Eurosensors 2026 Zürich

Eurosensors

Zurich | Switzerland | 2026

September 6 – 9, 2026

ABSTRACT BOOK

Proceedings

EUROSENSORS 2026

Zürich, Switzerland - Sept. 6th - 9th 2026

These proceedings cover the short papers of the lectures of the EUROSENSORS 2026 Conference.

The authors are responsible for form and content of the papers.

AMA Service GmbH accepts no responsibility for the correctness and completeness of the details and the consideration of private rights of third parties.

Herausgeber / Publisher:

AMA Service GmbH
Von-Münchhausen-Str. 49
31515 Wunstorf / Germany
Tel. +49 5033 9639-0
info@ama-service.com
www.ama-service.com / www.sensor-test.com
www.ama-science.org / www.smsi-conference.com

978-3-910600-12-6

© AMA Service GmbH, 2026

Sponsors & Opportunities

Platinum

SENSIRION
innovative Sensor Technology
Endress+Hauser
People for Process Automation

Silver

Zurich Instruments
NEXTRON
COMSOL
ABB
VAT
SGX SENSORTECH
An Amphenol Company
AMA
Verband für Sensorik + Messtechnik
Innovatoren verbinden
Hahn Schickard
HEIDELBERG INSTRUMENTS
QUANSCIENT
ams
OSRAM
ROYAL SOCIETY OF CHEMISTRY
SmarAct
metrology
VEOLIA
VEGA
HOME OF VALUES
MDPI
Argotech
JX Advanced Metals
IMT
PRECISION ON GLASS

Academic and Start-ups

SeniSens
ALiVION
optotune
.sensor. innovation hub.
microqubic

Custom Sponsorship

PalmSens
nano scribe
IMS CHIPS
SciSense
WILEY ADVANCED
ADVANCED SENSOR RESEARCH
VSparticle

Partners

ETH zürich
Stadt Zürich
Zürich, Switzerland.
VBZ Züri Linie
Umsteigen lohnt sich.
SWITZERLAND INNOVATION PARK ZURICH
HASLERSTIFTUNG
Schweizerischer Nationalfonds

Eurosensors 2026 Zürich

Dear Colleagues and Friends

On behalf of the Organizing Committee, it is my great pleasure to welcome you to EUROSENSORS 2026 in Zurich, Switzerland.

For nearly four decades, EUROSENSORS has brought together the global sensor community annually to exchange ideas, present scientific breakthroughs, foster interdisciplinary collaborations, and accelerate the translation of research into technologies that benefit society. This year's 38th edition of the conference has attracted participants from 40 countries across five continents, reflecting the truly international nature of our community. We are delighted to present an outstanding scientific program featuring six plenary lectures, delivered by internationally renowned leaders, 13 invited talks, 112 contributed oral presentations, and 16 industry presentations showcasing the latest scientific breakthroughs, technological developments and industrial innovations. We are particularly excited to feature two Special Sessions on Wednesday morning that highlight the growing impact of sensor technologies in healthcare. In addition, around 200 poster presentations will provide excellent opportunities for in-depth scientific discussions, networking, and the exchange of new ideas. Outstanding poster contributions will be recognized through our Poster Awards, celebrating exceptional work by early-career researchers.

This year also marks the inauguration of the EUROSENSORS Hackathon, a new initiative that complements the scientific conference by translating cutting-edge sensor research into real-world innovation. Over the weekend preceding the conference, multidisciplinary teams will tackle the challenge of developing "The Unhackable Scooter Immobilizer", an intelligent system combining gas sensing, biometrics, artificial intelligence, and cybersecurity to prevent unsafe e-scooter operation by detecting alcohol intoxication, helmet use, and multiple passengers. During the conference, participating teams will present their solutions, demonstrating

how advances in sensing technologies can address pressing societal challenges. We hope this inaugural hackathon will become a lasting tradition of EUROSENSORS, inspiring the next generation of sensor innovators and strengthening the connections between scientific discovery, engineering, and entrepreneurship.

This conference would not be possible without the generous support of our sponsors and partners. We would like to express our sincere gratitude to all of them for their commitment to the sensor community, and we are especially grateful to our Platinum Sponsors Sensirion, Innovative Sensor Technology (IST), and Endress+Hauser.

Beyond the scientific program, we hope you will enjoy the many opportunities to connect with colleagues in a relaxed atmosphere. We warmly invite you to our Welcome Reception on Sunday evening in the historic Main Building of ETH Zurich, offering a unique setting overlooking the city. On Monday evening, join us for our social event at the conference venue featuring live music by the Polyband. Finally, we look forward to celebrating together at the Conference Dinner on Tuesday evening at the beautiful Lake Side venue on the shores of Lake Zurich, hopefully with a spectacular view of the Alps.

We wish you an inspiring conference filled with stimulating discussions, new collaborations, exciting discoveries, and memorable moments in Zurich.

Andreas Güntner
General Chair

Plenary Talks

Plenary Talk 1

Nanophotonics: Enabling Technology for Next Generation Bioanaytical Devices 33
H. Altug, Ecole Polytechnique federale de Lausanne, Lausanne (Switzerland)

Plenary Talk 2

MEMS Sensors for the Body: From Wireless Implants to Transdermal Diagnostics 34
M. G. Allen, University of Pennsylvania, Philadelphia (USA)

Plenary Talk 3

Intelligent Robots with a Sense of Smell – Challenges, Current State, and Future Directions 36
A. J. Lilienthal, Technical University of Munich, München (Germany)

Plenary Talk 4

Wearable Sensors of Flux from the Skin 37
J. A. Rogers, Northwestern University, Evanston (USA)

Plenary Talk 5

Managing Health through Remote Monitoring 38
M. Snyder, Stanford University School of Medicine, Palo Alto (USA)

Plenary Talk 6

High-throughput optical biosensing with localized surface plasmon resonance imaging (LSPRi) 39
A. Bonyár, Budapest University of Technology and Economics, Budapest (Hungary)

Sessions

Session 1.1 Chemical Sensors

Sensor-on-LED: Visible-Light-Activated Gas Sensing Using Flame Spray Pyrolysis 40
X.-X. Wang, University of Bremen, Bremen (Germany), L. Mädler, Leibniz Institute for Materials Engineering IWT, Bremen (Germany)

Direct Capillary-Based Printing of Porous Coordination Networks on CMOS E-Nose Sensors for Plant Disease VOC Detection 42
S. Smit, Department of Precision and Microsystems Engineering, TU Delft, The Netherlands, C. Huang, J. Albertsma, Department of Chemical Engineering, TU Delft, The Netherlands, T. Shen, Y. Ouyang, Department of Microelectronics, TU Delft, The Netherlands, M. A. van der Veen, Department of Chemical Engineering, TU Delft, The Netherlands, F. Widdershoven, Department of Microelectronics, TU Delft, The Netherlands und NXP (Netherlands), P. G. Steeneken, M. K. Ghatkesar, Department of Precision and Microsystems Engineering, TU Delft, The Netherlands, J. Aghassi-Hagmann, M. Kabatas, Institute of Nanotechnology (INT), Karlsruhe Institute of Technology (KIT), Germany

Human Activity Recognition Using Distributed Colorimetric Chemical Sensors Based on CO2 and Formaldehyde Inks and Interpretable Machine Learning 44
I. Benito-Altamirano, Universitat Oberta de Catalunya (Spain), Y. Chen, O. Casals, C. Fabrega, University of Barcelona (Spain), M. Gonzalez-Gomez, J. D. Prades, Technische Universität Braunschweig (Germany)

Dielectric and DRIFTS Characterization of Ba-based NOx Storage Materials for Radio Frequency based Dosimeters 46
D. Schönauer-Kamin, F. Fütterer, J. Baumgärtner, T. Wöhrl, G. Hagen, R. Moos, University of Bayreuth, Bayreuth (Germany)

Session 1.2 Optical Sensors

Multiplexed, Label-Free InP Nanowire Photodetectors for Nanofluidic Single-Particle Sensing 48
L. Seggering, I. Fernandez-Cuesta, University of Hamburg, Hamburg (Germany), V. Flodgren, A. Das, T. K. Jensen, A. Mikkelsen, Lund University, Lund (Sweden), J. E. Sestoft, J. Nygård, University of Copenhagen, Copenhagen (Denmark)

Circuit-free Cardiovascular Monitoring via Electrically Passive Nanophotonic Patch for Sub-beat Hemodynamics 50
T. Steffensen, V. Stubberud, E. Winogrocki, E. Hennissen, N. K. Skjærvold, M. Steinert, A. Xomalis, Norwegian University of Science and Technology, Trondheim (Norway)

Polymer-based Fiber Fabry-Perot Interferometer for Temperature Monitoring of Operando Lithium-Ion Batteries 52
A. Hernández-Pascual, D. Monzón-Hernández, M. Alonso-Murias, E. Rodríguez-Sevilla, Centro de investigaciones en Óptica A.C., León (México), J. Villatoro, University of the Basque country EHU, Bilbao (Spain), Basque Foundation for Science

Trace Level Moisture Sensing using a Resonant Photoacousic Sensor with an LED as Light Source 54
C. Weber, A. Eberhardt, M. Benkendorf, K. Schmitt, J. Wöllenstein, Fraunhofer IPM, Freiburg (Germany)

Session 1.3 Sensing for Medical Diagnostics

Colorimetric point-of-care detection of Enterococcus faecalis in urinary tract infection 56
M. M. Morim, P. Rupper, S. Altenried, A. Meier, R. M. Rossi, Q. Ren, L. F. Boesel, G. Giovannini, Empa, St. Gallen (Switzerland)

Continuous Respiratory Rate Monitoring Using a Flexible Thermoelectric Sensor 58
A. Johnson-Brett, A. Angelopoulos, R. Zafeirelis, H. Akerman, I. Zeimpekis, N. Harris, N. White, K. A. Morgan, University of Southampton, Southampton (United Kingdom)

Comparative Assessment of Assimilating Probes and Molecular Beacons in Multiplex LAMP for Diagnostic 60
A. Mishra, T. L. Quyen, W. E. Svendsen, M. Dimaki, Technical University of Denmark, Kgs. Lyngby (Denmark)

Multimodal Textile-Based Wearable System for Upper-Limb Motion and Heart Rate Monitoring in Rehabilitation 62
C. Alglave, G. Jodin, J. Schoch, C. Depontailler, F. Razan, Univ Rennes, Rennes (France), A. Laarabi, SII Ouest, Cesson-Sévigné (France), A. Marin, Inria, Bruz (France), J. Prioux, Movement, Sport and Health Laboratory, Rennes (France)

Session 1.4 Sensor Applications: Environmental and Food Monitoring

Combined Physical and Digital Sensor Twin for Monitoring Fresh Fruits in the Cold Chain 64
R. Jedermann, University Bremen, Bremen (Germany), T. G. Hoffmann, P. V. Mahajan, Leibniz Institute for Agricultural Engineering and Bioeconomy, Potsdam (Germany)

Continious Monitoring of Glyphosate in Water 66
N. Budimirović, A. Beard, T. Kipfer, R. Pugin, S. Nicolay, Csem Sa, Neuchâtel (Switzerland)

Architecture-Dependent Emergence of Self-Powered Gas Sensing in Junction Engineered WSe2 Device 68
D. Mondal, V. Kamble, Indian Institute of Science Education and Research Thiruvananthapuram, Thiruvananthapuram (India)

Low-Cost Raman System for Continuous Measurement of Aqueous Ammonium Bicarbonate in Carbon Capture Processes 70
N. Schäuble, J. Jacob, C. Karnutsch, J. Hoinkis, Karlsruhe University of Applied Sciences, Karlsruhe (Germany), J. Wöllenstein, University of Freiburg, Freiburg (Germany), M. Graf, University of Hamburg, Hamburg (Germany)

Session 2.1 Microfluidic Devices, Lab on a Chip, µTAS, Organ on Chip Systems

Bimodal MEMS Sensor Cartridge for Prediagnostic Evaluation of Pleural Effusion 72
M. O. Güngör, A. Gümüştaş, S. Eroğlu, A. Fadaie, E. Yıldırım, ODTU MEMS Center, Ankara (Türkiye)

Real-World Chemical Plant Monitoring and Event Classification by Multi-Modal Low-Cost Sensor Network 74
A. Raffeiner, R. Pohle, Siemens AG, Munich (Germany), J. Kelleter, GTE Industrieelektronik GmbH, Viersen (Germany), S. Essel, Ish, Höchst (Germany)

Graphene Hall Sensor-Based Receiver for Magnetic Droplet-Based Communications 76
M. K. Zadeh, E. Akyol, A. Azmoudeh, M. Kuscu, Koç University, Istanbul (Turkey)

Interfacial Direct Printing (IDP) of SU-8: Fabrication of Molds with Smooth Round Channels 78
R. Dezauzier, M. Breitfeld, C. L. Dietsche, P. S. Dittrich, ETH Zürich, Basel (Switzerland)

Designing better biosensors from first principles 80
D. Juncker, McGill University, Montréal (CANADA)

Session 2.2 Optical Sensors

Raman and Photoluminescence Spectroscopy Detection of NO_2 gas Adsorbed on ZnO Nanowires 81
F. Rigoni, M. Ponzoni, M. Borsi, D. Zappa, E. Comini, Università di Brescia, Brescia (Italy)

A Lens-free Microscope with Edge AI Acceleration 83
L. Zhukova, I. Benito-Altamirano, Universitat Oberta de Catalunya, Barcelona (Spain), L. Yan, A. Dharmawan, J. D. Prades, Technische Universität Braunschweig, Braunschweig (Germany)

Digital Bone Metastasis: an AI-based Organ-on-chip Platform for Modeling Breast Cancer Bone Metastasis 85
M. D'Orazio, A. Mencattini, A. Agresti, S. Pescetelli, E. Martinelli, University of Rome Tor Vergata, Rome (Italy), L. Iafrate, G. Cidonio, Sapienza University of Rome, Rome (Italy), V. de Turris, G. Ruocco, Istituto Italiano di Tecnologia, Rome (Italy)

A Miniaturized Optical Online Sensor for the Detection of Oil Pollution on Water Surfaces 87
M. Brandl, T. Posnicek, A. Knecht, University for Continuing Education Krems, Krems (Austria)

Monolithic LED Emitter-Detector for colorimetric CO_2 gas sensor 89
M. Verdaguer Mallorquí, M. González-Gómez, C. Fàbrega, O. Casals Guillén, University of Barcelona, Barcelona (Spain), J. Hartmann, A. Waag, J. D. Prades, Technische Universität Braunschweig, Braunschweig (Germany)

A portable and Low-Cost Spirometer with Knife-Edge Optical Detection 91
S. Ulgaz, Ö. G. Akcan, O. Ferhanoglu, Istanbul Technical University, Istanbul (Türkiye), B. Yılmaz, Y. D. Gökdel, Istanbul Bilgi University, Istanbul (Türkiye)

Session 2.3 Sensing for Medical Diagnostics

Beyond Surface Area: Microfabrication-Compatible Electrode Nanostructuring for High-Performance Miniaturized Electrochemical and Bioelectrical Sensors 93
I. Taurino, KU Leuven, Leuven (Belgium)

Motion Artifact Removal for Moving FMCW Radar-Based Vital Sign Sensing Using IMU 94
N. Mascia, J. Fastier-Wooller, S. Muramatsu, M. Yamamoto, T. Itoh, The University of Tokyo, Tokyo (Japan)

Unchallenging the Debye Challenge in Field-Effect Biosensors 96
G. Shalev, Ben-Gurion University of the Negev, Beer-Sheva (Israel)

Development and Comparison of Innovative Sensing Modules to Support Pneumonia Diagnosis.....98
A. M. Tischer, E. Zanni, C. Bax, R. Dellacà, L. Capelli, Politecnico di Milano, Milan (Italy), F. Schmidt, U. Weimar, N. Barsan, University of Tuebingen, Tuebingen (Germany), L. Novelli, F. Di Marco, Azienda Ospedaliera Socio Sanitaria Territoriale Papa Giovanni XXIII, Bergamo (Italy)

Metabolic Monitoring at Home with a Smartphone-coupled Breath Sensing Device..... 100
S. Hersberger, L. Schmid, F. Kappeler, A. T. Güntner, ETH Zurich, Zurich (Switzerland), J. Van Den Broek, Alivion AG, Glattbrugg (Switzerland), P. A. Gerber, University Hospital Zurich, Zurich (Switzerland)

Session 3.1 Chemical Sensors

Free-space laser interrogation of Tantalum-Palladium Hydrogen sensor.....102
R. Gremaud, C. Yue, J.-M. Oppliger, P. Castro-Fernández, ABB Research, Baden-Dättwil (Switzerland)

Optimized Water-Based Colorimetric Carbon Dioxide Indicators for 455 nm Monolithic LED Emitter-Detector..... 104
M. Verdaguer Mallorquí, University of Barcelona, Barcelona (Spain), M. González-Gómez, Universitat de Barcelona, Barcelona (Spain) and Technische Universität Braunschweig, Braunschweig (Germany), C. Fàbrega, University of Barcelona, Barcelona (Spain), J. D. Prades, Technische Universität Braunschweig, Braunschweig (Germany), O. Casals, University of Barcelona, Barcelona (Spain)

Photolysis for Enhancing the Specificity of NO_x Electrochemical Sensors.....106
R. F. Wolffenbuttel, Delft University of Technology, Delft (The Netherlands), D. Bilby, J. H. Visser, Ford Motor Company, Dearborn (USA)

A new QEPAS sensor optimized for the use of multiple op-tical sources with reduced window absorption..... 108
I. Troadec, M. Duquesnoy, J.-M. Melkonian, R. Levy, M. Raybaut, Onera, Palaiseau (France)

Comparison of Self-Heating and Electrode Heating recoveries in a suspended-CNT CNFET NO2 Sensor.....110
I. Kraiem, D. Wolf, M. Haluška, C. I. Roman, C. Gentili, C. Hierold, ETH Zürich, Zürich (Switzerland)

Selective Benzene Gas Sensing with Flame-made Polytungstate Porous Film.....112
A. Baut, S. Kravecz, A. T. Güntner, ETH Zurich, Zurich (Switzerland)

Session 3.2 Biosensors

Single-Cell Impedance Cytometry: Recent Progress and Challenges Ahead..... 114
F. Caselli, University of Rome Tor Vergata, Roma (Italy)

Chip-Sized Biosensor for Multiparametric Monitoring.....115
S. Moncada-Madrazo, J. Canals, S. Moreno, A. Vilà, Á. Diéguez, Department of Electronic and Biomedical Engineering, Universitat de Barcelona, Barcelona (Spain) and Institute of Nanoscience and Nanotechnology of the University of Barcelona, Barcelona (Spain), N. Castro, C. Rodríguez-Gallo, Institute for Bioengineering of Catalonia, Barcelona (Spain), J. Ramón-Azcón, Institute for Bioengineering of Catalonia, Barcelona (Spanien) and Catalan Institution for Research and Advanced Studies, Barcelona (Spanien)

PEDOT:PSS coated Fully Printed Microelectrode Arrays for Neural Interfacing..... 117
A. Ziller, L. Kreuzberger, A. Corna, P. Werginz, G. Zeck, Technische Universität Wien, Vienna (AT)

An Electrochemical Aptasensor for Continuous Biomarker Monitoring.....119
H. Mirzajani, S. Carrara, Epfl, Neuchâtel (Switzerland)

Ferroelectric Microelectrode Array with System-Integrated Direct-Digitization ASIC for Neural Recording..... 121
M. Doering, D. Rossbach, P. Zimmer, D. Hoffmann, H. Trautner, M. T. Becker, Hahn-Schickard-Gesellschaft, Villingen-Schwenningen (Germany), R. Willaredt, M. Kuhl, Universität Freiburg, Freiburg (Germany), O. Amft, Hahn-Schickard-Gesellschaft, Villingen-Schwenningen (Germany) and Universität Freiburg, Freiburg (Germany)

Session 3.3 Physical Sensors

CO/HC Gas Sensor Using a Powder Aerosol Deposited Thermoelectric Material.....123
B. Streibl, T. Wöhrl, D. Paulus, J. Kita, D. Schönauer-Kamin, G. Hagen, R. Moos, University of Bayreuth, Bayreuth (Germany)

Micropillars patterned surface on in-plane MEMS resonator for enhanced airborne fine particles detection..... 125
J. SOREL, F. Marty, E. Algré, Univ Gustave Eiffel, Marne-la-Vallee (France), P. Didier, L. A. Ali Yahia, E. Géhin, Univ Paris-Est Creteil, Creteil (France)

From Materials to Systems: Passive, Low-Energy Sensors Based on Organic Mixed Ionic–Electronic Conductors.....127
T. Cramer, University of Bologna, Bologna (Italy)

A Mixed-Level Model for Force-Feedback Controlled Piezoelectric MEMS Microphones..... 128
T. Friebe, G. Schrag, Technical University of Munich (TUM), Munich (Germany), F. Schiller, C. Bretthauer, Infineon Technologies AG, Munich (Germany)

Microfluidic Integration of Interfacial Nanopores for Single-Molecule Sensing under FPGA-Based Closed-Loop Control.....130
L. Petrella, L. Dysli, J. Imfeld, J. N. Cronk, M. Aramesh, ETH Zürich, Zürich (Switzerland)

Session 4.1 Chemical Sensors

Printed and Light-activated CuO/Cu_2O-Based Chemiresistive Acetone Sensors with Carbon Electrodes..... 132
A. Chatterjee, J. Kosel, M. T. Vijjapu, Silicon Austria Labs GmbH, Villach (Austria), B. Jakoby, Johannes Kepler University Linz, Linz (Austria)

Enhanced Gas Sensing Performance of Pt-Coated Ag-Doped Ga_2O_3 via Surface Modification..... 134
M. M. Uddin, M. A. I. Bhuyan, L. Xiuqian, H. C. Kim, University of Ulsan, Ulsan (South Korea)

Re-examining Mechanisms, Materials and Measurement in Metal Oxide Gas Sensing.....136
C. Blackman, University College London (UCL), London (UK)

Session 4.2 Optical Sensors

Beyond the Ensemble: Resolving Sample Heterogeneity in Space and Time.....137
R. Quidant, ETH Zurich, Zurich (Switzerland)

Compact MicroLED-Based Lensless Microscope for Real-Time Airborne Cloud Droplet Sensing..... 138
A. B. Dharmawan, R. G. Gibilisco, J. D. Prades, Technische Universität Braunschweig, Braunschweig (Germany), J. Saturno, A. Nowak, C. Pöhlker, Physikalisch-Technische Bundesanstalt (PTB), Braunschweig (Germany)

Multi-wavelength Fiber-Optic Refractometer Based on Multimodal Interference and Surface Plasmon Resonance..... 140
E. D. Galván-Navarro, M. Alonso-Murias, D. Monzón-Hernández, Centro de Investigaciones en Óptica A.C., León de los Aldama (Mexico)

Session 4.3 Emerging Sensor Materials

Bio-sourced Polyester as Substrate for Sustainable Wireless Smart Tags Made by Printing..... 142
J. Bourely, D. Briand, Epfl, Neuchâtel (Switzerland), M. A. Hedou, L. P. Manker, J. S. Luterbacher, Epfl, Lausanne (Switzerland), R. Marti, HEIA-FR Chemtech, Fribourg (Switzerland)

A Torque Sensor using 3D Printed Conductive TPU.....144
T. Stein, M. Schärer, M. Meboldt, ETH Zurich, Zurich (Switzerland)

Soft and Stretchable Carbon Flower Sensors Detect Hormones and Neurotransmitters at High Sensitivity..... 146
I. C. Weber, Chalmers University of Technology, Göteborg (Sweden), D. U. Patino, K.-J. Hsu, Z. Bao, Stanford University, Stanford (USA)

Electrokinetic Self-Cleaning of Mixed-Phase Contaminants on Optical Sensors in Physical AI..... 148
D. J. Lee, T. H. Jang, Y. Kim, S. K. Chung, Myongji University, Yongin (South Korea), J. Lee, Microsystems Inc., Yongin (South Korea)

Session 4.4 Actuators

Programable hierarchical actuation schemes based on phase change composites arranged as a resistive network 150
W. Hilber, S. Lang, B. Jakoby, Johannes Kepler University Linz, Linz (Austria)

A 3D-Printed Monolithic Bender Bar Transducer Featuring a Fluid-coupled Thin-plate Backing and Flexural Hinges 152
M. J. Sim, Y. Je, H. Shim, K. Kim, Y. Cho, H. S. Seo, Agency for Defense Development, Changwon (Republic of Korea)

A Low-Power Printed Flexible Lorentz Force MEMS Switch with Electrostatic Hold-down 154
M. Meybodi, K. Nguyen, T. Chen, C. Shafai, University of Manitoba, Winnipeg (Canada)

Characterization of Biodegradable Magnetic Elastomers for Mechanical Stimulation in Organ-on-Chip Platforms 156
F. Pirim-Aslan, E. Aprea, P. M. Sarro, C. M. Boutry, Delft University of Technology, Delft (The Netherlands), M. K. Aslan, S. Stavrakis, A. deMello, ETH Zurich, Zurich (Switzerland)

Session 5.1 Microfluidic Devices, Lab on a Chip, µTAS, Organ on Chip Systems

Aptamer-based Optically Induced Dielectrophoresis for High-Resolution Single-Cell Phenotyping 158
J. Filippi, F. Corsi, P. Casti, A. Mencattini, G. Antonelli, A. Chamorro-Garcia, A. Idili, E. Martinelli, University of Rome Tor Vergata, Rome (Italy), A. Wheeler, University of Toronto, Toronto (Canada)

Multiplexed analysis of extracellular vesicles from single cells in an array with opposing microwells 160
L. R. Stöcklin, E. Kortus, P. S. Dittrich, ETH Zürich, Basel (Switzerland)

Microfluidic Synthesis of Piezoelectric-Magnetic Composite Microbeads for Wireless Neural Stimulation 162
T. Zhang, A. Bertsch, J. Luo, Y. Su, Y. Zhang, J. Brugger, Ecole Polytechnique Federale de Lausanne, Lausanne (Switzerland)

Label-free isolation of single cells for IVD cell therapy using impedance flow cytometry 165
M. Favrod-Coune, A. Stirnimann, F. Ille, P. Eberle, Lucerne University of Applied Sciences, Lucerne (Switzerland), O. Guenat, University of Bern, Bern (Switzerland)

Microdroplet arrays: Printing and analyzing liquid sample at high throughput 167
P. S. Dittrich, ETH Zurich, Basel (Switzerland)

Session 5.2 Emerging Sensor Materials

Bioelectronic Sensors for Understanding Plant Stress Responses 168
E. Stavrinidou, Linköping University, Norrköping (Sweden)

Measurement Method for Determining Solvent Exchange in Aerogels During Realization and Functionalization 169
J. kleine Piening, K. Tembekar, T. M. de Rijk, S. van den Driesche, M. J. Vellekoop, Universität Bremen, Bremen (Germany)

Biosensing and Healthcare Applications via Emerging Nanomaterials 171
K. Yadav, R. Sankar, Academia Sinica, Taipei (Taiwan), K. Yadav, National Taiwan University, Taipei (Taiwan) and Indian Institute of Science, Bangalore (India)

All-Dry Dual-Stencil Lithography for IGZO Thin-Film Transducers 173
C. Zhang, G. Boero, J. Brugger, École Polytechnique Fédérale de Lausanne (EPFL), Lausanne (Switzerland)

Ensemble Nuclearity Optimum in Chemoresistive Hydrogen Sensing 175
H. Shin, A. Güntner, ETH Zürich, Zürich (Switzerland)

Session 5.3 Sensor Arrays and Networks, Integrated Systems

A Polyimide-based In-situ Sensor and Actuator Platform for Battery Monitoring and Self-healing 177
V. Kuczius, P. Sarapukdee, E. Wallesch, S. Palzer, Technical University Dortmund, Dortmund (Germany), D. Kutluay, J. Fleming, T. Amietszajew, Coventry University, Coventry (United Kingdom), E. Comas, IDNEO Technologies, Barcelona (Spain), J. Sagu, A. Baker, L. Gill, D. Johnson, I. Manfren, K. Parkes, G. Brown, J. McClean, F. Tait, S. Chan, L. Evans, Centre for Process Innovation, Sedgefield (United Kingdom)

A Portable Ultrasound System Integrating a CMUT Sensor Array with an FPGA-Based Delay-and-Sum Beamformer 179
M. Doğan, M. O. Güngör, Metu, Ankara (Turkey), C. U. Ertenli, B. Karacaer, K AND K Müh. Tek. Ltd. Şti., Ankara (Turkey)

Addressing Calibration Transfer in Electronic Noses for Urine Headspace Analysis through Synthetic Reference Samples and Advanced Feature Extraction 181
L. Capelli, Politecnico di Milano, Milano (Italia)

A Two-Stage Encapsulation Procedure for Sterilization-Resistant MEMS Devices With Integrated SMA Actuator 182
D. Hoffmann, D. Schuhmacher, N. Burghardt, A. Dehé, Hahn-Schickard, Villingen-Schwenningen (Germany), A. Erben, Fraunhofer IWU, Dresden (Germany)

Continuous, Scalable Building Envelope Monitoring Using Low-cost Gas Sensor Networks 184
F. Sievers, N. Langer, M. Jakubowsky, Á. Ortiz Pérez, S. Braungardt, S. Palzer, Technical University Dortmund, Dortmund (Germany)

Session 6.1 Chemical Sensors

Microwave-based control of an SCR-based flue gas aftertreatment system for biomass combustion 186
B. Streibl, R. Moos, T. Wöhrl, G. Hagen, University of Bayreuth, Bayreuth (Germany), T. Ritter, H+H Engineering & Service GmbH, Sonnefeld (Germany)

Polymorph-Dependent Electronic Transduction in WO3 during Molecular Sensing through Experiment and DFT 188
M. Yin, K. Suzuki, Y. Chen, Tohoku University, Sendai (Japan), M. D'Andria, S. Neuhauser, A. T. Güntner, V. G. Mavrantzas, ETH Zurich, Zurich (Switzerland), V. G. Mavrantzas, University of Patras, Patras (Greece)

Hydrogel Beads-Based Sensing Technology For Measurement Of Insulin Growth Factor 1 (IGF1) In Saliva 190
K. Haliru, R. Gupta, University of Birmingham, Birmingham (UK), N. Goddard, Independent Researcher, Accrington (UK)

Controlling Interconnection Density in 3D ZnO Networks for Optimized Charge Transport and Multimodal Sensing 192
B. Chakraborty, L. Siebert, R. Adelung, Kiel University, Kiel (Germany), B. Junker -Reiss, Eberhard Karls Universität Tübingen, Tübingen (Germany)

High-Sensitivity and Reliable Gas Sensor by Hybridizing Laser-Induced Graphene and Molybdenum Trioxide with Metal-Organic Decomposition 194
A. Katsura, O. Okanishi, Y. Hirose, Y. Miura, W. Zhu, T. Sugahara, Kyoto Institute of Technology, Kyoto (Japan)

Corporation Effect of CuO and Fe_2O_3 Composites in VOC Sensing 196
C. Xiao, H. Jabal, U. Weimar, N. Barsan, University of Tübingen, Tübingen (Germany)

Session 6.2 Biosensors

Miniaturized, Flexible Electroosmotic Device Based on Laser-Patterned PEDOT:PSS Electrodes for Drug Delivery and Electrophysiological Biosensing 198
M. Mariello, F. Ahnaf, C. M. Proctor, University of Oxford, Oxford (UK)

Bespoke Laser Fabrication of High-Density PEDOT:PSS MEAs for Low-Impedance Cortical Neuronal Recordings 200
E. Rolando, D. Grojo, A. Casanova, Lp3 Umr 7341, Marseille (France)

Enzyme-Free Electrochemical Sensing for Real-Time In-Process Monitoring..... 202
A. Hasanzadeh, S. Neupane, E. Kazempour, N. Støvring, S. S. Keller, K. V. Gernaey, P. Ramin, Technical University of Denmark

Toward Rapid Water Quality Monitoring: QCM-Guided Bioin-terface Engineering of Graphene SGFET Biosensors for Escherichia coli Detection.....204
C. Beddok, V. Fabre, T. Alava, Cea, Leti, Grenoble (France), M. D. Alhindi, G. Fuks, A. M. Debela, Univ. Perpignan Via Domitia, Perpignan (France)

Bioimpedance Microsensor for Cell-Density Monitoring in Small-Scale Bioprocessing..... 206
P. Patschg, Y. Mermoud, R. Achor, S. Huber, OST.Eastern Switzerland University of Applied Sciences, Buchs (SG) (Switzerland), S. Schneider, M. Zumbihl, R. Eibl, ZHAW Zurich University of Applied Sciences, Wädenswil (Switzerland)

MXene-Functionalised U-Shaped SMF-NC-SMF Optical Fibre Sensor for Label-Free Detection of PFOA and PFOS in Water.....208
A. Faruq, Y. Fu, Z. Ghassemlooy, Q. Wu, Northumbria University, Newcastle (UK), Y. Semenova, Technological University Dublin, Dublin (Ireland)

Session 6.3 Signal Analysis, Machine Learning and Artificial Intelligence for Sensing

Mitigation of Chemical Sensor Drift through Calibration Transfer in Edge AI.....210
J. Fonollosa, Universitat Politècnica de Catalunya, Barcelona (Spain)

A Dual-Resolution Binary Neural Network Inference Engine for Fully Implantable Cochlear Implant Speech Processing..... 211
M. Doğan, H. Uluşan, H. Külah, Metu, Ankara (Turkey)

Tiltmeter-Based Forecasting and Anomaly Detection for Proactive Structural Monitoring of Railway Infrastructure..... 213
P. Saha, F. Hernandez-Ramirez, J. D. Prades, Technische Universität Braunschweig, Braunschweig (Germany)

Graph Deviation Networks for Schizophrenia Signatures Detection in Brain Organoids' MEA Signals.....215
A. Riccardi, A. Mencattini, G. Curci, E. Martinelli, University of Rome Tor Vergata, Rome (Italy), W. Zhang, Q. Meng, University of South China, Hunan (China)

Multidimensional Force Estimation in Laparoscopic Instruments with a CMOS-Based Force Sensor Chip.....217
T. Hehn, B. Folkmer, R. Nouna, S. Knappmann, O. Amft, Hahn-Schickard, Villingen-Schwenningen (Germany), W. Kunert, S. Axt, Universitätsklinikum Tübingen, Tübingen (Germany), J. Rolinger, A. Brodbeck, Erbe Elektromedizin GmbH, Tübingen (Germany)

Session 7.1 Chemical Sensors

Electrochemical Approaches for Monitoring PFOA in Aqueous Environments..... 220
A. Beard, N. Budimirovicr, T. Kipfer, S. Nicolay, Csem Sa, Neuchâtel (Switzerland), S. Piletsky, E. Piletska, University of Leicester, Leicester (UK)

Transient Graphene-Based Aptasensor on a Cellulose Substrate for Toxin Detection.....222
L. Travaglini, D. Briand, Epfl, Neuchâtel (Switzerland), Y. Abderrahim, Ecole Polytechnique, Palaiseau (France), H. Korri-Youssoufi, Université Paris-Saclay, Orsay (France)

Physics-Based Dynamic Estimation of NO_2 and H_2O Concentrations with CNT-FETs and Extended Kalman Filter.....224
C. Gentili, C. I. Roman, I. Kraiem, M. Haluska, C. Hierold, ETH Zürich, Zürich (Switzerland)

Gas sensing applications of CuO doped with metallic catalyst fabricated by spark ablation.....226
C. Maier, L. Egger, B. Kosednar-Legenstein, Materials Center Leoben Forschung GmbH, Leoben (Austria), N. Rising, L. Sacco, Vsparticle B.v., Delft (The Netherlands)

Session 7.2 Physical Sensors

A Functionalization-Free Acetone Detector Based on Low Frequency Interfacial Dielectric Relaxation.....228
S. K. Verma, M. Menon, A. N. Warrier, M. Gardill, H. Schenk, Brandenburg University of Technology Cottbus-Senftenberg, Cottbus (Germany), A. Mrosk, Fraunhofer Institute for Photonic Microsystems, Dresden (Germany)

Modelling of Moving Magnet Actuators for Haptic Sensing Applications..... 230
S. Lang, A. O. Niedermayer, J. Astl, D. Spira, B. Jakoby, Johannes Kepler University Linz, Linz (Austria)

In-Situ Spatial Mapping of Microjet Impingement with a Piezoresistive Silicon Nanowire MEMS Sensor..... 232
L. Demirkazik, I. N. Samci, M. J. Ghourichaei, O. Aydin, B. Aksoy, G. Nadar, U. Kerimzade, B. E. Alaca, Koç University, Istanbul (Türkiye), C. Aydogan, I. W. Rangelow, Technische Universität Ilmenau, Ilmenau (Germany), A. D. Yalcinkaya, Boğaziçi University, Istanbul (Türkiye), H. Bayraktar, Istanbul Technical University, Istanbul (Türkiye)

Dual-Resonance Indirect Photoacoustic Gas Sensing System for Sub-ppm Gas Detection..... 234
A. Srivastava, A. Bittner, Hahn-Schickard, Villingen-Schwenningen (Germany), A. Dehé, Albert-Ludwigs-Universität Freiburg, Freiburg (Germany)

Session 7.3 Sensor Fundamentals & Modelling

On the Interplay of Viscoelasticity and Air Permeation in Modelling the Dynamics of Embedded Tactile Sensors..... 236
K. Meier, F. Püntener, C. Hierold, C. Roman, ETH Zürich, Zürich (Switzerland)

Improved Angle Sensing by Shape-from-Motion Calibration of 3D Magnetic Sensors..... 238
B. Kar, P. Rutquist, O. Paul, University of Freiburg, Freiburg (Germany)

Geometrical Optimization of Planar Hall Sensors Dominated by 1/f Noise for Maximal Signal-to-Noise Ratio.....240
A. Fleck, O. Paul, University of Freiburg, Freiburg (Germany), L. Osberger, M. Cornils, M. C. Vecchi, TDK-Micronas GmbH, Freiburg (Germany)

Study of Width-over-length Aspect Ratio on Mode Ordering for 2D Nanomechanical Resonant Sensors..... 242
W. Zhou, C. I. Roman, C. Hierold, P. Zhang, ETH Zürich, Zürich (Switzerland)

Session 8.1 Chemical Sensors

Charge and Capacitance Sensitive Field-Effect Device for Room-Temperature Hydrogen Sensing..... 244
J. Boudaden, N. M. Mbachu, K. Neumeier, I. Eisele, Fraunhofer Institute for Electronic Microsystems and Solid State Technologies EMFT (Germany)

Triphenylene and Triptycene-Based MOFs as Chemiresistive Platforms for CO_2 and CH_4 Detection..... 246
Y. Mendoza-Gamero, S. Gonzalez-Martinez, A. Romano-Rodriguez, D. Sainz-Garcia, Universitat de Barcelona, Barcelona (Spain)

Ultra-Low Crosstalk Thermally-Compensated Monolithic AlGaN/GaN MISHEMT Sensor Array for Robust Gas Detection.....248
K. Bouzid, S. S. Venkatachalam, T. Moudakir, A. Juyal, S. Othmani, M. Petit, S. Gautier, Institut Lafayette, Metz (France)

Pd Decorated MoS_2 Nanosheet Deposited on Yolk-Shell (SiO_2-TiO_2) Nanosphere for Hydrogen Gas Sensing.....250
D. N. Liyanage, T. Thathsara, C. J. Harrison, P. Kingshott, M. Shafiei, Swinburne University of Technology, Hawthorn (Australia), H. Alluhaybi, Y. Sabri, Royal Melbourne Institute of Technology, Melbourne (Australia)

Development and Validation of a Portable GC-MOS System for High-Sensitivity and Selective Analysis of VOC..... 252
O. Brieger, A. Schütze, C. Bur, Saarland University, Saarbrücken (Germany), T. Sauerwald, G. Zeh, Fraunhofer IVV, Freising (Germany)

Unveiling Humidity-Enhanced Performance in Chemoresistive $CoCu_2O_3$ VOCs Sensors 254
M. D'Andria, H. Shin, A. T. Güntner, ETH Zurich, Zurich (Switzerland), Y.-H. Wu, Forschungszentrum Jülich GmbH, Erlangen (Germany), X. Meng, F. R. Wang, University College London (UCL), London (United Kingdom), P. Zeller, Fritz-Haber-Institut der Max-Planck-Gesellschaft, Berlin (Germany)

Session 8.2 Physical Sensors

On-Chip Label-Free Holographic NTA for Biophysical Characterization of Single Particles 256
C. Lombardo, B. Vignon, J. Ortega Arroyo, R. Quidant, ETH Zürich (Switzerland)

Systematic Method of Measuring and Evaluating Sensitivity and Linearity of a Micro-Fluxgate Sensor 258
J. Maier, P. Ripka, Czech Technical University in Prague, Prague (Czech Republic), P. Chen, National Taiwan University of Science and Technology, Taipei City (Taiwan)

A Next Generation HVM Process Platform for High Performance IMU Devices 260
T. Macha, A. Behroudj, D. Richter, C. Schwenk, H. Stahl, A. Grosse, Robert Bosch GmbH, Reutlingen (Germany)

Chip-scale Electrochemical Angular Accelerometer based on SOI Substrate 262
M. Zhu, Y. Lu, D. Chen, J. Wang, Aerospace Information Research Institute, Beijing (CN) and University of Chinese Academy of Sciences, Beijing (CN), B. Liu, Minzu University of China, Beijing (China)

Particle-based sensor materials enable plant-inspired upconverting I-Seeds as flying environmental sensors 264
A. Nexha, T. Kister, INM.Leibniz Institute for New Materials, Saarbrücken (Germany), K. Cikalleshi, S. Mariani, Istituto Italiano di Tecnologia, Genova (Italy)

ZnO@ZIF-8 Doubly Clamped Microbeam Resonator for Detection of VOCs 266
D. Rajagopal, C. Wang, B. P. Madeira, M. Kraft, KU Leuven, Leuven (Belgium), B. Chakraborty, A. Padunnappattu, N. Stock, R. Adelung, Kiel University, Kiel (Germany)

Session 8.3 Flexible and Wearable Sensors

Biodegradable Technologies for Medical and Environmental Applications 268
C. M. Boutry, TU Delft, Delft (The Netherlands)

Smartphone-enabled, Thin-Film Epidermal Electronic Systems for Cardiac Health Monitoring 269
S. Ingebrandt, D. Zhang, M. Eyvazi Hesar, Z. Gao, RWTH Aachen, Aachen (Germany), H. Gall, R. Schermuly, H. A. Ghofrani, Justus-Liebig-University Giessen, Giessen (Germany)

Transient Battery-Free Microphone-Integrated Face Mask 271
M. J. Bathaei, A. Golparvar, F. A. Cardoso, C. M. Boutry, Delft University of Technology, Delft (The Netherlands), S. Hashemizadeh, Foundation for Research on Information Technologies in Society, Zurich (Switzerland), D. Nikolayev, University of Rennes, Rennes (France)

Ultrathin Wearable Thermochromic Tattoo-Based Skin Sensor 273
K. Unger, R. Heer, P. Piller, Silicon Austria Labs GmbH, Graz (Austria)

Reduced Recovery Time after Free Flap Surgery by means of Textile Sensor Systems 275
E. Maevskaia, M. Camenzind, C. Lemière-Franzetti, R. M. Rossi, S. Annaheim, Empa, St. Gallen (Switzerland), L. Lotter, T. Eugster, V. J. Schmidt, HOCH Health Ostschweiz, St. Gallen (Switzerland), J. Gartmann, A. Kupferschmid, Empa, Dübendorf (Switzerland), A. Haag, FRTI Inter Spitzen AG, St. Gallen (Switzerland)

Special Sessions

Special 1.1 Continuous Health Monitoring in Medicine

Cortisol and Luteinizing Hormone. A Tale of Two Aptamers 277
S. Ben-Aissa, A. Cass, Imperial College London, London (UK)

A System For All Day Biosampling: Microdialysis and Wearables Collide 278
T. Upton, University of Bristol, Bristol (UK), E. Zavala, S. Lightman and the ULTRADIAN consortium, University of Manchester, Manchester (UK), P. Methlie, University of Bergen, Bergen (Norway), M. van Faassen, University Medical Center Groningen, Groningen (Netherlands)

Tissue corticosteroid rhythms are dysregulated mainly during sleep in primary aldosteronism 280
M. A. Grytaas, K. Løvås, T. Sjøgren, I. Løvik, A. Heie, G. Å. Ueland, Haukeland University Hospital, Bergen (Norway), T. Upton, G. Russell, S. L. Lightman, University of Bristol, Bristol (United Kingdom), I. Marinelli, University of Exeter, Exeter (United Kingdom), P. Methlie, M. Øksnes, B. E. Oftedal, E. S. Husebye, Haukeland University Hospital, Bergen (Norway) and University of Bergen, Bergen (Norway), D. A. Vassiliadi, D. Margaritopoulos, M. Balomenaki, S. Tsagarakis, Evangelismos General Hospital, Athens (Greece), S. Bensing, I. R. Botusan, K. Berinder, O. Kämpe, Karolinska University Hospital, Stockholm (Sweden) and Karolinska Institutet, Stockholm (Sweden), K. Simunkova, University of Bergen, Bergen (Norway), B. Lombard, University of Birmingham, Birmingham (United Kingdom), E. Zavala, University of Birmingham, Birmingham (United Kingdom) and University of Manchester, Manchester (United Kingdom)

Ultradian Monitoring in Adrenal Insufficiency 281
I. Botusan, K. Berinder, O. Kämpe, S. Bensing, Karolinska Institutet, Stockholm (Sweden) and Karolinska University Hospital, Stockholm (Sweden), E. Zavala, University of Manchester, Manchester (United Kingdom), T. Upton, G. Russell, S. Lightman, University of Bristol, Bristol (United Kingdom), P. Methlie, K. Simunkova, M. Grytaas, E. Husebye, M. Øksnes, University of Bergen, Bergen (Norway) and Haukeland University Hospital, Bergen (Norway), D. Vassiliadi, S. Tsagarakis, Evangelismos Hospital, Athens (Greece)

Special 1.2 Antimicrobial Resistance Diagnostics

Machine Learning for longitudinal data analysis in gas sensors: A case study in early subclinical ketosis in dairy cows 283
A. Belenguer-Llorens, C. R. Jutzeler, ETH Zurich, Zurich (Switzerland) and SIB Swiss Institute of Bioinformatics, Lausanne (Switzerland), J. Hendricks, A.-M. Reiche, F. Dohme-Meier, Agroscope, Posieux (Switzerland), J. Ko, A. T. Güntner, ETH Zurich, Zurich (Switzerland)

Metabolomics as a Tool for Rapid Urinary Tract Infection Diagnosis 285
G. Vasku, A. Vescovi, ETH Zürich, Zürich (Switzerland), E. W. Slack, ETH Zürich, Zürich (Switzerland) and Botnar Research Institute for Child Health, Basel (Switzerland)

Volatilomics for Medical Microbiology Diagnostics using Standard Bacterial Headspace Sampling 287
M. B. Bilgin, N. Toccalino, A. Güntner, ETH Zürich, Zürich (Switzerland), E. Slack, ETH Zurich, Zurich (Switzerland), Botnar Institute of Immune Engineering, Basel (Switzerland) and University of Oxford, Oxford (UK), A. Egli, University of Zurich, Zurich (Switzerland)

Special 2.1 Continuous Health Monitoring in Medicine

Electrochemical Sensors and Biosensors for Biomedical and Clinical Applications 289
D. O'Hare, A. Cass, E. Stadler, W. D. Boer, Imperial College London, London (United Kingdom)

From Rigid to Flexible and Stretchable Hollow Microneedle Patches: Integrated Microfluidic Platforms for Dermal Inter-stitial Fluid Extraction and Intradermal Therapeutic Delivery 291
W. Shu, T. Raicevic, ETH Zurich, Zurich (Switzerland), A. T. Güntner, ETH Zurich, Zurich (Switzerland) and University Hospital Zurich (USZ) and University of Zurich (UZH), Zurich (Switzerland)

Managing Data Integrity in Medical Wearables 293
W. Karlen, Universität Ulm, Ulm (Germany)

Mathematical Modelling at the Interface of Digital Endocrinology and Wearable Sensing Technologies 295
B. Lombard, University of Birmingham, Birmingham (United Kingdom), T. Upton, S. L. Lightman, University of Bristol, Bristol (United Kingdom), E. Zavala, University of Manchester, Manchester (United Kingdom)

"How are you today?" Harnessing speech as a window into life with a chronic disease 297
V. von Wyl, University of Zurich, Zurich (Switzerland)

Participatory AI in Endocrinology: Supporting Shared Deci-sion-Making Through Multimodal Sensing 299
L. Fernandez-Luque, Adhera Health SL, Sevilla (Spain)

Special 2.2 Antimicrobial Resistance Diagnostics

The cancer microbiome produces distinct volatile organic compounds 301
B. Vadhwana, P. Arya, N. Abdul Kader, P. Boshier, S. Jamel, I. Belluomo, Imperial College London, London (UK)

Base Gap Switches: Exploiting the Central Dogma of Molecular Biology to Detect Dis-ease 303
D. Richards, ETH Zürich, Zurich (CH)

Isolation and culturing of urinary bacteria for VOC-based rapid diagnostics 305
A. Vescovi, G. Vasku, E. Wetter Slack, ETH Zürich, Zürich (Switzerland)

Machine Learning and Gas Sensors for Antimicrobial Reisistence Identification 307
A. Belenguer-Llorens, E. Slack, A. T. Güntner, C. R. Jutzeler, ETH Zurich, Zurich (Switzerland), A. Egli, University of Zurich, Zurich (Switzerland), T. M. Kessler, Balgrist University Hospital, Zurich (Switzerland)

Diagnostics Needs for Urinary Tract Infections in the Era of Antimicrobial Resistance 309
L. Leitner, S. McCallin, T. M. Kessler, Balgrist University Hospital, Zürich (CH)

Industry Sessions

Industry Session 1

Pushing the Limits of Established Sensor Technologies 311
Y. Maret, ABB Measurement & Analytics, Dättwil (Switzerland), A. Riaud, ABB Corporate Research, Dättwil (Switzerland), B. Smith, ABB Measurement & Analytics, Bartlesville (USA), J. Schalkowski, ABB Measurement & Analytics, Frankfurt am Main (Germany)

Scaling up and Automating Nanodevice Fabrication with Parallelized Multi-tip Thermal Scanning Probe Lithography 313
J. Chaaban, J. Stark, E. Clerc, A. Ubezio, A. Damyanova, F. Könemann, K. Buddha, S. Bonanni, Heidelberg Instruments Nano AG, Zürich (Switzerland)

From Miniaturized Bioassays to 3D Imaging of Microfluidic Devices 315
Y. Temiz, Microqubic AG, Zug (Switzerland)

Industry Session 2

High-Precision 3D Printed Micro-Optics for Next-Generation Optical Sensor Integration 317
M. A. T. Yeşilyurt, Nanoscribe GmbH & Co. KG, Eggenstein-Leopoldshafen (Germany)

Active Optics for Enhanced Sensor Performance 318
W. Zesch, A. Saba Shirvan, A. Amrein, Optotune Switzerland AG, Dietikon (Switzerland)

A Hitchhiker's Wave Guide to Photonic Chips: Physics, fabrication, and the road to volume 319
J. Voigt, C. Bilgeri, M. Flemming, G.-A. Rezzoli, W. Arens, IMT Masken und Teilungen AG, Greifensee (Schweiz)

Industry Session 3

State of the Art Microsensors at Industrial Scale 321
T. Uehlinger, M. de Queiroz Tavares, L. Bürgi, Sensirion AG, Stäfa (Switzerland)

Alivion SmartSelect: Making Gas Sensors Work in the Real World 323
J. van den Broek, Alivion AG, Opfikon (Switzerland)

Accelerating Gas Sensor Material Development 325
L. N. Sacco, VSParticle B.V., Delft (The Netherlands)

Industry Session 4

microGauge – a Micro Resonator Gauge (MRG) Featuring a High-Stability Zero for Vacuum Process Control 326
S. Kühne, N. Wojtas, S. Demicheli, V. Barreiro Lomba, M. Trant, P. Rhyner, S. Kohler, U. Bartsch, VAT Vakuumventile AG, Haag (Switzerland)

Taking Sensor Simulations to New Frontiers: The COMSOL Perspective 328
S. Friedel, COMSOL Multiphysics GmbH, Zurich (Switzerland)

Poster by Topics

Actuators

Mo-ACT-01 **Temperature Dependence of Parametric Snap-Through in Bistable Piezoelectric ScAlN MEMS Plates** 330
P. Egger, M. Mortada, U. Schmid, M. Schneider, Technische Universität Wien, Wien (Austria)

Mo-ACT-02 **Electrodynamic Self-Cleaning Glass for Visibility Improvement of Autonomous-Driving Optical Sensors** 332
J. Yoon, L. Chai, D. J. Lee, S. K. Chung, Myongji University, Yongin (Republic of Korea), K. Y. Lee, Microsystems, Inc., Yongin (Republic of Korea)

Mo-ACT-03 **Asymmetric Snap-through Dynamics in Bistable Piezoelectric MEMS Plates** 334
M. Mortada, A. Kraus, J. Gruber, U. Schmid, M. Schneider, TU Wien, Vienna (Austria)

Biosensors/-electronics And Biomimetic Sensors

Mo-BBS-01 **Glyphosate Detection with Mass-sensitive sensors using Molecularly Imprinted Polymers: Polymerization Strategies and Application** 336
M. R. S. Castillo, P. A. Lieberzeit, University of Vienna, Vienna (Austria)

Mo-BBS-02 **Enhanced IgE Aptasensing via Scaffold-mediated Oriented Immobilization of DNA Aptamers** 338
Y. Chokki, A. Tanabe, I. Sasaki, M. Iijima, Tokyo Univ. Agric., Tokyo (Japan), H. Nakano, Nagoya Univ., Nagoya (Japan), S. Kuroda, Univ. of Osaka, Osaka (Japan)

Mo-BBS-03 **Reliable Cell Concentration Prediction Using a Temperature-Compensated Four-Electrode Impedance Sensor with Machine Learning** 340
X. Huo, L. Pan, D. Han, Y. Niu, J. Wang, J. Chen, Chinese Academy of Sciences, Beijing (China)

Mo-BBS-04 **3D Tubular Microelectrode Array Fabricated via Rotary Surface Exposure for Deep-Tissue Electrophysiological Monitoring of Organoids** 342
J. Ni, H. Ren, J. Wang, F. Ye, X. Guo, Z. Yang, Shanghai Jiao Tong University, Shanghai (China) und Nanyang Technology University, Singapore (Singapore)

Mo-BBS-05 **Design and Experimental Validation of an Impedance Based Position Sensor for Magnetic Microrobots** 344
M. Heuschkel, D. Principi, D. V. Freire, A. Roux, University of Applied Sciences and Arts Western Switzerland, Geneva (Switzerland), A. Savary, C. Besson, University of Applied Sciences and Arts Western Switzerland, Yverdon-les-Bains (Switzerland)

Mo-BBS-06 **Computational Design of Peptide Recognition Elements for Rapid Detection of Neurotoxin Exposure** 346
M. Al-gafari, A. Tayabali, Health Canada, Ottawa (Canada), A. Golshani, Carleton University, Ottawa (Canada)

Mo-BBS-07 **Raspberry Pi Platform for Multi-Modal Biosensing: Electrochemiluminescent and Colorimetric Analysis** 348
S. Rodríguez Muiña, F. J. del Campo, Basque Center for Materials, Leioa (Spain), G. Valenti, University of Bologna, Bologna (Italy), J. F. Rusling, University of Connecticut, Storrs (USA)

Mo-BBS-08 **MEMS-Based Flexible NiTi Shape Memory Alloy Micro Actuator for Cochlear Electrode Applications** 350
P. Ormancı, H. Külah, Middle East Technical University, Ankara (Turkey)

Mo-BBS-09 **Reproducibility and Biofouling in Graphene Foam Electrodes Assessed by Direct ELISA** 352
L. Cuasay, B. Mathmann, P. Pernod, A. Talbi, L. Manzanares, Univ. Lille, Lille (France), I. Manea, O. Hosu-Stancioiu, C. Cristea, Iuliu Haţieganu University of Medicine and Pharmacy, Cluj-Napoca (Romania), N. delos-Santos-Álvarez, Universidad de Oviedo, Oviedo (Spain)

Mo-BBS-10 **Investigation of a Plasmonic Aptamer-Based Biosensor for Heavy Metal Ion Detection** 354
R. Kovács, A. Bonyár, Budapest University of Technology and Economics, Budapest (Hungary), A. P. G. Rocha, T. Lednický, B. Li, A. Csáki, Leibniz Institute of Photonic Technology, Jena (Germany)

Mo-BBS-11 **Development of Plasmonic Biosensor Platform for Multiplex Sensing of miR-21** 356
N. Tarpataki, A. Bonyár, Budapest University of Technology and Economics, Budapest (Hungary), T. Lednický, Leibniz Institute of Photonic Technology, Jena (Germany), L. T. Csőke, Optimal Optik Ltd., Budapest (Hungary)

Mo-BBS-12 **High-Resolution Inkjet Printing of a Functional Polymer for On-Chip Biosensing** 358
F. Brossard, W. Rostain, Hitachi Cambridge Laboratory, Cambridge (UK), L. Fruk, University of Cambridge, Cambridge (UK)

Tu-BBS-01 **Design and Optimization of a Traveling Surface Acoustic Wave (TSAW) Microfluidic Platform for Controlled Liposome Manipulation** 360
Y. Je, H. N. Açıkgöz, S. Caneva, Delft University of Technology, Delft (The Netherlands)

Tu-BBS-02 **Bacteria collection from static millilitre sample using a DC field** 362
G. Sacco, C. Ciubotaru, M. Conti, D. Cojoc, CNR Istituto Officina Dei Materiali, Trieste (Italy), L. Gigli, Alifax S.r.l., Udine (Italy)

Tu-BBS-03 **Smart Lateral Flow Device with Embedded Gradient Nanoparticle Lines towards Enhanced Quantification via Smartphone** 364
S. Demuru, M. Markocic, S. Cattaneo, V. Zubkovs, Csem Sa, Landquart (Switzerland), P. Spies, D. Meinel, Fhnw, Muttenz (Switzerland), M. Schinz, S. Dobitz, Diabetes Center Berne, Bern (Switzerland)

Tu-BBS-04 **Development of multiplexing LAMP on lateral flow assay (LAMP-LFA) for rapid detection of respiratory viruses** 366
T. L. Quyen, A. Mishra, W. E. Svendsen, M. Dimaki, Technical University of Denmark, Kgs. Lyngby (Denmark)

Tu-BBS-05 **Rapid Temperature Cycling Miniaturized PCR Thermocycler with Switchable Heat Pipe Cooling** 368
P. Bamerni, C. Weber, J. Wöllenstein, University of Freiburg, Freiburg (Germany)

Tu-BBS-06 **Laser-induced graphene paper-based electrodes for detection of the pancreatic cancer biomarker CA19-9 in real samples** 370
G. O. do Nascimento Soares, G. G. Dalkiranis, B. B. Millan Torres, D. Gonçalves, University of São Paulo, São Carlos (Brazil), A. Coatrini Soares, Federal University of Amazonas, Manaus (Brazil)

Tu-BBS-07 **Electrochemical Biosensing of HPV: From Molecular Detection to Clinical Impact** 372
M. Bartosik, L. Moranova, J. Strmiskova, Masaryk Memorial Cancer Institute, Brno (Czech Republic), M. Anton, University Hospital Brno, Brno (Czech Republic)

Tu-BBS-08 **Decoupling Optical and Electrical Transduction Mechanisms in Peptide-Functionalized Graphene Biosensors for Immune Cell Detection** 374
A. Hasnain, H. Heilmann, B. Bufe, A. Tarasov, Kaiserslautern University of Applied Sciences, Zweibrücken (Germany)

Tu-BBS-09 **Electrochemical Redox Label Multiplexing on Single Carbon Electrodes for the Real-Time Detection of Bacterial Wound Infections** 376
D. Kleinknecht, M. Trotter, C. Keß, J. Kloeppel, N. Borst, F. von Stetten, A. Schreiber, Hahn-Schickard, Freiburg im Breisgau (Germany), D. Kiritsi, Medical Center – University of Freiburg, Freiburg im Breisgau (Germany)

Tu-BBS-10 **Development of a MEMS-Based Electrochemical Platform for Label-Free Viral Antibody Sensing.....378**
Z. Çağlayan Arslan, METU MEMS Center, Ankara (TR) and Middle East Technical University, Ankara (TR), E. Salmanlı, METU MEMS Center, Ankara (TR) and Ankara University, Ankara (TR), T. Tezcan, Gazi University, Ankara (TR), T. Karaoğlu, Ankara University, Ankara (TR), U. Tamer, METU MEMS Center, Ankara (TR) and Gazi University, Ankara (TR), H. Külah, METU MEMS Center, Ankara (TR) and Middle East Technical University, Ankara (TR)

Tu-BBS-11 **Gold-Mediated Functionalization of NEMS-FTIR Resonators for Selective Molecular Detection..... 380**
D. Suvara, K. Kanellopulos, H. Wursag, S. Prado-López, S. Schmid, TU Wien, Vienna (Austria)

Tu-BBS-12 **Design Rules for CMOS-Compatible OECTs: Impact of Geometry and Architecture on Ionic–Electronic Transport..... 382**
N. Mukhin, V. Issakov, L. Bakhchova, Technical University of Braunschweig, Braunschweig (Germany), G. L. Frey, Technion – Israel Institute of Technology, Haifa (Israel)

Tu-BBS-13 **Competitive Electrochemical Detection of SARS-CoV-2 Antigen on a 2D MoWSe2-Based Biosensor..... 384**
S. Anuthum, T. Yao, J. Jakmunee, K. Ounnunkad, Chiang Mai University, Chiang Mai (Thailand)

Tu-BBS-15 **Optimization of ssDNA Immobilization for a CRISPR/Cas12a Electrochemical Biosensor for Friedreich's Ataxia..... 386**
L. V. D. Souza, A. M. Faria, T. Mazon, Centro de Tecnologia da Informação Renato Archer, Campinas (Brazil)

Tu-BBS-16 **Biochemical Modulation of Ionic Transport in Asymmetric Nanochannels for Label-Free Biosensing.....388**
L. M. Hernandez Parra, W. Marmisollé, O. Azzaroni, M. L. Cortez, Universidad Nacional de La Plata (UNLP), La Plata (Argentina), M. E. Toimil-Molares, GSI Helmholtzzentrum für Schwerionenforschung, Darmstadt (Germany) and Technische Universität Darmstadt, Darmstadt-West (Germany)

Chemical Sensors

Mo-CHS-01 **Rapid and Selective Sub-ppm Hydrogen Sulfide Detection using rGO/ In2O3 Heterojunction Sensor.....390**
T. Sood, P. Poornesh, Manipal Institute of Technology, Manipal (India), S. Chattopadhyay, Manipal University Jaipur, Jaipur (India)

Mo-CHS-02 **Humidity Enhances the Isopropyl Alcohol Detection by Co-Mn Oxide..... 392**
R. dos Santos Theodoro, D. P. Volanti, São Paulo State University, São José do Rio Preto (Brazil), M. D'Andria, A. T. Güntner, M. Pereira Martins, ETH Zurich, Zurich (Switzerland)

Mo-CHS-03 **UV-light activated ZnO for ppb level NO_2 detection: Influence of modified Pechini synthesis route..... 394**
Y. Amokrane, M. Bendahan, S. Bernardini, Aix Marseille Univ, Marseille (France)

Mo-CHS-04 **Simultaneous Capacitance and DRIFTS Analysis of Zeolites for Dosimeter-Based Epichlorohydrin Sensing at Room Temperature.....396**
T. Wöhrl, R. Moos, D. Schönauer-Kamin, University of Bayreuth, Bayreuth (Germany)

Mo-CHS-05 **Engineering the Active Layer of SnO2 Chemoresistive Sensors: Influence of Deposition Methods and Film Thickness on NO2 Detection..... 398**
D. L. Ferreira, R. A. da Silva, R. A. da Silva, M. O. Orlandi, São Paulo State University (Brazil)

Mo-CHS-06 **Development of Platinum Heater by Inkjet Printing onto Polyimide Substrate..... 400**
M. Rieu, B. Le Porcher, M. Minot, J.-P. Viricelle, Mines Saint-Etienne, Saint-Etienne (France)

Mo-CHS-07 **Inkjet-printed TiO_2 Nanoparticles for Miniaturized Gas Sensors..... 402**
A. Debot, V. Rogé, S. Girod, R. Leturcq, Luxembourg Institute of Science and Technology, Belvaux (Luxembourg), I. Boehme, Sciosense Germany GmbH, Reutlingen (Germany)

Mo-CHS-08 **Highly Stable Pt-activated Graphene Gas Sensors with Antimony Oxide Coatings.....404**
A. B. Baloglu, M. Kodu, T. Kahro, R. Pärna, A. Kasikov, R. Jaaniso, University of Tartu, Tartu (Estonia)

Mo-CHS-09 **Electrosynthesized porous tin oxide film for gas sensors applications** **406**
A. Kumar, S. Sudalaimuthu, M. Minot, M. Rieu, Mines Saint-Etienne, Saint-Etienne (France)

Mo-CHS-10 **Sub-ppm Methane Sensing by Spark-Ablation-Synthesized Nano-SnO_2** **408**
D. Gounaris, G. Biskos, The Cyprus Institute, Nicosia (Cyprus), A. Baut, H. Shin, S. E. Pratsinis, A. Güntner, ETH Zürich, Zürich (Switzerland)

Mo-CHS-11 **Harnessing Multi-phase Interactions in Sn/SnO/SnO2 Tri-phase Material for Gas Sensing** **410**
G. Kim, A. Güntner, ETH Zürich, Zürich (Switzerland)

Mo-CHS-12 **Room-temperature Drift Reduction in Chemoresistive Gas Sensors by UV Illumination Tuning** **412**
P. Pellegrino, A. Romano Rodriguez, University of Barcelona (UB), Barcelona (Spain), G. Domènech-Gil, , Linköping University, Linköping (Sweden)

Mo-CHS-13 **Dataset: Odour sensing in turbulent plumes with high-speed e-nose and PLIF ground truth** **414**
N. Dennler, S. Collaku, A. T. Güntner, ETH Zurich, Zurich (Switzerland), E. Stark, A. Wahr, University of Colorado Boulder, Boulder (USA)

Mo-CHS-14 **Ethylene Glycol Detection in Pediatric Syrups: Rapid Screening MIP Based Electrochemical Sensor** **416**
E. Saritas, H. Kulah, Middle East Technical University, Ankara (Turkiye), B. Sen-Dogan, METU MEMS Center, Ankara (Turkiye)

Mo-CHS-15 **Tuning Selectivity of Electrochemical Sensors through Polymer Modifications** **418**
I. C. Weber, Chalmers University of Technology, Göteborg (Sweden), Y. Zosso, D. Uruchurtu Patino, L. Rijns, A. Düsselberg, Z. Bao, Stanford University, Stanford (USA)

Tu-CHS-01 **Manganese Spinels Boost Gas Sensitivity in Humid Environments** **420**
R. dos Santos Theodoro, D. P. Volanti, São Paulo State University, São José do Rio Preto (Brazil), M. D'Andria, T. E. Abi-Ramia Silva, A. T. Güntner, ETH Zurich, Zurich (Switzerland)

Tu-CHS-02 **Controlling DNA Translocation Velocities through Nanopores by in-situ Aperture Size Control** **422**
J. N. Cronk, A. Angeli Bufalini, M. Aramesh, ETH Zurich, Zurich (Switzerland)

Tu-CHS-03 **Sub-ppm Gas Detection with Metal Organic Frameworks Functionalized Quartz Microbalances** **423**
S. Murugaiyan, R. Capuano, G. Magna, M. Stefanelli, A. Catini, K. Pushparaj, V. Allegra, University of Rome Tor Vergata, Rome (Italy), Y. Sivalingam, Bannari Amman Inst. of Technology, Sathyamangalam (India)

Tu-CHS-04 **W-$Bi_2Sn_2O_7$ Ultrafine Nanocrystals for Chemiresistive Monitoring of Volatile Organic Compound** **425**
Y. Zhou, University of Mons, Mons (BE) und Yangzhou University, Yangzhou (CN), Z. Zheng, X. Nie, R. Hou, C. Zhang, Yangzhou University, Yangzhou (China), C. Bittencourt, University of Mons, Mons (Belgium)

Tu-CHS-05 **Engineering Selective Detection of Hazardous H? and NO? Using Pd Functionalized MXene/ WS? Gas Sensors.** **427**
M. Elsheshtawy, S. B. Malik, F. Güell, E. Llobet, F. E. Annanouch, Universitat Rovira i Virgili, Tarragona (Spain)

Tu-CHS-06 **Self-Powered Gas Sensing in Interface Engineered 2D layered Heterostructures** **429**
D. Mondal, V. Kamble, Indian Institute of Science Education and Research Thiruvananthapuram, Thiruvananthapuram (India)

Tu-CHS-07 **Pyrene-Based Probe with Tunable AIE-ICT Emissions for Amyloid Sensing and Imaging** **431**
D. Arumugam, S. Mandal, National Institute of Technology, Trichy (India)

Tu-CHS-08 **Morphology-Governed Diffusion Enables CH_4/H_2 Discrimination in Metal Oxide Chemiresistor** **433**
M. Verma, E. Llobet, Universitat Rovira i Virgili, Tarragona (Spain)

Tu-CHS-09 **AuAg Nanocage-based Colorimetric Sensor for Silver Detection** **435**
R. M. Sarza, S. F. Y. Li, X. Su, National University of Singapore, Singapore (Singapore), L. Sutarlie, Institute of Materials Research and Engineering, Singapore (Singapore)

Tu-CHS-10 **Pd Decorated Mesoporous TiO_2 Nanospheres for High Performance Hydrogen Gas Sensors at Room Temperature** 437
T. Thathsara, D. Liyanage, M. Shafiei, Swinburne University of Technology, Hawthorn (Australia), C. J. Parker, C. J. Harrison, Royal Melbourne Institute of Technology, Melbourne (Australia)

Tu-CHS-11 **Highly Selective Ethanol Sensor Based on SnO_2/MWCNTs Nanocomposite** 439
M. Aleksanyan, A. Sayunts, G. Shahkhatuni, Z. Simonyan, K. Hambardzumyan, G. Stepanyan, H. Kasaparyan, R. Papovyan, Yerevan State University, Yerevan (Armenia)

Tu-CHS-12 **A Physics-Informed Inverse Problem for Tracking Gas Chromatography Column Degradation** 441
A. Riaud, B. Toth, Y. Maret, K. Hencken, ABB Corporate Research Switzerland, Baden-Dättwil (Switzerland)

Tu-CHS-13 **Optimising Organic Bilayer Heterojunction Sensors through Device Geometry and Operating Bias** 443
M. Hruška, University of Chemistry and Technology, Prague (Czech Republic), P. Bečvář, M. Bouvet, Institut de Chimie Moléculaire de l'Université Bourgogne Europe (ICMUB), Dijon (France)

Emerging Sensor Materials

Mo-ESM-01 **Porous WS_2 Films for Selective and Humidity-robust NO_2 Sensing and Humidity-robust NO2 Sensing at Room Temperature** 445
S. Hersberger, M. Pereira Martins, S. Fassbind, A. T. Güntner, ETH Zurich, Zurich (Switzerland)

Mo-ESM-02 **Functionalized MXenes Chemiresistors for Room-Temperature NO Sensing** 447
E. Pargoletti, Università degli Studi di Milano, Milan (Italy), B. Davis, Y. Gogotsi, Drexel University, Philadelphia (US)

Mo-ESM-03 **Hybrid Nanomaterial Networks for Dynamic VOC Sensing** 449
L. Mielke, Y. Bhattacharjee, G. Carelli, H. Schlicke, Leibniz Institute of Polymer Research Dresden, Dresden (Germany), S. C. Bittinger, University of Hamburg, Hamburg (Germany)

Mo-ESM-04 **Plasma-Fabricated Metasurfaces for SERS Detection of Warfare Chemicals** 451
V. Shvalya, O. Baranov, U. Cvelbar, Jozef Stefan Institute, Ljubljana (Slovenia)

Mo-ESM-05 **Characterization of Aluminum Nitride on vertical side walls** 453
M.-T. Becker, M. B. Venkatesan, A. Bittner, A. Dehé, Hahn-Schickard, Villingen-Schwenningen (Germany)

Mo-ESM-06 **Direct Sputter Deposition of Gold Thin-Film Sensors on Wood Substrates toward Chip-on-Wood Integration** 455
P. Reber, N. Daupayev, M. Lang, S. Hirsch, Brandenburg University of Applied Science, Brandenburg/Havel (Germany)

Mo-ESM-07 **Synthesis of Nitrogen and Phosphorus doped carbon dots and study of their photoluminescence in the solid state** 457
S. N. Katsantonis, NCSR Demokritos, Athens (Greece), S. Gardelis, National and Kapodistrian University of Athens, Athens (Greece), M. Bošković, D. Randjelović, Institute of Chemistry, Technology and Metallurgy, Belgrade (Serbia), N. Vuković, S. Matijašević, Institute for Technology of Nuclear and Other Mineral Raw Materials, Belgrade (Serbia), S. Dean, M. A. Saeed, Kuwait Institute for Scientific Research, Kuwait city (Kuwait)

Mo-ESM-08 **Sputtered permalloy as novel material for THz-thin film technology: Fabrication process, physical and electro-magnetic properties** 459
P. Kondamarri, J. Petit, A. Kovacs, U. Mescheder, V. Bucher, Furtwangen University, Furtwangen im Schwarzwald (Germany), A. Badisa, M. Herbko, A. Zywica, M. Ziolkowski, P. Lopato, West Pomeranian University of Technology in Szczecin, Szczecin (Poland)

Mo-ESM-09 **A New Approach for Production of Nanofilament-Based Chemoresistive Sensors** 463
A. Schmidt-Ott, L. Sacco, VSParticle B.V, Delft (The Netherlands), K. Petallidou, G. Biskos, The Cyprus Institute, Nicosia (Cyprus), P. Kováčik, National Research Council of Canada, Ottawa (Canada)

Energy Harvesting For Sensors

Mo-EHS-01 **Multiplexed Power Management Circuit for Low-Power Thermoelectric Generators** 465
F. Leoncini, Università Degli Studi di Brescia, Brescia (Italy), M. Ridwan, F. Reverter, Universitat Politècnica de Catalunya—BarcelonaTech, Castelldefels (Spain)

Mo-EHS-02 **Powering a Sensor Node with an Organic PV Module Under Low-Light Indoor Conditions** 467
R. A. Retana-González, F. Reverter, M. Gasulla, Universitat Politècnica de Catalunya-BarcelonaTech, Castelldefels (Spain)

Flexible Stretchable And Wearable Sensors

Tu-FSW-01 **Fully Printed MWCNT/PEDOT: PSS/Ecoflex Tactile –Thermal Sensor with Dual-Mode Piezoresistive and Thermoresistive Transduction** 469
N. T. Beigh, M. Al Hadi, N. Alcheikh, Khalifa University, Abu Dhabi (United Arab Emirates)

Tu-FSW-02 **Influence of Piezoresistive Material and Thickness on the Electromechanical Response of Flexible Pressure Sensors** 471
R. Neveu, G. Jodin, S. Bretin, F. Razan, Univ Rennes, Rennes (France)

Tu-FSW-03 **Stretchable Carbon Flower Sensors for Sensitive Estradiol Detection** 473
I. Weber, M. Jayarame Gowda, Z. Bao, Chalmers University of Technology, Gothenburg (Sweden)

Tu-FSW-04 **Aerosol-jet printed carbon for stretchable sensors** 475
H. Zhu, N. Adjeroud, S. Glinsek, Luxembourg Institute of Science and Technology, Belvaux (Luxembourg), Y. Decoster, Goodyear Innovation Center Luxembourg, Colmar-Berg (Luxembourg)

Tu-FSW-05 **Stretchable Piezoelectrics Based on PVDF-Elastomer Blends** 477
G. Khurana, S. Glinsek, Luxembourg Institute of Science and Technology, Belvaux (Luxembourg), J. Zhao, The Goodyear Tire & Rubber company, Akron (United States)

Tu-FSW-06 **Flexible Wearable MXene – Based Printed Temperature Sensor for Multifunctional Applications** 479
H. Nawaz, N. T. Beigh, N. Alcheikh, Khalifa University, Abu Dhabi (United Arab Emirates)

Tu-FSW-07 **Endometrial Receptivity Monitoring by Impedance Technology on a Soft and Adhesive MEA** 481
D. Tang, L. Izmaylova, S. Ingebrandt, R. E. Leube, Z. Gao, RWTH Aachen University, Aachen (Germany)

Tu-FSW-08 **A Flexible Wearable Platform with On-Device TinyML for Context-Aware Bio-Signal Monitoring** 483
S.-W. Shen, S.-L. Lin, C. Buchowiecki, C.-H. Hong, J.-E. Lee, Y.-L. Chen, Y.-C. Yang, S.-Y. You, S.-Y. Hung, H.-F. Tseng, H. Fujita, C.-Y. Lo, National Tsing Hua University, Hsinchu (Taiwan)

Tu-FSW-09 **Natural Flax Fibres for Sustainble Sensor Applications** 485
Y. Chen, A. de Lena, S. Shen, R. Abbel, K. P., Bioeconomy Science Institute, Rotorua (New Zealand), S. Guessama, Inrae, Nantes (France)

Microfluidic Devices, Lab on a Chip, µTAS, Organ on Chip Systems

Mo-MLO-01 **Full-Hydrogel-based Real-Time Sensor and Drug Deliverer in Organ-on-Chip Devices** 487
G. Antonelli, E. Debbi, F. Corsi, A. Idili, A. Mencattini, E. Martinelli, University of Rome Tor Vergata, Rome (Italy)

Mo-MLO-02 **Microwell for EIS based Viability Analysis of Cells** 489
L. Bató, J. M. Bozorádi, HUN-REN Centre for Energy Research, Budapest (Hungary), Z. Vizvári, P. Fürjes, Óbuda University, Budapest (Hungary)

Mo-MLO-03 **Acquisition System for Real-Time Monitoring of Glucose and Lactate in Recirculating Multi-Organ-on-Chip** 491
K. Montiège, S. Renaud, Univ. Bordeaux, Talence (France), V. Saunier, M. Raoux, Univ. Bordeaux, Pessac (France), A. Pirog, Icl, Junia, Lille (France)

Mo-MLO-04 **Centrifugal Microfluidic Automation of Protein Sample Preparation for Nanopore Sensing** 493
C. Kleber, C. Hensel, University of Freiburg, Freiburg (Germany), I. Suppanz, G. Mittler, Max Planck Institute of Immunobiology and Epigenetics, Freiburg (Germany), M. Hinrichs, S. Gutsch, Hahn-Schickard, Freiburg (Germany), T. Hutzenlaub, F. von Stetten, N. Paust, A. Schreiber, J.-N. Klatt, University of Freiburg, Freiburg (Germany) und Hahn-Schickard, Freiburg (Germany)

Mo-MLO-05 **Integrated Resistive Heating Systems in a Microfluidic Platform for Biological Applications** 495
M. Żółtowski, A. Cieślak, A. Krakos, J. Detyna, R. Walczak, Wrocław University of Science and Technology, Wrocław (Poland)

Mo-MLO-06 **A miniaturized portable device for continuous sensing of environmental contaminants** 497
M. López, Á. Diéguez, Universitat de Barcelona, Barcelona (Spain), J.-P. Salvador, Csic, Barcelona (Spain), G. Saviozzi, Scuola Superiore Sant'Anna (SSSA), Pontedera (Italy)

Tu-MLO-01 **Electrohydrodynamic oscillatory deformation of viscoelastic droplets as an interfacial microrheometer** 499
C. K. Parashar, O. S. Deshmukh, D. Bandyopadhyay, Indian Institute of Technology Guwahati, Guwahati (India)

Tu-MLO-02 **Finite element modeling, design and characterisation of SAW transducers for acoustofluidic systems** 501
A. Bányai, E. Leelőssyné Tóth, P. Fürjes, HUN-REN Centre for Energy Research, Budapest (Hungary), M. Varga, 77 Elektronika Ltd., Budapest (Hungary)

Tu-MLO-03 **Towards a Bronchus-on-a-chip Device with Integrated Sensing for Monitoring of the Cell Culture** 503
E. Simioni, C. R. F. Caneira, Inesc Mn, Lisbon (Portugal), S. Macuvele, A. M. Fialho, Instituto Superior Técnico, Lisbon (Portugal)

Tu-MLO-04 **Fully Automated Skeletal Muscle-on-chip Platform for Contraction Analysis** 505
G. Curci, C. Mazzaglia, A. Mencattini, E. Martinelli, University of Rome Tor Vergata, Rome (Italy), D. Durante, M. Ballarino, Sapienza University, Rome (Italy)

Tu-MLO-05 **A Microreactor Workflow for Spatial Proteomics Sample Preparation** 507
M. Metzger, T. Hutzenlaub, N. Paust, J.-N. Klatt, Hahn-Schickard, Freiburg (Germany), M. Maldacker, O. Schilling, Medical Center – University of Freiburg, Freiburg (Germany)

Tu-MLO-06 **A Microfluidic Device Integrating Electrical Impedance Spectroscopy Enables Label-Free Monitoring of C. elegans in Egg-Laying** 509
S. Yu, Y. Geng, J. Fan, H. Lu, Z. Zhu, Southeast University, Wuxi (China)

Photonics And Optical Sensors

Mo-POS-01 **SPR-grating: spectral vs intensity interrogation for ethanol detection** 511
M. Giménez-Conejo, V. González -Morote, S. González-Martínez, I. Fort-Grandas, A. Estany-Macià, D. Sainz, A. Romano-Rodriguez, M. Moreno-Sereno, Universitat de Barcelona, Barcelona (Spain)

Mo-POS-02 **Real-time resonance tracking for acoustic resonator enhanced photoacoustic gas sensors** 513
D. Sieg, R. Patel, V. Kuczius, S. Palzer, Technical University Dortmund, Dortmund (Germany)

Mo-POS-03 **Atomic Structure and Temperature-dependent Photoluminescence of Si-doped Epitaxial Diamond Layer on Nitrogen-rich HPHT Single Crystal Diamond** 515
T. Izsak, I. Kozak, M. Hulman, A. Kozak, M. Varga, Slovak Academy of Sciences, Bratislava (Slovak Republic), V. Vretenar, M. Matko, Slovak University of Technology, Bratislava (Slovakia)

Mo-POS-04 **Enhanced Optical NO_2 Sensing at Room Temperature through Chemical Reaction-Mediated Plasmonic Interaction** 517
M. Pereira Martins, A. T. Güntner, ETH Zurich, Zurich (Switzerland)

Mo-POS-05 **DMOAP-Aligned Bimesogenic Dimers for Wide-Band Spectral Tuning** 519
R. Sonar, A. B. Dharmawan, I. Benito-Altamirano, J. D. Prades, Technische Universität Braunschweig, Braunschweig (Germany)

Mo-POS-06 **Real-time Imaging of Microcrystal Growth and Dynamics by Lensless Microscopy in a Cell** 521
A. Rybakov, A. B. Dharmawan, J. D. Prades, Technische Universität Braunschweig, Braunschweig (Germany)

Mo-POS-07 **Label-Free Detection of Exosome Components via a Novel SPR-Raman Platform** 523
Y. Ai Wu, N.-F. Chiu, J.-C. Lin, National Taiwan Normal University, Taipei (Taiwan), T.-H. Ku, Providence University, Taichung (Taiwan)

Tu-POS-01 **Rapid Vaccine Screening and Component Analysis via a SERS Platform with Plasmonic Concentric Nanostructure Enhancers** 525
I.-J. Chen, Y.-A. Wu, Y.-T. Cheng, H.-Y. Ko, N.-F. Chiu, National Taiwan Normal University, Taipei (Taiwan), K.-K. (. Kuo, Taipei Union Hospital for Women and Children, Taipei (Taiwan)

Tu-POS-02 **MEMS-based microplasma devices on glass substrates for optical emission spectroscopy** 527
E. Escobedo-Cousin, K. Milenko, M. Getz, D. C. H. Hoang, A. K. Herbjørnrød, E. Vereshchagina, SINTEF Digital, Oslo (Norway)

Tu-POS-04 **Interface-Controlled Transport and Broadband Photoresponse in ZnO photodetectors modified with Nitrogen and Phosphorus-Doped Carbon Dots** 529
N. Ganotis, S. N. Katsantonis, C. Tsamis, National Center for Scientific Research (NCSR) "Demokritos", Athens (Greece), S. N. Katsantonis, K. V. Kordatos, E. Hourdakis, National Technical University of Athens (NTUA), Athens (Greece), S. Gardelis, National and Kapodistrian University of Athens (NKUA), Athens (Greece), M. Bošković, D. Randjelović, Institute of Chemistry, Technology and Metallurgy (ICTM), University of Belgrade, Belgrade (Serbia), M. A. Saeed, S. Dean, Y. Malallah, Kuwait Institute for Scientific Research, Kuwait City (Kuwait)

Tu-POS-05 **A Low-Cost Fully 3D-Printed Automated Magnetic Bead Capture System with Real-Time Optical Monitoring** 531
P. Saluja, S. V. Feltrin, M. Dimaki, W. E. Svendsen, Technical University of Denmark, Kgs. Lyngby (Denmark)

Tu-POS-06 **Beyond iSCAT Sensitivity: Mechanistic Control of Photodamage in Label-Free Biosensing** 533
B. N. Küçük, A. Sottini, J. Ortega Arroyo, R. Quidant, ETH Zurich, Zurich (Switzerland)

Tu-POS-07 **Equivalent Emissivity of Poly-Si, SiO_2, and SiN_x for Accurate Heated-Membrane Optical Radiator Design** 535
R. F. Wolffenbuttel, Delft University of Technology, Delft (The Netherlands)

Tu-POS-08 **Irreversible Microstructured Optical RH Threshold Indicator with a Binary Visual Readout** 537
J. Orlikowski, J. Cybińska, Łukasiewicz Research Network – PORT Polish Center for Technology Development, Wrocław (Poland)

Tu-POS-09 **Nanowire Geometry Engineering for Enhanced Fluorescence Biosensing Performance** 539
F. A. Mou, N. Anttu, Åbo Akademi University, Turku (Finland)

Tu-POS-10 **Tailoring Acoustic Modes for Ultra-Sensitive Photoacoustic Gas Detection** 541
M. S. Moussa, J.-F. Lampin, S. Eliet, A. Mazzamurro, O. Bou Matar, Univ. Lille, Lille (France), R. Viard, Groupe Endress+Hauser, Fribourg-en-Brisgau (Allemagne), S. Khattou, M. Amrani, Univ. Mohammed I, Oujda (Morocco)

Physical Sensors

Mo-PHS-01 **Improving Cavity Pressure Stability as Enabler for High-Performance 2-Cavity MEMS Chips** 543
A. Breitling, Robert Bosch GmbH, Reutlingen (Germany)

Mo-PHS-02 **Surface-Micromachined 3-Omega Gas Sensor** 545
P. Raimann, G. L. Tchoffo, F. Hedrich, S. Billat, Hahn-Schickard, Villingen-Schwenningen (Germany), A. Dehé, Albert-Ludwigs-University Freiburg, Freiburg (Germany)

Mo-PHS-03 **Synthesis and sensing properties of SnS_2/rGO composite towards NO_2 gas at room temperature** 547
J. Coelho Tagliaferro, A. A. Komorizono, V. RobertoMastelaro, Institute of Physics of São Carlos, São Carlos (Brazil)

Mo-PHS-04 **Nanowire-based micro-sensor for wall pressure measurement in hydrodynamical flow** 550
A. Serrure, M. Manrique Reyes, M. Abolhassan Araghi, L. Simonet, L. Gimeno, V. Consonni, B. Salem, S. Hoerner, G. Ardila, C. Ghouila-Houri, Univ. Grenoble Alpes, Grenoble (France)

Mo-PHS-05 **Harmonic Generation to Improve Ultrasound Image Using Piezoelectrical Micromachined Ultrasound Transducers** 552
F. Torres, A. Uranga, N. Barniol, Universitat Autònoma de Barcelona, Cerdanyola del Vallès (Spain)

Mo-PHS-06 **Robust In-Cavity Thin-Film Temperature Sensor Array for Real-Time Flow-Front Monitoring in Recycled Material Injection Molding** 554
M. Rekowski, L. Zhao, A. Schott, C. Herrmann, Fraunhofer IST, Braunschweig (Germany)

Mo-PHS-07 **Development of a dipole antenna sensitive to corrosion of steel** 556
B. Mugabo Nduhura, S. Rioual, B. Lescop, P. Talbot, Univ Brest, Brest (France)

Mo-PHS-08 **Experimental Investigation of the Thermal Conductivity Behavior of Ne-Ar, Ne-N_2 and Ar-N_2 Binary Gas Mixtures** 558
S. Jung, M. Benkendorf, H.-F. Pernau, J. Wöllenstein, K. Schmitt, Fraunhofer IPM, Freiburg (Germany), M. Graf, L. M. Comella, University of Applied Sciences Karlsruhe, Karlsruhe (Germany)

Mo-PHS-09 **Enhancing Cardiac Magnetomechanical Sensing via a Tunable Non-Linear Spring Transduction Layer** 560
A. Ascani Orsini, Y. Lai, H. Xu, D. Guo, C. Liu, N. Thakor, Johns Hopkins University, Baltimore (USA)

Mo-PHS-10 **Piezoelectrically Induced Resonance Frequency Tuning of Buckled-Diaphragm MEMS Ultrasonic Sensors for Multi-Frequency Measurement** 562
K. Yamashita, J. Yamamoto, Kyoto Institute of Technology, Kyoto (Japan)

Mo-PHS-11 **Calculation of Far Field Acoustic Radiation from Transmission Line Models of PMUT–Horn Systems** 564
P. Möhrle, G. Schrag, Technical University of Munich, Munich (Germany)

Tu-PHS-01 **LVIT position sensor with improved linearity** 566
M. Mirzaei, J. Maier, P. Ripka, Czech Technical University, Prague (Czech Republic)

Tu-PHS-02 **Frequency Mixing Magnetic Detection for Viscosity Sensitive Biosensing Using Magnetic Nanoparticle Relaxation** 568
A. M. Pourshahidi, I. Nasr Allah, T. Bikulov, A. Abuawad, H.-J. Krause, Forschungszentrum Jülich, Jülich (Germany), A. Gholivand, University of Bonn, Bonn (Germany), U. M. Engelmann, FH Aachen University of Applied Sciences, Jülich (Germany)

Tu-PHS-03 **A Drift-Resistant Amine-based Chemiresistive Printed Sensor for Carbon Dioxide Monitoring** 570
P. Tzourmpakis, M. Vaseem, I. Getmanov, A. Shamim, King Abdullah University of Science and Technology, Jeddah (SA), A. S. Pillai, Edinburgh Napier University, Edinburgh (UK)

Tu-PHS-04 **Detection of the Oscillation of a Magnetic Artificial Cilium using an Electromagnetic Pickup** 572
J. Astl, W. Hilber, S. Lang, B. Jakoby, Johannes Kepler University Linz, Linz (Austria)

Tu-PHS-05 **Sensing of Microplastics in Water Using Gold Nanoparticle-Coated Multimode Optical Fiber** 574
V. Kumar, S. Shukla, M. A. Illarramendi, J. Villatoro, Upv/ehu, Bilbao (Spain)

Tu-PHS-06 **A Robust Capacitive Sensor Platform for On-Line Dielectric Constant Measurement of Liquid Mixtures** 576
P. Schläpfer, J. Schläpfer, M. Giger, Innovative Sensor Technology iST AG, Ebnat-Kappel (Switzerland)

Tu-PHS-07 **Overcoming Thermal Inertia in Robust Anemometers via Observer-Based Virtual Thermal Isolation** 578
S. Huber, M. Mächler, T. Lamprecht, L. Kamm, D. Bertsch, C. Würsch, OST Eastern Switzerland University of Applied Sciences, Buchs (Switzerland)

Tu-PHS-08 **LVDT Position Sensor with external armature** 580
M. Mirzaei, J. Maier, P. Ripka, Czech Technical University, Prague (Czech Republic)

Tu-PHS-09 **Investigating Slip-Induced Frequency Relationship in Dual-Channel PVDF Sensor Applied to Robotic Grippers** 582
Z. Wang, V. Kamat, S. Bhansali, Vanderbilt University, Nashville (USA)

Tu-PHS-10 **High Temperature Investigation of Polymer-Free Strain Gauges for Integration in DED-LB Components** 584
E. Müller, J. Eisfelder, R. Ottermann, F. Dencker, D. Klaas, M. C. Wurz, Leibniz University Hannover, Garbsen (Germany)

Sensing For Medical Diagnostics And Monitoring

Mo-SMD-01 **A Miniaturized Electrochemical Biosensor for Real-Time In Vivo Potassium Monitoring in the Inner Ear** 586
F. Arshadi, M. Esfandiari, C. Pastras, M. Asadnia, Macquarie University, Sydney (Australia), R. Gay, Y. L. Enke, Cochlear Limited, Sydney (Australia), N. Farbehi, University of New South Wales, Sydney (Australia)

Mo-SMD-02 **Enhanced Split-Ring Resonator Sensing Platform for Gas Monitoring in Medical Applications** 588
D. Bailey, M. Hitzemann, C. Thoben, T. Hennig, E. Rohloff, A. Schneider, A. Schaate, S. Zimmermann, Leibniz University Hannover, Hannover (Germany)

Mo-SMD-03 **Engineering Spatially Patterned Selective Membranes for Scalable Multiplex Electrolyte Sensors** 590
A. Nilghaz, N. H. Voelcker, Monash University, Parkville (Australia), C. Devendran, Proton Intelligence Australia Pty Ltd, Clayton (Australia)

Mo-SMD-04 **High-Sensitivity Electrochemical Detection of Point Mutations: Optimization of BRAF V600E Analysis from Liquid Biopsy** 592
L. Moráňová, Masaryk Memorial Cancer Institute, Brno (Czech Republic), K. Itterheimová, J. Strmisková, National Center for Biomolecular Research - Masaryk University, Brno (Czech Republic) and Masaryk Memorial Cancer Institute, Brno (Czech Republic), M. Bartošík, Masaryk Memorial Cancer Institute, Brno (Czech Republic)

Mo-SMD-05 **Online Bacterial Headspace Sampling Setup for Medical Microbiology Diagnostics with Sensors** 594
M. B. Bilgin, N. Toccalino, A. Güntner, ETH Zürich, Zürich (Switzerland), E. Slack, ETH Zurich, Zurich (Switzerland), A. Egli, University of Zurich, Zurich (Switzerland)

Mo-SMD-06 **Electrochemical and Electrochemiluminiscence in vitro Detection Methods of a Human Cytomegalovirus in Oncology Patients** 596
L. Moranova, A. Fried, K. Itterheimova, M. Bartosik, Masaryk Memorial Cancer Institute, Brno (Czech Republic), M. Hendrych, St. Anne's Univ. Hospital, Brno (Czech Republic)

Mo-SMD-07 **A Data Management Platform for Early Diagnosis and Follow-Up of Human Diseases: Architecture Design, Development and Analysis** 598
M. Sansone, J. Palmisani, A. Di Gilio, M. R. Nisi, L. Pastore, M. C. Mazzola, G. de Gennaro, University of Bari, Bari (Italy), E. De Benedetto, University of Naples Federico II, Naples (Italy)

Mo-SMD-08 **An Adaptable Electrochemical Platform for Detection of Oncogenic Point Mutations Using Rolling Circle Amplification** 600
S. Sevcikova, K. Itterheimova, M. Bartosik, Masaryk Memorial Cancer Institute, Brno (Czech Republic)

Mo-SMD-10 **High-Performance Miniaturized Reference Electrodes for Electrochemical Sensors** 602
D. Migliorelli, G. Bouilly, S. Demuro, J. Heidler, J. Kim, Csem, Landquart (Switzerland), A. Speck, University of Geneva, Geneva (Switzerland)

Tu-SMD-01 **Measurement of Stress Relaxation During the Indentaion of Human Gastric Tissues** 604
J. M. Bozorádi, HUN-REN Centre for Energy Research, Budapest (Hungary), G. Papp, Uzsoki Hospital, Budapest (Hungary), Z. S. Bérces, P. Fürjes, Óbuda University, Budapest (Hungary), K. Gáspár, Budapest University of Technology and Economics, Budapest (Hungary), G. Battistig, University of Debrecen, Debrecen (Hungary)

Tu-SMD-02 **A Non-Invasive Biosensor for Albumin Detection in Tear Fluid Based on Molecularly Imprinted Polymers** **606**
G. Ndege, S. D. Psoma, The Open University, Milton Keynes (United Kingdom)

Tu-SMD-03 **Fatigue Detection During Wall-Sit Exercise Using Statistical Features of Chest ECG-Derived EMG** **608**
C. Park, C. Huh, H. J. Park, Electronics and Telecommunications Research Institute (ETRI), Daejeon (Republic of Korea)

Tu-SMD-04 **Clinical Validation of a New Radar System for Multi-Parameter Vital Sign Detection in Patients** **610**
M. Gottinger, S. Kranz, N. Notari, T. Pittorino, C. Würsch, Ostschweizer Fachhochschule, Buchs (Switzerland)

Tu-SMD-05 **Miniaturized GC-MOS Platform for Exhaled Breath Analysis** **612**
A. Kalinichenko, A. R. Murgia, T. Kassabi, J. Mitrovics, JLM Innovation, Tübingen (Germany), C. Bur, A. Schütze, Saarland University, Saarbrücken (Germany)

Tu-SMD-06 **Enabling Large-Area Tactile Imaging via Multiplexed CB–PDMS Flexible Pressure Sensor Arrays** **614**
M. A. I. Bhuyan, M. M. Uddin, L. Xiuqian, H. C. Kim, University of Ulsan, Ulsan (South Korea)

Tu-SMD-07 **Sugar-Based Electrochemical Biosensors for Quantification of a Secreted Protein in Human Fluids** **616**
J. Guo, L. Salmon, H. Korri-Youssoufi, Université Paris-Saclay, Orsay (France), H. Le Stunff, Y. Benomar, Université Paris-Saclay, Gif-sur-Yvette (France)

Tu-SMD-08 **Inductive wireless power transfer for miniature rodent brain implants enabling untethered neural recordings** **618**
P. Haghshomar, K. M. Azadmehr, University of South-Eastern Norway, Borre (Norway), B. Nossum, E. Escobedo-Cousin, SINTEF Digital, Oslo (Norway), F. A. Dapsance, C. Ortiz, C. Boccara, University of Oslo, Oslo (Norway)

Tu-SMD-09 **Development of a transistor-based gas sensor for biomedical application** **620**
D.-L. NGUYEN, B. PIRO, ITODYS Laboratory, Paris (France), T.-T. VU, University of Science and Technology of Hanoi (USTH), Hanoi (Vietnam)

Tu-SMD-10 **Discriminating between viable and non-viable bacteria with a field-effect transistor based on Nano-Channels** **622**
G. Shalev, Ben-Gurion University of the Negev, Beer-Sheva (Israel)

Sensor Applications: Environment, Food And Space

Mo-EFS-01 **Remote Sensing for Monitoring Hydric Stress in Farm Animals** **624**
E. Saoutieff, S. Brulais, I. Sorrentino, M. Escudé, M. Benessalah, L. Gauthier, C. Verplanck, R. Anciant, I. Texier, CEA, Leti, Grenoble (France), C. Xavier, L. Hervé, A. Boudon, F. Gondret, inrae, Saint Gilles (France)

Mo-EFS-02 **Development of a Radiofrequency Sensor for Detecting Bacteria in the Food Industry** **626**
Y. Hsana, A.-G. Mathot, O. Couvert, Univ Brest, Quimper (France), P. Talbot, S. Rioual, B. Lescop, University Brest, Brest (France)

Mo-EFS-03 **Synthesis of Gold Nanostructures for Optical Fiber Biosensors Towards the Detection of Salmonella Typhimurium** **628**
K. I. Duerme, M. Ptak, Institute of Low Temperature and Structure Research, Wrocław (Poland), R. Scotti, University of Milano-Bicocca, Milan (Italy)

Mo-EFS-04 **Smell-Based Molecular Communication for Mobile Robots Using Gas Sensing** **630**
A. Abdali, H. Lee, Y. Deng, King's College London, London (UK), D. Bi, University of Glasgow, Glasgow (UK), R. Zhu, Imperial College London, London (UK)

Mo-EFS-05 **MOS Sensors Characterization for Fermentation Monitoring Using GC-SOMSA** **632**
L. Corrà, L. Capelli, Politecnico di Milano, Milan (Italy), G. Zeh, T. Sauerwald, M. Czerny, Fraunhofer Institute, Freising (Germany)

Mo-EFS-06 **Portable and Smart Ion Analyser for Automated Monitoring of Alkali Metals in Battery Recycling Industries** **634**
R. Gil, S. Silva, O. Dudik, Á. Geraldes, INL-International Iberian Nanotechnology Laboratory, Braga (Portugal)

Tu-EFS-01 **Direct Comparison between an Analog MOS Sensor Array and a Single Temperature-Modulated Digital MOS Sensor for Food Spoilage Status Classification** **636**
L. Corrà, C. Ratti, S. Bettinaglio, E. Zanni, R. Dellacà, L. Capelli, Politecnico di Milano, Milan (Italy), F. Pianca, Electrolux Italia s.p.a., Treviso (Italy)

Tu-EFS-02 **A Lensless Microscope-Based Sensor for 3D Displacement Measurement in Infrastructure Monitoring** **638**
L. Yan, A. B. Dharmawan, J. D. Prades, Technische Universität Braunschweig, Braunschweig (Germany), J. Gülink, QubeDot GmbH, Braunschweig (Germany), I. Zrazinska, F. Hernandez, Worldsensing S.L., Barcelona (Spain)

Tu-EFS-03 **From Measurements to Perceptions: Sensors and Structural Equation Modelling to Evaluate Indoor Comfort in University Buildings** **640**
C. Visentin, M. Pellegatti, University of Ferrara, Ferrara (Italy), A. Rossi, G. Magherini, B. Fabbri, University of Ferrara, Ferrara (Italy), M. Magoni, University of Ferrara, Ferrara (Italy) and Eurac Research, Bolzano (Italy), D. Azzolina, E. Marrocchino, M. G. Paletta, University of Ferrara, Ferrara (Italy), D. Iervolino, University of Padova, Padova (Italy), F. Aldegheri, Studio Tecnico Aldegheri, Ferrara (Italy)

Tu-EFS-04 **Design and Theoretical-Experimental Investigation of a Surface Acoustic Wave Sensor Based on Dual Substrates** **642**
H. Taleb, M. Vanotti, V. Blondeau-Patissier, FEMTO-ST Institute, Besançon (France)

Tu-EFS-05 **Magnetic Microfluidics Biosensor for Environmental Appli-cations: A Simulation Approach** **644**
F. Shanehsazzadeh, A. Rabehi, Sorbonne Université, Paris (France), R. Askari Moghadam, S. Neveu, Sorbonne University, Paris (France), G. Klisnick, (H.), K., Paris, France

Sensor Arrays And Networks, Integrated Systems

Mo-SAN-01 **Polymer-Coated Quartz Microbalance Array for Discriminating VOCs and Ammonia** **646**
F. Cortese, R. Capuano, A. Catini, C. Di Natale, Tor Vergata University of Rome, Rome (Italy), E. Stoleru, M. Brebu, “P. Poni” Institute of Macromolecular Chemistry, Iaşi (Romania)

Mo-SAN-02 **An Adaptive Embedded Readout System for Resistive Sensor Arrays** **648**
D. Balraj, P. Woias, S. Kundu, Albert-Ludwigs-Universität Freiburg, Freiburg (Germany), M. Tarique, L. Abelmann, TU Delft, Delft (Netherlands)

Mo-SAN-03 **Engineering Opposing Response Evolution in $ZnWO_4$–WO_3 Sensor Pair for Deterministic Decoding of NO_2 in Reducing Gas** **650**
S. K. Singh, C. Neeraj, A. K. Dwivedi, V. B. Kamble, Indian Institute of Science Education and Research, Thiruvananthapuram (India)

Tu-SAN-01 **Sensor Placement in Energy Systems Based on Residual Uncertainty** **652**
P. Kersten, S. Hirsch, University of Applied Sciences Brandenburg, Brandenburg an der Havel (Germany)

Tu-SAN-02 **A multisensor-array device for breath analysis: development of a data quality assessment framework and application in the clinical practice** **654**
V. Pizzillo, J. Palmisani, A. Di Gilio, G. de Gennaro, University of Bari Aldo Moro, Bari (Italy), A. Catino, A. Quarato, Istituto Tumori ‘Giovanni Paolo II’, Bari (Italy), S. I. Lopes, Instituto Politécnico de Viana do Castelo, Viana do Castelo (Portugal)

Tu-SAN-03 **Integrated Nitrate Sensor for Real-time Soil Monitoring** **656**
E. Saoutieff, A. Ohl, V. Elhorga, C. Boko, CEA, Leti, Grenoble (France), I. Vogeler, Christian-Albrechts-Universität, Kiel (Germany), N. Surendran, A. Wille, Fraunhofer Institute, Munich (Germany), H. Shao, A. O'Riordan, Tyndall National Institute, Cork (Ireland), P. Kalkowski, L. Kulas, Gdansk University of Technology, Gdansk (Poland), H. Trindade, University of Trás os Montes e Alto Douro, Vila Real (Portugal), S. Ullah, L. Kohl, University of Eastern Finland, Kuopio (Finland)

Tu-SAN-04 **Scalable flux using chamber embedded integrated selective multigas sensing** **658**
F. Sievers, M. Zimmer, Á. Ortiz Pérez, N. Schütz, S. Palzer, TU Dortmund, Dortmund (Germany)

Tu-SAN-05 **Biosensing Network for Real-time Water Monitoring** **660**
E. Saoutieff, C. Boko, A. Ohl, C. Garaffa, G. Nonglaton, L. Cuvillier, CEA, Leti, Grenoble (France), R. Murray, A. O'Riordan, S. Muzaffar, Tyndall National Institute, Cork (Ireland), A. G. Tibbe, J. Elias, Imec, Eindhoven (Netherlands), G. Dudnik, A. Falhi, A. Fivaz, Csem, Neuchâtel (Switzerland), C. Jimenez-Jorquera, Imb-cnm, Csic, Barcelona (Spain)

Tu-SAN-06 **Low-Cost Electronic Nose for Environmental Applications** **662**
G. Domènech-Gil, D. Bastviken, Linköping University, Linköping (Sweden)

Tu-SAN-07 **Is the initial response of gas sensors enough for gas recognition?** **664**
L. Miranda, Í. Santos, B. Dorizzi, D. Petrovska Delacretaz, M. Hariz, J. Boudy, Télécom SudParis, Palaiseau (France), N. Redon, A. Gregori, IMT Nord Europe, Douai (France), J. Montalvão, Universidade Federal de Sergipe, São Cristóvão (Brazil)

Sensor Fundamentals & Modelling

Mo-SFM-01 **Physics-Based Power-Law Discrimination of CO2 and Isoprene Using a Single NdFeO3 Perovskite Sensor** **666**
A. N. Eshore, S. Banerjee, P. Dutta, P. K. Guha, IIT Kharagpur, Kharagpur (India)

Mo-SFM-02 **Artificial Wind-Assisted Control of Hydrogen Gas Leaks for Improved Sensor Detection: A CFD Study** **668**
S. Dasgupta, ABB Corporate Research, Bangalore (India), P. Castro-Fernandez, A. Kramer, ABB Corporate Research, Baden-Dättwil (Switzerland)

Mo-SFM-03 **Impact of Water on the Temperature Homogeneity in a High-Temperature Gas Sensor** **670**
J. Herrmann, G. Hagen, R. Moos, University of Bayreuth, Bayreuth (Germany)

Mo-SFM-04 **Revealing and Modeling Frequency-Dependent Field Redistribution for Calibration-Free Wideband Four-Electrode Impedance Spectroscopy** **672**
L. Pan, D. Han, Y. Niu, J. Zheng, J. Wang, J. Chen, X. Huo, Chinese Academy of Sciences, Beijing (China)

Tu-SFM-01 **Precision in Gas Sensing: A Quantitative and Qualitative Analysis of Comparative Bias in Reported Metrics** **674**
P. P. Ortega, E. Longo, Federal University of São Carlos, São Carlos (Brazil), S. Gherardi, M. Astolfi, C. Malagù, SCENT S.r.l., Ferrara (Italy), M. A. Ponce, Cificen, Tandil (Argentina)

Tu-SFM-02 **PMUT and CMUT array – Design, technology and experimental validation** **676**
A. Shaporin, A. R. Dudhat, S. Mulay, C. Stöckel, Fraunhofer ENAS, Chemnitz (Germany), R. Nagaraja, A. Tweedie, A. Halbach, Quanscient, Tampere (Finland)

Tu-SFM-03 **A Metasurface Acoustic Fabry-Perot Interferometer for Ultrasonic Passive Strain Sensing** **678**
S. Bielefeldt, C. Hierold, M. Luisier, C. Roman, ETH Zurich, Zürich (Schweiz), R. Furrer, Empa, Dübendorf (Schweiz)

Tu-SFM-04 **Fast Tactile Sensor Array Normalization of an Artificial Silicone Fingertip Using a Pressure Chamber** **680**
K. Meier, F. Püntener, S. Bielefeldt, C. Hierold, C. Roman, ETH Zürich, Zürich (Switzerland)

Tu-SFM-05 **Efficient Prediction of Damping in Acceleration Sensors by Physical Compact Modelling** 682
F. Michael, G. Schrag, Technical University of Munich, Munich (Germany), K. Hiller, S. Weidlich, TU Chemnitz, Chemnitz (Germany), R. Forke, Fraunhofer Institute for Electronic Nano Systems ENAS, Chemnitz (Germany), S. Pregl, Infineon Technologies AG, Dresden (Germany)

Tu-SFM-06 **Engineering Nanopipettes for Probing Neuronal Communication at the Nanoscale** 684
A. Viol, M. Aramesh, J. Vörös, ETH Zürich, Zürich (Switzerland)

Tu-SFM-07 **A two-layer Micro-Electrical Impedance Tomography Platform for Three-Dimensional Image Reconstruction using Machine Learning** 686
C. Liu, Institute of Microtechnology, TUBS, Braunschweig (Germany) und Center of Pharmaceutical Engineering, TUBS, Braunschweig (Germany), T. E. Winkler, Institute of Microtechnolog, TUBS, Braunschweig (Germany) und Department of Micro and Nanosystems (MST), Digital Futures & SciLifeLab, KTH, Stockholm (Sweden), I. Constantinou, Institute of Microtechnolog, TUBS, Braunschweig (Germany) und Center of Pharmaceutical Engineering, TUBS, Braunschweig (Germany)

Signal Analysis, Machine Learning, Physics-Informed Machine Learning And Artificial Intelligence For Sensing

Mo-SML-01 **Reliable TVOC Sensing: A Lab-to-Field Calibration Approach** 688
J. Amann, A. Schütze, C. Bur, Saarland University, Saarbrücken (Germany), S. Schumacher, Institute of Energy and Environmental Technology e.V. (IUTA), Duisburg (Germany)

Mo-SML-02 **Progressive Domain Adaptation under Sensor Drift for Gas Classification with Limited Calibration Labels** 690
H. Fan, A. J. Lilienthal, Technische Universität München, Munich (DE) and Örebro University, Örebro (SE)

Mo-SML-03 **Characterizing Resonance Scaling in Cattle Eructation Sounds for Methane Emission Estimation** 692
Y. Hu, J. Fastier-Wooller, S. Muramatsu, M. Yamamoto, T. Itoh, The University of Tokyo, Tokyo (Japan)

Mo-SML-04 **Jacobian-Initialized Parametric Physics-Informed Neural Network for Anomaly Position and Size Estimation from Simulated Electrical Impedance Tomography Data** 694
S. Sharma, K. Eckert, Z. Lei, Helmholtz-Zentrum Dresden-Rossendorf, Dresden (Germany)

Tu-SML-01 **Recovery of Characteristic Thiabendazole Raman Peaks from Ethanol-Dominated Spectra Toward Microfluidic SERS-Based Pesticide Sensing** 696
K. Mileńko, K. A. H. Bakke, E. Verschegina, SINTEF Digital, Oslo (Norway), A. Baracu, A. Dinescu, National Institute for R&D in Microtechnologies - IMT Bucharest, Bucharest (Romania), O. Rasoga, National Institute of Materials Physics, Magurele (Romania), K. Giżyński, Polish Academy of Sciences, Warsaw (Poland)

Tu-SML-02 **Dual-Descriptor VAE Characterisation of AE-Band Structural Signals in Reinforced Concrete** 698
X. Zhang, HafenCity University Hamburg, Hamburg (Germany)

Tu-SML-03 **Field Measurement-Based Analysis of Impulsive Bridge Vibrations for Energy Harvesting** 700
S. Du, M. Illguth, G. Kapteina, HafenCity University Hamburg, Hamburg (Germany)

Tu-SML-04 **Impact of Sensor Selection on Signal Quality of Physiological Monitoring in Demanding Conditions** 702
A. F. Renz, E. Maevskaia, F. Bauer, R. M. Rossi, S. Annaheim, Empa, St. Gallen (Switzerland), A. Stier, Armasuisse, Bern (Switzerland), D. Bron, Swiss Air Forces, Dubendorf (Switzerland)

Tu-SML-05 **Multi-Season Field Evaluation of a Temperature-Modulated SMOX Sensor Array for NO2 and O3 Monitoring** 704
F. Schmidt, A. Kobald, U. Weimar, N. Barsan, University of Tuebingen, Tuebingen (Germany), P. Tosato, A. Gaiardo, Bruno Kessler Foundation, Trento (Italy)

Tu-SML-06 **Generation and Real-Time Detection of High-Fidelity Odour Plumes** 706
A. Gholivand, A. Padmanabhan, T. Ackels, University of Bonn, Bonn (Germany), F. P. Schmidt, Bielefeld University, Bielefeld (Germany)

Tu-SML-07 **Empowering Self-Powered Sensors via Agentic RAG: A Domain-Specific LLM Framework for Building Physics Retrieval** **708**
S. Saadatnasab, M. Li, Z. Wang, Hong Kong University of Science and Technology, Hong Kong

DOI 10.5162/eurosensors2026/PT1

Nanophotonics: Enabling Technology for Next Generation Bioanaytical Devices

Hatice Altug
Ecole Polytechnique federale de Lausanne, School of Engineering, Bionanophotonic Systems Laboratory, Lausanne, 1015, Switzerland
hatice.altug@epfl.ch

Abstract:

Healthcare is undergoing a paradigm shift from reactive treatment to preventive, personalized, and globally accessible care. Realizing this transformation requires fundamentally new bioanalytical and diagnostic technologies that can deliver rapid, accurate, and affordable results. Towards this goal, our laboratory is pioneering next-generation nanophotonic platforms that enable ultra-sensitive, quantitative, multiplexed, real-time detection of biomolecules through advances in optical biosensing, imaging, and spectroscopy. Nanophotonics provides a powerful technological foundation for bioanalytical devices by enabling strong light–matter interactions with confined lights at subwavelength scales. Building on this capability, we engineer nanophotonic metasurfaces operating over a broad spectrum from visible to mid-infrared to leverage complementary optical detection principles such as label-free refractometric sensing, molecular, structural and chiral sensitive surface enhanced spectroscopy, ultra-sensitive digital nanophotonic biosensing and multi-modal chemical-hyperspectral imaging approaches [1-5]. We develop wafer-scale nanofabrication processes compatible with low-cost and high-throughput manufacturing of disposable biosensor chips, and integrate them with microfluidics to enable rapid, automated, and efficient sample handling. In parallel, we employ advanced data science approaches to enhance the performance of our platforms by multiparametric analysis of spectrally, temporally, and spatially resolved data. This talk will highlight some of our recent work on these fronts with selected demonstrations.

Keywords:

Nanophotonic biosensing, metasurfaces, advanced vibrational spectroscopy, multi-modal imaging, lab-on-a-chip integration

References:

[1] A Saateh, R Allamehnejad, W Yang, YC Liu, GV Tolstonog, H Altug. Kinetic Profiling in One-Step Digital Immunoassays Enables Multiplex Quantification across an Ultrabroad Dynamic Range. *Journal of American Chemical Society*, 148, 5253-5263 (2026); doi.org/10.1021/jacs.5c17838

[2] I Sinev, A Cargioli, D Piciocchi, FU Brikh, J Faist, H Altug. Metasurface-Enhanced Mid-Infrared Imaging Spectroscopy with Broadband Quantum Cascade Lasers. *Nature Communications* (2026), doi.org/10.1038/s41467-026-71611-9

[3] D Kavungal, E Morro, ST Kumar, B Dagli, HA Lashuel, H Altug. Nanoplasmonic Infrared Microarray Sensor Enabling Structural Protein Biomarker-Based Drug Screening for Neurodegenerative Diseases. *Advanced Science*, e00320 (2025) doi.org/10.1002/advs.202500320Digital Object Identifier (DOI)

[4] J Lee, Y Wu, I Sinev, M Masharin, S Papadopoulos, EJC Dias, L Wang, et al. Plasmonic biosensor enabled by resonant quantum tunnelling. *Nature Photonics*, 19, 938-945 (2025). doi.org/10.1038/s41566-025-01708-y

[5] S Ansaryan, YC Chiang, YC Liu, P Reichenbach, M Irving, H Altug. Multimodal Nanoplasmonic and Fluorescence Imaging for Simultaneous Monitoring of Single-Cell Secretory and Intracellular Dynamics. *Advanced Science*, 12, 2415808 (2025). doi.org/10.1002/advs.202415808

[6] ML Brongersma, RA Pala, H Altug, F Capasso, et al. The second optical metasurface revolution: moving from science to technology. *Nature Reviews Electrical Engineering*, 2, 125-143 (2025). doi.org/10.1038/s44287-024-00136-4

[7] AJ El-Helou, Y Liu, C Chen, F Wang, H Altug, PJ Reece, Y Zhu. Optical Metasurfaces for the Next-Generation Biosensing and Bioimaging. *Laser & Photonics Reviews*, 19, 2401715 (2025) XXX doi.org/10.1002/lpor.202401715

DOI 10.5162/eurosensors2026/PT2

MEMS Sensors for the Body: From Wireless Implants to Transdermal Diagnostics

Mark G. Allen
University of Pennsylvania
Philadelphia, Pennsylvania, USA
mallen@upenn.edu

Abstract:

Microsystems are now being used to interface with the human body for sensing relevant parameters that impact the diagnosis and treatment of multiple diseases. As this technology continues to mature, many examples of both research and regulator-approved products are expected to become available. This paper highlights several such microsystem-based interfaces associated with our laboratory, including wireless endovascular permanent implants for detection of pulmonary artery pressure utilized in managing medication of patients with heart failure; wireless fingertip implants intended for sensing of normal and shear forces for restoration of sensation in diabetic patients; microneedle-based devices for transdermal detection of cytokines used in assessment of inflammation; and transdermal intramuscular oxygen sensors for replacement of muscle biopsies in the detection of mitochondrial-based metabolic dysfunction.

Keywords: Implant, biosensor, endovascular, tactile, cytokine

Introduction

Microsystems for medicine, including implants and transdermal devices, have been envisioned for decades. Nearly 70 years ago the 'endoradiosonde', a swallowable device reporting gastro-intestinal pressure, was published. The recent convergence of microfabrication, wireless communication, and low-power electronics has expanded this field tremendously, resulting in devices that measure physiological parameters from the body and transmit data, either wired or wirelessly, to guide treatment.

Endovascular pressure sensors

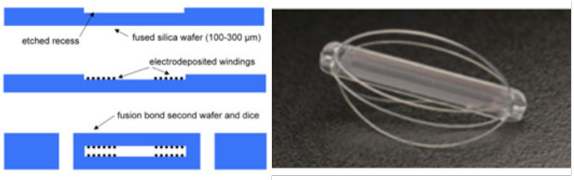

Wireless endovascular pressure sensors for catheter-based implantation within the pulmonary artery can guide titration of medication used to manage patients with congestive heart failure. These devices are realized using fused silica micromachining. The sensor comprises a passive LC resonator; pressure-induced deflection of the fused silica plates shifts its resonant frequency. An external reader detects this frequency shift and converts it to a pressure waveform.

Clinically, this sensor was validated in the CHAMPION trial, where 550 patients received implants. The device enabled clinicians to titrate therapy based on daily pulmonary artery pressure data. Patients whose treatment incorporated sensor data experienced a 30% reduction in heart-failure-related hospitalizations at six months and a 38% annualized reduction over the full follow-up period. These devices are now commercially available.

Implantable tactile sensors

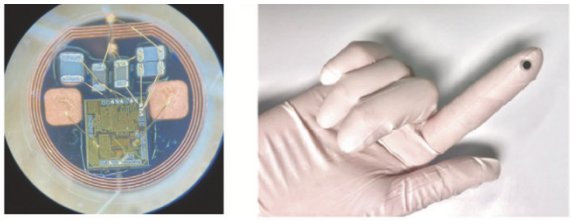

Building on this fabrication technology, wireless, battery-free tactile sensing systems designed to restore touch sensation in individuals with paralysis have been fabricated. Unlike wearable tactile sensors that such patients may struggle to don, a subdermal capacitive pressure sensor encapsulated in a hermetic fused-silica package, paired with a custom ASIC that enables wireless power transfer and data communication, is investigated. Ex vivo implantation in a macaque fingertip showed that the sensor could detect

physiologically relevant light-touch forces (<1 N) with a sensitivity of 0.8 pF/N, force resolution of 4.3 mN (comparable to natural mechanoreceptor thresholds), and reconstruction of dynamic forces with high fidelity ($R^2 = 0.94$).

Microneedle cytokine sensors

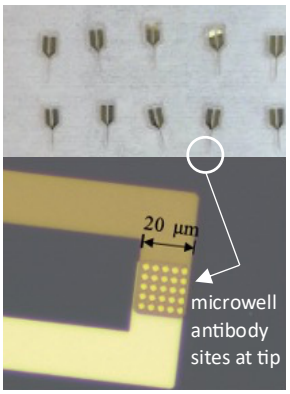

These devices are needle-shaped impedance sensors designed for rapid, label-free, and real-time detection of cytokines *in vivo.* The device inte-grates a 20 µm × 20 µm microwell array onto a fused-silica microneedle, enabling localized electrochemical sensing through impedance changes generated by specific antibody–antigen interactions within the microwells. This needle form factor supports minimally invasive transcutaneous or intramuscular deployment. Antibody immobilization and antigen binding produce reproducible impedance signatures. To validate *in vivo* functionality, the microneedle sensor was inserted into transgenic mice expressing human IL-8. Real-time impedance measurements correlated closely with ELISA-derived serum cytokine levels, enabling detection across four orders of magnitude with picomolar sensitivity, enabling a robust, minimally invasive tool for continuous cytokine monitoring, with potential applications in point-of-care diagnostics and real-time immune profiling.

Transdermal Oxygen Sensors

Monitoring oxygen levels in living tissues is essential for understanding metabolic function, disease progression, and physiological stress. A microfabricated electrochemical oxygen sensor that integrates a three-electrode gold system, a polyvinyl-alcohol (PVA) hydrogel electrolyte, and a dip-coated PDMS oxygen-permeable membrane on a flexible polyimide substrate is implemented. The resulting device is compact (2.4 mm diameter sensing region) and ultrathin (~100 µm), enabling insertion into soft tissues while maintaining structural robustness. The hydrogel electrolyte simplifies fabrication by eliminating the need for liquid reservoirs and leak-prone microfluidic chambers.

Electrochemical impedance spectroscopy confirmed comparable ionic conductivity between hydrogel- and saline-based devices, and chronoamperometry revealed effective oxygen diffusion through the PDMS-hydrogel stack, confirming the efficacy of the hydrogel electrolyte as stable, biocompatible medium that does not compromise selectivity or sensitivity.

Sensor functionality was validated *in vivo* using adult zebrafish, where it reliably measured intramuscular oxygen levels within the physiological range of 20–50 Torr. Measurements across multiple animals demonstrated reproducibility and agreement with expected tissue oxygenation. These findings establish such hydrogel-electrolyte oxygen sensors as a platform for minimally invasive, real-time monitoring of tissue oxygen levels, with strong potential for biomedical research and future clinical applications.

Acknowledgements

These selected examples of MEMS sensors for the body also represent the work of many students, postdocs, and collaborators over the years, which are detailed in the references below. Funding from DARPA, NIH, NSF, CDMRP, and private industry are gratefully acknowledged.

References

Mackay, RS and Jacobson, B. “Endoradiosonde,” *Nature* 179 (1957).

Allen MG. “Microfabricated implantable wireless microsystems: Permanent and biodegradable implementations,” *Proc. IEEE MEMS Conf* (2014).

Du L, Hao H, Ding Y, Gabros A, Mier TC, Van der Spiegel J, Lucas TH, Aflatouni F, Richardson AG, Allen MG. “An implantable, wireless, battery-free system for tactile pressure sensing,” *Microsystems & Nanoengineering*, 9(1):130 (2023).

Song N, Xie P, Shen W, Oh H, Zhang Y, Vitale F, Javanmard M, Allen MG. “A microwell-based impedance sensor on an insertable microneedle for real-time in vivo cytokine detection,” *Microsystems & Nanoengineering*, 7(1):96 (2021).

Venkatesh V, Burg L, Anderson VE, Zolkipli-Cunningham Z, Falk MJ, Allen MG. “Microfabricated electrochemical oxygen sensors with hydrogel electrolytes for in vivo applications,” *J. Micromechanics and Microengineering*, 35(12):125013 (2025).

DOI 10.5162/eurosensors2026/PT3

Intelligent Robots with a Sense of Smell – Challenges, Current State, and Future Directions

Achim J. Lilienthal
Technical University of Munich, Georg-Brauchle-Ring 60-62, 80992 München, Germany
achim.j.lilienthal@tum.de

Abstract:

In this plenary, I will describe how gas sensing, combined with the capabilities of intelligent robots, can be used for impactful real-world applications (e.g., environmental monitoring, industrial safety, infrastructure inspection, and emergency response) and the challenges that must be addressed to realize them.

I will present key results from my research on robots and sensor networks to detect, interpret, and map airborne chemicals, and autonomously localize gas sources using information-driven exploration to reduce search time. From early work that primarily highlights challenges of robotic gas sensing to the most recent approaches that combine chemical sensing, mobile robotics, probabilistic modeling, machine learning, and fluid dynamics. From naively using single gas sensors out-of-the-box to increasingly multimodal approaches combining gas (in situ or remote), wind, 3D, and increasingly visual sensing.

Finally, I'll describe ongoing and expected developments in the community towards more reliable, scalable, and adaptive robotic olfactory capabilities, highlighting dedicated measurement swarms, multimodal approaches combining physical models with data-driven intelligence, 3D modeling, Deep Learning-based gas distribution mapping, the possibility of large-scale self-supervised learning, offering the opportunity to move beyond handcrafted search strategies, and the emergence of olfaction foundation models that promise generalized olfactory reasoning from diverse experience.

Keywords:

Robotics, Artificial Olfaction, Sensor Networks, Gas Distribution Mapping, Gas Source Localization

References:

–

DOI 10.5162/eurosensors2026/PT4

Wearable Sensors of Flux from the Skin

John A. Rogers
Northwestern University, 2145 Sheridan Road, Evanston, IL 60208 USA
jrogers@northwestern.edu

Abstract:

Interdisciplinary research over the last fifteen years has established classes of advanced electronic and microfluidic systems that can conform to the soft, curved surfaces of the human body. Skin-interfaced, wireless wearable biophysical and biochemical sensors that leverage these technologies are now beginning to change the way that we approach patient care and health monitoring. This talk will briefly describe our on-going efforts in (1) microfluidic devices for collection, storage and biomarker analysis of microliter volumes of eccrine sweat [1,2] and (2) non-contacting sensors for quantitation of molecular gaseous flux into and out of the surface of the skin [3]. Highlighted activities span academic research to commercial translation.

Keywords:

wearables, sweat, transepidermal water loss, volatile organic compounds, wounds

References:

List and number all bibliographical references. When referenced within the text, enclose the citation number in square brackets, i.e. [1] (font Arial, font size 9, line spacing 1, spacing after 6 pt., alignment left)

[1] A. Koh, et al, A Soft, Wearable Microfluidic Device for the Capture, Storage, and Colorimetric Sensing of Sweat, *Science Translational Medicine* 8, 366ra165 (2016); doi 10.1126/scitranslmed.aaf2593

[2] D.S. Yang, R. Ghaffari, J.A. Rogers, Sweat as a Diagnostic Biofluid, *Science* 379, 760-761 (2023); doi: 10.1126/science.abq591

[3] J. Shin, et al, A Non-Contact Wearable Device for Monitoring Epidermal Molecular Flux, Nature 640, 375-383 (2025). doi: 10.1038/s41586-025-08825-2

DOI 10.5162/eurosensors2026/PT5

Managing Health through Remote Monitoring

Michael Snyder
Stanford University School of Medicine, 240 Pasteur Drive Palo Alto, CA 94304, USA
mpsnyde@stanford.edu

Abstract:

Our present healthcare system focuses on treating people when they are ill rather than keeping them healthy. We have been using remote monitoring approaches to monitor people while they are healthy to track their health and detect disease at its earliest moment presymptomatically. Using smartwatches we can detect disease early, including COVID-19. Using CGM we can subtype glucose dysregulation and monitor personalized responses to food. We have also developed microsampling technologies for monitoring responses to food and tracking physiological and biochemcial responses to lifestyle. We believe that advanced technologies have the potential to transform healthcare and keep people healthy.

Keywords:

Wearables, CGM, microsampling, precision medicine

References:

[1] Mishra, T., Wang, M., Metwally, A.A. *et al.* Pre-symptomatic detection of COVID-19 from smartwatch data. *Nat Biomed Eng* **4**, 1208–1220 (2020). https://doi.org/10.1038/s41551-020-00640-6

[2] Park, H., Metwally, A.A., Delfarah, A. *et al.* High-resolution lifestyle profiling and metabolic subphenotypes of type 2 diabetes. *npj Digit. Med.* **8**, 352 (2025). https://doi.org/10.1038/s41746-025-01728-6

[3] Shen, X., Kellogg, R., Panyard, D.J. *et al.* Multi-omics microsampling for the profiling of lifestyle-associated changes in health. *Nat. Biomed. Eng* **8**, 11–29 (2024). https://doi.org/10.1038/s41551-022-00999-8

DOI 10.5162/eurosensors2026/PT6

High-throughput optical biosensing with localized surface plasmon resonance imaging (LSPRi)

Attila Bonyár
Department of Electronics Technology, Faculty of Electrical Engineering and Informatics, Budapest University of Technology and Economics, Egry József Street 18., H1111, Budapest, Hungary
bonyar.attila@vik.bme.hu

Abstract:

Surface plasmon resonance (SPR) based biosensor devices have been on the market for more than four decades. Besides high sensitivity and label-free detection, the imaging capability of SPRi devices also enables high-throughput measurements with up to several thousand parallel measurement spots on a single sensor surface [1]. Localized surface plasmon resonance (LSPR) based sensors utilize nanostructures instead of thin films, and they offer several advantages compared to SPR, such as the possibility to maximize surface sensitivity by tailoring the nanoparticles' near field to the size of the used receptor/target molecules, and also the simpler, transmission-based optical setups [2]. However, to date, no LSPR imaging-based devices are on the market. The talk will address theoretical considerations for realizing and optimizing nanoparticle arrangements for use as LSPRi sensor elements and will present a technology for fabricating a tightly packed nanoparticle layer consisting of hexagonally arranged gold nanoellipsoids with tunable interparticle gaps, exhibiting high surface sensitivity [3]. A custom device that uses a simplified form of hyperspectral imaging to implement the LSPRi principle on a 4 mm by 5 mm sensor surface comprising patterned nanoparticle layers will also be introduced, along with practical applications for small-molecule sensing (DNA-DNA hybridization and aptamer-heavy-metal ion binding).

Keywords:

biosensors, plasmonics, LSPR imaging, nucleotide sensors, nanoparticles

References:

[1] J. Xu, P. Zhang, Y. Chen, Surface Plasmon Resonance Biosensors: A Review of Molecular Imaging with High Spatial Resolution, *Biosensors* 14(2), 84 (2024); doi: 10.3390/bios14020084

[2] A. Bonyár, Label-Free Nucleic Acid Biosensing Using Nanomaterial-Based Localized Surface Plasmon Resonance Imaging: A Review, *ACS Applied Nano Materials* 3(9), 8506–8521 (2020); doi: 10.1021/acsanm.0c01457

[3] T. Lednický, A. Bonyár, Large Scale Fabrication of Ordered Gold Nanoparticle–Epoxy Surface Nanocomposites and Their Application as Label-Free Plasmonic DNA Biosensors, *ACS Applied Materials & Interfaces* 12(4), 4804–4814 (2020); doi: 10.1021/acsami.9b20907.

DOI 10.5162/eurosensors2026/1.1.1

Sensor-on-LED: Visible-Light-Activated Gas Sensing Using Flame Spray Pyrolysis

Xiao-Xue Wang[1,2], Lutz Mädler[1,2]
[1] Mechanical Engineering and Process Engineering, University of Bremen, Germany
[2] Leibniz Institute for Materials Engineering IWT, Germany
x.wang@iwt.uni-bremen.de

Summary:

Visible-light-activated gas sensors require not only compact optical integration, but also sensing-layer fabrication compatible with wafer-level processing. In this work, we focus on the engineering of porous WO_{3-x} sensing layers directly deposited onto LED microchip arrays via flame spray pyrolysis (FSP). Using a 460 nm sensor-on-LED platform as a model system, we investigate how FSP deposition conditions define film thickness and surface chemistry. The resulting highly porous WO_{3-x} films enable efficient gas access, visible-light interaction, and scalable wafer-level integration without post-treatment.

Keywords: Flame spray pyrolysis, Visible-light-activation, LED-integration, Gas sensors, wafer-level.

Motivation

The physical separation between the light source and the gas-sensing layer remains a major limitation in visible-light-activated gas sensors, as it increases device complexity, optical losses, and integration challenges. Direct sensor-on-LED architectures offer a compact solution, but their practical implementation is often constrained by conventional SMOX sensing-layer fabrication processes, which may involve high-temperature post-treatment, extreme pH conditions, or mechanical stress. These factors can degrade LED luminescence and shorten device lifetime.

In this work, flame spray pyrolysis (FSP) provides a device-compatible direct-deposition route for porous WO_{3-x} layers on LED microchips. More importantly, FSP is not only an integration method, but also a processing tool for tailoring film thickness, nanoparticle-network structure, surface defect chemistry, and gas accessibility, all of which directly influence visible-light interaction and gas-sensing performance.

Method

Here, A GaN-based LED array was fabricated on one side of a 2-inch sapphire wafer, and WO_{3-x} gas sensing layer was deposited on the other side via FSP.

LED layer: GaN-based LED epitaxial layers, including an AlN buffer layer, Si-doped *n*-GaN layer, InGaN/GaN multiple quantum wells (MQWs), *p*-AlGaN electron blocking layer (EBL) and p-GaN layer were orderly grown on one side of a (0001) sapphire wafer *via* metal–organic chemical vapour deposition (MOCVD). Then, an array of flip-chip structures was fabricated on the GaN epitaxial layers. The size of each unit in the array was 600 µm × 600 µm, and the wavelength of the LED is 460 nm. By precisely adjusting the proportion of indium (In) within the material, the wavelength of the emitted light can be continuously and precisely controlled from the violet to the green range. After flip-chip fabrication, the sapphire substrate was thinned from the other side using mechanical grinding and subsequent chemical-mechanical polishing (CMP). This process reduced the wafer thickness to 150 µm while removing grinding-induced surface damage and maintaining optical and mechanical quality for further integration.

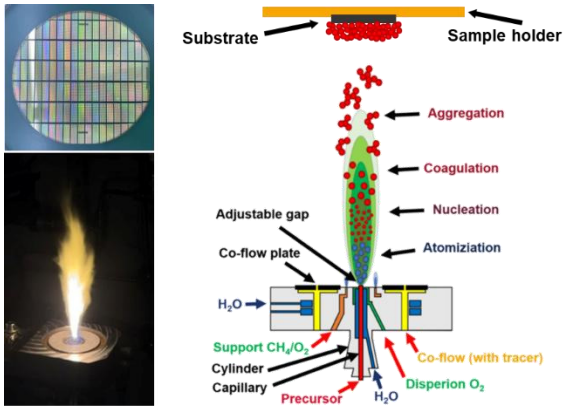

Fig. 1. FSP setup for the direct deposition of a porous sensing layer onto LED chips.

Gas sensing layer: Au interdigital electrodes were deposited on the opposite side of the sapphire wafer via photolithography and electron beam evaporation (EBE). The sensing layer was then directly deposited on top of the Au electrodes via FSP. During the deposition process, as shown in Fig. 1, the sample holder was placed at a defined height above the nozzle, and circulating cooling water was used to maintain the sapphire substrate temperature at approximately 120 °C. By adjusting FSP parameters such as precursor concentration, deposition time, methane/oxygen ratio, and dispersion oxygen flow rate, the WO_{3-x} film thickness, oxygen stoichiometry of WO_{3-x} surface defect chemistry can be tailored, thereby influencing light–matter interaction and gas sensing performance under visible-light excitation.

Results

As shown in Figure 2, The FSP-derived WO_{3-x} sensing layers formed highly porous nanoparticle networks directly on the LED microchip without post-deposition heat treatment. The films exhibited high crystallinity, approximately 97% porosity, nanoparticle sizes of about 15 nm, and a specific surface area of around 60 $m^2\ g^{-1}$. By adjusting FSP parameters, the film thickness, oxygen stoichiometry and defect-related surface chemistry could be tuned. These features regulate optical accessibility and charge-transport pathways under visible light illumination, thereby influencing visible-light-activated gas-sensing performance. The results demonstrate that FSP enables both wafer-level integration and process-controlled engineering of WO_{3-x} sensing layers for compact sensor-on-LED platforms.

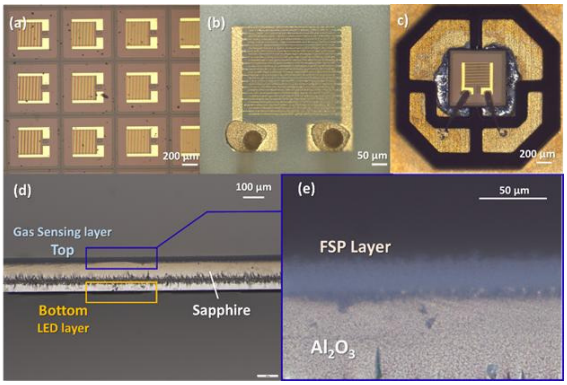

Fig. 2. Microscopy images of the (a) transparent gas sensing layer and Au interdigital electrodes (electrode spacing: 10 µm) after FSP, (b) and (c) after bonding; Cross-sectional microscopy images of (d) integrated microchip, (e) WO_3 gas-sensing layer by FSP.

References

[1] X.-X. Wang, S. Zhang, Y. Liu, J.-N. Dai, H.-Y. Li, X. Guo. Light-excited chemiresistive sensors integrated on LED microchips. *J. Mater. Chem. A*, 2021, 9, 16545–16553.

[2] B. Junker, A. Kobald, C. Ewald, P. Janoschek, M. Schalk, U. Weimar, L. Mädler, N. Barsan. Multivariate Analysis of Light-Activated SMOX Gas Sensors. *ACS Sens.* 2024, 9, 1584−1591.

DOI 10.5162/eurosensors2026/1.1.2

Direct Capillary-Based Printing of Porous Coordination Networks on CMOS E-Nose Sensor for Plant Disease VOC Detection

Stan Smit[1], Chunyu Huang[2], Jelco Albertsma[2], Tao Shen[3], Yihan Ouyang[3], Monique van der Veen[2], Frans Widdershoven[3,4], Peter G. Steeneken[1], Murali K Ghatkesar[1], Jasmin Aghassi-Hagmann[5] and **Murat Kabatas**[5,*]

[1]Department of Precision and Microsystems Engineering, TU Delft, The Netherlands
[2]Department of Chemical Engineering, TU Delft, The Netherlands
[3]Department of Microelectronics, TU Delft, The Netherlands
[4]NXP Semiconductors, The Netherlands
[5]Institute of Nanotechnology (INT), Karlsruhe Institute of Technology (KIT), Germany

**Contact:* m.kabatas@kit.edu

Summary:

Early detection of plant diseases can substantially reduce pesticide use, offering significant environmental and economic benefits. Agriculture consumes over 18,000 tons of pesticides annually in the EU alone, with 40–60% applied unnecessarily before disease symptoms manifest. Here, we present the surface functionalization of CMOS capacitive sensor arrays via SonoPlot direct writing of porous materials for low-power electronic nose (E-nose) applications. Utilizing advanced SonoPlot printing for precise material deposition, we functionalize sensor surfaces to optimize VOC adsorption, enabling real-time detection through capacitance changes. Our results show that a wide range of polymers and porous materials, including UV-curable inks, carbon nanoparticle-based polymers, metal-organic frameworks (MOFs) such as CAU-10 and CAU-23, and Prussian blue analogs (PBAs) such as CuPBA, exhibit high selectivity toward VOCs, including 1-nonanol, 2-nonanol, α-terpinene, tetradecane, 1-butanol, 2-butanol, 1-propanol, 2-propanol, ethanol, toluene, α-pinene, and water vapor. This research highlights the potential of SonoPlot printing technology to enable next-generation, high-performance, and cost-effective printable E-nose VOC sensors, offering significant promise for widespread environmental sensing applications.

Keywords: Metal organic frameworks (MOFs), Prussian blue analogues (PBAs), Volatile organic compounds (VOCs), Capacitive gas sensor, Electronic nose (E-nose)

Background, Motivation, and Objective

The intensification of global agriculture has led to a steep rise in pesticide use, with more than 18,000 tons applied annually in the EU, of which an estimated 40–60% is sprayed preventively before visible symptoms of plant disease appear [1]. This practice not only imposes high economic costs on farmers but also contributes to environmental pollution, biodiversity loss, and human health risks. Early, non-invasive detection of plant diseases is therefore essential to enable targeted treatment, reduce pesticide consumption, and support the UN Sustainable Development Goals on responsible production and climate action

Volatile organic compound (VOC) fingerprints emitted by plants and pathogens provide a powerful, label-free pathway for early disease diagnosis, often days to weeks before visual symptom onset. Electronic nose (E-nose) systems based on VOC sensing have shown promise in agriculture, environmental monitoring, industrial safety, and healthcare [2]. However, current E-nose platforms are often limited by high power consumption, poor selectivity, a lack of spatial-temporal resolution [3], and complex or costly

fabrication, hindering their deployment in large-scale, distributed sensor networks in the field.

A CMOS pixelated capacitive sensor (PCS) array offers an attractive route to low-power, highly integrated E-nose systems, but their performance critically depends on the functional materials and the changes in their dielectric constants upon VOC adsorption [4]. Each electrode (capacitor plate sensor) is 5 µm x 5 µm in size, separated from other sensors by 10 µm, in a 32 x 32 matrix format (Fig 1). Given their size, inkjet printing of diverse functional materials in pico-liter volumes with micrometer precision is a promising method for low-cost sensor functionalization [5].

The objective of this work is to demonstrate the feasibility of printing multiple inks with an ultrasonic-based inkjet printer (Sonoplot Inc., Germany) to detect multiple VOCs for plant disease detection. The CMOS-PCS array was printed with UV-curable polymer ink, carbon nanoparticle ink, and three types of porous coordination network (PCN) inks (within a binding UV-ink solution) – CAU-10, CAU-23, and CuPBA (Fig 1). Unprinted pixel sensors were used as reference sensors.

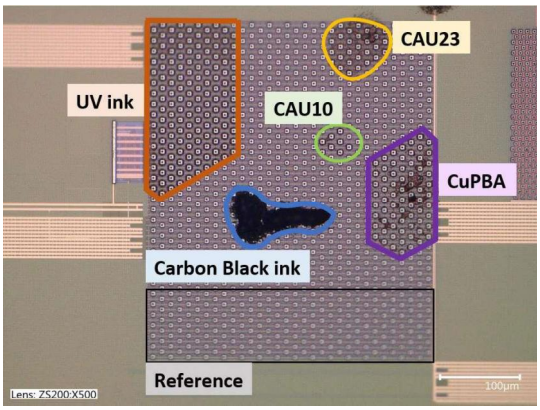

Fig. 1. Surface functionalized CMOS pixelated chip with multi-inks using an ultrasonic inkjet printer.

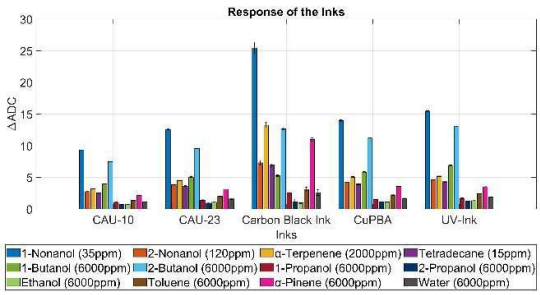

Fig. 2. E-Nose sensor's response to 11 different VOCs and humidity with 5 different inks functionalized on its surface. Tests were performed at parts-per-million (ppm) concentrations of VOCs.

The functionalized sensor array was tested for the detection of the following gases: 1-Nonanol, 2-Nonanol, α-Terpinene, Tetradecane, 1-Butanol, 2-Butanol, 1-Propanol, 2-Propanol, Ethanol, Toluene, α-Pinene, and water vapor (Fig. 2). Most of these VOCs are released by plants. The sensitivity in parts per million (ppm) and selectivity for VOCs of functionalized sensors are shown in Fig. 3. Our initial results indicate that the inks are selectively responsive to plant VOCs [4]. However, the inks of PCNs show a similar response to that of the pure UV ink. This indicates that the UV-ink in the ink solution plays a more dominant role than PCNs. Improving the ink formulation to address this point is ongoing work.

In conclusion, a low-power CMOS PCS array with 1024 sensors has been functionalized with 5 inks via inkjet printing and tested with 11 plant VOCs and humidity. The sensors respond to VOCs but lack selectivity, indicating that the response is dominated by the UV ink rather than the PBNs. As a next step, we optimize the ink formulation by increasing the PBN concentration.

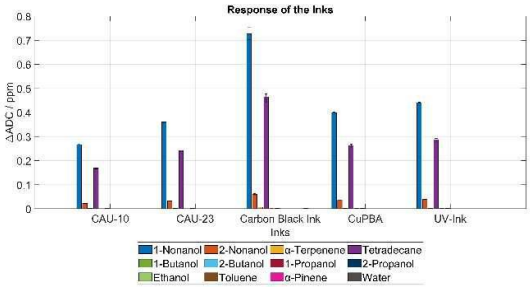

Fig. 3. E-Nose sensor's response to different concentrations of VOCs in ppm, indicating that inks can be very selective towards certain VOCs.

Funding:

This work is supported by the Karlsruhe Institute of Technology Excellence Strategy via the Young Investigator Group Preparation Program, by the Dutch National Growth Fund program NXTGEN High-tech (project Agrifood 11: Greenhouse Horticulture – Digital Twin), and by the Dutch Research Council (NWO) through the NWA-ORC 2020/21 program (grant NWA.1389.20.123).

References

1. Pereira, P., et al., *Impacts of agriculture intensification on biodiversity loss, climate change and ecosystem services.* Current Opinion in Environmental Science & Health, 2025. **46**: p. 100637.
2. Chen, Y., et al., *Hydrogen peroxide and hypochlorite responsive fluorescent nanoprobes for sensitive cancer cell imaging.* Biosensors, 2022. **12**(2): p. 111.
3. Chou, T.-I., et al., An Aging Drift Calibration and Device-Generality Network With Realistic Transfer Samples for Electronic Nose. IEEE Sensors Journal, 2023. 23(24): p. 30712-30719.
4. Kabatas, M., et al., *Capacitive Pixelated CMOS Electronic Nose.* arXiv preprint arXiv:2603.23537, 2026.
5. Najafabadi, S.A.N., et al., *Advancements in inkjet printing of metal- and covalent-organic frameworks: process design and ink optimization.* ACS Applied Materials & Interfaces, 2025. **17**(8): p. 11469-11494.

DOI 10.5162/eurosensors2026/1.1.3

Human Activity Recognition Using Distributed Colorimetric Chemical Sensors Based on CO2 and Formaldehyde Inks and Interpretable Machine Learning

Ismael Benito-Altamirano[2], Yansheng Chen[1], Maria Gonzalez-Gomez[3], Olga Casals[1], J. Daniel Prades[3], Cristian Fabrega[1]
[1] University of Barcelona, Marti i Franques 1 Spain,
[2] Universitat Oberta de Catalunya, Rambla del Poblenou, 154-156 Spain,
[3] Technische Universtität Braunschweig, ------ Germany
cfabrega@ub.edu

Summary:
This work presents a novel approach for human activity recognition based on distributed colorimetric chemical sensors using inks selective to carbon dioxide and formaldehyde. Sensor nodes were deployed in a pilot residential environment to capture spatial and temporal variations in indoor air composition during daily activities. Experiments followed a structured protocol and involved up to sixteen participants. Distinct activity dependent chemical signatures were observed. An interpretable machine learning model was used to classify activities from sensor data. Results demonstrate robust and privacy preserving activity recognition based on environmental chemistry.

Keywords: Colorimetric chemical sensors, Human activity recognition, Indoor air quality sensing, Distributed sensor Systems, Interpretable machine learning

Background, Motivation and Objective

Human activity recognition (HAR) is typically addressed using vision or motion-based systems, which may raise privacy concerns and require complex infrastructure. Chemical sensing provides an alternative by capturing indirect signatures of human activities through changes in indoor air composition. In this work, we explore HAR using distributed colorimetric sensors based on chemically selective inks for carbon dioxide (CO2) and formaldehyde (CH2O), combined with interpretable machine learning.

Description of the New Method or System

The sensing platform integrates two previously developed colorimetric inks: (i) a water-based ink for CO2 detection based on reversible amine–CO2 interactions and [1] (ii) a primary amine/pH-indicator ink for ppb-level formaldehyde detection based on imine formation reactions [2]. These inks were printed and embedded into multiple identical sensing nodes measuring CO2, CH2O, relative humidity, and temperature.

The sensing nodes were deployed at different locations within a pilot residential environment. A structured experimental protocol was designed to ensure reproducible activity patterns, including cooking, eating, dish cleaning, and hygiene-related tasks, each performed following predefined sequences and durations . Experiments were conducted under semi-controlled conditions involving up to 16 participants performing these activities across different locations within the dwelling.

The sensing system was implemented using a compact IoT platform integrating colorimetric sensors, environmental sensors, and a low-power microcontroller.

Results

Time-resolved measurements from the distributed sensing nodes reveal clear activity-dependent chemical signatures across different locations within the dwelling (Fig. 1). Cooking activities are characterized by strong temperature-driven responses and moderate CO2 variations, while cleaning-related activities, particularly dish cleaning, produce pronounced humidity increases and correlated CO2 responses, especially in sensors located near the kitchen sink. Formaldehyde signals exhibit lower amplitude but provide complementary information associated with specific indoor emission sources.

These results demonstrate that each activity generates a distinct temporal and spatial chemical fingerprint, enabling differentiation based on environmental sensing alone.

To further analyze the contribution of each sensing variable, a feature relevance analysis was

DOI 10.5162/eurosensors2026/1.1.3

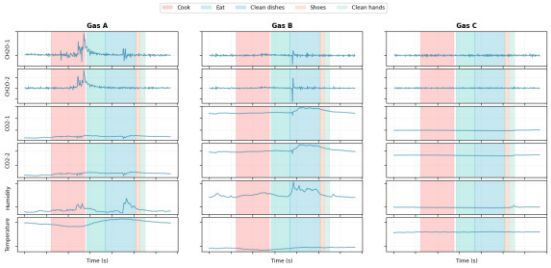

Fig. 1. Time-resolved signals from distributed colorimetric sensors based on CO2 and formaldehyde inks during controlled household activities. Distinct activity-dependent chemical signatures are observed across different sensing nodes, highlighting spatial and temporal variability in indoor air composition.

performed (Fig. 2). The results show that activity discrimination relies on localized sensor responses rather than global trends. Cooking activities are mainly associated with temperature and CO2 signals, particularly in specific sensing nodes, whereas cleaning activities are strongly correlated with humidity-driven responser and CO2 variations in other locations. This spatial differentiation highlights the importance of distributed sensing.

A lightweight and interpretable machine learning model was trained to classify activities from the sensor data. The results demonstrate robust discrimination between activities and improved generalization when combining multiple sensing locations. Feature importance analysis confirms that the model leverages physically meaningful variables, directly linked to the underlying

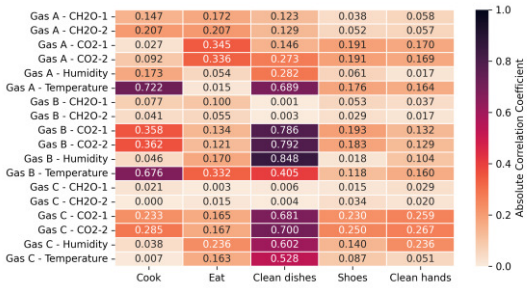

Fig. 2. Feature relevance analysis showing the contribution of each sensor signal to activity discrimination. Cooking activities are mainly associated with temperature and CO2-related responses, while cleaning activities are strongly correlated with humidity-driven signals, particularly in specific spatial locations.

sensing mechanisms of the inks. To better understand the contribution of each sensing variable, a feature relevance analysis was performed (Fig. 2).

Conclusions

This work demonstrates that combining chemically selective colorimetric inks with distributed sensing and interpretable machine learning enables reliable human activity recognition based solely on indoor air composition. The proposed approach provides a low-cost and privacy-preserving alternative to conventional HAR systems and highlights the potential of artificial olfaction for smart environment applications.

DOI 10.5162/eurosensors2026/1.1.4

Dielectric and DRIFTS Characterization of Ba-based NO_x Storage Materials for Radio Frequency based Dosimeters

Daniela Schönauer-Kamin, Fabian Fütterer, Johanna Baumgärtner, Thomas Wöhrl, Gunter Hagen, Ralf Moos
[1] Department of Functional Materials, University of Bayreuth, Universitätsstraße 30, 95447 Bayreuth, Germany
Correspondence to: functional.materials@uni-bayreuth.de

Summary:
A radio frequency-based approach for dosimeter-type NO_x detection using a Barium-containing NO_x storage material is demonstrated. Dielectric properties were investigated by the microwave cavity perturbation method during controlled NO_x storage. A clear linear correlation between dielectric losses and Ba-site utilization was established, demonstrating that the dielectric losses reliably reflect the stored NO_x dose. Operando DRIFTS and impedance measurements provided mechanistic insight, revealing nitrate and nitrite formation as the dominant storage species governing the electrical response.

Keywords: RF based NO_x dosimeter, Pt/Ba-Al_2O_3, Operando DRIFTS, Microwave Cavity Perturbation, dielectric properties, nitrite/nitrate formation

Motivation

Reliable detection and quantification of nitrogen oxides (NO_x) are of central importance in view of stringent air-quality regulations and the significant health impacts of NO_2. Conventional high-accuracy techniques such as chemiluminescence detectors are costly, maintenance-intensive, and only of limited suitability for widespread long-term monitoring. Classical gas sensors furthermore face challenges at low concentrations due to drift and signal noise. Gas dosimeters based on the temporal storage of NO_x going along with changes in materials properties offer clear advantages, especially for long-term measurements and direct detection of the NO_x dose. However, their applicability is often restricted by the low electrical conductivity of many NO_x storage materials. [1] Radio frequency (RF) based sensing concepts provide new opportunities, as they enable the detection of changes in dielectric properties. A detailed understanding of the relationship between NO_x storage properties and RF signal formation is therefore crucial for the development of robust RF-based NO_x dosimeters. DRIFTS investigations combined with impedance measurements provide mechanistic insights into the NO_x storage behavior.

Materials and Measurement Setup

A Barium-containing NO_x storage material with 16.9 wt.% Ba (NSC-Ba17) was prepared by impregnating a lanthanum-stabilized γ-Al_2O_3 support with an aqueous barium acetate solution. After calcination, $Pt(NH_3)_4Cl_2$ was added and a reduction step in forming gas was applied to form catalytically active platinum (0.6 wt%). [2]

The dielectric properties of the NO_x storage powders were determined using the microwave cavity perturbation (MCP) technique in a resonant cavity. The scattering parameter S_{21} was evaluated using a vector network analyzer. Shifts in the resonant frequency and quality factor of a defined resonance mode were used to derive the permittivity and dielectric losses. Measurements were performed at 350 °C in defined gas atmospheres during NO_x storage (here: 400 ppm NO_2) and regeneration. [3]

For operando DRIFTS and electrical characterization, screen-printed NO_x storage films were fabricated on heated alumina transducers equipped with interdigitated gold electrodes. These sensors were operated inside a DRIFTS cell that enabled simultaneous infrared spectroscopic and impedance spectroscopic measurements under defined NO_x exposure conditions. The time-resolved detection of nitrate and nitrite species was correlated with changes in the electrical properties of the storage films, allowing chemical storage processes to be directly linked to the resulting sensor signal. [4]

Results and Discussion

The NO_x sorption behavior and the dielectric properties of NSC-Ba17 investigated in the MCP setup at 350 °C are illustrated in Fig. 1. First, the course of measured NO_x concentration downstream the NSC-powder compared to the

reference NO_x concentration shows that NO_x is stored and the powder is almost fully loaded when a concentration of 400 ppm NO_x is reached downstream. The calculated Ba-site utilization $w_{Ba,NOx}$, which describes the proportion of available Ba sites converted during NO_x storage to Ba-nitrate, increases during NO_x storage and reaches a maximum loading of approx. 35 %. When the NO_x dosing is stopped (t = 300 min), desorption processes occur and by thermal initiated regeneration at 600 °C the sorbed NO_x species desorbs (visible by a distinct NO_x desorption peak in c_{NOx} and $w_{Ba,NOx}$ reaching zero). Meanwhile, the dielectric properties during NO_x loading are measured and the determined dielectric losses ε'' present a comparable behavior. ε'' increases during NO_x storage and becomes almost stable when the NSC-Ba17 is almost fully loaded with NO_x. A linear relationship between ε'' and the Ba-site utilization results, which is attributed to the formation of electrically more conductive nitrate and nitrite species during NO_x storage. This demonstrates that the dielectric losses provide a reliable cumulative measure of the NO_x dose, highlighting the suitability of this material for RF-based dosimeter-type NO_x sensing applications.

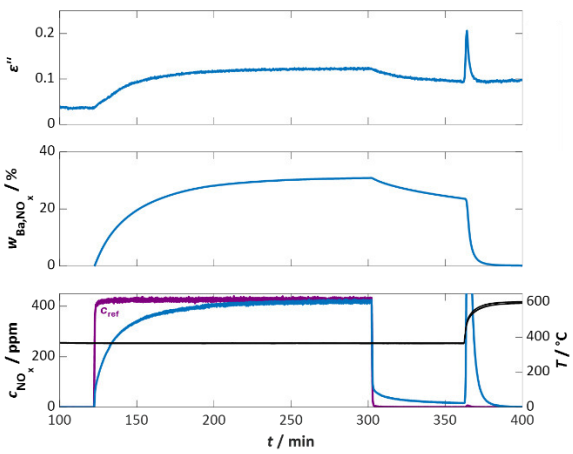

Fig. 1. Dielectric losses ε'' and NO_x storage behavior of NSC-Ba17 during NO_x sorption at 350 °C with calculated storage utilization $w_{Ba,NOx}$ and c_{NOx} measured downstream of the MCP setup by FTIR.

Operando DRIFTS measurements were conducted at 350 °C to elucidate the NO_x storage mechanism of NSC-Ba17 and its correlation with the capacitance (see Fig. 2). During exposure of a screen-printed NSC-Ba17 film to 2 ppm NO for 35 min, infrared spectra revealed the formation of both nitrite and nitrate species. The nitrite-related band (evaluated at 1220 cm^{-1}) rapidly saturates, while the nitrate band increases almost linearly throughout NO exposure. The course of the peak heights of the absorbance A of the nitrate and nitrite band clarifies this behavior. Simultaneously measured capacitance exhibited a pronounced increase ($\Delta C \approx 4$ fF), reflecting changes in dielectric permittivity associated with nitrite and nitrate formation. After stopping NO dosing, nitrite desorption was observed, whereas nitrate species remained stable and the capacitance signal stayed nearly constant. These results demonstrate that at 350 °C nitrite and nitrate formation dominate NO_x storage in NSC-Ba17 and that more stable nitrates seem to govern the observed electrical response, highlighting its suitability for dosimeter-type sensing.

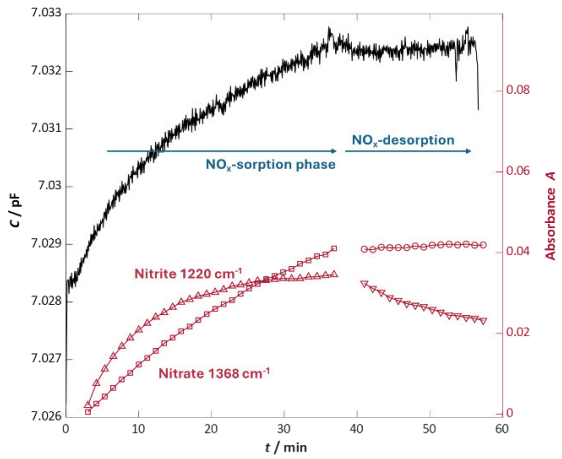

Fig. 2. Peak height of the absorbance A evaluated at 1220 cm^{-1} (denoted as nitrite) and 1368 cm^{-1} (denoted as nitrate) and the calculated capacitance C during 2 ppm NO exposure at 350 °C.

Combined RF characterization and operando DRIFTS provide consistent insights into the NO_x storage behavior of Ba-NSC-materials. Dielectric losses ε'' emerge as a robust, sensitive indicator of NO_x uptake, showing a clear linear correlation with stored NO_x and Ba site utilization until saturation. DRIFTS confirms formation of nitrite and nitrate species, with nitrates being stable and seem to predominantly govern the dielectric response. Overall, the results validate the dielectric properties as a reliable cumulative measure for RF-based dosimeter-type sensing.

References

[1] I. Marr, A. Groß, R. Moos, *Sensors* 13, 4428-4449 (2013); doi: doi:10.3390/s130404428

[2] S. Walter, J. Baumgärtner, G. Hagen, D. Schönauer-Kamin, J. Kita, R. Moos, *Sensors* 24, 2951 (2024); doi:10.3390/s24092951

[3] C. Steiner, S. Walter, V. Malashchuk, G. Hagen, I. Kogut, H. Fritze, R. Moos, *Sensors 20, 6024* (2020); doi:10.3390/s20216024.

[4] D. Schönauer-Kamin, I. Marr, M. Zehentbauer, C. Zängle, R. Moos, *Sens. Actuators, B* 320, 128568 (2020); doi:10.1016/j.snb.2020.128568.

Acknowledgment

Special thanks to the German Research Foundation (DFG, Deutsche Forschungsgemeinschaft) for funding the project ID: 465563965.

DOI 10.5162/eurosensors2026/1.2.1

Multiplexed, Label-Free InP Nanowire Photodetectors for Nanofluidic Single-Particle Sensing

Leon Seggering[1,2], Vidar Flodgren[3], Abhijit Das[3], Thomas Kjellberg Jensen[3], Joachim E. Sestoft[4], Jesper Nygård[4], Anders Mikkelsen[3], Irene Fernandez-Cuesta[1]
[1] University of Hamburg, Physics Department, 22761 Hamburg, Germany
[2] Deutsches Elektronen-Synchrotron (DESY), 22607 Hamburg, Germany
[3] Lund University, Department of Physics and NanoLund, 223 63 Lund, Sweden
[4] University of Copenhagen, Niels Bohr Institute, 2100 Copenhagen, Denmark
lseggeri@physnet.uni-hamburg.de

We demonstrate a label-free detection of single nanoparticles using individual InP nanowires integrated into nanofluidic chips. Nanochannels confine and guide liquid and particles, while nanowires transduce optical signals into electrical ones. A single nanowire resolves the transit of sub-micrometer particles as a transient dip in its photocurrent without fluorescent labels. A modular PCB readout setup is used to read the signal from the nanowires. This system has the potential to read multiple nanowires in parallel, which can be used in the future for multiplexing and to gain insights into particle characteristics, like size and flow speed.

InP nanowire, photodetector, nanofluidics, label-free detection, multiplexed readout.

Background, Motivation and Objective

Nanofluidic single-molecule analysis relies almost exclusively on fluorescence microscopy, which is limited to two optically aligned excitation spots per device and depends on fluorescent labelling of analytes [1]. Replacing this optical readout with an electrical one would eliminate alignment, remove labelling, and allow several sensing sites to be integrated along the same channel. Wafer-scale arrays of individually contacted InP p-i-n nanowires [2] enable a distributed electrical readout. We present a device in which nanowires, placed directly beneath a PMMA nanochannel, operate as label-free photoelectrical detectors of objects passing through the channel.

Device Concept

A single InP nanowire of 200 nm diameter contacted at both ends by Ti/Au builds a detection site. (Fig. 1) Shortage is prevented by a protective Al_2O_3 layer on top of the nanowire. A nanochannel is exposed directly above the nanowire by electron-beam lithography. The channel is sealed by a transparent polymer coverslip onto which microchannels and inlet holes have been transferred by UV-nano-imprinting [3].

Working Principle

Illumination from above generates photocarriers that drive a photocurrent. Transient changes in the photocurrent of then nanowire indicate a particle passing through the channel.

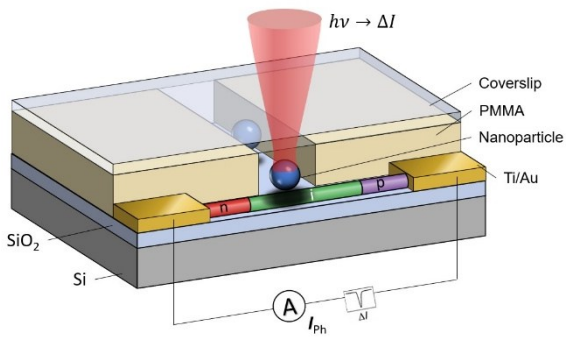

Fig. 1. Cross-section of the detection site. A 500 nm particle flowing through a 1 x 1 µm² PMMA nano-channel shadowing the laser. The InP p-i-n nanowire underneath produces a transient dip in the photocurrent. Each nanowire is individually contacted on both ends by Ti/Au contacts. The nanowire and contacts are covered with a 20 nm ALD Al_2O_3 layer to insulate from the analyte.

A two-board PCB readout addresses many detection sites in parallel. A microscope-slide-sized daughterboard holds the sample, with each nanowire wire-bonded to a PCB trace. A motherboard with BNC connectors accepts the daughterboard and routes each wire to its own measurement channel (Fig. 2). The modular format enables rapid sample exchange and parallel readout of several nanowires.

DOI 10.5162/eurosensors2026/1.2.1

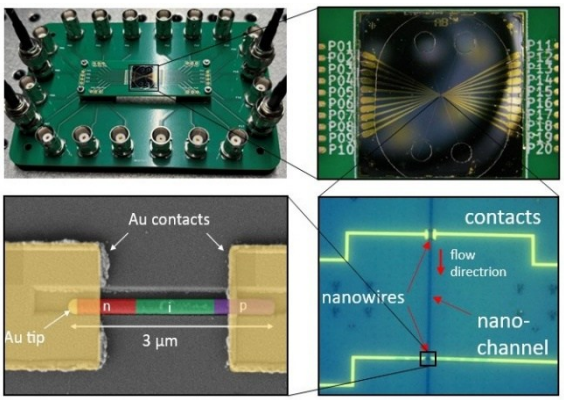

Fig. 2. Progressive zoom into the integrated sensor. From left to right: motherboard PCB with BNC outputs; daughterboard holding the wire-bonded sample; optical micrograph of the nanochannel crossing the nanowire array; and SEM of one nanowire contacted at n and p doped segment, nanochannel crosses perpendicular on top of the nanowire.

Results

Fig. 2 shows the device integration across different scales, from PCB to detection site.

The baseline photocurrent is stable under constant laser illumination and scales linearly with incident power (Fig. 3), consistent with the photoelectrical response reported for the same nanowire technology [2].

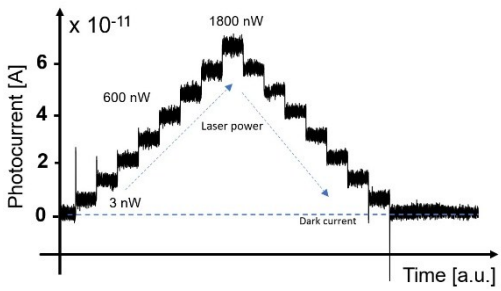

Fig. 3. Stepwise increase (3 nW → 1800 nW) and decrease of the incident laser power and the corresponding nanowire photocurrent. The current tracks the optical power in discrete, reversible steps and returns to the dark-current baseline, demonstrating the direct photoresponse of the contacted InP nanowire.

500 nm fluorescent polystyrene beads flown through the nanochannel produce each a transient dip in the nanowire photocurrent as they cross the illuminated region. Fig. 4 sketches the nanochannel at three consecutive time points (t_1, t_2, t_3) as a single bead travels through the laser spot above the nanowire. In the bottom Fig. 4 shows the corresponding photocurrent measurement. The dip reaches its minimum when the bead is directly over the wire (t_2) and recovers to baseline once the bead has left the focal spot (t_3). A simultaneous CCD recording confirms each dip corresponds to a single particle, not an electrical artefact.

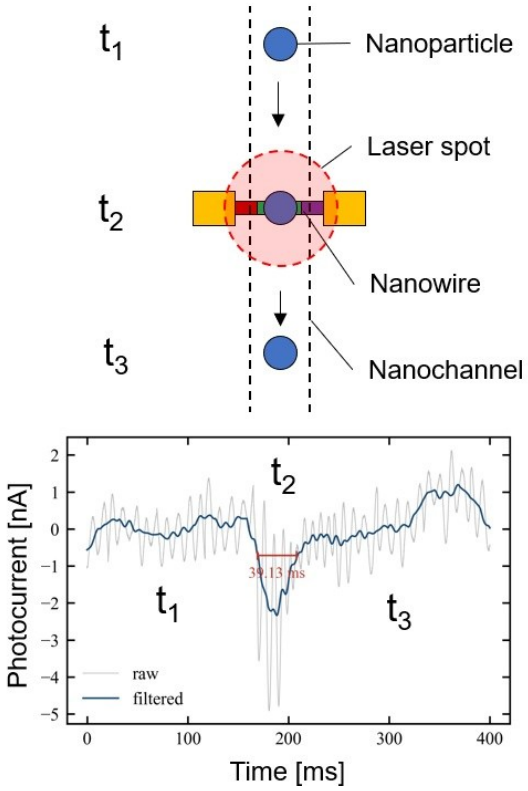

Fig. 4. (top) Sketch of a single nanochannel at three successive time points t_1, t_2, t_3. A nanoparticle flows top-to-bottom through the laser spot, crossing the nanowire at t_2. (bottom) Corresponding photocurrent trace (raw and filtered); the dip reaches its minimum at t_2 and recovers to baseline at t_3. FWHM ≈ 39 ms.

The readout is label-free and wavelength-agnostic above the InP bandgap (~925 nm) because it depends only on optical modulation at the nanowire. Combined with the multi-channel PCB, this yields a multiplexed, label-free platform for nanofluidic analyte detection.

Ongoing work targets three directions: parallel readout of several nanowires under one channel for on-chip time-of-flight velocimetry; channel geometries adapted to biomolecules; and full characterization of responsivity and noise floor using a supercontinuum source.

References

[1] F. M. Esmek et al., IEEJ Trans. Electr. Electron. Eng. 19, 840–844 (2024); doi: 10.1002/tee.24058

[2] V. Flodgren et al., Flexible fabrication of aligned multi-nanowire circuits for on-chip prototyping, Microelectron. Eng. 300, 112363 (2025); doi: 10.1016/j.mee.2025.112363

[3] I. Fernandez-Cuesta et al., J. Vac. Sci. Technol. B 29, 06F801 (2011); doi: 10.1116/1.365321

DOI 10.5162/eurosensors2026/1.2.2

Circuit-free Cardiovascular Monitoring via Electrically Passive Nanophotonic Patch for Sub-beat Hemodynamics

Torjus Steffensen[1], Vegar Stubberud[1], Eryk Winogrocki[1], Emilie Hennissen[1], Nils Kristian Skjærvold[1,2], Martin Steinert[1], Angelos Xomalis[1]

[1] Norwegian University of Science and Technology, Høgskoleringen 1, 7034 Trondheim, Norway
[2] St. Olav's University Hospital, Prinsesse Kristinas gate 3, 7030 Trondheim, Norway
torjus.l.steffensen@ntnu.no, angelos.xomalis@ntnu.no

Summary:

We report on a monolithic nanophotonic patch (OptoPatch) that converts arterial pulsation into camera-readable colour shifts via mechanochromic diffraction, removing the need for on-body electronics, batteries, or external optics. A single-material PDMS film carries a strain-sensitive metasurface on one face and a suction-cup adhesive on the other. In 13 volunteers recorded under hand-held smartphone imaging, OptoPatch recovers high-fidelity pulse waves, essential for highly deployable cardiovascular monitoring, and accesses inter-beat hemodynamics. Signal extraction is improved by gridded ROI tracking combined with harmonic SNR estimation.

Keywords: photonic, metasurfaces, mechanochromic sensing, wearable-sensor, smartphone, cardiovascular-monitoring, diffraction-based strain

Background

Continuous cardiovascular monitoring supports an expanding range of clinical and home-based care, but wearable sensors still rely on electrical transduction (electrocardiography (ECG), photoplethysmography (PPG)) with its associated circuitry, power and packaging overhead. Remote camera-based approaches such as remote PPG eliminate the on-body burden but access low-bandwidth features of the pulse wave through diffuse tissue transmission and remain sensitive to light-melanin interactions. Photonic-crystal and metasurface-based strain sensors have shown that mechanical-to-optical transduction can in principle be fully passive [1], yet published implementations typically require spectrometric readout, offsetting the practical advantage of a "wireless" front-end [2]. Truly circuit-free wearables recovering clinically meaningful pulse-wave morphology with commodity imaging hardware remain less explored.

We address this gap with OptoPatch, a single-material elastomeric patch whose surface diffracts ambient light into visible-spectrum colours that shift with the strain imposed by the underlying arterial pulse. The device avoids on-body electronics or complex optical interrogators; readout is by commodity RGB camera.

Sensor and Transduction Principle

OptoPatch is a monolithic poly(dimethylsiloxane) (PDMS) film carrying a surface-relief diffractive nano-patterned surface and a microscale structured adhesive surface on the opposite face. Both structures are replicated in a single casting step, using wafer-scale maskless photolithography and two-photon polymerization.The adhesive micro-suction-cup array provides residue-free, reusable adhesion to skin, allowing single-material pattern-transfer type fabrication.

Adhered over the radial artery, pulsatile arterial expansion elongates the diffractive structure along its periodic axis and locally tilts the film about the artery's curvature (Fig. 1) [3]. Both effects modulate the diffraction condition: periodicity elongation redshifts each order, and angular tilting changes which order reaches a fixed observation angle. Under broadband ambient illumination, the net result is a shift in observed colour. A camera recording the film surface produces an RGB time series that tracks diffraction-encoded deformation of the film induced by arterial diameter expansion. Because transduction occurs via surface diffraction at the film–air interface rather than through tissue-transmitted light, the mechanism is, by design, independent of dermal melanin absorption. As the active diffraction area spans several cm², and individual subregions experience non-uniform ambient illumination, local tissue curvature, and flexion.

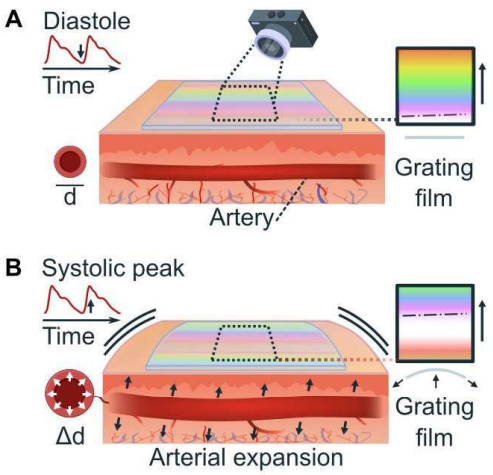

Figure 1: (A) OptoPatch above an artery. (B) The artery expands, shifting an observed diffraction pattern.

Single ROI-mean colour time series then dilutes the cleanest pulsatile regions with less informative ones. We divide the tracked ROI into an N × M patch grid and compute, for each patch and RGB channel, a harmonic signal-to-noise ratio (SNR) against a globally estimated fundamental frequency per sliding window. The output waveform is then the harmonic-SNR-weighted, polarity-aligned sum across patches and channels.

Results

In strain-mapped goniometry under uniaxial tension (0, 5, 10%) over observation angles 0–70° we observed RGB sequences matching Fresnel–CIE 1931 simulations. Alongside the broad angular window, in uniaxial tensiometer testing at P = 2100 nm, strains of order 0.2 - 2% produced colour shifts well above the camera noise floor, making hand-held imaging viable. No appreciable drift in amplitude was observed over 1000 strain cycles.

In 13 healthy, consenting volunteers, a 2100 nm period (3 × 3 cm² active area) OptoPatch was placed over the radial artery of the non-dominant hand and smartphone video recorded at 60 FPS under ceiling-panel illumination. Continuous non-invasive blood-pressure (cNIBP) reference (Finapres) was recorded simultaneously on the same limb. Fig. 2A compares patch fusion ("Composite") and conventional ROI-mean tracking ("Intensity). Fusion preserves harmonic structure across the full ~130 s recording; the ROI-mean trace degrades after ~40 s as the user shifts and the cleanest pulsatile pixels are averaged out. Fig. 2C shows beat-resolved correspondence. Ensemble-averaged OptoPatch and c-NIBP waveforms align, with reflected-wave onset resolvable in both channels. Median inter-channel magnitude-squared coherence from 0.5–8 Hz exceeded 0.7 across the cohort,

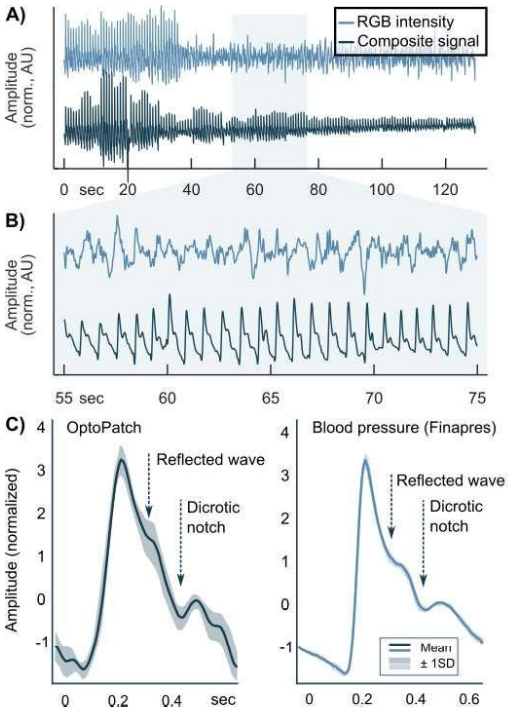

Figure 2: A: Recording from OptoPatch over 2 minutes. B: excerpt from A, indicating stability issues in simple ROI intensity tracking. C: Ensemble waveforms from OptoPatch (left) and cNIBP (right), indicating capture of sub-beat hemodynamic phenomena such as distal wave reflections.

demonstrating that the colorimetric signal preserves dynamic wave content beyond fundamental heart-rate tracking. Per-beat ensemble Pearson correlations had mean of 0.94, SD 0.034. These results indicate mechanochromic sensors as a potential avenue towards wireless, electrically passive cardiovascular sensors.

This work extends methods presented in [3].

References

[1] F. Romana Calabrò *et al.*, "Contactless pressure detection enabled by a hybrid 3D laser-printed nanophotonic sensor," *Journal of Materials Chemistry C*, vol. 12, no. 40, pp. 16478–16486, 2024, doi: 10.1039/D4TC01611D.

[2] R. Song, S. Cho, S. Khan, I. Park, and W. Gao, "Lighting the Path to Precision Healthcare: Advances and Applications of Wearable Photonic Sensors," *Advanced Materials*, p. 2419161, Jan. 2025, doi: 10.1002/adma.202419161.

[3] T. L. Steffensen *et al.*, "Circuit-Free Cardiovascular Monitoring via Smartphone-Readable Skin-Interfaced Nanophotonic Films," *Advanced Materials*, p. e74512, Aug. 2026, doi: 10.1002/adma.74512.

DOI 10.5162/eurosensors2026/1.2.3

Polymer-based Fiber Fabry-Perot Interferometer for Temperature Monitoring of *Operando* Lithium-Ion Batteries

Andrés Hernández-Pascual[1], David Monzón-Hernández[1], Monserrat Alonso-Murias[1], Erika Rodríguez-Sevilla[1], Joel Villatoro[2,3]*
[1] Centro de investigaciones en Óptica A.C., 37150, León, Guanajuato, Mexico
[2] Departamento de Ingeniería de Comunicaciones, University of the Basque Country UPV/EHU, 48013 Bilbao, Spain
[3] IKERBASQUE, Basque Foundation for Science, 48011 Bilbao, Spain
Corresponding Author's e-mail address: agustinjoel.villatoro@ehu.eus

Summary:
A microscopic Fabry-Perot interferometer made of a thermo-sensitive polymer deposited on the facet of a single-mode fiber is proposed for highly sensitive temperature sensing. The miniature interferometer was used for monitoring thermal effects in a rechargeable (lithium-ion) battery. The temperature changes in the battery due to electrochemical events that occur internally during the charge/discharge stages were successfully tracked, non-invasively, with the proposed sensor. Our sensors may be used for real-time diagnostics, safety assurance, and lifetime estimation of lithium-ion batteries.

Keywords: Optical fiber interferometer, temperature sensors, lithium-ion batteries.

Introduction

The use of lithium-ion batteries (LIBs) is being promoted globally due to their positive impact on achieving a carbon-neutral world. LIBs can be charged and discharged multiple times but is has associated risks such as fires and even explosions. Furthermore, maintaining the temperature controlled during the battery operation is crucial as overheating can affect stability, efficiency, capacity degradation, and hence the lifespan of such batteries. Thus, temperature in LIBs is a parameter that must be monitored continuously and ideally non-invasively.

Optical fiber sensors for rechargeable batteries have attracted considerable attention in the last few years [1]. These sensors provide electromagnetic immunity, are low weight, safe, and can provide precise temperature measurements in real-time. For example, it has been demonstrated that temperature sensors based on Bragg gratings are as accurate as electronic ones. Thus, fiber sensors have been used for temperature monitoring and control during battery charging/discharging processes.

Herein, we demonstrate that a polymer-capped fiber Fabry-Perot interferometer can be an alternative to monitor non-invasively temperature during the charging/discharging process of LIBs. We have selected a polymer as a temperature sensitive material because the temperature sensitivity of our interferometers is approximately one order of magnitude higher than that of sensors based on Bragg gratings.

Results

The structure of the interferometer is shown in Fig. 1. The fabrication steps are reported in [2]. Basically, a drop of commercial polymer (PMDS) is deposited on the flat facet of a conventional single mode fiber (SMF). Then, the polymer is cured at 60 ºC for 4 hours. The resulting dome had a height of 72 µm approximately. This polymer-capped fiber tip was calibrated as temperature sensor from 20°C to 60°C. To do so, we correlated the phase of the interference pattern with temperature. The phase observed at different temperatures and the calibration curve are shown in Fig. 1. The sensor exhibited a temperature sensitivity of 0.129 rad/°C. This is equivalent to 346.5 pm/°C, which is 34 times more sensitive than temperature sensors based on Bragg gratings (~10 pm/°C). Moreover, it is well known that polymers, PDMS in particular, respond faster than glass to temperature changes.

After the calibration of the sensor, it was used to monitor temperature changes in a commercial LIB (model INR18650-30Q) during the charge and discharge processes. The fiber interferometer was protected with a capillary tube to prevent its response from being influenced by other parameters such as humidity or dust particles. The protected sensor was positioned externally at the center of the battery.

DOI 10.5162/eurosensors2026/1.2.3

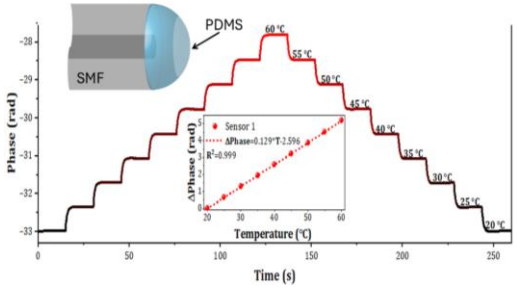

Fig. 1. Schematic of the polymer-based interferometer. SMF is single mode fiber. The graph shows the phase of the interference pattern at different temperatures. The calibration curve is shown in the inset graph.

A potentiostat was used for cycling the battery at different charge rates (C). The potentiostat was programmed to apply three charge/discharge stages with constant current densities at C-rates of C/5, C/3, and 1C. This cycling protocol was executed in conjunction with the acquisition of the optical signal from the interferometer. In this manner, the thermal changes in the LIB could be correlated with the voltage.

The voltage profiles obtained with the potentiostat over time and corresponding phase in the interference pattern and temperature changes are shown in Figure 2. It can be noted from the figure that during the discharge stages variations of approximately 1.5 ºC, 4°C and 14 °C for C-rates of C/5, C/3 and 1C, respectively, were measured with our device. As expected, more prominent phase or temperature changes were observed at faster charge rates.

The phase changes suffered by the interferometer are caused by the modification of the thermal properties of the PDMS cavity when the temperature in the battery increases. There is a greater temperature change during the charge/discharge stages at 1C rate in contrast with C/5. It can be principally associated to exothermic events that occur by electrochemical and resistive reactions of the battery.

The results shown in Fig. 2 demonstrate that minute temperature variations can be detected in the battery by means of the polymer-capped fiber tip. By tracking the phase of the interference pattern, the sensor response can also be more sensitive and accurate. Thus, monitoring temperature in a non-invasive manner can be reached without compromising the battery structure.

It is important to point out that currently, voltage differential analysis and temperature monitoring are used as quality parameters and lifespan of LIBs. The thermal evolution is usually associated with the degradation mechanisms in LIBs. In

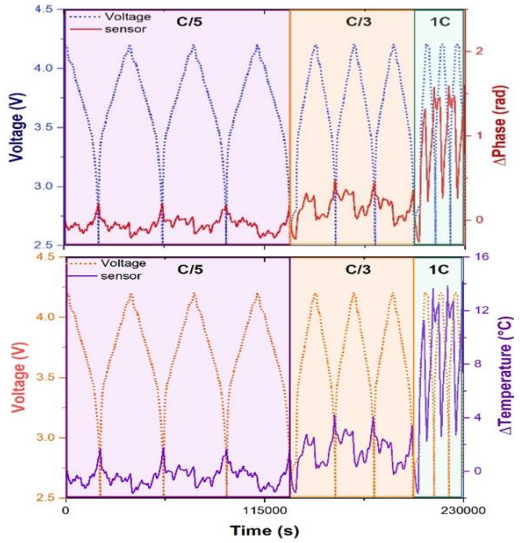

Fig. 2. Changes in phase (temperature) observed in the polymer-based interferometer during the charge and discharge stages of a rechargeable battery. The C-rates are indicated with the voltage profiles maintained.

some cases, the monitoring of temperature requires internal measurements due to the low sensitivity of the sensor used. In this work, we have shown how an easily manufactured, ultra-compact Fabry-Perot interferometer can be used to monitor non-invasively temperature changes of a LIB. More experiments are being carried out to investigate the feasibility of the sensor reported in the diagnosis for *operando* assessment of thermal behavior, safety conditions, and degradation pathway of LIBs. The results of these investigations will be presented at the conference.

ACKNOWLEDMENTS

This work was partially financed through the Spanish Ministry of Science, Innovation and Universities, the State Research Agency (MCIN/AEI/10.13039/501100011033) and the European Regional Development Fund (ERDF)/'European Union', under project PID2023-152763NB-I00.

References

[1] C. An, K. Zheng, S. Wang, T. Wang, H. Liu, L. Lin, Q. Deng, K. Zhang, N. Hu, “Advances in sensing technologies for monitoring states of lithium-ion batteries,” *Journal of Power Sources* 625, art. no. 235633 (2025). https://doi.org/10.1016/j.jpowsour.2024.235633.

[2] A. Hernández-Pascual, at al., “Non-invasive temperature monitoring of operando Lithium-ion batteries using polymer capped optical fiber tips,” Manuscript under review, *Journal of Power Sources* (2026).

DOI 10.5162/eurosensors2026/1.2.4

Trace Level Moisture Sensing using a Resonant Photoacousic Sensor with an LED as Light Source

Christian Weber[1,2], Andre Eberhardt[1], Mike Benkendorf[1], Katrin Schmitt[1,2], Jürgen Wöllenstein[1,2]
[1] Fraunhofer Institute for Physical Measurement Techniques IPM, 79110 Freiburg, Germany
[2] Department of Microsystems Engineering - IMTEK, University of Freiburg, 79110 Freiburg, Germany
christian.weber@ipm.fraunhofer.de

Summary:
Measuring the water content of gas mixtures is relevant in a large variety of industrial applications ranging from pressurized air to energy or process control applications. Here we present a novel photoacoustic sensor design that uses a LED with a wavelength of 2.7 µm and a radial resonator to achieve detection limits in the single-digit ppm region at averaging time of over 20 seconds. An 8-hour zero-gas measurement shows no drift over this period, enabling even lower detection limits with high averaging times.

Keywords: Photoacoustic, Resonant, LED, Water Sensing, Optical

Motivation

Trace-level moisture sensing is essential in a large variety of industrial applications [1]. Even very low water vapor concentrations in the low ppm to ppb range can cause damage to the productions equipment and reduce product quality in the semiconductor and chemical industries. Therefore, reliable detection methods are required for early detection of faulty conditions resulting in equipment failures, product recalls, and safety hazards while optimizing overall efficiency of processes.

Currently, trace level moisture is measured using a number of various methods that are either very complex (e.g. laser-spectrometers, dew point mirrors) or have slow response times are prone to drift and contamination, like capacitive sensors or quartz resonator sensors [2].

We present an LED driven photoacoustic (PA) moisture sensor that can bridge the gap between both technologies and provide a drift-stable sensing method with low sensor complexity.

Photoacoustic Sensor Design

High power LEDs are usually large and have an area of at least 1 mm². To guide a significant fraction of the light through a photoacoustic cell without wall interaction, a large cell aperture is necessary. The sensor presented in this work fulfills this requirement with a cylindrical resonator of 20 mm length and 8 mm length. The light of a mid-IR led with 2.7 µm peak wavelength and 3 mW optical power (nanoplus, Germany) is collimated by a parabolic mirror and a f=35 mm CaF_2 lens and then guided along the cylinder's axis through the cell. A silver-plated concave mirror (f=50 mm) at the outlet focuses the radiation back into the cell for a second pass. This concentrates the radiation intensity at the center of the cylindrical cell, leading to a high overlap integral with the first radial resonant mode. The radial mode also has a large Q-factor, making it ideal for photoacoustic measurements. With the dimensions of the cell, it is located around 21 kHz in air. The whole assembly, which is made of aluminum (see Fig. 1), has diameter of 48 mm and a length of 92 mm.

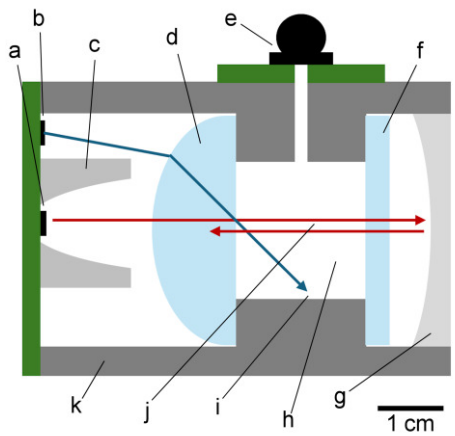

*Fig. 1. Simplified drawing of the Sensor setup: **a)** MIR-LED, **b)** tracking-LED, **c)** reflector, **d)** 35 mm CaF_2 lens, **e)** microphone, **f)** outlet CaF_2 window, **g)** concave mirror, **h)** resonant photoacoustic cavity, **i)** wall absorption providing a reference signal, **j)** photoacoustic signal generation in two passes, **k)** housing*

The acoustic signal is acquired by a MEMS microphone (SPV61A0L, Knowles, USA), amplified by a factor of 110 and bandpass filtered. It is then digitalized at 1 MSa/s and filtered by a point-by-

point FIR lock-in filter running on a PSoC6 (Infineon, Germany) based embedded system. The system also incorporates an LED driver and transmits the measured data to a host PC via USB. The resonance frequency is tracked by a second LED with 850 nm wavelength using the method described in [3].

Results and Discussion

The sensor was characterized in a gas measurement laboratory to determine its sensitivity and linearity. The time constant of the filter was set to 2 s and the LED was driven with 200 mA peak-to-peak. Relative humidity steps of 0 to 10% at 22°C at a flow rate of 0.1 l/min were applied to the sensor. The recorded measurement is shown in Fig. 2.

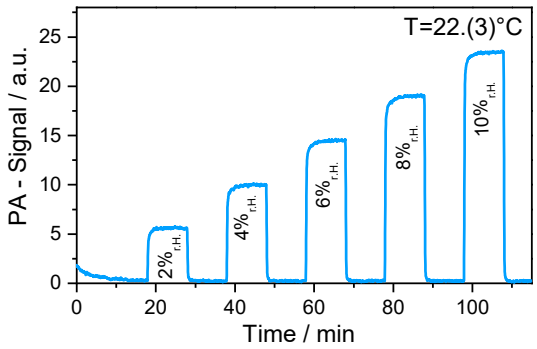

Fig. 2. Sensor response towards steps of 2 to 10% relative humidity in dry nitrogen.

Due to the low inner volume, the measurement values settle down with a time constant of approx. 2.4 s. A second time constant can be observed, that can probably be attributed to the water saturation of the sensor cell. All applied concentrations can clearly be resolved and no deviations in the nitrogen steps are observable, aside from the initial drop from ambient moisture. For a better evaluation of the linearity Fig. 3 shows the magnitude of each step along with the respective standard deviations. Typical for a PA sensor, the linearity is better than the noise in the system. A fit in Fig. 3 emphasizes this. The fit does not meet the Y-axis at 0 but rather at 1.25

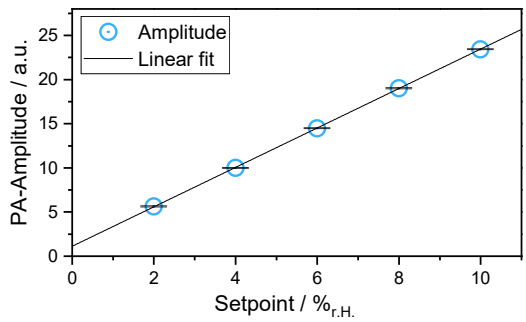

Fig. 3. Measured PA amplitude vs. Setpoint humidity together, along with the standard deviation of the steps. A fit emphasizes the sensor's linear behavior.

counts, which is also more than the offset in Fig. 2. This is likely caused by a systematic offset of the mass flow controller in the open state rather than being an actual measurement effect.

For the evaluation of the detection limits and noise, the sensor signal was recorded for 8.5 h with dry nitrogen applied. Fig 4. shows the result together with the Allan deviation calculated from it. The sensor signal was calibrated by a 1-point factor extracted from the 10%r.H. step (2650 ppm) from the previous measurement.

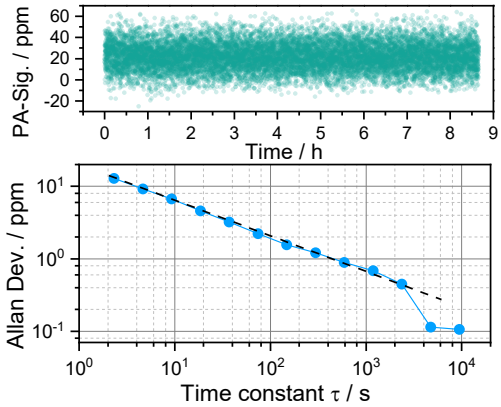

Fig. 4. Zero signal over a period of 8.5 h and the Allan deviation calculated from it. The dashed line indicates the slope of white noise.

The Allan plot shows no drift limitation over the observed time interval. Over a wide range of averaging times, the Allan deviation decreases by 10dB/decade indicating white noise. The noise equivalent concentrations are 12 ppm at 2s, 2 ppm at 60 s and 800 ppb at 1000 s. These correspond to noise equivalent dew points of -65°C, -72°C and -83°C.

Therse results demonstrate that photoacoustic sensing using mid infrared LEDs can provide a reliable and low-drift measurement of moisture down in the low ppm to the high ppb range. The sensor design can furthermore be compact and of low complexity.

References

[1] S. A. Ali, S. Malik, M. R. Mahboob and T. Islam, Moisture Measurement in Trace Level: Prospects, Challenges and Solutions, IEEE Instrumentation & Measurement Magazine vol. 28, no. 2, pp. 51-59, April 2025, doi: 10.1109/MIM.2025.10946254

[2] R. Fenner and E. Zdankiewicz, Micromachined water vapor sensors: a review of sensing technologies," IEEE Sensors Journal, vol. 1, no. 4, pp. 309-317 (2001), doi: 10.1109/7361.983470

[3] C. Weber, J. Kapp, J. Wöllenstein, K. Schmitt, Novel approach for efficient resonance tracking in photoacoustic gas sensor systems based on a light-induced wall signal, *Photoacoustics* 31 (2023); doi: 10.1016/j.pacs.2023.100495

DOI 10.5162/eurosensors2026/1.3.1

Colorimetric point-of-care detection of Enterococcus faecalis in urinary tract infection

*Maria M. Morim[1], Patrick Rupper[2], Stefanie Altenried[3], Adrian Meier[1], René M. Rossi[1], Qun Ren[3], Luciano F. Boesel[1] and Giorgia Giovannini[1]**
[1]Empa, Swiss Federal Laboratories for Materials Science and Technology, Laboratory for Biomimetic Membranes and Textiles, Lerchenfeldstrasse 5, CH-9014, St. Gallen, Switzerland.
[2]Empa, Swiss Federal Laboratories for Materials Science and Technology, Laboratory for Advanced Fibers, Lerchenfeldstrasse 5, CH-9014 St. Gallen, Switzerland
[3]Empa, Swiss Federal Laboratories for Materials Science and Technology, Laboratory for Biointerfaces, Lerchenfeldstrasse 5, St. Gallen 9014, Switzerland
.Corresponding Author: giorgia.giovannini@marionegri.it.

Summary:
Urinary tract infections are among the most common bacterial infections, often diagnosed through culture-based methods, which are time-consuming and costly. In this work, we developed a rapid, specific, and accurate point-of-care colorimetric sensor for indirect detection of *Enterococcus faecalis* in urine samples via its metabolite, L-lactate. The probe consists of silica nanoparticles loaded with MnO_2, functionalized with the enzyme lactate oxidase The probe allows both visual qualitative analysis and spectroscopy quantitative analysis.

Keywords: Point-of-Care device, Colorimetric sensor, Silica nanoparticle, Urinary tract Infection, ASSURED

Introduction

Urinary tract infections (UTIs) are among the most common bacterial infections, affecting up to 150 million people every year [1]. Currently, diagnosis is often made using culture-based methods, which are time-consuming, leading to the administration of antibiotics without a clear diagnosis [2]. Point-of-care (POC) devices may enable a fast and accurate UTI diagnosis, thereby improving treatment efficacy [3]**.** Colorimetric sensors, used as POC devices, present several advantages, including a colour change visible to the naked eye [4], being a simple, specific, and sensitive solution that supports the development of rapid, cost-effective, user-friendly, and affordable diagnostic tools that do not require complex or expensive equipment.

In this work, we developed a fast and cost-effective colour-based indirect method for the detection of *E. faecalis* in urine samples, through targeting its metabolic, L-lactate. The sensing probe (Lac@MnSNP) consists of silica nanoparticles loaded with manganese dioxide (MnSNP) and functionalized with the enzyme lactate oxidase. In the presence of L-lactate, an enzymatic cascade is triggered, with the production of hydrogen peroxide (H_2O_2). The presence of H_2O_2 reduces MnO_2 to MnO/Mn^{2+}, resulting in a visible colour change from brownish to colourless. The probe also allows a quantitative detection, through the monitoring of MnO_2 reduction by measuring the decrease in absorbance at 400 nm, apart from the qualitative detection.

Results

MnSNP particles were synthesized through the reverse microemulsion method and characterized through DLS and TEM, producing a homogenous suspension of nanoparticles with an average size of 158 $\pm$ 3 nm and a zeta potential of -34 $\pm$ 1 mV. The functionalization of MnSNP with lactate-oxidase led to an increase in the dynamic size to 1438 $\pm$ 52 nm, with the core particle size remaining similar to MnSNP (153 $\pm$ 1 nm for MnSNP and 105 $\pm$ 1 nm for Lac@MnSNP). The difference in dynamic size can be explained by the increase in surface charge in Lac@MnSNP to -13 $\pm$ 1 nm, which can promote nanoparticle agglomeration.

Lac@MnSNP at 2 mg/mL was treated against H_2O_2 with concentration ranging from 0 µM to

100 µM, to evaluate the detection efficacy of the probe. Results are reported as relative absorbance, calculated as the absorbance intensity at each H_2O_2 concentration divided by the untreated sample [I_n/I_0]. The absorbance signal of Lac@MnSNP decreased with increasing L-lactate concentration, decreasing in signal to 0.70 at 50 µM of L-lactate, and a calculated LOD of 31 µM (R^2 = 0.94) (Fig.1). These results confirm that Lac@MnSNP effectively catalyzes L-lactate, allowing a quantification through the detection of generated H_2O_2. The decrease in absorbance indicates the presence of *E. faecalis,* via the detection mechanism of the probe.

Urine is a complex matrix containing various components that could interfere with the probe's performance. To assess the potential matrix effect of the sample in the probe, Lac@MnSNP was tested in an artificial urine medium (AUM). Lac@MnSNP presented similar behaviour in both media, having a decrease in signal to 0.68 at 50 µM L-lactate in AUM, with an LOD of 47 µM (R^2 = 0.86), compared to 31 µM in DI water (Fig. 1). These findings indicate that the complex composition of AUM influences the sensitivity of the probe. Nevertheless, the probe remains suitable for the intended application, since bacteria associate with UTI's produce 59–241 µg/mL of L-lactate during UTIs [5], whereas normal urine does not typically contain L-lactate [6].

As a proof-of-concept, the responsiveness of the probe was evaluated, testing 2 mg/mL of Lac@MnSNP against the lactate-producing bacteria *E. faecalis* (Fig. 2). The increase of concentration of *E. faecalis* led to a linear decrease of the absorbance signal, reaching a saturation at 10^3 CFU/mL. Additional increase *of E. faecalis* to 10^4 and 10^5 CFU/mL resulted in higher absorbance signals, likely due to the detection range of the probe being exceeded. For bacterial concentrations up to 10^3 CFU/mL, it was calculated concentrations of L-lactate of 56 µM. The calculated concentrations of L-lactate are above the LOD of the probe (31 µM), showing the potential of the probe in detecting bacterial load up to 10^3 CFU/mL. Further details are available in the full manuscript [7].

Conclusion

We present a colorimetric probe for the indirect detection of *E. faecalis* in urine samples, based on its metabolite, L-lactate. This strategy enhances the reliability of detection in comparison to conventional pH-based methods. Additionally, the proposed method fulfills several criteria of the ASSURED criteria [2], being cost-efficient, with a simple preparation of the probe and the use of simple instrumentation for the measurement.

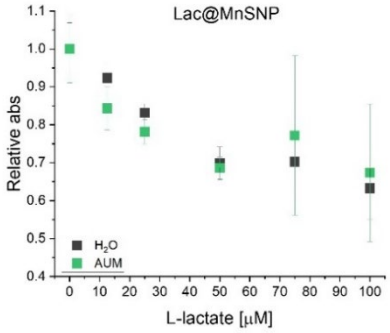

Fig. 1. Responsiveness of 2 mg/mL of Lac@MnSNP against L-lactate, in artificial urine medium (AUM) or water , after 4 h.

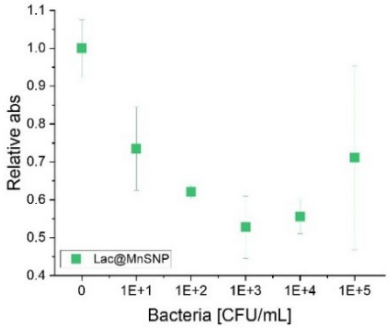

Fig. 2. Responsiveness of 2 mg/mL Lac@MnSNP against E. faecalis, after 5 h incubation

References

1. Medina, M. and E. Castillo-Pino, *An introduction to the epidemiology and burden of urinary tract infections.* Ther Adv Urol, 2019. **11**: p. 1756287219832172.
2. Pashchenko, O., et al., *A Comparison of Optical, Electrochemical, Magnetic, and Colorimetric Point-of-Care Biosensors for Infectious Disease Diagnosis.* ACS Infectious Diseases, 2018. **4**(8): p. 1162–1178.
3. Kettler, H., et al., *Mapping the landscape of diagnostics for sexually transmitted infections : key findings and recommendations / Hannah Kettler, Karen White, Sarah Hawkes*. 2004, World Health Organization: Geneva.
4. Rasheed, S., et al., *Advances and challenges in portable optical biosensors for onsite detection and point-of-care diagnostics.* TrAC Trends in Analytical Chemistry, 2024. **173**: p. 117640.
5. Gupta, A., et al., *1H-nuclear magnetic resonance spectroscopy for identifying and quantifying common uropathogens: A metabolic approach to the urinary tract infection.* BJU International, 2009. **104**(2): p. 236–244.
6. *<Aubron et al. - 2012 - Changes in urine composition after trauma facilitate bacterial growth.pdf>.*
7. Morim, M.M., et al., *Colorimetric point-of-care diagnostic to monitor Enterococcus faecalis causing urinary tract infection.* Journal of Materials Chemistry B, 2025. **13**(37): p. 11640–11651.

DOI 10.5162/eurosensors2026/1.3.2

Continuous Respiratory Rate Monitoring Using a Flexible Thermoelectric Sensor

Abi Johnson-Brett, Aimilios Angelopoulos, Rafail Zafeirelis, Harry Akerman, Ioannis Zeimpekis, Nick Harris, Neil White, Katrina A. Morgan
University of Southampton, Southampton, SO17 1BJ, United Kingdom
A.JohnsonBrett@soton.ac.uk

Summary:
Respiratory rate is an early indication of patient decline. A key limitation of continuous respiratory monitoring for hospital use is providing a non-invasive, low cost and easy to use system. Wearable sensors offer a continuous, lightweight and an unobtrusive solution. The proposed system combines a thin flexible thermoelectric sensor into a standard hospital grade oxygen mask with continuous Bluetooth connectivity and a selected algorithm. The proposed system is compared to a medical standard with a bias of -0.04, limits of agreement of -0.34 and +0.26 breaths per minute and successful apnoeic detection.

Keywords: Thermoelectric, Respiratory Monitoring, Clinical Comparison, Wearable, Flexible

Respiratory rate monitoring

Respiratory rate (RR) is a key physiological signal that can determine the beginning of patient deterioration for a significant number of medical conditions and if effectively monitored could allow for earlier intervention and improved patient outcomes [1]. Retrospective reviews show that abnormal vital signs including RR is prevalent up to 4 hours before an in hospital cardiac arrest [2]. Respiratory monitoring in hospitals is one of the most underdeveloped monitoring systems. General wards rely on nurses manually observing the RR of each patient. This measurement exhibits systematic bias with abnormal RR being underreported whilst causing a significant burden to clinical nursing staff.

Wearable sensors offer a continuous monitoring solution. They can spot abnormalities as they occur and reduce the burden on nursing staff by removing the need for spot checks. These sensors can improve patient comfort by improving mobility allowing for continuous monitoring whilst in the hospital. Fabricating a flexible, light, and sensitive sensor is a challenge. Current wearable respiratory sensors often require extra equipment leading to patient discomfort. Additionally commercial wearable devices have a focus on fitness which promotes miniaturisation over clinical accuracy.

Thermoelectric (TE) sensors convert the temperature gradients into a voltage output. During breathing, the temperature around the mouth fluctuates which produces a readable varying voltage output signal. TE sensors are self-powered therefore only the data logging and wireless connectivity require power producing a low power system. TE sensors can be flexible and lightweight hence easily integrable into wearable systems.

RR algorithms tend not to be publicly available, making comparison between different sensor systems difficult. This leads to problems in directly comparing the efficacy of a proposed system with a reference technology [3].

In summary, this work presents the development of a thin, lightweight TE sensor integrated into a standard oxygen mask providing wireless data transmission to a phone or laptop. The TE sensor and system layout is optimised for increased sensitivity whilst being easy to use. The RR algorithm, results and apneic detection is compared to a medical standard whilst maintaining a low power, low cost system.

RR sensing system development

A TE sensor with a planar structure has a high surface area allowing for a large active area which increases the sensor's sensitivity to small temperature fluctuations [4]. The optimum system layout includes a 3 TE pair in a planar structure with an active area thickness of 135µm and a Seebeck coefficient of 94 µV/K. The flexible sensor is integrated into a standard hospital grade oxygen mask through the ventilation gap. The location and adjustments of the sensor within the mask is optimised to maintain mask integrity whilst improving sensitivity and stability.

An external pcb (45mm x 25mm) is attached to the mask providing Bluetooth datalogging capabilities. The sensor system breathing detection and RR algorithm is compared to a medical standard. Final sensor system shown in figure 1.

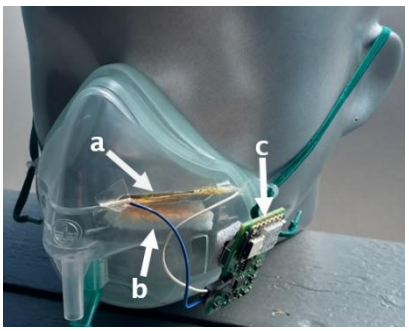

Figure 1. Image of TE based respiratory monitoring system in a standard oxygen mask worn by a life size mannequin. a - TE sensor. b - Foam barrier. c - External pcb.

Respiratory rate algorithm

The RR analysis was performed in MATLAB using a frequency-domain approach based on the fast Fourier transform (FFT) technique. The TE sensor voltage is detrended using a mean moving average as the baseline to remove any slow drift. A single sided FFT is applied to convert the time domain to frequency domain spectrum where the dominant frequency peaks correspond to the majority RR.

Respiratory rate measurements and results

The output respiratory signal of the complete sensor system (figure 2a) displays the key respiratory details including the expiratory pause.

The TE respiratory system is compared against the capnography machine, showing a bias of -0.04bpm (breaths per minute) and limits of agreement of [-0.34, +0.26] bpm for the RR algorithm calculations over a range of 8 to 18 bpm on one subject. The post-processed results from the TE sensor system (figure 2b) are compared with the proprietary post-processed results from capnography.

Testing abnormal respiratory breathing patterns is representative of real-world critical scenarios.

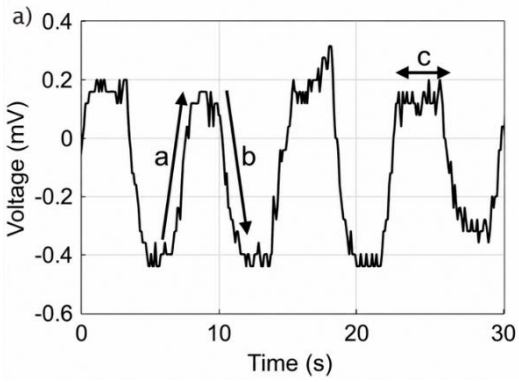

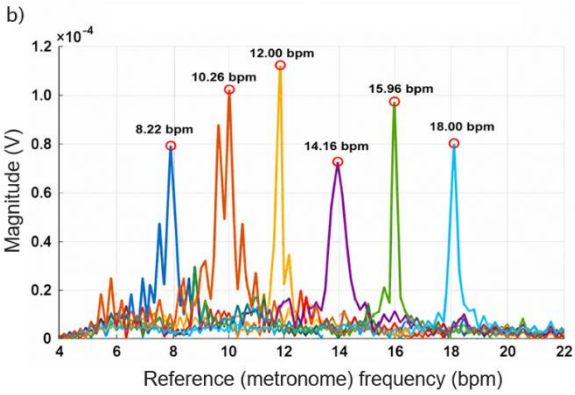

Figure 2. a) Output respiratory signal. a - Exhale. b - Inhale. c - Expiratory pause. b) Post processed RR FFT from range of 8 to 18 bpm.

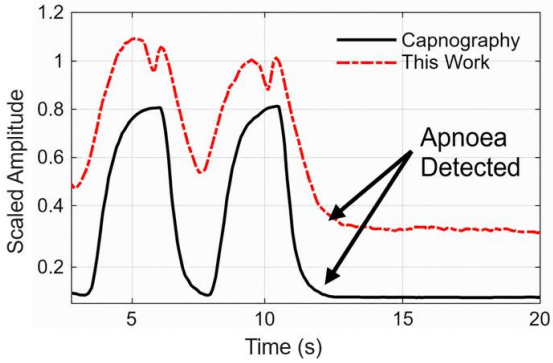

Figure 3. A comparison of the TE sensor system and the capnography results detecting apnoea.

The proposed sensor system closely matches the detection of the apnoea onset, figure 3. This demonstrates that the system can provide clinically relevant respiratory data while being minimally obtrusive. Future work will investigate a comparison between different respiratory algorithms for different respiratory types.

Funding

UKRI is funding Abi Johnson-Brett's PhD.

References

[1] S. A. S. Aglen et al., 'Respiratory Rate as a Predictor of Clinical Deterioration and Mortality: A Scoping Review', *Acta Anaesthesiol. Scand.*, vol. 69, no. 8 (2025) doi: 10.1111/aas.70113.

[2] L. W. Andersen *et al.*, 'The Prevalence and Significance of Abnormal Vital Signs Prior to In-Hospital Cardiac Arrest', *Resuscitation*, vol. 98, pp. 112–117 (2016) doi: 10.1016/j.resuscitation.2015.08.016.

[3] A.Nicolo et al., 'The Importance of Respiratory Rate Monitoring: From Healthcare to Sport and Exercise'. Sensors (2020) doi: 10.3390/s20216396

[4] X. Tang et al., 'Recent progress of biosensors based on thermoelectric effects for monitoring physical activity and environment monitoring', *Soft Sci.*, vol. 5, no. 1 (2025) doi: 10.20517/ss.2024.62.

DOI 10.5162/eurosensors2026/1.3.3

Comparative Assessment of Assimilating Probes and Molecular Beacons in Multiplex LAMP for Diagnostics

Ankita Mishra, Than Linh Quyen, Winnie Edith Svendsen, Maria Dimaki
DTU Bioengineering, Technical University of Denmark
DK-2800 Kgs. Lyngby, Denmark
Corresponding author: amis@dtu.dk

Summary:

Despite widespread use of fluorescent probes in LAMP diagnostics, role of probe architecture in contributing to threshold time (Tt), independent of primer efficiency, remains unclear in multiplex assays. This gap limits rational probe selection for point-of-care applications. Here, we present a structure/function analysis framework comparing assimilating probes (APs) and molecular beacons (MBs) in multiplex LAMP targeting respiratory viruses. Briefly, APs out performed MBs in Tt and signal-to-background ratio for most of the targets in singleplex and multiplex reactions. These findings highlight the critical role of probe selection in developing multiplex LAMP assays for rapid diagnostics.

Keywords: Loop mediated isothermal Amplification (LAMP), respiratory viruses, assimilating probes, molecular beacons, point-of-care (PoC) diagnostics.

Background

Recurrent outbreaks of respiratory and zoonotic viruses including avian influenza, COVID-19, and beyond, underscores urgent need for rapid, field deployable, multiplexed diagnostic assays. Loop mediated isothermal amplification (LAMP) is an ideal choice owing to its isothermal operation, specificity, and compatibility with resource limited settings. However, multiplex LAMP in a PoC format, is heavily affected by two major constraints i.e. inter-target primer competition that distorts amplification kinetics, and the choice of fluorescent probe architecture, which directly governs sensor response time, signal fidelity, and deployment feasibility. Assimilating probes (APs) operate via strand displacement, i.e. a fluorophore labelled oligonucleotide hybridizes to the amplicon loop region and displaces a quencher labelled complement, generating real-time signal and potentially accelerating amplification kinetics [1, 2].

Molecular beacons (MBs) are hairpin structures that fluoresce upon target-induced conformational opening, with locked nucleic acid (LNA) modifications conferring enhanced thermal stability and specificity [3, 4]. While each probe type has been individually deployed in LAMP assays, a fundamental mechanistic question remains unanswered: whether threshold time (Tt) in multiplex LAMP is only governed by differences in primer amplification efficiency and/or by probe architecture? Here, we present a structure/function analysis framework that involves parallel evaluation of both architectures within the same multiplex system.

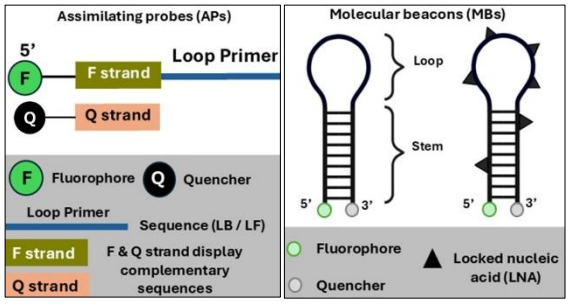

Figure 1: Left: Assimilating probe design; Right: Molecular beacon in closed conformation.

Methodology

For decoupling probe architecture from primer efficiency, APs and LNA-MBs were evaluated in parallel LAMP reactions targeting respiratory viruses and an eGFP reporter as internal amplification control, under identical conditions. Inner primer concentrations were systematically adjusted to mitigate inter-target amplification competition and restore balanced kinetics in the duplex format. Sensor performance was assessed based on quantitative fluorescence descriptors, like Tt, relative fluorescence signal ($\Delta F/F_0$), signal-to-background ratio (SBR) etc.

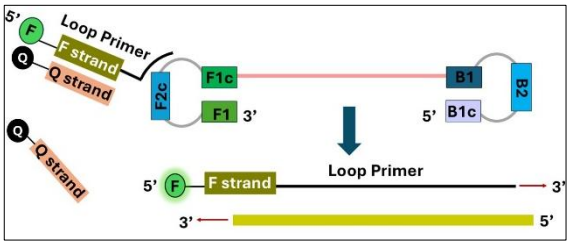

Figure 2A: Quencher strand displacement from F strand upon target recognition (working of APs).

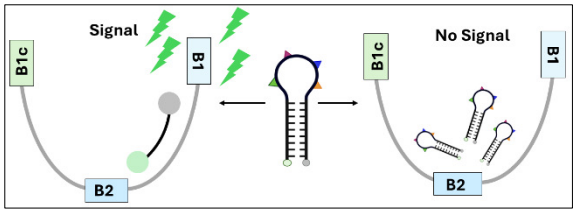

Figure 2B: Open and closed conformation of LNA incorporated molecular beacons.

Results

APs mostly outperformed LNA-MBs across tested reaction formats, for most of the performance descriptors. For instance, in singleplex, APs achieved a Tt of ~14 min, ~15 min, 9 min and 10 min for Influenza A, Influenza B, SARS-CoV-2 and eGFP, respectively. While LNA-MBs showed a Tt of <20 min (for Influenza A & B) and ~10 min (for SARS-CoV-2 & eGFP), respectively. Similarly, SBR for APs was higher for Influenza A & SARS-CoV-2. While SBR for eGFP was comparable among the two probe types.

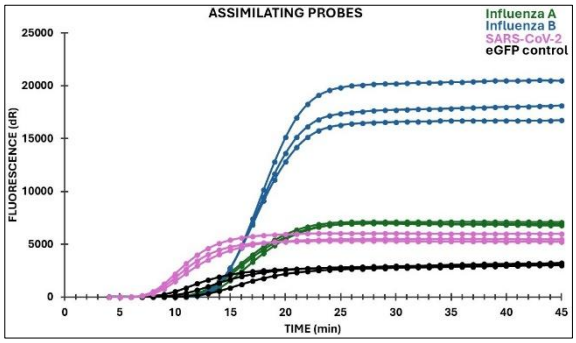

Figure 3A: Amplication plots with APs (singleplex).

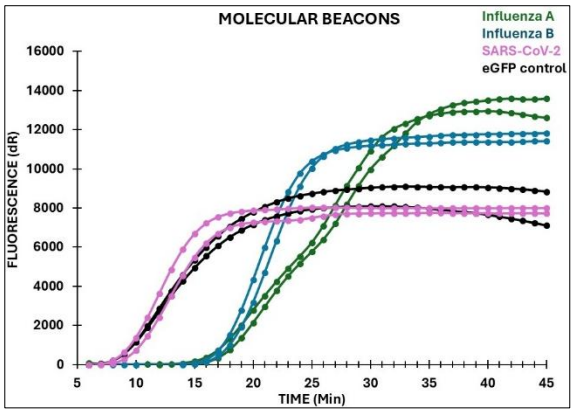

Figure 3B: Amplication plots with MBs (singleplex).

In case of duplex reaction, APs for Influenza A and SARS-CoV-2, with eGFP, respectively, showed a Tt of around ≤ 22 min. While MBs showed a Tt of 35 min and 25 min for Influenza A and SARS-CoV-2 with eGFP, respectively. Furthermore, in duplex reaction, MBs for Influenza A, B & SARS-CoV-2 displayed a reduced SBR, as compared to the performance in singleplex reaction. In general, amplification was delayed in duplex reactions as compared with singleplex assays. However, the delay was more pronounced for MBs than APs. Also, signal strength for MB influenza A was reduced, likely due to partial opening of the hairpin loop structure during isothermal amplification.

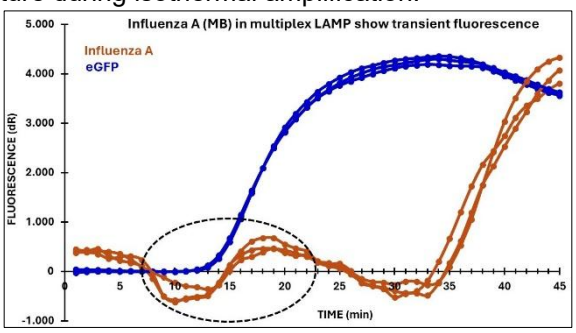

Figure 3C: Transient fluorescence observed for Influenza A (MB) in duplex reaction.

Overall, strand displacement mechanism of APs enabled an earlier fluorescence signal, as compared to conformational switching of LNA-MBs. Additionally, LNA integration in stem/loop region of MBs might also delay the opening and closing mechanism resulting in a late fluorescent signal. Both probe architectures demonstrated spectral orthogonality and channel independence. Additionally, lyophilized AP and MB probe types maintained their amplification capability after storage, demonstrating compatibility with cold chain independent deployment and the potential for shelf-stable, cartridge based diagnostics.

Conclusion

AP based multiplex LAMP architecture described here is scalable, field-deployable, and cost-effective. APs are particularly well-suited for optical point-of-care systems, owing to compatibility with lyophilization and low per-assay cost than alternatives. This platform holds translational potential for pandemic preparedness, zoonotic surveillance, and rapid field diagnostics.

References

[1] R. Kubota, A. M. Alvarez, W. W. Su, D. M. Jenkins, FRET-based assimilating probe for sequence-specific real-time monitoring of loop-mediated isothermal amplification (LAMP), *Biological Engineering Transactions* 4, 81–100 (2011); doi: 10.13031/2013.38509

[2] R. Kubota, D. M. Jenkins, Duplex loop-mediated isothermal amplification (LAMP) by assimilating probes, *International Journal of Molecular Sciences* 16, 4786–4799 (2015); doi: 10.3390/ijms16034786

[3] S. Tyagi, F. R. Kramer, Molecular beacons: Probes that fluoresce upon hybridization, *Nature Biotechnology* 14, 303–308 (1996); doi: 10.1038/nbt0396-303

[4] P. Bakthavathsalam, G. Longatte, S. O. Jensen, M. Manefield, J. J. Gooding, Locked nucleic acid molecular beacon for multiplex detection of loop mediated isothermal amplification, *Sensors and Actuators B: Chemical* 268, 255–263 (2018); doi: 10.1016/j.snb.2018.04.081

DOI 10.5162/eurosensors2026/1.3.4

Multimodal Textile-Based Wearable System for Upper-Limb Motion and Heart Rate Monitoring in Rehabilitation

C. Alglave[1], G. Jodin[1], A. Laarabi[2], J. Schoch[1], C. Depontailler[1], A. Marin[3], J. Prioux[4] and F. Razan[1]
[1] Univ Rennes, ENS Rennes, CNRS, IETR - UMR 6164, Rennes, 35170, France,
[2] SII Ouest, 3b Av. de Belle Fontaine, Cesson-Sévigné, 35510, France
[3] Inria, CNRS, ENS Rennes, Univ Rennes, IRISA, Bruz, France
[4] Movement, Sport and Health Laboratory (EA 1274), UFR APS, Rennes 2, France
Corresponding author: florence.razan@ens-rennes.fr

Summary:

Continuous upper-limb monitoring is essential for rehabilitation outside clinical environments. This paper presents a textile wearable system for synchronized motion and heart rate monitoring. A piezoresistive textile sleeve combined with an LSTM-based network enables elbow angle estimation, with a normalized error of 8.43% against Kinovea reference angles. Heart rate is estimated using photoplethysmography and an electrocardiography sensor with errors below 10%. The system enables unobtrusive monitoring of both kinematic and physiological parameters for rehabilitation assessment outside clinical settings.

Keywords: wearable sensing, textile sensors, multimodal monitoring, heart rate, upper-limb motion

Background, Motivation and Objective

Human motion analysis is essential for rehabilitation and functional assessment [1], especially for upper-limb monitoring in daily life. Optical motion capture systems such as Qualisys provide high accuracy but require controlled environments [2]. Markerless vision-based methods are more flexible but remain sensitive to occlusions and lighting variations [3], while wearable inertial sensors suffer from drift and cumulative errors [4]. Textile-based sensors offer a flexible alternative for motion capture [5]; however, their nonlinear behavior and inter-subject variability complicate accurate estimation, motivating data-driven modeling approaches [6]. Heart rate is widely used to assess exercise intensity and physiological state [7]. Although multimodal wearable systems are emerging [8], motion and physiological data are still often analyzed separately, limiting the understanding of their interaction. This work proposes a wearable multimodal system for synchronized analysis of kinematic and physiological signals, with potential relevance for rehabilitation monitoring. Kayaking-like movements were chosen as a demanding case study because they combine repetitive arm motion and varying intensity.

Description of the System

The system enables synchronized acquisition of motion and physiological signals using a textile-based sensing device with embedded modules. The device consists of a wearable sleeve embedding piezoresistive sensors around the elbow joint to measure deformation through resistance variations. Signals are acquired wirelessly via BLE. Experimental characterization reveals nonlinear behavior and inter-sensor variability due to non-uniform strain distribution, motivating data-driven modeling. Physiological data are collected using an electrocardiography (ECG) chest strap (Polar H9) and a photoplethysmography (PPG) module (WPSE340), the latter being processed for peak detection and heart rate estimation. Synchronization between camera and Arduino acquisitions enabled the extraction of Kinovea reference angles for model training and validation. Experiments were conducted on a SkiErg2 ergometer configured in kayak mode to reproduce kayaking posture and motion in a controlled environment (Fig.1).

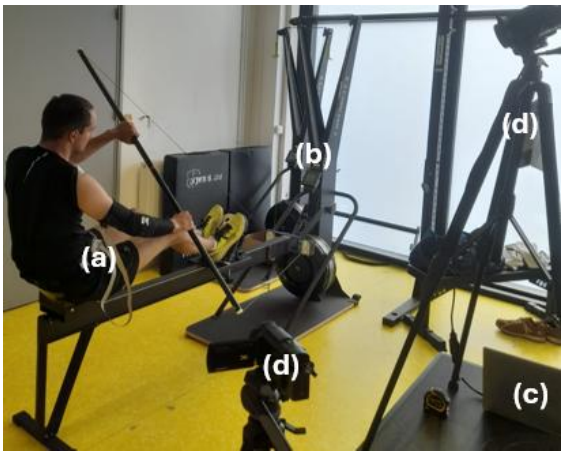

Fig. 1. Multimodal acquisition setup (M2S platform, Bruz, France): (a) textile sleeve and heart rate measurement, (b) ergometer, (c) acquisition system, (d) color (RGB) cameras.

Motion estimation was performed using an LSTM-based neural network, chosen because the textile sensor signals form temporal sequences and elbow angle evolution depends on previous time steps. The system combines textile sensing and physiological monitoring in a portable multimodal framework.

Results and Discussion

The system was evaluated on kayaking-like upper-limb movements under controlled dynamic conditions. The LSTM-based model enabled elbow angle estimation, with a normalized error of 8.43% against Kinovea reference angles. Model architecture and training details will be provided in the full presentation. The textile signals and predicted angle reflect movement dynamics across different phases (Fig. 2). Heart rate was estimated from PPG and ECG measurements, with errors below 10% during high-intensity activity.

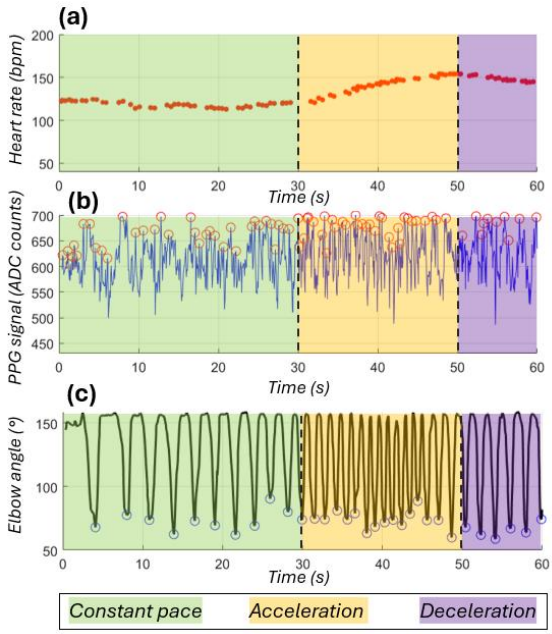

Fig. 2. Multimodal monitoring of upper-limb motion and physiological signals. (a) Heart rate measured using an ECG chest strap. (b) Raw PPG signal with detected peaks. (c) Predicted elbow angle. The shaded regions correspond to different movement phases (constant pace, acceleration, deceleration).

The synchronization of kinematic and physiological signals reveals a clear relationship between movement dynamics and cardiovascular response, illustrating the coupling between motion and physiological state. These results highlight the potential of combined motion and heart rate monitoring to assess exercise intensity during upper-limb activity, which is highly relevant for rehabilitation. Overall, the system enables robust multimodal monitoring in controlled dynamic conditions, extending its applicability to performance analysis and health monitoring.

Conclusion

This work presents a portable multimodal wearable system combining motion tracking and physiological monitoring. By capturing both kinematic and cardiovascular responses, the system enables accurate motion estimation and highlights the relationship between movement dynamics and physiological response. This approach opens the way to continuous and unobtrusive assessment of motor performance and exercise intensity outside clinical settings.

Acknowledgments

This work was supported by the ANR through the PIA EUR DIGISPORT project (ANR-18-EURE-0022) and the France 2030 program, ESOS (ANR-23-CMAS-0007), as well as by SII group (Paris, France).

References

[1] J. Strandberg, A. Pini, C. K. Häger, L. Schelin, *Analysis Choices Impact Movement Evaluation: A Multi-Aspect Inferential Method Applied to Kinematic Curves of Vertical Hops in Knee-Injured and Asymptomatic Persons*, Front. Bioeng. Biotechnol. 9 (2021) 645014. doi:10.3389/fbioe.2021.645014.

[2] B. Baker, Measuring walking: a handbook of clinical gait analysis, Mac Keith Press (2013).

[3] Z. Cao, G. Hidalgo, T. Simon, S. Wei, Y. Sheikh, OpenPose: Realtime multi-person 2D pose estimation using part affinity fields, IEEE Trans. Pattern Anal. Mach. Intell. 43, 172–186 (2021); doi: 10.1109/TPAMI.2019.2929257

[4] A. M. Sabatini, Inertial sensing in biomechanics: a survey of computational techniques bridging motion analysis and personal navigation, Sensors 11, 639–672 (2011); doi: 10.4018/978-1-59140-836-9.ch002

[5] L. Yin, X. Sun, Textile-based sensors for human motion sensing: recent developments and future perspectives, Nanocomposites 11, 79–98 (2025); doi: 10.1080/20550324.2025.2477392

[6] S. Gong, W. Schwalb, Y. Wang, et al., A wearable and highly sensitive pressure sensor with ultrathin gold nanowires, Nat. Commun. 5, 3132 (2014); doi: 10.1038/ncomms4132

[7] A. Achten, A. E. Jeukendrup, Heart rate monitoring: applications and limitations, Sports Med. 33, 517–538 (2003); doi: 10.2165/00007256-200333070-00004

[8] S. Patel, H. Park, P. Bonato, L. Chan, M. Rodgers, A review of wearable sensors and systems with application in rehabilitation, J. Neuroeng. Rehabil. 9, 21 (2012); doi: 10.1186/1743-0003-9-21

DOI 10.5162/eurosensors2026/1.4.1

Combined Physical and Digital Sensor Twin for Monitoring Fresh Fruits in the Cold Chain

Reiner Jedermann[1], Tuany Gabriela Hoffmann[2], Pramod Vasantrao Mahajan[2]
[1] University Bremen, IMSAS, 28205 Bremen, Germany,
[2] Leibniz Institute for Agricultural Engineering and Bioeconomy (ATB), 14469 Potsdam, Germany
rjedermann@imsas.uni-bremen.de

Summary:

The proposed sensor twin design enables easy installation and wireless measurement of fruit quality relevant parameters during cold storage. The system was tested using 11 sensor twins in a 50-ton commercial apple cold room. Comparing dew point and fruit temperature revealed critical conditions leading to condensation on the fruits. Reliable communication was achieved from within the fruit stacks for signal path lengths up to 4 m, with packet losses < 3.5%, signal-to-noise ratio > 5 dB, and signal attenuation of 16 dB/m.

Keywords: LoRa, physical twin, packet losses, cold chain, humidity sensors, LoRaWAN

Background, Motivation and Objective

Maintaining high fruit quality during cold storage and in the logistic chain requires keeping environmental parameters within recommended ranges and continuously tracking of deviations. Direct humidity measurement inside fruit stacks is essential to capture microclimatic conditions that are not represented by ambient air sensors. The temperature difference between fruit surface and surrounding air plays a key role in processes such as water condensation on the fruit, evaporation, mass loss and microbial growth.

Installation of wired probes is mostly not feasible in bins or boxes with fruits under commercial cold chain handling conditions. The performance of LoRa in industrial IoT applications was analyzed in [1] but data for fruit storage environments is still scarce. Wireless communication in such environments suffers from high signal attenuation by the high moisture content of fruits.

Description of the New Method or System

The proposed system combines extended sensing capabilities of a physical twin with its digital counterpart [2] to run prediction algorithms for condensation and mass loss, and later convert these indicators to a prediction of quality risks.

The physical twin mimics a cluster of 4 apples using plastic spheres of 8 cm diameter, filled with a hydrogel material, which provided similar thermal properties to real fruits (Fig. 1). The electronics consist of a Sensirion STS35 sensor for surface temperature of the spheres, SHT45 for air humidity and temperature, and wetness sensors for direct measurement of condensation. The latter one consists of a finger structure with 0.3 mm spacing on a 0.1 mm thick flexible PCB. Sensor data are processed on a STM32 Nucleo microcontroller and transmitted by a RN2483 LoRa radio. LoRa communication uses different spreading factors (SF). Lower SFs mean longer battery lifetime [3], shorter airtime, but reduced communication range.

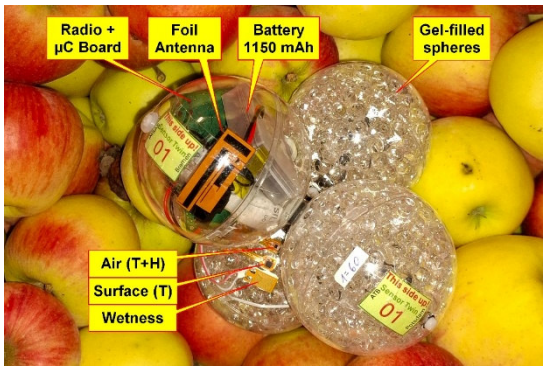

Fig. 1. Physical sensor twin components

The physical twins were placed in apple bins (1.2 m · 1 m · 0.75 m / 300 kg capacity) within the top layer of fruits. A commercial cold storage room was filled with 154 bins, arranged with vertical and horizontal gaps of 0.1 m width between bins. Two LoRa gateways were installed, one under the ceiling and one above the door.

Results

Various types of events, e.g., setpoint changes, can increase the dew point above the fruit surface temperature (Fig. 2). Such dew point undershoots (DPU) mark the beginning of water condensation on the fruit. In addition to an earlier

analysis of DPUs [4], this contribution focuses on the communication performance of LoRa in fruit cold storage. The 868 MHz band is less affected by fruits compared to standard 2.4 GHz communication [5].

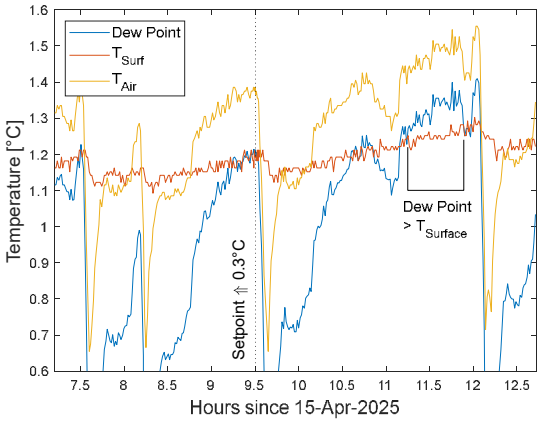

Fig. 2. Dew point rises above surface temperature after set point was increased by 0.3°C. Condensation on fruit surface is expected during the marked period

Signal-to-noise ratio (SNR), radio signal strength indicator (RSSI), packet losses, and sensor battery voltage were read out via The Things Network (TTN). Communication performance was tested for two scenarios: a) fixed SF values from 7 to 11, and b) automated setting of SF by the server.

RSSI is almost independent of SF and mostly depends on the length of the signal path through fruit (SPF). Signal attenuation was measured to 16.5 dB/m (Fig 3). Sensor-J had a higher RSSI due to the free air space at the door side.

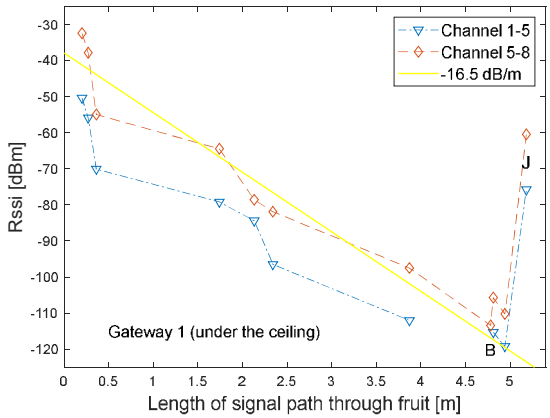

Fig. 3. Drop of signal strength (RSSI) by 16 dB/m

Additionally, a dependency on the radio channel was detected. The receiver implementation on the gateway uses different radio chips resulting in average RSSI that was 13.5 dB higher for channels 6 to 8 compared to channels 1 to 5.

Packet losses remained stable at max. 3.5% for SPF < 4 m. Combining the data of two gateways lowered to packet losses to 1.5%. Radio transmissions with SF 11 showed higher losses. SF 11 requires 4 times longer airtime than SF 9 and is, therefore, more affected by collisions and by occasional distortions, e.g., the gateway switching from receiver to transmission mode for downlink messages.

SNR drops for SPF > 4 m (Fig. 4). Sensor-B was buried between the apples. It had a 15 dB lower SNR than sensors in the top layer of fruits. Even for the highest SF, the packet losses increased to 14% or 64% for the two gateways.

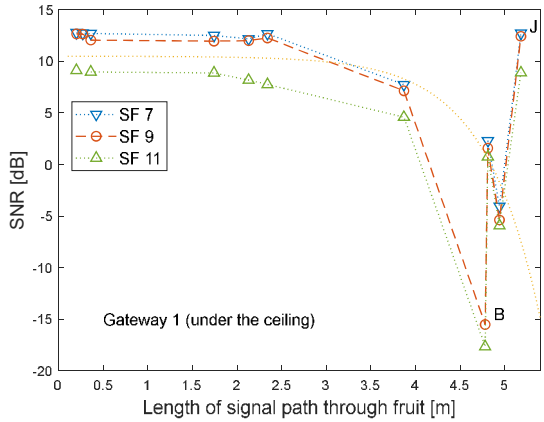

Fig. 4. Signal-to-noise ratio (SNR) for different SF

The theoretical battery life for transmissions in intervals of 150 s was calculated to 10 months. In practice, battery life of only 4 months was achieved due to low temperature conditions. Power consumption can be further reduced by collecting two sensor measurements before transmitting a combined packet.

References

[1] M. Luvisotto, F. Tramarin, L. Vangelista, S. Vitturi, On the Use of LoRaWAN for Indoor Industrial IoT Applications, *Wireless Communications and Mobile Computing* (2018); doi: 10.1155/2018/3982646.

[2] R. Jedermann, K. Singh, W. Lang, P. Mahajan, Digital twin concepts for linking live sensor data with real-time models, J. Sens. Sens. Syst. 12 (2023); doi: 10.5194/jsss-12-111-2023

[3] M.S. Philip, P. Singh, Energy Consumption Evaluation of LoRa Sensor Nodes in Wireless Sensor Network, *Advanced Communication Technologies and Signal Processing (ACTS),* IEEE, (2021); doi: 10.1109/ACTS53447.2021.9708341

[4] R. Jedermann, T.G. Hoffmann, D.A. Neuwald, F. Büchele, P.V. Mahajan, Dew point undershoot mechanisms driving surface condensation in commercial apple cold storage, *Postharvest Biology and Technology* 236 (2026); doi: 10.1016/j.postharvbio.2026.114264

[5] R. Jedermann, M. Borysov, N. Hartgenbusch, S. Jaeger, M. Sellwig, W. Lang, Testing Lora for food applications, *Procedia Manufacturing* 24 (2018); doi: 10.1016/j.promfg.2018.06.026

DOI 10.5162/eurosensors2026/1.4.2

Continious Monitoring of Glyphosate in Water

Nataša Budimirović[1], Alexandra Beard[1], Tristan Kipfer[1], Raphaël Pugin[1] & Sylvain Nicolay[1]
[1] Centre Suisse d'Electronique et de Microtechnique SA (CSEM), 2002 Neuchâtel, Switzerland
natasa.budimirovic@csem.ch

Summary:

Reliable detection of glyphosate remains challenging, particularly in real water samples. Here, we present a modification-free electrode that directly oxidizes glyphosate as a promising route to a robust detection system. Additionally, we show how dynamic conditions under microfluidic flow enhance mass transport and improve the detection limit compared with static operation, while a molecularly imprinted polymer preconcentrator mitigates matrix effects from common interferents. Together, these elements enable a proof-of-concept continuous sensing scheme for monitoring glyphosate in water.

Keywords: glyphosate, environmental monitoring, electrochemical sensor, microfluidics, molecularly imprinted polymer

Introduction

Glyphosate has been widely used since its commercialization in 1974, with further expansion following the adoption of glyphosate-tolerant crops [1]. Growing attention to potential health and environmental impacts has led to region-specific regulatory thresholds. In the European Union, authorization currently extends to 2033 and the drinking-water limit is set at 0.6 nM, whereas in the United States the corresponding limit is 4.1 μM [2]. Consistent with its extensive application, glyphosate and its main metabolite aminomethylphosphonic acid (AMPA) are frequently detected in soils, waters, and foods [3], underscoring the need for sensitive environmental monitoring.

Current reference methods for glyphosate quantification rely on laboratory-based chromatography, typically high-performance liquid chromatography (HPLC) coupled to fluorescence detection or mass spectrometry (including tandem MS) [2]. However, these approaches do not enable continuous, in-situ monitoring. In this regard, electrochemical sensing provides a potential route to field-deployable, real-time detection, and selectivity has been pursued using molecularly imprinted polymers (MIPs), aptamers, metal-organic frameworks, and enzyme layers. Despite encouraging results, translation to robust products remains limited by matrix effects in real samples and by manufacturing constraints that impact reproducibility, operational stability, and selectivity [4]. Here, we evaluate a functionalization-free electrochemical approach based on the direct oxidation of glyphosate at gold electrodes, aiming to improve robustness, reversibility, scalability, and long-term stability. We further assess dynamic operation under microfluidic flow to enhance mass transport and lower the limit of detection, and we integrate a MIP-based preconcentration step to mitigate matrix effects and enable detection at lower glyphosate concentrations.

Results

Direct electrochemical oxidation of glyphosate was first characterized by cyclic voltammetry (CV), comparing the response of the bare gold electrode in supporting electrolyte (blank) with that obtained after addition of glyphosate. A distinct oxidation peak is observed at ≈ 0.65 V vs Ag/AgCl (Fig. 1). This potential region was therefore selected for chronoamperometric detection using a fixed potential (Fig. 1, inset).

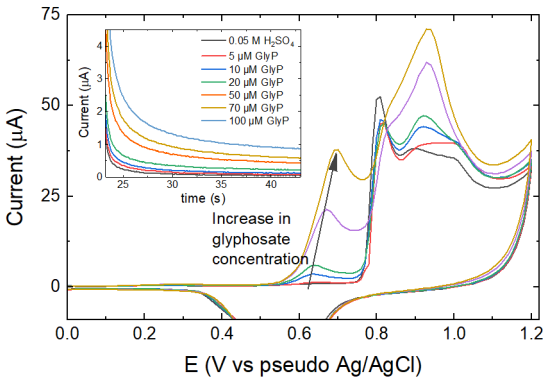

Fig. 1. Cyclic voltammetry of different glyphosate concentrations in 0.05 M H_2SO_4 (up to 1 mM) and inset showing chronoamperometry at 0.7 V vs Ag/AgCl.

Notably, the chronoamperometric current increases with increasing glyphosate concentration. The signal can be sampled at different times during the potential hold, yielding distinct

calibration sensitivities. Figure 2 shows calibration curves taken out at readout of 2 s in 0.05 M and 0.5 M H_2SO_4. Interestingly, the performance is comparable in both acidic solutions, with a limit of detection (LOD, ≈ 5 μM) and sensitivity (≈ 135 $nAmM^{-1}cm^{-2}$).

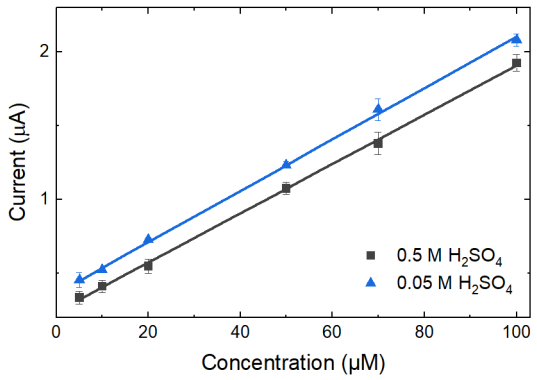

Fig 2. Calibration curves in 0.05 M and 0.5 M H_2SO_4 at 0.7 V and 0.75 V vs Ag/AgCl, respectively.

Although these results validate the sensing concept and agree with prior work [2], LOD remains substantially above the regulatory threshold for drinking water. To improve sensitivity, we implemented hydrodynamic measurements using a flow cell. Forced convection enhances mass transport to the electrode, increasing the oxidation current at a given glyphosate concentration. As shown in Fig. 3, this approach enables detection down to 0.05 μM leading to a 100-fold improvement relative to static operation.

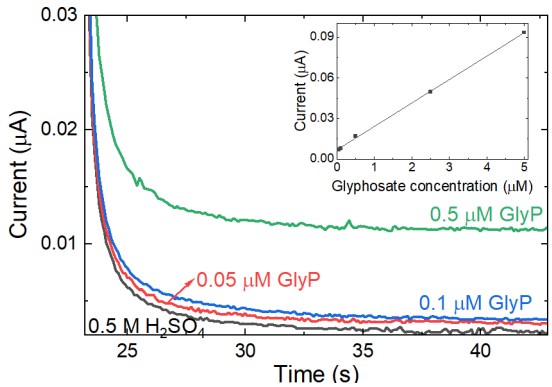

Fig 3. Chronoamperometric measurement in a microfluidic cell, at the flow of 1 mL/min, inset showing calibration curve in the range between 0.05 and 5 μM.

We further evaluated common ionic interferents found in water. Chloride (Cl^-) markedly affected glyphosate quantification due to its specific adsorption which lead to significant perturbation of glyphosate oxidation signal. To mitigate matrix effects and further lower the effective detection limit, we tested a commercially available MIP-based preconcentrator, as proposed by Uka et al. [2]. Using spiked water samples, we demonstrated a proof-of-concept for continuous glyphosate monitoring with the combined preconcentration and electrochemical detection scheme.

Conclusion

A functionalization-free gold electrode has been tested and evaluated for glyphosate detection, based on its direct oxidation. While static measurements yielded micromolar-level detection, operation under microfluidic flow enhanced mass transport and improved the LOD to 0.05 μM (100× versus static mode). Interference studies showed that chloride significantly perturbs the response due to its specific adsorption on gold and thus integrating an MIP-based preconcentrator mitigated matrix effects and enabled proof-of-concept measurements. Together, these results show the feasibility of a continuous, field-deployable glyphosate monitoring platform combining electrochemistry with upstream selective preconcentration.

References

[1] P. Neve, M. Matzrafi, L. Ulber, B. Baraibar, R. Beffa, X. Belvaux, et al., *Weed Research* 64, 181-196 (2024); doi: 10.1111/wre.12624

[2] B. Uka, J. Kieninger, G. A. Urban and A. Weltin, *ACS Sensors* 6, 2738-2746 (2021); doi: 10.1021/acssensors.1c00884

[3] A.D. González-Cruz, L.M. Anaya-Esparza, I. Valenzuela-Chavira, F. Martínez-Esquivias, J.M. Ruvalcaba-Gómez, J.M Silva-Jara, C.A. Velázquez-Carriles, I. Balderas-León, R.I. Arteaga-Garibay and Z. Villagrán, *Applied Sciences* 15, 6979 (2025); doi: 10.3390/app15136979

[4] A. L. Valle, F. C. C. Mello, R. P. Alves-Balvedi, L. P. Rodrigues and L. R. Goulart, *Environmental Chemistry Letters* 17, 291–317 (2019) ; doi: 10.1007/s10311-018-0789-5

Acknowledgment

This work is partially supported by the European Union Horizon Europe program Universwater (Grant agreement No. 101135422) and the Swiss Confederation (SERI).

DOI 10.5162/eurosensors2026/1.4.3

Architecture-Dependent Emergence of Self-Powered Gas Sensing in Junction Engineered WSe_2 Device

Dipanjana Mondal[1], Vinayak Kamble[1]*
[1] School of Physics, Indian Institute of Science Education and Research Thiruvananthapuram, Kerala, India, 695551
e-mail address: kbvinayak@iisertvm.ac.in

Summary:
Self-powered gas sensing in two-dimensional (2D) semiconductors remains limited by weak zero-bias response. Here, we investigate architecture-dependent NO_2 sensing in WSe_2 devices ranging from monolayer to stacked and networked configurations. A pronounced zero-bias response emerges only in heterogeneous networks, further enhanced under illumination. Further, with a mild response in the stacked system and no response for the single monolayer device. The results reveal a transition from bulk to junction-mediated transport governing sensing behaviour. This study establishes structural heterogeneity as a key design parameter for energy-efficient gas sensors.

Keywords: WSe_2, Self-powered gas sensor, Chemical Vapour Deposition, Junction effects, Photo-assisted sensing.

Background, Motivation and Objective

Self-powered gas sensors are essential for next-generation low-power and distributed sensing systems, particularly in applications such as wearable electronics, environmental monitoring, and remote sensing. However, achieving reliable gas detection at zero external bias in two-dimensional (2D) semiconductors remains challenging due to inefficient carrier separation and the lack of strong intrinsic electric fields [1-3]. As a result, most reported devices rely on external bias to achieve measurable sensitivity, which increases power consumption and limits their practical deployment in autonomous platforms.

In conventional device designs, sensing performance is often enhanced through engineered interfaces or external driving fields [4, 5]. While such approaches improve carrier transport and sensitivity, they introduce additional fabrication complexity and do not fundamentally address the limitations of zero-bias operation. An alternative route is to exploit intrinsic variations within the material system itself, where structural non-uniformity can give rise to spatially varying electronic landscapes, local potential barriers, and distributed internal fields that influence charge transport.

In this work, we investigate how device architecture, from monolayer to stacked and networked WSe_2 configurations governs gas sensing behaviour under zero-bias conditions. By systematically comparing these architectures, we aim to establish the role of junction formation and percolative transport pathways in enabling self-powered sensing. This study provides insight into how structural heterogeneity can be utilized as a design strategy to achieve energy-efficient gas sensing without relying on externally engineered interfaces.

Description of the New Method or System

Here, we have synthesized different configuration of WSe_2 by optimising different growing parameters in Chemical Vapour Deposition (CVD) method. Two electrode devices were fabricated first by patterning electrodes by photolithography method on the CVD grown flakes followed by metal deposition (Au/Ti) by e-beam deposition technique. WSe_2 devices were fabricated in three configurations: (i) monolayer flake, (ii) stacked few-layer flake, and (iii) percolative networks composed of interconnected flakes with varying thickness and orientation. The network architecture introduces a high density of inter-flake junctions arising from thickness variation, twist, and grain boundaries. These junctions are hypothesized to generate spatially distributed built-in electric fields, enabling carrier separation and modulation of transport pathways without external bias.

Results

Gas-sensing measurements toward NO_2 gas were performed under zero-biased dark and illuminated conditions. Monolayer devices exhibit negligible response at zero bias (Fig. 1(a)) and

weak sensitivity under applied bias. Stacked few layer structures show limited zero-bias response as shown in Fig. 1(b), indicating partial contribution from interfacial effects. In contrast, networked WSe_2 devices demonstrate a pronounced response at zero bias shown in Fig. 1(c), significantly enhanced under illumination. This behaviour suggests that sensing is governed by junction-mediated percolative transport, where gas adsorption modulates local barrier heights and transport pathways. The observed trend across device architectures highlights a transition from bulk-dominated to junction-controlled sensing mechanisms. Fig. 1 (d-f) demonstrates the schematic of the device configuration with the band alignment diagram for the devices.

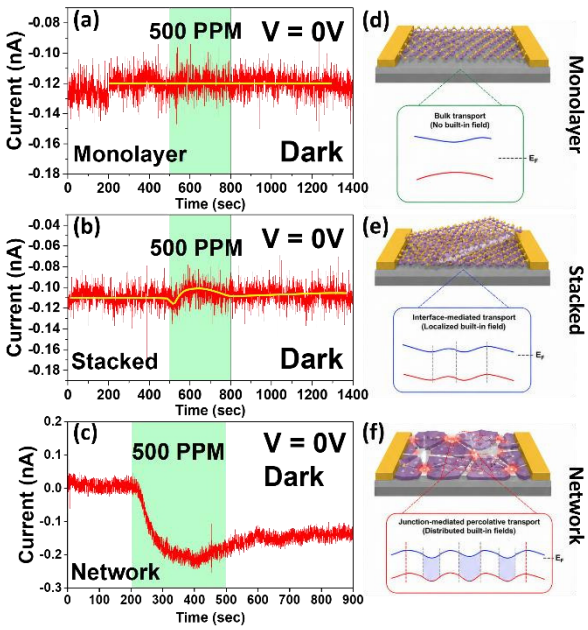

Fig. 1. Gas sensing response for 500 PPM of NO_2 gas at zero bias condition in dark for (a) Network, (b) Stacked (c) Monolayer WSe_2 device. Schematic and band diagram for the (d) Network, (e) Stacked and (f) Monolayer device.

Furthermore, photoexcitation enhances the sensing response across all device types, with the most significant improvement observed in the network architecture. This enhancement is linked to the interplay between photogenerated carriers and gas-induced modulation of local potential barriers, leading to increased sensitivity under illumination.

Conclusion

The presented results demonstrate that structural heterogeneity in WSe_2 enables a distinct sensing mechanism based on junction-mediated percolative transport, allowing measurable gas response under zero-bias conditions. The systematic comparison across device architectures highlights a transition from bulk-dominated to junction-controlled behaviour, with networked systems exhibiting the most pronounced response. Furthermore, photoexcitation enhances sensitivity by coupling photogenerated carriers with gas-induced modulation of local potential barriers. These findings establish an alternative pathway toward self-powered gas sensing in 2D materials and provide design guidelines for energy-efficient sensing platforms based on architecture-driven transport engineering.

References

[1] Wang, Q.H., Kalantar-Zadeh, K., Kis, A., Coleman, J.N. and Strano, M.S., 2012. Electronics and optoelectronics of two-dimensional transition metal dichalcogenides. *Nature nanotechnology*, *7*(11), pp.699-712.

[2] Furchi, M.M., Pospischil, A., Libisch, F., Burgdorfer, J. and Mueller, T., 2014. Photovoltaic effect in an electrically tunable van der Waals heterojunction. *Nano letters*, *14*(8), pp.4785-4791.

[3] Mondal, D., Sharma, D., R, K., N, A.M., Tiwary, C.S., Bhat, N. and Kamble, V.B., 2025. Native Oxide MoO_2–$MoSe_2$ Heterostructure-Based Self-Powered Gas Sensor for Selective NO_2 and H_2 Detection. *Small*, *21*(33), p.2503284.

[4] Late, D.J., Huang, Y.K., Liu, B., Acharya, J., Shirodkar, S.N., Luo, J., Yan, A., Charles, D., Waghmare, U.V., Dravid, V.P. and Rao, C.N.R., 2013. Sensing behavior of atomically thin-layered MoS2 transistors. *ACS nano*, *7*(6), pp.4879-4891.

[5] Patra, C., Guna, V.K., Chakraborty, S., Mondal, S. and Nandakishora, Y., 2025. Advances in 2D transition metal dichalcogenide-based gas sensors. *ACS sensors*, *10*(9), pp.6347-6379.

DOI 10.5162/eurosensors2026/1.4.4

Low-Cost Raman System for Continuous Measurement of Aqueous Ammonium Bicarbonate in Carbon Capture Processes

Nick Schäuble[1], Jennifer Jacob[1], Christian Karnutsch[1], Jan Hoinkis[1], Jürgen Wöllenstein[2,3], Markus Graf[1,4]
[1] Karlsruhe University of Applied Sciences, 76133 Karlsruhe, Germany
[2] Fraunhofer-Institute for Physical Measurement Techniques, 79110 Freiburg, Germany
[3] University of Freiburg, 79085 Freiburg, Germany
[4] University of Hamburg, 22761 Hamburg, Germany
markus.graf@uni-hamburg.de

Summary:
Raman spectroscopy is demonstrated as a direct and non-invasive method for quantifying dissolved inorganic carbon and ammonium species in aqueous solution. This paper presents a cost-effective setup that utilizes the strong concentration dependence of the bicarbonate band at 1022 cm^{-1} as the primary measurement feature. Ongoing work targets system optimization, advanced spectral analysis, equilibrium-based species modeling, and further cost reduction through simplified detector configurations.

Keywords: Raman sensor, spectroscopy, ammonium bicarbonate, low-cost, carbon capture.

Introduction

Aqueous ammonia is a promising solvent for carbon capture due to its high absorption capacity, low regeneration energy, and compatibility with circular utilization pathways [1,2]. However, practical implementation is limited by operational challenges, including ammonia slip, incomplete conversion, and limited real-time process monitoring [3]. These limitations are particularly critical due to the formation of high concentrations of ammonium bicarbonate ($H_2O + NH_3 + CO_2 \rightarrow NH_4HCO_3$), for which no reliable and cost-effective online sensors currently exist [4].

Raman spectroscopy has been used for speciation and quantification in CO_2-NH_3-H_2O systems, enabling the resolution of carbonate, bicarbonate, and carbamate species and the development of multivariate calibration models [4,5]. However, most studies employ excitation wavelengths in the visible range, which are more susceptible to fluorescence interference in complex aqueous systems [6]. In addition, conventional Raman instrumentation remains expensive, restricting broader implementation [7].

This paper describes the development of a Raman sensor based on a 785 nm excitation laser for the quantification of ammonium bicarbonate in aqueous solutions. The choice of excitation wavelength reduces susceptibility to fluorescence interference, while the system design follows a low-cost approach (<20 k€), addressing key practical limitations of existing Raman-based methods.

Methodology

Solutions with concentrations of 0.1 - 1.0 mol/L were prepared by dissolving solid ammonium bicarbonate (99%) in deionized water. The excitation source was a multimode diode laser (Thorlabs FPV785M) emitting at 785 nm with 600 mW. Samples were placed in a cuvette holder and measured using a non-contact probe with back-scattering collection geometry. The collected signal was filtered to remove Rayleigh-scattered light and analyzed with a Raman spectrometer (Ocean Optics QE Pro). Prior to analysis, dark spectra were subtracted to account for detector bias and non-laser-induced background signals, followed by subtraction of a deionized water reference spectrum to isolate solute-specific contributions. Characteristic spectral peaks were identified and assigned to corresponding ionic species based on literature data. Peak intensities were quantified based on peak height as a function of bicarbonate concentration.

Results

Figure 1 shows the measured Raman spectrum of a 1.0 mol/L ammonium bicarbonate solution.

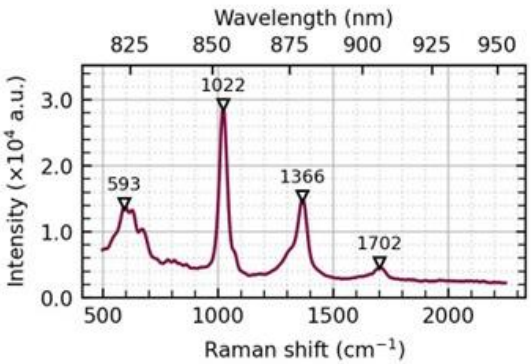

Fig. 1: Raman spectrum of an aqueous 1.0 mol/L ammonium bicarbonate solution with indicated peak positions.

The Raman spectrum is dominated by prominent peaks at 1022 and 1366 cm^{-1}, both attributed to bicarbonate [5,8]. Additional bands at 593 and 1702 cm^{-1} could be associated with ammonium but need further investigation [8].

Figure 2 presents the intensity of selected Raman peaks as a function of ammonium bicarbonate concentration. The data illustrates the relationship between the spectral signal and concentration for the investigated range.

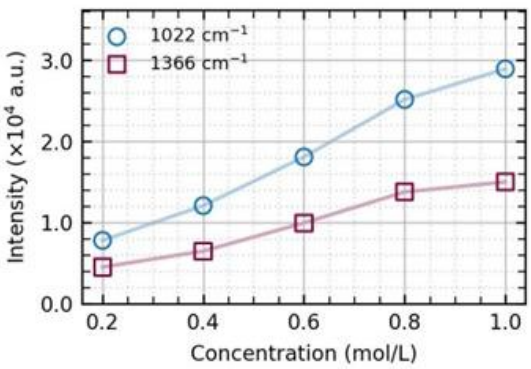

Fig. 2 Intensity of selected Raman peaks as a function of ammonium bicarbonate concentration in the range of 0.2 – 1.0 mol/L.

Both the 1022 cm^{-1} and the 1366 cm^{-1} bands show a slightly non-linear response with a possible saturation effect at higher concentrations, which requires further investigation. Nevertheless, the 1022 cm^{-1} band exhibits significantly higher overall sensitivity, making it the most suitable candidate for quantitative analysis and calibration.

Discussion

The strong and well-defined bicarbonate signal demonstrates the suitability of Raman spectroscopy for direct quantification of dissolved inorganic carbon species in ammonium-based systems. Ongoing work will extend these preliminary results through: (1) sensor optimization and limit of detection analysis, (2) extraction of ammonium signals using advanced spectral analysis algorithms, (3) development of a comprehensive model for complete quantification of NH_4^+ and HCO_3^- species incorporating pH measurements, and (4) replacement of the spectrometer with a filter-and-detector configuration to reduce sensor costs while maintaining analytical performance.

Acknowledgements

This study was funded by the Vector Stiftung (Project "CapBioCO_2") and supported by Endress+Hauser. N. Schäuble acknowledges support from the Deutsche Bundesstiftung Umwelt (DBU) in the form of a doctoral scholarship.

References

[1] A. Akinmoladun, O.S. Tomomewo, Advances and future perspectives in post-combustion carbon capture technology using chemical absorption process: A review, *Carbon Capture Sci. Technol.* 16, (2025); doi: 10.1016/j.ccst.2025.100461

[2] Schäuble, N., Greisner, B., Tenfelde, D., Hoinkis, J., Graf, M., Pilot scale wastewater treatment using a combined forward & reverse osmosis process to produce irrigation water for agriculture, *Recent Adv. Environ. Sci. Euro-Mediterr. Reg.,* (2024, in press).

[3] W. M. Budzianowski, Mitigation of NH_3 slip in ammonia-based CO_2 capture, *Energy* 37, 461–468 (2012); doi: 10.1016/j.energy.2011.11.014

[4] M. Halstensen, H. Jilvero, W.N. Jinadasa, K.-J. Jens, Equilibrium measurements of the NH_3-CO_2-H_2O system: speciation based on Raman spectroscopy and multivariate modeling, *J. Chem.*, (2017); doi: 10.1155/2017/7590506

[5] Q. Zhao, S. Wang, F. Qin, C. Chen, Composition analysis of CO_2-NH_3-H_2O system based on Raman spectra, *Ind. Eng. Chem. Res*. 50, (2011); doi: 10.1021/ie1010178

[6] M. Hardy, H.O.M. Chu, Laser wavelength selection in Raman spectroscopy, *Analyst* 150, (2025); doi: 10.1039/D5AN00324E

[7] Zgrablić, G.; Senkić, A.; Vidovic, N.; Užarević, K.; Capeta, D.; Brekalo, I.; Rakić, M. Building a Cost-Effective Mechanochemical Raman System: Improved Spectral and Time Resolution for *In Situ* Reaction and Rheology Monitoring. *Phys. Chem. Chem. Phys.* 2025 , *27* , 5909–5920; doi: 10.1039/d4cp04757

[8] Wen, N.; Brooker, M. H. Ammonium Carbonate, Ammonium Bicarbonate, and Ammonium Carbamate Equilibria: A Raman Study. *J. Phys. Chem.* 99, (1995); doi: 10.1021/j100001a054

DOI 10.5162/eurosensors2026/2.1.1

Bimodal MEMS Sensor Cartridge for Prediagnostic Evaluation of Pleural Effusion

Mehmet Oğulcan Güngör[1,2], Ayşen Gümüştaş[1], Seçkin Eroğlu[1,3], Amir Fadaie[1], Ender Yıldırım[1,3]
[1] ODTU MEMS Center, Ankara, Türkiye
[2] Micro and Nanotechnology, Middle East Technical University, Ankara, Türkiye
[3] Department of Mechanical Engineering, Middle East Technical University, Ankara, Türkiye
yender@metu.edu.tr

Summary:
This paper presents the design, fabrication, and integration of a compact (45x34x6 mm) bimodal microfluidic cartridge for the prediagnostic screening of pleural effusion. The system successfully integrates a MEMS-based sensor layer, featuring capacitive pressure and electrochemical LDH sensors, with a high-precision thermoformed styrenic block copolymer microfluidic layer. Adhering to ISO 22916 standards for inlet/outlet positioning and utilizing custom 3D-printed clamps for mechanical sealing, the platform demonstrates a robust and compact solution for multimodal biomarker detection.

Keywords: MEMS integration, Microfluidic cartridge, Bimodal sensing, Flexdym thermoforming, Prediagnostic platform

Background, Motivation and Objective

The accurate diagnosis of pleural effusion relies on the simultaneous analysis of multiple biomarkers, such as lactate dehydrogenase (LDH) activity and fluid viscosity, to distinguish between malignant and inflammatory conditions. Clinical studies indicate that viscosity levels above 1.6 mPa.s often signal severe infection, while levels below 1.4 mPa.s are associated with malignancy [1]. However, traditional in vitro diagnostic methods are time-consuming, require significant sample volumes, and typically assess a single biomarker at a time. This work addresses these limitations by developing a prediagnostic cartridge for the simultaneous measurement of LDH and viscosity from a small volume of pleural effusion sample, combining MEMS-based bimodal sensing with a compact microfluidic cartridge architecture.

Description of the New Method or System

The cartridge utilizes a four-layer architecture: a polymethyl methacrylate (PMMA) top cover, a thermoformed Flexdym microfluidic layer, a MEMS-produced sensor chip, and a PMMA support base. Each layer serves a distinct functional role, enabling delivery of pleural effusion samples to both sensing regions within a single integrated platform.

Integrated Sensor Layer: The core of the system is a bimodal sensor chip fabricated on a glass substrate using a specialized 10-step MEMS fabrication flow, integrating a Parylene-C based capacitive pressure sensor and gold/silver-based electrodes for electrochemical LDH activity measurement. Viscosity is assessed by measuring the pressure drop induced by sample flow through the serpentine microchannel, which is analytically related to fluid viscosity via the Hagen-Poiseuille framework and converted to a capacitance signal by the Parylene-C diaphragm [2]. Analytical modeling of the diaphragms was performed to ensure high sensitivity and linearity within the target 1.0-1.8 mPa.s viscosity range [3]. Electrochemical LDH detection is based on amperometric measurement of NADH oxidation, facilitated by a conducting polymer-modified electrode surface [4].

Microfluidic Channel Layer: The microfluidic network is produced from Flexdym, a biocompatible styrenic block copolymer (SBC), via a high-precision thermoforming process. This material provides excellent replication fidelity and inherent self-sealing properties when compared to traditional PDMS [5]. The channel layer features 100 µm wide serpentine geometries optimized for controlled sample delivery and the detection of viscosity-induced pressure drops. To ensure reliable electrochemical detection, phaseguide structures are incorporated into the reaction chambers to facilitate bubble-free wetting of the sensor electrodes, preventing signal artifacts. The channel geometry is replicated using a high-temperature Stereolithography (SLA) 3D-printed polymer insert as the thermoforming mold, enabling rapid tooling and precise feature transfer without the need for metal tooling.

Packaging and Integration: The entire assembly is secured by custom 3D-printed clamps that provide uniform mechanical pressure for leak-proof sealing without the need for permanent bonding or adhesives, as illustrated in Fig. 1. Precision alignment between layers is achieved through dedicated pockets machined into the PMMA layers via CNC milling. For fluidic operation, a magnetic interface integrates a Flexible Hydraulic Reservoir (FHR) pump, enabling dead-volume-free sample loading and precise flow control [6]. Port positions follow the ISO 22916 standard to ensure compatibility with other analysis platforms that conform to the same standard.

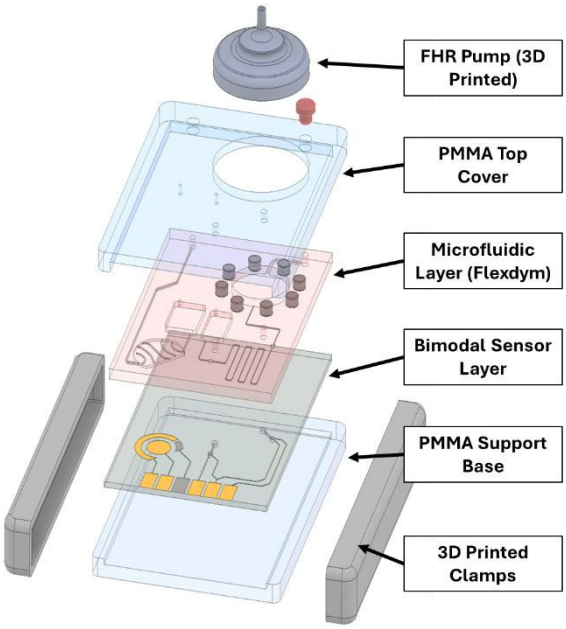

Fig. 1. Exploded view of the four-layer bimodal sensor cartridge architecture.

Results

The MEMS bimodal sensor chip, comprising the Parylene-C pressure sensor and electrochemical electrodes, was successfully fabricated and verified to be electrically functional prior to cartridge integration. The integration process successfully yielded a fully functional prediagnostic cartridge with portable dimensions of 45x34x6 mm, as shown in Fig. 2. Fabrication of the 100 µm microchannels in the Flexdym layer was verified using profilometry and electron microscopy, confirming high geometric fidelity with a mean surface roughness (Ra) of approximately 1.9 µm on channel walls. Sealing performance, facilitated by the elastic properties of the SBC layer and the mechanical pressure from the 3D-printed clamps, was confirmed to be completely leak-proof during operational flow tests. Furthermore, integrated phaseguide structures effectively ensured bubble-free filling of the sensor chambers, enabling reliable wetting of the electrodes even at varying flow rates. These results demonstrate a robust bimodal cartridge architecture capable of simultaneous multimodal biomarker detection from a single low-volume clinical sample.

Fig. 2. Photograph of the assembled bimodal sensor cartridge.

References

[1] D. C. Fitzgerald, et al., Pleural Infection: Diagnosis, Management, and Future Directions, *Journal of Clinical Medicine* 14, 1685 (2025); doi: 10.3390/jcm14051685

[2] S. Eroğlu, et al., Modeling of Microfluidic MEMS-Based Capacitive Pressure Measurement, *Lecture Notes in Mechanical Engineering*, 3–10 (2026); doi: 10.1007/978-3-032-16138-3_1

[3] A. C. Atik, et al., Modeling and fabrication of electrostatically actuated diaphragms for on-chip valving of MEMS-compatible microfluidic systems, *Journal of Micromechanics and Microengineering* 30, 115001 (2020); doi: 10.1088/1361-6439/aba16f

[4] A. Gümüştaş, et al., Conducting Polymer Based Amperometric Sensor for the Determination of Lactate Dehydrogenase, *Biosensors 2025: 35th Anniversary World Congress on Biosensors*, Lisbon, Portugal (2025)

[5] H. Salmon, et al., Facile engineering and interfacing of styrenic block copolymers devices for low-cost, multipurpose microfluidic applications, *Engineering Reports* 3, e12361 (2021); doi: 10.1002/eng2.12361

[6] A. Atay, et al., Flow rate-controlled pipetting for microfluidics: second-generation flexible hydraulic reservoir, *Microfluidics and Nanofluidics* 25, 1-10 (2021); doi: 10.1007/s10404-020-02402-x

Acknowledgement: This work was supported by the Scientific and Technological Research Council of Türkiye (TÜBİTAK) under grant number 22AG008

DOI 10.5162/eurosensors2026/2.1.2

Real-World Chemical Plant Monitoring and Event Classification by Multi-Modal Low-Cost Sensor Network

A. Raffeiner[1], R. Pohle[1], J. Kelleter[2], S. Essel[3]
[1] Siemens AG, Munich, Germany
[2] GTE Industrieelektronik GmbH, Viersen, Germany
[3] ISH, Höchst, Germany
aaron.raffeiner@siemens.com

Summary:
The project MIMOSE-A combines industry and academic efforts to improve monitoring of chemical industry parks. The goal is to detect and locate unwanted events such as gas leaks and fires using low-cost wireless sensor networks. Field tests at a chemical plant site deploy multi-modal sensor nodes equipped with metal oxide (MOX) volatile organic compound (VOC) sensors, and particulate matter (PM) sensors. A fire event near the plant site served as first real-world validation case. A preliminary statistical analysis of PM and VOC sensor responses demonstrates the ability to classify events and in combination with a wind analysis provides initial indicators for possible emission sources.

Keywords: sensor network, leakage detection, gas sensors, fire detection

Background, Motivation and Objective

Unintended gas leaks and fire events at industrial plants pose significant challenges for safety, operational efficiency, and regulatory compliance. Current plant monitoring relies on dedicated sensor systems designed for special applications, e.g. environmental compliance, usually associated with high costs. Trained human operators supplement these systems by detecting unusual or hazardous conditions through olfaction and visual inspection. A low-cost, sensor network could improve spatial coverage and enable continuous automated monitoring. In the project MIMOSE-A, a multi-modal wireless sensor network was proposed and deployed at two chemical facilities in Germany [1]. This paper aims to evaluate the feasibility of the multi-modal sensor network for event detection, classification, and source attribution by a statistical analysis.

Approach

This study presents a first analysis of real-world field test data from the chemical park ISH at Höchst. The sensor nodes, as described in [1], were installed at the plant site, covering an area of 4.6 km². Each node comprises sensors for environmental parameters such as temperature, humidity, gas and VOC (Sciosense ENS160), and PM (Sciosense APC1). The nodes were mounted on poles at heights of 2.0–2.5 m above ground. Meteorological data, including wind direction and wind speed, was obtained from the ISH environmental monitoring stations and integrated with the sensor data for joint analysis. A root cause analysis requires a documented reference event with known location and time to validate sensor responses against. A fire at the Woolworth store in proximity to the ISH site on 18.02.2025 [2], serves as validation case. The sensor and event locations are depicted in Fig.1. The fire emits PM and VOC, providing a signature detectable by the sensor [3]. The correlation between VOC and PM sensor responses is analyzed for event classification, and wind data is studied for source attribution.

Fig. 1 Positions of the sensor nodes, wind sensor (green arrow in mean wind direction) and fire event (red dot).

Results

The fire event was first reported at 17:30, a strong PM increase was recorded at a public environmental measurement station at Höchst main station at 19:00 [2]. At 20:00 the fire was reported to be under control [2]. Therefore, the period from 18:00 to 22:00, was considered in this study for all evaluations.

During this period, the ISH meteorological station recorded a prevailing wind direction of NNE (32.9°, σ = 10.1°) with speed 3.0 m/s (σ = 0.4 m/s), transporting the fire plume towards the sensor nodes, see Fig. 1.

The VOC responses recorded by the sensor nodes in Fig. 2 lack distinctive features attributable to specific sources. The observed PM magnitudes (Fig. 2) significantly exceed background levels from traffic or construction activity, indicating a large-scale combustion event. Clear PM peaks are visible in the time from 19:30 to 21:00, see Fig. 2. Node 40, closest (≈1.0 km downwind) to the fire, recorded the largest increase among all nodes. Smaller peaks are visible even ≈2.5 km downwind at nodes 42 and 43. Node 41 is located crosswind and shows the least significant response.

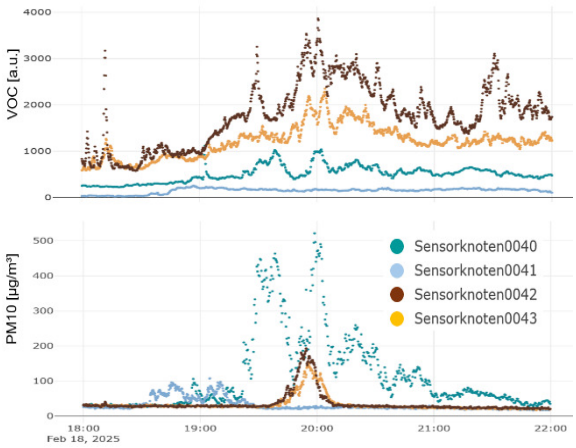

Fig. 2 VOC and PM10 sensor response in the period of the fire event. PM shows clear peaks. VOC responses show ambiguous features.

Fig. 3 depicts the Pearson correlation between VOC and PM responses during the period considered. Node 40, closest to the fire, shows a PM-VOC correlation of ≈0.81, consistent with co-located PM and VOC from a single source. At nodes 42 and 43 (≈2.5 km downwind), the local PM-VOC correlation drops to ≈0.40, indicating that VOC signals at this distance may reflect additional local emission sources rather than the fire plume. A cross-node correlation of ≈0.90 between VOC-VOC as well as PM-PM at node 42 and 43 supports this interpretation, as both nodes share a common industrial environment with possibly independent emitters.

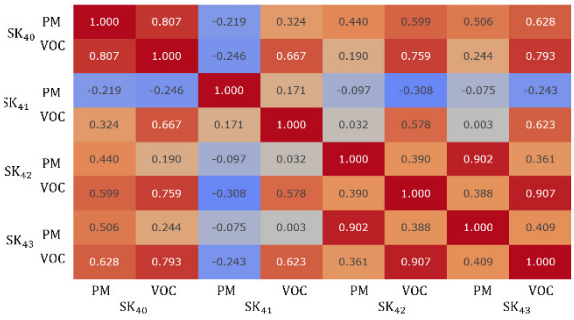

Fig. 3 Pearson correlation matrix of VOC and PM10 for individual nodes (SK) based on 1400 datapoints.

In conclusion, the significant increase in PM magnitudes - far exceeding background levels - indicates a large-scale combustion event as the primary source. A gas leakage, by contrast, produces a predominantly VOC response with negligible PM increase. The combined evaluation of both sensor modalities therefore enables classification of fire versus leakage events.

Summary and outlook

This study validates a low-cost multi-modal sensor network for event detection and classification at an industrial chemical park. PM sensors detect the fire plume up to 2.5 km downwind, while the combined PM-VOC correlation enables discrimination between combustion events and gas leakages. The sensor network thus provides a scalable complement to conventional plant monitoring at low cost.

Further work includes evaluation of temperature modulated MOX sensor signals, assessment of machine learning methods for the detection of unwanted events and methods for gas source localization.

Acknowledgements

The project “MIMOSE-A” is funded by the German Federal Ministry for Economic Affairs and Energy (BMWE) under the grant number 03EN4057A-G. We acknowledge support by the Project Management Jülich (PTJ). The authors want to thank all project partners for their good, ongoing cooperation.

References

[1] D. Arendes, et al., Multimodal Smart Sensor Networks for Plant Monitoring and Improved Energy Efficiency, SMSI 2025 Conference; DOI 10.5162/SMSI2025/B1.1

[2] Richter M., Großbrand zerstört Woolworth-Kaufhaus, *feuerwehrmagazin.de, 19.02.2025*

[3] Vorwerk P., et al., Distance-Based Analysis of Early Fire Indicators on a New Indoor Laboratory Dataset with Distributed Multi-Sensor Nodes. *Fire*. 2023; DOI 10.3390/fire6080323

DOI 10.5162/eurosensors2026/2.1.3

Maryam Kahvazi Zadeh[1,*], Eren Akyol[1], Aysa Azmoudeh[1] and Murat Kuscu[1]
[1]Department of Electrical and Electronics Engineering, Koç University, Istanbul, Turkey
[*]Corresponding author: mzadeh22@ku.edu.tr

Abstract

Integrating a CVD graphene Hall cross beneath a PDMS microfluidic channel, we demonstrate real-time, label-free detection of individual ferrofluid droplets through transient Hall voltage measurements. The exceptional carrier mobility of graphene enables sensitive transduction of the stray magnetic field of passing droplets, yielding reliable detection and size discrimination via pulse-width analysis with a linear response across the full operating field range. The compact, planar architecture eliminates the need for bulky optical or inductive instrumentation, establishing graphene Hall sensors as a practical, chip-scale magnetic transducer for microfluidic sensing and droplet-based communication platforms.

Keywords: Graphene Hall Sensor, Molecular Communication, Microfluidic chip

Introduction

The Internet of Bio-Nano Things (IoBNT) envisions networks of nanoscale devices operating within physiological environments, where molecular and particulate carriers replace conventional electromagnetic signals [1]. Within this paradigm, droplet-based communication has emerged as a promising scheme, offering deterministic transport and higher throughput than diffusion-based approaches [2]. Ferrofluid droplets carrying magnetic nanoparticles are particularly attractive carriers due to their biocompatibility and detectable magnetic signatures in biological media [3], and their negligible magnetic background in physiological environments renders magnetic detection advantageous over optical methods for deeply implanted systems [4]; a distinction that becomes critical when sensing must occur silently, in situ, and without external illumination (Fig. 1).

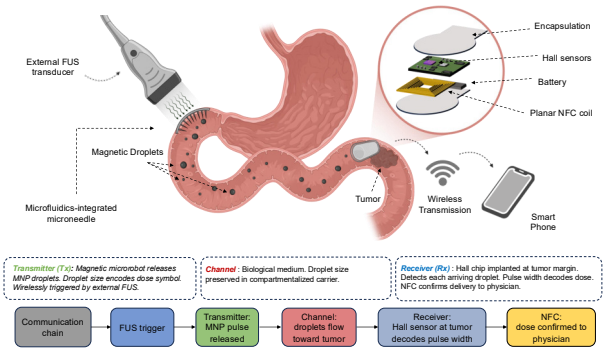

Figure 1. Conceptual illustration of a magnetic droplet-based communication system for in-body drug delivery, where a miniaturised Hall sensor receiver detects and decodes arriving magnetic droplets at the target site.

Realizing such systems, however, demands receivers that are not merely sensitive, but miniaturized, planar, and monolithically compatible with microfluidic architectures. Existing magnetic readout approaches based on susceptometers and inductive coils [5, 6] impose footprints and assembly constraints incompatible with implantable or lab-on-chip platforms. Hall-effect sensors offer a compelling alternative: a purely electronic, DC-operable transduction mechanism that converts localized magnetic flux into a measurable transverse voltage with no moving components [7]. Graphene elevates this principle further, as its monoatomic thickness and exceptional carrier mobility yield Hall coefficients that surpass conventional semiconductor implementations [8].

Yet graphene Hall sensors have not been applied to microfluidic droplet detection, leaving their considerable potential untapped at precisely the scale where it matters most. Here, we report a CVD graphene Hall cross integrated beneath a PDMS microfluidic channel that detects and size-discriminates individual ferrofluid droplets in real time through transient Hall voltage analysis, establishing a sensitive, chip-scale magnetic receiver architecture directly applicable to next-generation bio-nano communication and sensing systems.

Experimental

Device Fabrication

Fabrication began with patterning Ti/Au (5/50 nm) contacts on an n-type Si/SiO_2 substrate (525 µm Si, 90 nm thermal oxide) by photolithography and electron-beam evaporation followed by lift-off. CVD-grown graphene was wet-transferred onto the pre-patterned electrodes and defined into Hall-cross geometries (100 µm × 15 µm) by photolithography and O_2 plasma etching. The active channel was encapsulated with 20 nm Al_2O_3 deposited by atomic layer deposition (ALD), and contact-pad windows were opened by selective wet etching. A PDMS microfluidic channel fabricated by soft lithography was plasma-bonded to the chip, completing the integrated device (Fig. 2).

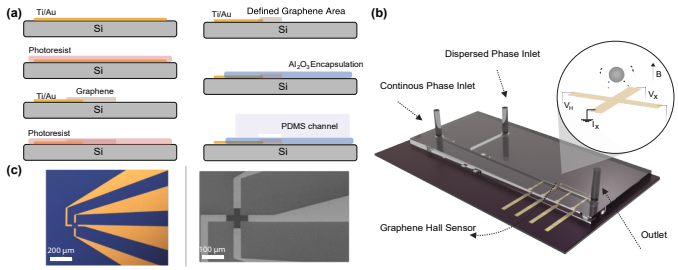

Figure 2. (a) Fabrication process flow of the graphene Hall sensor. (b) Schematic of the assembled device with integrated T-junction microfluidic channel and Hall measurement circuit. (c) Optical and SEM images of the fabricated graphene Hall cross.

Measurement Setup

Electrical characterisation was performed using a Keysight B2902B source measurement unit under perpendicular magnetic fields up to 40 mT generated by an external electromagnet. Water-based ferrofluid (EMG-705, Ferrotec) in silicone oil (100 cSt) was used as the droplet phase. Droplets were generated on-chip via a T-junction by independently controlling the dispersed- and

DOI 10.5162/eurosensors2026/2.1.3

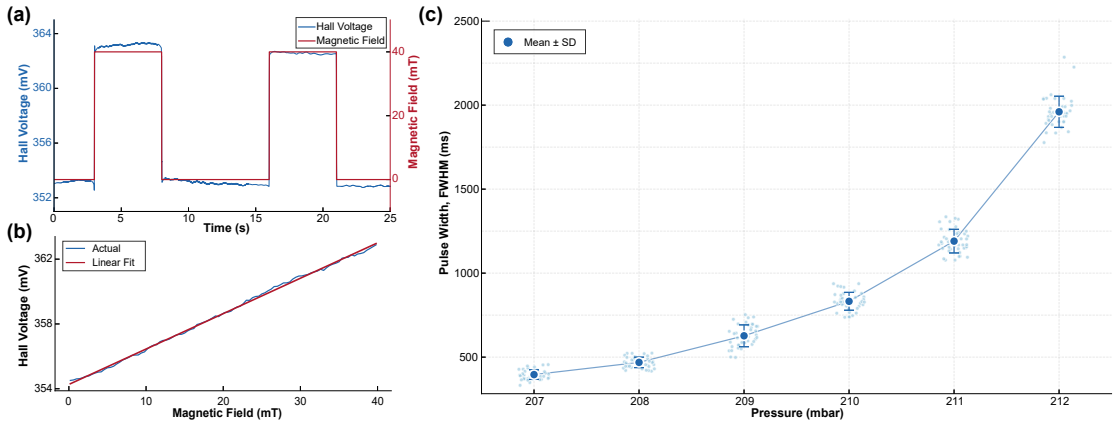

Figure 3. (a) Hall voltage response at $B = 0$ and $B = 40$ mT. (b) Hall voltage as a function of applied magnetic field with linear fit. (c) Mean pulse width ($\pm$ SD, $n = 40$) as a function of dispersed-phase pressure.

continuous-phase pressures, and the Hall voltage was recorded continuously as droplets transited over the sensor.

Results and Discussion

Sensor Characterisation

The Hall-cross geometry and contact integrity were confirmed by scanning electron microscopy (Fig. 2c). Electrical characterization under controlled out-of-plane magnetic fields revealed a linear Hall voltage response across the full 0–40 mT operating range (Fig. 3b), from which a sensitivity of 218.5 mV/T was extracted. This linear behaviour confirms the suitability of the graphene Hall cross as a quantitative magnetic transducer under the low-field conditions relevant to ferrofluid droplet detection.

Droplet Detection and Size Discrimination

Receiver performance was evaluated by varying the dispersed-phase pressure from 207 to 212 mbar while maintaining the continuous phase at 220 mbar, producing droplets of systematically increasing size. Each passing droplet induced a transient Hall voltage pulse (Fig. 3a), confirming real-time detection without optical access or additional labelling. As shown in Fig. 3c, the mean pulse width increases monotonically from 396 to 1960 ms with pressure, with clearly separated distributions at each operating point ($n = 40$ droplets per condition). The tight, non-overlapping distributions confirm both the stability of on-chip droplet generation and the repeatability of the Hall voltage readout, demonstrating reliable size discrimination across a nearly five-fold dynamic range.

Conclusions

We have presented a chip-integrated graphene Hall sensor capable of detecting and size-discriminating individual ferrofluid droplets in real time through transient Hall voltage analysis. The device achieves a sensitivity of 218.5 mV/T with a strictly linear response up to 40 mT, and resolves droplet sizes across a nearly five-fold pulse-width dynamic range with non-overlapping distributions, without optical access, external labelling, or bulky instrumentation. These characteristics, combined with the planar, CMOS-compatible architecture, position graphene Hall sensors as a compelling building block for next-generation lab-on-chip diagnostics, implantable magnetic sensing, and miniaturised receivers in bio-nano communication networks. Looking forward, implementing structured modulation schemes and multi-sensor array configurations will be key steps toward a fully integrated, programmable droplet-based communication platform operating within physiological environments.

Acknowledgements

This work was supported by The Scientific and Technological Research Council of Turkey (TÜBİTAK) under Grants No. 123E516 and No. 123C592.

[1] Murat Kuscu and Bige Deniz Unluturk. Internet of bio-nano things: A review of applications, enabling technologies and key challenges. *ITU J. Future Evol. Technol.*, 2(3):1–24, 2021.

[2] Eren Akyol, Aysa Azmoudeh, Iman Mokari Bolhassan, Pelin Kubra Isgor, and Murat Kuscu. Microdroplet-based communications with frequency shift keying modulation. *IEEE Trans. Mol. Biol. Multi-Scale Commun.*, 11(4):513–517, 2025.

[3] Quentin A Pankhurst, Jon Connolly, Stephen K Jones, and JJJ Dobson. Applications of magnetic nanoparticles in biomedicine. *Journal of physics D: Applied physics*, 36(13):R167–R181, 2003.

[4] David Issadore et al. Ultrasensitive clinical enumeration of rare cells ex vivo using a micro-hall detector. *Sci. Transl. Med.*, 4(141):141ra92, 2012.

[5] Harald Unterweger et al. Experimental molecular communication testbed based on magnetic nanoparticles in duct flow. In *Proc. IEEE Int. Workshop Signal Process. Adv. Wireless Commun. (SPAWC)*, pages 1–5, 2018.

[6] Wayan Wicke et al. Magnetic nanoparticle-based molecular communication in microfluidic environments. *IEEE Trans. Nanobiosci.*, 18(2):156–169, Apr. 2019.

[7] R. S. Popović. Hall-effect devices. *Sens. Actuators*, 17(1–2):39–53, 1989.

[8] Jan Dauber et al. Ultra-sensitive hall sensors based on graphene encapsulated in hexagonal boron nitride. *Appl. Phys. Lett.*, 106(19), 2015.

DOI 10.5162/eurosensors2026/2.1.4

Interfacial Direct Printing (IDP) of SU-8: Fabrication of Molds with Smooth Round Channels

Raphael Dezauzier, Maximilian Breitfeld, Claudius L. Dietsche, Petra S. Dittrich
Department of Biosystems Science and Engineering, ETH Zürich, Klingelbergstrasse 48, 4056 Basel, Switzerland
rdezauzier@ethz.ch

Summary:
In this study, we introduce a new process for the fabrication of microfluidic molds referred to as Interfacial direct printing (IDP). IDP allows the fabrication of smooth semi-round SU-8 structures on a glass slide, which is not possible with standard photolithography. The photoresist is deposited via a capillary on a moving substrate placed inside an oil bath, forming SU-8 lines with semi-round cross-section shaped by acting interfacial forces. After UV treatment and baking, the structures can be used for soft lithography. Round shaped channels are of particular interest for microfluidic organ-on-chip and diagnostic devices.

Keywords: printing, additive manufacturing, microfabrication, lithography, mold

Introduction

Photolithography has long been the gold standard to fabricate microfluidic molds used for replica molding. It provides very smooth and precise geometries, however, the structures have usually edged, often rectangular cross-sections. For many biological applications, notably organ-on-chip, circular geometries are preferred for cell cultivation. Indeed, they mimic the *in vivo* environment much better than edged forms. For example, spheroid/organoid assembly is favored in concave wells [1]. Also, rectangular structures provide zero flow regions, create additional shear stresses and can harm cells. Previous approaches to form round channels include CNC micromachining, laser ablation and 3D printing, which often result in irregular and rough surfaces [1,2,3]. Other methods include microfabrication techniques such as resist thermal reflow, or backside photolithography, but these lack good control over the final geometry, are hard to implement, and require a cleanroom [4,5]. In this work, we present a new SU-8 deposition technique which allows the formation of channels with semi-round profiles, without the need for cleanroom equipment.

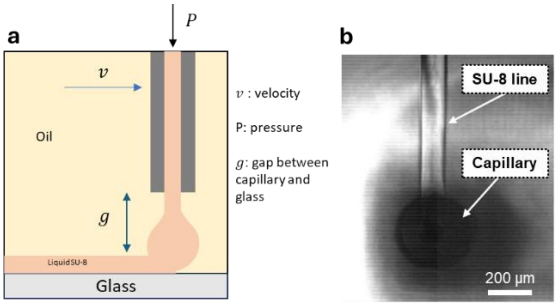

Figure 1: (a) Schematic illustrating the deposition of photoresist semi-round lines on substrate, by tuning three parameters, g, v and P. (b) Photo (top view) of line creation during deposition. Black spot is the capillary.

Interfacial direct printing (IDP)

The method builds on a previously introduced platform for liquid-in-liquid printing [6], here adapted to print viscous SU-8 photoresist. A substrate (a glass slide) is placed into a HFE 7500 oil bath (Figure 1a). A capillary is placed near the substrate, a gap g separating them. Application of pressure (P) pushes the SU-8 out, at the same time the glass slide moves at a defined velocity (v) relative to the capillary. When the parameters pressure, velocity and gap are tuned appropriately, the photoresist forms a continuous line on the substrate (Figure 1b). Due to the interfacial tension between the substrate, the oil and the photoresist, the deposited lines naturally forms a semi-circular shape. Subsequently, UV light is exposed on the substrate to cure the photoresist, and the oil bath is removed. The mold is then baked in an oven at 80°C overnight and can be used for soft lithography afterwards.

Printing results

Images of deposited lines are shown in Figure 2a,b. The cross-section of the line was measured with a profilometer (Figure 2c). Depending on the parameters, lines of different widths and heights are created. For example, by setting the pressure P to 200 mbar, the gap g to 20 µm, and the velocity v to 1 mm/s, the photoresist lines were 13.7 µm high and 105.9 µm wide, with

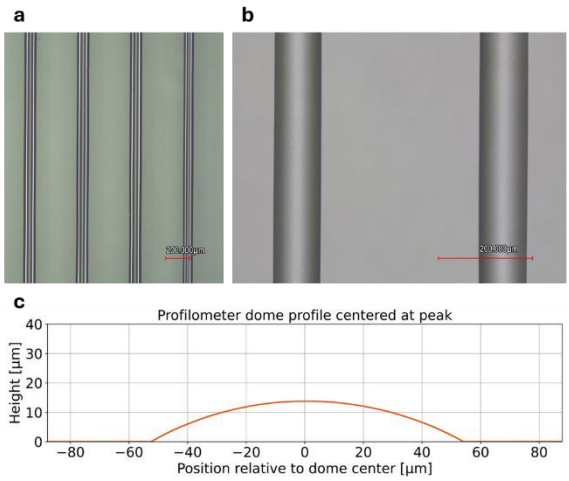

Figure 2: (a) Microscopy image of deposited lines 5x and (b) 20x. (c) Profilometer data displaying cross-section of a deposited line.

110.2 µm curvature radius, and 996 µm² in cross-section area. The contact angle θ was measured to be 29.2°. The cross-section area (A), height (h) and width (w) are dependent on pressure P and v as follows:

$$A = \frac{P}{R \cdot v}, \quad (1)$$

$$h = \sqrt{\frac{P \cdot (1-\cos\theta)^2}{R \cdot v \cdot (\theta - \sin\theta\cos\theta)}}, \quad (2)$$

$$w = \sqrt{\frac{P \cdot 4\sin^2(\theta)}{R \cdot v \cdot (\theta - \sin\theta\cos\theta)}}, \quad (3)$$

where R is the hydraulic resistance. By changing the pressure or the velocity, we define the geometry of the deposited lines. Moreover, it is important to note that the photoresist viscosity influences R and substrate surface energy impacts θ, and therefore both parameters also play a significant role in the shape and size of the deposition. The roughness was measured on the profilometric data. As the surface is curved, a 2nd degree polynomial was fitted on a 10-µm wide region of the cross-section profile (Figure 3a). Residual data could then be calculated by subtracting the fit to the profile, onto which arithmetic average R_a, mean roughness depth R_z and root mean square R_q value could be extracted (Figure 3b). The values (R_a: 5.0 nm, R_q: 5.9 nm and R_z: 27.6 nm) confirm the low roughness of the surface. After light exposure and baking, we also confirmed the tight binding of SU-8 to glass and formed PDMS devices from the molds. We also fabricated wells and more complex designs to show the suitability of the process for rapid prototyping.

Conclusion

IDP is a simple process to form molds with round, smooth photoresist lines without the need for a clean room in resolution suitable for lab-on-chip devices. We currently explore the method to build complex channel networks.

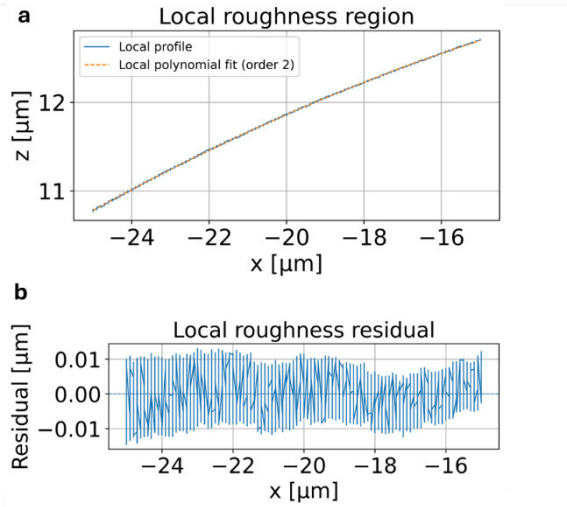

Figure 3: (a) Profilometer data (blue line) with 2nd degree polynomial fit (orange line) to detect curvature. (b) Residual data obtained by subtracting profile with 2nd degree polynomial.

References

[1] W. Guo, Z. Chen, Z. Feng,H. Li, M. Zhang, H. Zhang and X. Cui, Fabrication of Concave Microwells and Their Applications in Micro-Tissue Engineering: A Review. Micromachines (Basel), 9, 1555 (2022), doi: 10.3390/mi13091555

[2] S. Lee, N. Kim, S. Kim, S. Um and J. Y. Park, Biological and mechanical influence of three-dimensional microenvironment formed in microwell on multicellular spheroids composed of heterogeneous hair follicle stem cells, 13, 22742 (2023), https://doi.org/10.1038/s41598-023-49510-6

[3] C. Chen, V. Rengarajan, A. Kjar, Y. Huang, A matrigel-free method to generate matured human cerebral organoids using 3D-Printed microwell arrays, Bioactive Materials,6,4 (2021), https://doi.org/10.1016/j.bioactmat.2020.10.003

[4] Z. Lian, S. Hung, M. Shen, H. Yang, Rapid fabrication of semiellipsoid microlens using thermal reflow with two different photoresists, Microelectronic Engineering, 115, 46-50, (2014), https://doi.org/10.1016/j.mee.2013.10.025

[5] M. Fenech, V. Girod, V. Claveria, S. Meance, M. Abkarian, B. Charlot, Microfluidic blood vasculature replicas using backside lithography, *Lab Chip*, 19, 2096-2106, (2019) doi: 10.1039/C9LC00254E

[6] M. Breitfeld, R. Strutt, L. Fröhlich, C.L. Dietsche, S. Bargfrede, P.S Dittrich, Liquid-in-Liquid Prints: High-Density Biochemically Encoded Information Preserved in Microdroplet Arrays, Adv. Mater., 38,0935-9648, (2025), https://doi.org/10.1002/adma.202516338

DOI 10.5162/eurosensors2026/2.1.5

Designing better biosensors from first principles

David Juncker
McGill University
Biomedical Engineering Department and VP Dahdaleh Institute of Genomic Medicine
Montréal, CANADA
david.Juncker@mcgill.ca

Abstract:

Biosensors and microfluidics have yet to collectively meet necessary and desired benchmarks of high sensitivity, specificity, reproducibility, multiplexing and speed. Notably, scaling in multiplexed sandwich assays faces compounding cross-reactivity [1], while the trade-off between time-to-result and sensitivity remains stifling. Here, we will discuss conceptual frameworks and practical designs that transcend these limitations. Firstly, the colocalization-by-linkage assay on microparticles (CLAMP) enables scalable multiplexing on barcoded microparticles with standard flow cytometry readout [2,3]. Thousands of proteins can be detected in 20 µl with a turnaround of ~3 h only. Secondly, the microfluidic sieve detector (MFSD) rapidly 'sieves' hundreds of microliters of sample in 1 min, and detects individual proteins digitally following partitioning and enzymatic amplification [4]. The MFSD enables very rapid (< 5 min) and ultrasensitive (zeptomolar) assays with 7 OM dynamic range and low CVs (<15%) suitable for quantification; it can also detect nucleic acids (isothermally) more sensitively and faster than PCR. While classical mass action and transport theory apply, insight is gained from a proposed stochastic Brownian agent dynamics (SBAD) model with flow. We believe the MFSD sets a new standard for assays, and together with the CLAMP, and with SBAD, highlight the potential for new biosensing approaches and principles.

Keywords:

sandwich assays, multiplexing, digital assays, microfluidic sieve, stochastic Brownian agent dynamics.

References:

[1] D. Juncker *et al*. Cross-reactivity in antibody microarrays and multiplexed sandwich assays: shedding light on the dark side of multiplexing, *Curr. Op. Chem. Biol.* 18, 29-37 (2012) doi:10.1016/j.cbpa.2013.11.012.

[2] M. Dagher, M.Kleinman, A. Ng, and D. Juncker, Ensemble multicolour FRET model enables barcoding at extreme FRET levels, *Nature Nanotechnology*, 13, 925-932 (2018). doi:10.1038/s41565-018-0205-0

[3] M. Dagher, *et al*., nELISA: A high-throughput, high-plex platform enables quantitative profiling of the inflammatory secretome, *Nature Methods*, 22, 2375–2385 (2025). doi: 10.1038/s41592-025-02861-6

[4] G.Kim, M. L. Shen A. Ng, D. Juncker, Microfluidic sieve and detector for rapid ultrasensitive assays with single-molecule sensitivity, *bioRxiv*, 2025.10.30.685461 (2025). doi: 10.1101/2025.10.30.685461

DOI 10.5162/eurosensors2026/2.2.1

Raman and Photoluminescence Spectroscopy Detection of NO_2 gas Adsorbed on ZnO Nanowires

Federica Rigoni[1], Massimo Ponzoni[2], Matteo Borsi[2], Dario Zappa[1], Elisabetta Comini[1]
[1] Università di Brescia, via Branze 38, 25123, Brescia, Italy,
federica.rigoni@unibs.it

Summary:
NO_2 detection via optical techniques is of significant interest for gaining deeper insight into gas sensing mechanisms. ZnO nanowires represent an excellent model system due to their high surface-to-volume ratio and defect-mediated surface reactivity, which enhance sensitivity to adsorbed species. NO_2 adsorption induces charge transfer processes that modulate oxygen vacancy-related states, leading to measurable changes in both Raman spectra and photoluminescence emissions. The effect of NO_2 adsorption on the ZnO nanowires surface was investigated by Raman spectroscopy, observing an increase in the LO phonon band around 550 cm^{-1}, and related to the PL contribution.

Keywords: spectroscopic detection, Raman, Photoluminescence, ZnO nanowires, nitrogen dioxide

Background, Motivation and Objective

The detection of nitrogen dioxide (NO_2), a toxic and highly reactive pollutant, is crucial for environmental monitoring and industrial safety. Optical sensing approaches based on semiconducting metal oxides have attracted significant attention due to their high sensitivity, fast response, and potential for real-time, non-invasive detection. Moreover, these techniques possibly allow us for a deeper understanding of the interaction of the gas molecules with the material surface and ultimately to the gas sensing mechanisms. Among semiconducting metal oxides, ZnO nanowires (NWs) are known as perfect candidates for their wide band gap (~3.37 eV), large exciton binding energy, and high surface-to-volume ratio, which enhances gas adsorption and surface reactions [1,2]. Upon NO_2 adsorption, charge transfer processes occur at the ZnO surface, leading to modifications in defect states, particularly oxygen vacancies, and changes in both vibrational and electronic properties. Raman spectroscopy is sensitive to lattice disorder and defect-related features, such as the enhancement and broadening of longitudinal optical (LO) phonon modes (~550 cm^{-1}), indicative of oxygen vacancy-related surface defects [3]. Although direct in situ Raman studies on ZnO nanowires under NO_2 are limited, in-situ and operando Raman spectroscopy has been applied to gas sensors [4]. Complementarily, photoluminescence (PL) spectroscopy probes electronic transitions and defect levels, where NO_2 adsorption typically results in modulation of near-band-edge emission and deep-level luminescence associated with intrinsic defects [5]. In our previous work [6], it has been shown that the different PL contributions of ZnO NWs act differently during NO_2 exposure, giving rise to reversible and irreversible effects. NO_2 adsorption on ZnO nanowires modifies surface charge and defect states, which in turn affects not only electronic recombination but also lattice-related properties probed optically. The observed changes in surface and defect-related emissions imply a coupling between gas-induced charge transfer and polar optical modes, consistent with the sensitivity of ZnO longitudinal optical (LO) phonons to surface electronic conditions. In the present work, we investigated the effect of NO_2 adsorption on the ZnO nanowires surface in the LO phonon band around 550 cm^{-1}, in the Raman spectrum, and related it to the PL contribution.

Experimental Method

ZnO NWs were synthesized by hydrothermal method onto FTO substrate and characterized by scanning electron microscopy (SEM, Fig. 1).

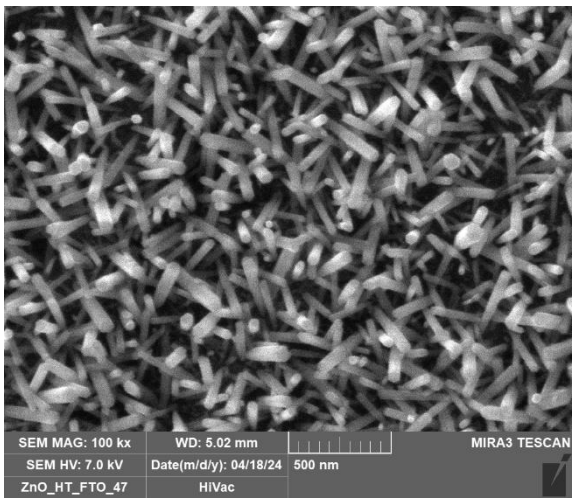

Fig. 1. SEM image at 100 kX magnification of ZnO NWs grown on FTO substrate.

Raman and photoluminescence spectroscopy were carried out on the ZnO NWs sample inside a Linkam stage (HFS600E-PB4), with a Horiba XploRA PLUS system, using a 50x Long Working Distance objective. For Raman spectra, excitation wavelength was 532 nm and grating 1800 l/mm; for PL excitation wavelength was 325 nm and grating 600 l/mm. Dry air and NO_2 gas (5 ppm) were flowed through mass flow controllers in the Linkam stage (V≈33 cm^3) with a rate of 50 sccm. All the experimental measurements were carried out at room temperature.

Results

Before NO_2 gas exposure, ZnO NWs and FTO substrate were characterized by Raman spectroscopy in dry air (RH=0) atmosphere (Fig. 2a). Typical Raman signal from ZnO was observed, with the main wurtzitic phase Raman modes: E_2^{high} (438 cm^{-1}), second order peaks at 200 cm^{-1} (overtone of the E_2^{low} mode out of detected range) and at ~330 cm^{-1} due to the combination of E_2^{high}-E_2^{low}. Linkam stage was then filled with 5 ppm NO_2 gas in dry air at 50 sccm for 30 minutes. In Fig. 2b, the Raman spectrum after NO_2 exposure (red solid line) of ZnO NWs is shown (acquisition time 5 s). An increase in the LO phonon band (~550 cm^{-1}) was observed. Later, a second spectrum with 60 s acquisition time was collected (not shown here), giving a prolonged laser (532 nm) exposure of the investigated area. The LO band decreased as shown in the second spectrum (red dashed line) of Fig. 2b, obtained with the same parameters (same acquisition time of 5 s). The decreasing of the LO band is interpreted as an effect of NO_2 laser-induced desorption from ZnO NWs surface.

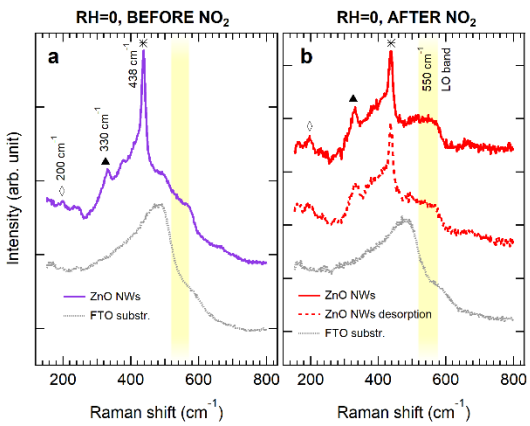

Fig. 2. Raman spectra of ZnO NWs on FTO substrate, (a) before and (b) after 5 ppm NO_2 exposure.

Further investigation is needed to better understand this effect. However, it is already possible to notice how the LO phonon mode variation is strongly related to the adsorbate on the surface. In our previous work [6], a different PL emission at 77 K of the isolated ZnO NWs with different diameters was observed (Fig. 3), allowing to discriminate "bulk" and surface effects. Three different PL regions were detected: the surface related spectral region around the peak at ~3.35 eV, the donor−acceptor pair (DAP) region centered at ~3.31 eV and the first order LO phonon replica of DAP (DAP-LO) at lower energy ~3.23 eV. The DAP-LO (signal related to "bulk" ZnO where the optical phonon can propagate) is the only PL region that shows a signal recovery [6] and this is consistent with Raman observation on bundles of ZnO NWs.

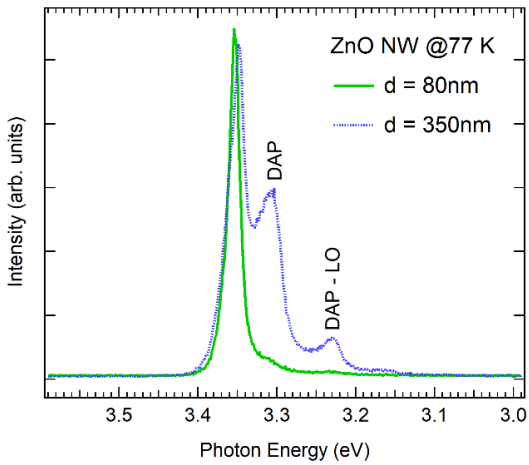

Fig. 3. Photoluminescence emission of two isolated ZnO NWs with different diameters (80 nm, green solid curve and 350 nm, blue dashed curve).

References

[1] Z.L. Wang, Zinc oxide nanostructures: growth, properties and applications, *J. Phys.: Condens. Matter* 16, R829–R858 (2004); doi:10.1088/0953-8984/16/25/R01

[2] Ü. Özgür, Ya. I. Alivov, C. Liu, A. Teke, M. A. Reshchikov, S. Doğan, V. Avrutin, S.-J. Cho, and H. Morkoç, A comprehensive review of ZnO materials and devices, *J. Appl. Phys.* 98, 041301 (2005); doi: 10.1063/1.1992666

[3] R. Bhujela, S. Raia, B.P. Swain, Spectroscopic characterization of CVD grown zinc oxide nanowires, M*aterials Science in Semiconductor Processing* 102, 104592 (2019); doi: 10.1016/j.mssp.2019.104592

[4] A.-K. Elger and C. Hess, Application of Raman Spectroscopy toWorking Gas Sensors: From In situ to Operando Studies, *Sensors*, 19, 5075 (2019); doi:10.3390/s19235075

[5] C. Klingshirn, ZnO: Material, Physics and Applications, *ChemPhysChem*, 8, 782 – 803 (2007); doi: 10.1002/cphc.200700002

[6] F. Rigoni, D. Zappa, C. Baratto, G. Faglia, E. Comini, Single ZnO Nanowire for Electrical and Optical NO_2 Gas Sensing: Origin of Reversible and Irreversible Gas Effects Investigated by Photoluminescence Spectroscopy, *ACS Sensors* 9, 4646-4654 (2024); doi: 10.1021/acssensors.4c00901

DOI 10.5162/eurosensors2026/2.2.2

A Lens-free Microscope with Edge AI Acceleration

Lena Zhukova[1,2], Luqi Yan[3], Agus Dharmawan[3], J. Daniel Prades[3], Ismael Benito-Altamirano[1,3,4]
[1] e-Health Centre & Faculty of Computer Science, Multimedia and Telecommunications, Universitat Oberta de Catalunya, Barcelona, Spain
[2] Centre for Sensors, Instruments and Systems Development (CD6), Universitat Politècnica de Catalunya, Barcelona, Spain
[3] Institute of Semiconductor Technology (IHT) & Laboratory for Emerging Nanometrology (LENA), Technische Universität Braunschweig, Braunschweig, Germany
[4] Department of Electronics and Biomedical Engineering, Universitat de Barcelona, Barcelona, Spain
ibenitoal@uoc.edu

Summary:
Lens-free microscopy offers a compact lab-on-a-chip solution but typically requires high external computational power for image reconstruction. This work introduces a lens-free system utilizing the Sony IMX500 sensor within the Raspberry Pi AI Camera. By removing the integrated lens, we leverage the sensor's internal AI accelerator to process in-line holographic images directly. Instead of traditional diffraction-based back-propagation, we employ Convolutional Neural Networks (CNNs) for real-time cell counting. Using a synthetic dataset for training, we applied post-training quantization to deploy our model onto the IMX500 hardware. Results demonstrate that the on-sensor AI performs comparably to a GPU, establishing a localized, low-power processing pipeline for portable lab-on-a-chip sensing.

Keywords: lens-free, microscopy, cell count, edge AI, deep learning

Introduction

Lens-free microscopy has become an easy solution for lab-in-a-chip solutions[1], despite this lens-less microscopy brings computational cost to the table which is often computed outside the lab-in-a-chip or in resource-intensive FPGA development boards. The post-processing pipeline for such images involve computer vision tasks (i.e. optical propagation, particle localization and counting, ...)[2].

In this work we introduce a new lens-free microscope based in the IMX500 sensor from Sony, packaged inside the Raspberry Pi AI Camera. The Sony IMX500 is a CMOS sensor that incorporates an AI accelerator inside the same chip, enabling running models like YOLO for human-activity recognition (see Fig.1).

By a small hardware modification of this camera, removing its lens system, we integrated it in our lens-free microscopy setup (see Fig.2a). We propose to use the AI accelerator inside the camera sensor for lens-free image processing. Rather than computing a back-propagation of the optical field using diffraction laws[2], we process the images with a CNN model to solve different task, like particle or cell counting directly from the in-line holographic image.

To train our CNN model, we created a synthetic dataset using the optical field propagation laws for several distributions of simulated samples resembling those from our laboratory (see Fig.b and Fig.c). Then, we trained the model on GPU, performed a quantization to the model, using the post-training quantization technique, and, finally, compiled the models for the IMX500 hardware. Models shown similar behavior in GPU and inside the IMX500 AI accelerator, enabling this technology for lab-on-a-chip sensing.

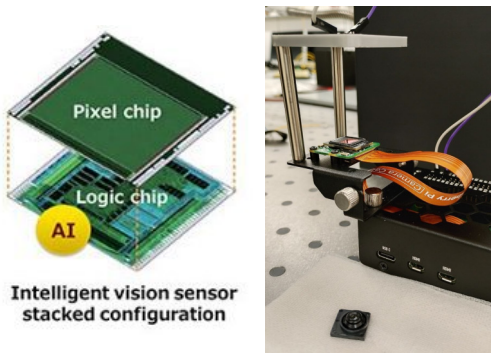

Fig. 1. (Left) The Sony IMX500 hardware stack (image from Sony). (Right) Provisional setup for a lens-less microscope based on a modified Raspberry Pi AI Camera. Image show the removed lens at the bottom.

DOI 10.5162/eurosensors2026/2.2.2

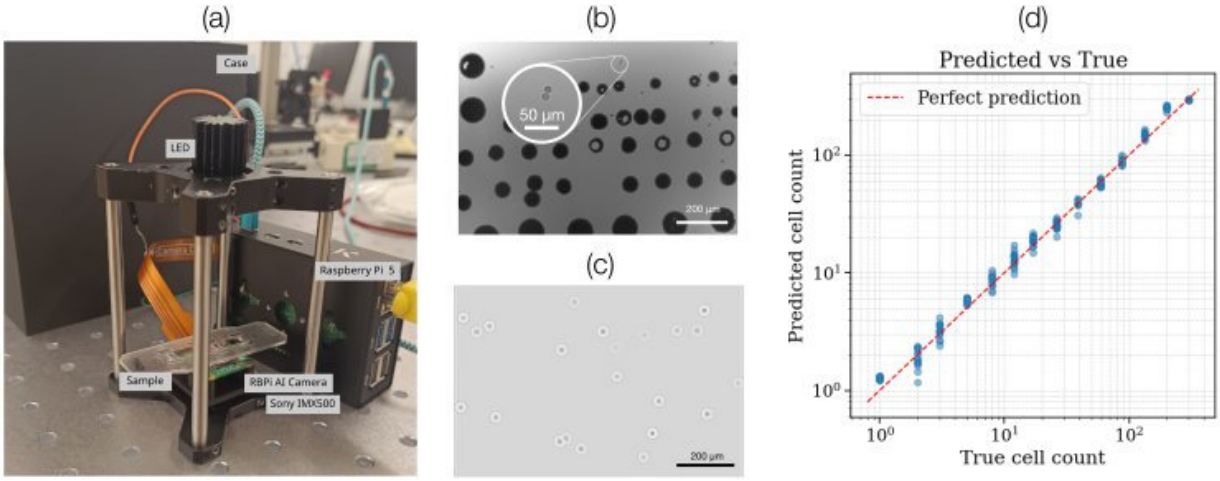

Fig. 2. (a) Our lens-free microscope setup, consists of: a case, an LED with a dissipation and a dampening filter, a sample, the modified AI camera a Raspberry Pi 5. (b) An actual image from a sample created with lithography from the IMX500 sensor. (c) A simulated image of a distribution of cells to train and to be predicted by the model. (d) Results from training a dataset of synthetic images.

Methodology

For the computational core of the system we defined a neural model, using PyTorch, this model consisted of a convolutional neural network (CNN) architecture designed for feature extraction through an 11-layer encoder, followed by a regression head for particle counting. To bridge the gap between high-level deep learning and resource-constrained sensing hardware, we quantized our model, this means we converted the model from a *float* model to a discrete logic model represented by *integer* logic.We used the Post-Training Quantization (PTQ) method[3], recommended by the IMX500 manufacturer. Using this technique, the model was optimized and compiled specifically for the IMX500 intelligent vision sensor's architecture. Enabling the sensor to perform on-chip inference directly from in-line holographic data.

The synthetic dataset was designed to cover a broad dynamic range of particle densities, utilizing a logarithmic distribution of cell counts ranging from 1 to 300. Each simulation modeled a 512 × 512 pixel window with a 2 µm pitch to match the IMX500 physical characteristics. To ensure model robustness and depth-of-field adaptability, we introduced stochastic physical parameters in the simulator: the sample-to-sensor distance was randomized between 400 µm and 1000 µm, and spherical illumination was applied based on a fixed 70 mm source-to-sensor distance. The training data was generated by applying Fresnel propagations[2] to objects with randomized cell morphologies and positions, rendering a total of 1.400 images.

Results

The model training was performed on GPU (NVIDIA GeForce RTX 2080 Ti) on a training split (1.190 samples), and successfully converged within 31 epochs, achieving a final validation MSE of 0.00054 and a MAE of 0.044 in log10 space. Then we used 10 random samples from the training set to perform the post-training quantization on the model, obtaining the quantized model. Finally, we observed the correlation between predicted and true cell counts over the test split (210 samples) remains highly linear across the entire dynamic range (see Fig.2d), demonstrating that the quantized model maintains high fidelity for counting tasks even when deployed on the resource-constrained IMX500 hardware.

Acknowledgments

I.B. ack. the support for the Spanish MCIU under the CAS24/00369 José Castillejo grant. Also, and the RA 2026 program from UOC. J.D.P. ack. the support from the Alexander von Humboldt Professorship of the Humboldt Foundation and the Federal Ministry for Education and Re-search (Germany), and the zukunft.niedersachsen program of the Lower Saxony MSC and the Volkswagen Foundation.

References

[1]A. B. Dharmawan et al., "Nonmechanical parfocal and autofocus features based on wave propagation distribution in lensfree holographic microscopy," Sci Rep, vol. 11, no. 1, p. 3213, Feb. 2021, doi: 10.1038/s41598-021-81098-7.

[2]I. Benito-Altamirano et al., "MicroVi: A Cost-Effective Microscopy Solution for Yeast Cell Detection and Count in Wine Value Chain," Biosensors, vol. 15, no. 1, p. 40, 2025.

[3]J. Zhang, Y. Zhou, and R. Saab, "Post-training quantization for neural networks with provable guarantees," SIAM journal on mathematics of data science, vol. 5, no. 2, pp. 373–399, 2023.

DOI 10.5162/eurosensors2026/2.2.3

Digital Bone Metastasis: an AI-based Organ-on-chip Platform for Modeling Breast Cancer Bone Metastasis

M. D'Orazio[1], A, Mencattini[1], L. Iafrate[2], V. de Turris[3], A. Agresti[1], S. Pescetelli[1], G. Ruocco[3], G. Cidonio[2,3], E. Martinelli[1]
[1] Department of Electronic Engineering, University of Rome Tor Vergata, Rome, Italy,
[2] Department of Mechanical and Aerospace Engineering (DIMA), Sapienza University of Rome, Rome, Italy
[3] Center for Life Nano- and Neuro-Science of Istituto Italiano di Tecnologia (IIT), Italy
Correspondence to: michele.d.orazio@uniroma2.it

Summary:

We present an integrated microfluidic and AI-based platform to model breast cancer (BC) bone metastasis on chip. We investigated how human bone marrow stromal cells (HBMSCs) influence BC cell motility, morphodynamics, and doxorubicin resistance. Our system captures rare motility phenotypes and increased invasion depth driven by stromal interactions. To decipher these behaviors, we developed the first agent-based model that reproduces the observed cellular dynamics, providing mechanistic insights into the metastatic process, ultimately bridging experimental and computational approaches.

Keywords: artificial intelligence, agent-based modeling, time-lapse microscopy, organ-on-chip, bone metastasis

Background, Motivation and Objective

Bone metastasis represents a major cause of morbidity and mortality in breast cancer (BC), largely due to microenvironment-mediated resistance to chemotherapy [1]. The bone niche provides biochemical and biomechanical cues that reprogram cancer cell phenotypes, promoting invasion and survival under treatment [2]. Conventional 2D cultures and animal models fail to capture the human-specific, dynamic interactions between BC cells and bone stromal cells that drive metastatic progression and drug resistance [3]. Organ-on-chip technologies offer a promising route to reproduce these interactions under controlled conditions [4], but quantitative, single-cell-resolved, and mechanistically interpretable frameworks are still lacking. Here we present an integrated bone-on-chip platform combined with artificial intelligence (AI) and agent-based modeling (ABM) to dissect stromal-driven chemoresistance in BC bone metastasis.

Description of the New Method or System

We engineered a microfluidic device hosting two adjacent compartments. Primary human bone marrow stromal cells (HBMSCs) were encapsulated in a 3D gelatin methacryloyl (GelMA)-Laponite® matrix. BC cells were seeded in an adjacent GelMA-coated chamber. Following BC cells invasion into the bone-like matrix, cultures were exposed to clinically relevant concentrations of doxorubicin and monitored for three days using confocal time-lapse microscopy (Fig. 1a). To quantitatively analyze cell motility and morphodynamics, we applied AI-based automated cell detection, tracking (Fig. 1b), and deep-learning-driven morphodynamic (Fig. 1c) and kinematic (Fig. 1d) cell profiling [5]. Finally, we developed an agent-based model (ABM) of breast-to-bone metastasis calibrated on experimental organ-on-chip data.

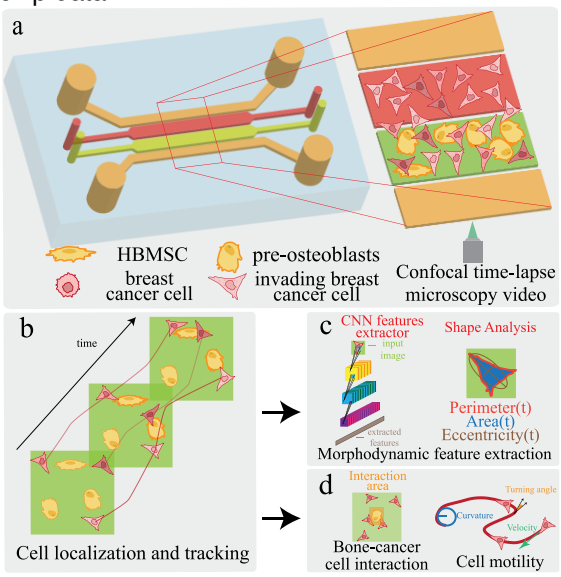

Fig. 1. (a) Schematic of the organ-on-chip model of the breast cancer bone metastasis. (b) Breast cancer cell localization and tracking. (c) Morphodynamic features extraction. (d) Kinematic features extraction.

Results

HBMSCs were found to induce heterogeneity in BC cell motility (Fig. 2a), characterized by the emergence of rare, highly motile “leader-like” cells that drive tissue penetration. Motility distributions were extracted from single-cell tracking on confocal time-lapse acquisitions and compared across conditions. Importantly, these extreme motility phenotypes persisted under doxorubicin treatment in the presence of HBMSCs, whereas chemotherapy significantly suppressed the highly motile BC cell population in their absence. This BC cell motility behavior was successfully qualitatively reproduced by the ABM model (Fig. 2b). Deep learning (DL)-based morphodynamic profiling, extracting time-resolved shape descriptors from segmented cell sequences, revealed that HBMSC interaction drives a distinct cancer cell state (Fig. 3a), largely insensitive to drug-induced morphological perturbations (Fig. 3b). On the contrary in the absence of HBMSCs a doxorubicin-induced switch in morphodynamic features was observed (Fig. 3c). We found doxorubicin significantly reduces BC cell interactions with HBMSCs measured in terms of interaction commitment (defined as the ratio between the interaction area and the total area of the cell) (Fig. 4a). This behavior was qualitatively reproduced by the *in silico* model (Fig. 4b).

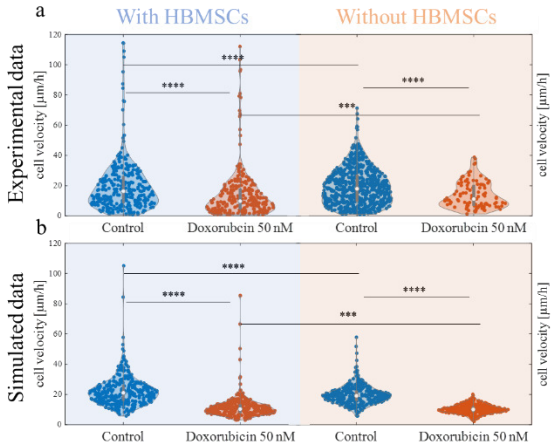

Fig. 2. Average cell velocity with (left-blue panel) and without (right-red panel) in experimental (a) and simulated (b) data.

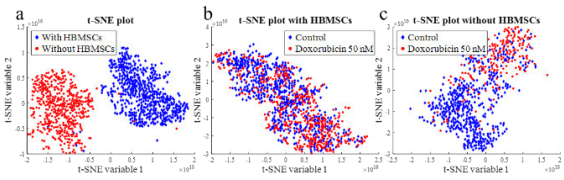

Fig. 3. t-SNE scatter plot of BC cell morphodynamic descriptors. With vs without HBMSC (a), Control vs Doxorubicin 50 nM with (b) and without (c) HBMSCs.

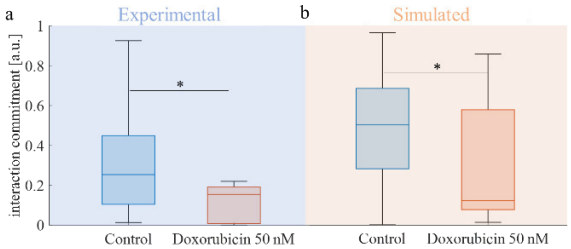

Fig. 4. Box-plot of BC cells-HBMSCs interaction commitment in control and Doxorubicin 50 nM treated scenarios in real (a) and simulated (b) data.

Direct quantification of cancer–stroma interactions demonstrated that interaction with HBMSCs significantly triggers a motility switch toward faster and more directed migration, as well as cell elongation and a change in DL-based morphodynamic descriptors (results will be presented at the conference). Viability assays confirmed that HBMSCs provide a protective niche, significantly attenuating doxorubicin-induced cytotoxicity (results will be presented at the conference), in agreement with previous reports on mesenchymal stromal cell-mediated drug resistance [6]. By explicitly incorporating cell–cell attraction, repulsion, matrix-dependent friction, and nutrient gradients, the ABM model identified intercellular interaction strength and chemotactic sensitivity as key regulators. This study demonstrates how advanced organ-on-chip biomaterials, AI-powered single-cell analytics, and mechanistic *in silico* modeling can be integrated into a predictive platform for metastatic disease. This approach will help link simplified *in vitro* models to complex physiological conditions observed *in vivo*, increasing the translational relevance of the obtained results.

References

[1] X. Lu, Y. Kang, Organotropism of breast cancer metastasis, *J. Mamm. Gland Biol. Neopl.*, 12, 153-162 (2007); doi: 10.1007/s10911-007-9047-3

[2] F. Salvador, et al., From latency to overt bone metastasis in breast cancer: potential for treatment and prevention, *J. of Pathology*, 249, 6-18 (2019); doi: 10.1002/path.5292

[3] M. Kapałczyńska, et al., 2D and 3D cell cultures – a comparison of different types of cancer cell cultures, *Arch. Med. Sci.*, 14, 910-919 (2018); doi: 10.5114/aoms.2016.63743

[4] M. Gonçalves, et al., Organ-on-a-Chip Platforms for Drug Screening and Delivery in Tumor Cells: a Systematic Review, *Cancers (Basel)*, 14, 1-25 (2022): doi: 10.3390/cancers14040935

[5] M. D’Orazio, et al., Machine learning phenomics (MLP) combining deep learning with time-lapse-microscopy for monitoring colorectal adenocarcinoma cells gene expression and drug-response, *Sci. Rep.*, 12, 8545 (2022); doi: 10.1038/s41598-022-12364-5

[6] T. Luo, et al.,Mesenchymal Stem Cell-Secreted Exosome Promotes Chemoresistance in Breast Cancer via Enhancing miR-21-5p-Mediated S100A6 Expression, *Mol. Ther. Oncolytics*, 19, 283 (2020); doi: 10.1016/j.omto.2020.10.008

DOI 10.5162/eurosensors2026/2.2.4

A Miniaturized Optical Online Sensor for the Detection of Oil Pollution on Water Surfaces

Martin Brandl[1], Thomas Posnicek[1], Anja Knecht[1]
[1] University for Continuing Education Krems, Department for Integrated Sensor Systems, 3500 Krems, Austria
Martin.Brandl@donau-uni.ac.at

Summary:
Oil contamination of surface waters poses serious environmental and economic risks, even at very low concentrations. To enable early detection, a miniaturized optical sensor based on UV-induced fluorescence was developed for real-time, contact-free monitoring of oil films on water surfaces. The system employs a UV LED excitation source and lock-in signal processing to achieve high sensitivity under varying environmental conditions. Laboratory tests demonstrate detection limits below 0.1 µl/cm² for mineral oils such as diesel, gasoline, and engine oil. Owing to its compact design, low power consumption, and robust performance, the sensor is well suited for permanent deployment in early warning networks for water quality monitoring.

Keywords: Oil pollution detection, UV fluorescence sensor, Online water quality monitoring, Miniaturized optical sensor, Early warning system

Introduction

Oil pollution of surface waters remains a major environmental concern due to its adverse effects on aquatic ecosystems, drinking water resources, and socio-economic activities. Even very thin oil films can impair gas exchange at the water–air interface, harm aquatic organisms, and promote the transport of hazardous substances over long distances in rivers and drainage systems [1,2]. Accidental spills, traffic runoff, and diffuse urban or industrial emissions contribute continuously to oil contamination, making early detection and continuous monitoring essential.

Conventional oil detection methods rely mainly on manual sampling and laboratory analyses, which are time-consuming and unsuitable for real-time warning scenarios. Remote sensing techniques, such as satellite or airborne systems, offer broad spatial coverage but often lack the sensitivity and temporal resolution needed to detect small-scale or early-stage pollution events in inland waters [2,3]. Therefore, compact in-situ sensors capable of autonomous and continuous operation are increasingly sought.

Optical sensing approaches based on ultraviolet (UV) excitation are particularly promising, as many oils show strong fluorescence and high reflectivity under UV illumination, whereas clean water exhibits only weak background signals [2,4]. Advances in UV LEDs and miniaturized optoelectronics have enabled compact, energy-efficient fluorescence sensors suitable for online water monitoring [3]. These developments form the basis of the sensor concept presented here.

Objectives

Oil pollution in surface waters poses significant environmental risks, even at very low concentrations. Thin oil films are difficult to detect visually but can already cause ecological damage. Consequently, there is a strong demand for robust, sensitive, and cost-effective sensors for continuous, real-time monitoring that can function as early warning systems. The goal of this work is the development of a miniaturized optical oil sensor that exploits UV-induced fluorescence to detect oil films on water surfaces using commercially available components and low power consumption.

Sensor Setup and Results

The optical setup consists of a UV LED with a central wavelength of 365 nm as excitation source, collimating and focusing optics to define a well-confined measurement spot on the water surface, and a fluorescence detection channel (~420nm) equipped with spectral filters and a photodiode (Fig. 1A). Dichroic optics are used to spatially separate excitation and emission paths, ensuring efficient suppression of scattered UV light. To minimize disturbances caused by ambient light, especially sunlight, the excitation

source is intensity-modulated, and the detected signal is processed using a lock-in amplification principle. This significantly improves the signal-to-noise ratio and allows reliable measurements under varying environmental conditions, including changing illumination, temperature variations, and moderate surface waves. All optical and electronic components are integrated into a compact, watertight housing with dimensions of approximately 10 × 10 × 5 cm³. The sensor operates contact-free at a distance of 10–20 cm above the water surface and can be installed in drainage channels, wastewater systems, riverbanks, or on floating platforms (Fig. 1B). The modular optical design enables adaptation to different deployment scenarios.

A)

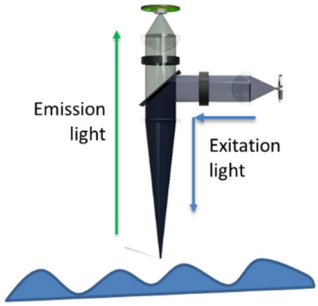

B)

*Fig. 1. **A)** Optical pathway of the confocal fluorescence detector. **B)** View of the assembled Detector.*

The determined limits of detection demonstrate the high sensitivity of the system. For mineral oils, detection limits (LOD) below 0.1 µl/cm² of water surface were achieved, corresponding to extremely thin oil films that are barely visible to the naked eye. For example, engine oil could be detected down to approximately 0.07 µl/cm². while diesel fuel and gasoline showed comparable detection thresholds (Fig. 2, Table 1). As expected, vegetable oil exhibited weaker fluorescence and thus higher detection limits; nevertheless, even rapeseed oil could be reliably detected at concentrations relevant for environmental monitoring. Temperature tests between 5 °C and 35 °C revealed moderate signal variations mainly caused by photodiode sensitivity, which can be compensated by calibration. Measurements under disturbed surface conditions confirmed reliable operation in dynamic water environments. Compared to conventional detection approaches, the presented sensor enables localization, real-time monitoring with low maintenance effort, no reagents, and reduced system cost. It is therefore well suited for integration into early warning networks for stormwater systems, industrial effluents, and sensitive surface waters.

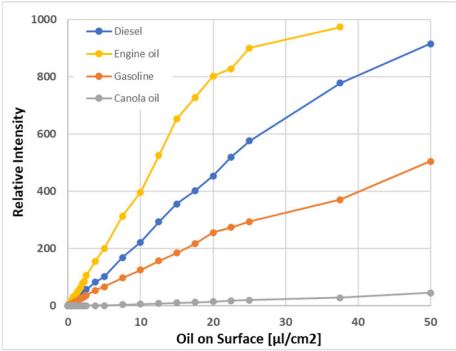

Fig. 2. Fluorescence intensity as a function of the amount of different types of oil.

Table 1. Limit of detection (LOD) for different types of oil.

	Diesel	Gasoline	Engine oil	Canola oil
LOD [µl]	12,24	13.26	27.68	155.76
LOD [µl/cm²]	0.17	0.19	0.39	2.20

Conclusions

A compact and cost-effective optical sensor for real-time detection of oil pollution on water surfaces was developed and validated. The combination of UV fluorescence sensing, lock-in amplification, and miniaturized optoelectronics results in a robust system with high sensitivity for environmental monitoring. Future work will focus on long-term field validation, further miniaturization, and intelligent data processing for autonomous sensor networks.

References

[1] Kvočka, D., Žagar, D., & Banovec, P. A review of river oil spill modeling. *Water*, 13(12), 1620, 2021.

[2] Fingas, M., & Brown, C. E. A review of oil spill remote sensing. *Sensors*, 18(1), 91, 2017.

[3] Duan, Z., Li, Y., Wang, J., Zhao, G., & Svanberg, S. Aquatic environment monitoring using a drone-based fluorosensor. *Applied Physics B*, 125(6), 2019.

[4] Carl von Ossietzky University of Oldenburg. Remote Sensing Using Lasers (SEOS Project).

DOI 10.5162/eurosensors2026/2.2.5

Monolithic LED Emitter-Detector for colorimetric CO_2 gas sensor

Martí Verdaguer Mallorquí[1], María González-Gómez[1,2], Jana Hartmann[2], Cristian Fàbrega[1], Andreas Waag[2], Joan Daniel Prades[2], Olga Casals Guillén[1]
[1] MIND/IN2UB, Dept. of Electronics and Biomedical Engineering, University of Barcelona, Marti i Franqués 1, Barcelona ES08028, Spain
[2] Institute of Semiconductor Technology (IHT) and Laboratory for Emerging Nanometrology (LENA), Technische Universität Braunschweig, D-38106 Braunschweig, Germany;
olga.casals@ub.edu

Summary: This work presents a monolithic GaN optoelectronic platform integrated with a colorimetric indicator layer for gas sensing applications. The system integrates an InGaN/GaN LED emitter and photodetector on the same chip, enabling optical interrogation without external alignment or discrete optical components. The exposure to CO_2 of the pH-sensitive colorimetric layer results in a color change that is measured as a decrease of photodiode current. The sensor shows reproducible responses to CO_2 concentrations from 1 to 40 % operating at power range of hundreds of microwatts.

Keywords: Nitride-based LED, Nitride-based photodiode, Monolithic integration, Carbon dioxide, Colorimetric gas sensor.

Background, Motivation and Objective

Colorimetric indicators offer a simple and low-cost route for detecting chemical and biochemical species through analyte-induced optical changes. Their practical use, however, is often constrained by external optical readers, controlled illumination, camera calibration, or bulky discrete components. InGaN/GaN multiple-quantum-well structures are attractive because the same epitaxial platform can be engineered for light emission and photodetection. Monolithic GaN LEDs, photodetectors, waveguides, and monitoring elements have demonstrated compact, robust, alignment-free optical systems [1,2], and recent gas-sensing prototypes have shown that color changes can be converted into electrical signals at chip scale [3].

Nevertheless, fully integrated GaN system-on-chip interrogation of colorimetric indicators remains underdeveloped. Outstanding challenges include optical crosstalk, efficient coupling between the indicator layer and the active devices, reproducible sensing-layer deposition, and robust calibration under varying environmental conditions. Here, we develop a monolithic GaN system-on-chip that combines integrated light emission and photodetection with colorimetric indicator layer for compact, low-power, and scalable colorimetric sensing.

Description of the New Method or System

The monolithic GaN optoelectronic transducer was fabricated from an InGaN/GaN LED epitaxial stack grown on sapphire. Two junctions were processed on the same chip: one is forward-biased as the emitter, whereas the second is operated as a short-circuit photodetector. Hereafter, this architecture is referred to as a monolithic LED emitter-detector (MLED). The emitter and detector mesas were defined by ICP-RIE and contacted individually while sharing a common n-GaN layer. The integrated configuration removes the need for external alignment between discrete optical components, reducing system complexity and power consumption. The LED device emits at around 455 nm, where the selected CO_2 indicator exhibits a measurable transmission change.

The sensing layer consists of a pH dye, m-cresol purple, immobilized in a hydroxyethyl cellulose matrix [4]. A thin film was spin-coated between the MLED emitter and detector. When CO_2 dissolves in the water contained in the matrix, the local pH decreases and the dye changes from deep purple-blue to yellow. The resulting change in optical absorption is detected as a reduction in the detector photocurrent.

Results

Figure 1 shows the response of the MLED device coated with the colorimetric indicator. The LED was powered with 750 µW, and the detector photocurrent was recorded under short-circuit conditions. Upon exposure to 6 pulses of three different CO_2 concentrations, 1, 10 and 40 % in synthetic air with 50 % of relative humidity, the photocurrent of MLED device shows a clear, stable and repetitive decrease. The photocurrent decrease scales with CO_2 concentration, and repeated pulses at the same concentration showed discrepancies as low as 0.6%.

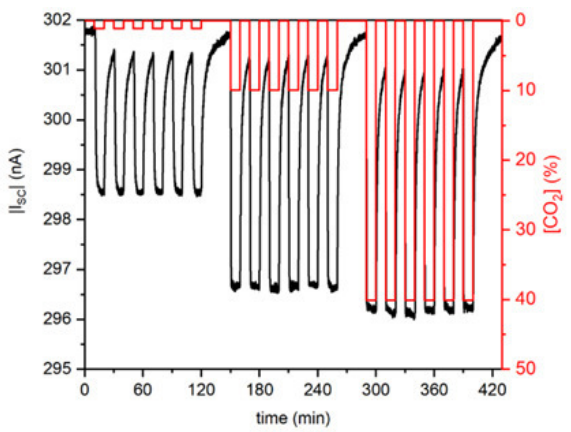

Fig. 1. Short-circuit photodiode current (photocurrent) measured with the LED power set to 750 µW while the colorimetric indicator is exposed to 6 pulses of three different CO_2 concentrations, 1, 10 and 40 % in synthetic air with 50 % of relative humidity (21°C and 1 atm).

For a given CO_2 concentration, the absolute photocurrent decrease depends on the power applied to the LED. In contrast, the relative photocurrent change is largely independent of LED power, as shown in Figure 2. The sensor response was therefore calculated from the photocurrent measured in synthetic air and under CO_2 exposure as:

$$S(\%) = \frac{I_{CO_2} - I_{SA}}{I_{SA}} \cdot 100 \qquad (1)$$

Accordingly, the relative response in Figure 2 can be directly related to the CO_2-dependent absorption change of the colorimetric indicator. Notably, these responses were obtained with LED powers between 125 and 750 µW, substantially below the 165 mW reported for an integrated microsystem based on off-the-shelf components [3].

Response times were estimated to be on the order of tens of seconds or less; the current experimental set-up requires at least 2 min to reach the target CO_2 concentration, which limits a more precise determination. Complete recovery of the baseline photocurrent was observed after CO_2 removal, although recovery times up to 10 min were required at the highest concentrations.

In summary, MLED devices enable electrical readout of absorption changes in colorimetric indicators and constitute a compact, low-power platform for CO_2 gas sensing.

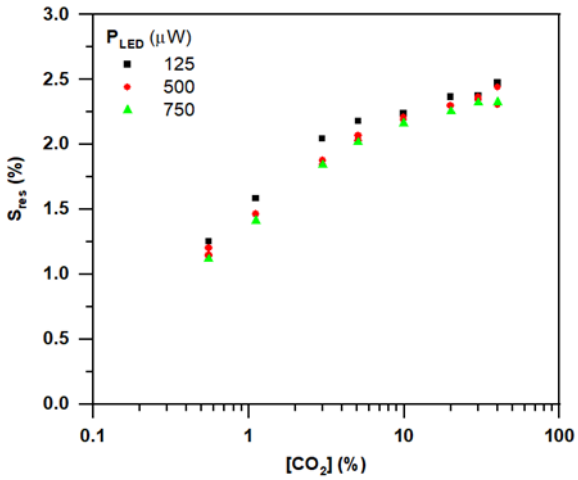

Fig. 2. Sensor Response versus the CO_2 concentration in synthetic air with a relative humidity of 50 % (21°C and 1 atm) for different LED powers.

References

[1] Li K, Fu W, Cheung Y, et al., Monolithically integrated InGaN/GaN light-emitting diodes, photodetectors, and waveguides on Si substrate, Optica 5, 564-569 (2018) doi:10.1364/OPITCA.5.000564

[2] Zhang H, Yan J, Ye Z, et al. Monolithic GaN optoelectronic system on a Si substrate. *Appl. Phys. Lett.*121, 181103(2022). doi:10.1063/5.0125324

[3] Driau C, Fàbrega C, Benito-Altamirano I, et al. How to implement a selective colorimetric gas sensor with off the shelf components? Sens Actuators B Chem. 293,41–44 (2019). Doi:10.1016/j.snb.2019.04.117

[4] González-Gómez M, Benito-Altamirano I, Prades JD, et al. Ultralow-Cost and Selective Water-Based Colorimetric Ink for Indoor CO_2 Monitoring. IEEE Sens J. 25,18722–18730 (2025). doi: 10.1109/JSEN.2025.3559593

DOI 10.5162/eurosensors2026/2.2.6

A Portable and Low-Cost Spirometer with Knife-Edge Optical Detection

Sena Ulgaz[1], Ömer Gökalp Akcan[1,3], Berkay Yılmaz[2], Onur Ferhanoglu[1], Yiğit Dağhan Gökdel[2]
[1] Department of Electronics and Communication Engineering, Istanbul Technical University, 34467, Istanbul, Türkiye.
[2] Department of Electrical and Electronics Engineering, Istanbul Bilgi University, 34060, Türkiye.
[3] Advanced Vocational Studies, Big Data Analytics, Istanbul Bilgi University, 34387, Istanbul, Türkiye.
ulgaz25@itu.edu.tr

Summary:
We present a portable, low-cost optical spirometer that overcomes moisture-induced degradation of resistive sensors. A compliant double-leaf structure modulates transmitted light intensity under airflow, eliminating electrical elements from the airflow path. We demonstrate a linear optical response up to 160 kPa input flow pressure and distinguishable breathing patterns across multiple subjects, confirming the system's potential as a scalable disposable respiratory monitoring device.

Keywords: Spirometer, Optical sensing, Knife-edge optics, MEMS airflow sensor, Disposable sensors.

Introduction

Spirometry is a widely used diagnostic tool for assessing pulmonary function, particularly in diseases such as asthma and chronic obstructive pulmonary disease (COPD). Conventional spirometers are susceptible to contamination from saliva during repeated use and inadequate hygiene [1]. Furthermore, existing research on various sensing mechanisms indicated that many current devices are difficult to fabricate and lack disposability, further exacerbating the risk of contamination [2]-[4]. In our previous work, a disposable airflow sensor based on graphite-coated paper demonstrated low-cost fabrication and promising sensitivity. However, the electrical readout mechanism exhibited degradation due to moisture and biological contaminants, limiting long-term reliability in real-world conditions [5]. To address these limitations, here we propose an optical spirometer that eliminates electrical sensing components within the airflow path. By employing a knife-edge readout, airflow-induced mechanical deformation is transduced into an optical signal. This design leverages additive manufacturing and standard optoelectronic components, offering a robust, moisture-resistant, and cost-effective solution suitable for scalable personal healthcare applications.

System Description

Fig. 1 illustrates the proposed optical knife-edge detection system for a portable spirometer. A red LED array, mounted inside an SLA-printed tube, illuminates a flexible sensor element positioned 6 cm away from the LED source. Air pressure impinges on the sensor, causing deflection that progressively unblocks the beam and modulates the transmitted light intensity. The diverging beam exiting the tube travels 9 cm before being collected by a convex lens, which the beam toward the photodetector positioned 3.5 cm beyond the lens. The resulting optical signal is converted to electrical domain via the photodetector and is recorded by a digital oscilloscope and transferred to a computer for post-processing.

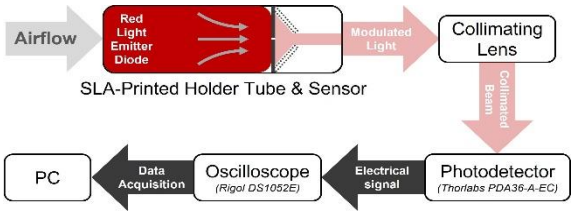

Fig. 1. Block diagram of the light-intensity-based air pressure measurement setup.

The proposed structure, shown in Fig. 2(a) and 2(b), illustrates the sensor geometry and FEM (Finite Element Method) analysis. The sensor consists of two semicircles, each with a radius (r_{dl}) of 9.5 mm and a thickness of 0.6 mm, separated by a gap (g_{dl}) of 1.4 mm in the initial (undeflected) position. The sensor is anchored inside the holder tube via cantilever beams of length (l_c) 3 mm attached to the semicircular leaves. This double-leaf structure is fabricated via SLA 3D printing (Anycubic® Photon Mono SE) using Anycubic® Tough Resin Ultra-Gray) (E = 1.35 GPa, ρ = 1118 kg/m3). Simulations were performed to evaluate the mechanical response of the sensor under applied pressure.

Under a load of 11.732 kPa, the FEM analysis yielded a maximum deflection of δ_{max}= 7.22 mm, confirming that the structure to support large deflections while remaining below the yield point. The geometry was optimized to ensure repeatable deflection while avoiding plastic deformation under typical spirometry pressure ranges [6].

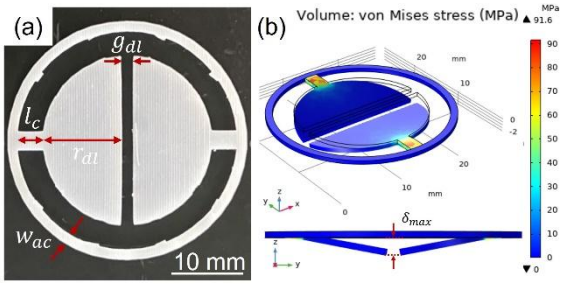

Fig. 2. (a) fabricated sensor with desing parameters, (b) FEM results of the double-leaf sensor (σmax = 91.6 MPa).

Results and Conclusion

Figure 3 presents controlled airflow tests using an air compressor connected to the proximal end of the device, with pressure levels ranging from 0 to 700 KPa. Data was acquired 3 times at each pressure.

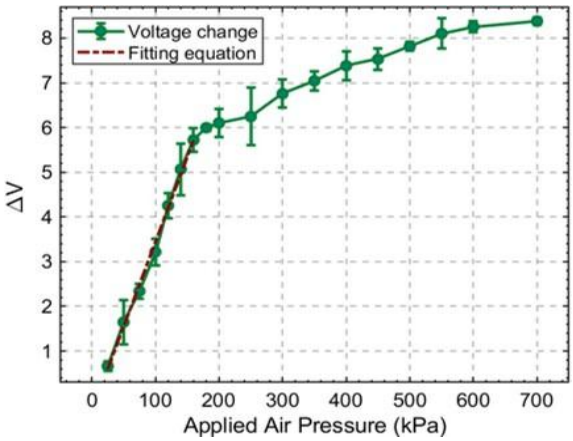

Fig. 3. Voltage response of the optical sensor versus applied pressure (f(x) = 0.0379x – 0.3514, R² = 0.995, RMSE = 0.1431). Error bars demonstrate 3 standard deviations of variability among experiments.

The sensor exhibited a linear response up to 160 kPa, with a sensivity of 0.04 V/kPa. In this regime, mechanical deformation remains elastic and transmitted light intensity scales proportionally with the opening area of the double-leaf structure. Beyond 160 kPa, nonlinear mechanical deformation and photodetector saturation drive the sensor into nonlinearity, highlighted the importance of co-designing mechanical and optical subsystems for extended dynamic range. Second, human subject testing was conducted with four participants performing forced exhalation and inhalation maneuvers. As shown Fig. 4, distinct breathing profiles were captured across subjects, with amplitude differences attributed to gender and smoking behavior (Subject 1 and Subject 2 are the only male smoker, and subject 4 is the only female subject). The results confirm the system's capability to extract meaningful physiological information, while the absence of electrical elements in the airflow path ensures moisture-resistant, stable operation addressing the primary failure mechanism of previously developed graphite-based sensors.

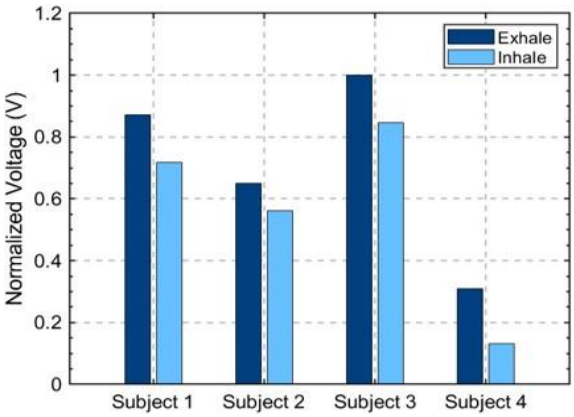

Fig. 4. Normalized exhale and inhale voltage responses recorded from four human subjects.

This work presents a low-cost optical spirometer replacing conventional electrical readout with optical modulation, demonstrating linear pressure response and successful capture of human respiratory patterns. Future work will target ray-tracing optimization, experimentation with a larger number of subjects and compact electronics integration for real-time portable healthcare applications.

References

[1] Kendrick, A. H., D. P. Johns, and J. P. Leeming. "Infection control of lung functipractical approach." *Respiratory medicine* 97.11 (2003): 1163-1179.

[2] Saroli, Vincenzo, et al. "Advancing flow rate measurement: innovations and challenges in spirometry and mechanical ventilation." *IEEE Sensors Reviews* (2025).

[3] Wang, Kaifeng, et al. "A High-Sensitivity and Wide-Range FBG-Based Flow Sensor for Pulmonary Function Tests." *IEEE Sensors Journal* (2026).

[4] Zhang, Zhang, et al. "A multifunctional airflow sensor enabled by optical micro/nanofiber." *Advanced Fiber Materials* 3.6 (2021): 359-367.

[5] Aygül, Beril, et al. "Disposable piezoresistive mems airflow sensor for chronic respiratory disease detection." *Journal of Microelectromechanical Systems* 34.1 (2024): 100-107.

[6] Pleil, Joachim D., et al. "The physics of human breathing: flow, timing, volume, and pressure parameters for normal, on-demand, and ventilator respiration." *Journal of breath research* 15.4 (2021): 042002.

DOI 10.5162/eurosensors2026/2.3.1

Beyond Surface Area: Microfabrication-Compatible Electrode Nanostructuring for High-Performance Miniaturized Electrochemical and Bioelectrical Sensors

Irene Taurino
KU Leuven, Kasteelpark Arenberg 10, 3001 Leuven, Belgium
irene.taurino@kuleuven.be

Abstract:

The progressive miniaturization of electro(chemical) sensors improves spatial resolution and integration capabilities but leads to reduced electroactive area and increased electrode impedance, limiting sensitivity and signal quality. These constraints apply broadly to both electrochemical detection and bioelectrical measurements. Conventional approaches relying on ex situ nanomaterial integration are often hindered by poor reproducibility, cleanroom incompatibility, binder-related artefacts, and limited mechanical stability.

This talk will present a microfabrication-enabled paradigm based on direct electrode modifications, delivering binder-free, scalable, and stable nano–microarchitectures. The resulting electrodes provide increased effective surface area, improved charge-transfer properties, and reduced interfacial impedance, enhancing performance across sensing modalities.

The approach will be illustrated through two applications: (i) non-enzymatic glucose sensing in chloride-rich physiological media, where electrode engineering, combined with *ad hoc* electroanalytical operation, enables transient catalytic activity and (ii) nanostructured silicon microneedle arrays for wearable EEG, showing improved signal-to-noise ratios.

These results demonstrate that electrode architecture, beyond simple surface area scaling, governs performance, and establish nanostructuration as a reproducible pathway toward high-performance miniaturized sensing systems.

Keywords:

electrode nanostructuring, microfabrication-compatible sensors, electrochemical and bioelectrical sensing, non-enzymatic glucose monitoring, EEG monitoring, wearable microneedle electrodes

References:

[1] M. Amir, R. Ding, N. Izni Rusli, N. Vercooren, F. Ceyssens, N. Kuznetsova, C. Wang, A. Bertrand, M. Kraft, I. Taurino, Microneedle Momina Platinum-Nanostructured Silicon Microneedles with Scalable Fabrication for EEG Biosensing. (2026). Accepted in *Microsystems & Nanoengineering*.

[2] M. Amir, M. Kraft, I. Taurino. High Performance Microneedle Patches for Biomedical Applications. (2026).

[3] F. Franceschini, I. Taurino. Designing Electrocatalytic Interfaces for Non-Enzymatic Glucose Sensing: from Metal Oxides to Porous Gold. (2026).

DOI 10.5162/eurosensors2026/2.3.2

Motion Artifact Removal for Moving FMCW Radar-Based Vital Sign Sensing Using IMU

Natsuhiko Mascia[1], Jarred Fastier-Wooller[1], Shun Muramatsu[1], Michitaka Yamamoto[1], Toshihiro Itoh[1]
[1] Department of Precision Engineering, Graduate School of Engineering, The University of Tokyo, 7-3-1 Hongo, Bunkyo-ku 113-8656, Tokyo, Japan
Email Adress: gmascia2002@g.ecc.u-tokyo.ac.jp

Summary:

We propose an IMU-based motion artifact removal algorithm for non-contact vital sign monitoring, in which a frequency-modulated continuous-wave (FMCW) millimeter-wave (mm Wave) radar and an inertial measurement unit (IMU) are co-mounted on a moving platform. A least mean squares (LMS) adaptive filter exploits the correlation between IMU acceleration and radar phase disturbance to suppress motion-induced artifacts. Phantom experiments demonstrated a mean signal-to-noise ratio (SNR) improvement of 31.85 dB after calibration, while the cardiac signal at 1 Hz was preserved.

Keywords: radar, vital sign sensing, motion artifact removal, IMU, adaptive filter

Introduction

In Japan, the rapid aging of society and the growing prevalence of single-person elderly households have created an urgent need for unobtrusive health monitoring systems. Companion animals and social robots offer a natural mobile platform for such monitoring, as they move freely within the living space without requiring the user to wear any device. Non-contact vital sign sensing using mm Wave FMCW radar has emerged as a promising approach, detecting subtle skin displacements caused by cardiorespiratory activity without wearables [1]. Recent studies have explored mounting radar on mobile platforms to enable room scale monitoring [2].

However, existing approaches assume that either the subject or the radar is stationary. When mounted on a moving platform, carrier motion introduces phase artifacts that are indistinguishable from vital sign signals.

In this paper, we propose co-mounting an FMCW mm Wave radar and an IMU on a pet collar, using IMU-acquired acceleration as a reference signal to suppress motion-induced artifacts via an LMS adaptive filter, as shown in Fig. 1.

Materials and Methods

The proposed vital sign monitoring system is shown in Fig.2. An FMCW mm Wave radar (Acconeer XE125) and an IMU (Adafruit Feather nRF52840) are co-mounted on a pet collar, enabling continuous cardiac monitoring in home environments. For a stationary radar, the phase shift due to small skin displacement $d(t)$ caused by respiration and heartbeat can be expressed as eq. (1), where λ is the wavelength of the transmitted signal.

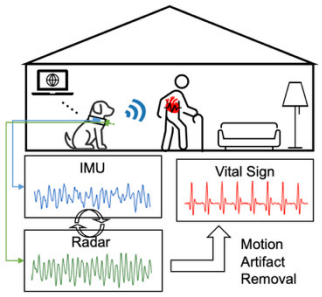

Fig.1. Overview of the proposed pet-collar mounted mm Wave radar system for non-contact vitals sign monitoring

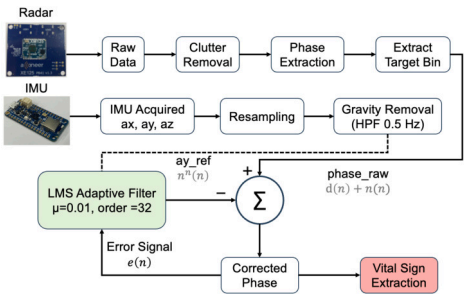

Fig.2. Block diagram of the proposed IMU-based motion artifact removal algorithm

$$\varphi(t) = \frac{4\pi}{\lambda} d(t) \tag{1}$$

However, when the radar itself undergoes motion, an additional phase component arising from the carrier's movement is superimposed, such that the measured phase becomes eq. (2).

$$\varphi_{\text{meas}}(t) = \frac{4\pi}{\lambda}[d(t) + d_{\text{noise}}(t)] \tag{2}$$

Since $d_{\text{noise}}(t)$ is correlated with the IMU-measured acceleration, it can be estimated and suppressed using the IMU signal as a reference, regardless of its spectral content.

To address this, the IMU simultaneously records the three-axis acceleration of the platform. The IMU-derived acceleration signal is resampled to match the radar frame rate and high-pass filtered at 0.5 Hz to remove gravitational components. The processed signal is fed as a reference input to an LMS adaptive filter (μ = 0.01, order = 32), which adaptively estimates and subtracts the motion-induced phase artifact via an error signal feedback loop, yielding a corrected phase signal. Heart rate is subsequently extracted through vital sign extraction.

To evaluate the proposed method, a phantom experiment was conducted in a controlled laboratory environment as shown in Fig.3. A chest phantom (servo motors driving a gel-padded surface at 1Hz) simulated cardiac motion, while a mechanical shaker vibrating at 3 Hz provided motion artifacts to the co-mounted radar and IMU. Data were collected simultaneously at approximately 54 FPS over 30 minutes and segmented into 35 non-overlapping 50-second windows for analysis. The SNR is defined as the ratio of PSD at the cardiac frequency (1 Hz) to that at the artifact frequency (3 Hz).

Results and Discussion

Figure 4 shows the PSD of the radar phase signal before and after calibration. The artifact component at 3 Hz was reduced by 24.2 dB, while the cardiac signal at 1 Hz was preserved with a change of only +0.13 dB. This selective suppression demonstrates a key advantage of the LMS adaptive filter: by exploiting the correlation between the IMU reference signal and the motion-induced phase artifact, the algorithm can remove the artifact without prior knowledge of its frequency.

Figure 5 shows the distribution of SNR across 35 measurement windows. Without calibration, the mean SNR was 0.42 ± 0.28 dB, indicating that artifact power was comparable to the cardiac signal and that heart rate estimation would be unreliable. After applying the proposed LMS-based motion artifact removal method, the SNR improved to 32.27 ± 4.25 dB, a mean improvement of 31.85 dB.

Conclusion

We proposed an IMU-based motion artifact removal method for non-contact vital sign monitoring using a co-mounted FMCW mm Wave radar and IMU. An LMS adaptive filter exploits the correlation between IMU acceleration and radar phase disturbance to suppress motion-induced artifacts without prior knowledge of the artifact frequency. Phantom experiments demonstrated a mean SNR improvement of 31.85 dB while preserving the cardiac signal with a PSD change of only +0.13 dB at 1 Hz. Future work will focus on validation with animal subjects and extension to scenarios where motion artifact and vital sign frequencies overlap.

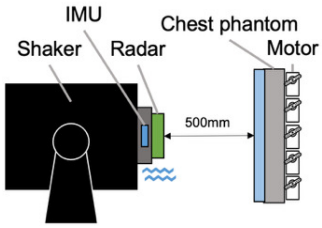

Fig.3. Experimental setup for evaluation

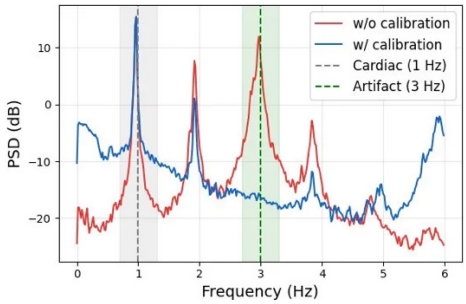

Fig.4. PSD of the radar phase signal before and after IMU-based calibration.

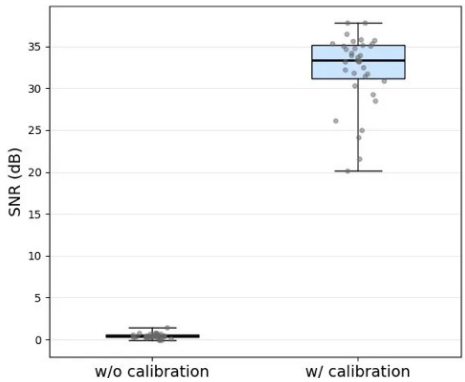

Fig.5. SNR comparison before and after IMU-based motion artifact removal (n = 35).

References

[1] M.Alizadeh, G.Shaker, J.C.M. De Almeida, P.P.Morita, and S. Safavi-Naeini, Remote monitoring of human vital signs using mm-wave FMCW radar, IEEE Access 7, 54958-54968 (2019); doi:10.1109/ACCESS.2019.2912956

[2] P. Zhao, C. X. Lu, B. Wang, C. Chen, L. Xie, M. Wang, N. Trigoni, and A. Markham, Heart Rate Sensing with a Robot Mounted mm Wave Radar, in Proc. IEEE Int. Conf. Robotics and Automation (ICRA), Paris, France, pp. 2812–2818 (2020); doi: 10.1109/ICRA40945.2020.9197431

Acknowledgements

The authors would like to thank Secom Science and Technology Foundation for its support in this research.

DOI 10.5162/eurosensors2026/2.3.3

Unchallenging the Debye Challenge in Field-Effect Biosensors

Gil Shalev[1,2]
[1] School of Electrical Engineering, Ben-Gurion University of the Negev, POB 653, Beer-Sheva 8410501 Israel
[2] The Ilse-Katz Institute for Nanoscale Science and Technology, Ben-Gurion University of the Negev, POB 653, Beer-Sheva 8410501, Israel
glshalev@bgu.ac.il

Summary:
The Meta-Nano-Channel (MNC) bioFET performs specific, label-free, and real-time quantitative sensing of C-reactive protein (CRP)—a key biomarker for inflammation and tissue damage. This sensor operates using tiny, 0.5 µL unprocessed samples of blood and sweat, successfully overcoming significant screening effects in environments with Debye lengths of 0.7 nm and 2.3 nm, respectively

Keywords: sweat, blood, bioFET, antigen-antibody, Debye length

Background, Motivation and Objective

While Biological field-effect transistors (bioFETs) are highly promising for the future of point-of-care and home diagnostics, they face a significant hurdle: Debye screening. In unprocessed physiological fluids, high ionic concentrations result in a Debye length of less than 1 nm, theoretically making bioFETs "blind" to any molecular interactions occurring further from the sensor surface [1] [2]. Traditionally, this limitation was thought to rule out the use of antibody-based receptors, as their large physical dimensions (typically 10–15 nm) would place the binding event far beyond the sensitive zone. This has sparked an intensive search for smaller, "short" receptors to bring the target interaction closer to the surface. However, recent findings suggest this may not be entirely necessary; observations of adsorbed antibodies show they often tilt sharply toward the surface, allowing binding events to occur much closer to the sensing area than previously expected.

Description of the New Method or System

This study utilizes the Meta-Nano-Channel (MNC) bioFET, a platform specifically engineered to overcome traditional interface challenges such as molecular gating and solution gating. The MNC bioFET's unique multi-gate architecture allows for the excitation of various conducting channels that differ in size, shape, and spatial orientation. This diversity ensures that each channel is uniquely coupled to the potential variations at the sensing area, which are often non-uniform due to the irregular distribution of molecular interactions. Furthermore, the device enables the switching of these channels between off and on states while preserving the electrochemical equilibrium of the solution and surface-bound biomolecules—a critical factor for accurate real-time measurements.

Results

The device achieves a limit of detection (LoD) of 100 fg/mL in blood and 10 fg/mL in sweat [3]. Across both mediums, the sensor demonstrates a remarkably wide dynamic range of eight orders of magnitude, characterized by exceptional sensitivity and high linearity. This study presents the first direct bioFET measurement of antibody-antigen interactions in raw physiological samples, achieved without any preprocessing or washing steps. The findings challenge the long-held "Debye screening" dogma within the bioFET community. The standard assumption—that surface-bound antibodies stand in a rigid, upright ("Fab-up") position—has led many to prematurely dismiss the possibility of sensing in physiological fluids. This work argues that such a view is an oversimplification of the complex sensing interface. By demonstrating exceptional performance in environments with physiological Debye lengths, this study proves that target molecules must interact in much closer proximity to the surface than previously thought, perhaps even involving direct interaction with the surface chemistry itself. Consequently, this research reaffirms that antibodies, with their superior specificity, remain the gold standard for bioFET receptors.

References

[1] M. Sun, C. Zhang, S. Lu, S. Mahmood, J. Wang, C. Sun, J. Pang, L. Han, H. Liu, Recent Advances in Graphene Field-Effect Transistor Toward Biological Detection, *Adv Funct Mater* 34 2405471 (2024). doi.org/10.1002/ADFM.202405471.

[2] X.W. Chen, N.T. Huang, Dual Ion-Selective Membrane Deposited Ion-Sensitive Field-Effect Transistor Integrating a Whole Blood Processing Microchamber for In Situ Blood Ion Testing, *ACS Sens* 8 904–913 (2023); doi.org/10.1021/ACSSENSORS.2C02603.

[3] Babbar, S. et al. Reassessing the challenge of Debye length in field-effect biosensors. Chemical Engineering Journal 527, 172070 (2026); doi.org/10.1016/j.cej.2025.172070

.

DOI 10.5162/eurosensors2026/2.3.4

Development and Comparison of Innovative Sensing Modules to Support Pneumonia Diagnosis

Ana Maria Tischer[1], Emanuele Zanni[2], Felix Schmidt[3], Carmen Bax[1], Luca Novelli[4], Udo Weimar[3], Nicolae Barsan[3], Raffaele Dellacà[2], Fabiano Di Marco[4,5], Laura Capelli[1]
[1] Department of Chemistry, Materials, and Chemical Engineering Giulio Natta, Politecnico di Milano, Milan, Italy,
[2] Department of Electronics, Information, and Bioengineering, Politecnico di Milano, Milan, Italy,
[3] Institute of Physical and Theoretical Chemistry, University of Tuebingen, Tuebingen, Germany,
[4] Azienda Ospedaliera Socio Sanitaria Territoriale Papa Giovanni XXIII, Bergamo, Italy,
[5] Università degli Studi di Milano, Department of Health Sciences, University of Milan, Milan, Italy
emanuele.zanni@polimi.it

Summary:
In this work we developed an add-on system for expanding the sensing capabilities of an existing commercial E-Nose used for breath analysis aiming at pneumonia diagnosis. The system integrates three sensing modules with analog fixed-temperature metal-oxide gas sensors and temperature-modulated digital sensors. Module-specific machine-learning models were developed to compare their ability to discriminate pneumonia from healthy controls. The platform enables breath measurements with different sensing modules and future data fusion studies.

Keywords: electronic nose, breath analysis, temperature modulation, pneumonia, medical diagnostics

Background, Motivation and Objective

Pneumonia remains a major cause of morbidity and mortality, and its diagnosis often requires integrating clinical history, imaging, microbiology, and response to therapy [1]. Breath analysis using electronic noses (E-Nose) offers a rapid, non-invasive alternative, but performance is still limited by low volatile compounds concentrations, humidity interference, and poor sensor selectivity [2]. In addition, many commercial instruments provide limited sensor diversity and flexibility for testing new sensing strategies, and were not specifically developed for medical applications.

To address these limitations, we developed an add-on system to expand the sensing capabilities of an existing commercial E-Nose, enabling multiple measurements. The aim is to compare the ability of the sensing modules to support the diagnosis of pneumonia when compared to the commercial E-Nose. In this preliminary study, we assessed the potential of the two add-on sensing modules to discriminate between breath samples from patients with pneumonia and healthy controls by developing module-specific data processing pipelines.

Description of the New Method or System

The measurement platform comprised three sensing modules (Fig. 1-A). The commercial sensing module was an EOS-AROMA (Sacmi, Italy) containing six fixed-temperature semiconductor metal-oxide (SMOX) gas sensors: four custom sensors based on ZnO, TiO_2, and SnO, and two commercial sensors (TGS2611 and TGS2610, Figaro Engineering), all operated at 400 °C.

Sensing Module 1 (SM 1) was integrated in series and included a digital gas-sensor module based on two temperature-modulated SGP40 sensors (Sensirion AG, Switzerland; STZ AO Action, Germany). Its operation mode was previously described in [3]. For the EOS-Aroma and SM 1, each analysis consisted of 20 min of sampling followed by 20 min of cleaning at 50 mL/min, with 1:1 dilution by carbon-filtered air.

Sensing Module 2 (SM 2) (Fig. 1-B) was developed as a complete E-Nose module with an independent flow system. It comprised an innovative sensing chamber designed to optimize flow distribution across all the sensors and a regulated pump for flow generation. SM 2 was operated in parallel with the commercial device and included an array of seven SMOX sensors from the TGS26XX line (Figaro Inc., Japan), a temperature and relative humidity sensor (SHT40, Sensirion, Switzerland) and one digital sensor operated under temperature modulation;

detailed specifications are intentionally omitted due to confidentiality agreements and non-disclosure obligations. SM 2 operated in parallel with the commercial E-Nose at 300 mL/min, with 6 min of sampling followed by 10 min of cleaning. Its operation was synchronized with that of the commercial E-Nose to ensure that the two systems never drew samples from the same line at the same time.

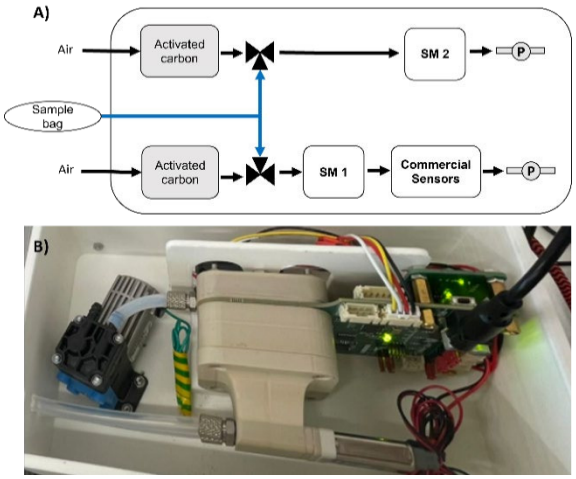

Fig. 1. (A) Illustration of the setup; (B) Prototype SM 2 installed inside the commercial E-Nose.

Breath samples were collected at ASST Papa Giovanni XXIII Hospital in Bergamo, Italy, under ethics approval no. 223/20. The present analysis focuses on the common subset of samples measured using all three sensing modules, currently consisting of 15 pneumonia cases and 11 healthy controls from an ongoing cohort. Exhaled breath was collected offline after a 3 min lung washout using a two-way non-rebreathing valve and medical air, as previously described in [2]. Samples were stored in Nalophan™ bags for 4-24 h in the E-Nose room to reduce humidity interference before analysis.

Different data processing pipelines were adopted for each sensing module. For the commercial E-Nose, the resistance curves were normalized with respect to clean air, and 12 features from the sampling phase were extracted for each fixed-temperature sensor. For the temperature-modulated sensors in SM 1, one steady-state temperature cycle was selected, log-transformed, and 6 features were extracted for each temperature modulation step, such as the mean value, maximum and minimum derivative and area under that temperature step. For the SM 2, the fixed-temperature sensors we processed as for the commercial E-Nose, whereas the temperature modulated sensor was processed as SM 1. Features of both sensing approaches were combined in a table before feature selection.

Boruta algorithm was used to select the top 15 most important features for each dataset, and the resulting feature table was used to train a linear SVM. Leave one out cross validation (LOOCV) was used to validate all models.

Results

Preliminary functional tests with acetone and ethanol (results not shown) indicated that the response time and sensitivity of TGS26XX sensors were improved for the SM 2 compared with the commercial E-Nose.

Breath analysis on the common subset provided a first indication of the diagnostic potential of the multi-module sensing system. Fig. 2 shows the PCA score plot obtained from SM 2, in which good separation between pneumonia and control samples is visible. Table 1 summarizes the LOOCV performance of the three module-specific models. Overall, the add-on modules performed better than the commercial E-Nose, suggesting that increase sensor diversity, temperature-modulated sensing, and optimized chamber fluid dynamics may improve information that can be extracted from the samples.

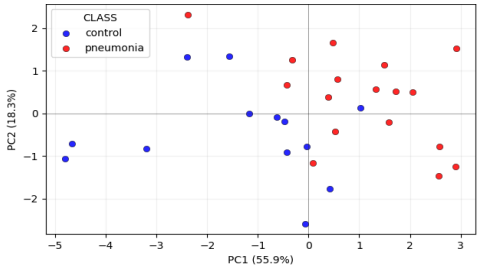

Fig. 2. PCA of breath samples from pneumonia (red) and control (blue) cases analyzed with SM 2.

Tab. 1: Performance of E-Nose in LOOCV in the discriminating pneumonia vs control breath samples.

Sensing Module	Accuracy (%)	CI95%
Commercial	72.7	54.9 – 85.4
SM 1	86.2	69.8 – 94.4
SM 2	90.0	74.4 – 96.5

References

[1] E. Prina, O. T. Ranzani, A. Torres, Community-acquired pneumonia, The Lancet 386, 1097-1108 (2015); doi: 10.1016/S0140-6736(15)60733-4

[2] C. Bax et al., An Experimental Apparatus for E-Nose Breath Analysis in Respiratory Failure Patients, Diagnostics 12, 776 (2022); doi: 10.3390/diagnostics12040776

[3] A. Kobald, U. Weimar, N. Bârsan, Towards understanding temperature modulated SMOX gas sensor arrays for outdoor air quality applications, Sensors and Actuators B: Chemical 440, 137879 (2025); doi: 10.1016/j.snb.2025.137879

DOI 10.5162/eurosensors2026/2.3.5

Metabolic Monitoring at Home with a Smartphone-coupled Breath Sensing Device

Simone Hersberger[1], Jan Van Den Broek[2], Lara Schmid[1], Fabienne Kappeler[1], Philipp A. Gerber, Andreas T. Güntner[1]
[1] Department of Mechanical and Process Engineering ETH Zurich, CH-8092 Zurich, Switzerland
[2] Alivion AG, CH-8152 Glattbrugg, Switzerland
[3] Department of Endocrinology, Diabetes, and Clinical Nutrition, University Hospital Zurich, CH-8091 Zurich, Switzerland.
simonehe@ethz.ch

Summary:
Human metabolism can be monitored through non-invasive breath analysis suitable for home use. We developed a handheld breath acetone detector for smartphone-guided metabolic monitoring that provides accurate and reproducible measurements with strong stability across time and humidity. Individual metabolic responses of volunteers during exercise and dietary interventions were captured with high agreement with mass spectrometry. This work establishes a validation framework for translating breath detectors from laboratory prototypes into healthcare applications.

Keywords: nanotechnology, electronic device, sensor, mobile health, metabolism

Background, Motivation and Objective

Overweight and obesity affect a large proportion of the global population and are major risk factors for chronic diseases such as diabetes, cardiovascular disorders and cancer [1,2]. Effective management increasingly relies on personalized metabolic monitoring to guide lifestyle interventions, including diet and exercise [3]. Breath analysis offers a non-invasive approach to monitor fat metabolism through acetone, a volatile byproduct of ketogenesis that reflects the systemic metabolic state [4]. Its suitability for frequent and convenient sampling makes it attractive for home-based monitoring. However, most existing sensing approaches remain confined to laboratory environments, and translation into reliable, user-friendly handheld devices is still lacking [5]. Key challenges include achieving sufficient sensitivity, selectivity and long-term stability under varying environmental conditions, as well as ensuring reproducible breath sampling. Here, we aim to bridge this translational gap by developing and validating a handheld breath acetone sensing system designed for accurate, reproducible and user-guided metabolic monitoring in real-world settings.

Description of the New Method or System

We present a fully integrated handheld device (Fig. 1) for non-invasive metabolic monitoring via breath acetone detection, designed for unsupervised home use. The system combines a modular mouthpiece with volume-guided breath sampling using a pressure sensor to ensure reproducible end-tidal sampling. Selective detection is achieved through a sorption column coupled to a chemoresistive sensor, enabling reliable acetone quantification. Automated sampling and regeneration cycles allow rapid and repeatable measurements. A smartphone interface provides real-time user guidance and data visualization, while cloud connectivity enables longitudinal tracking. This integration of controlled sampling, selective sensing and user feedback advances the translation of breath analysis from laboratory setups to practical everyday applications.

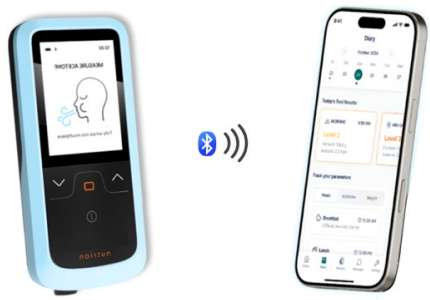

Fig. 1: *Smartphone-guided metabolic monitoring at home with a fully integrated breath acetone device. Smartphone app with Bluetooth connection for sampling control, result display and trend analysis.*

Results

The device demonstrated accurate and stable acetone quantification across the physiologically relevant range, with low inter-device variability

(5.6% at 1 ppm) and high repeatability (mean coefficient of variation (CV) of ~2.5%). Long-term measurements over 8 months showed no observable drift (inter-day variability 6.1%), and humidity robustness was confirmed with ≤4.2% bias up to 90% relative humidity. Pressure-guided sampling enabled reproducible end-tidal breath collection (CV ~3%), supporting reliable operation under user-controlled conditions. Validation against proton transfer reaction time-of-flight mass spectrometry (Fig. 2) showed excellent agreement across 0.2-43 ppm (R^2 = 0.990; r = 0.995; ~7.5% bias at 2 ppm), confirming analytical accuracy in human breath.

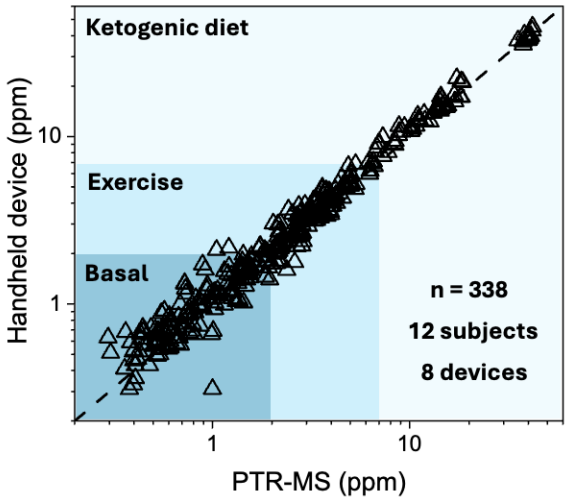

Fig. 2: *Correlation between breath acetone concentrations measured by the sensor and PTR-MS. A total of n = 338 breath samples were analyzed from 12 subjects using 8 devices during exercise and dietary interventions (R^2 = 0.990).*

Longitudinal home monitoring during dietary interventions (Fig. 3) demonstrated the ability to resolve individual metabolic adaptations over three weeks. Breath acetone remained low during habitual diet, increased substantially during ketogenic diet with subject-specific peak levels up to ~39 ppm, and decreased again during intermittent fasting, in agreement with PTR-MS measurements. The device closely tracked reference measurements and captured pronounced inter-individual differences in both magnitude and dynamics. These results highlight the capability of the system to monitor real-world metabolic changes over time, providing information complementary to blood ketones and continuous glucose measurements.

Conclusion

We present a validated handheld breath acetone sensing platform enabling accurate, non-invasive metabolic monitoring in real-world settings. By integrating controlled sampling, selective detection and digital guidance, the system reliably tracks individual metabolic dynamics over time, supporting personalized health applications such as dietary guidance, exercise optimization and preventive monitoring.

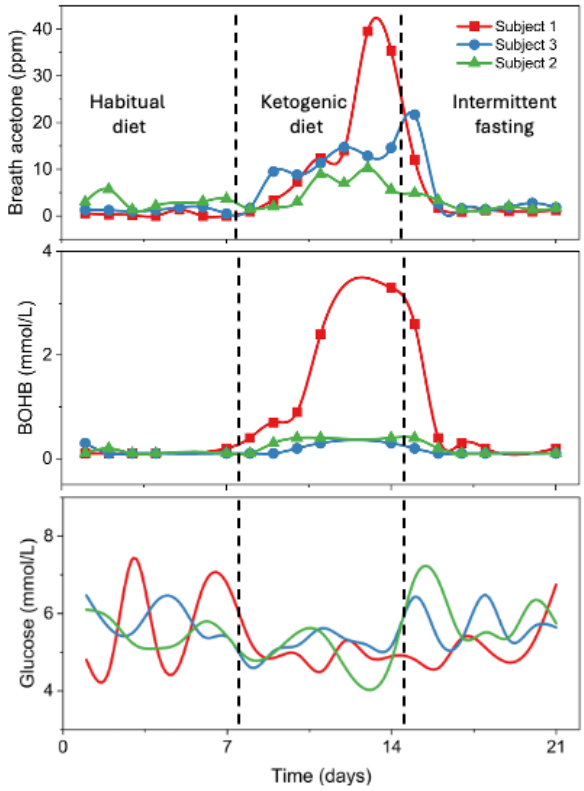

Fig. 3: *Longitudinal monitoring of **(a)** breath acetone measured by the sensor, **(b)** capillary blood BOHB and **(c)** ISF glucose during habitual diet (days 1-7), ketogenic diet (days 8-14), and intermittent fasting (days 15-21) for three subjects.*

References

[1] Nyberg, S. T. et al. Obesity and loss of disease-free years owing to major non-communicable diseases: a multicohort study. Lancet Public Heal. 3, e490–e497 (2018); doi: 10.1016/S2468-2667(18)30139-7

[2] Phelps, N. H. *et al.* Worldwide trends in underweight and obesity from 1990 to 2022: a pooled analysis of 3663 population-representative studies with 222 million children, adolescents, and adults. *Lancet* **403**, 1027–1050 (2024); doi: 10.1016/S0140-6736(23)02750-2

[3] Güntner, A. T. *et al.* Challenges and opportunities of wearable molecular sensors in endocrinology and metabolism. *Nat. Rev. Endocrinol.* **22**, (2025); doi: 10.1038/s41574-025-01175-z

[4] Musa-Veloso, K., Likhodii, S. S. & Cunnane, S. C. Breath acetone is a reliable indicator of ketosis in adults consuming ketogenic meals. *Am. J. Clin. Nutr.* **76**, 65–70 (2002); doi: 10.1093/ajcn/76.1.65

[5] Güntner, A. T. *et al.* Breath sensors for health monitoring. *ACS Sensors* **4**, 268–280 (2019); doi: 10.1021/acssensors.8b00937

DOI 10.5162/eurosensors2026/3.1.1

Free-space laser interrogation of Tantalum-Palladium Hydrogen sensor

Robin Gremaud, Chongsheng Yue, Jean-Marc Oppliger, Pedro Castro-Fernández
[1] ABB Research, ABB Switzerland Ltd, Baden-Dättwil, Switzerland
robin.gremaud@ch.abb.com

Summary: A free-space laser interrogation scheme of Hydrogen sensitive $Ta_{1-y}Pd_y$ thin film layers is presented. We focus on the design of the optical setup, by isolating systematically the potential sources of error and improving signal-to-noise ratio as well as stability of the signal, with the goal of optimizing remote Hydrogen sensors for industrial applications.

Keywords: Hydrogen sensing, hydride, laser, reflectivity, resistivity, Tantalum-Palladium

Background and Motivation

The rapid expansion of Hydrogen technologies across energy, industrial, and power-system applications has intensified the demand for reliable H_2 leak detection. Hydrogen is, however, intrinsically difficult to sense by conventional laser absorption methods because the H_2 molecule lacks strong vibrational–rotational absorption bands in the infrared and ultraviolet spectral regions. As a result, established free-space spectroscopic techniques such as TDLAS or open-path FTIR—successfully deployed for gases like methane or ammonia—are fundamentally unsuited for direct Hydrogen detection. Consequently, most optical Hydrogen sensors rely on interrogation of Hydrogen-sensitive materials, rather than on direct optical absorption by the gas itself.

Among these approaches, fiber-optic interrogation of Palladium-based sensing elements currently exhibits the highest technology readiness. Palladium and its alloys reversibly absorb H_2 to form hydrides, inducing changes in lattice constant, mechanical strain, and optical properties. Pd sensors can have issues with stability (microcracking, delamination), modest sensing range (difficult to detect low H_2 concentration) and intrinsic hysteresis. Alloying reduces this problem, but at the price of a reduced sensitivity. In fiber-optic Hydrogen sensors, these changes are transduced into intensity, phase, or wavelength shifts that can be read remotely through optical fibers. Reviews indicate that such systems have progressed from laboratory demonstrations to extended field trials and niche deployments, corresponding to TRL 4–6, depending on architecture and application.[1]

Fiber-based schemes benefit from intrinsic electrical isolation, immunity to electromagnetic interference, and compatibility with distributed sensing concepts. Representative implementations include Fabry–Pérot cavities formed by suspended palladium membranes at fiber tips, where Hydrogen-induced membrane deformation results in measurable interference shifts with ppm-level sensitivity, or direct measurement of optical reflectance at fiber tip (so-called micromirror configuration). In parallel, free-space laser interrogation, typically based on optical reflectometry or scattering from palladium-coated surfaces, represents a less mature but conceptually simpler alternative. In these schemes, a laser probes a Hydrogen-sensitive film directly, and Hydrogen exposure is inferred from changes in reflectance caused by Hydrogen-induced deformation or modified optical constants. While attractive for their simplicity and potential low cost, free-space interrogation concepts remain largely confined to laboratory environments and early validation experiments, corresponding to TRL 2–3. Their sensitivity to alignment, environmental contamination, and line-of-sight constraints poses significant barriers to deployment in industrial environment.[2]

Recently it was demonstrated that thin film $Ta_{1-y}Pd_y$ with high Ta content is an optical sensing material with extremely wide sensing ranges covering at least 7 orders of magnitude in Hydrogen pressure.[3] Nanoconfinement of the $Ta_{1-y}Pd_y$ layer suppresses the first-order phase transitions present in bulk and ensures a sensing response free of any hysteresis. It therefore represents a more appropriate alternative to pure palladium or high-content Pd thin film for Hydrogen sensing in a wide range of concentrations, also as a fiber optic sensor.[4]

Objective

In this contribution, we explore the potential of a free-space laser interrogation scheme of

Hydrogen sensitive $Ta_{1-y}Pd_y$ thin film layers. We focus on the design of the optical setup, with the goal of isolating the potential sources of error and improving signal-to-noise ratio as well as stability of the signal. Figure 1 shows the bench-top optical setup used to measure single-wavelength optical reflectance at 976nm. Besides the direct reflection path from the laser reflected into Ta-Pd sample (8) into the main detector (6), we divert a part of the light intensity into reference detector (7). Additionally, another part of the light is coupled after reflection on the Hydrogen sensitive layer to a camera (5).

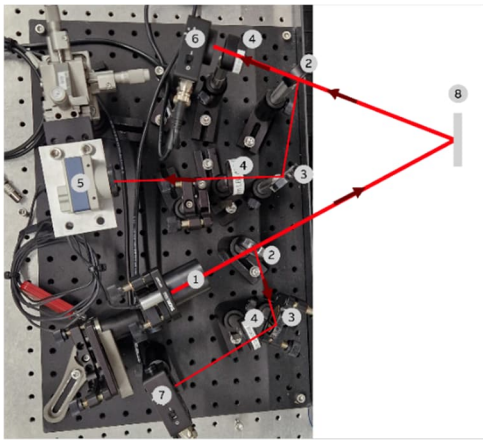

Figure 1. Initial optical setup: 1. IR Laser + neutral density filter: class 1 output at 976 nm (< 0.4 mW) (depicted: Thorlabs CPS980; a temperature-stabilized (with LDM9LP) LP980-SF15 fiber laser laser is used in a second stage. 2. Beamsplitters, 3. Mirrors, 4. Focus lenses 5. Teledyne Dalsa G3-GC10-C1280IF Genie Nano 1GigE Camera. 6. Main detector. 7.Reference detector. 8. Ta-Pd Sample.

Results

Figure 2 shows a comparison between the optical reflectance (top) and the electrical 4-point resistance (bottom) for 50, 100, 250, 500, 1000 and 10000 ppm in a nitrogen background for $Ta_{88}Pd_{12}$ Hydrogen sensing layers. At $2.3 \cdot 10^5$s, the laser has been switched off and on again, resulting in an intensity change that can be compensated with the reference signal (see inset). Between the cycles of Hydrogen application, samples are flushed with technical air or Nitrogen. Both readout schemes allow an accurate measurement of the hydrogen concentration in this range. The sensor response is slightly larger in the Nitrogen flushing case, indicating that presence of Oxygen in the environment reduces durably H_2 sensitivity.

Conclusion and Outlook

This free-space laser interrogation readout for Hydrogen sensing is valuable to test and improve remote H2 sensing readout schemes. The simultaneous 4-point measurement of electrical resistance provides a local reference and enables isolating various sources of error in the optical readout scheme. Next step is to add laser beam tracking by camera (5) to compensate for misalignments inherent to remote optical interrogation.

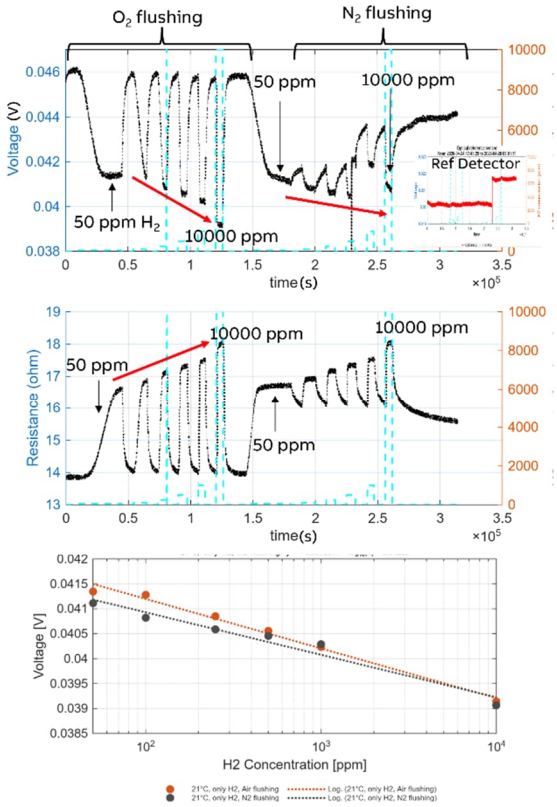

Figure 2. $Ta_{88}Pd_{12}$ response to various H_2 concentration in N_2.Top: 4-point resistance, Middle: reflectance. First serie: flushing with technical air (21% O_2 in N_2), second serie: flushing with N_2. Bottom: corrected optical detector voltage as function of H2 concentration.

Acknowledgement

We thank TU Delft (L. Bannenberg, H. Schreuders) for the Ta-Pd samples. See [3] for a full description of the thin film layer stacks used.

References

1. Nicolas, J., *Review on hydrogen leak detection: comparison between fiber optic sensors based on different designs with palladium.* Optical Engineering, 2015. **54**(3): p. 030901.
2. She, X., et al., *Pd films on soft substrates: a visual, high-contrast and low-cost optical hydrogen sensor.* Light: Science & Applications, 2019. **8**(1): p. 4.
3. Bannenberg, L., H. Schreuders, and B. Dam, *Tantalum-Palladium: Hysteresis-Free Optical Hydrogen Sensor Over 7 Orders of Magnitude in Pressure with Sub-Second Response.* Advanced Functional Materials, 2021. **31**(16): p. 2010483.
4. Verhoeff, D.J., H. Schreuders, and L.J. Bannenberg, *Tantalum-palladium alloy based optical micro-mirror hydrogen sensor.* Sensors and Actuators B: Chemical, 2025. **428**: p. 137229.

DOI 10.5162/eurosensors2026/3.1.2

Optimized Water-Based Colorimetric Carbon Dioxide Indicators for 455 nm Monolithic LED Emitter-Detector

Martí Verdaguer Mallorquí[1], María González-Gómez[1,2], Cristian Fàbrega[1], Joan Daniel Prades[2], Olga Casals[1]
[1] MIND/IN2UB, Dept. of Electronics and Biomedical Engineering, Universitat de Barcelona, Marti i Franqués 1, Barcelona ES08028, Spain
[2] Institute of Semiconductor Technology (IHT) and Laboratory for Emerging Nanometrology (LENA), Technische Universität Braunschweig, D-38106 Braunschweig, Germany;
mverdaguer@ub.edu

Summary:
A water-based m-cresol purple CO_2 indicator was optimized for sensing with a 455 nm monolithic LED emitter-detector platform. Printed films were evaluated under controlled CO_2 atmospheres using a commercial 455 nm LED setup. Single-factor and Design of Experiments studies identified individual and coupled formulation effects and supported selection of an optimized composition. Response models agreed well with an independently prepared formulation, and selected sensing layers produced clear concentration-dependent responses after integration on the monolithic device.

Keywords: Carbon dioxide, colorimetric sensor, m-cresol purple, blue LED, optical gas sensor.

Background, Motivation and Objective

Affordable CO_2 monitoring is increasingly relevant for indoor air-quality and ventilation assessment. Although nondispersive infrared sensors are widely used, their optical complexity and path-length requirements limit miniaturization [1]. Colorimetric indicators offer a complementary route by converting selective chemical interactions into measurable absorbance changes, but deployment requires stable films and compact electronic readout rather than bulky spectrophotometers, subjective visual inspection or illumination-sensitive camera methods [1,2].

This work builds on water-based m-cresol purple (MCP) CO_2 indicators, where CO_2 lowers the local pH and protonates the dye, producing a reversible optical change [3]. Water-based formulations are especially attractive because they have shown improved ambient lifetime compared with similar solvent-based indicators [3].

Recent compact colorimetric systems and water-based CO_2 inks demonstrate the relevance of this approach, but rely on different chemistries, device architectures or spectral ranges [1,2]. Here, the key challenge is matching the indicator to a monolithic blue LED emitter-detector platform operating near 455 nm. The objective is to adapt the water-based MCP formulation for 455 nm optical readout, enabling measurable CO2 sensing at reduced LED intensity and lower optical dose.

Description of the New Method or System

The proposed method is a device-constrained optimization of a water-based MCP CO_2 indicator for blue optical readout. Formulation variants are first printed on transparent polyester films and evaluated in a reference optical setup using a commercial 455 nm Oslon LED, selected to reproduce the emission range of the final device. The indicator film is placed between the LED and an IllumiaLite spectral flux analyser while controlled atmospheres with different CO_2 concentrations are generated. This setup allows the spectral transmission change of each formulation to be quantified under blue illumination.

The formulation is optimized by studying the amounts of the main indicator components: hydroxyethyl cellulose, glycerol, m-cresol purple and sodium bicarbonate. First, a one-factor-at-a-time approach is used to identify the individual influence of each component on the 455 nm response, response/recovery dynamics, film quality and stability. Then, a Design of Experiments approach is applied with hydroxyethyl cellulose held constant while sodium bicarbonate, glycerol and m-cresol purple are varied simultaneously. This links the chemical composition of the sensing film to the optical signal measurable at the wavelength of the target platform.

Selected formulations are then integrated on the monolithic emitter-detector LED device by spin-coating the indicator between the blue emitter and the matching blue receiver. In the final

sensor, CO_2-induced changes in the indicator absorbance modulate the blue light reaching the receiver and are measured as a change in the receiver signal. By maximizing the response at the available 455 nm band, the sensing layer enables measurable CO_2 readout at reduced LED intensity, thereby lowering the optical dose to the indicator.

Results

Formulation optimization focused on the optical response under 455 nm illumination, since this wavelength matches the blue LED emitter-detector platform. Measurements performed with the 455 nm Oslon LED showed that the water-based MCP indicator produces a clear CO_2-dependent decrease in transmitted blue flux, with the largest variation close to 450 nm. Complementary 2700 K white-LED spectra show that the dominant overall colorimetric change occurs around 590–600 nm, while a smaller CO_2-dependent feature is also present near the 455 nm region (Fig. 1). Together, these results show that the indicator can be read in the blue band, but that formulation optimization must be guided by the 455 nm signal rather than by the strongest broadband color change.

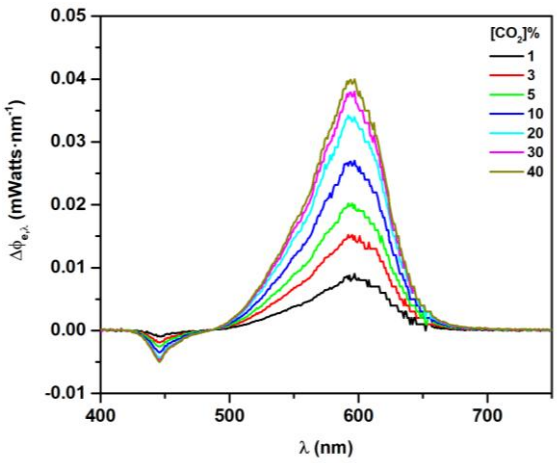

Fig. 1 CO_2-induced change in transmitted spectral flux of the water-based MCP indicator under 2700 K white LED illumination. The main spectral change occurs around 590–600 nm, while a smaller CO_2-dependent feature is observed near the 455 nm blue region.

The formulation study showed that the effect of composition depends strongly on the readout wavelength. This was particularly evident for sodium bicarbonate. Under 2700 K white illumination, lower bicarbonate content produced a stronger overall signal, with the lowest tested concentration giving the largest response. Under 455 nm illumination, sodium bicarbonate instead modified how the response developed across the tested CO_2 range: higher bicarbonate concentrations required more CO_2 to reach the same relative response. This confirms that formulations optimized from broadband or visual color change do not necessarily provide the most useful response for the blue LED platform.

The 455 nm one-factor-at-a-time study identified the individual role of each formulation component. Sodium bicarbonate influenced the response behavior and reversibility of the indicator. M-cresol purple increased the response amplitude, although excessive dye loading may compromise long-term stability by shifting the initial pH. Glycerol mainly affected response and recovery dynamics, while hydroxyethyl cellulose governed film homogeneity and processability with a weaker direct effect on the 455 nm response amplitude.

The Design of Experiments study was then used to evaluate coupled effects between formulation variables that could not be resolved by the one-factor-at-a-time study. In particular, the effect of glycerol on both response and recovery depended strongly on the sodium bicarbonate concentration. The DoE was also used to identify compositions that balance 455 nm response, recovery behavior, response across the tested CO_2 range and stability, and to construct response models relating formulation composition to the measured optical signal. These models showed good agreement with an independently prepared formulation.

After spin-coating on the monolithic emitter-detector LED platform, the selected sensing layers produced a clear concentration-dependent change in the receiver signal upon CO_2 exposure. This confirms that the formulation strategy developed under 455 nm reference illumination translates to the final blue LED readout configuration. By increasing the useful response at the available wavelength, the optimized indicator supports CO_2 sensing at reduced emitter intensity and lower optical dose to the sensing film.

References

[1] M. González-Gómez, I. Benito-Altamirano, J. D. Prades, O. Casals, and C. Fàbrega, Ultralow-Cost and Selective Water-Based Colorimetric Ink for Indoor CO_2 Monitoring, *IEEE Sensors Journal* 25, 18722 (2025); doi: 10.1109/JSEN.2025.3559593

[2] C. Driau, C. Fàbrega, I. Benito-Altamirano, P. Pfeiffer, O. Casals, H. Li, and J. D. Prades, How to implement a selective colorimetric gas sensor with off the shelf components?, *Sensors and Actuators B: Chemical*. 293, 41 (2019); doi: 10.1016/j.snb.2019.04.117

[3] A. Mills and G. A. Skinner, Water-based colourimetric optical indicators for the detection of carbon dioxide, *The Analyst* 135, 1912 (2010); doi: 10.1039/c000688b

DOI 10.5162/eurosensors2026/3.1.3

Photolysis for Enhancing the Specificity of NOx Electrochemical Sensors

Reinoud F. Wolffenbuttel[1], David Bilby[2], Jacobus H. Visser[2]
[1] Laboratory for Electronic Instrumentation, Department of Microelectronics, Delft University of Technology, 2628 CD Delft, The Netherlands,
[2] Research and Advanced Engineering, Ford Motor Company, Dearborn, MI 48121, USA
Corresponding Author's e-mail address: R.F.Wolffenbuttel@TUDelft.NL

Summary:

Operation of the electrochemical NOx gas sensor lacks specificity between NO and NO_2 detection. Radiation of a NO_X-containing exhaust gas mixture by UV light of 370 nm wavelength is investigated for photodecomposition of NO_2 into NO and atomic oxygen. The objective is to achieve sufficient modulation of the NO/NO_2 composition for significantly improving specificity of a commercially available sensor in a dynamic operating mode. A sufficient photolysis conversion efficiency is demonstrated using a 100 sccm flow in a quartz tube and commercially available LEDs for enabling NO/NO_2 selective detection.

Keywords: automotive sensor, exhaust sensor, electrochemical sensor, sensor specificity, photolysis

Background, Motivation and Objective

The increased emphasis by regulatory agencies on exhaust gas management has called for automotive gas sensors for a range of gases, each with demanding specifications and at low-unit costs for commercial viability in the automotive application. The electrochemical NOx sensor is a proven concept and satisfies these constraints. However, satisfying the tightening in levels of acceptable emission and the need for selectively monitoring other gases in the reduction chain from NO_2 to N_2, for instance N_2O, requires an NOx sensor for selectively measuring these constituents.

Photolysis of NO_2 in the atmosphere by UV light is well documented and is used here as a solution within the framework of the mantra 'learning from nature' for providing specificity in the measurement of the NO and NO_2 compositions in an exhaust gas, using an industrially available NOx electrochemical sensor in combination with gas illumination by UV light in a pulsed mode [1].

Description of the Approach

Photo-dissociation of NO_2 into NO is maximum at 370 nm wavelength [2, 3]. The absorption coefficient at ppm-level concentrations is sufficient for an absorption depth of several cm, which implies that an efficient conversion can be achieved using a gas flow in a quartz tube of practical dimensions (see Fig. 1). The NOx sensor is placed downstream the flow.

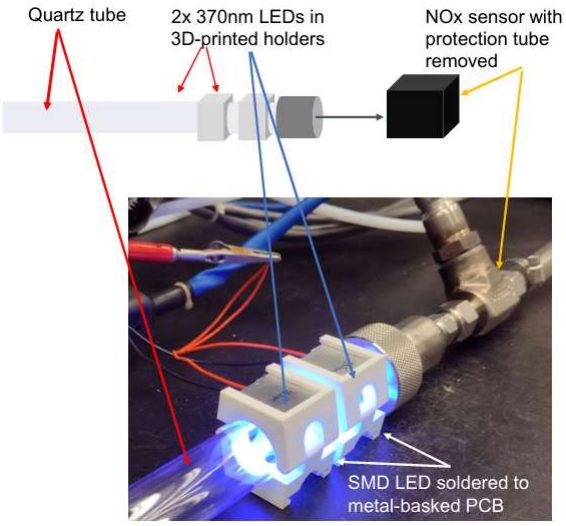

Fig. 1. Set-up for validating photo-dissociation of NO_2 at 370 nm and for measuring photolysis efficiency.

The generic effect is validated using the quartz tube in the transmission path of a spectrometer set-up (Ocean Optics Flame-S spectrometer-see Fig. 2). The spectral absorption is consistent with literature on NO_2 [4]. while the NO generation results in relatively small spectral absorption peaks in the 200-230 nm band [5].

Gas mixtures are applied with the LEDs operated in a pulsed mode (see Fig. 3). The response lags the LED cycle, because of the relatively low flow rate of 100 ppm. The NO_2 concentration is indeed reduced during an illumination phase and

recovers during the dark phase in between. The incomplete recovery results in a time dependent response, which can be circumvented by adding a purging phase.

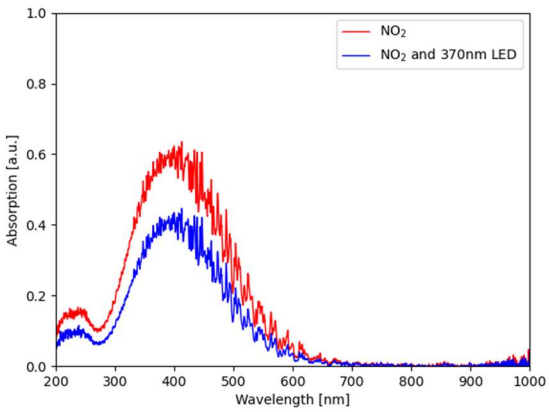

Fig. 2. Spectral absorption of NO_2 at 1000 ppm flow and without oxygen in the experiment, non-illuminated (red line) and radiated with LEDS at 370 nm wavelength (blue line)

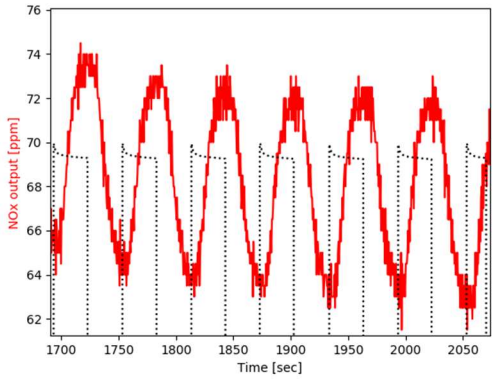

Fig. 3. Response of the NOx sensor and the exit of the quartz tube to a 100 ppm NO_2 at the input, with the state of the LED indicated by the dotted line. The slow response is due to the relatively low flow rate.

The response to an NO_2/NO mixture is shown in Fig. 4. The NO_2 concentration changes between 100 ppm and 80 ppm. During NO_2 at 80 ppm, the NO concentration is changed between 100 ppm, 60 ppm and 20 ppm.

Although the NOx sensor output signal for NO_2= 100 ppm is overlapping with the signal for NO_2=80/NO=20 ppm, the individual NO_2 and NO concentrations can in principle be resolved due to the pulsed mode operation using the peak-to-peak signal fluctuations. Therefore, detection using lock-in techniques can be applied.

In the simple set-up used only a part of the wall area of the quartz tube is covered by LEDs and a more significant modulation depth can be expected from an optimized design.

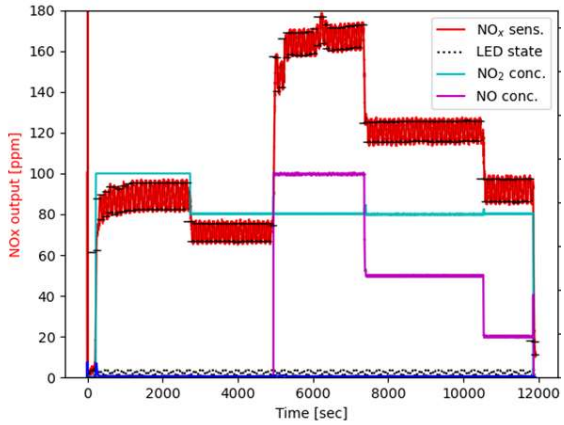

Fig. 4. Response of the NOx sensor at the exit of the quartz tube to different concentrations of a NO_2/NO mixture entered at the input line (note that the LED pulse series is too compressed to be clearly visible in this long time series).

Ozone generally plays a role in the effectivity of UV photolysis [6]. The thermodynamics of the equilibration reaction indicates a recovery rate of NO_2 from NO oxidation with ozone, which makes the reaction depend on the NO and O_2 concentrations. Optimization of the set-up and investigation of these dependencies are topics of future work.

References

[1] D. Bilby, R.F. Wolffenbuttel, Electrochemical Exhaust Gas Sensor with photolysis, Patent US12,259,357 B2, March 25, 2025

[2] E.P. Gardner, G.D. Sperry, J.G. Calvert, Primary Quantum Yields of NO_2 Photodissociation, J. Geophys. Res. 92, 6642-6652 (1987); doi: 10.1029/JD092iD06p06642

[3] C.L. Roehl, J.J. Orlando, G.S. Tyndall, R.E. Shetter, G.J. Vasquez, C.A. Cantrell, J.G. Calvert, Temperature dependence of the quantum yields for the photolysis of NO_2 near the dissociation limit, J. Phys. Chem. 98, 7837-7843 (1994); doi: 10.1021/j100083a015

[4] A. C. Vandaele, C. Hermans, P. C. Simon, M. Carleer, R. Colin, S. Fally, M. F. Mérienne, A. Jenouvrier, B. Coquart, Measurements of the NO2 Absorption Cross-section from 42000 cm^{-1} to 10000 cm^{-1} (238-1000 nm) at 220 K and 294 K, J. of Quantitative Spectroscopy and Radiative Transfer 59, 171-184 (1997)

[5] B.A. Thompson, P. Harteck, R.R. Reeves, Ultraviolet Absorption Coefficients of CO2, CO, H2O, N2O, NH3, NO, SO2, and CH4 between 1850 and 4000 Å, J. Geophys. Res. 68, 6431-6436 (1963); doi: 10.1029/JZ068i024p06431

[6] Y. Matsumi, M. Kawasaki, Photolysis of Atmospheric Ozone in the Ultraviolet Region, Chem. Rev. 103 (12), 4767-4782 (2003); doi: 10.1021/cr0205255

DOI 10.5162/eurosensors2026/3.1.4

A new QEPAS sensor optimized for the use of multiple optical sources with reduced window absorption

Ilona Troadec[1], Maxime Duquesnoy[1], Jean-Michel Melkonian[1], Raphaël Levy[1], Myriam Raybaut[1]
[1] ONERA, 6 Chemin de la Vauve aux Granges 91120 Palaiseau, France
ilona.troadec@onera.fr

Summary :

The development of sensitive, selective, multi-gas, fast and compact sensors to detect and identify polluting or toxic gases is a key challenge for public, industrial and military safety. We present a quartz-enhanced photoacoustic spectroscopy (QEPAS) sensor using a custom quartz tuning fork coupled to an acoustic resonator. The design was optimized with finite element method (FEM) and adapted for an optical multi-pass of laser arrays. It was validated experimentally by measuring C_2H_2, showing the expected acoustic mode, the reduction of window background and a sensitivity of 1.10^{-8} $W.cm^{-1}.Hz^{-1/2}$.

Keywords: Gas sensors, photoacoustic, spectroscopy, quartz, resonator

Context

The detection of greenhouse gases, toxic industrial chemicals (TICs) and chemical warfare agents (CWAs) has been identified as a major challenge for the public, industrial and military safety [1]. It has become necessary to develop compact, sensitive (ppbv level to reduce exposure), selective (to avoid interference), multi-gas (to cover more threats) and fast sensors [2]. Photoacoustic spectrometry is based on optical absorption of laser light by the rovibrational modes of molecules. When the molecular gas is periodically excited by a modulated light, acoustic waves are created and later detected by a mechanical resonator (microphone, tuning fork, cantilever…) [3]. Photoacoustic spectroscopy presents a good selectivity and could fulfill the mentioned applications requirements [4,5]. However, some challenges remain. Harmful gases and many pollutants have complex molecular structures and thus present large optical absorption spectrum features (~100 cm^{-1}) in the mid-infrared region (3-14 µm). To probe these features, quantum cascade laser arrays (QCL) or Interband Cascade Lasers (ICL) that are widely wavelength-tunable or incorporate several emitters at different wavelengths are essential. Also, periodic excitation of the absorption features is only effective with amplitude modulation, in contrast to wavelength modulation. These requirements strongly constrain the geometry of the opto-acoustical coupling and require a specific conception, which we patented [6] and describe in the next section.

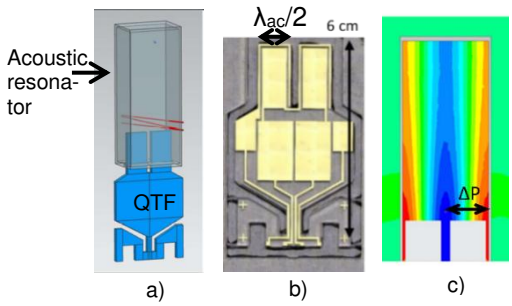

Fig. 1. a) CAD model of the sensor. b) Picture of the custom QTF. c) Simulation of the acoustic mode at resonance frequency (Red and blue: extrema of pressure with opposite phases. Green: pressure node)

New Sensor Design

A prototype using a quartz tuning fork (QTF) coupled with an acoustic resonator (fig.1a) has been designed and optimized through finite element method (FEM) simulations. The custom QTF (fig.1b) is dimensioned to be strongly coupled to an acoustic wave. Its prong width equal to half the acoustic wavelength $\lambda_{ac}/2$ was chosen in order to maximize the pressure amplitude between external and internal QTF faces. The QTF resonates at f_0 around 17450 Hz, resulting in an acoustic wavelength of 19.6 mm in air. The rectangular acoustic resonator is designed to present an acoustic mode adapted to maximize the pressure delta ΔP between the prongs (fig.1c). This maximizes the displacement of the prongs, i.e. the signal-to-noise ratio. Also, by design, the chosen acoustic mode presents pressure nodes (in green in fig. 1c) where the laser beam can enter and exit diagonally the resonator to minimize the background signal created by optical window absorption. At the resonator center, the beam passes through a pressure antinode to

maximize the photoacoustic signal. To further increase the signal-to-noise ratio, this patented design is adapted for an optical multi-pass (of around 10 passes for a QCL) in the resonator height, or can enable the use of multiple sources thanks to the multiple laser beam entry points around acoustic nodes (fig.1a).

Experimental Setup

The setup depicted in fig. 2 and showed in fig. 3 was used to carry out first photoacoustic measurements as proof of concept. A laser diode emitting around 20 mW and set at 6490.02 cm^{-1} to target a rovibrational line of C_2H_2 is modulated at $f_0/2$. The laser diode temperature and current are controlled. The acoustic resonator is filled with C_2H_2 1000 ppmv in air. The signal is fed to a FPGA-based lock-in amplifier and demodulated at f_0.

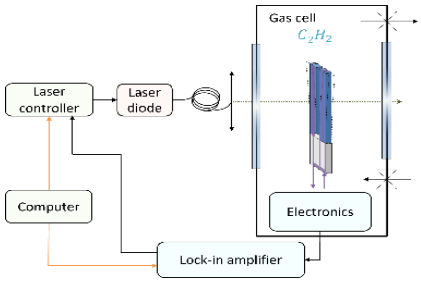

Fig. 2. Scheme of the experimental setup

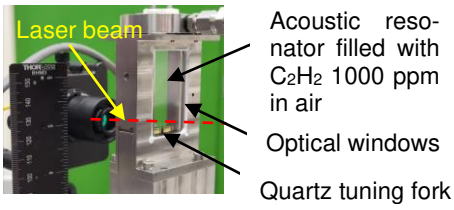

Fig. 3. Picture of the prototype

Results

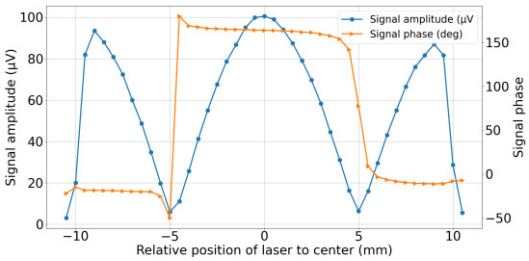

Fig. 4. Lateral scan of the acoustic mode by moving the laser beam in the resonator at f_0.

In order to validate the sensor concept, the acoustic mode at frequency resonance was verified. The laser beam was manually moved along a horizontal line above the QTF prongs and the signal amplitude and phase were collected, resulting in fig. 3. The amplitude curve has two local minima which represent pressure nodes (green in fig.1c) and three local maxima which represent pressure antinodes (blue and red in fig. 1c). Moreover, there is an inversion in the phase between local maxima which represents the opposite phase between prongs. A signal ratio of almost 17 was obtained between a node and an antinode, similar to simulation (ratio of 12). This result is promising for the decreasing of the background due to optical window absorption and validates the acoustic resonator concept.

The normalized noise equivalent absorption (NNEA) is the signal-to-noise ratio normalized by the generated signal and measurement bandwidth. To take into account all possible modulation schemes, the NNEA is defined as:

$$NNEA = \frac{H}{SNR \times \sqrt{\Delta f}} \qquad (1)$$

where H is the heat amplitude generated in $W.cm^{-1}$ due to gas excitation and relaxation. It takes in account the laser mean power, the overlap of the laser emission spectrum with gas absorption and the gas relaxation rate.

With a single pass and the laser beam centered in the resonator, a NNEA of 1.10^{-8} $W.cm^{-1}.Hz^{-1/2}$ was measured. It is important to note that the necessity of accommodating multiple optical sources with divergent beams while avoiding the acoustic window background results in a degraded NNEA. However, with the implementation of the optical multi-pass, the sensitivity will reach levels comparable to the state of the art.

Future work will concern the implementation of the optical multi-pass with QCL arrays in order to conduct measurements on CWAs simulants.

References

[1] L. Fiorani, C. Ciceroni, I. Giardina, F. Pollastrone. Rapid non-contact detection of chemical warfare agents by laser photoacoustic spectroscopy. Sensors 24(1), 201 (2024); doi: 10.3390/s24010201

[2] E. J. Pacsial-Ong, Z. P. Aguilar, Chemical warfare agent detection: a review of current trends and future perspective, Front. Biosci. (Schol Ed), 5(2), 516–543, (2013); doi: 10.2741/S387

[3] A.G. Bell. Upon the production of sound by radiant energy. (Gibbson brothers), 1881

[4] N. Liberatore, G. Felizzato, S. Mengali, R. Viola, F. S. Romolo, A novel signal processing approach enabled by machine learning for the detection and identification of chemical warfare agent simulants using a GC-QEPAS system, *Forensic Sciences Research*, Volume 10, Issue 3, (2025); doi : 10.1093/fsr/owaf002

[5] S. Xiong, X. Yin, Q. Wang, J. Xia, Z.Chen, H. Lei, X. Yan, A. Zhu, F. Qiu, B. Chen, Q. Wang, L. Zhang, K. Zhang, Photoacoustic Spectroscopy Gas Detection Technology Research Progress, Applied Spectroscopy, 78(2):139-158 (2024); doi: 10.1177/00037028231208712

[6] R. Levy, M.Duquesnoy, J-M. Melkonian, L. Tran, M. Guais, G. Aoust, Detector employing a photoacoustic effect, FR24.05894 (2025)

DOI 10.5162/eurosensors2026/3.1.5

Comparison of Self-Heating and Electrode Heating recoveries in a suspended-CNT CNFET NO_2 Sensor

Ines Kraiem[1], David Wolf[1], Miroslav Haluška[1], Cosmin I. Roman[1], Cristina Gentili[1], Christofer Hierold[1]
[1]Micro and Nanosystems, Department of Mechanical and Process Engineering, ETH Zürich, Switzerland
ikraiem@ethz.ch

Summary:
We compare self-heating (SH) and electrode-heating (EH) recovery of a carbon nanotube FET NO_2 sensor. Both methods sustained reproducible sensing across nine cycles, five cycles with EH and four cycles with SH; the post-reset operating point had comparable cycle-to-cycle spread for both methods, while EH delivered a 1.7–2.2× smaller standard deviation in NO_2 response amplitude.

Keywords: CNFET, NO_2 gas sensor, sensor recovery, self-heating, electrode heating.

Background, Motivation and Objective

Suspended Carbon nanotube field-effect transistor (CNFET) gas sensors detect NO_2 at parts-per-billion concentrations [1], but room-temperature desorption of NO_2 from CNTs is slow [2], so an active reset between measurements is required for continuous operation. Two heating-based reset strategies have been demonstrated: self-heating (SH), in which Joule heating the CNT channel is achieved by a drain-source voltage pulse [3], and electrode heating (EH) [4], in which a heater current flows through split, U-shaped source/drain electrodes that conduct heat into the contact-adjacent CNT region. SH targets the channel mid-section. EH heats the contacts directly. Because NO_2 adsorbs on the CNT and on the metal contacts in unpassivated devices, with both contributions reflected in the transfer characteristic [5], the two heating methods may show different characteristics in heating experiments. In this work, we run two consecutive gas experiments on a single suspended carbon nanotube CNFET, with reversed orders of EH and SH, to test the relative reset performance of the two methods on the same sensor.

Methods

The channel of the CNFET is formed by a single suspended carbon nanotube with split palladium source/drain electrodes (5 nm Cr / 35 nm Pd); the channel length is 1 µm, and the distance between the CNT and the gate electrode is 200 nm (air gap). Transfer characteristics (TCs) were continuously acquired (every ~1.5 s, V_{DS} =0.2 V, pulsed V_{GS} sweep, 5 ms on, 1 ms off, from 0 V to +10 V to -10 V back to 0 V) in a gas measurement chamber under constant flow of synthetic dry air and 500 ppb NO_2 exposures. From each TC's backward sweep, +10 V to -10 V, we extract two parameters: I_{on} as I_s at V_{GS} = -9V and the fixed-current threshold V_{th} represented by V_{GS} @ I_s=0.01 µA. The gas measurement protocol consisted of 1 h baseline in dry air, followed by ten consecutive 30 min adsorption steps at 500 ppb NO_2, separated by 10 times 1 s reset pulses each, and a final 1 h dry-air purge (*Fig. 1*). In Experiment 1, the first adsorption step was not preceded by a reset; the next five were each preceded by an EH-reset (V_{EH} = 2.5 V), and the last four by an SH-reset (V_{DS} = 1.7 V, V_{GS} = - 10 V). Experiment 2 was started on the same device 3 minutes later under identical conditions but with the reset order reversed: SH for the first five reset pulses, then EH for the last four.

Results

Representative TCs in dry air, after 30 min NO_2 exposure, and after EH or SH reset are shown in Fig. 2. Both reset methods qualitatively restore the transfer curve. In Experiment 1, the post-reset operating point showed comparable cycle-to-cycle standard deviations (SD) for EH and SH on both readouts I_{on} and V_{th} (Fig. 3a, c; Tab. 1). The mean NO_2 response amplitudes per cycle after reset (Fig. 3b, d) showed a smaller standard deviation for EH than for SH on both readouts: the standard deviation of ΔV_{th} was 1.7x smaller for EH, and that of ΔI_{on} 2.2x smaller. In Experiment 2, with the order reversed, I_{on} degraded monotonically across four SH-reset cycles while V_{th} remained stable, before the device failed abruptly during the fifth cycle (Fig. 1 c-d).

Conclusions

EH-reset and SH-reset gave comparable post-reset operating points but EH-reset delivered a smaller cycle-to-cycle standard deviation in NO_2 response amplitude. In Experiment 2, the

monotonic decline of I_{on} with stable V_{th}, ending in abrupt failure, is consistent with a progressive increase in contact resistance rather than a change in channel electrostatics. This pattern may indicate cumulative electro-thermal stress at the metal-CNT contacts under repeated SH pulses, consistent with the expectation that SH leaves the contact-adjacent CNT region cooler and less effectively recovered than EH. Multi-device experiments are needed to confirm this mechanism.

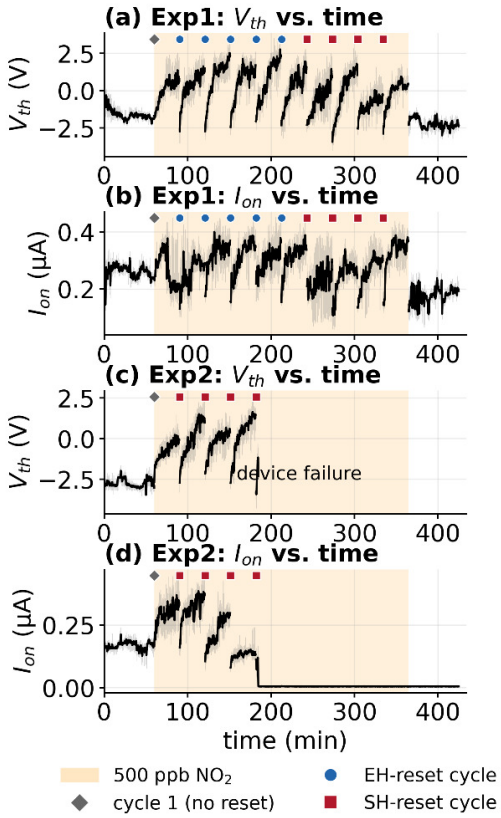

Fig. 1. Sensor signals over both gas experiments. (a, b) Exp1 and (c, d) Exp2 show V_{th} and I_{on} extracted from the backward sweep of every TC. Shaded orange regions mark continuous 500 ppb NO_2 exposure. Colored dots mark the start of each adsorption cycle: gray = cycle 1 (no preceding reset), blue = EH-reset, red = SH-reset. Exp1 sustains nine reset cycles (five EH, four SH); Exp2 fails during the fifth SH cycle.

Tab. 1: Per-cycle metrics for Exp1, mean ± 1 SD across n = 5 EH-reset and n = 4 SH-reset cycles.

Metric	EH-reset	SH-reset	SH/EH SD
Post-reset V_{th} (V)	-2.40 ± 0.37	-2.79 ± 0.49	1.3
Post-reset I_{on} (µA)	0.17 ± 0.04	0.15 ± 0.05	1.2
ΔV_{th} (V)	4.30 ± 0.49	3.28 ± 0.83	1.7
ΔI_{on} (µA)	0.18 ± 0.02	0.16 ± 0.04	2.2

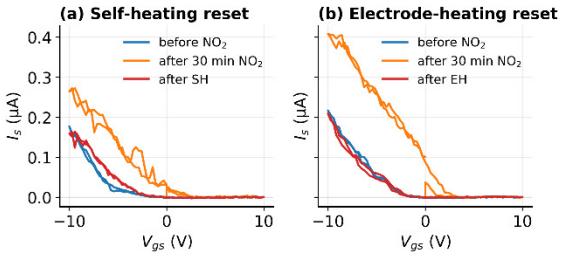

Fig. 2. Representative transfer characteristics (full sweep) before NO_2 exposure (blue), after 30 min at 500 ppb NO_2 (orange), and after a 10x1 s reset pulse (red).

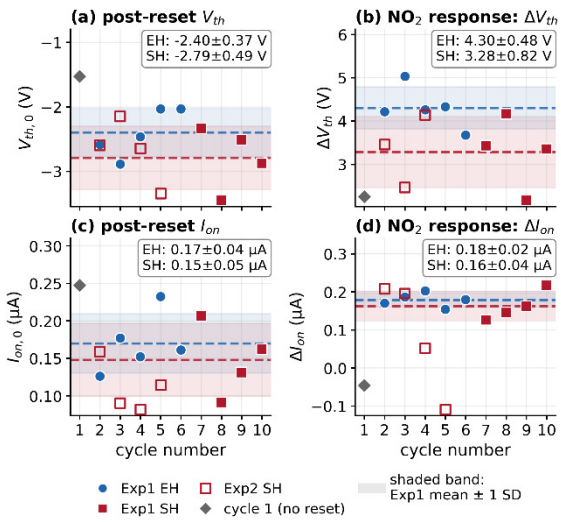

Fig. 3. Per-cycle metrics from each adsorption cycle. (a, c) Post-reset values y_0 (average of the first 5 s of each cycle) for V_{th} and I_{on}. (b, d) NO_2 response amplitudes $\Delta y = y_\infty - y_0$, where y_∞ is the average of the last 10 s of each cycle. Filled markers: Exp1 (circles = EH-reset, squares = SH-reset). Open squares: Exp2. Dashed lines and shaded bands indicate Exp1 mean ± 1 SD per reset method.

References

[1] S. Jung, C. Roman, and C. Hierold, "Fast Nitrogen Dioxide Sensing with Ultralow-Power Nanotube Gas Sensors". Adv. Sensor Res., 3: 2300081 (2024). https://doi.org/10.1002/adsr.202300081

[2] J. Kong, N.Franklin, C.Zhou, M.Chapline, S.Peng, K.Cho, H.Dai, "Nanotube Molecular Wires as Chemical Sensors". Science, vol. 287, pp. 622-625 (2000). https://doi.org/0.1126/science.287.5453.622

[3] K. Chikkadi, m. Muoth, V. Maiwald, C. Roman, and C. Hierold, "Ultra-low power operation of self-heated, suspended carbon nanotube gas sensors", Appl. Phys. Lett. 103, 223109 (2013). https://doi.org/10.1063/1.4836415

[4] I. Kraiem, C. Gentili, C. I. Roman, M. Haluska, and C. Hierold, "Reliable Gas sensor Recovery with Local Electrode Heating", Hilton Head Workshop (2026), unpublished.

[5] J. Zhang, A. Boyd, A. Tselev, M. Paranjape, and P. Barbara, "Mechanism of NO2 detection in carbon nanotube field effect transistor chemical sensors", Appl. Phys. Lett. 88, 123112 (2006). https://doi.org/10.1063/1.2187510

DOI 10.5162/eurosensors2026/3.1.6

Selective Benzene Gas Sensing with Flame-made Polytungstate Porous Film

Adrien Baut, Sebastian Kravecz, Andreas T. Güntner
Human-centered Sensing Laboratory, Sonnegstrasse 3, 8092, Zurich, Switzerland
andreas.guentner@hsl.ethz.ch

Summary:
Polytungstates are materials composed of highly oxidized tungsten polyhedral displaying a wide range of applicability due to their tunability. Their usual synthesis routes involve long reaction times and high temperatures, limiting their scalable production. In our work, we use flame aerosol, a rapid and scalable production method, to synthesize nanoparticulate powders and thin porous films. When used as gas sensors for air quality monitoring, these films are highly selective to benzene, even detecting concentrations down to 200 parts-per-billion while operated at 170 °C under 20% relative humidity.

Keywords: polytungstate nanoparticles, chemoresistive gas sensors, porous film, air quality monitoring, aerosol combustion.

Background, Motivation and Objective

Polytungstates are complex tungsten-oxide frameworks composed of edge- and corner-sharing WO_x polyhedra, widely studied for biomedical and functional applications. In particular, WO_6 octahedra can form hexagonal channel structures capable of incorporating alkali or other cations, enabling materials with promising uses in sensing. However, conventional synthesis routes (hydrothermal, solvothermal, and solid-state reaction) are limited by long reaction times, high temperatures, and poor scalability. Additionally, these routes can lead to micron-sized particles due to sintering effects [1], resulting in a loss of sensing performances.

Flame spray pyrolysis (FSP) is a one-step dry aerosol production method for nanoparticulate powders and thin film. It relies on the gas-solid conversion of the aerosol to form agglomerated particles that can be collected either on a filter or by thermophoresis on a sensing substrate to form highly porous films [2].

In our work [3], we leverage FSP technology to produce the pure phase polytungstate $K_2W_7O_{22}$ and determine the role of the production operational parameters on the sizes and composition of the particles produced. When deposited as a porous film, $K_2W_7O_{22}$ showed promising sensing performance for the detection of benzene.

Description of the New Method or System

Nanoparticles of $K_2W_7O_{22}$ have been produced for the first time by FSP. Additionally, their chemoresistive properties when used as porous film for the detection of benzene have been observed and reported.

Results

Figure 1 shows the X-Ray Diffractometer (XRD) patterns of various powder prepared by FSP for different precursor compositions, labelled by their potassium to tungsten atomic ratios (K/W). For K/W = 0.0, only ε- and γ-WO_3 are identified, as expected from literature [4]. As K/W increases, peaks attributed to $K_2W_7O_{22}$ emerge, while those attributed to WO_3 polymorphs shrink. At K/W = 0.29, only pure $K_2W_7O_{22}$ is identified as expected by its stoichiometric composition. Until K/W = 0.6, $K_2W_7O_{22}$ remains the only crystalline phase visible in the XRD, suggesting a high solubility of the potassium without disruption of the crystalline organization. When the stoichiometry is extended to K/W = 0.8 and 1, the $K_2W_7O_22$ peaks vanish and only large humps are observed, suggesting an amorphization of the powder.

Pure $K_2W_7O_{22}$ (K/W = 0.29) nanocrystals were directly deposited by thermophoresis onto a water-cooled sensing substrate to form a highly porous film (Fig. 2a). When operated at 170°C under an air flow at 20% relative humidity, the porous film was able to detect benzene concentrations from 2.5 parts-per-million (ppm) down to 0.2 ppm (Fig. 2b). This sensibility is of importance as benzene is a highly toxic air pollutant for which there are no safe levels of exposure according to the World Health Organization. Additionally, our sensor shows good selectivity over a wide range of analytes (Fig. 2c). In particular, the selectivity towards chemically similar

compounds xylene (18.7) and toluene (20.9) is substantially higher than other metal oxide-based sensors (e.g., [5]). Other sensing systems were able to better discriminate these three compounds, but usually really on additional elements such as filters [6] to increase the selectivity.

Illustrations, Graphs, and Photographs

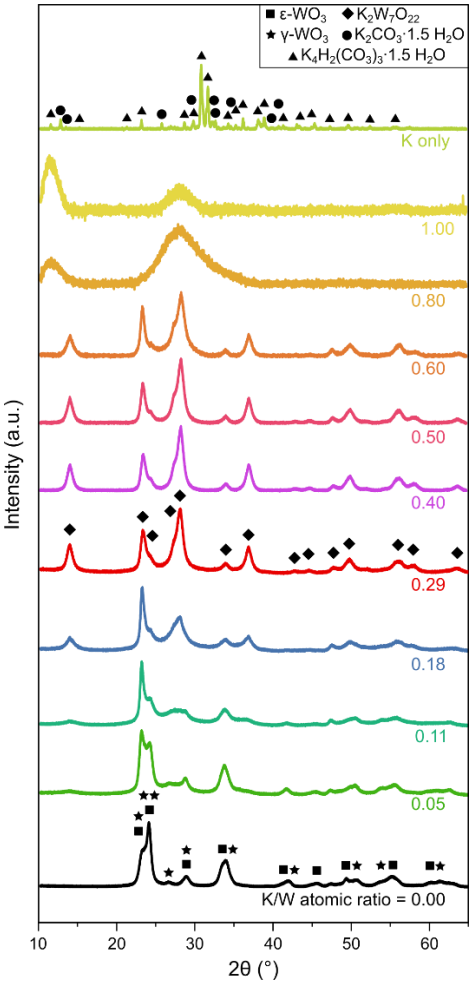

Fig. 1. (a) XRD patterns of nanoparticulate powders obtained by FSP for different K/W ratio. Reproduced from [3].

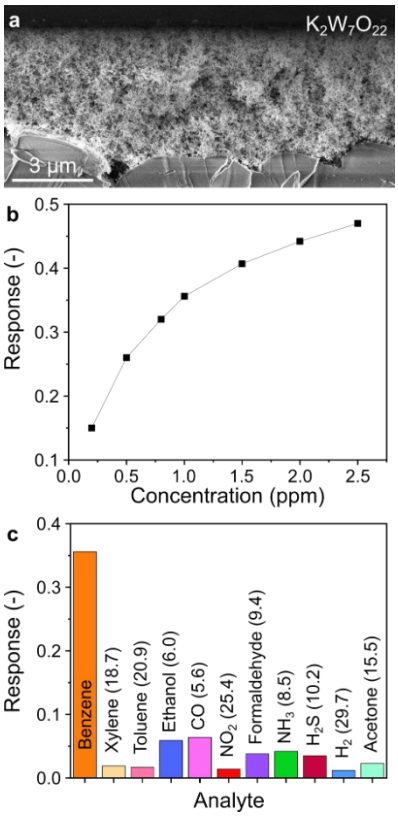

Fig. 2. (a) Scanning electron microscopy image of a porous $K_2W_7O_{22}$ sensing film. Response of a $K_2W_7O_{22}$ sensing film operated at 170°C under an air flow at 20% RH to various (b) benzene concentrations and (c) analytes at 1 ppm. Reproduced from [3].

References

[1] S.F. Solodovnikov et al., Resolving old problems with layered polytungstates related to hexagonal tungsten bronze: phase formation, structure, crystal chemistry and some properties, *Dalton Trans*. 52, 2770-2785 (2023); doi:10.1039/d2DT03895A.

[2] A.T. Güntner, N.J. Pineau, S.E. Pratsinis, Flame-made chemoresistive gas sensors and devices, Prog. Energy Combust. Sci. 90, 100992 (2022); doi: 10.1016/j.pecs.2022.100992.

[3] A. Baut, S. Kravecz, Andreas T. Güntner, Rapid dry synthesis of nanosized potassium polytungstate via flame aersol technology for benzene sensing, *Powder Technol.* 473, 122238 (2026); doi: 10.1016/j.powtec.2026.122238.

[4] M. Righettoni, A. Tricoli, S.E. Pratsinis, Thermally stable, silica-doped ε-WO_3 for sensing acetone in the human breath, *Chem. Mater.* 22, 3152-3157 (2010); doi: 10.1021/cm1001576.

[5] Y.J. Kwon et al., Enhancement of the benzene-sensing performance of Si nanowires through the incorporation of TeO2 heterointerfaces and Pd-sensitization, *Sens. Actuators B* 244, 1085-1097 (2017) doi: 10.1016/j.snb.2017.01.078.

. M. D'Andria et al. Metastable CoCu2O3 Nanocrystals from Combustion-Aerosols for Molecular Sensing and Catalysis, *Adv. Mater.* 36, 2408888; doi: 10.1002/adma.20240888.

DOI 10.5162/eurosensors2026/3.2.1

Single-Cell Impedance Cytometry: Recent Progress and Challenges Ahead

Federica Caselli
University of Rome Tor Vergata, via del Politecnico 1, 00133 Roma, Italy
caselli@ing.uniroma2.it

Abstract:

Microfluidic impedance cytometry (MIC) is a label-free technique that characterizes individual flowing cells based on their interaction with a multifrequency electric field [1]. It has been successfully applied across a range of domains, including life-science research, diagnostics, and environmental monitoring. In this talk, I will outline emerging trends that are expected to further expand the capabilities and adoption of MIC, together with the key challenges associated with these developments.

The presentation will focus on:

(i) The evolution from MIC to microfluidic impedance spectroscopy [2], in which thousands of single-cell spectra can be acquired within minutes and fitted to physically grounded models, enabling the extraction of cell dielectric parameters.

(ii) The integration of MIC with other microfluidic tools to create multifunctional single-cell analysis platforms [3]. MIC relies on a simple setup, making it naturally compatible with other microfluidic technologies.

(iii) The synergy with Artificial Intelligence (AI) [4–6]. As microfluidic systems gain functionality, they require a “brain” capable of interpreting signals from the sensing units and making task-level decisions. AI-based approaches are highly promising, as they enable real-time perception and decision-making in complex operational scenarios.

Keywords:

single-cell analysis, microfluidics, impedance cytometry, multifunctional platforms, artificial intelligence.

References:

[1] C. Honrado, P. Bisegna, N. S. Swami, F. Caselli, Single-cell microfluidic impedance cytometry: from raw signals to cell phenotypes using data analytics, *Lab on a Chip* 21, 22-54 (2021); doi: 10.1039/D0LC00840K

[2] M. Righetto, R. Reale, F. Carneri, A. Mistretta, M. De Zotti, D. Roversi, P. Bisegna, A. De Ninno, F. Caselli, Fast fourteen-frequency impedance spectroscopy of single erythrocytes and yeast cells in flow, *Biosensors and Bioelectronics*, 118757 (2026); doi: 10.1016/j.bios.2026.118757

[3] M. Righetto, C. Brandi, R. Reale, F. Caselli, Integrating impedance cytometry with other microfluidic tools towards multifunctional single-cell analysis platforms, *Lab on a Chip* 25, 1316-1341 (2025); doi: 10.1039/D4LC00957F

[4] F. Caselli, R. Reale, A. De Ninno, D. Spencer, H. Morgan, P. Bisegna, Deciphering impedance cytometry signals with neural networks, *Lab on a Chip* 22, 1714-1722 (2022); doi: 10.1039/D2LC00028H

[5] J. Jarmoshti, A. B. Siddique, A. Rane, S. Mirhosseini, S. J. Adair, T. W. Bauer, F. Caselli, N. S. Swami, Neural network-enabled multiparametric impedance signal templating for high throughput single-cell deformability cytometry under viscoelastic extensional flows, *Small* 21, 2407212 (2025); doi: 10.1002/smll.202407212

[6] M. Righetto, R. Reale, A. De Ninno, C. Brandi, D. C. Spencer, X. Zou, J. Jarmoshti, N. S. Swami, H. Morgan, P. Bisegna, F. Caselli, Segmentation of single-cell impedance signals using deep learning: a multi-dataset study, (2026); under revision

DOI 10.5162/eurosensors2026/3.2.2

Chip-Sized Biosensor for Multiparametric Monitoring

Sofia Moncada-Madrazo[1,2], Joan Canals[1,2], Sergio Moreno[1,2], Natalia Castro[3], Carolina Rodríguez[3], Javier Ramón-Azcón[3,4], Anna Vilà[1,2], Ángel Diéguez[1,2]
[1] Department of Electronic and Biomedical Engineering, Universitat de Barcelona, [2] Institute of Nanoscience and Nanotechnology (IN2UB), Universitat de Barcelona, [3] Institute for Bioengineering of Catalonia (IBEC), The Barcelona Institute of Science and Technology (BIST), [4] Institució Catalana de Recerca i Estudis Avançats (ICREA)
sofia.moncada@ub.edu

Summary: A chip-sized biosensor based on lensless digital holographic microscopy is introduced for continuous, in-incubator monitoring of *in vitro* models. The system integrates a CMOS sensor and a micro-LED display, enabling compact, label-free imaging, and quantitative parameter extraction across biological systems. Its capabilities were validated through angiogenesis and muscle-on-chip models, enabling quantification of both morphological parameters (network formation metrics), and functional parameters (contractile displacement). This work establishes a scalable, multiparametric biosensing platform for tissue monitoring.

Keywords: chip-sized microscopy, holography, angiogenesis, muscle-on-chip.

Background, Motivation and Objective

Continuous, non-invasive monitoring of cellular and tissue dynamics is critical for advanced in vitro assays. Conventional live-cell imaging typically depends on large, costly benchtop microscopy systems that are frequently shared and situated outside incubator environments. This arrangement restricts experimental flexibility, scalability, and the ability to maintain uninterrupted observation under physiological conditions.

To address these limitations, we present a compact chip-sized biosensing platform based on lensless digital holographic microscopy for continuous monitoring directly within standard incubator environments. It incorporates a CMOS sensor and a micro-LED array in an in-line configuration, allowing simplified optical architecture and parallel deployment of multiple devices within standard CO_2 incubators.

Existing lensless systems often reply on additional optical elements [1–2], increasing system complexity and limiting scalability. In contrast, the proposed platform uses a simplified illumination scheme and compact design, enabling robust operation within standard incubator environments.

The platform was validated across distinct biological models to demonstrate its capability for both morphological and functional biosensing. In angiogenesis assays, this approach provides continuous monitoring of vascular network formation and remodeling, which has been shown to be critical for capturing dynamic angiogenesis processes that cannot be resolved by endpoint analyses [4-5].

The platform is further applied to muscle-on-chip systems for the extraction of functional parameters under electrical stimulation. Contractile behavior in engineered skeletal muscle tissues is typically evaluated by measuring force, deformation, or displacement [6]. In the present study, contractility is quantified by tracking tissue displacement between flexible anchoring pillars providing a readout of muscle activity.

Description of the New Method or System

The platform has three acquisition modes: endpoint, time-lapse and video. For angiogenesis monitoring (Fig. 1), time-lapse imaging was performed every 30 min over 18 h and quantitative metrics were extracted using a custom image analysis pipeline.

For muscle-on-chip experiments (Fig. 2), video sequences were acquired at 60 frames per second during electrical stimulation using the MyoMoves system [7], to induce twitch (low-frequency) and tetanic (high-frequency) contractions. Tissue displacement was quantified by tracking pillar deflection using a custom algorithm, yielding time-resolved contractile dynamics.

The key innovation lies in a unified biosensing approach that extracts both morphological and functional parameters across distinct *in vitro* systems.

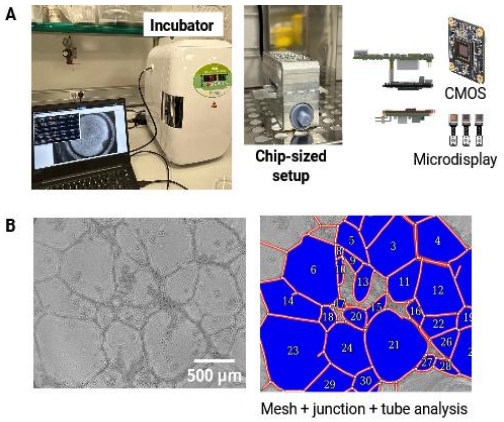

Fig. 1. (A) Chip-sized system inside incubator. (B) Example of a capture and its analysis.

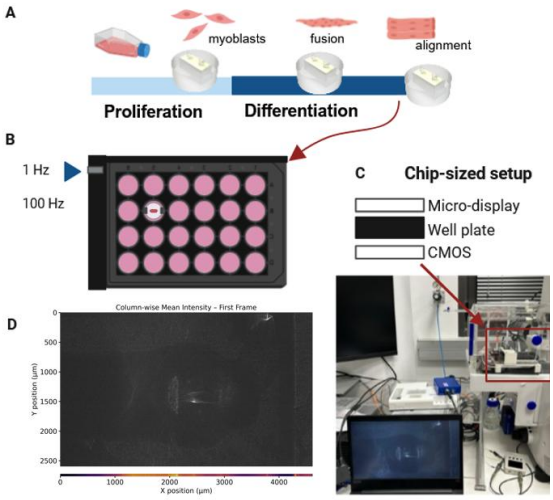

Fig. 2. (A) 3D muscle generation. (B) Electrical stimulation configuration. (C) Chip-sized system within a controlled chamber. (D) Representative analyzed frame of muscle contraction.

Results

Figure 3 presents the temporal evolution of angiogenesis metrics across two experiments. Tube length and junction number increase during early stages and decrease after reaching its peak.

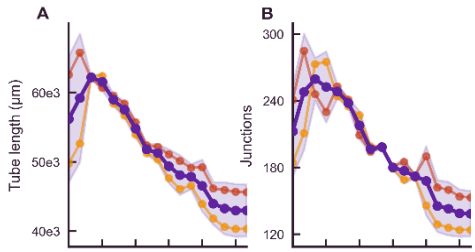

Fig. 3. Evolution of angiogenesis over an 18h experiment. Tube length, and number of junctions trends. Experiment 1, 2, and Mean ± SD (yellow, orange, purple plots).

Figure 4 shows displacement curves recorded during stimulation. At low-frequency stimulation, periodic displacement peaks correspond to individual twitch contractions, which are characterized by complete relaxation and low-amplitude responses. In contrast, high-frequency stimulation induces tetanic contractions, resulting in sustained, higher-amplitude displacements and slower relaxation dynamics due to temporal summation.

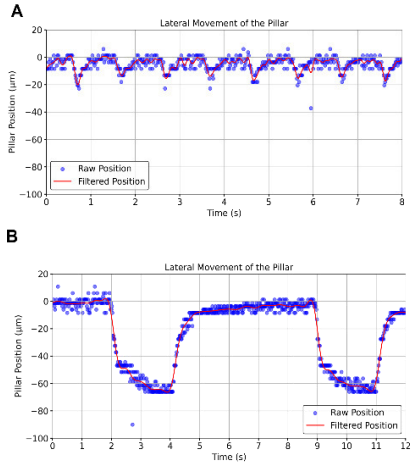

Fig. 4. Analysis of muscle contraction under (A) 1 Hz and (B) 100 Hz stimulation.

References

[1] S.V. Kesavan, F. Momey, O. Cioni, B. David-Watine, N. Dubrulle, S. Shorte, E. Sulpice, D. Freida, B. Chalmond, J.M. Dinten, X. Gidrol, C. Allier, High-throughput monitoring of major cell functions by means of lensfree video microscopy, *Sci. Rep.* 4, 5942 (2014); doi: 10.1038/srep05942.

[2] J.A. Picazo-Bueno, K. Trindade, M. Sanz, V. Micó, Design, Calibration, and Application of a Robust, Cost-Effective, and High-Resolution Lensless Holographic Microscope, *Sensors* 22, 553 (2022); doi: 10.3390/s22020553

[3] H. Lee, K.T. Kang, Advanced tube formation assay using human endothelial colony forming cells for *in vitro* evaluation of angiogenesis, *Korean J. Physiol. Pharmacol.* 22,705-712 (2018); doi: 10.4196/kjpp.2018.22.6.705.

[4] Z. Li, H. Zhang, Y. Sun, Z. Feng, B. Cui, J. Han, Y. Li, H. Liu, T. Sun, Live-cell imaging-based dynamic vascular formation assay for antivascular drug evaluation and screening, *iScience* 26, 106721 (2023); doi: 10.1016/j.isci.2023.106721.

[5] C. Vesga-Castro, J. Aldazabal, A. Vallejo-Illarramendi, J. Paredes. Contractile force assessment methods for in vitro skeletal muscle tissues, *elife* 11, e77204 (2022); doi: 10.7554/eLife.77204.

[6] M. Ruiz-Gutiérrez, A. Tejedera-Villafranca, S. Pujol-Pinto, J. Ramón-Azcón, J. M. Fernández-Costa, Myo-MOVES: a custom electrical stimulation system for functional studies of 3D bioengineered muscle, *Lab Chip* 25, 5677–5690 (2025); doi: 10.1039/d5lc00614g

DOI 10.5162/eurosensors2026/3.2.3

PEDOT:PSS coated Fully Printed Microelectrode Arrays for Neural Interfacing

Amelie Ziller[1], Lukas Kreuzberger[1], Andrea Corna[1], Paul Werginz[1], Günther Zeck[1]
[1] Institute of Biomedical Electronics, TU Wen, Vienna, Austria
guenther.zeck@tuwien.ac.at

Summary:
Inkjet printing enables scalable fabrication of flexible microelectrode arrays, but commonly used printable inks rely on suboptimal electrode materials. Here, gold electrodes on flexible substrates were coated with electropolymerized PEDOT:PSS, significantly reducing impedance and enhancing charge injection capability. Electrochemical characterization together with neuronal recording and stimulation demonstrate improved interface performance. These results highlight the potential of inkjet printed PEDOT:PSS coated electrodes for high performance neural interfacing.

Keywords: Inkjet printing, Microelectrode array, PEDOT:PSS, Neural interface, Flexible electronics

Introduction

Microelectrode arrays (MEAs) are widely used in neural interfaces for recording and stimulation of electrogenic activity [1]. Conventional fabrication techniques, such as photolithography, offer high precision but are often costly and limited in design possibilities. Inkjet printing has emerged as a promising alternative for the fabrication of flexible and customized electronic devices, enabling rapid prototyping and reduced manufacturing complexity [2].

However, printed metal electrodes can present challenges in terms of electrochemical performance, which may limit their suitability in neural recording and stimulation. Conductive polymers such as PEDOT (poly(3,4-ethylenedioxythiophene)) are known to significantly improve electrode-electrolyte interface properties by lowering impedance and increasing charge transfer capability [3].

In this work, we improved the impedance characteristics of fully inkjet-printed gold MEAs on flexible substrates by functionalization with PEDOT:PSS. We demonstrate their suitability for recording and stimulation of single unit neural activity in the ex vivo retina.

Methods

Gold MEAs, with electrode diameters ranging from 40 to 80 µm, were fabricated on flexible Polyethylene Naphthalate (PEN) substrates via inkjet printing. Both the gold and an epoxy-based SU-8 dielectric ink were deposited using commercial Dimatix Samba Materials Cartridges with a 2.4 pL drop volume. Following fabrication, the electrodes were coated with PEDOT:PSS via electropolymerization. The deposition was performed using a potentiostat in chronopotentiometry mode, applying constant current densities of 10-20 µA/mm² for 1 minute. The aqueous electropolymerization solution consisted of 0.01 M 3,4-ethylenedioxythiophene and 1 wt% poly(sodium-p-styrenesulfonate).

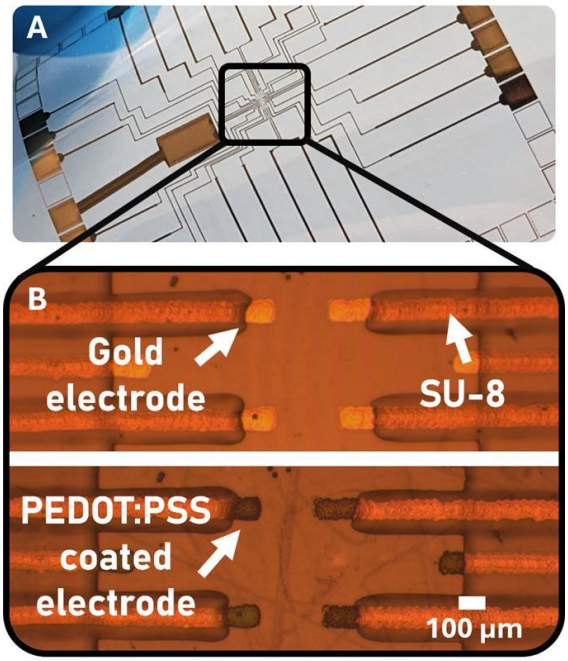

Fig. 1. Fabrication and morphology of the microelectrode array. (A) Photograph of an inkjet-printed flexible microelectrode array (MEA). (B) Magnified view of an individual electrode before (top) and after (bottom) PEDOT:PSS deposition.

Results

The deposition of PEDOT:PSS offers significant advantages over bare gold, primarily by reducing electrode impedance, which directly impacts recording performance. To quantify this, we performed electrochemical impedance spectroscopy (EIS) before and after deposition. The results show that the PEDOT:PSS coating substantially reduced impedance across the frequency spectrum (Figure 2). Specifically, at 1 kHz, the baseline impedance of the bare gold electrodes was 26 kΩ, which decreased approximately fivefold following PEDOT:PSS electrodeposition. Furthermore, the coated electrodes demonstrated greater consistency, as evidenced by the reduced impedance variation between individual recording sites (Figure 2, bottom).

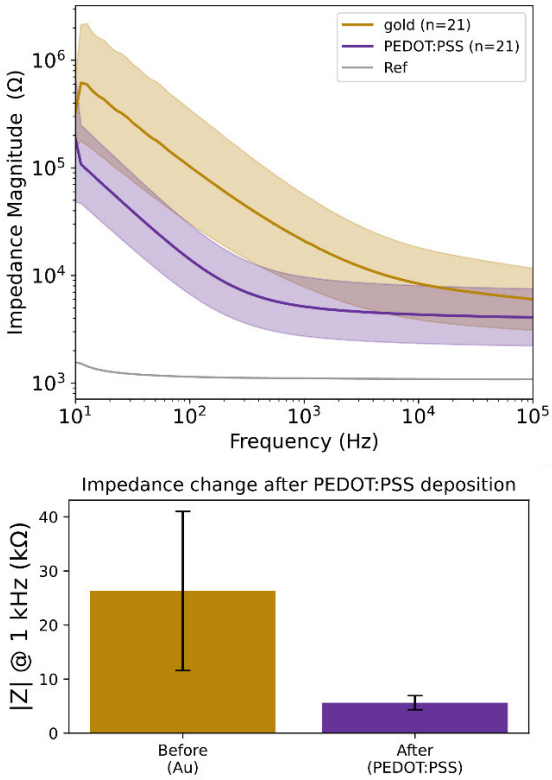

Fig. 2. Electrochemical impedance spectroscopy (EIS). (Top) Impedance magnitude of bare gold vs. PEDOT:PSS-coated electrodes. (Bottom) 1 kHz impedance comparison (n = 21), showing reduced magnitude and variability with PEDOT:PSS.

To confirm that these electrochemical improvements translate to functional performance, we conducted neuronal recordings and electrical stimulation experiments using ex vivo photodegenerated retinae. We recorded spontaneous activity from retinal ganglion cells (RGCs) (Fig. 3A), where PEDOT:PSS-coated MEAs yielded single-cell extracellular voltage waveforms with high signal-to-noise ratio. We then performed subretinal stimulation with PEDOT:PSS electrodes while simultaneously recording with patch-clamp electrodes, delivering voltage-controlled square-wave pulses. The recorded RGCs showed reliable activation with sub-millisecond precision (Figure 3B), with activation thresholds consistently below 1 V (Figure 3C), superior to printed gold electrodes [4].

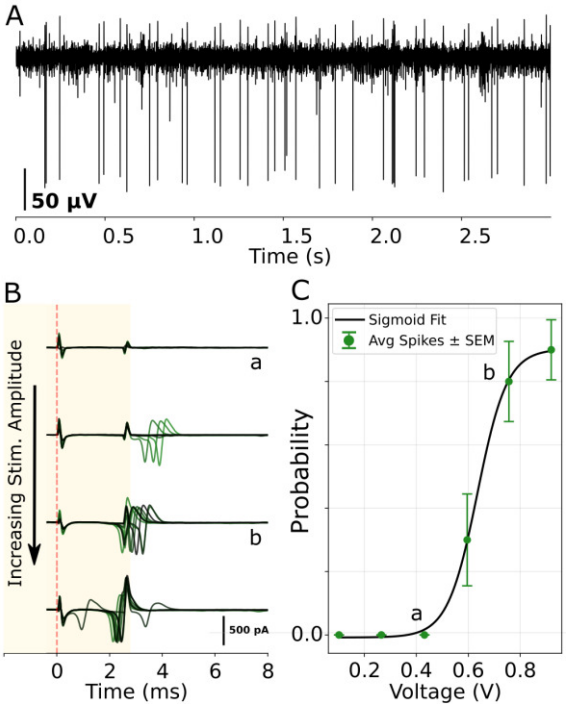

Fig. 3. Functional characterization of the PEDOT:PSS-coated electrodes. (A) Spontaneous retinal ganglion cell (RGC) activity. (B) RGC responses to stimulation, with increased spike count and reduced latency at higher strengths. (C) Sigmoidal stimulus–response curve with activation threshold < 1 V.

References

[1] Obien, M.E.J., Deligkaris, K., Bullmann, T., Bakkum, D.J., Frey, U., Revealing neuronal function through microelectrode array recordings, Front. Neurosci. 8. (2015); https://doi.org/10.3389/fnins.2014.00423

[2] Bachmann, B., Adly, N. Y., Schnitker, J., Yakushenko, A., Rinklin, P., Offenhäusser, A., & Wolfrum, B., All-inkjet-printed gold microelectrode arrays for extracellular recording of action potentials, *Flexible and Printed Electronics*, *2*(3), 035003 (2017); https://doi.org/10.1088/2058-8585/AA7928

[3] Pranti, A.S., Schander, A., Bödecker, A., Lang, W., PEDOT: PSS coating on gold microelectrodes with excellent stability and high charge injection capacity for chronic neural interfaces. Sensors and Actuators B: Chemical 275, 382–393. (2018); https://doi.org/10.1016/j.snb.2018.08.007

[4] Ziller, A., Corna, A. Bui, M.T., Werginz, P. Schneider, M., Schmid U., Zeck, G., Inkjet-printed Rough Gold Microelectrode Arrays on Flexible Substrates for Neural Recording and Electrical Stimulation, ACS Applied Materials and Interfaces, (2026); *(accepted)*

DOI 10.5162/eurosensors2026/3.2.4

An Electrochemical Aptasensor for Continuous Biomarker Monitoring

Hadi Mirzajani[1], Sandro Carrara[1]
[1] Bio/CMOS Interfaces (BCI) Laboratory, École Polytechnique Fédérale de Lausanne (EPFL), 2000 Neuchâtel, Switzerland,
hadi.mirzajani@epfl.ch

Summary:
This study presents a self-regenerating electrochemical aptamer biosensor for continuous biomarker sensing under controlled buffer conditions. Sensor renewal is achieved by modulating buffer flow, avoiding chemical stripping and enabling repeated measurement cycles. Gold nanorod modified electrodes enhance interfacial electron transfer and improve analytical sensitivity, yielding a concentration dependent response across three orders of magnitude with a subnanomolar detection limit. The platform also exhibits reversible operation, with faster baseline restoration at higher wash flow. Overall, these findings establish hydrodynamic control as a practical strategy for continuous affinity biosensing and a strong basis for future diagnostic systems including but not limited to wearable, implantable, and microfluidic devices for diagnostics in sweat, interstitial fluid, tears, urine, saliva and other human specimens.

Keywords: biosensors, bioelectronics, continuous monitoring, hormone monitoring, 17β-Estradiol.

Background and Motivation

Continuous hormone monitoring is crucial because endocrine signals evolve over time, and single blood draws often miss physiologically meaningful fluctuations linked to fertility, pregnancy, and women's health. Continuous affinity biosensing offers a path to time-resolved molecular readout, and electrochemical aptamer sensors are especially attractive because they support reagent-free transduction, miniaturization, and direct electronic measurement [1]. For continuous operation, however, affinity biosensors must reversibly track concentration changes without cumulative saturation, memory effects, or signal drift [2-3]. A remaining bottleneck, however, is regeneration. Once affinity sites are occupied, signal recovery often depends on chemical stripping or added reset hardware, which complicates wearable integration and sustained operation [4]. Here, we address this limitation with a flow-triggered self-regenerative electrochemical aptamer sensor for 17β-Estradiol (E2) sensing. By using buffer-flow modulation alone to restore the sensing interface, the platform enables repeated measurement-regeneration cycles, stable dynamic operation, and selective detection toward practical continuous use.

Description of the New Method

We report a flow-programmed electrochemical aptamer platform for continuous biomarker sensing, combining a methylene blue tagged recognition layer with square-wave voltammetric (SWV) transduction. The working electrode was nanostructured with AuNRs to enlarge electroactive area, improve electron-transfer efficiency, and increase sensitivity. Regeneration was achieved exclusively through modulation of buffer flow, which accelerated target dissociation and restored the baseline without chemical stripping. To the best of our knowledge, this is one of the first applications of flow-mediated regeneration in an electrochemical biosensor. The method was validated in E2 sensing in buffer to establish reversible operation and repeatable sensing-regeneration cycles.

Results

Figure 1A presents the time-resolved dose response of the E2 electrochemical aptasensor under continuous flow at 3 μL min^{-1}, where E2 solutions prepared in binding buffer with different concentrations were sequentially delivered into the sensing chamber. The sensor displayed well-defined, concentration-dependent current transitions, evidencing rapid target binding under dynamic conditions. The corresponding calibration plot in Figure 1B revealed an excellent quasi-linear dependence on the logarithm of concentration over three orders of magnitude, defining a dynamic range from 10 pM to 10 nM, an R^2 of 0.9982, and a limit of detection of 190 pM. Above 1 nM, the response approached saturation, consistent with progressive occupation of the available surface-confined aptamer binding sites.

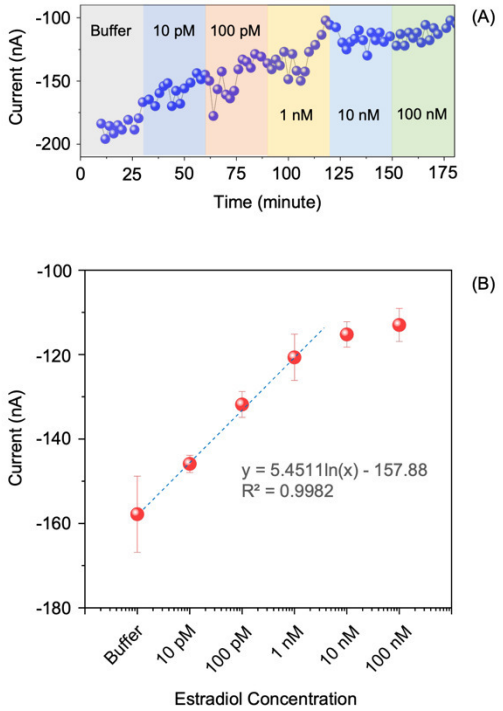

Fig. 1. Sensor characterization. (A) Dynamic dose-response, and (B) calibration curve of the sensor.

Figure 2 demonstrates that the E2 aptasensor preserves dynamic and reversible operation under continuous perfusion, with the measured current reflecting the coupled effects of target binding, fluid exchange, and interfacial re-equilibration. In Figure 2A, exposure to 100 nM E2 at 3 μL min^{-1} produces a clear time-dependent signal shift, indicating progressive occupation of the surface-confined aptamer layer and establishment of a new quasi-steady electrochemical state under flow. The non-instantaneous transition shows that the response is not governed solely by equilibrium binding, but also by analyte transport through the chamber and conformational switching of the redox-tagged probe layer. When the inlet is switched to blank buffer at the same flow rate, recovery is markedly slower and proceeds over a longer transition window, revealing incomplete washout of residual analyte and continued rebinding near the electrode surface. Figure 2B further confirms this mechanism. When E2 is introduced at 3 μL min^{-1} but the buffer flow is increased to 8 μL min^{-1}, the sensor undergoes faster and more reproducible regeneration between consecutive cycles. The shortened transition time at higher buffer flow indicates that signal reset is strongly mass-transport limited, with enhanced convection accelerating analyte clearance, thinning the diffusion layer, and reducing memory effects. Collectively, these results establish flow programming as an effective and non-chemical route for regeneration of the E2 biosensor.

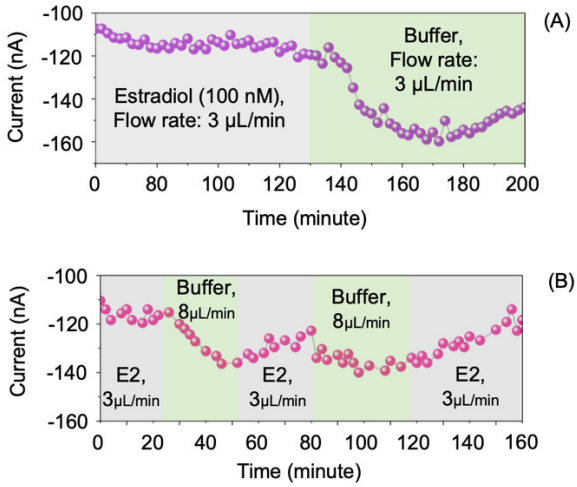

Fig. 2. Flow-induced regeneration. (A) Regeneration at buffer flow rate of 3 μL/min, and (B) 8 μL/min.

Conclusion and Outlook

This study establishes an electrochemical aptamer strategy for continuous biomarker monitoring in which sensitivity and reversibility are engineered together. AuNR nanostructuring strengthened SWV transduction and enabled dose-resolved E2 quantification over a broad log-linear range, while flow-programmed washing regenerated the interface without chemical stripping. The dependence of reset kinetics on buffer flow shows that recovery is governed by both aptamer dissociation and convective mass transport. These findings identify hydrodynamics as a controllable design variable for continuous affinity biosensors.

Acknowledgment

The research has been financially co-supported by the Innosuisse grant ¨MatPacth¨ (project # 116.366 IP-ENG) and by the European project SENSOTERIC, with direct funding from SEFRI (Grant No. 23.00481). The authors would like to thank Gian Luca Barbruni for useful discussions.

References

[1] Downs, A. M., & Plaxco, K. W. Real-time, in vivo molecular monitoring using electrochemical aptamer based sensors: opportunities and challenges. *ACS sensors*, *7*(10), 2823-2832 (2022); doi: 10.1021/acssensors.2c01428.

[2] Ye, C., Wang, and *et al*. A wearable aptamer nanobiosensor for non-invasive female hormone monitoring. Nature nanotechnology, 19(3), 330-337 (2024); doi: s41565-023-01513-0

[3] H. Mirzajani, and *et al*.. "Minimally invasive and in situ capacitive sensing of cardiac troponin I from interstitial fluid." *ACS sensors* 10, no. 12, 9335-9346 (2025); doi: 10.1021/acssensors.5c01691

[4] Zargartalebi, H., and *et al*. Active-reset protein sensors enable continuous in vivo monitoring of inflammation. *Science*, *386*(6726), 1146-1153 (2024); doi: 10.1126/science.adn2600.

DOI 10.5162/eurosensors2026/3.2.5

Ferroelectric Microelectrode Array with System-Integrated Direct-Digitization ASIC for Neural Recording

Moritz Doering[1], Roman Willaredt[2], Daniel Rossbach[1], Philip Zimmer[1], Daniel Hoffmann[1], Heiko Trautner[1], Oliver Amft[1,2], Matthias Kuhl[2], Maximilian T. Becker[1]
[1] Hahn-Schickard-Gesellschaft, 78052 Villingen-Schwenningen, Germany
[2] Universität Freiburg, Technische Fakultät, 79110 Freiburg, Germany
Moritz.Doering@hahn-schickard.de, Maximilian.Becker@hahn-schickard.de

Summary:

We present a bioelectronic interface platform comprising a passive ferroelectric microelectrode array (FeMEA) biochip directly connected to DC-coupled sigma-delta analog-to-digital converters (ADCs) with a power consumption of less than 10 µW per channel. The FeMEA biochip platform is validated with pre-recorded neuronal signals in the action potential band (0.3 – 10 kHz) and in the local field potential band (1 – 300 Hz), thereby demonstrating utility for *in-vitro* neurophysiology applications and future *in-vivo* neural probes with ferroelectric electrodes.

Keywords: Ferroelectric microelectrode arrays (FeMEAs), analog-to-digital converters (ADCs), neural recording, low-power consumption

Background, Motivation and Objective

Bioelectronic devices for targeted neural stimulation and recording of bioelectric signals, e.g., in implant systems or wearables, offers enormous opportunities for the treatment, prevention and rehabilitation of neurodegenerative disorders and chronic diseases [1,2]. Key prerequisites for the successful use of future bioelectronic devices are their long-term stability, sensitivity and safety, which are all largely determined by the properties of the bioelectronic interface.

The traditional approach to bioelectronic interfacing is based on metallic electrodes in contact with electrogenic cells or tissue [1,2]. However, when using metallic electrodes (e.g. Pt) for neural stimulation, it is difficult to avoid electrochemical degradation processes at the interface which can lead to corrosion and to cell and tissue damage [3]. One possible solution to avoid electrochemical degradation processes in bioelectronic applications are ferroelectric electrodes [4]. There, a metallic electrode is coated with a ferroelectric insulator, whereby electrochemical degradation processes are suppressed and the stimulation current corresponds to a displacement current induced by ferroelectric polarization reversal.

The read-out electronics require low-power consumption. Recently, the concept of in-situ digitization of neuronal signal utilizing DC-coupled sigma delta analog-to-digital converters (ADCs) has been introduced and validated with generic electrode materials including Pt and IrOx [5,6]. However, the combination of ferroelectric electrodes connected to low-power recording frontends formed by an application-specific integrated circuit (ASIC) has not been tested yet.

Description of the System

In this work, we introduce a bioelectronic interface platform comprising a passive ferroelectric microelectrode array (FeMEA) biochip directly connected to DC-coupled sigma-delta ADCs with a power consumption of less than 10 µW per channel [6]. An overview of the complete system is shown in Fig. 1(a). The FeMEA biochip is depicted in Fig. 1(b) and has 60 circular TiW electrodes (30 µm in diameter) which are coated with 8-nm ZrO_2 with field-induced ferroelectric properties [7]. The electrode pitch is 200 µm and the FeMEA biochip is also compatible with commercial MEA readout systems. The experimental configurations for testing the functionality of the recording ASIC and for measuring pre-recorded neural signals with the FeMEA connected to the recording ASIC are shown in Fig 1(c,d) respectively. It should be noted, that the first stage of the ADC is formed by a dedicated input transistor T_{IN} and hence, the ferroelectric electrode connected to the gate of T_{IN} corresponds to an extended-gate field-effect transistor (EGFET) sensor [8].

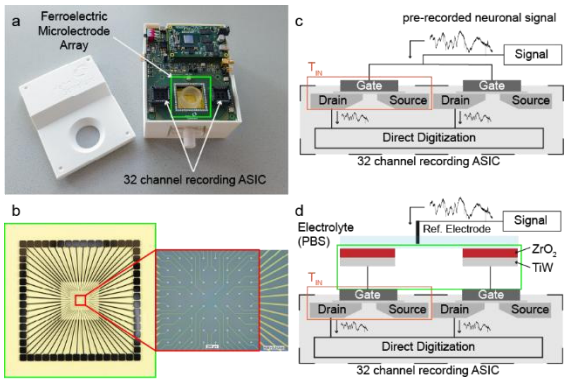

Fig. 1. (a) Overview of the prototype system. (b) FeMEA biochip. (c) Experimental set-up for ASIC testing. (d) Experimental set-up for measuring pre-recorded and pre-processed neural signals with FeMEA connected to the recording ASIC.

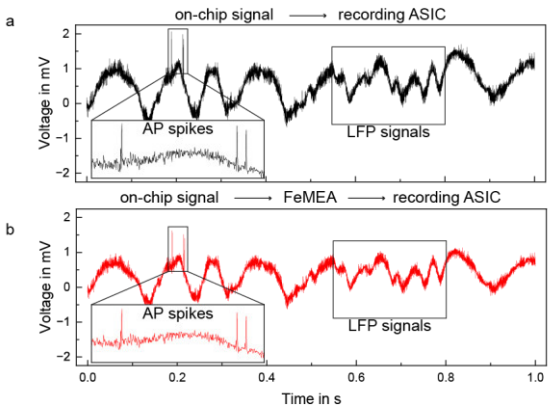

Fig. 2. Validation of the entire systems with pre-recorded neural signals. (a) Input Signal directly connected to recording ASIC. (b) Input signal applied to reference electrode in electrolyte and recorded with FeMEA electrode connected to recording ASIC.

Results

We developed and designed a system for evaluating the capabilities of recording neuronal signals with ferroelectric coated MEAs in combination with a direct-digitization frontend. Fig. 2a shows the recording of a pre-recorded and pre-processed neural signal applied directly to the designed neurorecording ASIC. In comparison, Fig. 2b contains the signal measured by the combination of ASIC and FeMEA biochip immersed in electrolyte. The artificial neural signals contain spikes induced by action potentials (APs, frequency band 0.3 – 10 kHz) and slower oscillations due to local field potentials (LFPs, frequency band 1 – 300 Hz). The measured signals with a FeMEA electrode connected to the ADC is shown in Fig. 2(b). AP spikes and LFPs are clearly visible, which demonstrates full functionality of the system. Moreover, our results demonstrate the possibility to utilize ferroelectric electrodes in EGFET sensors, which are so far operated solely with conductive (i.e., uncoated) electrodes [8].

The presented work serves as a basis for future highly-integrated in-vitro and in-vivo bioelectronic devices, including EGFET-based sensors, that combine ferroelectric electrodes with low-power readout electronics on a single chip.

References

[1] Schröter, Manuel, et al. "Advances in large-scale electrophysiology with high-density microelectrode arrays." *Lab on a Chip* 25.19 (2025): 4844-4885; doi: 10.1039/d5lc00058k

[2] Williams, Nathaniel P., et al. In vivo microelectrode arrays for neuroscience." *Nature Reviews Methods Primers* 5.1 (2025): 31: doi: 10.1038/s43586-025-00399-7

[3] M. Doering *et al.* Electrochemical microelectrode degradation monitoring: in situ investigation of platinum corrosion at neutral pH, *Journal of neural engineering* 19.1, 016005 (2022); doi: 10.1088/1741-2552/ac47da

[4] M. T. Becker, Charge injection capacity of ferroelectric microelectrodes for bioelectronic applications, *AIP Advances* 11, 065106 (2021); doi:10.1063/5.0049202

[5] D. De Dorigo *et al.* Fully immersible subcortical neural probes with modular architecture and a delta-sigma ADC integrated under each electrode for parallel readout of 144 recording sites, *IEEE Journal of Solid-State Circuits* 53, 3111 (2018); doi: 10.1109/JSSC.2018.2873180

[6] R. Willaredt, *et al.* A 0.00175 mm^2 and 9.62 µW per Channel Direct-Digitization Front End With EDO Compensation for Neural Probes With a Spatial Resolution of 35 µm, *IEEE Journal of Solid-State Circuits,* 2330 (2025); doi: 10.1109/JSSC.2025.3555007

[7] M. T. Becker *et al.* A Ferroelectric CMOS Microelectrode Array with ZrO_2 Recording and Stimulation Sites for In-Vitro Neural Interfacing, *2024 IEEE BioSensors Conference (BioSensors).* IEEE (2024); doi: 10.1109/BioSensors61405.2024.10712692

[8] S. A. Pullano *et al.* EGFET-based sensors for bioanalytical applications: A review, *Sensors* 18.11 (2018): 4042; doi: 10.3390/s18114042

DOI 10.5162/eurosensors2026/3.3.1

CO/HC Gas Sensor Using a Powder Aerosol Deposited Thermoelectric Material

Benedikt Streibl, Thomas Wöhrl, Daniel Paulus, Jaroslaw Kita,
Daniela Schönauer-Kamin, Gunter Hagen, Ralf Moos
Department of Functional Materials, Center of Energy Technology (ZET), University of Bayreuth, Bayreuth, 95447, Germany,
Correspondence to: functional.materials@uni-bayreuth.de

Summary:

This study presents a CO/HC gas sensor designed for operation at high temperatures in harsh environments, such as the flue gas of biomass combustion systems. The sensor principle is based on an indirect thermoelectric effect caused by exothermic reactions, which enables the detection of unburned flue gas components. A special feature of the sensor is its manufacturing process, whereby structured lines of a thermoelectric material are fabricated using the powder aerosol deposition method. As a result, significantly enhanced sensor sensitivity was achieved compared to the conventional sensor design.

Keywords:
Emission Monitoring, High Temperature Gas Sensor, Biomass Combustion,
Powder Aerosol Deposition (PAD), Thermoelectrics

Motivation

The increasing use of biogenic residual fuels such as wood for energy production requires reliable emission monitoring, particularly of carbon monoxide (CO) and hydrocarbons (HC) as indicators of incomplete combustion [1]. Conventional gas analysis systems are often expensive, maintenance-intensive, and limited in their suitability for continuous in-situ operation. Thermoelectric gas sensors offer a robust alternative well suited for harsh environments [2]. This work presents a CO/HC sensor that relies on an indirect thermoelectric sensing effect resulting from exothermic reactions at a catalytic active film. The manufacturing process of the thermoelectric components involves the use of the powder aerosol deposition method (PAD). This novel approach includes the production of structured, optimized functional films, which contribute to reliable emission monitoring during biomass combustion.

Sensor Setup and Fabrication

The sensor element is based on a ceramic substrate containing a screen-printed platinum heater structure on the reverse side. It is realized in a four-wire configuration and insulated by an additional cover layer [2]. On the front side, a thermopile structure is integrated to detect temperature differences across the sensor. This temperature difference is generated by a one-sided applied catalytically active film that exothermically converts unburned hydrocarbons (HC) and carbon monoxide (CO) [3]. Thus, the sensor provides a voltage signal that depends on the concentration of unburned flue gas components. A schematic image is shown in Fig. 1a) and a real sensor without the catalytic active film is shown in Fig. 1c).

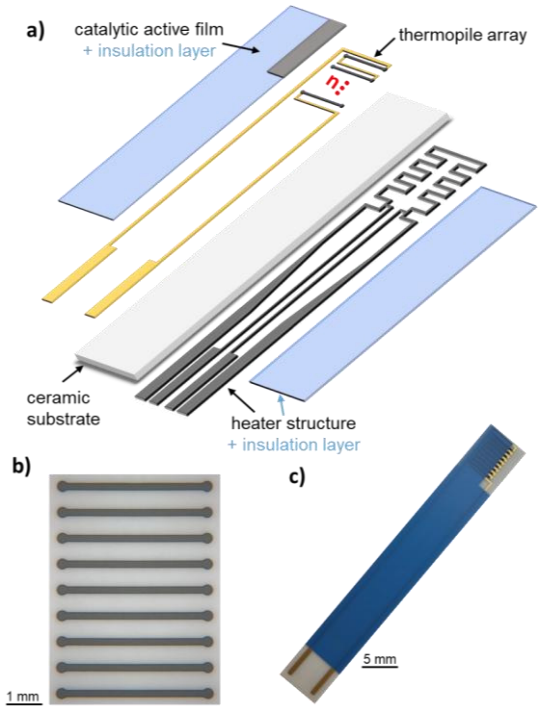

Fig. 1. Setup of the CO/HC sensor. a) Schematic picture. b) CCO thermocouple junctions with a line width of 200 µm, fabricated using the PAD method, c) real sensor without catalytic active film

In contrast to previous sensor designs, no gold–platinum combination is used for the thermopile structure. Instead, platinum is replaced by the thermoelectric material calcium cobalt oxide ($Ca_3Co_4O_9$, CCO), which offers a significantly higher relative Seebeck coefficient ($|S_{Au/CCO}(600\ °C)| \approx 160\ \mu V/K$ in comparison to $S_{Au/Pt}(600\ °C) \approx 19\ \mu V/K$) [4,5]. This thermoelectric material is deposited using the powder aerosol deposition method (PAD), in which the CCO powder is accelerated into a vacuum chamber and directly deposited onto the substrate at room temperature. This process enabled the fabrication of structured lines with widths of approximately 200 µm (see Fig 1b)).

Results and Discussion

The sensor characterization was carried out under laboratory conditions using sensors with nine thermocouple pairs. To provide a basis for comparison, sensors with Au/CCO thermopiles were evaluated along with reference sensors that had conventional Au/Pt thermopiles (according to [3]).

Fig. 2 shows the temporal response of the sensor signals measured at a sensor temperature of 600 °C. In this measurement, different concentrations of CO and C_3H_6 were dosed and the voltage change ΔU was evaluated.

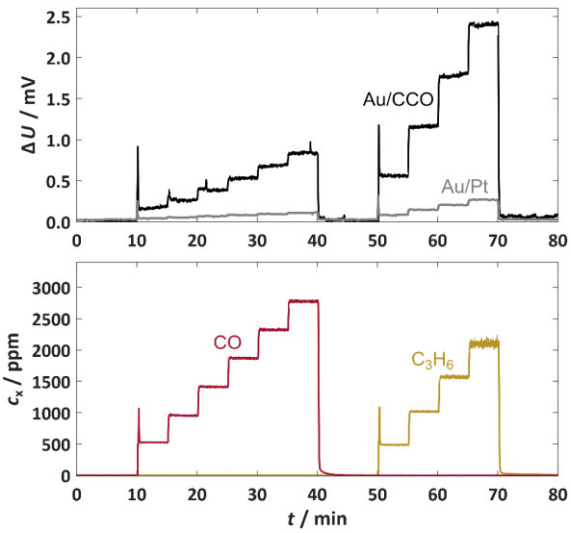

Fig. 2. Time course of sensor responses at varying CO and C_3H_6 concentrations at a sensor temperature of 600 °C, base gas: 15 vol% O_2, 5 vol% H_2O, 3 vol% CO_2 in N_2

The measurement shows that the voltage change obtained with the Au/CCO sensor is significantly higher than that of the Au/Pt sensor. For CO exposure, a sensitivity of 305 µV per 1000 ppm was determined, while propene generated a response of 1167 µV per 1000 ppm, corresponding to approximately a ninefold increase compared to the Au/Pt sensor (32 µV per 1000 ppm for CO and 121 µV per 1000 ppm for C_3H_6). Thus, the signal increase can be attributed to the Seebeck coefficient ratio of the thermopile combinations, assuming identical temperature differences at the sensors.

Further measurements demonstrated that cross-sensitivities to water vapor and oxygen were extremely low. Due to the nearly temperature-independent Seebeck coefficient of CCO around 600 °C, fluctuations in sensor temperature have only a minor impact on the sensor signal. This can contribute to a stable and robust sensor response under varying operating conditions. Further investigations will therefore focus on validating the sensor performance under realistic conditions by conducting measurements in the real flue gas of a wood-fired furnace.

References

[1] H. Kohler, B. Ojha, N. Illyaskutty, I. Hartmann, C. Thiel, K. Eisinger, M. Dambacher, In situ high-temperature gas sensors: continuous monitoring of the combustion quality of different wood combustion systems and optimization of combustion process, *Journal of Sensors and Sensor Systems* 7, 161-167 (2018); doi: 10.5194/jsss-7-161-2018

[2] G. Hagen, J. Herrmann, X. Zhang, H. Kohler, I. Hartmann, R. Moos, Application of a Robust Thermoelectric Gas Sensor in Firewood Combustion Exhausts, *Sensors* 23, 2930 (2023); doi: 10.3390/s23062930

[3] S. Wiegärtner, G. Hagen, J. Kita, W. Reitmeier, M. Hien, P. Grass, R. Moos, R, Thermoelectric hydrocarbon sensor in thick-film technology for on-board-diagnostics of a diesel oxidation catalyst, *Sensors and Actuators B: Chemical* 214, 234-240 (2015); doi: 10.1016/j.snb.2015.02.083.

[4] D. Paulus, S. Bresch, R. Moos, D. Schönauer-Kamin, Powder aerosol deposited calcium cobaltite as textured P-type thermoelectric material with power factors approaching single crystal values, *Journal of the European Ceramic Society* 44, 116717 (2024); doi: 10.1016/j.jeurceramsoc.2024.116717.

[5] F. Bernhard, Handbuch der Technischen Temperaturmessung, *Springer-Verlag Berlin, Heidelberg*, 1034-1040 (2014); doi: 10.1007/978-3-642-24506-0

DOI 10.5162/eurosensors2026/3.3.2

Micropillars patterned surface on in-plane MEMS resonator for enhanced airborne fine particles detection

Julien SOREL[1], Pierre Didier[2], Frédéric Marty[1], Evelyne Géhin[2],
Lyès Ait Ali Yahia[2], Emmanuelle Algré[1]
[1] Univ Gustave Eiffel, ESYCOM Laboratory, UMR 9007 CNRS, F-77454 Marne-la-Vallee, France
[2] Univ Paris-Est Creteil, CERTES, F-94010 Creteil, France

Summary:

In this paper, the impact of micropillars surface patterning on an in-plane MEMS resonator is described. Although lamé mode resonance frequency of patterned surface is found at a lower value than the plain one, the quality factor remains on the same order, confirming that particle detection is still feasible. Experiments involving inertial impaction of Polystyrene Latex (PSL) beads on these sensors, tend to show that ratio between pillars spacing and particle diameter is key to control local collection efficiency.

Keywords: MEMS, microbalance, resonator, airborne, collection efficiency, surface patterning

Background, Motivation and Objective

Numerous adverse effects on human health can be attributed to air pollution. The World Health Organization (WHO) global air quality guidelines set thresholds of mass concentration exposure for harmful pollutants, amongst which, one can find particulate matter with diameter lower than 10µm and 2.5µm (PM_{10}, $PM_{2.5}$) [1]. Gravimetric and optical sensors commonly used to obtain PM mass concentrations tend to be replaced by smaller and more sensitive ones like Quartz Crystal Microbalance (QCM). Micro Electromechanical Systems (MEMS) resonators are other serious candidates for this purpose with a high sensitivity allowing detection of mass at nanogram and even picogram order [2]. For airborne PM collection, inertial impaction is commonly used. Nevertheless, using smooth solid surfaces, bouncing effects occurs inducing a reduction in local collection efficiency (LCE). In order to increase collection, several surface modifications have been tried on QCM. Using printed 3D IP-DIP resin pillars on a QCM surface, Hajizadehmotlagh and Paprotny showed an increased airborne 4.8µm PSL beads collection with inertial impaction [3]. In this work, a new fabrication process leading to similar equally spaced pillars but etched within the active area of MEMS resonators is proposed. Electrical characterizations are performed to assess the impact on deposited mass detection. Finally, particles counting allows to control LCE for combinations of different pillars patterned surface densities and monodispersed particle sizes.

Fabrication and characterization methods

The MEMS resonator is fabricated from a doped silicon on insulator (SOI) wafer in several steps involving thermal oxidation, successive front and back deep reactive ion etching (DRIE), aluminum layers deposition, and anisotropic vapor hydrofluoric acid (VHF) etching. The detailed process is synthetized in Fig. 1.

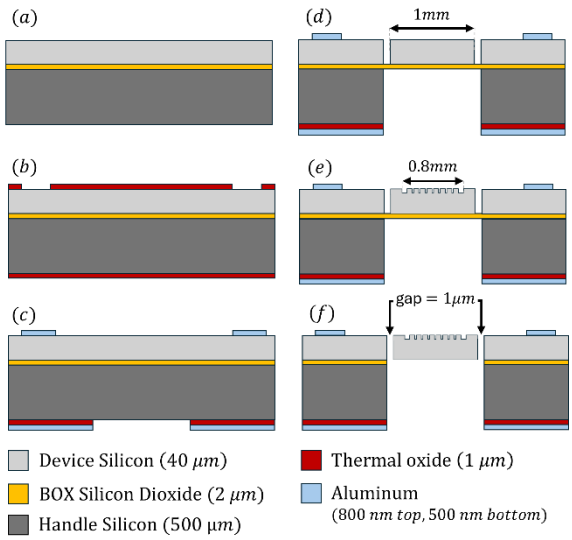

Fig. 1. Overview of the pillars patterned surface MEMS membrane fabrication process. (a) Initial SOI wafer. (b) Thermal oxidation creating an oxidation layer etched to form MEMS geometry. (c) Aluminum layers deposited on both sides then patterned to create electrode pads on top and the handle silicon cavity freeing the membrane. (d) & (e) Successive top and bottom DRIE employed to create the structure functionalization and 5µm diameter, 10µm height pillars patterned surface. (f) VHF release to eliminate the BOX layer remaining inside handle silicon cavity.

DOI 10.5162/eurosensors2026/3.3.2

The final device, which can be seen on Fig. 2, is a 6mmx6mm chip incorporating a free membrane consisting of a 1mmx1mm square and 40µm thickness silicon device linked to the chip thanks to T-shaped tethers on each corner. Equally spaced micropillars are patterned during DRIE steps. In this work pillars dimensions are 5µm diameter and 10µm height and are spaced lateral surface to surface either by 5µm (E5) or 10µm (E10). Four actuation electrodes are located on membrane's flanks, separated from it by a 1µm gap. A body terminal from one tether allows to sense the motional current created on the membrane while vibrating.

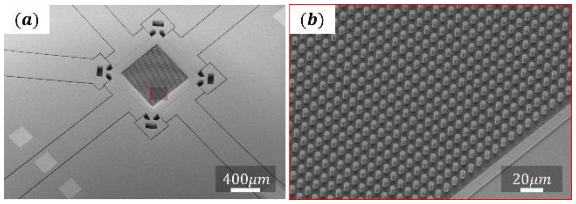

Fig. 2. MEMS resonator structure. SEM images of (a) E5 patterned membrane chip, (b) membrane zoom.

For lamé mode detection, electrical characterization is performed by injecting on two facing electrodes the same sum of two tensions V_{AC}=10V_{pp} (sine form) and V_{DC}=60V. The V_{AC} frequency is swept around resonance frequency. The body terminal is linked to a lock-in amplifier (LIA), allowing synchronous detection of induced motional current with exciting frequency as reference. In these experiments, resonance frequency and quality factor are determined by detecting signal peak while sweeping actuation frequency before and after inertial impaction of monodispersed 2.5µm and 7µm commercial PSL beads from Thermofisher's Duke Stand.™ 4000 series. Finally, during the impaction, particle generation counts and size is controlled with an APS (3321 APS-TSI) and deposited particles number is assessed by automatic counting using MATLAB language program from Zeiss Axio lab optical microscope image acquisitions of the MEMS resonator's membrane after impaction. LCE is calculated using ratio between these particles counts for each experiment.

Results and discussion

Fig. 3 resumes lamé mode resonance frequencies, quality factors and LCE for E5 and E10 pillars patterned surfaces before and after impaction of 2.5µm diameter PSL. All experiments were run in the same conditions (PSL generation, impaction time, air flows). These results are compared with those of a plain surface giving resonance frequencies and quality factor of f_0 = 4.109374 MHZ, Q_0 = 10170 before and f_p = 4.109020 MHz, Q_p = 8137 after impaction and CE of 3.3%.mm².

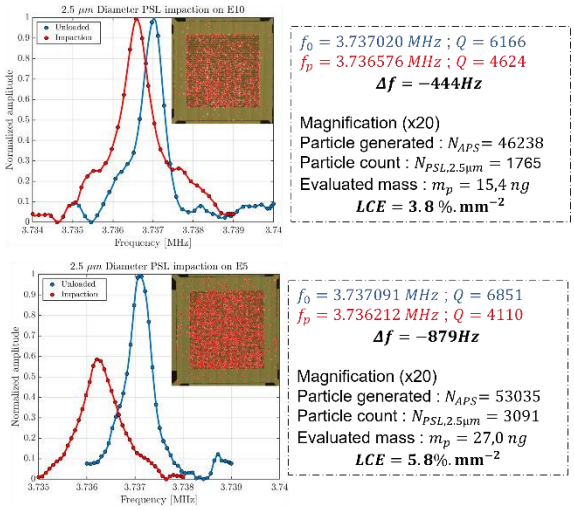

Fig. 3. Results of E10 and E5 2.5µm PSL impaction

Giving these results one can see a quality factor remaining high enough for detection. LCE is not significantly better for E10 structure (+0.5%) but almost doubled with E5. To go further, same experiment was done with a E5 surface but for 7µm PSL diameter to see the effect of diameter greater than pillar spacing, resulting in a CE of 33,9% with particles located on pillars surface.

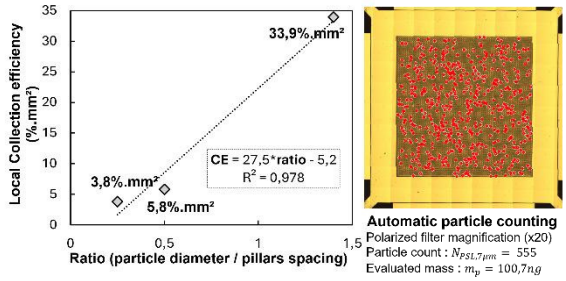

Fig. 4. Left : graph representing LCE vs ratio between particle diameter and pillars spacing. Right : particles counting after 7µm PSL impaction on E5.

These preliminary results are very encouraging, showing that surface patterning is feasible on MEMS resonator with small impact on detection and can increase LCE tuning pillars spacing according to particle diameter.

References

[1] World Health Organization. (2021). *WHO global air quality guidelines: Particulate matter (PM2.5 and PM10), ozone, nitrogen dioxide, sulfur dioxide and carbon monoxide*. Geneva: WHO.

[2] J.-S. Choi, W.-T. Park, MEMS particle sensor based on resonant frequency shifting, *Micro and Nano Syst Lett (2020);* https://doi.org/10.1186/s40486-020-00118-9

[3] M. Hajizadehmotlagh, I. Paprotny, Effect of micropillars with varying geometryand density on the efficiency of impaction based quartz crystal microbalance aerosol sensors, *J. Appl. Phys. 127, 184903 (2020);* https://doi.org/10.1063/1.5125895

DOI 10.5162/eurosensors2026/3.3.3

From Materials to Systems: Passive, Low-Energy Sensors Based on Organic Mixed Ionic–Electronic Conductors

Tobias Cramer
University of Bologna, Department of Physics and Astronomy, Viale Berti Pichat 6/2, 40127 Bologna, Italy
tobias.cramer@unibo.it

Abstract:

Organic mixed ionic–electronic conductors (OMIECs) are promising materials for bioelectronics and electrochemical sensing due to their ability to couple ionic and electronic charge transport at low operating voltages. Realizing fully passive and battery-free sensor systems based on OMIECs, however, requires understanding the fundamental limits of signal propagation and energy dissipation in these materials.

Here, we first investigate dissipative charge transport in OMIEC channels using electrical phase velocity measurements and modulated electrochemical atomic force microscopy.[1] Interpreting the results within a transmission line framework reveals that energy dissipation is governed by the ratio between electronic mobility and volumetric capacitance, establishing a key figure of merit for OMIEC materials beyond transistor amplification.

Building on this understanding, we demonstrate a fully passive oxygen sensor based on an organic electrochemical transistor (OECT).[2] By combining optimized device geometries with near-field communication (NFC) power harvesting, the system enables wireless and battery-free oxygen sensing in air and water. The interrogating NFC field is sufficient to power the electronics, acquire the sensor signal, and transmit the data wirelessly.

These results connect microscopic transport physics with the development of sustainable, ultra-low-power sensing systems based on OMIEC materials.

Keywords:

Organic mixed ionic–electronic conductors, Organic electrochemical transistors, Passive wireless sensing, Low-power bioelectronics, Near-field communication sensors

References:

[1] F. Bonafè, M. Bazzani, B. Fraboni, T. Cramer, *Nature Communications 16, 2499 (2025);* doi: 10.1038/s41467-025-57528-9

[2] L. G. D'Amico et al., *Advanced Materials Technologies 10, 2401875 (2025);* doi: 10.1002/admt.202401875

DOI 10.5162/eurosensors2026/3.3.4

A Mixed-Level Model for Force-Feedback Controlled Piezoelectric MEMS Microphones

Til Friebe[1], Ferdinand Schiller[2], Christian Bretthauer[2], Gabriele Schrag[1]
[1] Technical University of Munich (TUM), Munich Germany,
[2] Infineon Technologies AG, Munich Germany
til.friebe@tum.de

Summary:

We present a mixed-level model for a force-feedback controlled piezoelectric MEMS microphone. The approach combines a 2D axisymmetric FEM model of the piezoelectric transducer with an equivalent circuit describing parasitic electrical effects. The model enables accurate prediction of electromechanical behavior and electrical feedthrough over a wide frequency range up to 100 MHz. The implementation supports co-simulation with force-feedback controller models via LiveLink™ to Simulink.

Keywords: piezoelectric MEMS, MEMS microphones, force-feedback control, mixed-level modeling

Introduction

Advanced system-level modeling is essential for the design of force-feedback controlled MEMS sensors, as it enables performance optimization and controller co-design [1]. In piezoelectric MEMS microphones (PMICs), force-feedback control (FFC) improves linearity, increases resonance frequency, and raises the acoustic overload point [1,2]. This work presents a mixed-level model of a recently introduced PMIC design featuring a fully clamped corrugated single-layer membrane [3,4]. The pseudo-bimorphic architecture enables single-ended signal readout and force-feedback actuation. Previous studies identified electrical feedthrough (FT) as a key limitation for controllability [5]. While an equivalent circuit model addressing FT was introduced in [6], a complete system description requires coupling detailed membrane mechanics with circuit-level parasitics. We therefore combine a FEM-based mechanical and piezoelectric model with a lumped circuit model and implement the system in COMSOL Multiphysics. Using LiveLink™, the model supports co-simulation with controllers designed in Simulink. The functional principle and control scheme are shown in Fig. 1.

Device Description

Under acoustic excitation, membrane deflection induces compressive stress in corrugation peaks and tensile stress in valleys, resulting in a net charge sensed by electrodes placed as shown in Fig. 1 (sensing mode). Electrical actuation is achieved by applying a voltage V_{act} between peak and bottom electrodes, exploiting the inverse piezoelectric effect.

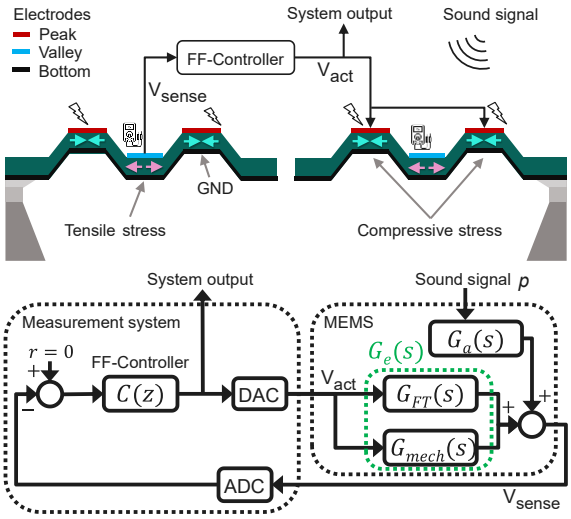

Fig. 1. Functional principle and control scheme of a force-feedback controlled piezoelectric microphone.

In force-feedback operation, the sensed voltage V_{sense} at the valley electrode is fed into a digital controller $C(z)$, whose output V_{act} counteracts membrane motion and minimizes V_{sense}. The effective sensor signal is therefore V_{act}. However, electrical feedthrough causes a direct coupling between actuation and sense electrodes, independent of mechanical deformation. Fig. 1 illustrates the corresponding control and measurement scheme. The transfer functions $G_{\mathrm{mech}}(s)$ and $G_{\mathrm{FT}}(s)$ describe the mechanical and electrical contributions to the electrical frequency response $G_e(s)$, while $G_a(s)$ models the acoustic path. The controller is implemented on an FPGA-based measurement system.

DOI 10.5162/eurosensors2026/3.3.4

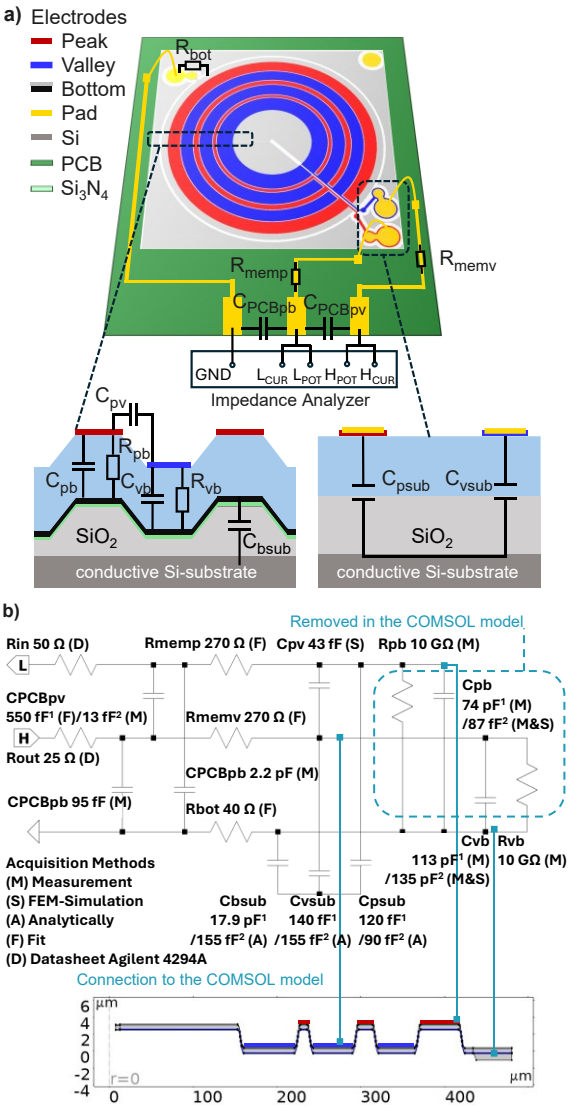

Fig. 2. (a) Schematic of the electrical frequency response measurement and (b) the equivalent circuit representing $G_{FT}(s)$ for co-simulation. Circuit parameters, values, and acquisition methods for [1]PMIC1 (non-released) and [2]PMIC3 (released).

Methods

The mixed-level model combines a 2D axisymmetric FEM model including solid mechanics, electrostatics, and the piezoelectric effect with a lumped circuit model representing parasitic circuitry of the real device. The equivalent circuit parameters were identified from LCR measurements on multiple samples (see Fig. 2 (a)). Measured admittance data are converted into the corresponding voltage response using (1).

$$V_{meas} = \frac{Q}{C} = \frac{I}{\omega\, C} = \frac{Y_{meas}\, V_{act}}{\omega\, C_{meas}} \qquad (1)$$

Capacitance values are additionally extracted from FEM simulations and analytical parallel-plate approximations of the material stack. The electrical feedthrough $G_{FT}(s)$ is obtained from a non-released membrane (PMIC1). Remaining parameters are obtained by fitting the model to the measured frequency response.

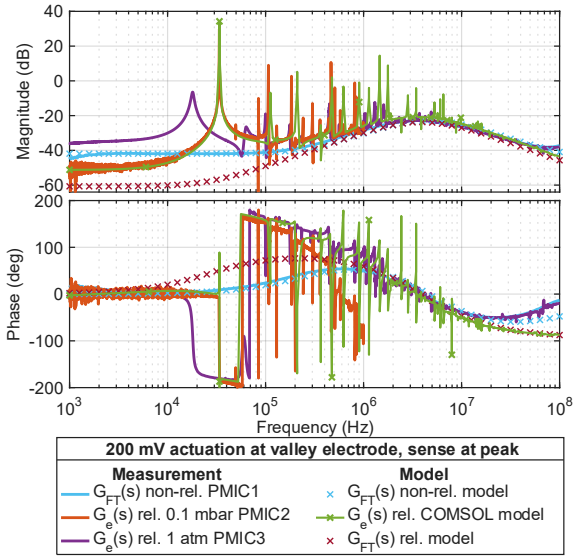

Fig. 3. Electrical transfer functions of a non-released membrane (PMIC1) and two released membranes (PMIC2, PMIC3). Feedthrough is modeled in LTspice, electromechanical response in COMSOL. PMIC3 data extend the frequency range to 100 MHz.

Results and Summary

Fig. 3 compares measured and simulated electrical transfer functions for different samples. Released samples show reduced parasitic capacitances to the conductive Si-substrate and between actuation and sense contacts. PMIC2 is bonded to an ASIC amplifier, enabling vacuum measurements but limiting the bandwidth to 1 MHz. To extend the frequency range to 100 MHz, PMIC3 is measured at atmospheric pressure without an ASIC. The mixed-level model accurately reproduces $G_e(s)$ of PMIC2 up to 1 MHz and closely follows the response of PMIC3 at higher frequencies, demonstrating its validity over the full measurement range. Due to the 2D axisymmetric formulation, only radially symmetric modes are captured. Angular resonances are therefore not represented.

The presented mixed-level model shows good agreement with experimental data and enables co-simulation of complex MEMS behavior with force-feedback controllers. Future work focuses on extending the model with a transmission-line formulation to include thermoviscous effects of the sound port inside the PCB.

References

[1] doi: 10.1002/9783527647132.ch16
[2] doi: 10.5162/sensoren2024/C3.2
[3] G. Bosetti, A Novel High-SNR Full Bandwidth Piezoelectric MEMS Microphone Based on a Fully Clamped Aluminum Nitride Corrugated Membrane. In: *2023 22nd International Conference on Solid-State Sensors, Actuators and Microsystems (Transducers)*, 366–369; 2023.
[4] doi: 10.1109/EuroSimE60745.2024.10491462
[5] doi: 10.30420/456614127
[6] doi: 10.1109/SENSORS59705.2025.11330565

DOI 10.5162/eurosensors2026/3.3.5

Microfluidic Integration of Interfacial Nanopores for Single-Molecule Sensing under FPGA-Based Closed-Loop Control

Lorenzo Petrella[1], Lena Dysli[1], Jonah Imfeld[1], Justin N. Cronk[1], Morteza Aramesh[1]
[1] Laboratory of Single-Molecule and Single-Cell Biophysics, Department of Information Technology and Electrical Engineering, ETH Zürich, Zürich, Switzerland
lpetrella@ethz.ch

Summary:

We present interfacial nanopores integrated into microfluidic devices as a versatile platform for single-molecule sensing in small-volume samples. On-chip integration combined with FPGA-based closed-loop control enables leak-free, mechanically stable nanopore formation with tunable resistance up to the hundred megaohm range. Initial tests on double-stranded DNA demonstrate the working principle, with single-cell secretomics envisioned as the target application.

Keywords: interfacial nanopore, microfluidics, single-molecule sensing, FPGA closed-loop control, secretomics

Background, Motivation and Objective

Achieving real-time, single-molecule sensitivity in highly diluted samples is a major challenge toward unlocking access to the wealth of information encoded in the secretions of single cells. Interfacial nanopores have emerged as a promising technique to address this challenge, owing to their ability to detect single molecules in diluted samples or in situ proximal to single cells [1]. Microfluidic platforms are well-established tools for the handling and analysis of small-volume samples in a cost-efficient fashion [2]. Building on the growing body of evidence supporting pipette–elastomer interfacial nanopores (PEINs) as controllable-size, clog-free single-molecule sensors with high spatiotemporal resolution, we aim to embed interfacial nanopores directly into microfluidic chips to leverage their versatile, high-throughput capabilities and expand the range of applications.

Description of the New Method or System

Interfacial nanopores were formed at the interface of a flexible surface and a submicron aperture. The geometry, assembly, and operation were optimized to enable stable ionic current measurements across the highly deformable channels. Nanomanipulators with single-nanometre resolution, patch-clamp amplifiers, and high-speed digitisers orchestrated by FPGA-based logic provide real-time, automated feedback control of the interfacial nanopores.

Results

We achieved on-chip integration of interfacial nanopores by establishing leak-free and mechanically stable nanopore formation with tunable resistance up to the 100 MΩ range in 2 M KCl solution. The power spectral density of an actuated interfacial nanopore measured in buffer shows rejection of electromagnetic interference at the power line and servo loop frequencies, and limited vibrational noise in the expected range despite the mechanical actuation of the system (Figure 1).

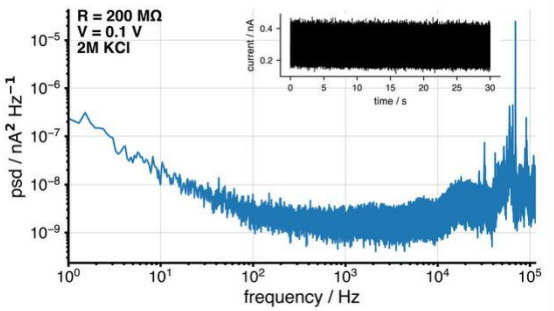

Fig. 1. Power spectral density of a 200 MΩ interfacial nanopore in 2 M KCl when a 100 mV bias is applied. The inset shows the 30 s current trace used to compute the PSD.

Combined with mechanical and electromagnetic noise rejection, the setup enabled the sensing of biomolecules such as double-stranded DNA (Figure 2), exhibiting voltage dependence of capture rate, dwell time and amplitude. Ultimately, we aim to establish a platform for single-cell secretomics that combines the single-molecule sensitivity of interfacial nanopores with the small-volume handling capabilities of microfluidics. Future work will focus on leveraging the low-latency FPGA-based control to influence the

translocation dynamics of individual analyte molecules, and on integrating multiple interfacial nanopores on a single device.

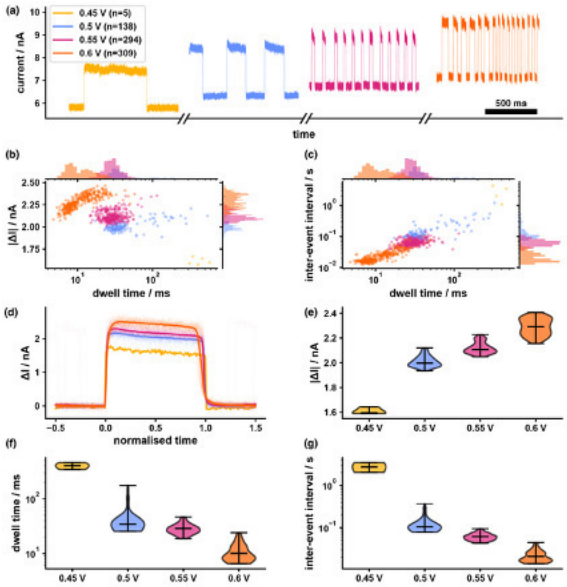

Fig. 2. Sensing of λ-DNA at varying pore bias in 2 M KCl with an 80 MΩ pore. (a) Representative traces of nanopore current at increasing pore bias; scatter plots of (b) event amplitude and (c) inter-event interval versus dwell time, with marginal distributions; (d) time-warped average event traces per pore bias condition; violin plots of (e) event amplitude (f) dwell time and (g) inter-event interval versus pore bias, with distributions shown for the 5th-95th percentile range.

References

[1] T. Schlotter, S. Weaver, C. Forró, D. Momotenko, J. Vörös, T. Zambelli, M. Aramesh, Force-Controlled Formation of Dynamic Nanopores for Single-Biomolecule Sensing and Single-Cell Secretomics. *ACS nano* 14(10), 12993–13003 (2020); doi:10.1021/acsnano.0c04281

[2] A.-G. Niculescu, C. Chircov, A. C. Bîrcă, A. M. Grumezescu, Fabrication and Applications of Microfluidic Devices: A Review. *International Journal of Molecular Sciences* 22(4) (2011); doi: 10.3390/ijms22042011

DOI 10.5162/eurosensors2026/4.1.1

Printed and Light-activated CuO/Cu_2O-Based Chemiresistive Acetone Sensors with Carbon Electrodes

Amit Chatterjee[1], Bernhard Jakoby[2], Jürgen Kosel[1], Mani Teja Vijjapu[1]
[1] Sensor System Division, Silicon Austria Labs GmbH, Europastraße 12, Villach 9524 Austria
[2] Institute for Microelectronics and Microsensors, Johannes Kepler University Linz, Austria
Correspondence: amit.chatterjee@silicon-austria.com

Summary:
Printed metal-oxide gas sensors commonly rely on thermal activation and metallic interdigitated electrodes (IDEs), typically silver, which increases cost and raises sustainability concerns. In this work, as a step toward more sustainable and cost-effective sensor fabrication, carbon-based IDEs were employed in place of conventional silver electrodes together with light activation. Carbon electrodes were screen-printed onto the glass substrates, followed by the deposition of copper layer on the carbon electrodes, and subsequently thermally oxidized to form CuO/Cu_2O sensing devices. Owing to the strong optical absorption of CuO/Cu_2O in the yellow spectral region, yellow light was used for sensor activation. The fabricated devices demonstrated repeatable room-temperature sensing of acetone, achieving a sensitivity of approximately 0.0264 %/ppm with efficient light-assisted recovery. These results highlight the potential of fully screen-printed, carbon-electrode-based platforms for developing cost-effective and more sustainable gas sensing systems.

Keywords: Carbon interdigitated electrodes (IDEs), Gas sensors, Light-activated sensors, Printed sensors

Introduction

Metal-oxide chemiresistive gas sensors widely use interdigitated electrodes (IDEs) to convert changes in the sensing layer's resistance into measurable electrical signals. Common IDE materials include conductive metals such as Ag, Au, Pt, and Pd owing to their high conductivity, low contact resistance, and compatibility with microfabrication or printing processes [1]. However, metallic electrodes can present drawbacks, including high material cost, electromigration, thermal diffusion, and dependence on precious metal resources [2]. Therefore, alternative electrode materials are interesting for low-cost and sustainable gas-sensor platforms. Carbon-based conductive inks offer low cost, abundance, chemical stability, corrosion resistance, lightweight nature, and compatibility with large-area printed electronics [3]. Screen-printed carbon IDEs have recently been explored in humidity, strain, and emerging gas-sensing devices, highlighting their promise as functional electrode alternatives.

In our previous work, we demonstrated light-activated CuO/Cu_2O-based acetone sensors; however, these devices employed silver electrodes [4]. In this work, screen-printed carbon IDEs are investigated as a sustainable and cost-effective alternative to conventional metallic IDEs for CuO/Cu_2O-based acetone sensors. Mixed-phase copper oxide sensing layers were fabricated on carbon electrodes via screen printing and thermal oxidation, followed by structural, optical, and acetone-sensing characterization under room-temperature, yellow-light-assisted operation.

Materials and methods

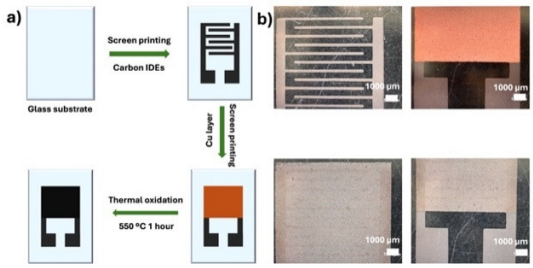

Fig 1. (a) Fabrication of the CuO/Cu_2O sensor on carbon IDEs. (b) Optical microscope images of the printed carbon IDE, Cu-coated device, and final oxidized sensor.

CuO/Cu_2O chemiresistive sensors were fabricated via a screen-printing and thermal oxidation route adapted from our previously reported process [4], employing a slightly increased oxidation temperature. Carbon IDEs were screen-printed onto glass slides (Sigma-Aldrich, 24 × 50 mm) using a carbon paste (DM-CAP-4402S, DYCOTEC MATERIALS) and cured at 120 °C for 10 min. A 1 × 1 cm² copper layer was then screen-printed over the IDE area using Cu ink (SARAL Cu 200, SARALON GmbH) and cured at 120 °C for 15 min. The printed Cu films were

subsequently oxidized in ambient air at 550 °C for 1 h on a hot plate to obtain mixed-phase CuO/Cu_2O sensing layers. A schematic of the fabrication process is shown in Fig 1. Structural characterization was performed by X-ray diffraction to determine the crystallographic phases of the CuO/Cu_2O sensing layer and to evaluate the structural state of the carbon IDEs before and after annealing. Optical absorption properties of the copper oxide layer were investigated using UV–Visible spectroscopy. Gas sensing measurements were conducted in a static VOC test chamber using acetone as the target analyte. Prior to exposure, the sensor was pre-activated under yellow LED (5mm commercial) illumination (350 µW optical power). Acetone was then introduced while the light source was simultaneously switched off to probe the sensing response under dark conditions, followed by light-assisted recovery through re-illumination. The sensor response was defined by:

$$\frac{\Delta R}{R_0} = \frac{R_g - R_0}{R_0} \times 100\%. \quad (1)$$

Results

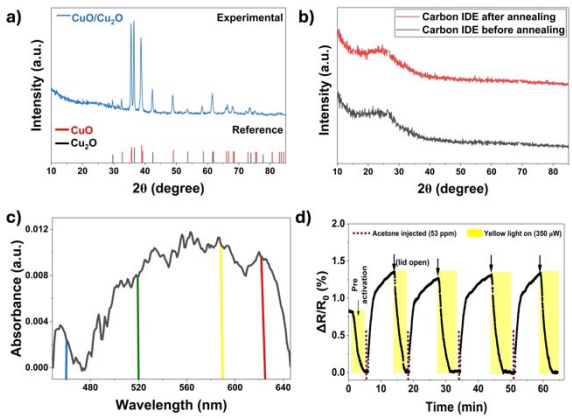

Fig 2. (a) XRD pattern of the CuO/Cu_2O-coated carbon IDE. (b) XRD of bare carbon IDE before and after annealing. (c) UV–Visible spectrum of the CuO/Cu_2O layer. (d) Repeated response/recovery cycles to 53 ppm acetone under yellow-light-assisted operation (350 µW) at room temperature.

Fig 2a shows the XRD pattern of the CuO/Cu_2O layer on carbon IDEs, where reflections matching CuO and Cu_2O confirm successful formation of mixed-phase copper oxides after thermal oxidation. Such phase coexistence may favor sensing through interfacial charge modulation [5]. Fig 2b presents the bare carbon IDE before and after annealing, both showing broad humps rather than sharp peaks, indicating a predominantly amorphous, thermally stable nature. The absorbance spectrum in Fig 2c reveals broad visible-light absorption with enhanced intensity in the yellow region, supporting the use of yellow light for activation. Sensing performance to an exposure to 53 ppm acetone is shown in Fig 2d. The carbon IDE-based CuO/Cu_2O sensor exhibits repeatable response/recovery cycles under the yellow-light-assisted protocol, reaching a maximum response of ~1.4%. The sensor signal fully recovers upon re-illumination. Additionally, the CuO/Cu_2O layer uniformly covers the carbon electrodes, minimizing their direct exposure to the environment and restricting their role to electrical interfacing for resistive measurements. This configuration enables stable room-temperature operation and demonstrates that carbon IDEs can effectively replace metallic electrodes, offering a lower-cost and more sustainable alternative.

Conclusion

Screen-printed carbon interdigitated electrodes were successfully demonstrated as a viable platform for CuO/Cu_2O chemiresistive acetone sensors. The fabricated device showed stable room-temperature operation, repeatable light-assisted sensing behavior, and a sensitivity of ~0.0264 %/ppm to acetone. These results highlight carbon electrodes as a promising route toward low-cost, scalable, and sustainable printed metal-oxide gas sensors.

Acknowledgements

This work has been jointly supported by the European Union under the MSCA COFUND project CRSTALLINE, grant agreement no. 101126571 and Silicon Austria Labs (SAL).

References

1. Barsan N, Weimar U. Conduction model of metal oxide gas sensors. *J Electroceram*. 2001;7(3):143-167. doi:10.1023/A:1014405811371/METRICS
2. Capone S, Forleo A, Francioso L, et al. SOLID STATE GAS SENSORS: STATE OF THE ART AND FUTURE ACTIVITIES. *Journal of Optoelectronics and Advanced Materials*. 2003;5(5):1335-1348.
3. Krebs FC. Fabrication and processing of polymer solar cells: A review of printing and coating techniques. *Solar Energy Materials and Solar Cells*. 2009;93(4):394-412. doi:10.1016/J.SOLMAT.2008.10.004
4. Chatterjee A, Zikulnig J, Jakoby B, Kosel J, Teja Vijjapu M. M1.1.1 - A Screen-Printed and Light-Activated Copper Oxide Sensor for Acetone Detection. *Lectures*. Published online September 22, 2025:38-39. doi:10.5162/eurosensors2025/m1.1.1
5. Khiavi ND, Katal R, Eshkalak SK, Masudy-Panah S, Ramakrishna S, Jiangyong H. Visible Light Driven Heterojunction Photocatalyst of CuO–Cu2O Thin Films for Photocatalytic Degradation of Organic Pollutants. *Nanomaterials*. 2019;9(7):1011. doi:10.3390/nano9071011

DOI 10.5162/eurosensors2026/4.1.2

Enhanced Gas Sensing Performance of Pt-Coated Ag-Doped Ga_2O_3 via Surface Modification

Md Mayen Uddin[1], Mohammad Ariful Islam Bhuyan[1], Liang Xiuqian[1], Hyeon Cheol kim[1]
[1] Department of Electrical, Electronic and Computer Engineering, University of Ulsan
93 Daehak-ro, Nam-gu, Ulsan 680-749, South Korea
hckim08@mail.ulsan.ac.kr

Summary:

In this paper, Gallium oxide (Ga_2O_3) thin films are studied for their n-type semiconducting behavior and stability at high temperatures, making them suitable for hydrogen sensing. The resistivity of Ga_2O_3 thin films is influenced by hydrogen concentration, which forms the basis for their use in hydrogen detection. Silver (Ag) doping and platinum (Pt) coating improve sensor performance, including response and recovery times. The films show strong hydrogen sensitivity at 400°C, with fast resistivity changes within seconds. Furthermore, Pt coated Ag doped Ga_2O_3 thin films show promise as catalytically inactive hydrogen sensors, provided that appropriate temperature compensation is applied to ensure measurement stability.

Keywords: H_2 sensor, Gallium Oxide, High-Temperature, Fast response/recovery, Ag doping

Background, Motivation and Objective

Hydrogen sensing is vital for safety and efficiency in energy, environmental, and industrial applications due to hydrogen's flammability and invisibility. Nanomaterials are widely studied for this purpose because of their high surface area and enhanced sensitivity. Gallium oxide (Ga_2O_3), a wide-bandgap semiconductor, stands out for its thermal stability and suitability for high-temperature sensing (400–1000°C). Its conductivity changes with hydrogen concentration due to interactions with lattice oxygen, enabling detection [1].

Research on Ga_2O_3 for gas sensing applications, including hydrogen detection, has shown promising results. For instance, Y. Ogo et al. [2] demonstrated that Ga_2O_3 nanomaterials exhibit excellent sensitivity to hydrogen, particularly when combined with noble metal catalysts such as platinum (Pt). Recent studies found that Ag doped Ga_2O_3 nanostructures exhibited faster response times and higher sensitivity to hydrogen compared to their undoped materials [3-4]. Ag promotes charge transfer at the gas-material interface, improving the sensing mechanism for hydrogen detection. Sensor performance can be significantly improved through doping and surface modification. Silver (Ag) doping enhances charge transport and gas interaction, leading to faster response and higher sensitivity. Platinum (Pt) is widely used in hydrogen sensors as a catalyst layer due to its exceptional catalytic activity in hydrogen dissociation. Several studies have demonstrated that Pt coating significantly boosts the hydrogen sensing performance of semiconductor materials, including Ga_2O_3 [5]. The performance of the Pt coated Ag doped Ga_2O_3 thin films sensor was prepared for catalytic analysis, as shown in Fig. 1. This study investigates Pt-coated, Ag-doped Ga_2O_3 nanomaterials, focusing on response, recovery, and stability. The combined approach offers a promising path for highly sensitive and durable hydrogen sensors with stable operation around 400°C.

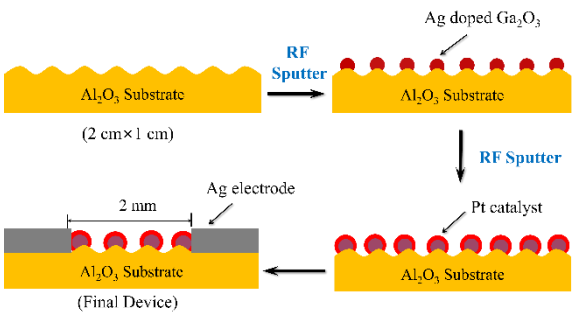

Fig. 1. Schematic diagram of a hydrogen sensor.

Results

The typical SEM images (Fig. 2) confirm the formation of nanoparticle (NP) thin films. The Ag-doped Ga_2O_3 sample shows a densely packed, uniform granular surface with well-dispersed particles, indicating good film coverage and microstructural quality. EDS mapping further

confirms the successful growth of Pt-coated, Ag-doped Ga_2O_3 NPs.

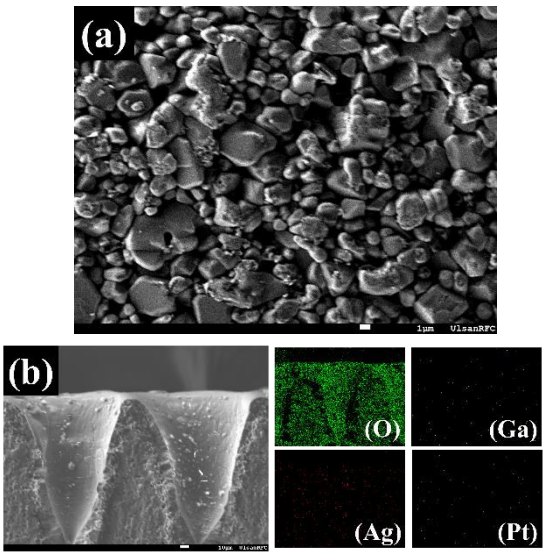

Fig. 2. SEM analysis of Pt coated Ag doped Ga_2O_3 NPs (a) Surface analysis (b) Cross-section and EDS mapping analysis

The response and recovery analysis for the Pt coated Ag doped Ga_2O_3 thin film sensor is shown in Fig. 3. The relatively quick response time (8 s) and recovery time (27 s) indicate that the Pt coated Ag doped Ga_2O_3 sensor can rapidly detect hydrogen and revert to its original state when the gas is no longer present. At 400°C operating temperature, the sensor has the greatest response of 2.7%.

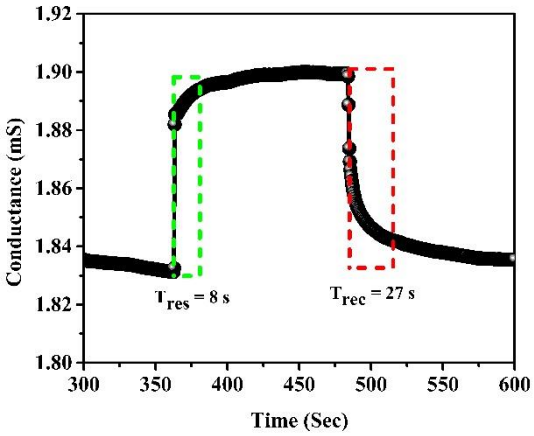

Fig. 3. Response-recovery analysis of Pt coated Ag doped Ga_2O_3 structure.

The repeatability of the gas sensor based on the Pt coated Ag doped Ga_2O_3 sensor is shown in Fig. 4 based on conductance change and response. The sensor shows consistent cyclic behavior in response to repeated hydrogen exposure cycles. Fig. 5 shows the sensing response of the Pt coated Ag doped Ga_2O_3 based sensor to different gases.

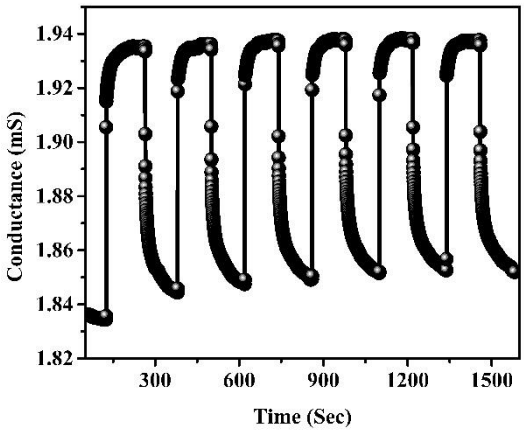

Fig. 4. Repeatability characteristics of the Pt coated Ag doped Ga_2O_3 sensor.

Among all tested gases, hydrogen generates an exceptionally high response (2.7%) nearly an order of magnitude higher than other gases, while O_2, CO, NO, CH_4, and C_3H_8 show negligible sensitivity.

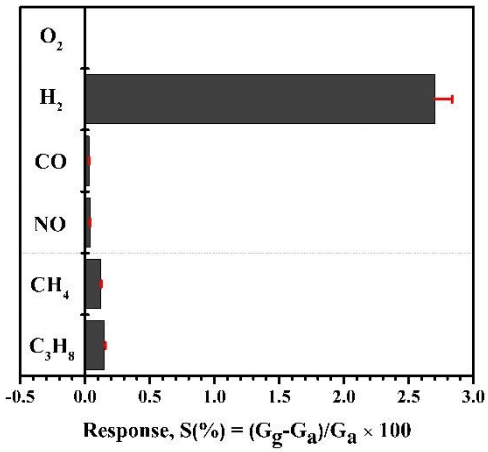

Fig. 5. Selectivity of the Pt coated Ag doped Ga_2O_3 sensor.

References

[1] Collins, S. E., Baltanás, M. A., & Bonivardi, A. L. (2005). Hydrogen chemisorption on gallium oxide polymorphs. *Langmuir*, 21(3), 962-970; doi: 10.1021/la0481389

[2] Y. Ogo, H. Hiramatsu, K. Nomura, H. Yanagi, T. Kamiya, H. Hosono, Ga2O3-based Schottky barrier diode for hydrogen gas sensors, *Appl. Phys. Lett.* 93 (2008) 032113; doi: 10.1063/1.2957046

[3] X. Wang, J. Zhang, Z. Zhu, Hydrogen sensing with Pt–Ga2O3 Schottky diodes, *Sens. Actuators B Chem.* 144 (2010) 220–225; doi 10.1016/j.snb.2009.10.040

[4] G. Frank, J. Stößel, Electrical properties of β-Ga2O3 single crystals, *Appl. Phys. A* 27 (1982) 197–206; doi: 10.1007/BF00617298

[5] Y. Hou, L. Zhang, G. Li, Gas sensing properties of Ga2O3 nanostructures, *Ceram. Int.* 38 (2012) 3035–3040; doi: 10.1016/j.ceramint.2011.12.021

DOI 10.5162/eurosensors2026/4.1.3

Re-examining Mechanisms, Materials and Measurement in Metal Oxide Gas Sensing

Chris Blackman
University College London (UCL),20 Gordon Street, London, WC1H 0AJ, UK
c.blackman@ucl.ac.uk

Abstract:

Despite widespread deployment of metal oxide semiconductor gas sensors, fundamental assumptions about how these devices operate, age and respond to complex gas environments can be poorly described. This talk will present a coherent body of work that revisits core gas sensing paradigms by combining operando spectroscopy, controlled sensing studies and critical analysis of prevailing models, by focusing on the mechanistic origins of the conductometric response in tin dioxide-based sensors. Using operando near-ambient pressure X-ray photoelectron spectroscopy (NAP-XPS) coupled with simultaneous electrical measurements, we demonstrate that dynamically changing surface and near-surface oxygen vacancy populations, rather than ionosorbed oxygen species, are likely to dominate the sensing response. These observations challenge long standing ionosorption based models and provide a more physically grounded framework linking surface stoichiometry to electronic transport.

Keywords:

Operando, XPS, mechanism, oxygen vacancy, tin dioxide

References:

[1] C. Blackman, Do We Need “Ionosorbed” Oxygen Species? (Or, “A Surface Conductivity Model of Gas Sensitivity in Metal Oxides Based on Variable Surface Oxygen Vacancy Concentration”), *ACS Sensors* 6, 3509–3516 (2021); doi: 10.1021/acssensors.1c01727

[2] S. Kucharski, P. Ferrer, F. Venturini, G. Held, A.S. Walton, C. Byrne, J.A. Covington, S.K. Ayyala, A.M. Beale and C. Blackman, Direct in situ spectroscopic evidence of the crucial role played by surface oxygen vacancies in the O_2-sensing mechanism of SnO_2, *Chemical Science*, 13, 6089-6097 (2022); doi: 10.1039/D2SC01738E

[3] S. Kucharski, M. Vorochta, L. Piliai, A.M. Beale, C. Blackman, Interplay between CO and Surface Lattice Oxygen Ions in the Vacancy-Mediated Response Mechanism of SnO_2-Based Gas Sensors, *ACS Sensors* 10 1898–1908 (2025); doi: 10.1021/acssensors.4c03047

[4] S. Kucharski, M. Vorochta, L. Piliai, A.M. Beale, C. Blackman, Spectroscopic Insight into the Role of Surface Oxygen Vacancies in the Detection of NO_2 in SnO_2-Based Chemoresistive Gas Sensors, *ACS Sensors* 11 747–755 (2026); doi: 10.1021/acssensors.5c04098

DOI 10.5162/eurosensors2026/4.2.1

Beyond the Ensemble: Resolving Sample Heterogeneity in Space and Time

Romain Quidant
Department of Mechanical and Process Engineering (D-MAVT), ETH Zurich, Zurich, Switzerland
rquidant@ethz.ch

Abstract:

Biological samples are inherently heterogeneous, yet traditional biosensing typically relies on ensemble measurements that mask critical information. In this talk, we present several optofluidic platforms that integrate advanced optical detection, microfluidics, and surface chemistry to resolve biological complexities at the single-analyte level.

We first introduce an optofluidic platform leveraging Interferential Scattering Microscopy (iScat) for the label-free fingerprinting of cell secretomes at the single-particle level. By implementing a multiplexed digital immunoassay, we extract high-dimensional data with sensitivity reaching the single-protein limit [1]. Furthermore, we incorporate polarization-sensitive detection to enable single-shot retrieval of optical activity images, uncovering spatial chirality variations that are typically invisible to bulk analysis [2].

The second part of the talk introduces a high-throughput, droplet-based platform for multiparametric kinetic analysis of aptamer-target interactions. By integrating picoliter-volume droplets with Förster resonance energy transfer (FRET), our approach allows for real-time monitoring of binding and structural switching with unprecedented spatiotemporal resolution. This methodology provides detailed insights into conformational dynamics and binding kinetics, overcoming the fundamental limitations of endpoint or low-resolution techniques [3].

Keywords:

Photonic sensing, cell secretome, digital assay, single molecule, microfluidics

References:

[1] A. Stollmann, J. Garcia-Guirado, J. Hong, P. Rüedi, H. Im, H. Lee, J. Ortega Arroyo, R. Quidant, Molecular fingerprinting of biological nanoparticles with a label-free optofluidic platform, *Nature Comm.* 15, 4109 (2024)

[2] R. Büchner, J. García-Guirado, J. Ortega Arroyo, R. Quidant, Wide-field spectroscopic imaging of optical activity, *Nature Photonics* https://doi.org/10.1038/s41566-025-01722-0 (2025)

[3] M. Sulliger, M. Peters, A. Sottini, A. Stuber, K. Yang, N. Nakatsuka, J. Ortega Arroyo, R. Quidant, Scalable Multiparametric Characterization of Aptamer–Target Interactions, *ACS nano* 20 2, 2387−2398 (2026)

DOI 10.5162/eurosensors2026/4.2.2

Compact MicroLED-Based Lensless Microscope for Real-Time Airborne Cloud Droplet Sensing

Agus Budi Dharmawan[1], Rodrigo Gaston Gibilisco[1,2], Jorge Saturno[3], Andreas Nowak[3], Christopher Pöhlker[3], J. Daniel Prades[1]
[1] Institute of Semiconductor Technology (IHT) and Laboratory for Emerging Nanometrology (LENA), Technische Universität Braunschweig, Braunschweig, Germany
[2] Laboratory of Atmospheric Studies (LEA), INQUINOA (CONICET–National University of Tucumán), Tucumán, Argentina
[3] Physikalisch-Technische Bundesanstalt (PTB), Braunschweig, Germany
e-mail: agus.dharmawan@tu-braunschweig.de

Summary:
We present a microLED-based lensless microscope, an imaging system that is compact, lightweight, energy-efficient, and capable of capturing airborne microdroplets. It consists of a microLED as a light source and a CMOS image detector and operates based on inline holographic microscopy. The microscope records holographic images of airborne microdroplets, which are then reconstructed using a Fourier-transform-based backpropagation algorithm. During testing, a microdroplet dispensing system was used to generate droplets with controlled sizes. The results showed that the LED-based lensless microscope could capture clear microdroplet images. After reconstruction, the images were comparable to those obtained using a lens-based camera. Based on the results, the proposed lensless microscope is suitable for monitoring airborne water droplets in both controlled laboratory environments and real-world field conditions.

Keywords: airborne droplets, lensless microscopy, microLED, meteorology

Background, Motivation and Objective

The study of airborne droplets is increasingly important in atmospheric science and climate research [1]. Cloud behavior depends strongly on droplet size distributions rather than solely on liquid water content (LWC) [2]. Therefore, accurate in situ measurements of droplet size distributions and LWC are essential for investigating aerosol–cloud interactions using both airborne and ground-based platforms.

Experimental studies are typically conducted either in controlled laboratory environments or under real-world field conditions. Laboratory setups require compact imaging systems that can operate within confined spaces such as environmental chambers.

In contrast, field measurements require lightweight, portable devices suitable for deployment on towers, drones, or other mobile platforms. Conventional optical systems are often limited in these scenarios due to their size, complexity, and power consumption.

To address these challenges, we developed a microLED-based lensless microscope that enables compact and energy-efficient imaging of airborne microdroplets.

Description of the setup

The LED-based lensless microscope consists of a microLED light source and a CMOS image detector, operating according to the principle of inline holographic microscopy, in which the sample is positioned between the illumination source and the detector. This configuration enables the recording of interference patterns generated by the interaction of light with the sample, which can later be computationally reconstructed. The microLEDs used in this work were developed in-house, emitting at a wavelength of 450 nm and featuring a pixel size of 20 µm. As the image sensor, a Basler monochrome CMOS camera was employed, with an active sensing area of 7.68 mm × 4.32 mm and a pixel pitch of 2 µm, providing high spatial sampling of the recorded holograms.

Image reconstruction is carried out using a Fourier-transform-based backpropagation algorithm, which enables the retrieval of high-quality images from the captured holographic patterns, achieving sub-micron spatial resolution [3]. The use of microLED illumination eliminates the need for high-power sources and complex optics, resulting in an energy-efficient system. Moreover, the dimensions of 4 cm × 4 cm × 4 cm and a

mass below 50 g make the system compact and suitable for both laboratory and field applications.

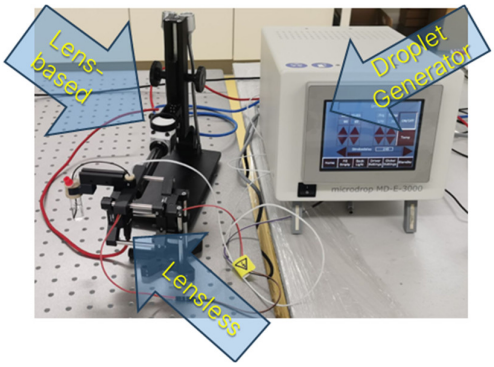

Fig. 1. The lensless microscope and lens-based imaging system were integrated to enable simultaneous image acquisition as a validation step. Furthermore, the strobe mode of the microdroplet generator was synchronized with the light sources of both the lensless microscope and the lens-based camera.

Results

In this experiment, a dispensing system, MD-E-3000 from Microdrop Technologies, Norderstedt, Segeberg, Germany, was used to generate droplets with well-defined sizes. The LED-based microscope was positioned horizontally to provide sufficient space for the microdroplet dispensing tip between the CMOS detector and the microLED (Fig. 1). During calibration and measurements, a lens-based camera was used to image microdroplets generated by the same dispensing tip used in the lensless microscope experiments. To synchronize the measurements and ensure that both imaging systems recorded the same microdroplets, the strobe output controlled by the droplet generator was connected in parallel to the microLED of the lensless microscope and to the illumination source of the lens-based camera.

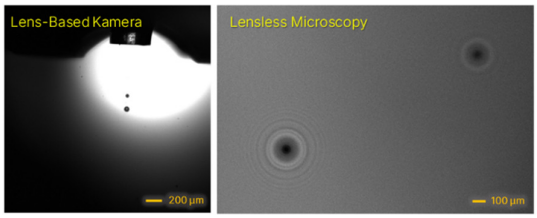

Fig. 2. The lensless microscope was capable of capturing droplet images in strobe mode. The droplet positions shifted accordingly when the frequency or strobe delay was adjusted, consistent with the observations obtained using the lens-based camera.

The results demonstrate that the lensless microscope can capture clear images of microdroplets. After applying the backpropagation reconstruction process, the LED-based lensless microscope produced images comparable to those obtained using the lens-based camera (Fig. 2). Based on the microdispenser parameters, namely a driving voltage of 80 V and a pulse duration of 60 µs applied to the piezoelectric nozzle, together with the calibration and synchronization of both imaging systems, the dispensing tip was found to generate droplets with a diameter of between 50 µm and 70 µm ± 5 µm.

Based on these results, it can be concluded that the proposed lensless microscope is suitable for monitoring airborne water droplets. Its compact and lightweight design makes it a promising candidate for droplet monitoring in both controlled laboratory environments and real-world field measurements. Therefore, the system enables lensless microscopy to be used as a portable tool that can be mounted on drones, kites, or even radiosondes for micro-meteorological studies (Fig. 3). This allows real-time measurements to be performed at various locations, e.g., mountainous sites such as Zugspitze, Schneefernerhaus, or Jungfraujoch in Switzerland, supporting long-term studies and sensing-stability evaluations.

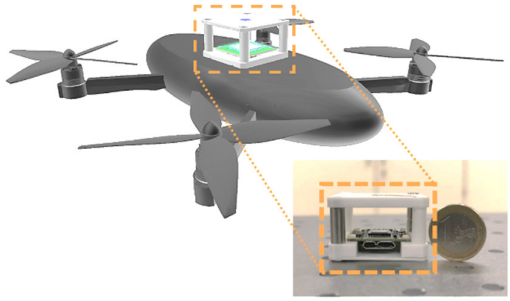

Fig. 3. Illustration of a lensless microscope on a drone to provide useful data for in-situ cloud microphysics studies.

Acknowledgement

This work is supported by the Alexander von Humboldt Professorship of the Humboldt Foundation, and the Federal Ministry for Education and Research, Germany.

References

[1] V. A. Kaikkonen, E. O. Molkoselkä, and A. J. Mäkynen, “A rotating holographic imager for stationary cloud droplet and ice crystal measurements,” Optical Review, vol. 27, no. 2, pp. 205–216, Mar. 2020, doi: 10.1007/s10043-020-00583-y.

[2] M. O. Andreae et al., “Smoking Rain Clouds over the Amazon,” Science, vol. 303, no. 5662, pp. 1337–1342, Feb. 2004, doi: 10.1126/science.1092779.

[3] A. B. Dharmawan et al., “Nonmechanical parfocal and autofocus features based on wave propagation distribution in lensfree holographic microscopy,” Scientific Reports, vol. 11, no. 1, p. 3213, Feb. 2021, doi: 10.1038/s41598-021-81098-7.

DOI 10.5162/eurosensors2026/4.2.3

Multi-wavelength Fiber-Optic Refractometer Based on Multimodal Interference and Surface Plasmon Resonance

Galván-Navarro E. Didier[1], Alonso-Murias Monserrat [1], and Monzón-Hernández David[1],
[1] Centro de Investigaciones en Óptica A.C., Loma del Bosque 115, Lomas del Campestre, 37150 León de los Aldama, Gto., Mexico.
egalvan@cio.mx

Summary:

We demonstrated a multi-wavelength fiber-optic refractometer using a multimode-coreless-multimode fiber structure, partially coated with a gold layer, in which multimodal interference and surface plasmon resonance are simultaneously excited. The transmission spectra exhibit three spectral dips, in the visible and the near-infrared regions whose wavelength position is determined by the refractive index of the surrounding medium. This enables the determination of the refractive index of a liquid sample at three different wavelengths to estimate its refrective index dispersion curve using Cauchy's equation.

Keywords: Fiber-optic sensors, multimodal interference, surface plasmon resonance, refractive index dispersion, acetaminophen concentrations.

Background, Motivation and Objective

The measurement of the refractive index is one of the most widely used methods for the determination of a sample purity. However, most optical fiber refractometers reported so far operate at a single wavelength [1,2], which limits the ability to provide information of the content of a mixed sample. To address this limitation, refractometers using different wavelength sources have been developed [3,4], however, these configurations increase the complexity and cost of the system.

In this work, we propose a fiber-optic device that, using an incoherent white-light source and an optical spectrum analyzer, enables the simultaneous measurement of the refractive index at three wavelengths [5]. Based on these measurements, the spectral dependence of the sample's refractive index can be estimated using the Cauchy model.

Description of the New Method or System

A fiber-optic refractometer was developed based on the simultaneous excitation of multimodal interference and surface plasmon resonance, enabling the measurement of the refractive index of liquids at three different wavelengths using a single broadband light source. With these refractive index values and using the Cauchy model, it is possible to estimate the dispersion of the liquid sample. The refractometer proposed here reduces the complexity and cost of measurements compared to setups that require multiple light sources. In addition, this optical fiber refractometer can be used for in situ measurements, making it suitable for monitoring and quality control applications.

Results

To construct the sensor, as shown in Fig. 1, two segments of multimode optical fiber are joined to a 29 mm segment of coreless fiber, which, through multimode interference, produces a transmission band at 790 nm and an attenuation band at 1560 nm. Subsequently, a 3 nm chromium adhesion layer and a 30 nm gold film, were deposited over section of 10 mm length of the coreless fiber to generate surface plasmon resonance in the visible region.

To calibrate the refractometer, the device was immersed in different Cargille oils with refractive index in the range of 1.30 to 1.40. As shown in Figs. 2(a), 3(a), and 4(a), the three dips in the transmission spectra exhibit a red shift as the refractive index increases, although with different sensitivities. From these spectra, the minimum of each dip is identified and used to obtain the polynomial calibration curves shown in Figs. 2(b), 3(b), and 4(b). With these curves is possible to determine the refractive index of an unknown substance by monitoring the wavelength position of the three dips minima in the transmission spectrum.

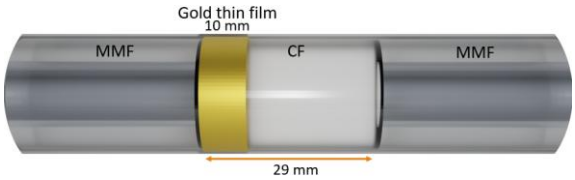

Fig. 1. Schematic of the fiber-optic refractometer.

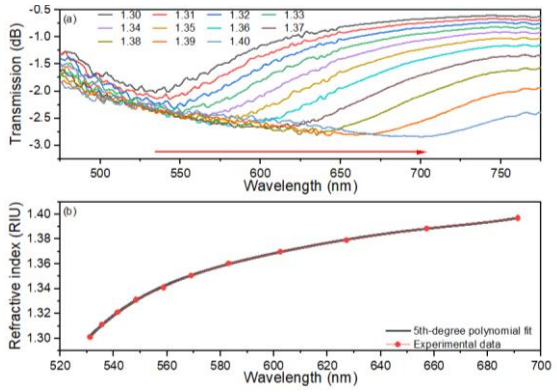

Fig. 2. (a) Partial transmission spectra of the plasmonic resonance as a function of the refractive index of the surrounding medium. (b) Corresponding calibration curve.

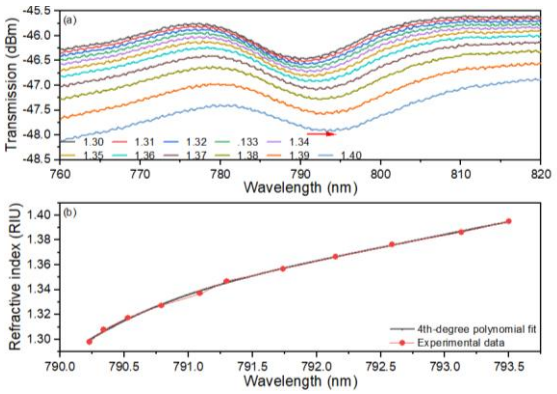

Fig. 3. (a) Partial transmission spectra of the transmission band as a function of the refractive index of the surrounding medium. (b) Corresponding calibration curve.

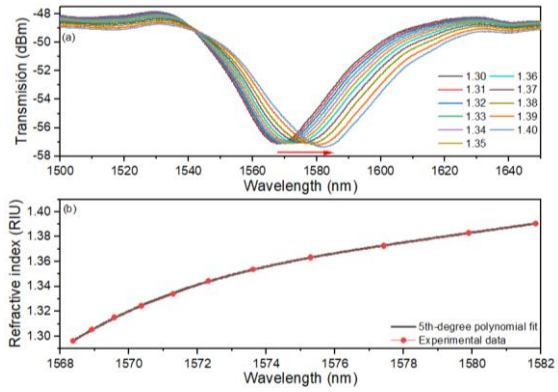

Fig. 4. (a) Partial transmission spectra of the attenuation band as a function of the refractive index of the surrounding medium. (b) Corresponding calibration curve.

To test the broadband refractometer, liquid samples of acetaminophen in water were prepared at concentrations of 1, 2, 4, and 6 mg/mL. Based on the obtained spectra, the refractive index values were interpolated at three different wavelengths; subsequently, their dispersion was calculated using Cauchy's equation. Fig. 5 shows these curves, which reveal an increament of the refractive index as the acetaminophen concentration increases; furthermore, the curves for 2, 4, and 6 mg/mL retain a similar shape.

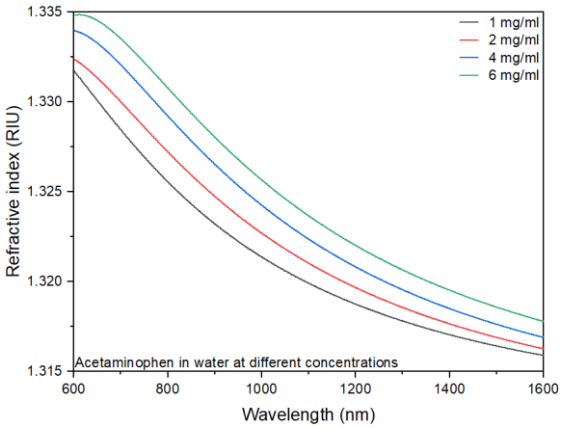

Fig. 5. Refractive index dispersion for different concentrations of acetaminophen in water.

References

[1] P. K. Rastogi, Optical Measurement Techniques and Applications, Artech House (1997).

[2] P. Gong, X. Li, X. Zhou, Y. Zhang, N. Chen, S. Wang, S. Zhang, Y. Zhao, Optical fiber sensors for glucose concentration measurement: A review, Optics & Laser Technology 139, 106981 (2021); doi: 10.1016/j.optlastec.2021.106981

[3] K. Karpienko, M. Wróbel, M. Szczerska, Determination of refractive index dispersion using fiber-optic low-coherence Fabry–Perot interferometer: Implementation and validation, Optical Engineering 53, 077103 (2014); doi: 10.1117/1.OE.53.7.077103

[4] D. Zhu, R. Chen, W. Jia, H. Zhu, Q. Zhang, S. Han, Refractive index measurement based on multi-wavelength laser interferometer, Proceedings of SPIE 11899, 118990Y (2021); doi: 10.1117/12.2601193

[5] E. Galván-Navarro, M. Alonso-Murias, E. Rodríguez-Sevilla and D. Monzón-Hernández, "Broad-spectrum all-fiber optic refractometer for alcoholic beverages identification," *Optics and Lasers in Engineering*, under review, 2026.M. Mouse, D. Duck, The Beagle Boys for President, *Journal of Applied Nonsense* 13, 123-134 (2011); doi: 10.1234/s10000

DOI 10.5162/eurosensors2026/4.3.1

Bio-sourced Polyester as Substrate for Sustainable Wireless Smart Tags Made by Printing

James Bourely[1], Maxime A. Hedou[2,3], Roger Marti[3], Lorenz P. Manker[2], Jeremy S. Luterbacher[2], Danick Briand[1]
[1] EPFL STI IGM LMTS, Rue de la Maladière 71b, 2002 Neuchâtel, Switzerland,
[2] EPFL SB ISIC LPDC, Bâtiment CH, Station 6, 1015 Lausanne, Switzerland,
[3] HEIA-FR Chemtech, HES-SO, Boulevard de Pérolles 80, 1700 Fribourg, Switzerland
danick.briand@epfl.ch

Summary:
We report on poly(hexylene xylosediglyoxylate), a bio-derived polyester from lignocellulosic sugars, as a sustainable substrate for printed electronics. The material is compatible with the additive manufacturing of a transient zinc ink for the realization of eco-friendly sensors and wireless tags. Applying the optimized sintering parameters, different transducers, resistors, capacitors and microstrip lines were patterned to evaluate the properties of the substrate and realize sensing structures. Using the zinc and bio-polyester combination, a wireless identification tag operating at 860–930 MHz was demonstrated.

Keywords: Bio-derived polyester, printed electronics, RFID, sensors, substrate, wireless

Background, Motivation and Objective

Recent advances in bio-derived polymers have enabled the development of high-performance polyesters from lignocellulosic sugars, providing sustainable alternatives to fossil-based plastics [1]. In parallel, alternative conductive materials such as zinc have emerged as promising low-cost and less toxic substitutes for conventional silver inks in printed electronics [2]. These developments align with the growing demand for eco-responsible short life smart tags with wireless and sensing capabilities. In this context, combining bio-sourced polyesters with eco-friendly conductive inks offers a pathway toward more sustainable electronic platforms.

In this work, we are investigating poly(hexylene xylosediglyoxylate) (PHX) as a bio-sourced substrate for printed electronics. We demonstrate its compatibility with the additive manufacturing of transient conductive ink applied to wireless and environmental sensing applications.

Description of the New Method and System

PHX is a bio-based polyester produced directly from the hemicellulosic fraction of lignocellulosic biomass. It is synthesized by functionalizing this biomass with glyoxylic acid to create a rigid tricyclic monomer (DMGX), which subsequently reacts with 1,6-hexanediol to form PHX. This carbohydrate-derived polyester exhibits PET-like properties (Tg = 72 °C and an ultimate tensile strength of 63 MPa) while allowing efficient chemical depolymerization back to its monomers under mild conditions [1].

The PHX powder was hot pressed to form 200 µm thick substrates. The zinc ink was made of zinc microparticles mixed with polyvinylpyrrolidone as binder and using diethylene glycol monobutyl as solvent. The zinc ink was screen printed on the substrate and sintered following the hybrid chemical and photonic process described in [2]. The photonic energy was tuned for an optimal sintering of conductive ink.

The radio-frequency characteristics of the PHX substrate were characterized using a printed zinc microstrip line. The influence of ambient humidity was evaluated using a climatic chamber. Interdigitated zinc electrodes were also patterned to form a capacitive transducer, and its humidity response was evaluated. The results for both structures were compared to those obtained on a PET (Melinex ST506) substrate used in printed electronics.

Finally, an RFID UHF tag was manufactured on PHX substrate. The tag is made of a zinc antenna integrated with an RFID chip. The tag can be interfaced with zinc based capacitive and resistive transducers for humidity and temperature sensing, respectively.

For the first time, bio-sourced PHX has been applied as a printed electronic substrate showing its compatibility with conductive inks, sensing and radio-frequency applications.

Results

The transient zinc ink was successfully printed and hybrid sintered on PHX. Fig. 1 presents the resistance value as a function of sintering energy, compared to zinc printed on paper, achieving higher conductivity. The optimal parameter to achieve the highest conductivity was found to be $3.7\,J/cm^2$. Above $4.4\,J/cm^2$ the integrity of the zinc pattern is affected, because of the PHX substrate melting locally. The thickness of the zinc layer on PHX was measured at $9.5 \pm 2\,um$ and its conductivity was measured at $2.1 * 10^6\,S/m$. These zinc resistors can be used as a temperature sensor thanks to their high temperature coefficient of resistance (TCR). Using these optimum parameters, zinc capacitive and radio-frequency structures were also printed and evaluated on PHX.

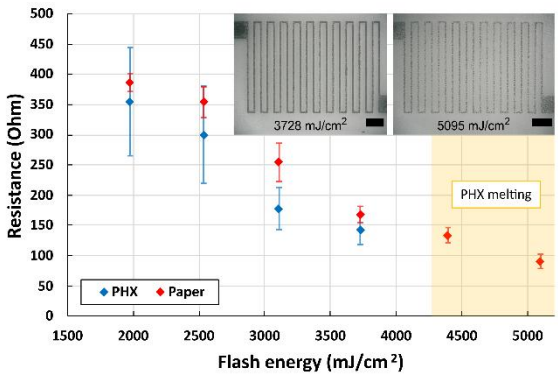

Fig. 1. Resistance of the zinc track vs flash lamp energy for PHX and paper substrates. Scale bar = 2 mm.

Fig. 2 shows the interdigitated electrodes capacitor and its capacitance evolution when exposed to dry air and air at 80% RH, both on PHX and PET substrates. PHX substrate is slightly more sensitive to humidity than PET, with its capacitance increasing by 5% in comparison to 1.5% for PET, when increasing the humidity from 0 to 80% RH. However, its recovery to 0% RH is much faster, leading to less hysteresis when cycling it up again to 80% RH, making the structure of interest as humidity sensor.

A microstrip line resonating at 1 GHz was also printed on PHX and PET and tested. Fig. 3 shows the S12 response of the resonator on PET and PHX where a change in resonance frequency of less than 5 MHz is observed when exposing the resonator to 0% and 80% RH. At 1 GHz, PHX exhibits a similar behavior as PET showing its suitability for high-frequency applications.

Finally, we manufactured a UHF (870-930 MHz) RFID tag with a zinc antenna, as seen in Fig. 4. The eco-friendly RFID tag was able to be detected at a distance up to 9.6 m using a commercial reader emitting at 0.5 W. The RFID chip having sensors' inputs, the tag can integrate a zinc RTD sensor and/or an IDE humidity transducer printed on PHX substrate at the same time as the antenna.

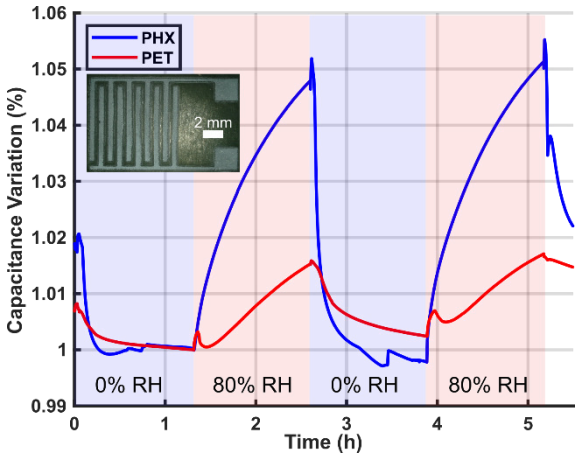

Fig. 2. Capacitance variation over time for zinc on PHX and on PET when cycling from 20% to 80% relative humidity at 20 °C.

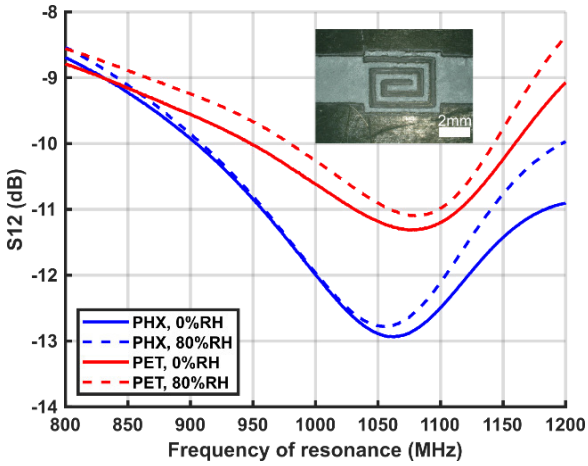

Fig. 3. S12 response vs frequency for the zinc strip line on PHX and PET substrates when exposed to 0 and 80% RH at 20 °C.

Fig. 4. Optical image of the zinc antenna printed on PHX and assembled to an UHF RFID chip.

This work shows the suitability of PHX as a bio-sourced substrate alternative to PET/PEN for printed electronics and wireless devices.

References

[1] Manker, L.P., Dick, G.R., Demongeot, A. et al. Sustainable polyesters via direct functionalization of lignocellulosic sugars. Nat. Chem. 14, 976–984 (2022). DOI: 10.1038/s41557-022-00974-5

[2] Fumeaux, N., Briand, D. Zinc hybrid sintering for printed transient sensors and wireless electronics. *npj Flex Electron* **7**, 14 (2023). DOI: 10.1038/s41528-023-00249-0

DOI 10.5162/eurosensors2026/4.3.2

A Torque Sensor using 3D Printed Conductive TPU

Tom Stein[1], Marc Schärer[1], Mirko Meboldt[1]
[1] Product Development Group Zurich, ETH Zurich, Zurich, Switzerland,
tstein@ ethz.ch

Summary: A fully 3D printed torque sensor was realized through FDM by embedding a conductive TPU helix inside a PA12 body. Torque loading changes the helical sensing path and causes a resistance increase. The printed devices show an approximately linear response up to 3.5 Nm. Repeated cycling between zero and 1 Nm remains detectable but shows baseline drift. These results demonstrate the potential of fully 3D printed sensors and highlight the main challenges for optimization.

Keywords: Additive Manufacturing, Torque Sensor, Printed Electronics, Fused Deposition Modeling, Conductive Filament

Background, Motivation and Objective

Conductive polymers have been used in fused deposition modeling (FDM) to directly print electrical interconnects and functional sensors into structural components, enabling a high degree of integration without post-assembly. Various studies have demonstrated 3D printed strain sensors based on conductive filaments [2], as well as soft tactile sensors embedded in compliant structures [3]. In addition, torque sensing has been explored using additively manufactured structures with conductive paths, by printing metallic silver inks, although this requires specialized processes not compatible with standard FDM workflows [4]. A common limitation across these approaches is the high electrical resistance of conductive polymer composites, compared to metal wiring, and their sensitivity to environmental and mechanical influences, resulting in drift, hysteresis, and limited long-term stability [1]. In this work, we exploit these characteristics to realize a fully 3D printed torque sensor, targeting applications such as human–robot interaction where the detection of small torque variations is essential.

Description of the Torque Sensor

We propose a small inline torque sensor that exploits the helical deformation along the path of a helical conductive structure. When subjected to torque, the elastic twist response of the helix causes a change in its length, which can be measured and correlated to the applied torque through the piezoresistive material behavior. The sensor is fabricated on a standard PrusaXL printer (Prusa Research a.s.) using fiberology PA12 (Fiberlab S.A.) as the structural material, due to its wide elastic deformation capabilities and low creep. The carbon black [1] enriched filaflex conductive TPU (Recreus Industries S.L.)

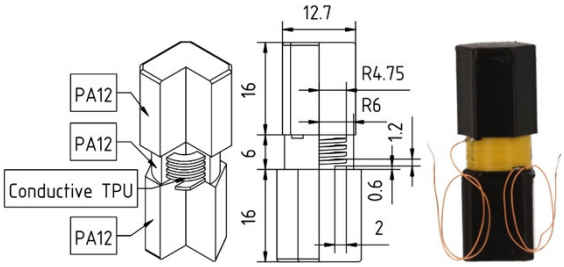

Fig. 1. Left & Middle: Dimensions (mm) of the torque sensor built from PA12 and a conductive TPU helix. Right: FDM fabricated sensor with wires.

is used for the sensor element. Filaments were dried and printed with 0.4 mm diameter nozzles at 100% concentric infill, 235 °C for TPU, and 265 °C for PA12. Specimens were stored in a dry box at room temperature after printing. As shown in Fig. 1, the helical sensing element is embedded in a PA12 cylinder between ½″ sockets. In total, 115.6 mm x 1.2 mm^2 of conductive material are expected to give a total resistance of 21.6 to 33.6 kΩ given the previously reported processed material resistivity of 22.4 to 34.9 Ωcm [1]. The volume ratio of conductive TPU of the cylinder is 20.4%. Short pieces of 0.2 mm enameled copper wire were tinned, heated, and inserted into the straight ends of the conductive helix. An Otti Ace (Qoitech AB) source measurement unit (SMU) was connected to the specimens to record current under a constant voltage of 1.0 V to study the piezoresistive response under load. The sensor is fully clamped in the sockets up to the inner cylinder in a vice and custom test fixture shown in Fig 2. Through a retaining pin, the system can be reset and kept in a baseline state without any applied torque or twist. Without the pin, a torque of up to 5 Nm can be applied by adjusting the weight on the lever arm.

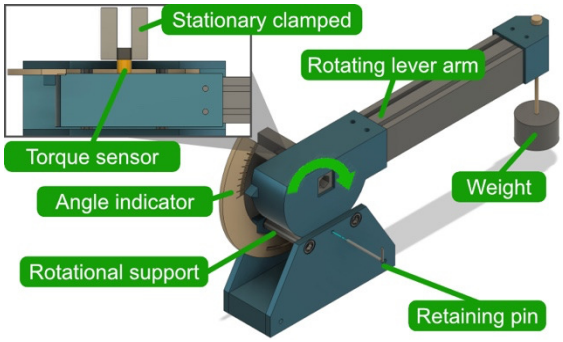

Fig. 2. Torque testing setup with an adjustable hanging mass on a lever arm inducing clockwise torque into the sensor and a 0° locking mechanism.

The rotational support minimizes bending loads but still allows for small height expansion. The expected rotational displacement θ (twist) of the cylinder can be calculated with eq. (1) using the material's shear modulus G, cylinder length $L = 6\,\mathrm{mm}$ and polar moment of inertia $J \approx 2.04 \cdot 10^{-9}\,\mathrm{m}^4$, given the diameter of 12 mm.

$$\theta = \frac{TL}{GJ} \quad (1)$$

Due to material heterogeneity and FDM-induced uncertainties, G cannot be determined precisely but is assumed constant in the linear-elastic regime. For reference, isotropic PA12 ($G = 0.5\,\mathrm{GPa}$)[5] yields $\theta \approx 1.7°$at $T = 5\,\mathrm{Nm}$.

Results

The torque sensors show an initial baseline resistance R_0 of 20.4±0.7 kΩ after printing (n=6) and were split into two sets for experimental study. During stepwise increasing static loading, the sensor shows a linear response up to a torque of 3.5 Nm with high resistive sensitivity of 15.3% and deformation of 7.3° (see Fig. 3). Further loading beyond 3.5 Nm causes saturation of the resistance and eventually irreversible resistance change. However, rotational deformation does not stop beyond 3.5 Nm and continues linearly up to 10.5° at 5 Nm. Cyclic loading tests in the linear range alternating between 0 Nm and 1 Nm torque (see Fig. 4), are detectable by a 3% difference but show a linear decrease in both the loaded and unloaded resistance readings throughout repeated cycles.

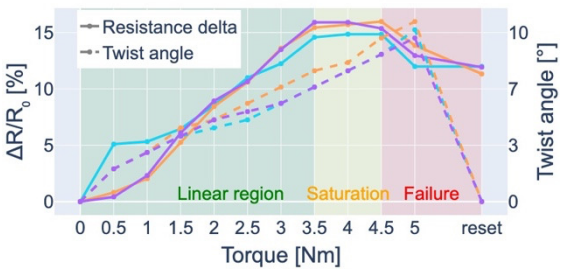

Fig. 3. Resistance and twist change under increasing static torque from 0-5 Nm for specimens 1-3.

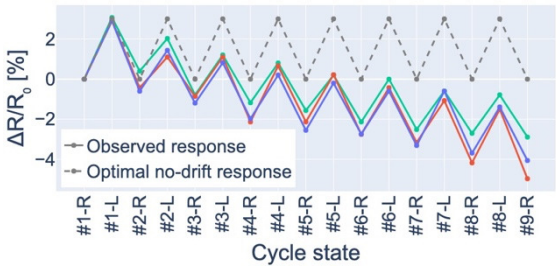

Fig. 4. Resistance change over repeated loading to 1 Nm (L) and forced relaxation to 0 Nm and 0° (R) for specimens 4-6 compared to an optimal theoretical behavior without drift.

The results indicate that conductive TPU can be used for small fully 3D printed torque sensors. However, resistance drift under repeated cycles limits the application to single-use scenarios. Additionally, the twist deformation of several degrees is undesirable for inline torque sensing. The current sensor geometry was derived from theoretical considerations but has not yet been optimized with respect to electrical recovery, mechanical stability, and long-term cyclic behavior. Future work should therefore explore alternative geometries, heat sintering [2], the influence of axial loading, and alternative transduction principles such as capacitive sensing.

References

[1] M. Nowka, K. Ruge, L. Schulze, K. Hilbig, T. Vietor, Characterization of the Anisotropic Electrical Properties of Additively Manufactured Structures Made from Electrically Conductive Composites by Material Extrusion, Polymers 16, 20, 2891 (2024); doi: 10.3390/polym16202891

[2] D. N. Pagonis, A. Stavros, I. Iakovidis, S. Dimitrellou, G. Kaltsas, A 3D Printed Strain Sensor Employing Conductive TPU for Marine Applications, Eurosensors 2025; doi: 10.5162/EUROSENSORS2025/MP1

[3] R. Antunes, L. Lang, M. L. de Aguiar, T. A. Dutra, P. D. Gaspar and N. J. Matos Pereira, Self-Sensing Soft Finger Produced from Conductive TPU for Adaptive Grasping and Force Sensing Applications, *ICARSC 2025,* pp. 39-44; doi: 10.1109/ICARSC65809.2025

[4] L. Stiglmeier, T. Wendt, N. Hangst, P. Gawron, S. Rupitsch, A guideline for the fabrication of fully 3D-printed torque sensor elements – demonstrated based on a real example, 22. GMA/ITG-Fachtagung Sensoren und Messsysteme 2024, 213–220 (2024); doi: 10.5162/sensoren2024/C1.2

[5] Polyamide 12 - Nylon 12 - PA 12, https://www.azom.com/properties.aspx?ArticleID=753, access on April 19th, 2026.

DOI 10.5162/eurosensors2026/4.3.3

Soft and Stretchable Carbon Flower Sensors Detect Hormones and Neurotransmitters at High Sensitivity

Ines C. Weber[1], Diego U. Patino,[2] Kuang-Jung Hsu,[2] Zhenan Bao[2]
[1] Chalmers University of Technology, Kemivägen 10, SE-412 96 Göteborg, SWEDEN
[2] Stanford University, 334 Via Ortega, 94305 Stanford, USA
inesc@chalmers.se

Summary:

Continuous monitoring of hormones, neurotransmitters, and metabolites in biofluids such as sweat and saliva holds great promise for personalized health. Yet, current sensor technologies lack the sensitivity, selectivity, and mechanical compliance needed for on-skin and real-life applications. We introduce carbon flowers, which are graphitic microparticles with flower-like morphology, as a novel electrochemical sensing material. These carbon flowers are synthesized through a bottom-up approach by polymerizing acrylonitrile and feature unique morphology with high conductivity and defect-rich structure. Fabricated via scalable spray-coating onto stretchable substrates, the sensors achieve nanomolar detection of serotonin, dopamine, melatonin, uric acid, estradiol, and ascorbic acid, outperforming state-of-the-art carbon materials. Simultaneous multi-analyte detection with excellent linearity ($R^2 > 0.97$) and robustness under physiological pH and salt conditions makes them promising for future wearable, real-time health monitoring.

Keywords: soft electronics, health monitoring, electrochemical sensor, multi-analyte detection, defective carbon

Background, Motivation and Objective

Sweat and saliva are biofluids rich in health information. They contain a plethora of hormones, neurotransmitters, and metabolites that reflect underlying physiological processes [1]. Monitoring such biomarkers continuously at the point-of-care could significantly advance personalized health, but suitable sensing technologies are missing. This is because current sensors lack the ***sensitivity*** to measure these biomarkers at physiological levels, the ***selectivity*** to measure individual biomarkers in the presence of other molecules, and the stability under real conditions. Finally, many sensors are ***rigid and require highly complex fabrication***, unsuitable for low-cost on-skin applications, as desired for sweat sensing. We introduce carbon flower (CF) electrodes to address these challenges [2]. CFs have previously shown interesting capabilities in electrocatalysis applications [3, 4], but have never been explored in electrochemical sensing. We demonstrate the use of such carbon flowers as soft, stretchable electrodes for the detection of a multitude of biomarkers and biomarker mixtures.

Description of the New Method or System

Carbon flowers are synthesized *bottom-up* from acrylonitrile polymerization and converted to graphitic, hierarchical CFs via stabilization and carbonization [5]. This in-house synthesis ensures controlled and uniform graphitic particles of ~1 µm diameter. A key advantage of the CFs is their high defect density, accessible surface sites, and good conductivity, ideal for electrochemical sensing [2].

The CFs are dispersed in chloroform with a polymeric binder using ultrasonication and spray-coated onto stretchable substrates. Each device features patterned silver interconnects and eight electrodes (2.5 × 0.5 mm) connected to a flexible cable for signal readout (Fig. 1a,b).

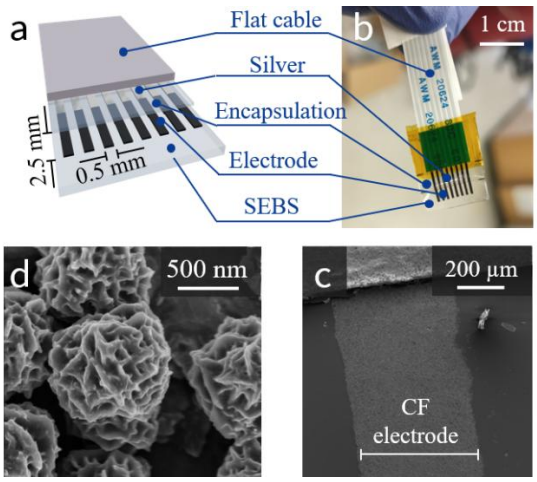

Fig. 1. (a) Sensor design. (b) Photograph of a sensor featuring 8 sensing electrodes on a flexible substrate. (c) SEM image of a carbon flower electrode. (d) SEM image of the carbon flowers.

The fabrication requires no cleanroom steps, enabling low-cost, scalable production of soft sensor arrays.

Results

A scanning electron microscopy (SEM) image of the carbon flower electrode with a zoom-in on the carbon flowers is shown in Fig. 1c,d. The particles exhibit a distinctive flower-like morphology with excellent uniformity in size; highly graphitic crystalline areas are revealed in XRD analysis, while Raman and XPS show high defect density and the presence of nitrogen sites stemming from the acrylonitrile precursor.

Most importantly, carbon flower sensors detect a variety of biomarkers, including dopamine, ascorbic acid, uric acid, serotonin, estradiol, and melatonin. The square wave voltammetry (SWV) detection of serotonin and melatonin is shown exemplarily in Fig. 2. The limits of detection (LOD) of 1 nM surpass state-of-the-art carbon-based sensors. We attribute the high sensitivity to the unique morphology of the CFs, in combination with high conductivity and a highly defective structure. Notably, the carbon flower sensors can be used for repetitive measurements and are robust to changes in salt and pH [2].

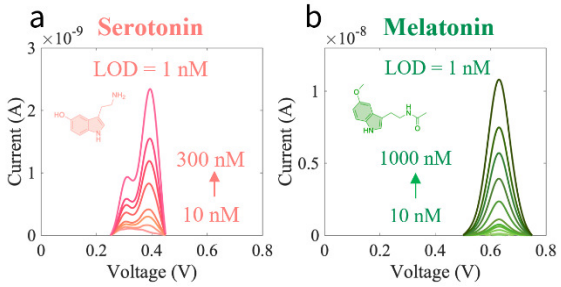

Fig. 2. SWV detection of (a) 10-300 nM serotonin and (b) 10-1000 nM melatonin

In addition, distinct oxidation peaks permit concurrent detection of biomarkers in mixtures. Fig. 3a shows the simultaneous detection of serotonin and estradiol, indicating that the oxidation peaks are clearly separated and allow for the selective detection of either molecule. This is possible also when testing the three biomarkers serotonin, estradiol, and melatonin in mixture (Fig. 3b): despite the increased complexity, the individual molecules remain clearly separable, and calibration curves in mixtures closely match single-analyte measurements ($R^2 > 0.97$). Yet, limitations arise when increasing mixture complexity further, e.g. through addition of ascorbic acid, which overlaps with serotonin. Combining the intrinsic selectivity shown here with sensor arrays or Nafion coatings could overcome this limitation and further advance multi-analyte sensing.

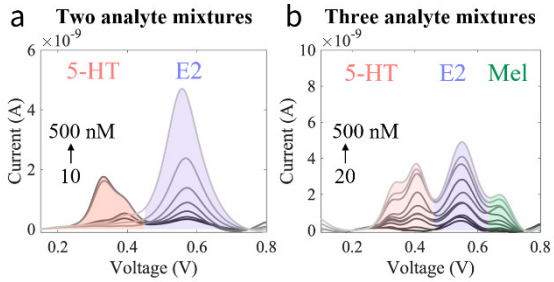

Fig. 3. (a) Simultaneous detection of 50-100 nM serotonin (5-HT) and 10-100 nM estradiol (E2). (b) Simultaneous detection of 20-500 nM serotonin, estradiol, and melatonin (Mel).

Conclusion

Carbon flower electrodes enable soft, stretchable electrochemical sensors with superior sensitivity, achieving nanomolar detection of serotonin, melatonin, estradiol, dopamine, uric acid, and ascorbic acid. Their scalable, cleanroom-free fabrication on stretchable substrates, combined with robust multi-analyte discrimination under physiological conditions, makes them a compelling platform for continuous wearable health monitoring.

References

[1] D. Sim, M. C. Brothers, J. M. Slocik, A. E. Islam, B. Maruyama, C. C. Grigsby, R. R. Naik, S. S. Kim, Biomarkers and Detection Platforms for Human Health and Performance Monitoring: A Review, *Advanced Science* 9, 7, 2104426 (2022). doi: 10.1002/advs.202104426

[2] I. C. Weber et al., Sensitive Hormone and Neurotransmitter Detection with Carbon Flower Electrodes, *Advanced Functional Materials* e28595 (2026). doi: 10.1002/adfm.202528595.

[3] H. Gong, L. Wei, S. Chen, Z. Chen, T. F. Jaramillo, Z. Bao, Carbon flowers as electrocatalysts for the reduction of oxygen to hydrogen peroxide, *Nano Research* 16, 9, 11556–11563 (2023). doi: 10.1007/s12274-023-5903-8

[4] S. Chen, H. Gong, B. Dindoruk, J. He, Z. Bao, Dense Carbon Nanoflower Pellets for Methane Storage, *ACS Applied Nano Materials* 3 (8), 8278–8285 (2020). doi: 10.1021/acsanm.0c01700.

[5] K. Parkatzidis, D. U. Patino, Y. Shi, K.-J. Hsu, I. Weber, H. S. Wang, Z. Bao, Polyacrylonitrile Flower-Like Particles with Tunable Size and Morphology via Scalable Oxygen-Tolerant Polymerization, *ACS Nano* 20, 5, 4455–4469 (2026). doi: 10.1021/acsnano.5c19392.

DOI 10.5162/eurosensors2026/4.3.4

Electrokinetic Self-Cleaning of Mixed-Phase Contaminants on Optical Sensors in Physical AI

Dong Joo Lee[1], Tae Hyeon Jang[1], Youngkwang Kim[1], Jeongmin Lee[2], Sang Kug Chung[1]
[1] Department of Mechanical Engineering, Myongji University, 116 Myongji-ro, 17058 Yongin, South Korea,
[2] Microsystems Inc., 116 Myongji-ro, 17058 Yongin, South Korea
skchung@mju.ac.kr

Summary: This paper presents an active electrokinetic cleaning device that integrates dielectrophoresis (DEP) and electrowetting-on-dielectric (EWOD) to simultaneously remove solid and liquid contaminants from optical sensors in Physical AI systems. By applying alternating current voltage to a transparent electrode, both particles and droplets are removed without mechanical moving parts. The restoration of object recognition accuracy in a contaminated optical sensor verifies the applicability of this approach.

Keywords: Physical AI, Electrokinetic cleaning, Dielectrophoresis, Electrowetting-on-dielectric, MEMS

Background

Artificial intelligence is integrated into various mechanical systems (e.g., automobiles, cameras, and robots) through on-device processing. This evolution toward Physical AI enables systems to autonomously perceive surroundings, make decisions, and execute physical actions. However, when these sensors are exposed to outdoor environments, solid particles (e.g., dust) and liquid droplets (e.g., raindrops) coexist and adhere to the surface. The resulting optical scattering causes degradation in object recognition accuracy and system reliability [1][2].

To address this challenge, active electrokinetic cleaning technology has garnered attention due to its lack of mechanical moving parts and rapid response [3]. The physical driving forces exerted on surface contaminants depend on the configuration of the non-uniform electric field and the underlying electrokinetic principles [4][5]. These factors dictate the cleaning efficiency of multiphase contaminants exhibiting diverse physicochemical properties. Consequently, it is essential to design a device architecture based on a dual-mechanism approach capable of simultaneously removing solid and liquid contaminants in operating environments.

This study proposes a self-cleaning device that integrates DEP and EWOD principles into a single transparent structure. We experimentally analyze the dynamic behavior of mixed-phase contaminants under AC voltage to quantitatively evaluate the surface cleaning efficiency.

Materials and methods

Electrokinetic removal utilizes non-uniform electric fields generated by applying AC voltage to multi-channel electrodes. Under this field, liquid droplets are driven by EWOD, which alters their contact angles and deforms the fluid interface, whereas solid particles are polarized and transported by DEP. To optimize the electrode geometry, a structural-electric field analysis was conducted using COMSOL Multiphysics. Based on these simulations, interdigitated electrodes were fabricated on a transparent glass substrate via semiconductor microfabrication processes (Fig. 1). Specifically, a 40 nm-thick indium tin oxide (ITO) layer was patterned as the electrode. Subsequently, a 2 μm-thick Parylene-C layer was deposited for electrical insulation, followed by a hydrophobic layer to control surface wettability, completing the multifunctional device.

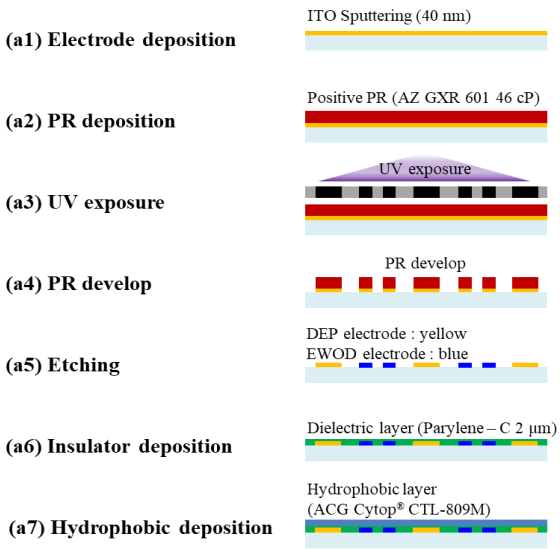

Fig. 1. Schematic images of microfabrication process.

Results

To evaluate the cleaning efficiency, the electrokinetic behavior of the contaminants was analyzed under a controlled environment (25 °C, 40 % RH). Initial removal experiments were conducted independently for each contaminant phase using the optimized interdigitated electrode pattern. Solid particles (50 µm diameter; glass beads, polymer beads, and iron powder) and liquid droplets of varying sizes were separately distributed on the device surface. AC voltage with varying frequencies was applied using a function generator coupled with a voltage amplifier. The dynamic response of the contaminants under the non-uniform electric field was recorded using a high-speed camera. Observations confirmed that liquid droplets were removed via EWOD-induced interface deformation, whereas solid particles were transported toward the electric field gradient via DEP (Fig. 2).

The surface states before and after the cleaning process were documented using an optical microscope. Residual contamination areas were quantitatively measured using ImageJ software. By analyzing the removal efficiency as a function of the applied voltage and frequency for each material, the optimal driving parameters were established. Subsequently, a mixed-phase contamination environment was simulated by co-depositing solid particles and liquid droplets on the surface. The simultaneous separation and removal of both phases were verified under the optimized parameters.

Finally, the proposed device was integrated into a surveillance camera module to validate its applicability. Artificial mixed-phase contamination applied to the optical sensor caused optical distortion, leading to object recognition failure. Upon activating the cleaning device, the contaminants were removed, and the recognition rate of the YOLOv26 object recognition model was restored to its pre-contamination baseline (Fig. 3).

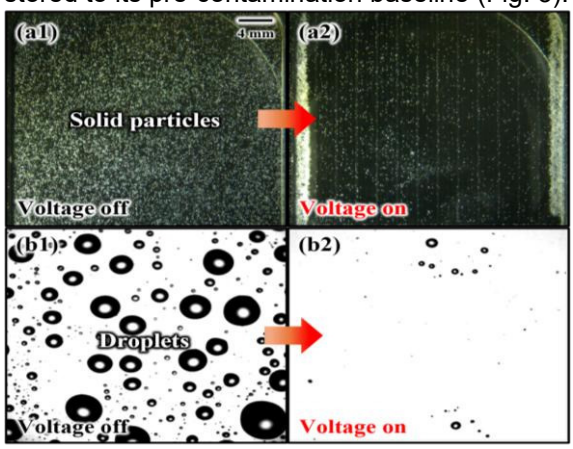

Fig. 2. Experimental results of contaminats removal using the active electrokinetic cleaning device: (a) solid particles; (b) Droplets

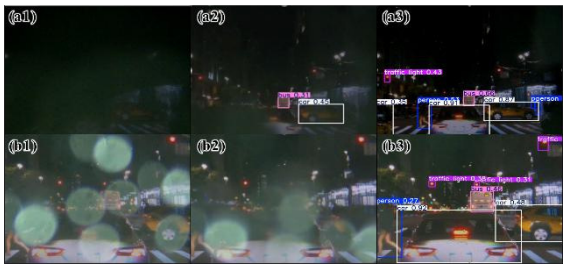

Fig. 3. Sequential snapshots of the electrokinetic removal of contaminants on an optical sensor and the restoration of object recognition: (a) Solid particles; (b) Droplets.

Conclusion

This study presents an active electrokinetic cleaning device that combines DEP and EWOD mechanisms for the simultaneous removal of mixed-phase contaminants. By restoring the object recognition accuracy of an obscured optical sensor, this technology demonstrates its potential as an active self-cleaning optical module to ensure the reliability of Physical AI systems, including autonomous driving and intelligent robotics.

Acknowledgements

This work was supported by the National Research Foundation of Korea (NRF) grant funded by the Korea government (MSIT) (RS-2025-25421959).

References

[1] M. Bijelic, T. Gruber, W. Ritter, Benchmarking Image Sensors under Adverse Weather Conditions for Autonomous Driving, Proc. IEEE Intelligent Vehicles Symposium (IV), 1773-1780 (2018); doi: 10.1109/IVS.2018.8500659

[2] E. Yurtsever, J. Lambert, A. Carballo, K. Takeda, A Survey of Autonomous Driving: Common Practices and Emerging Technologies, IEEE Access 8, 58443-58469 (2020); doi: 10.1109/ACCESS.2020.2983149

[3] D. Sun, K. F. Böhringer, Self-Cleaning: From Bio-Inspired Surface Modification to MEMS/Microfluidics System Integration, Micromachines 10, 101 (2019); doi: 10.3390/mi10020101

[4] K. Y. Lee, J. Hong, S. K. Chung, Smart Self-Cleaning Lens Cover for Miniature Cameras of Automobiles, Sensors and Actuators B: Chemical 239, 754-758 (2017); doi: 10.1016/j.snb.2016.08.032

[5] H. Kawamoto, T. Shibata, Electrostatic Cleaning System for Removal of Sand from Solar Panels, Journal of Electrostatics 73, 65-70 (2015); doi: 10.1016/j.elstat.2014.10.011

DOI 10.5162/eurosensors2026/4.4.1

Programable hierarchical actuation schemes based on phase change composites arranged as a resistive network

Wolfgang Hilber[1], Sebastian Lang[1], Bernhard Jakoby[1]
[1]Institute for Microelectronics and Microsensors, Johannes Kepler University Linz, Altenbergerstrasse 69, A-4040 Linz, Austria
wolfgang.hilber@jku.at

Summary:
In this contribution we present a concept for the utilization of an electrically conductive phase-change composite as a drive element for the realization of predefined and programmable micro-actuation schemes in space and time. For this purpose, segments of a composite of paraffin and carbon black with different cross-sectional areas are arranged in a predefined pattern, reflecting a resistive network. Applying electric current to this network triggers an actuation pattern defined in space and time that can, for instance, be used for complex actuation sequences in microfluidic chips.

Keywords: functional composites, phase change actuator, paraffin, carbon black, transducer network

Introduction

Phase-change materials based on paraffin have been widely used in various actuation schemes, in most instances confined within a small cavity and with an attached heater to gain control over temperature and thus the volume-change actuation mechanism associated with the phase transition from solid to liquid [1]. In a few studies the paraffin wax itself was made accessible for Joule heating by adding conducting particles [2]. Here, we advance this approach by arranging conductive paraffin as a resistive network, enabling predefined, sequential actuation schemes embedded in a single platform.

The Phase Change Composite

Carbon Black (CB) was added to pure paraffin wax (PW) in the molten state, well above 55 °C, until the resulting bulk composite featured a base resistance of approximately 10 kΩ at room temperature (~25 °C) when measured at a thick layer with probe tips with a 10 mm spacing.

Subsequently, the PW/CB composite was characterized with respect to its temperature behavior, with results shown in Fig. 1. As expected, the composite undergoes the solid-to-liquid phase change at around 50 °C, accompanied by a steep increase in electrical resistance. This is anticipated since, due to the volume increase, the average distance, and hence the overlap between conducting particles decreases, thus reducing the available electrical pathways and the electrical conductivity.

However, for temperatures well above 50 °C the electrical resistance of the liquid composite decreases again, although the volume still increases at a low rate. This effect is most likely attributed to electrophoretic migration and alignment of carbon particles in the liquid paraffin, as has been examined previously [3].

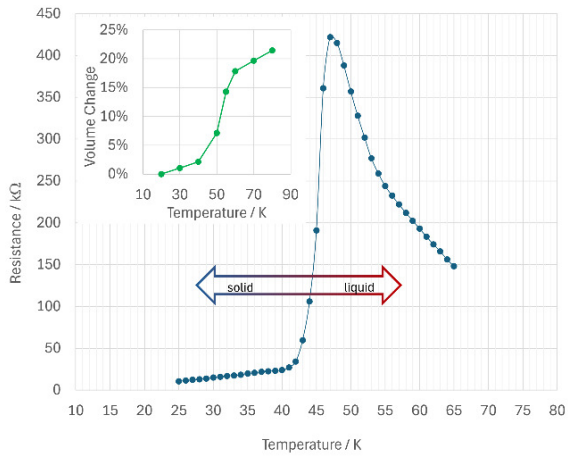

Fig. 1. Electrical resistance over temperature of the utilized PW/CB composite measured in the bulk with the probe tips featuring a distance of 10 mm. The inset shows the corresponding volume change determined separately via a volume displacement measurement.

The Operating Principle

The basic idea is to arrange conductive segments made of the devised composite with different cross-sectional areas and hence electrical conductivity in such a way that a resistive network is formed. Applying Joule heating to this network then leads to local heating and hence volumetric expansion, initially at the points of highest ohmic resistance. According to the chosen dimensioning of the single segments and

their arrangement relative to one another, a predefined hierarchical sequence of volumetric actuation can be released on demand.

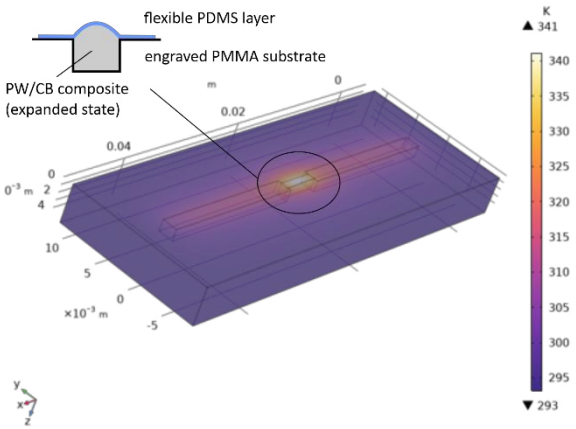

Fig. 2. FEM simulation (Comsol Multiphysics) illustrating the localized Joule heating effect at a geometric restriction of the PW/CB composite structure.

This actuation cascade, geometrically and chronologically predefined and reversible, can be utilized, e.g., for peristaltic actuation of fluid in an attached chip with an engraved fluid channel, as microfluidic switches or flow meters in general, or can be transformed into any other kind of mechanical displacement.

Proof of Principle, the first Actuation Chips

Fig. 3 shows, as proof of principle, the same geometry as in the simulation in Fig. 2, realized with laser-engraved channels in a PMMA substrate, filled with the PW/CB composite, and sealed with a thin elastic PDMS layer on top. In accordance with the geometric dimensions of the line segment (1 x 0.8 x 5 mm^3) and the measured volume expansion coefficient, as illustrated in Fig. 1, the achieved membrane deflection amounts to ~ 0.3 mm shortly after onset of the Joule heating due to the applied electric current.

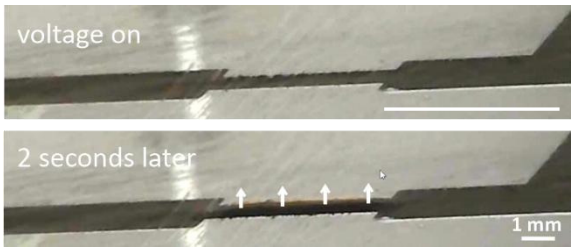

Fig. 3. Proof of principle, showing the volume expansion-induced deformation of a thin PDMS layer above the geometric restriction of the PW/CB structure directly after the onset of Joule heating (side view).

As a next step, a peristaltic actuation scheme from the center outward was examined by joining together segments with increasing cross-section. Applying current to this structure leads to a kid of peristaltic deformation of the elastic membrane on top, as illustrated in Fig. 4.

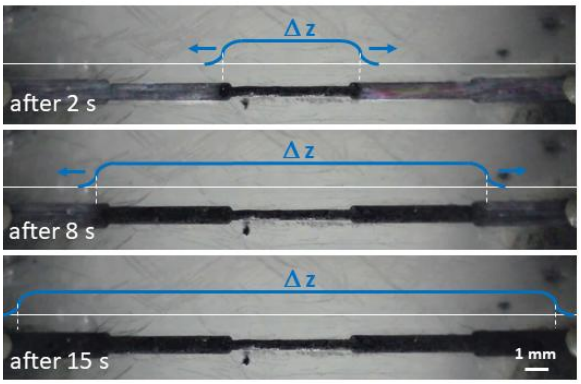

Fig. 4. Peristaltic deformation center outward of the covering PDMS layer on top, achieved with symmetric alignment of segments with different cross-sectional area (top view; expanded section indicated for better visibility).

Response time and actuation dynamics, as indicated in Fig. 3 and 4, strongly depend on the applied electric power and have not yet been examined in detail.

Conclusions and Outlook

In summary, it has been shown that an electrically conductive phase-change composite, arranged in connected segments as a resistive network, can be used to realize complex micro-actuation schemes predefined in space and time. For example, multilocal actuation can be implemented on a single microfluidic chip, either time-delayed or sequentially, as shown for the peristaltic membrane deflection in Fig. 4, or simultaneously at different spots for, e.g., switching and valving. Layout and dimensioning of the single segments for a specific actuation pattern are straightforward, since they simply reflect a resistive network subjected to ohmic heating as soon as a voltage or current source is activated.

A further degree of freedom in design can be achieved by combining the conductive composite segments with low-ohmic metallic lines in between in hybrid technology. This can, for example, be realized by using a standard PCB as the initial substrate and combining copper-based conductive paths with engraved and phase-change-composite filled channels.

References

[1] S. Ogden et al., *Microfluidics and nanofluidics* 17.1, 53-71 (2014); doi: 10.1007/s10404-013-1289-3

[2] H.J. Sant et al., *Journal of Micromechanics and Microengineering 20*(8), 085039 (2010); doi: 10.1088/0960-1317/20/8/085039

[3] M.N. Patel et al., *Journal of colloid and interface science* 345.2, 194-199 (2010); doi: 10.1016/j.jcis.2010.01.055

DOI 10.5162/eurosensors2026/4.4.2

A 3D-Printed Monolithic Bender Bar Transducer Featuring a Fluid-coupled Thin-plate Backing and Flexural Hinges

Min Jung Sim[1], Yub Je[1], Hayeong Shim[1], Kyungseop Kim[1], Yohan Cho[1], Hee Seon Seo[1]
[1]Agency for Defense Development,
Jinhae P.O. Box 18, Changwon, Gyeongnam 51678, Republic of Korea
Corresponding Author's e-mail address: sideze@add.re.kr

Summary:
A 3D-printed monolithic bender bar transducer featuring a thin-plate backing and flexural hinges is proposed to overcome the acoustic short circuit effect in low frequency underwater applications. Fabricated via powder bed fusion, this structure creates a narrow fluid gap that strongly couples with the thin plate, functioning as an effective dynamic boundary. Experimental results demonstrate that this compact design transforms the dipole radiation into an omnidirectional monopole pattern, significantly increasing acoustic radiation efficiency while offering a tunable acousto-structural framework for future applications.

Keywords: bender bar transducer, 3D printing, pressure release, dynamic boundary, acousto-structural coupling

Background, Motivation and Objective

Bender-type transducers are widely utilized for low-frequency underwater acoustic projectors due to their high-power output and compact size [1]. However, when operating in a free-field environment without backing structures, they act as dipole sources. At low frequencies, the out-of-phase radiation from the front and rear faces causes a severe acoustic short-circuit, which drastically reduces the radiation resistance and overall transmitting efficiency. Conventional approaches to prevent this issue rely on thick, heavy metal housings with air-backing or elastomeric backing materials, such as Corprene, to block rearward acoustic radiation and provide pressure release [2, 3]. While effective, these conventional methods significantly increase the volume and weight of the sonar system and limit the operational bandwidth. Therefore, the objective of this work is to introduce a novel, highly compact monolithic bender bar transducer utilizing a 3D-printed thin plate dynamic boundary.

We investigate the strong acousto-structural coupling mediated by a narrow fluid gap to achieve an effective pressure release condition of bender bar transducers without the bulk of conventional housings. We aim to demonstrate, through both finite element method (FEM) models and empirical lake tests, that the bender bar with thin-plate backing behaves to a pressure release condition, thereby maximizing acoustic output and transforming the dipole radiation into an omnidirectional monopole pattern.

Description of the New Method

The proposed transducer features a completely monolithic titanium mechanical body driven by a [011] poled Mn:PIN-PMN-PT piezoelectric single crystals which provide superior 32 piezoelectric properties for bending mode [4].

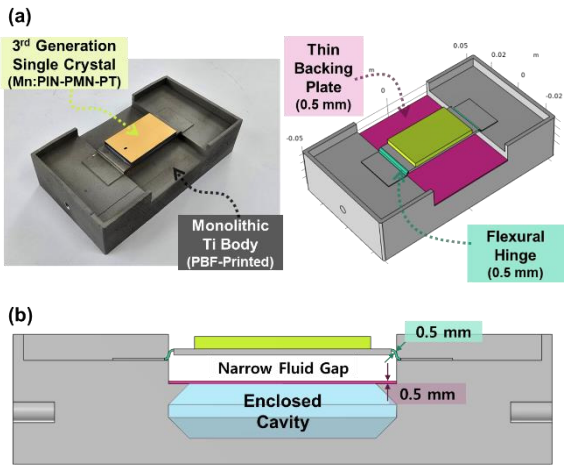

Fig. 1. Structure of the monolithic bender bar transduce (a) Photograph of the fabricated titanium prototype via powder bed fusion (PBF) incorporating the Mn:PIN-PMN-PT single crystal. (b) Cross-sectional view, detailing the 0.5 mm-thick flexural hinges, the narrow fluid gap, and the thin plate for dynamic boundary.

Unlike traditional assembled transducers, this entire titanium structure — encompassing the bender, flexural hinges, and thin-plate backing — is manufactured as a single entity using Powder Bed Fusion (PBF) 3D printing technology.

This ultra-precise fabrication enables the integration of a 0.5 mm-thick flexural hinge to realize a simply supported boundary condition at both ends of the bender bar, alongside a 0.5 mm thin metal plate positioned closely behind the bender bar to encapsulate an air cavity. Traditional machining cannot fabricate such a seamless, fully enclosed acoustic cavity without introducing mechanical losses at assembly joints. Thus, PBF 3D printing is a fundamental prerequisite for realizing the flexural hinges and dynamic boundary conditions in a physical prototype.

In our transducer design, a narrow fluid gap (approximately 5 mm) exists between the bender and the thin-plate backing. This fluid layer induces a strong acousto-structural coupling between the two components. Acoustically, this resonant thin-plate backing acts as an engineered dynamic boundary. The acoustic response is not merely dictated by the air volume, but is fundamentally governed by the engineered structural compliance of this PBF-printed thin-plate backing. At low frequencies, the plate's precise flexibility yields to the acoustic pressure through this coupling medium, effectively absorbing the rearward radiation and acting as an efficient pressure release boundary.

Results

The FEM simulations and subsequent lake tests rigorously validated the acoustic mechanism of the engineered dynamic boundary. FEM simulations were established comparing three conditions: a bare bender, a bender with an ideal pressure release (PR) boundary at the rear, and a bender with the proposed thin-plate backing. To provide a clear comparative analysis, the frequency axis was normalized to the primary resonance of the proposed model(f_0).

As shown in Fig. 2, the bare bender exhibited a typical dipole beam pattern with severe acoustic cancellation. Conversely, the proposed model revealed that the strong coupling between the bender and the thin plate mirrors the pressure release boundary around $1.0f_0$. This interaction successfully decoupled the rearward radiation, generating an omnidirectional monopole pattern. Notably, the dynamic boundary also induced an additional low-frequency resonance mode at approximately $0.44f_0$. This unique characteristic, absent in both bare and ideal PR models, demonstrates the profound influence of the acousto-structural coupling on the system's dynamic response. Consequently, by effectively eliminating the acoustic short-circuit, the radiation resistance was fully recovered. The lake test results confirmed these theoretical predictions; the measured transmitting voltage response (TVR) of the proposed design was substantially enhanced compared to the bare bender model, matching the acoustic performance of an ideal PR boundary while maintaining an extremely thin, monolithic profile.

Furthermore, this coupled fluid-structure system establish a versatile foundation for tuning resonance behaviors in future advanced transducer designs.

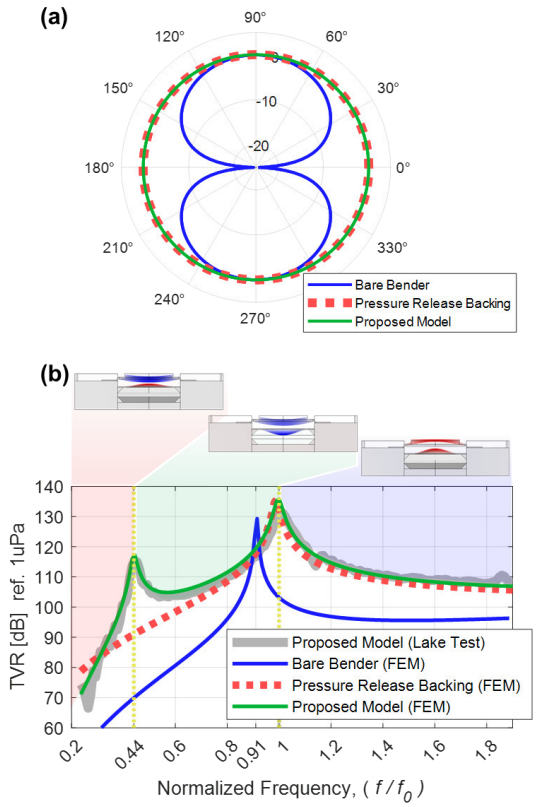

Fig. 2. Acoustic performance validation. (a) Simulated (FEM) beam patterns comparing the bare bender (dipole) to both an ideal pressure release (PR) condition and the proposed model (monopole). (b) Transmitting voltage response (TVR) illustrating the theoretical FEM comparisons and the empirical lake test results of the proposed transducer, demonstrating the elimination of the acoustic short-circuit and pressure enhancement due to the dynamic boundary.

References

[1] C. H. Sherman, J. L. Butler, Transducers and Arrays for Underwater Sound, Springer, 35-70 (2007); doi: 10.1007/978-0-387-33139-3

[2] Y. Zheng, W. Zhang, X. Wang, A High-Power and High-Efficiency Bender Transducer, *2019 IEEE International Symposium on Phased Array Systems and Technology*, 1-4 (2019); doi: 10.1109/SPAWDA48812.2019.9019242

[3] J. Zhang, Miniaturized flextensional transducers and arrays, Ph.D. Dissertation, The Pennsylvania State University (2004).

[4] S. Zhang, F. Li, High performance ferroelectric relaxor-PT single crystals: Status and perspective, *Journal of Applied Physics* 111, 031301 (2012); doi: 10.1063/1.3679521

DOI 10.5162/eurosensors2026/4.4.3

A Low-Power Printed Flexible Lorentz Force MEMS Switch with Electrostatic Hold-down

Mohammad Meybodi, Khoi Nguyen, Tao Chen, Cyrus Shafai
University of Manitoba, 75 Chancellors Circle, Winnipeg, MB, R3T 5V6, Canada
Cyrus.Shafai@umanitoba.ca

Summary:
This work presents a flexible, printed MEMS switch based on Lorentz force actuation with electrostatic hold-down. The Lorentz force drives the pull-down motion, while a low electrostatic force maintains the closed state, reducing power consumption. The device consists of a printed silver conductive layer on a polyimide substrate and is released using a plasma etching process. Simulation results show that a current of 120 mA produces approximately 110 µm displacement, enabling contact closure. The switch has a resonant frequency of 33 Hz, and a spring constant of 0.018 N/m. Experimental results demonstrate switching operation and validate the proposed concept.

Keywords: Printed MEMS, Flexible electronics, Lorentz force actuation, Electrostatic hold-down, Low power switching

Introduction

Micro-electromechanical systems (MEMS) switches are promising alternatives to conventional electronic switches due to their small size, low power consumption, and comparable switching performance [1]. They are widely used in RF systems, reconfigurable electronics, and low-power communication circuits. With the advancement of additive manufacturing, printed and flexible electronic systems have attracted attention due to their low-cost and fast fabrication and compatibility with large-area substrates [2]. MEMS switches rely on mechanical motion to enable or interrupt electrical conduction, which is typically driven by electrostatic or electromagnetic mechanisms [3]. Electrostatic actuation offers low steady-state power consumption but normally requires relatively high voltage, while Lorentz-force actuation enables low-voltage operation but requires continuous current to maintain closure, increasing power consumption [4]. Recently, micro-printing technologies has shown potential for printed MEMS [5].

In this work, we present a printed and flexible MEMS switch that combines these mechanisms. The Lorentz force is used for pull-down actuation, while an electrostatic force maintains the closed state, eliminating the need for continuous current. The device uses a four-spring suspension design and is fabricated on a polyimide substrate. Simulation and experimental results demonstrate its performance and operation.

Working principle

Fig. 1 illustrates the structure of the switch and its operation. A permanent magnet is placed beneath the device to generate a static magnetic field. A direct current is applied through the fixed anchor pads (P2 and P4), creating an in-plane current. As a result, an out-of-plane Lorentz force is generated, which pulls the movable shuttle downward. When the shuttle reaches the contact pads, the switch is in the closed state. Once closed state, a voltage applied to the bottom electrode maintains the contact through electrostatic force. At this stage, the driving current can be turned off, reducing power consumption while keeping the switch closed. Fig.1 also shows the experimental setup used to monitor the switching behavior. A 5 V power supply is connected to the device through a 1 kΩ resistor, and an oscilloscope is used to measure the voltage at the contact pad. When the switch is open, the measured voltage is 5 V. When the shuttle is pulled down and contact is established, the voltage drops to 0 V, indicating the closed state.

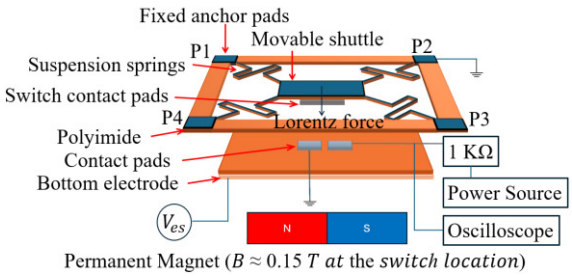

Fig. 1. Working principle of the MEMS switch.

Simulation and Experimental setup

A multiphysics finite element model was used in COMSOL Multiphysics to analyze the electromechanical response of the switch. The device is based on a printed silver layer (15 µm thickness, 100 µm line width, Voltera NOVA printer, ACI FS0142 silver ink) on a 25 µm thick polyimide substrate. The printed switch is released using oxygen plasma etching of surrounding polyimide. The switch closes when the vertical displacement reaches 110 µm, corresponding to contact with the bottom electrodes. Fig. 2 shows the simulated displacement distribution under Lorentz-force actuation. Its fundamental resonance frequency of approximately 33 Hz, and the effective spring constant is about 0.018 N/m.

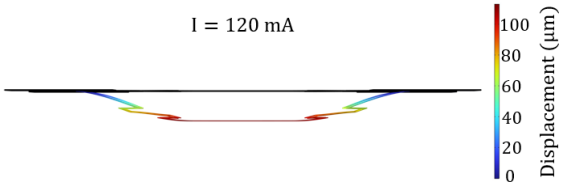

Fig. 2. Simulated displacement distribution.

Experiment Results

A fabricated switch is shown in Fig. 3. Experiments were conduced to measure the displacement versus current as shown in Fig. 4, along with simulation results. We can see that measurements follow the trend of simulation results. The dynamic response of the switch is shown in Fig. 5. In this test a square-wave excitation produces repeatable switching between open and closed states, with the contact voltage transitioning between 5 V (OFF state) and 0 V (ON state). Another test was conduced to explore the minimum voltage required to maintain the ON state. In this test the electrostatic voltage was swept down from 80 V to 0 with a step of 1 V, and at 28 V the switch released. Fig. 6 shows the results.

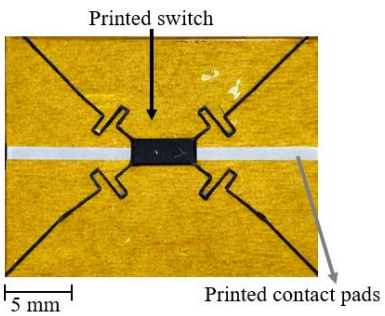

Fig. 3. Fabricated switch.

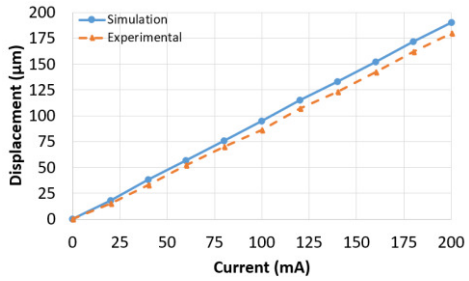

Fig. 4. Lorentz force displacement.

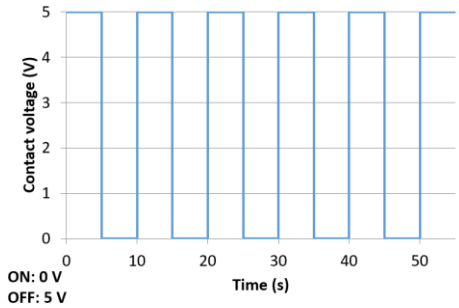

Fig. 5. Dynamic response of the switch.

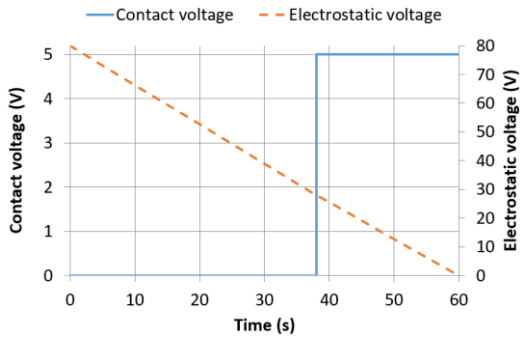

Fig. 6. Release voltage measurement.

References

[1] G. M. Rebeiz, RF MEMS: Theory, Design, and Technology, *John Wiley & Sons* (2004); doi: 10.1002/0471225282

[2] A. H. Espera Jr. et al., Advancing flexible electronics and additive manufacturing, Japanese *Journal of Applied Physics 61, SE0803 (2022)*; doi: 10.35848/1347-4065/ac621a

[3] X. Lv et al., A novel MEMS electromagnetic actuator with large displacement, *Journal of Sensors and Actuators A: Physical* 221, 22–28 (2015); doi: 10.1016/j.sna.2014.10.130

[4] J. Cheng et al., Recent design and application advances in micro-electro-mechanical system (MEMS) electromagnetic actuators, *Micromachines* 16, 670 (2025); doi: 10.3390/mi16060670

[5] D. Lagace et al., An extrusion printed Lorentz force actuated electromechanical relay, *Proc. of the International Conference on Micro and Nano Engineering (MNE)* (2025)

DOI 10.5162/eurosensors2026/4.4.4

Characterization of Biodegradable Magnetic Elastomers for Mechanical Stimulation in Organ-on-Chip Platforms

Feyza Pirim-Aslan[1], Elena Aprea[1], Mahmut Kamil Aslan[2], Stavros Stavrakis[2], Andrew deMello[2], Pasqualina M. Sarro[1], Clementine M. Boutry[1]
[1] Department of Microelectronics, Delft University of Technology, Delft, The Netherlands
[2] Institute of Chemical and Bioengineering, ETH Zurich, Switzerland
Corresponding Author's e-mail address: f.pirim@tudelft.nl

Summary:
This work reports the characterization of a biodegradable magneto-active elastomer composite based on poly(octamethylene maleate (anhydride) citrate) (POMaC) embedded with carbonyl iron particles (CIP). Biodegradable magneto-active elastomer composites with 10–40 wt.% CIP are characterized for morphology, magnetic response, mechanical behavior, and cytocompatibility. Processed into thin bilayer scaffolds, the optimized 20 wt.% composite delivers reproducible cyclic deformation with millimeter-scale tip displacement and ~7% tensile strain under 70 mT fields, with >97% cytocompatibility.

Keywords: magneto-active elastomer, biodegradable composite, POMaC, carbonyl iron particles, magnetic actuation

Background, Motivation and Objective

Magneto-active elastomers, soft polymers loaded with magnetic microparticles, are an attractive class of stimuli-responsive materials for wireless mechanical actuation. They enable contact-free, programmable deformation under externally applied magnetic fields and can be shaped into thin, compliant structures suitable for biological environments [1]. However, most magneto-active elastomers reported to date are based on non-degradable matrices such as PDMS or silicone rubbers, which limits their use in applications where transient mechanical function and eventual material resorption are desirable. Translating these materials into biodegradable formulations requires a polymer matrix that combines elasticity, processability, and cytocompatibility while accommodating high filler loadings without losing mechanical integrity. In this work, we characterize a biodegradable magneto-active composite based on POMaC loaded with carbonyl iron particles (CIP), focusing on the relationship between filler content, morphology, magnetic response, mechanical behavior, and cytocompatibility.

Description of the System

The composite is prepared by dispersing CIP within liquid POMaC pre-polymer and crosslinking the mixture into thin bilayer films (Fig. 1). The base layer consists of pure POMaC and provides a transparent, compliant substrate, while the upper layer incorporates the magnetically responsive POMaC–CIP composite. Patterned windows are introduced into the POMaC-CIP layer by laser processing to define the final scaffold geometry. SEM imaging confirms the homogeneous distribution of CIP particles within the POMaC matrix. Under an externally applied oscillating magnetic field, the embedded CIP particles experience a magnetic torque that translates into cyclic out-of-plane bending of the composite. This configuration removes the need for tethered or pneumatic actuation, while keeping the entire structure within a fully biodegradable material system.

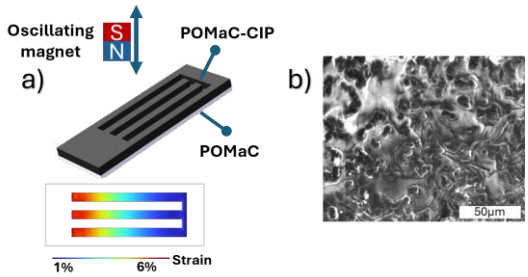

Fig. 1. (a) Bilayer POMaC–CIP composite scaffold and FEM strain distribution under a 70 mT magnetic field. (b) SEM morphology of the POMaC–CIP composite (scale bar: 50 µm).

Results

FEM simulations were used to evaluate the strain distribution within the bilayer composite under magnetic actuation (Fig. 1a). For the designed geometry, FEM predicts tensile strains of ~7% in the window region under a 70 mT magnetic field. The magnetic response of the

composite was characterized by SQUID magnetometry across the 10–40 wt.% CIP loading range (Fig. 2), confirming that the magnetization of the composite scales with CIP content while retaining the soft-magnetic, low-remanence behavior typical of carbonyl iron fillers.

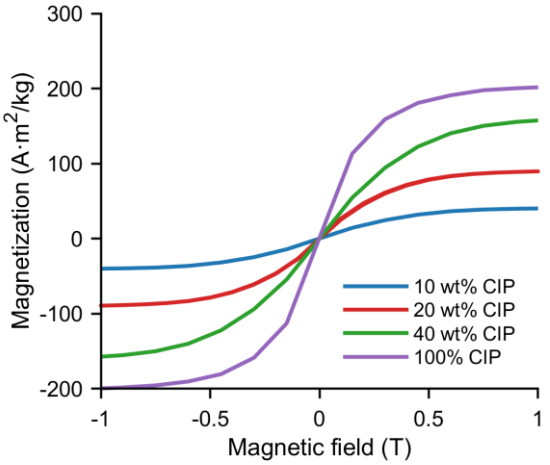

Fig. 2. SQUID magnetometry of POMaC–CIP composites at varying CIP loading.

Mechanical behavior of the composite was characterized by DMA across the 10–40 wt.% CIP loading range (Tab. 1). The Young's modulus increases from 9.5 kPa for pure POMaC to 130 kPa at 40 wt.% CIP, while strain at break decreases from 137.1% to 50.7%, consistent with the expected stiffening effect of rigid filler incorporation in an elastomer matrix. Among the tested formulations, 20 wt.% CIP provides the best compromise between magnetic responsiveness and elastomeric compliance and was selected for further evaluation. Cytocompatibility of the optimized formulation was assessed using LN229 cells exposed to POMaC and POMaC–CIP conditioned media, with viability remaining above 97% after 24 h, confirming that the composite is well tolerated under standard culture conditions (Fig. 3).

Tab. 1: DMA-derived Young's modulus and strain at break of POMaC–CIP composites at varying CIP loading

Sample	E(kPa)	Strain(%)
Pure POMaC	9.5	137.1%
10% POMaC-CIP	14.6	95.1%
20% POMaC-CIP	45	65.2%
40% POMaC-CIP	130	50.7%

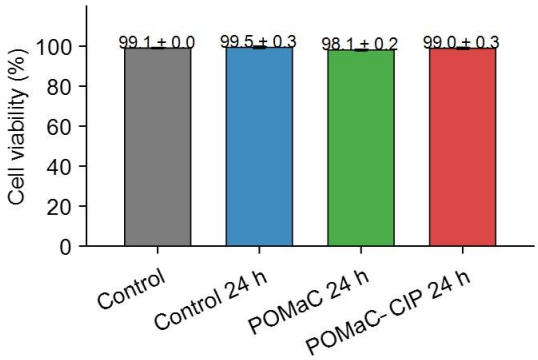

Fig. 3. Viability of LN229 cells exposed to POMaC and POMaC–CIP conditioned media for 24 h compared to untreated controls. Data are presented as mean ± SD.

Conclusions

This work characterizes a biodegradable magneto-active elastomer composite based on POMaC loaded with carbonyl iron particles. Combined SEM, SQUID magnetometry, and DMA characterization across 10–40 wt.% CIP loading establish the relationship between filler content, morphology, magnetic response, and mechanical behavior. The optimized 20 wt.% formulation maintains elastomeric compliance, exhibits cytocompatibility above 97%, and produces cyclic out-of-plane deformation with millimeter-scale tip displacement and ~7% tensile strain under low magnetic field (70 mT). These results establish the POMaC–CIP system as a wireless, biodegradable magneto-active elastomer suitable for further integration into compliant actuating structures.

References

[1] C. Gomez-Cruz, M. Fernandez-de la Torre, D. Lachowski, M. Prados-de-Haro, A. E. del Río Hernández, G. Perea, A. Muñoz-Barrutia, D. Garcia-Gonzalez, Mechanical and Functional Responses in Astrocytes under Alternating Deformation Modes Using Magneto-Active Substrates, Advanced Materials 36, 2312497 (2024); doi: 10.1002/adma.202312497.

Acknowledgements

This work was supported by the Netherlands Organ-on-Chip Initiative, an NWO Gravitation project (024.003.001) funded by the Ministry of Education, Culture and Science of the government of the Netherlands.

DOI 10.5162/eurosensors2026/5.1.1

Aptamer-based Optically Induced Dielectrophoresis for High-Resolution Single-Cell Phenotyping

J. Filippi[1], F. Corsi[2], P. Casti[1], A. Mencattini[1], G. Antonelli[1], A.Chamorro-Garcia[2], A. Wheeler[3], A. Idili[2], E. Martinelli[1]
[1] Department of Electronic Engineering, University of Rome Tor Vergata, Rome, Italy
[2] Department of Chemical Sciences and Technologies, University of Rome Tor Vergata, Rome, Italy
[3] Department of Chemistry, University of Toronto, Toronto, Canada
filippi@ing.uniroma2.it

Summary: Cellular heterogeneity is critical in oncology, where rare subpopulations drive tumor progression and therapy resistance. Here, we combine optically induced dielectrophoresis with receptor-specific aptamers to enhance single-cell resolution. Aptamers modulate membrane charge, amplifying sensitivity to receptor expression. By analyzing frequency-dependent cell dynamics using machine learning, this approach enables high-resolution phenotyping at the receptor level within cell subpopulations. The approach was validated on PC3 prostate cancer cells targeting αvβ3 and EGFR receptors.

Keywords: optically-induced dielectrophoresis, aptamers, lab-on-chip, machine learning, single-cell analysis.

Background, Motivation and Objective

Cellular heterogeneity plays a critical role in oncology, particularly at the single-cell level, where it drives functional variability among individual cells that collectively determine tumor behavior and treatment response. Conventional bulk analysis cannot resolve this complexity, as it averages signals and masks rare, clinically relevant subpopulations [1]. To address these limitations, optically induced dielectrophoresis (ODEP) has emerged as a powerful, label-free platform for single-cell manipulation and analysis. ODEP exploits light-patterned virtual electrodes projected onto a photosensitive surface to generate dynamic, non-invasive electric fields, enabling flexible and parallel control of individual cells [2]. Compared to conventional dielectrophoresis systems with fixed microelectrodes or optical tweezers requiring high-intensity laser exposure, ODEP provides a low-power, scalable, and minimally invasive alternative with reduced photodamage [2]. Recent advances combining ODEP with machine learning have enabled the extraction of single-cell dielectric fingerprints based on frequency-dependent electrokinetic behavior and cellular deformation, reflecting membrane structure and biochemical composition [3-4]. However, the discrimination of cellular subtypes remains challenging due to limited molecular specificity. Here, we propose an enhanced ODEP-based strategy based on the use of aptamers (artificially selected single-stranded oligonucleotides able to bind non-DNA targets) as receptors to selectively bind target cell surface receptors. The binding with the selected target allows aptamers to modulate the cell surface charge, introducing negative charges for the phosphate backbone of DNA strands. This increases the sensitivity and specificity of ODEP measurements, enabling the detection and amplification of functionally distinct subpopulations within heterogeneous samples. The proposed approach preserves global phenotypic information while enhancing receptor-level resolution, allowing broad characterization and high-resolution discrimination of cellular subtypes. It was validated using the castration-resistant prostate cancer cell line (PC3), targeting αvβ3 integrin and epidermal growth factor receptor (EGFR). Results demonstrate the capability of the system to resolve phenotypically distinct subpopulations, highlighting its potential for high-precision single-cell phenotyping and stratification at the single-receptor level.

Description of the New Method or Systems

Cells were detached and harvested, and aptamer binding was performed on cell suspensions in binding buffer [5]. A non-binding sequence was used as a negative control. After incubation, both targeted and control cells were washed with washing buffer [5] and subsequently resuspended in a low-conductivity buffer. Cells were then loaded into a lab-on-chip (LOC) device, where they were trapped and analyzed using the ODEP-based platform (see Fig.1a). An AC electric field was applied while

dynamic light patterns were projected onto a photosensitive (amorphous silicon) substrate, generating reconfigurable virtual electrodes. Cellular responses were evaluated using alternating rectangular light patterns at multiple frequencies (25–150 kHz) with a 10 Vpp amplitude. This enabled the acquisition of receptor-specific frequency-dependent response profiles, recorded via time-lapse microscopy (TLM) (see Fig.1b). Single-cell trajectories were extracted by tracking cell motion over time. Due to alternating electrode activation, cells exhibited frequency-dependent motion under ODEP. Both x- and y-direction components were used for spectral analysis. Feature extraction was performed using the wavelet scattering transform (WST), combined with machine learning algorithms for feature selection and classification, to identify the most discriminative patterns of single-cell dynamic (Fig.1c). To the best of our knowledge, this is the first platform integrating ODEP with selective aptamer-based functionalization of the cell membrane for high-resolution single-cell phenotyping. This approach enables probing of specific cell-surface receptor expression within a label-free electrokinetic framework. By combining receptor-targeted aptamer modulation with dielectric profiling, the proposed method enables the identification and amplification of distinct cellular subpopulations in heterogeneous samples, overcoming key limitations of conventional bulk assays and advancing single-cell analysis to receptor-level resolution.

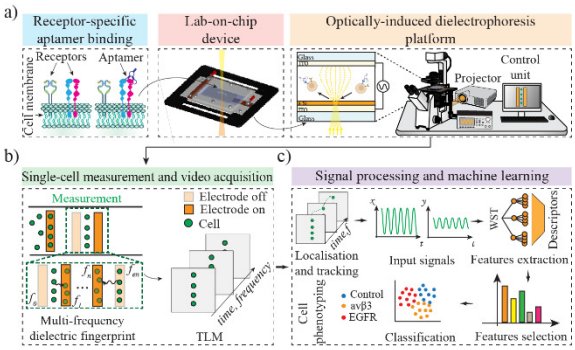

Fig. 1. Schematic representation of the proposed platform. (a) Aptamer-based cell targeting followed by resuspension in ODEP buffer and loading into LOC device for analysis. (b) Multi-frequency single-cell measurements with video acquisition. (c) Extraction of features from DEP-induced cell motion, including WST-based parameters, was used to build the classification model[4].

Results

Fluorescence images of the target aptamers were acquired to assess their binding to the receptor. The aptamers receptors modified with a fluorophore at their 5'-end, allowed direct visualization of their localization, thereby confirming their specificity and proper interaction with the target receptor. As shown in Fig. 2a, control aptamer does not exhibit specific binding and is effectively removed upon washing with the washing buffer. Differently, both aptamers, anti-avβ3 (Fig. 2b) and anti-EGFR (Fig. 2c), exhibit specific and stable binding to their respective targets. Fig. 2d shows the confusion matrix for the linear discriminant analysis (LDA) classification model, validated using Monte Carlo cross-validation (80% training and 20% test with 100 repetitions), across four classes, including the control group representing untreated cells without any specific or non-specific aptamer binding. As shown in the LDA scores plot in Fig. 2e, based on the first two discriminant directions, the two control groups appropriately overlap, whereas the two aptamer-treated groups are clearly separated. This result confirms the proposed approach's ability to recognize binding specificity and highlights its high-resolution capability.

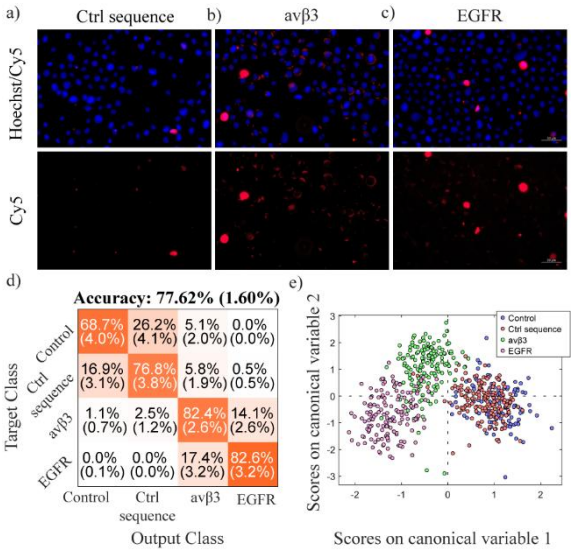

Fig. 2. Fluorescence images of PC3 cells treated with (a) control sequence, (b) anti-αVβ3 aptamer, and (c) anti-EGFR aptamer. Nuclei were stained with Hoechst, and aptamers were labeled with Cy5. Magnification 20x, scale bar: 50 µm. (d) Confusion Matrix of the LDA classification model with average accuracy (and standard deviation). (e) Scores on the canonical variable of the LDA model.

References

[1] S.J. Altschuler et al., *Cell* 141.4 (2010): 559-563; doi: 10.1016/j.cell.2010.04.033

[2] P. Y. Chiou, et al., Nature 436.7049: 370-372 (2005); doi: 10.1038/nature03831.

[3] J. Filippi, et al., *Small Methods*, 8(8), n. 2300923 (2024); doi: 10.1002/smtd.202300923.

[4] J. Filippi, et al., *Cyborg and Bionic Systems 6, 0234 (2025);* doi: *10.34133/cbsystems.0234.*

[5] X. Teng, et al., *Analytical Chemistry* 95.33 (2023): 12406-12418:doi:10.1021/acs.analchem.3c01995

DOI 10.5162/eurosensors2026/5.1.2

Multiplexed analysis of extracellular vesicles from single cells in an array with opposing microwells

Lucien R. Stöcklin[1], Erwin Kortus[1], Petra S. Dittrich*
[1]ETH Zürich, Department Biosystems Science and Engineering, CH-4056 Basel, Switzerland
*Corresponding Author's email Address: petra.dittrich@bsse.ethz.ch

Summary:
Single-cell analysis can help to resolve the heterogeneous and complex biogenesis of extracellular vesicles (EVs), thereby improving our understanding of EVs' role in signalling and cell-cell communication. Here, we introduce a method to detect up to five membrane proteins in EVs secreted from single cells. Two microwell arrays, one for single-cell trapping and another one for capturing fluorescently barcoded beads pre-functionalized with EV-capture antibodies, are aligned during incubation. Then, membrane proteins of bead-bound EVs are analysed by immunostaining for four breast-derived cell lines.

Keywords: single cell, extracellular vesicles, microfluidics, sandwich immunoassay, epifluorescence microscopy.

Introduction

Extracellular vesicles (EVs) mediate intercellular communication between a parental cell and a recipient cell, both in healthy and pathological states. In the context of cancer, EVs can promote metastasis, tumour vascularization, suppress the local immune response, or contribute to treatment resistance via exiting pathways [1]. EV phenotypes are highly heterogeneous due to the various biogenesis and secretion pathways. To reduce complexity in the analysis of EVs, recent efforts focused on the development of single-cell EV analysis methods [2].

Here, we present a method, where we align two microwell arrays for the multiplexed analysis of EVs by immunostaining. We co-detect five distinct EV membrane proteins from the breast cancer cell line MDA-MB-231. Moreover, we compare EV secretions from four distinct breast cell lines.

Microfluidic Platform Description

The microfluidic device builds on our previous work [3]. It consists of a polydimethylsiloxane (PDMS) layer with over 2700 square wells (60x60x60 µm^3) for capturing individual cells, aligned with an upper array made of glass, which contains smaller microwells to trap paramagnetic beads functionalized with specific EV capture antibodies (Fig. 1). The intensity ratios between two far-red fluorophores serves as barcode and enables to assign a bead to the specific EV capture antibody (Fig. 2). All captured EVs are detected afterwards with another antibody targeting the tetraspanin CD9 which is labelled with the fluorescent protein phycoerythrin (PE).

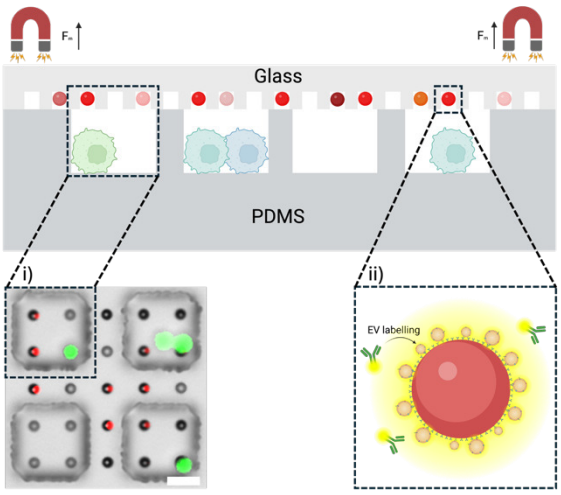

Fig. 1. Schematic of the microfluidic device during incubation. i) Microscopy image with cells (green) and beads (red). Scale bar = 60 µm. ii) Bead-bound EVs are labelled with a phycoerythrin-conjugated detection antibody via a two-step sandwich immunoassay.

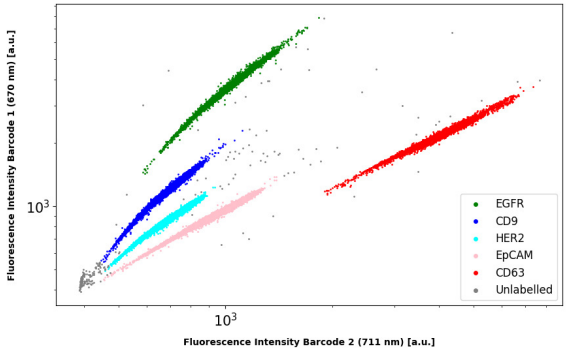

Fig. 2. Bead classification, where each bead is assigned to a specific EV capture antibody (Procartaplex™).

The experimental workflow consists of coating both arrays with a 1% bovine serum albumin

(BSA) solution, before loading the beads and cells. Both arrays are then aligned and clamped to seal the individual microwells. Following a 16-hour incubation, the arrays are unclamped, and bead-bound EVs are detected by addition of the PE-labelled antibody. Images of the two microwell arrays are acquired with an epifluorescence microscope, then processed and analysed with an in-house Python-based software. Thereby, the average fluorescence intensity measured on the beads in one well can be assigned to the corresponding co-incubated single cell, stained with cellTracker® Green. Wells with no cells, dead cells or multiple cells are discarded.

Results & Discussion

First, the platform was used to detect five distinct EV phenotypes from triple negative breast cancer cell line MDA-MB-231 (Fig. 3). Secreted EVs were selectively immobilised via one of five membrane proteins: tetraspanins (CD9, CD63), HER2, EGFR or EpCAM. All EVs were detected via anti-CD9 detection antibody. The overall high intercellular heterogeneity and larger signals observed for tetraspanin-positive EVs is aligned with existing literature [4]. The lower fluorescent signals for EpCAM-positive EVs confirms the mesenchymal phenotype of MDA-MB-231 cells, and the low level of HER2 is in accordance with prior observation [5].

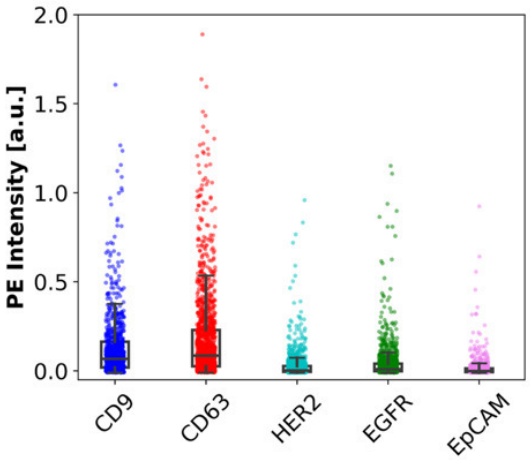

Fig. 3. EV detection from MDA-MB-231 cells. Secreted EVs were immobilized via one of five capture antibodies and labelled with CD9 detection antibody.

Last, EVs from different breast cell types were compared: one benign breast cell line MCF-10A and three breast cancer lines MCF-7, SkBr3 and MDA-MB-231. EVs were captured on the beads via CD63 and detected via anti-CD9 detection antibody (Fig. 4). Significant differences in average fluorescence intensity can be observed between the cell types. The data confirm the co-expression of the tetraspanins CD63 and CD9 in all four cell types, with high levels in at least one of the proteins for MCF-7 and MDA-MB-231. The signal variation in all data reflect the general heterogeneity of EVs with regard to protein levels.

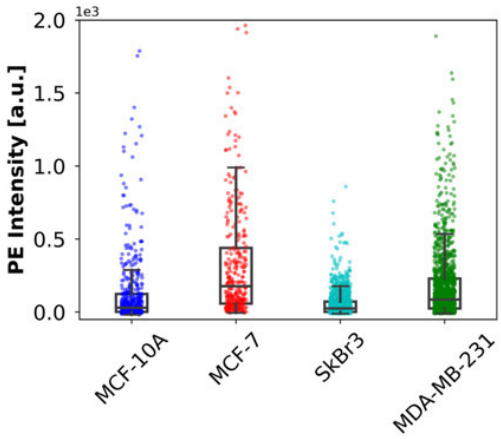

Fig. 4. EV detection from four breast cell lines. Secreted EVs were immobilized via CD63 capture antibody and labelled with CD9 detection antibody.

Conclusions

We present a microwell array for the analysis of extracellular vesicles derived from single cells. The use of barcoded functionalised beads enables to measure distinct EV phenotypes on a single device. In future work, we intend to investigate the changes in EV secretions upon drug treatment to evaluate the potential of EVs as a biomarker for therapy success.

References

[1] R. Xu, A. Rai, M. Chen, W. Suwakulsiri, D. W. Greening, R. J. Simpson, Extracellular vesicles in cancer — implications for future improvements in cancer care, *Nature Reviews Clinical Oncology* **15**, 617-638 (2018); doi: 10.1038/s41571-018-0036-9.

[2] J. M. Nikoloff, M. A. Saucedo-Espinosa, A. Kling, P. S. Dittrich, Identifying extracellular vesicle populations from single cells, *Proceedings of the National Academy of Sciences of the United States of America* **118**(38), e2106630118 (2021); doi: 10.1073/pnas.2106630118.

[3] C. L. Dietsche, L. R. Stöcklin, R. Strutt, P. S. Dittrich, Nested Nanowell Arrays for High-Throughput Quantitative Analysis of Cytokines from Single Macrophages, *ACS Nano Medicine* (2026); doi: 10.1021/acsnanomed.5c00149.

[4] L. R. Stöcklin, C. L. Dietsche, P. S. Dittrich, A High-Density Microchamber Array for the Analysis of Extracellular Vesicles Derived from Single Cells under Drug Treatment, *Analytical Chemistry* **98**(2), 1460-1469 (2026); doi: 10.1021/acs.analchem.5c0562

[5] Y. Peng, Z. Wu, Z. Pang, L. Zhang, D. Song, F. Liu, Y. Li, T. Lin, Manufacture and evaluation of a HER2-positive breast cancer immunotoxin 4D5Fv-PE25, Microbial Cell Factories 22, 100 (2023); doi: 10.1186/s12934-023-02115-0.

DOI 10.5162/eurosensors2026/5.1.3

Microfluidic Synthesis of Piezoelectric-Magnetic Composite Microbeads for Wireless Neural Stimulation

Tao Zhang[1], Arnaud Bertsch[1], Jiabei Luo[2], Yuyan Su[2], Yujia Zhang[2], Juergen Brugger[1]
[1]Microsystems Laboratory, Ecole Polytechnique Federale de Lausanne, 1015 Lausanne, Switzerland,
[2]Laboratory for Bio-Iontronics, Ecole Polytechnique Federale de Lausanne, 1015 Lausanne, Switzerland
tao.zhang@epfl.ch

Summary:
This work presents a microfluidic approach for manufacturing piezoelectric–magnetic composite microbeads for wireless neural stimulation. By integrating particle-laden droplet generation with UV polymerization, uniform functional microbeads with a diameter of 100 µm are produced at a generation frequency of about 20 Hz. The system combines magnetic steering and ultrasound-triggered piezoelectric response, enabling remotely controlled actuation. The approach offers a scalable route toward multifunctional microbead-based systems for bioelectronic applications.

Keywords: droplet microfluidics, composite beads, piezoelectric materials, magnetic particles, neural stimulation

Background, Motivation and Objective

Wireless neural stimulation has emerged as a promising alternative to conventional electrode-based interfaces, offering reduced invasiveness and improved spatial control compared to conventional tethered electrode-based systems [1]. Although the piezoelectric effect is well known, recent studies have shown that piezoelectric nanomaterials can transduce ultrasound-induced mechanical energy into electrical signals sufficient to stimulate neuronal activity. [2]. Integrating magnetic components in such materials further enables remote positioning and guidance of such stimulators [3]. However, such approaches typically rely on high particle concentration suspensions (e.g., in the mg/mL range) to achieve a reliable and sufficiently strong response to external fields such as ultrasound, due to their stochastic distribution and activation at the microscale.

Droplet microfluidic technologies enable deterministic control over droplet generation and precise encapsulation of functional materials, providing a scalable route to engineer uniform, multifunctional micro-components with well-defined composition and architecture [4], [5]. In parallel, our previous work on particle-laden inks demonstrated that particle concentration strongly influences droplet formation through coupled effects on viscosity and interfacial tension, enabling controlled generation of uniform microbeads [6]

Building on this foundation, the objective of this work is to develop a microfluidic platform for producing composite mirobeads containing both piezoelectric ($BaTiO_3$, 200 nm) and magnetic (Fe_3O_4, 100 nm) particles, targeting applications in wireless neural stimulation.

Description of the New Method or System

We propose a microfluidic-based fabrication approach for generating polymerizable droplets encapsulating multiple functional particles. An acrylate-based resin (PEGDA 250) containing 5 wt% photoinitiator (DMPA) is loaded with 20 wt% piezoelectric particles and 5 wt% magnetic nanoparticles, followed by ultrasonication for 30 seconds to ensure homogeneous dispersion. The resulting suspension is then processed using a flow-focusing PDMS microfluidic device.

The system leverages insights from particle-laden droplet dynamics: the particle concentration modifies both viscosity and interfacial tension, which together determine the capillary number and govern droplet formation regimes [6]. By tuning flow conditions, stable dripping regimes are achieved, producing highly uniform droplets.

These droplets are collected in a glass vial together with the continuous liquid phase, and then polymerized using UV irradiation (365 nm, 114 mW/cm^2, exposure time about 2 min) to form solid composite beads. The resulting particles combine magnetic responsiveness for spatial control and piezoelectric functionality for ultrasound-triggered electrical output. Compared to surface-coating approaches [3], this method allows the incorporation of functional particles

throughout the bead volume, resulting in higher particle loading per bead and potentially leading to an enhanced response under stimulation.

Results

Microfluidic processing enabled the generation of monodisperse composite droplets that were subsequently solidified into spherical microbeads, as shown in Fig. 1 (A, B). Consistent with prior findings, stable dripping regimes produced highly uniform bead sizes, while increased particle loading influenced droplet size and formation behavior. In Fig. 1 (C-F), scanning electron microscopy (SEM) and energy dispersive X-ray spectroscopy (EDX) confirm homogeneous distribution of $BaTiO_3$ and Fe_3O_4 nanoparticles on the bead surface.

The beads exhibit magnetic responsiveness, allowing controlled motion and positioning under external magnetic fields generated by five permanent magnets (5 mm in diameter), including translation in Fig. 2 (A, B) and rotation in Fig. 2 (C, D). While piezoelectric actuation has not yet been experimentally characterized, the incorporation of piezoelectric nanoparticles is designed to enable ultrasound-induced electrical responses. Together, these features establish a foundation for future development of localized, wireless neural stimulation systems.

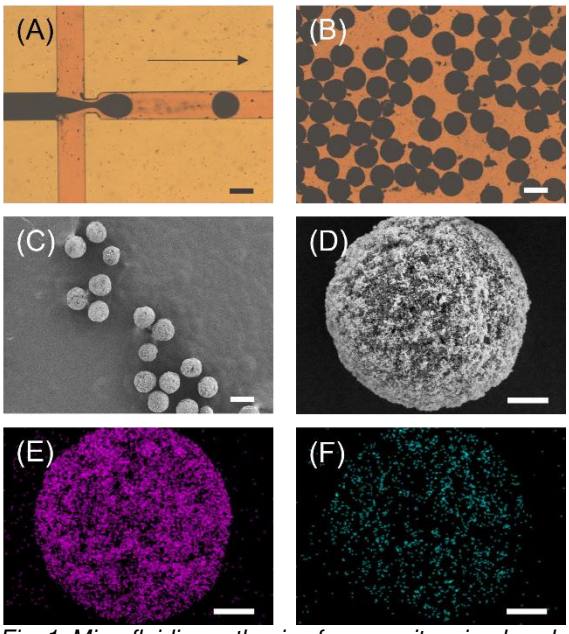

Fig. 1. Microfluidic synthesis of composite microbeads encapsulating 20 wt% piezoelectric ($BaTiO_3$) and 5 wt% magnetic (Fe_3O_4) particles. (A) Optical image of the microfluidic junction illustrating droplet generation in the dripping regime. (B) Droplets collected prior to UV curing. (C-D) SEM images of the solidified beads. (E, F) Elemental mapping indicating the spatial distribution of barium and iron on the bead surface. Scale bars: (A-C) 100 µm, (D-F) 20 µm.

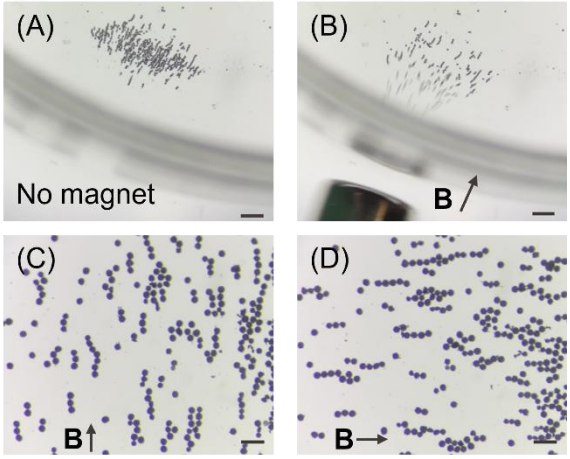

*Fig. 2. Magnetic actuation of composite microbeads (approximately 300 beads) in water. (A, B) Beads are attracted toward a permanent magnet placed outside a glass vial. (C, D) Beads rotate in response to the rotation of a nearby permanent magnet. Arrows next to **B** indicate the direction of the applied magnetic field. Scale bars: (A, B) 1 mm; (C, D) 500 µm.*

Conclusion

This study demonstrates a microfluidic strategy for fabricating multifunctional piezoelectric–magnetic composite beads. By combining controlled droplet generation with particle-laden ink design, the approach enables precise tuning of bead size, composition, and functionality.

The integration of magnetic guidance and piezoelectric activation offers a promising pathway toward wireless, minimally invasive neural interfaces. More broadly, this work establishes a foundation for microfluidic-based additive manufacturing of functional micro-objects with applications in bioelectronics and smart materials. The approach enables continuous production with high yield and uniformity at a throughput of ~20 Hz per channel, and is inherently scalable via parallelization of microfluidic modules to further increase production capacity.

Acknowledgements

Authors acknowledge funding from the Swiss National Science Foundation (SNSF, grant number: 219165). We thank Prof. Véronique Michaud and Jean-Baptiste Desbrest for their $BaTiO_3$ particles.

References

[1] I. Bok *et al.*, “Wireless agents for brain recording and stimulation modalities,” *Bioelectron Med*, vol. 9, no. 1, p. 20, Sep. 2023, doi: 10.1186/s42234-023-00122-5.

[2] A. Cafarelli *et al.*, “Piezoelectric Nanomaterials Activated by Ultrasound: The Pathway from Discovery to Future Clinical Adoption,” *ACS Nano*, vol. 15, no. 7, pp. 11066–11086, Jul. 2021, doi: 10.1021/acsnano.1c03087.

[3] M. Han *et al.*, “Janus microparticles-based targeted and spatially-controlled piezoelectric neural stimulation via low-intensity focused ultrasound,” *Nat Commun*, vol. 15, no. 1, p. 2013, Mar. 2024, doi: 10.1038/s41467-024-46245-4.

[4] A. Ofner *et al.*, “High-Throughput Step Emulsification for the Production of Functional Materials Using a Glass Microfluidic Device,” *Macromolecular Chemistry and Physics*, vol. 218, no. 2, p. 1600472, 2017, doi: 10.1002/macp.201600472.

[5] Y. Cao *et al.*, “Permanent magnetic droplet–derived microrobots,” *Science Advances*, vol. 11, no. 28, p. eadw3172, Jul. 2025, doi: 10.1126/sciadv.adw3172.

[6] T. Zhang, S. Jiguet, A. Bertsch, and J. Brugger, “Microfluidic synthesis of alumina particle-laden beads via capillary number tuning for varying particle concentrations,” *Microfluid Nanofluid*, vol. 30, no. 6, p. 49, Jun. 2026, doi: 10.1007/s10404-026-02905-z.

DOI 10.5162/eurosensors2026/5.1.4

Label-free isolation of single cells for IVD cell therapy using impedance flow cytometry

M. Favrod-Coune[1,2,3], A. Stirnimann[1,2], O. Guenat[3], F. Ille[1] and P. Eberle[1]
[1] Lucerne University of Applied Sciences, Switzerland
[2] Graduate School for Cellular and Biomedical Sciences, University of Bern, Switzerland
[3] University of Bern, ARTORG Center, Switzerland
patric.eberle@hslu.ch

Summary: Impedance flow cytometry (IFC) is an emerging label-free, high-throughput sorting method that reads cell-specific electrical signatures across frequencies. This work demonstrates the feasibility of isolating presumptive nucleus pulposus progenitor cells (NPPC) and benchmarks its performance to FACS. Results suggest that IFC accurately identifies and sorts NPPCs, representing a significant advancement for cell-based therapies targeting intervertebral disc degeneration.

Keywords: Label-free sorting, progenitor cells, impedance flow cytometry, microfluidics, intervertebral discs

Introduction

Intervertebral disc (IVD) degeneration is a primary cause of low back pain, a global health issue affecting around 7% of the population [1] and costing billions to society [2]. Existing interventions, such as tissue resection and spinal fusion fail to regenerate disc tissue. Population aging and limitations of current treatments motivate the development of alternative therapies.

While nucleus pulposus cells (NPC), which reside within the inner region of IVD, exhibit limited regenerative capacity, their progenitor cells (NPPC) are believed to play a pivotal role in developing novel therapies [3], provided they can be effectively isolated. NPPC differ from mature NPC by expressing the Angiopoietin-1 receptor, also called Tie2.

Single-cell isolation is essential in biology, biotechnology, precision medicine [4]. While fluorescence-activated (FACS) and magnetic-activated cell sorting (MACS) are well established, high-throughput sorting methods, they present significant drawbacks: expensive reagents, time-consuming labeling protocols, and the absence of specific markers for certain cell types [5], limiting their applicability in cell therapy [6]. Several label-free alternatives are under development, including impedance flow cytometry (IFC), which discriminates cells based on electrical properties across multiple frequencies.

This study assesses the potential of IFC for NPPC isolation compared to FACS, evaluating the impact of both technologies on cell viability and phenotype.

Methods

A previously developed impedance flow cytometer [7], utilizing a transimpedance amplifier, FPGA, and co-planar electrodes, was coupled with a piezo-based sorting mechanism [8, 9] to enable single-cell sorting based on the measured electrical characteristics of cells.

Bovine coccygeal tails obtained from a local abattoir provided nucleus pulposus tissue from proximal discs, which was minced, sequentially digested with pronase and collagenase II, then filtered and washed with PBS. The resulting NPC were then suspended in 1x PBS at a concentration of 1M/mL. Electrical characteristics were measured at 1 and 10 MHz with a 1.2 V peak-to-peak excitation. Initially, Tie2+ and Tie2- populations were isolated via FACS using the antibody bs-1300R-BF488 (Bioss), and their electrical signatures were compared to raw bovine NPCs (Fig. 1, 2). Subsequently, the impacts of FACS, IFC, and the handling after the IFC (dillution, centrifugation) on the sorted populations were investigated with a FACS (Table 1) and the distributions compared to the initial FACS. Finally, the IFC system sorted bovine NPCs, and the resulting populations were analyzed by FACS. These latter results are currently under evaluation and will be presented at the conference.

Results

Impedance analysis of bovine NPCs sorted by FACS revealed that both Tie2+ and Tie2– cells form clusters that partially overlap (Fig. 1). However, with the data of both frequencies, a quadratic support vector machine (SVM) achieves an identification accuracy exceeding 90% (Fig. 2). Furthermore, both Tie2+ and Tie2- clusters were discernible within the unsorted unstained population, providing strong evidence that these subpopulations can be resolved via IFC.

Analysis of the IFC sorter's impact (Table 1) indicated minimal effects on the cell population: post-sorting, the proportion of Tie2+ cells decreased by approximately 9.3%, with 7.5% attributable to sample preparation artefacts (di-

DOI 10.5162/eurosensors2026/5.1.4

Tab. 1: Changes of the distribution of Tie2- / Ti2+

Process	Tie2-	Tie2+
FACS	+34.9%	-28.0%
IFC	+10.8%	-1.8%
Handling after IFC	-16.4%	-7.5%

lution, centrifugation, pipetting) or temperature changes.

Conversely, FACS exhibited more pronounced effects: from an initial Tie2+ percentage of 38% following the first sort, only 10% were recovered upon re-analysis. It is suspected that some of the stained cells adhered to the tube or were lost during preparation.

These results suggest that IFC can effectively sort label-free nucleus pulposus progenitor cells with less cell loss than FACS. Although currently lower-throughput than FACS, IFC enables label-free isolation that facilitates downstream analyses and accelerates cell therapy adoption.

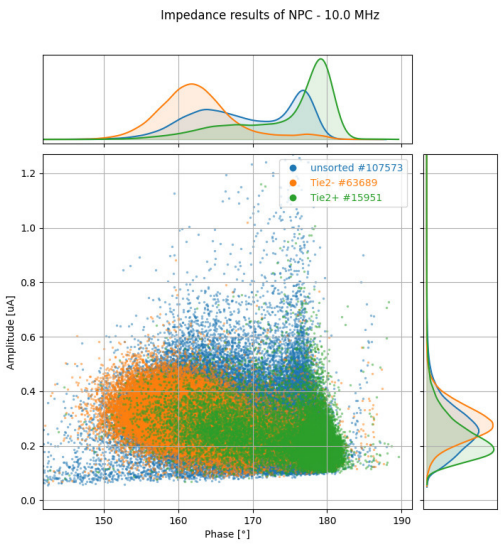

Fig. 1: Scatter plot of cell impedances at 10 MHz of unsorted bovine NPC and sorted Tie2-/Tie2+ bovine NPC. Cells were obtained from four different animals. (#nb of cells)

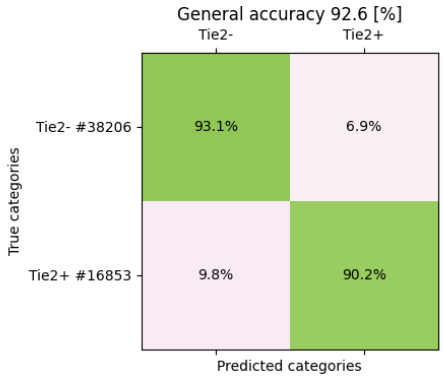

Fig. 2: Confusion matrix given by a quadratic SVM algorithm. Cells were obtained from two different animals. (#nb of cells)

References

[1] A. Wu, L. March, X. Zheng, J. Huang, X. Wang, J. Zhao, F. M. Blyth, E. Smith, R. Buchbinder, and D. Hoy, "Global low back pain prevalence and years lived with disability from 1990 to 2017: Estimates from the global burden of disease study 2017," *Annals of Translational Medicine*, vol. 8, p. 299–299, Mar 2020.

[2] D. Chang, A. Lui, A. Matsoyan, M. M. Safaee, H. Aryan, and C. Ames, "Comparative review of the socioeconomic burden of lower back pain in the united states and globally," *Neurospine*, vol. 21, p. 487–501, Jun 2024.

[3] J. Schol, L. Ambrosio, C. Ruiz-Fernandez, L. Schlagenhof, C. Voskamp, L. T. Laagland, E. Matsushita, H. Soma, T. Warita, G. Vadalà, and et al., "Tie2-positive cells in the nucleus pulposus with a purpose: The who, what and why," *Journal of Biomedical Science*, vol. 33, Mar 2026.

[4] C. Wyatt Shields IV, C. D. Reyes, and G. P. López, "Microfluidic cell sorting: a review of the advances in the separation of cells from debulking to rare cell isolation," *Lab Chip*, vol. 15, pp. 1230–1249, 2015.

[5] M. Xavier, R. O. Oreffo, and H. Morgan, "Skeletal stem cell isolation: A review on the state-of-the-art microfluidic label-free sorting techniques," *Biotechnology Advances*, vol. 34, no. 5, pp. 908–923, 2016.

[6] C. A. Lazarski and P. J. Hanley, "Review of flow cytometry as a tool for cell and gene therapy," *Cytotherapy*, vol. 26, pp. 103–112, Feb. 2024.

[7] M. Favrod-Coune, O. Guenat, and P. Eberle, "Sensitive cell identification in impedance flow cytometry using optimized dielectric buffer properties and low cost microchannels," in *EUROSENSORS XXXVII*, 2025.

[8] S. Sakuma, Y. Kasai, T. Hayakawa, and F. Arai, "On-chip cell sorting by high-speed local-flow control using dual membrane pumps," *Lab Chip*, vol. 17, pp. 2760–2767, 2017.

[9] K. Zhang, Z. Xia, Y. Wang, L. Zheng, B. Li, and J. Chu, "Label-free high-throughput impedance-activated cell sorting," *Lab on a Chip*, vol. 24, no. 20, p. 4918–4929, 2024.

DOI 10.5162/eurosensors2026/5.1.5

Microdroplet arrays: Printing and analyzing liquid sample at high throughput

Petra S. Dittrich
ETH Zurich, Department Biosystems Science and Engineering, Schanzenstrasse 44, 4056 Basel, Switzerland
petra.dittrich@bsse.ethz.ch

Abstract:

High throughput analysis is the ultimate challenge in many applied fields across the life sciences such as biotechnology, single-cell analysis, drug screening or screening for reaction conditions. The key parameters are the number of samples that can be analysed, and the time needed for the analysis. The current gold standard for high-throughput screening are microtiter plates, which are highly standardized platforms that enable parallel analysis of commonly 96, 384 or even 1536 samples. We overcome inherent limitations of these classical platforms by employing microdroplet-based methods on an open platform.[1] Thousands of aqueous nL-droplets are deposited on a custom-made glass slide with a defined hydrophilic-hydrophobic surface pattern. The droplets are covered by fluorinated oil and remain stable for several days. We employ optical microscopy for droplet assessment as well as MALDI-MS imaging for analysis of the droplet content. In this presentation, I will show recent technological developments of the printing mechanism, where we control the size of the droplets, form chemical gradients and add compounds in defined patterns and at a defined time. Various applications will be discussed, such as encoding chemical information [2], label-free kinetic analysis of enzymatic reactions [3], microbial growth and antibiotic drug testing [4].

Keywords:

Droplet microfluidics, droplet arrays, high-throughput analysis, drug screening, label-free analysis

References:

[1] R. Strutt, B. Xiong, V. F. Abegg, P. S. Dittrich: Open Microfluidics: Droplet Microarrays as Next Generation Multiwell Plates for High Throughput Screening, *Lab Chip* 24, 1064-1075 (2024); doi: 10.1039/D3LC01024D

[2] M. Breitfeld, R. Strutt, L. Fröhlich, C. L. Dietsche, S. Bargfrede, P. S. Dittrich: Liquid-in-Liquid Prints: High-Density Biochemically Encoded Information Preserved in Microdroplet Arrays, *Adv. Mat.* 38, e16338 (2026); doi: 10.1002/adma.202516338

[3] M. Breitfeld, C. L. Dietsche, M. A. Saucedo-Espinosa, S. F. Berlanda, P. S. Dittrich: Ultrafast formation of microdroplet arrays with chemical gradients for label-free determination of enzymatic reaction kinetics, Small 21, 2410275 (2025); doi: 10.1002/smll.202410275

[4] B. Xiong, M. Breitfeld, P. S. Dittrich: Two-Layer Droplet Arrays Enable Dynamic Manipulation of Cell Microenvironment During High-Throughput Bacterial Cultivation, *Small Meth.* 9, e01417 (2025); doi: 10.1002/smtd.202501417

DOI 10.5162/eurosensors2026/5.2.1

Bioelectronic Sensors for Understanding Plant Stress Responses

Eleni Stavrinidou
Laboratory of Organic Electronics, Department of Science and Technology, Linköping University, 601 74, Norrköping, Sweden
eleni.stavrinidou@liu.se

Abstract:

Climate change and a growing global population call for plants with enhanced tolerance to biotic and abiotic stress, as well as increased productivity. In this talk, I will present our recent advances in interfacing bioelectronic tools with plants, with the aim of enabling new discoveries and expanding possibilities in plant science. Electrical signals in plants mediate long-distance communication and are closely linked to stress responses. We have developed conformable multielectrode arrays based on organic electronics for large-scale, high-resolution plant electrophysiology. This technology has enabled precise spatiotemporal mapping of fast electrical signals associated with plant movement. We are now extending this approach to other plant species to advance the mechanistic understanding of plant responses to environmental stress. In parallel, we have developed a multimodal sensing platform that correlates electrical signals with ionic and biochemical processes, allowing us to investigate the role of specific genes in regulating and coordinating these signaling pathways. Beyond monitoring, we also explore the use of electric fields to actively stimulate plant processes. I will present our recent work on bioelectronic platforms that not only deepen our understanding of plant biology but also have the potential to contribute to more sustainable food production.

Keywords:

plants, agriculture, electrophysiology, stress signaling

DOI 10.5162/eurosensors2026/5.2.2

Measurement Method for Determining Solvent Exchange in Aerogels During Realization and Functionalization

Jan kleine Piening[1,2], Khyati Tembekar[1], Tim M. de Rijk[1,2], Sander van den Driesche[1,2,3], Michael J. Vellekoop[1,2,3]
[1]Institute for Microsensors, -actuators and -systems (IMSAS), Universität Bremen, Bremen, Germany
[2]Microsystems Center Bremen (MCB), Universität Bremen, Bremen, Germany
[3]MAPEX Center for Materials and Processes, Universität Bremen, Bremen, Germany
klpiening@uni-bremen.de

Summary:
In this work a measurement method for determining solvent exchange in an aerogel-filled microfluidic channel is investigated. For this purpose, the dye Eosin Y is applied to examine the diffusion using a fluorescence microscope. The measurements confirm the suitability of the measurement method for determining the diffusion behavior in aerogel. This enables the optimization of solvent exchange after the aging step of the sol-gel process and will facilitate the use of aerogel-based sensors in microfluidic channels.

Keywords: aerogel, diffusion, solvent exchange, microfluidic channel, MEMS

Background, Motivation and Objective

Aerogels refer to a group of materials characterized by their high porosity, low density, and low thermal conductivity [1]. Aerogels typically have a porosity of 80 % to 99.8 %, a specific surface area of 500 m^2/g to 1200 m^2/g, and a density of 0.003 g/cm to 0.5 g/cm. Silica-based aerogels are the most commonly used [2]. The use of aerogels as a material for sensors offers great potential. For example, gas sensors or bio sensors often rely on the use of sensing materials. Due to the high specific surface area and highly interconnected porous structure aerogels are attractive as a support material for these. The Agglomeration of the sensing material that is being taken up into the aerogel can be reduced by the porous network. Furthermore, the high porosity ensures that the active sites of the sensing material remain accessible for the stimuli [3]. In the sol-gel process for silica aerogels, one of the most important steps is the aging process. This process strengthens the network, resulting in a stable porous network [2]. After this process, different solvents are regularly replaced to achieve specific properties for the aerogel [4]. However, in order to enable the integration of aerogels in chips, there is a lack of fundamental research on the diffusion of solvents in aerogels. In this work the solvent exchange in aerogel within a microfluidic channel is investigated.

Description of the New Method or System

The silica aerogels used in this work were synthesized using the sol-gel process. This process is done in two phases. First TEOS, ethanol, and water are mixed. To start the hydrolysis HCL is added to this mixture. After 1.5 h, ammonia is added to initiate condensation, causing the gelation. After gelation is achieved which takes around 50 min, the gel is filled into a microfluidic channel [4]. The used channels have a width of 1.6 mm and consist of a glass-silicon-glass structure with two openings in the top glass wafer. The aerogel in the channel was aged afterwards and kept in a beaker filled with ethanol. To be able to investigate the diffusion in a porous silica aerogel structure the dye Eosin Y from Merck is used. This dye has fluorescent properties which makes is possible to investigate the diffusion using a fluorescence microscope. For the measurement, the chip filled with aerogel was placed in a beaker with an Eosin Y ethanol solution. The aerogel was loaded with the dye for 30 min and then put into a Petri dish filled with ethanol without the dye to avoid evaporation of the liquid during the measurement. This Petri dish is then placed under a fluorescence microscope and images were automatically take every 5 min. The camera settings were kept constant to avoid any influence from changing settings.

Results

In Fig. 1 a selection of images illustrating the diffusion into the aerogel is shown. Time intervals of 30 min, 45 min, and 5 h were selected. The reason for this is that the diffusion is significantly faster at the beginning and slows down as the dye concentration increases. After

approximately 5 h, the color is saturated, and no further change in intensity can be observed. It is visible, that the green color of the Eosin Y dye is not evenly distributed across the channel. The reason for this could be the inhomogeneity of the aerogel structure. The porous network is denser in some areas than in others, resulting in slightly different diffusion rates.

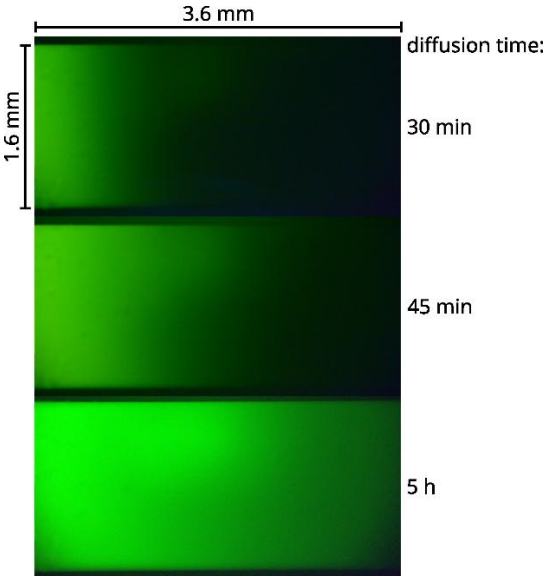

Fig. 1. Diffusion of Eosin Y in ethanol into aerogel in a 1.6 mm wide and 3.6 mm long microfluidic channel.

Using the images from the measurements the intensity of the green color can be extracted. The intensity is normalized to the maximum measured value using an 8-bit color profile. The resulting intensity profile can be seen in Fig. 2. The figure shows the average of the green color across the entire channel width. As the aerogels were loaded for 30 min the first measurement was taken at 30 min.

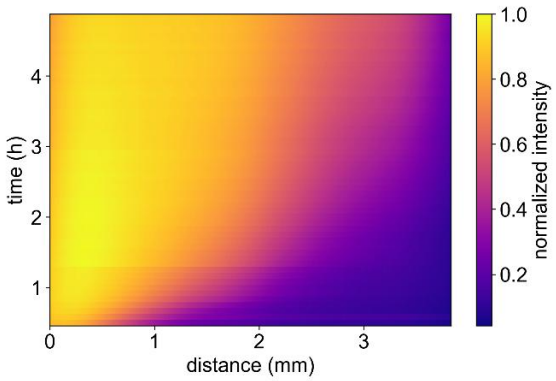

Fig. 2. Fluorescence intensity profiles of the diffusion measurement.

It can be seen that the diffusion is initially much faster and slows down as the dye concentration in the channel increases. To observe this behavior more closely, the diffusion distance at a normalized intensity of 0.75 is plotted over the time in Fig. 3. The measurement results were shifted to the origin to allow fitting the data.

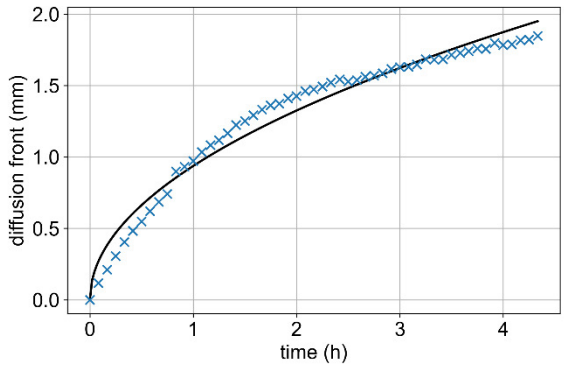

Fig. 3. Diffusion front at a normalized intensity of 0.75 over time.

The data shows that diffusion in a wet aerogel can be described by the function $x \approx \sqrt{2\mathrm{Dt}}$. The curve fitting results in an apparent diffusion constant of $D = 1.2e^{-10}\ m^2/s$. For comparison, the self-diffusion coefficient of ethanol at 25 °C is $D \approx 1.1e^{-9}\ m^2/s$ [5]. This difference of about a factor of 10 is to be expected, since diffusion slows down noticeably due to the size of the dye molecules and the porous network of the aerogel. The measurement performed demonstrates the ability to determine the diffusion coefficient of Eosin Y in an aerogel-filled microfluidic channel. Using the presented method, it is possible to determine the diffusion of the solvents used for the solvent exchange. This would allow for adjusting the intervals between solvent exchanges or determining the maximum still practical length of the microfluidic channels.

References

[1] A. C. Pierre and G. M. Pajonk, ‘Chemistry of Aerogels and Their Applications’, *Chem. Rev.*, vol. 102, no. 11, pp. 4243–4266, Nov. 2002, doi: 10.1021/cr0101306.

[2] H. Maleki, L. Durães, C. A. García-González, P. del Gaudio, A. Portugal, and M. Mahmoudi, ‘Synthesis and biomedical applications of aerogels: Possibilities and challenges’, *Adv. Colloid Interface Sci.*, vol. 236, pp. 1–27, Oct. 2016, doi: 10.1016/j.cis.2016.05.011.

[3] J. Yang *et al.*, ‘Versatile Aerogels for Sensors’, *Small*, vol. 15, no. 41, p. 1902826, Oct. 2019, doi: 10.1002/smll.201902826.

[4] A. L. Silveira Fiates, R. S. M. Almeida, M. Wilhelm, K. Rezwan, and M. J. Vellekoop, ‘Silica Aerogel in Microfluidic Channels: Synthesis, Chip Integration, Mechanical Reinforcement, and Characterization’, *ACS Omega*, vol. 9, no. 40, pp. 41480–41490, Oct. 2024, doi: 10.1021/acsomega.4c05019.

[5] S. Meckl and M. D. Zeidler, ‘Self-diffusion measurements of ethanol and propanol’, *Mol. Phys.*, vol. 63, no. 1, pp. 85–95, Jan. 1988, doi: 10.1080/00268978800100081.

DOI 10.5162/eurosensors2026/5.2.3

Biosensing and Healthcare Applications via Emerging Nanomaterials

Kanchan Yadav* [1,2,3,4], ***Raman Sankar*** [2,3]

[1] *Department of Chemistry, National Taiwan University, Taipei, Taiwan*

[2] *Nano Science and Technology Program, Taiwan International Graduate Program, Academia Sinica, Taipei, Taiwan*

[3] *Institute of Physics, Academia Sinica, Taipei, Taiwan*

[4] *Department of Materials Engineering, Indian Institute of Science, Bangalore, India*

E-mail of presenting author: kanchanyadav@iisc.ac.in

Eurosensors_Summary: The project focus on the fluorescence biosensing via Fluorescence Resonance Energy Transfer (FRET) mechanism based on the fluorescence quenching and recovery. There have been several reports based on the applications of transition metal chalcogenides (TMDs) 2-Dimensional nanosheets (2D-NSs) for FRET based fluorescence-based sensing for varieties of Nucleic Acid, proteins, food toxins, pesticides, and wide varieties of biomolecules, etc, [1-4]. But the application of fluorescence biosensor in physiological or real samples is a big challenge because of the interference from the complex matrix of sensing medium. To solve this issue, the present study focuses on the introduction of antifouling agent (polyethylene glycol) in the biosensing system. The polyethylene glycol modification enhances the stability and detection sensitivity by preventing the aggregation of 2D-NSs and minimizing the interferences in the complex matrix. TMDs single crystals have been grown via chemical vapor transport method followed by exfoliation to form nano-sheets via ultrasonication method and then PEGylated nanosheets were prepared. Then, multiplexed detection of aflatoxins in diverse complex sensing mediums based on the high fluorescence quenching abilities and affinities towards the aptamers was demonstrated via PEGylated nanosheets. Aflatoxins are fungal toxins which not only contaminate food, but also adversely affect human health if consumed and function as biomarkers for liver cancer and other dreadful diseases. The designed sensor demonstrates a multiplexed detection, ultrasensitive (limit of detection in picomolar), wide span of linear working range (around 5 orders of analyte concentrations), target selectivite, quick detection and cost-effective method. Consequently, the designed strategy is highly promising not only for the food industry, but also for the clinical diagnosis of numerous disease (such as cancer) biomarkers in physiological environments. Overall, our project focuses on food and health safety and overall well-being of society. Hence this project provides a substantial footstep and extensive impact on practical healthcare and fundamental research. Inspired by the above research, our future work is to focus on employment of 2D materials-biopolymer for the development of portable point of care device and wearable biosensor for the early detection of cancer and other dreadful disease and for the development of intelligent and sustainable food packaging system for food and health safety.

Eurosensors_Keywords: Fluorescence biosensing, 2-Dimensional nanosheets, antifouling agent, ultrasensitive, selective.

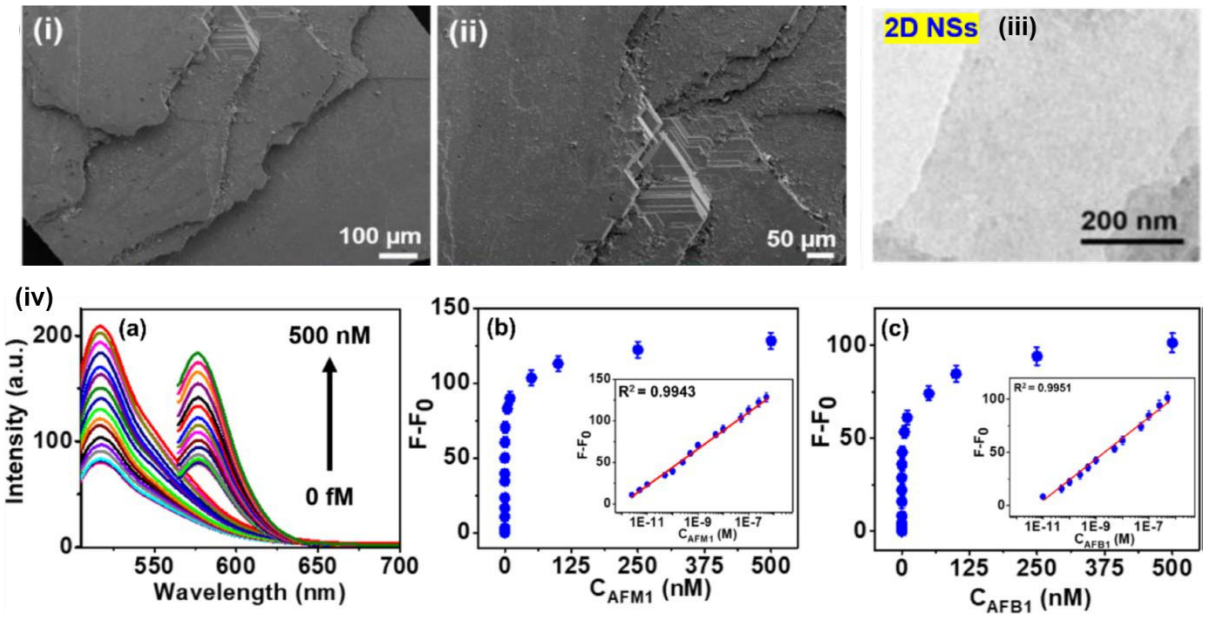

Fig.1 (i, ii) SEM of transition metal chalcogenides bulk crystal (iii) TEM of transition metal chalcogenides nanosheets, (iv) (a) Fluorescence spectra of Fam-Apt-M1 and Tam-Apt-B1 with varying concentrations of AFM1 and AFB1, respectively in PBS for multiplexed sensing via 2D NSs. Fluorescence intensity response (F-F0) of (b) Fam-Apt-M1 and (c) Tam-Apt-B1 versus C_{AFM1} and C_{AFB1}, respectively. Inset in (b, c) shows the plot of (F-F0) versus C_{AFM1} or C_{AFB1}, respectively to determine the LOD and LWR.

Eurosensors_References

[1] S. K. Setlem, B. Mondal, S. Ramlal, A fluorescent aptasensor for the detection of Aflatoxin B1 by graphene oxide mediated quenching and release of fluorescence, Journal of Microbiological Methods 193 (2022) 106414. https://doi.org/10.1016/j.mimet.2022.106414

[2] C. Zhu, Z. Zeng, H. Li, F. Li, C.H. Fan, H. Zhang, Single-Layer MoS_2-Based Nanoprobes for Homogeneous Detection of Biomolecules, J. Am. Chem. Soc. 135 (2013) 5998-6001.

https://doi.org/10.1021/ja4019572

[3] Y. Zhang, B. Zheng, C. Zhu, X. Zhang, C. Tan, H. Li, B. Chen, J. Yang, J. Chen, Y. Huang, L. Wang, H. Zhang, Single-Layer Transition Metal Dichalcogenide Nanosheet Based Nanosensors for Rapid, Sensitive, and Multiplexed Detection of DNA, Adv. Mater. 27 (2015) 935-939. **https://doi.org/10.1002/adma.201404568**

[4] N. Dhenadhayalan, K. Yadav, M.I. Sriram, H.L. Lee, K.C. Lin, Ultra-sensitive DNA sensing of a prostate-specific antigen based on 2D nanosheets in live cells, Nanoscale 9 (2017) 12087-12095. **https://doi.org/10.1039/C7NR03431H**

DOI 10.5162/eurosensors2026/5.2.4

All-Dry Dual-Stencil Lithography for IGZO Thin-Film Transducers

Chenxiang Zhang, Giovanni Boero, Jürgen Brugger
Microsystems Laboratory, École Polytechnique Fédérale de Lausanne (EPFL), 1015 Lausanne, Switzerland
chenxiang.zhang@epfl.ch

Summary:
Amorphous indium-gallium-zinc oxide (IGZO) is attractive for active thin-film transducer stacks processed at near-room temperature. Here, dual stencil lithography with alignment was used to fabricate an IGZO thin-film-transistor (TFT) stack, without photoresist or wet etching, with a maximum process temperature of 150 $°C$. The devices show clear field-effect operation, low gate leakage, and stable transfer characteristics. A preliminary white-light switching test confirms an electrically measurable response, suggesting an all-dry route toward IGZO transducer platforms for processing-sensitive sensor systems.

Keywords: IGZO, dual stencil lithography, all-dry fabrication, thin-film transistor, transducer

Introduction

Emerging sensing systems, such as agricultural or implantable sensors that need to degrade after their lifespan, increasingly require both sensing elements and electronics on processing-sensitive substrates. Amorphous IGZO is attractive for such a system because it can be deposited at room temperature while maintaining a mobility of $10-50\ cm^2V^{-1}s^{-1}$ in amorphous films [1], better than a-Si:H or most of the organic semiconductors. Beyond electronics, IGZO TFTs have also been explored as optoelectronic and chemical sensing elements, suggesting that the same material can contribute to both electronics and sensing [2].

From a processing perspective, solvent-sensitive, swelling-prone, or biodegradable polymeric substrates can benefit from resist-free and wet-etch-minimized fabrication. Stencil lithography offers such a dry-patterning route through direct deposition or etching [3].

In our work, stencil lithography with deposition is used as a dry and resist-free route to create an IGZO-based active stack on a Si substrate. The highest temperature in the entire process reached 150 °C during annealing. Using two sequentially aligned stencils with an alignment accuracy below 5 µm, sputtered SiO_2, sputtered IGZO, and evaporated Ti/Au electrodes were integrated into a TFT configuration. The resulting device shows clear field-effect operation, with a saturation mobility of $4.88\ cm^2V^{-1}s^{-1}$, a threshold voltage of 9.93 V, and a subthreshold swing of $226\ mV\ dec^{-1}$. A proof-of-concept illumination experiment further reveals a distinct white-light-induced current response from the IGZO channel. This dual functionality indicates that stencil-defined IGZO can serve as a dry-patterned active stack for both transistor and photo-responsive transducer in emerging sensor systems that require low-temperature and solvent-minimized patterning.

Methods

Devices were fabricated on a $2\times2\ cm^2$ p-type Si chip used as the global back gate. A 100 nm SiO_2 gate insulator was RF sputtered with O_2 addition to reduce oxygen-deficient oxide formation [4]. A 10 nm IGZO layer was then RF sputtered through a first SiN_x stencil as shown in Fig.1(a). The stencil-substrate gap was ~1-3 µm, estimated by microscope focus plane. After removing the first stencil, a second stencil was aligned and placed with an alignment accuracy below 5 µm, and 5/50 nm Ti/Au source/drain electrodes were evaporated. The representative transistor has a W/L ratio of 5/50 µm and was annealed in air at 150 °C for 1 h. The stack of fabricated devices is shown in Fig.1(b).

The patterns were characterized by optical microscopy and atomic force microscopy (AFM). Transfer and output characteristics were measured with a semiconductor analyzer. For a preliminary light-response test, V_g and V_d were fixed at 20 V and 5 V, respectively, while a white-light source was manually switched on and off.

Results

Among 4 fabricated devices on the same chip, all of them showed measurable field-effect operation. The representative device in Fig.1(c) has

a clearly defined channel, with IGZO visible between the Ti/Au electrodes. The AFM profiles in both Fig.1(c) and (d) show that the evaporated metal edges are sharper than the sputtered IGZO edges, consistent with the more directional flux during evaporation. The IGZO edge blurring is approximately 1 µm over a 10 nm thickness. Therefore, the channel length is mainly defined by the evaporated source/drain electrodes rather than by the sputtered semiconductor boundary.

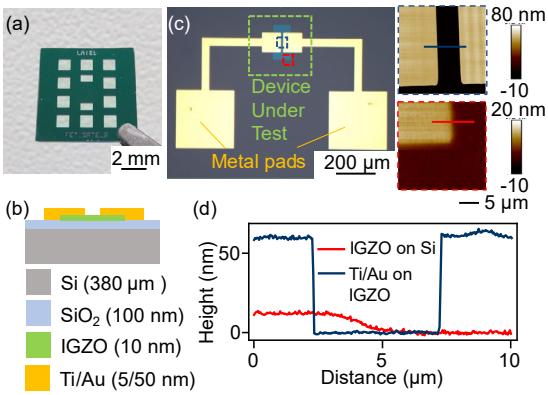

Fig.1. Stencil lithography patterned IGZO device. (a) Stencil chip with alignment marks. (b) Schematic cross-section of the SiO₂/IGZO/Ti/Au stack on a Si substrate. (c) Optical image of the device under test, with AFM scans from the marked regions. (d) Cross-section profiles extracted along the AFM cutting lines.

Fig.2. shows the field-effect operation of the fully stencil-patterned stack shown in Fig.1(c). The device exhibits $V_{th} = 9.93\ V$, an on/off current ratio of approximately 10^5, subthreshold swing $SS = 226\ mV\ dec^{-1}$, and $\mu_{sat} = 4.88\ cm^2V^{-1}s^{-1}$. The gate leakage remains near $10^{-11} - 10^{-10}\ A$, and the forward/backward transfer sweeps nearly overlap. These transfer, output, leakage, and hysteresis characteristics demonstrate that the dual-stencil-defined stack provides a functional transistor-type transducer platform

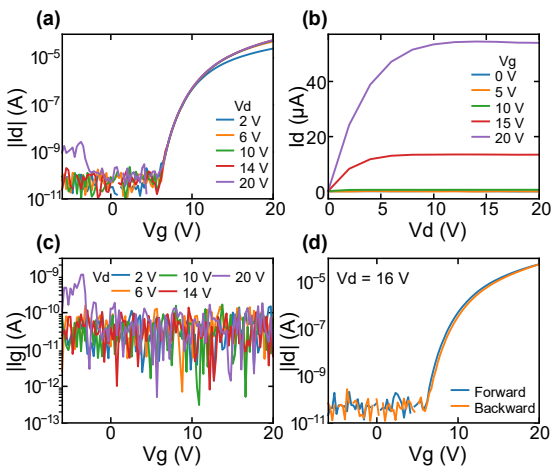

Fig.2. Characteristics of a representative IGZO TFT patterned by stencil lithography. (a) Transfer characteristics at different drain voltages. (b) Output characteristics at different gate voltages. (c) Gate leakage current. (d) Forward and backward transfer sweeps.

The same IGZO channel also shows a measurable light response, as shown in Fig. 3. Switching on white light increases the drain current, with a relative response of 65-75% calculated as $(I_{light} - I_{dark})/I_{dark}$. After the light is turned off, the recovery contains a fast component and a slower tail, suggesting a persistent photoconductivity (PPC) [5].

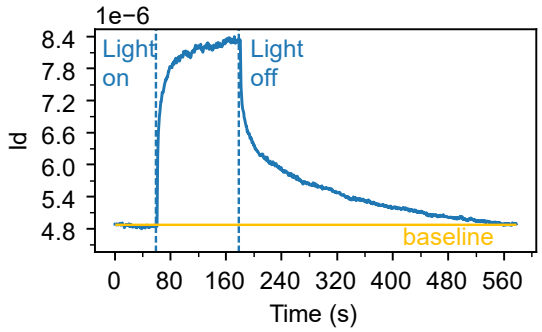

Fig.3. Time-resolved white-light response of the IGZO device patterned by stencil lithography, measured at $V_g = 20\ V$ and $V_d = 5\ V$, under white light.

In this work, dual-stencil lithography with alignment was used to fabricate an IGZO TFT device with a maximum thermal budget below 150 °C, supporting compatibility with processing-sensitive and biodegradable substrates. The device shows transistor operation and a qualitative response to white-light illumination. Further quantitative measurements are ongoing and will be presented at the conference.

References

[1] K. Nomura, et al., Room-temperature fabrication of transparent flexible thin-film transistors using amorphous oxide semiconductors, Nature 432, 488–492 (2004); doi: 10.1038/nature03090.

[2] Y. Han, et al., IGZO-based electronic device application: advancements in gas sensor, logic circuit, biosensor, neuromorphic device, and photodetector technologies, Micromachines 16, 118 (2025); doi: 10.3390/mi16020118.

[3] O. Vazquez-Mena, et al., Resistless nanofabrication by stencil lithography: a review, Microelectronic Engineering 132, 236–254 (2015); doi: 10.1016/j.mee.2014.08.003.

[4] S. Suyama, et al., The effects of oxygen–argon mixing on properties of sputtered silicon dioxide films, Journal of The Electrochemical Society 134, 2260–2264 (1987); doi: 10.1149/1.2100867.

[5] K. Park, et al., Endurable IGZO/SnSx/IGZO heterojunction phototransistor arrays for image sensors, ACS Applied Materials & Interfaces 17, 3620–3630 (2025); doi: 10.1021/acsami.4c18491.

DOI 10.5162/eurosensors2026/5.2.5

Ensemble Nuclearity Optimum in Chemoresistive Hydrogen Sensing

Hamin Shin[1], Andreas Güntner[1]
[1]Human-centered Sensing Laboratory, Department of Mechanical and Process Engineering, ETH Zürich, CH-8092, Zürich, Switzerland,
hashin@ethz.ch

Summary:
Chemoresistive hydrogen sensing with Pd-functionalized oxides still depends largely on empirical optimization, as the atomic-scale descriptor governing performance remains unclear. Here, we establish ensemble-defined Pd motifs with controlled nuclearity (Pd1-Pd3) on a nanostructured oxide and identify a non-monotonic nuclearity-performance relationship with an intermediate ensemble as the optimum. Combined experiments and density functional theory calculations show that this trend originates from nuclearity-specific hydrogen adsorption and activation rather than oxygen-centered surface descriptors.

Keywords: hydrogen sensing, palladium nuclearity, Chemoresistive sensor, atomic ensembles, Predictive materials design

Background, Motivation and Objective

Pd functionalization is a common strategy to enhance oxide chemoresistors for hydrogen sensing,[1] but material selection and optimization remain largely empirical because the structural descriptor that predicts performance is still unclear. This limitation is particularly pronounced when Pd is distributed as heterogeneous surface species, where the contribution of discrete atomic ensembles cannot be isolated and a direct structure-performance relationship cannot be established.

This work addresses that gap by testing Pd nuclearity as a motif-resolved design variable for chemoresistive hydrogen sensing. The objective was to construct ensemble-defined Pd1, Pd2, and Pd3 motifs [2] on a flame-made nanostructured oxide,[3] verify their local structures using complementary experimental and computational methods, and determine how ensemble nuclearity governs hydrogen adsorption and activation and thereby controls sensor response, selectivity, and limit of detection.

Description of the New Method or System

We developed a structure-validated chemoresistive hydrogen sensing platform based on ensemble-defined Pd motifs with controlled nuclearity on a flame-made nanostructured oxide. Using a solution-phase functionalization strategy, discrete Pd1, Pd2, and Pd3 ensembles were introduced while preserving the support structure, enabling direct comparison of motif-dependent sensing behavior within a single material system. The local structures of these Pd motifs were then validated by complementary spectroscopy, microscopy, and atomistic modelling, providing a rare platform in which the atomic configuration of the sensitizer is explicitly resolved rather than treated as a heterogeneous PdO_x decoration.

The methodological advance lies in combining motif-controlled synthesis, structure validation, mechanistic screening, and device-level comparison to identify Pd nuclearity as a predictive design variable for hydrogen sensing. Rather than attributing performance trends to generic oxygen-related effects, the system allows nuclearity-dependent hydrogen adsorption and activation to be isolated as the dominant differentiator. This establishes ensemble nuclearity as a practical motif-resolved descriptor and provides a general framework for predictive design of Pd-functionalized oxide chemoresistors.

Results

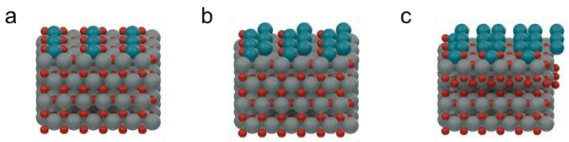

Fig. 1. Visual illustration of a) Pd1, b) Pd2 and c) Pd3 ensembles on a metal oxide support.

A structure-validated Pd nuclearity series was established on the flame-made nanostructured oxide, enabling direct comparison of Pd1, Pd2, and Pd3 motifs within a common support framework. Atomistic modelling identified distinct local

geometries and stabilization modes for each ensemble, and complementary structural characterization verified the targeted motifs, confirming that the sensing platform captures discrete Pd nuclearity as a controlled surface variable. This structural definition provides the basis for the observed performance trend and is summarized in Fig. 1, where the different Pd ensembles are represented as motif-resolved surface structures. Across the full sensing dataset, hydrogen response followed a clear non-monotonic dependence on nuclearity, with the intermediate ensemble consistently delivering the optimum performance over the measured temperature range, as reflected in the temperature-dependent sensor data shown in Fig. 2.

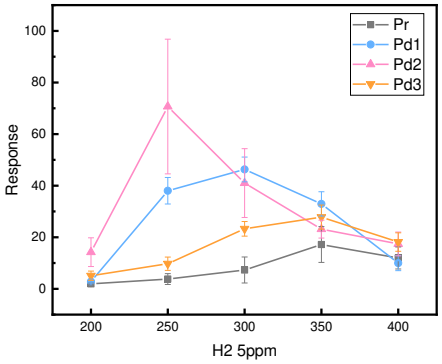

Fig. 2. Temperature-dependent chemoresistive hydrogen sensing performance of pristine oxide and the Pd-functionalized oxide sensors with controlled Pd nuclearity.

The origin of this nuclearity-dependent sensing behavior was then resolved by combining mechanistic screening experiments with density functional theory calculations. Surface adsorbed oxygen species and surface lattice oxygen reducibility did not correlate with the sensor trend, excluding oxygen-centered descriptors as the dominant origin of performance differences in this system. H_2-temperature-programmed reduction and calculated hydrogen adsorption energetics identified a nuclearity-specific hydrogen adsorption and activation landscape, which explains why the intermediate Pd ensemble outperforms both the monomeric and trimeric motifs. This motif-resolved reactivity trend was consistent with the device-level comparison across response, selectivity against representative interferents, and limit of detection, establishing ensemble nuclearity as a practical descriptor for predictive chemoresistive hydrogen sensing.

References

[1] W.-T. Koo, H.-J. Cho, D.-H. Kim, Y. H. Kim, H. Shin, R. M. Penner, I.-D. Kim, Chemiresistive Hydrogen Sensors: Fundamentals, Recent Advances, and Challenges, *ACS Nano* 14, 14284-14322 (2020); doi: 10.1021/acsnano.0c05307

[2] E. Vorobyeva, E. Fako, Z. Chen, S. M. Collins, D. Johnstone, P. A. Midgley, R. Hauert, O. V. Safonova, G. Vilé, N. López, S. Mitchell, J. Pérez-Ramírez, Atom-by-Atom Resolution of Structure–Function Relations over Low-Nuclearity Metal Catalysts *Angewandte Chemie International Edition* 58, 8724-8729 (2019); doi: 10.1002/anie.201902136

[3] A. T. Güntner, N. J. Pineau, S. E. Pratsinis, Flame-made chemoresistive gas sensors and devices, *Progress in Energy and Combustion Science* 90, 100992 (2022); doi: 10.1016/j.pecs.2022.100992

DOI 10.5162/eurosensors2026/5.3.1

A Polyimide-based In-situ Sensor and Actuator Platform for Battery Monitoring and Self-healing

Vincent Kuczius[1], Pongsak Sarapukdee[1], Emanuel Wallesch[1], Deniz Kutluay[2], Joe Fleming[2], Tazdin Amietszajew[2], Enric Comas[3], Jagdeep Sagu[4], Andrew Baker[4], Lilly Gill[4], David Johnson[4], Ian Manfren[4], Kevan Parkes[4], Gavin Brown[4], John McClean[4], Frances Tait[4], Sam Chan[4], Louise Evans[4], Stefan Palzer[1]

[1]Technical University Dortmund, Professorship for Sensors, Otto-Hahn-Straße 8, 44227 Dortmund, Germany

[2]Coventry University, C-ALPs building, Coventry University, Cheetah Road, CV1 2TL

[3]IDNEO Technologies, Career Rec de Dalt 3, Barcelona, Spain

[4]Centre for Process Innovation, The Coxon Building, John Walker Road, Sedgefield, TS21 3FE United Kingdom

stefan.palzer@tu-dortmund.de

Summary:

This work introduces a 30 µm-thick flexible array for in-situ battery monitoring and triggering of self-healing mechanisms. By combining temperature sensing with localized thermal actuation, the polyimide-based platform is able to trigger healing mechanisms at specific locations inside the battery without heating the entire cell. Simulations and experiments confirm spatial heat confinement. This enables a shift from pure diagnostics to active, closed-loop battery management capable of autonomously detecting and mitigating battery failure mechanisms.

Keywords: in-situ sensors, battery monitoring, battery, self-healing, battery system

Introduction

Next-generation battery systems employ high-energy materials and complex architectures that exhibit stronger thermo-mechanical coupling accompanied by higher safety sensitivity. This necessitates real-time monitoring to provide direct insight into internal processes to enable early detection of degradation and more precise control of battery operation [1, 2]. Embedded flexible sensors including thin-film thermocouples, piezoresistive sensors, and strain gauges, allow for real-time monitoring of corresponding internal battery parameters. They may be integrated on flexible substrates such as polyimide for in-situ, multiphysics monitoring within electrode stacks or separators with minimal impact on cell performance [3, 4]. While these technologies significantly improve diagnostics and battery management, they remain largely passive monitoring tools.

Here a sensor-actuator platform tailor-made for batteries that incorporate self-healing materials is presented. In this scenario detection alone is insufficient, since many healing mechanisms such as bond reformation require thermal activation [5]. Heating the entire cell is inefficient and may accelerate degradation or introduce safety risks. Therefore, the array enables localized heat deposition to deliver heat only at damaged regions and initiate healing processes within safe limits. By combining in-situ sensing with localized thermal actuation, this approach extends current flexible battery sensor technologies towards active self-healing battery systems capable of both detecting and autonomously mitigating degradation.

Processing

The fabrication process for the sensing platform starts with a glass wafer used as a temporary support substrate. A photosensitive polyimide (PIM) layer is first deposited by spin coating to form the flexible base layer. The electrical structures are produced via physical vapor deposition (PVD) of Aluminium (Al) metallization usiung maskless photolithographic patterning. The fabrication of resistive temperature detectors is achieved using a serpentine structure and array of 3x3 temperature sensors with a respective area of 149.47 mm^2.

Electrical insulation and chemical protection to prevent corrosion and electrolyte interaction from the battery environment is achieved by a second spin-coated polyimide layer. Finally, the devices are singulated using wafer sawing and released from the glass carrier by laser ablation resulting in a free-standing flexible sensor structure with a total thickness of ~30 µm. The process flow is shown in Figure 1 including a photograph of the finished device.

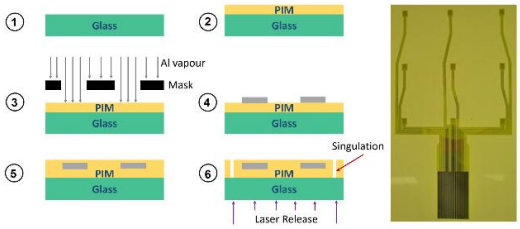

Fig. 1. Fabrication process for the sensing platform. The photograph on the right shows the finished device.

Experimental

The thermal behavior of the system has been modelled to understand heat generation and dissipation within the sensor structure and battery. To this end, the spatio-temporal behaviour is simulated using the finite-element method (FEM) and material parameters and dimensions for a single Pouch cell using a Li-S chemistry. The sensor array is calibrated to establish the relationship between the electrical resistivity of each temperature sensing area and the actual temperature. The heating performance is then experimentally characterized by analyzing both the temporal evolution of temperature and the spatial temperature distribution across the device to ensure localized heat deposition.

Results

The simulation results indicate that the generated heat remains strongly confined around the active heating element, with a spatial spread of approximately 15 mm (FWHM) as shown in Figure 2.

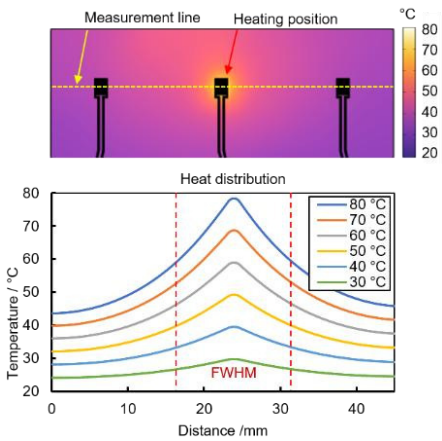

Fig. 2. COMSOL simulation of the micro-heater array (top) and the corresponding lateral temperature distribution profiles (bottom) at various setpoints from 30 °C to 80 °C.

The vertical temperature decreased by approximately 1.7°C at the aluminum current collector interface and 2°C at the sulfur layer relative to the peak heater temperature.

This confirms that the device design enables highly localized thermal actuation. Experimental validation was conducted by heating a single temperature sensing site to 51.8 °C. The measured temperature response agrees well with the simulation results, confirming localized heat deposition without significantly affecting neighboring sites. Based on the calibrated sensor signals, the temperature distribution across the array was reconstructed during operation. The reconstructed heat map in Figure 3 visualizes the thermal profile and demonstrates controlled, localized heating within the flexible sensor structure.

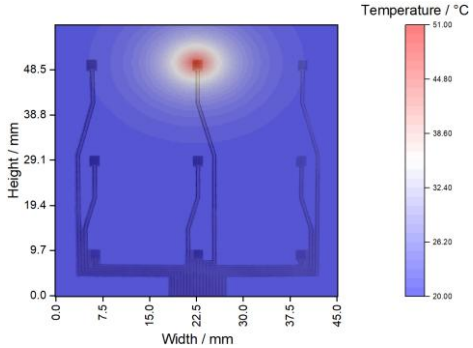

Fig. 3. Interpolated temperature distribution on an aluminum foil substrate with a 3x3 resistor array.

Conclusion

This work introduces a flexible, quasi-2D microsensor for in-situ temperature monitoring and localized heating in batteries. Experiments and simulations confirm precise thermal control with minimal spread. By combining embedded sensing with targeted actuation, this platform offers a pathway for self-healing battery chemistries. Future integration with management systems will enable responsive, intelligent energy storage through closed-loop thermal control.

References

[1] R. Xiong, X. Sun, X. Meng, *et al.*, “Advancing fault diagnosis in next-generation smart battery with multidimensional sensors,” *Appl. Energy*, vol. 364, p. 123202, Jun. 2024, doi: 10.1016/J.APENERGY.2024.123202.

[2] A. Manzini *et al.*, “Sulfur cathodes for next-generation batteries,” *Communications Materials 2026 7:1*, vol. 7, no. 1, pp. 108-, Apr. 2026, doi: 10.1038/s43246-026-01133-w.

[3] F. Cheng *et al.*, “In situ and real-time monitoring of the internal temperature, pressure, and current of lithium-ion batteries for long cycle life safety using a flexible multi-parameter sensor array,” *J. Mater. Chem. A Mater.*, vol. 14, no. 19, pp. 11663–11675, Mar. 2026, doi: 10.1039/D5TA09703G.

[4] X. Zeng and M. Berecibar, “Emerging sensor technologies and physics-guided methods for monitoring automotive lithium-based batteries,” *Communications Engineering 2025 4:1*, vol. 4, no. 1, pp. 44-, Mar. 2025, doi: 10.1038/s44172-025-00383-9.

[5] X. Wan, T. Mu, and G. Yin, “Intrinsic Self-Healing Chemistry for Next-Generation Flexible Energy Storage Devices,” *Nanomicro Lett.*, vol. 15, no. 1, p. 99, Dec. 2023, doi: 10.1007/S40820-023-01075-9

DOI 10.5162/eurosensors2026/5.3.2

A Portable Ultrasound System Integrating a CMUT Sensor Array with an FPGA-Based Delay-and-Sum Beamformer

Mert Doğan[1], Can Ufuk Ertenli[2,3], Mehmet Oğulcan Güngör[4], Berkay Karacaer[2]
[1]Department of Electrical and Electronics Engineering, METU, Ankara, Turkey
[2]K AND K Müh. Tek. Ltd. Şti., Ankara, Turkey
[3]Department of Computer Engineering, METU, Ankara, Turkey
[4]Department of Micro and Nanotechnology, METU, Ankara, Turkey
brk@knktechs.com

Summary:
A portable ultrasound imaging system combining a custom CMUT array, fabricated via a novel SOI-based MEMS process under patent review, with a real-time FPGA delay-and-sum beamformer is presented. The 64-channel array is scanned in eight sequential groups of 8 via analog multiplexing, with on-chip receive beamforming at 100 MHz yielding ~33 ms per focal depth within a 7.9 W total system power budget. Phantom experiments at 1 and 10 MHz validate point-target resolution and tissue-mimicking contrast, confirming feasibility for handheld point-of-care ultrasound.

Keywords: CMUT, FPGA beamforming, portable ultrasound, MEMS, point-of-care imaging

Background, Motivation and Objective

Point-of-care ultrasound (POCUS) demands transducer technology and signal-processing electronics that are simultaneously high-performance, compact, and power-efficient. Capacitive Micromachined Ultrasonic Transducers (CMUTs) are a compelling alternative to conventional piezoelectric arrays, offering batch-fabrication compatibility, wide acoustic bandwidth, and potential for monolithic CMOS integration [1], but translating them into functional imaging systems requires careful co-design of the sensor and downstream beamforming hardware.

FPGAs support parallel receive processing at deterministic latency and far lower power than GPU or CPU-based pipelines [2], and storing all working data in on-chip block RAM eliminates the PCB area and power overhead of external memory. We present a complete sensor-to-image pipeline in which a custom CMUT array, fabricated via a novel Silicon-on-Insulator based MEMS process, is interfaced with an FPGA running a Verilog delay-and-sum beamformer.

Description of the System

The imaging system (Fig. 1a) comprises three subsystems: a CMUT array front-end, a high-voltage pulser and analog receive chain, and an FPGA-based digital beamformer.

The CMUT array is fabricated utilizing custom Silicon-on-Insulator wafers. The process achieves well-controlled membrane geometry: across a 15-wafer lot, the device layer thickness was 1.93 ± 0.09 µm wafer-to-wafer (interwafer CoV 4.5%), confirming consistent membrane definition across the lot. The assembled sensor module comprising the CMUT die wirebonded to a custom PCB with acoustic matching and isolation layers is shown in Fig. 1b, alongside optical microscope images of individual array elements and cells. Devices target a resonant frequency in the 1–10 MHz diagnostic range and operate in pre-collapsed mode to maximize coupling efficiency. Specific array geometry, element count, and process-layer details are withheld pending patent review.

Transmit pulses are produced by a high-voltage pulser board (EV28J28A and HV7351) with programmable bipolar excitation. Received echoes are conditioned by a low-noise amplifier and anti-aliasing filter before digitization via an AD9671 analog front-end IC. A custom multiplexer board enables element addressing, reducing the simultaneous digital channel count to eight which is a practical power and area trade-off at the prototype stage.

The beamformer is implemented in Verilog HDL on a Nexys Video FPGA (Artix 7- XC7A200T) development board clocked at 100 MHz. The full 64 channel array is scanned in eight sequential groups of 8 channels via the analog multiplexer, with each group digitized and receive-beamformed independently. For each output

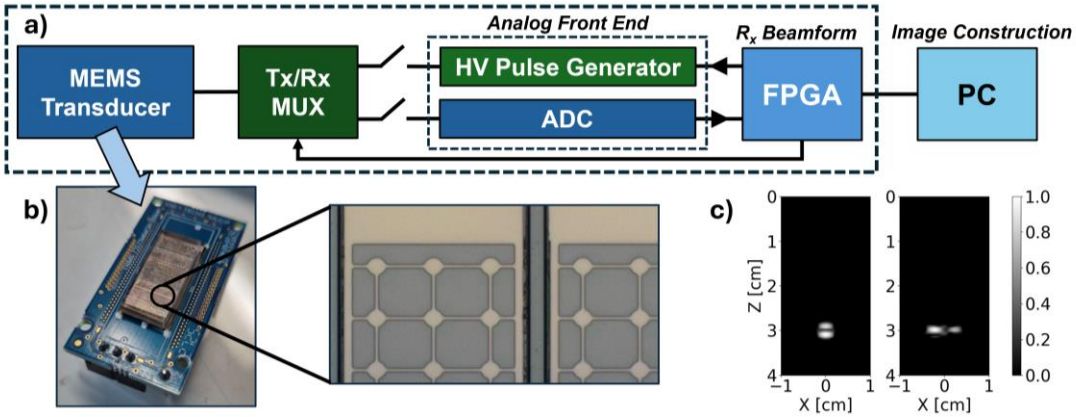

Fig. 1. (a) System block diagram of the signal chain from MEMS transducer to PC reconstruction. (b) Assembled sensor module and optical microscope image of the CMUT array elements. (c) B-mode images of wire targets at the same axial (left) and lateral (right) positions.

pixel, the round-trip delay to each element is computed from the element positions with tissue sound speed of 1540 m/s. The corresponding sample is selected from a per-channel BRAM buffer and all eight contributions are summed. Delay arithmetic uses fixed-point integers to minimize DSP tile usage and log compression is applied via a look-up table. All working data, reside entirely in on-chip BRAM, eliminating external DDR memory. Beamformed frames from all eight groups are streamed over USB to a host PC, where they are coherently combined and processed for envelope detection, dynamic range selection, scan conversion, and display. At 100 MHz, a single frame requires 3.3 M cycles per group, corresponding to 33 ms per focal depth per group. Table 1 summarizes the implementation parameters.

Results

Phantom imaging experiments (Fig. 1c) were conducted using a wire-target and a tissue-mimicking gelatin phantom at two operating frequencies, characterising the resolution–penetration trade-off across the 1–10 MHz bandwidth of the transducer. Point spread function measurements were obtained from 0.1 mm-diameter wire targets, with lateral and axial resolution extracted at the −6 dB level. At 10 MHz, axial resolution remains stable between 1.13 and 1.46 mm over 1–9 cm depth, degrading to 2.06 mm at 10 cm due to frequency-dependent tissue attenuation. Lateral resolution degrades from 0.51 mm at 1 cm to 1.42 mm at 10 cm (0.10 mm/cm), reflecting the tighter beam at higher frequency. At 1 MHz, axial resolution spans 1.23–2.50 mm across the full range, while lateral resolution degrades more steeply (0.92 mm/cm) to 18.6 mm at 20 cm, consistent with the longer wavelength and fixed single-focus transmit configuration. Tissue-mimicking phantom experiments confirm imaging of hypo- and hyperechoic inclusions at both frequencies, with no significant grating-lobe artefacts observed.

Tab. 1: FPGA implementation summary.

Parameter	Value / Description
Samples / channel	32,768 × 16-bit
Beamformed image	100×100 × 32 bit ≈ 400 KB
Total memory	≈4.4 MB (BRAM)
Beamforming cycles	~3.3 M (100×100×32,768)
Frame time	~33 ms ≈ 30 fps theoretical
Delay arithmetic	Fixed-point integer
Log compression	LUT-based

The total system power consumption is 7.9 W. The analog front-end draws 5.2 W during active transmission (3.72 W pulser + 1.44 W ADC and peripherals across 8 channels), and the FPGA digital back-end consumes 2.7 W. These results confirm the feasibility of the sensor–FPGA co-integration approach for portable operation; dynamic transmit focusing is identified as the primary next step toward improved lateral resolution at depth.

Acknowledgements

This work was supported by the Scientific and Technological Research Council of Turkey (TÜBİTAK) under grant no. 7230798.

References

[1] G. Caliano et al., “Design, fabrication and characterization of a capacitive micromachined ultrasonic probe for medical imaging,” IEEE Trans. Ultrason. Ferroelectr. Freq. Control, vol. 52, no. 12, pp. 2259–2269, 2005; doi: 10.1109/TUFFC.2005.1561630

[2] E. Boni et al., “ULA-OP 256: A 256-channel open scanner for development and real-time implementation of new ultrasound methods,” IEEE Trans. Ultrason. Ferroelectr. Freq. Control, vol. 63, no. 10, pp. 1488–1495, 2016; doi: 10.1109/TUFFC.2016.2566458

DOI 10.5162/eurosensors2026/5.3.3

Addressing Calibration Transfer in Electronic Noses for Urine Headspace Analysis through Synthetic Reference Samples and Advanced Feature Extraction

Laura Capelli
Politecnico di Milano, Department of Chemistry, Materials and Chemical Engineering "Giulio Natta"
Piazza Leonardo da Vinci 32, 20133 Milano
laura.capelli@polimi.it

Abstract:

The widespread adoption of electronic noses (e-Noses) in biomedical applications is hindered by sensor-to-sensor variability, which requires each individual device to be calibrated separately. This limitation severely affects system scalability and becomes particularly critical when dealing with biological samples such as human urine, whose collection, storage, and standardization are inherently challenging.

This work presents a methodological framework to address calibration transfer e-Nose devices based on Metal-Oxide (MOX) sensors for urine headspace analysis. The proposed approach relies on Direct Standardization (DS), a transfer learning technique requiring the measurement of reproducible transfer samples on both "master" and "slave" devices. For this purpose, synthetic urine formulations were specifically developed starting from literature data on urine volatile composition, with the objective of reproducing representative urine headspace characteristics while ensuring high repeatability and availability. These synthetic standards were then used to support the transfer of calibration models across different e-Nose units.

In parallel, advanced feature extraction and engineering strategies were investigated to improve the robustness and discriminative power of the generated models under realistic operating conditions, where both biological and instrumental variability typically affect performance. The combination of calibration transfer and enhanced feature extraction represents a promising step toward scalable and deployable e-Nose systems for biomedical applications.

Keywords:

Electronic nose; training; direct standardization; transfer samples; diagnosis

DOI 10.5162/eurosensors2026/5.3.4

A Two-Stage Encapsulation Procedure for Sterilization-Resistant MEMS Devices With Integrated SMA Actuator

Daniel Hoffmann[1], Dietmar Schuhmacher[1], Nico Burghardt[1], Andreas Erben[2], Alfons Dehé[1,3]
[1] Hahn-Schickard, Wilhelm-Schickard-Str. 10, Villingen-Schwenningen, Germany
[2] Fraunhofer IWU, Nöthnitzer Str. 44, Dresden, Germany
[3] University of Freiburg, Georg H. Endress Chair for Smart Systems Integration, Freiburg, Germany
Daniel.Hoffmann@Hahn-Schickard.de

Summary:

In this paper we propose a wafer level encapsulation approach for heterogenous integration of SMA wire actuators at low temperatures. The approach is based on the combination of anodic pre-bonding and laser bonding. For the first time, a MEMS-based sterilization counter device was realized withstanding the harsh conditions associated with cleaning and sterilization procedures applied for medical instruments. A reliability of up to 93% was achieved for recording of 125 performed reprocessing cycles.

Keywords: Heterogeneous integration, SMA wire actuator, sterilization counter, laser bonding

Introduction

Reprocessing of reusable medical instruments requires a critical, multi-stage process in order to remove all organic debris and microbial life. Key steps include cleaning, disinfection and sterilization. Due to the high thermal load acting on the medical instruments during sterilization, there is a demand to monitor the number of times a product has been sterilized [1]. However, detection and recording of sterilization events on individual medical devices remain a challenging task [2]. Electronic, battery-based data loggers available on the market are too large in size and too expensive for integration on instrument level [3].

A new concept for autonomous sensing of sterilization events on medical instruments was proposed by Pagel et al. and is based on a micromechanical system with an integrated shape memory alloy (SMA) actuator [4]. Heterogeneous integration of standard SMA wires into silicon microstructures was demonstrated by Hoffmann et al. [5]. However, achieving a robust encapsulation remains a major challenge, as the, SMA material limits processing temperatures to approximately 200°C. Adhesive bonding techniques have failed so far, as the robustness in the autoclave has proven to be very limited with a maximum cycle count below 20.

In this paper we propose a novel wafer level approach for robust encapsulation of SMA wire actuators. This approach enables MEMS devices withstanding the harsh conditions associated with cleaning and sterilization of medical instruments. For the first time, a robustness of 125 sterilization cycles has been demonstrated. The new approach enabled to characterize functional prototypes of the sterilization cycle counter device inside a steam autoclave giving valuable findings about performance and reliability.

Materials and Methods

The micromechanical counter system is realized in the device layer (100 µm thickness) of an SOI wafer. A specific feature of the device is, that the gear wheel and the embedded SMA wire actuator (76 µm diameter) are loose elements. Consequently, special procedures are required, in particular for encapsulation of the device. The silicon device wafer and the glass cap wafer are aligned using a standard mask aligner. However, the glass wafer needs to be loaded first in upside-down orientation. Consequently, after alignment of the wafers on the bond chuck, the silicon wafer is facing up with its bottom side. This means, there is no optical access for direct laser bonding. Therefore, an anodic pre-bond is performed with temperatures below 200°C. The voltage is set to be very low (< 300 V) in order to prevent sticking of the gear wheels on the glass wafer. The anodic prebond is strong enough for handling the wafer stack without debonding or

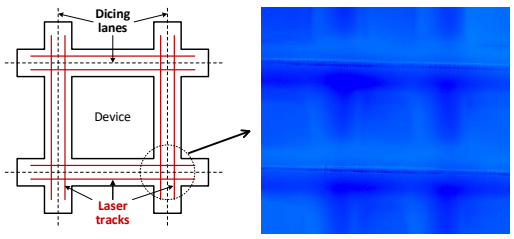

Fig. 1. Left: schematic view of bond frame and scan pattern; Right: laser bond tracks in the glass wafer

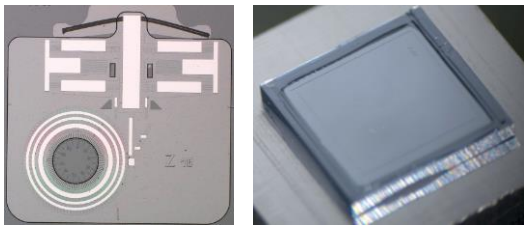

Fig. 2. Left: encapsulated device with integrated SMA wire actuator; right: test chip after tensile test

dealignment. After prebonding, the final bond is generated by using a continuous wave Laser with a wavelength of 1070 nm. The spot size is 200 µm and the Laser power is controlled by a Pyrometer. The travelling speed of the Laser spot is 2 mm/s. The wafer stack is bonded by scanning a grid-like pattern generating a bond frame for each chip (Fig. 1 left). The tracks of the laser bond lines that form in the glass wafer, are shown in Fig. 1 right. The wafer is then conventionally diced to release individual chips (Fig. 2 left). To determine the bond strength, specific test chips were characterized using a standard tensile test. The sterilization resistance of the encapsulation was accessed by performing 50 and 125 reprocessing cycles including cleaning and disinfection with chemical agents as well as steam sterilization at 134°C for up to 10 minutes.

Results and Discussion

The tensile test revealed a well-defined fracture pattern (Fig. 2 right) indicating a solid bond between the wafers in the region of the bond frame. Fig. 3 shows the fracture strength of 8 samples (mean value and standard deviation) for different wafers of a test series. By tuning and optimizing relevant parameters of the process chain (pretreatment, anodic prebonding and laser boning), the fracture strength is significantly increased. In particular, the pretreatment of the silicon device wafer, starting with wafer R2W12, has a significant effect. For comparison, the fracture strength of laser welded glass chips with equal geometry is also shown (Ligthfab). The behavior of encapsulated devices is shown in Fig. 4. After 125 reprocessing cycles, counter devices showed no signs of moisture ingress, confirming a steriliza-

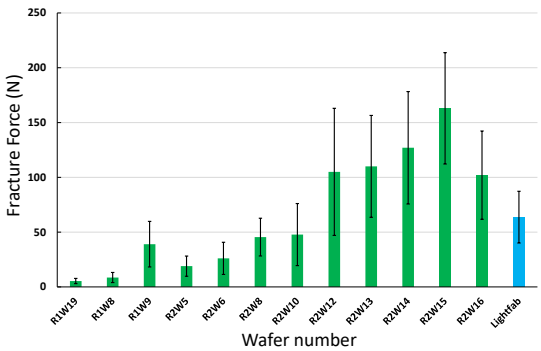

Fig. 3. Fracture strength for different wafers of a test series with variable process parameters

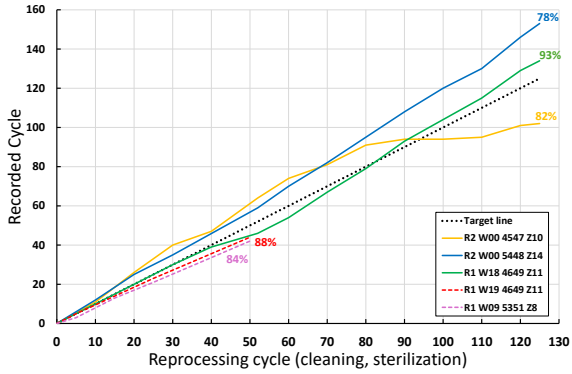

Fig. 4. Characterization of counter devices: number of recorded cycles vs number of cycles performed.

tion-resistant encapsulation. The reliability of recording performed sterilization cycles is currently up to 93%. Counting errors are caused by a variation of the switching point. Further research is required to reduce the impact of tolerances and to achieve a more reliable device behavior.

Conclusions

The presented results demonstrate the feasibility of a two-stage encapsulation process for heterogeneous integration of SMA wire actuators at low temperatures without damaging the SMA material. Through tests in the application environment, a sterilization-resistant encapsulation was verified. For the first time, a MEMS-based sterilization counter device was realized withstanding 125 reprocessing cycles. The reliability of counting sterilization cycles reached a maximum of 93%. The successful integration of SMA wire actuators opens up new senor- and actuator applications beyond the sterilization cycle counter.

References

[1] European medical device regulation (EU-MDR), www.eumdr.com

[2] E. A. Jacuzzi et al., Novel sterilization counter for medical applications, *Proceedings SMST 2010*

[3] L. Boehler et al., Sensors in the Autoclave-Modelling and Implementation of the IoT Steam Sterilization Procedure Counter; *Sensors 2021*, 21, 510; doi: 10.3390/s21020510

[4] K. Pagel et al., Development of a shape memory alloy actuator for a micromechanical sterilization cycle counter, *Proceedings SMASIS 2020*; doi: 10.1115/SMASIS2020-2242

[5] D. Hoffmann et al., Hybrid Integration of A Shape Memory Alloy Actuator For Micro Thermal Mechanical Systems, *Proceedings IEEE MEMS 2022*; doi: 10.1109/MEMS51670.2022.9699649

Acknowledgement

This work was funded by the German Federal Ministry of Economic Affairs and Energy (BMWE) as part of the industrial collective research (IGF-Project „ProAuSter“, 23003BG).

DOI 10.5162/eurosensors2026/5.3.5

Continuous, Scalable Building Envelope Monitoring Using Low-cost Gas Sensor Networks

Fabian Sievers[1], Nils Langer[1], Michael Jakubowsky[1], Álvaro Ortiz Pérez[1], Sibylle Braungardt[1], Stefan Palzer[1]
[1]Technical University Dortmund, Professorship for Sensors, Otto-Hahn-Straße 8, 44227 Dortmund, Germany
stefan.palzer@tu-dortmund.de

Summary:
Air exchange in buildings affects energy consumption, indoor air quality, and occupant health, and varies dynamically. Continuous monitoring of the air exchange rate (AER) is therefore important to understand real ventilation conditions and detect changes in building performance. Conventional methods only allow for short snapshots and cannot capture this variability during normal operation. Here continuous monitoring combined with automated mass-balance analysis is shown to yield scalable comparison of air exchange rates across rooms and building sections for real-time analysis of ventilation behavior.

Keywords: air exchange, sensor network, building envelope, long-term monitoring, digital twin

Introduction

Buildings exhibit complex temporal and spatial dynamics that influence ventilation, energy performance, and indoor air quality. In educational buildings, ventilation conditions directly affect both energy consumption and occupant health and performance. The air tightness and the associated air exchange rate (AER) are therefore key parameters for understanding the interaction between the building envelope, occupant behavior, and environmental conditions.

Conventional methods for determining air tightness and AER, such as blower door or artificial tracer gas tests, provide accurate results but are limited to short-term measurements under controlled conditions. As a result, they cannot capture the temporal variability and spatial heterogeneity of ventilation processes during normal building operation. With increasing building sensorization, distributed networks of low-cost sensors now continuously monitor parameters such as temperature, humidity, and carbon dioxide (CO_2) [1]. Occupant-generated CO_2 can be used as a natural tracer gas, and its temporal evolution reflects the balance between generation and removal through ventilation [2].

Recent research highlights significant spatial and temporal variability of indoor CO_2, motivating spatio-temporal sensor network analysis to capture heterogeneous concentration distributions and airflow dynamics [3]. However, large-scale, long-term applications of such approaches for assessing air exchange behavior in naturally ventilated school buildings remain limited.

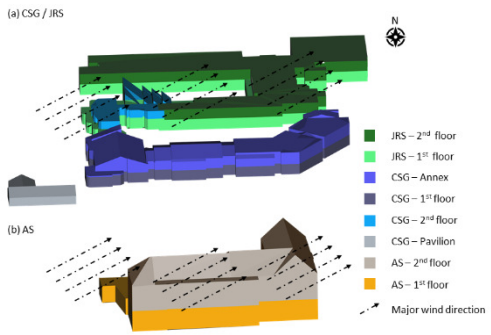

Fig 1: Digital twins of the three schools with building parts marked in color and the predominant wind direction indicated with arrows.

Here a tracer-gas modeling is combining with multi-sensor time-series analysis to determine ventilation behavior and air exchange processes under real operating conditions.

Experimental

Three schools in Holzwickede, Germany were instrumented to monitor indoor environmental conditions. The buildings, constructed between 1927 and 1994, each have two floors and are predominantly naturally ventilated, with a small number of laboratory classrooms equipped with mechanical ventilation. A total of 134 classrooms across the schools were equipped with sensor nodes measuring CO_2 concentration, temperature, and humidity. Each node records CO_2 every 30 s and transmits the data via a Wi-Fi

mesh network (ESP32-based) to an InfluxDB time-series database for continuous monitoring.

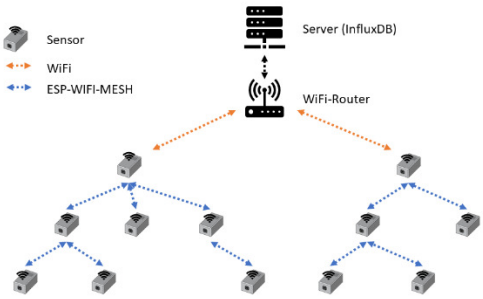

Fig 2: Schematic representation of the sensor network setup consisting of a central server, Wi-Fi access points for internet connection, and sensor nodes interconnected by ESP-WIFI-MESH protocol.

Indoor CO_2 concentration in a classroom is described using a mass-balance model that relates concentration changes to room volume, outdoor CO_2, ventilation airflow, and indoor CO_2 generation by occupants. During classes, metabolic CO_2 production causes a roughly linear increase in concentration, while after occupancy ends the concentration decays exponentially toward the outdoor level. This decay behavior enables estimation of the air exchange rate (AER) by fitting the measured CO_2 decrease to an exponential model. To automate the analysis, sensor data are smoothed and filtered for quality, and only days with sufficient CO_2 buildup and decay are used for the nonlinear fit used to determine AER.

Results

Continuous CO_2 measurements enable analysis of both occupancy patterns and ventilation behavior by examining concentration increases during occupancy and decay periods caused by ventilation or vacancy.

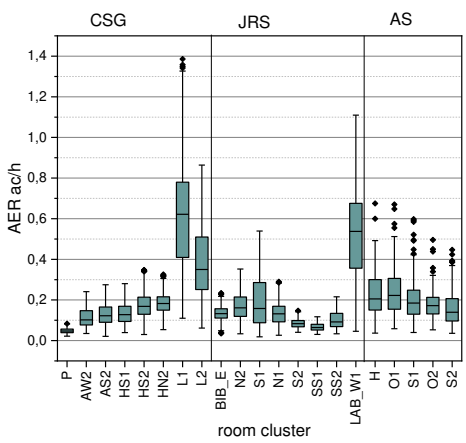

Fig 3: AER distribution for room clusters allow for identifying weak spots or abnormal user behaviour.

The final CO_2 decay after school hours provides an estimate of the undisturbed natural AER, while earlier decays during the school day indicate higher AER due to window opening or temporary vacancy. Analysis of the decay-derived AER shows that window-opening behavior depends on outdoor temperature, with windows more frequently left open at higher temperatures, and that AER varies with environmental drivers such as wind speed and temperature. Spatial differences in AER between rooms and building sections further allow the identification of potential weaknesses in the building envelope, while mechanically ventilated laboratories exhibit significantly higher AER values than naturally ventilated classrooms.

Conclusion

Estimating the natural air exchange rate from CO_2 decay using a non-linear mass-balance analysis provides a robust method for long-term monitoring. The approach is largely independent of absolute sensor calibration and does not require an external measurement of ambient CO_2.

The results show that after-hours CO_2 decay can be used to compare relative air tightness across naturally ventilated classrooms and provide building-level insights into the envelope. However, weather conditions influence the measured AER, with observable dependencies on outdoor temperature and wind speed, which should be considered when comparing results.

Reliable application requires adequate CO_2 buildup before the decay period and well-mixed indoor air, which makes school building ideal for this approach. Despite potential influences such as interzonal air exchange, the method provides a scalable and non-invasive way to analyze air tightness and ventilation behavior using large sensor datasets.

References

[1] A. Ortiz Perez, B. Bierer, L. Scholz, J. Wöllenstein, and S. Palzer, " *Wireless Gas Sensor Network to Monitor Indoor Environmental Quality in Schools Sensors,* (Basel, Switzerland), 18, 12, 2018, doi: 10.3390/s18124345

[2] W. W. Nazaroff, *Residential air-change rates: A critical review*, Indoor air, 31, 282–313, 2021, doi: 10.1111/ina.12785.

[3] D. Marín, A. Alegría-Sala, L. Canals Casals, M. Macarulla, J. Fonollosa. *The Reliability of CO2 Measurements Using Low-Cost Sensors: A Study of Sensor Positioning and Ventilation Strategies in Classrooms*, Indoor Air, 5517242, 2025113363, 2023, doi: 10.1016/j.enbuild.2023.113363.

DOI 10.5162/eurosensors2026/6.1.1

Microwave-based control of an SCR-based flue gas aftertreatment system for biomass combustion

Benedikt Streibl[1], Ralf Moos[1], Thomas Wöhrl[1], Thomas Ritter[2], Gunter Hagen[1]
[1] Department of Functional Materials, Center of Energy Technology (ZET), University of Bayreuth, 95447 Bayreuth, Germany,
[2] H+H Engineering & Service GmbH, Birkenleite 2, 96242 Sonnefeld, Germany
Correspondence to: functional.materials@uni-bayreuth.de

Summary:

Selective catalytic reduction (SCR) is essential for reducing NO_x emissions from biomass-fired plants, where fluctuating fuel composition leads to strongly varying raw emissions. Conventional SCR control relies on fixed calibration curves or gas sensors, which can cause inefficiencies and NH_3 slip. This work investigates a radio frequency (RF)-based approach in which the catalyst itself acts as a sensor by monitoring its electromagnetic properties. Experiments show a clear correlation between RF signals and NH_3 storage on commercial vanadia-based catalysts. The results indicate that RF-based control enables more precise and robust SCR operation than conventional gas sensor-based methods.

Keywords:
Flue gas, microwave cavity perturbation, selective catalytic reduction (SCR), ammonia loading, catalyst state-diagnosis, nitrogen oxides

Motivation

Selective catalytic reduction (SCR) is a widely applied technology to remove nitrogen oxides (NO_x) from flue gases produced by combustion processes. It has long been used in coal-fired power plants or waste incineration plants and is increasingly applied in biomass-fired boilers and combined heat and power (CHP) systems. NO_x emissions from biomass combustion arise predominantly from fuel-bound nitrogen. Biomass fuels such as wood chips, bark, straw, and agricultural or biogenic residues often show large variations in nitrogen content, leading to strongly fluctuating NO_x raw emissions [1].

Primary mitigation measures like air or fuel staging, or flue gas recirculation reduce NO_x formation. However, their NO_x reduction potential is often not sufficient to meet the emission limits. Therefore, flue gas aftertreatment systems such as SCR become necessary. The SCR process is based on the catalytic reduction of NO and NO_2 by ammonia (NH_3) to form nitrogen (N_2) and water (H_2O). Ammonia is supplied either directly or generated in-situ from urea-water solutions. SCR reactions occur on an oxide catalyst, mostly based on vanadium-tungsten oxides supported on titanium dioxide (V_2O_5-WO_3/TiO_2, abbreviated VWT) or on zeolite-based materials [2].

For high NO_x conversion and high selectivity (suppression of undesired oxidation reactions), SCR systems are typically operated between ca. 200 °C and 400 °C. Compared to selective non-catalytic reduction (SNCR), SCR provides substantially higher NO_x removal efficiencies, that exceeds 80%. This is particularly relevant for biomass-fired plants, where variable fuel composition and fluctuating load conditions occur. Here, SCR is the preferred technology when very low emission limits must be met [2].

To date, sensors (NO_x) have been used solely for plant monitoring. The dosing of the reducing agent is generally based on calibration curves, which are suitable only for a narrow range of fuel and operating parameters. If this range is exceeded, increased exhaust emissions occur.

To ensure that the SCR process can always be operated within the optimal range of possible NO_x reduction rates, automated control of reducing agent supply based on the operating conditions is necessary. This simultaneously prevents overdosing with unwanted NH_3 slip. A major general disadvantage of gas sensor-controlled systems is that an overdose is only detected once breakthrough has occurred and NH_3 slip has already taken place. For this reason, the automotive industry has shifted to determine the NH_3 loading of the SCR catalyst based on gas sensor signals and engine operating parameters, and to control it to a defined NH_3 loading [3].

DOI 10.5162/eurosensors2026/6.1.1

A novel approach utilizes radio frequency (RF)-technology. This involves measuring the electrical properties of the catalyst material using microwaves, thereby using the catalyst itself as a sensor. It has already been demonstrated that RF-based control works for zeolites used as SCR catalysts in automotive exhaust gas [4]. This study investigates whether this is also possible for VWT catalysts, which are typically used for the aftertreatment of biomass flue gases.

Measurement Setup

Generally, the catalyst is installed in an exhaust manifold within a metal canning. This metal casing of the ceramic catalyst acts as a cavity resonator when electromagnetic waves are coupled in (Fig. 1). Using this setup, the loading state of the catalyst can be determined in situ by measuring the dielectric properties of the catalyst material, since NH_3 sorption influences these properties. A frequency shift of the resulting resonance modes (f_0) or an attenuation of the input power occurs. The measurement involves either the reflection of the electromagnetic waves or their transmission through the catalyst material.

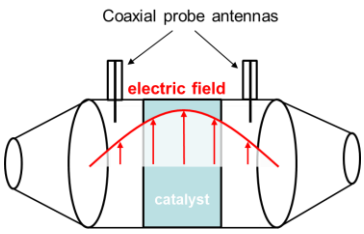

Fig. 1. Basic experimental setup using antennas to measure the electrical properties of the catalyst material within the cavity of the catalyst housing.

The initial measurements in Fig. 2 were performed with a commercial VWT catalyst at around 300 °C using a typical flue gas composition that includes water, CO_2, O_2, and N_2. NO and NO_2 were added as well as NH_3 in concentration that are shown also in Fig. 2 (b) as dotted lines. The FTIR-measured concentrations of NO, NO_2, and NH_3 downstream of the SCR catalyst are shown in Fig. 2 (b) as drawn lines.

Results and Discussion

Fig. 2 (b) shows the decrease in NO_x concentration when the NH_3 concentration increases. Already in a range where less NH_3 is added than required stoichiometrically for full NO_x reduction, NH_3 is stored in the catalyst. This can be seen in for instance at t = 100 min in Fig. 2 (c), where the NH_3 mass is balanced and the stored NH_3 mass in the catalyst is plotted. Both RF-derived data reflect the mass of stored NH_3 very well: the resonant frequency f_0 and the reciprocal quality factor Q_0^{-1} that reflects the attenuation.

Conclusion

This setup seems to be suitable to determine the mass of stored NH_3, and the RF-parameters may serve as variables to control SCR systems. It is interesting to see that NH_3 storage occurs despite no NH_3 overdosing and no NH_3 slip occurs. This demonstrates that RF-based control may be superior to gas sensor-based control.

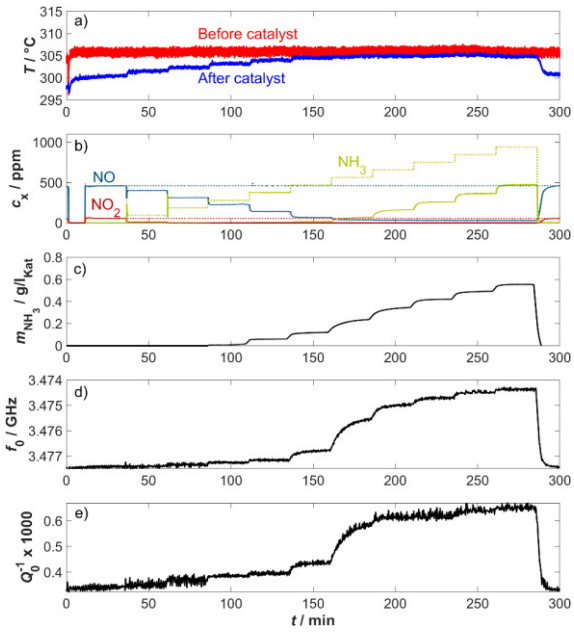

Fig. 2. Experimental Data; (a) temperature of the VWT catalyst, (b) gas concentrations up- and downstream of the catalyst, (c) stored NH_3 mass (derived from b), (d) resonant frequency, and (e) reciprocal quality factor, both measured with a vector network analyzer.

References

[1] M. König, M. Müller, I. Hartmann, Emission reduction process for the energetic use of biogenic residues, *IOP Conference Series: Earth and Environmental Science* 642, 1–10 (2021); doi: 10.1088/1755-1315/642/1/012006.

[2] S. Elkaee, A.D. Phule, J.H. Yang, Advancements in (SCR) technologies for NOx reduction: A comprehensive review of reducing agents, *Process Safety and Environmental Protection* 184, 854–880 (2024); doi: 10.1016/j.psep.2024.02.046.

[3] T.V. Johnson, Review of Selective Catalytic Reduction (SCR) and Related Technologies for Mobile Applications. In: Nova, I., Tronconi, E. (eds) Urea-SCR Technology for deNOx After Treatment of Diesel Exhausts. Fundamental and Applied Catalysis. *Springer, New York*, NY (2014); doi: 10.1007/978-1-4899-8071-7.

[4] M. Dietrich, C. Steiner, G. Hagen, R. Moos, Radio-Frequency-Based Urea Dosing Control for Diesel Engines with Ammonia SCR Catalysts, *SAE International Journal Engines* 10 (4), 1638-1645 (2017); doi: 10.4271/2017-01-0945.

Acknowledgement

Work was funded by the German Federal Ministry for Economic Affairs and Energy, grant 03EI5490B.

DOI 10.5162/eurosensors2026/6.1.2

Polymorph-Dependent Electronic Transduction in WO_3 during Molecular Sensing through Experiment and DFT

Meng Yin[1], Matteo D'Andria[2], Stefan Neuhauser[2],
Vlasis G. Mavrantzas[3 4], Ying Chen[5], Ken Suzuki[1], and Andreas T. Güntner[2]
[1] Green X-Tech Center, Green Goals Initiative, Tohoku University, Sendai, Miyagi, Japan,
[2] Human-Centered Sensing Laboratory,
Dept. of Mechanical and Process Engineering, ETH Zurich, Zurich, Switzerland,
[3] Macromolecular Engineering Laboratory,
Dept. of Mechanical and Process Engineering, ETH Zurich, Zurich, Switzerland
[4] Department of Chemical Engineering, University of Patras
& Institute of Chemical Engineering Sciences (ICE–HT/FORTH), Patras, Greece
[5] Global Learning Center, Tohoku University, Sendai, Miyagi, Japan
Corresponding Author's e-mail address: meng.yin.c3@tohoku.ac.jp

Summary:

Tungsten trioxide (WO_3) polymorphs have been widely studied for molecular sensing, yet the origin of their different chemoresistive behaviors remains unclear. Here, structural and spectroscopic characterization, in situ DRIFTS, and density functional theory (DFT) simulations reveal that both γ- and ε-WO_3 exhibit similar surface-level activation of acetone, whereas only ε-WO_3 stabilizes analyte-induced electronic states derived from W(5d) orbitals. These subsurface electronic rearrangements may explain its superior transduction efficiency despite similar receptor chemistry. Our findings provide a new framework for rational transducer design rooted in intrinsic electronic structure.

Keywords: WO_3, polymorphism, gas sensors, DFT, electronic structure

Background, Motivation and Objective

WO_3 is one of the most widely studied metal oxides for chemoresistive gas sensing. Besides the thermodynamically stable γ-phase, the metastable ε-WO_3 polymorph has shown higher responses, for example, toward acetone [1]. Despite its promising performance in advanced sensing applications, including non-invasive metabolic monitoring, the mechanistic origin of its superior response remains unclear. Conventional surface-chemical explanations based on adsorbate binding, oxygen activation, or intermediate speciation have not adequately explained the performance difference. In particular, the influence of crystal polymorphism on electron transfer and localized electronic states during molecular sensing remains largely unexplored. Here, using acetone as a model analyte, we investigate polymorph-dependent electronic transduction in WO_3 through a combined experimental and DFT approach.

Methodology

γ-WO_3 and ε-WO_3 nanoparticles were synthesized by the flame spray pyrolysis method. Structural characterization was performed by XRD, HR-TEM, XAFS, and XANES, while the

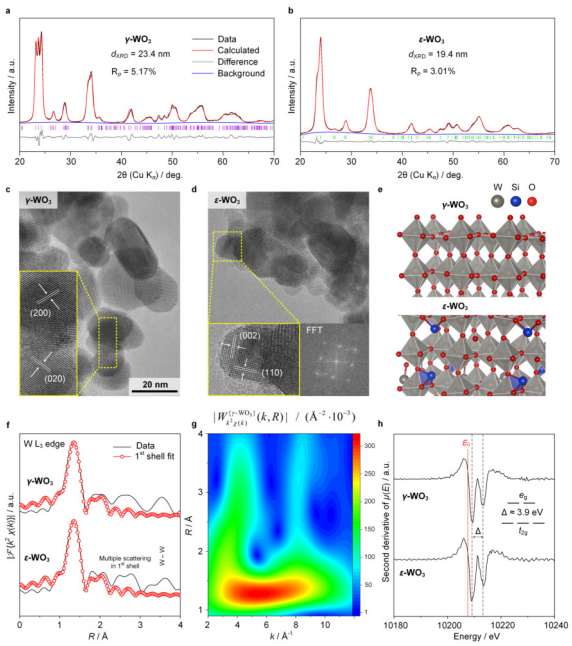

Fig. 1. Structural and spectroscopic characterization of γ-WO_3 and ε-WO_3: (a,b) XRD patterns and Rietveld refinements, (c,d) high-resolution TEM, (e) DFT-relaxed structures, (f) W-L_3-edge Fourier transforms, (g) wavelet transform magnitude for γ-WO_3, and (h) second derivative of XANES.

DOI 10.5162/eurosensors2026/6.1.2

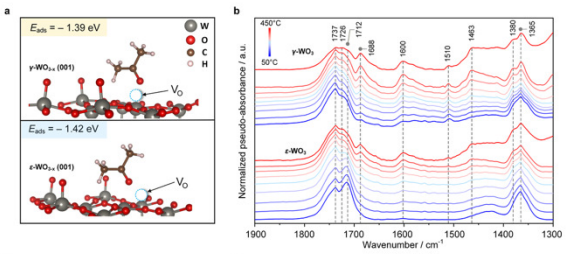

Fig 2. (a) Equilibrium structures of γ-WO_{3-x} (001) and ε-WO_{3-x} (001) with an adsorbed acetone molecule. Shown are the adsorption energies obtained by DFT. (b) In situ DRIFT spectra of adsorbed acetone (2 vol% C_3H_6O) between 50 – 450 °C in steps of 50 °C.

analyte induced changes were probed by in situ DRIFT spectroscopy, chemoresistive sensing and related experiments. In parallel, DFT calculations were carried out to determine the adsorption energy, charge transfer, differential charge density, and band structure upon acetone adsorption. This combined approach enabled us to correlate molecular interaction with polymorph-dependent electronic transduction in WO_3.

Results

Structural identity of WO_3 polymorphs

Using flame spray pyrolysis [2], we synthesized γ-WO_3 and Si-stabilized ε-WO_3 nanoparticles. As shown in Fig. 1, XRD and HR-TEM confirmed phase-pure γ- and ε-WO_3 with faceted nanocrystals. DFT suggests that Si is incorporated interstitially, forming distorted SiO_x units that locally strain and stabilize the metastable ε-phase. W-L_3-edge XAFS shows similar W–O bond lengths and reduced coordination numbers in both polymorphs, indicating comparable local WO_6 environments with oxygen vacancies. Wavelet-transform analysis reveals additional Si-related distorted structures in ε-WO_3 beyond the first W coordination shell. Despite these differences, second-derivative XANES indicates nearly identical W^{6+} oxidation states and ligand-field splitting, showing that Si stabilizes ε-WO_3 without significantly perturbing the local WO_6 framework.

Acetone adsorption and surface chemistry

To clarify analyte–surface interactions, we combined DFT calculations within situ DRIFT spectroscopy. DFT-relaxed structures show that acetone preferentially adsorbs via its carbonyl oxygen on under-coordinated W sites *next* to oxygen vacancies in both γ- and ε-WO_{3-x} (Fig. 2a). The calculated adsorption energies are nearly identical (−1.39 eV for γ-WO_{3-x} and −1.42 eV for ε-WO_{3-x}), together with comparable charge transfer, indicating similar surface binding in the two polymorphs. In situ DRIFTS during acetone exposure further shows similar surface chemistry for γ- and ε-WO_3 (Fig. 2b). Acetone adsorption

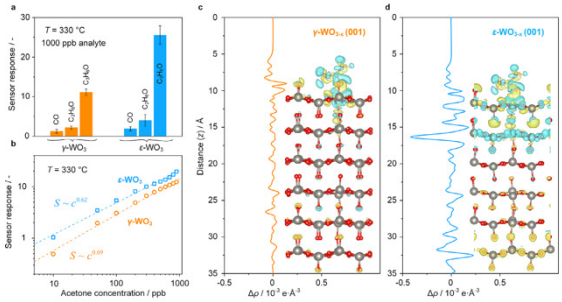

Fig. 3. (a)Sensor response of γ-WO_3 (orange) and ε-WO_3 (blue) toward 1000 ppb CO, ethanol, and acetone as well as (b) response vs. concentration characteristics of these for acetone ranging between 10 and 1000 ppb. CDD maps as well as plane-averaged differential density (Δρ) plot as a function of z-coordinate (i.e., normal to the slab) of acetone adsorbed on (001) surfaces of (c) γ-WO_{3-x} and (d) ε-WO_{3-x}.

gives perturbed C=O bands, indicating interaction with surface W sites, while a weaker low-wavenumber component suggests more strongly activated species. Importantly, within the typical sensing range of 300–400 °C, both polymorphs exhibit nearly identical surface reactivity, indicating that their response difference does not primarily arise from receptor chemistry.

Transducer function and electronic structure

Despite similar acetone adsorption and surface chemistry, ε-WO_3 shows higher chemoresistive responses than γ-WO_3, indicating that the performance difference arises from transduction rather than receptor chemistry. As shown in Fig. 3a, this polymorph-dependent response is most pronounced for acetone compared with CO and ethanol. DFT-calculated charge-density-difference (CDD) analysis reveals pronounced subsurface charge redistribution only in ε-WO_3 after acetone adsorption (Fig. 3c, d). This behavior can be understood from the electronic structure. In contrast to γ-WO_3, ε-WO_3 more readily accommodates analyte-induced electrons in conduction-relevant W(5d)-dominated states close to the conduction-band edge, thereby providing an efficient pathway for conductivity modulation. Together with the orbital-resolved analysis and local W–O distortions, these results suggest the formation of delocalized electron polarons across several subsurface W atoms. Thus, polymorphism in WO_3 governs chemoresistive sensing behavior mainly by tuning the density and accessibility of conduction-relevant states.

References

[1] M. Righettoni et al., Chemistry of Materials 22, 3152-3157 (2010); doi: 10.1021/cm1001576

[2] A. T. Güntner et al., Progress in Energy and Combustion Science 90, 100992 (2022); doi: 10.1016/j.pecs.2022.100992

[3] M. D'Andria, M. Yin et al., Advanced Materials e16840 (2026); doi: 10.1002/adma.202516840

DOI 10.5162/eurosensors2026/6.1.3

Hydrogel beads-based sensing technology for measurement of insulin growth factor 1 (IGF1) in saliva

Khalid Haliru[1], Nicholas Goddard[2], Ruchi Gupta[1]
[1] School of Chemistry, University of Birmingham, Birmingham, B15 2TT, UK
[2] Independent Researcher, Accrington, BB5 2SB, UK

r.gupta.3@bham.ac.uk

Summary:

We report a hydrogel beads-based sensing technology for the measurement of a protein biomarker, insulin growth factor 1 (IGF1) with a limit of detection of 0.03 ng/mL and dynamic range of 0-1.6 ng/mL. We showed that concentrations of IGF1 were successfully measured in human saliva samples using hydrogel beads. In comparison to the gold standard method, enzyme-linked immunosorbent assay (ELISA), the use of beads was beneficial because the measurements were not influenced by the dilution factor of samples and the buffer used for sample dilution.

Keywords: Hydrogel, beads, enzyme-linked immunosorbent assay (ELISA), proteins, saliva

Background, Motivation and Objective

Salivary proteins can serve as biomarkers of diseases and health conditions. For example, salivary insulin growth factor 1 (IGF1) can be a biomarker of skeletal maturity, which can be useful for orthodontic treatment planning [1]. The concentration of salivary IGF1 in adults and adolescents is <0.9 ng/mL and ~4 ng/mL, respectively [2]. The state-of-the-art method for the measurement of proteins is enzyme-linked immunosorbent assay (ELISA) [3], which can require sample preparation and optimization of (diluent, block and wash) buffers for each protein/ sample, is tedious and time-consuming.

Our motivation is to devise technologies for accurate, easy, and rapid detection of biomarkers in body fluids. Our objective is to determine the utility of our hydrogel beads-based sensing technology [4] for measurement of salivary IGF1 and benchmark against ELISA.

Hydrogel beads-based sensing technology

As shown in Fig. 1, proteins were covalently captured by the reaction between the isothiocyanate reactive group and amines in the polyethylene glycol (PEG) hydrogel and proteins, respectively. Proteins were pre-concentrated because the volume of the hydrogel was lower than the sample. Equally, interferents were removed because the hydrogel was designed to serve as a molecular weight cut-off filter. When the hydrogel was exposed to light, fluorophores labelled proteins were released. The released proteins were selectively captured by antibodies and quantified by fluorescence.

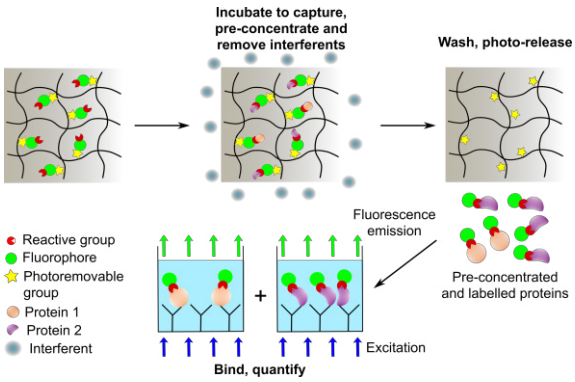

Fig. 1. Measurement of proteins using hydrogel.

Experimental

Each hydrogel bead was formed by polymerizing 4 µL solution, containing a crosslinker as well as active and inactive monomers with their chemical structures shown in Fig. 2 (a).

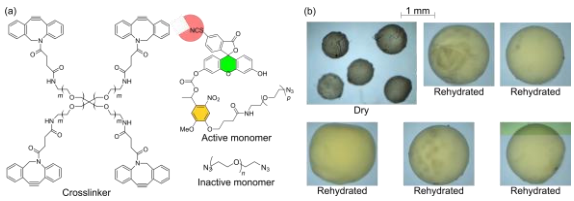

Fig. 2. (a) Chemical structures of the crosslinker and monomers used to make PEG hydrogel and (b) images of dried and rehydrated beads

Fig. 2 (b) shows that the diameters of dried and rehydrated beads were 0.49±0.03 mm and 1.03±0.46 mm, respectively. 20% (w:v) hydrogel beads were used because they were suited for pre-concentration of IGF1 and removal of

macromolecular interferent, mucin, which is present in large excess in saliva [4].

4 beads were incubated with 200 µL sample for 60 min while shaking, washed in 10 mM phosphate buffered saline (PBS, pH 7.4), immersed in 50 µL PBS, and then exposed to 365 nm light for 10 min. The released proteins were pipetted in a microtiter plate well coated with IGF1 antibody. The solution was left in the well for 30 min and then the well was washed with PBS containing 0.05% Tween-20. The sensing performance of the beads was compared against an ELISA kit (DuoSet DY291, Bio-Techne).

The wells were coated with IGF1 antibody by leaving 100 µL of 4 µg/mL antibody prepared in 50 mM bicarbonate buffer (pH 9.6) in wells overnight and then washing the wells with PBS containing 0.05% Tween-20. PBS containing either 1% bovine serum albumin (BSA, buffer 1) or 5% Tween-20 (buffer 2) was used to dilute samples, prepare biotinylated detection antibody and streptavidin labelled horseradish peroxidase enzyme for ELISA, and block wells after immobilization of capture antibody.

Saliva samples were collected from healthy individuals visiting the University of Birmingham Dental Hospital with approval from the local research ethics committee (ethics code 24/SW/0100, project code DRTB002.2029). Samples were stored at −80 °C prior to use.

Results

The calibration curves of IGF1 using ELISA and beads are provided in Fig. 3. The ELISA calibration curves were non-linear over the entire range of the protein concentration. In contrast, the beads calibration curves were linear for up to 1.6 ng/mL IGF1. The limit of detection (LOD) for IGF1 using the beads was 0.10 ng/mL and 0.03 ng/mL when the protein was prepared in PBS with 1% BSA and 5% Tween-20, respectively. Thus, the LOD and dynamic range of beads-based sensing technology is sufficient to measure IGF1 in saliva of adults.

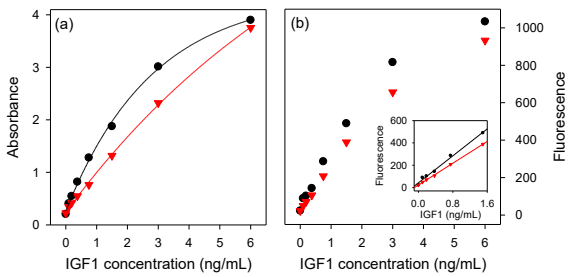

Fig. 3. Calibration curves of IGF1 in buffer 1 (black) and buffer 2 (red) using (a) ELISA and (b) beads.

Table 1 lists IGF1 concentrations measured using beads and ELISA in undiluted saliva using buffer 1, showing good agreement.

Tab. 1: Comparison of salivary IGF1 concentration determined using beads and ELISA

Method	IGF1 concentration (ng/mL) in sample			
	1	2	3	4
Beads	0.31 ±0.06	0.26 ±0.06	0.32 ±0.06	0.21 ±0.06
ELISA	0.28 ±0.03	0.25 ±0.02	0.29 ±0.03	0.20 ±0.02

Fig. 4 (a) shows that for each saliva sample, when measured using beads, the concentration of IGF1 was comparable irrespective of the sample dilution factor and buffer type. In contrast, as shown in Fig. 4 (b), these factors had a strong effect on the measurement of IGF1 concentration using ELISA. Thus, our conclusion is that hydrogel bead-based sensing technology is more robust than ELISA for the measurement of salivary IGF1.

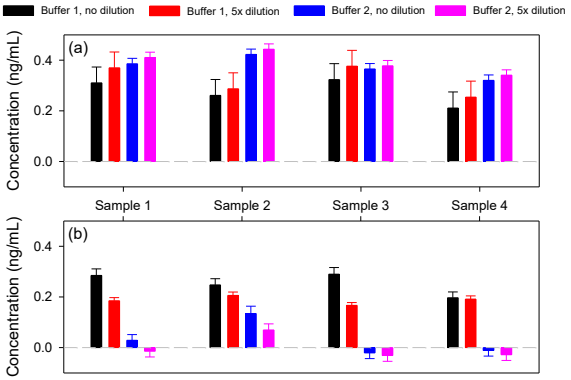

Fig. 4. Concentration of salivary IGF1 determined using (a) beads and (b) ELISA for different sample dilution factors and buffers used for sample dilution.

References

[1] R. Wadia, Salivary Biomarkers as Skeletal Maturity Indicators, *British Dental Journal* 234, 1786 (2023), doi: 10.1038/s41415-023-5463-z.

[2] A. Almalki, J.T. Thomas, A.R.A. Khan, B. Almulhim, A. Alassaf, S.A. Alghamdi, B. Joseph, A. Alqerban, S. Alotaibi, Correlation between Salivary Levels of IGF-1, IGFBP-3, IGF-1/IGFBP3 Ratio with Skeletal Maturity Using Hand-Wrist Radiographs, *International Journal of Environmental Research and Public Health* 19, 3723 (2022), doi: 10.3390/ijerph19063723.

[3] S. Aydin, A Short History, Principles, and Types of ELISA, and Our Laboratory Experience with Peptide/ Protein Analyses Using ELISA, *Peptides* 72, 4 (2015), doi: 10.1016/j.peptides.2015.04.012.

[4] K. Haliru, S. Li, N.J. Goddard, R. Gupta, Novel Functional Hydrogels for the Measurement of Low Molecular Weight Proteins in the Presence of Serum Albumin, *Sensors and Actuators B: Chemical* 444, 138404 (2025), doi: 10.1016/j.snb.2025.138404.

DOI 10.5162/eurosensors2026/6.1.4

Controlling Interconnection Density in 3D ZnO Networks for Optimized Charge Transport and Multimodal Sensing

Barnika Chakraborty[1], Benjamin Junker -Reiss[2], Leonard Siebert[1], Rainer Adelung[1*]
[1] Chair for Functional Nanomaterials, Department for Materials Science, Kiel University, Kaiserstr. 2, 24143, Kiel, Germany
[2] Mathematisch-Naturwissenschaftliche Fakultät Institut für Physikalische und Theoretische Chemie, Eberhard Karls Universität Tübingen, AG Weimar, Auf der Morgenstelle 15, 72076, Tübingen, Germany
Corresponding Author's e-mail address : ra@tf,uni-kiel.de

Summary:

Three-dimensional (3D) tetrapodal ZnO (t-ZnO) networks are promising for multifunctional sensing but often suffer from poor interparticle connectivity, which limits charge transport and sensitivity. We introduce interconnection density as a tuneable design axis governing both electronic and sensing behaviour in 3D semiconductor frameworks. Through a UV-driven photoelectrochemical approach, nanoscale ZnO bridges are selectively formed between tetrapodal arms, enabling controlled tuning of network connectivity. The optimized interconnected networks show a 25-fold enhancement in UV response and highly efficient gas detection (10x enhancement), while preserving low-cost and scalable fabrication. Interconnection engineering thus emerges as a general route toward next-generation multimodal sensors [5].

Keywords: ZnO, nanobridge interconnections, photoelectrochemical growth, UV sensing, gas sensing

Background, Motivation and Objective

Tetrapodal ZnO networks [1,2] feature large surface area and mechanical stability, offering a suitable platform for UV and gas sensing. Yet, their performance is constrained by random and poorly defined inter-tetrapod junctions that impede carrier transport [4]. Traditional synthesis routes like CVD, hydrothermal or sputtering cannot independently control network connectivity.

This work decouples building-block formation from connection engineering and introduces interconnection density [2] as a fundamental design variable. The targeted goal is to establish how controlled nanoscale bridging affects charge transport, photoresponse, and gas-sensing behavior in a 3D ZnO framework.

Description of the New Method or System

A UV-pulse driven photoelectrochemical process was developed to induce localized ZnO nanobridges between t-ZnO arms (Fig 1(b)). The mechanism combines photocatalytic growth with selective chemical dissolution. Spatial and temporal control is achieved by modulating the UV pulse duration, which defines bridge density without high-temperature processing. The method is inherently scalable and compatible with 3D-printed ZnO architectures [4] (Fig 1(a)), using direct-ink writing with a printable binder.

The controlled formation of nanobridged interconnections enhances the percolation network within the 3D architecture, facilitating the transition from percolation-limited to optimized charge transport and significantly improving carrier mobility across the network.

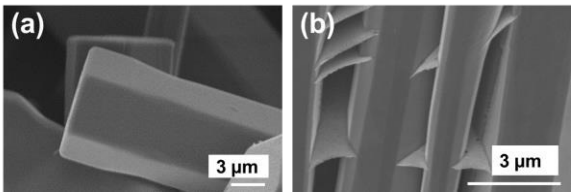

Fig. 1. SEM comparison of (i) point-contact-limited pristine t-ZnO and (ii) nanobridged IC t-ZnO, demonstrating the formation of interconnected junctions and increased contact area.

Results

SEM and TEM confirm controlled bridge formation, transforming discrete point contacts into a continuous percolating network. The interconnection-controlled ZnO (IC-t-ZnO) exhibits markedly higher conductivity and faster transient photoresponse than pristine t-ZnO,

with nearly 25× higher photocurrent under UV illumination (Fig 2(a)).

Gas-sensing tests for acetone reveal a multi-fold increase in response [3] and improved recovery kinetics, particularly in moderately interconnected samples (Fig 2(b)).

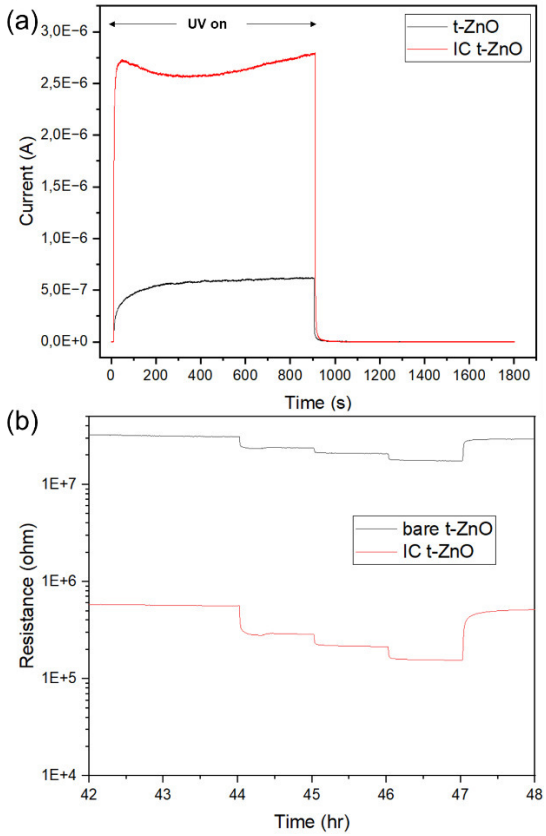

Fig. 2. (i) UV photoresponse and (ii) acetone sensing response of t-ZnO and IC t-ZnO, highlighting enhanced response magnitude and improved sensing performance in the interconnected network

The nanobridged interconnections increase effective contact area and enable efficient charge transfer, resulting in improved sensitivity and stability down to ppb-level concentrations (up to 125 ppb). A non-monotonic dependence [3] on interconnection density is observed, where optimal connectivity maximizes performance, while overly dense networks suffer from recombination and diffusion limitations.

Equations

The transient photoresponse was analyzed using a combined exponential–diffusive model, capturing both rapid surface-controlled recombination and slower diffusion-limited transport. The model shows excellent agreement with experimental data, enabling extraction of characteristic time constants and diffusion contributions. This fitting reveals a transition from percolation-dominated to diffusion-influenced transport with increasing interconnection density.

The UV sensing response was quantified using the normalized photocurrent change, defined as Response $= \frac{I_{UV}}{I_{dark}}$, capturing the relative increase in conductivity under illumination. For gas sensing, the sensor response was calculated as Response $= \frac{R_{air}-R_{gas}}{R_{gas}}$, reflecting resistance modulation upon exposure to reducing gases [3]. These formulations enable consistent comparison of sensitivity across different operating conditions and interconnection densities.

Table 1. Comparative overview of ZnO sensor architectures highlighting performance

System	Response	Key Limitation
ZnO Nanowires	Moderate	Poor Connectivity
ZnO Thin Films	Low - Moderate	Limited Pathways
Hierarchi-cal ZnO	High	Complex Synthesis
This work	**Very High**	**Limited control over junction formation**

References

[1] Ü. Özgür, Y. I. Alivov, C. Liu, A. Teke, M. A. Reshchikov, S. Doğan, V. Avrutin, S. J. Cho, H. Morkoç, A comprehensive review of ZnO materials and devices, *Journal of Applied Physics* 98, 041301 (2005); doi: 10.1063/1.1992666

[2] Y. K. Mishra, R. Adelung, ZnO tetrapod materials for functional applications, *Materials Today* 21, 631–651 (2018); doi: 10.1016/j.mattod.2017.11.003

[3] N. Yamazoe, K. Shimanoe, Theory of power laws for semiconductor gas sensors, *Sensors and Actuators B: Chemical* 128, 566–573 (2008); doi: 10.1016/j.snb.2007.07.036

[4] S. Kirkpatrick, Percolation and conduction, *Reviews of Modern Physics* 45, 574–588 (1973); doi: 10.1103/RevModPhys.45.574

[5] B. Chakraborty, L. Ramío I Matas, S. Bayan, B. Junker-Reiss, C. Lupan, M.-I. Terasa, M. Elis, E. Osman, R. Madurawala, K. Meurisch, J. Carstensen, O. Lupan, A. Gutierrez Galvez, L. Siebert, R. Adelung, Interconnection engineering in 3D ZnO networks for enhanced charge transport and multimodal sensing, *(to be published elsewhere)*

DOI 10.5162/eurosensors2026/6.1.5

High-Sensitivity and Reliable Gas Sensor by Hybridizing Laser-Induced Graphene and Molybdenum Trioxide with Metal-Organic Decomposition

Akihiro Katsura[1], Otoya Okanishi[1], Yukiko Hirose[1], Yuma Miura[1], Wenliang Zhu[1], Tohru Sugahara[1]
[1] Kyoto Institute of Technology, Matsugasaki, Sakyo-ku, Kyoto, 606-8585, Japan
katsura.akihiro.1025@gmail.com

Summary:
Volatile organic compounds are attracting increasing attention in health monitoring, environmental assessment, and industrial process control. Therefore, simple strategies for developing gas sensors with high sensitivity and rapid response are strongly desired. In this work, laser-induced graphene is employed as a conductive scaffold and molybdenum trioxide as a gas-reactive material to construct a hybrid sensing platform through metal-organic decomposition. This approach provides a simple route to hybrid sensing materials for high-performance volatile organic compound sensing.

Keywords: Laser-Induced Graphene, Molybdenum Trioxide, Metal-Organic Decomposition, Gas Sensor, Volatile Organic Compounds

Introduction

Volatile organic compounds are attracting increasing attention in health monitoring, environmental assessment, and industrial process control. In particular, methanol, ethanol, 1-propanol, and 2-propanol have been investigated as representative volatile organic compounds related to metabolic disorders, alcohol consumption, bacterial infections, and diabetic ketoacidosis, respectively [1-2]. Therefore, gas sensors with high sensitivity, rapid response, and stable operation are strongly desired for practical volatile organic compound monitoring. Metal oxide semiconductors have been widely studied as gas sensing materials because of their high sensitivity and rapid response originating from surface redox reactions [3]. However, their low carrier mobility and high electrical resistivity often impose a substantial electrical burden on sensor devices. Hybridization with conductive carbon materials has recently attracted attention as an effective way to address these drawbacks and enhance sensing performance [4]. In particular, laser-induced graphene offers high electrical conductivity, large surface area, and simple fabrication directly on polymer substrates, making it an attractive platform for hybrid gas sensors [5]. However, a facile strategy for integrating highly crystalline gas-reactive metal oxides with laser-induced graphene has not been sufficiently established. In this study, laser-induced graphene was employed as a conductive scaffold and molybdenum trioxide as a gas-reactive material, and a metal-organic decomposition strategy was adopted to integrate both components into a hybrid sensing platform for volatile organic compound detection.

Experimental

Laser-induced graphene was fabricated on polyimide films by direct laser irradiation using a YVO_4 laser marker. For hybridization, a precursor solution containing ammonium molybdate, citric acid, and N,N-dimethylformamide was deposited onto the laser-induced graphene by spin coating, followed by sintering in air at 673 K for 15, 30, and 60 min to form molybdenum oxide. The resulting structures were analyzed by field-emission scanning electron microscopy, X-ray diffraction, X-ray photoelectron spectroscopy, and Raman spectroscopy to evaluate their morphology, crystal structure, and chemical states. Gas sensing performance was evaluated by monitoring resistance changes toward methanol, ethanol, 1-propanol, and 2-propanol under heated conditions.

Results and Discussion

Fig. 1(a) shows the surface morphology of laser-induced graphene optimized as a conductive platform for gas sensing. The laser-induced graphene exhibited a wave-like porous network structure, which is favorable for providing both continuous electrical conduction pathways and a large specific surface area. Fig. 1(b) shows the surface morphology of the LIG/α-MoO_3 hybrid material after the synthesis using metal-organic

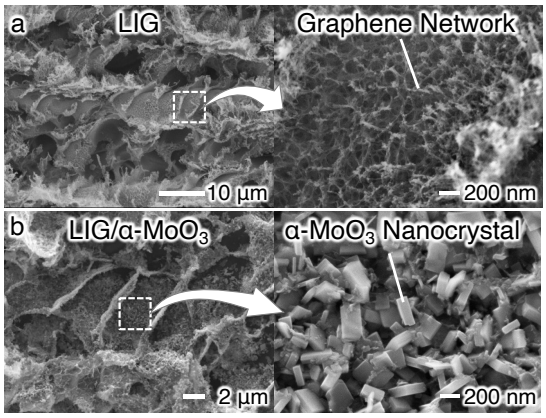

Fig. 1. Surface morphology of (a) laser-induced graphene (LIG). (b)LIG/α-MoO_3 hybrid materials.

decomposition. Nanostructured α-MoO_3 was densely formed on the graphene network while the underlying laser-induced graphene framework was preserved, indicating that the metal-organic decomposition process successfully hybridized the gas-reactive oxide with the conductive scaffold without severe degradation of the carbon structure. This hybrid structure is expected to combine efficient charge transport through laser-induced graphene with abundant gas-reaction sites from α-MoO_3. Fig. 2(a) shows the sensing properties of LIG/α-MoO_3 toward various volatile organic compounds at approximately 350 ppm. The hybrid sensor responded to all tested gases, including methanol, ethanol, 1-propanol, and 2-propanol, and the response strongly depended on the gas species. In particular, methanol showed the largest response, followed by 1-propanol, 2-propanol, and ethanol, demonstrating selective discrimination among alcohol-based volatile organic compounds. Fig. 2(b) shows the repeatability of the sensor response to 44.7 ppm methanol under repeated injection cycles. A stable cyclic response was observed with a coefficient of variation of 3.62%, indicating good repeatability at low concentration. These results demonstrate that the hybridization of laser-induced graphene and α-MoO_3 effectively improved volatile organic compound sensing by combining conductive charge transport with dense gas-reactive nanostructures.

Conclusion

In this study, laser-induced graphene and α-MoO_3 were integrated by metal-organic decomposition to construct a hybrid gas-sensing platform. The resulting hybrid showed clear responses toward volatile organic compounds, with the highest response and stable repeatability toward methanol. These results demonstrate that metal-organic decomposition is a simple and effective strategy for fabricating high-performance hybrid gas sensors.

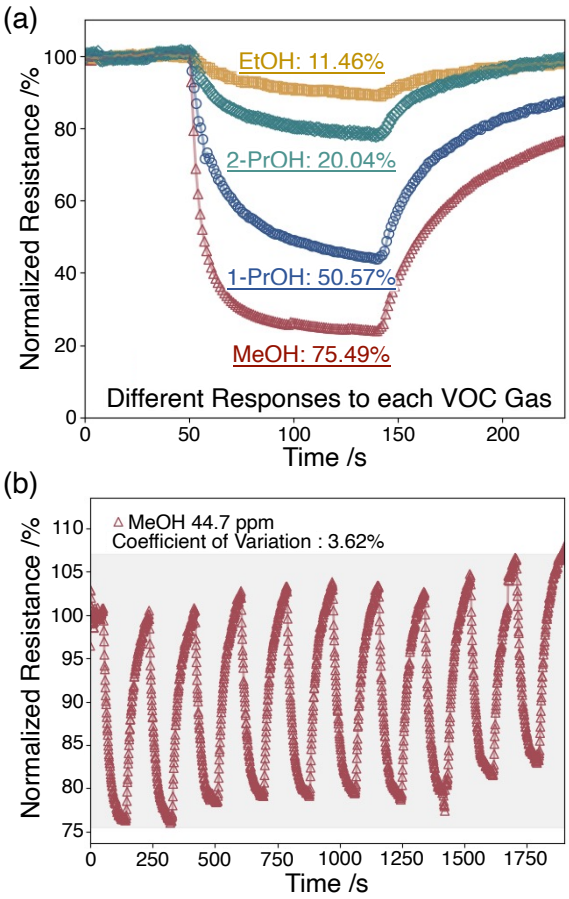

Fig. 2. (a) Sensing properties of LIG/α-MoO_3 hybrid gas sensor toward volatile organic compounds gases. (b) Repeatability of the sensor responses toward 44.7 ppm methanol.

References

[1] H. Jin, N. Tang, Q. C. Li, C. L. Xue, Y. N. Zhang, Y. Zhou, D. X. Cui, H. Haick, "Wearable Sensors for Detection of Human Health Using Volatile Biomarkers," in Volatile Biomarkers for Human Health: From Nature to Artificial Senses, ed. H. Haick, *The Royal Society of Chemistry*, 2022, pp. 401–415

[2] T. E. A.-R. Silva, F. Burisch, A. T. Güntner, "Gas sensing for space: Health and environmental monitoring," Trends in *Analytical Chemistry*, 2024, 177, 117790.

[3] A V.-M. Dospinescu, A. Tiele, J. A. Covington, "Sniffing Out Urinary Tract Infection—Diagnosis Based on Volatile Organic Compounds and Smell Profile," *Biosensors*, 2020, 10, 83.

[4] H. Lim, H. Kwon, H. Kang, J. E. Jang, H.-J. Kwon, "Laser-Induced and MOF-Derived Metal Oxide/Carbon Composite for Synergistically Improved Ethanol Sensing at Room temperature," *Nano-Micro Letters*, 2024, 16, 113.

[5] Y. Li, D. X. Luong, J. Zhang, Y. R. Tarkunde, C. Kittrell, F. Sargunaraj, Y. Ji, C. J. Arnusch, J. M. Tour, "Laser-Induced Graphene in Controlled Atmospheres: From Superhydrophilic to Superhydrophobic Surfaces," *Advanced Materials*, 2017, *29*, 1700496.

DOI 10.5162/eurosensors2026/6.1.6

Corporation Effect of CuO and Fe_2O_3 Composites in VOC Sensing

Changlin Xiao[1], Harindrasing Jabal[1], Udo Weimar[1], Nicolae Barsan[1],
[1] Institute of Physical and Theoretical Chemistry, University of Tübingen, 72076 Tübingen, Germany
nb@ipc.uni-tuebingen.de

Summary:
We demonstrated improved VOC sensing using composites of p-type CuO and n-type Fe_2O_3 metal oxide semiconductors. The composites were prepared using both chemical mixing (sol–gel method) and physical mixing. Both composites showed higher sensor signals and faster response and recovery speeds compared to the pure phase, while the physically mixed sample maintained the baseline resistance and sensitivity of Fe_2O_3. Operando DRIFTS measurements confirmed consistent surface chemistry, indicating that the improvements originate from the electronic coupling effect between CuO and Fe_2O_3.

Keywords: SMOX sensor, VOCs, CuO, Fe_2O_3, corporation effect

Introduction

Semiconducting metal oxides (SMOXs)-based gas sensors, as one of the most important types of chemical sensors, have attracted widespread scientific attention. However, their practical applications are still limited by several drawbacks, such as slow response and recovery speeds, especially toward low-concentration VOC gases. Our previous work demonstrated that Fe-containing materials exhibit better performance in VOC sensing; however, they also suffer from slow response and recovery kinetics, as observed in both Fe-containing perovskites and Fe_2O_3. This limitation can be mitigated by increasing the operating temperature to accelerate surface reactions and enhance charge carrier transport. However, elevated temperatures also increase power consumption and reduce the sensor signal. Fe-containing spinels, on the other hand, exhibit much faster response and recovery kinetics, despite their relatively poor sensitivity. Therefore, we explored another Fe-containing spinel, $CuFe_2O_4$. However, we accidentally obtained a mixture of CuO and Fe_2O_3, which exhibited improved performance, including higher sensor signals and faster response and recovery. We therefore performed a series of characterizations to elucidate the underlying mechanisms.

Materials and Methods

We first attempted to synthesize $CuFe_2O_4$ via a sol–gel method at different calcination temperatures ranging from 300 to 800 °C. The samples are denoted as CFO, followed by a suffix indicating the calcination temperature. CuO and Fe_2O_3 were synthesized using the same method and calcined at 500 °C. Characterization results revealed that the products obtained at lower temperatures (below 700 °C) consist of mixtures of CuO and Fe_2O_3. These mixtures, however, exhibited superior performance during the sensing tests. We then physically mixed CuO and Fe_2O_3 powders; the resulting material retained the baseline resistance of Fe_2O_3 while showing faster response and recovery speeds toward formaldehyde, as well as other VOCs. We therefore performed operando DRIFTS measurements to investigate the differences in surface chemistry among these materials. All sensors were fabricated using screen printing, and the sensing tests were conducted in a dynamic gas-mixing system with multiple VOC channels.

Results and Discussion

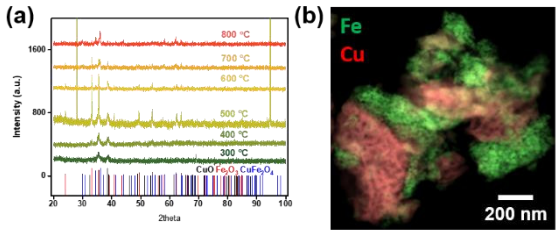

Fig. 1. (a) The XRD results of all synthesized materials. (b) The EDS mapping of CFO500 sample.

The crystallographic information was evaluated by X-ray diffraction (XRD), as summarized in Fig. 1(a). Incomplete crystallization at low temperatures (300 and 400 °C) leads to weak and broad diffraction peaks in the patterns. At 300 °C, only the CuO phase can be observed. Fe_2O_3 starts to

form at temperatures above 400 °C. Notably, the sharp peaks appearing at around 28 and 94.7° originate from the silicon substrate. At temperatures above 700 °C, CuO and Fe_2O_3 begin to convert into the spinel phase $CuFe_2O_4$, and at 800 °C, a pure spinel phase is obtained. Samples prepared between 400 and 700 °C consist of mixed phases of CuO and Fe_2O_3. The sample calcined at 500 °C shows better crystallinity and was therefore selected to evaluate the phase and elemental distribution by EDS mapping (see Fig. 1(b)). Clearly, the CuO and Fe_2O_3 particles are closely connected, which provides the possibility for forming more n–p heterojunctions.

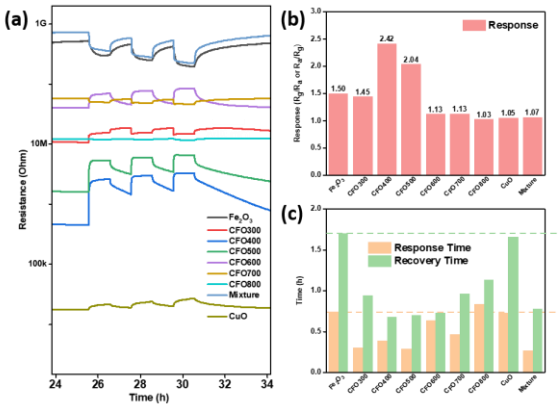

Fig. 2. (a) Output curves of all fabricated sensors toward 50, 100, and 200 ppb formaldehyde. (b) Calculated response values and (c) response and recovery times of all fabricated sensors toward 200 ppb formaldehyde. The sensor operating temperature was 150 °C.

The response curves of the fabricated sensors toward different concentrations of formaldehyde are shown in Fig. 2(a). Pure CuO, shown at the bottom, has a conductivity advantage, as indicated by its lowest baseline resistance. However, the limited sensor signals reveal its lower surface activity. The sample calcined at 300 °C exhibits an n-to-p conduction inversion, which is an intrinsic property of Fe_2O_3 [1]. However, this inversion is not observed in other mixtures, including the samples calcined at 400, 500, and 600 °C, nor in the physically mixed sample. The conduction type of Fe_2O_3 is inverted only when conduction band electrons are depleted and oxygen begins to extract electrons from the valence band. This strongly supports the interaction between CuO and Fe_2O_3. Electrons spontaneously transfer from the conduction band of Fe_2O_3 to the valence band of CuO, resulting in a decrease in the electron concentration of Fe_2O_3, which makes it more easily depleted, i.e., more prone to a change in conduction type.

The sensor responses are shown in Fig. 2(b). The samples calcined at 400 and 500 °C exhibit higher sensitivity, which originates from the increased formation of n–p junctions within the material. At higher temperatures, particle growth occurs and the spinel phase, which exhibits poor sensitivity, begins to form, resulting in decreased sensor signals. The response and recovery times, summarized in Fig. 2(c), clearly show that both the response and recovery speeds of the mixtures, including the chemically mixed and physically mixed samples, are faster than those of the pure phases.

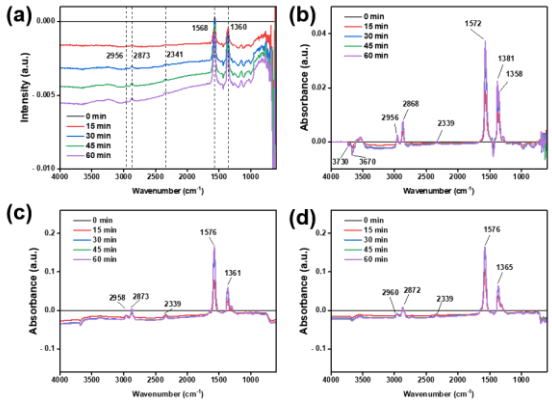

Fig. 3. DRIFT absorbance spectra of (a) CuO, (b) Fe_2O_3, (c) CFO400 and (d) CFO500 toward 10 ppm formaldehyde, collected with 15 min intervals.

The operando DRIFTS results are shown in Fig. 3. Intermediate products from the oxidation of formaldehyde, including bridged formate and dioxymethylene, can be clearly observed in the spectra of all samples[1]. Terminal formate species are observed in the spectra of Fe_2O_3. The peak at 2341 cm^{-1} is attributed to carbon-containing species introduced by the organic precursors; this species is still under investigation. Apparently, the absorbance intensity of CuO is the lowest among the four samples. This further confirms its poor catalytic activity, which is consistent with the low sensor signal. The mixtures, including CFO400 and CFO500, exhibit significantly higher absorbance, indicating a higher concentration of surface species, which is induced by the cooperation between CuO and Fe_2O_3.

Referenc

[1] Gurlo, A.; Bârsan, N.; Oprea, A.; Sahm, M.; Sahm, T.; Weimar, U. An n- to p-type conductivity transition induced by oxygen adsorption on α-Fe_2O_3. Applied Physics Letters. 2004, 85, 2280-2282, DOI: 10.1063/1.1794853

[2] Gomes, J. R. B.; Gomes, J. A. N. F. A theoretical study of dioxymethylene, proposed as intermediate in the oxidation of formaldehyde to formate over copper. Surface Science. 2000, 446, 283-293, DOI: 10.1016/S0039-6028(99)01157-7

DOI 10.5162/eurosensors2026/6.2.1

Miniaturized, Flexible Electroosmotic Device Based on Laser-Patterned PEDOT:PSS Electrodes for Drug Delivery and Electrophysiological Biosensing

Massimo Mariello[1], *Farabi Ahnaf*[1], *Christopher M Proctor*[1]
[1] Department of Engineering Science, Institute of Biomedical Engineering, University of Oxford, Oxford, UK

massimo.mariello@eng.ox.ac.uk

Summary:

Electroosmotic micropumps use electric fields to precisely control fluid flow in microdevices. They are attractive for implantable bioelectronic devices due to their simple electrode-based design and compatibility with miniaturization. This study presents a low-voltage bioelectronic pumping and sensing device with thin-film interdigitated electrodes achieving very low flow rates (~0.5 nL/min). Laser-fabricated designs and simulations optimize flow and reduce vortices. PEDOT:PSS improves efficiency and electrode stability. A flexible implantable prototype demonstrates potential for biomedical applications like drug delivery and electrophysiological biosensing, specifically for the treatment of neurological disorders.

Keywords: bioelectronics, drug delivery, electrophysiology, flexible, implantable.

Background, Motivation and Objective

Electroosmotic (EO) actuators are suitable for microfluidic applications because they can produce high pressures and precise flow. In these devices an electrolyte is pumped by applying an electric field to the Debye layer, which is formed by the ions due to electric screening of the immobile charges on the walls of the liquid channels within the pump [1, 2]. The EO pumping mechanism is one of the simplest ones for fluidic control, since it is based only on electrode arrays, therefore it is very suitable for the design and fabrication of bioelectronic implantable micro-devices with applications in drug delivery or biofluid sampling [3]. Currently, these pumps are designed to trigger large flow rates (~1-10 μL min^{-1}), they are based on thick electrodes and their sizes are mostly not compatible with miniaturized advanced bioelectronics.

In this work, we aim to design and characterize an AC electroosmotic micropump based on thin-film interdigitated electrodes, as a proof-of-concept prototype capable of generating ultra-low flow rates while operating at significantly reduced voltages. The objective is to demonstrate a scalable and efficient platform for controlled fluid delivery in biomedical applications, where drug delivery and biofluid sampling can be coupled with electrophysiological biosensing.

Description of the Methodology

An AC electroosmotic micropump based on asymmetric thin-film interdigitated electrode (IDE) designs is developed. Different AC electrical waveforms are applied to drive the flow of a phosphate buffer solution (PBS) containing 1 μm polystyrene microbeads, enabling optical visualization of fluid motion. The pumps are characterized in vitro using microfluidic channels with sub-50 μm dimensions, fabricated through PDMS replica molding from laser-patterned metal molds. IDEs with both symmetric and asymmetric configurations are patterned using nanosecond and femtosecond pulsed lasers on thin films of gold (Au) and PEDOT:PSS deposited by DC sputtering. The laser microfabrication provides an ultra-fast, effective and maskless method to pattern thin films deposited by DC sputtering. The resolution offered by different pulse durations is used to design IDEs within a wide range of dimensions, from 10μm to 100μm trackwidth. Finite-element-modelling (FEM) simulations are used to predict the fluid dynamics due to electroosmosis, systematically showing a strong dependence on the flow rate on the electrode designs and the microfluidic channels size. Additionally, it is possible to predict the formation of fluidic vortexes in the gaps between the electrodes or above each electrode. Tuning the channel height, the trackwidth and the inter-electrode gaps contributes to regulate more uniformly the fluid flow.

Results

Simulations reveal a strong dependence of flow rate on electrode geometry and microchannel dimensions, and predict vortex formation that can be mitigated through design optimization.

The contribution of the organic conductive material (PEDOT:PSS) is two-fold. First, PEDOT:PSS significantly increases the effective electrode capacitance due to its mixed ionic–electronic conductivity and volumetric charge storage capability. Unlike bare metal electrodes, where capacitance is limited to the electric double layer, PEDOT:PSS enables additional capacitive contributions within its bulk, effectively behaving as a distributed network of nanoscale capacitors [4, 5]. This enhanced capacitance reduces the electrode impedance and allows efficient charge transfer at lower applied voltages, thereby decreasing the voltage required to achieve a given electroosmotic flow rate.

Second, PEDOT:PSS improves the stability and durability of gold (Au) electrodes under electrical operation. The polymer coating reduces electrode polarization and increases the charge injection capacity, mitigating electrochemical degradation processes that typically occur at higher voltages [6]. Additionally, PEDOT:PSS exhibits excellent electrochemical stability and strong adhesion to Au surfaces, forming a protective interface that limits corrosion and prolongs electrode lifetime in electrolyte environments [7].

In vitro experiments enable to quantify the dependence of the resulting flow rate and the applied voltage amplitude, the AC driving frequency, the applied DC offset and the electrode design. Flow rates in the order of ~0.5 nL min^{-1} can be achieved with ultra-low peak-to-peak voltages (~0.8-3 V) (Fig.1).

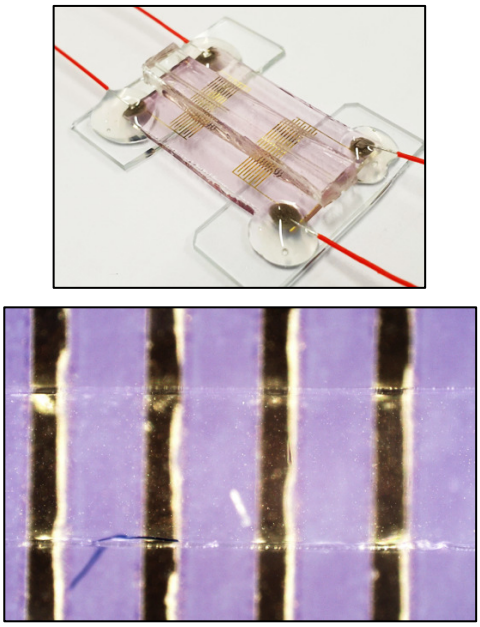

Fig. 1. Top: In vitro platform to test the PEDOT:PSS based electrodes with a PDMS microfluidic channel. Bottom: optical micrograph showing the microbeads flowing at a speed of ~0.5 nL min^{-1} within a microfluidic channel filled with PBS on top of interdigitated electrodes.

Additionally, a flexible proof-of-concept AC electroosmotic pump, designed in the form of an implantable probe (Fig.2), is successfully demonstrated and tested in vitro in an agarose gel phantom.

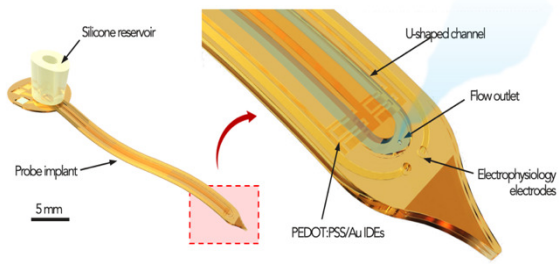

Fig. 2. Illustration of a flexible pump based on the PEDOT:PSS/Au electrodes for drug delivery and electrophysiological biosensing.

Conclusions

The proposed PEDOT:PSS-based electroosmotic pumps pave the way for the realization of implantable bioelectronic probes for biomedical applications, in particular for the treatment of neurological disorders (e.g., epilepsy, Parkinson's disease, chronic pain, etc.). Designs with arrays of multiple pumps are envisioned for more complex and sophisticated microfluidic systems for fluid control and biosensing.

References

[1] Guy RH, Kalia YN, Delgado-Charro MB, et al. Iontophoresis: electrorepulsion and electroosmosis. *Journal of Controlled Release* 2000; 64: 129–132.
[2] Kusama S, Sato K, Matsui Y, et al. Transdermal electroosmotic flow generated by a porous microneedle array patch. *Nat Commun* 2021; 12: 658.
[3] Mariello M, Eş I, Proctor CM. Soft and Flexible Bioelectronic Micro-Systems for Electronically Controlled Drug Delivery. *Advanced Healthcare Materials*; n/a: 2302969.
[4] Calabia Gascón N, Terryn H, Hubin A. The role of PEDOT:PSS in (super)capacitors: A review. *Next Nanotechnology* 2023; 2: 100015.
[5] Kauth A, Wegener J, Jiang H, et al. PEDOT:PSS Electropolymerization Protocol for Microelectrodes Enabling Low-Cost Impedance-Based Cellular Assays. *Applied Research* 2025; 4: e202400087.
[6] Pranti AS, Schander A, Bödecker A, et al. PEDOT:PSS coating on gold microelectrodes with excellent stability and high charge injection capacity for chronic neural interfaces. *Sensors and Actuators B: Chemical* 2018; 275: 382–393.
[7] Dijk G, Rutz AL, Malliaras GG. Stability of PEDOT:PSS-Coated Gold Electrodes in Cell Culture Conditions. *Advanced Materials Technologies* 2020; 5: 1900662.

DOI 10.5162/eurosensors2026/6.2.2

Bespoke Laser Fabrication of High-Density PEDOT:PSS MEAs for Low-Impedance Cortical Neuronal Recordings

Enzo Rolando[1], David Grojo[1], Adrien Casanova[1]
[1] LP3 UMR 7341, 163 Av. de Luminy, 13009 Marseille, France
enzo.rolando@univ-amu.fr

Summary:
We explore a cleanroom free fabrication route to prototype high density PEDOT:PSS microelectrode arrays with 256 recording sites for neuronal interfacing. Electrochemical impedance spectroscopy indicates low-impedances around 30 kΩ at 1 kHz, consistent with PEDOT:PSS microelectrodes suitable for extracellular recordings. Preliminary tests with primary rat cortical neurons show detectable spontaneous activity on multiple channels but also highlight limitations in long term stability and cell culture performance that motivate further optimisation of the materials stack.

Keywords: laser microfabrication, PEDOT:PSS, microelectrode arrays, electrochemical impedance spectroscopy, neuronal recordings

Background, Motivation and Objective

Microelectrode arrays (MEAs) are key bioelectronic tools to monitor the electrical activity of electrogenic cells and neuronal networks with high spatial and temporal resolution [1]. However, conventional MEA fabrication relies on multi-step cleanroom processes and photolithography, which are costly, rigid in design, and poorly suited to rapid on-demand prototyping of customised layouts [2]. Each new electrode configuration typically requires a dedicated mask set and full process run, making it difficult for research laboratories to iterate quickly on electrode density, geometry, or contact routing. Conducting polymers such as PEDOT:PSS have enabled low-impedance electrodes for high-quality extracellular recordings, while also offering mechanical compliance closer to that of soft tissues. Yet PEDOT:PSS is most often integrated through standard microfabrication routes [3], limiting its accessibility to facilities with established microfabrication infrastructure. There is thus a strong demand for rapid and bespoke cleanroom-free fabrication strategies that combine high-density layouts, low-impedance PEDOT:PSS microelectrodes and robust neuronal recordings on a single platform, while remaining compatible with stable long-term operation in electrolyte and cell culture. The objective of this work is to explore a bespoke laser-based fabrication process for high-density PEDOT:PSS MEAs and to provide a proof-of-concept assessment of its electrochemical and electrophysiological performance with primary cortical neurons. We specifically aim to investigate whether a laser route can (i) pattern the full MEA circuitry and define 30 µm-diameter PEDOT:PSS recording sites (Fig. 1A–C), and (ii) yield electrode impedances and neuronal recordings compatible with standard in vitro network studies (Fig. 1D–F), while identifying limitations that motivate further materials and process optimisation. By doing so, we highlight laser microfabrication as a promising route for cleanroom-free, on-demand prototyping of advanced bioelectronic interfaces.

Description of the New Method or System

We developed a dual-wavelength laser microfabrication platform that combines an infrared beam for rapid large-area material removal with a UV beam for high-resolution patterning and selective ablation, all operated without cleanroom facilities. Glass substrates are first coated with a Ti (PVD) followed by PEDOT:PSS (dropcasted) stack. The MEA circuitry, electrode sites and contact pads are then defined entirely by laser ablation steps (Fig. 1A,B). An insulating PDMS passivation layer is spin-coated on top and a final laser ablation step open the recording sites and contact pads through the passivation layer (Fig. 1C).

This laser process is used here to prototype 256-electrode high-density MEAs with a radial routing layout, distributing 252 recording channels and four reference electrodes over a 49 × 49 mm footprint using LaserDesk software, as illustrated in Fig. 1A. The close-up view in Fig. 1C highlights the regular array of exposed PEDOT:PSS microelectrodes and their alignment with the underlying titanium tracks.

DOI 10.5162/eurosensors2026/6.2.2

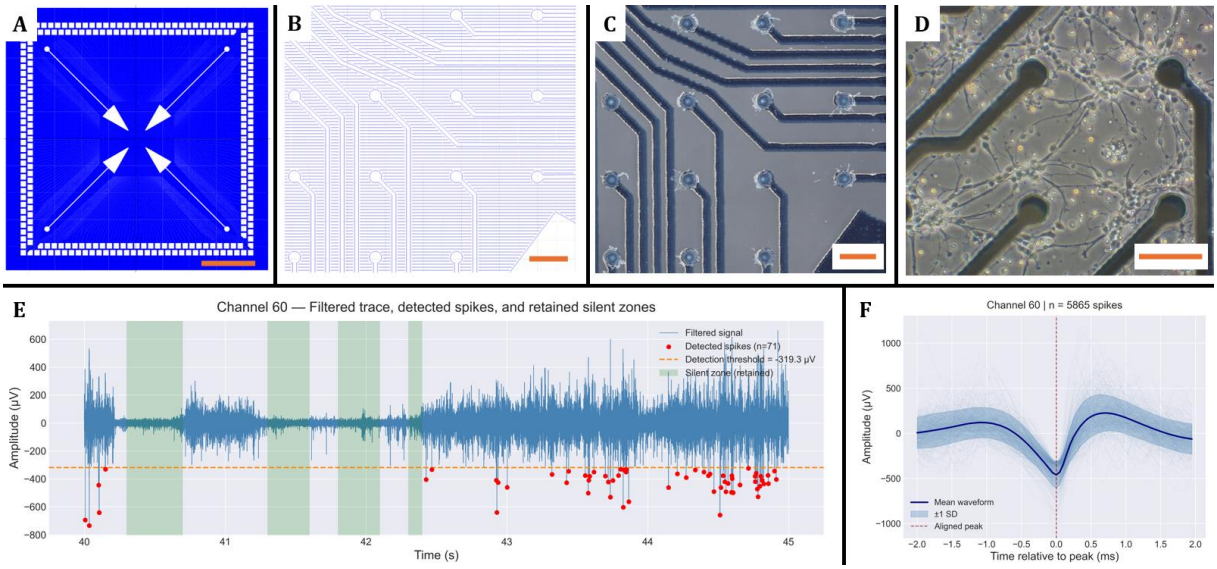

Fig. 1. (A) Entire MEA layout in LaserDesk software; the blue region indicates the ablated area (scale bar 10 mm). (B) Close-up of the central electrode array with 25 electrodes/mm² and approximately 30 µm electrode diameter (scale bar 100 µm). (C) UV-opened electrodes with PDMS passivation (scale bar 100 µm). (D) Primary cortical neurons at DIV8 cultured on the MEA (scale bar 100 µm). (E) Bandpass filtered (300-5000 Hz) extracellular recording on channel 60 over 5 s, with detected spikes highlighted in red and the threshold indicated by the dashed line. (F) Mean spike waveform on channel 60 (n = 5865 spikes); shading indicates ±1 SD and the dashed line marks the negative peak at 0 ms.

Results

Electrochemical impedance spectroscopy (EIS) was used to characterise the electrical performance of the laser-fabricated PEDOT:PSS microelectrodes in phosphate-buffered saline (PBS). Mean electrode impedances at 1 kHz are on the order of 30 kΩ for 30 µm-diameter sites, within the expected range for PEDOT:PSS microelectrodes of similar dimensions and indicative of suitability for extracellular measurements. These measurements provide a first quantitative link between the device architecture in Fig. 1A, B and its electrical behaviour, while leaving possibility for further optimisation of the materials stack and encapsulation.

Preliminary biological tests were performed with primary rat cortical neurons cultured directly on the laser-fabricated MEAs (Fig. 1D). By eight days in vitro, spontaneous bursting activity was observed on multiple channels, and bandpass-filtered traces showed clearly identifiable spikes with representative average spike waveforms on selected electrode (Fig. 1E,F). For more mature cultures beyond two weeks in vitro, however, limitations became apparent, with a degradation of network stability that we attribute to long-term PEDOT:PSS behaviour in immersion and to the intrinsic hydrophobicity of the PDMS passivation layer, which is less critical for indirect microfluidic contact but becomes determinant for in vitro neuronal cultures. To address these issues, we have begun exploring surface functionalisation strategies for PDMS such as polydopamine coatings, initial results are mixed but encouraging and motivate ongoing efforts to improve the electrode stack and passivation layer in future work.

References

[1] A. Angelovski, M. Bébarová, The microelectrode array technique - a crucial tool for studying excitable tissue disorders and drug testing: an update on recent advances, *Progress in Biophysics and Molecular Biology* (2025); doi: 10.1016/j.pbiomolbio.2025.07.005

[2] A. Tanwar, H. Gandhi, D. Kushwaha, J. Bhattacharya, A review on microelectrode array fabrication techniques and their applications, *Materials Today Chemistry* (2022); doi: 10.1016/j.mtchem.2022.101153

[3] J. Pas, C. Pitsalidis, D.A. Koutsouras, P.P. Quilichini, F. Santoro, B. Cui, L. Gallais, R.P. O'Connor, G.G. Malliaras, R.M. Owens, Neurospheres on patterned PEDOT:PSS microelectrode arrays enhance electrophysiology recordings, *Advanced Biosystems* **2**, 1700164 (2018); doi: 10.1002/adbi.2017001

DOI 10.5162/eurosensors2026/6.2.3

Enzyme-Free Electrochemical Sensing for Real-Time In-Process Monitoring

Aliyeh Hasanzadeh[1], Shova Neupane[1], Elaheh Kazempour[1], Nicolai Støvring[2]

Stephan Sylvest Keller[2], Krist V. Gernaey[1], Pedram Ramin[1]

[1]Center for Process Engineering and Technology (PROSYS), Department of Chemical and Biochemical Engineering, Technical University of Denmark
[2]National Centre for Nano Fabrication and Characterization Nanofabrication, Technical University of Denmark
alhas@dtu.dk

Summary:

Real-time monitoring is essential for scalable bioprocessing, yet key metabolites are still measured off-line. We present an enzyme-free electrochemical sensor for continuous in-line and on-line operation under industrial conditions. The platform enables accurate, stable, and sterilizable monitoring in complex media. Performance is demonstrated during fermentation with high linearity, low detection limits, and long-term stability.

Keywords: process analytical technology, electrochemical sensing, glucose monitoring, bioprocessing, enzyme-free sensor

Background, Motivation and Objective

Process analytical technology (PAT) is a key enabler for the transition from empirical bioprocessing toward data-driven and autonomous operation [1]. However, most industrial and laboratory-scale processes still rely on off-line measurements for critical metabolites such as glucose. This limits temporal resolution and process insight.

Biosensors are very attractive due to their operational simplicity, low cost, and rapid analysis. They have been used effectively for real-time monitoring platform in a yeast fed-batch fermentation [2]. However, most electrochemical biosensors rely on enzymes, such as glucose oxidase, and this creates several practical limitations. The enzyme can lose activity over time, which leads to limited stability and short operational lifetime. These systems also often depend on oxygen, which can be a problem in some bioprocess conditions. In addition, they are usually sensitive to sterilization and may require frequent calibration or replacement.

Description of the New Method or System

We present an enzyme-free electrochemical sensing platform for monitoring of key metabolites such as glucose, lactate and ammonium. The system is intended for both in-line use inside the bioreactor and on-line operation using an external flow-through setup. The overall idea is to enable continuous measurements under realistic bioprocess conditions, where traditional biosensors often have limitations.

The sensing principle is based on a solid-state electrode structure with synthetic sensing layers, so no biological components are used. The electrodes are fabricated as 3D pyrolytic carbon microstructures in a three-electrode chip configuration. This is done using photolithography followed by pyrolysis of SU-8 photoresist, which forms stable carbon structures [3].

The sensing itself is based on electrochemical reactions occurring at the electrode surface. The electrode is coated with selective materials that interact with the target molecules, and this leads to a measurable current signal. On top of this, a membrane layer is used to control diffusion of molecules to the surface and to reduce interference from larger compounds or particles in the medium. Additional coating layers are used to improve stability and reduce fouling during operation. The combination of coating and membrane is important to get a stable signal over time

and to make the sensor usable in complex fermentation media

For the in-line configuration, the sensor is integrated into a probe. The design helps to have more controlled mass transport at the sensor surface and reduces effects from bubbles and mixing in the reactor. For the on-line configuration, a flow-through cell is used, where the liquid is circulated outside the reactor and passes over the sensor. This makes it easier to handle and test the system.The platform is operated with a compact in-house potentiostat, which is used to control the measurement and record the signal.

Results

The glucose, lactate and ammonium sensors demonstrate a dynamic range of 0.1–150 mM, linearity above $R^2 > 0.996$, and detection limits below 0.05 mM. Accuracy and precision were below 5% and 7%, respectively, with response times of 1–3 minutes. The sensor maintains a stable and linear response after gamma sterilization (50 kGy) (Fig. 1). While a slight decrease in absolute signal is observed after irradiation, the linear relationship between current and glucose concentration is preserved across the full measurement range. This indicates that the sensing mechanism remains intact, and calibration can be maintained post-sterilization.

On-line glucose monitoring was performed using a flow-through setup during yeast fermentation (Fig. 2). The sensor shows stable operation over time and follows the general trend of glucose consumption thought-out the 8 hours. The measurements are in reasonable agreement with HPLC data, which were collected every hour, following sampling and off-line analysis.

At a later stage, a glucose spike was intentionally introduced to check if the sensor is still responsive. This appears as a sharp increase in the signal. After this, the signal goes back to the expected level. This confirms that the sensor is still active, responds quickly to changes, and does not lose functionality during operation.

Conclusion

The presented enzyme-free electrochemical platform enables robust in-line and flexible on-line monitoring of multiple key metabolites. By combining sterilizability, long-term stability, and multi-analyte capability, this work addresses key limitations of existing biosensors and provides a practical route toward scalable PAT and autonomous bioprocessing.

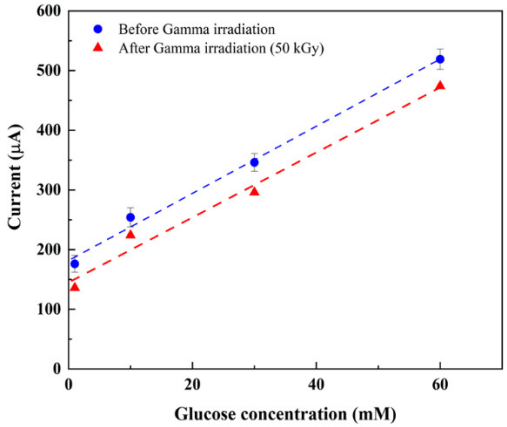

Fig. 1. Stable and linear glucose response is maintained after gamma sterilization, confirming sensor robustness.

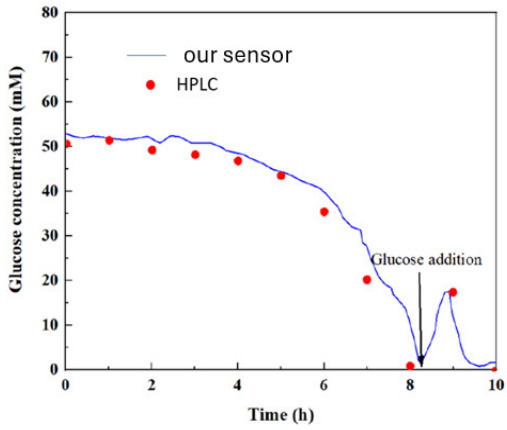

Fig. 2. On-line Glucose Monitoring During a yeast fermentation

References

[1] C. L. Gargalo, P. C. Lopez, A. Hasanzadeh, I. A. Udugama, and K. V. Gernaey, *On-line monitoring of process parameters during fermentation*. INC, 2022. doi: 10.1016/b978-0-323-91167-2.00003-4.

[2] K. Pontius, D. Semenova, Y. E. Silina, K. V. Gernaey, and H. Junicke, “Automated Electrochemical Glucose Biosensor Platform as an Efficient Tool Toward On-Line Fermentation Monitoring: Novel Application Approaches and Insights,” *Front. Bioeng. Biotechnol.*, vol. 8, May 2020, doi: 10.3389/FBIOE.2020.00436.

[3] S. Esmail Tehrani *et al.*, “Hydrogen Peroxide Detection Using Prussian Blue-modified 3D Pyrolytic Carbon Microelectrodes,” *Electroanalysis*, vol. 33, no. 12, pp. 2516–2528, 2021, doi: 10.1002/elan.202100387.

DOI 10.5162/eurosensors2026/6.2.4

Toward Rapid Water Quality Monitoring: QCM-Guided Bio-interface Engineering of Graphene SGFET Biosensors for *Escherichia coli* Detection

Claire Beddok[1], Mohammad Danish Alhindi[2], Gad Fuks[2], Ahmed Mehdi Debela[2], Victor Fabre[1], Thomas Alava[1]
[1] Univ. Grenoble Alpes, CEA, LETI, Grenoble 38054, France
[2] Univ. Perpignan Via Domitia, CRIOBE, Perpignan 66400, France
talava@cea.fr

Summary:

This work presents a QCM-guided biointerface engineering strategy for graphene SGFET biosensors dedicated to rapid *Escherichia coli* detection in water. The bio-functionalization process is optimized using Quartz Crystal Microbalance to ensure controlled antibody immobilization while preserving graphene electrical properties. The optimized protocol is successfully transferred to SGFET devices, enabling concentration-dependent Dirac point shifts upon bacterial exposure.

Keywords: graphene biosensor, SGFET, Escherichia coli, QCM, water quality

Title

Toward Rapid Water Quality Monitoring: QCM-Guided Biointerface Engineering of Graphene SGFET Biosensors for Escherichia coli Detection

Introduction

Microbial contamination of coastal waters represents a major public health and socio-economic challenge for coastal territory management. It directly impacts both the sanitary safety of shellfish production and the opening of recreational bathing areas, which rely on monitoring bacterial indicators such as *Escherichia coli* [1,2]. Increasing contamination events associated with human activities and climate-driven environmental variability have strengthened the demand from public authorities and economic stakeholders for rapid microbial risk assessment tools. Current surveillance frameworks, based on laboratory culture analyses requiring extended processing times, limit monitoring frequency and delay decision-making.

In addition, graphene has emerged as an attractive material for biosensing applications due to its atomically thin structure, high surface-to-volume ratio, and accessible π-electron system. These properties make graphene well suited for surface-dominated transduction schemes, including field-effect transistors [3,4], and mass-sensitive platforms such as quartz crystal microbalance (QCM) devices [5]. In this context, this work aims at functionalizing graphene for *E. coli* detection in water.

Methods

In this work, we developed a non-covalent bio-interface engineering strategy based on a novel tripodal structure that enable robust and stable antibody immobilization (see Fig. 1). The bio-functionalization was first optimized using QCM to ensure efficiency and reproducibility prior to device integration. The optimized protocol was then transferred to graphene SGFET devices and used for bacterial detection.

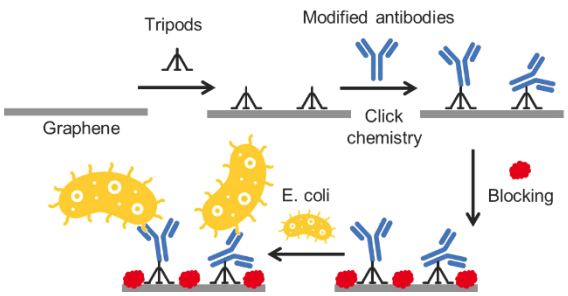

Fig. 1. Schematic representation of the graphene biofunctionalization steps.

Results

The biofunctionalization strategy was validated using QCM where each functionalization step induced reproducible and well-defined frequency shifts (see Fig. 2) confirming successful and stable layer-by-layer assembly. In particular, no

antibody desorption was observed, and the bacterial binding step induces a significant frequency shift, proportional to bacterial concentration in sample. The initial deposition of the tripodal linker on graphene, performed prior to QCM measurements, was independently confirmed by Raman spectroscopy.

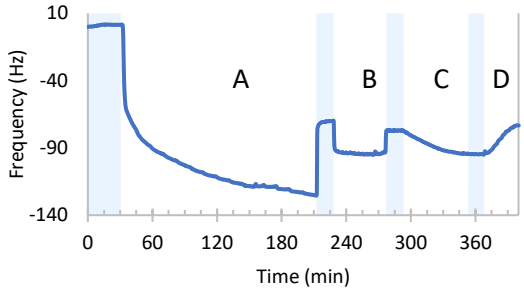

Fig. 2. QCM frequency response (third harmonic) during biofunctionalization and detection steps: (A) modified antibody immobilization, (B) blocking, (C) E. coli *exposure (2.5 × 10^7 CFU/mL), and (D) water rinsing. Intermediate blue regions correspond to buffer rinsing steps.*

The optimized biofunctionalization protocol was successfully transferred to graphene SGFETs. Upon exposure solutions of *E. coli* in aqueous media, systematic Dirac point shifts were observed, demonstrating reliable bacterial detection (see Fig. 3).

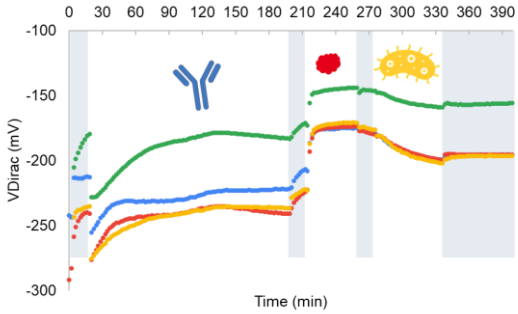

Fig. 3. Dirac point tension during functionalization and exposure to 10^7 CFU/mL solution of E. coli on 4 SGFET replicates. Intermediate blue regions correspond to buffer rinsing steps.

Conclusion

This work demonstrates an effective graphene biofunctionalization strategy enabling specific bacterial capture while preserving its electronic properties. The successful transfer of a QCM-optimized protocol to SGFET devices highlights the robustness and reproducibility of the approach. The observed electrical responses upon *E. coli* exposure show promising potential toward bacterial detection, paving the way for the development of rapid graphene-based biosensors for water quality monitoring.

References

[1] R. F. Vaccaro, M. P. Briggs, C. L. Carey, B. H. Ketchum, Viability of Escherichia coli in Sea Water, American Journal of Public Health and the Nation's Health 40, 1257–1266 (1950)

[2] F. Petronella, D. De Biase, F. Zaccagnini, V. Verrina, S.-I. Lim, K.-U. Jeong, S. Miglietta, V. Petrozza, V. Scognamiglio, N. P. Godman, D. R. Evans, M. McConney, L. De Sio, Label-Free and Reusable Antibody-Functionalized Gold Nanorod Arrays for the Rapid Detection of Escherichia coli Cells in a Water Dispersion, Environmental Science: Nano 9, 3343–3360 (2022); doi: 10.1039/D2EN00425K

[3] A. Béraud, M. Sauvage, C. M. Bazán, M. Tie, A. Bencherif, D. Bouilly, Graphene Field-Effect Transistors as Bioanalytical Sensors: Design, Operation and Performance, Analyst 146, 403–428 (2021); doi: 10.1039/D0AN01661F

[4] S. K. Krishnan, N. Nataraj, M. Meyyappan, U. Pal, Graphene-Based Field-Effect Transistors in Biosensing and Neural Interfacing Applications: Recent Advances and Prospects, Analytical Chemistry 95, 2590–2622 (2023); doi: 10.1021/acs.analchem.2c03399

[5] P. Hampitak, et al., A Point-of-Care Immunosensor Based on a Quartz Crystal Microbalance with Graphene Biointerface for Antibody Assay, ACS Sensors 5, 3520–3532 (2020); doi: 10.1021/acssensors.0c0164

DOI 10.5162/eurosensors2026/6.2.5

Bioimpedance Microsensor for Cell-Density Monitoring in Small-Scale Bioprocessing

Philip Patschg[1], Yves Mermoud[1], Samuel Schneider[2], Muriel Zumbihl[2], Raneem Achor[1], Regine Eibl[2], Samuel Huber[1]
[1] Institute of Microtechnology and Photonics, OST - Eastern Switzerland University of Applied Sciences, Buchs (SG), Switzerland,
[2] Institute of Chemistry and Biotechnology, School of Life Sciences and Facility Management, ZHAW Zurich University of Applied Sciences, Wädenswil, Switzerland
yves.mermoud@ost.ch

Summary:
Small-scale bioprocessing systems are increasingly used in biopharmaceutical applications from bioprocess optimization to patient-scale therapy manufacturing. In these confined formats, inline monitoring of process parameters such as viable cell density (VCD) is limited by the lack of miniature sensing probes. Here, we demonstrate in CHO cell cultures that bioimpedance VCD sensing can be miniaturized to a 1 × 10 mm footprint and 25 µL working volume with performance close to conventional probes.

Keywords: cell density monitoring, process analytical technology (PAT), electrochemical impedance spectroscopy (EIS), bioimpedance, small-scale bioprocessing

Introduction

Small-scale bioprocessing systems are increasingly used in the biopharmaceutical industry to advance high-throughput bioprocess development, support intensified manufacturing, or enable flexible, patient-scale, production of personalized therapies [1-2].

Timely measurement of key process parameters is essential to ensure performance and product quality, as encouraged by the FDA's Process Analytical Technology (PAT) initiative. However, real-time PAT solutions compatible with small-scale bioprocessing systems remain limited. This is particularly true for viable cell density (VCD), a key parameter directly linked to process performance and product titer [2-3].

Inline VCD measurement relies on biocapacitance probes that are too large for small-scale bioprocessing systems [1,4]. Alternatively, offline determination by trypan blue exclusion method is possible, but the need for sampling limits its practical use.

Here, we present a miniature VCD sensor with a reduced footprint of 1 × 10 mm and a working volume of 25 µL. Using microfabrication techniques, tetrapolar microelectrodes for Electrical impedance spectroscopy (EIS) were patterned on a glass microchip. Bioimpedance analysis of Chinese hamster ovary (CHO) cell suspensions showed a linear correlation (R^2=0.92) with reference VCD in the range 10^6-10^8 cells mL^{-1}.

Materials and Methods

Miniaturized VCD sensors made of evaporated Pt thin films (250 nm) were fabricated on a 100 mm fused silica wafer using photolithography and lift-off processes, followed by dicing into 15 × 15 mm microchips. The chips were mounted in a holder providing fluidic routing and electrical connection to an impedance analyzer (Zurich Instruments) (Fig. 1a). Each chip consists of two VCD sensors positioned within two microfluidic channels with a sample volume of about 25 µL each (Fig. 1b). Samples were manually dispensed into the channels using a pipette. EIS measurements were made from 10 kHz to 5 MHz with an amplitude of 200 mV in a tetrapolar configuration (Fig. 1c). Impedance spectra were calibrated using an open-short-load procedure with supernatant as reference.

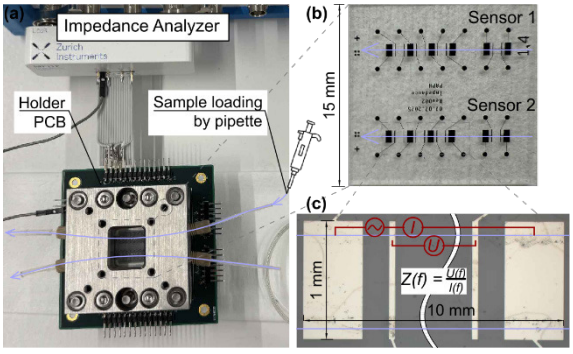

Fig. 1 Measurement setup. (a) Holder for fluidic and electrical interface to the chip. (b) Image of a chip with the two VCD sensors. (c) Close-up of a VCD sensor and schematic of the tetrapolar EIS measurement.

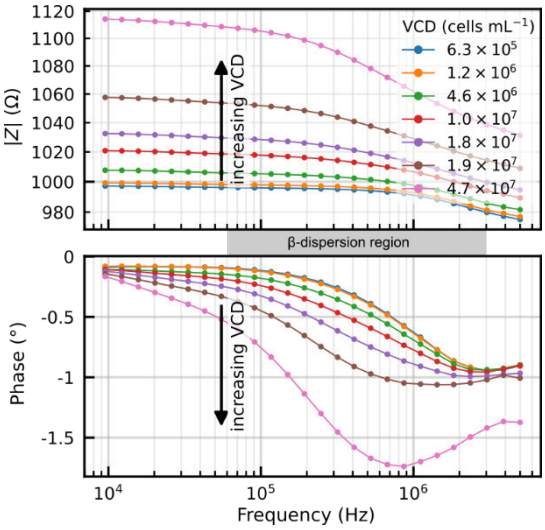

Fig 2. Bode plots showing calibrated impedance spectra of CHO cell suspensions at different VCDs. The lines are guides for the eye.

Finally, the biocapacitance C(f) was derived at each frequency from a parallel RC model circuit.

ExpiCHO-S cells were cultured in Efficient-Pro Medium (Thermo Fisher Scientific) as described previously [5] and sampled during the exponential growth phase at VCD of 4.6×10^6 cells mL^{-1} and mean cell diameter of 13.6 µm. Cells were then centrifuged at 300 RCF for 5 min and resuspended in supernatant at defined concentrations. Reference VCD measurements were made using a Cedex HiRes Analyzer (Roche).

Results and Discussion

VCD measurement by bioimpedance models cells as core-shell spheres suspended in an electrolyte. Under an alternating electric field, such cell suspensions exhibit β-dispersion (kHz to MHz) due to Maxwell-Wagner interfacial polarization, resulting in VCD-dependent permittivity changes [6]. This behavior is visible in the calibrated EIS Bode plots shown in Fig. 2, where CHO cell suspensions of increasing VCD exhibit stronger capacitive effects.

As shown in Fig. 3, the biocapacitance C(f) extracted from the calibrated EIS spectra at 55 kHz

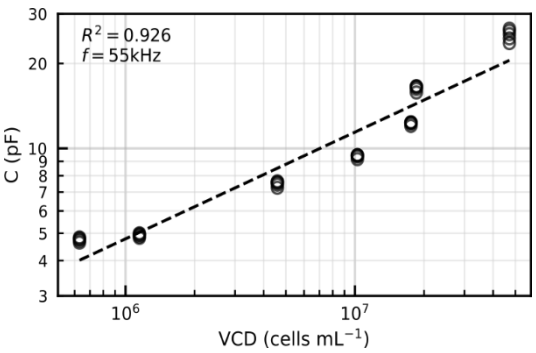

Fig 3. Extracted biocapacitance C(f) at 55 kHz versus reference VCD, with linear fit (dashed line). Each sample was measured 5 times.

shows a coefficient of linearity R^2=0.92 with reference VCD measurements, matching the performance of conventional probes [4]. Likewise, deviations from linearity below 0.8×10^6 and above 2×10^7 cells mL^{-1} are similar to commercial probes, reflecting detection limits (~0.5×10^6 cells mL^{-1}) and crowding effects beyond Maxwell–Wagner assumptions [4].

Conclusion and Outlook

Addressing the lack of inline VCD monitoring in small-scale bioprocessing systems is essential for their broader adoption. Here, we demonstrate that chip-based miniaturization of VCD sensing can achieve performance comparable to conventional probes with a significantly reduced footprint, enabling monitoring at the smallest scale.

Future work will focus on continuous monitoring over up to 14 days, with focus on biofouling effects. Ultimately, our miniaturized chip-based approach will allow integration of additional sensors, paving the way for multi-parameter PAT microchips tailored to small-scale bioprocessing.

References

[1] J. I. Betts and F. Baganz, Miniature bioreactors: current practices and future opportunities, Microb Cell Fact, 5 (2006); doi: 10.1186/1475-2859-5-21

[2] R. K. Iyer, P. A. Bowles, H. Kim, and A. Dulgar-Tulloch, Industrializing Autologous Adoptive Immunotherapies: Manufacturing Advances and Challenges, Frontiers in Medicine 5 (2018); doi. 10.3389/fmed.2018.00150

[3] M. M. Hewitt, N. Trainor, N. Ostrout, and E. Abraham, Cell therapy manufacturing: process analytic technologies needed to achieve flexible, feedback-driven automation, Current Opinion in Biomedical Engineering, 20 (2021); doi: 10.1016/j.cobme.2021.100358

[4] A. Bergin, J. Carvell, and M. Butler, Applications of bio-capacitance to cell culture manufacturing, Biotechnology Advances, 61 (2022), doi: 10.1016/j.biotechadv.2022.108048

[5] J. Ott, V. Ott, P. Neubauer, D. Eibl, and R. Eibl, Process intensification by inoculating antibody production bioreactors directly from cryovials, Chemie Ingenieur Technik (2024); doi: 10.1002/cite.202300189

[6] H. P. Schwan, Determination of biological impedances, Electrophysiological Methods (1963); doi: 10.1016/B978-1-4831-6743-5.50013-7

Acknowledgements

This work was supported by Innosuisse, the Swiss Innovation Agency, under Project Number 118.678 IP-LS.

We thank the staff at the Sensor Innovation Hub (https://si-hub.ch) for their support with sensor fabrication.

DOI 10.5162/eurosensors2026/6.2.6

MXene-Functionalised U-Shaped SMF-NC-SMF Optical Fibre Sensor for Label-Free Detection of PFOA and PFOS in Water

Adeel Faruq[1], YongQing Fu[1], Zabih Ghassemlooy[1], Yuliya Semenova[2], Qiang Wu[1],
[1] School of Engineering, Physics and Mathematics, Northumbria University, Newcastle, NE1 8ST, UK
[2]School of Electrical and Electronic engineering, Technological University Dublin, Ireland
adeel.faruq@northumbria.ac.uk

Summary: A U-shaped single-mode–no-core–single-mode (SMF-NC-SMF) optical fibre sensor functionalised with a sequential PEI/PDADMAC/MXene ($Ti_3C_2T_x$) multilayer interface is presented for the label-free, real-time detection of perfluorooctanoic acid (PFOA) and perfluoro octane sulfonate (PFOS) in aqueous media. Exploiting evanescent wave interactions at the fibre–solution interface, the sensor transduces analyte binding events as measurable wavelength shifts. PFAS contaminants produced clear, concentration-dependent responses spanning 0.1–100 pg/mL, establishing the platform's suitability for sensitive water quality monitoring applications.

Keywords: PFAS, PFOA, PFOS, optical fibre sensor, MXene, evanescent wave, water quality monitoring

Background, Motivation and Objective

Per- and polyfluoroalkyl substances (PFAS) comprise a family of over 4,700 synthetic chemicals characterised by exceptionally strong carbon–fluorine bonds that confer extreme environmental persistence and biological accumulation [1]. Among these, PFOA and PFOS are the most globally regulated, having been detected in surface water, groundwater, and treated drinking water at concentrations associated with hepatotoxicity, immunosuppression, endocrine disruption, and elevated cancer risk [2]. Under the European Union's revised Drinking Water Directive (EU 2020/2184), a combined permissible limit of 0.1 µg/L has been set for 20 listed PFAS compounds [3], placing stringent requirements on detection sensitivity. While liquid chromatography–tandem mass spectrometry (LC-MS/MS) remains the benchmark analytical technique, its dependence on centralised laboratory facilities, labour-intensive sample preparation, and specialist expertise significantly constrains its utility for real-time or on-site monitoring. Label-free optical fibre sensors based on evanescent wave interactions offer a compelling alternative, providing real-time, in-situ measurements in a miniaturised, low-cost format without the need for fluorescent labels [4]. This work presents a U-shaped SMF-NC-SMF fibre sensor with a layered PEI/PDADMAC/MXene functionalisation for sensitive detection of PFOA and PFOS.

Description of the New Method or System

The sensing element was fabricated by fusion splicing a segment of no-core fibre (NC, ∼125 µm outer diameter, no guiding core) between two sections of standard single-mode fibre (SMF-28), forming an SMF-NC-SMF multimode interference structure. This structure was tapered to (∼ 9 µm) then assembly was bent into a U-shape (∼4 mm bend radius), significantly enhancing evanescent field penetration depth at the fibre–solution interface and increasing sensitivity to local refractive index changes induced by surface-bound analytes.

Surface functionalisation employed a sequential layer-by-layer (LbL) electrostatic deposition strategy. First, polyethylenimine (PEI), a branched polycation, was adsorbed onto the cleaned fibre surface to act as a primer layer and introduce abundant cationic binding sites. Second, poly(diallyldimethylammonium chloride) (PDADMAC), a strongly cationic polyelectrolyte, was deposited to build up the positive surface charge and improve adhesion of the subsequent layer. Finally, $Ti_3C_2T_x$ MXene nanosheets—two-dimensional transition metal carbide materials bearing abundant terminal functional groups (–OH, –F, =O) were electrostatically adsorbed as the terminal sensing layer [5]. The inherent fluorophilicity of MXene surfaces, combined with hydrophobic interactions, facilitates preferential capture of perfluorinated analytes. Sensing measurements were performed using a broadband light source and optical spectrum analyser; PFAS binding events were transduced as red shifts (Δλ) in the fibre transmission spectrum.

Results

Figure 1 presents the real-time Δλ response of the PFOA sensor following introduction of analyte solutions at 0.1, 1, 10, and 100 pg/mL, alongside a deionised water (DI) blank. After a stable baseline period, PFOA introduction produced an immediate and sustained red shift,

with response magnitude increasing monotonically with concentration. The highest tested concentration (100 pg/mL) produced a maximum Δλ of ~0.23 nm, while even at 0.1 pg/mL a distinguishable shift was recorded, indicating that sub-pg/mL detection limits are achievable with further optimisation. The DI blank yielded no measurable shift, confirming negligible non-specific response from the sensing interface.

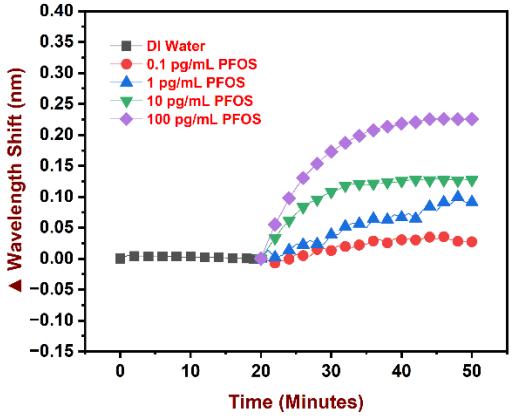

Fig. 1. Real-time wavelength shift (Δλ) of the MXene-functionalised SMF-NC-SMF sensor upon exposure to PFOA at concentrations of 1, 10, 100, and 1000 pg/mL, and DI blank.

PFOS produced analogous concentration-dependent wavelength shifts (Fig. 2), with Δλ magnitudes broadly comparable to those recorded for PFOA across the same concentration range. This correspondence is consistent with the structural similarity of the two compounds and their equivalent fluorophilic affinity towards the MXene sensing layer. For both analytes, responses reached steady-state within approximately 15–20 minutes of introduction, a behaviour characteristic of diffusion-limited binding kinetics at the MXene–solution interface.

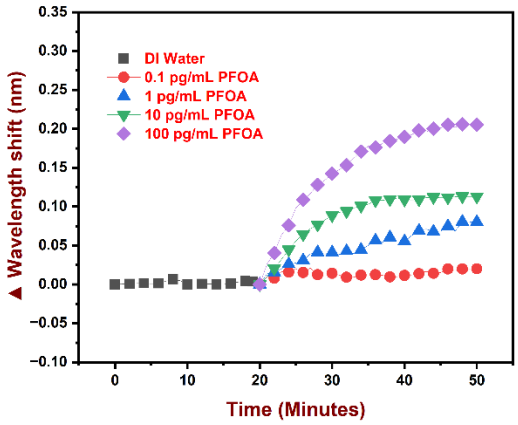

Fig. 2. Real-time wavelength shift (Δλ) of the MXene-functionalised SMF-NC-SMF sensor upon exposure to PFOS at concentrations of 1, 10, 100, and 1000 ng/mL, and PBS blank (0 ng/mL).

SEM analysis confirmed successful MXene deposition on the functionalised fibre surface. At magnifications discrete near-spherical MXene nanostructures are visible across the silica surface, a morphology consistent with $Ti_3C_2T_x$ self-assembly under LbL electrostatic deposition conditions. Nanostructure clustering along the fibre surface suggests effective immobilisation via the PEI/PDADMAC scaffold, and the homogeneous surface coverage observed across both fields of view reflects a reproducible sensing interface capable of sustaining consistent evanescent wave interaction with PFAS analytes.

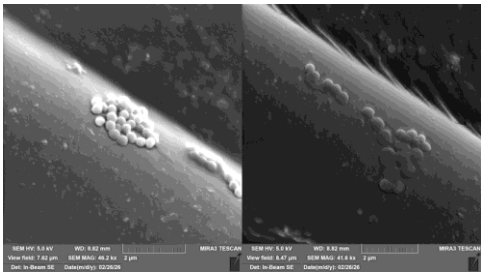

Fig. 3. SEM micrograph confirming MXene nanostructure deposition on the fibre surface.

The reproducible, dose-dependent shifts observed for PFOA and PFOS collectively confirm the effectiveness of the PEI/PDADMAC/MXene architecture for evanescent wave-based PFAS sensing, supporting the platform's applicability to water quality monitoring.

References

[1] Zexi Zhang, Kaixuan Chen, Bruno Ameduri, and Mao Chen, *Chemical Reviews* **2023** *123* (22), 12431-12470; DOI: 10.1021/acs.chemrev.3c00350

[2] Grandjean P, Clapp R. Perfluorinated Alkyl Substances: Emerging Insights Into Health Risks. New Solut. 2015 Aug;25(2):147-63. doi: 10.1177/1048291115590506.

[3] Marco Dettori, Antonella Arghittu, Giovanna Deiana, Paolo Castiglia, Antonio Azara, the revised European Directive 2020/2184 on the quality of water intended for human consumption. Environmental Research, Volume 209, 2022, 112773, ISSN 0013-9351; doi.org/10.1016/j.envres.2022.112773.

[4] Fan X, White IM. Optofluidic Microsystems for Chemical and Biological Analysis. Nat Photonics. 2011 Oct 1;5(10):591-597; doi:0.1038/nphoton.2011.206.

[5] B. Anasori, M.R. Lukatskaya, Y. Gogotsi, Nat. Rev. Mater. 2, 16098 (2017); doi: 10.1038/natrevmats.2016.98

DOI 10.5162/eurosensors2026/6.3.1

Mitigation of Chemical Sensor Drift through Calibration Transfer in Edge AI

Jordi Fonollosa
Institut de Recerca i Innovació en Salut (IRIS), Universitat Politècnica de Catalunya, Av. Diagonal, 647, 08028 Barcelona, Spain
jordi.fonollosa.m@upc.edu

Abstract:

The deployment of chemical sensor arrays in continuous industrial monitoring requires mitigating severe performance degradation caused by temporal drift, environmental variability, and device-to-device heterogeneity [1-2]. Traditional calibration transfer methods adapt chemometric models to reduce the number of expensive and impractical full recalibrations [3]. Recently, modern Edge AI architectures introduce new dimensions for long-term applications since running calibration models on local hardware devices reduce network load, privacy concerns, and latency. On the other hand, models may run on strict resource budget in terms of computational throughput and power [4-5]. This work shows calibration sustainability principles with resource-aware neural network scaling. Five Temporal Convolutional Networks (TCNs) are evaluated under strict parameter budgets (8K to unconstrained) and benchmarked across eleven multi-domain datasets and an 11-month industrial electronic nose dataset undergoing real-world seasonal drift. Results show that macro-F1 performance scales with parameter capacity rather than architectural configuration itself. Although seasonal variations inevitably trigger progressive degradation, mid-sized models optimize the trade-off between accuracy and hardware constraints, while lighter models achieve smaller latencies. This framework bridges the gap between algorithmic model adaptation and edge deployment, establishing sustainable strategies that reduce recalibration frequency in long-term autonomous sensing.

Keywords:

Calibration transfer, Electronic nose, Edge AI, Sensor drift, Deep Learning

References:

[1] Li, R. *et al.,* A Comprehensive Review of Algorithms for Drift Compensation in Metal Oxide Semiconductor Gas Sensor Arrays, *Chemosensors* 14(6), 143-172 (2026); doi: 10.3390/chemosensors14060143

[2] Jiang, K. *et al.,* Gas Sensor Drift Compensation Using Semi-Supervised Ensemble Classifiers with Multi-Level Features and Center Loss, *ACS Sensors* 10(4), 2906-2918 (2025); doi: 10.1021/acssensors.4c03655

[3] Fonollosa, J. *et al*., Calibration transfer and drift counteraction in chemical sensor arrays using Direct Standardization, *Sensors and Actuators B: Chemical* 236, 1044–1053 (2016); doi: 10.1016/j.snb.2016.05.089

[4] Heydari, S. and Mahmoud, Q.H., Tiny Machine Learning and On-Device Inference: A Survey of Applications, Challenges, and Future Directions, *Sensors* 25(10), 3191-3214 (2025); doi: 10.3390/s25103191

[5] Miller, T. *et al.,* Federated Learning for Environmental Monitoring: A Review of Applications, Challenges, and Future Directions, *Applied Sciences* 15(23), 12685-12709 (2025); doi: 10.3390/app152312685

DOI 10.5162/eurosensors2026/6.3.2

A Dual-Resolution Binary Neural Network Inference Engine for Fully Implantable Cochlear Implant Speech Processing

Mert Doğan[1], Hasan Uluşan[1,2], Haluk Külah[1,2]
[1]Department of Electrical and Electronics Engineering, METU, Ankara, Turkey
[2]ODTÜ MEMS CENTER, Ankara, Turkey
mertd@metu.edu.tr

Summary:

A dual-resolution Binary Neural Network inference engine replaces conventional filterbanks in cochlear implant speech processing. A 1 kHz split applies a 256-sample window (75% overlap) to low-frequency channels and a 128-sample window (50% overlap) to high-frequency channels, with a shared 64-sample hop. The architecture matches fixed N=256 intelligibility (STOI 0.826 vs 0.830) while halving high-frequency channel latency and reducing L1 inference cost and size by ~25%, at <2 mW inference power. The approach can be applied to edge AI sensor SoCs requiring low-power spectral analysis.

Keywords: cochlear implant, binary neural network, dual-resolution, embedded ML, implantable SoC

Background

Cochlear Implant (CI) users struggle with speech-in-noise due to two main limitations: the limited feature extraction capability of current processors [1], and suboptimal stimulation patterns. In sound processing, long windows resolve pitch and vowel formants for low frequencies, while short windows capture consonant transients and no single length serves both [2]. Additionally, conventional IIR/FFT filterbanks used in CIs are too power-hungry for fully implantable SoCs [3], and recent deep learning CI approaches [4, 5] remain offline-only. BNNs can bridge this gap via low-cost XNOR-popcount operations [6], enabling real-time embedded inference at implantable power levels. To the best of the authors' knowledge, this work presents the first implantable-scale neural CI speech processor SoC with embedded ML inference.

Method

Unlike single-window CI processors, a 1 kHz frequency split assigns a longer window to low-frequency channels (200–1000 Hz, 256 samples, 10.7 ms, 75% overlap) where wider spectral resolution benefits pitch and vowel encoding, and a shorter window to high-frequency channels (1–11 kHz, 128 samples, 5.3 ms, 50% overlap) where reduced latency and inference cost are prioritized. A shared 64-sample hop ensures both paths produce electrode envelopes at identical update rates, maintaining synchronisation without additional hardware complexity.

Envelope extraction replaces conventional multiply-accumulate-heavy IIR/FFT operations with a BNN that operates directly on the raw I²S bitstream from the MEMS microphone, eliminating preprocessing entirely. XNOR-popcount reduces inference to single-cycle bitwise logic ($\boldsymbol{w}^{\mathsf{T}}\boldsymbol{a} = 2\,\mathrm{popcount}(\overline{\boldsymbol{w} \oplus \boldsymbol{a}}) - N$). A single pipelined 2048-bit engine is time-multiplexed across all layers of both paths (4-cycle, 48 MHz), completing inference in 0.111 ms (Fig. 1(a)). Bitwise output encoding maps 128 binary activations directly to 8-bit electrode envelopes, enabling positionally-weighted per-bit loss supervision during training. Binary weights are stored in on-chip BRAM; BatchNorm parameters are absorbed offline into fixed popcount thresholds, adding no runtime overhead. Reprogrammable weights enable post-implantation patient-specific adaptation: retraining on ECAP-derived cochlear maps [7] emphasizes channels with intact spiral ganglion populations without hardware modification.

Training uses synthetic windows with log-normal frequency distribution (centred at 2500 Hz, σ = 0.8 decades) and Beta(1,5) amplitudes across up to 32 sinusoidal components, biasing coverage toward the perceptually critical mid-speech range. Windows are normalized to unit peak before 8-bit signed quantization, matching the hardware MEMS pipeline exactly. The combined loss (1) sums peak-weighted MSE (2) and per-bit BCE (3). The MSE term applies peak-emphasis (α = 10) with Gaussian band-weighting over the formant region (400–3000 Hz); BCE is weighted by bit significance ($w_b \propto 2^{-b}$, MSB weighted 128× over LSB), with separate loss instances per path.

$$\mathcal{L} = \lambda_{\mathrm{MSE}}\mathcal{L}_{\mathrm{MSE}} + \lambda_{\mathrm{BCE}}\mathcal{L}_{\mathrm{BCE}} \qquad (1)$$

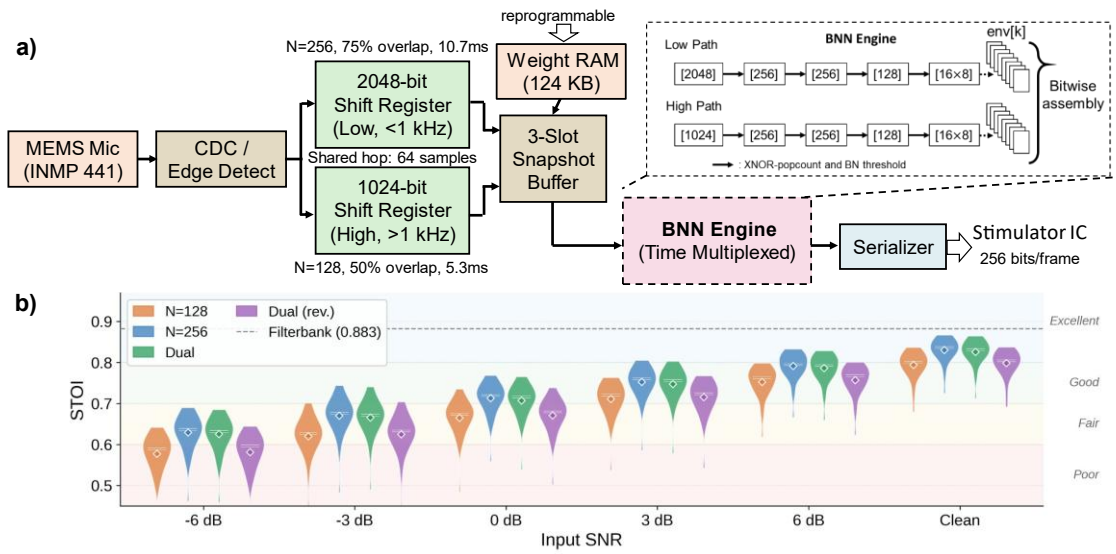

Fig. 1. (a) Top-level system architecture: dual-path dataflow from MEMS microphone through asymmetric shift registers and time-multiplexed BNN engine to serial electrode output. (b) STOI distributions across SNR conditions for fixed N=128, N=256, dual-res. and reverse dual-res. BNN, dashed line indicates clean filterbank ceiling.

$$\mathcal{L}_{\text{MSE}} = \frac{1}{NB}\sum_{n,k}(1+\alpha y_{nk})(\hat{e}_{nk}-y_{nk})^2 \cdot w_k^{\text{band}} \quad (2)$$

$$\mathcal{L}_{\text{BCE}} = \frac{1}{8NB}\sum_{n,k,b} w_b^{\text{bit}} \cdot w_k^{\text{band}} \cdot \text{BCE}\left(\mathrm{l}_{nkb}, y_{nkb}^{\text{bit}}\right) \quad (3)$$

Results

Table 1 and Fig. 1(b) summarize the four-way STOI [8] comparison across input SNR conditions. The reversed split (N=128 low / N=256 high) performs comparably to uniform N=128, while the proposed split (N=256 low / N=128 high) consistently outperforms both across all SNR conditions. This confirms that the direction of the frequency-window assignment is the critical design choice. The dual-resolution architecture achieves equivalent intelligibility to fixed N=256 (clean STOI 0.826 vs 0.830, difference within variance) while halving high-frequency channel latency from 10.7 ms to 5.4 ms and reducing weight memory from 156 KB to 124 KB. Both satisfy the 6–20 ms clinical latency target [1]. The design occupies 63 BRAM36 tiles (17.3%) and 757 LUTs (<1%) on the XC7A200T with 2 mW BNN dynamic power, supporting a <500 µW ASIC projection at 65 nm CMOS. The XNOR-popcount engine further generalizes to edge AI sensor SoCs where FFT or IIR filtering is computationally prohibitive.

Tab. 1: Performance and hardware results

Metric	128	256	Dual (rev)	Dual
Clean STOI	0.794 ± 0.034	0.830 ± 0.030	0.798 ± 0.033	0.826 ± 0.032
High-path latency	5.4 ms	10.7 ms	10.7 ms	5.4 ms
Infer.Lat.	0.111 ms			
Memory	92 KB	156 KB	124 KB	124 KB
Usage	BRAM: 63 (17.3%) / LUT: 757 (<1%)			

Acknowledgements

This work was supported by TUBITAK under grant no.123C554 and partially by no. 112C340.

References

[1] F.-G. Zeng et al., “Cochlear implants: System design, integration, and evaluation,” IEEE Rev. Biomed. Eng., vol. 1, pp. 115–142, 2008.

[2] J. H. Won et al., “Maximizing the spectral and temporal benefits of two clinically used sound processing strategies for cochlear implants,” Trends Amplif., vol. 16, no. 4, pp. 201–210, 2012.

[3] H. Uluşan et al., "A full-custom fully implantable cochlear implant system validated in vivo with an animal model," Commun. Eng., vol. 3, p. 132, 2024; doi: 10.1038/s44172-024-00275-4

[4] E. H.-H. Huang et al., “ElectrodeNet: A deep-learning-based sound coding strategy for cochlear implants,” IEEE Trans. Cogn. Dev. Syst., vol. 16, no. 1, pp. 346–357, 2024.

[5] T. Gajecki et al., “A deep denoising sound coding strategy for cochlear implants,” IEEE Trans. Biomed. Eng., vol. 70, no. 9, pp. 2700–2709, 2023.

[6] F. Conti et al., “XNOR Neural Engine: A hardware accelerator IP for 21.6-fJ/op binary neural network inference,” IEEE Trans. CAD, vol. 37, no. 11, 2018

[7] C. Garcia et al., “The panoramic ECAP method:,” J. Assoc. Res. Otolaryngol., vol. 22, no. 5, 2021.

[8] C. H. Taal et al., "An algorithm for intelligibility prediction of time-frequency weighted noisy speech," IEEE Trans. Audio Speech Lang. Process., vol. 19, no. 7, pp. 2125–2136, 2011.

DOI 10.5162/eurosensors2026/6.3.3

Tiltmeter-Based Forecasting and Anomaly Detection for Proactive Structural Monitoring of Railway Infrastructure

Puspita Saha[1], Francisco Hernandez-Ramirez[1,2], J. Daniel Prades[1]
[1.] Institute of Semiconductor Technology (IHT) and Laboratory for Emerging Nanometrology (LENA), Technische Universität Braunschweig, 38106 Braunschweig, Germany
[2.] Worldsensing SL, 08014, Barcelona, Spain
Email: puspita.saha@tu-braunschweig.de

Summary:
Railway operators increasingly require predictive tools that transform continuous tiltmeter sensing into actionable structural health indicators. This work presents a physics-informed data-driven framework for rail and sleeper monitoring and validates it on a dataset collected from several tiltmeters with hourly sampling deployed in Spain over more than two years. The pipeline combines robust preprocessing, feature engineering, multi horizon forecasting and temperature aware anomaly detection. Results show accurate one week forecasting and effective separation of temperature-driven behaviour from structural deviations, supporting earlier maintenance decisions. The framework is designed for real-world deployment and scalability across large railway networks.

Keywords: tiltmeter sensors, time-series forecasting, anomaly detection, structural health monitoring, railway infrastructure monitoring.

Background, Motivation and Objective

Continuous sensing is gaining importance in railway asset management because conventional inspections are episodic while structural degradation can evolve between interventions. Structural health monitoring provides a route toward earlier detection and condition-based maintenance [1]. In railway infrastructure, distributed sensing and smart track instrumentation are increasingly regarded as enablers of safer and more sustainable operation [2].

Tiltmeter signals capture slow structural rotations and thermal responses. However, they are noisy, non-stationary, and strongly temperature-dependent. This work addresses that gap by developing an operator-oriented forecasting and anomaly-detection framework for long-term railway tiltmeter data, aimed at detecting faults and operational risks in infrastructure, thereby supporting operational decision-making. This enables earlier detection of structural issues, reduces inspection costs, and facilitates the transition toward predictive maintenance strategies.

Description of the New Method

Standard unsupervised methods and general-purpose forecasting models are unable to separate normal thermal variability from structural deviations in this dataset [3], motivating the physics-informed approach adopted here. The proposed system processes hourly measurements from 42 rail and sleeper tiltmeters installed in a rail facility in Spain, from November 2023 to December 2025, including temperature and tilt angles (x, y, and z axis, in degrees). A robust preprocessing pipeline integrates outlier filtering, gap filling, changepoint detection, and signal smoothing. A set of 226 engineered features captures temporal, lag, rolling, trend, and temperature-correlation behavior. Multi-horizon forecasting is performed with a stacked Long Short-Term Mem-ry (LSTM) neural network, a deep learning model designed to capture patterns in sequential data [4]. The anomaly detection step finally models how the track normally responds to temperature. Deviations from the expected temperature-driven response are flagged as potential structural anomalies. Changepoints identified by PELT algorithm (Pruned Exact Linear Time) [5] are retained rather than removed, as they may indicate structural shifts or emerging instabilities.

Fig. 1. Wireless tiltmeter installed on a railway sleeper for real-time track monitoring.

Results

A representative output obtained with the proposed pipeline is shown in Fig. 2 for a rail tiltmeter. One-week forecasts achieved R^2 (coefficient of determination) values between 0.81 and 0.998 across the three tilt axes and temperature, with consistently low prediction errors and the best performance for z axis and temperature due to their regular thermal cycles.

These high R^2 values indicate that the proposed model explains between 81% and 99.8% of the variance in the observed data, demonstrating a strong predictive capability and a close agreement between forecasts and measurements.

In comparison, generic statistical (SARIMAX, Prophet) and machine-learning (XGBoost, CatBoost, N-HITS) baselines produced negative R^2 at the same horizon, meaning that their predictions perform worse and fail to capture the underlying temporal dynamics.

This stark contrast highlights the superiority of the proposed approach, which is specifically tailored to the characteristics of tilt-meter data and significantly outperforms standard off-the-shelf methods for long-term forecasting in railway infrastructure monitoring.

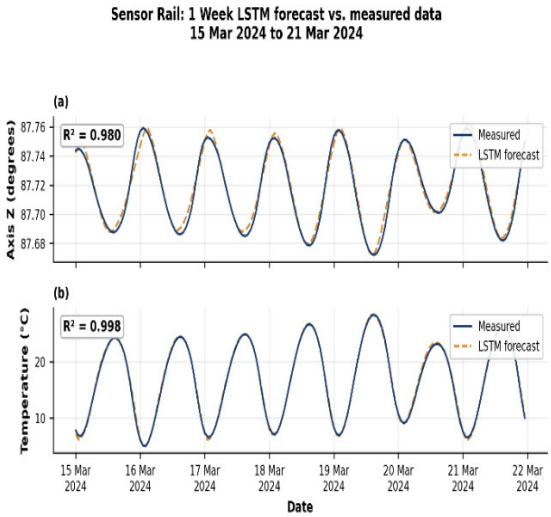

Fig. 2. Zoomed forecast versus measured data for rail sensor 75288 (z axis and temperature, one-week window). Blue: actual; orange dashed: LSTM forecast

For anomaly detection, synthetic validation showed that the pipeline recovered 84.6 percent of injected events, with full (100%) event-level recall for sustained level shifts and gradual drifts. These results are promising, as they demonstrate the capability of the approach to reliably identify relevant structural changes, and provide a solid foundation for its application to real-world event analysis in operational railway infrastructure. This demonstrates the importance of incorporating physical context into data-driven models for infrastructure monitoring.

This work introduces a novel framework that combines temperature-aware anomaly detection with multi-horizon forecasting in a unified pipeline for railway tiltmeter data. The results demonstrate that integrating physics-informed modelling with data-driven approaches provides a robust decision-support tool for proactive infrastructure monitoring. This capability directly addresses the growing demand for advanced monitoring solutions that enhance operational safety, improve risk mitigation, and enable predictive maintenance in railway systems.

References

[1] C. R. Farrar, K. Worden, An introduction to structural health monitoring, Philosophical Transactions of the Royal Society A 365, 303-315 (2007); doi: 10.1098/rsta.2006.1928

[2] J. M. Castillo-Mingorance, M. Sol-Sanchez, F. Moreno-Navarro, M. C. Rubio-Gamez, A critical review of sensors for the continuous monitoring of smart and sustainable railway infrastructures, Sustainability 12, 9428 (2020); doi: 10.3390/su12229428

[3] R. Rabadán-Arroyo, E. Simó, F. Aguiló-Gost, F. Hernández-Ramírez, X. Masip-Bruin, An adaptive IoT-based forecasting framework for structural and environmental risk detection in tailings dams, Electronics 15, 658 (2026); doi: 10.3390/electronics15030658

[4] S. Hochreiter, J. Schmidhuber, Long short-term memory, Neural Computation 9, 1735-1780 (1997); doi: 10.1162/neco.1997.9.8.1735

[5] R. Killick, P. Fearnhead, I. A. Eckley, Optimal detection of changepoints with a linear computational cost, Journal of the American Statistical Association 107, 1590-1598 (2012); doi: 10.1080/01621459.2012.737745

Acknowledgments

This work is supported by the Alexander von Humboldt Professorship of the Humboldt Foundation, and the Federal Ministry for Education and Research, Germany. We also gratefully acknowledge Ferrocarrils de la Generalitat de Catalunya (FGC) for granting access to their railway facilities and enabling the data collection that made this study possible.

DOI 10.5162/eurosensors2026/6.3.4

Graph Deviation Networks for Schizophrenia Signatures Detection in Brain Organoids' MEA Signals

Alessia Riccardi[1,2], Arianna Mencattini[1,2], Giorgia Curci[1,2], Wendiao Zhang[3,4], Qingtuan Meng[3,4], Eugenio Martinelli[1,2]
[1]Department of Electronic Engineering, University of Rome Tor Vergata, 00133 Rome, Italy,
[2] InterdisciplinaryCenter for Advanced Studies on Lab-on-Chip and Organ-on-Chip Applications (ICLOC), 00133 Rome, Italy,
[3] The First Affiliated Hospital, Multi-Omics Research Center for Brain Disorders and Department of Neurology, Hengyang Medical School, University of South China, Hunan 421001, China,
[4] The First Affiliated Hospital, Clinical Research Center for Immune-Related Encephalopathy of Hunan Province, Hengyang Medical School, University of South China, Hunan 421001, China
Corresponding Author's e-mail: alessia.riccardi@uniroma2.it

Summary:

We present a Graph Deviation Network (GDN) framework to detect early alterations in the neuronal network of human Forebrain Organoids (hFOs) associated with schizophrenia risk. MEA-recorded signals from PCCB-knockdown hFOs are preprocessed into amplitude-modulated spike arrays and represented as time-varying graphs. Topological descriptors extracted from these graphs feed a linear discriminant analysis classifier, achieving 91% accuracy in distinguishing PCCB-knockdown from control hFOs at early time sessions. This approach provides a powerful tool for identifying disease-relevant electrophysiological signatures in neuronal organoid models.

Keywords: brain organoids, graph deviation network, schizophrenia, multi-electrode arrays, deep learning.

Background, Motivation and Objective

Human Forebrain Organoids (hFOs) are self-organized 3D cell aggregates that faithfully recapitulate the cellular architecture of the human brain, representing a powerful in vitro platform for studying brain development and neurological disorders. Their functional characterization is greatly facilitated by multi-electrode arrays (MEAs), which enable non-invasive, long-term acquisition of electrical signals directly correlated with organoid activity, capturing the spike and burst dynamics of developing neuronal networks. Among the disorders that can be investigated through this approach, schizophrenia (SCZ) stands out as a severe psychiatric condition with complex environmental and genetic etiology. Notably, hFOs have been used to demonstrate the involvement of Propionyl-CoA Carboxylase Subunit Beta (PCCB), a nuclear-encoded gene, in SCZ risk [1]: PCCB knockdown induces mitochondrial dysfunction that disrupts GABA production, leading to measurable alterations in hFO electrical activity. However, MEA-recorded signals are commonly reduced to temporal averages such as mean firing rate or burst rate, thereby discarding the most informative spatiotemporal patterns for identifying disease-relevant signatures. To overcome this limitation, we introduce a Graph Deviation Network (GDN) [2], a deep learning framework based on graph theory, to detect early network alterations in hFO activity associated with SCZ risk, enabling anomaly identification from only a few milliseconds of electrical signal [3].

Description of the New Method or System

Neural activity from PCCB-knockdown hFOs and controls was recorded across multiple time sessions using 16-electrode MEA platforms (see Fig. 1a). Prior to GDN processing, raw recordings undergo a preprocessing step that extracts amplitude-modulated (AM) signals centered around each detected spike event (see Fig. 1b), preserving the informative content surrounding neuronal firing [3]. The resulting AM-spike arrays (see Fig. 2a) constitute the input to the GDN, a deep learning framework that models MEA dynamics as time-varying graphs: each node represents an electrode, and directed edges encode asymmetric, potentially causal interactions among them (see Fig. 2b). The GDN operates by predicting future signal samples from learned

past values. To this end, signals are first projected into low-dimensional space through embedding vectors; a directed graph is then derived from their pairwise similarities, capturing the evolving relational structure of the network. From each graph instance, topological descriptors are extracted to quantify network dynamics over time [3]. These descriptors feed a linear discriminant analysis (LDA) classifier, trained to distinguish PCCB-knockdown from control conditions across recording wells.

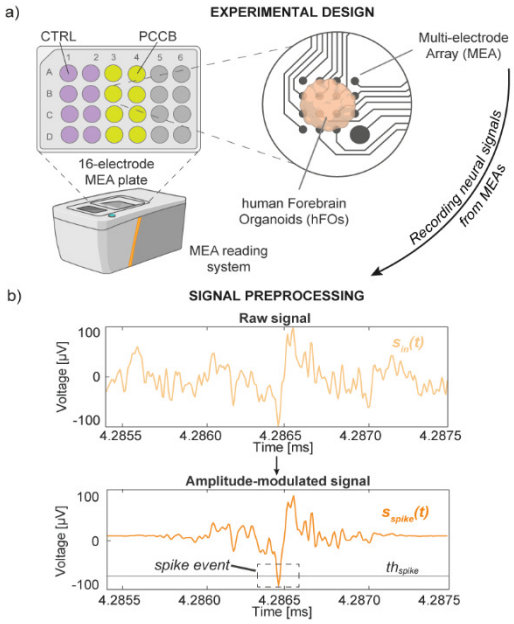

Fig. 1. a) Experimental design showing the MEA reading system, the 16-electrode MEA platform in which hFOs are cultured, and a detailed view of the MEA electrodes-coupled hFOs. b) MEA-acquired data undergo preprocessing, resulting in amplitude-modulated (AM) signals where spike events are detected.

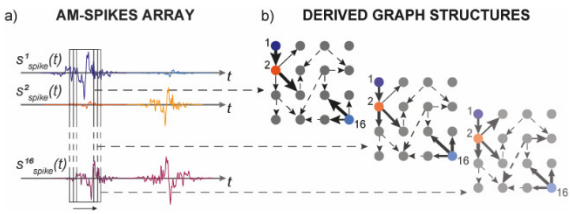

Fig. 2. a) AM-spike signals coming from one electrode are concatenated along the time axis, and vertically with the other MEA data, resulting in an AM-spikes array. b) AM-spikes arrays are encoded as graph structures from which topological features are extracted.

Results

The proposed pipeline was evaluated across five recording sessions spanning approximately 80 hours of organoid development (11h, 27h, 46h, 57h, 80h). The LDA classifier, trained on topological descriptors extracted from GDN-derived graph representations, consistently distinguished PCCB-knockdown hFOs from controls across the entire observation window (see Table 1). At the earliest time point (11h), the model achieved its highest classification accuracy of 91%, confirming that the GDN framework can detect disease-relevant electrophysiological signatures from very early stages of network activity. At this stage, organoid maturation is still limited, and PCCB-mediated mitochondrial dysfunction leaves a clearly measurable imprint on network topology, making the two conditions well separable in the topological feature space. As recording sessions progressed, a gradual yet consistent decline in classification accuracy was observed, dropping from 86% at 27h to 76% at 80h. Inspection of the confusion matrices (see Fig. 3) revealed that this trend is primarily driven by an increasing number of misclassified samples over time. This pattern is consistent with the progressive maturation of the organoids. Actually, as neuronal connectivity consolidates and network dynamics become more complex, maturation-driven signals increasingly dominate electrophysiological activity, gradually masking condition-specific alterations induced by PCCB knockdown and reducing inter-class separability.

Tab. 1: Classification accuracy achieved for each time session applying an LDA model.

Time session	11h	27h	46h	57h	80h
Accuracy	91%	86%	83%	78%	76%

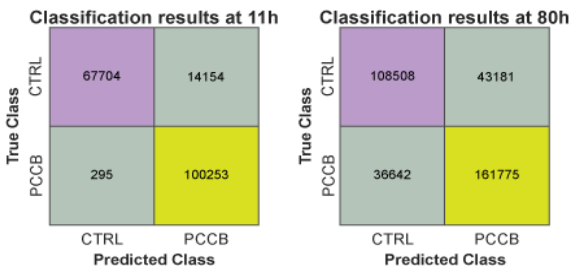

Fig. 3. Classification results for the first and last time sessions, showing how the LDA model tends to misclassify samples of the two classes.

References

[1] Zhang, W., Zhang, M., Xu, Z. et al. Human forebrain organoid-based multi-omics analyses of PCCB as a schizophrenia associated gene linked to GABAergic pathways. Nat Commun 14, 5176 (2023); doi: 10.1038/s41467-023-40861-2

[2] Deng, A., & Hooi, B. (2021). Graph Neural Network-Based Anomaly Detection in Multivariate Time Series. Proceedings of the AAAI Conference on Artificial Intelligence, 35(5), 4027-4035. Doi: 10.1609/aaai.v35i5.16523

[3] A. Mencattini, G. Curci, A. Riccardi, et al. MEA-Based Graph Deviation Network for Early Autism Syndrome Signatures in Human Forebrain Organoids. Cyborg Bionic Syst. 2025;6:0441. doi: 10.34133/cbsystems.0441

DOI 10.5162/eurosensors2026/6.3.5

Multidimensional Force Estimation in Laparoscopic Instruments with a CMOS-Based Force Sensor Chip

Thorsten Hehn[1], Bernd Folkmer[1], Rachid Nouna[1], Stephan Knappmann[1], Wolfgang Kunert[2], Steffen Axt[2], Jens Rolinger[3], Achim Brodbeck[3], Oliver Amft[1,4]
[1] Hahn-Schickard, Wilhelm-Schickard-Straße 10, 78052 Villingen-Schwenningen, Germany
[2] Universitätsklinikum Tübingen, Chirurgische Technologie & Training (CTT), Waldhörnlestraße 22, 72072 Tübingen, Germany
[3] Erbe Elektromedizin GmbH, Waldhörnlestraße 17, 72072 Tübingen, Germany
[4] Albert-Ludwigs-Universität Freiburg, Institut für Informatik, Intelligente Eingebettete Systeme (IES), Georges-Köhler-Allee 304, 79110 Freiburg, Germany
Thorsten.Hehn@Hahn-Schickard.de

Summary:
Minimally invasive surgery lacks haptic feedback, limiting the surgeon's ability to assess tissue interaction forces. This work presents a miniaturized CMOS-based multisensor chip integrated in laparoscopic instruments for multidimensional force sensing. Finite element modeling was used to optimize sensor placement. Machine learning models reconstruct axial, lateral, and gripping forces from 32 sensors per chip. A Random Forest model reached near-perfect accuracy between 0.0001 N and 0.0048 N. Results demonstrate the feasibility of compact, high-precision force sensing in smart surgical instruments.

Keywords: force sensing, CMOS sensor, laparoscopic instruments, machine learning, multidimensional force estimation

Background, Motivation and Objective

Minimally invasive surgical procedures including laparoscopy have significantly improved patient outcomes by reducing trauma and recovery time. However, the instruments currently used in laparoscopy limit the surgeon's tactile perception, as interaction forces between instrument and tissue are strongly attenuated [1]. The loss of haptic feedback can lead to surgical errors and unintentional tissue damage [2].

Existing approaches can be broadly classified into direct sensor integration and indirect estimation methods. Indirect approaches are easier to integrate but generally less accurate [2]. Microelectro-mechanical systems (MEMS) are particularly promising for direct force sensing due to their small size and integrability. However, existing solutions (e. g. [3]) often lack full system integration or remain limited in practical applicability.

The objective of this work is to develop a compact and integrated sensing system capable of reconstructing multidimensional interaction forces in laparoscopic instruments with high precision. The approach combines a CMOS-based multisensor chip, model-based sensor integration, and data-driven force estimation algorithms, as illustrated in Figure 1.

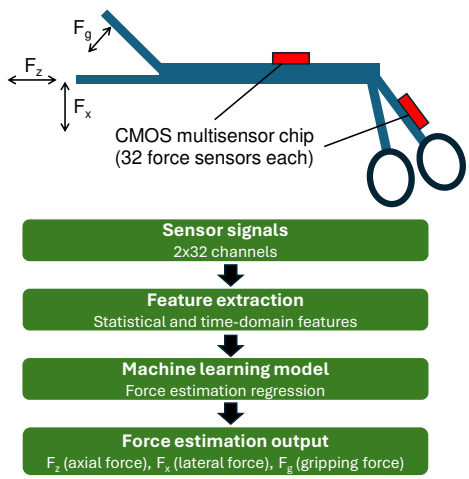

Figure 1: Concept of the proposed force sensing system for laparoscopic instruments: CMOS multisensor chips combined with machine learning for multidimensional force reconstruction.

Force Measurement Concept and System Integration

At the core of the system is a miniaturized CMOS multisensor chip comprising 32 spatially distributed sensors within a footprint of 2.0 x 2.5 mm² and a thickness of 0.3 mm, including readout electronics providing a digital output signal [4]. The chip measures local mechanical stress based on the piezoresistive effect; thus, the force

sensor chip can resolve deformations of the instrument in different axes.

The sensor chip was integrated into a laparoscopic instrument from Erbe Elektromedizin GmbH. The sensors were mounted and electrically connected using flexible interconnects. The sensor was placed at the shaft to capture tool-center-point forces and at the handle to capture gripping forces. Due to the instrument's complex mechanical structure, the resulting signals are nonlinear, requiring advanced modeling for force reconstruction.

Finite element modeling was used to identify optimal sensor placement within the laparoscopic instrument, aiming at a distinct and interpretable stress distribution across the sensor surface. The simulations consider nonlinear effects including contact, friction, and deformation during the opening and closing of the instrument.

Force Estimation Methods

Force estimation was formulated as a supervised regression problem. The input features include 32 sensor values, statistical features (standard deviation and variance), temperature, shaft rotation, and lever arm geometry (45 features in total).

Four regression models were evaluated: Linear, Ridge, Lasso, and Random Forest, each using an 80/20 train-test split including five-fold cross-validation. Feature normalization was applied for the linear models, while the Random Forest model was trained on raw data.

The dataset was acquired using dedicated test setups, where defined axial, lateral, and gripping forces were applied to the instrument. Reference forces were generated using calibrated weights and force sensors, while the corresponding multisensor signals were recorded simultaneously. Both static and dynamic load cases were considered to capture a wide range of operating conditions.

Temperature effects were explicitly investigated, as thermal expansion differences between sensor and instrument introduce measurement drift. Models with and without temperature as an input feature were compared to assess its impact.

Results and Discussion

All evaluated models were capable of reconstructing force components from the sensor data. However, clear differences in performance were observed. The Random Forest model achieved the highest accuracy when including temperature as an input feature, with coefficients of determination of up to $R^2 \approx 1.000$ and mean absolute errors (MAE) of 0.0001 N for lateral force, 0.0027 N for axial force and 0.0048 N for gripping force (see Figure 2). Linear models also showed strong performance with R^2 values above 0.96, but with higher estimation errors.

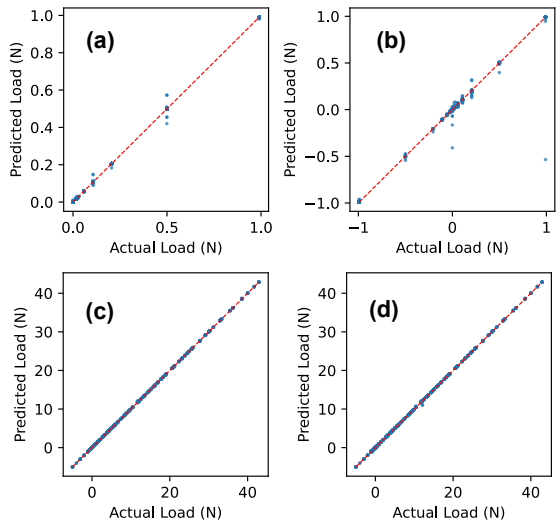

Figure 2: Comparison between measured and predicted load values for Random Forest model. (a) shows lateral force, (b) axial force, (c) and (d) gripping force. Whereas (a) to (c) use the temperature feature, (d) ignores the temperature.

The investigation of temperature influence revealed that linear models only marginally benefit from the inclusion of temperature as an input feature. In contrast, the Random Forest model clearly benefits from temperature as additional feature: As an example, the gripping force MAE can be reduced from 0.0081 N without temperature feature (see Figure 2d) to 0.0048 N with temperature feature (see Figure 2c).

The proposed approach can reliably estimate axial, lateral, and gripping forces despite complex mechanical coupling within the instrument. Our results demonstrate the effectiveness of combining spatially resolved sensing with data-driven modeling.

Conclusions and Acknowledgment

The results demonstrate that the presented multisensor force chip is well suited for measuring mechanical loads in laparoscopic instruments with millinewton accuracy.

The Random Forest model provides maximum accuracy. Our results suggest that it is feasible to use force sensing in laparoscopic instruments to provide real-time force feedback and thus improve surgical safety for both manual and robotic surgery.

The authors thank the Ministry of Economic Affairs, Labour and Tourism of Baden-Württemberg for funding the project "Intelligente Chirurgische Instrumente (InXI)" under grant number BW8_1387/01.

References

[1] J. Miller *et al.,* "Impact of haptic feedback on applied intracorporeal forces using a novel surgical robotic system-a randomized cross-over study with novices in an experimental setup," *Surg Endosc*, vol. 35, no. 7, pp. 3554–3563, 2021, doi: 10.1007/s00464-020-07818-8.

[2] W. Wang, J. Wang, Y. Luo, X. Wang, and H. Song, "A Survey on Force Sensing Techniques in Robot-Assisted Minimally Invasive Surgery," *IEEE transactions on haptics*, vol. 16, no. 4, pp. 702–718, 2023, doi: 10.1109/TOH.2023.3329172.

[3] A. Nakai, K. Kuwana, K. Saito, T. Dohi, A. Kumagai, and I. Shimoyama, "MEMS 6-axis force-torque sensor attached to the tip of grasping forceps for identification of tumor in thoracoscopic surgery," in *2017 IEEE 30th International Conference on Micro Electro Mechanical Systems (MEMS)*, Las Vegas, NV, USA, Jan. 2017 - Jan. 2017, pp. 546–548.

[4] M. Kuhl *et al.,* "A wireless stress mapping system for orthodontic brackets using CMOS integrated sensors," *IEEE Journal of Solid-State Circuits*, vol. 48, no. 9, pp. 2191–2202, 2013.

DOI 10.5162/eurosensors2026/7.1.1

Electrochemical Approaches for Monitoring PFOA in Aqueous Environments

Alexandra Beard[1], Natasa Budimirovicr[1], Tristan Kipfer[1],Sergey Piletsky, Elena Piletska [2], Sylvain Nicolay[1]
[1] Swiss Center for Electronics and Microtechnology CSEM SA, 2002 Neuchâtel, Switzerland

[2] Department of Chemistry, University of Leicester, University Rd, LE1 7RH Leicester, UK
alexandra.beard@csem.ch

Summary:
Perfluorooctanoic acid (PFOA) is commonly used as a marker of per- and polyfluoroalkyl substances (PFAS) contamination in aqueous environments due to its persistence and widespread occurrence. This work explores electrochemical approaches for PFOA monitoring, combining interfacial studies at electrode surfaces with the development of selective sensing materials. Molecularly imprinted polymers (MIPs) are investigated as recognition elements, while complementary electrochemical analyses are performed to identify suitable transduction mechanisms.

Keywords: PFAS, PFOA, electrochemical sensors, MIP, EIS

Background, Motivation and Objective

Per- and polyfluoroalkyl substances (PFAS) are persistent pollutants associated with adverse effects on human health and the environment. Their widespread use and resistance to degradation have led to increasing regulatory pressure to monitor and limit their presence in water systems. However, effective mitigation requires reliable detection: contaminants must first be identified and quantified before they can be controlled or eliminated.

In this context, PFOA is commonly used as a marker of PFAS contamination.[1] The objective of this work is to explore electrochemical strategies for its detection, aiming for selective response and low detection limits compatible with current and emerging regulatory requirements. Particular attention is given to interfacial phenomena and the development of selective recognition layers, such as molecularly imprinted polymers.

Description of the New Method or System

Due to the high chemical stability and low intrinsic electroactivity of PFOA, direct electrochemical detection is challenging. This work proposes a detection strategy based on interfacial phenomena. The approach exploits the adsorption properties of the carboxylic group of PFOA at electrode interfaces, either on platinum (Pt) surfaces or on electrodes modified with quaternary ammonium functional polymers. These interactions alter the structure of the electrochemical double layer. The resulting changes in double-layer capacitance are measured and quantified using electrochemical impedance spectroscopy as a function of PFOA concentration.

In parallel, MIP nanoparticles are synthesized and deposited on electrode surfaces to introduce molecular selectivity. In this case, detection relies on an indirect (mediated) mechanism, where binding events within the imprinted sites modulate the electrochemical response of the interface. [2]

Results

The voltammetric behaviour of PFOA was first investigated at platinum (Pt) electrode surfaces using microfabricated silicon-based electrodes. Measurements were performed in both acidic (50 mM H_2SO_4) and carbonate (0.5 M K_2CO_3) electrolytes (Fig. 1).

Under these conditions, PFOA does not appear fully electrochemically inert. At higher concentrations (≈1 mM), an oxidation peak is observed starting at around 0.6 V vs. reference electrode. More notably, significant modifications are observed in the hydrogen underpotential deposition (HUPD) region, along with changes in the double-layer current. These features suggest specific adsorption of PFOA molecules at the Pt surface. The observed oxidation process at higher potentials may be associated with adsorbed species, although the mechanism is not yet fully understood and requires further investigation.

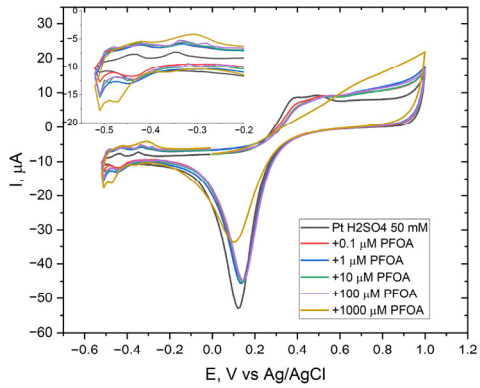

Fig. 1.Cyclic voltammograms of PFOA at a Pt electrode in 50 mM H_2SO_4 at varying concentrations (scan rate: 100 mV s^{-1}).

Based on these observations, changes in the electrochemical double-layer capacitance were quantified using electrochemical impedance spectroscopy. Measurements were performed at −0.2 V vs. reference electrode, and capacitance values were extracted at 100 Hz. A dependence of capacitance on PFOA concentration was observed, confirming that interfacial adsorption significantly influences the electrochemical response.

The obtained capacitance values are summarized in Fig. 2, comparing measurements in acidic and carbonate electrolytes, as well as results obtained with bare Pt electrodes and Pt electrodes modified with an anion exchange membrane (AEM, Fumatech®). The capacitance shows distinct trends depending on the electrolyte and surface modification. In acidic conditions (H_2SO_4), capacitance decreases with increasing PFOA concentration, consistent with surface adsorption and partial blocking of the electrode. In contrast, in carbonate electrolyte, a slight increase is observed, suggesting a different interfacial organization. The presence of the AEM layer leads to lower and more stable capacitance values, indicating a modified interaction mechanism. Overall, these results highlight the strong influence of both electrolyte composition and surface functionalization on PFOA interfacial behavior.

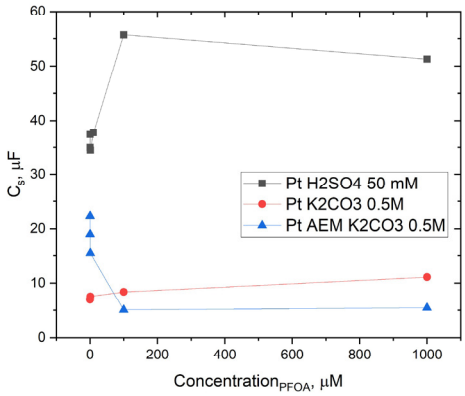

Fig. 2. Evolution of double-layer capacitance with PFOA concentration at Pt and AEM-modified Pt electrodes in different electrolytes, extracted from EIS measurements at 100 Hz.

Conclusions

This work demonstrates that PFOA, despite its low intrinsic electroactivity, can be detected through adsorption-induced modulation of interfacial electrochemical properties. The observed dependence of capacitance on electrolyte composition and surface modification highlights the complexity of the sensing mechanism, which requires further investigation. Nevertheless, these findings establish a foundation for adsorption-based electrochemical detection strategies. The integration of MIP modified electrodes, aimed at enhancing selectivity, will be discussed.

References

[1] D. Thomson, N. Zolfigol, Z. Xia, Y. Lei, Recent progress in per- and polyfluoroalkyl sunstances sensing: A critical mini-review, Sensors and Acuators Reports 7, 100189 (2024); doi.org/10.1016/j.snr.2024.100189

[2] M. Costa, J. Peters, S. Di Masi, S. A. Piletsky, C Zaleski, C. Malitesta, A. Garcia Cruz, E. Beij , G. E. De Benedetto, Nanoengineered electrochemical sensor for trace-level monitoring of perfluorooctanoic acid in aqueous environments using electroactive molecularly imprinted nanoparticles, Microchemical Journal 216, 114645 (2025).; doi.org/10.1016/j.microc.2025.114645

Acknowledgements

This work is partially supported by the European Union Chips Joint Undertaking program Genesis (Grant agreement No 101194246) and the Swiss Confederation (SERI).

DOI 10.5162/eurosensors2026/7.1.2

Transient Graphene-Based Aptasensor on a Cellulose Substrate for Toxin Detection

Lorenzo Travaglini[1], Yassar Abderrahim[2], Hafsa Korri-Youssoufi[3], Danick Briand[1]
[1] Ecole Polytechnique Fédérale de Lausanne (EPFL), Soft Transducers Laboratory (LMTS), Rue de la Maladière 71b, Neuchâtel, Switzerland,
[2] Ecole Polytechnique, CNRS, IPP, LPICM, Route de Saclay, Palaiseau, France,
[3] Université Paris-Saclay, CNRS, Institut de Chimie Moléculaire et des Matériaux d'Orsay (ICMMO), 17 Av. des Sciences, Orsay, France
lorenzo.travaglini@epfl.ch

Summary:
We report a transient aptasensor for food toxin detection based on screen printed interdigitated electrodes (IDEs) fabricated using graphene ink printed on cellulose substrate. The aptamer is covalently-functionalized to provide selective biorecognition of the target food toxins on this transient platform. Electrochemical impedance spectroscopy reveals concentration-dependent impedance features, driven by interfacial modification due to the aptamer-toxin binding at the electrode surface. Compared to conventional single working and counter electrode configuration, the IDE electrode configuration enables a clear differentiation between the target concentrations in the high frequency range. The materials and fabrication process ensure eco-friendly and compatible device with low-cost, scalable manufacturing. This approach supports the development of sustainable biosensing technologies for rapid food safety screening adaptable for point of care (POC) detection system.

Keywords: Transient biosensor, graphene-carbon transducer, interdigitated electrodes, aptasensor, high frequency impedance spectroscopy

Background, Motivation and Objective

Impedimetric biosensors use EIS to detect biorecognition-induced changes at the electrode–electrolyte interface. In conventional single large-area electrodes, the response is dominated by double-layer capacitance and charge-transfer resistance, mainly at low frequencies. However, low-frequency operation can reduce stability and limit POC integration, motivating faster and more robust readout strategies.

Here we propose an interdigitated electrode (IDE) transducer made of printed graphene on a cellulose substrate. Compared with single-electrode designs, IDEs provide higher sensitivity to surface binding and support measurements at higher frequency and the use of an optimized single-frequency readout for rapid target detection of various concentrations.[1,2]

In parallel, the field is shifting toward transient and more sustainable electronics to reduce e-waste. Cellulose substrates and printable carbon-based functional inks provide a scalable and eco-responsible route to disposable devices. This approach is particularly relevant for food safety screening, where single-use sensors are intended at low-cost and easy field deployment. Foodborne toxins remain a persistent risk in supply chains, positing a significant for public health threat, motivating the development of sensors for point-of-need food safety analysis beyond immunoassays and chromatography. Mycotoxin, such as Othratoxin A (OTA), produced by fungal contamination of staple food, poses a severe long-term threat to human health and requires a sensor for point-of-use detection.[3]

We report on an OTA aptasensor based on interdigitated graphene electrode printed on cellulose substrate. The sensor exhibits centration-dependent impedance signature compatible with high-frequency readout on a transient platform.

Description of the New Method

The sensor consists of interdigitated working and counter electrodes (WE–CE) (Fig. 1). The IDEs were fabricated by screen printing a graphene-carbon ink onto a cellulose substrate followed by curing. The electrode surface was functionalized by OTA-specific aptamer via covalent link to form the recognition layer. Upon binding of OTA, the aptamer layer undergoes conformational modifying their structure and leading to measurable changes in the electrical interfacial properties.

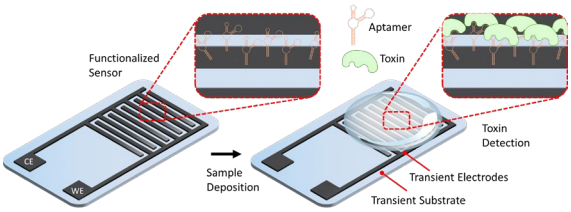

Fig. 1. Schematic representation of the sensor's IDE configuration functionalized with aptamers and its interaction with the toxin, resulting in impedance change due to conformational rearrangement.

Device performance was assessed by Electrochemical Impedance Spectroscopy (EIS), analyzing both Nyquist and Bode spectra over a broad frequency range (0.1 Hz to 500 kHz). The data were fitted with an equivalent-circuit model to extract interfacial electrical properties linked to surface modification and target capture. Measurements were performed for both graphene/aptamer functionalized electrode and bare electrode as a control before and after exposure to OTA at relevant concentrations of 0.1 nM, 1 nM, and 10 nM.

Results

The graphene-carbon IDE aptasensor exhibits a concentration-dependent impedance signature upon toxin exposure at concentrations of 0.1 nM, 1 nM, and 10 nM, relative to the aptamer-functionalized electrode measured in toxin-free solution (0 nM control). This demonstrates effective toxin sensing on the transient cellulose platform. As shown in Fig. 2, the Nyquist spectra show a high variation at high frequency range with increasing toxin concentration. The Bode magnitude plot shows clear impedance change after OTA biding across a wide frequency range, 500 kHz to 1kHz. In parallel, a sensor based on a single-electrode layout exhibited a markedly smaller response at high-frequency, indicating that the interdigitated configuration enhances signal transduction at elevated frequencies.

The sensor displays a linear-log dependence of impedance magnitude on analyte concentration (Fig.2). Sensitivities of 626 ± 22 Ω/dec, 641 ± 48 Ω/dec, 615 ± 13 Ω/dec and 550 ± 15 Ω/dec were derived at 1 kHz, 10 kHz, 100 kHz and 500 kHz, respectively. These results demonstrate the good response at high frequency of our toxin aptasensor on cellulose enabled by using interdigitated graphene-carbon electrodes. The limit of detection and selectivity are under evaluation and will be presented at the conference.

To support interpretation of the sensing mechanism, the impedance spectra were fitted with an equivalent circuit consisting of a solution resistance in series with two interfacial time constants including resistance of charge transfer and capacitance. These two contributions arise form electrical parameters variation of the graphene electrode interface and the aptamer-modified recognition layer. The fitted capacitance and resistance values show consistent increase with toxin concentration, demonstrating progressive surface modification and blocking effects following aptamer-toxin recognition.

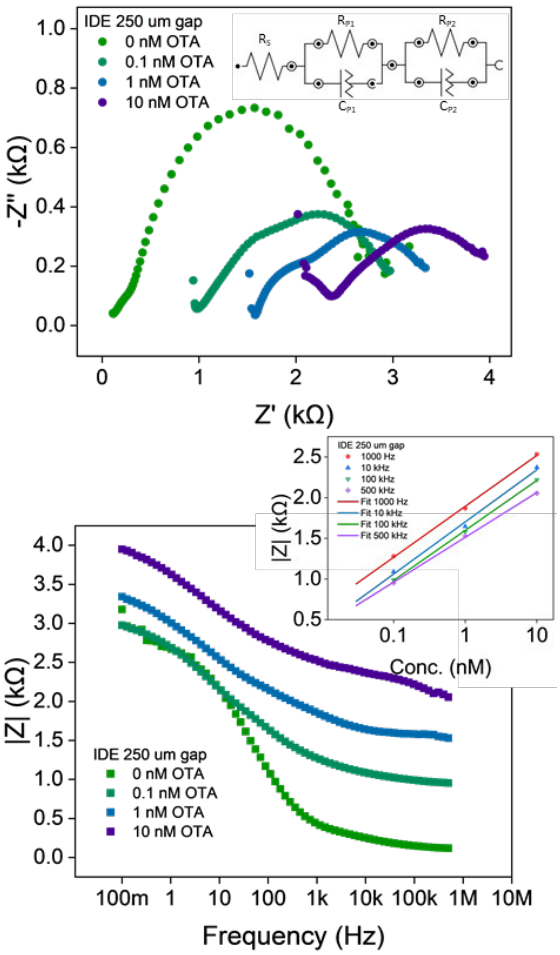

Fig. 2. Impedance characterization of IDE aptasensor. (Top) Nyquist plots showing concentration-dependent changes in the impedance spectra. (Bottom) Impedance magnitude as a function of frequency, highlighting clear separation between concentrations from 500 kHz to 1kHz.

References

[1] Lakeya, A. et al. Impedimetric array in polymer microfluidic cartridge for low-cost point-of-care diagnostics, *Biosensors and Bioelectronics* 129,147 (2019); doi: 10.1016/j.bios.2018.12.054

[2] Jiang, T, et al. Sensitivity studies and optimization of an impedance-based biosensor for point-of-care applications, *Biosensors and Bioelectronics: X*, 18,100479 (2024); doi:10.1016/j.biosx.2024.100479

[3] Wang, K. et al. Review of Electrochemical Biosensors for Food Safety Analysis. *Biosensors* 12(11), 959 (2022); doi: 10.3390/12110

DOI 10.5162/eurosensors2026/7.1.3

Physics-Based Dynamic Estimation of NO_2 and H_2O Concentrations with CNT-FETs and Extended Kalman Filter

Cristina Gentili[1], Cosmin I. Roman[1], Ines Kraiem[1], Miroslav Haluska[1], Christofer Hierold[1]
[1]Micro and Nanosystems, Department of Mechanical and Process Engineering, ETH Zürich, Zürich
cgentili@ethz.ch

Summary:
We present a Langmuir-based Extended Kalman Filter (EKF) framework for real-time estimation of NO_2 at ppb-level concentrations in humid air at room temperature. Two CNT-FETs gas sensors were exposed to a gas-mixture experiment involving different NO_2 and humidity (H_2O) concentrations, with threshold voltages (V_T) extracted from sensors transfer characteristics over time. The V_T signals were first fitted using a two-gas Langmuir isotherm-based model; next, an Extended Kalman Filter (EKF) enabled dynamic NO_2 and H_2O simultaneous estimation.

Keywords: Carbon Nanotube Gas Sensor, Signal Processing, Dynamic Modeling, Real-time Prediction, Extended Kalman Filter (EKF).

Background, Motivation and Objective

Carbon nanotubes (CNTs) are 1D materials known for their gas sensing capabilities and high sensitivity to nitrogen dioxide (NO_2). In this work, we fabricate NO_2 gas sensors based on CNT field-effect transistors (CNT-FETs), where a pristine CNT is suspended between platinum source and drain electrodes, with the gate located beneath the channel (Fig. 1a). The device is a p-type transistor, in which NO_2 adsorbed onto the CNT p-dopes the channel through electron withdrawal. This effect is visible in the transfer characteristics (i.e., drain current I_D as a function of gate voltage V_{GS} at fixed V_{DS}), where NO_2 adsorption on the CNT induces a threshold voltage V_T shift [1]. Humidity (H_2O) produces an opposite, though weaker, effect (Fig. 1b). The objective of this work is to estimate NO_2 and H_2O concentrations dynamically over time. In previous works, we extracted multiple features from transfer characteristics [2] and used quasi-steady-state data to predict gas concentrations via machine learning [3]. Here, we move from a static to a dynamic approach by modeling the temporal evolution of V_T induced by gas adsorption/desorption, using a two-gas Langmuir model applied to two CNT-FETs [4]. Following a calibration phase in which the model parameters are fitted, NO_2 and H_2O concentrations are estimated online using an Extended Kalman Filter (EKF) [5]. With respect to our most recent work [6], the present study introduces the following novelties. First, two devices are used, demonstrating that the Langmuir based-model is reproducible across different CNT-FETs. Second, the experimental dataset is split into a calibration subset (phase I) for model fitting and a subsequent test subset (phase II), designed to mimic a realistic gas exposure scenario, for gas concentrations estimation; previously, the EKF was validated on the same data used for model fitting, while real-scenario testing was limited to synthetic data. Finally, whereas H_2O was assumed known, here we simultaneously estimate both NO_2 and H_2O concentrations.

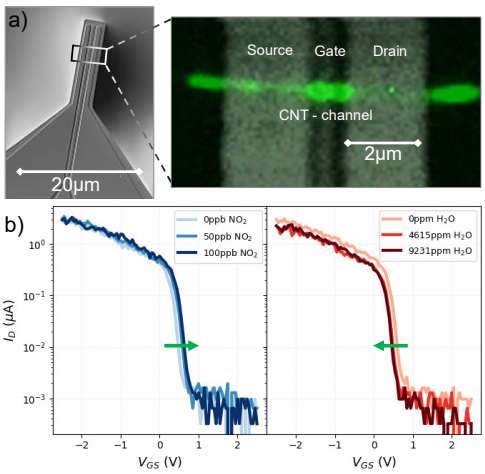

Fig. 1. a) CNT-FET, with CNT identified by Raman spectroscopy (representative). b) Transfer characteristics for different NO_2 and H_2O at V_{DS}=0.1 V (devA). Each curve was subtracted by its minimum value.

Gas Experiment

Two CNT-FETs devices (devA and devB) were exposed to the same gas experiment at room temperature, as shown in Fig. 2a. The experiment can be divided into two phases. In phase I, NO_2 and H_2O concentrations were changed

DOI 10.5162/eurosensors2026/7.1.3

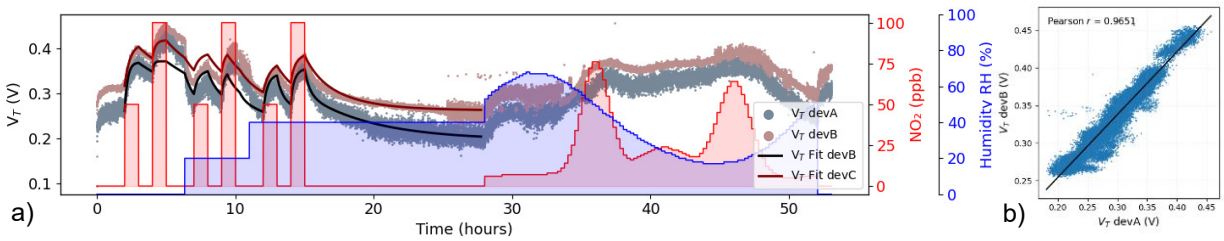

Fig. 2. a) Gas experiment: threshold voltage (V_T) *and dynamic model fit (phase I). b) Scatter plot of V_T (devA) vs. V_T (devB) and Pearson correlation coefficient.*

stepwise. In phase II, the gas profiles were designed to mimic a realistic 24-hour scenario: H_2O follows a sinusoidal-like variation, higher during the night and early morning and lower during the day, while NO_2 exhibits two peaks corresponding to high-traffic times and lower levels at night. During the experiment, transfer characteristics were acquired every 5 s.

Methods: Dynamic-model-based Prediction

The threshold voltage V_T signals were fitted over time for devA and devB using the following model, assuming that V_T is proportional to the surface coverage θ of the two gases, and that the steady-state θ follows a bi-component Langmuir isotherm [4]:

$$V_T(t) = \alpha_1\theta_1(t) + \alpha_2\theta_2(t) + \beta; \quad 1: NO_2, \quad 2: H_2O$$

$$K_{1,2} = \frac{K_{a1,2}}{K_{d1,2}}; \theta_{SS1,2} = \frac{K_{1,2}p_{1,2}}{1 + K_{1,2}p_{1,2} + K_{2,1}p_{2,1}}; \theta_{01,2} = \theta_{1,2}\big|_{t=0}$$

$$\theta_{1,2}(t) = \left(\theta_{SS1,2} - \theta_{01,2}\right)\left(1 - e^{-(K_{a1,2}p_{1,2} + K_{d1,2})t}\right) + \theta_{01,2}$$

where p_1 and p_2 are NO_2 and H_2O concentrations, respectively. The fitted parameters include the conversion coefficients $\alpha_{1,2}$, the adsorption constants $K_{a1,2}$ and the desorption constants $K_{d1,2}$. The fitting results are illustrated in Fig. 2a. Continuous-time NO_2 estimation is achieved using an Extended Kalman Filter (EKF), that estimates the state of a dynamic system by optimally combining noisy measurements with a predictive model, with covariance matrices tuned empirically [5]. Here, the system state is defined as: $\hat{\boldsymbol{x}} = [\theta_1, \theta_2, p_1, p_2]$, and the continuous-time EKF correction equation is given by: $\dot{\hat{\boldsymbol{x}}}(t) = \boldsymbol{f}(\hat{\boldsymbol{x}}(t)) + \boldsymbol{K}(t)(\boldsymbol{V_T}(t) - \boldsymbol{h}(\hat{\boldsymbol{x}}(t)))$, where $\boldsymbol{K}$ is the Kalman gain, $\boldsymbol{f}()$ describes the state dynamics and $\boldsymbol{h}()$ maps the state to the $\boldsymbol{V_T}$ signals.

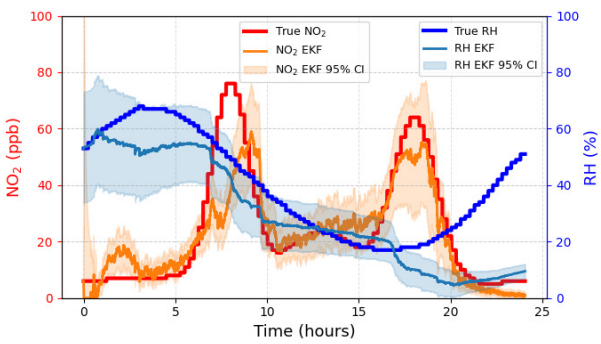

Fig. 3. EKF NO_2 and H_2O predictions. Mean Absolute Error (MAE) is 6.81 ppb for NO_2 and 2604 ppm (~11% RH: Relative Humidity at 20˚C) for H_2O.

Results and Discussion

NO_2 and H_2O estimations obtained though EKF are shown in Fig. 3. The dynamic modeling-based prediction approach represents a realistic framework for continuous NO_2 and H_2O tracking. It should be noted that CNT-FETs exhibit higher sensitivity to NO_2 than to H_2O, and that the V_T signals of the two devices are strongly correlated (Fig. 2b). Ideally, improved selectivity could be achieved by using devices with different sensitivities to the two gases. Nevertheless, the proposed method enables ppb-level NO_2 estimation in the presence of unknown humidity, representing a promising approach for real-world gas sensing applications.

References

[1] I. Heller, A. M. Janssens, J. Männik, E. D. Minot, S. G. Lemay, C. Dekker, Identifying the mechanism of biosensing with carbon nanotube transistors, *Nano letters* 8, no. 2, pp. 591-595, 2008; doi: 10.1021/nl072996i

[2] C. Gentili, C. Hierold, C. Roman, Physics-informed autoencoder for feature extraction from multidimensional sensor measurement data, *Applied Intelligence 55*, 1063, 2025; doi: 10.1007/s10489-025-06892-6

[3] C. Gentili, C. Roman, I. Kraiem, C. Hierold, Resolving NO_2, O_3 and H_2O Concentrations in Gas Mixtures with Dual CNT-FET Sensors and Machine Learning, 2025 *Transducers*, pp. 1030-1033; doi: 10.1109/Transducers61432.2025.11111144

[4] A. Amrutha, G. Jeppu, C. Girish, B. Prabhu, K. Mayer, Multi-component adsorption isotherms: review and modeling studies, *Environmental processes* 10, no. 2, p. 38, 2023; doi: 10.1007/s40710-023-00631-0.

[5] S. S. Haykin, Kalman filtering and neural networks (Vol. 284), *New York: Wiley*, 2001; doi: 10.1002/0471221546

[6] C. Gentili, C. Roman, I. Kraiem, M. Haluska, C. Hierold, Predicting NO_2 Concentration Dynamics Under Varying Humidity with a CNT-FET Sensor, 2026 *Hilton Head*, unpublished.

DOI 10.5162/eurosensors2026/7.1.4

Gas sensing applications of CuO doped with metallic catalyst fabricated by spark ablation

Christian Maier[1], Larissa Egger[1], Barbara Kosednar-Legenstein[1], Nigel Rising[2], Leandro Sacco[2]
[1] Materials Center Leoben Forschung GmbH, Roseggerstraße 12, 8700 Leoben, Austria
[2] VSPARTICLE B.V. Oostingel 209, 2612HL Delft, The Netherlands

Correspondence: christian.maier@mcl.at; +43 3842 45922 - 681

Summary:

In this work, we present chemical nanosensors based on thin CuO films, which are fabricated by spark ablation paired with a dry printing system and subsequent oxidation on Si_3N_4-based micro-hotplate chips. The sensors are tested against various target gases like carbon monoxide (CO), carbon dioxide (CO_2), hydrocarbons (HC_{Mix}) and formaldehyde (CH_2O). An investigation was conducted into various combinations of metallic catalysts, with a particular focus on the CuO, with the objective of reducing the operational temperature.

Keywords: metal oxide, CuO, nanomaterials, spark ablation, gas sensors

Introduction

The detection of hazardous or toxic gases—such as volatile organic compounds (VOCs), CO_2, CO and CH_2O—that adversely affect human health has become essential for monitoring both indoor and outdoor air quality. Conductometric gas sensors operate by measuring changes in the electrical conductivity of a gas-sensitive material when it interacts with surrounding gases. Metal oxides such as SnO_2, ZnO, and CuO are commonly used for this purpose because they exhibit high sensitivity to a wide range of gases [1]. The performance of these sensors can be further optimized through doping with metallic nanoparticles, such as Au, Pd, or Pt, which is considered a promising strategy for enhancing sensor selectivity. [2,3] In particular, the use of CuO is a promising candidate, as it demonstrates significant potential for functionalization with Au nanoparticles, which can enhance the detection of CO_2. [4] In this study, we investigate a solvent-free printing system based on spark ablation, a novel fabrication technique, to print CuO thin layers with metallic catalysts such as Au for gas sensing applications.

Sensor Fabrication

The fabrication technique for producing the sensitive gas-sensing layer of CuO is the patented technology from VSParticle based on spark ablation that can locally deposit the material without use of any patterning/lithography step. Then, the layer is printed directly onto the Si_3N_4 micro hotplate chip with an electrode structure covering an area of 340 × 340 µm². The principle behind spark ablation involves generation of high-energy electrical sparks between two bulk electrodes (metals or properly doped semiconductors) in a hermetically sealed chamber at atmospheric pressure, with a high purity gas (Ar) being flown through the system. In summary, the spark ionizes the gas and ablates the material from the electrodes. This process creates a vaporized material that rapidly cools down due to the temperature difference between the spark zone and the surrounding environment. [5] The present study focuses on a specific aspect of the spark ablation process, namely the variation of layer thickness, post-annealing temperatures and mixtures with Au metal catalysts during the printing step by using two generators in parallel.

Sensor Characterization & Results

The sensor devices have been operated at 150 and 300 °C and tested against CO, CO_2, HC_{Mix} (an equal mixture of 500 ppm of acetylene, ethane, ethene and propene) and formaldehyde. Synthetic air consisting of 80% N_2 and 20% O_2 with 50% relative humidity (r.h.) has been used as the background gas. A comparison has been made between bare CuO sensors and CuO/Au sensors. Fig. 1 shows the electrical resistance behaviour of CuO/Au sensors when exposed to 0.1, 1 and 5 ppm formaldehyde, measured at an operating temperature of 150 °C. The resistance of the baseline of the bare CuO is enhanced with an increase of Au in the sensing layer. The sensors demonstrate a rapid response time and an extended recovery time.

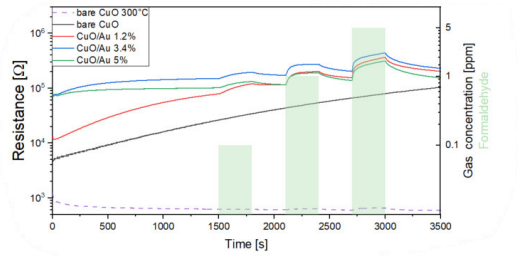

Fig. 1. Resistance measurement during exposure to 0.1 / 1 / 5 ppm formaldehyde at 150 °C (black), 300 °C (violet) operation temperature and 50% r.h. of CuO fabricated by spark ablation, and CuO with different Au content (red 1.2%, blue 3.4% and green 5%)

As illustrated in Fig. 2, the responses of CuO mixed with different concentrations of Au are compared. The sensor response (S), has been calculated according to the following formula:

$$S = \frac{R_{gas} - R_{air}}{R_{air}} * 100\% \qquad (1)$$

where R_{gas} is the sensor resistance in the presence of the test gas and R_{air} is the sensor resistance in pure synthetic air. The sensors are operating at an optimal temperature of 150 °C. The sensors have already reached a state of saturation at low concentrations of each test gas, with the exception of formaldehyde. As demonstrated, the sensors with the highest Au content (5%) correspond to the highest sensor response for each test gas. The highest sensor response was achieved for CO_2, with a result of 77%. Conversely, the sensor response of formaldehyde is not influenced by the Au content; all three Au concentrations demonstrate a comparable sensor response. Notably, these results suggest distinct optimal operating temperatures depending on the target gas with a concentration-dependent response: CuO/Au at 150 °C is well suited for formaldehyde detection, while bare CuO at 300 °C is suited for CO_2.

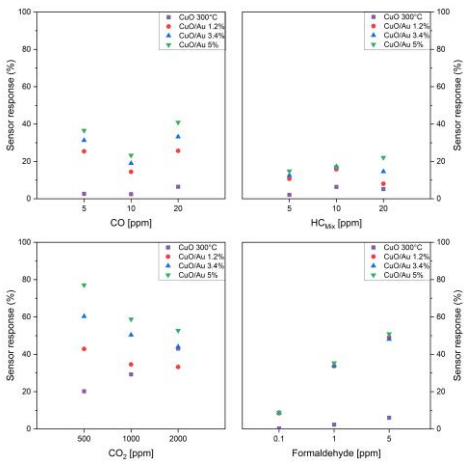

Fig. 2. Sensor response of bare CuO at 300 °C and CuO with different Au content operated at 150 °C towards CO, HC_{Mix}, CO_2 and formaldehyde at different concentrations.

Discussion & Conclusion

We have demonstrated that a combination of CuO and Au is sensitive towards different test gases. The highest sensor response of 77% was achieved for CO_2 with 5% Au content. Typically, CuO gas sensors are operated at 300°C to ensure optimal sensor response. However, the incorporation of Au serves to reduce this operating temperature from 300 °C to 150 °C, thereby decreasing the energy requirements of the entire system. In addition, the drift of the baseline resistance of the CuO/Au mixture is reduced in comparison with that of the bare CuO.

It is asserted that the pathway for enhancing sensitivity to different test gases with low-energy consuming devices, as outlined here, is a highly promising approach for the development of chemoresistive based sensors to be commercialized.

References

[1] M. V. Nikolic, V. Milovanovic, Z. Z. Vasiljevic, Z. Stamenkovic, Semiconductor Gas Sensors: Materials, Technology, Design, and Application. *Sensors* (Basel, Switzerland) 2020, 20 (22) https://doi.org/10.3390/s20226694.

[2] C. Maier, L. Egger, A. Köck, K. Reichmann, A Review of Gas Sensors for CO_2 Based on Copper Oxides and Their Derivatives, Sensors 24 (17). https://doi.org/10.3390/s24175469

[3] [2] J. Guo, J. Zhang, H. Gong, D. Ju and B. Cao, Au nanoparticle-functionalized 3D SnO_2 microstructures for high performance gas sensor, Sens. Actuators, B, 2016, 226, 266–272 https://10.1016/j.snb.2015.11.140.

[4] C. Maier, L. Egger, A. Köck, K. Reichmann, S. Becker, J. S. Niehaus, K. Reichmann, Investigation of the gas-sensing performance of CuO sensors functionalized with different stabilized Au nanoparticles, J. Sens. Sens. Syst. 2025 14 (1), S. 55–65. DOI: 10.5194/jsss-14-55-2025.

[5] R. Raymond und M. Akram, "Temporal investigation of a fast spark discharge in chemically inert gases, “Journal of Physics D: Applied Physics, 30, 1125 (1997); DOI:10.1088/0022-3727/30/7/010

Funding

The work has been performed within the projects “RealSens- Advanced Nanomaterials for Real-time Environmental Monitoring Sensor System (project No 922632), which receive funding from the Austrian Funding Agency FFG.

DOI 10.5162/eurosensors2026/7.2.1

A Functionalization-Free Acetone Detector Based on Low Frequency Interfacial Dielectric Relaxation

Satish K. Verma[1], Mahesh Menon[1], Aravind N. Warrier[1], Andreas Mrosk[2], Markus Gardill[1] and Harald Schenk[1,2]
[1] Brandenburg University of Technology Cottbus-Senftenberg, 03046 Cottbus, Germany
[2] Fraunhofer Institute for Photonic Microsystems, Maria-Reiche-Str. 2, 01109 Dresden, Germany
Corresponding Author's e-mail address: vermas@b-tu.de

Summary:
A novel concept for miniaturized, low-power gas detection without surface functionalization or elevated temperatures, is presented using acetone as a model analyte. MEMS Si-electrodes apply electric fields exceeding 1 MV/m to induce Maxwell-Wagner-Sillars interfacial polarization at device-gas interface. This yields a dielectric loss peak with relaxation time ≈0.45 ms as an acetone-specific signature. Loss peak scales with concentration attaining over 20 dB SNR for 25 ppm acetone. The detector consumes ~6 µw below 1 kHz, making it well suited for battery operated and MEMS-integrated sensing platforms.

Keywords: acetone detection, dielectric relaxation, MWS polarization, low-power sensing, functionalization-free.

Introduction

Acetone is a clinically volatile biomarker for non-invasive point-of-care diagnostics. Industrial exposure monitoring and food quality control represent additional application domains where compact, battery operated and low-cost detectors are needed [1]. Existing acetone sensors mostly relies on surface-functionalized sensors operating at elevated temperatures (200-400 °C), limiting scalability and power efficiency [2]. Here, we take fundamentally different approach where the sensor exploits the intrinsic dielectric properties of acetone vapor rather than relying on a chemical reaction between acetone and functional surface [3], [4]. This enables reagent free, thermally passive and low power detection with CMOS–MEMS compatible platforms.

Theory

The sensing cell consists of parallel electrodes separated by gas domain (Fig. 1a), forming a two-layer dielectric interface that supports Maxwell-Wagner-Sillars (MWS) interfacial polarization. When acetone enters gap between sensing cells, it alters the dielectric contrast at interface producing MWS polarization, measurable in the low frequency impedance spectrum. Fig. 1b shows the microscopic image of Si-electrode device (~200 sensing cells with 5 µm gap). For a bilayer system with electrode and gas regions of permittivity ε_i and conductivity σ_i, the MWS relaxation time is $\tau_{mws} = (\varepsilon_1 + \varepsilon_2)/(\sigma_1 + \sigma_2)$. A 5V electrodes DC bias establishes dielectric

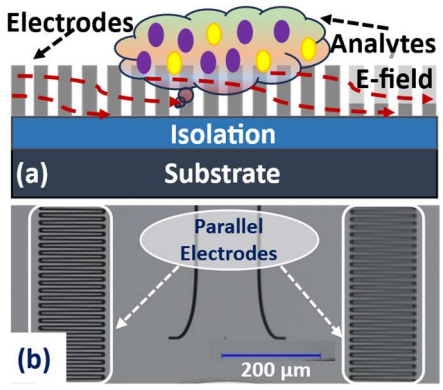

Fig. 1. (a) Schematic of the sensing principle. (b) Microscopic image of parallel Si-electrode device.

contrast at interface due to high electric field of 1MV/cm. A 0.5 V superimposed AC sweeps the frequency range from 20 Hz to 100 kHz to map the impedance response. Complex permittivity $\varepsilon^*(\omega)$ is extracted via broadband dielectric spectroscopy, while the electric modulus $M^*(\omega) = 1/\varepsilon^*(\omega)$ is employed to isolate intrinsic MWS

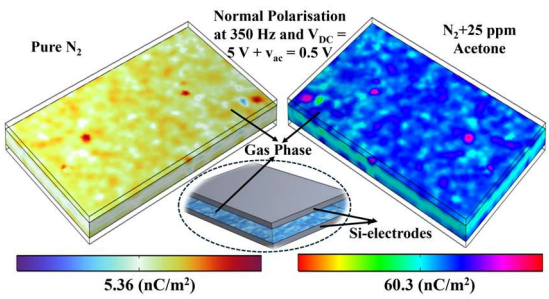

Fig. 2. Simulated normal polarization in the gas region at 350 Hz for N_2 and N_2+25 ppm acetone.

DOI 10.5162/eurosensors2026/7.2.1

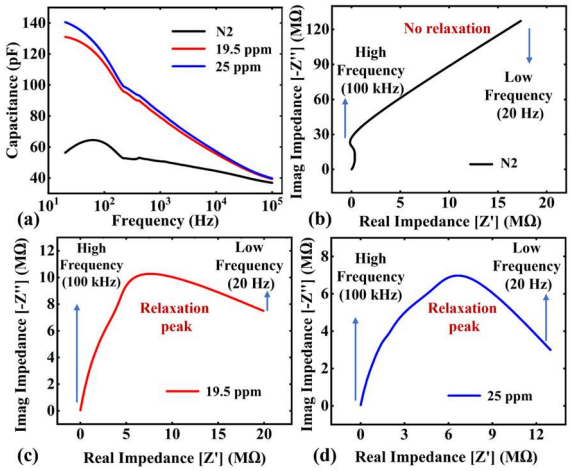

Fig. 3. (a) Measured capacitance vs. frequency at ambient conditions for various gas concentrations. Nyquist responses for (b) N_2, (c) 19.5 ppm acetone, and (d) 25 ppm acetone, showing semi-arc relaxation.

relaxation from electrode polarization and parasitic conductance artifacts. COMSOL based finite element analysis show that normal polarization between the electrodes increases from 5.36 nC/m² (in N_2) to 60.3 nC/m² (N_2 + 25 ppm acetone) at 350 Hz under V = 5 V DC + 0.5 V AC, confirming the dielectric contrast induced by acetone vapor as shown in Fig. 2.

Detection Performance

The sensor performance is evaluated in N_2 and N_2-acetone mixtures. Fig. 3a shows that the static capacitance increases from 60 pF in N_2 to 140 pF at 25 ppm acetone, reflecting an enhancement in the effective permittivity of the gas mixture. In contrast to the featureless Nyquist response of pure N_2 (Fig. 3b), Figs. 3c-d reveal semicircular arcs of progressively reduced diameter with increasing acetone concentration, indicating a polarization-driven relaxation process.

Fig. 4a demonstrates an asserted dispersion in the real permittivity (ε') between N_2 and the acetone mixture, consistent with enhanced polarizability of the analyte. The imaginary permittivity (ε'') spectra in Fig. 4b exhibit a loss peak near 353 Hz for the acetone mixture, absent in N_2, confirming the presence of a dielectric relaxation mechanism. The peak amplitude scales from 0.28 at 19.5 ppm to 0.319 at 25 ppm acetone, reflecting a concentration-dependent response with signal-to-noise (SNR) ratio ~20.3 dB for 25 ppm. Moreover, the electric modulus formalism decouples the bulk conductivity contributions. The real (M') and imaginary (M'') components (Figs. 4c-d) reproduce the 353 Hz peak, corroborating the relaxation signature independently of ohmic effects. Cole–Cole plots provide further insight. The ε'-ε'' arc (Fig. 5a) appears only for acetone mixtures. The M'-M'' plot (Fig. 5b) yields a characteristic relaxation time $\tau \approx 0.45$ ms.

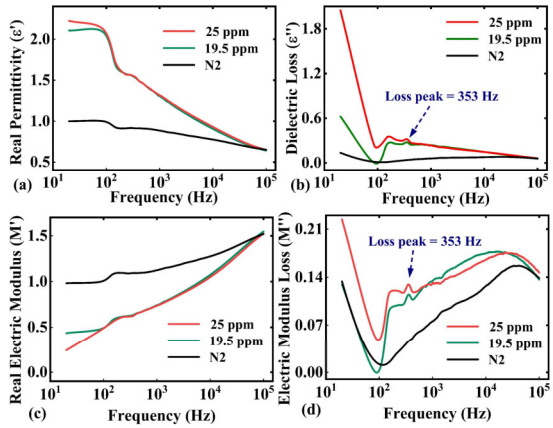

Fig. 4. Measured: (a) ε', (b) ε'' (loss), (c) M', and (d) M'' spectra for various gas concentrations.

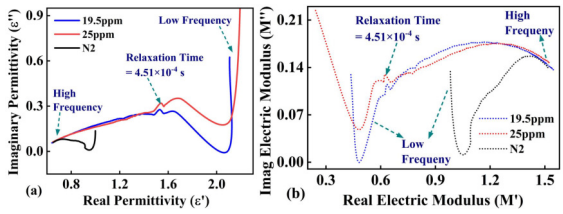

Fig. 5. Cole–Cole plots of: (a) ε' vs. ε'' and (b) M' vs. M'' for various gas concentrations.

Collectively, these results confirm interfacial polarization-driven relaxation within the gas-electrode system. The sensor power consumption is ~6 µw below 1 kHz.

Conclusion

This work demonstrates a functionalization-free, low-power acetone vapor detector using MEMS parallel Si-electrodes. High field (>1 MV/m) induced MWS polarization yields a concentration-scalable, acetone-specific distinct dielectric loss peak at 353 Hz with 20.3 dB SNR at 25 ppm. At ~6 µW below 1 kHz, the platform is inherently compatible with battery-operated and MEMS-integrated deployment, offering a route toward portable, label-free VOC sensing.

References

[1] Ertai *et al.*, “Ultrasensitive Acetone Gas Sensor Based on a K/Sn–Co_3O_4 Porous Microsphere for Noninvasive Diabetes Diagnosis,” in *ACS Sensors,* 9, 11, 6148–6156, 2024, doi: 10.1021/acssensors.4c02009.

[2] Potyrailo *et al.*, “Extraordinary performance of semiconducting metal oxide gas sensors using dielectric excitation,” in *Nature Electronics*, 3, 280-289, 2020, doi: 10.1038/s41928-020-0402-3.

[3] Mertens *et al.*, "Dielectric Spectroscopy: Revealing the True Colors of Biological Matter," in *IEEE Microwave Magazine*, 24, 4, 49-62, 2023, doi: 10.1109/MMM.2022.3233510.

[4] F. Kremer and A. Schönhals, Eds., *Broadband Dielectric Spectroscopy*. Springer Science & Business Media, 2002.

DOI 10.5162/eurosensors2026/7.2.2

Modelling of Moving Magnet Actuators for Haptic Sensing Applications

Sebastian Lang[1], Alexander O. Niedermayer[1], Jonas Astl[1], Daniel Spira[1], Bernhard Jakoby[1]
[1] Johannes Kepler University Linz, Altenbergerstrasse 69, 4040 Linz, Austria,
sebastian.lang@jku.at

Summary:
Haptic feedback is a key component of human interface devices as it allows for intuitive interaction. A common way to give haptic feedback is via vibrations, depending on either the user's inputs or the state of the device. One difficulty of such devices, vibration actuators in particular, is the influence of the outside environment on the actuator's performance. In this work, we show a way to model how the coupling of the outside environment affects the impedance response of a moving magnet actuator for haptic vibrational feedback and to, in turn, extract the properties of the actuator's surroundings. To achieve this, we derived an electrical equivalent circuit from a linear two-degree-of-freedom mechanical model and calculated the resulting electrical impedance of the actuation coil. After calibration, impedance spectra were measured in different user scenarios, and the contributions to the impedance which are related to the environment (e.g., the user's hands) were extracted, showing the possibility to measure the characteristics of a surrounding system via the impedance spectrum.

Keywords: haptic sensors, resonance, modelling, equivalent electrical circuit

Introduction

Integrating haptic feedback into electronic interfaces supports intuitive interaction between user and device [1,2]. In particular, so-called Moving Magnet Actuators (MMAs), which utilize the electromagnetic actuation of vibrating permanent magnets, enable such feedback to the user [3]. MMAs have different designs, most of which can be described as a magnet suspended by springs inside a housing comprising a coil for electromagnetic actuation, as shown in Fig. 1.

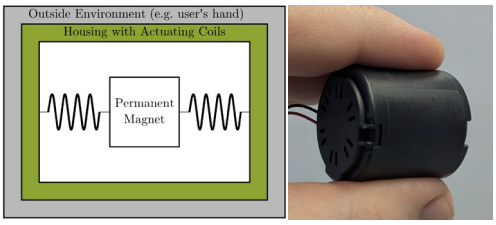

Fig. 1 Simplified sketch of the inner structure of an MMA (left) and a picture of an MMA held in the user's hand (right).

Interaction with the external environment remains an issue for all types of mechanical oscillators, including MMAs, resulting in changes in resonance frequency in particular. In MMAs, the interaction causes a change in vibration amplitude depending on the way a user holds the device, resulting in a measurable change in electrical impedance [4].

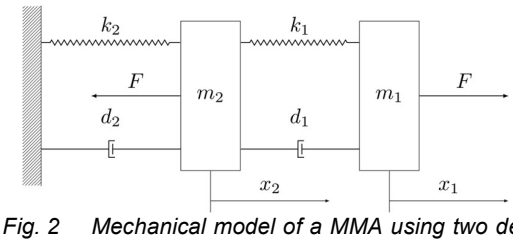

Fig. 2 Mechanical model of a MMA using two degrees of freedom x_1 and x_2. The Mass m_1, with the spring k_1 and damper d_1 represent the magnet and the spring connecting it to the housing with Mass m_2. The components k_2 and d_2 model the user's hand or materials surrounding the MMA.

This effect can be considered to be spurious, but it could also be utilized for sensing and possibly controlling the vibration amplitude in various environments and handling situations. Hence, a mechanical model is devised, which can be further translated into an equivalent circuit for the actuation coil's impedance.

Mechanical and Electrical Model

Based on the linear two-degree-of-freedom mechanical model shown in Fig. 2, a transformer model coupling the electrical and mechanical quantities at the actuation coil via a constant coupling factor $a = \frac{F}{i} = \frac{u_{\text{ind}}}{\dot{x}}$ and by introducing mechanical admittances connecting velocity and applied force $Y_{\text{mech}} = \frac{v}{F}$, an equivalent circuit was derived as shown in Fig. 3.

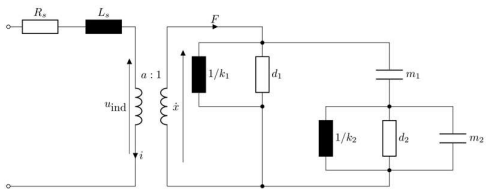

Fig. 3. Equivalent circuit representing the mechanical system together with the ohmic resistance R_s and self-inductance L_s of the coil yielding the impedance of the actuation coil.

Measurements

As described in our previous work [4], the electrical impedances of multiple MMAs in different baseline and user scenarios were measured using an impedance analyzer. These spectra in Fig. 4 (solid) show that holding or clutching an MMA with different forces leads to strongly varying resonances.

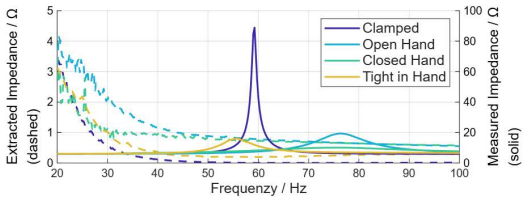

Fig. 4. Measured(solid) and extracted(dashed) impedance spectra of multiple user scenarios of the MMA shown in Fig.1.

Using calibrated system parameters as well as the aforementioned model, the characteristics of the "outer" system, represented by k_2, d_2 and m_2, can be extracted as shown in Fig. 4 (dashed; impedance) and Fig. 5 (admittance). These spectra represent the properties of the surrounding environment (e.g., a user's hand).

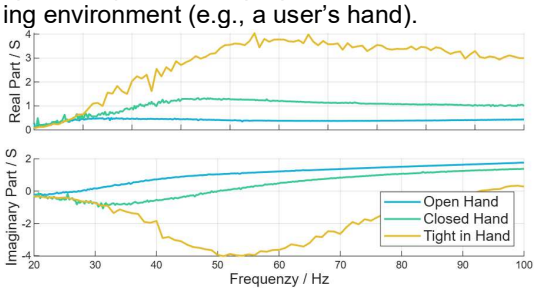

Fig. 5. Real and Imaginary parts of the extracted admittances of the "outer" system.

The parameters d_2 and k_2, responsible for the plateau in the real part and the shape of the imaginary part in Fig. 5, respectively, show a clear increase over the increase in grip strength. The increase in stiffness k_2 from $100\,\mathrm{N/m}$ (closed hand) to $300\,\mathrm{N/m}$ (tight in hand) is also consistent with reported similar observations [5], indicating that these parameters are well suited to be used as measurement metrics for the grip strength, thus enabling sensor functionality of these actuators.

Observed Challenges

The desired parameters are nested within the rather complex impedance spectrum of the whole system, and consequently, inaccuracies during the calibration process lead to significant errors in the extracted "outer" impedance. Additionally, many MMAs are constructed without any magnetic field guides, resulting in a coupling factor a that is dependent on the position of the inner magnet, which results in a significant variation of the impedance spectrum depending on the displacement amplitude, in addition to various other non-linearities that can be encountered.

Conclusion

This work illustrates the modeling of an MMA for haptic applications. From a linear mechanical two-degrees-of-freedom model, a model for the observed electrical impedance, as well as an electrical equivalent circuit are derived. This model, with additional calibration measurements, can be used to extract the characteristics of the surrounding environment (e.g., a user's skin tissue), which would enable sensing associated parameters in the environment. This can, in turn, allow for active control of the vibration amplitude of haptic feedback elements.

Acknowledgment

This work was supported by the K2 Center for Symbiotic Mechatronics, Linz Center of Mechatronics, within the framework of the Austrian COMET-K2 Program, as well as the Austrian Research Promotion Agency under the project 'Adaptec'.

References

[1] J. Tan, Y. Ge, X. Sun, Y. Zhang, Y. Liu, User Experience of Tactile Feedback on a Smartphone: Effects of Vibration Intensity, Times and Interval, in: 2019: pp. 397–406. https://doi.org/10.1007/978-3-030-22577-3_29.

[2] E. Hoggan, S. Brewster, J. Johnston, Investigating the effectiveness of tactile feedback for mobile touchscreens, 2008. https://doi.org/10.1145/1357054.1357300.

[3] A. Hassan, A. Bijanzad, I. Lazoglu, Dynamic Analysis of a Novel Moving Magnet Linear Actuator, IEEE Trans. Ind. Electron. 64 (2017) 3758–3766. https://doi.org/10.1109/TIE.2016.2645506.

[4] S. Lang, N. Doppelhammer, A.O. Niedermayer, T. Mitteramskogler, B. Jakoby, Sensitivity of Resonant Moving Magnet Actuators to Haptic Environments, IEEE Sens. Lett. 9 (2025) 1–4. https://doi.org/10.1109/LSENS.2025.3585347.

[5] H. Höppner, M. Große-Dunker, G. Stillfried, J. Bayer, P. van der Smagt, Key Insights into Hand Biomechanics: Human Grip Stiffness Can Be Decoupled from Force by Cocontraction and Predicted from Electromyography, Front. Neurorobotics 11 (2017) 17. https://doi.org/10.3389/fnbot.2017.00017.

DOI 10.5162/eurosensors2026/7.2.3

In-Situ Spatial Mapping of Microjet Impingement with a Piezoresistive Silicon Nanowire MEMS Sensor

Levent Demirkazik[1], Ipek Nil Samci[1], Masoud Jedari Ghourichaei[1], Onur Aydin[1], Bekir Aksoy[1], Cemal Aydogan[2], Gokhan Nadar[1], Ivo W. Rangelow[2,3], Arda Deniz Yalcinkaya[4], Halil Bayraktar[5], Umut Kerimzade[1,6], Burhanettin Erdem Alaca[1,6,7]
[1] Mechanical Engineering Department, Koç University, Istanbul, Türkiye
[2] Department of Electrical Engineering and Information Technology, Institute of Micro- and Nanoelectronics, Ilmenau University of Technology, Ilmenau, Germany
[3] nano analytik GmbH, Ehrenberg Str. 3, Ilmenau, Germany
[4] Department of Electrical and Electronics Engineering, Boğaziçi University, Istanbul, Türkiye
[5] Department of Molecular Biology and Genetics, Istanbul Technical University, Istanbul, Türkiye
[6] n²STAR, Koç University, Istanbul, Türkiye
[7] KUYTAM, Koç University, Istanbul, Türkiye
ealaca@ku.edu.tr

Summary:
We present an in-situ sensing framework for spatial mapping of impinging microjet plume-surface interaction at the sub-mm nozzle scale using a piezoresistive silicon nanowire (SiNW) MEMS sensor. A bilinear response surface in jet momentum (J) and stand-off ratio (h/d) measures resistance change ($\Delta R/R_0$) across h/d = 2.5–10. Spatial maps acquired with 20 µm along-track sampling and sub-nW power resolve stand-off-dependent changes in both peak loading and spatial structure of the impingement.

Keywords: MEMS, force sensor, piezoresistive silicon nanowires, jet impingement, flow sensing

Background, Motivation and Objective

Impinging microjets govern near-wall loading in applications from micro-propulsion plume-surface interaction [1] to compact cooling, printing, and needle-free injection. Optical diagnostics such as µPIV deliver microscale vector fields but suffer from depth-of-correlation averaging, reflections, and seeding constraints at small stand-off [2]. Physical sensing at sub-mm nozzle scale remains rare; a pressure sensor for jet momentum spatial distribution has been demonstrated [3], and point-wise jet impingement on suspended SiNW MEMS sensors showed initial feasibility [4]. However, in-situ spatial mapping of micro-jet plume-surface interaction across a broad stand-off range has not been addressed.

Description of the New Method or System

The sensing element is a suspended shuttle with SiNW piezoresistors (<110>, p-type, 10^{17} cm^{-3}) (Fig. 1) [5]. A nitrogen jet from a d = 200 µm nozzle impinges on the shuttle, generating strain in the SiNWs; gas delivery, electrical readout, and stage motion are coordinated through a DAQ system (Fig. 2). Sensor characterization at h/d = 2.5–10 and three momentum setpoints (~9–13 mN) establishes the response surface in (J, h/d) (Fig. 3). For raster mapping across h/d = 2.5–10, the sensor remains fixed while the nozzle rasters 8 passes over x/d = ±10, stepping increments of $\Delta(y/d)$ = 0.5 from y/d = 3.5 to 0 at 400 µm/s, giving 20 µm along-track sampling at 20 Hz.

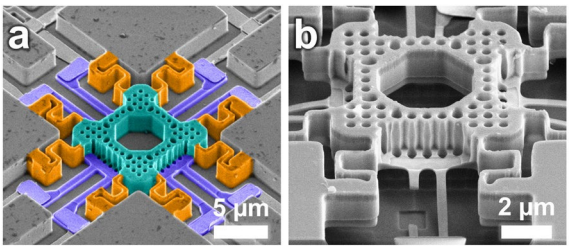

Fig. 1 a) SEM image of the sensor shows 10×10 µm² MEMS shuttle (teal), anchors connected by springs (orange) and SiNW piezoresistors (purple) of length 5 µm, b) SEM image after FIB cut exposing the SiNW cross-section (width × height = 500 × 280 nm²).

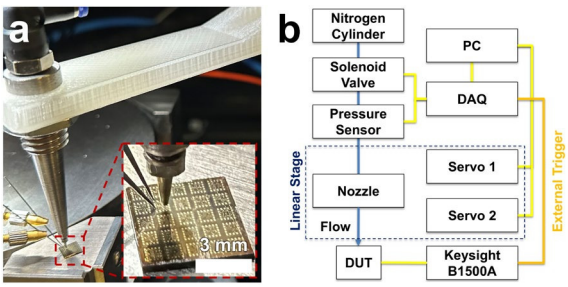

Fig. 2. a) Picture of the experimental setup showing the DUT, probe tips, and nozzle (inset: DUT–nozzle close-up). b) Block diagram of the experimental setup.

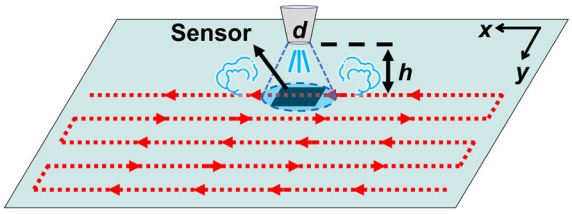

Fig. 3 Measurement workflow schematic showing the chip (cyan) with on-chip sensor (black) and nozzle positioning for centered characterization and raster mapping (red arrows indicate the scan trajectory).

Results

With the sensor biased at 50 nA (R_0 = 190.4 kΩ, <0.5 nW), the response surface increases with J and decreases with h/d (Fig. 4). The fit yields local sensitivities of -7.35×10^{-4} $(h/d)^{-1}$ and 1.22×10^{-3} mN^{-1}. The raster scan at h/d = 7.5 (Fig. 5a) shows a clear $\Delta R/R_0$ maximum at y/d = 0 decaying with lateral displacement. Across each map, the 95th percentile $\Delta R/R_0$ reaches 1.54%, 1.23%, and 1.14% at h/d = 2.5, 7.5, and 10 respectively. While J primarily scales response magnitude, increasing stand-off narrows the peak response region while weaker loading persists across the field (Fig. 5b). The platform resolves these patterns with sub-nW power in a 10×10 µm^2 pixel, supporting in-situ mapping across a wide stand-off operating range. This framework opens direct wall-referenced characterization to applications in microscale cooling, additive manufacturing, and needle-free injection where near-field loading governs process outcomes.

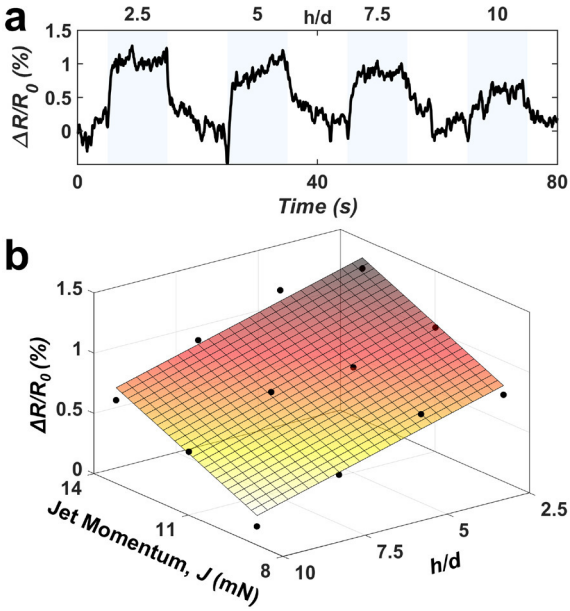

Fig. 4. a) $\Delta R/R_0$ vs. time at $J \approx 11$ mN for h/d = 2.5–10; shaded intervals indicate flow-on periods. b) Response surface (bilinear fit) to 12-cycle averages from three independent tests in (J, h/d); R^2 = 0.93.

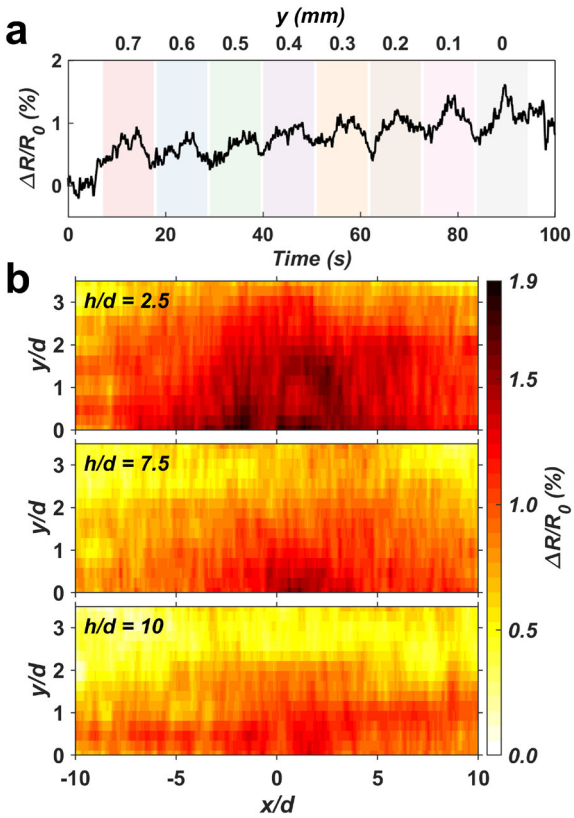

Fig. 5. a) Eight-pass raster scan at J = 11.8 mN, h/d = 7.5. $\Delta R/R_0$ is plotted against time and corresponding y position. b) $\Delta R/R_0$ maps at h/d = 2.5, 7.5, and 10 on a common color scale.

References

[1] C. Ngalande, T. Lilly, M. Killingsworth, et al., Nozzle Plume Impingement on Spacecraft Surfaces: Effects of Surface Roughness, Journal of Spacecraft and Rockets 43, 1013-1018 (2006); doi: 10.2514/1.19321

[2] R. Lindken, M. Rossi, S. Große, et al., Micro-Particle Image Velocimetry (µPIV): Recent developments, applications, and guidelines, Lab on a Chip 9, 2551 (2009); doi: 10.1039/b906558j

[3] A. Bottega, C. Dongiovanni, A new sensor for the analysis of jet momentum spatial distribution, Sensors and Actuators A: Physical 269, 283-293 (2018); doi: 10.1016/j.sna.2017.11.041

[4] L. Demirkazik, U. Kerimzade, M. Jedari Ghourichaei, et al., Gas Flow Sensing with a Piezoresistive Silicon Nanowire-Based MEMS Force Sensor, 2025 IEEE 38th International Conference on Micro Electro Mechanical Systems (MEMS), 809-812 (2025); doi: 10.1109/MEMS61431.2025.10917650

[5] M. Jedari Ghourichaei, U. Kerimzade, L. Demirkazik, et al., Multiscale Fabrication and Characterization of a NEMS Force Sensor, Advanced Materials Technologies 10, 2400022 (2025); doi: 10.1002/admt.202400022

Acknowledgements

This work was supported by the Scientific and Technological Research Council of Türkiye (TÜBİTAK) under Grants No. 120N361 and 118C155.

DOI 10.5162/eurosensors2026/7.2.4

Dual-Resonance Indirect Photoacoustic Gas Sensing System for Sub-ppm Gas Detection

Ananya Srivastava[1], Achim Bittner[1], Alfons Dehé[1,2]
[1] Hahn-Schickard, Wilhelm-Schickard-Str. 10, 78052 Villingen-Schwenningen, Germany,
[2] Georg H. Endress Chair of Smart Systems Integration, IMTEK, Albert-Ludwigs-Universität Freiburg, Georges-Köhler-Allee 103, 79110 Freiburg, Germany
ananya.srivastava@hahn-schickard.de

Summary:
This work presents a dual-resonance photoacoustic (PA) gas sensing system that exploits the spectral overlap between resonances of a Helmholtz acoustic cell and a piezoelectric MEMS cantilever to achieve enhanced sensitivity for carbon dioxide detection. The system employs a chopper-based modulation and a distributed feedback (DFB) laser operating near 4225 nm, targeting a strong absorption line of carbon dioxide. Lock-in-based photoacoustic measurements demonstrate a detection resolution of ca. 250 ppb of carbon dioxide in nitrogen at the atmospheric pressure.

Keywords: Photoacoustic gas sensing, Dual resonance, Piezoelectric MEMS cantilever, Helmholtz resonator, Carbon dioxide detection

Introduction

Photoacoustic spectroscopy (PAS) is a trace gas detection technique in which modulated infrared radiation absorbed by target gas molecules generates a periodic acoustic pressure wave whose amplitude is proportional to the gas concentration [1]. Conventional systems exploit a single resonance—either an acoustic cell mode or a detector mechanical mode—to amplify the signal. However, the achievable quality factor at a single resonance is limited by viscous and thermal losses in miniaturized geometries [2]. In this work, a dual-resonance approach is presented in which the Helmholtz resonance of a custom acoustic cell is deliberately matched to the fundamental resonance of a piezoelectric MEMS cantilever. At the shared frequency, both amplification mechanisms act simultaneously, yielding a multiplicative signal enhancement. Sub-ppm CO_2 detection is demonstrated using a DFB laser near 4225 nm with a chopper and amplitude modulation scheme, achieving a resolution of 250 ppb.

System Design and Operating Principle

The sensing system, shown in Fig. 1, comprises a modified Helmholtz acoustic resonator cell and a piezoelectric MEMS cantilever transducer. The Helmholtz cell is an H-shaped structure with a central front cavity illuminated by the laser beam, connected via a narrow neck to a larger back volume. An adjacent narrow channel also connects the front volume to the reference microphone. The cell geometry is dimensioned such that its damped Helmholtz mode coincides with the first flexural resonance of the cantilever. The dampness comes due to the introduction of MEMS

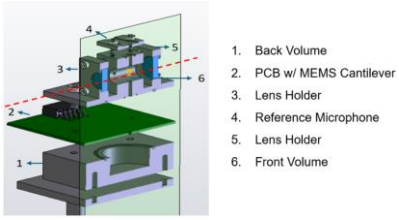

Fig. 1.CAD cross-section of the PA system

cantilever in between the Helmholtz neck and back volume. The dual-resonance operating point thus yields an overall enhancement scaling as $Q_{CellDamp} \times Q_{cant}$ relative to the off-resonance baseline.

Laser Source and Target Line

The target absorption line was selected using the HITRAN spectroscopic database [3]. Fig. 2 shows the laser power as the function of current and also the targeted CO_2 absorption spectrum in the mid-infrared region [4]. A specific line near 4.22 µm (~2370 cm−1) was chosen for its strong line strength and minimal interference from other gas species.

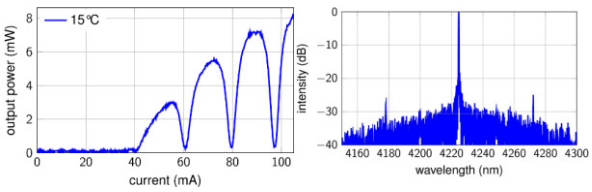

Fig. 2. DFB laser & gas absorption parameters

Experimental Setup

The DFB laser beam is modulated by a mechanical chopper at the dual-resonance frequency. The modulated beam passes through the measurement channel with variable and controlled

DOI 10.5162/eurosensors2026/7.2.4

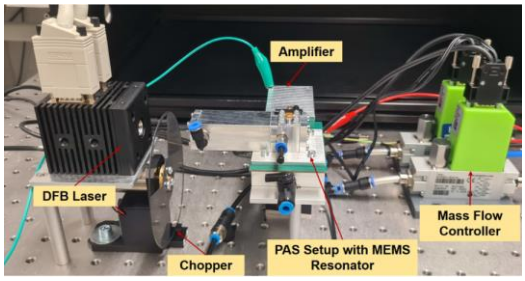

Fig. 3. PAS system measurement setup

CO_2 gas concentration, prepared using known gas mixtures and mass flow controllers, and a Helmholtz cell containing high concentration (>80%) CO_2. The photoacoustic pressure wave generated within the cell drives the MEMS cantilever, whose piezoelectric output voltage is demodulated by a lock-in amplifier referenced to the chopper frequency. The in-phase and quadrature signal components are recorded as a function of gas concentration. The temperature and humidity of the setup are monitored using a reference sensor. The separation of variable gas volume with the reference gas volume ensures minimal influence on the position of the resonance frequency. This is further also corroborated by the use of the phase-locked loop technique.

Results and Discussions

The dual-resonance design was first validated through independent frequency sweep characterization. The cell transfer function was measured using PAS signal and a reference microphone.

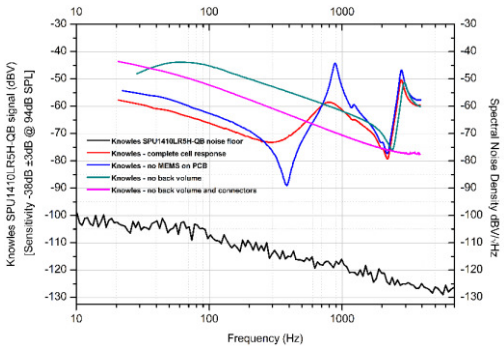

Fig. 4. Influence of different components on the measured PAS frequency response of the cell

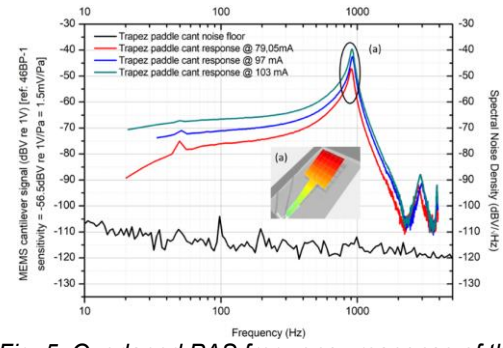

Fig. 5. Overlaped PAS frequency response of the trapezoidal cantilever w/ the cell resonance at different laser currents

Fig. 4 presents both cell responses in different configurations and the combined system transfer function, confirming spectral overlap at the target frequency (f_{res} ~ 910 Hz). The combined quality factor at the matched point is significantly higher than that of either subsystem alone. For example, the complete cell response shown by the red curve in Fig. 4 can be compared to the cantilever response in Fig. 5. The signal-to-noise ratio for the current generation of cantilevers at f_{res} is ~155 dB, which corresponds to the current gas measurement range. This is forecasted to improve with the next generation of cantilevers with better material parameters.

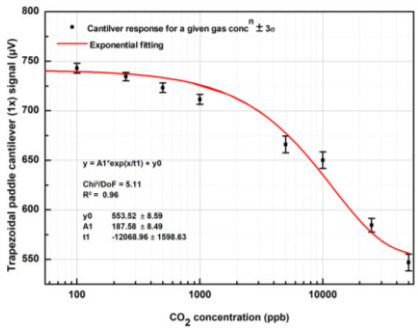

Fig. 6. PAS signal vs. CO_2 concentration @ f_{res}

The photoacoustic sensing performance was evaluated by varying the CO_2 concentration from ambient levels to sub-ppm. Fig. 5 presents the lock-in amplifier output versus concentration. An expected negative exponential relationship, following Beer-Lambert's law, is observed between the cantilever signal and change in the gas concentration. With a ±3σ deviation, the 250 ppb of CO_2 is distinctly and repeatably measurable.

Conclusions

A dual-resonance photoacoustic gas sensor has been demonstrated by spectrally matching a Helmholtz cell acoustic mode with a MEMS cantilever mechanical resonance, yielding multiplicative signal enhancement. Using a mid-infrared DFB laser near 4225 nm targeting a HITRAN-identified CO_2 absorption line and a chopper-based AM scheme, a detection resolution of 250 ppb was achieved. This work offers a strategy towards highly selective, high-sensitivity photoacoustic sensors, which can be extended to different target gases.

References

[1] A. Miklós, P. Hess, and Z. Bozóki, "Application of acoustic resonators in photoacoustic trace gas analysis and metrology," Rev. Sci. Instrum., vol. 72, no. 4, pp. 1937–1955, 2001.

[2] T. Kuusela and J. Kauppinen, "Photoacoustic gas analysis using interferometric cantilever microphone," Appl. Spectrosc. Rev., vol. 42, no. 5, pp. 443–474, 2007.

[3] I. E. Gordon et al., "The HITRAN2020 molecular spectroscopic database," J. Quant. Spectrosc. Radiat. Transf., vol. 277, p. 107949, 2022.

[4] nanoplus Nanosystems and Technologies GmbH, "4000 nm - 4600 nm Distributed Feedback Laser." Accessed: Jan. 23, 2026.

DOI 10.5162/eurosensors2026/7.3.1

On the Interplay of Viscoelasticity and Air Permeation in Modelling the Dynamics of Embedded Tactile Sensors

Katja Meier[1], Florin Püntener[1], Christofer Hierold [1], Cosmin Roman[1]
[1] Micro and Nanosystems, Dept. of Mechanical and Process Engineering, ETH Zürich, Switzerland
croman@ethz.ch

Summary: We investigate via experiments and finite element simulations the dynamic behavior of soft artificial fingertips. While viscoelasticity is a well-recognized dynamical mechanism, here we reveal air diffusion through silicone layers to be an equally important mechanism influencing dynamics. A series of experiments, performed in air and submerged in oil to reduce air diffusion, support unambiguously the participation of both dynamical mechanisms. A finite-element model further supports these findings, reproducing qualitatively the main dynamical features of the measurements.

Keywords: tactile artificial fingertip, soft materials, viscoelasticity, air diffusion through silicone

Background and Motivation

Tactile sensing is a key enabler for dexterous robotic manipulators [1]. Integration of tactile sensor arrays into soft materials will enable human-like fingertips suitable for delicate and precise object grasping. Such a technology, that we introduced in [2] is shown in Fig. 1. However, using soft materials such as silicones introduces several complexities stemming from hyper- and viscoelastic effects, entailing nonlinear deformations and dynamical effects.

In this work we draw attention to an additional effect, namely air diffusion, that may co-influence the dynamics of sensors integrated into soft materials. This is particularly important when the sensors incorporate an air-filled gap as the one illustrated in Fig. 1.

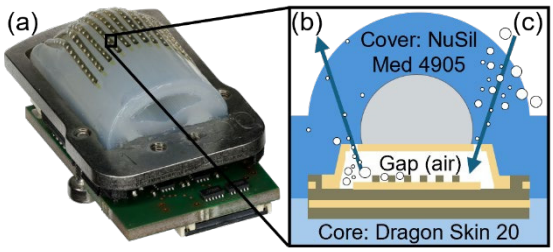

Fig. 1. ***Technology overview****. (a) Artificial fingertip with embedded tactile array (12x12 taxels) [2]. (b, c) Cross-section of a taxel showing the air gap (cavity) and ~400 µm cover layer, with pressure-difference driven air diffusion between cavity and ambient (schematic, not to scale).*

Description of the New Method

Experiments were conducted with the artificial fingertip either placed directly in an air pressure chamber or partially submerged in oil to prevent air diffusion into the taxel air gap.

Finite-element simulations were performed with COMSOL Multiphysics, to get insight into the physics of the observed dynamical effects. The applied pressure P and number of molecules n were interconverted via the ideal gas law. A diffusion-based simulation, as illustrated in Fig. 2(b), was utilized to compute n (and corresponding pressure P) within the air gap of the taxel. The pressure difference ΔP was used subsequently in an electromechanical taxel model to predict capacitance changes ΔC.

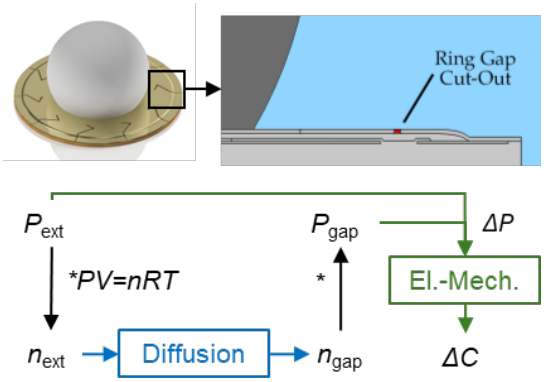

Fig. 2. ***Finite-element simulation framework.*** *Detailed representation of 2D axisymmetric taxel with cover layer (top). Schematic representation of simulation flow with decoupled diffusion simulation to predict pressure in the air gap and electro-mechanical simulation to predict ΔC (bottom).*

For computational efficiency, a 2D axisymmetric model was derived from the 3D geometry. The membrane spring cut-outs (Fig. 2) were simplified, replacing them with a single equivalent air opening. Material parameters and diffusion constants were taken from literature, experiments, and previously reported work, (see Table 1).

Tab. 1: Material parameters of silicone rubber and diffusivity constants for Nitrogen used in simulation

Neo-Hookean Lamé μ	82'124 N m^{-2}
Generalized Maxwell model parameters	Rt =0.35 s Ef = 10
Pressure reduction factor	4.5
N_2 self-diffusion [$cm^2\ s^{-1}$]	0.209 [3]
N_2 in silicone rubber [$cm^2\ s^{-1}$]	$1.5*10^{-5}$ [4]

Results and Discussion

For linear pressure ramps up to 3000 mbar in oil viscoelastic effects of the silicone layer dominate (Fig. 3). Slower ramps result in higher ΔC values, particularly during loading, as silicone has more time to undergo creep. During unloading, the responses are more similar, indicating partial compensation of these effects. Hysteresis decreases with increasing ramp time.

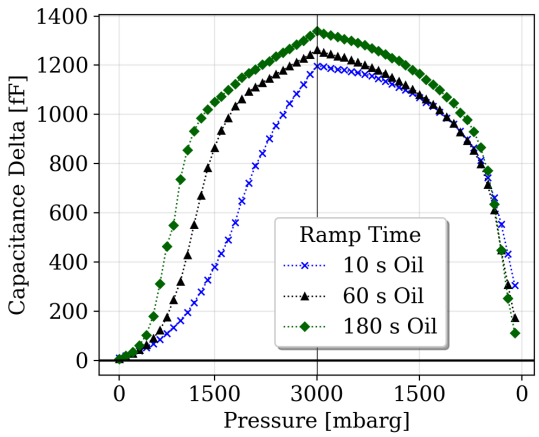

*Fig. 3. **Viscoelastic dynamic effects** for linear pressure ramps up to 3000 mbar for different ramp times with artificial finger submerged in oil. Slower ramps show higher response but lower hysteresis.*

Fig. 4 compares the capacitance response (ΔC) in air and oil environments after switching the pressure up to 500 mbar holding it for 90 s and then releasing it back to ambient pressure. Comparing air and oil measurements, supported by simulation, reveals the influence of diffusion. During the first 10 s, similar behavior is observed across all cases. Past the 15 s mark, the behavior starts to differ, with ΔC starting to decrease for air (w/ diffusion) as opposed to oil (w/o diffusion). This behavior is attributed to air diffusing through the silicone cover layer into the membrane cavity, which reduces the effective pressure difference ΔP and restores the initial membrane configuration. The effect becomes significant after 20 s, with approximately 10% of the applied pressure establishing within the taxel gap. No such relaxation is observed in oil measurements or simulations with disabled diffusion, confirming this effect.

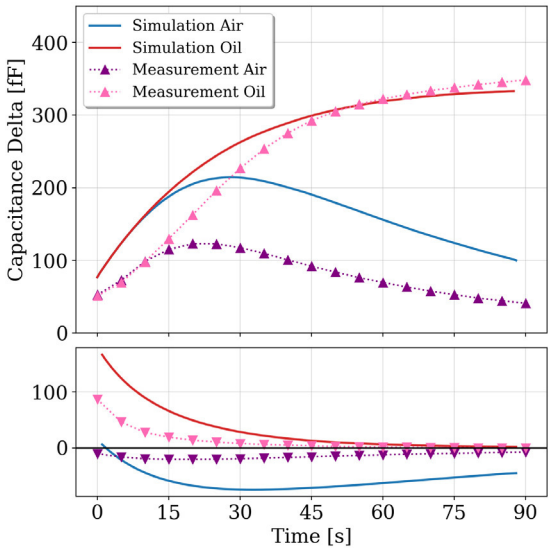

*Fig. 3. **Impact of air diffusion.** Comparison of simulations with and without diffusion to experiments in air and oil (no diffusion). (top) Taxel response in simulation and taxel array average of experimental data after switching the chamber pressure up to 500 mbar and holding it for 90 s and (bottom) after returning to ambient pressure. Fast transients (<2s) not shown.*

In addition to well-known viscoelastic effects, air diffusion should be considered when analyzing the dynamics of sensors that contain soft and permeable silicone covers. In our case, for artificial fingertips, a linear ramp duration of 30 s or a pressure hold duration of up to 15 s provides a suitable balance between reduced viscoelastic effects and limited diffusion. Furthermore, intentionally varying ramp speed can provide additional insight into the electromechanical behavior of the taxels, enabling more advanced model-based normalization strategies.

References

[1] S. Wistreich, et al, DexSkin: High-Coverage Conformable Robotic Skin for Learning Contact-Rich Manipulation, *arXiv preprint* (2025); doi: 10.48550/arXiv.2509.18830

[2] Weichart et al, Tactile Sensing With Scalable Capacitive Sensor Arrays on Flexible Substrates, *IEEE Eplore* (2021); doi:10.1109/JMEMS.2021.3104352

[3] Donald R Burgess Jr, et al, Self-diffusion and binary-diffusion coefficients in gases, Tech. rep. NIST TN 2279, National Institute of Standards and Technology (U.S.), (2024); doi: 10.6028/NIST.TN.2279.

[4] W. L. Robb, et al, Thin silicone membranes-their permeation properties and some applications. *Annals of the New York Academy of Sciences* 146.1 (1968), pp. 119–137. doi: 10.1111/j.1749-6632.1968.tb20277.x.

DOI 10.5162/eurosensors2026/7.3.2

Improved Angle Sensing by Shape-from-Motion Calibration of 3D Magnetic Sensors

Bibhu Kar, Per Rutquist, Oliver Paul
Laboratory for Microsystem Materials, IMTEK, University of Freiburg, Germany
bibhu.kar@imtek.uni-freiburg.de

Summary:
Axis non-orthogonality in multi-axis magnetic sensors introduces cross-talk, distorts the reconstructed magnetic field, and limits measurement accuracy. In this contribution, we present a shape-from-motion-based method to estimate and compensate for axis non-orthogonality in a 3D magnetic sensor by exposing the sensor to a magnetic field of constant magnitude at six orientations. The key advantage of this approach is that it does not require precise control of the field directions nor the magnitude. In the reported case, we demonstrate the improvement of the measured relative angles by a factor of 3.5.

Keywords: Magnetic sensors, sensor calibration, axis non-orthogonality, inverse calibration, Shape-from-motion method

Introduction

In order to reconstruct a magnetic field reliably, accurate calibration of multi-axis magnetometers is essential. In practice, fabrication tolerances and assembly imperfections lead to gain mismatch, offset, and non-orthogonality between the sensor axes.

Conventional calibration of magnetic sensors requires an application of known magnetic fields in well-defined orientations, typically using Helmholtz coil systems. However, coil setups are prone to their own imperfections. To overcome these limitations, we implement a calibration method based on the shape-from-motion (SfM) method. SfM was originally developed in computer vision to recover 3D structures from multiple observations [1], and was later applied by Kim et al. [2] for the calibration of 2D MEMS force sensors.

SfM exploits the structure of the measured data acquired at different orientations, allowing the simultaneous estimation of sensor response parameters. In contrast to [2], in this work, we extend SfM to a 3D magnetic sensor. Furthermore, we demonstrate the capability of the method to improve angle sensing, even if the magnitude of the calibration magnetic field is not accurately known.

Method: Shape-from-motion calibration

A 3D magnetic sensor provides a measurement vector $z \in \mathbb{R}^3$, in response to a magnetic field vector $m \in \mathbb{R}^3$. Assuming a linear model, the relationship between z and m is expressed using a sensor response matrix S as:

$$z = mS. \tag{1}$$

For N measurements acquired under different sensor orientations in a magnetic field of constant magnitude, the model can be written in matrix form as:

$$Z = MS, \tag{2}$$

where $Z \in \mathbb{R}^{N\times 3}$ contains the measurement data and $M \in \mathbb{R}^{N\times 3}$ contains the corresponding field vectors.

Nevertheless, the matrix Z can be factorized using singular value decomposition (SVD) as:

$$Z \approx \hat{M}\hat{S}\,. \tag{3}$$

This factorization is not unique and, for non-collinear measurement orientations, defined up to an unknown invertible linear transformation. This ambiguity is resolved by exploiting the constant magnitude of the applied magnetic field, which introduces a quadratic constraint on the reconstructed vectors and enables the recovery of the sensor response matrix. A detailed explanation is available in [2].

In this contribution, only six measurement orientations are used for 3D calibration. These are sufficient to estimate the sensor response matrix S up to an unknown rotation and, if the calibration field magnitude is inaccurately known, up to a scaling factor.

The calibration matrix $C = S^{-1}$ is then used to reconstruct the applied magnetic field vectors from measured data. Further, we evaluate the axis non-orthogonality by computing the angles

between the effective sensing directions derived from C.

Measurements

For validating the method, we used a Bosch BMM350 sensor. This 3D magnetometer is mounted at the center of a Helmholtz coil setup generating a quasi-uniform magnetic field. The sensor was rotated using a stepper motor to acquire measurements under different orientations. To ensure sufficient excitation of all three sensor axes, we rotated the sensor around two different axes, as shown in Fig. 1.

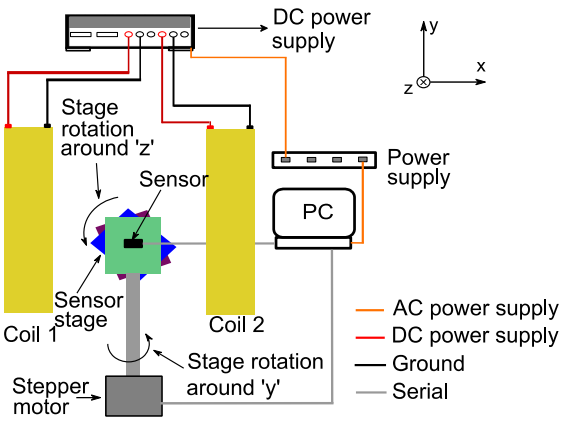

Fig. 1. Helmholtz coil setup with a rotational stage providing 2 DOF for sensor orientation.

Results

We measure the magnetic field components B_x, B_y, and B_z at six sensor orientations under a constant field. Fig. 2 shows the measured data and the reconstructed field vectors after SfM-based calibration.

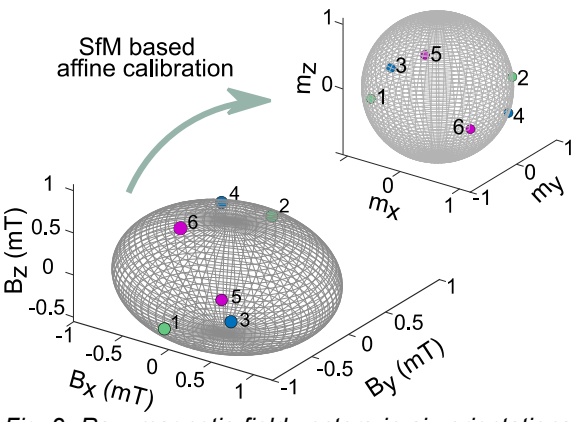

Fig. 2. Raw magnetic field vectors in six orientations and after SfM-based affine calibration. For visualization, the non-sphericity of the ellipsoid is exaggerated by a factor of 25.

The measurements form a distorted ellipsoid due to gain mismatch and axis misalignment. The SfM calibration reconstructs vectors that lie close to a unit sphere, indicating effective compensation of these distortions.

To validate the model, the sensor is rotated over 360° in three different planes, yielding 72 measurements per plane. Fig. 3 shows the angular deviation as a function of the reference angle for raw and SfM-calibrated data.

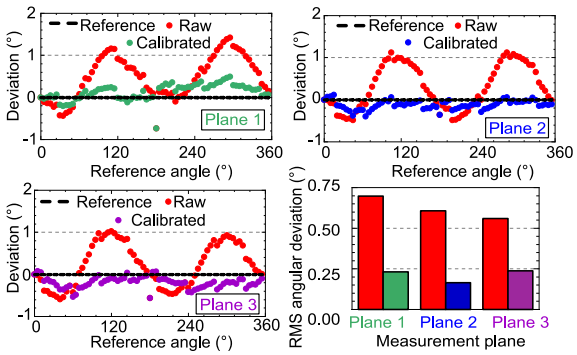

Fig. 3. Angular deviation vs. reference angle (raw vs. SfM-calibrated) for three planes (72 points each); bottom-right: RMS angular deviation before and after calibration.

SfM reconstructs the magnetic field vectors on a unit sphere; the remaining arbitrary rotation does not affect the determination of relative angles, as relative angles are rotation invariant [3]. The effective sensing directions are obtained directly using $\boldsymbol{C}$ and the angles between them are computed as:

$$\alpha_{ij} = \cos^{-1} \frac{m_i . m_j}{|m_i| . |m_j|} . \quad (4)$$

Tab. 1 summarizes the resulting inter-axis angles. All angles are close to 90°, with deviations below 0.6°. Further, the uncertainty estimated from repeated measurements is around 0.1°, indicating that the observed non-orthogonality is small but statistically significant.

Tab. 1: Angles between pairs of sensor axes, showing minor deviations from 90°

Axis pair	x-y	x-z	y-z
Angle α (°)	89.85 ± 0.09	89.48 ± 0.10	90.49 ± 0.06

References

[1] C. Tomasi, T. Kanade, Shape and motion from image streams under orthography: a factorization method, International Journal of Computer Vision 9, 137-154 (1992); doi: 10.1007/BF00129684

[2] K. Kim, Y. Sun, R.M. Voyles, B.J. Nelson, Calibration of multi-axis MEMS force sensors using the shape-from-motion method, IEEE Sensors Journal 7, 344-351 (2007); doi: 10.1109/JSEN.2006.890141

[3] Q. Li, J. G. Griffiths, Least squares ellipsoid specific fitting, Geometric Modeling and Processing Proceedings (IEEE), 335-340 (2004); doi: 10.1109/GMAP.2004.1290055

DOI 10.5162/eurosensors2026/7.3.3

Geometrical Optimization of Planar Hall Sensors Dominated by $1/f$ Noise for Maximal Signal-to-Noise Ratio

Anja Fleck[1], Laurent Osberger[2], Martin Cornils[2], Maria Cristina Vecchi[2], Oliver Paul[1]
[1] Dept. of Microsystems Eng. (IMTEK), University of Freiburg, Freiburg, Germany,
[2] TDK-Micronas GmbH, Freiburg, Germany
anja.fleck@imtek.uni-freiburg.de

Summary:
This work introduces a voltage-related geometry factor for arbitrarily shaped planar Hall devices dominated by $1/f$ noise and derives a corresponding signal-to-noise (SNR) geometry factor. The geometry factors are simulated for disk-, square-, and cross-shaped Hall sensors. The results are supported by measurements on cross-shaped GaAs Hall sensors and confirm a trade-off between Hall signal and noise performance. Optimal cross geometries provide the highest SNR geometry factor, namely 0.59, while optimal disk and square geometries reach only 0.56 and 0.52, respectively.

Keywords: Hall sensor, signal-to-noise ratio (SNR), $1/f$ noise, optimization, geometry factor

Introduction

The signal-to-noise ratio (SNR) is a key figure of merit for Hall sensors. It is defined as the ratio of Hall signal to noise signal over a frequency f range of interest. Here, we introduce a geometry factor for $1/f$-dominated noise compatible with Hooge's relation [1] and derive a SNR geometry factor for arbitrarily shaped planar four-terminal devices. This framework is used to identify the SNR-optimal geometry of disk-, square-, and cross-shaped Hall sensors, cf. Fig. 1.

Theory

For planar Hall sensors of in-plane area *A*, homogenous planar charge carrier density n_{2D} and mobility in the conductive sensor region Ω, and operated in measurement modes *a* and *b*, cf. Fig. 2, at constant current I, the geometry dependence of the Hall voltage in mode *a* is given by the voltage-related Hall geometry factor [2]

$$G_{H,V} = \frac{\int_\Omega (\boldsymbol{i}_{a0} \times \boldsymbol{i}_{b0})_z \, dA}{\int_\Omega \boldsymbol{i}_{a0} \cdot \boldsymbol{i}_{a0} \, dA}, \qquad (1)$$

where $\boldsymbol{i}_{a0}$ and $\boldsymbol{i}_{b0}$ denote the normalized in-plane line current densities in the two measurement modes at zero magnetic field, and $(\boldsymbol{i}_{a0} \times \boldsymbol{i}_{b0})_z$ is the z component of their cross product.

Analogously, a voltage-related geometry factor for $1/f$-dominated noise can be derived as

$$G_{1/f,V} = \frac{A \int_\Omega (\boldsymbol{i}_{a0} \cdot \boldsymbol{i}_{b0})^2 \, dA}{\left(\int_\Omega \boldsymbol{i}_{a0} \cdot \boldsymbol{i}_{a0} \, dA\right)^2}. \qquad (2)$$

A geometry dependence of $1/f$-dominated output signal noise in terms of an effective area was

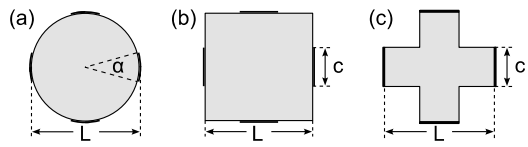

Fig. 1. Hall sensor geometries of characteristic dimension L: (a) Disk with contact opening angle α, (b) square, and (c) cross geometry with aspect ratio c/L.

first discussed in [3]. Here, this dependence is cast into the dimensionless voltage-related factor $G_{1/f,V}$. This formulation allows a straightforward generalization of the empirical Hooge relation [1]. In fact, the normalized voltage power spectral density (PSD) becomes

$$\frac{S_V}{V^2} = \frac{\alpha_{1/f}}{Nf} G_{1/f,V} = \frac{\alpha_{1/f}}{n_{2D} f} \frac{1}{L^2} \frac{1}{k_A^2} G_{1/f,V}, \qquad (3)$$

where $\alpha_{1/f}$ is the Hooge factor, N the number of free charge carriers, and $k_A = \sqrt{A}/L$ a shape-dependent area-utilization factor. The standard Hooge relation is recovered for $G_{1/f,V} = 1$, holding for two-contact devices with homogeneous 1D current densities. Increasing the lateral sensor dimensions reduces $1/f$ noise at the expense of a larger footprint. The analysis is therefore restricted to a fixed characteristic dimension L of the structures, cf. Fig. 1. The resulting

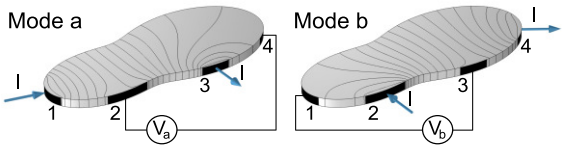

Fig. 2. Measurement configurations for modes a and b of an arbitrarily shaped planar four-terminal device operated with constant drive current I, yielding the output voltages V_a and V_b, respectively.

differences in the active sensor area are accounted for by k_A, listed in Tab. 1. Under this constraint, relying on the third expression in (3), we define the SNR geometry factor as

$$G_{SNR} = \frac{G_{H,V}}{\sqrt{G_{1/f,V}}} k_A = \frac{\int_\Omega (\boldsymbol{i}_{a0} \times \boldsymbol{i}_{b0})_z \, dA}{\sqrt{A \int_\Omega (\boldsymbol{i}_{a0} \cdot \boldsymbol{i}_{b0})^2 \, dA}} k_A \,. \quad (4)$$

It enables the direct comparison between different sensor shapes of identical L.

Numerical Simulation and Experiment

Finite-element simulations of $G_{H,V}$ and $G_{1/f,V}$ were performed using COMSOL, yielding G_{SNR}. The simulation results were supported by measurements on cross-shaped samples of GaAs Hall sensor test structures, featuring either varied aspect ratios c/L or uniform scaling at constant $c/L \approx 0.58$, cf. Fig. 1 (c), in a temperature-controlled setup at $T = 25$ °C. $G_{H,V}$ was obtained from van-der-Pauw measurements [4], and $G_{1/f,V}$ from PSD measurements at $V = 1$ V for all specimens, evaluated at $f = 1$ kHz after subtraction of the white-noise spectral background. The active sensor area A was estimated from the device layout. The Hooge factor was taken as $\alpha_{1/f} = 3 \times 10^{-4}$, based on its reported mobility dependence [1].

Results

As shown in Fig. 3, the investigated sensor geometries reveal a clear trade-off between signal and noise performance. With increasing design parameter ξ, defined as $\xi = \alpha$ for disks and $\xi = c/L$ for square and cross sensors, $G_{1/f,V}$ increases monotonically, whereas $G_{H,V}$ reaches a maximum at intermediate ξ. In general, the SNR-optimal sensor geometry does not coincide with the optimal Hall signal geometry. For all three shapes, $G_{1/f,V}$ increases strongly at large ξ values, since the current flow in both modes becomes more aligned, particularly between adjacent contacts, cf. Fig. 4. The $G_{H,V}$ values extracted from measurements and shown in Fig. 3 (c) are in very good agreement with the simulations. The extracted $G_{1/f,V}$ values reproduce the simulated trend well. However, their absolute value depends on $\alpha_{1/f}$ taken from literature [1] and may therefore be subject to systematic scaling. As expected, measurements on uniformly scaled crosses confirm that the geometry factors are invariant under scaling. The optimal SNR values extracted from the simulation data are listed in Tab. 1. Crosses show the best SNR performance with coinciding Hall-signal- and SNR-optimal geometries. Disks outperform squares. For both, the SNR optimum is found at small ξ, differing from the Hall-signal-optimal geometry.

Tab. 1: Area-utilization factor and optimal SNR values.

	Disk	Square	Cross
k_A (-)	$\sqrt{\pi}/2$	1	$\sqrt{2c/L - (c/L)^2}$
Max. G_{SNR}	0.56	0.52	0.59
ξ_{opt}	2.87°	0.07	0.58

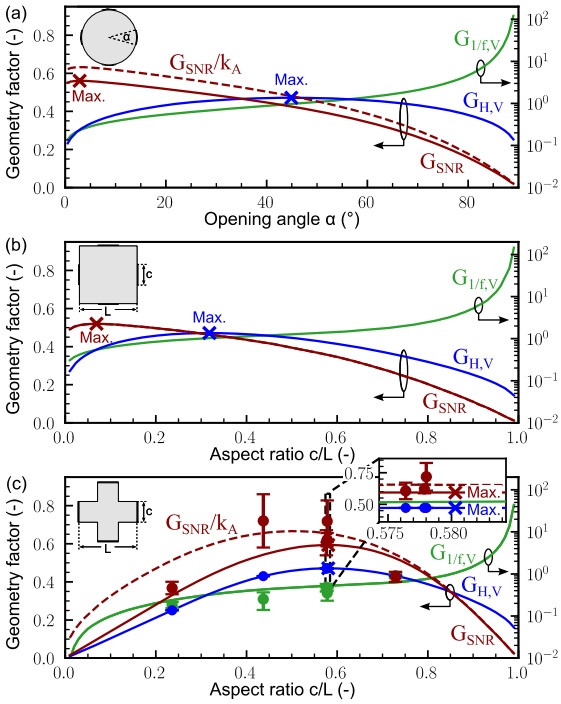

Fig. 3. Simulated geometry factors for (a) disk, (b) square, and (c) cross geometries. The blue and red ×-symbols mark the maximum $G_{H,V}$ and G_{SNR}, respectively. For the cross geometries, the simulations are supported by measurements.

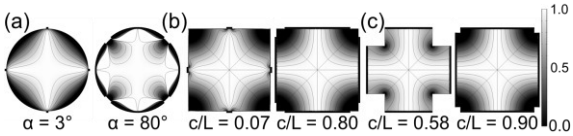

Fig. 4. Simulated spatial distributions of $k_A\,(\boldsymbol{i}_{a0} \times \boldsymbol{i}_{b0})_z / \sqrt{A(\boldsymbol{i}_{a0} \cdot \boldsymbol{i}_{b0})^2}$ for pairs of different (a) disk, (b) square, and (c) cross geometries.

References

[1] F.N. Hooge, 1/f Noise Sources, *IEEE Transactions on Electron Devices* 41, 1926-1935 (1994); doi: 10.1109/16.333808

[2] O. Paul, M. Cornils, Explicit connection between sample geometry and Hall response, *Applied Physics Letters* 95, 232112 (2009); doi: 10.1063/1.3272267

[3] L.K.J. Vandamme, W.M.G. van Bokhoven, Conductance noise investigations with four arbitrarily shaped and placed electrodes, *Applied Physics* 14, 205-215 (1977); doi: 10.1007/BF00883091

[4] M. Cornils, O. Paul, Sheet resistance determination of electrically symmetric planar four-terminal devices with extended contacts, *Journal of Applied Physics* 104, 024503 (2008); doi: 10.1063/1.2956333

DOI 10.5162/eurosensors2026/7.3.4

Study of Width-over-length Aspect Ratio on Mode Ordering for 2D Nanomechanical Resonant Sensors

Weixin Zhou, Cosmin Ioan Roman, Christofer Hierold and Pengcheng Zhang**
Micro and Nanosystems, Department of Mechanical and Process Engineering,
ETH Zürich, 8092 Zürich, Switzerland
**Corresponding Authors' e-mail addresses: cosmin.roman@micro.mavt.ethz.ch, zpengchen@ethz.ch*

Summary: Two-dimensional (2D) nanoelectromechanical system (NEMS) resonators, which offer high sensitivity, show strong potential for sensing applications. Among them, the fundamental mode is typically used as the operating mode for detecting external physical quantities such as pressure, mass, and force. Operating in this mode maximizes the sensor's displacement amplitude, which translates to a stronger output signal and enhanced overall sensitivity. However, a comprehensive and systematic understanding of how to identify the working mode is still lacking. In this work, we analyze how the width-to-length aspect ratio affects the ordering of resonant modes in doubly clamped 2D MoS2 NEMS resonators. Through finite element method (FEM) simulation, the longitudinal fundamental mode remains largely insensitive to device width, whereas the eigenfrequencies of transverse modes vary strongly with aspect ratio. This leads to clarify mode-crossing events and a reordering of the overall mode sequence.

Keywords: Two-Dimensional materials, Nanomechanical resonant sensors, Eigenmodes, Width-over-length aspect ratio, FEM simulation

Background, Motivation and Objective

NEMS resonators are ideal ultrasensitive sensors due to their extremely small size, high frequency and low power consumption [1]. Physical perturbations such as mass adsorption (Fig. 1 (a)) or temperature changes, measurably shift the fundamental resonance peak (Fig. 1 (b) and (c)). However, reliable characterization requires a clear distinction of the working mode shapes. This work provides a comprehensive study how to differentiate these modes by FEM simulation as width-over-length ratio varies.

Simulation Setup and Theoretical Model

In our study, we model a doubly clamped MoS_2 membrane, a prevalent material in 2D NEMS (Fig. 1 (a)). Key properties include length (l), width (w), width-over-length aspect ratio $(a = w/l)$, thickness (t), i^{th} resonance frequency (f_i). For highly narrow devices $(a \ll 1)$, the membrane behaves like an ideal one-dimensional beam with predictable frequencies [2][3]:

$$f_i = \frac{\lambda_i^2 \cdot t}{2\pi \cdot l^2 \cdot \sqrt{12}} \cdot \sqrt{\frac{E}{\rho \cdot (1-\nu)}} \qquad (1)$$

where E is Young's modulus, ρ is density, ν is Poisson's ratio and λ_i are solutions from the characteristic equation of doubly clamped boundary condition $cos(\lambda_i)cosh(\lambda_i) = 1$. This lead to values of $\lambda_1 = 4.73, \lambda_2 = 7.85$, etc.

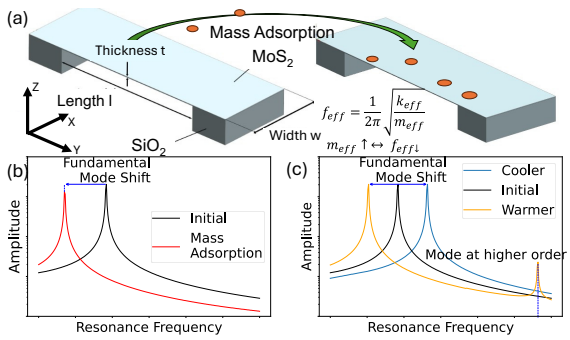

Fig. 1. (a) Schematic of device structure and mass adsorption. (b) Illustration of the frequency shift due to mass adsorption (c) Impact to temperature change

Tab. 1: Theoretical frequency of example device

Properties [4]	Result	
$l = 2\mu m$	Mode	Eigenfrequency
$t = 10nm$	Fundamental	19.40 MHz
$E = 270GPa$		
$\nu = 0.23$	Secondary	53.49 MHz
$\rho = 5000kg/m^3$		

Through calculation based on Tab. 1, the 1st and 2nd modes of an example device are 19.40 MHz and 53.49 MHz, respectively. However, as w increases, the 1D approximation might fail to cover all. To identify the fundamental mode and classify the 2D oscillation of the membrane, we introduce the notation (m, n), where m describe the mode order along the free direction and n the

DOI 10.5162/eurosensors2026/7.3.4

clamped direction. The spatial mode shape (x, y) (Fig. 1(a)) and frequency are [5]:

$$(x, y) = k \cdot cos\left(\frac{m \cdot x \cdot \pi}{w}\right) \cdot sin\left(\frac{n \cdot y \cdot \pi}{l}\right) \quad (2)$$

$$f_{mn} \propto \sqrt{\left(\frac{m}{w}\right)^2 + \left(\frac{n}{l}\right)^2} = \sqrt{\left(\frac{m}{a \cdot l}\right)^2 + \left(\frac{n}{l}\right)^2} \quad (3)$$

where k acts as a scaling constant.

Results and Discussion

For a purely clamped mode $(0, n)$ where no transversal bending occurs (Fig. 2), the approximation in Tab. 1 remains highly valid, respectively, regardless of the increasing width.

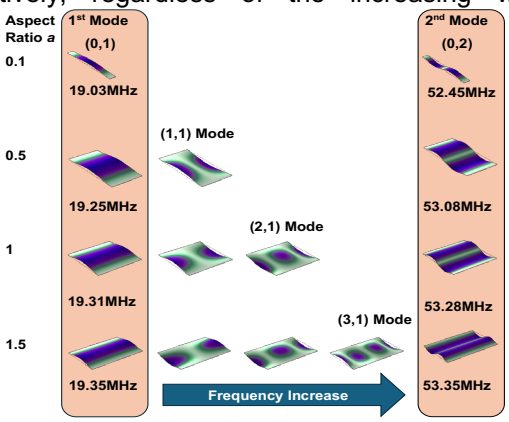

Fig. 2. Demonstration of 2D mode order varying with aspect ratio.

Complex transversal modes m begin to emerge when the aspect ratio a exceeds $a > 0.1$. In the intermediate aspect ratio $0.3 < a \leq 1$, the frequencies of transverse modes spread widely across 100MHz (Fig. 3). As an example, it can be observed that mode$(1,1)$ cross mode $(0,2)$ at $a \approx 0.25$ (Fig. 3 (a)). Because the frequencies of higher order (m, n) modes asymptotically converge toward the frequencies of the fundamental $(0, n)$ modes (Fig. 3(b)), it remains reasonable to use the $(0, n)$ approximation for device with an exceptionally high aspect ratio $(a \gg 10)$.

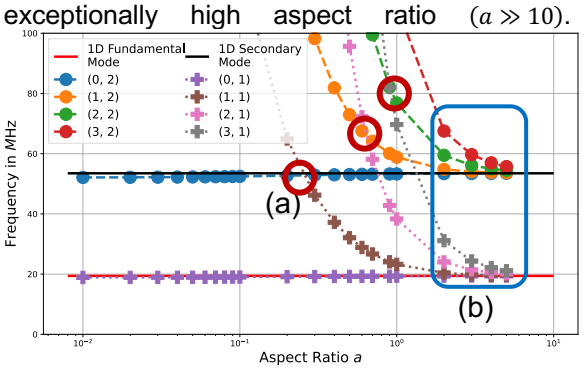

Fig. 3. Modeled frequencies of various (m,n) modes against the aspect ratio. (a) Mode-crossing. (b) Convergence

To experimentally validate these findings, we use an RF down-mixing detection scheme to measure the resonance of doubly clamped 2D MoS_2 resonators [6], detecting the same frequency shift shown by the simulations (Fig. 4).

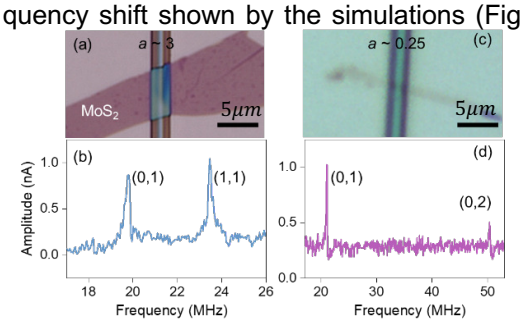

Fig. 4. (a)(b) Measured modes of a device with a~3. (c)(d) Measured modes of a device with a~0.25. Reprinted in part with permission from ref [7]. Copyright 2026 IEEE.

Conclusion

In summary, this study shows the mode-crossing induced by the width-over-length aspect ratio in 2D MoS_2 resonant sensors. Highly accurate sensing can be achieved at a strongly asymmetric width-over-length geometry, either $a \ll 1$ to isolate the frequencies, or $a \gg 10$ to merge the non-fundamental modes to fundamental ones.

Acknowledgments

We thank Ines Kraiem for fabricating the receiving substrate.

References

[1] B. Xu, P. Zhang, et al., Nanomechanical Resonators: Toward Atomic Scale, *ACS Nano* 16(10), 15545-15585 (2022)

[2] O. Brand, H. Baltes, Micromachined Resonant Sensors – an Overview, *Sensors Update* 4(1), 3-51 (1998)

[3] X. L. Feng, R. He, P. Yang, M. L. Roukes, Very High Frequency Silicon Nanowire Electromechanical Resonators, *Nano Letters* 7(7), 1953-1959 (2007)

[4] J. Joswig, T. Lorenz, et al., Optics, Mechanics, and Energetics of Two-Dimensional MoS2 Nanostructures from a Theoretical Perspective, *Acc. Chem. Res* 48(1), 48-55 (2015)

[5] J. García-Pérez, D. Granados, et al., Electromechanical Mode Imaging of MoS_2 Drum Resonators, *Mater. Res. Express* 12(7), 1075002 (2025)

[6] P. Zhang, M. Vollmann, I. Kraiem, M. Haluska, C. Gentili, C. Roman, C. Hierold, Strain Dilution in Thermoelastic Damping in Two-Dimensional MoS_2 Resonators, *Nano Letters* 26(9), 3141-3148 (2026)

[7] T. Platten, C. Roman, C. Hierold, P. Zhang, Accurate Model of RF Frequency Tuning in 2D NEMS using a Fringing-Sensitive Capacitance, *2026 IEEE 39th International Conference on Micro Electro Mechanical Systems (MEMS)*, 1414-1417 (2026)

DOI 10.5162/eurosensors2026/8.1.1

Charge and Capacitance Sensitive Field-Effect Device for Room-Temperature Hydrogen Sensing

Jamila Boudaden[1], Nnaemeka Michael Mbachu[1], Karl Neumeier[1], Ignaz Eisele[1,2]
[1] Fraunhofer Institute for Electronic Microsystems and Solid State Technologies EMFT, GERMANY
[2] Center Integrated Sensor Systems (SENS), Universität der Bundeswehr München, GERMANY
Jamila.boudaden@emft.fraunhofer.de

Summary:
We present the sensing properties of a CMOS-compatible Charge- and Capacitance-Sensitive Field-Effect Transistor (CCSFET) operated in gaseous environments. The device comprises two sensing areas, each integrating a chemically sensitive capacitor and a potential probe that together form the floating gate of a MOS transistor. In addition, the potential probe is connected to an operational amplifier (OpAmp), enabling robust electrical readout via both the MOSFET and the OpAmp. The CCSFET is flip-chip packaged onto a flexible substrate, which improves mechanical robustness and ensures reliable signal acquisition. As a demonstration, we investigate room-temperature hydrogen sensing using a thin Pd layer deposited on two different sensing layers, Si_3N_4 and Ta_2O_5 of CCSFT.

Keywords: CCSFET, MOSFET, OpAmp, H_2 sensing, CMOS technology, Pd//Si_3N_4, Pd//Ta_2O_5

Background, Motivation and Objective

In this work, we introduce the CCSFET, a fully CMOS-compatible device concept for sensing application that overcomes the limitations of previously proposed miniaturized systems as it is designed to operate in both liquid and gaseous environments. The CCSFET measures changes in both charge and capacitance of chemically sensitive layers [1–3]. Our objective is to demonstrate, on a single-chip platform, hydrogen detection in air at atmospheric pressure and room temperature using both sensing systems, Pd//Ta_2O_5 and Pd//Si_3N_4, integrated on the same CCSFET chip.

Description of CCSFET

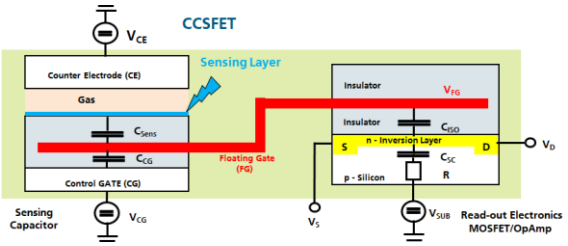

Fig. 1. Schematic of CCSFET device with sensing area, counter electrode, floating gate), control gate and MOSFET and OpAmp read-out.

The CCSFET is fabricated in CMOS technology on a 200 mm silicon substrate. The chip has a footprint of 4.5 × 4.5 mm² and incorporates two circular sensing areas with diameters of 820 µm and 520 µm (Fig. 1). The sensing areas, consisting of Si_3N_4 and Ta_2O_5, that are capacitively coupled to a MOSFET and OpAmp readout via a floating gate. Si_3N_4 was deposited by PECVD. 50nm Ta_2O_5 was sputtered on Si_3N_4 grown by LPCVD. The gold counter electrode acts as Faraday cup for gas. CCSFET configuration has the advantage of a clear separation between the sensing areas and the electronic readout.

To improve robustness and simplify handling, the CCSFET is flip-chip bonded onto a flexible foil, as described in [4]. This hybrid packaging approach yields a compact and mechanically compliant sensor module. Only the sensing areas are exposed to the gas to be sensed, while the contact pads and interconnects remain protected. This design reduces parasitic effects and enhances long-term stability in real environments.

For sensing H_2 at room temperature, the counter electrode is connected to a grounded Faraday cup, which provides shielding and prevents chemical reactions at the cup surface from influencing the sensor response. This is particularly important because the gas capacitance is very small, and parasitic effects must be minimized. A 5 nm Pd layer sputtered on Si_3N_4 and Ta_2O_5 enables detection of H_2 between 500 ppm and 1.6% in synthetic air at atmospheric pressure. The sensors are placed inside a tight PEEK gas chamber. The counter electrode is grounded,

DOI 10.5162/eurosensors2026/8.1.1

and the control gate is used to define the operating point of the CCSFET and to extract the MOSFET input characteristics (Fig. 2).

Results

In Fig. 2, we show the MOSFET input characteristics as a function of control gate voltage for different hydrogen concentrations for both sensing systems, Pd//Ta_2O_5 and Pd//Si_3N_4. In Fig. 3, we plot the change in control gate voltage, extracted at $I_{source\text{-}drain}$ = 300µA, as a function of H_2 concentration.

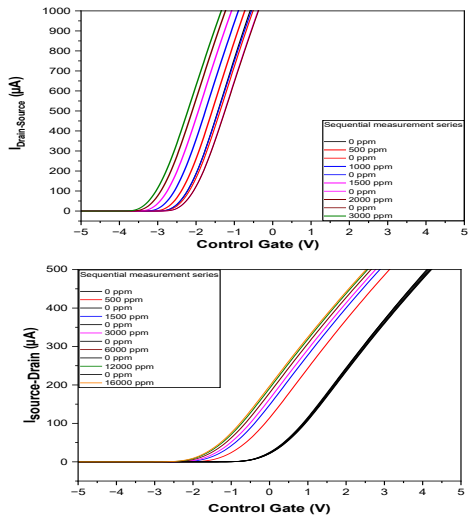

Fig. 2. CCSFET input characteristics: Source-drain current (I_{SD}) vs control gate voltage for sensing system Pd//Ta_2O_5 (Top) and Pd//Si_3N_4 *(Bottom).*

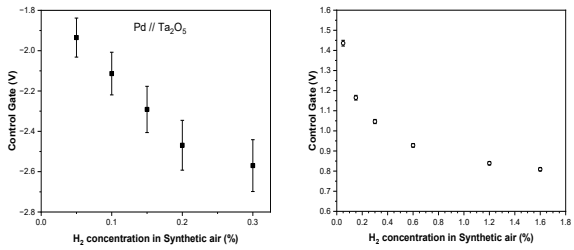

Fig. 3. Control voltage versus H_2 concentration at $I_{source\text{-}drain}$ = 300 µA for sensing system Pd//Ta_2O_5 (Left) and *Pd//Si_3N_4* (Right).

For both sensing systems, a shift of the MOSFET threshold voltage V_{th} to lower values is observed with increasing H_2 concentration, demonstrating a clear response to the presence of hydrogen. V_{th} is correlated with the chemical interaction of H_2 with the Pd//Ta_2O_5 and Pd//Si_3N_4 sensing systems, which induces charges at the sensing areas and leads to a potential change at the floating gate. This potential shift is then converted into a measurable electrical response by the MOSFET readout.

Only the Pd//Si_3N_4 system shows reversible and reproducible sensing behavior toward H_2 at room temperature (Fig. 2, bottom). The detection limit reaches 1.2%. In contrast, Pd//Ta_2O_5 system doesn't recover after H_2 exposure: the sensing error exceeds 5%, restricting reliable measurements to about 0.3% H_2.

Our results contrast with recently published work [5], which reports reversible H_2 sensing for a Pd//Ta_2O_5 system. We attribute the irreversibility observed in Fig. 2 top, to the fact that both Pd and Ta_2O_5 are permeable to hydrogen, whereas Si_3N_4 remains essentially impermeable to H_2. In the Pd//Si_3N_4 system, H_2 absorbed in Pd can rapidly desorb once the H_2 atmosphere is removed. In contrast, H_2 captured in Ta_2O_5 likely requires elevated temperatures (around 150 °C) for efficient release, as suggested in [5]. To the best of our knowledge, no prior experimental or theoretical studies report H_2 detection using Pd//Ta_2O_5 and Pd//Si_3N_4 sensing systems at room temperature.

Conclusion

The CCSFET introduces a new class of CMOS-compatible field-effect devices for sensing charge formation in the sensing layer induced by the reaction of H_2 with Pd. The H_2 sensitivity of Pd depends strongly on the composition of the underlying layer on which Pd is sputtered. Among the investigated systems, Pd//Si_3N_4 emerges as a promising sensing stack for room-temperature H_2 detection.

References

[1] I. Eisele, J. Boudaden and K. Neumeier, "Charge and Capacitance Sensitive Field Effect Transistor (CCSFET) for Chemical Sensing," in IEEE Sensors Journal, vol. 25, no. 20, pp. 37622-37629, 15 Oct.15, 2025, doi: 10.1109/JSEN.2025.3596216

[2] I. Eisele, "Fluid Sensor and Method for Examining a Fluid," US patent 9,716,140 B2, 2017.

[3] I. Eisele, J. Boudaden, K. Neumeier, "Sensor Device and Corresponding Methods," Patent application EP24191571.9, 2024.

[4] M. Steinmaßl, J. Boudaden, W. Hell, C. Kutter, "Simple and powerful encapsulation through hybrid packaging for electrochemical transducers," Smart Systems Integration (SSI) Conference, 2021.

[5] J. Tong, Y. Lv, Z. Zhuang, J. Yang, B. Feng, J. Zhao, S. Huang, D. Zhang, Y. Zhu, G. Cuniberti, L. Wang, Wafer-Scale Pd-decorated Ta2O5/SnO2 Heterojunction Sensor for Ultrafast and Sensitive Hydrogen Detection, Sensors & Actuators: B. Chemical 451 (2026) 139432.

DOI 10.5162/eurosensors2026/8.1.2

Triphenylene and Triptycene-Based MOFs as Chemiresistive Platforms for CO_2 and CH_4 Detection

Yuzelfy Mendoza-Gamero[1,2,3], Sergi Gonzalez-Martinez[1,2,3], Albert Romano-Rodriguez[1,2], Daniel Sainz-Garcia[2,3]
[1] Electronic and Biomedical Engineering Department, Universitat de Barcelona, Barcelona, Spain
[2] Institute of Nanoscience and Nanotechnology (IN2UB), Universitat de Barcelona, Barcelona, Spain
[3] Inorganic and Organic Chemistry Department, Universitat de Barcelona, Barcelona, Spain
Corresponding author: yuzelfymendoza@ub.edu

Summary:

Triphenylene-based metal-organic frameworks (MOFs) (Cu-HTAT and Ni-HTAT) show reproducible resistance responses to CO_2 and CH_4 under variable humidity. In parallel, triptycene-derived MOFs (HHTT, M = Cu, Ni, Zn, Co) are introduced as a complementary three-dimensional platform. The combined approach enables correlating ligand structure with gas accessibility and electrical response. Our results demonstrate measurable gas-induced modulation of conductivity, highlighting the potential of these MOFs for environmental sensing.

Keywords: metal-organic frameworks, triphenylene, triptycene, chemiresistive sensor, carbon dioxide, methane

Background, Motivation and Objective

Conductive metal–organic frameworks (MOFs) based on π-conjugated ligands (planar) have emerged as promising candidates for gas sensing due to their tunable porosity, accessible active sites, and intrinsic charge transport properties. Triphenylene-based MOFs have demonstrated chemiresistive responses toward polar analytes, although the detection of weakly interacting gases, such as CO_2 and CH_4 remains challenging, especially in the presence of water [1,2,3].

These conductive MOFs' sensors rely on planar aromatic linkers, however, the impact of ligand dimensionality on gas diffusion and adsorption remains underexplored [1].

In this work, we compare the performance of triphenylene-based MOFs (Cu- and Ni-HTAT) with a series of triptycene-derived frameworks (M-HHTT; M = Cu, Ni, Zn, Co). By introducing a rigid 3D scaffold with intrinsic free volume, we investigate how modifying the ligand dimensionality influences gas diffusion and adsorption. This comparative study will help clarifying the role of framework topology in modulating the electrical response to non-polar analytes in realistic environments.

Synthesis and fabrication Methods

Two complementary ligand systems were employed to construct conductive MOF platforms with distinct structural dimensionality. The triphenylene-based (HTAT) ligand was synthesized from triphenylene via bromination, followed by Pd-catalyzed Buchwald–Hartwig amination with tert-butylamine. In parallel, the triptycene-derived hexahydroxy (HHTT) ligand was prepared through a two-step procedure involving Cu(I)-assisted methoxylation of a brominated triptycene precursor, followed by demethylation using boron tribromide to yield the corresponding hexahydroxy ligand [4,5,6]. Both ligands were obtained and characterized by NMR, ATR-FTIR, and ESI-MS.

MOFs based on HTAT (M-HTAT, M: Cu,Ni) and HHTT (M-HHTT, M: Cu, Ni, Zn, Co) were obtained by solvothermal coordination using the corresponding metal salts under mild conditions. The resulting powders were dispersed in H_2O/EtOH mixtures and deposited onto platinum or gold interdigitated electrodes by drop casting. These chips were next bonded on TO-8 packages for electrical characterization. Sensing experiments were carried out in a self-designed miniaturized chamber equipped with mass-flow controllers, enabling precise delivery of CO_2 and CH_4 pulses in synthetic air. Humidity was adjusted between 0 and 40% RH using a bubbler system. Electrical measurements were performed using a source-measure unit, recording resistance changes in real time under alternating gas exposure and purge cycles.

Results and discussion

PXRD confirms the formation of crystalline MOFs for both HTAT- and HHTT-based systems. Under CO_2 and CH_4 exposure, HTAT-based MOFs show a chemiresistive response that depends on relative humidity. As humidity increases, the baseline resistance decreases, in line with transport dominated by planar π-conjugated pathways. HHTT-based MOFs display a

similar trend, although some differences in signal modulation are observed, suggesting changes in gas accessibility and adsorption behavior associated to their three-dimensional structure. In both systems, the response is more pronounced at intermediate humidity levels, pointing to a combined effect of water and gas adsorption. Overall, these observations indicate that ligand topology plays a role in the sensing mechanism, with HTAT-based frameworks mainly governed by surface interactions, while HHTT-based systems introduce additional diffusion pathways that influence gas adsorption and electrical response.

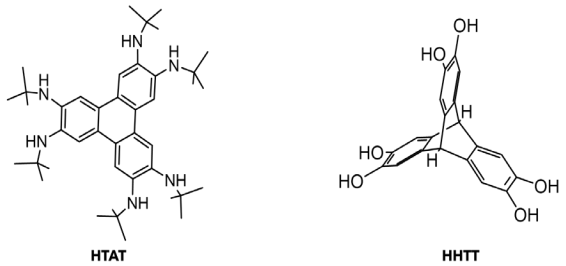

Figure 1. Chemical structures of the triphenylene-based (HTAT) and triptycene-based (HHTT) ligands

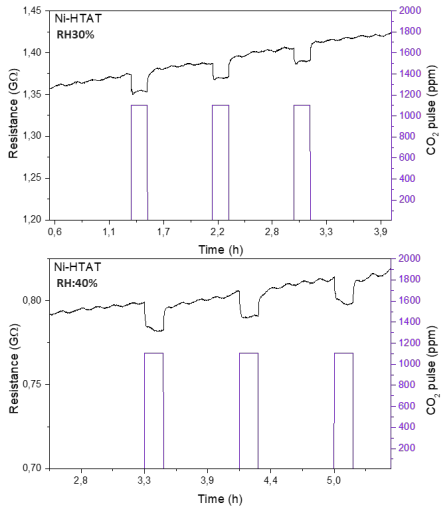

Figure 2 Chemiresistive response of Ni-HTAT to CO_2 pulses at 30% and 40% relative humidity.

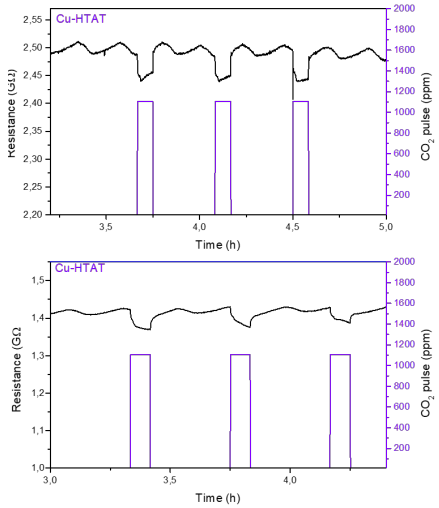

Figure 3 Chemiresistive response of Cu-HTAT to CO_2 pulses at 30% and 40% relative humidity.

In this work, we will describe the ligand synthesis, the MOF formation and characterization, and discuss their chemiresistive response upon greenhouse gas exposure, with particular emphasis on the role of humidity.

References

[1] M. G. Campbell, S. F. Liu, T. M. Swager, M. Dincă, Chemiresistive Sensor Arrays from Conductive 2D Metal-Organic Frameworks, *J. Am. Chem. Soc. 137*, 13780-13783 (2015); doi: 10.1021/jacs.5b09600

[2] I. Fort-Grandas, M. Martínez-Belmonte, J. Benet-Buchholz, R. M. Gomila, A. Frontera, A. Romano-Rodríguez, A. Vidal-Ferran, Layered Nickel-HHTP Networks for Efficient Chemiresistive Sensing of Greenhouse Gases, *ACS Small* (2026, under review

[3] T. Chen, J.-H. Dou, L. Yang, C. Sun, N. J. Libretto, G. Skorupskii, J. T. Miller, M. Dincă, Continuous Electrical Conductivity Variation in M3(hexaiminotriphenylene)2 (M = Co, Ni, Cu) MOF Alloys, *J. Am. Chem. Soc. 142*, 12367-12373 (2020); doi: 10.1021/jacs.0c04458

[4] S. Gonell, M. Poyatos, E. Peris, Triphenylene-Based Trinuclear Mercury N-Heterocyclic Carbene Complexes, *Angew. Chem. Int. Ed. 52*, 7009-7013 (2013); doi: 10.1002/anie.201302686

[5] Q. Chen, A. Afugu, Y. Shuku, Z.-F. Liu, K. Awaga, Z. Zhang, Triptycene-Based 2.5-Dimensional Metal–Organic Frameworks: Atomically Accurate Structures and Anisotropic Physical Properties from Hydrogen-Bonding Bridged Protonated Building Units, *J. Am. Chem. Soc 147*, 28215–28225 (2025); doi: 10.1021/jacs.5c08703

[6] Y. Lin, C. Kong, L. Chen, Amine-functionalized metal-organic frameworks: structure, synthesis and applications, *RSC Adv. 6*, 32598-32614 (2016); doi: 10.1039/C6RA01536K

DOI 10.5162/eurosensors2026/8.1.3

Ultra-Low Crosstalk Thermally-Compensated Monolithic AlGaN/GaN MISHEMT Sensor Array for Robust Gas Detection

Karim Bouzid[1], Sri Saran Venkatachalam[1], Tarik Moudakir[1], Abhishek Juyal[1], Safa Othmani[1], Mickaël Petit[1], Simon Gautier[1]
[1] Institut Lafayette, 2 rue Marconi 57070 Metz, France
karim.bouzid@institutlafayette.eu

Summary:
This work presents the impact of an optimized micro-fabrication process on monolithically integrated AlGaN/GaN MIS-HEMT (High Electron Mobility Transistor) sensors. We demonstrate exceptional electrical isolation with inter-device crosstalk, gate and off-state leakage currents in the pA range. This enables a multi-pixel differential measurement scheme to enhance signal stability and reject thermal common mode noise. Compact integration was achieved in an industry grade LCC16 package. Platform performance is validated through temperature compensated hydrogen detection with a thermal Common Mode Rejection Ratio (CMRR) of -60 decibels and operational stability exceeding 180 hours of continuous measurement, repeated over the span of 8 months.

Keywords:
AlGaN/GaN HEMT, Hydrogen Sensor, Sensor Array, LCC16 Packaging, Differential Sensing.

Background, Motivation and Objective

Gas safety necessitates reliable, high-sensitivity sensors, where AlGaN/GaN HEMTs excel due to their robustness in industrial environments. [1,2] However, scaling from discrete devices to consistent monolithically integrated arrays is typically hindered by inter-device crosstalk and parasitic leakage. [3] This work presents an optimized monolithic MIS-HEMT-based gas sensing platform, achieving leakage currents in the picoampere range through optimized mesa isolation and gate dielectrics. This technical foundation enables a distributed differential sensing scheme, validated via high-stability hydrogen detection, establishing a robust manufacturing framework for industrial-grade multi-pixel chemical sensing modules.

Description of the New Method or System

Our gas sensor platform consists of a monolithically integrated HEMT array on a 3.15 x 3.15 mm² die (see Fig. 1). The die is packaged in a standardized LCC16 package, allowing for plug-and-play integration into LCC16 sockets. Exceptional crosstalk current leakage performance and extremely low gate-source leakage enabled the simultaneous use of multiple devices of the array. A differential sense-reference topology is thus employed to rule out the contribution of environment fluctuation and low-frequency noise and provide a stable output signal. In this implementation, one type of pixel is functionalized for H_2 detection, while adjacent reference pixels remain passivated, and which signals serve as a real-time environmental baseline.

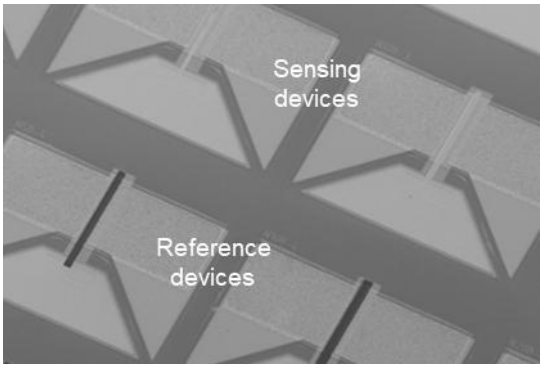

Fig. 1. SEM micrograph of the HEMT array showing the sensing (top) and reference (bottom) devices.

Results

In order to achieve the performance described, the following process flow is applied to 2” wafers with an AlGaN/GaN HEMT epitaxial structure grown by MOCVD. [4] Ohmic contacts were formed by a Ti/Al/Ni/Au metal scheme annealed at 850°C. Mesa etching was performed via optimized Cl_2/BCl_3 ICP etching until the buffer layer. A TMAH post treatment was then applied as Sun et al [5], followed by a PECVD SiN passivation layer, with openings for contact access. HfO_2

was then deposited by ALD to form the gate oxide. A thin film of Pt was deposited by sputtering to form the functionalized gate (200 x 10 µm). A final SiN layer was deposited to passivate the gates of the reference devices. This process allowed for crosstalk leakage current density of 7E-11 A/mm at Vds=5V, off state current density of 5E-11 A/mm at (V_{gs};V_{ds})=(-10V;5V) and gate leakage current of 3E-11 A/mm at (V_{gs};V_{ds})=(-10V;10V). Wafer level mapping of electrical characteristics confirms very high uniformity of typical HEMT KPIs (saturation current, transconductance, Rds_{on}, threshold voltage, gate leakage current, off-state current, crosstalk current) as well as high device yield (>95%).

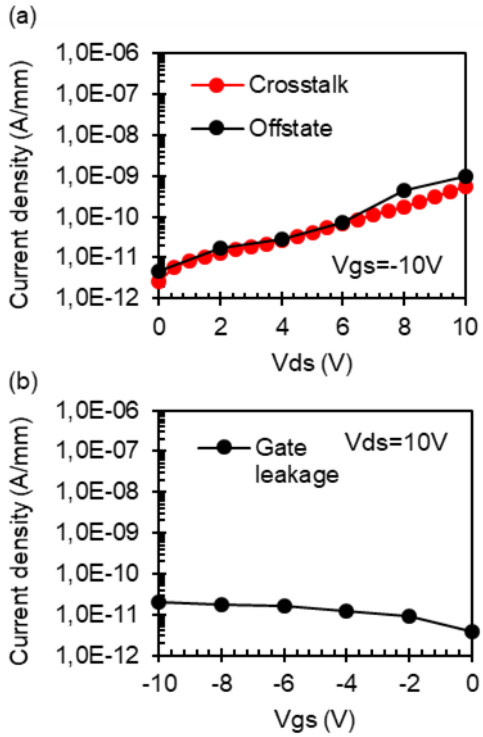

Fig. 2. a) Crosstalk and off-state leakage current densities vs applied voltage (for off-state leakage, V_{gs} = -10 V). b) Gate leakage current density vs gate-source voltage (V_{ds} = 10V).

After dicing and packaging, chips were exposed to different gas compositions. During testing, gate and source were connected together, and 5V was applied to the drain. Drain-source currents were monitored for both sensing and reference devices. As a primary validation case, the platform was characterized in N_2 with H_2 concentrations from 1 to 100 ppm at 20°C. Sensitivity, defined as the difference in currents between sensing and reference devices normalized by the baseline current of the sensing device, was observed between 6% and 10%. Crucially, the differential measurement architecture achieves a thermal CMRR of down to -60 dB at low concentrations, effectively suppressing thermal noise and baseline fluctuations (see Fig. 3). Long-term testing (several test cycles of 180 hours of continuous operation repeated over the span of 8 months) demonstrates a remarkably stable baseline recovery for the differential measurement signal (see Fig. 4).

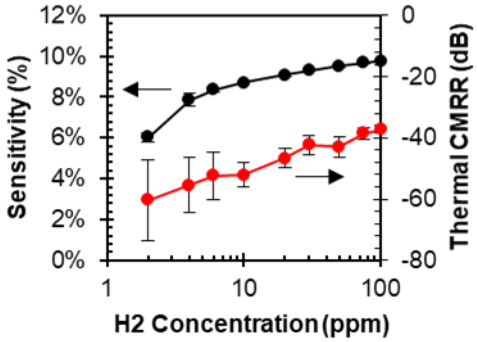

Fig. 3. Differential pair sensitivity (Black line) and thermal Common Mode Rejection Ratio (Red line) vs. H_2 concentration (1-100 ppm) at 20°C.

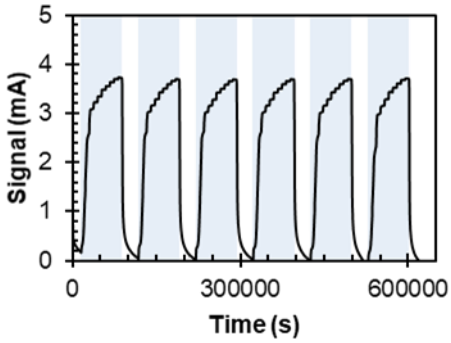

Fig. 4. Differential measurement output showing 6 detection cycles (Light blue zones) over 650,000 seconds (1 week). Full recovery is demonstrated after each H_2 exposure cycle in N_2 (1 to 100 ppm).

Additionally, a preliminary testing in ambient air showed no cross-sensitivity to common industrial interferents including IPA, acetone, water vapor, and butane/propane mixture, while sensitivity to H_2 remains unaffected. This test provides early insight into the selectivity of the sensor, paving the way for a higher Technology Readiness Level.

References

[1] Bhat, A. M. et al, *Micro and Nanostructures*, 176, 207528 (2023); doi: 10.1016/j.micrna.2023.207528

[2] Jiang, Y. et al, *Journal of Materials Chemistry C*, 11(30), 10121-10148 (2023); doi: 10.1039/D3TC01126G

[3] Garg, T. et al, *IEEE Electron Devices Reviews*, 1, 16-30 (2024); doi: 10.1109/EDR.2024.3491716

[4] Taher, M. I. B. et al, *International Journal of Hydrogen Energy*, 55, 1514-1522 (2024); doi: 10.1016/j.ijhydene.2023.12.070

[5] Sun Y. et al, *Nanomaterials*, 10(4), 657 (2020); doi: 10.3390/nano10040657

Pd Decorated MoS_2 Nanosheet Deposited on Yolk-Shell (SiO_2-TiO_2) Nanosphere for Hydrogen Gas Sensing

Dulani N. Liyanage[1], Hamidah Alluhaybi[2], Thilini Thathsara[1], Christopher J. Harrison[1,2], Peter Kingshott[1], Ylias Sabri[2], Mahnaz Shafiei[1]*
[1]Swinburne University of Technology, Hawthorn, VIC, 3122, Australia
[2]Royal Melbourne Institute of Technology, Melbourne, VIC, 3001, Australia
Corresponding author: mshafiei@swin.edu.au

Summary:

In this research, we explore a highly sensitive chemiresistive hydrogen gas sensor based on Pd-decorated MoS_2 nanosheets deposited on yolk–shell (SiO_2–TiO_2) nanospheres. This novel architecture was synthesized using a two-step facile hydrothermal method. The sensor shows a response of 317.3 towards 10,000 ppm hydrogen at 30 °C under a 9 V bias, with response and recovery times of 78 s and 39 s, respectively. The synergistic effect of Pd nanoparticles and MoS_2 deposited on the yolk–shell structure enhances the sensor performance and confirms its capability for real-world hydrogen sensing applications.

Keywords: Molybdenum disulfide, Pd nanoparticles, hydrogen sensor, yolk-shell structure.

Background, Motivation and Objective

Hydrogen plays an important role as a clean and sustainable energy carrier and has significant potential to replace fossil fuels [1]. It is widely used across various industries, including ammonia and methanol synthesis, water splitting, fuel cells, aerospace and medical applications. However, hydrogen is highly flammable and explosive, which limits its safe use. Therefore, reliable hydrogen gas sensors are essential for real-time detection to mitigate these risks. Existing hydrogen gas sensors suffer from many issues including higher operating temperatures, low response and recovery [2]. Hence, to overcome these limitations, new sensor materials need to be developed. Molybdenum disulfide (MoS_2) has gained significant attraction for gas sensing applications due to its intrinsic properties, such as higher surface to volume ratio, ability to functionalized with other materials, tunable band gap and flexibility to integrate in to modern electronics [3]. This research explores synthesis of a novel material, Pd decorated MoS_2 nanosheets deposited on yolk-shell (SiO_2-TiO_2) nanospheres (NS) (Pd@MoS_2 YS(SiO_2-TIO_2) NSs) for hydrogen sensing. This architecture provides a solid core, internal void space, and a porous shell, which facilitates a higher surface to volume ratio and enhances hydrogen adsorption.

Method

S two step hydrothermal method was used to synthesize Pd@MoS_2 YS(SiO_2-TIO_2) NSs. Initially, monodispersed SiO_2 NSs were synthesized using the Stöber method [4], which were then coated with TiO_2 to obtained yolk-shell NSs using a hydrothermal method and calcination. Subsequently, two-dimensional (2D) MoS_2 nanosheets were deposited on the YS NSs using a hydrothermal method. Finally, Pd nanoparticles were deposited via a simple reduction method.

Results

According to the scanning electron microscope (SEM) and transmission electron microscope (TEM) images shown in Fig. 1 (a), the presence of a well-defined spherical morphology with an internal SiO_2 yolk and TiO_2 shell structure with approximate diameters of 106 nm and 299 nm, respectively is confirmed. Furthermore, Fig. 1 (b) shows Pd-decorated MoS_2 nanosheets deposited on yolk–shell (SiO_2–TiO_2) NSs, along with the formation of a void space and a porous shell. This unique architecture provides a higher surface to volume ratio, allowing more hydrogen to be adsorbed for enhancing sensor performance. Energy-dispersive X-ray spectroscopy (EDS) mapping shown in Fig. 1 (c-f) demonstrates the uniform distribution of elements throughout the NSs.

The sensing performance of the synthesized Pd@MoS_2 YS (SiO_2–TiO_2) NSs were evaluated using a custom-built, fully automated gas chamber. The sensor response (R) was calculated using Equation (1), where I_{air} and I_{gas} represent the sensor current in air and under hydrogen exposure, respectively.

$$R = \frac{(Igas - Iair)}{Iair} \quad (1)$$

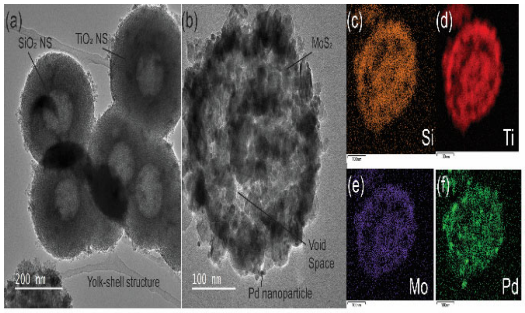

Fig. 1. (a-b) TEM images of yolk-shell (SiO_2 -TiO_2) NS and Pd@MoS_2 YS (SiO_2-TIO_2) NS, corresponding EDS elemental mapping: (c) Si (d)Ti (e) Mo and (f) Pd.

According to Fig. 2 (a) the sensor response was analyzed for hydrogen (500 -10,000 ppm) at different operating temperatures (25 °C, 30 °C, 40 °C, and 50 °C) under a 9 V bias. The sensor (Fig. 2 (b)) showed a response of 317.3 towards 10,000 ppm hydrogen at 30 °C, with a response time of 78 s and a fast recovery of 39 s. Furthermore, the sensor illustrated a noticeable response of 3.61 at a lower hydrogen concentration of 1,000 ppm. Sensitivity, calculated from the linear region (2000-8000 ppm) was approximately 0.038 ppm^{-1}, indicating correlation between sensor response and concentration. The significant sensor response is attributed to the synergistic effect of Pd nanoparticles and MoS_2 nanosheets, where Pd nanoparticles act as a catalyst for hydrogen molecule dissociation forming PdH_x, and the 2D MoS_2 nanosheets heterojunction with TiO_2, provides more active sites and enhancing charge transfer efficiency [5]. Further, corresponding linear fitting curves at 30 °C and 40 °C (Fig. 2 (c)) demonstrate good linearity, with R^2 values of 0.96 and 0.97, respectively. All these results conclude that novel Pd@MoS_2 YS (SiO_2–TiO_2) NS sensor is promising and has potential for real world applications.

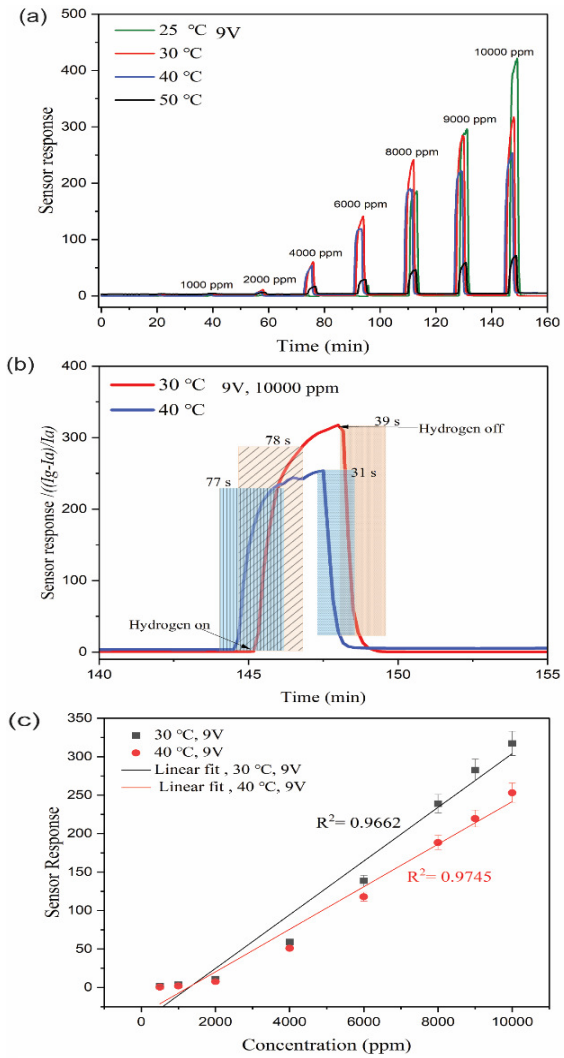

Fig. 2. Dynamic response towards hydrogen: (a) at different operating temperatures, (b) response and recovery times at 10,000 ppm, and (c) calibration curves at 30 °C and 40 °C.

Acknowledgements

The authors greatly appreciate the financial support from the Future Energy Exports Cooperative Research Centre (FEnEx CRC, 2026/24.RP2.0199.PHD-FNX-MILE0950) and the Australian Renewable Energy Agency (Contract No. 2018/RND012) and scholarship form Swinburne University of Technology

References

[1] T. Hübert, L. Boon-Brett, G. Black, and U. Banach, Hydrogen sensors–a review, *Sensors and Actuators B: Chemical,* 157, 329-352 (2011); doi: 10.1016/j.snb.2011.04.070.

[2] S. Luo, Z. Fan, Y. Ye, X. Li, and D. Yang, Metal oxide semiconductor-based hydrogen gas sensors: A comprehensive review, *International Journal of Hydrogen Energy,* 206, 153405 (2026); doi: 10.1016/j.ijhydene.2026.153405

[3] D. N. Liyanage, T. Thathsara, C. J. Harrison, P. Kingshott, and M. Shafiei, Recent advances in hydrogen gas sensors based on molybdenum disulfide (MoS_2), *International Journal of Hydrogen Energy,* 161, 150685 (2025); doi: 10.1016/j.ijhydene.2025.150685.

[4] B. Zhang, F. Yang, X. Zhang, N. Wu, B. Liu, and Y. Li, Construction of graphene-wrapped Pd/TiO_2 hollow spheres with enhanced anti-CO poisoning capability toward photoassisted methanol oxidation reaction, *ACS Sustainable Chemistry & Engineering,* 9,1352-1360 (2021); doi: 10.1021/acssuschemeng.0c08129.

[5] Q. Zhang *et al.*, MoS_2 yolk–shell microspheres with a hierarchical porous structure for efficient hydrogen evolution, *Nano Research,* 9, 3038-3047 (2016); doi: 10.1007/s12274-016-1186-7.

DOI 10.5162/eurosensors2026/8.1.5

Development and Validation of a Portable GC-MOS System for High-Sensitivity and Selective Analysis of VOC

Oliver Brieger[1], Tilman Sauerwald[2], Gina Zeh[2], Andreas Schütze[1], Christian Bur[1]
[1] Saarland University, Lab for Measurement Technology, Saarbrücken, Germany
[2] Fraunhofer IVV, Department of Sensory Analytics and Technologies, Freising, Germany
c.bur@lmt.uni-saarland.de

Summary:

This study presents the development, setup, and validation of a miniaturized gas chromatography system using a metal oxide semiconductor gas sensor as detector and a pre-concentrator based on metal-organic frameworks as injector. The system addresses the need for cost-effective, portable solutions for monitoring chemical markers in complex gas phases. It was first validated in the lab showing a good separation of an aldehyde mix, which is used as calibration standard for fat oxidation markers. To evaluate real-world performance, the system was deployed in a quality control lab at a chocolate factory. The device successfully detected hexanal, a critical biomarker used to determine the freshness of nuts. Additionally, initial results indicate the suitability in bio-medical application, too.

Keywords: gas chromatography, MOS-detector, Metal-Organic Framework

Introduction

High-precision gas analysis has historically been restricted to specialized laboratories due to the substantial costs and technical complexity of traditional analytical equipment. In various sectors ranging from food quality control to medical diagnostics, there is an urgent need for the rapid and reliable detection of chemical markers in the gas phase. One of the major challenges of sensor systems in real world applications is the poor selectivity whereas the sensitivity of metal oxide semiconductor (MOS) gas sensors is typically sufficient. To overcome this limitation a gas chromatography (GC) column has been utilized for separation of VOCs prior to the MOS sensor [1, 2]. However, sampling and injection of samples into the system still remain a challenge, in particular for inexpensive portable devices, as well as poor quality of the chromatograms [3] resulting from large dead volumes in the system affecting the acceptance of such systems so far.

In this study, a GC-MOS system using a metal-organic framework (MOF) for pre-concentration and sharp sample injection into a GC column is presented and field validated in the food industry to determine the freshness of hazelnuts.

Technological realization

Fig. 1 shows the schematic of the GC-MOS system consisting of a pre-concentrator as injector, a GC column, and MOS sensor as detector. The entire system design is optimized for a small bill of materials and low integration and operating costs. As pre-concentrator and sampling unit a MOF, i.e., UiO-66-BDC, on a ceramic heater substrate (Umweltsensortechnik, Germany) was used, similar to the solid phase micro extraction of common GC-MS approach. A membrane pump (NMP03KPDC, knf Neuberger, Germany) enables a constant sampling flow of the headspace of a sample onto the pre-concentrator. A portion of the desorbed volatiles are injected into the separation column (3-meter oxygen-resistant FS-5MS Supreme with 250 µm ID) column by a 3/2 cartridge valve (Bürkert, Germany). The column is temperature controlled by a custom-built GC-oven between 30 °C and 100 °C. During analysis and for flushing the column, a second pump is used downstream the MOS sensors which provides a negative pressure in the sensor chamber. This pressure gradient over the separation column leads to a constant flow through the column. As detector a MOS sensor, i.e., GGS1530 (Umweltsensortechnik, UST), is employed. The setup allows for an optional make-up flow in the sensor chamber for, e.g., rapid flushing. The GC system was optimized in terms of low dead volume allowing for sharp peaks.

Measurement

For validation of the GC-MOS system, a test measurement with an aldehyde mixture was performed. Five aldehydes, i.e., propanal up to

heptanal with 25 ppm each were solved into rapeseed oil. The expected headspace concentrations are 40.7, 11.5, 2.9, 0.9, and 0.2 ppm, respectively.

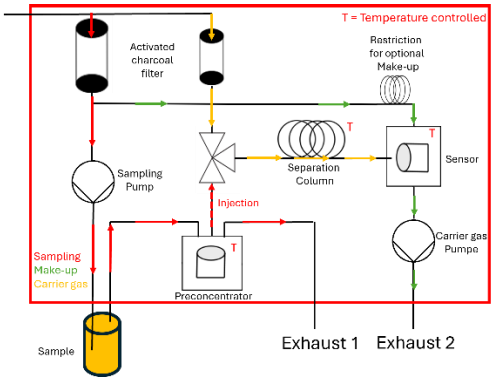

Figure 1: Schematic of the GC-MOS system.

A droplet (~1 mL) of this mixture was put onto a tissue and put into a 50 mL borosilicate sampling vial. The sampling flow was 200 mL/min which lowers the estimated headspace concentration. The headspace was sampled for 150 s at 20 °C. After this period the pre-concentrator was heated to 200 °C for 30 s for desorption and the first 3 s of this period were injected onto the column. The column and the sensor were temperature controlled at 35 °C and 400 °C, respectively.

Results

Figure 2 shows the sensor response and the derivative of the sensor response of the GGS1530 at 400 °C for five consecutive injections of the aldehyde mix. It was observed that the intensity of propanal and butanal decline strongly with each consecutive measurement. This is due to the considerably higher volatility compared to other aldehydes in the mixture. The peak for hexanal and heptanal was quite stable over the measurement. Each aldehyde was well detected by the GC-MOS system.

In addition to the aldehyde mix, the fat oxidation, and with that the decay of freshness, of real hazelnuts harvested in 2023, 2024, and 2025 were tested. The derivative of the sensor response in Fig. 3 shows a clear peak for hexanal and octanal increasing with the age of the nuts – both known as biomarkers for the oxidation process.

Discussion

The results of the aldehyde mix proved that the GC-MOS system can separate each substance of the mixture within 180 s cycle time. This is a reasonable duration for the quality control in the food industry. The system was further validated with real food samples, i.e., hazelnuts. The unambiguous determination of hexanal as biomarker proofs the suitability of the system for food quality applications.

Preliminary experiments (data not shown in this abstract) with propofol (intravenous anaesthetic) and pentanal (biomarker for oxidative stress and lung injury) have shown, that concentrations in the single digit ppb range can be detected reliably. This underscores the systems versatility and potential for medical applications.

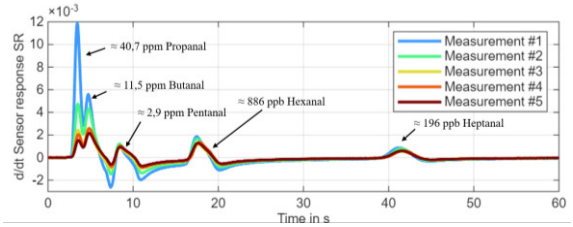

Figure 2: Derivative of the sensor response at 400 °C for five consecutive injections of the aldehyde mix.

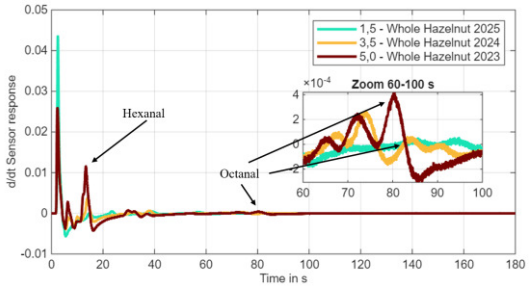

Figure 3: Derivative of the sensor response at 400 °C for hazelnuts (different harvest years) with some degree of oxidation due to age.

With different pump and make-up-flow setups a better separation is achievable. Further optimization of system parameters (i.e., sampling temperature and adsorption time of the pre-concentrator) will allow for measuring much lower concentrations. However, the presented results are meant to be a proof of principle.

Acknowledgement

Financial support was provided by Federal Ministry for Economic Affairs and Climate Action un-der the grant number 22938 N for the project SENT-GC-MOS.

References

[1] S. Zampolli et al., Selectivity enhancement of metal oxide gas sensors using a micromachined gas chromatographic column, *Sens. Actuators B Chem.*, 105, (2), 400–406 (2005); doi: 10.1016/j.snb.2004.06.036.

[2] M. Koehne et al., Development of a gas chromatography system coupled to a metal-oxide semiconductor (MOS) sensor, with compensation of the temperature effects on the column for the measurement of ethene, *J. Sens. Sens. Syst.*, 12 (2). 215–223 (2023), doi: 10.5194/jsss-12-215-2023.

[3] O. Brieger et al., Setup for characterization of MOS gas sensors as GC detector, *Sens. Actuators B Chem.*, 444, 138396 (2025), doi: 10.1016/j.snb.2025.138396.

DOI 10.5162/eurosensors2026/8.1.6

Unveiling Humidity-Enhanced Performance in Chemoresistive $CoCu_2O_3$ VOCs Sensors

Matteo D'Andria[1], Hamin Shin[1], Yi-Hsuan Wu[2], Xiangchao Meng[3], Patrick Zeller[4,5], Feng Ryan Wang[3], Andreas T. Güntner[1]
[1] Department of Mechanical and Process Engineering, ETH Zurich, CH-8092 Zurich, Switzerland
[2] Helmholtz-Institute Erlangen-Nürnberg for Renewable Energy (IET-2), Forschungszentrum Jülich GmbH, 91058 Erlangen, Germany
[3] Department of Chemical Engineering, University College London (UCL), London WC1E 7JE, United Kingdom
[4] Fritz-Haber-Institut der Max-Planck-Gesellschaft, Department of Inorganic Chemistry, Berlin, Germany
[5] Helmholtz-Zentrum Berlin für Materialien und Energie GmbH, Chemical Energy Division, Berlin, Germany
Speaker's email address: *mdandria@ethz.ch*
Corresponding author's email address: andregue@*ethz.ch*

Summary:
Oxidation chemistry is centered around understanding the electron flow that involves reactants, products, and reaction-derived adsorbate species. In chemical sensing, this electron flow results in electrical conductivity modulations in a thin film of semiconductor (oxide) nanoparticles. Therein, understanding which surface-adsorbed species are electronically coupled to the material is crucial. Here, we develop a methodology that separates ionized from dipolar surface populations, to elucidate the unusual promoter effect of humidity on metastable, nanocrystalline $CoCu_2O_3$. Our results outline strategies to turn humidity from detrimental to a functional advantage in gas sensor performance.

Keywords: oxidation catalysis, cobalt-copper oxides, electronic properties, molecular sensor.

Background, Motivation and Objective

Understanding how electrons are transferred, stored, and redistributed during surface redox is central to metal oxides, widely deployed in chemoresistive gas sensing. Therein, even modest perturbations (e.g., oxygen vacancy population, surface adsorbates) can change adsorption properties and electron flow throughout a catalytic turnover. Such perturbation may arise from background molecules, most notably H_2O, omnipresent in realistic sensor scenarios. It is essential to develop strategies to render the performance of conventional sensing materials more humidity-tolerant, to achieve stable and long-term operation in ambient air (e.g., air quality monitoring [1]).

In chemoresistive metal-oxide gas sensors, reaction-derived surface species that are not ionized remain electrically neutral and act as surface dipoles mainly affecting electron affinity, whereas ionized vacancies and adsorbates contribute directly to band bending and charge-carrier populations. Investigating the effect of H_2O on such *ionized* vs. *dipolar* distribution is essential for addressing the humidity-induced inhibition of chemical sensors, e.g., ~3-fold response-reduction in 90% relative humidity (RH) [2]. In mixed transition metal oxides, redox chemistry and charge-carrier modulation may not be confined to the same sites: one sublattice could be more directly involved in bond activation, whereas the other stabilizes ligand states that govern conductivity. Cobalt-copper oxides are an appealing platform to investigate these effects, owing to their rich valence chemistries that make them widely used in oxidation catalysis and gas sensing.

In this work, we employ $CoCu_2O_3$ as a mixed-oxide model system to unveil H_2O-induced modifications of receptor and transducer functions in a *p*-type semiconductor. To this end, we combined *operando* electrophysical measurements (DC resistance and work function), chemisorption analysis, and oxidation kinetics with surface-sensitive, *in situ*, near-ambient-pressure (NAP) X-ray photoemission and absorption spectroscopies.

Methodology

$CoCu_2O_3$ nanoparticles are fabricated by flame-aerosol technology as described in our previous work [3]. Chemoresistive films are obtained by direct flame-aerosol deposition on top of microfabricated substrates with interdigitated Pt electrodes and an integrated meander-shaped Pt resistive heater. These sensors are mounted onto MACOR® holders and placed in PTFE-made chambers, connected to a gas delivery manifold

comprising several thermal mass flow controllers. The resistance is measured between the interdigitated electrodes with a multimeter, and sensors' heating elements are heated to 200 °C *via* a DC power supply. For simultaneous work function (ϕ) measurements, the same MACOR®–supported sensor substrates are installed into aluminum chambers, with a hole drilling on the top that allows the Au tip (2 mm) of the Kelvin oscillator probe to approach the sample at working distances of approx. 0.5 mm. Temperature-programmed (TP) chemisorption characterization is performed to assess analyte-/oxidant-induced reactivity under either (i) dry or (ii) humid constant backgrounds.

The soft X-ray–based NAP spectroscopies are accomplished at the CAT@EMIL endstation of the Bessy II storage ring operated by the Helmholtz-Zentrum Berlin (HZB) für Materialien und Energie. Several reactive environments under different $CO:O_2:H_2O$ and $xylene:O_2:H_2O$ mixtures are obtained, at a total pressure of 1 mbar. X-ray photoemission (C and O 1s, Co and Cu 2p core levels) and absorption (O-K, Co- and Cu-$L_{2,3}$ edges) spectra are recorded.

This combination of techniques allows to elucidate the electron flow [4]. In dry conditions, electrons from reducing molecules are exclusively allocated to O(2p)–Cu(3d) states, while building up a considerable fraction of carbonaceous species that are neutral, i.e., do not affect electrical conductivity but rather *trivially* shift electron affinity (χ). In the presence of humidity, despite slower lattice O^{2-}–driven turnover, the removal of such carbonaceous dipoles is promoted, with up to approx. 50 meV χ-gains ($\Delta\chi_{gain}$). This has a significant influence on $CoCu_2O_3$ operated at 200 °C ($k_B T \approx 40\ meV$), decreasing its ligand-hole concentration by a factor of $\exp\left(\frac{\Delta\chi_{gain}}{k_B T}\right)$.

In conclusion, electrons are re-routed from Cu(3d)-only ligand-hole states (sub-optimally allocated) to O(2p)–Co(3d), activating Co-redox and yielding enhanced conductivity modulations, i.e., sensor performance.

Results

We quantified the electronic modulation of Co and Cu in $CO:O_2:H_2O$ mixtures. We focused on the evolution of Co valence inferred from its Co 2p envelope and the Cu^+/Cu^{2+} balance, as shown in **Figure 1**, while gradually increasing CO partial pressure in an O_2 environment, in either (i) dry, (ii) 20% or (iii) 70% H_2O constant backgrounds. As can be observed, in dry conditions, increasing CO pressure exclusively affects the Cu–O sublattice, with a growing Cu^+ fraction, and unaltered Co-spin distribution (from Co L_3-NEXAFS, not shown), showing even a slight net oxidation.

On the other hand, under 20% and 70% H_2O, modest increments of CO pressure decrease the Co-2p-inferred valence. Therein, under humid conditions, the burden of oxygen-vacancy formation and associated electron uptake is redistributed across Co–O and Cu–O, harnessing rerouted electrons which were sub-optimally placed in electrophilic carbonaceous species.

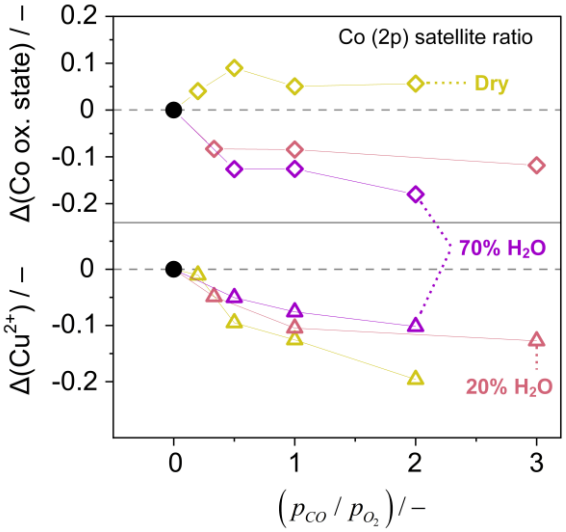

Fig. 1. Summary of $CoCu_2O_3$ evolution during CO dosing, starting from a CO-free baseline in either (i) dry, (ii) 20% or (iii) 70% H_2O backgrounds, showing the shift in Co oxidation state (inferred from Co 2p satellite analysis) and Cu^{2+} amount.

References

[1] R.S. Theodoro, G.S.M. Santos, M. D'Andria, H.S. Gropelo, S. Kravecz, A.T. Güntner, D.P. Volanti, *ACS Applied Materials & Interfaces* 18, 14473-14520 (2026), doi: 10.1021/acsami.5c24099

[2] M. D'Andria, F. Krumeich, Z. Yao, F.R. Wang, A.T. Güntner, *Advanced Science* 11, 2308224 (2024); doi: 10.1002/advs.202308224

[3] M. D'Andria, T. Elias Abi-Ramia Silva, E. Consogno, F. Krumeich, A.T. Güntner, *Advanced Materials* 36, 2408888 (2024); doi: 10.1002/adma.202408888

[4] M. D'Andria, H. Shin, Y.-H. Wu, X. Meng, P. Zeller, F.R. Wang, A.T. Güntner, „*Tailoring Electron Flow in the Redox Reactions of $CoCu_2O_3$ Nanocatalyst with Surface Hydroxyls for Humidity-Enhanced Molecular Sensing*"; doi: 10.26434/chemrxiv.15000437/v1

DOI 10.5162/eurosensors2026/8.2.1

On-Chip Label-Free Holographic NTA for Biophysical Characterization of Single Particles

Chiara Lombardo[1], Benoit Vignon[1], Andrea Sottini[1], Jaime Ortega Arroyo[1], Romain Quidant[1]
[1] ETH Zürich Switzerland,
chiaralo@ethz.ch

Summary:
We present an integrated optofluidic platform combining off-axis holographic microscopy with microfluidics for label-free tracking and characterization of heterogeneous nanoparticles. It extends tracking volumes and uses scattering contrast to simultaneously determine the size and refractive index of freely diffusing nanoparticles. We successfully classified synthetic nanoparticles and characterized biological ones without prior labeling.

Keywords: nanoparticle tracking, digital holography, microfluidics, label-free sensing, single-particle characterization, refractive index sensing

Background, Motivation and Objective

Classifying heterogeneous nanoparticle ensembles is essential for fundamental research and quality control. Conventional Nanoparticle Tracking Analysis (NTA) determines hydrodynamic diameter from Brownian motion. However, standard implementations image only a thin focal slab (~10 µm). Fast-moving particles quickly diffuse out, yielding truncated trajectories and high statistical sizing errors [1]. To address these challenges, we are developing an integrated optofluidic platform combining an off-axis digital holography microscope (Fig. 1a) with a custom two-layer microfluidic chip (Fig. 1b).
Off-axis digital holography overcomes these limitations by recording the interference of scattered and reference light to simultaneously capture intensity and phase [2]. Intensity provides insights into polarizability (related to size and refractive index), while encoded phase information enables numerical axial propagation. This allows volumetric sample reconstruction from a single 2D interferogram. Extending NTA to this holographic configuration (holoNTA) substantially increases the effective imaging volume (Fig. 1c). Capturing longer 3D trajectories allows accurate measurement of the 3D mean squared displacement to extract the diffusion coefficient and derive the hydrodynamic diameter via the Stokes-Einstein equation. Once the diameter is known (Fig. 1d), its scattering cross-section—derived from the reconstructed amplitude—is used to retrieve its refractive index based on Mie theory.
Preliminary measurements happen in a sealed circular imaging chamber (2 mm diameter, 100 µm height) formed by a silicone spacer between two glass coverslips, which suppresses residual flow for drift-free Brownian tracking. This architecture enables rigid optical alignment and complete volume confinement. A two-layer chip with push-up valves enclosing the same 2 mm × 100 µm volume is in development for automated sample exchange via fluidic washing, minimizing reagent use and contamination risks.
Although holoNTA offers superior tracking, the computational burden of volumetric reconstruction typically precludes real-time analysis. This was tackled by introducing a GPU-accelerated, physics-informed detection pipeline.

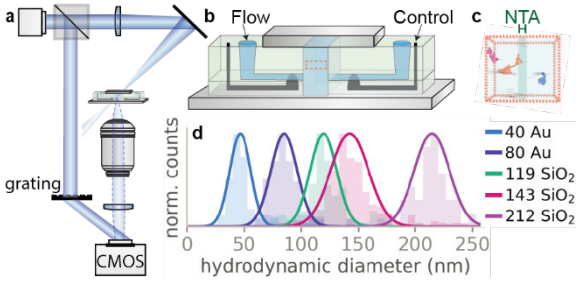

Fig. 1. Optofluidic holoNTA platform. (a) Off-Axis holography microscope. (b) Two-layer microfluidic chip design. The flow layer is used to fill the imaging chamber, which is sandwiched between two glass plates. Push-up valves in the control layer close the imaging chamber. (c) HoloNTA significantly increases the accessible imaging volume compared to the semi 2D conventional NTA. (d) The diffusion trajectories are used to compute the particle's hydrodynamic diameter.

Description of the New Method or System

We developed a custom-built off-axis holographic microscope (Fig. 1a) operating in

transmission dark field, achieved by illuminating at a high angle beyond the collection NA (0.75), at a 488 nm laser wavelength. The system provides a ~ 100 × 100 µm² field of view that can be propagated along 100 µm, resulting in a ~1 nL instant imaging volume at 60x effective magnification. A CMOS camera (Basler ace) records interference holograms with rapid exposures (20–100 µs) to freeze the Brownian motion of small analytes.
The acquired holograms are then Fourier transformed and the reconstructed complex field is propagated to 100 planes across a depth of 100 µm, with GPU acceleration propagating the full 1 nL volume simultaneously. Candidate particles are detected as local maxima of the amplitude contrast across the volume. The candidates are validated by directly fitting the physical PSF model to the complex field [3]. Besides confirming the detection, this step serves to refine the 3D localization and extract the scattering amplitude. Confirmed detections are linked into 3D trajectories with a Kalman-filter-based linker using adaptive statistical gating, globally optimal frame-to-frame assignment, and gap closing. For each trajectory, the mean squared displacement yields the diffusion coefficient and hence the hydrodynamic diameter via the Stokes–Einstein equation. The refractive index of the particles can be retrieved by calibrating the system on known samples via Mie theory.

Results

As proof of principle, 80 nm AuNP were measured at three different concentrations. A total of 2, 8 and 89 AuNP trajectories were retrieved at the three concentrations, corresponding to measured concentrations of 2.2×10^6, 7.8×10^6 and 5.8×10^7 NP/ml. The retrieved hydrodynamic diameters were 75, 83 and 81 nm respectively, in agreement with the TEM spec of 79 nm (CV 8.9%). Five monodisperse samples were then measured individually (40/80 nm Au, 119/143/212 nm SiO2, Fig. 1d). Populations whose size distributions overlap significantly still form distinct clusters in the contrast vs diameter map. This capability was proven on a heterogeneous mixture of 40 nm Au, 100 nm PS and 119 nm SiO_2, of which the relative concentrations were not known. Five different 1 nL volumes were measured and resulted in a total count of 1150 trajectories. Mapping the trajectories in the 2D contrast vs diameter plane (Fig. 2a) allowed us to classify each datapoint and retrieve the absolute concentrations of Au, PS and SiO_2, namely $5.1\pm1.6\times10^7$, $14.3\pm1.6\times10^7$ and $7.5\pm1.9\times10^7$ NP/ml. Individual measurements of 40 nm AuNP (N=179) and 80 nm AuNP (N=148) were taken to fit a Mie curve and calibrate the contrast to the corresponding refractive index (Fig. 2b). The 40 nm AuNPs classified from the mixture (N=201) fall right on the individually measured 40 nm AuNP, and thus on the Mie curve. The medians of the SiO_2 (N=286) and PS (N=524) fall on the Mie bands predicted by literature (n=1.43-1.48 for SiO_2 and 1.58-1.68 for PS) [4]. Measurements were extended to heterogeneous biological nanoparticles (e.g. EVs, liposomes), demonstrating label-free detection and tracking. Ultimately, this integrated optofluidic platform provides a versatile, real-time tool for rapid nanoparticle classification and biophysical characterization.

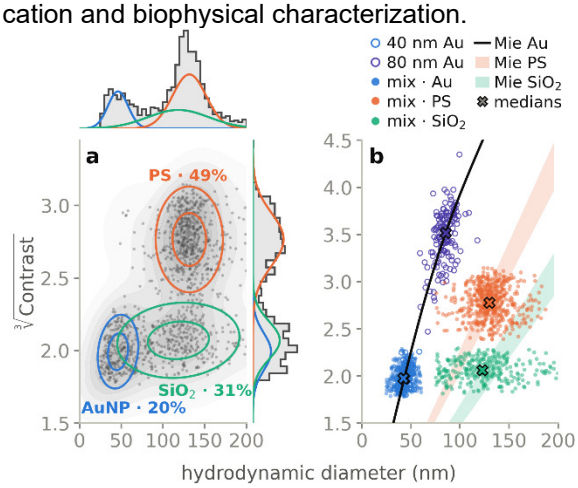

Fig. 2. Single-particle classification of a heterogeneous nanoparticle mixture. (a) The mixture (N=1150 trajectories) in the contrast vs diameter plane. Three populations are resolved, with classified fractions of 20% AuNP, 49% PS and 31% SiO_2. (b) The individually measured 40 nm and 80 nm AuNP fall on the Mie curve for gold; the medians of the PS and SiO_2 populations classified from the mixture fall within the Mie bands predicted from literature refractive indices.

References

[1] U. Ortiz-Orruno et al., Simultaneous Sizing and Refractive Index Analysis of Heterogeneous Nanoparticle Suspensions, *ACS Nano* 17 (1), 221-229 (2023); doi: 10.1021/acsnano.2c06883

[2] J. Ortega Arroyo, M. Liebel, The Next Dimension: Digital Holography for 3D Interferometric Scattering, ACS Nano 19 (44), 38630–38640 (2025); doi: 10.1021/acsnano.5c13224

[3] L. Wei, *et al.* Fast 3D localization of nano-objects in wide-field interferometric scattering microscopy via vectorial diffraction model-derived analytical fitting. *npj Nanophoton.* 2, 21 (2025); doi: 10.1038/s44310-025-00068-3

[4] A. D. Kashkanova et al., Precision size and refractive index analysis of weakly scattering nanoparticles in polydisperse mixtures, Nat. Methods 19, 586–593 (2022); doi: 10.1038/s41592-022-01460-z

DOI 10.5162/eurosensors2026/8.2.2

Systematic Method of Measuring and Evaluating Sensitivity and Linearity of a Micro-Fluxgate Sensor

Jiri Maier[1], Pavel Ripka[1], Poki Chen[2]
[1] Czech Technical University in Prague, Technicka 2, 160 00 Prague, Czech Republic
[2] National Taiwan University of Science and Technology, Taipei City 106335, Taiwan
maierjir@fel.cvut.cz

Summary:
We describe a rigorous method of measuring open-loop sensitivity of a fluxgate sensor. The most important aspects are to ensure that the applied magnetic field lies inside the linear range and select the optimal phase at which the output voltage is detected. The phase and open-loop sensitivity are required to correctly calculate the noise of the sensor, which is a very important characteristic.

Keywords: Fluxgate, micro-fluxgate, magnetic sensor, measurement, open-loop sensitivity

Introduction

Fluxgate sensors are widely used in various applications, such as navigation, geophysics, and industrial automation. The principle of their operation is based on the saturation of a magnetic core by an alternating excitation field and measuring an induced voltage in a pick-up coil. Voltage signal proportional to the measured field is detected at even harmonics of the excitation frequency.

Important parameters of a fluxgate sensor are the sensitivity and noise. While open-loop sensitivity is not critical for closed-loop sensor operation, its value is required to correctly calculate the noise.

Our team focuses on miniaturization of fluxgate sensors using microfabrication technology. Our first-generation design was published in [1]; with following design improvements published in [2]. Comparing different designs requires a robust approach to conducting automated measurements and evaluating important characteristics.

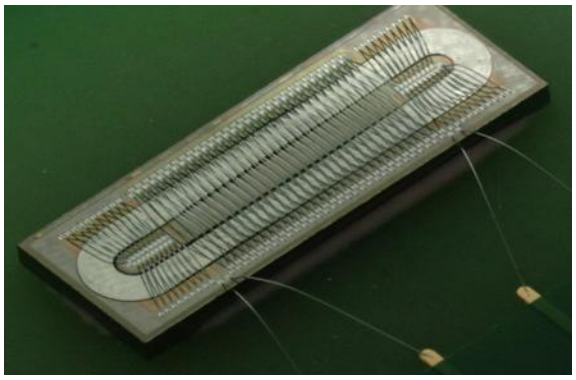

Fig. 1. Micro-fluxgate with racetrack core and solenoid coils made using wire-bonding [1]

Measurement setup

Lock-in amplifier is used to measure the output signal (pick-up coil induced voltage). Excitation current is used as the reference signal. For simplicity, sinusoidal excitation signal is used in the following example. Excitation signal parameters are 1 MHz, 40 mA, which is an optimum operating point of the used sensor.

Sensitivity Measurement

Measurement of fluxgate's sensitivity requires placing the fluxgate in a known magnetic field. The basic method of doing that is to place Helmholtz coils in such way, that the horizontal component of Earth's magnetic field is perpendicular to the axis of the coils, so that the field is zero in the coils' direction. A current is then passed through the coils to create the desired field. The sensitivity will then be the output voltage divided by the applied field.

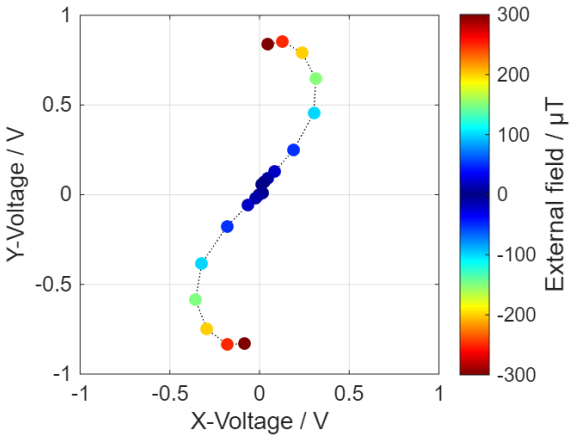

Fig. 2. X and Y components of the induced voltage at 2nd harmonic in pick-up coil for applied external fields in range ±300 µT. Results are composed of positive and negative halves, measured separately.

Selecting the strength of the field is a peculiar task. The Earth's field might not be perfectly zeroed out in the sensitivity axis, and the fluxgate might have some offset. When the applied field is low, those inaccuracies cause high relative error. On the other hand, if the applied field is large enough for the offset to be neglected, it is possible that the field is outside the linear range.

Figure 2 shows results of such measurement. We can see that the phase of the output is constant up to around 50 µT and then it starts changing dramatically. The magnitude is also not linearly dependent on the field for larger fields.

There is a distortion or discontinuity at the plot's origin (zero field). This is caused by the positive and negative half being measured separately, while environmental conditions might have slightly changed in-between. It would be more suitable to cover the low-field range by continuous measurement.

An Alternative Approach

Instead of placing the Helmholtz coils perpendicular to Earth's field, we can place them parallel to its horizontal component. The field created by the coils will then oppose Earth's field. This way, we can smoothly transition between negative and positive direction of applied field without swapping polarity of the Helmholtz coil current.

This way, we also get rid of any possible cross-field effects (there is no field perpendicular to the fluxgate's sensitivity direction in the horizontal plane.) We still have the vertical component of Earth's field, but this should not have any effect, as the thin flat core [2] has very high demagnetization factor in the vertical direction.

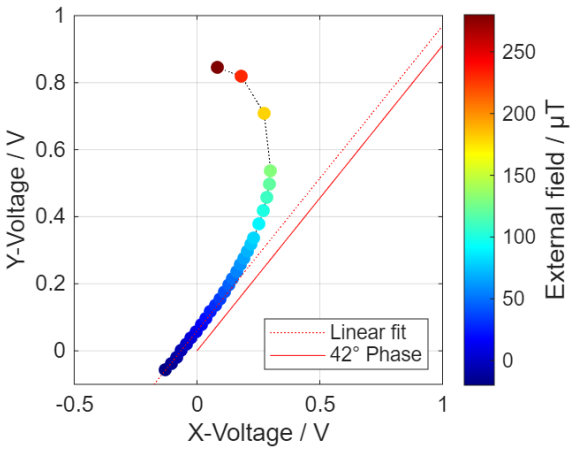

Fig. 3. X and Y components of the induced voltage at 2nd harmonic in pick-up coil for applied external fields in range 0 to 300 µT biased by 20 µT Earth's field

Figure 3 shows the results. With the horizontal component of Earth's field being approximately 20 µT at the location (Prague), the applied field can be swept from -20 µT to any positive value, giving us a continuous ±20 µT interval where we can linearly fit the data and obtain the phase of the useful signal, which in this case is 42°.

By projecting the data onto the 42° phase (rotate by -42° and use the new X), we obtain the relation between field and voltage, from which we determine the sensitivity, as shown in Figure 4.

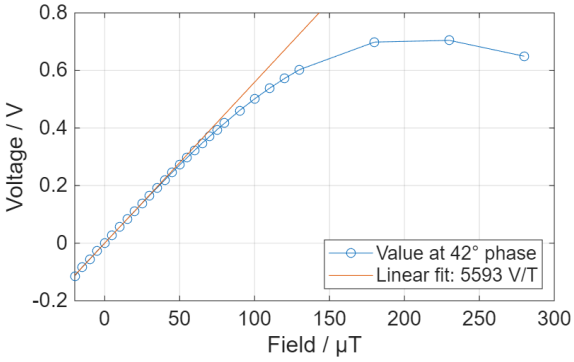

Fig. 4. Linear dependency of signal at the previously determined phase on the external (measured) field.

Conclusion

We presented a systematic method for measuring the open-loop sensitivity and linearity of a micro-fluxgate sensor. By aligning the Helmholtz coils parallel to the horizontal component of Earth's magnetic field rather than perpendicular to it, we achieved a continuous sweep through both polarities of the applied field without reversing the coil current. This eliminates discontinuities near zero field and does not require manually swapping polarity of the power source, which makes it suitable for automated measurements.

The method allows reliable determination of the signal phase within the linear range. Projecting the lock-in output onto this phase yields a clean linear relationship between the applied field and the output voltage, from which the sensitivity is easily determined. Crucially, the exact value of the Earth's field bias does not need to be known, since sensitivity is determined from the slope of the fit rather than its constant term.

The described approach is well suited for automated characterization of multiple sensor designs, enabling consistent and reproducible comparison. Accurate knowledge of both the sensitivity and the detection phase is essential for correctly computing the sensor noise, which is the main figure of merit in our ongoing miniaturization effort.

References

[1] J. Maier, P. Ripka, P. Chen, CMOS-based micro-fluxgate with racetrack core and solenoid coils, Sensors and Actuators A: Physical 379, 115886 (2024); doi: 10.1016/j.sna.2024.115886

[2] J. Maier, P. Ripka, P. Chen, High-Frequency Low-Power Microfluxgate, IEEE Sensors Letters 9, 1-4 (2025); doi: 10.1109/LSENS.2025.3585367

DOI 10.5162/eurosensors2026/8.2.3

A Next Generation HVM Process Platform for High Performance IMU Devices

Tobias Macha[1], Arezo Behroudj[1], Daniel Richter[1], Christof Schwenk[1], Heiko Stahl[1], Axel Grosse[1]
[1] Robert Bosch GmbH, Reutlingen, Germany,
tobias.macha@de.bosch.com

Summary:
We report on our next generation high-volume manufacturing (HVM) process platform for high performance inertial-measurement unit (IMU) devices. While footprint is reduced, it achieves a 40% increase in sensitivity for gyroscope and accelerometer with reduced noise level and improved vibration robustness. New process modules have been implemented and combined to accomplish stable production and application requirements.

Keywords: IMU, MEMS, high-volume mass production, process platform, 30µm Epi, SiRiN

Background, Motivation and Objective

Over the past years, the currently running, HVM proven, process platforms have enabled many successful products [1], but its limitations have become a bottleneck for next-gen IMU devices. Chip size and height constraints in combination with increasing performance demands required an evolution of a new process platform. Since it is not desirable to extend the footprint of a MEMS device, the performance boost in sensitivity is only achievable by significantly increasing the sensor core mass and capacity density. This goal was reached by vertically raising the sensor core mass, combined with other process adaptations. This paper presents the results and challenges of this new process platform development.

Description of the New Method or System

The process platform features a 30 µm thick, low-stress Epi layer and thus a higher aspect-ratio trench for unchanged electrode gaps. This allows for a higher capacitance within the same electrode area, compared to our former 20 µm Epi platform [2]. We also introduce a sacrificial oxide-etch protection using Silicon-Rich silicon Nitride (SiRiN) with a high selectivity, enabling accelerometer designs with very compact anchors, which in turn improve signal offset performance [3]. Furthermore, since wiring traces are no longer underetched, they can be more compact, which makes the parasitic capacitances smaller. To compensate for the conductivity loss of narrow wiring traces, we increased their thickness and doping level. The usage of thick, sacrificial, oxide layers between wiring and functional poly-Si layers enables large gaps for out-of-plane movement of our sensor masses, which makes the signal detection very robust against external disturbances.

Results

We optimized the new process platform with 50% higher Epi thickness and higher buried topography to achieve a comparable distribution of Epi thickness values after CMP. In fact, as for the previous platform, we still reach a comparable Gaussian standard deviation value over high volumes, as depicted in Figure 1. Simultaneously, increasing the Epi thickness does not lead to compromises in process or design variations, i.e. the critical dimensions or etch loss after trench. Results are comparable to current 20 µm Epi platform settings as exemplified in Figure 2. The spread of drive frequency is kept very small over high statistics and proves capability for HVM. Implementing the insulating SiRiN material required identifying a mass-production-safe gap width between wiring traces to minimize the probability of electrical bypasses. This was achieved using a dedicated test structure (Figure 3), which confirmed that a 2µm gap is sufficient for robust insulation. The new process platform clearly fulfills intended requirements and is ready to launch.

References

[1] J. Classen et al., "Advanced surface micromachining process — A first step towards 3D MEMS," 2017 IEEE 30th International Conference on Micro Electro Mechanical Systems (MEMS), Las Vegas, NV, USA, 314-318, 2017, doi: 10.1109/MEMSYS.2017.7863404

[2] M. Fürtsch, “Mechanical Properties of Thick Polycrystalline Silicon Films Suitable for Surface Micromachining”, PhD Thesis, Duisburg University, Shaker Verlag GmbH, 1999

[3] M. Williams, J. Smith, J. Mark, G. Matamis, and B. P. Gogoi, "Development of a low-stress silicon-rich silicon nitride film for micromachined sensor applications", Proc. SPIE 4174, Micromachining and Microfabrication Process Technology VI, 436-442, 2000, doi: 10.1117/12.396464

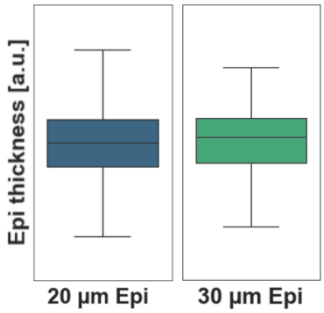

Fig. 1. The EP thickness is evaluated in a test structure, and the data is shown with equal increments. The 30 µm Epi thickness (right) lies well within the targeted thickness range and promises a similar series production capability as the 20 µm equivalent (left).

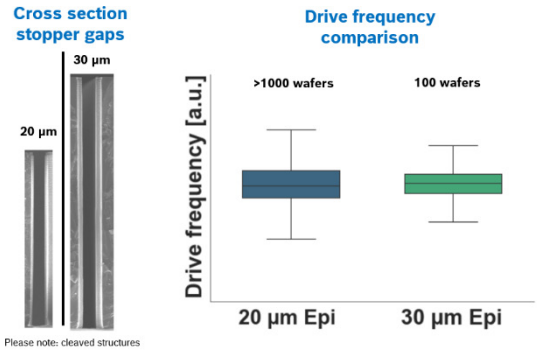

Fig. 2. A SEM cross section of stopper gaps reveals a comparable trench behavior of 20 µm and 30 µm Epi thickness types (left). The achievable etch loss distribution is also comparable (right).

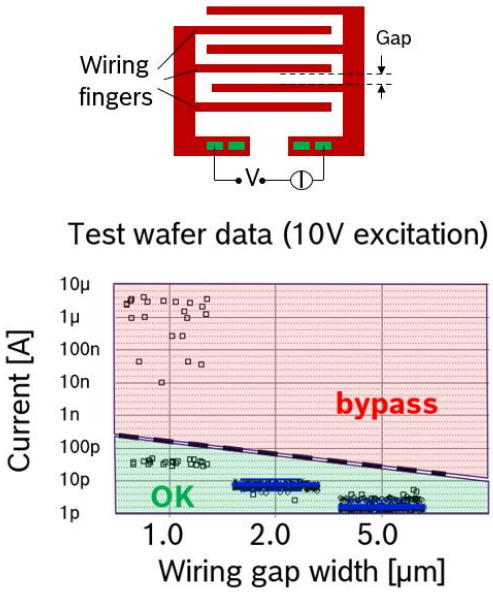

Fig. 3. Test structure (left) to measure the electrical isolation properties of SiRiN. Results (right) indicate that a 2µm gap is sufficient for insulation.

The results are supported by the Federal Ministry for Economic Affairs and Climate Action on the basis of a decision by the German Bundestag, by the Ministry for Economic Affairs, Labor and Tourism of Baden-Württemberg based on a decision of the State Parliament of Baden-Württemberg, the Bavarian State Ministry for Economic Affairs, Regional Development and Energy, as well as co-financed with tax funds on the basis of the budget adopted by the Saxon State Parliament and financed by the European Union - NextGenerationEU.

DOI 10.5162/eurosensors2026/8.2.4

Chip-scale Electrochemical Angular Accelerometer based on SOI Substrate

Maoqi Zhu[1,2], Yulan Lu[1,2], Bowen Liu[3], Deyong Chen[1,2], Junbo Wang[1,2]
[1] Aerospace Information Research Institute, Chinese Academy of Sciences, Beijing 100190, CHINA,
[2] University of Chinese Academy of Sciences, Beijing 100049, CHINA
[3] Minzu University of China, Beijing 100081, CHINA
jbwang@mail.ie.ac.cn

Summary:

This paper reports a chip-scale MEMS electrochemical angular accelerometer (EAA) based on an SOI substrate, featuring a monolithically integrated microchannel and sensitive electrodes. By employing 3D plate electrodes with a reduced 10 μm gap, redundant silicon area is minimized. Enhanced high-frequency sensitivity and lowered noise levels are achieved within a compact 10 × 10 × 1.5 mm³ footprint, making the device well-suited for unmanned aerial vehicle (UAV) attitude detection and control.

Keywords: Electrochemical angular accelerometer, SOI, Chip-scale integration, 3D plate electrode, UAV attitude detection and control.

Background, Motivation and Objective

Angular acceleration detection is the core foundation for achieving stable flight and safe control of unmanned aerial vehicles (UAVs). However, UAV angular acceleration is primarily detected through gyroscope differentiation, which suffers from high latency and low accuracy. While miniaturized electrochemical angular accelerometers (EAAs) [1-3] have been proposed, they are often hindered by rapid sensitivity decay and high noise levels. In this work, an SOI-based EAA is presented that overcomes depth-to-diameter ratio limits. By significantly reducing anode-cathode spacing, the device achieves enhanced bandwidth and high-frequency sensitivity. Furthermore, the optimization of planar electrodes into 3D plate structures minimizes redundant area and lowers the noise floor, effectively addressing the inherent limitations of conventional EAAs.

Description of the New Method or System

A chip-scale sensor microfabrication process utilizing an SOI substrate (300-μm handle / 2-μm buried oxide (BOX) / 40-μm device layer) is proposed. Initially, deep reactive ion etching (DRIE) is performed on the backside to remove the handle layer, followed by reactive ion etching (RIE) of the BOX layer to create through-silicon vias (TSVs). Subsequently, a Ti/Pt bilayer is sputtered for electrode metallization. By leveraging the 40 μm SOI device layer to surpass conventional etching constraints, 3D plate electrodes are defined by DRIE, enabling a significant reduction in anode-cathode spacing from 50 μm to 10 μm. Finally, the processed SOI substrate is bonded to a glass lid through anodic bonding, and the device fabrication is completed by sputtering metal into the electrode vias.

Results

Experimental results show that the proposed EAA achieves a peak sensitivity of 1 V/(rad/s²) at 0.01 Hz, featuring improved high-frequency response and broader bandwidth. Furthermore, the noise level is reduced to 4.52×10^{-6} rad/s²/√Hz (-106.90 dB) at 1 Hz, significantly outperforming the reference devices in Tab 1. The noise reduction stems from optimized anode-cathode spacing, enhanced convection suppression by 3D plate electrodes, and the parasitic-free SOI substrate. These findings offer a valuable reference for developing high-performance miniaturized inertial sensors for drone and aircraft platforms.

References

[1] Zaitsev D L, Agafonov V M,. Precession Azimuth Sensing with Low-Noise Molecular Electronics Angular Sensors. *Journal of Sensors 2016*, 6148019 (2016), doi: 10.1155/2016/6148019.

[2] T Liang, Z Sun, Microelectrochemical Rotational Vibration Sensor With SOI-Based Microelectrodes Used for Seismic Monitoring, *IEEE Transactions on Instrumentation and Measurement* 73, 1-8 (2023), doi: 10.1109/TIM.2023.3330213.

[3] M Zhu, J Wang, Chip-Level Packaged Electrochemical Angular Accelerometer with a Wide Measurement Range, *IEEE Sensors Journal 25*, 18941-18951 (2025), doi: 10.1109/JSEN.2025.3561182.

Figures

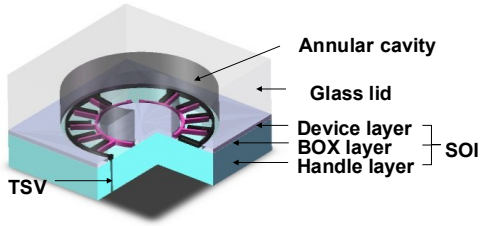

Fig. 1. Diagram of chip-scale EAA based on SOI substrate.

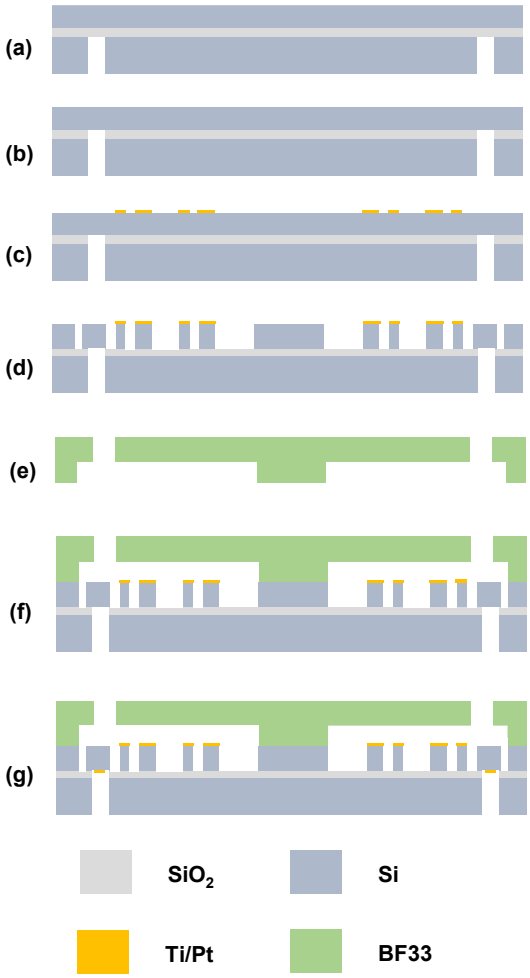

Fig. 2. Fabrication process of the proposed chip-scale EAA.

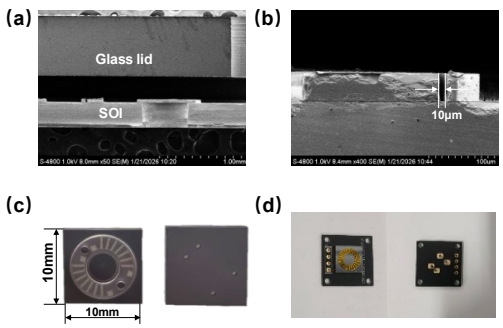

Fig. 3. SEM diagram and physical image of the proposed chip-scale EAA.

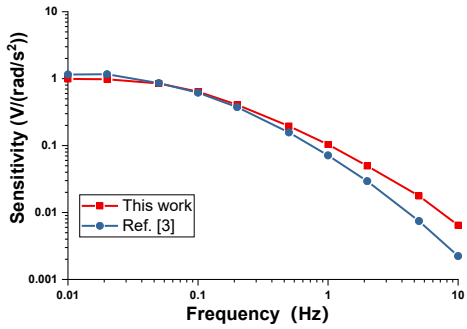

Fig. 4. Graph of sensitivity vs frequency for this work and Ref. [3].

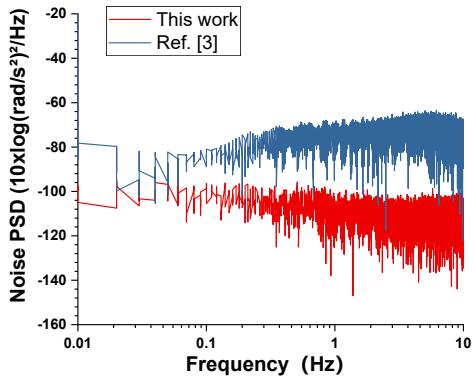

Fig. 5. Graph of Noise Power Spectral Density (PSD) vs frequency for this work and Ref. [3].

Tables

Tab. 1: Performance comparison of the chip-scale EAA fabricated in this study with other devices.

	[1]	[3]	This work
Sensitivity (V/(rad/s^2))	0.5	1	1
Linear range (°/s^2)	297	500	500
Noise level at 1Hz ((rad/s^2) /√Hz)	10^{-4}	7.94×10^{-6}	4.52×10^{-6}
Size(mm^3)	Φ 9×7	10×10×1.5	10×10×1.5

Acknowledgement

This work was funded by the Deep Earth Probe and Mineral Resources Exploration - National Science and Technology Major Project under grant 2024ZD1002503, in part by the National Natural Science Foundation of China under Grant 62571516, Grant 52335012 and Grant U23A20362, in part by Beijing Natural Science Foundation under Grant 4242012, in part by the Youth Innovation Promotion Association CAS under Grant 2023134.

DOI 10.5162/eurosensors2026/8.2.5

Particle-based sensor materials enable plant-inspired upconverting I-Seeds as flying environmental sensors

Albenc Nexha,[1,*] Kliton Cikalleshi,[2] Thomas Kister,[1] Stefano Mariani,[2] Barbara Mazzolai,[2] and Tobias Kraus[1,3]

[1] *INM - Leibniz Institute for New Materials, 66123, Saarbrücken, Germany*
[2] *Bioinspired Soft Robotics Laboratory, Istituto Italiano di Tecnologia, 16163, Genova, Italy*
[3] *Saarland University, Colloid and Interface Chemistry, 66123, Saarbrücken, Germany*
**e-mail: albenc.nexha@leibniz-inm.de*

Environmental parameters are a critical basis for decision-making in precision agriculture, remediation, and emergency management. State of the art probes for remote read-out require electronics based on complex materials that produce *e*-waste.[1] Here, we discuss self-deployable, biocompatible, flying I-Seeds as alternative probes. The bioinspired seeds are designed to provide optical sensor signal to be read using drones equipped with fluorescence light detection and ranging (fLIDAR) technology.

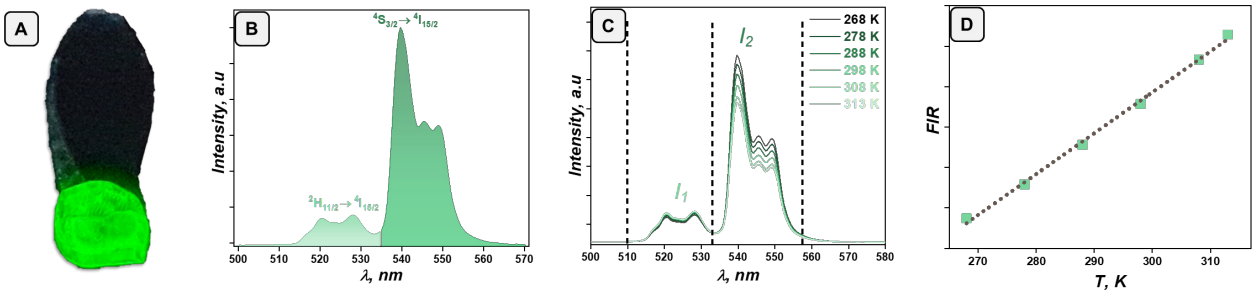

Figure 1: Environmental sensors with ratiometric read-out.[4] (A) I-Seeds were 3D-printed from sensor materials that provide (B) upconverting photoluminestence. (C) Ratiometric analysis of the optical emission enables the reconstruction of environmental parameters, e.g. (D) temperature.

We make I-Seeds from "sensor materials" with upconverting, plasmonic, and fluorescent nanoparticles that are embedded a permeable polymer matrix. The particles are electromagnetically coupled and arranged such that some of them react to environmental conditions or analytes. Others provide reference signals for ratiometric read-out.[2] For example, Hg^0 is detected based on its absorption by gold that causes a plasmonic shift and alters the emission of an upconverting lanthanide-doped particle.[3]

The I-Seeds are designed based on shapes of natural seeds.[4] They are lightweight and carried passively by the wind and dispersed over large distances and areas. We 3D-printed artificial models to emulate the morphometric and aerodynamic characteristics of the natural seeds. Biodegradable polymers (polylactic acid (PLA) and cellulose) are used as matrices to reduce environmental impact.

DOI 10.5162/eurosensors2026/8.2.5

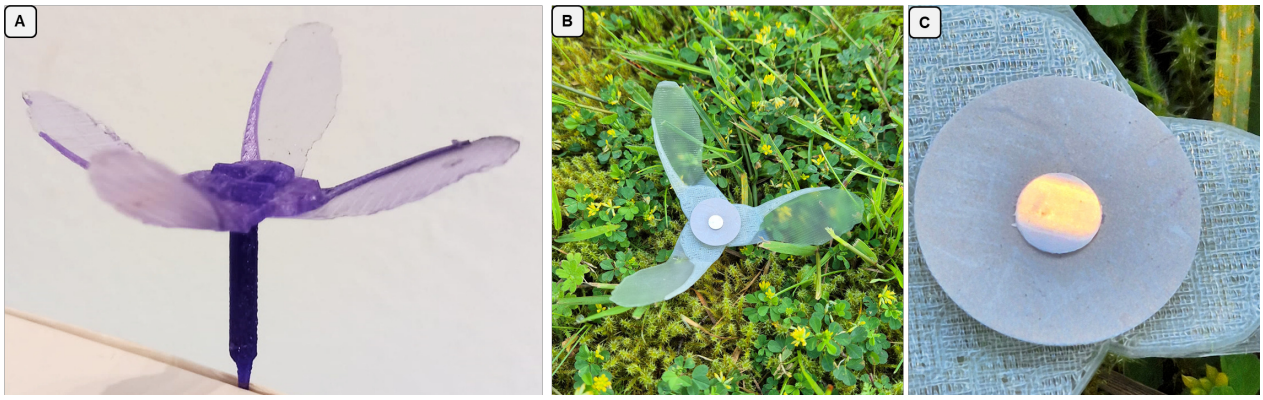

Figure 2: A mercury-sensing I-Seed. (A) The shape was designed to optimize dispersion properties and (B) enable upright landing. (C) The sensor patch detects Hg^0 concentration and can be read from a drone.

We will show I-Seed with upconverting lanthanide doped particles that emit in the red, green and blue (RGB) wavelengths when excited with near infrared (NIR) lasers. The intensity of their fluorescence bands depends on temperature, humidity, CO_2 or Hg^0 concentration. Ratios of different emission bands (in the R, G or B regions) are used to provide robust values for environmental monitoring.

References

[1] R. Ouni, K. Saleem, *Sustainability* **14**, 8356-8382 (2022).
[2] A. Nexha, S. Mariani, K. Cikalleshi, T. Kister, B. Mazzolai, T. Kraus, *Nanoscale* **31**, 18143-18152 (2025).
[3] T. Kister, C. Kaier, T. Kraus: German patent application (2025).
[4] K. Cikalleshi, A. Nexha, T. Kister, M. Ronzan, A. Mondini, S. Mariani, T. Kraus, B. Mazzolai, *Sci. Adv.* **9**, eadi8492 (2023).

DOI 10.5162/eurosensors2026/8.2.6

ZnO@ZIF-8 Doubly Clamped Microbeam Resonator for Detection of VOCs

Divya Rajagopal[1], Chen Wang[1], Barnika Chakraborty[2], Ajay Padunnappattu[3], Bernardo Pereira Madeira[1], Norbert Stock[3], Rainer Adelung[2], and Michael Kraft[1],
[1]Department of Electrical Engineering ESAT, Micro and Nano Systems (MNS), KU Leuven, Leuven, Belgium-3001,
[2]Chair for Functional Nanomaterials, Department of Material Science, Kiel University, Kaiserstr.2, Kiel, Germany- 24143
[3]Institute of Inorganic Chemistry, Kiel University, Max-Eyth-Str. 2, Kiel, Germany-24118
divya.rajagopal@kuleuven.be

Summary:

This paper reports the fabrication and characterization of a doubly clamped ZnO@ZIF-8 microbeam resonator for the detection of volatile organic compounds (VOCs), in which a single heterostructure material provides both actuation and gas sensing functionality. The ZIF-8 layer, with its tuneable porosity and molecular sieving capability, enables selective adsorption of VOC molecules, while the ZnO core ensures efficient piezoelectric actuation. The ZnO@ZIF-8 device exhibits a resonance frequency of 4.5 MHz with a quality factor (Q) of 204. Upon exposure to 300 ppm ethanol, a frequency shift (Δf) of 732 Hz is observed, demonstrating the potential of the proposed structure for VOC sensing applications.

Keywords: ZnO@ZIF-8, microbeam resonator, MOF-based sensor, gas sensing, piezoelectric resonator

Background

Sensitive and selective detection of volatile organic compounds (VOCs) is important for indoor air monitoring and non-invasive diagnostics such as breath analysis. Metal–organic frameworks (MOFs), particularly ZIF-8, are widely studied due to their tuneable porosity and selective adsorption, enabling differentiation between VOC species [1]. These materials operate at room temperature and release adsorbates upon mild heating, making them suitable for low-power sensing.

In contrast, conventional chemiresistive sensors require elevated temperatures (>150 °C) [2], limiting portability. MEMS piezoelectric resonators functionalized with ZIF-8 offer a promising alternative, combining room-temperature operation with high sensitivity. A ZnO@ZIF-8 doubly clamped resonator provides a simpler and more stable platform compared to coupled or multi-degree-of-freedom designs. This work builds on previous studies of ZnO nanowire oscillators [3] and ZnO@ZIF-8 surface conversion techniques [4].

Description of the New Method

This work introduces a ZnO@ZIF-8 microbeam resonator in which a single heterostructure material provides both piezoelectric actuation and gas sensing. The use of tetrapodal ZnO arms with a single-crystalline structure enables efficient charge transport and enhanced piezoelectric performance compared to conventional ZnO nanowires. In this approach, the entire surface of the microbeam is converted into ZnO@ZIF-8, increasing the effective surface area for gas adsorption, while the porous ZIF-8 layer provides molecular sieving capability for selective VOC adsorption. This selectivity is demonstrated through comparative adsorption behaviour of ethanol and toluene in ZnO and ZnO@ZIF-8 devices.

Experimental Procedure

The fabrication sequence is illustrated in Fig. 1. A p-doped Si (100) wafer with a 200 nm thermally grown SiO_2 layer was used as the substrate. Au/Cr electrodes were patterned using UV lithography, RF sputtering, and lift-off, with a gap of 20 µm between pads.

Tetrapodal ZnO (t-ZnO) was synthesized and converted into ZnO@ZIF-8 via surface chemical transformation [4]. The material was dispersed in DI water, drop-cast onto the substrate, and dried at 100 °C for 30s. Individual ZnO@ZIF-8 arms were then positioned across the electrodes using an Omniprobe micromanipulator, dual-beam

SEM/FIB system and fixed by Pt deposition, forming a doubly clamped resonator (Fig. 2). The device was excited using an AC voltage (V_{sd}^{ac} = 0.8 V), and the resonant response was measured using a laser Doppler vibrometer.

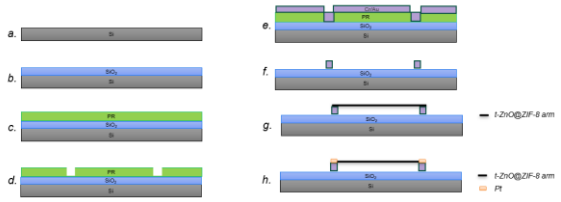

Fig.1. Fabrication process flow of a single ZnO@ZIF-8 doubly clamped microbeam a. substrate preparation, b. thermal oxidation, c. photoresist (PR) spincoating, d. UV exposure and development, e. RF sputtering, f. lift-off photolithography, g. ZnO@ZIF-8 arm pick and placement using Omniprobe micromanipulator, h. Pt deposition for fixing ZnO@ZIF-8 arm.

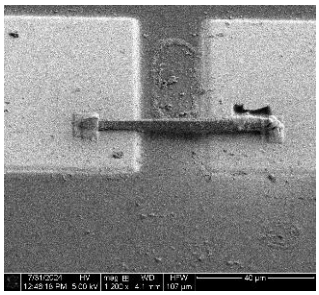

Fig. 2. SEM Image of ZnO@ZIF-8 doubly clamped microbeam

Results

The ZnO@ZIF-8 microbeam resonator exhibited a resonance frequency of approximately 4.5 MHz with a quality factor (Q) of 204 under piezoelectric excitation (V_{sd}^{ac} = 0.8 V). The resonance response was recorded at three stages: t_0 (baseline at room temperature), t_1 (after activation by heating at 100 °C overnight followed by 2 h storage in N_2), and t_2 (after gas exposure for 20 min in a 1.4 L chamber with 1 µL of 99% ethanol). Compared to the bare ZnO device, the ZnO@ZIF-8 microbeam shows ~2x higher response to ethanol than toluene. Upon exposure to 300 ppm ethanol, a frequency shift (Δf) of +1709 Hz and +732 Hz and an amplitude shift of +8E-05 m/s and +40E-05 m/s were observed in bare ZnO and ZnO@ZIF-8 respectively. Notably, the frequency increases upon gas adsorption, which deviates from the conventional mass-loading behaviour of resonant sensors. This suggests that adsorption-induced changes in effective stiffness and surface stress is dominant over the mass loading effect in doubly clamped single crystalline ZnO-based microbeam.

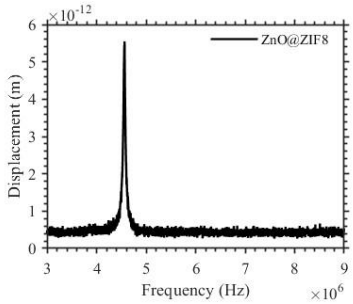

Fig. 3. Resonance spectrum of the ZnO@ZIF-8 doubly clamped microbeam resonator under piezoelectric excitation (V_{sd}^{ac} = 0.8 V), showing a resonance frequency of 4.56 MHz and a quality factor of Q = 204

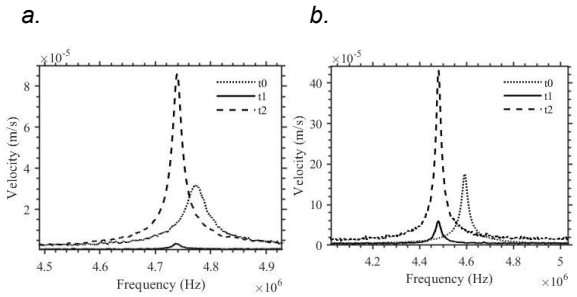

Fig. 4. Resonance response of microbeam resonators under exposure to 300 ppm ethanol in a. Bare ZnO microbeam resonator, b. ZnO@ZIF-8 microbeam resonator. Curves correspond to t_0 (before activation), t_1 (after activation), and t_2 (after exposure).

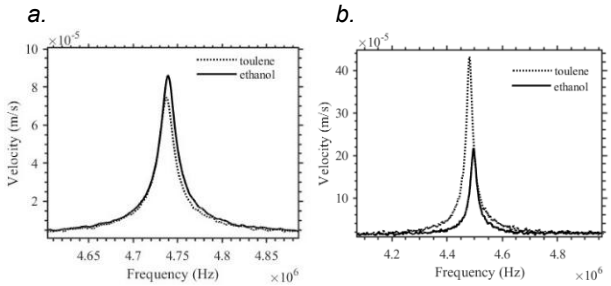

Fig. 5. Gas adsorption characteristics of ethanol and toluene in a. ZnO microbeam resonator, b. ZnO@ZIF-8 microbeam resonator

Acknowledgement

Funded by the European Union (Marie Skłodowska-Curie grant agreement no 101072845 (SENNET)) HORIZON Europe.

References

[1] M. Tu et al., Adv. Funct. Mater. 25, 4470–4479 (2015); doi: 10.1002/adfm.201500333
[2] R. Lv et al., Sensors 21, 4069 (2021); doi: 10.3390/s21124069
[3] R. Zhu et al., Nanotechnology 19, 285712 (2008); doi: 10.1088/0957-4484/19/28/285712
[4] M. P. M. Poschmann et al., ACS Appl. Mater. Interfaces 15, 38674–38681 (2023); doi: 10.1021/acsami.3c08873

DOI 10.5162/eurosensors2026/8.3.1

Biodegradable Technologies for Medical and Environmental Applications

Clementine M. Boutry
TU Delft, Mekelweg 4, 2628 CD Delft, The Netherlands
c.m.f.viellard-boutry@tudelft.nl

Abstract:

Interfacing biological tissues with artificial implants for therapeutic purposes presents significant challenges. Devices must be miniaturized without compromising performance, and wireless operation is crucial to limit infection risks and improve patient comfort. In some applications, biodegradability offers an additional benefit by enabling implants to safely resorb after use. While biomedical MEMS have driven major advances, including cochlear implants and spinal cord stimulators, their roots in conventional semiconductor manufacturing make them not always suited to the soft and dynamic environment of the human body. Materials and fabrication approaches must therefore evolve to meet biomedical constraints. Soft, stretchable materials enhance mechanical compatibility and reduce inflammation, while biodegradable systems avoid secondary surgeries and minimize long-term tissue damage.

Our work aims to establish a new class of fully biodegradable, wireless MEMS integrating sensors, actuators, and electronics. We develop bioresorbable microsystems for wearable and organ-on-chip platforms, implants with integrated actuation and micropumping for peripheral nerve repair, ultrathin silicon-based devices for cardiac transplant monitoring, and soft robotic systems designed to support and restore cardiac function.

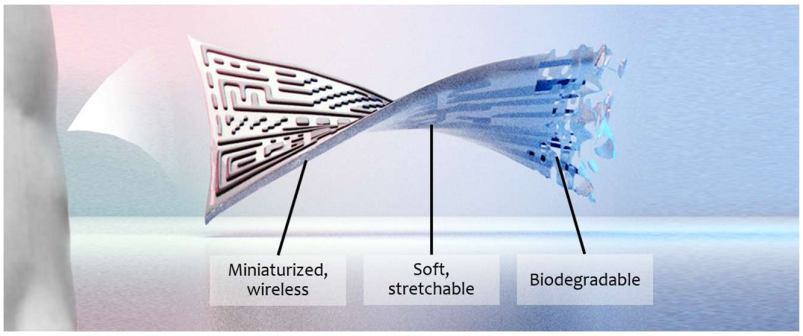

Fig. 1 - Biodegradable MEMS for medical applications

Keywords:

Biodegradable MEMS, Implantable medical devices, Wireless bioelectronics, Soft robotics, Bioresorbable materials

References:

[1] M. J. Bathaei, A. Golparvar, D. Nikolayev, F. Arroyo Cardoso, C. M. Boutry, Biodegradable, Battery-free, Smart Face Mask Embedded Passive Antenna for Continuous Acoustic Biomarkers Monitoring in Pulmonology, ACS Sensors (2026); accepted for publication

[2] E. Aprea, F. Pirim-Aslan, F. Stallone, V. Gkouzioti, L. Abelmann, J. P. Frimat, L. Sarro, C. M. Boutry, A biodegradable implantable micropump for biomedical applications, focusing on peripheral nerve repair, Nano Research (2025); accepted for publication

[3] P. Uliss, W. Hanggai, F. Kahler, E. Aprea, Q. Jia, V. Gkouzioti, J. P. Frimat, E. Brück, C. M. Boutry, Burn-Safe Biodegradable Magnetocaloric Composites for Temperature-Controlled Biomedical Applications, Advanced Science e09914 (2025)

[4] M. J. Bathaei, Y. Bathaei, Z. Liao, M. Yazdanmehr, S. S. Sethi, D. Nikolayev, F. Arroyo Cardoso, C. M. Boutry, Environmental and Ecological Monitoring with Biodegradable Technologies, Advanced Science e11452 (2025)

[5] Z. Liao, A. Golparvar, M. J. Bathaei, F. Arroyo Cardoso, C. M. Boutry, Wearable and Implantable Devices for Continuous Monitoring of Muscle Physiological Activity: A Review, Advanced Science e09934 (2025)

DOI 10.5162/eurosensors2026/8.3.2

Smart phone enabled, thin-film epidermal electronic systems for cardiac health monitoring

Sven Ingebrandt[1], Dongli Zhang[1], Milad Eyvazi Hesar[1], Henning Gall[2], Ralf Schermuly[2], Hossein Ardeschir Ghofrani[2], Ziyu Gao[1]
[1] RWTH Aachen University, Institute of Materials in Electrical Engineering 1, Aachen, Germany
[2] Justus-Liebig-University Giessen, Department of Internal Medicine, Giessen, Germany
ingebrandt@iwe1.rwth-aachen.de

Summary:

We present several skin-close, hybrid Epidermal Electronics Systems (EES) for cardiac monitoring. They combine electrodes for electrocardiography (ECG) and piezoelectric thin-film sensors for seismocardiography (SCG). We utilized the near field communication (NFC) functionality of a smart phone to power the systems, to pre-process and classify the data and to transfer it via RFID. Our modular EESs ensure versatility, while providing comfort and high signal quality, enabling accurate and real-time cardiac health monitoring. We demonstrate that the EESs can be used for cardiac diagnosis.

Keywords: Wearable sensors, cardiac monitoring, cardio-pulmonary hypertension, sensor fusion, AI-based data analysis

Introduction

Cardiac monitoring is essential for early detection and management of heart conditions, yet conventional devices are often bulky and uncomfortable, limiting patient compliance. We present advanced, thin-film embedded monitoring systems capable of measuring ECG and SCG simultaneously. The synchronous data acquisition allows for accurate extraction of systolic time intervals (STI), which provide insights into dynamic cardiac function. We tested the systems on a group of patients suffering from pulmonary hypertension and were able to distinguish healthy from diseased patients. Building on these promising results, we developed a next system offering enhanced integration, modularity, and functionality. To enable long-term monitoring away from bed side application, we aim to combine the EES systems with smart textiles as Hybrid E-Tattoos.

Background, Motivation and Objective

The different EESs developed in the clean room of IWE1 at RWTH Aachen university comprise a flexible circuit module based on polyimide (PI) and either a flexible unit based on PI or a stretchable electrode module made from Flexdym™. The circuit module was fabricated using a cleanroom microelectronics process, including photolithography, evaporation, and electroplating, ensuring precise patterning and high-quality connections. The stretchable module was produced via a screen-printing process, providing excellent elasticity and adaptability. Both modules were then interconnected either by direct gluing or by using magnetic snaps, enabling easy assembly and separation.

Results

The classical method to detect the excitation of the heart is ECG, where several electrodes are positioned on the chest of a person on precise locations and different lead signal shapes are combined to analyze the condition of the heart. In many wearable solutions, only the first lead signals are measured (left to right arm), a functionality which is for instance also integrated into modern smart watches.

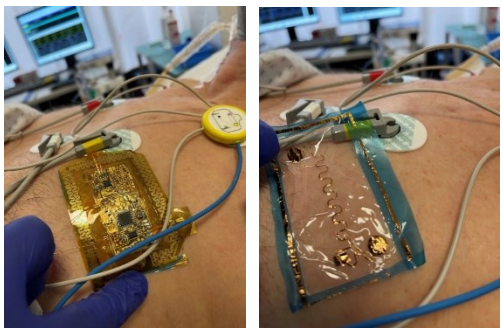

Figure 1: *A modular EES generated with a stretchable thin film material and a flexible, reusable part is used in the intensive care unit in the clinic of Giessen University on the chest of a test person.*

An older method for cardiac monitoring, which is experiencing a renaissance nowadays, is based on vibration sensing and sub-summed in the term ballistography. A special from of this

method is SCG, where sensitive vibration sensors are positioned at the chest of a test person very closely at similar locations as for classical ECG. In earlier works it was described that in SCG traces the action of cardiac valves such as aortic opening (AO) and aortic closing (AC) can be seen as similar characteristic fiducial points like the QRS complex in ECG. The precise understanding of the signal origins and signal shapes measured from different points at the chest is typically based on signal conditioning, filtering and precise timing analysis [1].

In a first approach for a wearable EES, we integrated a thin-film sensor based on the piezoelectronic polymer polyvinylidene fluoride (PVDF) into a polyimide based multilayer system and recorded ECG traces with a second system in a synchronized manner [2].

In the next generation of EES devices, a wearable, flexible, wireless and smartphone-enabled system-in-a-foil with synchronous first-lead ECG and SCG functionality was fabricated using state-of-the-art cleanroom technologies. The timing between the Q peak of ECG and the AO and AC peaks of SCG was automatically analyzed by AI-enabled classification of peaks and extraction of the timing between the STI parameters pre-ejection period (PEP) and left ventricular ejection time (LVET). For this purpose, we developed a machine-learning algorithm and trained it on public ECG data and SCG signals to annotate peaks and analyze their precise timing. The ratio between both peaks is called the Weissler's index, which can be used as prognostic parameter for hypertension. Tests with healthy control persons and patients with cardiopulmonary hypertension showed a promising prognostic performance (Fig. 1) [3].

Next step towards a modular EES

For the next step in the project, the skin-mounted part of the EES was realized in the thermoplastic elastomer styrene-ethylene-butylene-styrene (SEBS), a skin-friendly stretchable material. This stretchable module was produced via a screen-printing process with liquid metal as conductive tracks, providing excellent elasticity and adaptability [4].

Figure 2: *A schematic of the hybrid and modular design concept of the EES. It integrates a reusable circuit module and a disposable on-skin module. Both modules can be combined by magnetic snaps.*

Both modules were then interconnected using magnetic snaps, enabling easy assembly and separation (Fig. 2).
In the newer, modular version a MEMS-based 3-axis accelerometer was used to detect the SCG signals while offering additional functions such as body conditions such as lying, walking or running.

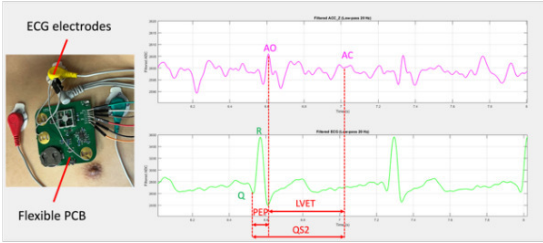

Figure 3: *Left: Measurement setup with the prototype PCB. Right: A section of the measured SCG traces (top) and ECG traces (bottom) signals, highlighting key waveform components - AO and AC in SCG, and the QRS complex in ECG.*

Conclusion and Outlook

A proof-of-concept EES with a thin-film electronics design was demonstrated through successful prototyping. The next phase in our project will focus on fabricating and assembling both flexible and stretchable modules, further advancing the functionality and integrity of the EES. To enable a better comfort for the persons, we combine the on-skin wearables with smart textiles to enable long-term recording.

References

[1] M. Eyvazi Hesar, W. Madhat Munief, A. Müller, N. Ponon, S. Ingebrandt, *Current Directions in Biomedical Engineering* 6, 583-586 (2022); doi: 10.1515/cdbme-2020-3149

[2] M. Eyvazi Hesar, D. Khan, N.S. Seyedsadrkhani, S. Ingebrandt, *ACS Applied Electronic Materials* 3, 11-20 (2021); doi: 10.1021/acsaelm.0c00768

[3] M. Eyvazi Hesar, N.S. Seyedsadrkhani, D. Khan, A. Naghashian, M. Piekarski, H. Gall, R. Schermuly, H.A. Ghofrani, S.Ingebrandt, *Biosensors and Bioelectronics* 241, 1, 115693 (2023); doi: 10.1016/j.bios.2023.115693

[4] M.E. Hesar, D. Khan, S. Ingebrandt, *De Gruyter* 8, 757-760 (2022); doi: 10.1515/cdbme-2022-1193

Acknowledgements

Funding came from the project KMU-innovative SINDynamik "Single-point sensor system for non-invasive, dynamic measurement of cardiac function" (13GW0180B), from the CORNET project "Hybrid E-Tattoo: a platform for sensor fusion of smart textiles and skin adhesives for the next generation of smart wearables" (IGF 351 EN) and from the RWTH Aachen University. Throughout the years, several bachelor and master students of RWTH Aachen University were involved in the technical developments.

DOI 10.5162/eurosensors2026/8.3.3

Transient Battery-Free Microphone-Integrated Face Mask

Mohammad Javad Bathaei[1], Ata Golparvar[1], Sina Hashemizadeh[2], Denys Nikolayev[3], Filipe Arroyo Cardoso[1], and Clementine M. Boutry[1]
[1] Department of Microelectronics, Delft University of Technology, Delft, 2628 CD, The Netherlands
[2] Foundation for Research on Information Technologies in Society (IT'IS), Zurich, 8004, Switzerland
[3] Institut d'électronique et des technologies du numérique (IETR UMR 6164), French National Center-for Scientific Research (CNRS) / University of Rennes, Rennes, 35042, France
C.M.F.Viellard-Boutry@tudelft.nl

Summary:

We introduce a transient, battery-free intelligent face mask for cough acoustic monitoring in pulmonology. It integrates a flexible passive microphone with a 3×3 membrane array coupled with a patch antenna, converting cough-induced vibrations into shifts in the electromagnetic reflection coefficient measured in zero-span mode. Fabricated from laser-patterned cellulose acetate, poly(lactic acid), and zinc, and stacked via a solvent- and adhesive-free low-temperature lamination process, the system enables detection of various cough intensities in humans, with over 90% degradation within 100 days.

Keywords: Smart face mask, Transient electronics, Green manufacturing, Patch antenna, Cough acoustics sensing

Background, Motivation and Objective

Cough is a fundamental early symptom of respiratory disease, and its acoustic characteristics—such as frequency, amplitude, and spectral features—offer a non-invasive and diagnostically specific modality for disease assessment [1]. Recent advances in wearable technologies have enabled continuous monitoring of respiratory health through chemical (e.g., volatile organic compounds in exhaled breath), physiological (e.g., respiratory rate, tidal volume), and acoustic signals. However, chemical sensing approaches are often limited by cross-sensitivity to environmental and metabolic factors, while physiological metrics lack specificity due to variability induced by non-respiratory conditions [2]. In contrast, cough acoustics provide event-driven signatures with high diagnostic specificity and robustness. Despite these advantages, existing wearable and mask-based systems predominantly rely on active microphones and bulky, non-biodegradable electronics powered by batteries that require periodic replacement, thereby limiting user compliance and scalability while exacerbating electronic waste [3]. Accordingly, this work aims to develop a scalable, battery-free, and biodegradable platform for continuous cough acoustic monitoring, leveraging sustainable materials and environmentally responsible fabrication processes. This abstract presents preliminary results from our platform, as part of our recent work [4].

Description of the New Method or System

To address the need for scalable, sustainable cough-monitoring technologies, we introduce a biodegradable passive acoustic sensing system integrated into a single-use face mask. In contrast to conventional battery-powered, non-biodegradable mask-based systems, the proposed device performs acoustic sensing via a membrane-coupled patch antenna, in which sound-induced vibrations modulate the antenna's electromagnetic reflection coefficient. The system is fabricated entirely from sustainably sourced materials using a green manufacturing approach that combines laser processing with thermal lamination, enabling scalable production of fully biodegradable sensing devices.

Results

The device was fabricated using CO_2 laser machining (λ = 10.6 µm) followed by stepwise thermal lamination. Zinc (Zn, 10 µm), polylactic acid (PLA, 50 µm), and cellulose acetate (CA, 25–500 µm) films were laser patterned; the Zn as antenna conductor (patch and ground) was cut at 50 W and 1 cm/s (see Fig. 1a). Aligned layers were stacked using alignment marks and laminated between Teflon sheets. A 25 µm CA membrane was first bonded to a 100 µm CA base at

150 °C. The antenna stack (PLA/CA/Zn) was then laminated at 120 °C, above the PLA glass transition temperature (Tg = 50–65 °C), ensuring strong bonding. The PLA (50 µm) layer served as an encapsulating lamination pouch. The resonator was assembled using 100 µm PLA spacers to realize the final membrane-integrated patch antenna device (see Fig. 1b). The final device was integrated into a PLA-based surgical face mask (Fig. 1c).

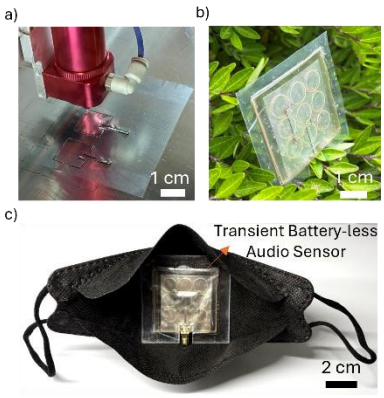

Fig. 1. a) Laser cutting of Zinc foil. b) Assembled device. c) Smart face mask integrated with a patch antenna-based device.

The dimensions of the patch antenna and acoustic resonator were optimized in CST Microwave Studio under face mask size constraints to achieve resonance at ~6 GHz.

Figure 2 shows the membrane response under 500 Hz acoustic excitation. The setup (Fig. 2a) uses a loudspeaker to excite the cellulose acetate membrane and a confocal sensor to measure the membrane displacement. The time-domain signal (Fig. 2b) shows three bursts, each reaching a peak displacement of ~11 µm. The Fast Fourier Transform (FFT) (Fig. 2c) exhibits a dominant peak at 500 Hz, which matches the sound frequency. The Short-Time Fourier Transform (STFT) (Fig. 3d) confirms sustained oscillation at 500 Hz with weaker harmonics at ~1 kHz

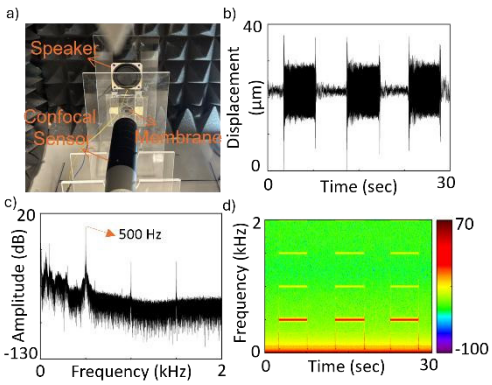

Fig. 2. a) Measurement setup. b) Time-domain displacement plot. c) FFT peak at 500 Hz. d) STFT spectrogram showing 500 Hz with harmonics (intensity in dB).

and ~1.5 kHz, indicating nonlinear excitation. The lower displacement at lower frequencies reflects viscoelastic, mass-controlled behavior, with increasing damping at higher frequencies.

Figure 3a presents the STFT spectrogram of the reflection coefficient ($|S_{11}|$) recorded in zero-span mode using a vector network analyzer (VNA), capturing real cough events. Distinct STFT signatures differentiate cough severity: mild (<200 Hz, low intensity), moderate (~300 Hz), and severe (broad, high-intensity spectrum up to ~600 Hz). Industrial composting was simulated using water-saturated compost soil with controlled moisture and gas flow (see Fig. 3b). The PLA-based mask half embedded in soil fully degraded within 20 days, while the device lost ~90% of its weight after 100 days (Fig. 3c).

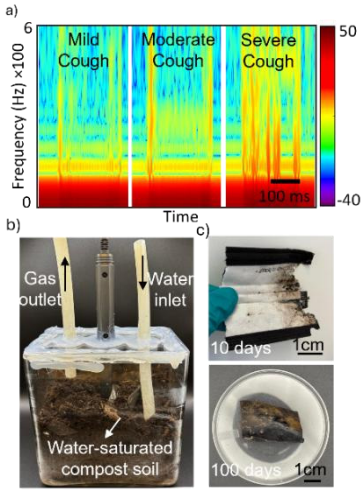

Fig. 3. a) STFT of $|S_{11}|$ (zero-span mode) showing mild, moderate, and severe cough signatures (intensity in dB). b) Industrial composting setup. c) Degradation of the facemask and device in soil.

References

[1] L. E. Witjaksono, et al., Cough Monitoring Systems in Adults with Chronic Respiratory Diseases: A Systematic Review, *Eur. Respir. Rev*. 34, 175 (2025); doi: 10.1183/16000617.0212-2023.

[2] M. Basanta, et al., Exhaled Volatile Organic Compounds for Phenotyping Chronic Obstructive Pulmonary Disease: A Cross-Sectional Study, *Respir. Res.* 13, 1 (2012); doi: 10.1186/1465-9921-13-72.

[3] Z. Ye, et al., A Breathable, Reusable, and Zero-Power Smart Face Mask for Wireless Cough and Mask-Wearing Monitoring, *ACS Nano.* 16, 5874–5884 (2022); doi: 10.1021/acsnano.1c11041.

[4] M. J. Bathaei, et al., Biodegradable Smart Face Mask for Cough Acoustic Sensing, *ACS Sensors. 11,* 5535-5552 (2026); doi: 10.1021/acssensors.5c04572.

Acknowledgement

MJB, FAC, and CMB acknowledge support from the Dutch High Tech for a Sustainable Future (HTSF) 4TU Green Sensors grant.

DOI 10.5162/eurosensors2026/8.3.4

Ultrathin Wearable Thermochromic Tattoo-Based Skin Sensor

Katrin Unger[1], Rudolf Heer[1], Paulina Piller[1]
[1] Silicon Austria Labs GmbH, 8010 Graz, Austria
paulina.piller@silicon-austria.com

Summary:

Continuous, non-invasive skin temperature monitoring is essential for healthcare and sports applications. We present an ultrathin, skin-conformal thermochromic temporary tattoo sensor. Its flexible, permeable structure enables intimate skin contact and high wearing comfort. The sensor, based on tattoo paper functionalized with a leuco-dye layer, exhibits a thickness of (1.7 ± 0.2) µm and changes color from purple to pink at (27.2 ± 0.5) °C, enabling the detection of abnormal skin temperatures associated with impaired perfusion.

Keywords: Ultrathin Temporary Tattoo-Based Sensor, Wearable Thermochromic Sensor, Leuco Dye, Colorimetric Sensing, Skin Temperature Sensing

Background, Motivation and Objective

Human skin serves not only as a protective and sensory organ but also as a crucial interface for thermal exchange with the environment. Spatial variations in skin surface temperature provide valuable diagnostic information for pathological conditions such as vascular disorders, inflammation, and cancer. Infrared thermography is a widely used non-invasive technique for mapping skin temperature. However, it is limited by motion artifacts, sensitivity to measurement geometry, and restricted accuracy in detecting small or localized abnormalities. [1]

To overcome these limitations, alternative approaches based on wearable thin-film sensors have been developed, employing electronic and/or colorimetric readout mechanisms. [2-3] These systems typically consist of flexible substrates combined with thermosensitive materials and must be designed to minimize thermal interference with the skin. Achieving ultrathin architecture is essential to ensure accurate measurements and maintain soft, conformal contact with the epidermis during natural movement. While electronic sensors can reach sub-micron thicknesses, reported colorimetric devices are generally thicker, and ultrathin implementations remain scarce despite their inherent advantages, such as battery-free operation. [4-6]

Temporary tattoo substrates provide a promising platform for transferring ultrathin sensors on the skin. These systems enable intimate skin contact through a simple transfer process and have already been applied in electrochemical and electrophysiological sensing. [7-8] Building on this concept, they offer significant potential for the development of minimally invasive, conformal skin temperature sensors.

Description of the New System

In this work, a temporary tattoo paper substrate is utilized to realize an ultrathin thermochromic skin sensor with a total thickness below 2 µm. This represents a significant reduction compared to previously reported colorimetric wearable sensors, which typically exhibit thicknesses in the tens of micrometers to millimeter range. By functionalizing commercially available tattoo paper with a thin layer of thermochromic leuco dye, the presented system constitutes, to the best of our knowledge, the thinnest colorimetric on-skin temperature sensor reported to date.

Leuco dyes exhibit reversible switching between colorless and colored state in response to external stimuli such as temperature, light, or pH. Their thermochromic behavior enables straightforward, power-free temperature sensing and has previously been exploited in wearable systems. However, their implementation in ultrathin, tattoo-based platforms has not yet been demonstrated at this thickness scale. [9]

The proposed approach advances the state of the art by combining sub-2 µm thickness, conformal tattoo transfer, and battery-free colorimetric sensing in a single platform. This enables minimally invasive, highly compliant skin sensors

with reduced thermal interference and improved adaptability to natural skin motion.

Results

A thin leuco dye layer was successfully deposited onto temporary tattoo paper, which appears macroscopically homogeneous and retains full transferability onto skin, enabling reliable transfer and yielding an ultrathin, mechanically compliant system with strong conformity to skin microtopography (Figure 1).

(a) (b) (c)

Fig. 1. (a) As-prepared tattoo sensor showing a localized area of temperature change upon exposure to a fingertip. (b) Applied tattoo sensor on a cooled arm, showing localized color change induced by underlying arterial heating. (c) Tattoo sensor applied conformally on skin.

Thickness analysis via optical and laser confocal microscopy reveals a transfer layer thickness of (610 ± 50) nm and a total sensor thickness of (1.7 ± 0.2) µm. This is significantly thinner than previously reported colorimetric skin sensors (~ 40 µm [6]), representing an approximate 20-fold reduction and enabling improved skin conformity and reduced thermal interference.

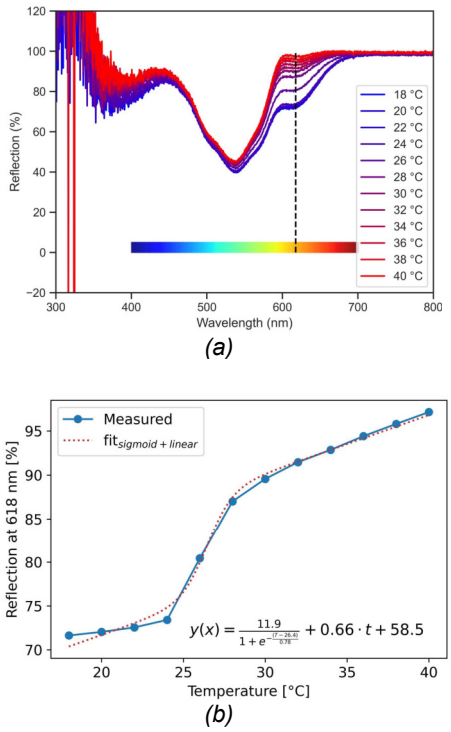

Fig. 2. (a) Reflection spectra of the sensor at temperatures between 18 – 40 °C. (b) Reflection at 618 nm of the sensor in relation to the temperature.

Optical measurements show temperature-dependent changes between 18 – 40 °C, with a characteristic decrease in absorption at 618 nm upon heating (Figure 2a). The reflectivity at this wavelength increases from 64 % to 87 %, following a sigmoidal trend corresponding to the thermochromic transition of the leuco dye. A transition temperature of T_C = (26.4 ± 0.3) °C is determined (Figure 2b).

The sensor exhibits a fully reversible thermochromic response over multiple temperature cycles, changing from purple to pink upon heating above the defined transition temperature, confirming the switching behavior of the leuco dye. This stable and repeatable performance demonstrates the feasibility of an ultrathin, conformal, and reliable colorimetric skin temperature sensor based on temporary tattoo substrates for non-invasive, real-time skin temperature monitoring and related thermally responsive applications.

References

[1] Liu, Q. et al. Infrared thermography in clinical practice: a literature review, *European journal of medical research* 30, 33 (2025); doi: 10.1186/s40001-025-02278-z

[2] Anbuselvam, B. et al. Wearable biosensors in cardiovascular disease, *Clinica Chimica Acta* 561 (2024); doi: 10.1016/j.cca.2024

[3] Mo, F. et al. Review of Conductive Hydrogel-Based Wearable Temperature Sensors, *Advanced Healthcare Materials* 13 (2024); doi: 10.1002/adhm.202401503

[4] Gao, L. et al. Epidermal photonic devices for quantitative imaging of temperature and thermal transport characteristics of the skin, *Nat Commun* 5 (2014); doi: 10.1038/ncomms5938

[5] Zhao, S. & Zhu, R. Electronic Skin with Multifunction Sensors Based on Thermosensation, *Advanced Materials* 29 (2017); doi: 10.1002/adma.201606151

[6] He, Y. et al. Facile flexible reversible thermochromic membranes based on micro/nanoencapsulated phase change materials for wearable temperature sensor, *Appl Energy* 247, 615–629 (2019); doi: 10.1016/j.apenergy.2019.04.077

[7] Ferrari, L. M. et al. E. Conducting polymer tattoo electrodes in clinical electro-and magneto-encephalography, *Nature* 4 (2020); doi: 10.1038/s41528-020-0067-z

[8] Spanu, A. et al. Parylene C-Based, Breathable Tattoo Electrodes for High-Quality Bio-Potential Measurements, *Front Bioeng Biotechnol* 10 (2022); doi: 10.3389/fbioe.2022.820217

Gudadur, K. S. & Kumar, A. Wearable reversible based polyoxymethylenmelamine blue 63 methyl stearate thermochromic membrane for temperature sensing, *Polymer* 325 (2025); doi: 10.1016/j.polymer.2025.128225

DOI 10.5162/eurosensors2026/8.3.5

Reduced Recovery Time after Free Flap Surgery by means of Textile Sensor Systems

Ekaterina Maevskaia[1], Luisa Lotter[2], Jonas Gartmann[3], André Kupferschmid[3], Martin Camenzind[1], Alexander Haag[4], Charlotte Lemière-Franzetti[1,5], Tessa Eugster[2], René M. Rossi[1], Volker J. Schmidt[2], Simon Annaheim[1]

[1] Empa, Laboratory for Biomimetic Membranes and Textiles, Lerchenfeldstrasse 5, 9014 St. Gallen, Switzerland

[2] HOCH, Health Ostschweiz, Department of Plastic Surgery and Handsurgery, Rorschacher Strasse 95, 9007 St. Gallen, Switzerland

[3] Empa, Transport at Nanoscale Interfaces Laboratory, Überlandstrasse 129, 8600 Dübendorf, Switzerland

[4] FRTI Inter Spitzen AG, Flurhofstrasse 150, 9000 St. Gallen, Switzerland

[5] ENSISA, 12 Rue des Frères Lumière, 68093 Mulhouse, France

ekaterina.maevskaia@empa.ch

Summary:

Continuous postoperative perfusion monitoring enables individualized patient care after free microsurgical flap reconstruction of complex wound defects. Pressure and tissue perfusion are key parameters influencing recovery, motivating the development of a sensing system for their monitoring. The individual sensors were developed and demonstrated sufficient sensitivity and reliable performance, and are now being integrated into a single textile-based system, which will be further evaluated in clinical settings.

Keywords: Reconstructive microsurgery, free flaps, postoperative monitoring, pressure sensing, tissue perfusion

Background, Motivation and Objective

Free flap soft tissue reconstruction involves transferring a vascularized tissue from a donor site to a recipient site by means of microsurgical techniques. A common postoperative treatment following lower limb reconstruction with free flaps is the dangling procedure which is used to reduce the risk of complications such as partial or total flap necrosis due to early hydrostatic stress. During dangling, the reconstructed limb containing the transferred free flap is gradually subjected to systematic hydrostatic stress loading by placing the leg in a temporarily vertical position according to a defined protocol. This results in an increase in pressure within the flap due to the absence of lymphatic vessel connections, and may also lead to reduced perfusion at the tip of the flap relative to the supplying pedicle vessel [1]. Both these parameters are essential for successful recovery. Excessive or prolonged pressure impairs microcirculation and delays healing [2], while inadequate perfusion may lead to hypoxia and tissue necrosis [3]. Therefore, continuous monitoring of both parameters is essential to gain a better understanding about the healing conditions. Further, the technique should identify flaps that are early adapted to hydrostatic stress in order to circumvent the routinely used dangling protocol that is usually performed over 5 days during the acute hospital stay. A detailed knowledge about the individual stress response would support clinical decision-making and enable a more personalized and shorter dangling protocol. Providing this information through a system integrated into a bandage would facilitate practical implementation. The aim of this study is therefore to develop a textile-based sensing system capable of continuously monitoring pressure and oxygen saturation.

Description of the New Method or System

The sensing system consists of oxygen saturation sensors integrated into a pressure sensing textile. The pressure sensing system was developed by FRTI a Business Unit of Inter Spitzen AG (St. Gallen, Switzerland) using the embroidered pressure sensing technology. The sensors based on piezoresistive fibers were arranged in a woven textile structure comprising 32 sensing elements (4 x 8 grid) with a sensing area of 10 x 22 cm².

Applied pressure induces changes in electrical resistance in each sensing element separately, enabling measurement of both pressure magnitude and spatial distribution across the flap reconstructed wound and the surrounding healthy

tissue. Conductive fibers integrated into the textile allow signal transmission to external electronics. The system was characterized within a pressure range of 0.5–5 kPa with step sizes of 0.1 kPa, 0.25 kPa, and 0.5 kPa. This range was selected to correspond to previously reported interstitial muscle flap pressures [4].

To simulate 3D conditions, the pressure sensors were tested using an artificial leg model consisting of a manikin limb covered with an inflatable sleeve. By inflating the sleeve, the stiffness of the structure increases, simulating oedema and inflammatory conditions. The applied air pressure was adjusted to represent normal and oedemic tissue states, as assessed by palpation performed by clinical personnel.

Electronics for the saturation sensor arrays were developed at the Transport at Nanoscale Interfaces Laboratory at Empa (Dübendorf, Switzerland). The system consists of eight sensors connected to a single control unit, allowing simultaneous measurements. Each sensor array integrates a pulse oximetry and heart rate biosensor module (MAX30102, Analog Devices, Inc., Wilmington, MA) connected to a PCA9615DP that converts the standard I^2C interface to differential I^2C signaling. This configuration provides signal integrity and proper line termination at both ends, one at the sensor node and one at the eight channel hub, ensuring reliable data communication over cable lengths of up to approximately 3 m. The battery powered system is managed by a central control unit equipped with an SD card slot for local data storage, a Bluetooth interface for wireless configuration, and a USB port for data transfer.

The presence of red and infrared LEDs enables measurement of absorption differences between oxygenated and deoxygenated hemoglobin. LED intensities were optimized individually for different anatomical locations (finger, forearm, thigh, calf, and neck). To ensure suitability for postoperative monitoring, the influence of bandaging on signal quality was also evaluated. Finally, sensor performance was validated against a commercial pulse oximeter (WristOx2 Model 3150, Nonin, Tilburg, Netherlands).

The two systems are currently being integrated into a single textile-based system. It is further laminated with polyurethane layer to ensure durability and allow cleaning between participants. Pressure and oxygen saturation measurements will be repeated to confirm that the integrated system maintains performance and that interaction between sensors remains minimal. This includes evaluation of measurement repeatability as well as comparison of sensor behavior before and after integration.

Results

The pressure sensing system demonstrated stable and repeatable responses under both increasing and decreasing pressure conditions. Pressure changes above 1 kPa could be reliably detected, with a sensitivity of approximately 0.1 kPa. Tests on the leg model confirmed the ability of the pressure sensing system to detect simulated inflammation by changes in local stiffness.

For the oxygen saturation sensors, signal quality was influenced by LED intensity, sensor location, and applied pressure. Optimal LED settings were determined for each anatomical site. When compared with the reference device, the developed sensors demonstrated good agreement with a root mean square error of 1.4% SpO_2, supporting their potential use for perfusion monitoring applications. Additionally, the application of a bandage improved the signal-to-noise ratio (SNR), increasing it from 19.2 dB (no bandage) to 25.6 dB (bandage). The bandaged configuration also exhibited more stable periodic pulsations, supporting the system's potential applicability in clinical settings.

Future studies will involve healthy participants, where the system will be tested under varying bandage conditions. Subsequently, clinical studies in patients undergoing free flap surgery are planned to compare standard monitoring methods during the dangling procedure with the developed system. This approach aims to enable data-driven personalization of the dangling protocol and ultimately improve postoperative outcomes.

References

[1] D. D. Krijgh et al., Is dangling of the lower leg after a free flap reconstruction necessary? Study protocol for a large multicenter randomized controlled study, Trials, 20(1), 558 (2019); doi: 10.1186/s13063-019-3665-0

[2] A. Leal-Junior, J. Guo, R. Min, A. J. Fernandes, A. Frizera, and C. Marques, Photonic smart bandage for wound healing assessment, Photonics Res., 9(3), 272–280 (2021); doi: 10.1364/PRJ.410168

[3] P. Mostafalu, W. Lenk, M. R. Dokmeci, B. Ziaie, A. Khademhosseini, and S. R. Sonkusale, Wireless Flexible Smart Bandage for Continuous Monitoring of Wound Oxygenation, IEEE Trans. Biomed. Circuits Syst., 9(5), 670–677 (2015); doi: 10.1109/TBCAS.2015.2488582

[4] J. S. Isenberg, A. Siegal, and R. Sherman, Quantitative Evaluation of the Effects of Gravity and Dependency on Microvascular Tissue Transfer to the Lower Limb, with Clinical Applications, J. Reconstr. Microsurg., 13(01), 25–29 (1997); doi: 10.1055/s-2008-1063937

DOI 10.5162/eurosensors2026/SP 1.1.1

Cortisol and Luteinizing Hormone. A Tale of Two Aptamers

[1]S.Ben-Aissa, Anthony Cass[1]
[1]Imperial College London, White City Campus, London UK,
t.cass@imperial.ac.uk

Summary:
This presentation draws together several threads of our recent research in the area of electrochemical aptamer based (EAB) sensors as applied to continuous hormone measurements (CHM). These threads range from the computational; modelling the structures of aptamer-target complexes through workflows for sensor interface engineering using statistical approaches, to surface chemistry and the control of the aptamer sensor surface interface.

Keywords: nanoporous gold, response surface methodology, molecular dynamics, G-quadruplexes, voltammetry

Background, Motivation and Objective

Continuous hormone measurements (CHM) are currently generating considerable interest amongst the medical and sensor communities. There are several reasons for this, including the success of continuous glucose measurement (CGM) technologies, both for clinical applications (diabetes management) and as a dietary and wellness aid. Within this space, there are often parallels drawn between CGM and CHM, parallels that can obscure the very real differences, both physiological and sensor-dependent, between the two. Some of these are summarised in Table 1.

Description of the New Method or System

The use of computational methods (structure prediction and DoE) combined with experimental feedback can help to optimize sensor performance at both the molecular and the device levels.Results

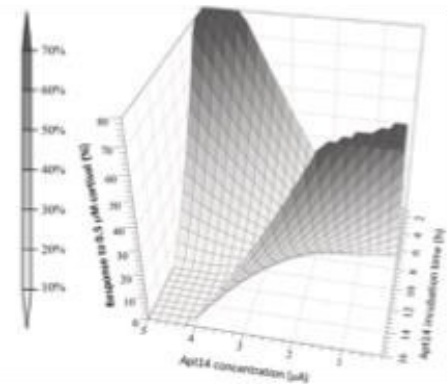

Figure 1 shows a typical response surface for the optimisation of aptamer loading and incubation time for a small (14nt) cortisol-binding aptamer.

Tab. 1: Comparison between CGM and CHM

Sensor	CGM	CHM
# of analytes for clinical decision	One	Several
Measurement Range	2-20mM	nM-pM
Analyte diversity	Low A single molecule	High Proteins, steroids
Sensing Modality	Catalytic	Affinity

References

[1] Ben-Aissa S. & Cass, A. E. G. Systematic optimisation of an integrated electrochemical aptamer-based sensor for cortisol detection. *Sens. Actuators B: Chem.* **444**, 138284 (2025).*doi.org/10.1016/j.snb.2025.138284*
[2] Liang, S. *et al.* Measuring luteinising hormone pulsatility with a robotic aptamer-enabled electrochemical reader. *Nature Communications* **10**, 852 (2019) *doi.10.1038/s41467-019-08799-6*

DOI 10.5162/eurosensors2026/SP 1.1.2

A System For All Day Biosampling: Microdialysis and Wearables Collide

Thomas Upton[1], Eder Zavala[2], Paal Methlie[3], Martijn van Faassen[4], Eystein Husebye[3], Stafford Lightman[1] and the ULTRADIAN consortium
[1] University of Bristol, Bristol, UK,
[2] University of Manchester, Manchester, UK
[3] University of Bergen, Bergen, Norway
[4] University Medical Center Groningen, Groningen, Netherlands

Thomas.upton@bristol.ac.uk

Summary:
Recent developments in wearable sensor technology have increased the ability to perform research in real-world settings. However, a challenge has been to link wearable signals with biological measures. In this paper, examples of ambulatory hormone profiling combined with wearable devices are used to illustrate the potential value for future studies in health and disease.

Keywords: microdialysis; hormones; wearables; chronomedicine

Background, Motivation and Objective

Human physiology is organized across the 24-hour day by timing systems that shape endocrine secretion, sleep, activity, temperature, metabolism, and responses to the external environment. Until relatively recently, it has only possible to capture dynamic changes in biological systems in contrived laboratory settings. As a result, key features of these important systems have been difficult if not impossible to observe in everyday life. At the same time, multiple kinds of wearable devices have emerged and have been applied for use as indirect proxies of environmental and physiological signals A key gap has been the ability to anchor proxy signals with real biological markers in ambulatory, real life situation..

Ambulatory microdialysis and wearables: Narrowing the gap between biological and passive monitoring

Portable microdialysis coupled to automated fraction collection can generate high resolution profiles of hormones over 24-hours or more in home based-setting, including during sleep [1,2]. These initial studies established proof-of principle feasibility and signposted the value of dense endocrine sampling. The aim of these methods is to improve diagnosis and treatment of health conditions by providing critical insights into dynamics and the links between wearable-measured signals and underlying biology.

Dynamics in everyday life

We used ambulatory microdialysis to quantify 24hr patterns of adrenal hormones in 214 healthy people [3] defining normal healthy variation and establishing reference for comparisons with disease [4].

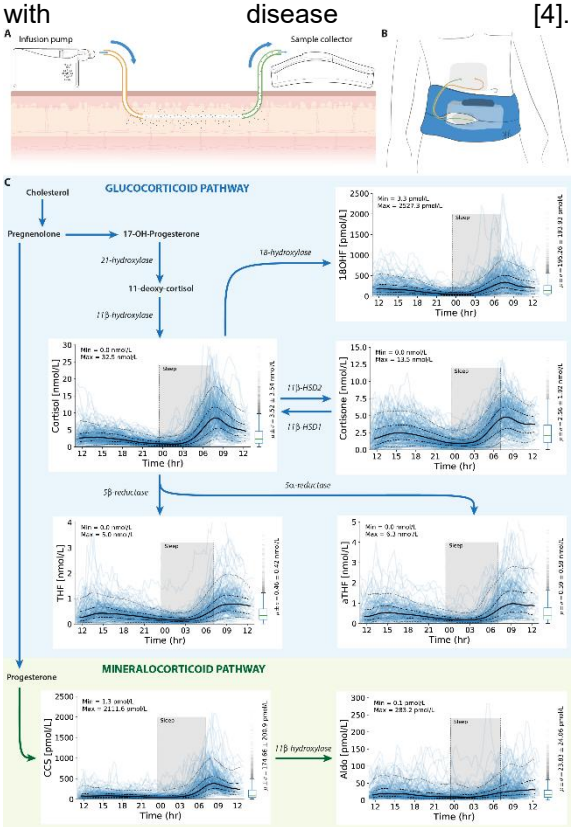

Fig. 1. Patterns of 7 adrenal steroids in n=214

healthy volunteers collected during normal daily life [3].

Broadening the horizon

A series of pilot studies have demonstrated the feasibility of integrating wearable devices into ambulatory microdialysis protocols.

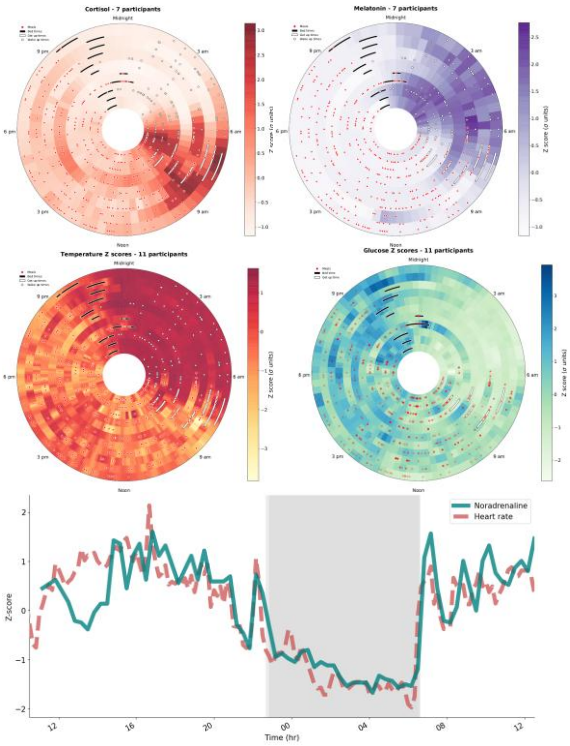

Fig. 2. 24hr heatmaps illustrate 24hr variation in hormones, skin temperature and glucose. Bottom: Free noradrenaline tracking with heart rate in a healthy volunteer (Author's unpublished data)

Advanced analysis methods now permit quantification of a wider variety of hormones and metabolites in interstitial fluid, including melatonin and free catecholamines (Fig 2).

The future of digital endocrinology and health

The combination of ambulatory biosampling and digital wearables opens doors for a potential revolution in the understanding of health and disease. The upcoming Endotrain DTP (10.3030/101227148) will train doctoral candidates across eight countries in this exciting new era where research innovation, digital solutions, and clinical care intersect.

References

[1] Bhake, R., Leendertz, J., Linthorst, A., & Lightman, S. (2013). Automated 24-hours sampling of subcutaneous tissue free cortisol in humans. *Journal of medical engineering & technology*, 37(3), 180-184.

[2] Bhake, R., Kluckner, V., Stassen, H., Russell, G., Leendertz, J., Stevens, K., Linthorst, A., & Lightman, S. (2019). Continuous free cortisol profiles—circadian rhythms in healthy men. *The Journal of Clinical Endocrinology & Metabolism*, 104(12), 5935-5947.

[3] Upton, T. J., Zavala, E., Methlie P. et al. High-resolution daily profiles of tissue adrenal steroids by portable automated collection. *Science Translational Medicine*, 15(701), eadg8464. https://doi.org/doi:10.1126/scitranslmed.adg8464

[4] Grytaas, M, Upton TJ et al. Home measurement of 24-hour corticosteroid dynamics in primary aldosteronism, 27 February 2025. PREPRINT (Version 1) available at Research Square [https://doi.org/10.21203/rs.3.rs-6095171/v1]

DOI 10.5162/eurosensors2026/SP 1.1.3

Tissue corticosteroid rhythms are dysregulated mainly during sleep in primary aldosteronism

Marianne A. Grytaas[1,†], Thomas Upton[2,†], Isabella Marinelli[3,‡], Paal Methlie[1,4,‡], Marianne Øksnes[1,4,‡], Dimitra A. Vassiliadi[5], Sophie Bensing[6,7], Georgina Russell[2], Kristian Løvås[1], Dimitris Margaritopoulos[5], Ileana R. Botusan[6,7], Katerina Simunkova[4], Maria Balomenaki[5], Katarina Berinder[6,7], Belinda Lombard[8], Thea Sjøgren[1], Ida Løvik[9], Bergithe E. Oftedal[1,4], Anette Heie[10], Grethe Å. Ueland[1], Olle Kämpe[6,7] Stylianos Tsagarakis[5], Stafford L. Lightman[2], Eder Zavala[8,11], Eystein S. Husebye[1,4]

Shared first author†; Shared second author‡

[1] Department of Medicine, Haukeland University Hospital; 5021 Bergen, Norway.
[2] Henry Wellcome Laboratories for Integrative Neuroscience and Endocrinology, Translational Health Sciences, Faculty of Health Sciences; University of Bristol; BS1 3NY Bristol, United Kingdom.
[3] Department of Mathematics and Statistics, University of Exeter, EX4 4QF, Exeter, United Kingdom.
[4] Department of Clinical Science, University of Bergen, 5021 Bergen, Norway.
[5] Department of Endocrinology and Metabolism, Diabetes Centre, Evangelismos General Hospital, European Reference Network on Rare Endocrine Conditions (Endo-ERN), 106 76 Athens, Greece.
[6] Department of Endocrinology, Karolinska University Hospital; 171 76 Stockholm, Sweden.
[7] Department of Medicine Solna, Karolinska Institutet, 171 77 Stockholm, Sweden.
[8] School of Mathematics, University of Birmingham, B15 2TT, Birmingham, United Kingdom.
[9] Department of Pathology, Haukeland University Hospital, 5021 Bergen, Norway.
[10] Department of Surgery, Haukeland University Hospital, 5021 Bergen, Norway.
[11] Centre for Biological Timing; Division of Diabetes, Endocrinology & Gastroenterology; Faculty of Biology, Medicine and Health; University of Manchester; M13 9PT, Manchester, United Kingdom.

Abstract

Primary aldosteronism affects 5–20% of the hypertensive population and is associated with increased cardiovascular and metabolic risk compared with primary hypertension. Alterations in the dynamics of aldosterone secretion are key, but these are not well captured by current diagnostic pathways, and the disease is often missed. In this proof-of-concept study, we utilized ambulatory microdialysis sampling to continuously monitor tissue corticosteroid dynamics in primary aldosteronism over 24 hours. In a cohort of 60 patients, we found prominent and pulsatile nocturnal hypersecretion of aldosterone and the hybrid steroids 18-hydroxycortisol and 18-oxocortisol with a preserved daily rhythm. This was most prominent in unilateral disease, with normalization after adrenalectomy. Our findings confirm that a key pathophysiological feature of primary aldosteronism is disruption of corticosteroid rhythms, rather than persistent elevation of hormones. We show that ambulatory dynamic hormone profiling is a viable technique that offers substantially more information than current diagnostic approaches relying on single time-point hormone measurements. In the future this offers the opportunity to investigate more subtle dynamic phenotypes and potentially earlier detection of disease.

Keywords

Primary aldosteronism, ultradian rhythms, dynamic hormone profiling, aldosterone, microdialysis

DOI 10.5162/eurosensors2026/SP 1.1.4

Ultradian Monitoring in Adrenal Insufficiency

Botusan Ileana[1], Zavala E [2], Upton T [3], Berinder K[1] , Methlie P[4], Simunkova K [4], Vassiliadi D[5], Grytaas M[4], Russell G[3], Tsagarakis S[5], Lightman S [3], Husebye E [4], Kämpe O [1], Øksnes M [4], Bensing S[1]
[1] Karolinska Institutet, Karolinska University Hospital, Dept of Medicine, Stockholm, Sweden,
[2] Centre for Biological Timing, University of Manchester, Manchester, United Kingdom,
[3]University of Bristol, Bristol, United Kingdom
[4]University of Bergen, Haukeland University Hospital, Medicine, Bergen, Norway,
[5] Evangelismos Hospital, Athens, Greece
ileana.botusan@ki.se

Summary:

Ultradian platform enables ambulatory, tissue-level profiling of steroid hormones, every 20 minutes over 24 hours. We applied this wearable microdialysis platform in patients with primary adrenal insufficiency receiving different glucocorticoid replacement regimens. Compared with healthy reference profiles, patients spent less time within the physiological cortisol range.These findings reveal dynamic treatment mismatches that conventional sparse sampling cannot capture. Ultradian platform provides a route toward precision endocrine monitoring and individualized glucocorticoid replacement.

Keywords: Ultradian; U-Rhythm; ambulatory biosampling; tissue steroid profiling; primary adrenal insufficiency.

Background, Motivation and Objective

Endocrine function is intrinsically dynamic, yet clinical hormone monitoring still relies mainly on sparse blood sampling. In primary adrenal insufficiency [1], loss of adrenal corticosteroid production requires lifelong glucocorticoid replacement therapy [2, 3].

We used the ambulatory U-RHYTHM system [4], a portable microdialysis-based biosampling platform, to capture high-resolution tissue corticosteroid dynamics in patients with primary adrenal insufficiency receiving different glucocorticoid replacement regimens.

Methods

Forty-one patients with autoimmune primary adrenal insufficiency were studied during treatment with hydrocortisone, cortisone acetate, or modified-release hydrocortisone. Free steroid hormones were sampled by microdialysis from abdominal subcutaneous tissue every 20 minutes over 24 hours using U-RHYTHM under ambulatory real-life conditions, including overnight sampling (Fig 1). Steroids were quantified by ultrasensitive LC-MS/MS [5] and compared with a healthy reference cohort of 214 individuals.

Time-resolved reference ranges were used to derive dynamic biomarkers, including time in range, time at extreme concentrations, area under the curve, peak concentration, rate of post-dose increase, and peak timing.

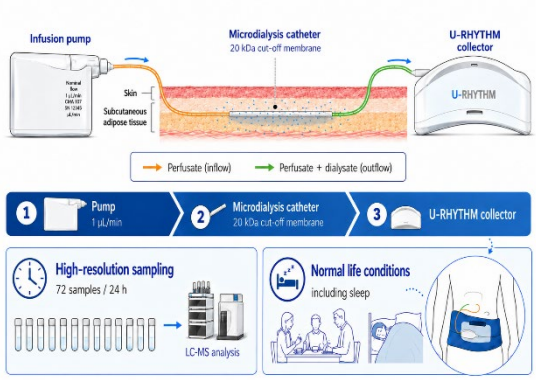

Fig. 1. Schematic representation of ambulatory microdialysis sampling using U-RHYTHM

Results

Ambulatory 24-hour tissue steroid profiling was feasible in patients with primary adrenal insufficiency without disturbing sleep. Across replacement regimens, time within the physiological cortisol range remained low, averaging below 35%, with more than 25% of the day spent at extreme concentrations. The normal pre-awakening rise in cortisol and cortisone observed in healthy individuals was absent. Instead, hormone levels remained very low during the early morning hours and increased only after morning glucocorticoid intake.

Post-dose hormone peaks were delayed and showed altered exposure, transition speed, and morphology compared with healthy controls.

Conclusions

The U-RHYTHM-based ultradian platform enables wearable, high-temporal-resolution steroid phenotyping at the tissue level under ambulatory conditions. In primary adrenal insufficiency, this approach reveals a persistent mismatch between current replacement regimens and physiological hormone dynamics. This platform provides precision endocrine monitoring and creates the premises for individualized optimization of glucocorticoid replacement therapy.

References

[1] Hahner S, Ross RJ, Arlt W, Bancos I, Burger-Stritt S, Torpy DJ, Husebye ES, Quinkler M. Adrenal insufficiency. Nat Rev Dis Primers. 2021 Mar 11;7(1):19. doi: 10.1038/s41572-021-00252-7

[2] Debono M, Ghobadi C, Rostami-Hodjegan A, Huatan H, Campbell MJ, Newell-Price J, Darzy K, Merke DP, Arlt W, Ross RJ. Modified-release hydrocortisone to provide circadian cortisol profiles. J Clin Endocrinol Metab. 2009 May;94(5):1548-54. doi: 10.1210/jc.2008-2380. Epub 2009 Feb 17

[3] Johannsson G, Nilsson AG, Bergthorsdottir R, Burman P, Dahlqvist P, Ekman B, Engström BE, Olsson T, Ragnarsson O, Ryberg M, Wahlberg J, Biller BM, Monson JP, Stewart PM, Lennernäs H, Skrtic S. Improved cortisol exposure-time profile and outcome in patients with adrenal insufficiency: a prospective randomized trial of a novel hydrocortisone dual-release formulation. J Clin Endocrinol Metab. 2012 Feb;97(2):473-81. doi: 10.1210/jc.2011-1926. Epub 2011 Nov 23.

[4] T. J. Upton et al., High-resolution daily profiles of tissue adrenal steroids by portable automated collection. Sci Transl Med 15, eadg8464 (2023). DOI: 10.1126/scitranslmed.adg8464

[5] P. Methlie *et al.*, Multisteroid LC-MS/MS assay for glucocorticoids and androgens, and its application in Addison's disease. *Endocr Connect* **2**, 125-136 (2013). DOI: 10.1530/EC-13-0023

DOI 10.5162/eurosensors2026/SP 1.2.1

Machine Learning for longitudinal data analysis in gas sensors: A case study in early subclinical ketosis in dairy cows

Albert Belenguer-Llorens[1,2], Jonas Hendricks[3], Jaehyun Ko[4] , Anna-Maria Reiche[3] , Frigga Dohme-Meier[3] , Andreas T. Güntner[4] , Catherine R. Jutzeler[1,2]

[1] Department of Health Sciences and Technology (D-HEST), ETH Zurich, Switzerland
[2] SIB Swiss Institute of Bioinformatics, Lausanne, Switzerland
[3] Ruminant Nutrition and Emissions, Agroscope, Posieux, Switzerland
[4] Human-centered Sensing Laboratory, Department of Mechanical and Process Engineering, ETH Zurich, Zurich, Switzerland
jutzelec@ethz.ch

Summary:

Machine learning offers powerful opportunities to transform continuous sensor measurements into clinically or biologically predictions. However, translating raw sensor signals into robust diagnostic models requires careful consideration of temporal dynamics, feature engineering, latent-state modeling, and interpretability. In this tutorial, we present a generalizable pipeline for developing predictive diagnostic models from sensor measurements, illustrated through a real-world case study: the early detection of subclinical ketosis in dairy cows using breath acetone measured by gas sensors.

Keywords: Gas Sensors, Machine Learning, Dairy science, Sensor Data Analysis, XGBoost

Background, Motivation and Objective

Modern sensor systems generate increasingly rich time-series data, yet many sensing applications still rely on threshold-based or linear analyses that underutilize the available information. Machine learning (ML) enables the identification of dynamic patterns that can improve predictive performance while providing insight into the underlying system dynamics.

This tutorial presents a practical workflow for converting longitudinal sensor measurements into predictive models. The proposed framework addresses common challenges encountered in data analysis for sensing applications, including temporal windowing, feature engineering, latent-state inference, validation under limited sample sizes, and model interpretability.

To illustrate the methodology, we use a case study on early diagnosis of subclinical ketosis (SCK) in dairy cows. SCK is a prevalent metabolic disorder that significantly affects milk production, animal welfare, and farm economics [1]. Current diagnosis relies on invasive and expensive blood β-hydroxybutyrate (BHB) measurements, whereas breath acetone provides a promising non-invasive biomarker measurable by gas sensors [2]. The example demonstrates how sensor measurements can be transformed into actionable predictions several days before disease onset using a ML-based pipeline.

Materials and Data Collection

The proposed pipeline consists of five consecutive stages:

- Sensor Data Acquisition: Collection of longitudinal gas sensor measurements together with reference clinical labels (SCK or healthy) based on reference BHB measurements.
- Temporal Representation: Construction of rolling temporal windows that preserve the evolution of the sensor signal and define prediction horizons relevant for prospective diagnosis.
- Feature Engineering: Extraction of dynamic descriptors including slopes, rates of change, acceleration, volatility, cumulative exposure (KAUC), and

trend characteristics that summarize acetone behavior over time.

- Latent State Modeling: Use of Hidden Markov Models (HMM) to identify latent physiological states linking sensor measurements with the underlying biological process. During training, both sensor (acetone) and reference measurements (BHB) calibrate the latent states, while inference relies only on sensor measurements.
- Predictive ML: Integration of temporal measurements, engineered features, and latent-state transition probabilities into an interpretable XGBoost classifier validated through nested cross-validation and explained using SHapley Additive exPlanations (SHAP) values [4].

Although demonstrated using breath acetone sensing, this methodology is applicable to many longitudinal sensor systems where complex temporal dynamics encode predictive information.

Case Study: Early Detection of Subclinical Ketosis

The case study uses breath acetone measurements collected with a novel sampling mask developed by ETH Zurich and Agroscope [3] together with blood BHB measurements from 31 dairy cows monitored before and after calving.

Using seven-day temporal windows and prediction horizons of 7–9 days, the proposed pipeline learns dynamic signatures preceding disease onset. The resulting predictive model achieved balanced and competitive performance across validation folds in both Area Under the Curve (AUC) and balanced accuracy, demonstrating that temporal sensor patterns contain substantial predictive information beyond instantaneous measurements (Table 1).

Tab. 1: Classification performance (mean ± std) of our proposed algorithm stratified by group. AUC: Area under the curver; ACC: Accuracy

Cohort	AUC	Balanced Acc
ALL	0.785 ± 0.071	0.778 ± 0.027
CON	0.832 ± 0.043	0.801 ± 0.034
SCK	0.744 ± 0.027	0.734 ± 0.124

Interpretability analysis using SHAP identified cumulative exposure (KAUC), acceleration, and temporal lag measurements among the most relevant predictors, illustrating how ML can simultaneously improve prediction and generate physiological hypotheses (Figure 1).

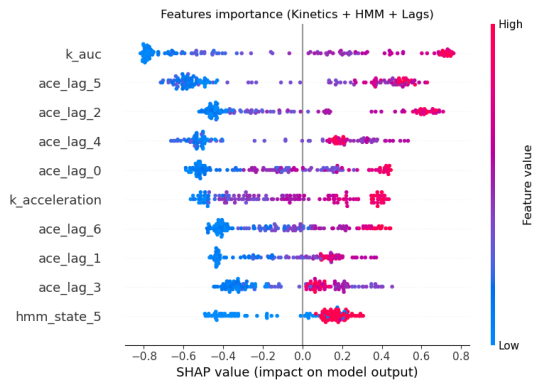

Fig. 1. SHAP values of the top 10 most relevant features found by XGBoost.

The proposed pipeline is computationally efficient and lightweight, making it suitable for deployment on resource-constrained embedded devices. Its transparent design and interpretability ensure compliance with the EU AI Act for high-risk AI support systems, supporting its potential translation to a broad range of medical and diagnostic applications.

Conclusions and Future Lines

This work presents a generalizable ML-based framework to extract predictive patterns from sensor measurements. By combining temporal feature engineering, probabilistic latent-state modeling, and interpretable ML algorithms, the proposed pipeline provides a practical blueprint for sensor scientists interested in developing predictive algorithms from longitudinal measurement data.

The dairy cow application serves as an illustrative example, but the methodology is broadly transferable to environmental sensing, wearable technologies, industrial monitoring, breath analysis, and other sensor-driven diagnostic applications. Future work will focus on extending the framework to larger datasets, additional ML architectures, and multimodal sensing platforms.

References

[1] Mostert, P. F., et al. Estimating the economic impact of subclinical ketosis in dairy cattle using a dynamic stochastic simulation model. *Animal* 12.1 (2018): 145-154; doi: 10.1017

[2] Rico, J. Eduardo, et al. Invited review: Ketone biology—The shifting paradigm of ketones and ketosis in the dairy cow. *Journal of Dairy Science* 107.6 (2024): 3367-3388; doi: 10.3168

[3] Ko, Jaehyun, et al. Mask for Individual Sampling of Tidal and Ruminal Gas Contaminated Breath in Dairy Cows. (2026); chemrxiv; doi: 10.26434

[4] Lundberg, Scott M., and Su-In Lee. A unified approach to interpreting model predictions. *Advances in neural information processing systems* 30 (2017).

DOI 10.5162/eurosensors2026/SP 1.2.2

Metabolomics as a Tool for Rapid Urinary Tract Infection Diagnosis

Glenda Vasku[1], Anne Vescovi[1], Emma Wetter Slack[1,2]
[1] Laboratory for Mucosal Immunology, Institute for Food, Nutrition and Health, D-HEST, ETH Zürich, Zürich, Switzerland
[2] Botnar Research Institute for Child Health, Basel, Switzerland
emma.slack@hest.ethz.ch

Summary:

Urinary tract infections caused by *Escherichia coli* are increasingly resistant to first-line antibiotics, yet current culture-based diagnostics require 2 to 4 days, driving empiric broad-spectrum therapy that accelerates resistance spread. Diagnostic gaps persist, with low-level and fastidious organisms frequently missed by standard methods, while rapid susceptibility testing remains unavailable in most settings. To address this challenge, we developed an untargeted and targeted metabolomics approach to identify urinary metabolite signatures specific to UTI-causing bacteria. Using 75 *E. coli* strains grown in artificial urine medium and analysed by complementary liquid chromatography–mass spectrometry methods, we identified differential metabolite production patterns including increased succinate and depleted mannitol in bacterial cultures. These metabolomic signatures offer potential biomarkers for rapid bacterial identification independent of culture. This approach could enable faster, more specific UTI diagnostics to reduce inappropriate antibiotic use and combat antimicrobial resistance.

Keywords: untargeted metabolomics, targeted metabolomics, UTI metabolites, UTI rapid diagnostics

Introduction

Urinary tract pathogens are increasingly resistant to first-line antibiotics, while empiric broad-spectrum therapy drives further resistance spread [1]. Meanwhile, diagnostic gaps persist, with low-level and fastidious organisms missed by standard methods, and rapid susceptibility testing technologies remain unavailable and not specific in most settings [2]. In our current efforts to address this issue, we aimed at developing an untargeted metabolomics approach that would screen for urinary metabolites in the presence of infection due to different urinary tract bacteria. At a second time we aimed at targeting specific amine and short chain fatty acids to quantify them, to check bacterial growth behavior specific to UTI bacteria. Finally, this data, completed with genomic sequence could draw a bigger picture into identifying robust metabolite biomarkers specific to different UTI infections.

Untargeted and targeted metabolomics for UTI

Two untargeted complementary methods (normal phase hydrophilic interaction liquid chromatography HILIC and reverse-phase C18) were used to analyze 75 E. coli strains after ensuring robust growth in an artificial urine medium. After metabolite extraction, samples were analyzed in a high-resolution mass spectrometer (Orbitrap Exploris 240). The complementarity of these methods assured the identification of different metabolites, polar and apolar present in the 75 strains. Artificial urine served as a controllable medium and as a baseline for matrix effects to avoid false identification due to contamination.

Results

Growth of the 75 E. coli strains in the artificial urine was comparable with several outliers (data not shown). The medium of artificial urine presents a constant stress to the bacterial growth with abundant salts and a highly saturated solution which could potentially destabilize the bacterial cells. However, given that the growth was steady and comparable throughout strains we continued the metabolomics extraction of the extracellular metabolites for untargeted and targeted metabolomics (Fig.1).

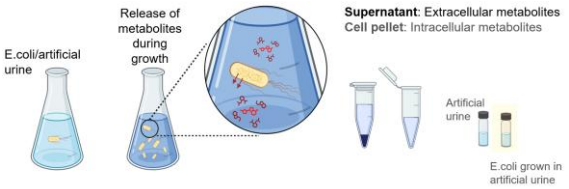

Fig. 1. Untargeted and targeted metabolomics of 75 E. coli strains grown in artificial urine for extracellular bacterial metabolites identification

Samples were extracted and polar metabolites were analyzed in HILIC conditions, where several total ion chromatograms were extracted and compared (Fig.2). In negative ionization HILIC conditions several different relative peak intensities were visible between blank (artificial urine) and grown E. coli in artificial urine (Fig.2). Succinate showed higher relative intensity in E. coli samples compared to artificial urine, potentially suggesting an overproduction due to bacterial growth. Conversely mannitol showed lower abundances in the E. coli samples suggesting that it was likely consumed by bacteria to ensure growth. Such differences in metabolite intensities need to be further confirmed with several standards to ensure a more accurate quantification. Nevertheless, this data suggests that following upon different changes of the bacterial metabolites one can possibly target those as specific to bacteria with the bigger aim of identifying bacterial infections based on metabolite production as a starting point.

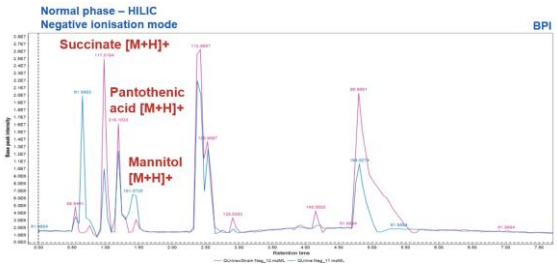

Fig. 2. Superimposed negative ionization chromatogram peaks of artificial urine (blank, blue) and E. coli grown in artificial urine (pink). BPI: baseline peak intensity

References

[1] M. R. Timm, S. K. Russell, S. J. Hultgren, Urinary tract infections: pathogenesis, host susceptibility and emerging therapeutics, Nature Reviews Microbiology 23(2), 72–86 (2025); doi: 10.1038/s41579-024-01092-4

[2] A. B. Bellankimath, S. Branders, I. Kegel et al., Metagenomic sequencing enables accurate pathogen and antimicrobial susceptibility profiling in complicated UTIs in approximately four hours, Nature Communications 17, 187 (2026); doi: 10.1038/s41467-025-66865-8

DOI 10.5162/eurosensors2026/SP 1.2.3

Volatilomics for Medical Microbiology Diagnostics using Standard Bacterial Headspace Sampling

Mehmet Berk Bilgin[1], Norma Toccalino[1], Emma Slack[2,3,4], Adrian Egli[5], Andreas Güntner[1]
[1] Human-centered Sensing Laboratory, D-MAVT, ETH Zürich, Zürich, Switzerland
[2] Laboratory for Mucosal Immunology, Department of Health Sciences and Technology, ETH Zurich, Zurich, Switzerland
[3] Botnar Institute of Immune Engineering, Basel, Switzerland
[4] Sir William Dunn School of Pathology, University of Oxford, Oxford, UK
[5] Institute of Medical Microbiology, University of Zurich, Zurich, Switzerland
andreas.guentner@hsl.ethz.ch

Summary:
This presentation advocates for the use of volatilomics as an alternative rapid microbiological testing method. A critical bottleneck is the reliable and controlled sampling of volatile biomarkers in the headspace of bacterial species. We will show exemplarily volatilome measurement with an online headspace sampling setup to track metabolic activity via headspace microbial volatile compound (mVOC) concentrations by mass spectrometry. We identify key translational gaps impending clinical adoption.

Keywords: Volatilomics, Headspace sampling, Antibiotic susceptibility testing, Microbiological sensing, Novel diagnostics.

Background, Motivation and Objective

Detection and identification of bacteria based on their mVOC emissions is a promising approach for rapid diagnostics [1,2]. Although some bacterial odors have been utilized in infection diagnostics since early modern times[3], the advent of high-resolution analytical techniques, like mass spectrometry, has enabled accurate mVOC quantification, paving the way for targeted biomarker analysis to reduce the time-to-result for AST from 48 hours to just a few hours (Figure 1) using compact, selective, and sensitive sensors [4–6]. Rapid point-of-care testing can drastically improve the disease prognosis and significantly contribute to the antibiotic stewardship efforts. Such clinical devices for fast pathogen discrimination can only be realizable with representative and reproducible sampling of the headspace to extract the volatilome at different timepoints. However, the critical role of sampling has been overlooked, and the variability in sampling methodologies has hindered direct comparability across studies. To date, no approach has established a standardized, robust method for longitudinal volatilome monitoring. This inconsistency undermines reproducibility and has left the relationship between volatilome composition and microbial metabolism insufficiently understood. The presented system aims to close the critical gap between mVOCs and microbial functions by proposing a reliable way of controlled volatilome extraction for both mass spectrometric and chemoresistive sensor measurements. The presentation starts with the outline of the envisioned workflow for an alternative microbiological diagnostic test. Individual steps for a successful test are discussed with an emphasis on the sampling approach. The recent advancements in the field are discussed with a future outlook.

Description of the Approach

We start with the proposed rapid volatilomics pathway as an diagnostic alternative. Sampling is the first step of the analysis: the extracted headspace volume must be a representative part of the bacterial volatilome. To ensure accuracy, we present the online headspace sampling setup for reliable and reproducible controlled volume extraction. As a crucial part of the system, parametric sweep of the dilution ratio was performed to meet the dynamic range limits of the analytical tool. The sampling accuracy is validated with mass spectrometry and analyte gas standards. Headspace mVOC concentrations are obtained from preliminary bacteria measurements for biomarker identification, which are particularly important for onsite testing, as target biomarker information must be available for selective detection of volatiles using compact sensors. The resulting multidimensional sensor data can be processed with machine learning algorithms to create a diagnostic report.

Results

The proposed setup is validated with acetone, ethanol, benzene, and acetaldehyde gas standards for reliable volume extraction down to ppb-level concentrations. *Escherichia coli* metabolic changes across different stages of incubation, and these changes are reflected in the preliminary headspace concentrations (Figure 2). Although the acetaldehyde concentrations serve as the main indicator of the growth phase, the results show that tracking similar volatiles with mass spectrometry and sensors can yield bacterial metabolic information for pathogen characterization. Finally, we emphasize the role of machine learning for the interpretation of such complex data for diagnostics.

Conclusion:

Volatilomics holds exceptional promise for rapid microbiological diagnostics, particularly in rapid antibiotic susceptibility testing. By establishing a standardized, reproducible headspace sampling platform compatible with both analytics and point-of-care sensors, our work bridges a critical gap between volatilome dynamics and microbial physiology. Combining the presented system with compact, sensitive, and selective sensor to unlock complex volatile data using machine learning algorithms, we envision volatilomics as an enabler for same-hour clinical diagnostics, antimicrobial stewardship enhancement, and a significant improvement of clinical infection management.

Figures

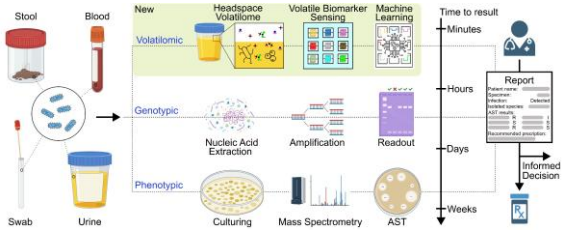

Fig. 1. Envisioned volatilomics and current workflows in medical microbiological pathogen and AST diagnostics [6]

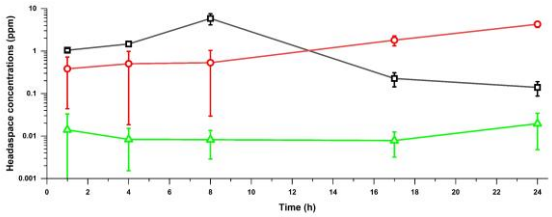

Fig. 2. Temporal profiles of the headspace concentrations of selected molecules from Escherichia coli culture

References

[1] K. Żuchowska, W. Filipiak, Modern approaches for detection of volatile organic compounds in metabolic studies focusing on pathogenic bacteria: Current state of the art, Journal of Pharmaceutical Analysis 14, 100898 (2024); doi: 10.1016/j.jpha.2023.11.005

[2] Q. Ding, W. Zhang, Y. Guo, J. Wang, H. Chen, L. Zhang, β-Lactamase Sensitive Probe for Rapid Detection of Antibiotic-Resistant Bacteria with Gas Chromatography-Tandem Mass Spectrometry, Analytical Chemistry 95, 6098–6106 (2023): doi: 10.1021/acs.analchem.3c00381.

[3] C.D. Cox, J. Parker, Use of 2-aminoacetophenone production in identification of Pseudomonas aeruginosa, Journal of Clinical Microbiology 9, 479-84 (1979); doi: 10.1128/jcm.9.4.479-484.1979

[4] J. van den Broek, S. Abegg, S.E. Pratsinis, A.t. Güntner, Highly selective detection of methanol over ethanol by a handheld gas sensor. Nature Communications 10, 4220 (2019); doi: 10.1038/s41467-019-12223-4

[5] I.C. Weber, H.P. Braun, F. Krumeich, A.T. Güntner, S.E. Pratsinis, Superior Acetone Selectivity in Gas Mixtures by Catalyst-Filtered Chemoresistive Sensors, Advanced Science 7, 2001503 (2020); doi: 10.1002/advs.202001503

[6] M.B. Bilgin, H. Shin, C.R. Jutzeler, T.M. Kessler, E. Slack, A. Egli, A.T. Güntner. Microbial and antimicrobial resistance diagnostics by gas sensors and machine learning, Cell Biomaterials 1, 100125 (2025); doi: 10.1016/j.cellbio.2025.100125

DOI 10.5162/eurosensors2026/SP 2.1.1

Electrochemical Sensors and Biosensors for Biomedical and Clinical Applications

Danny O'Hare[1], A Cass[2], E. Stadler[3], W de Boer[1,3]
[1] Department of Bioengineering, Imperial College, London SW7 2BP
[2] Department of Chemistry, Imperial College London W12 0BZ [3]Department of infectious Diseases, Imperial College London SW7 2AZ
d.ohare@imperial.ac.uk

Summary:
Electrochemical sensors offer many advantages for point-of-care and wearable sensors. Clinical and biomedical applications present unique challenges for sensors ranging from sensor fouling to signal interpretation. I shall provide an overview of the field drawing on my own research. Topics covered will include biofouling, sample selection, exhaled condensed breath, microneedles, signal processing and validation,

Keywords: Electroanalysis, wearables, point-of-care, biosensors, clinical applications.

Background

Point-of-care (PoC) and wearable devices[1] have demonstrable real world benefits for patients in the diagnosis of disease and in the management of chronic conditions. This is seen clearly in greatly improved outcomes in diabetes with PoC and in the vibrant and growing research into distributed healthcare [2], driven in part by healthcare needs of ageing populations [3].

There are significant scientific and engineering challenges associated with clinical measurement throughout the signal chain: selection of sampling site and medium, sensor fouling, selective molecular recognition, transduction, analogue front-end design, signal processing and unambiguous presentation of results to patients and their clinicians.

Sensor fouling arising from foreign body response causes, *inter alia* diffusional blocking, partitioning of analytes into adsorbed layers, deactivation of electrocatalytic sites, and compromised recognition chemistry performance. From the patient perspective adverse problems include inflammation and consequent analyte entrainment, blood vessel occlusion, pain, bleeding and risk of infection.

Minimally-invasive sampling

We have been investigating two minimally-invasive approaches to clinical measurement: Microneedle biosensors implanted into viable epidermis have been applied to β-lactam antibiotics [4], [5] for closed-loop control of drug levels and to lactate concentrations [6],[7] . Lactate has applications in sepsis and septic shock, respiratory diseases and fitness monitoring.

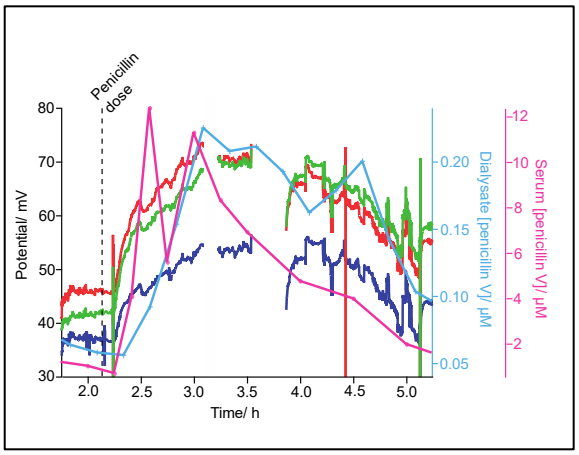

Fig.1. Microneedle determination of benzyl penicillin in a healthy volunteer. Red, green, dark blue traces are sensor data, Pink and pale blue traces are free drug conctrations from venous draws and microdialysis determined by LC-MS

Exhaled condensed breath (EBC) is a non-invasive analytical matrix and source of biomarkers. We have developed a novel portable device for the collection of EBC that enables correction for natural breathing patterns and optimization with respect to target analyte concentration [8]. We have applied this to lactate measurements in humans [9] and undertaken a preliminary clinical

evaluation in healthy volunteers and COPD patients [10]

a)

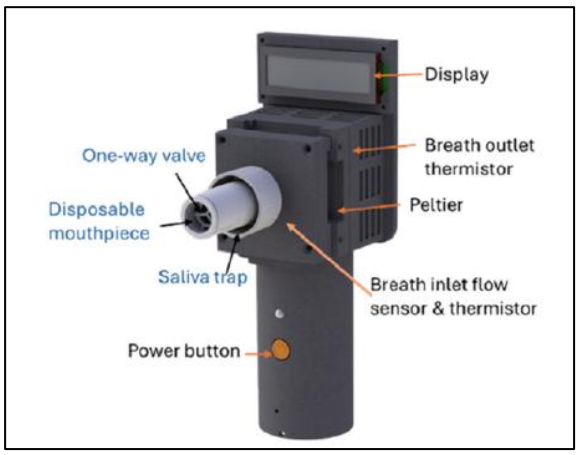

b)

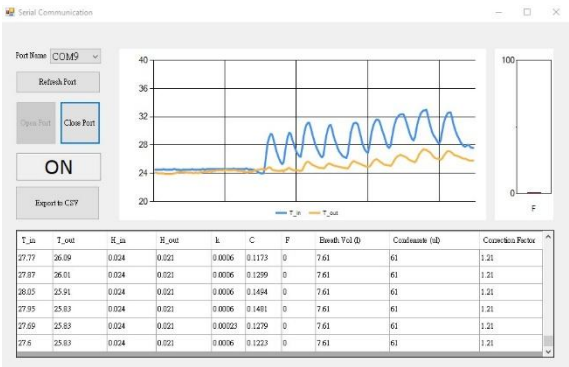

Fig 2 (a)The EBC collector and (b) typical data enabling on-the-fly correction for flow velocities and temperature

Electrodes and scaleability

Biosensor fouling and foreign body responses are inevitable. There is no 'magic bullet' fix: consequences depend on timescale, target analyte and application, and fixes are typically bespoke. We have shown that electrode materials such as boron-doped diamond are generally less affected [11], [12] but this comes at considerable costs of manufacturing that are incompatible with single use PoC devices.

Signal processing strategies can usefully be employed to improve selectivity. We have shown that the Hilbert transforms of electrode responses to frequency-modulated voltages improve selectivity and monitor changes in double-layer capacitance, an important marker of sensor fouling [13]

Scaleable manufacture is frequently considered too late in biosensor design, yet is essential for any clinical study as well as potential commercial exploitation. Collaboration with Respire Diagnostics Ltd has led to low cost (< €1 ea.) disposable glassy carbon electrodes which are sufficiently reproducible to be single use, need no pre-calibration and have applied them to biomarker measurement (xanthine oxidase) and therapeutic drug monitoring. Preliminary data of of nitrofurantoin, a first-line antibiotic used in urinary tract infections are shown in Figure 3.

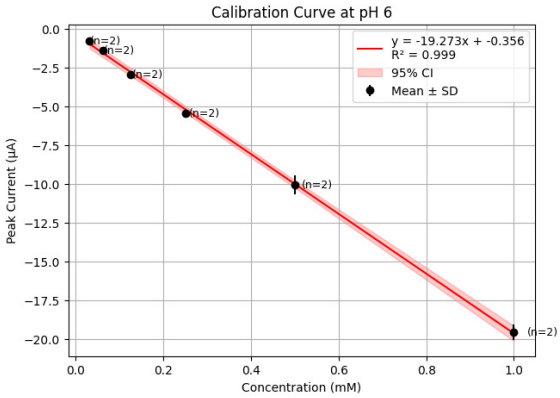

Fig. 3 Disposable GC sensor DPV calibration for nitrofurantoin in spiked artificial urine. Each concentration used two separate sensors. The pink shading is the 95% confidence limit of the fit.

Endotrain activities

Minimally invasive sensing for cortisol and other adrenal hormones. The first task will be development of the electrochemical aptasensor. We have a new approach using three-dimensional conducting polymer-hydrogel electrodes to stabilise local environment and minimise the impact of aptamer losses. We hope to apply this strategy to minimally-invasive EBS and microneedle samples following validation in plasma and venous draws.

[1] *The future of wearable technologies* doi.org/10.25561/88893
[2] "*Biosensorsand Bioelectronics* 21.10 (Apr. 2006), pp. 1887–1892. $%&: 10.1016/j.bios.2005.10.027.
[3] *J Clin Transl Sci*. 2025 Sep 9;9(1):e207. doi: 10.1017/cts.2025.10149
[4], *ACS Sensors* **4** 1072-1080 (2019) doi.org/10.1021/acssensors.9b00288
[5] *Lancet Digital Health* **7(1)** PE335-343 (2019) doi.org/10.1016/S2589-7500(19) 30131-1
[6] *ACS Sensors* (2023) **8** (4) 1639–1647.
[7] *BMJ Innovations* doi: 10.1136/bmjinnov-2021-000864
[8] *Analyst* 145, 3549-3556 (2020) DOI: 10.1039/c9an02438g
[9] *ACS Sensors* **7(12)** 3809-3816 (2022) doi. 10.1021/acssensors.2c01739
[10] R*espiratory Medicine* **257** 108813 (2026).
[11] *Physical Chemistry Chemical Physics* **13** 5422-5429 (2011)
[12] *Electrochimica Acta* **55(22)** 6586-6595 (2010).
[13] *Anal. Chem.* **78(19)** 6990-6998 (2006).

DOI 10.5162/eurosensors2026/SP 2.1.2

From Rigid to Flexible and Stretchable Hollow Microneedle Patches: Integrated Microfluidic Platforms for Dermal Interstitial Fluid Extraction and Intradermal Therapeutic Delivery

Wenting Shu[1], Raicevic, Teodora[1], Andreas T. Güntner[1,2]
[1] Human-Centered Sensing Laboratory, Department of Mechanical and Processing Engineering, ETH Zurich, 8092 Zurich, Switzerland
[2] Department of Endocrinology, Diabetology, and Clinical Nutrition, University Hospital Zurich (USZ) and University of Zurich (UZH), 8091, Zurich, Switzerland
andregue@ethz.ch

Summary:

Dermal interstitial fluid is an attractive biofluid for minimally invasive and longitudinal biomarker monitoring. Here, we develop a flexible hollow microneedle patch that combines two-photon-polymerised hollow microneedles, an elastomeric backing layer, and soft microfluidic channels. Building on 3D-printed microneedles integrated with silicon microfluidics, this platform improves skin conformity while maintaining reliable dermal access. Preliminary insertion, optical, and fluidic tests demonstrate effective skin interfacing, microneedle penetration, and microchannel connectivity. This mechanically compliant approach supports wearable interstitial-fluid sampling and future closed-loop sensing systems.

Keywords: hollow microneedles, flexible patch, dermal interstitial fluid, wearable biofluid sampling, soft microfluidics.

Background, Motivation and Objective

Continuous access to physiological biomarkers is increasingly important for personalised medicine, endocrine monitoring, and closed-loop therapeutic systems. Dermal interstitial fluid has emerged as a promising alternative to blood because it contains clinically relevant small molecules and can be accessed with reduced invasiveness [1, 2]. Hollow microneedles are particularly attractive for this purpose, as they can extract interstitial fluid on demand and separate the sampling interface from the downstream sensing element [3]. Previous work demonstrated the direct two-photon-polymerisation printing of polymer hollow microneedles on silicon-based microfluidic chips, achieving mechanically robust skin insertion and in vivo interstitial-fluid extraction [4].

However, rigid chip-based microneedle platforms may have limited conformity to curved or dynamically moving skin surfaces. This can reduce interfacial stability, affect insertion reliability, and restrict long-term wearable operation. The objective of this work is therefore to develop a flexible and stretchable hollow microneedle patch that preserves the precision of 3D-printed microneedles while introducing an elastomeric skin-interfacing architecture for improved conformity and dermal access.

Description of the New Method or System

The proposed platform consists of two-photon-polymerised hollow microneedles partially embedded within a soft elastomeric backing layer and integrated with microfluidic channels for interstitial-fluid extraction and local delivery. The microneedle geometry includes a central lumen and side openings to enable fluidic access after insertion into the skin. A needle-base anchoring structure is introduced to improve mechanical retention between the printed microneedle and the soft backing layer, while reducing the risk of channel blockage during bonding.

In contrast to rigid silicon-based devices, the flexible backing layer is designed to conform to curved skin surfaces and accommodate local deformation during body movement. The soft microfluidic layer can be fabricated using mould-based soft lithography and bonded to the microneedle-bearing substrate to form a continuous fluidic pathway. This architecture decouples the requirements of the microneedle, which must be sufficiently stiff for skin insertion, from those of the patch substrate, which must be compliant for wearable skin interfacing.

Results

Preliminary fabrication demonstrates the feasibility of integrating hollow microneedles with a flexible and stretchable elastomeric microfluidic

platform. Optical inspection confirms that the hollow microneedle geometry is preserved after embedding and bonding, while the compliant backing layer allows the integrated patch to undergo bending, stretching, and twisting without visible structural failure (see Fig. 1). These deformation tests indicate that the platform can better accommodate curved and dynamically moving skin surfaces than rigid chip-based designs.

Skin-insertion tests using dye-assisted visualisation show successful microneedle penetration and local dermal access. Pre- and post-insertion imaging indicates that the microneedles remain structurally intact after insertion, supporting their suitability for repeated handling and skin interfacing. To verify the fluidic function of the integrated platform, coloured-liquid perfusion was used as a preliminary validation method. These tests confirmed continuous connectivity between the hollow microneedle lumen and the soft microfluidic channels, demonstrating the potential of the device for dermal interstitial-fluid extraction and intradermal therapeutic delivery.

Beyond fluid extraction and delivery, the microfluidic architecture provides a route for integration with downstream biosensors. By guiding extracted interstitial fluid from the hollow microneedles towards an external or embedded sensing region, the platform can decouple the skin-access interface from the sensing element. This design therefore supports future wearable systems for longitudinal biomarker monitoring, closed-loop sensing, and personalised therapeutic intervention.

Overall, this work advances hollow microneedle biofluid sampling from rigid microfluidic chips towards a conformal, mechanically compliant and biosensor-compatible wearable platform.

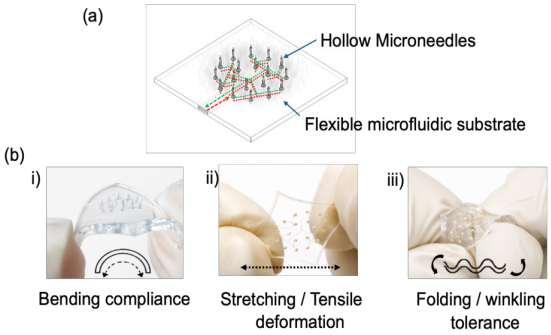

Fig. 1. Flexible and stretchable hollow microneedle patch integrated with a soft microfluidic platform. The concept combines a hollow microneedle array with a compliant microfluidic backing layer for dermal interstitial-fluid extraction and intradermal delivery. Bending, stretching, and twisting tests illustrate the mechanical compliance of the integrated patch for conformal skin interfacing.

References

[1] 1. Vora, L.K., et al., Microneedle-based biosensing. Nature Reviews Bioengineering, 2024. 2(1): p. 64–81.

[2] Friedel, M., et al., Opportunities and challenges in the diagnostic utility of dermal interstitial fluid. Nat Biomed Eng, 2023. 7(12): p. 1541–1555.

[3] Jiang, X. and P.B. Lillehoj, Microneedle-based skin patch for blood-free rapid diagnostic testing. Microsystems & Nanoengineering, 2020. 6(1): p. 96.

[4] Elias Abi-Ramia Silva, T., et al., 3D-printed polymer hollow microneedles on microfluidic platforms for minimally invasive interstitial fluid extraction. Cell Biomaterials, 2025. 1(1): p. 100008.

DOI 10.5162/eurosensors2026/SP 2.1.3

Managing Data Integrity in Medical Wearables

Walter Karlen
Universität Ulm, Albert-Einstein-Allee 45, 89081 Ulm, Germany
walter.karlen@ieee.org

Summary:

The shift to wearable medical monitoring introduces critical challenges in data integrity. This talk examines integrity across technical, temporal, and clinical dimensions. We propose addressing these gaps through uncertainty quantification, multimodal sensor fusion, and automated edge-based quality control. By prioritizing integrity-by-design, mHealth systems can deliver the trustworthy, actionable insights necessary for clinical adoption and remote healthcare.

Keywords: wearables, mHealth, Endotrain, quality, sensor fusion, checklist

Introduction

The transition of medical monitoring from controlled clinical environments to the unconstrained environments of everyday life via wearables is revolutionizing healthcare. However, this shift to remote, unsupervised settings introduces a significant challenge: uncertainty regarding the integrity of the generated data. For a wearable device to be clinically actionable, the data it produces must be more than just available; it must be trustworthy, precise, and contextually relevant.

In this special session, we explore the multiple dimensions and mechanisms of data integrity in mobile health (mHealth) systems, drawing specifically on medical time series from wearable sensors. We emphasize the intersection of signal processing, clinical validation, and the practical deployment of health technologies in resource-constrained or mobile settings.

Background

In the context of medical wearables, data integrity is a multidimensional construct requiring cross-domain expertise. This extends beyond the traditional definition of integrity as a security concept (e.g., the C-I-A triad), which focuses on preventing unauthorized modification. To ensure a correct diagnosis or treatment delivery, data must satisfy several criteria:

Technical Integrity (Signal Quality): This refers to the physical fidelity of the data. Wearables are prone to motion artifacts, sensor displacement, and environmental noise. High technical integrity requires sophisticated signal-quality algorithms to distinguish physiological processes from noise.

Temporal Integrity: Data must be accurately timestamped and synchronized. In multi-sensor arrays (e.g., matching heart rate with SpO_2), a lag of even a few seconds can lead to incorrect clinical interpretations. This is particularly challenging in body area networks or where devices are orchestrated across multiple sites and time zones.

Contextual Integrity: Data is only actionable if the context in which it was collected is known. For instance, a heart rate of 120 beats per minute has different clinical implications depending on whether the user is hiking or sleeping.

Completeness: Integrity is compromised by data gaps. These can often be caused by battery failures, connectivity issues, or synchronization errors.

Consistency: Consistency ensures that data remains unaltered and reproducible across platforms and during cloud transfers.

Clinical Integrity (Accuracy): The degree to which the wearable's digital output matches the "gold standard" clinical measurement. This involves objective and transparent validation against traditional medical devices.

Usability: A lack of usability in a medical system is a significant source of data integrity issues. With medically untrained users, poor interface design or ergonomic discomfort can lead to improper sensor placement and subsequent data degradation.

Approach

Our research group's approach focuses on making health monitoring smarter rather than just more frequent. We tackle the integrity gap through several methodological pillars:

Estimating uncertainty: We have introduced several metrics that allow us to quantify the severity of an integrity breach and to estimate the usefulness of the data for a given task. These metrics are highly application-specific. For example, a signal quality index (SQI) may be tuned to detect photoplethysmography distortions that prevent respiratory rate estimation while still allowing for reliable heart rate tracking [1]

Reliability through context-aware filtering: Sensor fusion enables systems to distinguish physiological anomalies from environmental noise. By fusing multimodal streams (physiological, environmental, and inertial), systems can increase specificity. While machine learning approaches for multimodal fusion show high potential, the challenge remains in obtaining robust, in-the-wild ground-truth labels.

Automated Quality Control and closed-loop feedback: Real-time algorithms at the edge can detect and flag low-quality data at the point of recording. By integrating these checks into a feedback loop, the system can alert users to adjust their devices immediately, preventing extensive data gaps. A practical example of this is the use of automated image quality checks in wound self-assessment [2].

Integrity-by-design: Maintaining integrity despite varying user expertise is a design-phase requirement. We advocate integrating ethics consultations and usability assessments early in the development of mHealth platforms [3], particularly for vulnerable users or in low-resource settings, and using quality checklists to help implementers anticipate challenges without requiring exhaustive multi-domain knowledge [4].

Conclusion

Managing data integrity goes beyond administrative data management plans or adherence to FAIR Data Principles [5]. It is an indispensable pillar of mobile health. As we move toward more autonomous medical systems, the quantity of data is never a substitute for quality. Future developments will likely focus on Explainable AI (XAI) to provide transparent justifications for including or excluding data, further bridging the gap between wearable technology and clinical trust.

References

[1] W Karlen *et al* Photoplethysmogram signal quality estimation using repeated Gaussian filters and cross-correlation *Physiol. Meas.* **33,** 1617, (2012); **doi:** 10.1088/0967-3334/33/10/1617

[2] Zhang J, *et al*. Wound Image Quality From a Mobile Health Tool for Home-Based Chronic Wound Management With Real-Time Quality Feedback: Randomized Feasibility Study *JMIR Mhealth Uhealth* (7),:e26149 (2021); doi: 10.2196/26149

[3] Ettinger, K. M., et al. Building quality mHealth for low resource settings. *Journal of Medical Engineering & Technology*, *40*(7–8), 431–443. (2016); doi: 10.1080/03091902.2016.1213906

[4] Zhang J, *et.al*. Data Integrity–Based Methodology and Checklist for Identifying Implementation Risks of Physiological Sensing in Mobile Health Projects: Quantitative and Qualitative Analysis *JMIR Mhealth Uhealth* 6(12), e11896 (2018); doi: 10.2196/11896

[5] Wilkinson, M., *et al.* The FAIR Guiding Principles for scientific data management and stewardship. *Sci Data* **3**, 160018 (2016); doi: 10.1038/sdata.2016.18

DOI 10.5162/eurosensors2026/SP 2.1.4

Mathematical Modelling at the Interface of Digital Endocrinology and Wearable Sensing Technologies

Belinda Lombard[1], Thomas Upton[2], Stafford L. Lightman[2], Eder Zavala[1,3]
[1] School of Mathematics, University of Birmingham, Birmingham, United Kingdom, [2] Laboratories for Integrative Neuroscience and Endocrinology, University of Bristol, Bristol, United Kingdom, [3] Centre for Biological Timing, University of Manchester, Manchester, United Kingdom.
eder.zavala@manchester.ac.uk

Summary:

Mathematical models are essential tools for fundamental understanding of hormonal dynamics within the Hypothalamic-Pituitary-Adrenal axis. Novel hormonal biosensing technologies from interstitial fluid require validating their dynamic fidelity against high resolution serum profiles. Computational methods can integrate our mathematical understanding of endocrine systems with multimodal wearable device datasets to quantify individual variability. This can help identify reliable proxies of endocrine function for precision medicine applications.

Keywords: mathematical model, hormones, interstitial fluid, wearables, rhythms.

Background, Motivation and Objective

The Hypothalamic-Pituitary-Adrenal (HPA) axis is a vital neuroendocrine system that maintains homeostasis by regulating stress hormone secretion through tightly controlled circadian and ultradian rhythms. Despite misaligned hormonal rhythms being associated with morbidity [1], we still lack a quantitative understanding of their variability across sub-populations, their mechanistic origin, pathogenicity and dynamic adaptation in diseased states.

Dynamic 24-hr hormonal profiles collected via high frequency biosampling have demonstrable potential to advance precision endocrinology [2]. Currently, clinical decision making is predominantly based on single time point measurements typically collected from blood, saliva or urine. While novel technologies for minimally invasive subcutaneous biosampling of interstitial fluid are developing rapidly [2, 3], a barrier for their adoption is quantifying their fidelity versus the gold standard of serum hormone concentrations. This is particularly important for assessing dynamic responses to perturbations (e.g., stressors, diagnostic tests, physical activity) which can manifest through rapid changes in adrenal steroid hormones away from their dynamic equilibrium.

Mathematical modelling and computational data analysis can address this challenge by testing our understanding of hormonal regulation and formulating new hypotheses about endocrine function. We extend this approach to gain insight on the mechanisms governing HPA axis activity, including circadian and ultradian rhythms as well as dynamic responses to stressors. This theoretical framework informs the analysis of non-invasive wearable device data to identify digital biomarkers for precision endocrinology [4].

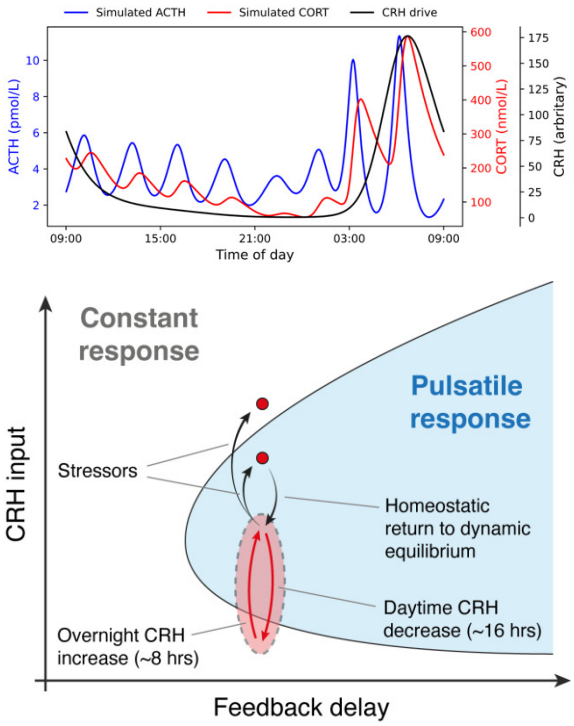

Fig. 1. Mathematical modelling of human HPA axis hormones in blood (top). The model predicts ultradian oscillations are governed by hypothalamic CRH and the delay within the pituitary-adrenal feedback loop (bottom). Figure adapted from Lombard et al. 2026 (under review).

Description of the New Method or System

We analyse 24-hour high-frequency hormonal profiles from healthy humans to quantify individual variability in HPA axis hormone rhythms. We use these profiles to develop and calibrate a mathematical model of the human HPA axis and perform computer simulations to understand the regulation of hormonal rhythms and their dynamic responses to stressors. We also analyse multimodal wearable device data in ambulatory humans to shed light on the dynamic relationship between endocrine markers and their variability across individuals.

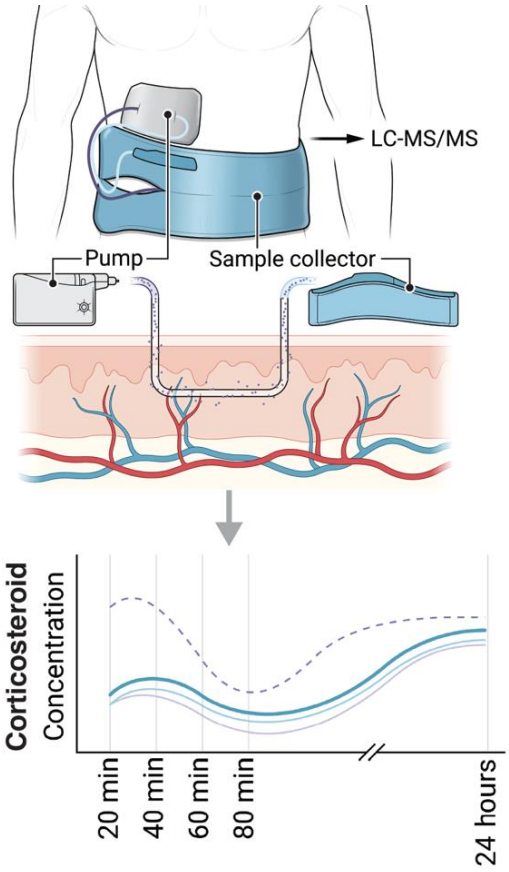

Fig. 2. Novel wearable technologies for high frequency hormonal sampling are enabling understanding of endocrine function. Computational analysis of this data allows quantification of variability, paving the way for digital endocrinology and precision medicine applications. Figure adapted from [5].

Results

The model reproduces distinct human-specific features of HPA axis dynamics, including an asymmetric circadian rhythm peaking at waking and ultradian oscillations with period and phase consistent with clinical observations. We show that the nonlinear delayed negative feedback between the pituitary and adrenal glands suffices to produce ultradian pulsatility and is critically dependent on the CRH drive and feedback delay. Computational simulations of the model predict how stressors of different intensity, duration and timing perturb HPA axis dynamics, allowing qualitative comparisons with stress responses observed during heart surgery. We also show how combining novel biosampling techniques with mathematical and computational analysis methods can support the development of digital tools for clinical decision-making. This includes digital biomarkers that help quantify variability of daily profiles of HPA axis rhythms, define normative ranges in health, and signal endocrine dysfunction [6].

Taken together, our work provides a theoretical framework for integrating novel data from wearable sensing technologies and understanding human HPA axis regulation. Our models offer quantitative insights into the robustness, fragility and individual variability of hormonal rhythms and their role in the stress response. Computational analysis of non-invasive wearable device data can help identify surrogates of hormonal rhythm misalignment. By shifting from a qualitative to a quantitative description of endocrine function, these insights will take us a step closer to personalised clinical interventions for which timing is key.

References

[1] Zavala E. Misaligned hormonal rhythmicity: Mechanisms of origin and their clinical significance. *Journal of Neuroendocrinology* **34**(6):e13144 (2022) doi:10.1111/jne.13144

[2] Upton TJ, Zavala E, Methlie P, *et al*. High-resolution daily profiles of tissue adrenal steroids by portable automated collection. *Sci. Transl. Med.* **15**:eadg8464 (2023) doi:10.1126/scitranslmed.adg8464

[3] Friedel M, Thompson IAP, Kasting G. *et al.* Opportunities and challenges in the diagnostic utility of dermal interstitial fluid. *Nat. Biomed. Eng.* **7**:1541–1555 (2023) doi:10.1038/s41551-022-00998-9

[4] Grant AD, *et al*. Analysis of wearable time series data in endocrine and metabolic research. *Curr. Op. Endo. Metab. Res.* **25**:100380 (2022) doi:10.1016/j.coemr.2022.100380.

[5] Mohan DR, Lerario AM. Closing the loop on adrenal health, dysfunction, and disease. *Sci. Transl. Med.* **15**:eadg4450 (2023) doi:10.1126/scitranslmed.adh4450

[6] Grytaas MA, Upton TJ, *et al.* Home measurement of 24-hour corticosteroid dynamics in primary aldosteronism, *PREPRINT* v1 (2025) doi:10.21203/rs.3.rs-6095171/v1

DOI 10.5162/eurosensors2026/SP 2.1.5

“How are you today?” Harnessing speech as a window into life with a chronic disease

Viktor von Wyl[1]
[1] Digital & Mobile Health Group; Epidemiology, Biostatistics & Prevention Institute (EBPI); University of Zurich, Zurich, Switzerland
viktor.vonwyl@uzh.ch

Summary:
This presentation will illustrate the usefulness of complementing wearable sensor studies with speech and patient narratives for better measurement contextualization and deeper insights into the lived experiences of persons with chronic diseases. Moreover, I will showcase a new tool for harnessing speech in health studies and outline a roadmap for its application and continued development within our Endotrain project.

Keywords: Remote Monitoring, Speech, Natural Language Processing, Person-Centered Research, Chronic Diseases.

Background

Sensor-based digital biomarkers hold promise for remote real-time monitoring of chronic diseases. Yet, they may offer only a limited perspective into health, symptoms, patient-led disease management, or lifestyle factors, which are relevant for clinical decision making. [1]

Speech-based descriptions or personal narratives can complement digital biomarkers by enabling such further insights into important aspects of life, but their analysis requires substantial expertise and manual efforts.

Objectives

In this presentation, I will illustrate how recent developments in large language models and natural language processing can increase feasibility and usability of speech-based information in sensor-based health studies and research in general.

Presentation Outline

Based on two study examples, I will showcase how we have leveraged speech data and patient narratives 1) for contextualizing sensor measurements [3], and 2) to characterize life circumstances and longer-term disease histories from a person-perspective [4].

Building on these studies, I will offer insights into the ongoing development of our software tool SpHeRe (acronym for Speech in Health Research). SpHeRe aims to facilitate the collection and analysis of speech and patient-narratives in health studies at scale.

I will conclude with remarks on our plans for applying SpHeRe in our Endotrain SDC17 project, as well as on our development roadmap for closing existing analysis tool gaps.

Conclusion

Integrating speech and personal narratives can meaningfully complement sensor information by providing more depth (e.g. into symptom descriptions) or offering additional context in which to interpret sensor signals (e.g. reasons for signal interruptions).

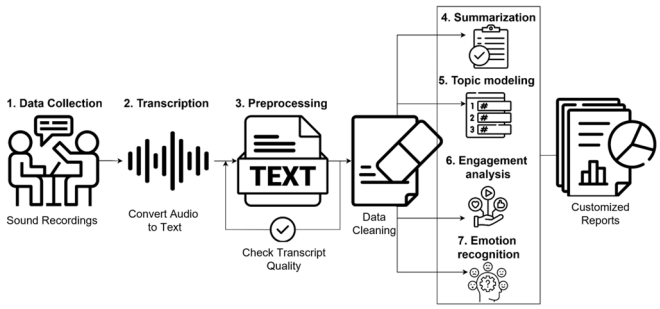

Fig. 1. Speech-to-text transcription and analysis workflow as integrated into our SpHeRe (Speech in Health) research tool.

References

[1] Azodo I, Williams R, Sheikh A, Cresswell K. Opportunities and Challenges Surrounding the Use of Data From Wearable Sensor Devices in Health Care: Qualitative Interview Study. J Med Internet Res;22(10):e19542 (2022); https://doi.org/10.2196/19542

[2] Daniore, P., Nittas, V., Haag, C. et al. From wearable sensor data to digital biomarker development: ten lessons learned and a framework

proposal. npj Digit. Med. 7, 161 (2024); https://doi.org/10.1038/s41746-024-01151-3

[3] Lu Z, Signer T, Sylvester R, Gonzenbach R, von Wyl V, Haag C, Implementation of Remote Activity Sensing to Support a Rehabilitation Aftercare Program: Observational Mixed Methods Study With Patients and Health Care Professionals. JMIR Mhealth Uhealth;11:e50729 (2023); https://doi.org/10.2196/50729

[4] Haag C, Steinemann N, Chiavi D, Kamm CP, Sieber C, Manjaly Z-M, et al. Blending citizen science with natural language processing and machine learning: Understanding the experience of living with multiple sclerosis. PLOS Digit Health 2(8): e0000305 (2023); https://doi.org/10.1371/journal.pdig.0000305

Acknowledgements

This work is funded by the Swiss National Science Foundation Spark grant CRSK-3_229057 and by the University of Zurich Teaching Fund open_innovation grant. Endotrain is funded by the HORIZON.1.2 - Marie Skłodowska-Curie Actions (MSCA) - Grant agreement ID: 101227148.

I would also like to thank the SpHeRe team from the Digital & Mobile Health Group: Dr. Sofia Strukova, Jonas Fabian, and Dr. Sintieh Ekongefeyin

DOI 10.5162/eurosensors2026/SP 2.1.6

Participatory AI in Endocrinology: Supporting Shared Decision-Making Through Multimodal Sensing

Luis Fernandez-Luque[1]
[1] *Adhera Health SL, Sevilla, Spain*
luis@adherahealth.com

Summary: Endocrine disorders require continuous interpretation of physiological, behavioral, and biopsychosocial information. We present a human centered multimodal sensing framework developed at Adhera Health to better understand the needs of people living with chronic conditions including obesity, diabetes, and growth disorders. The framework integrates wearable derived signals, patient reported outcomes, behavioral interaction patterns, and patient generated language to support contextualized care and shared decision making between patients, caregivers, and clinicians. Combining approaches from Artificial Intelligence and Human Computer Interaction, this work establishes the foundation for the ENDOTRAIN project on multimodal AI systems for adrenal insufficiency management in the context of the PhD project DC7.

Keywords: multimodal sensing, biopsychosocial data, endocrine disorders, human centered AI, shared decision making

Background

Endocrine disorders such as obesity, diabetes, growth disorders, and adrenal disorders require continuous longitudinal management involving heterogeneous physiological and contextual information. While wearable and mobile sensing technologies have significantly expanded the availability of patient-generated health data, many systems remain limited in their ability to integrate psychosocial context, behavioral patterns, and psychosocial data into clinically meaningful use cases, including also the shared decision making between patients and clinicians in the context of self-management and patient education. Chronic endocrine conditions are strongly influenced by stress, symptom perception, caregiver dynamics, treatment burden, and lifestyle adaptation, motivating biopsychosocial approaches to digital health solutions. This is particularly evident in adrenal disorders where the hormone of cortisol is also affected by aspects such as stress, sleep and other factors.

Adhera Health Platform

The initiative will leverage the Adhera Caring platform, a digital health platform designed to support the creation of longitudinal, multimodal cohorts in chronic conditions through continuous patient engagement and real-world data capture. The platform combines longitudinal real-world data collection capabilities with participant engagement and self-management support functionalities that facilitate continuous follow-up and contextual understanding of the treatment experience in real-world settings. The platform supports the collection of active and passive patient-generated health data, patient-reported outcomes, behavioral and psychosocial measures, treatment experience data, engagement metrics, and contextual family-level information over time.

Unlike traditional patient-centric approaches, the Adhera Caring platform incorporates a family-centered framework that enables the capture of household routines, family support dynamics, caregiver perspectives, and shared lifestyle factors that may influence treatment persistence and long-term obesity management. This approach is particularly relevant in obesity and obesity-related comorbidities, where health behaviors and treatment experiences are often shaped within the family environment.

The Adhera Caring platform has been successfully deployed across multiple chronic conditions, including type 1 diabetes [1], type 2 diabetes [2], growth hormone disorders [3,4], and obesity [5], and is currently being expanded to additional therapeutic areas and chronic disease populations.

Open Research Challenges

Current approaches in endocrine digital health increasingly rely on multimodal data combining wearable derived physiological time series, structured clinical variables, patient reported outcomes, behavioral interaction patterns, and biopsychosocial dimensions relevant to chronic disease management. However, major research gaps remain regarding how Artificial Intelligence systems and Digital Twin approaches can

transform heterogeneous multimodal data into representations that are clinically meaningful, trusted, and useful for both patients and clinicians in the context of daily life with chronic conditions.

Existing AI driven approaches often focus on prediction accuracy while providing limited understanding of how biopsychosocial context, lived experience, emotional burden, treatment routines, and family dynamics influence self management and clinical decision making. In endocrine disorders such as adrenal insufficiency, clinically relevant events are strongly affected by stress, behavioral adaptation, symptom interpretation, and contextual factors that are difficult to capture through isolated physiological measurements alone.

Another important challenge relates to trust, explainability, and usability of AI supported Digital Twin systems. Current approaches often conceptualize trust as an individual user attribute, while chronic disease management is inherently collaborative and involves multiple stakeholders including patients, caregivers, clinicians, and increasingly AI systems and AI Agents. There is limited knowledge regarding how trust should be managed when AI generated outputs are interpreted differently by different actors. For example, an AI recommendation may be trusted by clinicians but not by patients, particularly when the recommendation affects daily life, self-management routines, emotional wellbeing, or lifestyle adaptations. In such contexts, shared decision making becomes critical, requiring AI systems that not only provide technically accurate outputs, but also support negotiation, communication, contextualization, and alignment between stakeholders.

These challenges introduce important opportunities at the intersection of Artificial Intelligence, Human Computer Interaction, and Computer Supported Cooperative Work. Understanding how humans interact, negotiate, and build trust with AI mediated representations remains an open research question, particularly in chronic endocrine care where decision making is continuous, longitudinal, and highly contextual.

Expected Results in Endotrain

Prior deployments of multimodal digital health interventions at Adhera Health in obesity, diabetes, and growth disorders demonstrated the feasibility of integrating physiological, behavioral, and biopsychosocial information into longitudinal endocrine care pathways. Participatory studies highlighted the relevance of contextual factors including emotional burden, treatment routines, family dynamics, symptom interpretation, and behavioral adaptation for understanding the needs of people living with chronic conditions.

Building on this foundation, the Adhera Health DC7 subproject within ENDOTRAIN is expected to contribute to the development and evaluation of multimodal Artificial Intelligence systems capable of integrating wearable derived physiological time series, structured clinical data, patient reported outcomes, biopsychosocial measures, and patient generated natural language reports in adrenal insufficiency. The project will explore multimodal fusion strategies for combining heterogeneous data modalities into contextualized patient representations supporting personalized care and shared decision making between patients, caregivers, and clinicians. The DC7 project will also contribute Human Computer Interaction methodologies for transforming multimodal biopsychosocial data into interpretable visual and language-based representations that facilitate shared decision making and improve communication around complex endocrine conditions.

Funding

This work was supported by the EndoTrain Digital Endocrinology Training Network project “Endotrain Digital Endocrinology Training Network to Combat Adrenal Diseases” (Grant Agreement No. 101227148).

References

[1] de Arriba Muñoz, Antonio, et al. "Empowering Caregiver Well-Being With the Adhera Caring Digital Program for Family Caregivers of Children Living With Type 1 Diabetes: Mixed Methods Feasibility Study." *JMIR Pediatrics and Parenting* 8 (2025): e66914.

[2] Rodríguez Montes, Oscar Eduardo, et al. "Efficacy of a mobile application for glycemic control in type 2 diabetes: a randomized clinical trial." (2025).

[3] de Arriba Muñoz, A., e.t. al (2025). Enhancing Adherence and Mental Well-Being in Pediatric Growth Hormone Therapy: Feasibility Prospective Observational Study of a Family-Centered Digital Companion. *JMIR Pediatrics and Parenting*, *8*(1), e67102.

[4] Savage, M. O., et al.. (2022). Adherence to r-hGH therapy in pediatric growth hormone deficiency: current perspectives on how patient-generated data will transform r-hGH treatment towards integrated care. *Patient preference and adherence*, 1663-1671.

[5] de Arriba Muñoz, A., et. Al. Clinical Outcomes Associated with the Use of a Family-Based Digital Support Program in Patients with Pharmacologic Treatment for Obesity. *Journal of Clinical Medicine*, *15*(1), 222.

DOI 10.5162/eurosensors2026/SP 2.2.1

The cancer microbiome produces distinct volatile organic compounds

Bhamini Vadhwana[1], Pallavi Arya[1], Nayaab Abdul Kader[1], Piers Boshier[1], Sara Jamel[1], Ilaria Belluomo[1], Philip Leung[1], Patrik Španěl[2], Lesley Hoyles[3], George B Hanna[1]
[1] Department of Surgery and Cancer, Imperial College London, Du Cane Road, London, UK
[2] Department of Chemistry of Ions in Gaseous Phase, J. Heyrovský Institute of Physical Chemistry, Prague, Czech Republic
[3] School of Science and Technology, Nottingham Trent University, Nottingham, UK
Corresponding Author: g.hanna@imperial.ac.uk

Summary:
Oesophagogastric cancer harbours a distinct microbiome that produces volatile short chain fatty acids. Bacterial headspace VOCs were characterised using an optimised, reliable, high-throughput TD-GC-ToF-MS and two-dimensional GC-MS with quality-controlled protocols.

Keywords: cancer, bacteria, VOC, GC-MS

Title
The cancer microbiome produces distinct volatile organic compounds.

Headlines
This study utilises an optimised and reliable method for headspace VOC sampling of liquid bacterial cultures, using a thermal desorption-gas chromatography-time of flight-mass spectrometer.

Background, Motivation and Objective

The detection of bacterial volatile organic compounds (VOCs) has established utility in healthcare. [1,2] VOCs produced by the cancer microbiome offers a novel non-invasive platform for early disease detection. Our previous work identified volatile short chain fatty acids (SCFAs) in the exhaled breath of patients with oesophagogastric cancer, demonstrating the potential for a breath-based diagnostic test in a cancer of unmet clinical need. [3,4] This research aims to investigate the differential oesophagogastric cancer-related microbiome as the source of VOCs detected in exhaled breath.

Description of the New Method or System

Bacterial headspace VOCs were extracted using an automated sampling device onto thermal desorption tubes and analysed by mid-polar TD-gas chromatography-time of flight-mass spectrometry (TD-GC-ToF-MS) and two-dimensional GC-MS for structural identification. Stringent quality control and a robust analytical pipeline supported both untargeted and targeted approaches, enabling high-throughput dynamic sampling.

Results
Bacteria from cancer tissue and saliva were cultured and underwent whole genome sequencing demonstrating an abundance of *Lactobacillus*, *Prevotella*, *Veillonella*, *Fusobacterium*, and *Streptococcus*. Liquid bacterial cultures were established under anaerobic conditions, with growth curves to identify peak metabolic activity for VOC production. Bacteria cultured from oesophagogastric cancer patients demonstrated significantly higher volatile SCFA production, with responsible metabolic pathways identified through metagenomic sequencing. This proof-of-concept study supports a novel breath test based on the cancer's distinct bacterial VOC profile. The breath test will offer a cost-effective, non-invasive, and patient-friendly approach to identifying high-risk individuals presenting with non-specific upper gastrointestinal symptoms.

Fig. 1. Automated headspace sampling of volatile organic compounds produced by liquid bacterial cultures onto thermal desorption tubes.

References

[1] Graham DY, Klein PD, Evans DJ Jr, Evans DG, Alpert LC, Opekun AR, Boutton TW. Campylobacter pylori detected noninvasively by the ^{13}C-urea breath test. Lancet. 1(8543):1174–7 (1987); doi: 10.1016/s0140-6736(87)92145-3

[2] Metz G, Gassull MA, Drasar BS, et al. Breath-hydrogen test for small-intestinal bacterial colonisation. Lancet. 1:668–669. (1976); doi: 10.1016/s0140-6736(76)92779-3

[3] Markar SR, Wiggins T, Antonowicz S, Chin ST, Romano A, Nikolic K, Evans B, Cunningham D, Mughal M, Lagergren J, Hanna GB. Assessment of a Noninvasive Exhaled Breath Test for the Diagnosis of Oesophagogastric Cancer. JAMA Oncol. 4(7):970-976 (2018). doi: 10.1001/jamaoncol.2018.0991.

[4] Booth ME, Clements HA, Helbrow J, Baxter MA, Bleaney CW, Hawkins MA, Markar SR, Peters CJ, Smyth EC, Crosby TDL; UK and Ireland Oesophagogastric Cancer Group. United Kingdom and Ireland Oesophagogastric Cancer Group Cancer Update 2023. Clin Oncol (R Coll Radiol). 36 (2024). doi: 10.1016/j.clon.2024.04.013

DOI 10.5162/eurosensors2026/SP 2.2.2

Abstract Preparation Guidelines for the Eurosensors 2026

Yukina Partington[1], Beatrice Dalla Via[1], Fabrice Abgottspon[1], Isaure de Geyer[1], Piet Cools[2], Andrew J. deMello[1], Daniel A. Richards[1]*
[1] ETH Zürich, DCHAB, Vladimir-Prelog-Weg 1, 8093, Zürich, Switzerland
[2] Ghent University, Faculty of Medicine, Corneel Haymenslaan10, 9000, Ghent, Belgium
daniel.richards@chem.ethz.ch

Summary:

Base Gap switches are programmable transcriptional regulators activated DNA, which can be used to sense disease. In this talk, I will detail how these switches are easy to install, exert strong control over expression, and are highly orthogonal. I will show that Base Gap switches can be combined with Recombinase Polymerase Amplification to achieve single-copy detection of targets and be leveraged to differentiate single-nucleotide mismatches. Finally, I will discuss how we will apply Base Gap switches to detect drug-resistant infections. This talk will discuss the results of our recently published work.[1,2]

Keywords: Synthetic gene circuits, IVTT, multiplexing, transcriptional regulation, SNVs.

Title

Base Gap Switches: Exploiting the Central Dogma of Molecular Biology to Detect Disease

Background, Motivation and Objective

Proteins are ideal signalling molecules. Their chemical diversity enables a broad range of readily detectable biochemical processes, including fluorescence, luminescence, reduction, oxidation, hydrolysis, ligation, and more. As such, linking protein expression to the presence of disease markers presents a powerful opportunity for sensing. Such methods rely on manipulating the replication–transcription–translation pathway (the “central dogma” of molecular biology). This is achieved using regulatory components, commonly termed “switches”, that control various mechanisms essential for protein expression.[3] Unfortunately, contemporary switches are hampered by poor sensitivity and specificity, largely due to expression in the absence of the target, a phenomenon we call “leakage”. The objective of this work was to develop less leaky methods for manipulating protein expression in response to disease targets.

Description of the New Method or System

The most common tools for controlling protein expression in response to disease targets are toehold switches.[4] These rely on target RNA binding inducing a conformational change in an mRNA, which in turn enables *translation* of this mRNA into a functional protein. These leak because of conformational changes that occur even in the absence of the target mRNA. Thus, we reasoned that removing the reliance on conformational changes would reduce leakage. To do this, we developed a DNA-based switch that controls *transcription*. In these switches, we introduce a gap into the template strand of a gene encoding a signalling protein. This gap prevents elongation by RNA Polymerase, halting transcription and thus protein expression. This gap is engineered to be specific to a DNA target, which can “fill” the gap and allow transcription to resume (**Fig. 1A$_{i}$**). Since this gene-silencing method does not rely on conformational changes, but rather total physical disruption of transcription, we hypothesised that it would reduce leakage. Moreover, since these switches are built from DNA, rather than RNA, we reasoned that they would be easier to work with and more robust. We termed these new transcriptional switches “Base Gap” switches.

Results

As a proof-of-concept, we installed a Base Gap switch onto a gene encoding the fluorescent protein mNeonGreen (**Fig. 1A$_{ii}$**). We observed target-dependent expression as a function of single- and double-stranded DNA targets (switch ON) (**Fig. 1B**). In this proof-of-concept experiment, we observed no leakage (Switch OFF). We also performed cross-validation of seven orthogonally designed Base Gap switches, demonstrating excellent orthogonality (**Fig. 2A**). We exploited this orthogonality by installing three orthogonal switches onto genes encoding for blue, orange, and red fluorescent proteins, and demonstrated one-pot multiplexing of three tar-

gets (**Fig. 2B**). Next, we combined Base Gap switches with Recombinase Polymerase Amplification (RPA) to achieve single-copy-number sensitivity for *Trichomonas vaginalis* (**Fig. 3A**). Finally, we showed that Base Gap switches could be used to detect Single Nucleotide Variants (SNVs) within circulating tumour DNA (ctDNA) associated with Epidermal Growth Factor Receptor (EGFR) mutations (**Fig. 3B**).

Illustrations, Graphs, and Photographs

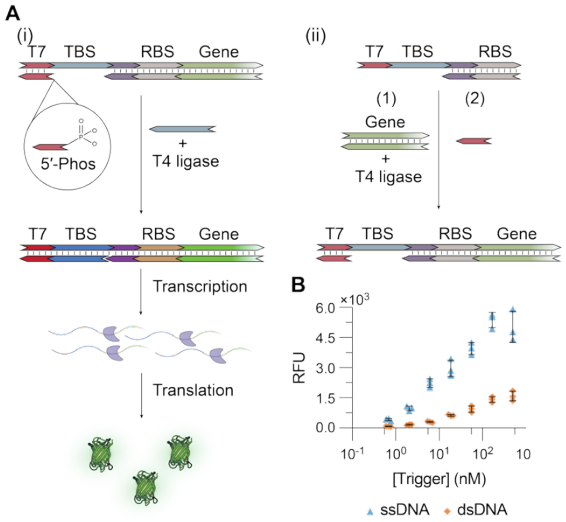

Fig. 1. (A) (i) A diagrammatic representation of the mechanism of Base Gap switches. (ii) The ligation-based installation of Base Gap switches onto genes. (B) Expression of mNeonGreen under the control of a Base Gap switch in response to single-stranded (ssDNA) and double-stranded (dsDNA) DNA. Figures are adapted from our published work [1,2].

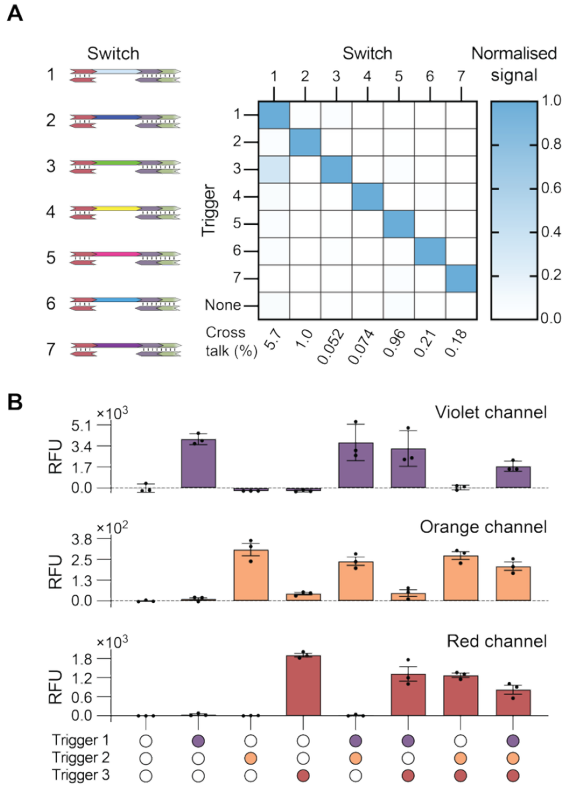

Fig. 2. (A) Cross-validation of seven targets against seven Base Gap switches to demonstrate orthogonality. (B) One-pot multiplexing of three targets using three Base Gap switches controlling the expression of blue, orange, and red fluorescent proteins. Figures are adapted from our published work [1,2].

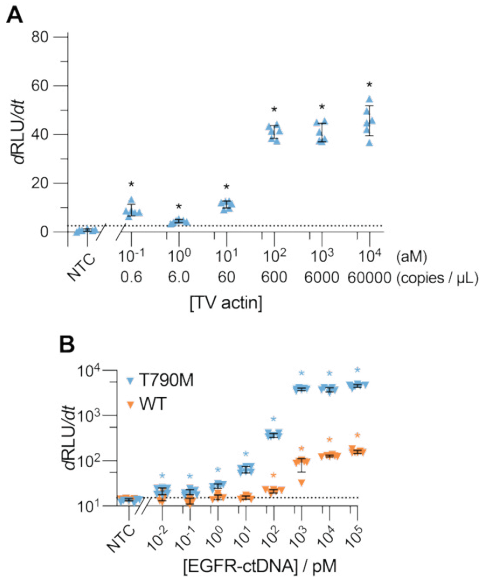

Fig. 3. (A) Detection of the actin gene of Trichomonas vaginalis (TV) using Base Gap switches, combined with RPA. (B) Differentiation of the T790M and wild type (WT) EGFR gene in ctDNA. Figures are adapted from our published work [1,2].

References

[1] Y. Partington, B. Dalla-Via, F. Abgottspon, I. de Geyer, P. Cools, A. J. deMello, D. A. Richards, Base Gap Switches as Transcriptional Regulators and Their Applications as Biosensors, *Nature Sensors*, just accepted. (2026)

[2] Y. Partington, B. Dalla-Via, F. Abgottspon, I. de Geyer, P. Cools, A. J. deMello, D. A. Richards, Base Gap Switches as Transcriptional Regulators and Their Applications as Biosensors, *ChemRxix.* (2026) https://doi.org/10.26434/chemrxiv.15001046/v1

[3] F. Sedlmayer, D. Aubel, M. Fussenegger, Synthetic Gene Circuits for the Detection, Elimination and Prevention of Disease. *Nat. Biomed. Eng.* *2*, 399–415. (2018) https://doi.org/10.1038/s41551-018-0215-0.

[4] A. A. Green, P. A. Silver, J. J. Collins, P. Yin, Toehold Switches: De-Novo-Designed Regulators of Gene Expression. *Cell*, *159*, 925–939. (2014) https://doi.org/10.1016/j.cell.2014.10.002.

DOI 10.5162/eurosensors2026/SP 2.2.3

Isolation and culturing of urinary bacteria for VOC-based rapid diagnostics

Anne Vescovi[1], Glenda Vasku[1], Emma Wetter Slack[1,2]
[1] Laboratory for Mucosal Immunology, Institute for Food, Nutrition and Health, D-HEST, ETH Zürich, Zürich, Switzerland
[2] Botnar Research Institute for Child Health, Basel, Switzerland
emma.slack@hest.ethz.ch

Summary:

Rapid alternatives to traditional 2 - 4 day urine culture are urgently needed to improve patient recovery and combat antimicrobial resistance. Volatile organic compound (VOC) sensing offers a powerful, non-invasive route to bacterial identification, but establishing reproducible metabolic markers requires a workflow that accounts for both pathogen diversity and variable growth dynamics. Using expanded urine culture, we isolated bacteria from 80 patient samples, revealing 35 distinct genera and pronounced inter-individual compositional variability. Growth kinetics of 75 *E. coli* strains were benchmarked under urinary-like conditions, revealing significant lag-time variation that motivates rigorous standardization for reproducible VOC profiling.

Keywords: UTI pathogens, method development, UTI rapid diagnostics, expanded urine culture

Introduction

Urinary tract infections (UTIs) are among the most prevalent bacterial infections worldwide. Generalized antibiotic therapy is often administered, contributing significantly to antimicrobial resistance [1]. Volatile organic compound (VOC) profiling of bacterial cultures offers a promising, non-invasive route to rapid pathogen identification: bacteria produce characteristic metabolic volatiles detect-able within hours [2]. However, translating VOC signatures into reliable diagnostics requires a well defined, reproducible culture workflow that accounts for the full diversity of urinary pathogens and their variable growth dynamics. This work presents the building of such a workflow, from patient-derived isolate collection to standardized cultivation under urinary-like conditions.

Methods

Urine samples were collected from 80 patients. Expanded urine culture (EUC) was applied to enhance recovery of slow-growing and low-abundance organisms: samples were plated on multiple media types (BHIS-blood agar, chromogenic agar, MRS) and incubated for up to 5 days under both aerobic and anaerobic conditions. All isolated colonies were identified by MALDI-TOF mass spectrometry. 75 E. coli strains were selected to benchmark growth kinetics. Strains were cultivated in anaerobic artificial urine medium at 37°C, and optical density (OD600) was measured every 20 minutes for 22 hours using an automated plate reader. Growth curves were normalized to initial OD (ΔOD600) and subjected to k-means clustering (k = 4) based on lag time and maximum growth rate.

Results

We isolated 35 different bacterial genera originating from 80 patients. Escherichia was the most prevalent genus (n = 28 patients), followed by Streptococcus (n = 19), Enterococcus (n = 16), Klebsiella and Staphylococcus (n = 9 each), as shown in Fig. 1. Beyond the dominant uropathogens, a pronounced “long tail” of low-prevalence genera (e.g., Veillonella, Actinomyces, Facklamia) was observed. These genera were isolated from fewer than 5 patients, highlighting the remarkable inter-individual compositional variability of the urinary microbiome.

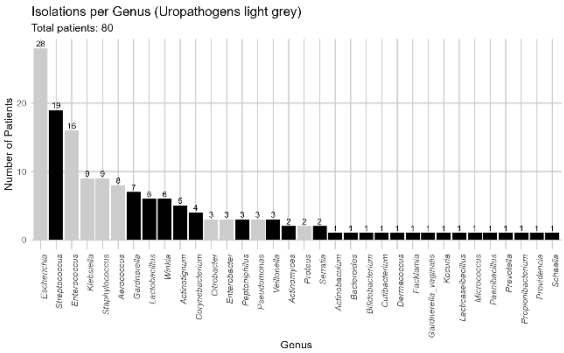

Fig. 1. Isolations per genus from 80 patient urine samples (EUC). Uropathogens shown in light grey. A pronounced long tail highlights low abundance non-uropathogenic genera.

Growth kinetics of 75 E. coli strains in artificial urinary media under anaerobic conditions revealed four distinct growth clusters (Fig. 2). The majority of strains (Clusters 1 and 2, n = 68) showed moderate growth with ΔOD600 reaching 0.3–0.4 after 22 hours, while Cluster 0 (n = 6) displayed markedly slower kinetics. Notably, one outlier strain (Cluster 3, n = 1) exhibited substantially faster and higher-amplitude growth (ΔOD600 ≈ 0.95), with a steep exponential phase beginning around hour 5. The observed variation in lag times (ranging from under 1 to over 5 hours) underscores why a fixed time-point sampling strategy can lead to inconsistent growth phases, followed by inconsistent VOC profiles. These results motivate the use of growth-phase-aware, standardized cultivation protocols to ensure reproducibility across strains and growth phases.

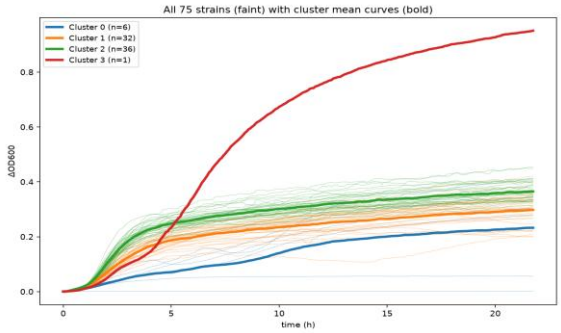

Fig. 2. Growth curves (ΔOD600) of 75 E. coli strains in anaerobic artificial urine medium over 22 hours. Individual strain curves (faint) and cluster mean curves (bold) are shown for four clusters.

References

[1] M. R. Timm, S. K. Russell, S. J. Hultgren, Urinary tract infections: pathogenesis, host susceptibility and emerging therapeutics, Nature Reviews Microbiology 23(2), 72–86 (2025); doi: 10.1038/s41579-024-01092-4

[2] W. Filipiak et al., Towards the Identification of Antibiotic-Resistant Bacteria Causing Urinary Tract Infections Using Volatile Organic Compounds Analysis, *Int. J. Mol. Sci.* 21(23), 9297 (2020); doi: 10.3390/ijms21239297

DOI 10.5162/eurosensors2026/SP 2.2.4

Machine Learning and Gas Sensors for Antimicrobial Resistence Identification

Albert Belenguer-Llorens[1,2], Emma Slack[3,4,5], Adrian Egli[6,7] . Thomas M. Kessler[8] , Andreas T. Güntner[9], Catherine R. Jutzeler[1,2]
[1] Department of Health Sciences and Technology (D-HEST), ETH Zurich, Switzerland;
[2] SIB Swiss Institute of Bioinformatics, Lausanne, Switzerland
[3] Laboratory for Mucosal Immunology, Institute for Food, Nutrition and Health, Department of Health Sciences and Technology, ETH Zurich, Zurich, Switzerland
[4] Basel Institute for Child Health, Basel, Switzerland
[5] Sir William Dunn School of Pathology, University of Oxford, Oxford, UK
[6] Institute of Medical Microbiology, University of Zurich, Zurich, Switzerland
[7] Swiss National Reference Center for Emerging Antibiotic Resistance (NARA) Network, University of Fribourg, Fribourg, Switzerland
[8] Department of Neuro-Urology, Balgrist University Hospital, University of Zurich, Zurich, Switzerland
[9] Department of Mechanical and Process Engineering, ETH Zurich, Zurich, Switzerland.
abelenguer@ethz.ch

Summary:
The global rise of antimicrobial resistance (AMR) requires a paradigm shift away from slow, culture-based diagnostics toward more rapid, data-driven approaches. We propose a novel pipeline that integrates high-resolution volatilomics extracted from gas sensors with machine learning (ML) techniques to bypass traditional time-consuming workflows, enabling rapid identification of resistance profiles directly from microbial emissions. This approach aims to provide a scalable foundation for point-of-care diagnostics, with the potential to reduce antibiotic overuse and support timely, precision-guided therapy.

Keywords: Machine Learning, Volatilomics, Antimicrobial Resistance, Microbiology, Gas Sensors

Background, Motivation and Objective

The global rise of antimicrobial resistance (AMR) is one of the current most concerning and rising public health problems, estimated to cause more than 8 million deaths by 2050 [1]. The AMR crisis is driven and exacerbated by the misuse (e.g. premature discontinuation of antibiotic treatment) and their overuse in both healthcare and the food industry. A major contributing factor is that current clinical diagnostics cannot adequately counter this trend in real time. Conventional microbial identification and susceptibility testing are predominantly culture-based, combining techniques such as matrix-assisted laser desorption ionization time-of-flight mass spectrometry (MALDI-TOF-MS) and antibiotic susceptibility testing (AST), which usually requires from 24 hours to several weeks. Thus, this inherent delay forces clinicians to rely on empirical broad-spectrum antibiotic therapy, a practice that can compromise patient outcomes and facilitate the emergence of resistant strains.

To address these challenges, we aim to propose a new diagnostic pipeline to bypass the limitations of traditional microbiology using volatilomics data captured by gas sensors [2]. Microbial metabolism produces specific volatile organic compounds (VOCs) that can serve as rapid biomarkers for both species identification and resistance profiling. Although volatilomics is not yet as widely established in clinical routines as other omics modalities (such as genomics or proteomics), there are recent growing evidence of its utility in bacterial identification [3]. The complexity and high dimensionality of volatilomic data require robust computational frameworks to be clinically actionable. In this context, Machine Learning (ML) algorithms have already demonstrated strong performance in related modalities, such as in genomics and mass spectrometry, where they are used to identify biological signatures.

To this end, we propose a novel ML pipeline designed to identify AMR profiles directly from the headspace of clinical samples. By combining high-resolution discovery using mass spectrometry with the development of tailored

chemoresistive sensor arrays, we aim to establish a rapid, data-driven diagnostic workflow.

Volatilomics in microbiology

Microbial volatilomics involves the systematic characterization of low-molecular-weight metabolites (primarily VOCs) secreted during bacterial proliferation and metabolic shifts under specific conditions such as antibiotic stress. These data represent a high-dimensional space, where target analytes (e.g., indoles, ketones, or short-chain fatty acids) often coexist with complex background matrices at trace-level concentrations (parts-per-billion or trillion).

The technical challenge lies in the dynamic nature of these emissions: VOC profiles are not static but exhibit distinct temporal kinetics (Figure X). Thus, requiring from complex computational methods to analyze the different metabolites interactions/tendencies across time.

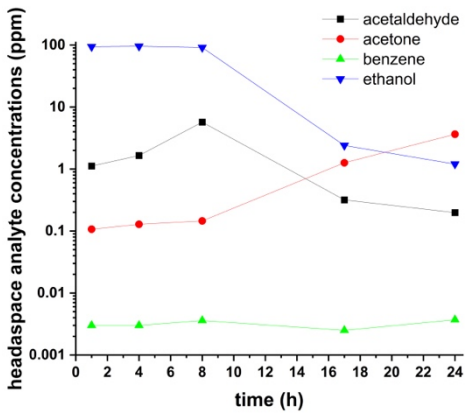

Fig. 1. Example of variation in concentration (ppm) of VOCs for a specific bacteria across time.

Description of the New Method or System

To extract meaningful diagnostic patters from the VOCs dynamics, we propose a locally deployable ML pipeline designed for integration into resource-constrained diagnostic devices. To ensure compliance with the EU AI Act for high-risk Class III medical devices, our architecture prioritizes interpretability over "black-box" deep learning (DL) models, which are also unsuitable for the limited sample size of these datasets, typical of early-stage clinical studies [4].

The pipeline initiates with a Hidden Markov Model (HMM) layer to characterize the VOCs emission dynamics of resistance vs non-resistance bacteria. That is, given the dynamics over time of new sample, calculate their probability to belong to one of both. To improve performance, we will extract other kinetic-based features such as signal entropy or tendency using a rolling window. Then, to capture the potential non-linear relations without sacrificing transparency, the final variable set (HMM-derived and kinetic features) will be used to train an ensemble of interpretable algorithms, including XGBoost, Random Forests, Support Vector Machines (SVMs), and Generalized Additive Models (GAMs).

A critical stage of the pipeline is a robust feature selection protocol, which the above models can natively perform with regularization techniques. This identifies the minimal subset of high-impact biomarkers required for accurate AMR prediction, directly informing the design of miniaturized sensor arrays tailored for a specific, limited number of target molecules.

Discussion and on-going work

The proposed pipeline aims to effectively integrate high-dimensional volatilomics and ML for microbial diagnosis in a portable gas sensor-based device. A central hypothesis of our work is that AMR identification cannot rely on isolated VOC analysis; instead, it requires the simultaneous assessment of collective analyte dynamics. Interactions between different volatile families, such as ratios among metabolic byproducts, are expected to yield more robust and specific signatures than single biomarkers alone. Disentangling these complex multi-analyte relationships using ML is key to reducing the dimensionality of the problem. By identifying the minimal optimal set of VOCs required for accurate classification, we can reduce system complexity and thereby enable device miniaturization. Furthermore, the transition from centralized, high-cost laboratory equipment to a streamlined, ML-driven sensor array offers a scalable pathway for the democratization of diagnostics.

On-going work is currently focused on the longitudinal data collection using clinical samples to train and validate our ML pipeline.

References

[1] Naghavi, Mohsen, et al. Global burden of bacterial antimicrobial resistance 1990–2021: a systematic analysis with forecasts to 2050. *The Lancet* 1199-1226 (2024); doi; 10.1016/S0140-6736(24)01867-1.

[2] Bilgin, Mehmet Berk, et al. Microbial and antimicrobial resistance diagnostics by gas sensors and machine learning. *Cell Biomaterials* 1.7 (2025); doi; 10.1016/j.celbio.2025.100125.

[3] Kemmler, Emanuel, et al. mVOC 4.0: a database of microbial volatiles. *Nucleic Acids Research* 53.D1 (2025); 10.1093/nar/gkae961.

[4] Aboy, Mateo, Timo Minssen, and Effy Vayena. Navigating the EU AI Act: implications for regulated digital medical products. *NPJ Digital Medicine* 7.1 (2024): 237; doi; 10.1038/s41746-024-01232-3.

DOI 10.5162/eurosensors2026/SP 2.2.5

Diagnostics Needs for Urinary Tract Infections in the Era of Antimicrobial Resistance

Lorenz Leitner[1,2], Shawna McCallin[1,2], Thomas M. Kessler[1,2]
[1] Department of Neuro-Urology, Balgrist University Hospital, University of Zürich, Zürich, CH;
[2] Spinal Cord Injury Center, Balgrist University Hospital, University of Zürich, Zürich, CH
Lorenz.leitner@balgrist.ch

Summary:
Urinary tract infections (UTIs) are among the leading indications for antibiotic prescription worldwide and are increasingly complicated by antimicrobial resistance (AMR). Current diagnostic workflows remain slow and insufficiently precise for modern anti-infective strategies. Here, we present our hospital's experience with UTI microbiology, AMR, and development of novel urine-based diagnostics, including companion diagnostics for phage therapy. Our findings highlight the urgent need for rapid, functionally informative diagnostics capable of supporting antimicrobial stewardship and future precision therapies.

Keywords: antimicrobial resistance, urine, diagnostics, urinary tract infections, phage therapy, antibiotic susceptibility testing

Background, Motivation and Objective

Urinary tract infections (UTIs) affect hundreds of millions of patients annually and represent one of the largest drivers of empirical antibiotic use. Increasing antimicrobial resistance (AMR), particularly among *Escherichia coli* and other uropathogens, has substantially complicated antibiotic treatment selection and contributed to recurrent infection, treatment failure, and healthcare burden.

Current diagnostic workflows rely primarily on symptom assessment, urinalysis, and urine culture. While urinalysis provides rapid but indirect information, urine cultures typically require 24–72 h, with additional time needed for antimicrobial susceptibility testing (AST). In polymicrobial or recurrent infections, clinically actionable results may require several days. Consequently, antibiotic therapy is frequently initiated empirically before microbiological confirmation.

These workflows were developed in an era of broadly effective antibiotics and are increasingly strained by AMR. Furthermore, emerging precision anti-infective strategies, including bacteriophage therapy, require greater diagnostic resolution, including rapid pathogen identification and strain-level susceptibility testing.

The objective of this work was to evaluate limitations in current UTI diagnostic pathways and to investigate new urine-based diagnostic approaches capable of supporting future precision therapies.

Description of the New Method or System

In clinical practice, we adhere to the current guidelines from the European Association of Urology (EAU). Our research is focused on developing and testing new therapies and diagnostics for UTIs, with a specific focus on recurrent and catheter-associated UTIs.

A prospective epidemiological study was conducted to characterize microbiology and AMR patterns within our patient population [1], while the ongoing MiLUT observational study longitudinally collects urine samples and clinical metadata for metabolomic, transcriptomic, proteomic, microbiome, and immunological analyses. These studies provide urine samples with associated clinical metadata and bacterial isolates for evaluation of next-generation therapies and diagnostics.

Using patient-derived urine and bacterial isolates, we validated a nano-luciferase-based companion diagnostic assay capable of simultaneously detecting *E. coli* and phage susceptibility directly in urine samples [2]. The assay is being developed to support patient enrollment and treatment selection in an upcoming phage therapy RCT.

Results

During a one-year prospective observation period, 2615 urine samples from 1820 patients underwent routine microbiological analysis and

AST. Culture-based diagnostic workflows required approximately 48–72 h to obtain susceptibility results, and resistance rates against commonly used antibiotics ranged from 1–38%. Within this cohort, standard urinalysis was a poor discriminator between asymptomatic bacteriuria and UTI, particularly in patients exposed to urinary catheters, the population in whom rapid, reliable diagnosis is most urgently needed. Catheter-stratified receiver-operating-characteristic curves (ROC) analysis (Fig. 1) showed only modest performance of leukocyte counts (AUC 0.59, 95 % CI 0.54 to 0.65) and essentially no discrimination of bacterial sediment counts (AUC 0.52, 95 % CI 0.45 to 0.58) in catheter-exposed patients, whereas in non-catheterized patients leukocytes performed substantially better (AUC 0.75, 95 % CI 0.64 to 0.86; bacteria AUC 0.63, 95 % CI 0.50 to 0.76). These findings indicate that conventional urinalysis cannot reliably guide antibiotic prescribing or trial enrolment decisions, motivating the development of rapid, pathogen-specific point-of-care diagnostics.

Using isolates and urine samples obtained through these studies, we validated a nano-luciferase-based assay for direct urine testing of phage susceptibility. Preliminary findings demonstrate the feasibility of simultaneous pathogen detection and functional susceptibility assessment directly in patient urine, with greatly reduced time-to-result compared to conventional microbiology. Ongoing work focuses on assay stabilization, integration of internal controls, and selection of clinically actionable readouts.

As therapeutic strategies become increasingly personalized, diagnostic systems must evolve from simple presence/absence testing toward adaptive platforms capable of supporting individualized treatment decisions directly from patient-derived samples. Further thought should be given to distribution and implementation in high AMR burden, low resource settings, such as in hospitals in low- and middle- income countries (LMICs).

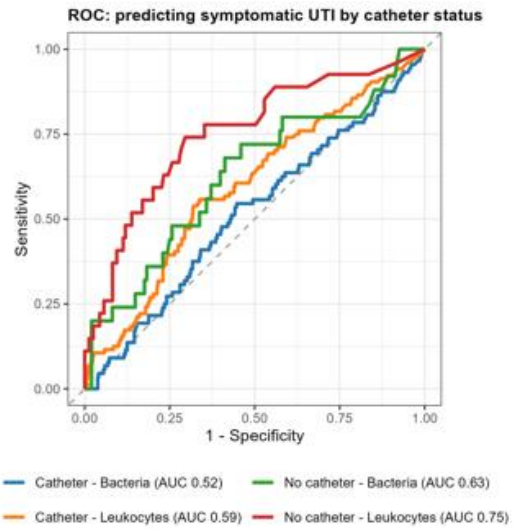

Fig. 1. Urinalysis as a discriminator between asymptomatic bacteriuria and UTI, stratified by catheter status. Top: leukocyte counts (Leu/µL, log10) in urine sediment. Middle: bacterial counts (Bact/µL, log10). Bottom: receiver-operating-characteristic curves for predicting UTI n = 1271 catheter-exposed and n = 244 non-catheter visits with paired urinalysis and clinical assessment.

References

[1] V. Neumeier, F.P. Stangl, et al. Indwelling catheter vs intermittent catherization: is there a difference in UTI susceptibility? *BMC Infect Dis*. 23(1):507. doi: 10.1186/s12879-023-08475-7

[2] S. Meile, J. Du, et al. Engineered reporter phages for detection of Escherichia coli, Enterococcus, and Klebsiella in urine. *Nat Comm*. 14(1):4336. doi: 10.1038/s41467-023-39863-x

DOI 10.5162/eurosensors2026/IS 1.1

Pushing the Limits of Established Sensor Technologies

Yannick Maret[1], Antoine Riaud[2], Brian Smith[3], Jens Schalkowski[4]
[1] ABB Measurement & Analytics, Segelhofstrasse 1K, 5405 Dättwil, Switzerland,
[2] ABB Corporate Research, Segelhofstrasse 1K, 5405 Dättwil, Switzerland,
[3] ABB Measurement & Analytics, 7051 Industrial Boulevard, Bartlesville, OK 74006, USA
[4] ABB Measurement & Analytics, Stierstädterstraße 5, 60488 Frankfurt am Main, Germany,
Corresponding Author's e-mail address: yannick.maret@ch.abb.com

Summary:
Regulatory tightening and increasingly demanding applications are driving sensor and measurement systems toward performance levels that were not anticipated in the original designs. Rather than pursuing new sensing technologies, a structured engineering approach can unlock substantial performance gains in existing systems, often with minimal hardware changes. This paper presents two industrial examples that illustrate the gains obtained through systematic modelling of measurement uncertainty, identification of dominant error contributors, and targeted mitigations.

Keywords: FTIR, Gas Chromatograph, Emission Monitoring, Established Technologies

Methodology

A complete error budget decomposes total uncertainty into individual contributors (noise, drift, cross-sensitivity, thermal effects, etc.), ranking them to reveal high-leverage "knobs." Targeted engineering effort on dominant contributors achieves required performance improvement efficiently.

Notably, this systematic approach yields substantial gains without novel sensing technologies.

CEMS for Waste Incineration

ABB ACF5000 is a multi-component FTIR-based analyser certified for Continuous Emission Monitoring (CEMS) of combustion plants [1].

Best Available Techniques Conclusions (BATc) under Directive 2010/75/EU establish emission limit values based on industry best practices. The updated 2019 BATc for waste incineration introduced significantly tighter limits for several components. For example, HCl and NH_3 limits were reduced substantially compared to the previously certified ranges [2].

Meeting these new limits required a rigorous analysis of measurement uncertainty as defined by DIN EN15267-3 [3]. The standard imposes two seemingly independent requirements: noise must be ≤2% of measurement range, and cross-interference between specified gas pairs must be ≤0.5% for relevant pairs, with the sum of all relevant cross-interferences <4% of range.

A critical statistical insight emerged during error budget analysis: when the noise limit is narrowly satisfied at 2%, measurement uncertainty is too high to reliably quantify cross-interference between gas pairs. In this regime, the sum of all relevant cross-interference cannot be verified to stay below the 4% requirement. This revealed the true requirement: achieve noise at approximately 1% of measurement range, creating sufficient statistical margin to measure and control cross-interference accurately.

Error budget analysis then identified the dominant physical contributors to excess noise and cross-interference: ambient temperature fluctuations inside the analyser cabinet, which degraded signal stability at very low concentration ranges, and insufficient heating in sample handling components for reactive gases such as HCl and NH_3, causing adsorption losses before the gas cell.

Targeted interventions addressed precisely these contributors: the cabinet cooling was mandated as air-conditioned only, and the heated sample probe design was changed to one providing a higher and more stable wall temperature. Gas cell optics were also updated, and processor capacity was increased to support parallel spectral evaluation models. The test infrastructure itself was recognized as a contributor; improved gas supply control and automation eliminated test-set-up-induced artifacts.

The resulting product, the ACF5000 LCS achieved a measurement performance improvement of up to factor 10 relative to the previous

platform, delivering successful certification for emission monitoring in 2026 with certified ranges [4][5] shown in Table 1. Those are the lowest certified ranges of any CEMS available.

Table 1, certified measurement range in mg/m³

Component	*Standard ACF5000*	*ACF5000 LCS*
CO	0–75	0–15
NO	0–150	0–50
NO_2	0–80	0–60
SO_2	0–75	0–7.5
HCl	0–15	0–3
HF	0–3	0–1.35
NH_3	0–5	0–3

Chromatography of trace gases using a Thermal Conductivity Detector (TCD)

An upcoming variant of ABB GCPro Series Gas Chromatograph [6] includes an advanced TCD designed to achieve ultra-low detection limits (~0.3 ppm) for trace gas analysis. Development employed systematic multi-physics modelling to understand and control the complete error chain.

Detailed simulations (combining thermal dynamics, fluid mechanics, heat transfer, and electronics noise) revealed the dominant uncertainty contributors. Critically, baseline noise at peak frequency (~0.1 Hz) was identified as the repeatability limiter; Figure 1 depicts the main elements influencing the noise. Three key physical knobs emerged: thermal wall temperature stability within the detector chamber (requiring ±50 µK control), baseline electronics noise across frequency band of interest (from A/D converter, signal conditioning, and thermal fluctuations), and detector geometry and gas flow patterns affecting heat transfer uniformity.

Three coordinated improvements emerged: miniaturized multi-plate geometry via diffusion bonding; advanced electronics (8-9× lower noise spectral density); optimized signal processing. Thermal stability required precision heater control and shielding.

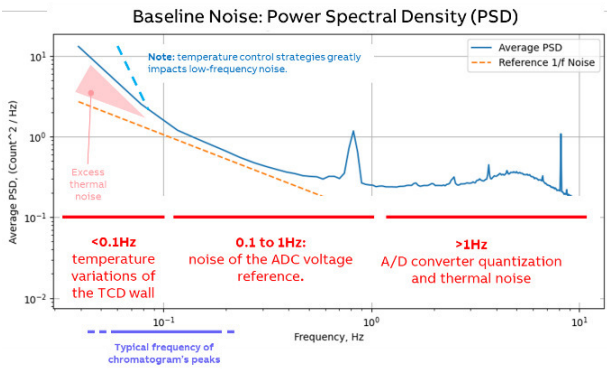

Figure 1. TCD noise model with main contributors

These coordinated physical improvements delivered a 6× enhancement in peak repeatability for low-ppm analytes compared to the previous TCD detector, translating to detection limits of 0.3 ppm with 0.05 ppm standard deviation. Signal processing algorithms alone contributed a 2× improvement in repeatability, demonstrating the importance of systematic optimization across the measurement and processing chain.

Both examples share a common pattern. In the ACF5000 case, the critical step was understanding that the normative noise requirement was not the true requirement: achieving 2% noise makes the cross-interference specification statistically unachievable. Recognizing this hidden constraint unlocked the path forward. In the GCPro TCD case, multiphysics simulation exposed that thermal wall stability at the sub-millikelvin level was the binding constraint, not electronics or geometry alone. In both cases, the performance breakthrough came not from incremental trial-and-error tuning, but from first building a sufficiently complete model of the error chain to know which knobs mattered.

Conclusions

Both examples demonstrate that systematic error modelling, grounded in physics-based understanding of the complete measurement chain, is a powerful and efficient route to extending the performance envelope of established sensor technologies.

The common thread across both is this: identify the dominant error contributors early through rigorous modelling, then apply focused engineering only to those high-leverage knobs. This approach can deliver up to factors 6-10 improvement without fundamentally new sensing principles. The methodology applies broadly across established sensor technologies, systematically transforming performance limitations into opportunities for significant improvement without costly redesigns.

References

[1] Hot/wet extractive system ACF5000, https://new.abb.com/products/measurement-products/analytical/cga-system-solution/acf5000

[2] Commission Implementing Decision (EU) 2019/2010, https://eur-lex.europa.eu/eli/dec_impl/2019/2010/oj

[3] DIN EN15267-3, Assessment of air quality monitoring equipment Part 3

[4] TÜV Zertifikatsnummer 0000053802_02

[5] TÜV Zertifikatsnummer 0000089096_00

[6] GCPro Series, https://new.abb.com/products/measurement-products/analytical/gas-chromatograph-analyzers/gcpro-series

DOI 10.5162/eurosensors2026/IS 1.3

Scaling up and Automating Nanodevice Fabrication with Parallelized Multi-tip Thermal Scanning Probe Lithography

Jana Chaaban, Julia Stark, Eliott Clerc, Andrea Ubezio, Antoaneta Damyanova, Fabian Könemann, Kartik Buddha, Simon Bonanni, Emine Çağın
Heidelberg Instruments Nano AG, Bändliweg 30, 8048 Zürich, Switzerland
Jana.chaaban@himt.ch

Summary:
Thermal Scanning Probe Lithography (t-SPL) with the NanoFrazor by Heidelberg Instruments allows high-resolution, damage-free nanoscale patterning using localized thermal stimulation from an ultra-sharp tip. The Decapede, its first multi-tip version, scales up t-SPL while maintaining resolution through parallel tip operation, enabling the creation of multiple designs simultaneously. This talk will highlight Decapede applications in nanophotonics, including the creation of a photonic sieve and a metalens, demonstrating parallel patterning of complex structures in silicon.

Keywords: thermal scanning probe lithography, nanofabrication, parallelization, nanophotonics.

Thermal Scanning Probe Lithography (t-SPL), using the NanoFrazor by Heidelberg Instruments, is an established direct-write nanolithography technique that utilizes an ultra-sharp thermal tip for creating and inspecting nanoscale structures, while also integrating direct laser sublimation (DLS) for hybrid lithography of nanodevices [1]. This unique method employs precise localized thermal stimulation to achieve high-resolution, damage-free patterning, enabling direct physical and chemical modifications of various materials [2]. Combined with markerless second layer alignment, automation features, and single-nanometer precise grayscale lithography, the NanoFrazor effectively addresses complex fabrication challenges across diverse applications in fields such as quantum nanoelectronics [3], nanophotonics [4], and nanobiosystems [5].

Fig. 1. (left) NanoFrazor in-situ microscope showing the Decapede over a resist-coated substrate, writing features in both 2D high-resolution and in grayscale. (right) Simulated image of the Decapede patterning different features, alongside the integrated laser writehead.

The Decapede, which is the first multi-tip version of the NanoFrazor, scales up the t-SPL technology without compromising resolution, see Figure 1. By enabling parallel tip operation, the Decapede minimizes overhead time and facilitates seamless patterning of large-area, high-resolution geometries, allowing for the independent and simultaneous creation of ten designs on a single surface.

In this talk, we will explore the working principles of NanoFrazor lithography, highlighting successful applications of Decapede patterning, particularly in nanophotonics. In one example, we will showcase the creation of a photonic sieve, seen in Figure 2, through rapid single indentation patterning. The patterned nanoholes are then turned into nanopillars etched in silicon through a series of standard microfabrication steps. In another example, we will demonstrate the patterning of a metalens by the multi-tip configuration, covering an area of 690 µm x 690 µm, comprising 2 million high-resolution rectangular elements etched 1.5 µm deep into silicon, as illustrated in Figure 3.

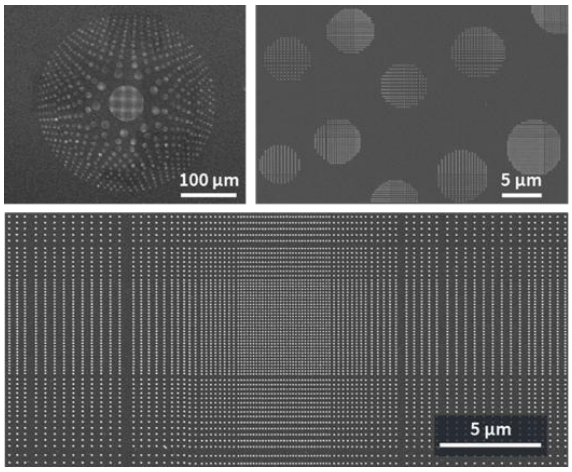

Fig. 2. SEM images of a final photon sieve with structures following a bisinusoidal distribution. The structures were created by single tip indentations with a pitch of 75 nm, and then etched 200 nm deep into Si.

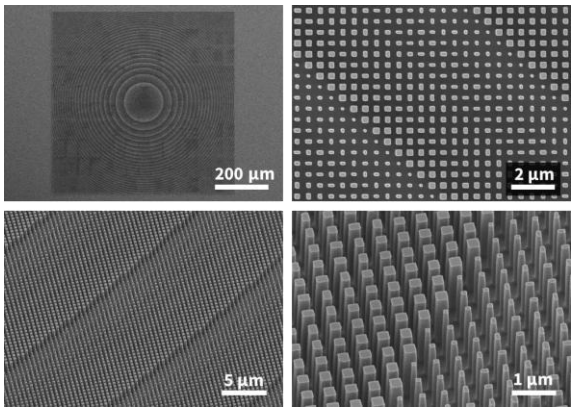

Fig. 3. SEM images of the full metalens (top left), and close-ups of its individual components, highlighting the Nanofrazor decapede's large-area high-resolution patterning capability.

References

[1] S. T. Howell et al., Microsyst. Nanoeng. 6 21 (2020).

[2] E. Albisetti et al., Nature Reviews Methods Primers 2 32 (2022).

[3] L. Shani*, J. Chaaban* et al., Nanotechnology 35 255302 (2024).

[4] N. Lassaline et al., Nature 582 506-510 (2020).

[5] X. Liu et al., Advanced Functional Materials 31 2008662 (2021)

DOI 10.5162/eurosensors2026/IS 1.4

From Miniaturized Bioassays to 3D Imaging of Microfluidic Devices

Yuksel Temiz[1]
[1] Microqubic AG, Feldpark 29, 6300 Zug, Switzerland
yuksel@microqubic.com

Summary:

This paper presents the evolution of capillary-driven microfluidic systems for miniaturized biosensing applications and the subsequent development of a programmable 3D microscopy platform designed to address the optical inspection challenges associated with these devices. The presentation will take the audience from my early work on bioassay development and the associated fabrication and inspection challenges to the founding of Microqubic AG to support the sensor and microfluidics community with dedicated imaging solutions.

Keywords: microfluidics, biosensors, microscopy, inspection, imaging

Background, Motivation and Objective

The development of point-of-care diagnostics using microfluidics requires precise fabrication, fluidic control, reagent integration, and quality assurance. While developing and scaling lab-on-a-chip devices for production is demanding, inspection and quality control remain equally important and are often underestimated in research. Microfluidic devices are commonly fabricated from highly transparent materials such as PDMS, glass, and thermoplastics, highly reflective substrates such as silicon, or hybrid combinations of both. Sealed channels, embedded reagents, electrodes in some cases, and liquid flow further complicate optical inspection. In addition, these devices may be physically large, exceeding the field of view of standard microscopes, while containing features down to only a few micrometers, often combined with variations in channel depth. Conventional microscopes struggle to capture the complex 3D topography and sidewalls of these structures for both characterization and presentation-quality full-device imaging.

Development of Novel Microfluidic Concepts

During my tenure at IBM Research-Zurich, we addressed several of these hurdles by introducing novel microfluidic concepts integrated with dedicated electronic and optical systems. We developed electro-actuated valves enabling programmable stop-and-go flow control from a smartphone [1] (see Fig. 1). We also introduced self-coalescing flow concepts for pulse-shaped reagent delivery [2]. Using ultra-miniaturized chips supporting capillary-driven flow and localized dried-reagent reconstitution, we realized one-step immunoassays [3] and devices containing up to 10,000 localized biochemical reaction sites [4] (see Fig. 2). This research frequently required custom imaging solutions in our laboratory, including 3D inspection systems.

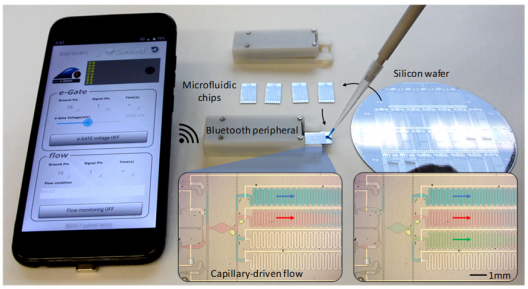

Fig. 1. Programmable smartphone-controlled flow of multiple liquids in capillary-driven microfluidic devices without active pumps.

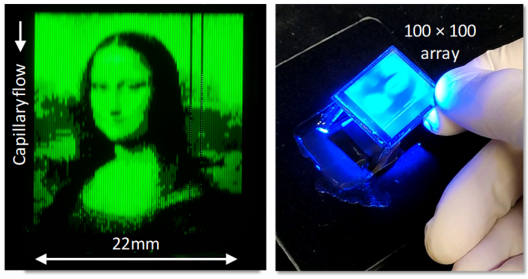

Fig. 2. Localized reconstitution of dried reagents using self-coalescing flow, imaged with a custom-built fluorescence microscope.

Programmable 3D Microscopy System

Imaging requirements in our research motivated me to develop a dedicated programmable 3D microscopy platform. Although high-end 3D microscopes exist, they are typically expensive, difficult to adapt to custom experimental setups,

and not optimized for microfluidic sensors. Driven by the need for a versatile and accessible inspection tool, I initially built a fully motorized microscope prototype using Lego components (see Fig. 3). Following its publication [5], the system attracted significant attention from the microfluidics and sensors communities, highlighting the value of multi-angle optical inspection. This motivated me to found Microqubic AG to commercialize modular, programmable, and affordable 2D/3D microscopes (see Fig. 4). The microscopes incorporate seven motorized actuators enabling X-Y translation, sample rotation, focus, zoom, and camera tilting. To image challenging samples effectively, the system integrates five illumination sources, including a proprietary curved LED matrix and coaxial illumination.

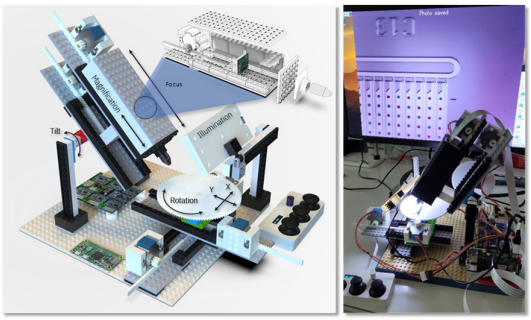

Fig. 3. Motorized Lego microscope developed for imaging microfluidic chips (github.com/IBM/Microscopy).

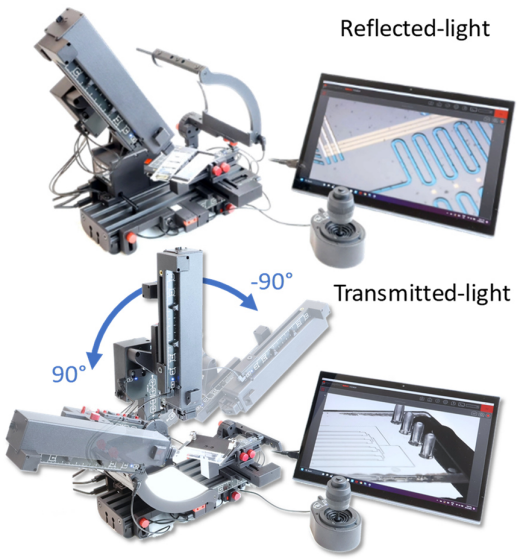

Fig. 4. Microqubic's motorized, programmable, and modular 3D microscope for imaging transparent and opaque microfluidic chips (www.microqubic.com).

Results and System Impact

Combined with MRCL Viewer software developed in-house, the platform supports autofocus, automatic focus stacking, HDR imaging, 4K video capture, automated imaging and live 2D/3D measurements (see Fig. 5). The systems are now used in more than 100 laboratories across 25 countries and continue to evolve with features such as fluorescence imaging and automated chip inspection.

Historically, researchers have often had to adapt their experimental setups to rigid microscopy systems. Microqubic platforms aim to reverse that traditional paradigm by providing compact and reconfigurable tools tailored to the experiment itself. For the sensor community, this approach enables rapid, precise, and affordable characterization of next-generation microfluidic devices, biosensors, and MEMS.

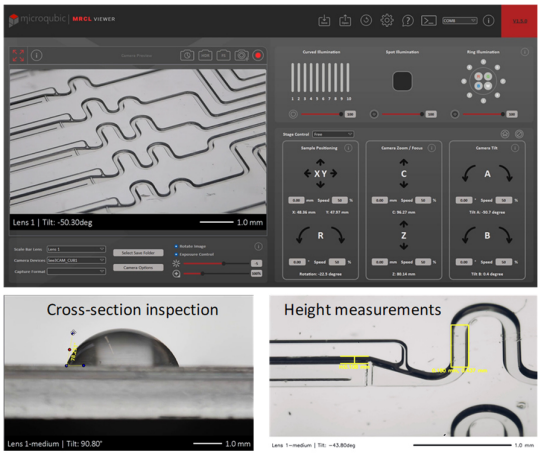

Fig. 5. Microqubic's software supporting advanced features such as 3D measurements, autofocus and focus stacking.

References

[1] Temiz, Y.*, Arango, Y.*, Gökçe, O., et al., "Electro-Actuated Valves and Self-Vented Channels Enable Programmable Flow Control and Monitoring in Capillary-Driven Microfluidics," **Science Advances**, 2020; doi: 10.1126/sciadv.aay8305

[2] Gökçe, O., Castonguay, S., Temiz, Y., Gervais T., Delamarche, E., "Self-Coalescing Flows in Microfluidics for Pulse-Shaped Delivery of Reagents," **Nature**, 2019; doi: 10.1038/s41586-019-1635-z

[3] Hemmig, E., Temiz, Y., Gökçe, O., et al., "Transposing Lateral Flow Immunoassays to Capillary-Driven Microfluidics Using Self-Coalescence Modules and Capillary-Assembled Receptor Carriers," **Anal. Chem.**, 2020; doi: 10.1021/acs.analchem.9b03792

[4] Temiz, Y.*, Gervais, T.*, et al., "Large-Scale Dried Reagent Reconstitution and Diffusion Control Using Microfluidic Self-Coalescence Modules," **Small**, 2022; doi: 10.1002/smll.202105939

[5] Temiz, Y., "The lego microscope: A valuable lab tool began as a diy project," **IEEE Spectrum,** 2020; doi: 10.1109/MSPEC.2020.9078448

DOI 10.5162/eurosensors2026/IS 2.1

High-Precision 3D Printed Micro-Optics for Next-Generation Optical Sensor Integration

Mina A. T. Yeşilyurt[1]
[1] *Nanoscribe GmbH & Co. KG,*
Hermann-von-Helmholtz-Platz 6,
76344 Eggenstein-Leopoldshafen, Germany
yesilyurt@nanoscribe.com

Summary:
Recent advances in optical sensing require compact, high-performance, and application-specific photonic architectures. We demonstrate how two-photon polymerization enables fabrication of high-resolution micro-optical components directly on substrates, fibers, and photonic interfaces for sensing applications. Additive microfabrication enables rapid prototyping of freeform optical elements while reducing assembly complexity. The presented approach highlights the potential of 3D printed micro-optics for next-generation optical sensors and integrated photonic systems.

Keywords: Two-photon polymerization, micro-optics, optical sensors, integrated photonics, additive manufacturing.

Recent advances in optical sensing require increasingly compact, high-performance, and application-specific photonic architectures. Conventional fabrication methods often limit the realization of complex optical interfaces, particularly when optical-quality freeform surfaces, 3D geometries, and precise alignment to existing photonic components are required simultaneously. As optical sensors continue to evolve toward higher integration density and miniaturized form factors, new fabrication approaches are needed to overcome the limitations of planar manufacturing and conventional assembly processes.

In this talk we demonstrate how two-photon polymerization enables fabrication of high-resolution micro-optical components directly on substrates, optical fibers, and photonic interfaces based on Two-Photon Grayscale Lithography (2GL®) and Aligned Two-Photon Lithography (A2PL®) for the fabrication and integration of high-resolution freeform micro-optics for sensing applications. Our approach allows the realization of complex 3D geometries with high spatial resolution and design freedom, enabling rapid prototyping and customization of optical functionality for application-specific sensor architectures.

2GL® enables the fabrication 2.5D and truly 3D microstructures by locally controlling the exposure dose during the printing process. In contrast to conventional layer-by-layer approaches, 2GL® allows continuous surface profiles and fabrication of complex freeform optical structures with smooth surfaces (R_a < 5 nm) and advanced geometries that are difficult or impossible to realize using conventional planar manufacturing technologies. Importantly, optical-quality freeform structures can be fabricated without significantly increasing printing time, enabling efficient prototyping and production of sophisticated 3D micro-optical components for integrated photonics and optical sensing applications.

A2PL® enables direct fabrication of micro-optics onto optical fibers, photonic chips, and other functional substrates with sub-micron alignment accuracy. By aligning printed optical structures directly to pre-existing optical interfaces, the technology enables highly compact and assembly-efficient photonic integration. This approach reduces packaging complexity, improves coupling efficiency, and enables rapid realization of application-specific optical interfaces for fiber-optic sensing, integrated photonics, spectroscopy, and miniaturized analytical instrumentation.

The presented approaches highlight the potential of additive micro-optics as a scalable enabling technology for next-generation optical sensors and integrated photonic systems. By combining high-resolution 3D design freedom, optical-quality finish with precise aligned integration, advanced two-photon lithography technologies open new opportunities for highly integrated and application-specific photonic sensor architectures.

DOI 10.5162/eurosensors2026/IS 2.3

Active Optics for Enhanced Sensor Performance

Wolfgang Zesch, Amirhossein Saba Shirvan, Andreas Amrein
Optotune Switzerland AG, CH-8953 Dietikon
wolfgang.zesch@optotune.com

Abstract

Optical sensing systems are increasingly required to deliver higher spatial resolution, faster acquisition rates, and improved 3D imaging capabilities. However, their performance remains constrained by fundamental physical limits, fabrication complexity, and cost. This work demonstrates how active optical elements combined with dedicated control strategies can significantly extend the capabilities of conventional imaging systems.

First, focus-tuneable liquid lenses enable high-speed, inertia-free focusing with millisecond response times. This allows continuous focus stacking without mechanical motion, providing extended depth of field in high numerical aperture systems, post-acquisition focal plane selection, and depth reconstruction from image stacks.

Second, the spatial resolution of image sensors — typically limited by pixel count, sensor size, and manufacturing yield — is enhanced using dynamic beam shifters. By introducing controlled sub-pixel lateral displacements and combining multiple acquisitions, the effective sampling density is increased. This approach enables resolution gains of up to 4× for RGB Bayer sensors and up to 16× for hyperspectral sensors with super-pixel architectures.

Finally, large field-of-view (FOV) imaging with high detail is addressed using high-speed scanning mirrors. These systems either reconstruct gigapixel-scale images from multiple sub-frames or dynamically direct the field of attention to regions of interest identified by overview sensors. Integration with focus-tuneable optics ensures sharp imaging across varying object distances within the extended FOV.

The presented approaches illustrate how adaptive optical components can overcome conventional trade-offs in resolution, depth of field, and FOV, enabling enhanced performance in applications such as machine vision, surveillance, and advanced sensing systems.

Keywords

Active optics, focus-tuneable lens, focus stacking, pixel shifting, field of view expansion, image stitching

DOI 10.5162/eurosensors2026/IS 2.4

A Hitchhiker's Wave Guide to Photonic Chips
Physics, fabrication, and the road to volume

Jan Voigt, Christian Bilgeri, Marcel Flemming, Gian-Andrea Rezzoli and Winfried Arens
IMT Masken und Teilungen AG, Im Langacher 46, 8606 Greifensee, Schweiz
jvoigt@imtag.ch

Summary:
Evanescent field sensing enables the measurement of small refractive index changes at the interface of a planar optical waveguide and its surface coating. It has been researched in academic environments for the past 30 years. One of the recently emerging technologies is Grating-coupled Interferometry (GCI), which enables label-free, real-time analysis of molecular interactions at surfaces.

A key challenge of this technology is the fabrication of waveguide coatings and Grating Couplers at scale. This work shows how we, IMT Masken und Teilungen AG, produce glass- based coplanar waveguide chips in volume, leveraging wafer-based manufacturing techniques of the semiconductor industry. In particular, the in-house developed characterization method will be emphasized.

Keywords: Waveguide, Evanescence, Lithography, Glass, Grating

Background, Motivation and Objective

Evanescent field sensing brings together interesting branches of photonics technology. The main pillar is the sputter coating of a planar waveguide materials and surfaces. Second, light needs to enter the waveguide in some convenient way. This is achieved by fabricating phase gratings with submicron feature sizes, which requires a firm grip on lithography processes. I will provide an overview of the underlying physics and shine light on what challenges we were facing, bringing such technology to a scale of a few thousand chips per batch.

For waveguiding microchips leaving production, not only the structural specification must be met, but also the optical functionality must be verified. Therefore, we developed a custom-built measurement setup that allows for the optical characterization of the waveguide chips.

Description in-house developed characterization tool.

Our wafer-based inspection tool (Fig. 1) consists of rotating motorized axes with Laser, Diodes, Cameras and an XY-Stage in its center.

We know the total light power P_{tot} introduced into a grating coupler via reference diode. Furthermore, we measure transmitted and reflected power P_T and P_R via diodes on the two rotary arms.

$$P_{tot} = P_T + P_R + P_{Scatter} + P_{Couple} \quad (1)$$

Neglecting diffusely scattered power loss $P_{Scatter} \approx 0\ W$ enables measurements of grating coupler efficiency, expressed as a fraction of coupled light power to total light power P_{Couple}/P_{tot}. This is an interesting property for the final sensing application. The amount of light power coupled into the system directly affects signal-to-noise ratio and sensitivity in the application our chips are part of.

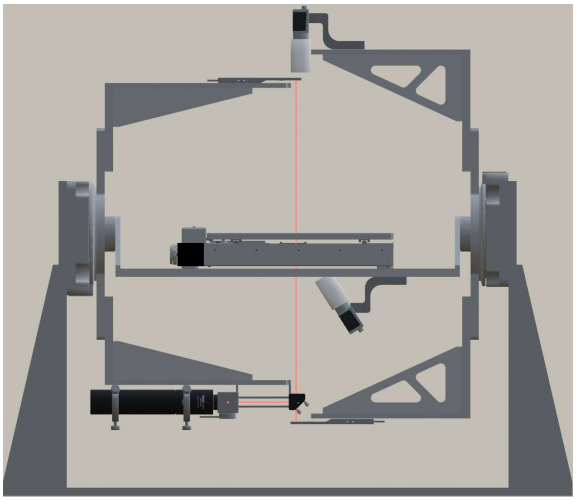

Fig. 1. Sketch of our R&D-built measurement setup for Waveguide and Grating Coupler characterization.

One camera is installed close to the waveguide surface (< 5 cm, below the stage). With that, we can get a good estimate of the attenuation of our coatings by analyzing the decay of scattered light within the waveguides.

Results

In Fig. 2, an example for a coupling curve of a typical waveguide can be seen.

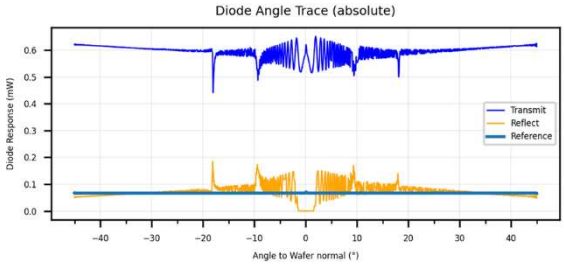

Fig. 2. Diode Angle Trace of a typical grating Coupler for visible light Evanescent sensing.

The grating coupler exhibits birefringence, that is, a polarization dependence on the refractive index. Therefore, we can find two resonances, “Coupling Angles” in positive and negative direction. Those are commonly referred to as TM and TE modes. Once the coupling angles are analyzed and considered proper, the system can be driven to the desired angle and light of the desired polarization will be coupled into the coating. Subsequently, scattered light along the incident beam can be analyzed with a scattering camera (see Fig. 3).

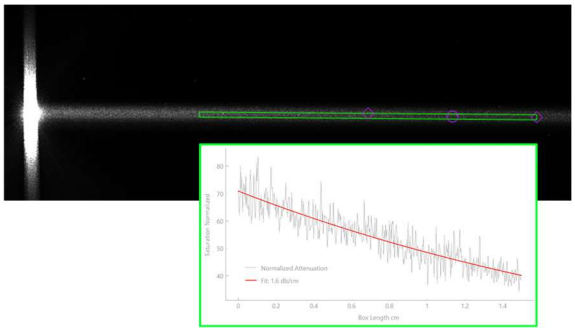

Fig. 3. Attenuation Analysis. With a length-calibrated camera image, the decay constant is given as $\alpha = 1.6\ db/cm$.

The decay of the signal within the coating is calculated within a Region of Interest (ROI, green box). Due to imperfections within the amorphous Ta_2O_5 layer, we can observe the decay of the signal as “scatter light” along the incident beam.

We can describe its exponential decay with the definition of optical attenuation $I(x) \sim 10^{-\alpha \cdot x/10}$, resulting in the given value of 1.6 db/cm.

In close collaboration with our customers, we are constantly improving our manufacturing processes to produce the highest possible refractive indices with lowest possible attenuation.

References

[1] P. Cheben, R. Halir, J.H. Schmid et al., Subwavelength integrated photonics, Nature 560, 565–572 (2018); doi: 10.1038/s41586-018-0421-7

[2] R. Halir, P.J. Bock, P. Cheben, A. Ortega-Moñux, C. Alonso-Ramos, J.H. Schmid, J. Lapointe, D.-X. Xu, J.G. Wangüemert-Pérez, Í. Molina-Fernández, S. Janz, Waveguide sub-wavelength structures: a review of principles and applications, Laser & Photonics Reviews 9, 25–49 (2015); doi: 10.1002/lpor.201400083

[3] K. Schmitt, K. Oehse, G. Sulz, C. Hoffmann, Evanescent Field Sensors Based on Tantalum Pentoxide Waveguides – A Review, Sensors 8, 711–738 (2008); doi: 10.3390/s8020711

[4] K. Cottier, M. Wiki, G. Voirin, H. Gao, R.E. Kunz, Label-free highly sensitive detection of (small) molecules by wavelength interrogation of integrated optical chips, Sensors and Actuators B: Chemical 91 (2003); doi: 10.1016/S0925-4005(03)00117-5

DOI 10.5162/eurosensors2026/IS 3.1

State of the Art Microsensors at Industrial Scale

Thomas Uehlinger[1], Marina de Queiroz Tavares[1], Lukas Bürgi[1]
[1] Sensirion AG, Laubisruetistrasse 50, 8712 Stäfa, Switzerland,
marina.dequeiroztavares@sensirion.com

Summary:
Sensirion develops and manufactures microsensors based on CMOSens® technology, integrating sensing elements and readout electronics on a single chip or within highly integrated sensor modules. This enables scalable, high-volume production of precise and reliable sensors for environmental, medical and mobility applications. Key sensing principles, including capacitive, chemoresistive, thermal and optical methods, are implemented in miniaturized systems. Each sensor is individually calibrated during production, ensuring high accuracy out of the box. The article highlights how industrial R&D translates microscale sensing concepts into robust, mass-produced solutions.

Keywords: CMOSens, MEMS, gas sensing, environmental sensing, high-volume manufacturing

Innovative and Reliable Microsensors at Industrial Scale

Microsensors are key enabling technologies for addressing challenges in climate action, energy efficiency, and healthcare. Applications range from indoor air quality monitoring to medical ventilation and industrial process control. Sensirion, founded in 1998 as an ETH Zürich spin-off, produces around 200 million sensors annually. The heart of each sensor is a combined MEMS structure with integrated electronics enabled by the company CMOSens® technology. Fig. 1 shows an overview of the sensing principles.

Sensing Principles: MEMS core

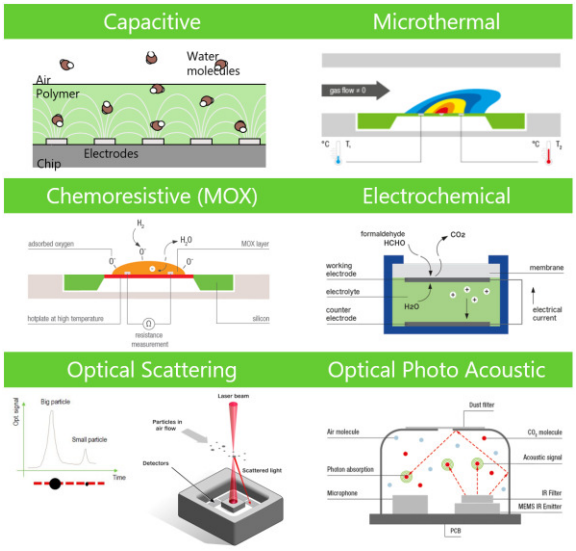

Fig. 1. capacitive, microthermal, MOX, electrochemical and optical (including scattering for particulate matter).

CMOSens® integrates sensing elements and CMOS electronics either monolithically or in highly integrated modules. Key sensing principles include capacitive humidity sensing, chemoresistive MOX gas sensing, microthermal sensing (thermal flow and thermal conductivity), optical absorption (NDIR and photoacoustic), and optical scattering for particulate matter. These technologies enable highly selective and scalable sensing solutions across a wide range of applications.

Products and Applications

These sensing principles are implemented across a broad portfolio of products.

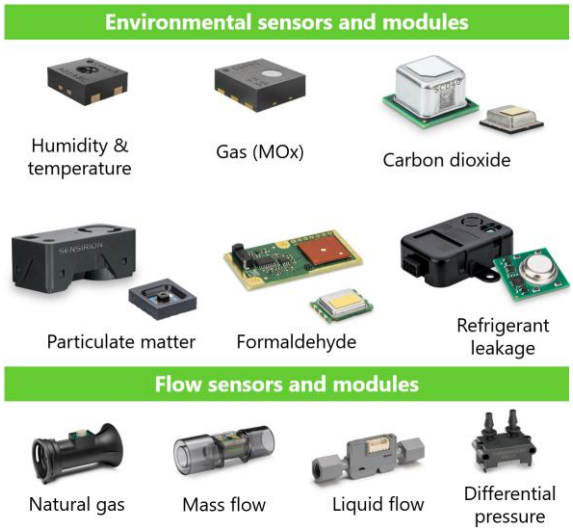

Fig. 2. Sensirion product portfolio overview across application domains.

These products serve a wide range of applications across environmental monitoring, mobility

and automotive, medical, life sciences and diagnostics, industrial, and consumer markets. Typical use cases include indoor air quality monitoring, HVAC systems (e.g. refrigerant leakage), gas metering, climate control in vehicles, medical ventilation and anesthesia monitoring [1]. An overview of the product portfolio and application domains is shown in Fig. 2.

Industrialization and Manufacturing

Scaling microsensor technologies from concept to millions of units requires not only robust design but also a deep integration of development and manufacturing processes, including MEMS and ASIC design, cleanroom fabrication, packaging, automated testing, and system integration. A key differentiating element is the individual calibration of every sensor during production, performed using dedicated automated calibration systems. This ensures high accuracy, reproducibility, and interchangeability, enabling reliable “out-of-the-box” sensor deployment at scale. Product development follows iterative design–test cycles over several years, bridging the gap from prototype to industrialization while maintaining a strong pace of innovation.

A representative example of technology evolution is the miniaturization of carbon dioxide sensing. Earlier solutions based on non-dispersive infrared (NDIR) absorption required relatively large optical paths, limiting their use in compact devices. The transition to photoacoustic sensing enabled a significant reduction in size by detecting pressure waves generated by modulated infrared absorption in a confined cavity. This approach allows highly compact sensor modules while maintaining high accuracy and stability, demonstrating how new sensing concepts can be successfully industrialized and scaled.

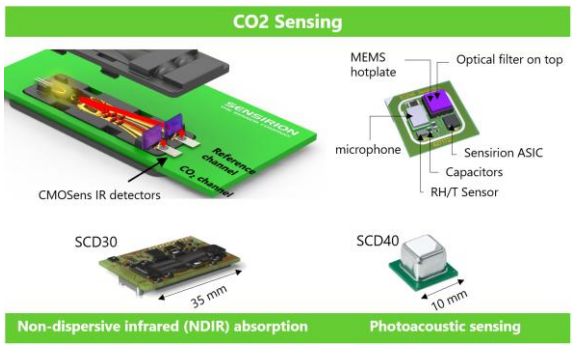

Fig. 3. Evolution of CO_2 sensing technologies: from NDIR to photoacoustic miniaturized modules.

Bridging Academia and Industry

Industrial microsensor development differs from academic research by emphasizing scalability, reproducibility, and cost efficiency in addition to sensitivity. Interdisciplinary collaboration and strong integration between R&D and operations are essential. Approximately 20% of revenue is invested in R&D, supporting continuous innovation. This approach has enabled the transformation of a university spin-off into a global company, with more than 1,150 full-time equivalents across three continents, and an interdisciplinary research and development team of more than 300 employees.

From Sensor to System Solutions

A strong focus on customer needs drives the evolution from discrete sensor components to complete system solutions. Modern sensing solutions increasingly integrate:

– Advanced packaging enabling system-in-package integration

– Sensor modules as hardware platforms

– Embedded signal processing

– Connectivity and data analytics

Such integration enables the transformation of raw sensor data into actionable information. Examples include refrigerant leakage detection modules, which provide ready-to-use sensing solutions, and methane emissions monitoring systems, where sensor data is transmitted, processed, and analyzed to enable real-time detection, localization, and quantification of leaks. These developments illustrate the growing importance of combining sensing technologies with system-level integration and digital capabilities.

Conclusion

CMOSens® technology and highly integrated modules enable scalable, high-performance sensing across environmental, medical and mobility applications. Individual calibration, advanced manufacturing, and interdisciplinary development are key to transforming scientific concepts into mass-produced solutions.

References

[1] Sensirion AG, “Applications and Products,” available at: https://www.sensirion.com/en/applications and https://www.sensirion.com/en/products, accessed May 2026.

DOI 10.5162/eurosensors2026/IS 3.3

Alivion SmartSelect: Making Gas Sensors Work in the Real World

Jan van den Broek[1]
[1] Alivion AG, Flughofstrasse 42, 8152 Opfikon, Switzerland
jan.vandenbroek@alivion.ch

Summary:
Gas sensors are attractive for compact, scalable analysis, but often fail when moved from controlled laboratories into real-world applications. Alivion SmartSelect is a system-level platform that makes gas sensors work reliably outside the lab by combining selective sampling, separation, calibration, algorithms and digital workflows. We demonstrate this approach with Nutrion for breath acetone and Spark for methanol and ethanol analysis in liquids.

Keywords: gas sensors, SmartSelect, selective detection, breath analysis, liquid headspace analysis

Background, Motivation and Objective

Gas sensors are attractive for compact, scalable chemical analysis outside the laboratory, but often fail under real-world conditions. Changing humidity, temperature, interferents, complex backgrounds and uncontrolled sampling can make sensor signals unreliable, even when laboratory performance appears promising [1].

Lab-based instruments such as GC-MS, PTR-MS or FTIR solve these challenges through controlled sampling, separation, calibration and advanced data analysis, but they are too bulky, costly and complex for decentralized or high-frequency measurements. Here, we present SmartSelect as a system-level approach to bring lab-like selectivity and workflow control into compact gas-sensing systems. We demonstrate the concept with Nutrion for breath acetone monitoring and Spark for methanol/ethanol analysis in liquids.

SmartSelect Platform Concept

SmartSelect addresses selectivity at the system level rather than relying on the gas sensor alone. The platform combines application-specific sampling, analyte preselection, separation or filtration, calibration routines, quality control and signal-processing algorithms. This creates a controlled measurement environment around compact gas sensors and reduces the influence of humidity, temperature variation and changing chemical backgrounds.

The approach builds on selective gas-sensing architectures in which separation or preselection is combined with compact sensors to overcome cross-sensitivity, as previously shown for methanol detection in ethanol-rich samples [2]. Depending on the application, SmartSelect can be implemented as a handheld instrument or as an OEM sensing module for integration into existing workflows.

Application Examples: Liquid and Breath Analysis

The same SmartSelect architecture is demonstrated in two different matrices: liquid headspace and human breath. Spark applies controlled liquid headspace sampling, selective separation and temperature-corrected signal analysis to quantify methanol and ethanol in liquids (Fig. 1). It enables compact analysis of complex liquid matrices, including alcoholic beverages with high ethanol background, and has been validated in an ISO 5725 interlaboratory study [3].

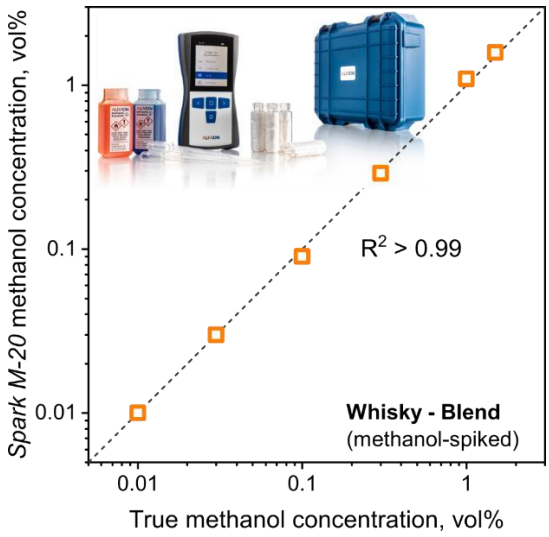

Fig. 1. Validation of Spark handheld methanol detector. Measured methanol concentrations show excellent agreement with true concentrations over 0.01–1.55 vol% in spiked whisky samples.

Nutrion applies the same system-level approach to breath analysis (Fig. 2a). It combines controlled end-tidal breath sampling, µ-GC separation and guided digital workflows to quantify breath acetone, a marker of lipid oxidation and metabolic state. The system enables repeated user-operated measurements outside the laboratory while reducing the influence of humidity, variable exhalation profiles and other breath compounds [4].

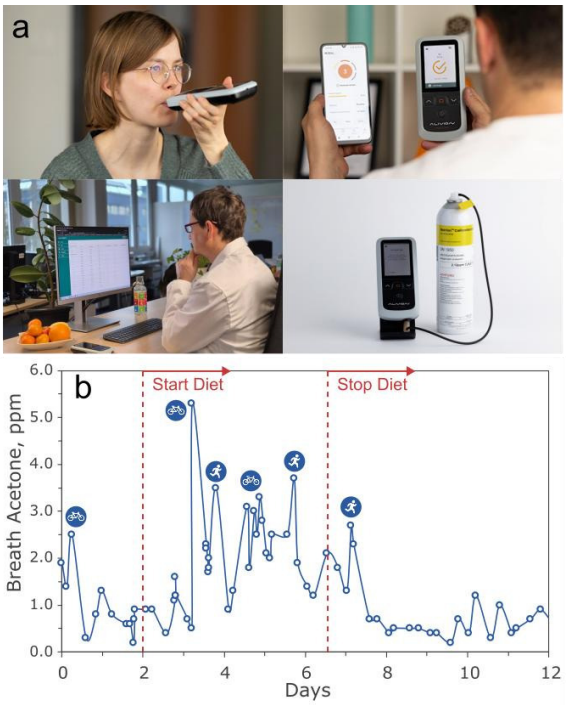

Fig. 2. Nutrion platform and longitudinal breath acetone monitoring. (a) Handheld device, smartphone app and researcher dashboard for guided at-home breath measurements. (b) Representative breath acetone profile during diet and exercise interventions, showing dynamic metabolic changes outside the laboratory.

Results and Discussion

For liquid analysis, Spark was validated in an ISO 5725 interlaboratory trial with 17 independent participants from six countries and 119 measurements. The handheld detector quantified methanol in alcoholic beverages within 2 min, down to 0.01 vol% in liquid, with repeatability below 5.4%, reproducibility below 9.5% and bias below 0.012 vol%. Additional tests showed excellent linearity over 0.01–1.55 vol% methanol (Fig. 1), effective temperature correction from 19–33 °C, and robust recovery across different beverage matrices including whisky, rum, gin, vodka, tequila, port, sherry and liqueur [3].

For breath analysis, Nutrion was validated against PTR-MS using 312 breath samples from 12 volunteers across 8 devices. The system showed strong agreement with the laboratory reference over 0.2–45 ppm acetone, with r = 0.995 and R^2 = 0.990. It also showed ~2.5% CV repeatability over 0.5–25 ppm, low inter-device variability, ~4.2% humidity-induced bias from 0–90% RH, and stable operation over 8 months without observed drift [4]. In at-home use, repeated measurements captured dynamic breath acetone changes during diet and exercise interventions (Fig. 2b).

Together, Spark and Nutrion demonstrate that SmartSelect can translate gas sensors into validated and commercially deployable analytical systems across different sample types. Both examples follow the same principle: controlling the sample, adding selectivity before detection, and using calibration and algorithms to deliver reliable measurements outside the laboratory.

Conclusion and Outlook

SmartSelect demonstrates how compact gas sensors can be transformed into robust analytical systems by combining controlled sampling, separation, calibration, correction algorithms and application-specific workflows. Spark and Nutrion show this principle in two different real-world settings: liquid headspace analysis for food and beverage applications, and breath analysis for longitudinal metabolic monitoring.

These examples highlight a broader platform strategy in which selectivity is engineered at the system level rather than expected from the sensor alone. Future work will focus on extending SmartSelect into further application-specific modules and OEM integrations, enabling reliable chemical measurements in decentralised workflows where laboratory instruments are impractical.

References

[1] A. Lewis, P. Edwards, Validate personal air-pollution sensors, *Nature* 535, 29–31 (2016); doi: 10.1038/535029a

[2] J. van den Broek, S. Abegg, S. E. Pratsinis et al., Highly selective detection of methanol over ethanol by a handheld gas sensor, *Nature Communications* 10, 4220 (2019); doi: 10.1038/s41467-019-12223-4

[3] J. van den Broek, S. D. Keller, I. Goodall et al., Handheld methanol detector for beverage analysis: interlaboratory validation, *Analytical Methods* (2024); doi: 10.1039/D4AY00919C

[4] S. Hersberger, J. van den Broek, L. Schmid et al., Self-monitoring of Metabolic Status with a Smartphone-assisted Breath Sensing Device, *ChemRxiv preprint* (2025); doi: 10.26434/chemrxiv.15000216/v1

DOI 10.5162/eurosensors2026/IS 3.4

Accelerating Gas Sensor Material Development

Leandro Nicolas Sacco
VSParticle B.V., Oostsingel 209, 2612 HL, Delft, The Netherlands
l.sacco@vsparticle.com

Abstract:

The identification of optimal sensing materials is essential for advancing selective chemiresistive gas sensors [1]. This work presents a high-throughput platform based on spark ablation technology for the rapid discovery and optimization of gas sensor materials. Spark ablation is a fully dry, environmentally friendly process that produces highly pure nanoparticles without chemical precursors, resulting in pristine nanoporous sensing layers. Its versatility enables the synthesis of pure metals, alloys, and doped semiconductors, offering broad compositional flexibility. Using the VSP-P1 nanoprinter, nanoparticles are directly deposited onto a platform chip in a single step, enabling the fabrication of both nanoporous sensing layers [2]. The platform chip is integrated with an active learning loop that can iteratively optimizes key sensing metrics of a gas sensor. As a case study, we targeted formaldehyde detection at ppb concentrations while evaluating specificity against CO, CO_2, toluene, and a hydrocarbon mixture. The results demonstrate that material composition strongly influences sensing performance, enabling the identification of sensors with high specificity and sensitivity toward formaldehyde after only a few iterations. This approach demonstrates the potential of combining spark ablation with active learning as an efficient platform for accelerating gas sensor material discovery and enabling rapid implementation in sensor fabrication.

Keywords:

Gas Sensors, Nanoparticles, Spark Ablation, Dry Printing, Active Learning Loop.

References:

[1] R. Theodoro, G. Santos, M. D'Andria, H. Gropelo, S. Kravecz, A. Güntner, D. Volanti, "Air Pollution Monitoring with Nanoscaled Materials in Chemoresistive Gas Sensors". ACS Appl. Mater. Interfaces (2026); 18 (10): pp. 14473–14520. DOI:10.1021/acsami.5c24099.

[2] L. Sacco, N. Schouten, L. Egger, M. Popov, A. Köck, C. Dösinger, and L. Romaner, "Multiarray Gas Sensors Based on Nanoporous Layers Produced à la carte by Spark Ablation Using Metal Oxides, Binary and Ternary Alloys," 2024 IEEE SENSORS, Kobe, Japan, (2024), pp. 1-4, DOI: 10.1109/SENSORS60989.2024.10785068.

DOI 10.5162/eurosensors2026/IS 4.2

microGauge – a Micro Resonator Gauge (MRG) Featuring a High-Stability Zero for Vacuum Process Control

Stéphane Kühne[1], Nina Wojtas[1], Samuele Demicheli[1], Vanessa Barreiro Lomba[1], Mathis Trant[1], Philip Rhyner[1], Stephan Kohler[1], Ulrich Bartsch[1]
[1]VAT Vakuumventile AG, Rütistrasse 4, 9469 Haag, Switzerland
Stephane.Kuehne@vatgroup.com

Summary:
VAT has developed a micro resonator-based pressure sensor enabling high zero-stability. This is achieved by designing a resonator featuring a high-aspect-ratio gap and driving it in a closed loop configuration in order to use the resulting squeeze-film damping as a measure for the pressure. Additionally, a thermo-mechanical decoupling of the MEMS transducer is minimizing environmental disturbances. A zero stability below 10^{-2}mTorr is being demonstrated over a period of nine months, offering the means to ensure repeatable control in vacuum processing applications for semiconductor manufacturing.

Keywords: micro resonator, pressure sensing, vacuum gauge, semiconductor, process control

Introduction

The semiconductor manufacturing industry is heading towards new challenges in process control, as highlighted in the respective technology roadmaps (e.g. [1]). Atomic sized features, new materials and shrinking process parameter windows are asking for more repeatable and robust pressure control across the entire vacuum tool chain in the production line. Therefore, pressure control requires improvements in many aspects, but in particular the feedback signal from the pressure sensor must be stable and reliable.

Today's prevailing pressure sensor technology for process control is based on capacitance diaphragm gauges (CDG). This type of sensors is known as a direct measurement method, based on the physical concept of measuring pressure by means of the deflection of a membrane. This approach has been optimized for many decades and is known for its repeatable sensitivity and fast response [2]. However, the sensors lack in performance regarding the stability of the zero level, typically caused by mechanical degradation and the cross-sensitivity to temperature and vibrations. This is mainly related to physical limitations, e.g. minimal membrane thickness and size, and the long-term stability of the gauge reference pressure for absolute sensors.

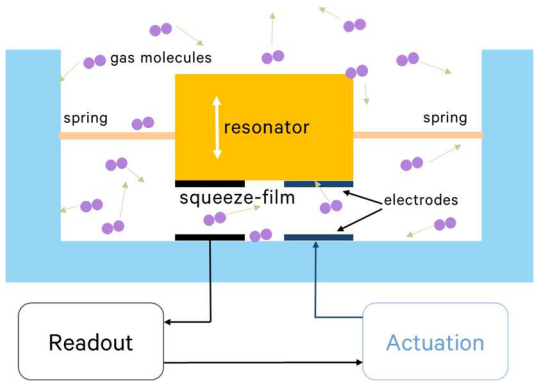

Fig. 1. Schematic cross-section of the MEMS transducer showing the closed-loop operation of a squeeze-film damped resonator.

Resonator-based concepts offer the opportunity to overcome these limitations. We are presenting an approach using rarefied gas damping of a resonator as well as decoupling the MEMS transducer from the environment for achieving high-stability zero and excellent sensitivity down to the high vacuum range.

Micro Resonator Gauge (MRG) Principle

Rarefied gas damping of MEMS structures is a well-known phenomenon [3]. In contrast to using the free-damping of a resonator structure [4], we take advantage of the squeeze-film effect [5]. As shown in Figure 1, the resonator and the surrounding substrate and electrodes form a high-aspect-ratio gap and a corresponding squeeze-film. The damping effect can be correlated to pressure by driving the resonator at a constant amplitude in closed-loop feedback control. As this approach does not rely on a reference pressure, this is a clear advantage over the conventional pressure sensing techniques to achieve ultimate stability of the zero level. To extend the device sensitivity to the high vacuum range, a high-aspect-ratio gap of close to 1000 is fabricated. Therewith, the sensitivity of the transducer can be extended to 0.1mTorr and below.

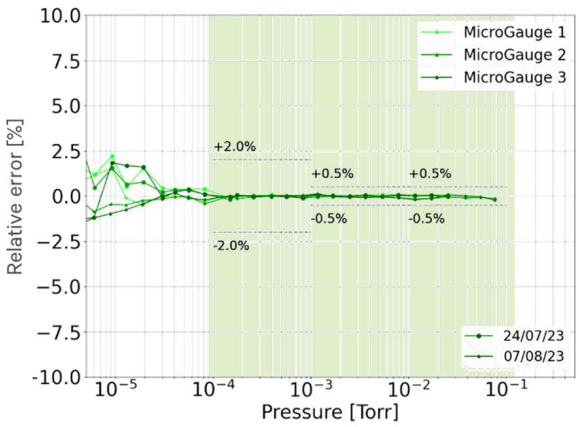

Fig. 2. Accuracy/repeatability of three MRG acquired in two different datasets over an interval of 2 weeks.

MRG Environmental Decoupling

The measurement principle would be significantly impacted by environmental disturbances without an effective decoupling approach. This is mostly related to thermal influence and mechanical noise/vibrations generated by mechanical components and propagated through the whole vacuum equipment.

The MEMS transducer allows for an effective decoupling – no clamping of a membrane, small dimension and local heating for thermal stabilization. The isolation from vibrations proves to be more challenging [6]. The required performance level is obtained by using a tailored mass spring system as a mechanical low pass filter.

Results: Demonstrated MRG Performance

Figure 2 shows the relative error of three MRG sensors with respect to the reference pressure. Two datasets are compared in the time span of two weeks. The dashed lines indicate relative error levels that correspond to the typically achieved ranges for commercial high-end process pressure gauges (CDG type). Our MRG sensors not only stay in these specified tolerance bands, but they show the capability to extend the measurement range by at least one decade without lowering the accuracy and repeatability specification.

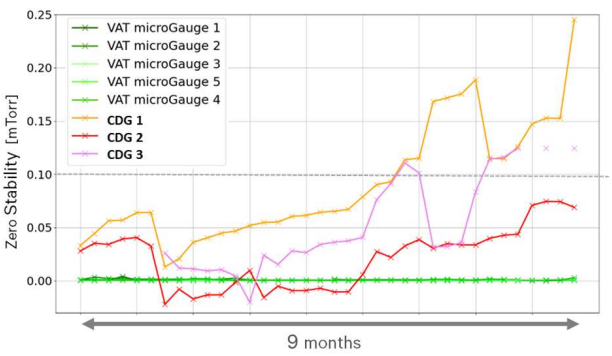

Fig. 3. Comparison of the zero stability of MRG and CDG sensors monitored over a period of 9 months.

The zero-stability of five MRG sensors is depicted in Figure 3. The zero output of the sensors was measured at 10^{-7} Torr or lower, over a period of nine months. These results demonstrate a zero stability below 10^{-2} mTorr across the entire duration of the measurement campaign. This illustrates the technological advantages implemented in the MRG sensor design: the micro resonator based on the squeeze-film damping and an effective thermo-mechanical decoupling from the environment.

Conclusions

A micro resonator gauge (MRG) pressure sensor relying on the squeeze-film damping effect was optimized to extend the range of accurate pressure measurement. Combining the improved sensor performance with an effective decoupling and thermal stabilization of the transducer demonstrated exceptional zero long-term stability. These benefits offer an attractive sensor system that is suitable to meet the challenging requirements for pressure control in semiconductor manufacturing applications.

Acknowledgements

The authors would like to thank Prof. Ch. Hierold (Micro- and Nanosystems, ETH Zurich) for the continuous support since the very early stage of the technology development, as well as the whole microGauge team and colleagues from the clean room operational team at BRNC for their extraordinary contributions along the way.

References

[1] https://www.imec-int.com/en/articles/smaller-better-faster-imec-presents-chip-scaling-roadmap

[2] K. Jousten, Simon Naef, On the stability of capacitance-diaphragm gauges with ceramic membranes, J. Vac. Sci. Technol. A 1 January 2011, doi: 10.1116/1.3529023

[3] Corigliano, A., Ardito, R., Comi, C., Frangi, A., Ghisi, A. and Mariani, Damping in Microsystems, Mechanics of Microsystems, Wiley (2018), doi: 10.1002/9781119053828.ch15

[4] M. Ono, M. Hirata, K. Kokubun, H. Murakami, F. Tamura, H. Hojo, H. Kawashima, H. Kyogoku, Design and performance of a quartz oscillator vacuum gauge with a controller, J. Vac. Sci. Technol. A 1 May 1985, 1746–1749, doi: 10.1116/1.573012

[5] Minhang Bao, Heng Yang, Squeeze film air damping in MEMS, Sensors and Actuators A: Physical, Volume 136, Issue 1, 2007, Pages 3-27, doi: 10.1016/j.sna.2007.01.008

[6] Sang Won Yoon, Sangwoo Lee, Noel C Perkins and Khalil Najafi, Analysis and wafer-level design of a high-order silicon vibration isolator for resonating MEMS devices, J. Micromech. Microeng. 21, doi: 10.1088/0960-1317/21/1/015017

DOI 10.5162/eurosensors2026/IS 4.4

Taking Sensor Simulations to New Frontiers: The COMSOL Perspective

Sven Friedel[1]
[1] *COMSOL Multiphysics GmbH, Technoparkstrasse 1, 8005 Zurich, Switzerland*
sven.friedel@comsol.com

Summary:
Modeling and simulation have become major drivers of sensor design and innovation. What began with multiphysics coupling has evolved into a broader ecosystem that now includes optimization, uncertainty quantification, surrogate modeling, simulation apps, digital twins, and large language models.

Keywords: Modeling, Simulation, Multiphysics, Surrogate

Introduction

Sensors are inherently multiphysics devices. Translating a physical phenomenon (such as the concentration of a biomarker) into a measurable signal (often electrical) involves multiple interacting domains, including fluidics, optics, and electrochemistry. These interactions are typically described through coupled balance equations for mass, momentum, energy, and charge, or through fundamental frameworks such as Maxwell's or Schrödinger's equations. The resulting couplings may arise from mutual loads or complex material behavior.

To capture that complexity, modeling and simulation have become commonplace in academic and industrial research, helping to better understand sensor systems, refine their response, and inspire numerous innovative methods and designs. Thanks to its rigorous Multiphysics concept and homogeneous architecture, COMSOL Multiphysics® software [1] has been a key driver of innovation in the sensor community for more than 30 years.

A typical multiphysics model for a sensor, incorporating several coupled partial or ordinary differential equations, is often just the starting point. In practice, these models are increasingly embedded in larger algorithmic structures, such as parametric sweeps, optimization, sensitivity analysis, uncertainty quantification (UQ), model order reduction (MOR) and data analysis, as well as interactive platforms for different classes of users (simulation apps).

These new frontiers reflect the insatiable desire for more performance and more ease. Conquering them involves the integration of the key technologies of our days into simulation algorithms: scalable hardware in clouds and on GPUs, machine learning (ML) as well as large language models (LLM) and other AI concepts.

Optimization

The ultimate goal of simulation-driven sensor design is no longer just to predict a response but also to optimize design and operational parameters, including dimensions, materials, and control functions.

With the COMSOL Optimization Module, scientists and engineers can use a range of gradient-based and gradient-free optimization algorithms with the same ease of use as when selecting PDEs for physics. In parameter optimization, a set of inputs serves as the control, whereas shape optimization allows the parametrization of smooth surfaces defined by polynomials. In topology optimization, a material density function serves as the control variable, enabling unexpected, generic designs that can also incorporate manufacturing constraints. The latest innovations include time-dependent optimizers for optimal control and global optimization (EGO Solver), as well as Design of Experiments (DoE) and surrogate modeling.

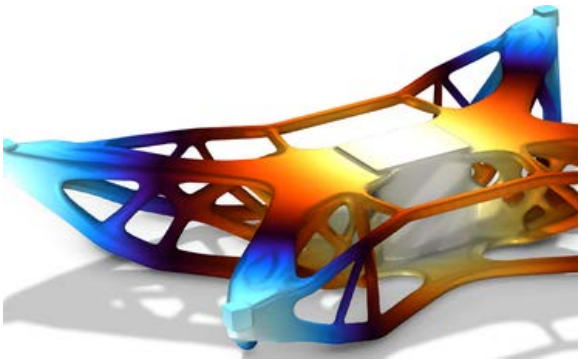

Fig. 1. Topology optimization of a drone.

Uncertainty quantification

The objective function for sensor optimization may include several quantities of interest: sensitivity, size, cost, and robustness. To extract measures of robustness, we need to account for the fact that all input parameters in a design are subject to statistical distributions, and consequently, so is sensor performance.

The COMSOL Uncertainty Quantification Module effectively evaluates model assumptions, simplifies models, identifies key inputs for the quantities of interest, explores their probability distributions, assesses design reliability, and calibrates unknown input parameter distributions. Confirming model accuracy and gaining a better understanding of the quantities of interest help reduce costs in production, development, and manufacturing.

Such analyses cannot rely solely on Monte Carlo-type calls to sensor simulations because complex multiphysics models can be computationally expensive and preclude brute-force mapping of a multidimensional parameter space. To advance, recent COMSOL releases make use of Latin Hypercube sampling (LHS) and, again, surrogate modeling, specifically Gaussian processes (GP) or polynomial chaos expansion (PCE).

Surrogate modeling

Surrogate models approximate the results of full finite element models. They are generally simpler, more compact, and require fewer computational resources than the full models. The path to obtaining a surrogate model typically involves two steps: data generation and training. During data generation, a DoE algorithm, e.g., one based on LHS, effectively maps the parameter space and produces a comprehensive design table. Each row contains a set of input parameters and corresponding outputs. In a training session, the design table is used to train a suitable surrogate (e.g., DNN, GP, or PCE). The surrogate model can then be called as a (fully differentiable) function, providing an approximate response for the sensor instantly. Typical use cases include fast optimization, uncertainty quantification, instantaneously responsive simulation apps, and digital twins.

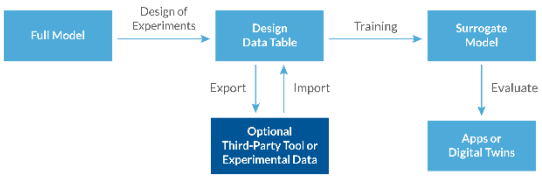

Fig. 2. Workflow of surrogate model design, training, and use. Optionally, measured data can be included. Surrogate models can also be exported.

Simulation Apps and Digital Twins

Simulation apps in COMSOL make sensor simulations accessible to lab technicians, managers, physicians, customers, and patients. Physics-based models include GUIs for safe use by non-experts and can connect with instruments, databases, and external codes.

Apps can be deployed in two ways: With COMSOL Compiler® apps can be compiled into royalty-free, standalone software for Windows, Linux, or macOS, which users can distribute either free of charge or for sale. Alternatively, a web server-based solution, COMSOL Server®, can host apps that are readily accessible from any web browser, including those on tablets and smartphones.

With server-side computation and the integration of surrogate models, these apps can deliver near real-time results. This capability is particularly important for digital twins, where live data from physical systems continuously updates and refines the virtual model, enabling predictive monitoring and improved decision-making.

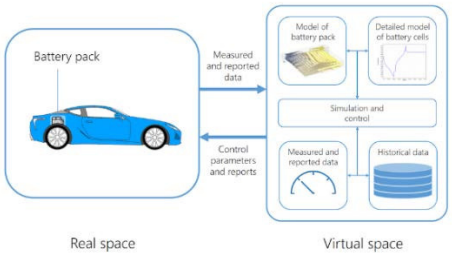

Fig. 3. Concept of an interaction of a battery pack in a real car and its digital twin in the virtual space.

Chatbot integration

State-of-the-art simulation tools are increasingly integrating large language models into their architecture. In COMSOL, users can integrate their OpenAI-compatible chatbot of choice to assist with modeling, generate code that can be executed directly, or saved in powerful methods. Thanks to the uniform object-oriented software architecture, it is already possible to build simple educational PDE models solely through prompting. Sharing models with chatbots makes bug checking straightforward, even for more complex models. Future versions are expected to expand interoperability with LLMs.

Conclusion: Sensor simulations today go far beyond physics and significantly accelerate the workflows of engineers and scientists by integration of cutting-edge algorithmic innovations.

References

[1] COMSOL Multiphysics® v. 6.4. www.comsol.com COMSOL AB, Stockholm, Sweden.

DOI 10.5162/eurosensors2026/Mo–ACT–01

Temperature Dependence of Parametric Snap-Through in Bistable Piezoelectric ScAlN MEMS Plates

Patrick Egger[1], Mahdi Mortada[1], Ulrich Schmid[1], Michael Schneider[1]
[1] Institut für Sensor- und Aktuatorsysteme, TU Wien, Gusshausstrasse 27-29, 1040 Wien, Austria
patrick.egger@tuwien.ac.at

Summary:

For the first time the temperature dependence between 30 °C and 80 °C of snap-through behaviour of bistable piezoelectric MEMS plates is shown. By exploiting mismatch in thermal expansion coefficients between ScAlN and Si the residual in-plane stress, and thus the buckling height, is tuned. An optimized measurement procedure allows for recording over 40 responses per second, enabling a high resolution parametric study. Understanding how dynamic characteristics of bistable plates are modified with ambient temperature change is a crucial step for future development towards commercial applications.

Keywords: MEMS, bistable, PMUT, nonlinear, temperature

State of the Art

In recent years bistable piezoelectric MEMS plates have emerged as promising candidates for applications requiring large stroke levels, like ultrasound generation [1, 2]. The static and small-signal response of such structures has been studied previously for a range of temperatures [3], as has the nonlinear parametric snap-through behaviour at room temperature [4]. The change in snap-through behaviour with temperature however has not been investigated so far. This study focuses on exploring the changes in the inter-well dynamics of the bistable piezoelectric MEMS plates for a temperature range from 30 °C to 80 °C through both metrics of number of snap-throughs and time to first snap-through. Additionally, the minimum voltage for initiating snap-through is investigated.

Methods

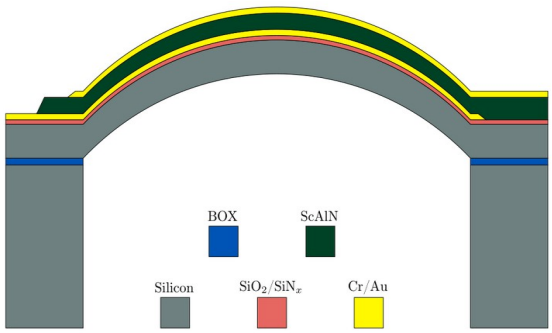

Fig. 1: Schematic, cross-sectional view of the device. The device is made from an SOI wafer with a 2.5 µm device layer. The piezoelectric layer (AlN or ScAlN, 400 nm) is sandwitched between Cr/Au electrodes. The plate is buckled due to the residual stress (up to -1 GPa) introduced in the ScAlN layer during sputter-deposition.

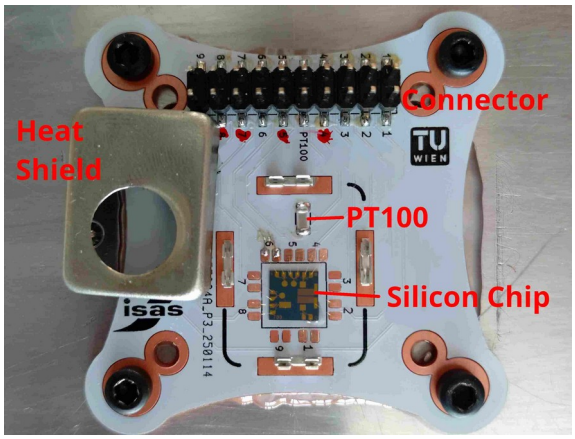

Fig. 2: Sample mounted on copper PCB for efficient thermal transfer. On the Si chip there are mutliple plates (rectangular and circular), as well as a gold resistor for on-chip temperature sensing. The PCB incorporates an SMD temperature sensor (Pt100) for precise temperature tracking. Heat shield is removed for illustrative purpose.

The studied device consists of a clamped circular plate with a diameter of 700 µm, with a total thickness of 3.2 µm. Bistability is achieved by engineering the piezoelectric layer ($Sc_{33}Al_{66}N$) to exhibit compressive residual stress (up to -1 GPa), leading to buckling of the plates. A schematic view of a bistable device can be seen in Fig. 1. The fabrication process is described in detail in [2]. The wafer is diced and each die is mounted on a PCB for subsequent tests (see Fig. 2). To study the snap-through behaviour parametrized sine pulses with varying amplitude, frequency and number of cycles are applied to the plate, inspired by [4]. The plate movement in response to the electrical signals is recorded with a Laser-Doppler-Vibrometer. To study the

impact of temperature the measurement setup includes a Peltier heater/cooler to control the device temperature. An example of a recorded signal is shown in Fig. 3.

Experimental Results

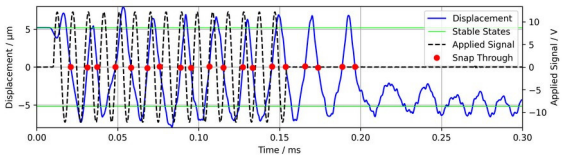

Fig. 3: Example of a recorded signal. Excitation parameters: 104.5 kHz, 24.875 Vpp, 15 pulses, temperature is 65 °C. The device switched, as shown by the sustained change in displacement for t > 0.2 ms.

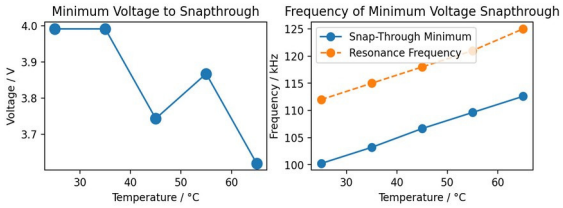

Fig. 4: Snap-through behaviour at different temperatures. Number of pulses is 15. Increasing the temperature shifts resonance frequency upwards, the frequency shift of the minimum voltage snapthrough point shifts by a similar amount.

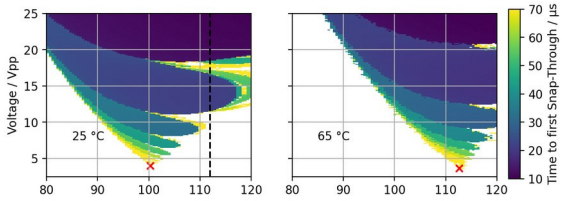

Fig. 5: Time to first snap-through for two example temperatures. The red 'x' represents the points from fig. 4. Each region represents a certain number of oscillations prior to snap-through. For example, the measurement from Fig. 3 has one oscillation before the first snap-through, it would be located in the darkest region at the top of the map.

The parameter space consists of 81 frequency steps by 181 voltage steps, 14,661 sets of parameters in total. Each measurement is repeated 5 times to check for consistency, resulting in 73,305 measurements performed. The fastest achieved time was 25 minutes, or about 48 measurements per second. Fig. 4 shows the analysis of the snap-through behaviour for different temperatures. With increasing temperature, the frequency at which the lowest voltage is required to achieve snap-through (marked by the red 'x' in Fig. 5) increases. This increase correlates well with the increase in the small-signal resonance frequency of the device. This finding supports the hypothesis that the location of the tongue-like shapes in the parameter space (Fig. 5), and therefore the highly nonlinear snap-through behaviour is linked to the small-signal resonance frequency of the device. In the upper regions of the map (Fig. 5) there is a shift to higher voltages as the temperature increases, which is also comparable to small-signal behaviour [3]. In contrast to that, the minimum voltage to snap-through decreases slightly with increasing temperature. This could be explained by different vibrational modes showing different temperature dependence, but further studies are needed to explain this phenomenon. The distinct regions in Fig. 5 representing a fixed number of oscillations before snap-through, shift smoothly and do not change their shape erratically, which ensures predictable device behaviour. This stability and predictability in behaviour across temperatures highlights the robustness of this nonlinear mechanism, ensuring consistent device behaviour even under fluctuating ambient operating conditions.

References

[1] M. Dorfmeister et al., Switching performance of bistable membranes activated with integrated piezoelectric thin film transducers, *Journal of Micromechanics and Microengineering* 29, 095011 (2019); doi: 10.1088/1361-6439/ab3185

[2] M. Dorfmeister, M. Schneider and U. Schmid, *A Bistalbe Ultrasonic MEMS Device with an Integrated Piezoelectric Scandium-AlN Thin Film Actuator for Switching*, *20th International Conference on Solid-State Sensors, Actuators and Microsystems & Eurosensors XXXIII (TRANSDUCERS & EUROSENSORS XXXIII),* 853-856 (2019) , doi: 10.1109/ TRANSDUCERS.2019.8808203.

[3] P. Moll et al., *Temperature-Dependence of Static and Dynamic Deflection of Bistable Piezoelectric Mems Membranes*, *IEEE 38th International Conference on Micro Electro Mechanical Systems (MEMS),* 744-747 (2025), doi: 10.1109/MEMS61431.2025.10918004.

[4] M. Mortada et al., *High-resolution parametric characterization of snap-through behaviour in bistable PiezoMEMS membranes*, Sensors and Actuators A: Physical 389, 116548 (2025); doi: 10.1016/j.sna.2025.116548.

DOI 10.5162/eurosensors2026/Mo–ACT–02

Electrodynamic Self-Cleaning Glass for Visibility Improvement of Autonomous-Driving Optical Sensors

Jungwoo Yoon[1], Lin Chai[1], Dong Joo Lee[1], Sang Kug Chung[1] and Kang Yong Lee[2]
[1] Department of Mechanical Engineering, Myongji University, Yongin, 17058, Republic of Korea
[2] Microsystems, Inc., Yongin, 17058, Republic of Korea
skchung@mju.ac.kr, kylee@microsystems.co.kr

Summary:

In this study, we propose a liquid-dielectrophoresis (L-DEP)-based self-cleaning glass capable of removing both conductive and non-conductive droplets from autonomous driving optical sensors. The device features a multichannel interdigitated electrode (IDE) array on a transparent glass substrate, with operating conditions systematically optimized through the analysis of voltage- and frequency-dependent droplet dynamics. Crucially, its practical applicability was validated through automated cleaning tests, demonstrating the complete restoration of object-recognition rates previously degraded by contamination.

Keywords: Autonomous-driving, Self-cleaning glass, Sensor cleaning, Liquid-dielectrophoresis (L-DEP)

Background, Motivation and Objective

Optical sensors are key components of autonomous driving systems because they acquire critical environmental information analogous to human vision [1-2]. However, in real-world driving environments, these sensors are continuously exposed to external liquid contaminants such as rain, snow, and oil. This exposure severely degrades image quality and sensing performance, potentially leading to fatal malfunctions in autonomous operations.

Various active cleaning approaches based on electric fields, heat, and acoustic waves have been developed to address this issue. Among them, electrowetting-based cleaning methods have attracted significant attention because of their rapid response, low power consumption, and ease of integration [3]. However, conventional electrowetting is primarily effective for conductive liquids and remains limited in manipulating non-conductive liquids such as oil, thereby restricting the range of removable contaminants.

To overcome this limitation, this study proposes a Liquid-dielectrophoresis (L-DEP)-based self-cleaning glass capable of removing both conductive and non-conductive liquid contaminants from physical AI optical sensor surfaces.

Description of the New Method or System

The proposed self-cleaning device utilizes a multichannel Interdigitated electrodes (IDE) array to transport both conductive and non-conductive droplets through sequential electrode actuation for contaminant removal (Fig.1).

The droplets undergo interfacial deformation under a dielectrophoretic force induced by liquid polarization in a non-uniform electric field. By sequentially activating the electrodes in a preprogrammed manner, the droplets are guided across the surface, enabling removal of various liquid contaminants. This planar electrode architecture eliminates the need for mechanical moving parts and offers advantages for compact packaging and seamless system-level integration with miniaturized optical sensor modules. Consequently, the device provides a scalable, sensor-integrable self-cleaning platform that fundamentally enhances the operational reliability of automotive optical sensors.

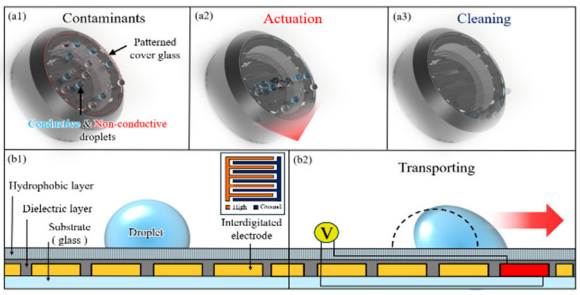

Fig. 1. Schematic of L-DEP based self-cleaning glass with sequential electrode control for the removal of conductive and non-conductive droplets

Results

First, to maximize the L-DEP force, the electric-field distribution in a parallel electrode configuration was numerically analyzed. The simulations revealed that strong fringing electric fields form at the electrode edges, generating a pronounced electric-field gradient primarily along the electrode-finger direction. Furthermore, the analysis further showed that minimizing the electrode gap increased the electric-field gradient, thereby enhancing the driving L-DEP force. Based on these findings, a six-channel IDE structure was designed, and interlocking electrode fingers with a width of 50 µm and a gap of 50 µm were incorporated between adjacent channels to enable continuous droplet transport. The designed L-DEP-based self-cleaning glass, consisting of IDE patterns, a dielectric layer, and a hydrophobic layer, was subsequently fabricated using standard semiconductor microfabrication processes (Fig. 2).

The fabricated device was then characterized in terms of device geometry, surface roughness, and optical transmittance to confirm its suitability for optical sensor applications.

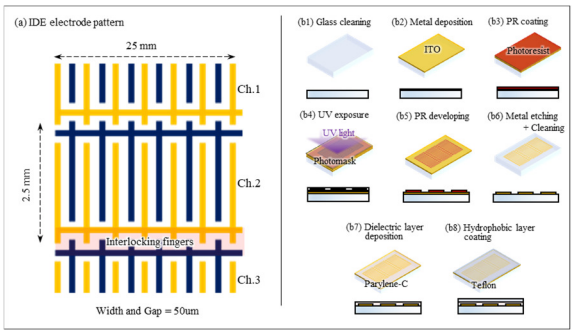

Fig. 2. Design and fabrication for L-DEP based self-cleaning glass: (a) IDE electrodes design; (b) Microfabrication processes

To investigate liquid-specific L-DEP response, the contact-angle variations of droplets with distinct electrical properties, including deionized water, propylene glycol, and silicone oil, were measured under different applied voltages and frequencies. For each liquid, the contact-angle modulation peaked near a characteristic actuation frequency and increased with applied voltage, thereby identifying the liquid-specific L-DEP response characteristics.

Based on these results, a programmable electrode-switching sequence for linear droplet transport was implemented on the proposed self-cleaning glass using an I/O board and a relay board. This precisely timed sequence enabled the linear transport and subsequent removal of both conductive and non-conductive droplets. Notably, this capability fundamentally broadens the spectrum of removable contaminants well beyond the intrinsic limits of conventional electrowetting-based cleaning systems.

In addition, to maximize cleaning efficiency, the transport velocity of individual droplets was quantitatively measured under different applied voltages. The results showed that the transport velocity varied with liquid type, increased with applied voltage, and was higher for liquids with higher permittivity. Based on these findings, the electrode-switching interval for sequential cleaning was determined. And, The cleaning performance was quantitatively assessed with ImageJ through time-dependent analysis of the cleaning efficiency under mixed conductive and non-conductive liquid contaminant conditions.

Finally, when integrated into a camera module, the device effectively removed surface contaminants, and the object-recognition rate degraded by contamination was fully restored following automated cleaning.

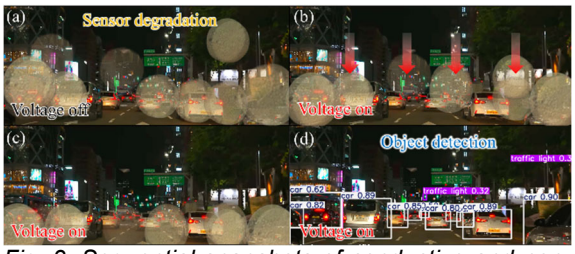

Fig. 3. Sequential snapshots of conductive and non-conductive droplet cleaning on L-DEP-based self-cleaning glass for autonomous driving optical sensors

References

[1] D. J. Yeong, G. Velasco-Hernandez, J. Barry, J. Walsh, Sensor and Sensor Fusion Technology in Autonomous Vehicles: A Review, Sensors 21, 2140 (2021); doi: 10.3390/s21062140

[2] A. Ziebinski, R. Cupek, H. Erdogan, S. Waechter, A Survey of ADAS Technologies for the Future Perspective of Sensor Fusion, in Computational Collective Intelligence: 8th International Conference, ICCCI 2016, Halkidiki, Greece, September 28–30, 2016, Lecture Notes in Computer Science 9876, 135–146 (2016); doi: 10.1007/978-3-319-45246-3_13

[3] K. Y. Lee, J. Hong, S. K. Chung, Smart Self-Cleaning Lens Cover for Miniature Cameras of Automobiles, Sensors and Actuators B: Chemical 239, 754–758 (2017); doi: 10.1016/j.snb.2016.08.032

Acknowledgement

This work was supported by the National Research Foundation of Korea (NRF) grant funded by the Korea government (MSIT) (RS-2025-25421959).

DOI 10.5162/eurosensors2026/Mo–ACT–03

Asymmetric Snap-through Dynamics in Bistable Piezoelectric MEMS Plates

Mahdi Mortada[1,2], Andreas Kraus[1,2], Jakob Gruber[1,2], Ulrich Schmid[1], Michael Schneider[1,2]
[1] Institute of Sensor and Actuator Systems, TU Wien,
[2] Christian Doppler Laboratory for Piezoelectric Silicon MEMS with Enhanced Sensitivity and Responsivity, Institute of Sensor and Actuator Systems, TU Wien
Gußhausstraße 27-29, 1040, Vienna, Austria
mahdi.mortada@tuwien.ac.at

Summary:
This study experimentally compares the switching behavior of a bistable piezoelectric MEMS plate actuated by an aluminium nitride (AlN) thin film from both ground states using pulse trains with varying voltages and frequencies to investigate nonlinear dynamics. The results show an asymmetry in the double-well potential with a preference for the upper state and demonstrate that adding an additional thin AlN layer to a buckled device modifies the potential energy, enabling tuning of voltage thresholds and snap-through responses, which is valuable for future PMUT applications.

Keywords: Snap-through, Bistability, Asymmetricity, Aluminum nitride, Piezoelectric MEMS

Background

Experimental analysis [1] reveals how controlled asymmetries influence the dynamics and efficiency of a bistable energy harvester. Similarly, the study in [2] discussed and showed the asymmetry contribution both in the potential energy model and the unequal energy requirements for switching withing bistable piezoelectric MEMS plates, from the lower to the upper state and vice versa. This asymmetry was attributed to the layers stack deposited on top of the plate. Generally, the upper state was observed to be the preferrable state. In [3], the authors introduced a better measurement approach using lock-in phase analysis for state detection to characterize snap-through behaviour in bistable piezoelectric MEMS. However, their study was only focused on switching starting from the upper ground state. In this work, we characterize this asymmetry and show the impact of tuning the stress of a bistable plate of 900 µm diameter (Figure 1) behaviour by adding additional layers.

Method

Different electrical pulses are applied with varying the voltage and frequency from 10 to 50 Vpp and 45 to 95 kHz, respectively. Laser Doppler Vibrometry (Single point VibroFlex from Ploytec) is used to obtain the velocity of the plate centre and a Multifrequency lock-in amplifier (MLA3) from IMP is utilized as signal generator and lock-in amplifier to detect the phase of the plate to distinguish its ground state. Subsequently, after characterizing the behaviour of the bistable plate, an additional layer of AlN is deposited onto its top electrode with a thickness of 35 nm and stress +100 MPa. Similar measurements were done subsequently to study the impact of this additional layer.

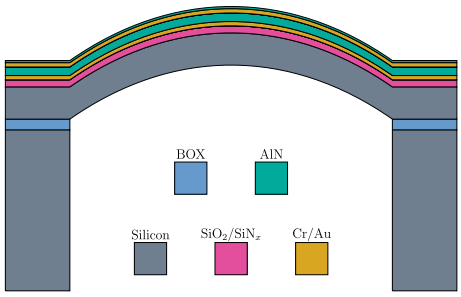

Fig. 1. Scheme of the bistable piezoelectric MEMS device with an additional top AlN layer.

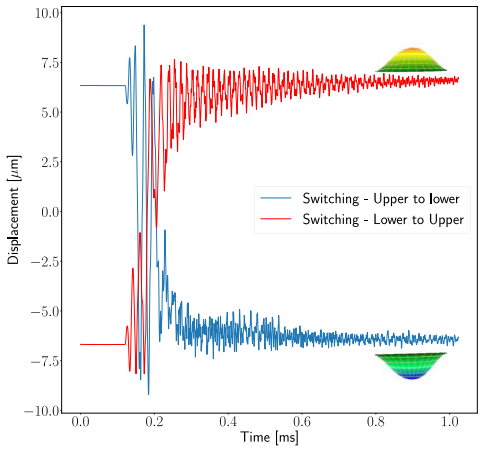

Fig. 2. Two switching events starting from different ground states showing different snap-through events.

Results

An example of switching behaviours are shown in Figure 2 and theoretical potential-well energies are shown in Figure 3. The obtained results showed a fractal nature behaviour of the parameter space similar to that presented in [3] as can be seen in Figures 4 and 5. The dynamic behavior reveals a clear asymmetry in the plates. Switching probabilities in Figure 4 indicate an overall higher probability of switching from the lower to the upper state confirming the asymmetry and the preference for the upper state. This is further supported by the lower voltage thresholds needed to initiate inter-well oscillations in the lower state.

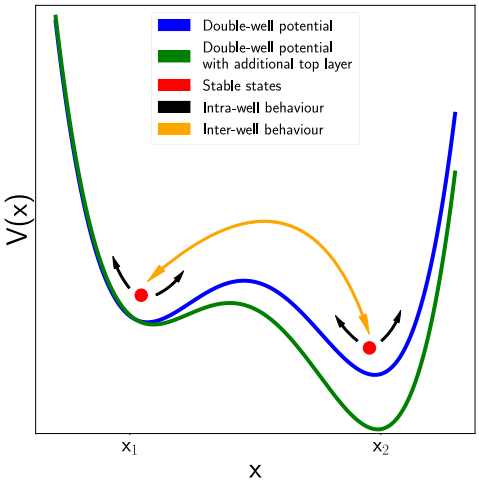

Fig. 3. Expected theoretical potential wells of bistable device where V(x), x_1 and x_2 represent the potential energy, lower and upper ground states positions respectively.

We also show that careful thin-film deposition on a fully fabricated plate can alter its potential energy, thereby affecting its dynamic behavior. Specifically, the results showed that the upper state acquires a lower potential energy and requires about 5 V higher voltage levels for snapping, whereas the lower state retains its original required voltage (see Figure 5). Adding an additional layer, primarily increases thickness rather than stress and therefore shifts the neutral axis upward further, favoring the upper state. By carefully adding layers on the top or bottom of the plate, the device can be made more symmetric improving the uniformity of its dynamic response. Also, it is observed that the modifications primarily affect the required voltage levels while the frequency and snap-through dynamics remain largely unchanged as evidenced by the similar alignment along the frequency axis and comparable ranges of snap-through counts.

References

[1] Norenberg, João Pedro, *et al.*, Nonlinear Dynamics 114.1 (2026): 22, DOI: 10.1007/s11071-025-11893-8

[2] Dorfmeister, Manuel, *et al.*, Journal of Micromechanics and Microengineering 29.10 (2019): 105008, DOI: 10.1088/1361-6439/ab3185

[3] Mortada, Mahdi, *et al.*, Sensors and Actuators A: Physical 389 (2025): 116548, DOI: 10.1016/j.sna.2025.116548

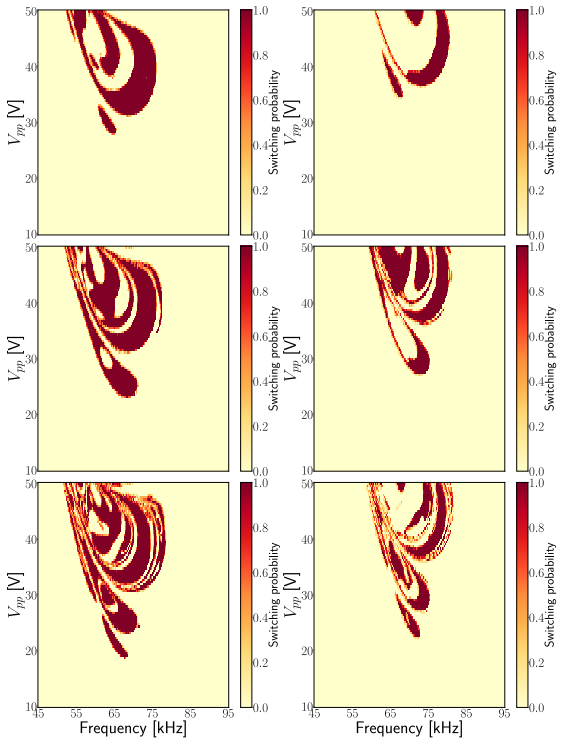

Fig. 4. Switching probabilities without the top AlN layer for 3, 4, and 5 pulses; left: lower state as initial state, right: upper state as initial state.

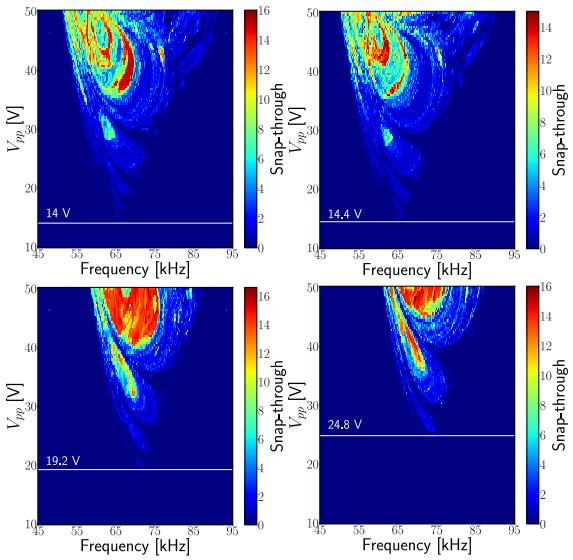

Fig. 5. Snap-through parametric presentation before(left) and after(right) deposition of AlN top layer starting from the lower state(top) and upper state (bottom) for 15 applied electrical pulses. White horizontal line serves as the threshold voltage for inter-well oscillations initiation.

DOI 10.5162/eurosensors2026/Mo−BBS−01

Glyphosate Detection with Mass-sensitive sensors using Molecularly Imprinted Polymers: Polymerization Strategies and Application

Ma Robellene S. Castillo[1,2], Peter A. Lieberzeit [1,2]
[1] University of Vienna, Faculty of Chemistry, Department of Physical Chemistry, 1090 Vienna, Austria
[2] University of Vienna , Doctoral School of Chemistry (DoSChem),1090 Vienna , Austria
a12405725@unet.univie.ac.at

Summary:

Molecularly imprinted polymer (MIP) coatings were fabricated on quartz crystal microbalance (QCM) sensors for the detection of glyphosate (Gly). The 16-mercaptohexadecanoic acid (16-MHDA) coupled with 2-hydroxyethyl methacrylate (2-HEMA) functionalized gold surface of the QCM was confirmed by Attenuated Total Reflectance - Fourier Transform Infrared Spectroscopy (ATR-FTIR). The MIP demonstrated enhanced binding to glyphosate compared to the non-imprinted polymer (NIP). The optimized MIP exhibited a high imprinting factor, achieved using a 60:40 citrate:ethanol solvent system and a 1:8:24 glyphosate:itaconic acid (ITA):N,N,N'-methylenebisacrylamide (BIS) molar ratio. These findings highlight the potential of the MIP-coated QCM sensor for glyphosate detection.

Keywords: Molecular Imprinted Polymer, Glyphosate, Quartz Crystal Microbalance, Maximum Residue Limit (MRL)

Introduction

Glyphosate is a widely used organophosphorus herbicide for weed control. It has been classified as a "probable human carcinogen" by the International Agency for Research on Cancer (IARC) [1]. Detecting glyphosate is particularly challenging due to its high polarity and lack of chromophores.

Residues of glyphosate in food, water, and the environment pose a significant threat to human health. Glyphosate inhibits acetylcholinesterase, an enzyme essential for proper central nervous system function. Therefore, monitoring glyphosate residues is critical to ensure they do not exceed the established MRL of 0.1 mg/kg [2]

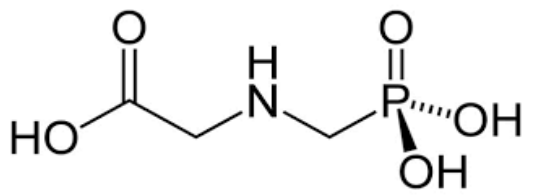

Fig. 1. Glyphosate Structure

MIPs are synthetic materials with highly selective recognition sites complementary in shape, size, and functional groups to a target molecule. In this study, MIPs were developed as selective coatings for QCM sensors to enable sensitive and selective detection of glyphosate.

Description of the New Method or System

The QCM gold surface was first functionalized with 16-MHDA to form a self-assembled monolayer. This was followed by coupling 2-HEMA to it via EDC/NHS chemistry to introduce polymerizable groups for covalent attachment. The MIP was synthesized using ITA as the functional monomer, BIS as the crosslinker, 2,2′-Azobis(2-methylpropionamidine) dihydrochloride (AAPH) as the initiator, and Gly as the template. The pre-polymerization mixture was heated to 60 °C until the gel point was reached, then spin-coated onto the functionalized QCM surface. The NIP was prepared under identical conditions without adding the template molecule.

Sensor Measurements

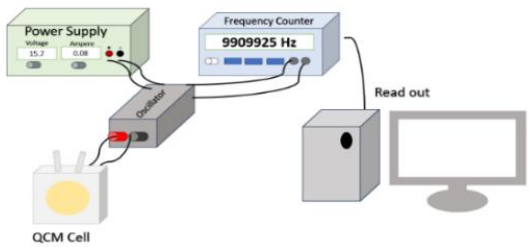

Fig. 2. QCM Measurement Setup

Figure 2 shows the QCM measurement setup. The dual-electrode QCMs were custom-made by screen-printing gold paste onto quartz blanks. The measurement setup consisted of an

oscillator connected to a QCM cell, a frequency counter, and a laboratory power supply. Resonance frequency changes were recorded and analyzed using a computer interface.

Results

Functionalization of QCM Surface

The functionalization of the QCM Surface is confirmed by ATR-FTIR. The 16- MHDA has a C-H band at 2920 cm^{-1} from its Alkyl chain. A peak at 1723 cm^{-1}, Ester C=O indicates successful coupling of MHDA and 2-HEMA.

QCM Sensor Response

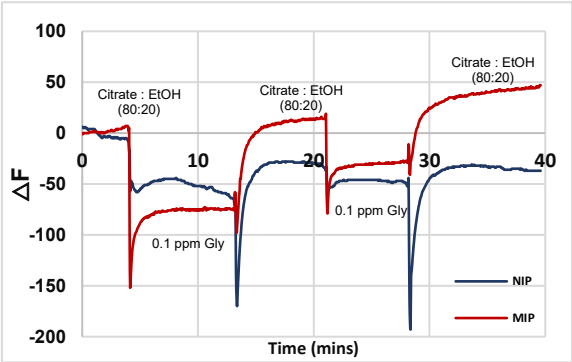

Fig. 3 QCM Measurement Graph of Coated Sensor (1:8:20 Gly:ITA: BIS)

The MIP-coated QCM (Fig.3) exhibits a 32 hz frequency shift than larger the NIP, indicating stronger, binding interactions with glyphosate. This confirms successful imprinting.

Optimization of Polymerization Parameters

The molar ratio of template: monomer: crosslinker governs MIP recognition capacity and selectivity [3].

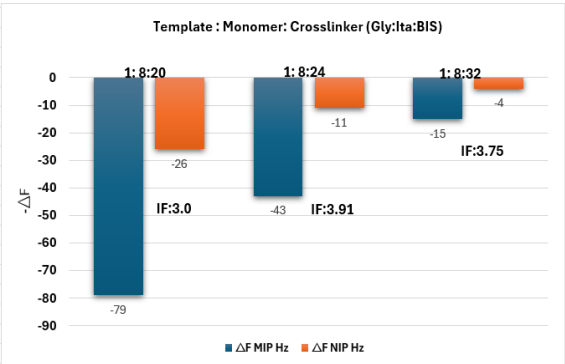

Fig. 4. Template: Monomer: Crosslinker Ratio (60:40 Citrate: Ethanol, 0.1 ppm Gly)

Fig 4 shows that 1:8:24 (Gly:Ita:BIS) produces the highest imprinting factor. Crosslinking density is sufficient to restrict the non-specific diffusion through the NIP network.

The 1:8:24 Gly:Ita:BIS formulation, combined with the previously optimized solvent system (60:40 Citrate:EtOH), defines the current optimized parameters for the glyphosate-MIP QCM Sensor. Further work will be performed, including optimization of the pH, calibration curve, and selectivity. It will establish analytical performance for the evaluation of the QCM Sensor

References

[1] International Research Agency for Cancer - WHO. *IARC monograph on glyphosate*. World Health Organization. (2018) https://www.iarc.who.int/featured-news/media-centre-iarc-news-glyphosate (accessed on 26 January 2026)

[2] Food and Agriculture Organization of the United Nations (2002). International Code of Conduct on the Distribution and Use of Pesticides. Retrieved 1-28-18

[3] Adeleke, V.T.; Ebenezer, O.; Lasich, M.; Tuszynski, J.; Robertson, S.; Mugo, S.M. Design and Optimization of Molecularly Imprinted Polymer Targeting Epinephrine Molecule: A Theoretical Approach. *Polymers 16*, 2341. (**2024**). https://doi.org/10.3390/polym16162341

DOI 10.5162/eurosensors2026/Mo–BBS–02

Enhanced IgE Aptasensing via Scaffold-mediated Oriented Immobilization of DNA Aptamers

Yuto Chokki[1], Akiko Tanabe[2], Izumi Sasaki[2], Hideo Nakano[3], Shun'ichi Kuroda[4], Masumi Iijima[1,2]
[1] Dept. Nutr. Sci. Food. Saf., Grad. Sch. Appl. Bioci., Tokyo Univ. Agric., JAPAN
[2] Dept. Nutr. Sci. Food. Saf., Fac. Appl. Bioci., Tokyo Univ. Agric., JAPAN
[3] Dept. Appl. Bioci., Grad. Sch. Bioagric. Sci., Nagoya Univ., JAPAN
[4] SANKEN, Univ. of Osaka, JAPAN
mi206786@nodai.ac.jp

Summary:

We developed a scaffold based on a single-chain Cro (scCro)-displaying bio-nanocapsule (scCro-BNC) that enables the oriented immobilization of DNA aptamers, thereby achieving highly sensitive detection in an aptasensor system. Herein, scCro-BNC was applied to a quartz crystal microbalance-based aptasensor for the detection of immunoglobulin E, an important biomarker for allergy diagnosis. This approach improved the sensitivity by approximately 30-fold compared with direct immobilization, demonstrating that scCro-BNC is an effective scaffold for enhancing aptasensor performance.

Keywords: aptasensor, oriented immobilization, scaffold, bio-nanocapsule, scCro

Background, Motivation and Objective

Aptasensors employing DNA aptamers, which have emerged as promising alternatives to antibodies in recent years, are widely applied to the detection of a broad range of target analytes—including food allergens, pathogenic microorganisms, and metal ions—using techniques such as quartz crystal microbalance (QCM), fluorescence resonance energy transfer (FRET), and immunochromatography [1]. For the immobilization of DNA aptamers onto sensor chips, various strategies have been developed, including nonspecific adsorption via electrostatic interactions as well as oriented immobilization using scaffold molecules such as crosslinkers, self-assembled monolayers, and thiol groups [1]. However, complete control over orientation remains challenging, often leading to reduced detection sensitivity.

To address this issue, we focused on single-chain Cro (scCro) [2], a DNA-binding domain that recognizes a specific 17-base pair sequence, and developed a nanoparticle-based bio-nanocapsule (scCro-BNC; Fig. 1) that displays scCro in an oriented manner on its surface [3]. The scCro-BNC is a hollow nanoparticle composed of a lipid bilayer and scCro-L proteins, in which part of the N-terminal region of the hepatitis B virus surface antigen L protein is replaced with scCro, and is produced in *Saccharomyces cerevisiae*. We previously demonstrated that appending a scCro-binding sequence to a thrombin-binding DNA aptamer, followed by its oriented immobilization on an scCro-BNC-treated QCM aptasensor, enhanced thrombin detection sensitivity by ~6000-fold compared with direct immobilization method [3].

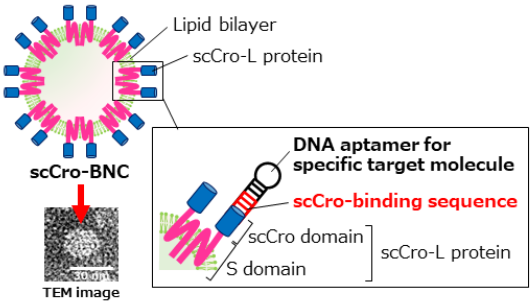

Fig. 1. Capsule structure of scCro-BNC.

In this study, we targeted immunoglobulin E (IgE), a key biomarker in allergy diagnostics, and aimed to enhance the sensitivity of an IgE-detecting aptasensor by using scCro-BNC as a scaffold, with the goal of enabling practical applications.

Description of the New Method or System

The IgE-binding DNA aptamer (37-mer) [4] was modified by appending a 17-base scCro-binding sequence to its terminus. The secondary structure of the modified aptamer was predicted by RNAfold WebServer (http://rna.tbi.univie.ac.at/).

The binding between the IgE-binding DNA aptamer and IgE was evaluated using a QCM instrument (Single-Q, As One, Osaka, Japan) in 500 µL of phosphate-buffered saline containing 2 mM $MgCl_2$ at 25°C with stirring at 540 rpm. The QCM sensor chip (As One) was first treated with scCro-BNC (6 µg/mL), followed by immobilization of the DNA aptamer (2 µg/mL). The sensor surface was then blocked with 5% (w/v) bovine serum albumin. IgE (0–6.2 µg/mL) was subsequently added, and a frequency change of less than 3 Hz per minute was considered indicative of signal stabilization. The maximum frequency change was defined as the binding response. As a control, DNA aptamers were directly immobilized onto the sensor chip. A frequency change of 1 Hz (ΔF) corresponds to a mass change of 0.6 ng/cm² according to the Sauerbrey equation. All measurements were performed in triplicate.

Results and Discussion

The maximum binding capacities of scCro-BNC and the IgE-binding DNA aptamer were determined using QCM. The amount of scCro-BNC immobilized on the sensor chip was estimated as 223.2 ± 9.5 ng/cm² based on a frequency change (ΔF) of −372.0 ± 15.8 Hz. After BSA blocking, the binding amount of DNA aptamer was 120.0 ± 21.1 ng/cm² (ΔF = −200.0 ± 35.1 Hz). Based on the molecular masses of scCro-L protein (~48 kDa) and the IgE-binding DNA aptamer (~21.8 kDa), approximately one aptamer molecule was estimated to bind per scCro-L protein, indicating an approximately 1:1 stoichiometric ratio.

IgE binding was evaluated using two immobilization methods: direct immobilization of the DNA aptamer and immobilization via scCro-BNC (Fig. 2). Calibration curves were constructed by plotting IgE concentration against binding amount on a log–log scale, followed by fitting to an exponential function. The direct immobilization method showed linearity in the range of 2.2–6.6 µg/mL, whereas the scCro-BNC method exhibited linearity across a broader range of 0.02–6.6 µg/mL. The limit of detection (LOD) of the QCM system was 2 ng/cm² (ΔF = −3.3 Hz), corresponding to ~0.61 µg/mL for the direct method and 0.02 µg/mL for the scCro-BNC method. These results demonstrate that the use of scCro-BNC expands the dynamic range and enhanced detection sensitivity by ~30-fold. Furthermore, the amount of IgE (~190 kDa) bound per mole of DNA aptamer also increased by ~2.5-fold, suggesting that scCro-BNC promotes oriented immobilization of DNA aptamers on the surface, thereby reducing steric hindrance and enhancing binding efficiency.

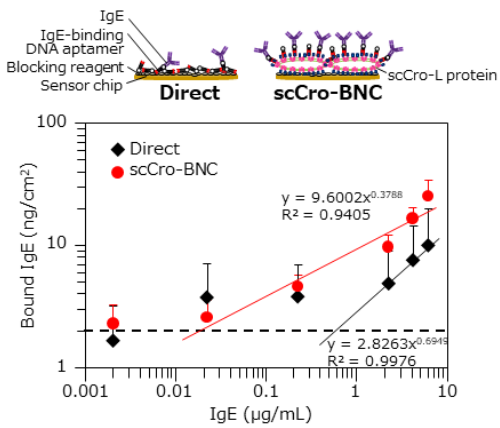

Fig. 2. Enhanced IgE detection sensitivity by scCro-BNC-mediated immobilization in QCM aptasensors.

Conclusions

These findings indicate that scCro-BNC serves as an effective scaffold for enabling highly sensitive detection of a wide range of target analytes in aptamer-based sensors. Future work will focus on extending this approach to various aptasensor platforms, with applications in food quality control, clinical diagnostics, and broader areas of the life sciences.

References

[1] X.F. Chen, X. Zhao, Z. Yang, Aptasensors for the detection of infectious pathogens: design strategies and point-of-care testing, *Microchimica Acta* 189, 443 (2022); doi: 10.1007/s00604-022-05533-w

[2] R. Jana, T.R. Hazbun, J.D. Fields, M.C. Mossing, Single-chain Lambda Cro Repressors Confirm High Intrinsic Dimer-DNA Affinity, *Biochemistry* 37, 6446-6455 (1998); doi: 10.1021/bi980152v

[3] M. Iijima, Y. Yamada, H. Nakano, T. Nakayama, S. Kuroda, Bio-nanocapsules for oriented immobilization of DNA aptamers on aptasensors, *Analyst* 147,489-495 (2022); doi: 10.1039/d1an02278d

[4] E. Katilius, C. Flores, N.W. Woodbury, Exploring the sequence space of a DNA aptamer using microarrays, *Nucleic Acids Research* 35, 7626-7635 (2007); doi: 10.1093/nar/gkm922

Acknowledgements

This research has been supported by JST FOREST Program (JPMJFR2102, Japan, to MI) and KAKENHI Grant-in-Aid for Scientific Research (C, 26K08149 to MI).

DOI 10.5162/eurosensors2026/Mo–BBS–03

Reliable Cell Concentration Prediction Using a Temperature-Compensated Four-Electrode Impedance Sensor with Machine Learning

Xiaoye Huo[1], Lihong Pan[12], Ding Han[1], Yongyao Niu[1], Junbo Wang[12]*, Jian Chen[12]**

[1] State Key Laboratory of Transducer Technology, Aerospace Information Research Institute, Chinese Academy of Sciences, Beijing 100190, People's Republic of China.

[2] School of Advanced Interdisciplinary Sciences, University of Chinese Academy of Sciences, Beijing 100049, People's Republic of China.

Xiaoye Huo[1]: huoxy@aircas.ac.cn*

Summary:

This work presents a compact PCB-based four-electrode impedance sensor for reliable live-cell concentration prediction under electrode polarization and temperature drift. The four-electrode configuration suppresses double-layer capacitance, while temperature compensation stabilizes impedance features. Based on compensated spectra, machine learning enables robust prediction under small-sample conditions. Experiments demonstrate improved stability and accurate prediction, with LASSO achieving the best performance, showing the system's potential for broader biosensing applications.

Keywords: Electrical impedance spectroscopy (EIS), Four-electrode configuration, Temperature compensation, Cell concentration prediction, Machine learning

Background

Electrical impedance spectroscopy (EIS) is widely used for label-free live-cell analysis [1]. However, its practical application is limited by electrode polarization and temperature-induced impedance drift, which degrade feature reliability and hinder quantitative analysis. At low frequencies, double-layer capacitance masks cellular signals [2], while temperature variations introduce additional fluctuations in impedance measurements. Although differential schemes can mitigate these effects [3], they in-crease system complexity and limit real-time applicability. Therefore, achieving stable and reliable impedance-based cell concentration prediction under practical conditions remains a challenge.

Description of the System

A compact PCB-based four-electrode impedance sensing system is developed for cell concentration monitoring (Fig. 1). A sinusoidal excitation signal from 10 kHz to 10 MHz is applied, and impedance and temperature are simultaneously recorded. The four-electrode configuration suppresses electrode polarization and enhances low-frequency sensitivity. Temperature compensation is performed to correct impedance drift and stabilize feature behavior. The compensated multi-frequency impedance features are then processed using PCA and used to train regression models for concentration prediction, enabling robust and real-time analysis.

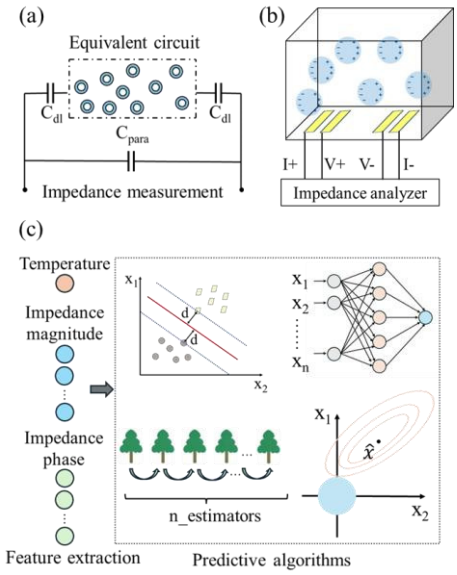

Fig. 1. Overview of the cell concentration prediction system. (a) Equivalent circuit representation of the impedance measurement. (b) Impedance spectra are acquired using an impedance analyzer (E4990A, Keysight, USA). (c) Measured impedance and temperature data are processed to extract features for training predictive models of cell concentration.

Results

Figure 2 shows that the four-electrode design effectively suppresses the double-layer capacitance seen in two-electrode systems, thereby revealing cellular polarization features at low frequencies.

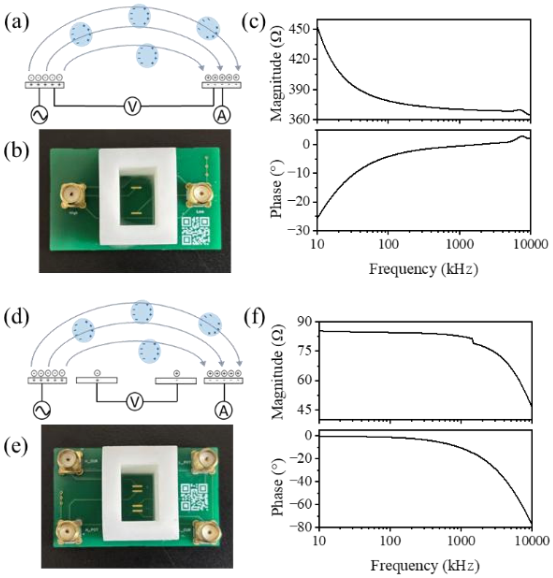

Fig. 2. Suppression of double-layer capacitance by the four-electrode configuration. Schematics, PCB structures, and impedance results of (a)–(c) two-electrode and (d)–(f) four-electrode.

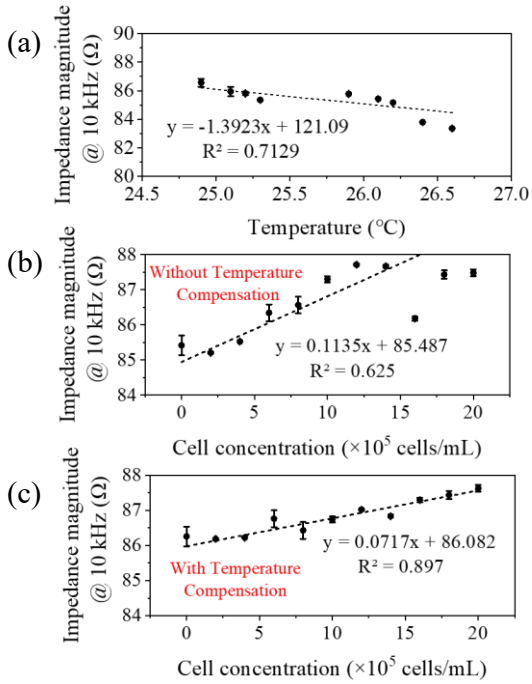

Fig. 3. Temperature dependence and compensation of impedance. (a) Low-frequency impedance shows a temperature coefficient of ~−1.39 Ω/°C. (b)–(c) Fitting results before and after compensation, showing improved monotonic and consistent impedance–concentration relationship.

Figure 3 further demonstrates that the low-frequency impedance magnitude is strongly temperature-dependent, with a temperature coefficient of −1.39 Ω/°C, and that temperature compensation improves its monotonic correlation with cell concentration. Based on the compensated multi-frequency spectra, machine learning models were trained for concentration prediction. As summarized in Table 1 and Figure 4, LASSO achieved the best performance under small-sample, high-dimensional conditions, indicating that feature-selective linear models can be highly effective in constrained biosensing tasks.

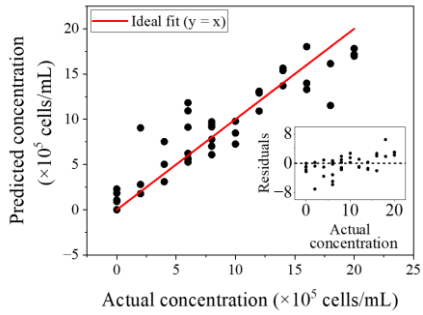

Fig. 4. LASSO fitting curve and residual distribution for cell concentration prediction.

Tab. 1: Performance comparison of different regression models in cell concentration prediction.

Predictive Model	RMSE	MAE	R^2
SVM	3.15	2.44	0.770
FNN	2.86	1.91	0.811
XGBoost	2.78	1.44	0.821
LASSO	2.28	1.60	0.880

References

[1] Y. Xu, X. Xie, Y. Duan, L. Wang, Z. Cheng, J. Cheng, A review of impedance measurements of whole cells, Biosensors and Bioelectronics 77, 824-836 (2016); doi: 10.1016/j.bios.2015.10.027

[2] A. R. Duarte, F. Batalioto, G. Barbero, A. M. Figueiredo Neto, Measurement of the Impedance of Aqueous Solutions of KCl: An Analysis Using an Extension of the Poisson-Nernst-Planck Model, Applied Physics Letters 105, 022901 (2014); doi: 10.1063/1.4890386

[3] M. Ashoorirad, R. Baghbani, A. Fallah, N. Jooyan, M. Gaffari, A Collagen Thin Film-Based Bioimpedance Sensor for Cell Proliferation Rate Assessment, IEEE Sensors Journal 22, 61-67 (2022); doi: 10.1109/JSEN.2021.3129351

Acknowledgements

Natural Science Foundation of Beijing: 4254075
National Natural Science Foundation of China：62501573

DOI 10.5162/eurosensors2026/Mo–BBS–04

3D Tubular Microelectrode Array Fabricated via Rotary Surface Exposure for Deep-Tissue Electrophysiological Monitoring of Organoids

Jie Ni[1], Han Ren[2] , Jiaxiang Wang[1], Fengming Ye[1], Xiaojun Guo[1], Zhuoqing Yang[1]
[1] National Key Laboratory of Advanced Micro and Nano Manufacture Technology, Shanghai Jiao Tong University, Shanghai, 200240, China
[2] Institute for Digital Molecular Analytics and Science (IDMxS), Nanyang Technological University(NTU), 59 Nanyang Drive, Experimental Medicine Building, Level 6 & 7, Singapore
yzhuoqing@sjtu.edu.cn

Summary:
A microelectrode array (MEA) was micro-fabricated and integrated onto the surface of a cylindrical polymer capillary for deep-tissue electrophysiological monitoring of organoids. By employing a rotary surface exposure system, platinum (Pt) functional electrodes were patterned on a 300 μm outer-diameter polyimide (PI) tube and encapsulated with biocompatible Parylene. This micron-scale tubular MEA configuration facilitates low-damage penetration into the organoid matrix, circumventing the constraints of traditional planar microelectrode arrays in accessing the internal electrophysiology of 3D tissue models.

Keywords: 3D microelectrode array, Rotary surface exposure, Tubular bioelectronics, Organoids, Deep-tissue monitoring

Background

While organoids have emerged as transformative in vitro models for recapitulating human tissue complexity, their functional characterization remains bottlenecked by destructive morphological analysis or the 2D spatial constraints of conventional planar microelectrode arrays [1]. To bridge this dimensionality gap, we present a flexible, miniaturized 3D microelectrode array (MEA) integrated onto a 300 μm polyimide (PI) tubular substrate (Fig. 1). By leveraging a high-precision rotary surface exposure process, this probe enables minimally invasive penetration into the organoid matrix, providing a robust solution for high-resolution, deep-tissue electrophysiological recordings [2]. This platform overcomes the spatial limitations of traditional technologies, offering a high-content functional analysis tool for next-generation organoid research and drug screening [3].

Description of the New Method

The fabrication strategy for the proposed 3D tubular microelectrode array (MEA) is detailed in Fig. 2, leveraging a specialized rotary surface exposure system for high-precision patterning on non-planar substrates [2]. The process sequence includes:

a. Using a curved-surface lithography system, a photoresist film was patterned on the capillary based on the programmable microstructure of the electrode array.
b. A 120-nanometer-thick platinum (Pt) film was deposited via magnetron sputtering onto the surface of the capillary with the patterned photoresist.
c. The photoresist film was removed via a stripping process, yielding a patterned Pt microstructure on the capillary surface.
d. A 500-nm-thick Parylene film is deposited.
e. A 2-μm photoresist layer was spray-coated and patterned via a secondary alignment (overlay) exposure.
f. oxygen plasma reactive ion etching was employed to selectively etch the Parylene, successfully exposing the electrode sites.
g. PEDOT:PSS was selectively applied onto the exposed microelectrode sites to reduce interfacial impedance and enhance the charge injection capacity.

Results

Fig. 3 and Fig. 4 illustrate the fabrication precision after etching. SEM images (Fig. 3) show the clear surface morphology post-Parylene-C etching, while EDS mapping (Fig. 4) confirms the successful removal of the encapsulation layer and precise platinum patterning.

The interface modification is shown in Fig. 5, comparing the bare (left) and PEDOT: PSS-coated (right) electrodes. The resulting electrochemical enhancement is validated in Fig. 6. CV curves (Fig. 6a) exhibit excellent stability and high charge storage capacity over multiple cycles. Additionally, the EIS Bode plot (Fig. 6b) shows low interfacial impedance and optimized charge-transfer kinetics, providing a high-

performance platform for long-term organoid monitoring.

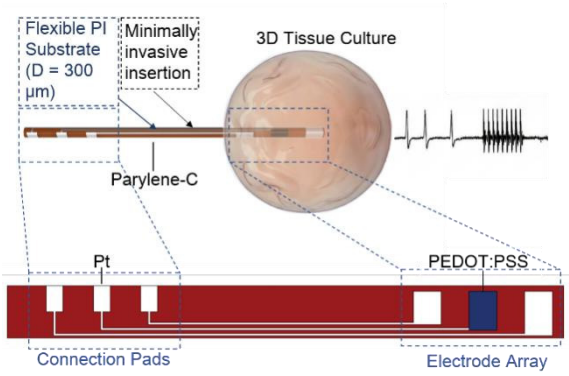

Fig. 1. Schematic of the integrated flexible PI-based microelectrode system for in-situ organoid signal recording.

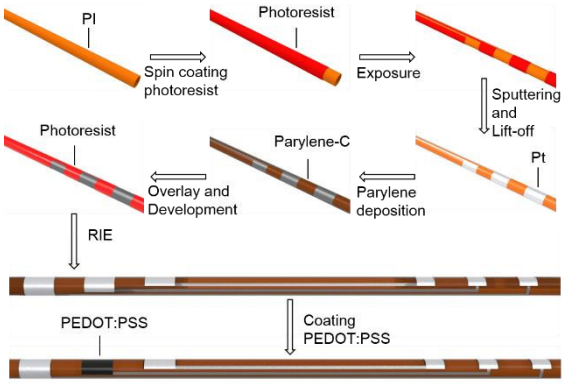

Fig. 2. Fabrication workflow of the microelectrode array on a 300 µm diameter PI substrate.

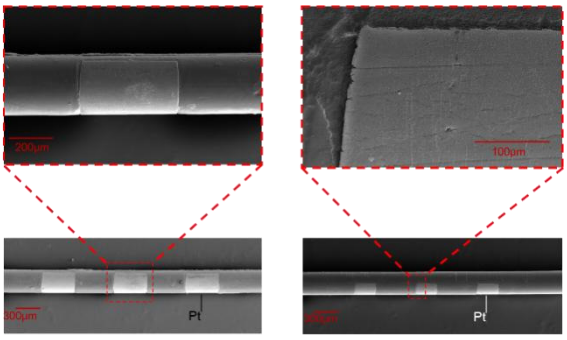

Fig. 3. Scanning electron microscopy (SEM) micrograph of the Parylene layer following the plasma etching process.

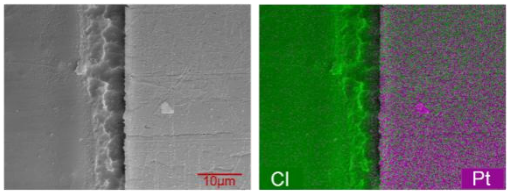

Fig. 4. Energy-dispersive X-ray spectroscopy (EDS) analysis of the substrate surface after Parylene etching.

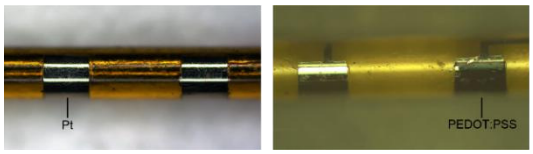

Fig. 5. Microscopic images of the electrode before (left) and after (right) PEDOT: PSS modification.

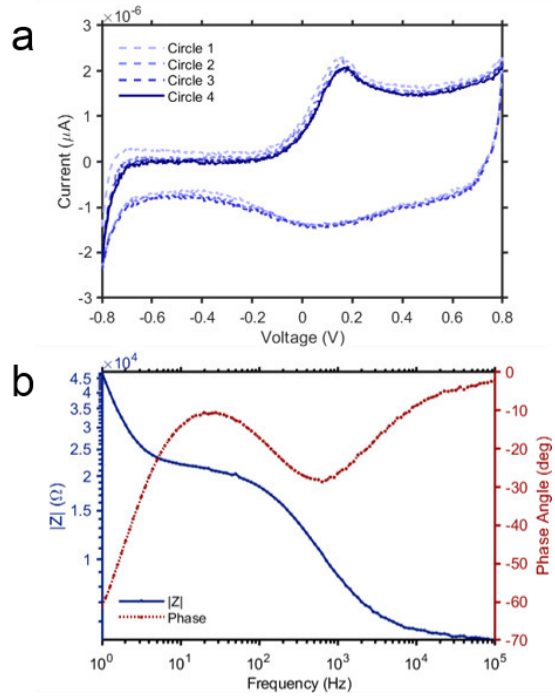

Fig. 6. Electrochemical characterization of the MEA: (a) CV curves; (b) EIS Bode plot.

References

[1] M. E. Spira, A. Hai, Multi-electrode array systems for external and intracellular recording from networks of cultured neurons, *Nature Nanotechnology* 8, 83–94(2013); doi:10.1038/nnano.2012.265

[2] A. Fatehullah, S. H. Tan, N. Barker, Organoids as an in vitro model of human development and disease, *Nature Cell Biology* 18, 246–254(2016);doi: 10.1038/ncb3312

[3] Z. Yang, Y. Zhang, Flexible Implantable Micro temperature Sensor Fabricated on Polymer Capillary by Programmable UV Lithography With Multilayer Alignment for Biomedical Applications, *Journal of Microelectromechanical Systems*, 23, 21-29(2014), doi:10.1109/JMEMS.2013.2269674.

DOI 10.5162/eurosensors2026/Mo−BBS−05

Design and Experimental Validation of an Impedance Based Position Sensor for Magnetic Microrobots

M.O. Heuschkel[1], D. Principi[1], D. Varela Freire[1], A. Savary[2], C. Besson[2], A. Roux[1]
[1] School of Engineering, Architecture and Landscape of Geneva (HEPIA), University of Applied Sciences and Arts Western Switzerland (HES-SO), Geneva, Switzerland
[2] School of Engineering and Management Vaud (HEIG-VD), University of Applied Sciences and Arts Western Switzerland (HES-SO), Yverdon-les-Bains, Switzerland
adrien.roux@hesge.ch

Summary:
Magnetic microrobots are investigated for minimally invasive applications, but their use remains limited by the lack of robust localization methods. An impedance-based sensing platform using a multiplexed electrode array is presented for spatial localization and tracking of a conductive magnetic milli-gripper in physiological saline solution. Experimental results demonstrate localized impedance variations that shift consistently with milli-gripper position across electrode pairs. Continuous measurements further enable real-time tracking during controlled displacement inside the sensing chamber.

Keywords: impedance tomography, microrobots, localization, electrode array, real-time tracking

Title

Design and Experimental Validation of an Impedance Based Position Sensor for Magnetic Microrobots

Background, Motivation and Objective

Magnetic microrobots are increasingly explored for minimally invasive manipulation, targeted drug delivery, and microscale interventions, but their use in conductive media remains limited by the lack of robust and scalable localization methods. Optical tracking is constrained by line-of-sight limitations, while imaging-based approaches increase system complexity and are difficult to integrate into compact platforms [1].

Electrical impedance tomography offers an alternative by reconstructing conductivity perturbations induced by objects, enabling non-invasive localization from boundary electrode measurements [2]. Recent studies have shown its suitability for real-time tracking of microrobots using low-cost instrumentation [3].

This work aims to develop a compact impedance-based sensing platform for real-time localization of a magnetic microrobot in a conductive saline environment using a multiplexed electrode array.

Description of the New Method or System

The proposed system integrates a magnetic microrobot platform, a conductive liquid sensing chamber, and a multiplexed impedance acquisition architecture.

The microrobot used in this study consists of a conductive magnetic milli-gripper measuring 7 × 7 × 1 mm³, including a titanium body with two embedded NdFeB magnets (see Fig.1). Helmholtz coils generate homogeneous magnetic fields enabling orientation, while Maxwell coils produce magnetic field gradients allowing translation within the liquid environment. Variations of the magnetic field amplitude generate magnetic torques enabling controlled opening of the gripper, while passive closing occurs when the external field is removed.

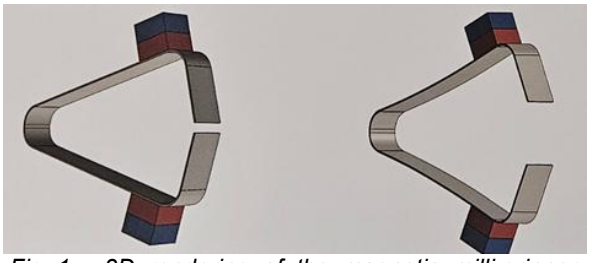

Fig. 1. 3D rendering of the magnetic milli-gripper illustrating its closed (left) and open (right) states.

The sensing chamber consists of two parallel plates, each integrating eight planar electrodes (4 mm²) arranged in opposing pairs and is filled with physiological saline solution (0.9% NaCl). The channel length is 30 mm, with two tested inter-plate distances of 10 mm and 15 mm.

The electronic architecture relies on multiplexed electrode selection using analog multiplexers controlled via an I²C interface. A dedicated impedance front-end generates an AC excitation signal and performs synchronous acquisition. Measurement frequencies between 40 kHz and

60 kHz were selected to minimize capacitive effects.

Experimental validation was conducted by magnetic actuation of the milli-gripper within saline-filled chambers, while continuous impedance measurements were acquired across electrode pairs (see Fig.2). The resulting impedance variations were quantified according to eg. (1), where Z_0 is the baseline impedance, i.e. only saline solution between measurement electrodes, and Z is the impedance measured in the presence of the milli-gripper.

$$\Delta Z = \frac{|Z - Z_0|}{Z_0} * 100 \quad (1)$$

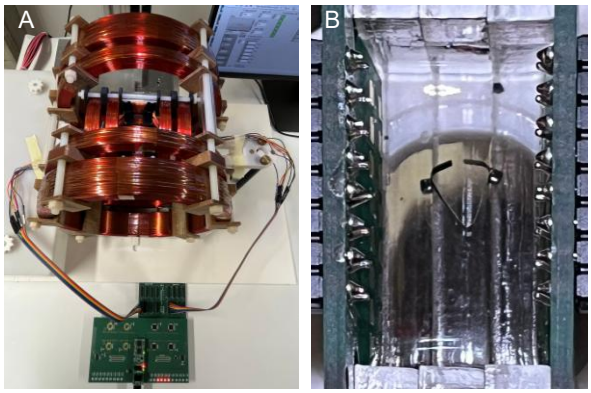

Fig. 2. (A) Complete system including magnetic field coils, external electronic board, and central measurement chamber. (B) Close-up of the chamber showing the eight electrode pairs and the milli-gripper positioned at its center.

Results

Results demonstrate that the presence of the milli-gripper induces localized decreases in impedance centered around electrode pairs closest to its position.

In the 10 mm chamber configuration, typical impedance variations of approximately 2 to 3 percent were measured at electrode pairs located directly near the milli-gripper. Adjacent electrode pairs exhibited smaller variations in the range of 1 to 2 percent, while more distant pairs showed variations below 1 percent. This spatial distribution confirms that impedance perturbations remain localized around the object position. Similar localization behavior was observed in the 15 mm chamber configuration, with impedance variations remaining within comparable ranges. Table 1 summarizes the impedance variations measured with the microrobot positioned at E2 for chamber width of 10 mm and 15 mm.

Continuous acquisition demonstrated real-time tracking capability, where the microrobot position is estimated by identifying the electrode pair with maximum impedance variation. The temporal evolution of impedance maps showed coherent spatial shifts during controlled displacement of the milli-gripper. No mutual interference was observed between magnetic actuation and impedance-based localization, confirming reliable parallel operation.

Electrode pairs	Width: 10 mm ΔZ[%]	Width: 15 mm ΔZ[%]
E1	1.5	1.8
E2	3.1	2.7
E3	1.5	1.9
E4	0.6	0.8
E5	0.6	0.3
E6	0.6	0.3
E7	0.3	0.3
E8	0.3	0

Tab. 1. Relative impedance variation (ΔZ) measured for each electrode pair with the milli-gripper positioned at E2, for chamber width of 10 mm and 15 mm. Green (>2%), orange (1–2%), and red (<1%).

Conclusion

The proposed impedance-based sensing system enables reliable localization and tracking of a conductive magnetic milli-gripper in saline environments using paired electrode measurements. Local impedance variations of 2–3% consistently identify the microrobot position in 10 mm and 15 mm chambers. Continuous acquisition enables real-time tracking during controlled motion, demonstrating the feasibility of a scalable impedance-based approach for microrobot localization in conductive media.

References

[1] Cai Z, et al., Performance evaluation of a magnetically driven microrobot for targeted drug delivery. *Micromachines (Basel)* 12(10), 1210 (2021); doi: 10.3390/mi12101210.

[2] Mansouri S, et al., Electrical impedance tomography – recent applications and developments. *Journal of Electrical Bioimpedance* 12(1), 50–62 (2021); doi: 10.2478/joeb-2021-0007.

[3] Daguerre H, et al., A localization method for untethered small-scale robots using electrical impedance tomography. *IEEE/ASME Transactions on Mechatronics* 27(5), 3506–3516 (2022) ; doi: 10.1109/TMECH.2022.3142924.

DOI 10.5162/eurosensors2026/Mo–BBS–06

Computational Design of Peptide Recognition Elements for Rapid Detection of Neurotoxin Exposure

Mustafa Al-gafari[1,2], Ashkan Golshani[2], Azam Tayabali[1,2]
[1] Biotechnology Laboratory, Environmental Health Science and Research Bureau, Healthy Environments and Consumer Safety Branch, Health Canada, Ottawa, Ontario, Canada, K1A 0K9
[2] Department of Biology, Carleton University, Ottawa, Ontario, Canada K1S 5B6
*azam.tayabali@hc-sc.gc.ca

Summary:

This project aims to identify neurotoxic exposure to organophosphate compounds by developing peptides that bind to acetylcholinesterase (AChE). Peptides were generated using the In-Silico Protein Synthesizer (InSiPS) platform to bind human acetylcholinesterase. Peptide interaction with native and inhibited enzyme structures was modeled using molecular docking to predict interaction affinities and binding confirmations. The best peptides demonstrated confirmation-dependent interaction patterns, which will be used for laboratory validation and future field-deployable chemical detection applications.

Keywords: peptide, acetylcholinesterase, molecular recognition elements, chemical hazards, field-deployable

Background, Motivation and Objective

Rapid identification of exposure to chemical hazards, including organophosphate compounds, remains an important challenge in chemical threat defense and emergency response. Acetylcholinesterase (AChE) is a relevant target in this context because inhibition of the enzyme is closely associated with toxic exposure [1]. Synthetic peptides offer a flexible and scalable route for developing recognition elements that may be adapted for a future chemical exposure detection platform. Additionally, peptides are more suitable for cold-chain independent deployment when compared to standard molecular affimers available. In this study, peptides were generated using the In-Silico Protein Synthesizer (InSiPS) platform [2] to bind AChE and were further evaluated using comparative docking analysis.

Description of the New Method or System

A panel of AChE-binding peptides was generated through the InSiPS workflow for downstream structural and experimental evaluation. InSiPS was used to identify peptide candidates targeting human AChE based on sequence-level recognition features, while accounting for off-target binding. This generated peptide panel formed the basis for subsequent structural assessment and future laboratory testing. To further evaluate peptide-AChE interactions, the candidates were subjected to preliminary HADDOCK docking [3] against selected native and inhibited human AChE structures. Docking was used to visualize likely peptide binding conformations in a three-dimensional space and compare predicted interaction behavior between enzyme states. This workflow combines sequence-based peptide generation with structure-based evaluation of peptide interactions with native and inhibited AChE, providing additional context for upcoming experimental validation (Fig. 1).

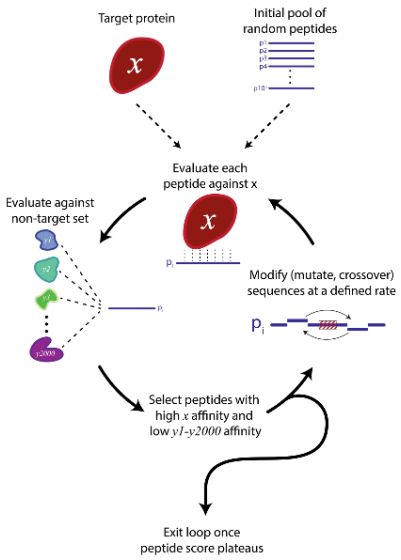

Fig. 1. Schematic overview of the InSiPS workflow used to generate candidate acetylcholinesterase-

DOI 10.5162/eurosensors2026/Mo–BBS–06

binding peptides for downstream docking analysis and experimental validation [4]

Results

Representative docking analysis of peptide P8 against native and inhibited human AChE provided a three-dimensional view of likely peptide binding regions on the enzyme surface. Comparative visualization suggested that peptide positioning and surface contacts differed between the two AChE conformations. P8 also showed a more favorable mean HADDOCK docking score for the inhibited structure than the native structure, supporting its use as a representative example of conformation-dependent docking behavior.

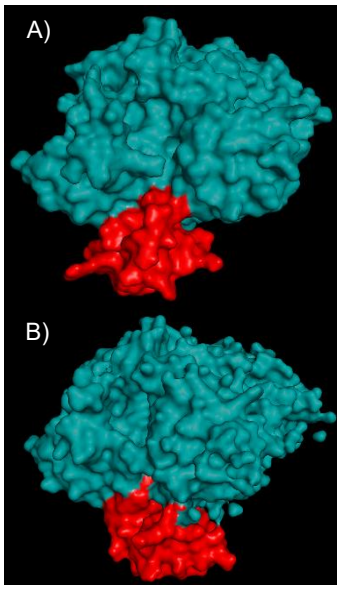

Fig. 2. Representative docking of peptide P8 against human acetylcholinesterase. (A) Docking pose of P8 with native AChE. (B) Docking pose of P8 with inhibited AChE. The models illustrate likely peptide binding regions in three-dimensional space.

Comparative mean docking scores showed mixed interaction behavior across the peptide panel. Five peptides (P8, P1, P10, P2, and P7) had more favorable mean docking scores for inhibited AChE than for native AChE, while five (P5, P6, P3, P9, and P4) showed the opposite trend. The strongest shift toward inhibited AChE was observed for P8 (Δ = -2.336), followed by P1 (Δ = -2.141) and P10 (Δ = -1.801). In contrast, P4 showed the largest shift toward native AChE (Δ = +7.802), followed by P9 (Δ = +4.053). These preliminary docking results indicate that peptide-AChE interactions vary across enzyme conformations and provide initial observation of peptide affinity ahead of laboratory validation of the full peptide set.

Tab. 1: Comparative mean HADDOCK docking scores of top 5, AChE-binding peptides against native and inhibited human AChE. Negative Δ values indicate more favorable docking to inhibited AChE, whereas positive Δ values indicate more favorable docking to native AChE.

Peptide name	Native mean	Inhib-ited mean	Δ
P8	-16.447	-18.783	-2.336
P1	-15.376	-17.517	-2.141
P10	-11.473	-13.274	-1.801
P2	-23.461	-24.640	-1.179
P7	-12.096	-12.361	-0.265
P5	-23.081	-22.789	+0.292
P6	-16.340	-14.824	+1.516
P3	-19.927	-17.650	+2.277
P9	-25.972	-21.919	+4.053
P4	-32.514	-24.712	+7.802

Conclusions

These preliminary docking results provide structural context for AChE-binding peptides and support ongoing laboratory validation toward future field-deployable detection of chemical hazard exposure.

References

[1] Lionetto MG, Caricato R, Calisi A, Giordano ME, Schettino T. Acetylcholinesterase as a Biomarker in Environmental and Occupational Medicine: New Insights and Future Perspectives. Biomed Res Int. 2013 Jan 1;2013(1):321213. doi:https://doi.org/10.1155/2013/321213

[2] Burnside D, Schoenrock A, Moteshareie H, Hooshyar M, Basra P, Hajikarimlou M, et al. In Silico Engineering of Synthetic Binding Proteins from Random Amino Acid Sequences. iScience. 2019 Jan 25;11:375–87. doi:10.1016/j.isci.2018.11.038

[3] Honorato R V, Trellet ME, Jiménez-García B, Schaarschmidt JJ, Giulini M, Reys V, et al. The HADDOCK2.4 web server for integrative modeling of biomolecular complexes. Nat Protoc. 2024;19(11):3219–41. doi:10.1038/s41596-024-01011-0

[4] Kazmirchuk TDD, Bradbury-Jost C, Withey TA, Gessese T, Azad T, Samanfar B, et al. Peptides of a Feather: How Computation Is Taking Peptide Therapeutics under Its Wing. Genes (Basel). 2023;14(6). doi:10.3390/genes14061194

Acknowledgments

The authors gratefully acknowledge funding support from the Canadian Safety and Security Program (CSSP).

DOI 10.5162/eurosensors2026/Mo−BBS−07

Raspberry Pi Platform for Multi-Modal Biosensing: Electrochemiluminescent and Colorimetric Analysis

Stephania Rodríguez Muiña[1], Francisco Javier del Campo[1], Giovanni Valenti[2], James F. Rusling[3]
[1] Basque Center for Materials, Applications and Nanostructures. UPV/EHU Science Park, Leioa, Bizkaia E-48940, Spain
[2] Department of Chemistry "G.Ciamician", University of Bologna, UE4, Via. P. Gobetti 85, 40129, Bologna, Italy
[3] Department of Chemistry, University of Connecticut, Storrs, CT 06269-3060, USA
Javier.delcampo@bcmaterials.net

Summary:

A Raspberry Pi-based imaging platform is presented to characterise camera modules and imaging parameters for two contrasting optical detection modes: light-emitting (electrochemiluminescence, ECL) and light-absorbing (ELISA) biochemical assays. A monochrome and a color camera without IR filter are evaluated for ECL, while a color camera with IR filter is characterised for absorbance detection. Key imaging parameters (focus, resolution, gain, exposure), file format, and image analysis are systematically optimised for each mode, delivering a unified framework for versatile optical biosensing.

Keywords: Raspberry Pi, optical biosensing, electrochemiluminescence, ELISA, biosensor.

Background, Motivation and Objective

Optical readout is central to many biochemical assays, but not all assays generate signals in the same way. In sandwich immunoassays, the detection antibody label determines the readout modality: ECL [1] and chemiluminescence (CLIA) generate photons requiring low-light detection, while colorimetric assays such as ELISA rely on enzyme-mediated absorption or transmitted color changes [2]. These contrasting principles impose distinct requirements on imaging hardware, acquisition settings, and analysis strategy.

Recent advances in smartphone cameras, single-board computers, and compact optics have enabled low-cost, portable imaging systems for point-of-care applications [1,2,3]. However, most platforms allow a single detection mode, limiting flexibility when workflows require switching between emission and absorption readouts.

This work presents a unified Raspberry Pi–based imaging platform [1] capable of supporting both luminiscence and colorimetric assays within a single instrument, and establishes an experimentally validated framework to guide the selection of camera configuration, image format, and analysis strategy according to the optical nature of the assay signal.

Description of the New Method or System

A Raspberry Pi 4B controller integrated with a PalmSens EmStat4s potentiostat and interchangeable camera modules (monochrome OV9281 and color IMX477 with and without IR filter) coupled to a 16 mm industrial lens with adjustable focus by tuning sensor-lens distance, was validated for both ECL [1] and colorimetric ELISA detection.

For ECL, all camera configurations were compared using a custom screen-printed electrode loaded with IL-8 IgG antibody labelled with $Ru(bpy)_3$-NHS ester (6 µg/mL, 2.5 µL), with emission triggered by chronoamperometry at 2 V for 5 s in 180 mM TPrA, 0.3 M phosphate buffer (pH 6.8) [1]. Background and signal frames were acquired inside a dark enclosure under fixed conditions (maximum analogue gain, 8 s exposure, auto white balance disabled, high resolution). Images were recorded in 16-bit TIFF, and 8-bit linear and gamma-encoded PNG formats. Quantification was performed using ROI-integrated background-corrected intensity, and signal-to-noise ratio (SNR) was calculated as the mean signal divided by the standard deviation of the background (n = 3).

For colorimetric ELISA, the IR-filtered color camera was used to record TMB substrate development in a TNF-α ELISA (DY210) before and after reaction stopping under fixed acquisition conditions (low resolution, 30 fps, auto white balance enabled). Four pixel aggregation strategies (mean, median, trimmed mean, and threshold mean) were compared across 16-bit TIFF, 8-bit linear and gamma PNG. Standard curves were fitted for blank (no analyte) corrected data using a four-parameter logistic model [2] (4PL, $Y = A + (D - A) / (1 + (C/x)^B)$, where A and D are the lower and upper asymptotes, B the Hill slope, and C the

concentration at inflexion point); limit of detection (LOD) was defined as a signal three standard deviations above the blank, SNR at the lowest standard relative to blank variability, and performance benchmarked against a plate reader absorbance (450–570 nm).

Results

For ECL detection of Ru-labelled antibodies emitting at ~620 nm (Figure 1), the signal was quantified as integrated intensity over the full electrode area to capture emission from spatially distributed labels. The monochrome camera achieved the highest signal per pixel and stable SNR across formats (47–57) by collecting all incident photons without spectral losses. For quantitative analysis, both 16-bit TIFF and 8-bit linear PNG are suitable, with higher bit depth providing improved dynamic range at low signal levels. When using non-linear gamma-encoded PNG, which enhances low-intensity signals, the tone response must be explicitly modelled [3].

The color camera with Bayer RGB and IR filters showed the poorest performance (SNR < 9), as the IR filter attenuates emission in the red/near-IR region where $Ru(bpy)_3^{2+}$ emits, while the Bayer pattern further reduces effective per-pixel signal by splitting photons across RGB color channels. Removing the IR filter substantially improved sensitivity; in this configuration, only the red channel provides a meaningful signal (SNR 83 amplified by gamma-encoding), as green and blue channels contain negligible emission and noise predominates [3].

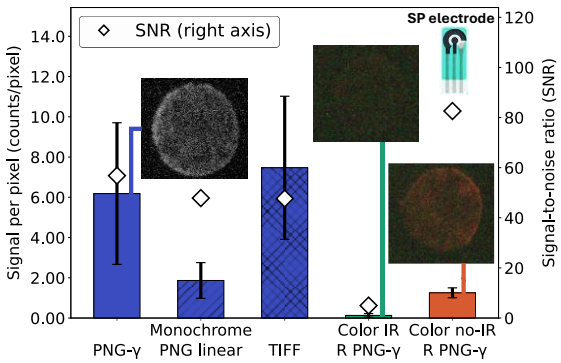

Fig. 1. Signal per pixel (bars) and SNR (diamond marker) for Ru-labelled IL-8 antibody detection across camera configurations and image formats. Error bars represent standard deviation (n=3). Representative ECL images are displayed with automatic brightness and contrast adjustment for visualization.

For colorimetric ELISA (Figure 2), the IR-filtered color camera was used, with pixel averaging over the colored well area as the core metric. Median aggregation outperformed all other strategies by suppressing outlier pixels from illumination inhomogeneity. Bit depth had no meaningful impact; 16- vs 8-bit linear formats were analytically indistinguishable for the averaged signal. Channel selection followed complementary color logic: before stopping, the blue TMB substrate made the R channel optimal (LOD 9.3 pg/mL, R^2 = 0.999997, Hill slope 1.294 vs plate reader reference 1.303); after stopping, the color shift to yellow made the B channel optimal (LOD 7.8 pg/mL, R^2 = 0.99991). Under gamma encoding, saturation of the red channel, consistent with gamma amplifying low-intensity signals at the cost of saturating high-intensity ones, shifted the best performer to the G channel before stopping (LOD 10.3 pg/mL, R^2 = 0.99996). Despite comparable calibration metrics to the plate reader, image-based methods showed lower SNR (~4 vs 62.6), reflecting the higher precision of monochromatic photometric detection.

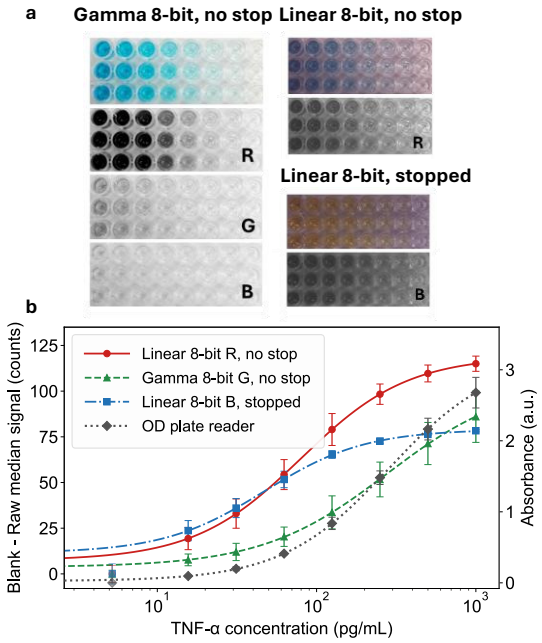

Fig. 2. Colorimetric TNF-α ELISA. (a) Representative 8-bit gamma and linear PNG image crops of the ELISA plate before and after reaction stopping, with R, G, and B channel splits. (b) 4PL standard curves for the best-performing image channels and plate reader absorbance.

References

[1] S. Rodríguez Muiña, G. Giagu, G. Valenti, F. J. del Campo, Versatile ECL Imaging Platform for Multiplexed Biosensing and Point-of-Care Application, *Chemical & Biomedical Imaging,* (2026); doi:10.1021/cbmi.5c00274.

[2] C. M. McGeough, S. O'Driscoll, Camera phone-based quantitative analysis of C-reactive protein ELISA, *IEEE Trans Biomed Circuits Syst* 7, 655–659 (2013); doi: 10.1109/TBCAS.2012.2234122

[3] S. Rodríguez Muiña, R. K. R. Gajjala, E. Fernández Martín, F.J. del Campo, Gamma Correction and Color Space Transformations for Quantitative Analysis of ECL Images Using Smartphone Cameras, *Chemical & Biomedical Imaging* 3, 767–778 (2025); doi:10.1021/cbmi.5c00056

DOI 10.5162/eurosensors2026/Mo–BBS–08

MEMS-Based Flexible NiTi Shape Memory Alloy Micro Actuator for Cochlear Electrode Applications

Pelin Ormancı[1,2], Haluk Külah[1,2]
[1] METU-MEMS Research and Application Center, Middle East Technical University, Ankara, Turkey; pormanci@mems.metu.edu.tr ; kulah@metu.edu.tr
[2] Dept. of Electrical and Electronics Engineering, Middle East Technical University, Ankara, Turkey

Summary:

This work presents a MEMS-based flexible NiTi micro actuator using co-sputtered thin films for cochlear electrode applications. Film composition was tuned to $Ni_{51.3}Ti_{48.7}$ by adjusting Ti sputtering power, followed by vacuum annealing at 400°C for 2 hours. Crystallization was confirmed by XRD, and EDX verified composition. The films exhibit a two-way shape memory effect with reversible actuation around 65 °C, demonstrating potential for integration into biomedical MEMS systems.

Keywords: Co-sputtering, MEMS actuators, NiTi thin films, shape memory alloys, thermal actuation

1. Background and Motivation

Shape memory alloys are widely used due to their unique ability to recover predefined shapes upon thermal stimulation, making them highly attractive for micro-actuation applications. This functionality enables their use in biomedical microsystems, where controlled deformation and recovery are critical [1]. Cochlear electrode systems represent a demanding application, as they must conform precisely to the spiral geometry of the cochlea to ensure effective neural interfacing, while simultaneously providing controlled mechanical compliance and actuation to enable smooth insertion and minimize trauma to delicate cochlear tissues [2]. For such biomedical applications, the phase transformation temperature must also be compatible with body temperature to ensure safe and effective operation.

This work aims to fabricate and characterize NiTi thin films via co-sputtering on a flexible substrate and evaluate their functional behavior for potential use in cochlear implant applications.

2. Materials and Methods

NiTi shape memory alloys were selected in this work because their phase transformation temperature can be tuned close to body temperature by controlling composition, which is critical for cochlear implant applications. Achieving this precise tuning requires strict compositional control, since even ~1% variation in Ni content can shift the transformation temperature by nearly 100 °C [3]. To enable this level of control, co-sputtering from separate Ni and Ti targets was employed, allowing independent adjustment of elemental contributions despite their different sputtering yields [4,5]. The as-deposited amorphous films were crystallized by high-temperature post-deposition annealing to activate shape memory behavior [6].

2.1. Fabrication Process

Fig.1 illustrates the fabrication process flow of the NiTi-based actuator. PI-2610 was used as a flexible substrate due to its high temperature resistance and mechanical flexibility, making it suitable to withstand the post-deposition annealing required for NiTi crystallization while enabling safe deformation during cochlear electrode insertion and operation. A 1 µm NiTi thin film is deposited by co-sputtering. Top and bottom PI layer thicknesses are intentionally made different so that the neutral axis does not lie within the NiTi layer, resulting in a predefined curvature upon release, thereby forming a permanently bent electrode structure that conforms to the shape of the cochlea. Upon heating, the structure straightens, enabling atraumatic insertion into the cochlea with no damage.

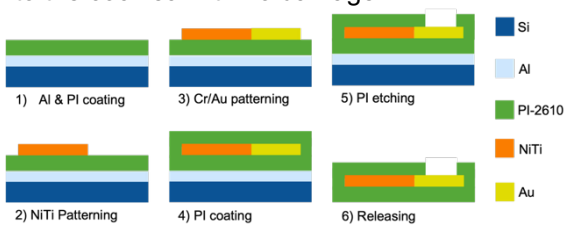

Fig. 1. Fabrication flow of the flexible SMA actuator

2.2. Characterization Methods

The chemical composition of the co-sputtered NiTi thin films was analyzed using EDX to evaluate the effectiveness of the compositional

optimization. The crystalline structure and phase formation were investigated using XRD measurements. Thermal behavior and shape memory response of the fabricated devices were evaluated through a heating test, where the actuation behavior of the NiTi thin films were observed.

3. Results

To enable actuation near body temperature, a slightly Ni-rich composition (~51 at. % Ni) was targeted as a higher Ni content would significantly shift the phase transformation temperature beyond the desired range. The Ni sputtering power was kept constant while the Ti sputtering power was varied to tune the film composition. Table 1 shows the dependence of the film composition on the applied powers.

Tab.1: EDX results for NiTi co-sputtering optimization

Process	Target Power (W)		Composition (at %)
	Ni	Ti	
1	42	200	$Ni_{57.8}Ti_{42.2}$
2	42	225	$Ni_{54.5}Ti_{45.5}$
3	42	250	$Ni_{51.3}Ti_{48.7}$

$Ni_{51.3}Ti_{48.7}$ film annealed at 400 °C for 2 h under vacuum conditions. Fig.2 presents the XRD patterns of the as-deposited amorphous film and the annealed film, highlighting crystallization after annealing. The diffraction peaks observed at 41.41°, 43.40°, and 46.19° are attributed to the martensitic phase of NiTi [3], indicating that the film is predominantly in this phase at room temperature. This suggests that the phase transformation to austenite occurs at higher temperatures.

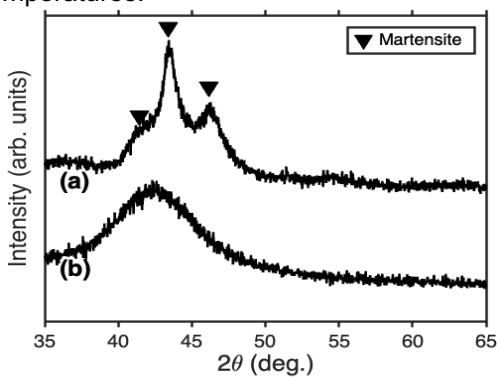

Fig. 2. XRD profiles of $Ni_{51.3}Ti_{48.7}$ (a) annealed at 400 °C for 2h (b) as deposited

Fig.3 shows the released die and the die heated on a hot plate at 65 °C for 3 minutes. As expected, the heated dies straighten, recovering the flat shape defined during annealing. Moreover, once removed from the hot plate, the samples return to its original shape at around 25 °C within approximately one minute, indicating a two-way shape memory effect. The shape memory alloy can also be actuated electrically by applying a voltage, for example by attaching the die to a PCB using epoxy, as shown in Fig. 3(c).

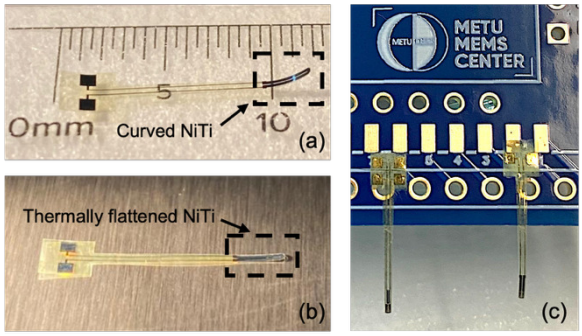

Fig.3. (a) Released die, (b) die heated on a hot plate at 65 °C for 3 min, and (c) die attached to a PCB

The results demonstrate promising potential for shape memory alloys in cochlear electrode applications, with rapid shape recovery observed at around 65 °C. The phase transformation temperature can be further tuned closer to body temperature by optimizing annealing parameters such as temperature and duration. This approach enables an actively reconfigurable electrode architecture compared to conventional passive designs, offering reduced insertion trauma and improved conformity to the cochlear spiral, and highlights the feasibility of integrating MEMS-fabricated shape memory alloys into next-generation cochlear interfaces. As a future work insertion tests can be performed using a cochlear model for further validation.

References

[1] K. Chaudhary et al., *A review of shape memory alloys in MEMS devices and biomedical applications*, Materials Today: Proceedings (2024); doi: 10.1016/j.matpr.2024.04.105

[2] A. Dhanasingh et.al, *An overview of cochlear implant electrode array designs*, Hearing Research 356, 93–103 (2017); doi: 10.1016/j.heares.2017.10.005

[3] S. Sanjabi et.al, *Growth and characterization of Ti_xNi_{1-x} shape memory thin films using simultaneous sputter deposition from separate elemental targets*, Materials Science and Engineering A 417, 289–296 (2006); doi: 10.1016/j.msea.2005.11.035

[4] W. D. Westwood, *Sputtering yields and related phenomena*, in: *Sputter Deposition*, Elsevier (2010); doi:10.1016/B978-1-4377-3483-6.00002-4B

[5] V. Karki et.al, *Synthesis of co-sputter deposited Ni–Ti thin alloy films and their compositional characterization using depth sensitive techniques*, Thin Solid Films (2020); doi: 10.1016/j.tsf.2020.137800

[6] A. G. Ramirez et.al, *Crystallization of amorphous sputtered NiTi thin films, Materials Science and Engineering: A* (2006); doi: 10.1016/j.msea.2006.01.118

DOI 10.5162/eurosensors2026/Mo–BBS–09

Reproducibility and Biofouling in Graphene Foam Electrodes Assessed by Direct ELISA

Lei Cuasay[1], Ioana Manea[2,3], Baptiste Mathmann[1], Oana Hosu-Stancioiu[2], Cecilia Cristea[2], Noemí de-los-Santos-Álvarez[3,4], Philippe Pernod[1], Abdelkrim Talbi[1], Lorena Manzanares[1]
[1] Univ. Lille, CNRS, Centrale Lille, JUNIA, Univ. Polytechnics Hauts-de-France, UMR 8520 - IEMN - Institute of Electronics, Microelectronics and Nanotechnology, 59800 Lille, France,
[2] Department of Analytical Chemistry, Iuliu Haţieganu University of Medicine and Pharmacy, 4 Pasteur Street, 400349, Cluj-Napoca, Romania,
[3] Departamento de Química Física y Analítica, Universidad de Oviedo, Av.Julián Clavería 8, 33006 Oviedo, Spain,
[4] Instituto de Investigación Sanitaria del Principado de Asturias, Av. Roma s/n, 33011, Oviedo, Spain
lei.cuasay@centralelille.fr

Summary:
Graphene foam is an emerging electrode material in the field of biosensors. Here, we evaluate graphene foam electrodes in terms of reproducibility and biofouling using electrochemical direct ELISA. The electrodes exhibited significant inter-batch variability and elevated nonspecific blank signals in comparison to conventional screen-printed carbon electrodes. Overall, surface heterogeneity and nonspecific adsorption in graphene foam limit its analytical reliability, highlighting challenges for practical biosensing applications despite its high sensitivity potential.

Keywords: graphene foam, electrochemical immunosensor, biofouling, reproducibility, direct ELISA

Introduction

Single-use electrodes are widely employed in electrochemical biosensing due to their sensitivity, portability, and simplicity for rapid in situ analysis. Three-dimensional (3D) graphene foam electrodes, with their porous networks, offer high surface area, biocompatibility, and efficient biomolecule immobilization, enhancing antibody–antigen interactions [1]–[3]. However, their complex architecture can introduce interfacial heterogeneity and nonspecific adsorption, limiting reproducibility and analytical performance. Additionally, performance is often assessed under idealized conditions that overlook these constraints. Biofouling and batch-to-batch variability remain underexplored, and both represent key challenges affecting reliability. This study systematically evaluates the reproducibility and antifouling performance of commercial graphene foam electrodes using a direct electrochemical enzyme-linked immunosorbent assay (ELISA) as a controlled model system.

Materials and Methods

Gii-Sens Integrated Graphene electrodes were purchased from iGii (Stirling, UK). DropSens 110 carbon electrodes were obtained from Metrohm (Spain) for comparison. In an electrochemical direct ELISA, an HRP-labeled antibody reacts with the substrate 3,3',5,5'-tetramethylbenzidine (TMB) to generate a current response, measured using chronoamperometry. Covalent immobilization anchored the target (IgG) to the graphene surface, using pyrene carboxylic acid to introduce carboxyl groups through π–π interactions and EDC/NHS coupling chemistry to anchor the antibody to the surface.

Results

Graphene foam electrodes owing to their porous structure (Fig. 1a), show promising electroanalytical performance due to their high surface area resulting in 3-4 times higher cathodic and anodic peak currents compared to planar carbon electrodes (Fig. 1c).

However, important challenges around reproducibility and biofouling were found when performing a direct electrochemical ELISA (Fig. 2a) on graphene foam electrodes. Chronoamperograms shown in Fig. 2b reflect up to 61% of inter-batch variation in the recorded signals for graphene electrodes, in contrast to 12% inter-batch variation for carbon electrodes. Overall, CoV values across multiple experiments on the same batch of graphene electrodes spanned from 9 to 149%, whereas for carbon it was systematically below 12%.

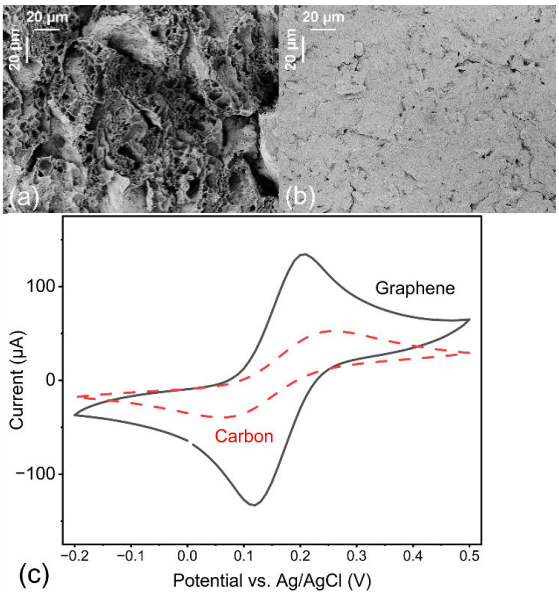

Fig. 1. SEM images of the bare working electrode of (a) graphene foam and (b) carbon. (c) Cyclic voltammograms of the graphene foam and carbon electrodes recorded in 5 mM ferro/ferricyanide in 0.1 M KCl aqueous solution at a scan rate of 100 mV s⁻¹.

Furthermore, graphene exhibited a 9 times higher blank signal compared to that recorded with carbon, indicating poor antifouling properties despite surface passivation using ethanolamine. Consequently, the signal-to-blank ratio for graphene was approximately threefold lower compared to carbon. Alternative blocking strategies were also evaluated, but all resulted in a 1.2-1.4-fold increase in the average current response for blank measurements. These findings demonstrate that surface heterogeneity and nonspecific interactions present on these electrodes critically impact the analytical performance of the proposed electrochemical immunosensor assay.

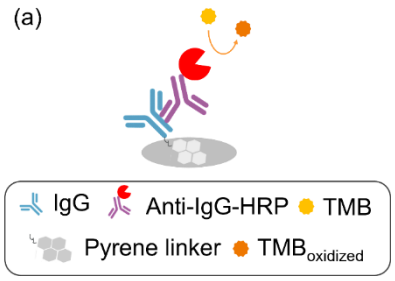

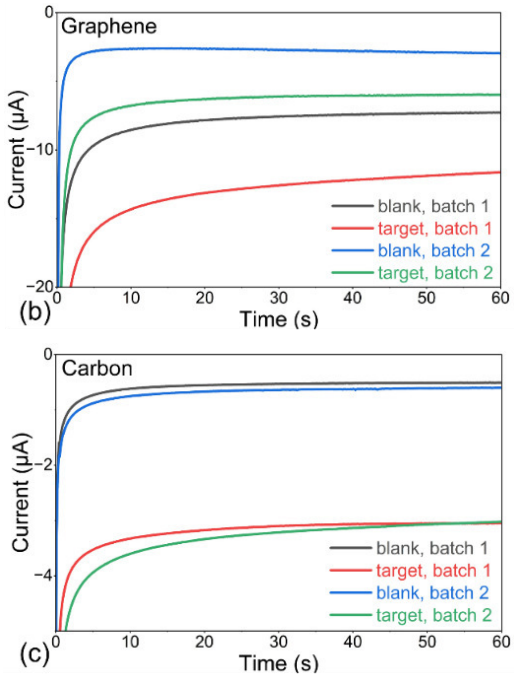

Fig. 2. (a) Schematic illustration of direct ELISA on the electrode surface. Surface passivation was done using 3 M (pH 9) ethanolamine. (b) Chronoamperometric responses (current vs. time) recorded for graphene foam electrodes, comparing blank and target conditions across two independent electrode batches. (c) Chronoamperometric responses for carbon electrodes under analogous conditions.

Acknowledgements

This work was supported by the European Union's Horizon Europe research and innovation programme under the Marie Skłodowska-Curie Doctoral Networks (MSCA-DN) project CanDoIt, grant agreement no. 101120186.

References

[1] S. Nazir, M. Dogan, Y. Wei, G. Pan, Electrochemical Immunosensor Using COOH-Functionalized 3D Graphene Electrodes for Sensitive Detection of Tau-441 Protein, *Biosensors* 15, 465 (2025); doi: 10.3390/bios15070465

[2] I.A. M. Frias, N. Zine, M. Sigaud, P. Lozano-Sanchez, M. Caffio, A. Errachid, Non-covalent π–π functionalized Gii-sense® graphene foam for interleukin 10 impedimetric detection, *Biosensors and Bioelectronics*, 222, 114954 (2023); doi: 10.1016/j.bios.2022.114954

[3] M.-J. Treanor, P. Lozano-Sanchez, Y. Bunga, R. Schaub, M. Caffio, Implementation of a simple functionalisation of graphene (Gii-Sens) in the determination of a suitable linker for use in biocatalytic devices, *Applied Surface Science*, 680, 161426 (2025); doi: 10.1016/j.apsusc.2024.161426

DOI 10.5162/eurosensors2026/Mo–BBS–10

Investigation of a Plasmonic Aptamer-Based Biosensor for Heavy Metal Ion Detection

Rebeka Kovács[1], André P. G. Rocha[2], Tomáš Lednický[2], Baihui Li[2], Andrea Csáki[2], Attila Bonyár[1]
[1] Department of Electronics Technology, Faculty of Electrical Engineering and Informatics, Budapest University of Technology and Economics, Budapest, Hungary,
[2] Leibniz Institute of Photonic Technology, Albert-Einstein-Str. 9, 07745 Jena, Germany
kovacs.rebeka@vik.bme.hu

Summary:
Optical biosensing devices offer a cost-effective approach to examining molecular interactions and detecting specific molecules; therefore, they are widely used for the detection of proteins, nucleic acids, and heavy metal ions. In this research, a localized surface plasmon resonance (LSPR) biosensing measurement device is studied to investigate the presence and quantity of arsenic ions in water samples, with the help of plasmonic nanostructures and aptamers, which can specifically bind to a target molecule to enable the selective detection of toxic arsenic(III)-ions in water samples.

Keywords: Plasmonic biosensing, localized surface plasmon resonance (LSPR), Microfluidic devices, refractive index sensing, heavy metal ion detection

Background, Motivation and Objective

Agricultural activities and increasing industrial and transport emissions are causing a global issue by polluting surface and ground waters with heavy metal ions, which can accumulate in animal and plant tissues consumed by humans. These ions are non-biodegradable and chronic posioning can lead to severe health problems: damage to the central nervous system, liver, kidneys, reproductive organs, mucus tissues, and can result in carcinogenic effects in humans and animals. The monitoring of the level of toxic heavy metal ions is indispensable in environmental protection, disease prevention and effective treatment of patients [1, 2]. In most biological and environmental samples, many interfering matrix components affect the reliability of detection; therefore, it is crucial to develop a highly selective approach. [3]

Localized surface plasmon resonance (LSPR) is a phenomenon caused by the interaction of visible light and metal nanoparticles. The wavelength of the absorption peaks is very sensitive to changes in the refractive index of the surrounding medium; hence, the presence of the target molecules can be observed in a real-time, label-free manner. To selectively capture the target molecules/ions, aptamers can be utilized (optical aptamer sensors are called aptasensors). These are artificial oligonucleotide probes created by an *in vitro* process, called SELEX (systematic evolution of ligands by exponential enrichment) [4]. Their main advantages are high binding affinity, excellent sensitivity and selectivity, and stability. These nucleic acid molecules, with a defined 3D structure, can be modified to bind a wide range of target molecules, cells, ions, and proteins, making them ideal for heavy-metal ion sensing [5, 6, 7]. Single-stranded deoxyribonucleic acid (ssDNA) and ribonucleic acid (RNA) aptamers are often used in biosensing devices. They can be chemically modified with certain ligands (thiols, amino groups); however, DNA aptamers are more stable [8]. Aptamers can bind heavy metal ions via electrostatic interactions, and, with different three-dimensional structures, they can exhibit specific affinity for certain ions, such as arsenic [9, 10]. These aptamers are attached to the surface of the gold nanoparticles, and when a bounding event to the ions occurs, a local refractive index change can be observed in the change of the LSPR extinction peak wavelength.

Description of the New Method or System

The measurement was carried out in an LSPR setup consisting of a *Tungsten* halogen light source, an *Ocean Insight* UV/VIS spectrometer. The plasmonic chip was integrated into a microfluidic channel, and the precise fluid control was achieved using a *Masterflex Ismatec Reglo* peristaltic pump. The plasmonic chip contained 80 nm gold (Au was deposited on chemically-modifyed cover slips) [11]. The samples are cleaned by O_2 plasma etching prior to each experiment. Arsenic aptamer aliquots were prepared by dilution with ultrapure water. The assay was

performed using 0.95× CB buffer (coupling buffer), with 10 mM MOPS (3-(N-morpholino)propanesulfonic acid, pH 7.4, supplemented with 2 mM $MgCl_2$) as the running buffer. Aptamer (5 µM) was introduced and the system was equilibrated, followed by CB and buffer exchange to MOPS. Surface blocking was carried out using 1 mM MCH (Mercaptohexanol, 1.37 µL in 10 mL MOPS). The system was incubated for 3 h to allow aptamer folding. Salmon sperm DNA (2 µL in 198 µL MOPS) was then added, followed by rinsing. A 10 µM As(III) standard solution (100 µL) was introduced, and the assay concluded with a final MOPS rinse.

Results

In the first phase of the experiment, the CB buffer was pumped into the microfluidic chip to ensure the correct pH and environmental conditions for the aptamer immobilization step, during which the aptamers attached to the nanoparticle surface, resulting in a distinct shift in the spectra. Then a passivation step is needed to ensure that only the target molecule can interact with the aptamer, while the other parts of the surface were blocked. A long conformational folding step is required for the aptamers to reach their proper 3D structure therefore the experiment was paused for 3 hours. In the last section, the green circles represent the binding of the As(III)-ions to the folded aptamers, which resulted in a 0.82 nm change in the stabilized final step compared to the signal caused by the folding of the aptamers.

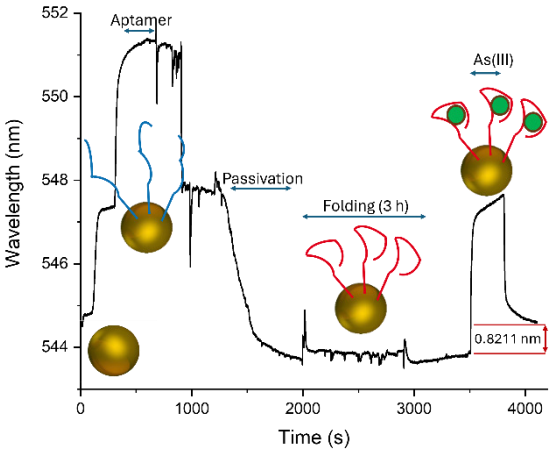

Fig. 1. The arsenic(III) detection process calculated from a centroid-based analysis

References

[1] T.A. Saleh, V.K. Gupta, A.A. Al-Saadi, Adsorption of lead ions from aqueous solution using porous carbon derived from rubber tires: experimental and computational study, *J. Colloid Interface Sci*. 396 (2013) 264–269.

[2] M.A. Ginya, M.B. Idris, U.A. Zakariyya, D. Singh, H.M. Yakasai, N. Sani, The role of some antioxidants on absorption, desorption and elimination of lead and iron: an in vivo study, Eur. J. Biomed. Pharm. Sci. 3 (2016) 528–531.

[3] Farzin, L., Shamsipur, M., & Sheibani, S. A review: Aptamer-based analytical strategies using the nanomaterials for environmental and human monitoring of toxic heavy metals. Talanta, 174, 619–627. (2017); doi: https://doi.org/10.1016/j.talanta.2017.06.066

[4] Tuerk, C.; Gold, L. Systematic evolution of ligands by exponential enrichment: RNA ligands to bacteriophage-T4 DNA-polymerase. Science, 249, 505–510. (1990)

[5] W. Zhou, J. Ding, J. Liu, 2-Aminopurine-modified DNA homopolymers for robust and sensitive detection of mercury and silver, *Biosens. Bioelectron*. 87 (2017) 171–177.

[6] Y. Guo, Y. Chen, Y. Wei, H. Li, C. Dong, Label-free fluorescent aptasensor for potassium ion using structure-switching aptamers and berberine, *Spectrochim. Acta A Mol. Biomol. Spectrosc*. 136 (2015) 1635–1641

[7] T. Wang, J. Liu, X. Gu, D. Li, J. Wang, E. Wang, Label-free electrochemical aptasensor constructed by layer-by-layer technology for sensitive and selective detection of cancer cells, *Anal. Chim. Acta* 882 (2015) 32–37.

[8] S. Spagnolo, K. Sontakke., L. Dubbert., M. Urban, T. Lednicky, A. Csaki., K. Wondraczek., W. Fritzsche. T. Hianik. Application of the combined QCM-D/LSPR aptasensor for penicillin G detection. *Biosensors*, 15(10), p.652. (2025); https://doi.org/10.3390/bios15100652

[9] B. Chatterjee, N. Kalyani, A. Anand, E. Khan, S. Das, V. Bansal, et al. GOLD SELEX: a novel SELEX approach for the development of high-affinity aptamers against small molecules without residual activity. *Microchim Acta*.;187:618.(2020)

[10] J. D. Munzar, A. Ng, D. Juncker. Duplexed aptamers: history, design, theory, and application to biosensing. *Chem Soc Rev*.;48:1390–419.(2019)

[11] Kastner, S.; Pritzke, P.; Csáki, A.; Fritzsche, W., The effect of layer thickness and immobilization chemistry on the detection of CRP in LSPR assays. *Scientific Reports* (2022), *12* (1), 836. 10.1038/s41598-022-04824-9

Acknowledgement

The research was supported by the National Research and Innovation Office under project number: 2020-1.2.3-EUREKA-2022-00030. The project is also supported by the Doctoral Excellence Fellowship Programme (DCEP) is funded by the National Research Development and Innovation Fund of the Ministry of Culture and Innovation and the Budapest University of Technology and Economics, under a grant agreement with the National Research, Development and Innovation Office. This project was implemented with the support provided by the National Research, Development and Innovation Fund of Hungary, financed under the NKKP_26 ADVANCED 153153 funding scheme.

DOI 10.5162/eurosensors2026/Mo−BBS−11

Development of Plasmonic Biosensor Platform for Multiplex Sensing of miR-21

Nóra Tarpataki[1], Tomáš Lednický[2], Lóránt Tibor Csőke[3], Attila Bonyár[1]
[1] Department of Electronics Technology, Faculty of Electrical Engineering and Informatics, Budapest University of Technology and Economics, Egry József street 18, H-1111, Budapest, Hungary
[2] Leibniz Institute of Photonic Technology, Albert-Einstein-Str. 9, 07745 Jena, Germany
[3] Optimal Optik Ltd., Dayka Gábor Street 6/b, H-1118 Budapest, Hungary
tarpatakin@edu.bme.hu

Summary:
The long-term aim of this research is to create a highly sensitive, localized surface plasmon resonance-based biosensor enabling the multiplex detection of microRNA-21. This molecule is an important cancer biomarker, and as miRNAs in general, has a low abundance in biological samples, therefore the need for low limit of detection (LOD). In this paper, we present the current state of this research, including the device used for multiplex sensing, experiments regarding the detection of the target molecule and possible ways to improve the LOD.

Keywords: localized surface plasmon resonance (LSPR), microRNA, limit of detection (LOD), microfluidics, hybridization chain reaction.

Background, Motivation and Objective

There is an increasing research and interest in miRNAs, as these small, non-coding RNAs can serve as biomarkers for a wide range of diseases, including various types of cancers, cardiovascular and neurodegenerative diseases [1]. These molecules have the potential to provide a faster diagnosis, and thus treatment, which can decrease mortality. The main obstacles to use them in clinics include low concentration in bodily fluids and the need to measure several different ones for a complete and accurate diagnosis [2].

The goal of this study is to provide a biosensor capable of meeting these requirements. The sensor element consists of gold nanoparticles which exhibit a phenomenon known as localized surface plasmon resonance: when interacting with light at the resonance wavelength, the electrons of the nanoparticles start to oscillate, leading to an absorption peak in the spectrum [3]. The resonance wavelength is affected by the refractive index of the surrounding medium, thus the presence of the analyte (which increases the refractive index) can be measured.

Description of the New Method or System

Usually, plasmonic sensors rely on optical spectroscopes for determining the wavelength shift. The drawback is that measurement can only be conducted in a single spot. Our custom-made device uses LEDs and a camera to enable multiplex detection, thus several measurements can be carried out parallelly, and in the future, several miRNAs can be detected simultaneously. Fig. 1. an image of the experimental setup.

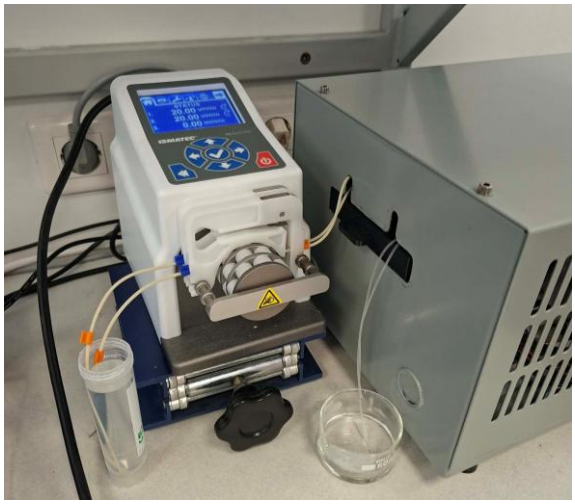

Fig. 1. LSPR imaging measurement setup.

Glass slides serve as substrates for the nanoparticles and are integrated in a microfluidic system with polydimethyl siloxane cells. Thiolated oligonucleotides are used as receptors.

Results

First, experiments were carried out to immobilize the probe (receptor) molecules on the surface of

the gold nanoparticles, then oligonucleotides modelling miR-21(same nucleotide sequence) were introduced.

Fig. 2. shows the results of one of these measurements during evaluation. The different colors represent the different areas on the sensor element. The position of the LSPR peak (in nanometers) is displayed in the function of time (in seconds).

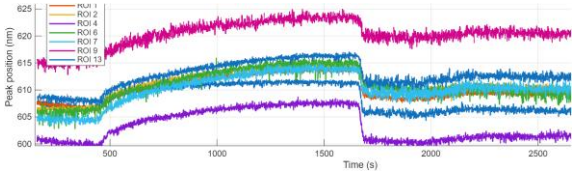

Fig. 2. Evaluation of wavelength peak shift during probe immobilization and target binding.

The first segment, until around 450 seconds, shows the flow of the buffer, then the probe oligonucleotide is introduced, the immobilization leads to a 5-8 nm shift in the spectrum. This is followed by a change of buffers, which causes the drop, then at 2000 seconds, a solution containing the target molecule enters the microfluidic cell. An increase of the peak's wavelength of 1-3 nm is observable.

In order to improve the LOD, several steps can be taken. The signal to noise ratio can be increased during evaluation by using appropriate filters, the buffers and other technical parameters (time, pH, concentration etc.) can be optimized, contributing to a better LOD. An additional approach is to use some kind of signal amplification technique, such as the hybridization chain reaction. Briefly, two hairpin oligonucleotides are added, binding to the target then each other alternatingly, increasing the LSPR peak shift [4].

All of the above-mentioned methods are currently being investigated, and the final paper will report the results.

References

[1] C. E. Condrat *et al.*, "MiRNAs as biomarkers in disease: Latest findings regarding their role in diagnosis and prognosis," Feb. 01, 2020, *Multidisciplinary Digital Publishing Institute (MDPI)*. doi: 10.3390/cells9020276.

[2] M. Cui *et al.*, "Circulating MicroRNAs in Cancer: Potential and Challenge," *Front. Genet.*, vol. 10, Jul. 2019, doi: 10.3389/fgene.2019.00626.

[3] Q. Duan, Y. Liu, S. Chang, H. Chen, and J. H. Chen, "Surface plasmonic sensors: Sensing mechanism and recent applications," Aug. 02, 2021, *MDPI AG*. doi: 10.3390/s21165262.

[4] A. Miti, S. Thamm, P. Müller, A. Csáki, W. Fritzsche, and G. Zuccheri, "A miRNA biosensor based on localized surface plasmon resonance enhanced by surface-bound hybridization chain reaction," *Biosens. Bioelectron.*, vol. 167, Nov. 2020, doi: 10.1016/j.bios.2020.112465.

Acknowledgments

The research was supported by the National Research and Innovation Office under project number 2020-1.2.3-EUREKA-2022-00030 and was implemented with the support provided by the National Research, Development and Innovation Fund of Hungary, financed under the NKKP_26 ADVANCED 153153 funding scheme and supported.

DOI 10.5162/eurosensors2026/Mo–BBS–12

High-Resolution Inkjet Printing of a Functional Polymer for On-Chip Biosensing

Frederic Brossard[1], William Rostain[1], Ljiljana Fruk[2]
[1] Hitachi Cambridge Laboratory, Ray Dolby Centre, J J Thomson Avenue, Cambridge CB3 0US
[2] Department of Chemical Engineering and Biotechnology, University of Cambridge, Philippa Fawcett Drive, Cambridge, CB3 0AS
fsfb2@cam.ac.uk, frederic.brossard@hitachi-eu.com

Summary

We present a surface functionalisation method based on high-resolution electrohydrodynamic inkjet printing of an azide-functional polymer bearing a reversible protein reporter layer for small-molecule detection. As proof of principle, we demonstrate a fluorescence assay of biotin on a silicon chip and localised functionalisation of a packaged photonic crystal, opening a route towards highly multiplexed label-free biosensing.

Keywords: Functional polymers, localised surface functionalisation, electrohydrodynamic inkjet printing, photonic integrated circuit, photonic crystals.

1. Introduction

In conventional on-chip assays, bioreceptors are delivered via microfluidics, which limits the minimum footprint available for multiplexing. Inkjet printing enables local functionalisation to reduce this footprint [1], and printing a target-specific functional polymer adds a further level of control [2]. However, conventional inkjet printing is limited to feature sizes larger than 20 µm and thus far these polymers have not yet been applied to photonic sensors. In contrast, electrohydrodynamic inkjet (EHD) printing can reach sub-micrometre resolution [3] but has mostly served flexible electronics and light-emitting diodes (LEDs) [4]. Here we demonstrate, for the first time, detection of a small molecule (biotin) by EHD printing of a commercially available functional polymer, and its local application on a packaged photonic crystal (PhC), expanding our previous work on printed polymer [5].

2. Materials and Methods

The reporter layer is a double-stranded alkyne-DNA (ds-alk-DNA) covalently grafted to EHD printed azide-polystyrene via copper-catalysed azide-alkyne cycloaddition (CuAAC). The DNA carries desthiobiotin, enabling reversible, competitive displacement of the protein streptavidin by biotin [6]. Az-PS at 2 mg/ml in dichlorobenzene was EHD-printed on untreated silicon with a sub-2 µm nozzle (SIJ-S050, SIJ Technology Inc.), then reacted by CuAAC with desthiobiotinylated ds-alk-DNA and incubated with Alexa Fluor 647–streptavidin for fluorescence readout (FV1200 confocal microscope). Printing was also performed on a fibre-packaged SOI photonic integrated circuit containing PhCs, characterised by transmission around telecom wavelengths (~1.55 µm).

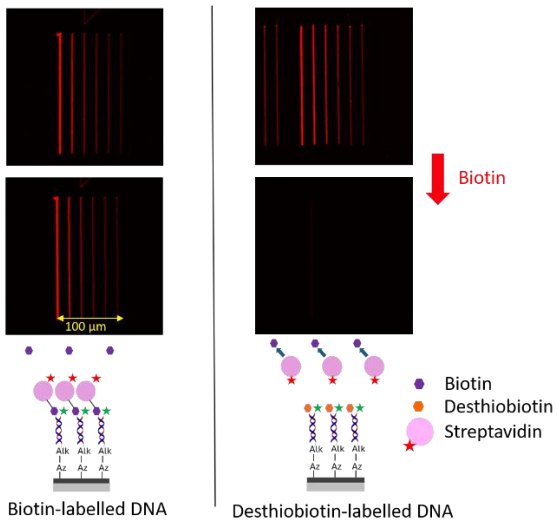

Fig. 1. Biotin sensing with streptavidin-bound to EHD-printed az-PS strips of variable thicknesses (~100 nm to ~10 nm left to right). The fluorescence microscopy images were obtained from the fluorophore on the streptavidin (5% laser power)

3. Discussion

Az-PS strips ~3 µm wide and 10–100 nm thick (AFM) were printed on untreated silicon. Following click chemistry with ds-alk-DNA and

incubation with streptavidin the fluorescence signal was localised to printed strips, scaling with strip height, with S/N > 40, confirming specific binding to the DNA-bound polymer (Fig. 1). Incubation in 1 mM biotin for 30 min returned the signal to near noise level for the desthiobiotinylated DNA while a biotin-modified DNA control showed no significant change, as expected. The result was reproduced on a nanostructured PhC surface and the surface regenerated by re-injecting streptavidin, demonstrating reversible biotin sensing (not shown here). On a slotted PhC packaged with optical fibres, post-printing transmission showed a photonic stop-gap with a sharp resonance, consistent with cavity creation at the printed centre (Fig. 2). This constitutes a clear demonstration of post-fabrication enhancement of a photonic stopgap by high-resolution inkjet printing while simultaneously establishing a route to local biofunctionalisation using the same clickable polymer platform. The polymer can subsequently be removed in an appropriate solvent to recover the initial PhC state.

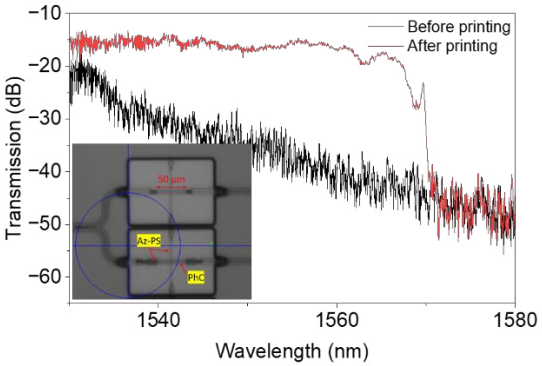

Fig. 2. Transmission spectra in water of a slotted PhC before and after EHD-printed az-PS. Inset: optical micrograph of the packaged PhC sensor with printed az-PS across and along the PhC waveguide.

References

[1] L. J. Donato *et al.*, “Evaluation of the genalyte maverick SARS-CoV-2 multi-antigen serology panel,” *Journal of Clinical Virology Plus*, vol. 1, no. 3, Sep. 2021, doi: 10.1016/j.jcvp.2021.100030.

[2] L. Sola, F. Damin, and M. Chiari, “Array of multifunctional polymers for localized immobilization of biomolecules on microarray substrates,” *Anal. Chim. Acta*, vol. 1047, pp. 188–196, Jan. 2019, doi: 10.1016/j.aca.2018.10.006.

[3] J.-U. Park *et al.*, “High-resolution electrohydrodynamic jet printing,” *Nat. Mater.*, vol. 6, no. 10, pp. 782–789, 2007, doi: 10.1038/nmat1974.

[4] Z. Yin *et al.*, “Electrohydrodynamic printing for high resolution patterning of flexible electronics toward industrial applications,” Feb. 01, 2024, *John Wiley and Sons Inc*. doi: 10.1002/inf2.12505.

[5] F. S. F. Brossard, V. Pecunia, A. J. Ramsay, J. P. Griffiths, M. Hugues, and H. Sirringhaus, “Inkjet-Printed Nanocavities on a Photonic Crystal Template,” *Advanced Materials*, vol. 29, no. 47, 2017, doi: 10.1002/adma.201704425.

[6] J. D. Hirsch *et al.*, “Easily reversible desthiobiotin binding to streptavidin, avidin, and other biotin-binding proteins: uses for protein labeling, detection, and isolation,” *Anal. Biochem.*, vol. 308, pp. 342–357, 2002, doi: 10.1016/S0003-2697(02)00241-1

DOI 10.5162/eurosensors2026/Tu–BBS–01

Design and Optimization of a Traveling Surface Acoustic Wave (TSAW) Microfluidic Platform for Controlled Liposome Manipulation

Yugyeong Je[1], Hande Nur Açıkgöz[1], Sabina Caneva[1]
[1] Department of Precision and Microsystems Engineering, Delft University of Technology, Mekelweg 2, 2628 CD Delft, The Netherlands
S.Caneva@tudelft.nl

Summary:
We report on the design and optimization of a traveling surface acoustic wave (TSAW)-based microfluidic platform for controlled manipulation of vesicle-sized particles. The study focuses on device geometry, acoustic field distribution, and flow conditions to maximize manipulation efficiency. The optimized structure enables stable and tunable particle deflection, providing a foundation for future integration with sensing and sorting functionalities.

Keywords: acoustofluidics, surface acoustic wave, SAW, TSAW, liposome sorting, fluorescence detection

Background, Motivation and Objective

Surface acoustic wave (SAW)-based microfluidic platforms have been widely explored for contactless manipulation of microparticles and biological samples [1]. In particular, traveling surface acoustic waves (TSAWs) provide flexible actuation for particle deflection and have been successfully applied to high-speed cell handling in microfluidic systems [2, 3]. However, most previous studies have focused on sorting performance in rigid particles or living cells, while the device-level requirements for fragile vesicles like liposomes remain much less understood.

This limitation is especially important for liposomes and other soft vesicle-like objects, which are widely used as model systems for synthetic cells and as carriers in bottom-up synthetic biology [4]. The manipulation of such vesicles is governed not only by acoustic radiation forces but also by their susceptibility to deformation, rupture, and flow-induced instability. Systematic investigation of how channel geometry, transducer configuration, and operating conditions affect stable vesicle deflection is still lacking.

In this work, we focus on the design and optimization of a TSAW-based microfluidic platform for controlled manipulation of liposomes. Our objective is to identify key structural and operational parameters that enable stable and reproducible acoustic deflection, thereby establishing a device architecture suitable for future integration with fluorescence-assisted liposome sorting.

Method

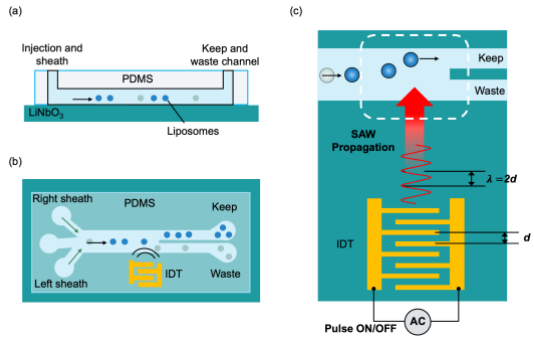

Fig. 1. Schematic of the TSAW-based microfluidic platform for liposome manipulation. (a) Cross-sectional view showing liposome flow within a PDMS channel on a $LiNbO_3$ substrate. (b) Top view of the microfluidic device with sheath flow focusing and separation into keep and waste outlets. (c) Working principle of TSAW actuation: acoustic waves generated by the IDT induce lateral deflection of selected liposomes toward the target outlet.

The proposed platform consists of a microfluidic channel integrated on a piezoelectric substrate ($LiNbO_3$) with interdigital transducers (IDTs) for generating TSAWs. Both straight and focused IDT geometries were implemented to investigate their influence on acoustic field distribution and particle manipulation performance.

To systematically analyze device behavior, finite element simulations were performed using COMSOL Multiphysics to model acoustic wave

propagation and the resulting pressure fields within the fluid channel. The simulations were used to compare acoustic energy localization, beam width, and intensity distribution between straight and focused IDT configurations.

Experimentally, microfluidic channels were fabricated and aligned with the IDTs, and vesicle-sized particles were introduced under controlled flow conditions. Liposomes were prepared using electroformation and polyvinyl alcohol (PVA) swelling methods to provide vesicles for manipulation experiments. Key design parameters, including IDT geometry, channel position relative to the acoustic propagation path, RF input power, and flow rate, were varied to evaluate their impact on particle deflection. Particular attention was given to identifying configurations that enhance acoustic energy confinement while maintaining stable flow conditions, which is critical for the manipulation of soft and deformable liposomes.

Results

The results demonstrate controlled lateral deflection of vesicle-sized particles under TSAW actuation in the proposed microfluidic platform. The observed particle trajectories show a clear dependence on both acoustic input power and device geometry, confirming the critical role of structural optimization.

COMSOL simulations reveal distinct differences in acoustic field distribution between straight and focused IDT configurations. The focused IDT generates a more confined acoustic beam with higher localized pressure intensity, whereas the straight IDT produces a broader and less concentrated acoustic field. These trends are consistent with experimental observations, confirming the enhanced deflection efficiency of the focused IDT.

An operational window was identified in which stable and reproducible particle deflection can be achieved without disrupting the flow profile. Within this regime, particles are consistently displaced from their original streamline, while maintaining continuous and stable flow conditions. Outside this range, either insufficient deflection or unstable trajectories were observed, indicating sensitivity to both acoustic and hydrodynamic parameters.

These results provide initial validation of the proposed device architecture and establish key design guidelines for vesicle-scale acoustofluidic manipulation. Ongoing work focuses on extending the optimized conditions to lipid vesicles and integrating fluorescence-based detection for selective liposome sorting.

References

[1] J Friend, LY Yeo, Microscale acoustofluidics: Microfluidics driven via acoustics and ultrasonics, *Reviews of Modern Physics* 83.2 (2011): 647-704; doi: 10.1103/RevModPhys.83.647

[2] K Mutafopulos, P Spink, CD Lofstrom, PJ Lu, H Lu, JC Sharpe, T Franke, DA Weitz, Traveling surface acoustic wave (TSAW) microfluidic fluorescence activated cell sorter (μFACS), *Lab on a Chip 19.14 (2019): 2435-2443*; doi: 10.1039/c9lc00163h

[3] AA Nawaz, D Soteriou, CK Xu, R Goswami, M Herbig, J Guck, S Girardo, Image-based cell sorting using focused travelling surface acoustic waves. Lab on a Chip 23.2 (2023): 372-387; doi: 10.1039/D2LC00636G

[4] SF Fenz, K Sengupta, Giant vesicles as cell models, *Integrative Biology*, 4(9) (2012): 982-995; doi: 10.1039/c2ib00188h

DOI 10.5162/eurosensors2026/Tu–BBS–02

Bacteria collection from static millilitre samples using a DC field

Giuseppina Sacco [1, 2], Catalin Ciubotaru [1], Lucia Gigli [3], Martina Conti [1], Dan Cojoc [1]
[1] CNR Istituto Officina Dei Materiali, Area Science Park Basovizza, 34149 Trieste, Italy
[2] Department of Physics, University of Trieste, Via A. Valerio 2, 34127 Trieste, Italy
[3] Alifax S.r.l., Via Merano 30, Nimis, 33045 Udine, Italy
Corresponding Author's e-mail address: giuseppina.sacco@phd.units.it,

Summary:
Efficient bacterial collection from millilitre-scale liquid samples remains challenging for preconcentration-based analyses. We present a device that uses a DC electric field to transport and deposit bacteria onto an agarose pad in a static chamber. The system operates at physiological ionic strength while preserving cell viability by limiting electrochemical reactions. Accumulation of live bacteria at low concentrations (10^3 CFU/mL) is demonstrated at 5V. Transport, viability, and collection efficiency are confirmed by microscopy and plate assays. This approach enables rapid bacterial pre-enrichment and detection.

Keywords: Electrokinetic bacterial collection, Milliliter scale sample processing, Low-concentration bacteria detection, Agarose pad collection

Background, Motivation and Objective

Efficient bacterial collection and concentration are critical for diagnostics and analytical sample preparation. Bacterial cells typically possess a negative net surface charge under physiological conditions and hence, they undergo electrophoretic motion when exposed to a direct current (DC) electric field. Electrophoretic deposition and more sophisticated electrokinetic manipulation strategies like dielectrophoresis (DEP) or ion concentration polarization (ICP) have been widely explored at the microscale, particularly in microfluidic systems for bacterial concentration and sensing [1][2]. Despite these advances, most electrokinetic bacterial concentration strategies rely on microfluidic architectures operating at microliter volumes and often require low-conductivity media to avoid excessive current and electrode reactions. One strategy to mitigate these effects involves electrically coupling the electrodes to the sample chamber through salt bridges or hydrogel interfaces [3]. Such configurations allow ionic current to pass through the system while physically separating the electrodes from the biological suspension, thereby suppressing electrode electrochemistry within the sample volume. Agarose-based salt bridges are widely used in electrophysiological and electrochemical measurements for this purpose [4]. Unlike most electrokinetic bacterial concentration approaches that rely on microfluidic geometries and microliter-scale sample volumes, the present work explores electric field-driven bacterial collection in a milliliter-scale chamber operating under physiologically relevant buffer conditions. This approach seeks to bridge the gap between electrokinetic manipulation techniques developed in microfluidics and practical bulk sample preparation methods required for analytical and diagnostic workflows.

Description of the New Method or System

We developed a novel milliliter-scale electrokinetic device to collect live bacteria on the surface of an agarose pad. The system consists of a 1 mL bacterial chamber electrically connected to Ag electrodes through agarose salt bridges, which allow electrical conduction while isolating the electrodes from the sample volume. This setup is integrated within a control system, as illustrated in Fig 1. By applying a DC bias (5 V), a current of approximately 1 mA is established across the system. Under the DC electric field, negatively charged bacterial cells undergo electrophoretic transport toward the positive electrode where they adhere on the agarose surface. The device configuration, comprising salt bridges, enables electrophoretic transport of live bacteria under physiologically relevant ionic strengths while suppressing electrode electrochemistry. Under these optimized parameters, bacterial collection from 1 mL sample in about 1.5 h can be accomplished. Remarkably, the collected bacteria remain viable and can be recovered by extracting the agarose pad for downstream analysis.

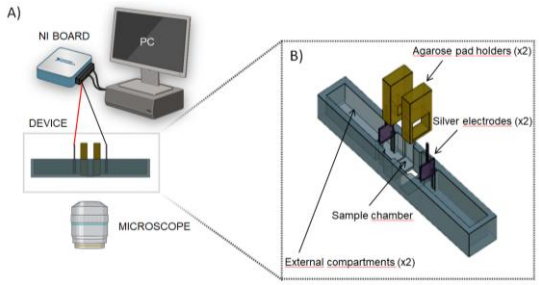

Fig 1. Experimental setup A) Integration of the device with the control system and optical microscopy for real-time observation. B) Zoom on the device showing the silver electrodes, agarose pads, and the 3D-printed PLA chamber compartmentalization

Results

We fabricated the device in Fig 1 by 3D printing in PLA. A sample chamber was implemented between two agarose pads which isolated it from the electrode compartments. A pair of electrochemically chlorinated silver (Ag/AgCl) electrodes were placed outside the bacterial sample, in two compartments containing 1.5 mL of 0.1x PBS. The agarose salt bridge (3% agarose salt bridges, 4 mm thick) enables ionic continuity and electrical connectivity while acting as a collecting surface for bacteria. By combining the agarose salt bridges with a low-current DC field and chlorine-free chemistry, we effectively eliminated the formation of toxic electrolysis by-products, thereby preserving the physiological integrity of the sample. The transport dynamics were monitored by using an inverted Olympus microscope (40x objective) interfaced with a National Instruments (NI) card and a power supply, controlled by custom developed software. The velocity, v of a bacteria cell driven by a DC electric field, depends on the bacteria electrophoretic mobility, μ and the intensity of the electric field, E: $v = \mu E$. Electrophoretic mobility depends on the zeta potential of the bacteria surface (about -40 mV), and permittivity and viscosity of the liquid in which the bacteria is immersed. With a potential V= 5V, distance d= 20 mm, between the two electrodes and ~50% attenuation of the electric field inside the sample chamber, the driving velocity is v ~2.1 µm/s, which corresponds to the experiments. For a 1 mL cubic chamber with the width w= 1 cm, the estimated time required to collect all the bacteria on the agarose pad is t ~80 min. Since this is quite time-consuming experiment, for the proof of concept we run experiments lasting only 15 min and extrapolated the results. *E. coli* bacteria at 10^3 CFU/mL concentration were used as sample and the collection evaluated by the plate-count method. Agarose pads were extracted, and collected bacteria were recovered by centrifugation and then plated. After 24 h of incubation, significantly more colonies were observed on the anode pad than on the cathode for DC field, and similar few colonies on both pads for control (no field), confirming transport and collection of viable bacteria as expected (Fig 2a). On average, about 17% of the initial bacterial population was recovered on the positive electrode after 15 min (n= 5 experiments). Extrapolating to the theoretically estimated time, a collection efficiency of 90% could be reached in 80 min. The presence of the bacteria on the anode and cathode pads was checked also with stained bacteria (NucRed) by confocal microscopy (Fig 2b). The normalized amounts of collected bacteria on the two pads, in the presence and without electric field are presented in Fig 2c, showing the net accumulation on the anode pad under the application of the DC field. These preliminary results demonstrate that by combining milliliter-scale operation, biocompatible electrolytes, and suppression of electrode electrochemistry, one can obtain a simple electrokinetic system and practical approach for bacterial preconcentration and detection in analytical and diagnostic workflows.

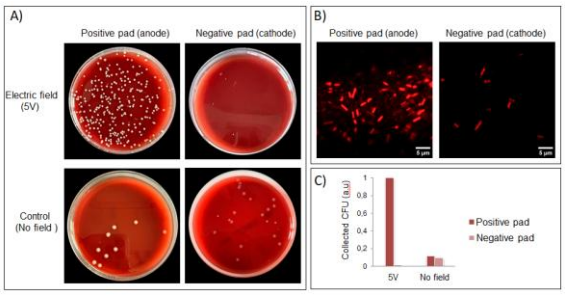

Fig 2. Recovery and viability analysis. A) Rapresentative agarose pads after culture. B) Confocal images of labeled bacteria collected on agarose pads. C) Statistical CFU count comparing transport vs. control

References

[1] MP. Hughes, Strategies for dielectrophoretic separation in lab-on-a-chip systems, Electrophoresis 23, 2569–2582 (2002); doi: 10.1002/1522-2683(200208)23:16%3C2569::aid-elps2569%3E3.0.co;2-m

[2] S. Park, Continuous dielectrophoretic bacterial separation and concentration from physiological media of high conductivity, *Lab Chip* 17, 2893-900 (2011); doi: 10.1039/c1lc20307j

[3] PH. Barry, Liquid junction potentials and salt bridges in electrophysiological measurements, *J. Membr. Biol* 121, 101–117 (1991); doi: 10.1007/BF01870526

[4] A.J. Bard, Electrochemical Methods: Fundamentals and Applications, 2nd ed.; *Wiley* (2001)

DOI 10.5162/eurosensors2026/Tu–BBS–03

Smart Lateral Flow Device with Embedded Gradient Nanoparticle Lines towards Enhanced Quantification via Smartphone

Silvia Demuru[1], Miha Markocic[1], Peter Spies[2], Dominik Meinel[2], Stefano Cattaneo[1], Maren Schinz[3], Stefanie Dobitz[3], Vitalijs Zubkovs[1]
[1] Centre Suisse d'Electronique et de Microtechnique SA (CSEM), Landquart, Switzerland
[2] University of Applied Sciences and Arts Northwestern Switzerland (FHNW), Muttenz, Switzerland
[3] Diabetes Center Berne (DCB), Bern, Switzerland
vitalijs.zubkovs@csem.ch

Summary:

Smartphone-based lateral flow assays enable accessible point-of-care diagnostics but suffer from limited quantitative reliability. To address this limitation, this work introduces a lateral flow device with embedded gradient nanoparticle lines for on-strip optical calibration. The calibration gradient enables direct normalization of test signals at the time of image acquisition. A custom smartphone-supported web application performs automatic image recognition and signal processing. The proposed approach supports customizable quantitative healthcare and drug tests at low-cost without external optical accessories.

Keywords: lateral flow assay, nanoparticle calibration, smartphone sensing, quantitative diagnostics, point-of-care

Background, Motivation and Objective

Lateral flow assays (LFAs) are widely used for rapid diagnostics and are increasingly combined with smartphones to enable quantitative point-of-care and home-based testing, generally supported by dedicated optics or controlled imaging conditions [1]. Performance is often limited by illumination sensitivity and device-dependent bias, which restrict quantitative robustness in real-world use [2]. These limitations motivate calibration strategies that are intrinsic to the assay and independent of external accessories, potentially enabling improved quantification while keeping the cost as low as standard LFAs.

The objective of this work is to develop a smart lateral flow device integrating embedded gradient nanoparticle lines as on-strip optical references together with optimized image acquisition and signal processing, to enable robust, customizable, and accessory-free quantitative lateral flow readout using a smartphone.

Description of the New Method or System

- On-strip gradient nanoparticle calibration lines (GNLs) using the same gold nanoparticles (NPs) as the assay.
- Custom cassette markers for automatic region-of-interest (ROI) detection.
- Custom software for gradient extraction and test line quantification.

Results

The proposed smart LFA is envisioned for user-friendly, accessory-free operation in point-of-care or home-use settings. After applying the sample (Fig. 1a), the user captures a single image of the smart lateral flow cassette using a smartphone (Fig. 1b).

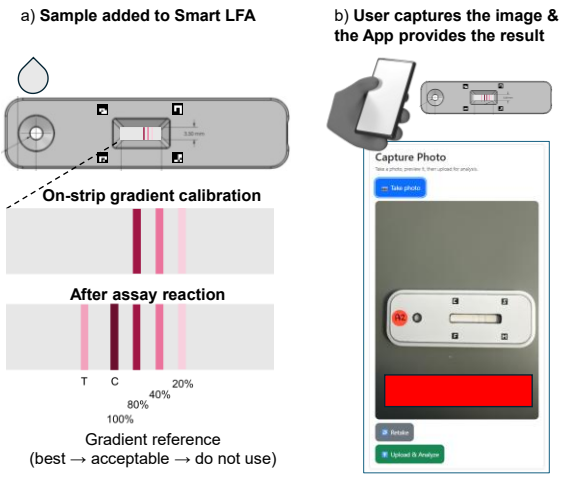

Fig. 1. Envisioned use of the smart LFA device with embedded gradient calibration and smartphone readout (a), with an example of a test result for checking sample degradation (b).

The custom application performs automated quantification, with the aim of providing a clear and actionable result for the user.

As a proof of concept, the envisioned calibration gradient composed of lines at increasing NPs concentrations (Fig. 1a) is fabricated using a BioDot AirJet dispenser (Model XYZ3210). Solutions of 40 nm gold nanoparticles (nanoComposix, AUCR40-5M), linearly diluted in standard buffer, are directly deposited onto FF120HP nitrocellulose membranes (Whatman GE Healthcare). The resulting five-line model nanoparticle gradient is integrated into a custom laser-cut cassette with engraved QR codes used as recognition markers (Speedy 300, TROTEC), as illustrated in Fig. 2a. This configuration enables automatic ROI identification and alignment as validated in Fig. 2b. All acquired images are processed using the developed custom modular software architecture for smartphone image analysis. The framework combines configurable analysis pipeline with reusable processing modules to ensure robust marker detection, ROI extraction, and quantitative analysis of intensity profile based on the GNLs.

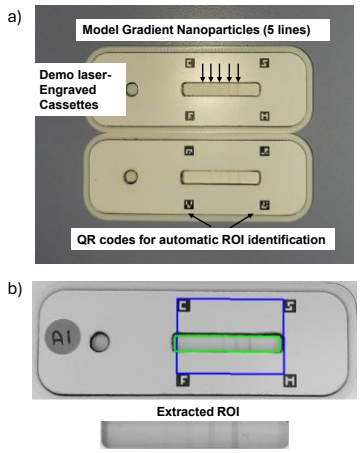

Fig. 2. Demonstration of the GNLs on-strip concept into customized cassettes with different engraved recognition markers (a), and example of automatic ROI quantification via the developed software (b).

The model nanoparticle gradient serves also as a tool for testing variability across different image acquisition platforms and generating a database for testing the developed algorithm, using stable, simulated test lines for repeatable measurements (Fig. 3). Direct images from various smartphones yield comparable results (Fig. 3b,c). All nitrocellulose strips were prewetted with PBS 1X before image acquisition to mimic real assay conditions, as wetting alters GNL optical properties without affecting line morphology. Ongoing work focuses on integrating the calibrated GNLs into a functional assay (Fig. 4), embedding recognition markers into the LFA cassette, and refining the mobile app for direct gradient and test-line quantification to validate the smart LFA concept.

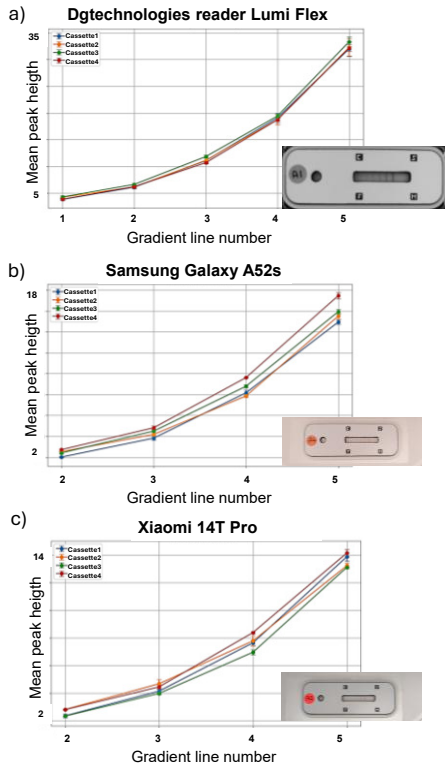

Fig. 3. Extracted GNL intensities comparing three different image acquisition tools for n=4 customized cassettes. With smartphones (b,c), the weakest GNL (line 1) cannot be detected.

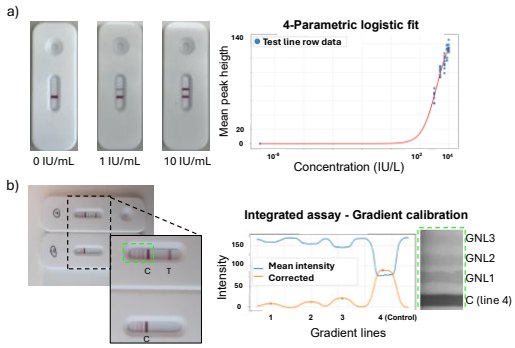

Fig. 4. Initial studies on a real model assay for hCG detection at different concentrations (a), and integration of 3 GNLs with the same assay (b).

References

[1] Thakur, R. et al. Development of Smartphone-Based Lateral Flow Device for the Quantification of LH and E3G Hormones. *IEEE Sens J* 20, 14491–14500 (2020); doi: 10.1109/jsen.2020.3008566

[2] Michaelis, S. et al. Performance evaluation of a smartphone-based home test for fecal calprotection. *Clin Chem Lab Med* 63, 139–146 (2025); doi: 10.1515/cclm-2024-0422

Acknowledgements

This work was funded through the Swiss Innovation Agency under grant 119.383 IP-LS

DOI 10.5162/eurosensors2026/Tu–BBS–04

Development of multiplexing LAMP on lateral flow assay (LAMP-LFA) for rapid detection of respiratory viruses

Than Linh Quyen, Ankita Mishra, Winnie Edith Svendsen, Maria Dimaki.
Department of Biotechnology and Biomedicine, Technical University of Denmark (DTU-Bioengineering), DK-2800 Kgs. Lyngby, Denmark.
Corresponding Author's e-mail address: quylin@dtu.dk

Summary:
Respiratory viruses such as influenza viruses and coronaviruses are among the most significant contributors to emerging infectious diseases due to the substantial threat they pose to public health. Diagnostics of respiratory viruses have become increasingly important. Here we report the development of lateral flow assay for rapid detection of respiratory viruses based loop-mediated isothermal amplification (LFA-LAMP). This assay enables rapid, sensitive, and user-friendly detection without the need for the complex laboratory infrastructure. The proposed method has potential applications in point-of-care testing and large-scale screening, particularly in resource-limited settings.

Keywords: Point-of-care (POC), LAMP-LFA, respiratory viruses, Lateral flow assay (LFA), Loop-Mediated isothermal amplification (LAMP).

Background

Respiratory viral infection remains a persistent challenge to global health systems, causing seasonal epidemics and occasional pandemics [1,2]. Influenza viruses and coronaviruses have demonstrated their capacity to spread rapidly across populations [3,4]. Their high mutation rates and zoonotic potentials contribute to the continuous emergence of new variants. Effective surveillance and early detection are critical to limiting transmission and reducing disease impact [7]. However, standard method techniques such as polymerase chain reaction (PCR) are often time-consuming and dependent on centralized laboratory facilities [8]. This creates a gap in timely diagnosis, especially in remote or low-resource settings [9]. As a result, there is increasing in developing rapid and portable diagnostic tools [10]. Isothermal amplification methods, such as loop-mediated isothermal amplification (LAMP), offer a promising alternative due to their speed, simplicity and sensitivity [11]. Coupling LAMP with lateral flow assay enables easy interpretation of results without specialized equipment [12]. These advances highlight the importance of developing innovative diagnostic strategies for improved management of respiratory viral infections.

Principles of LAMP-LFA

The principles of LAMP-LFA include 2 main steps. In the first step, multiplexing LAMP is carried out to produce products labeled with biotin, which serve as detectable targets in the second step using LAMP-LFA strip. To enable this, an additional oligo is attached to the 5' end of loop primers (Figure 1). Furthermore, a complementary sequence to this added oligo is modified with biotin at 5' end.

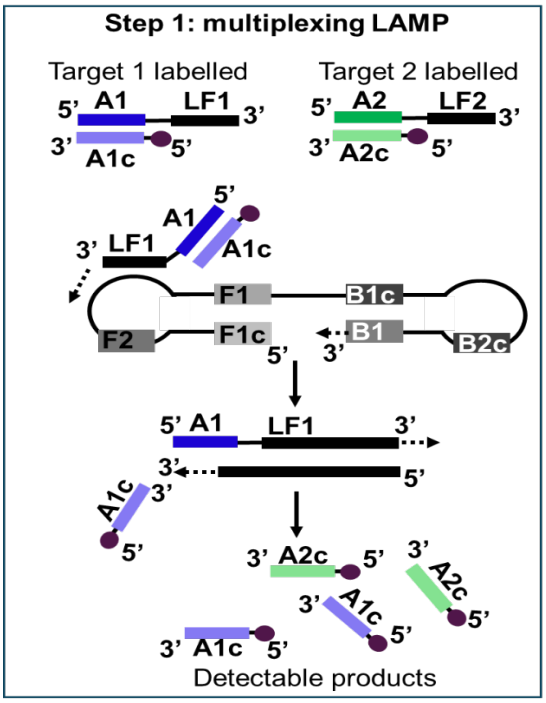

Figure 1. Multiplexing LAMP to produce detectable products.

During LAMP amplification, this biotin-labeled oligo is released. The released complementary oligo then binds to the nitrocellulose paper membrane. Subsequently, a streptavidin-gold nanoparticle complex (SA-GNP) attaches to the biotin on the membrane, generating a detectable signal (Figure 2).

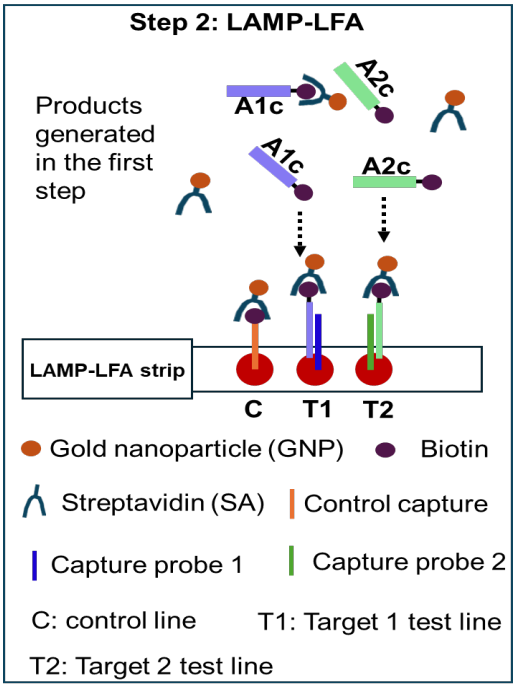

Figure 2. LAMP-LFA principle.

Results

The multiplexing LAMP assay was successfully developed to detect three targets SARS-CoV-2, influenza B, and an internal control (enhance green fluorescent protein, eGFP) within 20 min.

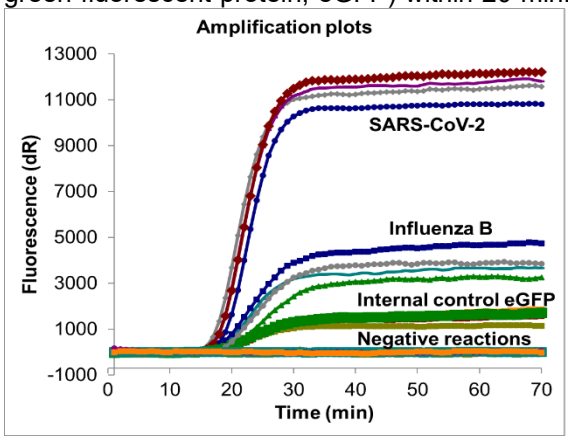

Figure 3. Multiplexing LAMP assay for detection of three targets.

Detection was achieved using assimilating probes, with a fluorescent label attached to the 5' end of the additional oligo on the loop primers and a quencher incorporated into its complementary sequence, enabling efficient signal generation. The results demonstrate the robustness of the amplification assay and its compatibility with downstream detection strategies. Furthermore, successful incorporation of biotin-labeled products indicates that the assay can be efficiently adapted to a LFA format, where lableled products can be captured on the strip and visualized via SA-GNP detection, supporting its potential for rapid POC diagnosis (Figure 4).

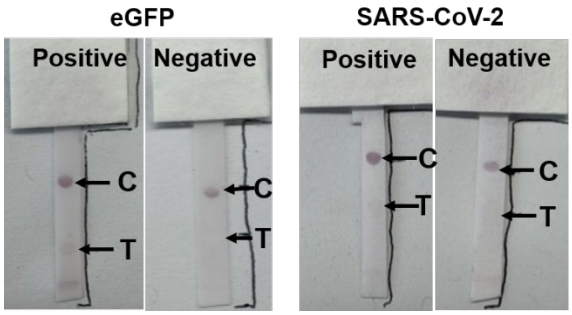

Figure 4. Primary LAMP-LFA results.

References

[1] Morens, D. M., Fauci, A. S., Emerging pandemic diseases: How we got to COVID-19, *Cell* 182, 1077–1092 (2020); doi:10.1016/j.cell.2020.08.021

[2] Iuliano, A. D., Roguski, K. M., Chang, H. H., et al., Estimates of global seasonal influenza associated respiratory mortality, *Lancet* 391, 1285–1300 (2018); doi:10.1016/S0140-6736(17)33293-2

[3] Paules, C., Subbarao, K., Influenza, *Lancet* 390, 697–708 (2017); doi:10.1016/S0140-6736(17)30129-0

[4] Petersen, E., Koopmans, M., Go, U., et al., Comparing SARS-CoV-2 with SARS-CoV and influenza pandemics, *Lancet Infect Dis* 20, e238–e244 (2020); doi:10.1016/S1473-3099(20)30484-9

[5] Webster, R. G., Bean, W. J., Gorman, O. T., et al., Evolution and ecology of influenza A viruses. *Microbiol Rev* 56, 152–179 (1992); doi:10.1128/mr.56.1.152-179.1992

[6] Cui, J., Li, F., Shi, Z. L. Origin and evolution of pathogenic coronaviruses. *Nat Rev Microbiol* 17, 181–192 (2019); doi:10.1038/s41579-018-0118-9

[7] World Health Organization, Diagnostic testing for SARS-CoV-2. WHO Guidelines (2020); https://www.who.int

[8] Carter, L. J., Garner, L. V., Smoot, J. W., et al., Assay techniques and test development for COVID-19 diagnosis, *ACS Cent Sci* 6, 591–605 (2020); doi:10.1021/acscentsci.0c00501

[9] Drain, P. K., Hyle, E. P., Noubary, F., et al., Diagnostic point-of-care tests in resource-limited settings, Lancet Infect Dis 14(3): 239-49 (2014); doi: 10.1016/S1473-3099(13)70250-0

[10] Peeling, R. W., Olliaro, P. L., Boeras, D. I., Fongwen, N. Scaling up COVID-19 rapid antigen tests. *Lancet Infect Dis* 21, e290–e295 (2021); doi:10.1016/S1473-3099(21)00048-7

[11] Notomi, T., Okayama, H., Masubuchi, H., et al. Loop-mediated isothermal amplification of DNA. *Nucleic Acids Res* 28, e63 (2000); doi:10.1093/nar/28.12.e63

[12] Posthuma-Trumpie, G. A., Korf, J., van Amerongen, A. Lateral flow immunoassay: Its strengths and weaknesses. *Anal Bioanal Chem* 393, 569–582 (2009); doi:10.1007/s00216-008-2287-2

DOI 10.5162/eurosensors2026/Tu–BBS–05

Rapid Temperature Cycling Miniaturized PCR Thermocycler with Switchable Heat Pipe Cooling

Passar Bamerni[1], Christian Weber[1], Jürgen Wöllenstein[1]
[1] University of Freiburg, Georges-Köhler-Allee 102, Germany,
passar.bamerni@imtek.uni-freiburg.de

Summary:
We present a highly miniaturized PCR thermocycler based on an aluminum oxide ceramic with an integrated micro-well structure, integrated heating and switchable thermal coupling for cooling. A platinum microheater enables rapid temperature changes, while pneumatically coupled heat pipes provide efficient heat dissipation during the cooling phase. The combination of low thermal mass and actively controllable heat transport enables significantly accelerated thermal cycling compared to conventional systems. Process monitoring is performed using fluorescence-based real-time detection. This approach offers potential for compact and high-performance point-of-care diagnostic systems.

Keywords: PCR, Thermal Cycler, Heat Pipe, Microheater, Point-of-Care

Background, Motivation and Objective

Fast and portable PCR (Polymerase Chain Reaction) systems are becoming increasingly important for point-of-care diagnostics and decentralized applications [1,2,3]. However, conventional thermocyclers are limited by large thermal masses and slow temperature transitions.
Advances in microsystem technology enable compact systems with significantly improved heating and cooling rates [4,5]. Nevertheless, efficient and controlled cooling in particular remains a key challenge.
The goal of this work is to develop a miniaturized PCR thermocycler based on a well-integrated ceramic structure with an embedded heating function and actively controlled thermal coupling for rapid temperature cycling. In particular, the decoupling of heating and cooling remains challenging, as continuous thermal coupling leads to parasitic heat losses and limits achievable temperature ramp rates.

Description of the New Method or System

To address this limitation, a thermocycler concept with switchable thermal coupling is proposed, enabling active control of heat transfer during different phases of the PCR cycle. The overall architecture is shown in Fig. 1. The system is based on a 5 × 5 × 5 mm³ Al_2O_3 cube with an integrated microcavity. Heating is provided by a platinum-based microheater. Cooling is achieved by pneumatically coupling two heat pipes to the ceramic, thereby establishing a switchable thermal contact. An integrated fluorescence detection unit enables real-time monitoring of DNA amplification, thereby combining rapid thermal cycling and optical readout within a compact system.

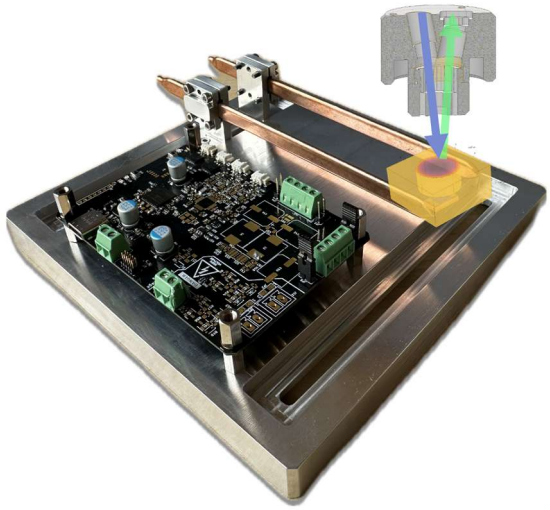

Fig. 1. Design of the miniaturized Thermocycler with integrated microheater, switchable heat pipe cooling, and fluorescence detection.

As illustrated in Fig. 2, the heat pipe operates on a closed two-phase cycle. A working fluid evaporates at the hot contact surface and transports latent heat along the heat pipe. At the cold end, the fluid condenses and releases the heat. The condensate is returned to the evaporation zone by capillary forces, enabling highly efficient heat transfer with low thermal resistance.

This principle allows heat transfer to be activated only during the cooling phase, while thermal coupling is minimized during heating. The thermal

behavior of the thermocycler can be approximated using simplified heat transfer models.

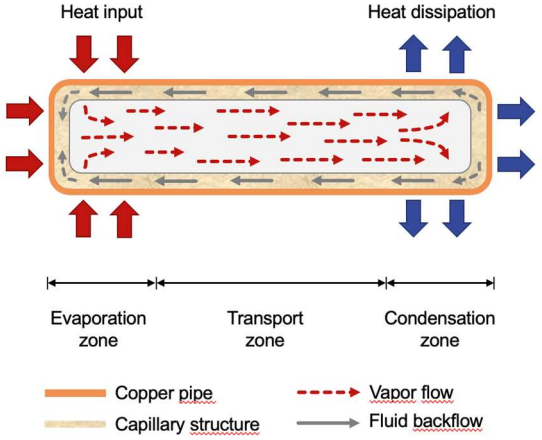

Fig. 2. Schematic illustration of the operating principle of a heat pipe.

Heat transfer within the system can be approximated by Fourier's law

$$q = -k \cdot \nabla T \qquad (1)$$

where q is the heat flux, k is the thermal conductivity, and ∇T is the temperature gradient. However, heat pipes exhibit a significantly higher effective thermal conductivity k, which can exceed that of solid materials [6]. The amount of heat transferred can be described simply by

$$Q = h \cdot A(T_{hot} - T_{cold}) \qquad (2)$$

where Q is the heat transfer rate, h is the effective heat transfer coefficient, A is the effective heat transfer area, T_{hot} is the temperature of the hot side, and T_{cold} is the temperature of the cold side. The effective heat transfer coefficient h is significantly enhanced by phase-change processes within the heat pipe. Pneumatic coupling specifically reduces the thermal resistance R_{th} during the cooling phase

$$R_{th} = \frac{\Delta T}{Q} \qquad (3)$$

where R_{th} is the thermal resistance and ΔT the temperature difference across the thermal interface. This minimizes heat loss during the heating phase while enabling high cooling rates.

Results

To evaluate the thermal performance of the proposed concept, the PCR protocol, including temperature levels and typical dwell times, is summarized in Table 1. As shown in Fig. 3, the normalized cooling curves demonstrate a significant improvement in thermal dynamics due to the use of heat pipes. Once the denaturation temperature is reached, cooling occurs significantly faster than without a heat pipe. This leads to accelerated transitions between the denaturation and annealing temperatures. Without a heat pipe, cooling proceeds significantly slower and exhibits lower effective cooling rates. The improved heat dissipation reduces cycle times and increases the overall efficiency and performance of the PCR process. These results demonstrate the effectiveness of the proposed switchable

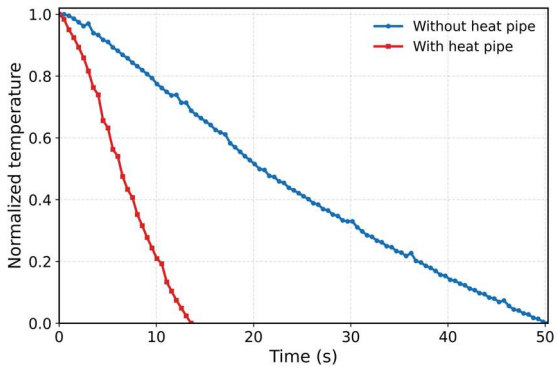

Fig. 3. Normalized cooling curves from 96 °C to 55 °C for operation without and with heat pipe.

heat pipe cooling concept for enabling rapid and efficient PCR thermal cycling in miniaturized systems.

Tab. 1: Process parameters for a PCR cycle, including the respective temperature steps and durations.

Process step	Temperature T / °C	Typical duration
Denaturation	96	10 – 30 s
Annealing	55	10 – 30 s
Elongation	68	20 – 60 s

References

[1] M. Marchesini et al., Point-of-Care Nucleic Acid-Detection: From Molecular Design to Integrated Systems, ACS Omega (2025); doi: 10.1021/acsomega.5c02914

[2] G. Papadakis et al., Portable real-time colorimetric LAMP device for rapid nucleic acid detection, Scientific Reports (2022); doi: 10.1038/s41598-022-06632-7

[3] A. M. Foudeh et al., Microfluidic designs and techniques using lab-on-a-chip devices for pathogen detection for point-of-care diagnostics, Lab on a Chip 12, 3249–3266 (2012); doi: 10.1039/c2lc40630f

[4] P. Neuzil, J. Pipper, T.M. Hsieh, Disposable real-time microPCR device: lab-on-a-chip at a low-cost. Molecular bioSystems 2.6-7 (2006): 292-298; doi: 10.1039/B605957K

[5] P. Bamerni et al., Design and Validation of a High-Speed Miniaturized Thermocycler with Peltier Elements for Efficient PCR Thermal Cycling, Sensors 25(22), 7046 (2025); doi: 10.3390/s25227046

[6] H. Jouhara, D. Reay, R. McGlen, P. Kew, J.McDonough, Heat Pipes: Theory, Design and Applications, 7th ed., Butterworth-Heinemann, 2023; ISBN: 978-0-12-823464-8

DOI 10.5162/eurosensors2026/Tu–BBS–06

Laser-induced graphene paper-based electrodes for detection of the pancreatic cancer biomarker CA19-9 in real samples

Gabriella Onila do Nascimento Soares[1], Andrey Coatrini Soares[2], Gustavo G Dalkiranis[3], Bruno Bassi Millan Torres[3], and Débora Gonçalves[3]

[1] Materials Engineering Department, Engineering School, University of São Paulo, São Carlos, São Paulo 13563-120, Brazil,
[2] Department of Physics, Federal University of Amazonas, Manaus, Amazonas 69067-005, Brazil,
[3] Institute of Physics of São Carlos, University of São Paulo, São Carlos, São Paulo 13566-590, Brazil.
gabriellaonila@usp.br

Summary: Pancreatic cancer has a high mortality rate due to challenges in early detection. This research reports the optimization, structural characterization, and biosensing performance of laser-induced graphene (LIG) electrodes fabricated on paper substrates for CA19-9 detection. Preliminary analyses of urine samples suggest that the paper electrodes show promising results for point-of-care applications.

Keywords: Biosensor, pancreatic cancer, CA19-9, Laser-induced graphene (LIG), paper-based electrodes.

Introduction

Pancreatic cancer remains one of the most significant challenges in modern oncology due to its high mortality and late diagnosis, which limit treatment options and reduce survival rates [1]. According to the American Society of Clinical Oncology (2023) [2], the 5-year relative survival rate is only 3% when diagnosed at an advanced stage. The absence of sensitive, selective, and practical early detection methods hinders effective treatment. Innovative, accurate, and non-invasive diagnostics offer strong potential to improve outcomes and support public healthcare [3]. Functional material-based biosensors, especially using the EIS technique, offer new paths for early diagnosis [4]. Beyond sensitivity and specificity, these devices offer portability, flexibility, and multifunctionality [3].

Experimental Procedure

Paper substrates were treated with sodium tetraborate, dried, and pressed, followed by hydrophobization using rosin in ethanol and a second pressing step. Laser processing was applied to form interdigitated graphene electrodes, with parameters optimized by varying power and speed. Morphological and structural characterization was performed using SEM-EDS and Raman spectroscopy. Capacitance measurements were assessed via EIS (Solartron SI 1260). Data analysis was conducted using Interactive Document Maps (IDMAP) generated with the Projection Explorer Sensors software (PEx-Sensors). For biosensor validation, urine samples from patients were analyzed and compared with ELISA reference measurements. Measurement conditions are still being optimized to improve sensitivity and calibration. All procedures involving human samples were ethically approved.

Results

The formation of interdigitated electrodes (IDEs) was optimized by systematically varying laser power (3–8% of 22 W) and scanning speed (300–800 mm/min). Based on this, the best condition was achieved at 7% power and 300 mm/min for digit formation (Fig. 1), while for the terminals and contacts, the optimized parameters were 6% power and 500 mm/min (Fig. 2), with sheet resistance of 230.12 ± 28.07 $\Omega\ sq^{-1}$ (Fig. 3). Morphological evaluation via scanning electron microscopy (SEM) revealed well-defined porous graphene structures. Energy-dispersive spectroscopy (EDS) confirmed the presence of carbon, oxygen, and calcium, principally. Raman spectroscopy further validated the synthesis of multilayer porous graphene, evidenced by the characteristic D, G, and 2D bands (Fig. 4). Electrochemical impedance spectroscopy (EIS) demonstrated that electrodes (terminal and contacts) produced

at 6% power and 500 mm/min exhibited the lowest resistivity values when compared to other conditions. Furthermore, a post-synthesis mechanical pressing step was found to significantly reduce real impedance by increasing the packing density of the graphene sheets. The optimized platform was applied as a capacitive biosensor for the CA19-9 biomarker. The sensing data followed a Langmuir–Freundlich model (R^2 = 0.99), yielding a limit of detection (LOD) of 2.38 U/mL and a limit of quantification (LOQ) of 7.86 U/mL. Preliminary analyses of urine samples (Fig. 5) show promising results for point-of-care applications. Enhancements in the measurement protocol are needed to develop a calibration curve that can more accurately quantify the biomarker, aligning more closely with the results obtained from the ELISA technique.

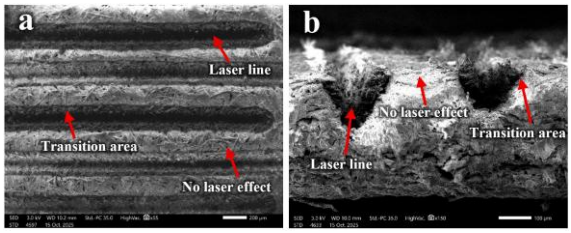

Fig. 1. SEM images of (a) top view and (b) cross-section of the interdigitated area.

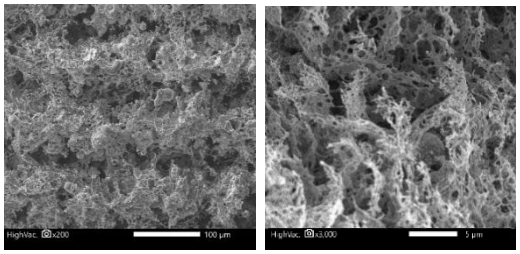

Fig. 2. SEM micrographs of LIG electrodes fabricated under 6.0% power, 500 mm min⁻¹.

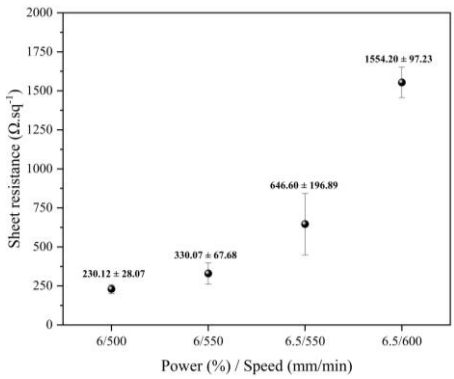

Fig. 3. Sheet resistance of different conditions of electrodes processing

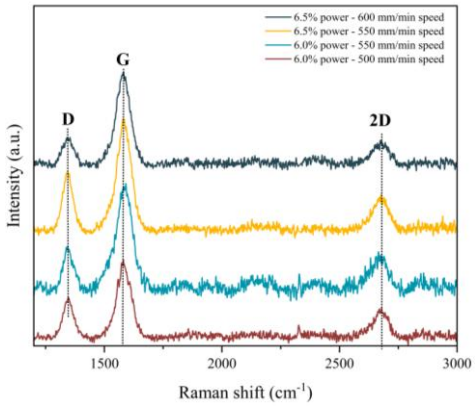

Fig. 4. CA19-9 measurements of urine samples using ELISA and Paper-based biosensor analysis.

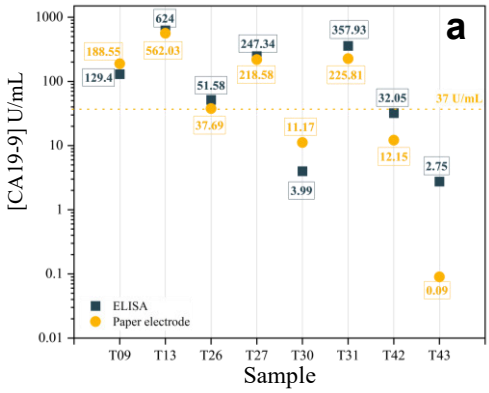

Fig. 5. CA19-9 measurements of urine samples using ELISA and Paper-based biosensor analysis.

Conclusions

Preliminary results show that LIG paper-based electrodes were successfully optimized. Urine sample analyses indicate promising performance for point-of-care applications.

Acknowledges

National Council for Scientific and Technological Development (CNPq, Brazil) (grant numbers 446650/2024-2, 107555/2024-7); National Institute of Organic Electronics INEO/FAPESP/INCT (grant number 314845/2025-9) and São Paulo Research Foundation (FAPESP) (grant number 2024/06362-6).

References

[1] J.D. Mizrahi, R. Surana, J.W. Valle, R.T. Shroff, Pancreatic cancer, *Lancet* 395, 2008–2020 (2020); doi: 10.1016/S0140-6736(20)30974-0

[2] American Society of Clinical Oncology, Pancreatic Cancer: Statistics (2023). Available: https://www.cancer.org/cancer/types/pancreatic-cancer/about/key-statistics.html (accessed 17 April 2026).

[3] S. Sarkar, S. Hazra, S. Patra, M. Gogoi, Biosensors for cancer detection: A review, *TrAC Trends Anal. Chem* 180, 1-18 (2024); doi: 10.1016/J.TRAC.2024.117978.

DOI 10.5162/eurosensors2026/Tu–BBS–07

Electrochemical Biosensing of HPV: From Molecular Detection to Clinical Impact

Martin Bartosik[1], Milan Anton[2], Ludmila Moranova[1], Johana Strmiskova[1]
[1] Masaryk Memorial Cancer Institute, Brno, Czech Republic
[2] Department of Obstetrics and Gynecology, University Hospital Brno and Medical Faculty, Masaryk University, Brno, Czech Republic
martin.bartosik@mou.cz

Summary:

Persistent infection with high-risk human papillomavirus (HPV) is the primary cause of cervical cancer and is also associated with anogenital and head and neck cancers. HPV testing improves diagnostics but remains costly and complex. Electrochemical (EC) detection offers a low cost user friendly alternative with minimal sample consumption. Combined with loop mediated isothermal amplification it enables sensitive and fast analysis. We developed EC biosensing platforms for HPV DNA and RNA detection in cervical precancerous lesions and we currently extend this approach to urine, blood and oral samples.

Keywords: HPV, cancer, biosensor, electrochemistry, LAMP

Background, Motivation and Objective

Persistent infection with high-risk human papillomavirus (HPV) is a primary etiological driver of cervical cancer. Incorporating HPV testing into screening programs has significantly improved the effectiveness of cytological diagnostics [1]. Beyond cervical cancer, HPV is also implicated in a range of anogenital malignancies as well as head and neck cancers [2]. Current HPV detection methods often rely on costly reagents, sophisticated instrumentation, and trained personnel, limiting their broader clinical implementation. Electrochemical (EC) detection approaches offer a compelling alternative, enabling rapid analysis using compact, low-cost, and user-friendly devices. When integrated with isothermal amplification strategies such as loop-mediated isothermal amplification (LAMP), these platforms achieve high sensitivity and reduced assay time. In our work, we have developed a series of EC biosensing platforms coupled with LAMP for the detection of HPV in cervical samples from patients with precancerous lesions, demonstrating their potential for rapid and accessible molecular diagnostics [3-6].

Description of the New Method or System

We employed LAMP for the rapid amplification of HPV nucleic acids (30-40 min) from the two most oncogenic genotypes, HPV16 and HPV18. The reaction was performed in the presence of biotinylated dUTP nucleotides, enabling affinity-based handling of the amplicons. The LAMP products were then hybridized to sequence-specific capture probes immobilized on magnetic beads, allowing efficient separation and target enrichment. EC readout was then performed using amperometric detection based on a peroxidase-mediated reaction, providing a sensitive and quantitative signal for HPV detection.

Results

Our group has reported a series of rapid and simple EC-LAMP assays for the detection of HPV16/18 in cervical cell lines and clinical smears from women with precancerous lesions. Following optimization [3], the method was validated on 61 clinical samples and benchmarked against PCR-based techniques and the INNO-LiPA genotyping assay, achieving specificity and predictive values above 90% [4]. The workflow was further streamlined by eliminating DNA extraction, enabling direct analysis of crude lysates prepared by simple heat treatment, which reduced assay complexity and minimized contamination risk [5]. More recently, we developed an RNA-based electrochemical biosensing platform that integrates reverse transcription LAMP (RT-LAMP) with rapid and simple EC readout [6]. Such diagnostics, capable of distinguishing between episomal and integrated HPV infections, can provide valuable insight into the risk of lesion progression. Our platform, termed eRT-LAMP, targeted the electrochemical detection of two key

viral mRNAs, E2 and E7. E2 is normally expressed at physiological levels, where it regulates E7 and helps prevent excessive cell proliferation. However, when the virus integrates into the host genome, the E2 gene is frequently disrupted or deleted at the integration site, resulting in loss of its regulatory role. This leads to uncontrolled E7 expression, pushing host cells toward a malignant state. The ratio of E2 to E7 expression could thus be an important biomarker for assessing the status of HPV infection. We measured these levels in cervical samples containing HPV16 using our EC-based method (Fig. 1).

Very recently, we have shifted our focus toward HPV analysis in urine samples from women with cervical precancerous lesions as a noninvasive alternative to conventional sampling. This approach is supported by studies suggesting a possible concordance between HPV detection in urine and cervical smears, indicating that urine may represent a promising and patient-friendly specimen for HPV diagnostics [7]. Our results demonstrate that HPV16 in patients is readily detectable in cervical smears, however viral loads in urine were considerably lower (Fig. 2). Finally, we have expanded our focus to the analysis of HPV in patients with oropharyngeal carcinoma (OPC), where HPV has been shown to play a critical role in tumor development and is associated with distinct clinical outcomes. In this study, we will compare oral rinse, oral swab, and plasma samples for the detection of HPV infection, evaluating their utility as prognostic biomarkers in OPC.

Financial support from the Czech Science Foundation (No. 25-15990S), project SALVAGE (OP JAC; reg. no. CZ.02.01.01/00/22_008/0004644), and institutional grant SUp 8/25 from University Hospital Brno is greatly acknowledged.

Illustrations, Graphs, and Photographs

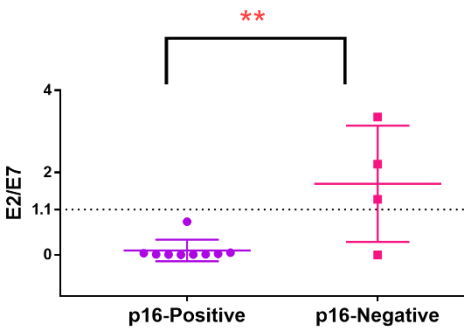

Fig. 1. Scatter plot for HPV16 comparing our EC signals (shown as E2/E7 current ratios obtained from two distinct mRNAs, left) with immunohistochemical analysis of p16. After HPV integration into the genome, E2 levels drop and E7 levels rise. This correlates with p16 positivity and disease progression. Adapted from reference [6].

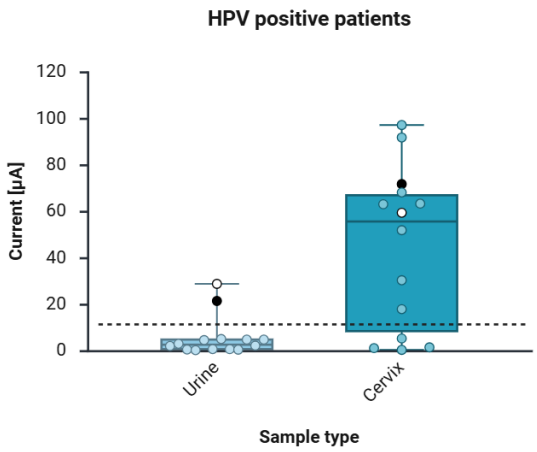

Fig. 2. Preliminary data on HPV16 detection in DNA extracted from paired samples - urine and cervical swabs - of 14 HPV16-positive patients.

References

[1] E. T. H. Fontham et al., Cervical cancer screening for individuals at average risk: 2020 guideline update from the American Cancer Society, *CA Cancer J Clin* 70, 321-346 (2020); doi:10.3322/caac.21628

[2] M. Lechner, J. Liu, L. Masterson, T. R. Felton, HPV-associated oropharyngeal cancer: epidemiology, molecular biology and clinical management, *Nat Rev Clin Oncol* 19, 306-327 (2022); doi: 10.1038/s41571-022-00603-7

[3] M. Bartosik, L. Jirakova, M. Anton, B. Vojtesek, R. Hrstka, Genomagnetic LAMP-based electrochemical test for determination of high-risk HPV16 and HPV18 in clinical samples, *Anal Chim Acta* 1042, 37-43 (2018); doi: 10.1016/j.aca.2018.08.020

[4] M. Anton, L. Moranova, R. Hrstka, M. Bartosik, Application of an electrochemical LAMP-based assay for screening of HPV16/HPV18 infection in cervical samples, *Anal Methods* 12, 822-829 (2020); doi: 10.1039/C9AY02383F

[5] N. Izadi, R. Sebuyoya, L. Moranova, R. Hrstka, M. Anton, M. Bartosik, Electrochemical bioassay coupled to LAMP reaction for determination of high-risk HPV infection in crude lysates, *Anal Chim Acta* 1187, 339145 (2021); doi: 10.1016/j.aca.2021.339145

[6] N. Izadi, J. Strmiskova, M. Anton, J. Hausnerova, M. Bartosik, LAMP-based electrochemical platform for monitoring HPV genome integration at the mRNA level associated with higher risk of cervical cancer progression, *J Med Virol* 96, e70008; doi: 10.1002/jmv.70008

[7] N. Pathak, J. Dodds, J. Zamora, K. Khan, Accuracy of urinary human papillomavirus testing for presence of cervical HPV: systematic review and meta-analysis, *BMJ* 349, g5264 (2014); doi:10.1136/bmj.g5264

DOI 10.5162/eurosensors2026/Tu–BBS–08

Decoupling Optical and Electrical Transduction Mechanisms in Peptide-Functionalized Graphene Biosensors for Immune Cell Detection

Ahmar Hasnain[1], Heiko Heilmann, Prof. Dr. Bernd Bufe, Prof. Dr. Alexey Tarasov[1]
[1] Faculty of Computer Sciences and Microsystems Technology, Kaiserslautern University of Applied Sciences, Amerikastr. 1, 66482, Zweibrücken, Germany
ahmar.hasnain@hs-kl.de

Summary:
We present a comparative graphene-enhanced peptide-based assay for the real-time detection of immune cell receptors. By directly comparing real-time optical (graphene-enhanced surface plasmon resonance, SPR) and electrical (graphene field-effect transistors, gFET) responses from identical peptide-functionalized graphene interfaces, this proof-of-concept study highlights the potential of graphene- based platforms for real-time sensing of living cells in point-of-care diagnostic applications.

Keywords: graphene biosensors, surface plasmon resonance, immune receptors, peptides,

Background, Motivation and Objectives

Graphene-based biosensors offer a highly sensitive and selective approach to detecting biological interactions. These sensors are generally based on the measurement of signal changes resulting from biomolecular events occurring at the interface between a transducer surface and functionalized biomolecular layers [1]. In recent years, peptide-functionalized surfaces have emerged as powerful tools for selective biosensing, as they can mimic biological recognition sites and enable controlled interaction with target receptors.

Among the various biological systems, immune cell receptors such as formyl peptide receptor 2 (FPR2) play a critical role in inflammation and disease progression. Specifically, peptides can selectively bind to these receptors, enabling targeted detection of immune cell activity. Consequently, peptide-based interfaces are regarded as promising candidates for real-time monitoring of receptor-ligand interactions.

However, challenges remain, including non-specific interactions that introduce false signals and differences in transduction mechanisms that complicate data interpretation and comparison. In this study, we present the development of a peptide-functionalized graphene-based sensing platform for the detection of HEK(FPR2) cells. The graphene surfaces were functionalized using PBA as a linker, followed by EDC/NHS activation to enable amine coupling of target and control peptides (see Fig. 1). The target peptide is designed to specifically bind FPR2 receptors, while the control peptide lacks affinity, enabling selective validation [2]. This approach ensures stable peptide immobilization while maintaining sensitivity to cell-surface interactions. This strategy minimizes non-specific interactions while enabling selective binding of HEK(FPR2) cells. The peptide interface is applied to graphene-coated SPR sensor surfaces for optical measurements and to graphene field-effect transistor (gFET) devices for electrical measurements. The assay was initially developed and monitored in real time using state-of-the-art SPR technology. Subsequently, real-time analysis was performed using gFETs, considering their potential for translation into point-of-care diagnostics. Real-time optical and electrical responses from identical interfaces enable evaluation of binding behavior.

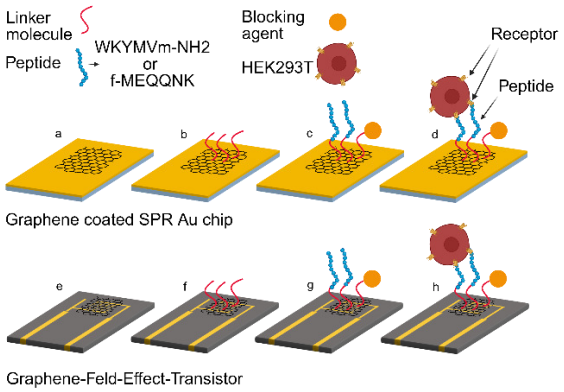

Fig. 1. Schematic illustration of the biosensing strategy of the proposed peptide-based cell detection assay using SPR and gFET.

Research novelty

A cross-platform validation strategy is introduced by directly comparing real-time SPR and gFET

responses from identical biointerfaces. This comparison was enabled by using CVD-grown monolayer graphene as the common sensing surface across both platforms, while enhancing SPR sensitivity.

The platform enables label-free, real-time detection of immune cell receptors directly on living cells, moving beyond conventional detection of soluble biomarkers. The results demonstrate correlated target-specific responses with minimal control interaction, confirming assay selectivity across both modalities.

Overall, this study establishes a framework for translating laboratory-grade SPR assays into scalable gFET-based sensing systems.

Results

SPR measurements show a clear increase in response upon exposure to HEK(FPR2) cells on the target peptide, while the control exhibits minimal signal, confirming selective binding. The signal increase reflects cell accumulation, and partial retention after washing indicates stable interaction.

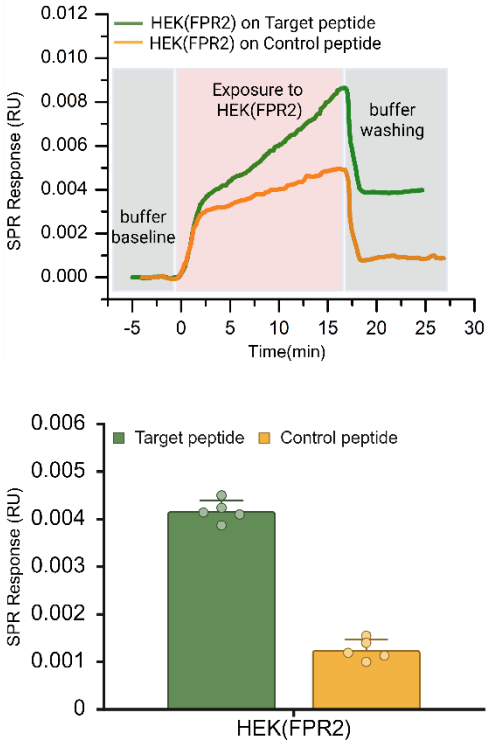

Fig. 2. SPR sensogram showing the peptide baseline, its exposure to HEK(FPR2) cells, followed by buffer washing. The target peptide exhibits a strong increase in response and remains above the baseline after washing, indicating stable binding. In contrast, the control shows minimal response and returns close to the baseline. The lower panel shows the mean response ± SD (n = 5). Adapted from [2].

Similarly, gFET measurements show a rapid increase in normalized current ($\Delta Ids/Ids_0$) for the target peptide, with negligible response for the control. The stable signal during exposure reflects changes in the local electrical environment. All mmeasurements were performed at a concentration of 10,000 cells/ml under physiological buffer conditions.

Both platforms consistently show higher responses for the target peptide. These results demonstrate selective, real-time detection of HEK(FPR2) cells, with complementary optical (SPR) and electrical (gFET) readouts, supporting translation toward point-of-care sensing.

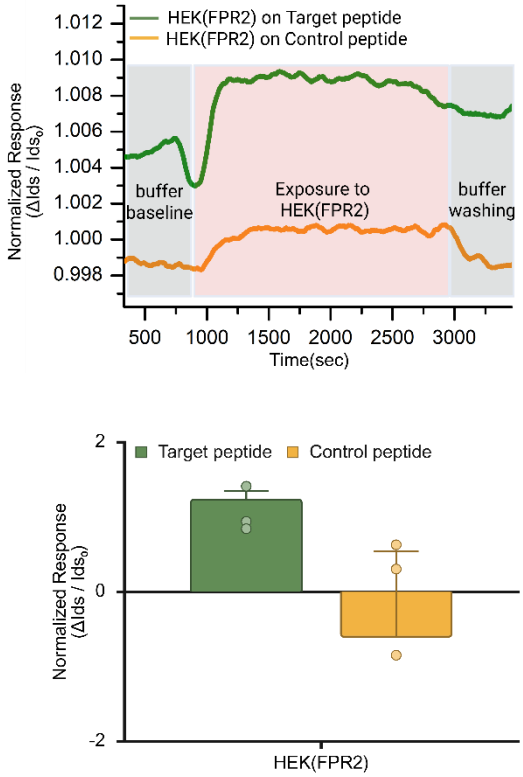

Fig. 3. gFET sensogram showing the baseline, its exposure to HEK(FPR2) cells, followed by buffer washing. The target peptide exhibits a strong increase in electrical response and remains above baseline after washing, while the control shows minimal change and returns close to baseline. The lower panel shows mean normalized response ($\Delta Ids/Ids_0$ ± SD, n = 3).

References

[1] A. Hasnain, H. Heilmann, N. L. P. Le, et al. “Graphene-Enhanced Plasmonic Interfaces: A General Strategy for Highly Sensitive Detection of Biomolecular Interactions.” Adv. Healthcare Mater.14, no. 31 (2025): e01723.; doi: 10.1002/adhm.202501723

[2] A. Hasnain, H. Heilmann, A. Pohl, C. Weber, B. Bufe, and A. Tarasov, “Cross-Platform Biosensing of Immune Receptors Using Peptide-Functionalized Graphene.” Adv. Sci.13, no. 18 (2026): e19436.; doi:10.1002/advs.202519436

DOI 10.5162/eurosensors2026/Tu–BBS–09

Electrochemical Redox Label Multiplexing on Single Carbon Electrodes for the Real-Time Detection of Bacterial Wound Infections

Dominic Kleinknecht[1,2], Martin Trotter[1], Cornelia Keß[1], Justus Kloeppel[1], Dimitra Kiritsi[3,4], Nadine Borst[1,2], Felix von Stetten[1,2], Andreas Schreiber[1,2]
[1] Hahn-Schickard, Georges-Köhler-Allee 103, 79110 Freiburg im Breisgau, Germany
[2] Laboratory for MEMS Applications, IMTEK – Department of Microsystems Engineering, University of Freiburg, Georges-Köhler-Allee 103, 79110 Freiburg im Breisgau, Germany
[3] Department of Dermatology, Medical Center – University of Freiburg, Hauptstraße 7, 79104 Freiburg im Breisgau, Germany
[4] First Department of Dermatology, Aristotle University of Thessaloniki, AUTh Campus, 54124 Thessaloniki, Greece
Corresponding Authors:
dominic.kleinknecht@hahn-schickard.de; andreas.schreiber@hahn-schickard.de

Summary:

We introduce redox label multiplexing and demonstrate the first real-time electrochemical duplex LAMP assay [1] enabling simultaneous detection of two nucleic acid targets on a single carbon electrode. Distinct redox labels combined with universal surface probes enable multiplexed signal-on detection within one reaction volume. Preliminary validation with patient wound swab samples demonstrates robust and highly specific performance in complex biological matrices. The presented platform establishes a scalable route toward low-cost, highly multiplexed point-of-care molecular testing.

Keywords: electrochemical detection, LAMP, multiplex diagnostics, point-of-care, biosensors

Background, Motivation and Objective

Electrochemical detection of loop-mediated amplification (LAMP) reactions is a promising approach to make sensitive, miniaturized molecular diagnostics available at the point-of-care. Emerging probe-based LAMP methodologies have adopted universal designs that increase analytical specificity and significantly simplify the development process [2]. However, these approaches are limited to the detection of only one target per working electrode. Multiplexed detection at the point-of-care remains challenging when sample volumes are limited, and robust multiplexing methods within a single reaction cavity are lacking [1]. Here we introduce redox label multiplexing on a single electrode using generic surface probes to overcome this limitation, demonstrating duplex detection with methylene blue and anthraquinone labels and thereby expanding the electrochemical mediator displacement (eMD) LAMP toolbox.

Description of the New Method or System

We demonstrate redox label multiplexing with the first real-time electrochemical duplex LAMP assay using distinct redox-active molecules on a single carbon working electrode. The platform approach builds on a generic surface functionalization strategy employing universal DNA capture probes, enabling modular assay design independent of target-specific surface modifications. Target-specific amplification is coupled to signal generation via labeled mediator strands displaced during the LAMP cascade. Each target is associated with a displaced mediator modified with a distinct redox label, producing separate and identifiable electrochemical signals at defined potentials when hybridized to the surface probes (see Fig. 1). This label-based multiplexing strategy allows simultaneous, real-time detection of multiple amplification reactions within a single chamber. The presented approach overcomes key limitations of existing electrochemical LAMP systems by combining (i) real-time signal-on detection, (ii) multiplex capability without geometric or electrode-based partitioning, and (iii) compatibility with simple and scalable PoC device architectures.

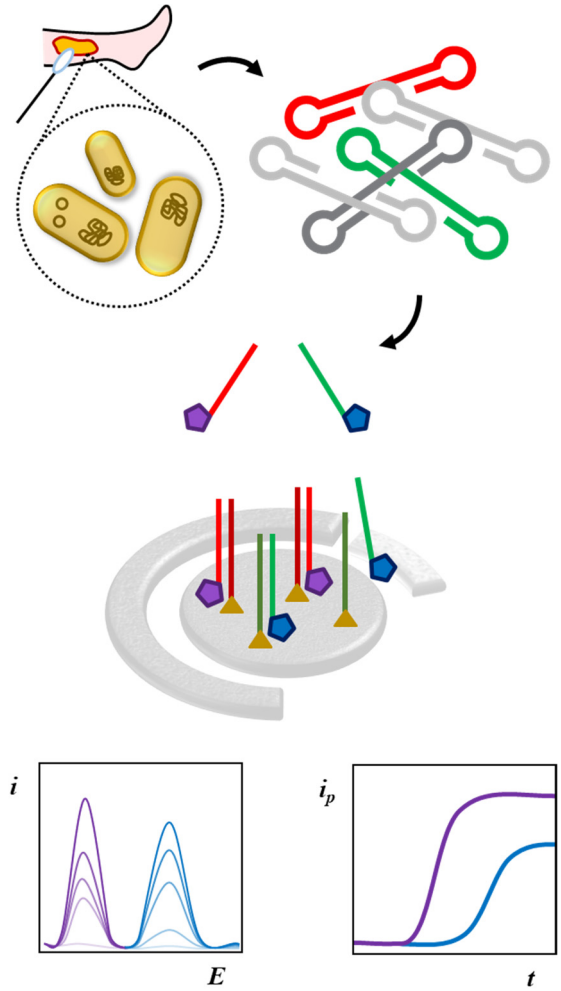

Fig. 1. Schematic visualization of the electrochemical duplex eMD LAMP realized on a single carbon electrode with redox label multiplexing. LAMP detection of lysed bacteria from patient wound swab samples (top) causes target-specific displacement of redox-labeled mediator sequences (red and green). Hybridization of displaced mediators to complementary surface probes allows for the co-detection of anthraquinone (purple) and methylene blue (blue) redox labels on a single electrode (middle). Both labels have discreet redox potentials, allowing for the simultaneous resolution in real-time (bottom left). Plotting the label-specific peak currents over time (bottom right) reveals the LAMP amplification plot, allowing for real-time electrochemical duplex LAMP detection. Figure adapted from [1].

Results

The *uidA E. coli* housekeeping gene and the *CTX-M1* antibiotic resistance gene found in ESBL *E. coli* are both successfully detected in singleplex down to 10 CFUs per reaction and show semi-quantitative amplification signals. Our novel electrochemical real-time LAMP assays show equal sensitivity and similar time-to-positive as their optical counterparts while improving the signal-to-noise ratio for the used primer sets. The combined duplex LAMP allows for detection of both targets within 40 min, and its clinical matrix compatibility was preliminarily validated using five clinical wound swab samples (see Fig. 2). The duplex LAMP specifically detects the *E. coli*–positive sample in presence of eleven other wound-associated bacterial species. Our label-based real-time multiplexing approach doubles the detection capabilities per working electrode and presents the first real-time probe-based electrochemical signal-on duplex LAMP detection, paving the way for miniaturized sample-to-answer point-of-care devices, with further redox labels available for an even higher degree of multiplexing. In combination with electrode-based multiplexing, highly multiplexed assay formats become possible that can far exceed what is currently possible in a single reaction volume.

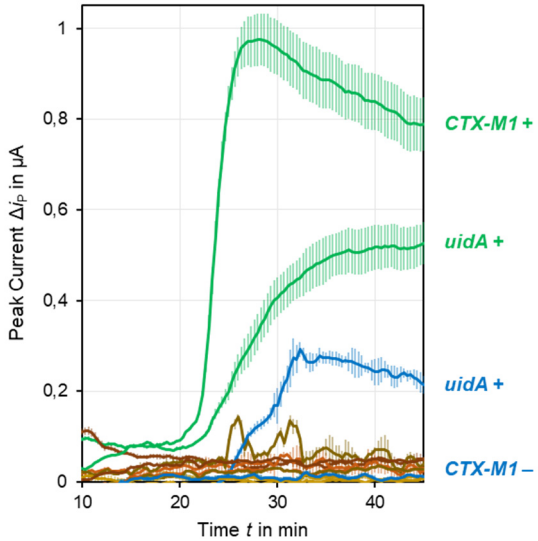

Fig. 2. Patient wound swab samples tested with eMD LAMP duplex assay. One E. coli-negative matrix sample with spiked-in CTX-M1 (10^2 CFUs/rx.) and uidA (10^4 CFUs/rx.) lysate (green) was used as the control reaction. In addition, one E. coli-positive wound swab sample (blue) and four E. coli-negative wound swab samples with various other wound colonizing bacterial strains (gold-brown hues) were tested. The eMD LAMP correctly identified the positive E. coli sample and did not yield false positive signals within 45 min, demonstrating diagnostic sensitivity and specificity in clinical samples. Figure adapted from [1].

References

[1] D. Kleinknecht et al., Electrochemical duplex LAMP on single carbon electrodes for the real-time detection of bacterial wound infections, *Biosensors and Bioelectronics: X* 29, 100754 (2026); doi: 10.1016/j.biosx.2026.100754

[2] M. Trotter et al., Pathogen-Specific Electrochemical Real-Time LAMP Detection Using Universal Solid-Phase Probes on Carbon Electrodes, *ACS Sensors* 10(3) (2025), doi: 10.1021/acssensors.4c0249

DOI 10.5162/eurosensors2026/Tu–BBS–10

Development of a MEMS-Based Electrochemical Platform for Label-Free Viral Antibody Sensing

Zeynep Çağlayan Arslan[1,4], Ezgi Salmanlı[1,2], Tuğba Tezcan[3], Taner Karaoğlu[2], Uğur Tamer[1,3], Haluk Külah[1,4]
[1] METU MEMS Center, 06530 Ankara, Türkiye,
[2] Department of Virology, Faculty of Veterinary Medicine, Ankara University, 06070 Ankara, Türkiye,
[3] Department of Analytical Chemistry, Faculty of Pharmacy, Gazi University, 06330 Ankara, Türkiye,
[4] Department of Electrical and Electronics Engineering, Middle East Technical University, 06800 Ankara, Türkiye
zcaglayan@mems.metu.edu.tr

Summary:
Monitoring of antibody levels plays a critical role in evaluating immune response and disease control. In this work, a MEMS-based electrochemical sensing platform is developed for label-free viral antibody sensing using impedance measurements. The platform exhibits a concentration-dependent impedance response at the picogram (pg) level, while at higher concentrations (nanogram, ng) it shows a nonlinear response, suggesting surface-related limitations in binding. Selective detection is achieved with minimal non-specific interference, demonstrating a compact and scalable sensing approach.

Keywords: MEMS, electrochemical biosensor, impedance spectroscopy, label-free detection, antibody sensing

Background, Motivation and Objective

Protection against infectious diseases is largely based on humoral immunity, making antibody monitoring essential for evaluating immune response, vaccine efficacy, and population-level protection [1]. Conventional serological methods, including ELISA and lateral flow immunoassays, remain limited in terms of protocol complexity, reproducibility, and applicability for on-site testing. These limitations highlight the need for reliable antibody detection platforms. Electrochemical biosensors offer advantages due to their sensitivity and suitability for label-free measurements [2]. In particular, MEMS-based electrochemical platforms enable precise electrode structuring, reduced sample volumes, and scalable device architectures, providing a promising route for high-performance antibody sensing. In this context, a MEMS-based electrochemical sensing platform is developed for label-free viral antibody detection using impedance measurements. Antibody recognition is achieved through binding to a bioengineered protein expressed in a recombinant system, enabling a miniaturized and scalable sensing approach [3].

Sensor Design and Experimental Methods

MEMS-based electrochemical sensors were fabricated in the cleanroom facilities of METU MEMS Center (Ankara, Turkey). The platform is based on a planar three-electrode configuration with a gold (Au) working electrode (WE), a platinum (Pt) counter electrode (CE), and a silver (Ag) reference electrode (RE) on a glass substrate, as shown in Fig. 1. Thin-film metal layers (Ti/Au, Ti/Pt, Ti/Ag; ~50/500 nm) were patterned using standard photolithography and lift-off processes [4]. The working electrode was designed as a circular structure (≈1000 µm in diameter) surrounded by concentric counter and reference electrodes. For surface functionalization, a self-assembled monolayer (SAM) was formed on the gold electrode using 5 mM 11-mercaptoundecanoic acid (11-MUA) in ethanol, followed by EDC/NHS activation for antigen immobilization. After rinsing, the antigen was introduced, and non-specific sites were blocked using bovine serum albumin (BSA). Subsequently, target and non-target antibody solutions were applied, and interfacial changes were monitored via impedance measurements, enabling label-free sensing.

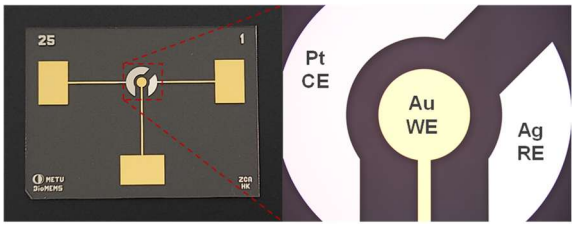

Fig. 1. Photograph of the fabricated MEMS-based sensor with a magnified view of the electrode region.

Electrochemical impedance spectroscopy (EIS) measurements were performed in a 5 mM ferricyanide/ferrocyanide solution using an Autolab PGSTAT128N system with a frequency response analyzer (FRA) module (Metrohm, Switzerland). Measurements were carried out from 0.1 Hz to 50 kHz using a 10 mV sinusoidal perturbation. The impedance spectra were analyzed with a Randles-type equivalent circuit, and charge transfer resistance (R_{ct}) was used as the sensing parameter. The sensing performance was evaluated over a concentration range from 10 pg to 5 ng, and responses were normalized with respect to the lowest concentration condition (10 pg).

Results

The sensing performance of the platform was evaluated by monitoring the impedance response as a function of antibody concentration (Fig. 2). The normalized R_{ct} was plotted against the logarithm of concentration, exhibiting a clear concentration-dependent behavior over a wide range. A progressive decrease in normalized R_{ct} was observed with increasing antibody concentration, indicating enhanced interaction at the electrode interface. At lower concentrations in the pg range, the response is gradual and well-resolved. In contrast, at higher concentrations (ng range), the response becomes nonlinear with reduced incremental signal change, suggesting surface-related limitations in binding and partial saturation of available sites. This behavior is highlighted in the inset of Fig. 2.

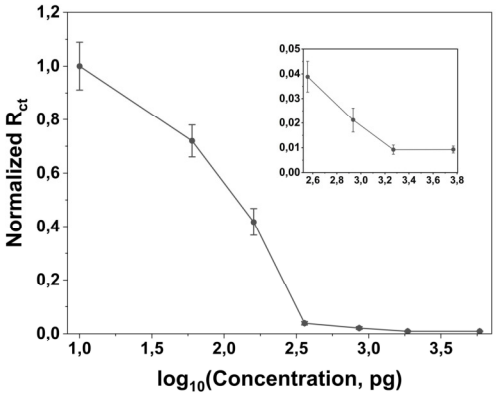

Fig. 2. Normalized R_{ct} versus logarithmic antibody concentration (picogram, pg). Inset shows the high-concentration regime.

The selectivity of the platform was evaluated at a representative concentration of 200 pg/mL by comparing the response of the target antibody with non-target species, including a model protein (BSA) and a non-target bacterial antibody (Fig. 3). The target analyte exhibited a pronounced decrease in normalized R_{ct}, whereas non-specific species showed significantly higher R_{ct} values. In particular, the responses for BSA and the bacterial antibody were approximately 10-fold and 30-fold higher than that of the target, respectively. These results indicate that target binding reduces interfacial resistance, while non-specific interactions do not produce a comparable effect, confirming minimal cross-reactivity and high selectivity of the sensing interface.

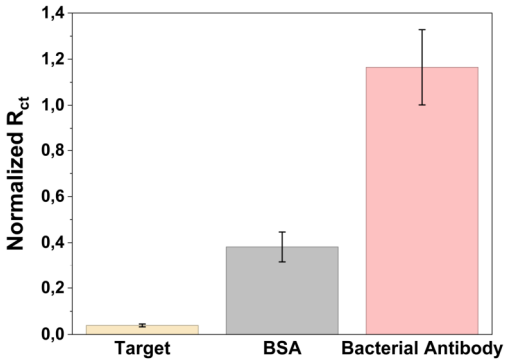

Fig. 3. Normalized R_{ct} for the target antibody, BSA, and a non-target bacterial antibody at 200 pg.

Conclusion

In this study, a MEMS-based electrochemical sensing platform for label-free viral antibody sensing was demonstrated. The system exhibited a concentration-dependent impedance response, with nonlinear behavior at higher concentrations, suggesting surface-related limitations in binding. Selective sensing of the target antibody was achieved with minimal interference from non-specific species, confirming the specificity of the sensing interface. The integration of a microfabricated electrode architecture with impedance-based readout enables a compact, label-free, and scalable sensing approach. These results highlight the potential of the platform for reliable and miniaturized antibody sensing.

References

[1] S. A. Ejazi, S. Ghosh, N. Ali, Antibody detection assays for COVID-19 diagnosis: an early overview, *Immunology & Cell Biology* 99, 21–33 (2021); doi: 10.1111/imcb.12397

[2] L. Guo et al., Electrochemical protein biosensors for disease marker detection: progress and opportunities, *Microsystems & Nanoengineering* 10, 65 (2024); doi: 10.1038/s41378-024-00700-w

[3] E. Salmanli, T. Tezcan, T. Karaoglu, A novel lateral flow immunochromatographic assay using a recombinant VP2 antigen for total antibody detection of canine parvovirus-2, *Analytical Methods* 16, 551–557 (2024); doi: 10.1039/d3ay01870a

[4] Z. Çağlayan Arslan, M. Okan, H. Külah, Pre-enrichment-free detection of hepatocellular carcinoma-specific ctDNA via PDMS and MEMS-based microfluidic sensor, *Microchimica Acta* 191, 229 (2024); doi: 10.1007/s00604-024-06315-2

Acknowledgements

This work was supported by the Scientific and Technological Research Council of Türkiye (TÜBİTAK), Grants 119E628 and 22AG008.

DOI 10.5162/eurosensors2026/Tu–BBS–11

Gold-Mediated Functionalization of NEMS-FTIR Resonators for Selective Molecular Detection

Dragana Suvara[1], Kostas Kanellopulos[1], Hanna Wursag[2], Sonia Prado-López[2], Silvan Schmid[1]
[1] TU Wien, Institute of Sensor and Actuator Systems, Gußhausstraße 27-29, 1040 Vienna, Austria,
[2] TU Wien, Institute of Solid State Electronics, Gußhausstraße 25-25a, 1040 Vienna, Austria
dragana.suvara@tuwien.ac.at

Summary:
NEMS-FTIR has recently demonstrated picogram-level limits of detection for both airborne and aqueous samples, with chemical specificity provided by the analyte's mid-IR fingerprint. However, the analysis of complex samples remains limited by overlapping molecular signatures and labor-intensive sample preparation. To address this, a gold-mediated functionalization strategy is introduced to enable selective analyte capture directly on the NEMS surface, demonstrated by the immobilization of a CD66e antibody and verified through the characteristic mid-IR fingerprint of the bound bioreceptor layer.

Keywords: NEMS-FTIR, molecular detection, photothermal sensing, functionalization, biosensing

Introduction

Nanoelectromechanical Fourier-transform infrared spectroscopy (NEMS-FTIR) has recently demonstrated picogram-level chemical identification of nanoplastics in aqueous samples [1] and of submicrometer atmospheric aerosols [2]. This high sensitivity enables the analysis of minute sample quantities, such as nanolitre volumes in aqueous samples [1], and reduces the sampling time required for ultrafine aerosols from hours to minutes [2].

Although the NEMS-FTIR platform can provide spectroscopic fingerprints, interpreting complex matrices remains challenging. Therefore, this work introduces gold-mediated surface functionalization to create selective biorecognition layers on NEMS membranes via stable Au-S bond formation, as schematically depicted in Fig. 1. The strong affinity between thiol groups and gold enables robust attachment of thiol-containing crosslinkers, providing a stable interface for bioreceptor immobilization and subsequent specific detection of target analytes in complex biological samples.

Methods

The central element of the NEMS-FTIR platform is a silicon nitride (SiN) membrane, which serves simultaneously as photothermal sensor and sample carrier. The chips consist of 5 mm × 5 mm, 380 µm thick silicon substrates supporting a 50 nm low-stress SiN membrane, patterned by UV lithography and released by backside KOH etching. Electrical transduction is enabled by 10 µm lithographically defined gold electrodes [2].

After chip fabrication, an additional circular gold pad was deposited on the backside of the released membrane by physical vapor deposition (PVD) through a laser-cut stainless-steel shadow mask. The 600 µm diameter pad consisted of a 10 nm chromium adhesion layer, followed by a 50 nm gold layer. This configuration provided sufficient surface area for functionalization and high IR reflectance, while minimizing added mass and preserving the resonator's thermomechanical dynamics.

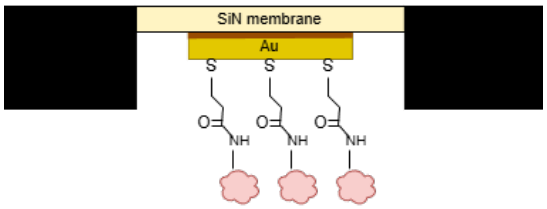

Fig. 1. Schematic representation of the biofunctionalized NEMS chip, illustrating the silicon nitride membrane with a localized gold pad serving as the functional interface for immobilization of the biorecognition element, enabling selective capture of the target analyte through specific functional-group interactions.

To demonstrate this concept, an antibody against the Carcinoembryonic Antigen (CEA), also known as CD66e, was immobilized on the gold-coated, oxygen plasma-treated NEMS surface using dithiobis(succinimidyl propionate) (DSP). DSP dissolved in dimethyl sulfoxide (DMSO) was first chemisorbed onto the gold

through its disulfide group by incubating the chip in a 10 µg/µL solution for 30 min, leaving NHS-reactive groups exposed at the surface. These groups then reacted with the primary amines of the 1 µg/µL CD66e antibody during incubation for 1 h. This facilitates covalent bonding between the protein and the surface of the resonator. The chip was then rinsed thoroughly with water to remove any unbound protein and by-products from the reaction.

The measurements were performed using a nanoelectromechanical IR analyzer (EMILIE, Invisible-Light Labs GmbH, Austria), coupled to a FTIR spectrometer (Vertex 70, Bruker Optics, MA, USA), that was operated under high-vacuum conditions (10^{-5} mbar) to reduce air damping and enable sensitive resonance-frequency tracking. The FTIR spectrometer served as a broadband mid-infrared light source over the range of 4000-400 cm^{-1}. The resonator frequency shifts were recorded in closed-loop operation and correlated with the FTIR wavenumber scan to reconstruct nanomechanical infrared spectra. The final spectra were background-corrected and normalized to remove substrate and baseline contributions [2].

Results

The NEMS-FTIR spectrum after DSP-mediated immobilization of the anti-CD66e antibody is shown in Fig. 2. The most pronounced DSP-related features are observed in the 2000-1750 cm^{-1} region and are assigned to NHS ester/ester carbonyl stretching vibrations. Additional DSP contributions are observed at 1251 cm^{-1} and 1112 cm^{-1}, corresponding to characteristic succinimide/NHS ester vibrations, including C-N-C and N-C-O stretching modes [3]. The remaining bands in the 1700-1000 cm^{-1} region are mainly attributed to fingerprint vibrations of the antibody. The bands at 1640 cm^{-1} and 1537 cm^{-1} correspond to amide I and amide II vibrations, respectively, which serve as key indicators of CD66e antibody immobilization [4]. These spectral features remained unchanged after multiple washing-measurement cycles, suggesting stable antibody immobilization rather than weak physical adsorption.

The predominance of DSP-related carbonyl bands is attributed to the strong spectral contribution of the linker layer, resulting from the relatively high DSP concentration, which could be addressed by optimizing the surface chemistry.

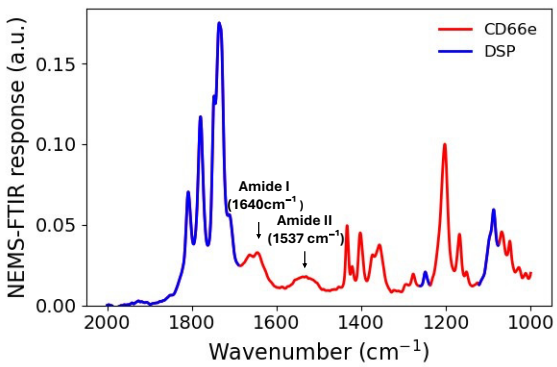

Fig. 2. NEMS-FTIR spectrum of a gold-coated resonator after DSP-CD66e immobilization, obtained following incubation with DSP cross-linker in DMSO at 10 µg/µL for 30 min, subsequent incubation with CD66e at 1 µg/µL for 1 h, and thorough washing with water.

Conclusion

This work demonstrates successful functionalization of NEMS-FTIR resonators through gold-thiol chemistry, confirmed by characteristic DSP- and antibody-related spectral features and their stability after repeated washing-measurement cycles. These results demonstrate the potential of introducing molecular selectivity to NEMS membranes. With further optimization of chip design, transduction, and surface chemistry, this approach could broaden the application of NEMS-FTIR to complex biological samples and support the development of next-generation biosensing technologies.

References

[1] M. Surdu, et al., Quantifying submicrometer atmospheric aerosol chemical composition using nanoelectromechanical Fourier transform infrared spectroscopy. *Science Advances* 12, eaeb2254 (2026); doi: 10.1126/sciadv.aeb2254.

[2] J. Timarac-Popović, et al, Picogram-Level Nanoplastic Analysis with Nanoelectromechanical System Fourier Transform Infrared Spectroscopy: NEMS-FTIR, ACS Nano 20, 11193-11208 (2026); doi: 10.1021/acsnano.5c22099

[3] H. Stevenson, et al., Ultrasensitive and Rapid-Response Sensor for the Electrochemical Detection of Antibiotic Residues within Meat Samples, ACS Omega 4, 6324-6330 (2019); doi: 10.1021/acsomega.8b03534

[4] Y. Du, et al., Breast cancer early detection by using Fourier-transform infrared spectroscopy combined with different classification algorithms, Spectrochimica Acta Part A: Molecular and Biomolecular Spectroscopy 283, 121715 (2022); doi: 10.1016/j.saa.2022.121715

DOI 10.5162/eurosensors2026/Tu–BBS–12

Design Rules for CMOS-Compatible OECTs: Impact of Geometry and Architecture on Ionic–Electronic Transport

Nikolay Mukhin[1], Gitti L. Frey[2], Vadim Issakov[1], Liubov Bakhchova[1]
[1] Institute for CMOS Design, Technical University of Braunschweig, 38106 Braunschweig, Germany
[2] The Science and Engineering of Organic Electronics Research Group, Department of Materials Science and Engineering, Technion – Israel Institute of Technology, Haifa 3200003, Israel
nikolay.mukhin@tu-braunschweig.de, gitti@technion.ac.il, liubov.bakhchova@tu-braunschweig.de

Summary:
Organic electrochemical transistors (OECTs) are promising for biosensing, but their CMOS integration is limited by insufficient understanding of geometry-dependent transport. Here, we show that OECT behavior deviates from simple scaling due to non-uniform electrochemical doping. Using physics-based finite element modeling calibrated with experiments, we analyze short-channel planar and vertical accumulation-mode OECTs. Device architecture controls electric-field distribution and active channel volume, leading to deviations from the Bernards–Malliaras model. These results establish design rules for CMOS-compatible OECTs.

Keywords: organic electrochemical transistors (OECTs), organic mixed ionic–electronic conductors (OMIECs), device performance, geometry and architecture, CMOS compatibility

Motivation and Objectives

Organic electrochemical transistors (OECTs) are promising for biosensing due to their low-voltage operation, high transconductance (g_m), and compatibility with biochemical and flexible platforms [1]. For practical sensing systems, OECTs must be integrated with compact readout and control electronics, making CMOS-compatible operation essential. Although OECTs based on PEDOT derivatives are widely studied, recent advances in accumulation-mode OMIECs are driving a shift toward alternative materials [2,3]. Thus, accumulation-mode behavior is a key requirement, as CMOS circuits rely on normally-off transistors with low static power consumption. Accumulation-mode OECTs therefore provide a more suitable basis for complementary integration than depletion-mode devices due to their off-state operation at zero gate bias and reduced standby losses [3]. Moreover, ambipolar OMIECs [4] are of special interest as they offer additional potential for CMOS integration.

However, despite rapid materials progress, predictive modeling of accumulation-mode OECTs remains limited, particularly in understanding how geometry and architecture govern ionic transport, volumetric doping, switching dynamics, and performance trade-offs.

In this work, we address this gap by systematically investigating the influence of device geometry and architecture on the electrochemical and electronic performance of accumulation-mode n- and p-type OMIEC-based OECTs using physics-based finite element modeling (FEM) in COMSOL Multiphysics, informed by experimental data, to derive design-relevant trends for CMOS-compatible architectures.

Methodology

We employ a physics-based FEM in COMSOL Multiphysics to simulate coupled ionic–electronic transport in accumulation-mode OMIEC-based OECTs. The model self-consistently solves the Poisson–Nernst–Planck equations for ion transport and drift–diffusion equations for electronic carriers, capturing volumetric electrochemical doping within the channel. Device parameters are calibrated using experimental data to ensure physically meaningful material and transport properties. A parametric study is performed across planar, coplanar, and vertical device geometries to evaluate the impact of architecture on key performance metrics, including transconductance, switching behavior, and ionic charging dynamics. Electrochemical doping in the model is described by:

$$\mathrm{OMIEC^0 + An^- + h^+ \leftrightarrow OMIEC^+An^-}; \quad (1)$$

$$\mathrm{OMIEC^0 + Cat^+ + e^- \leftrightarrow OMIEC^-Cat^+}, \quad (2)$$

for p- and n-type OMIECs, respectively. Here, $\mathrm{OMIEC^0}$ denotes the neutral material, h^+ and e^- are hole and electron carriers, and An^- and Cat^+ represent electrolyte anions and cations. These reactions couple ionic uptake to electronic carrier density and govern channel conductivity.

Results and Discussion

To elucidate structure–property relationships in OMIEC-based OECTs, we compare planar (Fig. 1a) and vertical (Fig. 1b) architectures, focusing on how device geometry governs electric-field distribution, mixed ionic–electronic transport, and volumetric doping dynamics.

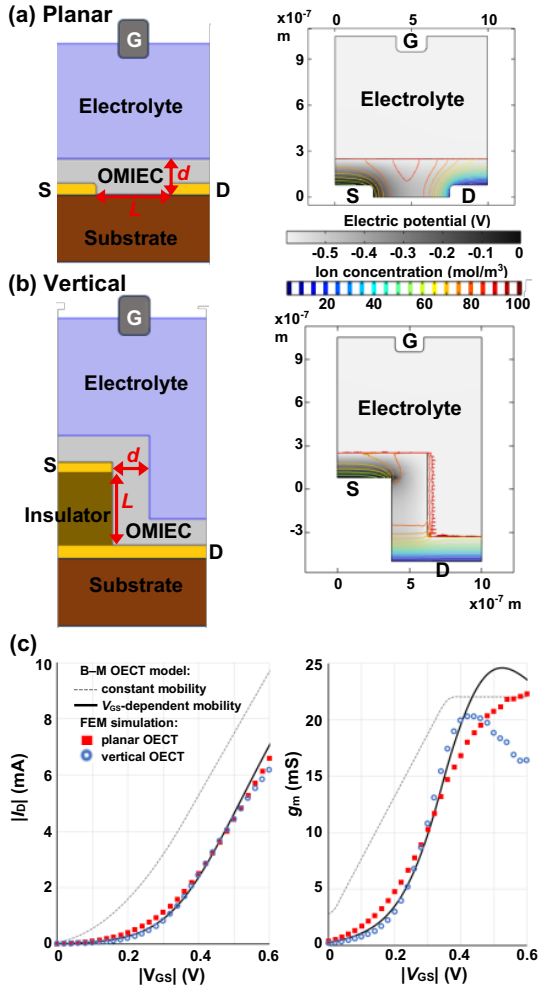

Fig. 1. (a,b) Schematic and simulated spatial distributions of electrostatic potential and anion concentration for planar (a) and vertical (b) OECTs with the same channel length (L) and height (d). (c) Transfer characteristics of a p(g2T-TT)-based OECT at V_{DS} = −0.4 V. The standard Bernards–Malliaras (B–M) model with constant mobility (grey dashed) and the modified B–M by gate voltage V_{GS}-dependent mobility (black) deviate from FEM simulations (colored dots).

Widely used Bernards–Malliaras (B–M) model [5] exhibits uniform channel penetration and geometric scaling, suggesting that planar and vertical OECTs can be described by the same simplified approximation form. However, in real cases of accumulation mode operation, charge transport is anisotropic and Fig. 1a,b suggests that electrochemical doping is spatially inhomogeneous, indicating that only a fraction of the channel volume is actively contributing to conduction. To quantify these effects, the B–M model was benchmarked against FEM simulations for both planar and vertical device configurations (Fig. 1c). Comparison of the simulated drain current (I_D) and g_m characteristics reveals systematic deviations, which can be also explained by the fact that not the entire channel volume is electrochemically active due to (i) finite ion penetration depth, (ii) contact effects, and (iii) non-uniform electric field distribution across the channel thickness (d). These effects become increasingly pronounced with decreasing channel length (L). Moreover, this limitation becomes evident in Fig. 1c, where the standard B–M model with constant mobility (grey dashed lines) systematically deviates from both FEM simulations and the gate voltage-dependent mobility modified B–M model. Despite the fact that the channel dimensions (d and L) were taken to be the same for the planar and vertical architectures (Fig. 1a,b), the FEM simulation showed different results in I_D and g_m (Fig. 1c). Decreasing L is desirable because it enables higher g_m and faster transistor response, both of which are particularly important for sensing applications. However, L-scaling introduces a trade-off between enhanced switching dynamics and increasingly dominant contact-related limitations.

Our results show that OECT performance is governed by the coupled interplay of geometry, architecture, and transport physics, and cannot be captured by simple scaling laws. These results establish geometry and architecture-aware design rules and highlight the need for V_{GS}-dependent mobility in predictive modeling of CMOS-compatible OECTs.

References

[1] N. Mukhin, A. Dietzel, V. Issakov, L. Bakhchova, Balancing Performance and Stability Characteristics in Organic Electrochemical Transistor, *Biosensors and Bioelectronics* 281, 117476 (2025); doi: 10.1016/j.bios.2025.1174

[2] E. Reyn, S. Simotko, Y. Yadav, N. Moscovich, G.L. Frey, Tunable electrochemical doping and charge transport in non-OMIEC:OMIEC blends by microstructure design, *J. of Mat. Chem. C* 14, 1164-1176 (2026); doi: 10.1039/D5TC03284A

[3] I. Uguz, D. Ohayon, S. Yilmaz, S. Griggs, R. Sheelamanthula, J.D. Fabbri, I. McCulloch, S. Inal, K.L. Shepard, Complementary integration of organic electrochemical transistors for front-end amplifier circuits of flexible neural implants, *Science Advances* 10, (2024); doi: 10.1126/sciadv.adi9710

[4] E. Stein, S. Simotko, Y. Yadav, P. Cavassin, I. McCulloch, N. Banerji, G.L. Frey, Synergistic effects in ambipolar blends of mixed ionic–electronic conductors, *Materials Horizons* 12, 5733-5748 (2025); doi: 10.1039/D5MH00293A

[5] D.A. Bernards, G.G. Malliaras, Steady-State and Transient Behavior of Organic Electrochemical Transistors, *Adv. Funct. Mat.* 17, 3538-3544 (2007); doi: 10.1002/adfm.200601239

DOI 10.5162/eurosensors2026/Tu–BBS–13

Competitive Electrochemical Detection of SARS-CoV-2 Antigen on a 2D $MoWSe_2$-Based Biosensor

Siriporn Anuthum, Tengfei Yao, Jaroon Jakmunee, Kontad Ounnunkad
Department of Chemistry, Faculty of Science, Chiang Mai University, Chiang Mai 50200, Thailand
kontad.ounnunkad@cmu.ac.th

Summary:
The ongoing spread of severe acute respiratory syndrome coronavirus 2 (SARS-CoV-2) has posed significant global public health challenges, highlighting the need for rapid and reliable surveillance strategies. A competitive electrochemical biosensor based on two-dimensional molybdenum tungsten diselenide was developed for SARS-CoV-2 antigen detection in wastewater. Using antibody-conjugated polyethyleneimine-coated gold nanoparticles as nanotags and thionine as a signal amplifier, the sensor achieves sensitive detection with a low limit of detection, a wide detection range, stability, and selectivity.

Keywords: electrochemical immunosensor, competitive detection, SARS-CoV-2, 2D $MoWSe_2$, PEI-AuNPs

Background, Motivation, and Objective

On March 11, 2020, the World Health Organization officially declared the COVID-19 outbreak a global pandemic. Since then, a diverse array of biosensing technologies has been developed to enable efficient and accurate detection of the virus [1]. Biosensors targeting the spike (S) protein have attracted significant attention due to their critical role in viral entry via ACE2 receptor binding. The urgent need for reliable virus monitoring, especially in complex matrices such as wastewater, has driven rapid advancements in biosensor development [2,3]. Here, we present a competitive electrochemical immunosensor for rapid SARS-CoV-2 detection utilizing a novel single-component 2D $MoWSe_2$ material integrated onto a screen-printed carbon electrode (SPCE), adapted from previous research [4], offering a more time-efficient and accessible alternative to conventional diagnostic methods.

Description of the New Method or System

A competitive immunosensor was developed using RBD antibody (Ab)/PEI-AuNPs nanotags for the detection of SARS-CoV-2 protein via differential pulse voltammetry (DPV). The detection mechanism relies on competitive binding between the target antigen and nanotags. Only unbound RBD Ab/PEI-AuNPs nanotags attach to the electrode surface, while antibody-antigen immune complexes are subsequently washed away. Consequently, the electrochemical signal is directly proportional to unbound nanotags and inversely related to antigen concentration. The sensing platform was fabricated by modifying SPCE with 2D $MoWSe_2$, followed by thionine adsorption, SARS-CoV-2 protein immobilization, and BSA blocking, yielding BSA/SARS-CoV-2 protein/TH/2D $MoWSe_2$-SPCE. Unlike conventional competitive assays, where signals decrease with antigen, reduced surface-bound nanotags in our design lower steric hindrance, enhancing electron transfer through the TH redox mediator and producing an increasing electrochemical signal, as illustrated in Fig. 1.

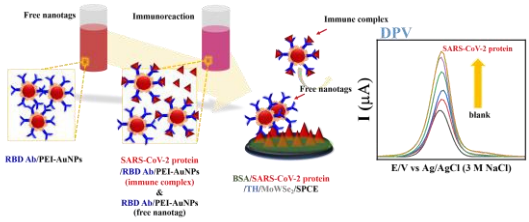

Fig. 1. Fabrication of a competitive immunosensor for the detection of SARS-CoV-2 proteins.

Results

SEM images confirmed successful modification of SPCE with uniform rectangular $MoWSe_2$ nanosheets (Fig. 2). Electrochemical characterization in PBS (pH 7.4) with 5.0 mM $[Fe(CN)_6]^{4-/3-}$ showed enhanced peak currents (i_{pa}: 93.15 μA, i_{pc}: −82.28 μA) and reduced peak separation (0.249 V) for 2D $MoWSe_2$-SPCE compared to bare SPCE (Fig. 3a). EIS confirmed improved conductivity, with charge transfer resistance (R_{ct}) decreasing from 1383 to 829.4 Ω (Fig. 3b). Thionine (5.0 mM) was adsorbed as a signal amplifier, followed by SARS-CoV-2 protein immobilization and BSA blocking, yielding the final platform: BSA/SARS-CoV-2 protein/TH/2D $MoWSe_2$-SPCE (Fig. 1). For competitive

detection, a mixture of RBD Ab/PEI-AuNPs nanotags and SARS-CoV-2 protein was incubated and applied to the modified electrode, followed by DPV measurement. The current response increased with antigen concentration due to the competitive binding mechanism (Fig. 4a). A linear relationship was observed between the peak current and the logarithm of antigen concentration: I (μA) = 4.44 log [SARS-CoV-2 proteins (pg/mL)] − 1.97 (R^2 = 0.991), over a range of 0–50,000 pg/mL (Fig. 4b). The LOD was 0.496 ng/mL. The sensor demonstrated strong potential for sensitive SARS-CoV-2 detection in environmental and clinical samples.

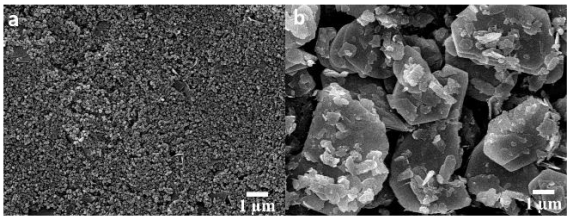

Fig.2. SEM images of (a) bare and (b) 2D $MoWSe_2$-modified SPCEs.

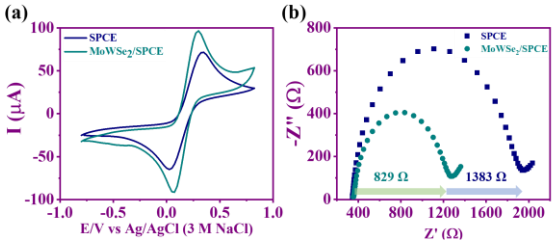

Fig. 3. (a) CVs and (b) Nyquist plots of bare and 2D $MoWSe_2$-modified SPCE in contact with 0.010 M PBS (pH 7.4) containing 5.0 mM $[Fe(CN)_6]^{3-/4-}$.

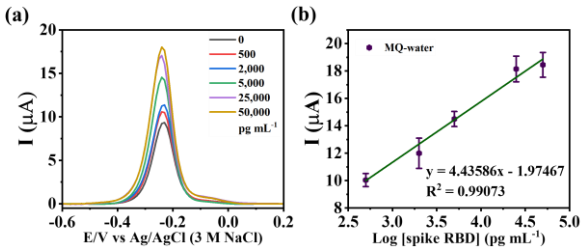

Fig. 4. (a) DPV responses and (b) corresponding calibration curve obtained from the detection of SARS-CoV-2 protein at various concentrations.

References

[1] D. Shahdeo, A. Roberts, G.J. Archana, N.S. Shrikrishna, S. Mahari, K. Nagamani, and S. Gandhi, “Label free detection of SARS CoV-2 receptor binding domain (RBD) protein by fabrication of gold nanorods deposited on electrochemical immunosensor (GDEI)”, Biosensors and Bioelectronics, 212 (2022) 114406.

[2] H. Zhao, F. Liu, W. Xie, T.-C. Zhou, J. OuYang, L. Jin, H. Li, C.-Y. Zhao, L. Zhang, J. Wei, Y.-P. Zhang, and C.-P. Li, “Ultrasensitive supersandwich-type electrochemical sensor for SARS-CoV-2 from infected COVID-19 patients using a smartphone”, Sensors and Actuators B, 327 (2021) 128899.

[3] D. Kadadou, L. Tizani, V.S. Wadi, F. Banat, H. Alsafar, A.F. Yousef, and S.W. Hasan, “Detection of SARS-CoV-2 in clinical and environmental samples using highly sensitive reduced graphene oxide (rGO)-based biosensor”, Chemical Engineering Journal, 453 (2023) 139750.

[4] S. Anuthum, J. Jakmunee, and K. Ounnunkad, “Dual-mode electrochemical biosensor based on gold nanoparticles/two-dimensional $MoWS_2$/graphene oxide composite for detection of glycated albumin and glucose”, ACS Applied Bio Materials, 8 (2025) 5215-5228.

DOI 10.5162/eurosensors2026/Tu–BBS–15

Optimization of ssDNA Immobilization for a CRISPR/Cas12a Electrochemical Biosensor for Friedreich's Ataxia

Luana Vohlbrecht de Souza[1], Aline Macedo Faria[1], Talita Mazon[1]
[1]Centro de Tecnologia da Informação Renato Archer, Ministério da Ciência, Tecnologia e Inovação, Campinas, São Paulo, Brazil,
talita.mazon@cti.gov.br

Summary:

An electrochemical biosensor based on CRISPR-Cas12a was developed by optimizing ssDNA immobilization on gold electrodes. Electrochemical impedance spectroscopy (EIS) was employed to characterize each modification step and the collateral cleavage activity. The optimized interface allowed Cas12a accessibility and resulted in a decrease in charge transfer resistance after collateral DNA cleavage. These results demonstrate that precise interface control is essential for developing CRISPR-based diagnostic platforms.

Keywords: CRISPR Cas12a, electrochemical biosensor, DNA immobilization, gold electrode

Introduction and Objective

Friedreich's ataxia is a rare inherited neurodegenerative disorder. However, their early diagnosis remains a critical challenge due to the low concentration of biomarkers [1]. Electrochemical biosensors emerge as a powerful analytical tool to overcome this limitation, offering outstanding sensitivity and specificity [2]. Nevertheless, the performance of DNA-based electrochemical sensors relies heavily on the structural organization of the sensing interface. Specifically, controlling the DNA probe density and immobilization dynamics is crucial to optimize signal transduction and ensure accessibility for Cas12a collateral activity, a mandatory requirement for CRISPR-based platforms. In this work, we investigate the influence of ssDNA surface density and immobilization time on the electrochemical behavior of screen-printed gold electrodes.

Methodology

The miniaturized platform consists of a gold working electrode, a counter electrode, and an Ag reference electrode. To modulate the surface coverage, a thiolated ssDNA probe (27-mer) was immobilized at varying concentrations (2.5 and 5.0 µM) and incubation periods (1 and 2 h). Subsequently, the sensing interface was backfilled with 6-mercapto-1-hexanol (MCH) to ensure proper probe orientation and prevent nonspecific binding. The stepwise interfacial modifications were monitored by electrochemical impedance spectroscopy (EIS) using a $[Fe(CN)_6]^{3-/4-}$ redox probe. The schematic illustration of the working principle for detection by a CRISPR/Cas12a system are illustrated in Figure 1.

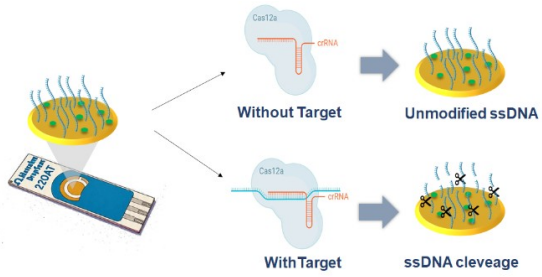

Fig. 1. Schematic illustration of the working principle for detection by a CRISPR/Cas12a system.

Results

Polyacrylamide gel electrophoresis (PAGE) was used to evaluate the molecular components of the CRISPR/Cas12a system before electrochemical characterization. Individual lanes confirmed the integrity of the crRNA, ssDNA reporter and the target oligonucleotide. The control reactions lacking either the target DNA or the crRNA showed electrophoretic profiles distinct from the complete CRISPR reaction, indicating that activation of Cas12a depends on the simultaneous presence of both components. The different migration pattern observed for the complete reaction is consistent with target-dependent activation of Cas12a and supports the subsequent electro-chemical evaluation of the sensing platform.

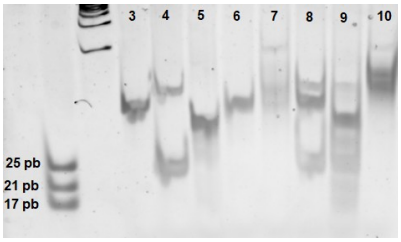

Fig. 1. 20% PAGE analysis of the CRISPR/Cas12a system. Lanes 1–2: DNA ladder; lane 3: crRNA; lane 4: ssDNA reporter; lane 5: target DNA; lane 6: crRNA/Cas12a; lane 7: crRNA/Cas12a +target DNA; lane 8: crRNA/Cas12a + ssDNA reporter; lane 9: CRISPR reaction without crRNA; lane 10: complete CRISPR/Cas12a reaction.

To optimize the sensor fabrication, the effect of ssDNA reporter concentration was first investigated (Figure 2a). The higher charge transfer resistance (R_{ct}) obtained with 2.5 µM ssDNA suggests the formation of a well-oriented and homogeneous DNA/MCH mixed monolayer, which effectively repels the anionic redox probe through electrostatic and steric hindrances. In contrast, a higher probe concentration (5 µM) may induce steric crowding during immobilization, hindering proper molecular rearrangement and efficient MCH backfilling. This can lead to a less organized interfacial layer with disordered DNA alignment, allowing easier access of the redox probe to the electrode surface and resulting in lower R_{ct} values. Using the optimized ssDNA concentration (2.5 µM), the effect of immobilization time was evaluated (Figure 2b). Although a slightly lower R_{ct} was observed after 2 h compared to 1 h, the longer incubation time was selected because it may favor the rearrangement of the immobilized DNA into a more ordered monolayer. Such structural reorganization can improve probe orientation and produce a more homogeneous sensing interface without necessarily increasing the R_{ct}. Therefore, an immobilization time of 2 h was adopted for the subsequent experiments.

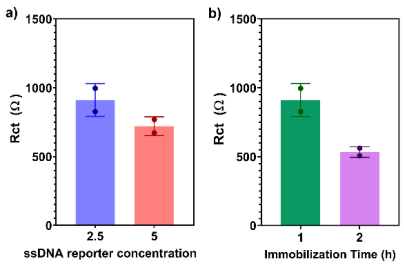

Fig. 2. Optimization of sensor modification conditions (R_{ct}): (a) ssDNA reporter concentration (fixed time: 2 h); (b) immobilization time (fixed concentration: 2.5 µM).

The electrochemical response of the sensor during the stepwise modification process is shown in Figure 3. The initial immobilization of the ssDNA reporter on the bare gold electrode led to a characteristic impedance profile, confirming successful probe attachment. Subsequent surface backfilling with MCH resulted in a slight R_{ct} increase, indicating the successful displacement of nonspecifically adsorbed DNA segments and the passivation of remaining bare gold sites. This modification ensures proper probe orientation while preventing nonspecific interactions. After incubation with the activated CRISPR/Cas12a complex, a decrease in R_{ct} was observed (Figure 3, blue curve), consistent with the collateral cleavage of the immobilized ssDNA reporter. This partial removal of the negative DNA layer facilitates electron transfer of the redox probe, confirming the efficiency of the Cas12a trans-cleavage activity at the sensing interface.

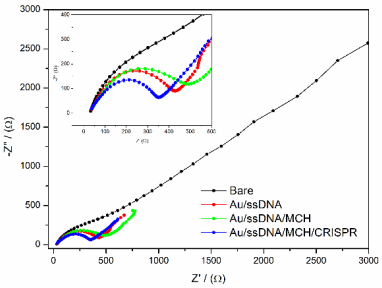

Fig. 3. Nyquist plots for the stepwise modification procedure. The inset shows an enlarged view of the modification steps.

The proposed platform was applied to the detection of a model target, demonstrating its potential for CRISPR-based electrochemical detection, with potential applications in genetic disorders such as Ataxia de Friedreich. These results highlight the critical role of probe density and surface organization in the design of efficient electrochemical CRISPR biosensors.

Acknowledgements

The authors thank FINEP, Vistobio and CNPq (406191/2024-7) for financial support.

References

[1] S. H. Khatami, H. Khanifar, A. Movahedpour, M. Taheri-Anganeh, S.Ehtiati, H. Khanifar, Electrochemical biosensors in early detection of Parkinson disease, *Clinica Chimica Acta* 565, 120001 (2025); doi: 10.1016/j.cca.2024.120001

[2] A. Cetinkaya, S. I. Kaya, S. A. Ozkan, Biomedical field applications of electrochemical biosensors as diagnostic tools: A short review, *Current Opinion in Electrochemistry* 53, 101738 (2025); doi: 10.1016/j.coelec.2025.101738

DOI 10.5162/eurosensors2026/Tu–BBS–16

Biochemical Modulation of Ionic Transport in Asymmetric Nanochannels for Label-Free Biosensing

L. Miguel Hernandez Parra[1,2],
M. Lorena Cortez[1], Maria Eugenia Toimil-Molares[2,3], Waldemar Marmisollé[1], Omar Azzaroni[1]
[1] Instituto de Investigaciones Fisicoquímicas Teóricas y Aplicadas (INIFTA), Departamento de Química, Facultad de Ciencias Exactas, Universidad Nacional de La Plata (UNLP), CONICET, Boulevard 113 y 64, La Plata 1900, Argentina,
[2] GSI Helmholtzzentrum für Schwerionenforschung, Darmstadt 64291, Germany
[3] Technische Universitat Darmstadt, Darmstadt 64287, Germany
lumihe@inifta.unlp.edu.ar

Summary:
Biomimetic solid-state asymmetric nanochannels serve as platforms for the integration of enzymes and functional polymers. Enzymatic reactions generate localized pH variations near the nanochannel surface, which are transduced by polymeric layers into measurable changes in iontronic current through acid–base-dependent modulation of surface charge within the multilayer assembly. The asymmetric bullet-shaped nanochannel geometry enhances the sensing response through nanoconfinement effects and amplified ionic current rectification, providing a promising strategy for the development of label-free biosensing platforms.

Keywords: Solid-state nanochannels, Ion-current rectification, Biosensing, Bioelectronics.

Background, Motivation and Objective

Nanofluidic systems based on asymmetric nanochannels have emerged as promising platforms for biosensing due to their ability to translate molecular interactions into measurable ionic current responses. Their sensing mechanism relies on the modulation of surface charge properties and ionic conductance within confined nanochannels, enabling the detection of chemical and biochemical processes without the need for molecular labeling. By integrating functional materials, we investigate the development of iontronic sensing platforms based on enzyme–polyelectrolyte-functionalized asymmetric nanochannels, where variations in the local physicochemical environment are transduced into changes in ionic current. This approach provides a versatile framework for the development of label-free biosensors for biomarker detection [1]. Current efforts focus on optimizing sensor performance, strategies toward real sample analysis are being implemented, together with improvements in fabrication and functionalization processes, to evaluate the potential of these systems for practical sensing applications.

Description of the New Method or System

The ion-track etching technique (Fig.1) provides a robust and well-established approach for the fabrication of solid-state nanochannels, and previous studies have demonstrated the proof-of-concept of nanochannel-based biosensing approaches [2]. However, the optimization of these systems toward practical applications, including measurements in complex samples, remains a significant challenge. In this work, we report the evaluation of asymmetric nanochannel-based biosensing platforms under real and complex sample conditions. Furthermore, we are developing sample pretreatment strategies and improving fabrication protocols to enable reliable single-nanochannel-based biosensing. These advances aim to bridge the gap between fundamental iontronic sensing mechanisms and their implementation in practical analytical applications.

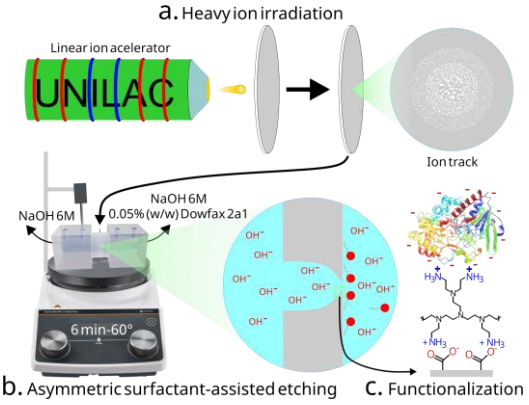

Fig. 1. Ion-track etching technology for bullet-shaped solid-state nanochannel fabrication. (a) Irradiation, (b) Wet etching, (c) Electrostatic surface modification.

Results

In this work, we present a biomimetic sensing platform based on asymmetric bullet-shaped nanochannels fabricated in polyethylene terephthalate (PET) membranes and functionalized through layer-by-layer supramolecular assembly of enzymes and poly(allylamine hydrochloride) (PAH) or polyetherimide (PEI). The cationic polyelectrolyte acts both as a structural component and as a pH-responsive transducer, converting enzyme-induced local pH variations into surface charge modulation within the nanochannel. These changes directly influence ionic transport, generating an iontronic signal that correlates with the enzymatic reaction occurring in the presence of the target analyte. The sensing strategy is applicable to different enzymatic systems capable of producing local physicochemical changes, providing a versatile framework for the detection of multiple biomarkers.

The platform was evaluated in terms of response time, pH dependence, storage stability, inter- and intra-batch reproducibility, and selectivity toward potential interfering species. In addition, sample pretreatment strategies were developed to reduce nonspecific adsorption and improve sensor performance in complex matrices. These results demonstrate the potential of enzyme–polyelectrolyte-functionalized asymmetric nanochannels as a robust and adaptable platform for label-free iontronic biosensing in practical analytical applications.

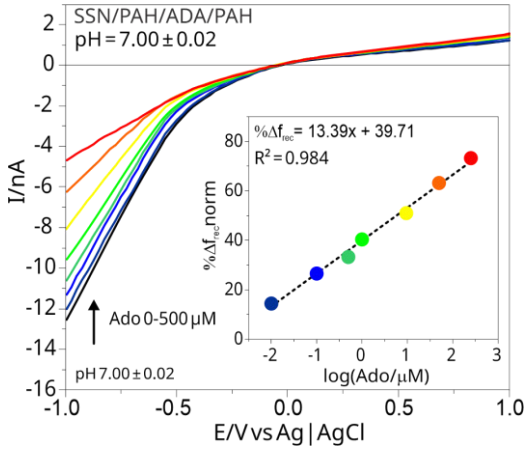

Fig. 2. Sensing performance of an adenosine deaminase (ADA)/PEI modified nanochannel to adenosine (Ado) in 10 mM KCl-0.05 mM HEPES.

The nanochannel response was quantified by the rectification factor (f_{rec}), as defined in Eq. (1,2). This parameter reflects the degree of ionic current rectification at steady state for each fixed substrate concentration (See Fig. 2).

Eq. 1. $f_{rec} = +\frac{I(-1V)}{I(1V)}$

Eq. 2. $\%\Delta f_{rec}norm = \left(\frac{|f_{rec}initial| - f_{rec}}{|f_{rec}initial|}\right) * 100$

To evaluate the performance of the platform in complex matrices, a simulated body fluid (SBF) containing high concentrations of BSA, ATP, and inorganic phosphate was selected as a model sample. A pretreatment and dilution strategy was implemented to minimize nonspecific interactions and matrix effects, enabling the analysis of spiked SBF samples using the functionalized nanochannel (Fig. 3).

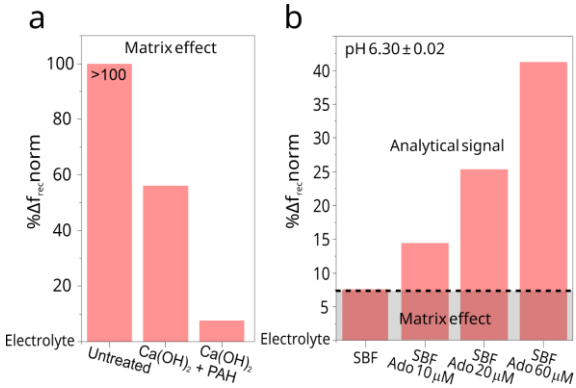

Fig. 3. Response of an ADA/PEI-functionalized nanochannel for Ado detection in SBF using 10 mM KCl and 0.05 mM HEPES as the supporting electrolyte. (a) Sample pretreatment procedure. (b) Measurement of adenosine-spiked pretreated SBF samples.

Although the matrix effect was effectively reduced by approximately 93%, it still affected the analytical performance of the system. In complex samples, the quantification limit increased and linear range decreased compared with measurements performed in electrolyte solution (Tab. 1). Nevertheless, the iontronic response of the functionalized nanochannels remained well correlated with substrate concentration in both electrolyte solution and diluted SBF, demonstrating the feasibility of the proposed sensing strategy for complex sample analysis [3].

Tab. 1: ADA/PEI-functionalized nanochannel sensing parameters.

Sample	LOQ (µM)	Linear range (µM)
Electrolyte	0.01	0.01-500
SBF	10	10 - 300

References

[1] P. Apel, Track etching technique in membrane technology, *Radiation measurements* 34 (1-6), 559-566(2001); doi: 10.1016/S1350 4487(01)00228-1

[2] L. M. Hernandez Parra, O. Azzaroni, W. A Marmisollé, Enzyme-Based Single Solid-State Nanochannel Biosensors, *Chemosensors* 13(8), 275(2025); doi: 10.3390/chemosensors13080275

[3] L. M. Hernandez Parra, M. E. Gramajo, , L. O. Maffoni, G. Laucirica, A. S. Peinetti, M. L. Cortez, M. E. Toimil-Morales, W. Marmisollé, Omar Azzaroni, Single nanochannel-based iontronic detection of adenosine, *Sensors and Actuators B: Chemical* 452, 139453(2026); doi: 10.1016/j.snb.2026.139453

DOI 10.5162/eurosensors2026/Mo–CHS–01

Rapid and Selective Sub-ppm Hydrogen Sulfide Detection using rGO/ In_2O_3 Heterojunction Sensor

Tanya Sood[1], P. Poornesh[1], Saikat Chattopadhyay[2]
[1] Manipal Institute of Technology, Manipal Academy of Higher Education, Manipal, India
[2] Department of Physics, School of Basic Sciences, Manipal University Jaipur, Jaipur 303007, India
Corresponding Author's e-mail address soodtanya31@gmail.com

Summary:

Trace level detection of toxic gases using chemiresistive sensors remain a significant challenge. In this work, spin coated reduced graphene oxide/ Indium oxide nanocomposite sensor was developed for hydrogen sulfide sensing. The sensor showed rapid response and concentration dependent sensing behavior at the optimized operating temperature. The improved sensing performance is attributed to structural defects, porous morphology, and heterojunction assisted interfacial effects in the nanocomposite. These results highlight the potential of the nanocomposite for trace level hydrogen sulfide detection.

Keywords: rGO/ In_2O_3 heterojunction, hydrogen sulfide sensing, sub-ppm detection, porous morphology, chemiresistive sensor

Title

Rapid and Selective Sub-ppm Hydrogen Sulfide Detection using rGO/ In_2O_3 Heterojunction Sensor.

Background, Motivation and Objective

H_2S is a highly toxic and corrosive gas, and its reliable detection at low concentrations is essential for environmental monitoring and health protection. Although metal oxide semiconductor sensors have been widely studied for H_2S sensing, their practical use is often limited by poor selectivity. In this context, rGO-based heterostructures have attracted considerable attention because of their large surface area, porous morphology, and ability to promote rapid charge transport [1]. In_2O_3 is also a promising sensing material due to its good electrical conductivity, chemical stability, and defect-assisted surface activity [2]. In this work, a sol gel assisted spin coated rGO/ In_2O_3 nanocomposite sensor is developed for enhanced H_2S detection, with emphasis on the role of heterojunction assisted interfacial effects in the sensing mechanism.

Description of the New Method or System

This work presents a sol gel assisted spin coated rGO/ In_2O_3 nanocomposite sensor for selective trace level H_2S detection. The novelty lies in integrating rGO with In_2O_3 to create a heterojunction-based sensing platform that combines enhanced charge transport with defect rich surface reactivity. The sensor achieved sub-ppm detection down to 0.5 ppm and showed a response of 66 ± 2 % at 4 ppm H_2S at an operating temperature of 250 ℃. The observed performance is attributed to structural defects, porous morphology, which assists adsorption, and interfacial resistance modulation within the nanocomposite. Graphene oxide was synthesized by a modified Hummers' method and mixed with In_2O_3 precursor to form a homogeneous coating solution. The sensing film was deposited by spin coating, followed by preheating and annealing to obtain the active layer as shown in Fig. 1. These results demonstrate a simple and scalable approach for improved H_2S sensing.

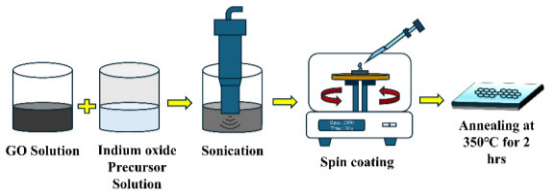

Fig. 1. Schematic diagram of spin coated rGO/ In_2O_3 thin film.

Results

Structural and Morphological Investigations

Fig. 2 (a) shows the XRD patterns of the rGO/ In_2O_3 composite films, confirming the polycrystalline cubic bixbyite structure of In_2O_3. The characteristic rGO peak was not distinctly visible, likely due to its low concentration and weak diffraction intensity. Fig. 2 (b) shows the Raman spectra with the characteristic D and G bands,

further confirming the successful formation of the rGO/ In_2O_3 composite sensing layer.

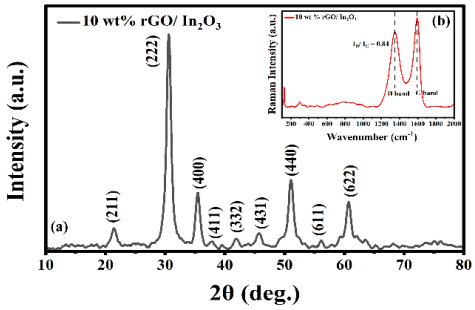

Fig. 2. (a) XRD pattern (b) Raman spectra of rGO/ In_2O_3 nanocomposites.

Fig. 3 (a) shows the surface morphology of the rGO/ In_2O_3 film, indicating a porous nanostructured surface. Fig. 3 (b) shows the EDX spectrum, confirming the elemental composition of the nanocomposite sensing layer.

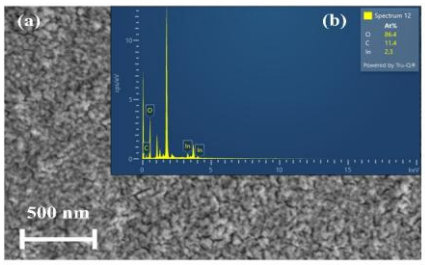

Fig. 3. (a) FESEM and (b) EDS spectra of rGO/ In_2O_3 nanocomposites.

Gas Sensing Measurements

Fig. 4 illustrates the gas sensing mechanism of the rGO/ In_2O_3 nanocomposite, governed by oxygen adsorption and heterojunction assisted charge modulation at the interface. In air, adsorbed oxygen species induce electron depletion, while exposure to H_2S releases electrons back to the sensing layer and decreases the resistance. The enhanced response is attributed to interfacial charge transfer and surface reactions within the nanocomposite.

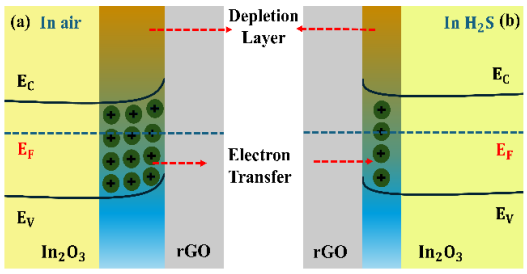

Fig. 4. Schematic representation of rGO/ In_2O_3 gas sensing mechanism (a) in air (b) in H_2S.

Fig. 5 shows the dynamic response curves of the sensor, revealing a progressive increase in response with increasing H_2S concentration and confirming effective concentration dependent sensing. The response and recovery times, along with the sensor response values, are summarized in Tab.1. The sensor response was calculated using Eq.(1).

$$Sensor\ Response\ (\%) = \frac{R_a - R_g}{R_a} \times 100 \qquad (1)$$

The response process was consistently faster than recovery, suggesting rapid surface adsorption followed by slower desorption. The sensor achieved a maximum response of 66 ± 2 % at 4 ppm H_2S and detected concentrations as low as 0.5 ppm, demonstrating its potential for trace level gas monitoring.

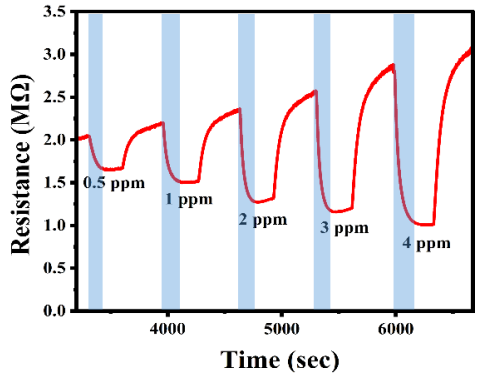

Fig. 5. Dynamic response curves of rGO/ In_2O_3 gas sensor for varying H_2S gas concentration.

Tab. 1: Response Time, recovery time and sensor response of rGO/ In_2O_3 sensor.

Concentration (ppm)	Response Time (s)	Recovery Time (s)	Sensor Response (%)
0.5	69 ± 6	141 ± 26	18 ± 6
1	76 ± 7	153 ± 18	30 ± 5
2	80 ± 7	174 ± 12	39 ± 10
3	73 ± 7	167 ± 15	57 ± 1
4	119 ± 12	168 ± 7	66 ± 2

References

[1] P. Leangtanom, A. Wisitsoraat, A. Tuantranont, N. Chanlek, P. Pookmanee, S. Satienperakul, S. Phanichphant, V. Kruefu, Microwave-assisted hydrothermal/ impregnation synthesis of Cu_2O-decorated rGO/ In_2O_3 nanorices for sensitive SO_2 gas sensors, ACS Applied Nano Materials 6, 12980-12990 (2023); doi: 10.1021/acsanm.3c01712.

[2] Tanya Sood, Saikat Chattopadhyay, P. Poornesh, Predictive mixed-gas detection using rGO/ In2O3 nanocomposite sensors assisted by machine learning, Nanoscale Advances 8, 1958-1974 (2026); doi: 10.1039/D5NA01092F.

DOI 10.5162/eurosensors2026/Mo–CHS–02

Humidity Enhance the Isopropyl Alcohol Detection by Co-Mn Oxide

Reinaldo dos Santos Theodoro[1,2], Matteo D'Andria[2], Michael Pereira Martins[2] Diogo Paschoalini Volanti[1], Andreas T. Güntner[2]
[1] São Paulo State University (UNESP), Rua Cristóvão Colombo 2265, 15054-000 São José do Rio Preto, Brazil,
[2] ETH Zurich, CH-8092 Zurich, Switzerland
andreas.guentner@hsl.ethz.ch

Summary:
Humidity is considered a major challenge in gas sensing applications. In this context, manganese-based sensing materials have attracted increasing interest due to their tolerance to humid environments. Here, we report a cobalt-manganese mixed oxide capable of detecting isopropyl alcohol at ppb levels under high humidity conditions. Remarkably, humidity enhances the sensing performance, resulting in a boost in sensitivity.

Keywords: Metal oxides, manganese-based oxides, gas sensing, humidity-enhanced sensing, isopropyl alcohol

Background

Isopropyl alcohol (IPA) is a volatile organic compound (VOC) that, together with acetone, can serve as a potential biomarker in diabetic breath analysis and lipid metabolism studies [1]. In addition, IPA can be used as a marker of air quality in controlled environments, such as cleanrooms in pharmaceutical and device manufacturing [2]. In this context, IPA emerges as an alternative marker for various field applications. However, a major limitation is the influence of humidity, which often compromises the sensing performance of many metal oxide (MO_x) sensors [3]. Here, we describe a p-type cobalt–manganese oxide capable of detecting IPA under high humidity conditions, where the sensing material exhibits enhanced sensitivity toward IPA.

Experimental

Cobalt–manganese oxide-based sensors and nanoparticles were fabricated by flame spray pyrolysis (FSP) [4]. The precursor solution consisted of Co(II) 2-ethylhexanoate and Mn(II) 2-ethylhexanoate dissolved in xylene, which were atomized and combusted in a flame with a precursor/dispersion (P/D) ratio of 5/5. The resulting nanoparticles were directly deposited onto Al_2O_3 substrates with interdigitated Pt electrodes and an integrated resistance temperature detector. In parallel, nanoparticles were collected on a filter positioned above the flame. Both samples were subsequently annealed at 500 °C for 5 h.

The sensor was mounted on dedicated holders and connected to a gas mixing system using hydrocarbon-free synthetic air and calibrated mass flow controllers to achieve the desired gas composition [5]. The sensitivity (S) was defined as follows:

$$S = Rg/Ra - 1 \quad (1)$$

Results

Co-Mn oxide synthesized by the FSP was characterized by X-ray diffraction (XRD, Fig 1), scanning electron microscopy (SEM), and energy-dispersive X-ray spectroscopy (EDX).

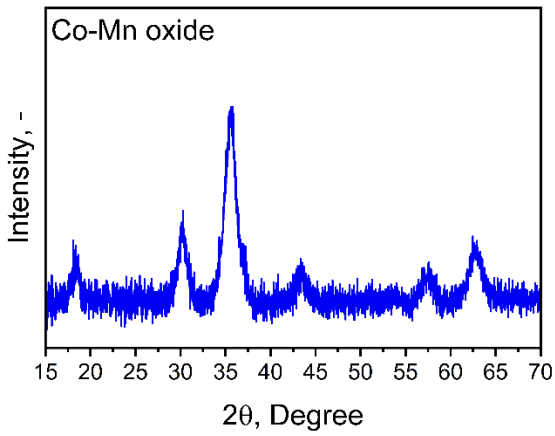

Fig. 1. XRD data of Co-Mn oxide.

Fig. 2 shows sensor response of the Co-Mn oxide sensor when exposed to IPA (1000 ppb) at 310 °C under different relative humidity levels (0

– 90% RH). Under humid conditions, the Co-Mn oxide sensor exhibits greater conductivity modulation than in dry air, suggesting a boosting effect of surface-adsorbed hydroxyl groups during interaction with IPA. This enhanced conductivity modulation reflects higher sensitivity under humid conditions.

These findings highlight the remarkable ability of manganese oxides to withstand humidity effects. Moreover, water vapor does not act as an interfering factor; instead, it plays a critical role in enhancing the sensing performance for the detection of gases and VOCs. Therefore, Mn oxide-based sensing materials present strong potential to overcome a common challenge in gas sensing and enable improved performance in real-world applications.

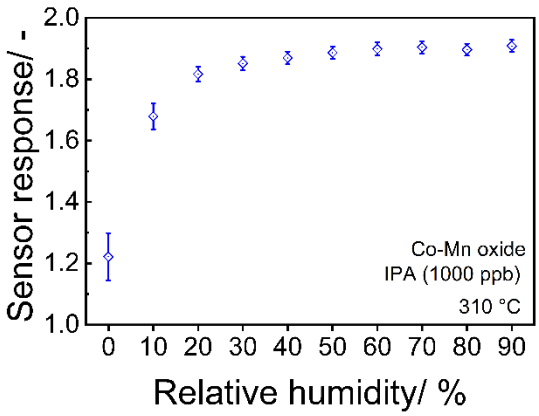

Fig. 2. Sensor response of Co-Mn oxide sensor to 1000 ppb of IPA under different relative humidity (RH) conditions.

The combination of cobalt and manganese oxides for IPA detection under humid conditions highlights the intrinsic ability of manganese-based materials to overcome humidity-related limitations. This finding opens new avenues for the rational design of advanced sensing materials, where the incorporation of manganese with transition metals, rare earths, or noble metals can further enhance sensitivity, selectivity, and long-term stability. Notably, humidity robustness – typically a major challenge in gas sensing – is inherently addressed by manganese oxides, positioning them as key materials for next-generation sensors in real-world applications.

References

[1] Li, W.; Liu, Y.; Liu, Y.; Cheng, S.; Duan, Y. Exhaled Isopropanol: New Potential Biomarker in Diabetic Breathomics and Its Metabolic Correlations with Acetone. RSC Adv. 2017, 7 (28), 17480–17488. doi: 10.1039/C7RA00815E.

[2] T. Eaton, Cleanroom airborne particulate limits and 70% isopropyl alcohol: a lingering problem for pharmaceutical manufacturing?, PDA Journal of Pharmaceutical Science and Technology 63, 559–567 (2009); doi:10.5731/pdajpst.2009.00634

[3] Theodoro, R. S.; Santos, G. S. M.; D'Andria, M.; Gropelo, H. S.; Kravecz, S.; Güntner, A. T.; Volanti, D. P. Air Pollution Monitoring with Nanoscaled Materials in Chemoresistive Gas Sensors. ACS Appl. Mater. Interfaces 2026, 18 (10), 14473–14520. doi:10.1021/acsami.5c24099

[4] Mädler, L.; Kammler, H. K.; Mueller, R.; Pratsinis, S. E. Controlled Synthesis of Nanostructured Particles by Flame Spray Pyrolysis. J. Aerosol Sci. 2002, 33 (2), 369–389. doi:10.1016/S0021-8502(01)00159-8.

[5] D'Andria, M., Krumeich, F., Yao, Z., Wang, F. R., Güntner, A. T. (2024). Structure-Function Relationship of Highly Reactive CuO_x Clusters on Co_3O_4 for Selective Formaldehyde Sensing at Low Temperatures. Advanced Science, 11(10), 2308224, (2024); doi:10.1002/ADVS.202308224

Acknowledgements

This work was sponsored by São Paulo Research Foundation (FAPESP); Process numbers: 2020/06421-1, 2022/05381-1, and 2024/12700-1.

DOI 10.5162/eurosensors2026/Mo–CHS–03

UV-light activated ZnO for ppb level NO_2 detection: influence of modified Pechini synthesis route

Amokrane Yasmine, Bendahan Marc, Bernardini Sandrine
Aix Marseille Univ, Univ Toulon, CNRS, IM2NP, Marseille, France
Corresponding Author's e-mail address: yasmine.amokrane@im2np.fr

Summary:

Zinc oxide (ZnO) nanoparticles have been successfully synthesized by modified Pechini process. To investigate the effect of additives on low temperature NO_2 detection, citric acid (CA), ethylene glycol (EG) and nitric acid (HNO_3) were used. The results showed that all sensors were able to detect NO_2 at near-room temperature, while the addition of ethylene glycol and nitric acid led to the highest response under UV light illumination. This study provides an easy and efficient way to obtain ZnO nanoparticles highlighting their potential for low temperature gas sensing.

Keywords: ZnO, polymer precursor method, gas sensing, drop coating, light irradiation.

Background, Motivation and objective

Resistive gas sensors based on semiconducting metal oxide are the mainly focus for atmospheric pollutants detection due to their high sensitivity and low cost. However, they present the disadvantage of elevated operating temperatures (up to 500°C) to activate gas-solid interactions [1], leading to high energy consumption and long-term instability.

Light activation has emerged as a promising strategy to enable room temperature gas detection by modulating the concentration of photo-generated electron-hole pairs, thereby enhancing sensing performances. This approach aligns with the growing demand for high precision and low power air quality monitoring networks, driven by concerns over rising global mortality rates linked to environmental risk factors. Thus, the development of low power semiconducting metal oxides sensors (SMOX) with low NO_2 detection limit is of particular importance, given its toxicity at concentrations as low as 100 ppb [2].

This work investigates ZnO thin films synthesized via a modified Pechini method for NO_2 sensing. This polymeric gel route is based on the use of a hydroxyl carboxylic acid (citric acid) and a polyhydroxyl alcohol (ethylene glycol) [3]. While the amount of ethylene glycol and solution pH are known to influence ZnO morphology [4], their role in UV-light assisted gas sensing has received less attention. Therefore, the objective of this work is to correlate Pechini synthesis parameters with ZnO morphology and NO_2 sensing performance at low operating temperature.

Methodology and experimental setup

All analytic grade reagents were used as received. Zinc nitrate ($Zn(NO_3)_2.6H_2O$, 99%), and ACS grade citric acid (CA) were obtained from Sigma Aldrich. Ethylene glycol (EG, 99%) and nitric acid (HNO_3, 68%), were acquired from Emplura and VWR Chemicals, respectively. Deionized water (18 MΩ.cm) was also utilized in preparing solutions. In brief, zinc nitrate was dissolved in 50 mL deionized water and certain amounts of EG, CA, and HNO_3 were added to prepare different sols under constant stirring and heating at 200°C for 2 h until the final solutions were homogeneous and without any precipitation.

The precursors were drop coated onto Si/SiO_2 substrates with 100 nm-thick interdigitated platinum electrodes. After deposition, the wet thin films were dried at 80°C and annealed at 500°C for 2 h in the ambient atmosphere. The sensors were labeled as ZnO:CA, ZnO:CA:EG, ZnO:EG and ZnO:EG:HNO_3 according to the additives used.

All sensors have been measured in an automated gas measurement setup using synthetic air as the carrier gas at a constant flow rate of 250 $mL.min^{-1}$, while it was adjusted upon the injection of target gas. The resistance changes of the sensor upon exposure to NO_2 were measured at a constant operating temperature

(30±2°C), and continuous UV light irradiation at a wavelength of 395 nm.

The sensor's normalized response was calculated by comparing the fully saturated resistances after exposure to dry air (R_{air}) and NO_2 (R_{gas}), according to (eq.1):

$$\textbf{Response} = \frac{\mathbf{R_{gas}}}{\mathbf{R_{air}}} \qquad (1)$$

Results and discussion

Fig. 1a shows the nanorod like morphology of ZnO:CA, whereas ZnO:CA:EG shows homogeneous spherical nanoparticles (Fig. 1b). It can be observed that grain agglomeration leading to a compact sensing layer, is much more evident in ZnO:EG:HNO_3 (Fig. 1c) than in ZnO:EG (Fig. 1d).

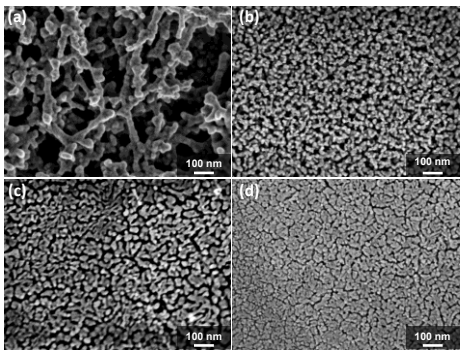

Fig. 1. SEM images of ZnO thin films: (a) ZnO:CA (b) ZnO:CA:EG (c) ZnO:EG and (d) ZnO:EG:HNO_3.

Fig. 1 illustrates the dynamic resistance changes in the presence of NO_2 of ZnO-based films, prepared using different additives. All sensors presented an increase in resistance independently of the additive, characteristic of n-type semiconducting behavior. The ZnO:EG:HNO_3 sensor showed significantly enhanced response, reaching resistance changes of nearly two orders of magnitude at sub-ppm range, suggesting that the addition of ethylene glycol and nitric acid leads to a higher sensitivity under light illumination.

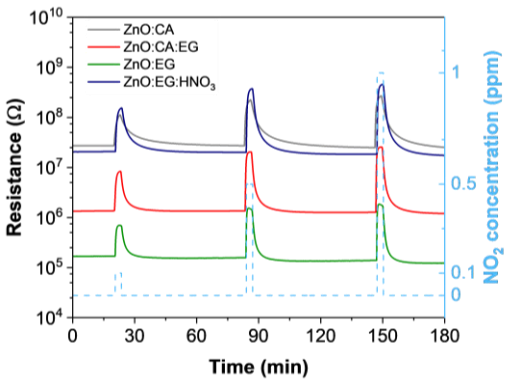

Fig. 2. Resistance variations of ZnO sensors under 395 nm light irradiation at different NO_2 concentrations (0.1, 0.5 and 1 ppm).

The ZnO:EG:HNO_3 sensor was initially exposed to NO_2 at 30°C in the dark, a slight response was observed with a longer recovery time. When exposed to NO_2 under UV illumination, the response was enhanced over that without any illumination.

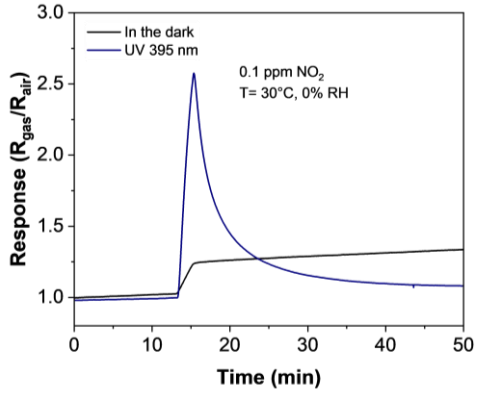

Fig. 3. NO_2 response of ZnO:EG:HNO_3 sensor in dark (black curve) and under UV-light irradiation (blue curve) towards 0.1 ppm of NO_2.

Conclusion

This work reported a facile and scalable route to synthesize ZnO nanoparticles, for the detection of ppb-level of NO_2 at a relatively low temperature of 30°C. Gas sensing experiments at different operating temperatures, in comparison to operating under LED illumination as well as under humidity conditions, have been performed and will be discussed at the conference.

References

[1] N. Yamazoe, Toward innovations of gas sensor technology, Sensors and Actuators B: Chemical 108, 2-14 (2005); doi: 10.1016/j.snb.2004.12.075.

[2] C. S. Prajapati, N. Bhat, ppb level detection of NO_2 using a WO_3 thin film-based sensor: material optimization, device fabrication and packaging, RSC Advances, 2018, 8, pp. 6590-6599; doi: org/10.1039/C7RA13659E.

[3] B. S. Barros, R. Barbosa, N. R. D. Santos, T. S. Barros, M. A. Souza, Synthesis and X ray diffraction characterization of nanocrystalline ZnO obtained by the Pechini method, Inorganic Materials 42, 1348-1351 (2006); doi: 10.1134/s0020168506120119.

[4] I. A. Farbun, I. V. Romanova, S. A. Kirillov, Optimal design of powdered nanosized oxides of high surface area and porosity using a citric acid aided route, with special reference to ZnO, Journal of Sol-Gel Science and Technology 68, 411-422 (2013); doi: 10.1007/s10971-013-3024-7.

DOI 10.5162/eurosensors2026/Mo–CHS–04

Simultaneous Capacitance and DRIFTS Analysis of Zeolites for Dosimeter-Based Epichlorohydrin Sensing at Room Temperature

Thomas Wöhrl, Ralf Moos, Daniela Schönauer-Kamin
Department of Functional Materials, Center of Energy Technology (ZET), University of Bayreuth, Bayreuth, 95447, Germany,
Correspondence to: functional.materials@uni-bayreuth.de

Summary:
This work investigates a dosimeter-based sensing concept for the detection of carcinogenic trace gases using a Cu-exchanged MFI zeolite. Simultaneous capacitance measurements and DRIFTS analysis were employed to monitor both the electrical response and molecular adsorption of epichlorohydrin under exposure at room temperature. The capacitance signal shows a concentration-dependent cumulative behavior, indicating adsorption of the analyte. DRIFT spectra confirm this interpretation by revealing characteristic bands of adsorbed epichlorohydrin, enabling dosimeter-type trace gas sensing.

Keywords:
DRIFTS Analysis, Dosimeter-based Gas Sensing, Carcinogenic Trace Gases, Zeolite Adsorption, Capacitance Measurement

Motivation

The detection of carcinogenic trace gases is highly relevant for protecting human health, as long-term exposure even at very low concentrations can exceed regulatory workplace exposure limits and present serious health risks [1]. In many applications, the critical factor for risk evaluation is the cumulative dose rather than short-term concentration peaks.

Dosimeter-type sensors are therefore particularly suitable, as they integrate the gas exposure over time and directly reflect the total amount of hazardous substances [2]. Zeolites are promising materials in this context due to their strong and selective adsorption of different gas species [3].

Combining capacitance measurements with DRIFTS analysis enables a deeper understanding of adsorption mechanisms and supports the development of reliable dosimeter-based sensing concepts for carcinogenic trace gases.

Measurement Setup

For the characterization of the zeolite material, two measurement techniques were used simultaneously. The investigated sensing film consisted of a copper-exchanged MFI zeolite with a SiO_2/Al_2O_3 ratio of 200, which was processed into a screen-printable paste and deposited onto an interdigital electrode (IDE) structure.

This configuration allows the determination of dielectric properties via a capacitance measurement at an excitation frequency of 32 kHz. In parallel, Diffuse Reflectance Infrared Fourier Transform Spectroscopy (DRIFTS) was used to monitor adsorbed species on the zeolite. DRIFTS enables the in-situ observation of adsorption processes without extensive sample preparation [4, 5].

The schematic layout of the setup is shown in Fig. 1.

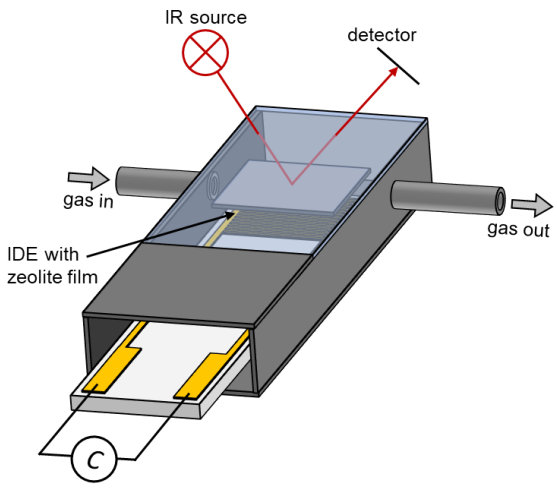

Fig. 1. Schematic diagram of the measurement setup for simultaneous capacitance measurement and DRIFTS characterization of a Cu-MFI zeolite film on an interdigital electrode structure.

The measurements were performed at room temperature using gaseous epichlorohydrin (ECH) in the low-ppm concentration range. This test gas is known to be carcinogenic. The adsorption of the analyte onto the zeolite is expected to result in both a detectable change in the adsorbed species visible in the IR spectrum and a change in the dielectric properties, which affects the capacitance measurement [6].

Results and Discussion

Fig. 1 shows a room-temperature experiment in which the epichlorohydrin (ECH) concentration was varied between approximately 2 and 7 ppm while capacitance signals and DRIFT spectra were recorded simultaneously.

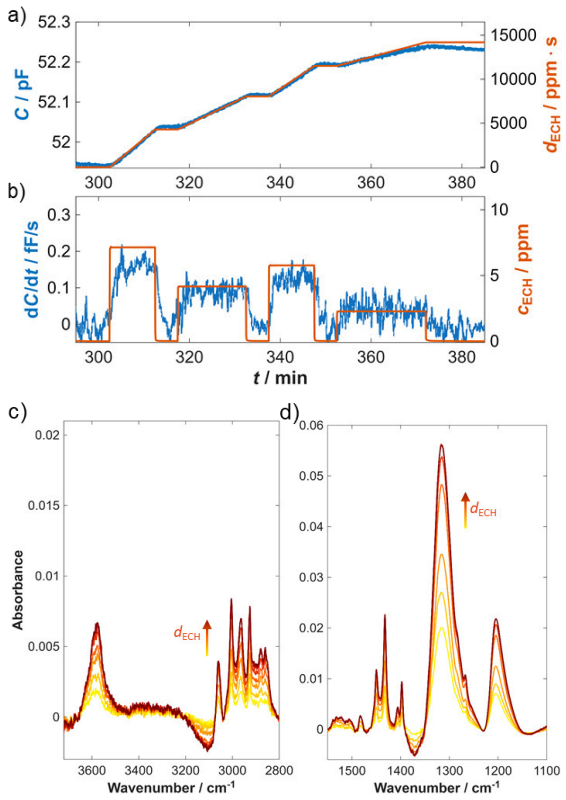

Fig. 2. Measurements during the dosing of different ECH concentrations. a) Time course of the capacitance signal versus the ECH dose (calculated from the concentration values of the dosed gases). b) Time derivative of the sensor capacitance versus the ECH concentration. c) and d) DRIFT spectra with increasing ECH loading.

The capacitance signal exhibits a clear dependency on the ECH dose. Following a dosimeter-type behavior, the signal increases linearly during gas exposure and remains at an elevated, nearly constant level once the ECH supply is stopped (see Fig. 1a)). The slope of the signal shows a linear dependency on the applied ECH concentration (see Fig. 1b)). This behavior supports the assumption of an adsorption process of ECH on the Cu-exchanged MFI zeolite.

The DRIFTS results confirm this interpretation. During ECH exposure, distinct absorption bands emerge mainly in the spectral regions between 1150 and 1500 cm^{-1} and between 2800 and 3600 cm^{-1} (see Figs. 1c) and d)). The intensity of these bands increased with higher ECH dose.

According to literature on the adsorption properties of zeolites towards hydrocarbons, these bands can be assigned to CH_2 deformation modes, C–O–C stretching vibrations of the epoxide ring, and C–H stretching vibrations of adsorbed organic species [4]. The persistence of these spectral features after ending of the ECH dosing further indicates stable adsorption onto the zeolite. The combined electrical and spectroscopic results therefore demonstrate that the observed capacitance response directly reflects the accumulation of carcinogenic ECH molecules in the zeolite. This confirms the suitability of this sensor setup for dosimeter-based trace gas sensing at room temperature.

References

[1] M. Woellner, S. Hausdorf, N. Klein, P. Mueller, M.W. Smith, S. Kaskel, Adsorption and Detection of Hazardous Trace Gases by Metal-Organic Frameworks, *Advanced Materials* 30, 1704679 (2018); doi: 10.1002/adma.201704679.

[2] I. Marr, A. Groß, R. Moos, Overview on conductometric solid-state gas dosimeters, *Journal of Sensors and Sensor Systems* 3, 29-46 (2014); doi: 10.5194/jsss-3-29-2014.

[3] D.T. Hayhurst, Gas adsorption by some natural zeolites, *Chemical Engineering Communications* 4, 729-735 (1980); doi: 10.1080/00986448008935944.

[4] D. Schönauer-Kamin, I. Marr, M. Zehentbauer, C. Zängle, R. Moos, Characterization of the sensitive material for a resistive NO_x gas dosimeter by DRIFT spectroscopy, *Sensors and Actuators B: Chemical* 320, 128568 (2020); doi: 10.1016/j.snb.2020.128568.

[5] L. Ohlin, P. Bazin, F. Thibault-Starzyk, J. Hedlund, M. Grahn, Adsorption of CO_2, CH_4, and H_2O in Zeolite ZSM-5 Studied Using In Situ ATR-FTIR Spectroscopy, *The Journal of Physical Chemistry C* 117, 16972-16982 (2013); doi: 10.1021/jp4037183.

[6] R. Wagner, D. Schönauer-Kamin, W. Bäther, R. Moos, Concept study with experimental proof for a new type of detector for gas chromatography, *Sensors and Actuators B: Chemical* 346, 130490 (2021); doi: 10.1016/j.snb.2021.130490.

Acknowledgement:

Special thanks to the German Research Foundation (DFG, Deutsche Forschungsgemeinschaft) for funding the project “Kapazitives Gasdosimeter zur Detektion kleinster Mengen kanzerogener Spurengase mit gasadsorbierenden MFI-Zeolithen als sensitive Schichten“ (ID: 533084795)

DOI 10.5162/eurosensors2026/Mo–CHS–05

Engineering the Active Layer of SnO_2 Chemoresistive Sensors: Influence of Deposition Methods and Film Thickness on NO_2 Detection

Davi Ladislau Ferreira[1], Rafael Aparecido da Silva[1], Ranilson Angelo da Silva[1] and Marcelo Ornaghi Orlandi[1]
[1] São Paulo State University, Chemistry Institute. Brazil,
davi.ladislau@unesp.br

Summary:
The influence of deposition technique and film thickness on SnO_2 chemoresistive sensors for NO_2 detection was investigated. Films were fabricated by screen-printing, drop-casting, and spin-coating, achieving thicknesses from ~380 nm to 30 µm. Thin spin-coated films enabled detection down to 0.2 ppm without saturation up to 10 ppm, while thick films showed early saturation due to diffusion limitations. The best device reached a response of 186 with high stability and repeatability. These results demonstrate that thickness control is a key parameter for optimizing gas sensor performance.

Keywords: Chemoresistive gas sensors, SnO_2 thin films, NO_2 detection, Film thickness, Deposition techniques.

Introduction

Chemoresistive gas sensors based on semiconducting metal oxides have been widely studied due to their high sensitivity, low cost, and simple device architecture [1]. Among these materials, SnO_2 stands out as one of the most widely used sensing layers for NO_2 detection, owing to its favorable electronic and surface properties. However, sensor performance is not determined solely by the intrinsic characteristics of the material. Processing parameters, particularly the deposition technique and resulting film thickness, play a critical role in defining film microstructure, gas diffusion pathways, and charge transport mechanisms, thereby directly impacting sensing behavior [2].

In this work, the influence of different deposition methods on the functional performance of SnO_2-based chemoresistive sensors is systematically investigated to establish structure–performance relationships governing gas sensing behavior. Films are fabricated using screen-printing, drop-casting, and spin-coating, enabling the production of sensing layers with a wide range of thicknesses and morphologies. The relationship between deposition technique, film architecture, and gas-sensing performance is evaluated through NO_2 detection tests, with emphasis on sensitivity, detection limit, stability, and repeatability.

Methodology

SnO_2 sensing films were fabricated from commercial nanopowder (<100 nm) using screen-printing, drop-casting, and spin-coating. For screen-printing, pastes were prepared with propylene glycol at 20–35 wt%. Drop-casting dispersions were prepared at 20 mg.mL^{-1} in isopropanol. Spin-coating was performed using a Laurell WS-400B-6NPP/LITE system, depositing 25 µL per cycle at 2000 rpm for 10 s, producing films with 10–40 layers and intermediate drying at 70 °C for 3 min. All devices were thermally treated at 400 °C for 2 h after deposition to remove organic residues and promote film calcination.

The thickness of screen-printed and drop-cast films was determined by cross-sectional analysis via controlled substrate fracture, followed by SEM-FEG (JEOL JSM-IT500HR). Multiple regions were analyzed to obtain representative average thickness values. For spin-coated films, thickness was measured using focused ion beam (FIB, FEI Helios NanoLab 600i) after deposition of protective platinum layers and cross-section milling.

Electrical characterization was performed in a controlled stainless steel chamber, with resistance monitored using a Keysight DAQ970A system. Heating (100–300 °C) was controlled via a PID system with a PT100 sensor and a Sorensen DLM 40-15 power supply. Gas flow (200 sccm) was regulated by MKS controllers

with dry air as baseline. Sensors were exposed to NO_2 (0.2–10 ppm) using 20 min exposure and 60 min recovery cycles. Stability and drift were evaluated under continuous exposure (1–10 ppm, 2 h per step), while reproducibility was assessed over 20 cycles at 4 ppm. Response time and relative standard deviation (RSD) were calculated from cyclic measurements at 4 ppm, while stability was further evaluated through RSD and temporal drift rate at the same concentration.

Results

Screen-printed films exhibited average thicknesses ranging from 14 to 30 µm. These sensors showed a detection limit of 0.4 ppm; however, signal saturation was observed from 2 ppm onward. This behavior is attributed to the large film thickness, which likely hinders gas diffusion and limits effective charge transfer within the sensing layer.

In contrast, spin-coated films presented significantly lower thicknesses, ranging from ~380 nm (10 layers) to ~900 nm (40 layers). These devices enabled detection down to 0.2 ppm and did not exhibit saturation up to 10 ppm, indicating improved gas diffusion and more efficient surface interaction.

Among the investigated techniques, the best performance was achieved with the 40-layer spin-coated film, which exhibited a response of 186 at 10 ppm of NO_2. Repeatability tests over 20 cycles showed a RSD of 3.54% and a response time of 340 s. Stability tests at 4 ppm revealed low signal fluctuation, with an RSD of 1.4% and a drift rate of 4.30% h^{-1} during continuous exposure.

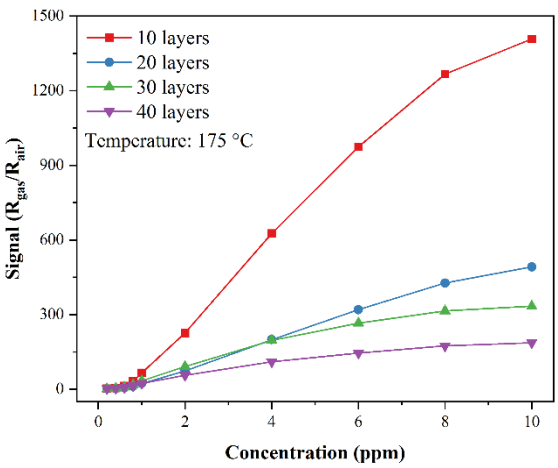

Fig. 1. Detection response of SnO_2 sensors fabricated by spin-coating under NO_2 exposure.

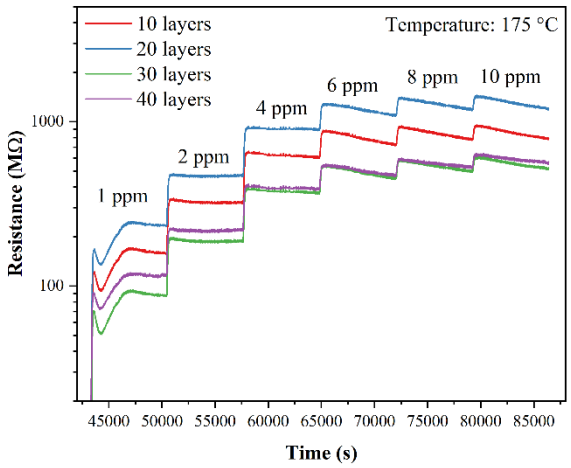

Fig. 2. Electrical stability of the SnO_2 sensor during 2 h of continuous NO_2 exposure.

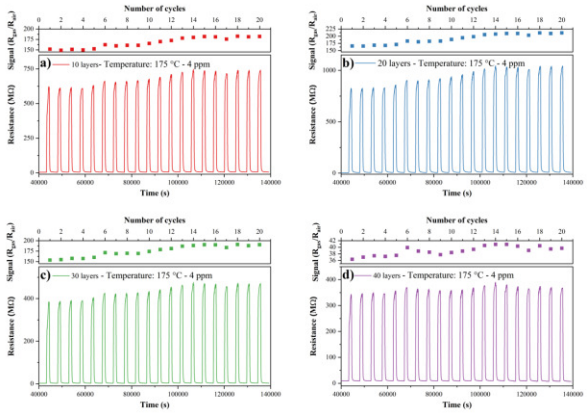

Fig. 3. Repeatability assessment of the SnO_2-based sensor over 20 consecutive exposure/recovery cycles to NO_2 at 4 ppm.

Overall, thinner films demonstrated enhanced sensitivity, improved stability, and more consistent signal profiles, highlighting the critical role of deposition technique and thickness control in optimizing the performance of SnO_2 chemoresistive sensors for NO_2 detection [3].

References

[1] S. Mobtakeri, et al., Simultaneous amperometric and gasochromic measurements of a-MoO3 gas sensors optimized with controlled content of Pd sensitizer and device configuration, Applied Surface Science, 704, 1-15 (2025); doi: 10.1016/j.apsusc.2025.163446

[2] A. Mirzaei, S.S. Kim, H.W. Kim., Resistance-based H2S gas sensors using metal oxide nanostructures: A review of recent advances, Journal of Hazardous Materials, 357, 314-331 (2018); doi: 10.1016/j.jhazmat.2018.06.015

[3] A. Tanwar, et al., LPG gas sensing performance of the SnO2 thin films influenced by the dieletric and conducting properties, Discover Applied Sciences, 7, 1-14 (2025), doi: 10.1007/s42452-025-06527-y

DOI 10.5162/eurosensors2026/Mo−CHS−06

Development of Platinum Heater by Inkjet Printing onto Polyimide Substrate

Mathilde RIEU, Bastien LE PORCHER, Maxime MINOT, Jean-Paul VIRICELLE
Mines Saint-Etienne, Univ Lyon, CNRS, UMR 5307 LGF, Centre SPIN, F-42023 Saint-Etienne, France
rieu@emse.fr

Summary:
Platinum inks were developed from nanoparticle suspensions obtained through a polyol synthesis route. These suspensions were then mixed with solvents such as ethylene glycol, water, and propan-2-ol to produce printable inks. After optimizing the deposition parameters onto polyimide substrates and the thermal treatment, functional platinum coatings were obtained. A sensor printed with our homemade inks on a flexible substrate was exposed to CO and NO_2 gases, and its response was found to be comparable to the one obtained for a sensor printed with commercial inks.

Keywords: Inkjet printing, platinum, metallic inks, gas sensors

Background, Motivation and Objective

This work is part of the development of a full inkjet-printed resistive sensor with controlled ink composition. Indeed, commercial inks are of unknown composition that can degrade sensors performances. We already worked on the feasibility of this kind of fully printed sensor, working on different aspects, SnO_2 [1,2], inkjet printing of commercial inks [1,3], development of homemade gold inks [4]. The objective of this new work was to complete the sensor with the heating element, in platinum, at the back side of the sensing layer.

Description of the New Method or System

For this, we proposed the development of a platinum ink. We study the formulation and the printability until getting a stable ink for a Dimatix DMP 2850 inkjet printer.

Results

For the fabrication of platinum conductive inks, the first objective was the synthesis of platinum nanoparticles (PtNPs) via polyol route. Polyol process is a type of liquid-phase synthesis that allows the production of finely divided metals from salts by reaction with polyalcohols. We choose to use ethylene glycol as the solvent and reducing agent, polyvinylpyrrolidone (PVP) as the stabilizer, and hexachloroplatinic acid as the platinum precursor.

After optimization of the synthesis parameters (reaction time, temperature and concentrations), platinum nanoparticles of 9 nm were obtained and are aggregated with 2 to 6 particles on average as reported in figure 1 (DLS analysis and TEM micrograph).

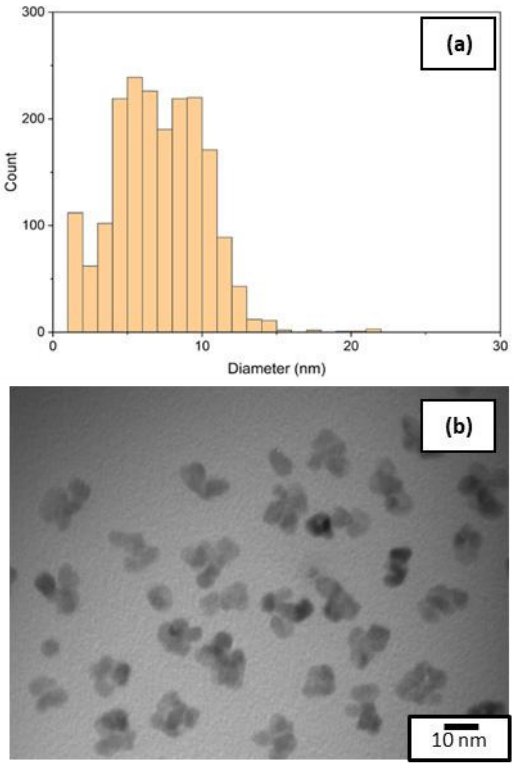

Fig. 1. Solution of PtNPs: (a) particle diameter distribution by DLS, (b) TEM micrograph.

Then, we formulated an ink by mixing the previous suspension with propan-2-ol in appropriate proportions in order to get viscosity and surface tension within the ranges of required values for inkjet printing, 12.5 mPa.s and 28.9 mN/m, respectively.

After several trials with the inkjet printer parameters, spherical drops without satellite droplets were obtained. As reported in figure 2, the spread drops have a diameter of 36 micrometres and by decreasing the distance between the drops, it is possible to obtain homogeneous and continuous lines.

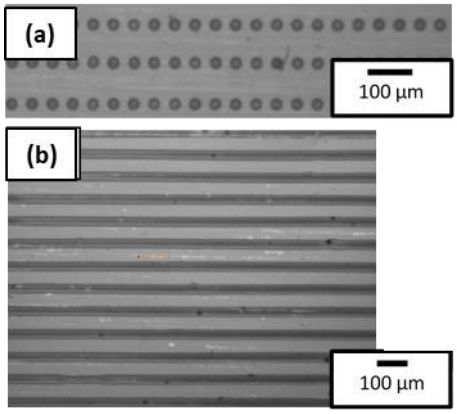

Fig. 2. Images obtained via the printer camera for a deposition of (a) droplets of PtNPs ink spread on polyimide and (b) lines.

Multi-layered films were thus deposited. Drying steps or intermediate curing were evaluated in regards of the final coating. After a final heat treatment at 400°C, a continuous coating was obtained. A SEM micrograph is reported in figure 3. The film was composed of very fine compacted particles.

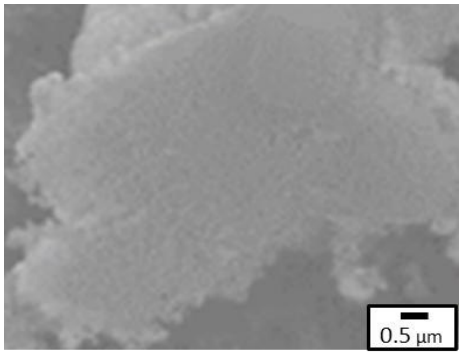

Fig. 3. SEM micrograph of the surface of a platinum coating

Finally, conductive layers were obtained and a pattern of a heater was printed in order to confirm the feasibility. Resistance and temperature coefficient of the heating element are under evaluation.

Conclusion

Finally, we formulated a stable and printable platinum ink to design the heating element. We succeeded in the preparation of a platinum heater to finalize our resistive gas senor onto polyimide foil. It was possible to produce several platinum nanoparticle-based inks and print them using inkjet technology. Very few commercial platinum inks are available for inkjet printing. This synthesis technique is similar to existing options but is nonetheless promising for ink production, especially since the resulting mixture is very stable and perfectly meets inkjet printing requirements.

This work opens the way to new applications, as resistive temperature sensors for example.

References

[1] M. Rieu, M. Camara, G. Tournier, et al. Fully inkjet printed SnO_2 gas sensor on plastic substrate. Sensors and Actuators B: Chemical 236:1091–1097. (2016) https://doi.org/10.1016/j.snb.2016.06.042

[2] O. Kassem, M. Saadaoui, M. Rieu, S. Sao-Joao, J.P Viricelle Synthesis and inkjet printing of sol-gel derived tin oxide ink for flexible gas sensing application, Journal of Materials Science, 53, p12750–12761 (2018) DOI: 10.1007/s10853-018-2577-9

[3] O. Kassem, M. Saadaoui, M. Rieu, J.P Viricelle, A novel approach to a fully inkjet printed SnO_2-based gas sensor on a flexible foil, Journal of Materials Chemistry C, 7, 12343-12353 (2019) https://doi.org/10.1039/C9TC04170B

[4] B. Le Porcher, M. Rieu, JP. Viricelle, Development of Gold Inks for Inkjet Printing of Gas Sensors Electrodes on Plastic Support. Electronics 13:2110. (2024) https://doi.org/10.3390/electronics13112110

DOI 10.5162/eurosensors2026/Mo–CHS–07

Inkjet-printed TiO_2 Nanoparticles for Miniaturized Gas Sensors

Alice Debot[1], Vincent Rogé[1], Stephanie Girod[1], Inci Boehme[2], Renaud Leturcq[1]
[1] Luxembourg Institute of Science and Technology, 41 rue du Brill, L4422, Belvaux, Luxembourg
[2] Sciosense Germany GmbH, Gerhard-Kindler-Straße 8, 72770 Reutlingen, Germany
Corresponding Author: alice.debot@list.lu

Summary

This work demonstrates the development of a gas sensor based on inkjet-printed titanium dioxide as a step toward multipixel gas sensing platforms. We demonstrate the reliable formulation of ink based on these nanoparticles and the resulting high-resolution deposition on interdigitated electrodes. The measured gas sensing properties are consistent with results obtained for drop-casted TiO_2 material. Through this approach, we aim to significantly address the limited selectivity typically associated with conventional chemiresistive gas sensors, while relying on a fabrication method that is compatible with scalable, industrial-level manufacturing.

Keywords: Inkjet printing, metal oxides, multi pixels, gas sensing

Introduction

Metal-oxide chemiresistive sensors are commonly employed for gas detection because of their strong sensitivity and rapid response times. Their operating principle relies on monitoring changes in the electrical resistance of metal-oxide layers, where these variations are directly linked to the concentration of target gases[1]. Despite these advantages, a key drawback is their limited selectivity, as they tend to respond to a range of gases rather than a single species, making accurate identification more challenging [2].

To overcome this issue, multi-pixel sensor platforms incorporating different sensing materials on each pixel have been proposed. While such approaches have been widely explored in academic research [3], their transition to commercial products remains constrained by the absence of scalable fabrication techniques capable of integrating multiple metal oxides onto a single chip. As a result, most commercially available multi-pixel sensors still rely on identical materials across all pixels, providing little improvement in selectivity compared to single-material devices. Inkjet printing offers a promising solution, as it allows the controlled and selective deposition of diverse materials onto multi-pixel architectures, with strong potential for straightforward scalability.

Description of the New Method

In this study, titanium dioxide nanoparticles were deposited via a drop-on-demand inkjet printing technique to fabricate miniaturized gas sensors. The resulting thin films exhibited electrical conductivity and showed sensitivity to both oxidizing and reducing gases.

Results

The nanoparticles are spherical, commercially available titanium dioxide (Aeroxide P25). Their primary particle size is around 20 nm; however, they tend to form solid aggregates with dimensions on the order of several hundred nanometers (Fig. 1). The ink formulation contained 5 wt% of these nanoparticles and was deposited using a pre-industrial inkjet printhead with a nominal droplet volume of 30 pL. The nozzle diameter is approximately 40 µm, which ensures stable jetting while minimizing the risk of clogging.

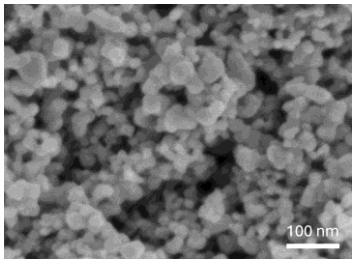

Fig. 1. SEM image of commercial TiO_2 nanoparticles

Individual droplets were deposited onto a silicon substrate. The resulting patterns are uniform, with no observable coffee-ring effect (Fig. 2 (a)). Each droplet has a diameter of approximately 50 µm, corresponding to a resolution comparable to that of electrodes in a multipixel platform.

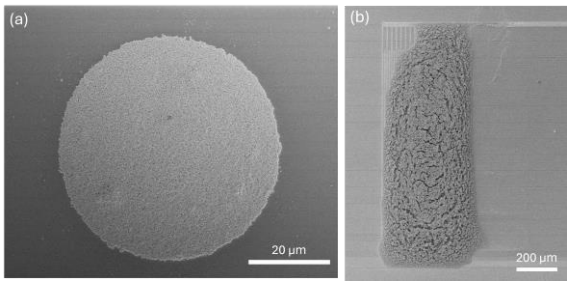

Fig. 2. SEM of inkjet-printed (a) TiO_2 droplet and (b) TiO_2 film on interdigitated electrodes

A carefully optimized ink formulation was developed to achieve both uniform deposition and adequate electrical conductivity. Establishing efficient interparticle contacts is critical to enable charge transport. This strongly depends on the ink composition, which must promote the formation of continuous conductive pathways throughout the film.

As a baseline approach, the optimized ink was inkjet-printed onto interdigitated electrodes (Fig. 2 (b)), using three different thicknesses corresponding to 1, 5, and 15 printed layers.

The baseline resistance of each device was measured at 200 °C under a flow of 100 sccm of dry air. Gas sensing tests were then carried out using diluted gas mixtures in dry air. The applied concentrations were 1 ppm for NO_2, H_2S, and CO; 10 ppm for NH_3; 21 ppm for MeOH; and 1000 ppm for H_2. The corresponding sensor responses are presented in Fig. 3 and expressed using the following relationship:

$$\text{Relative response} = (I_{gas}-I_b)/I_b \qquad (1)$$

Where I_b is the baseline current measured prior to gas exposure, and I_{gas} is the current recorded at the maximum response under the target gas atmosphere.

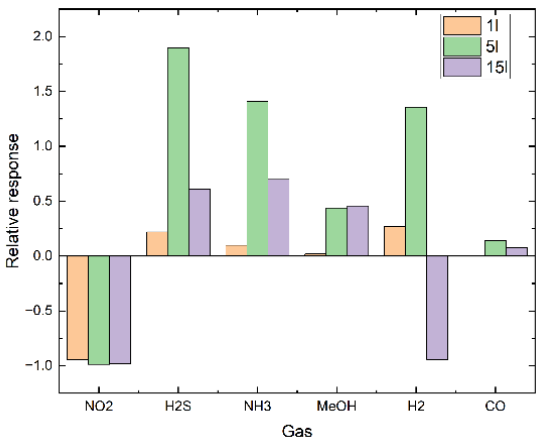

Fig. 3. Relative response of TiO_2 devices (1, 5 and 15 layers) to NO_2, H_2S, NH_3, MeOH, H_2 and CO

The film consisting of 5 layers exhibits a higher response than both the 1-layer and 15-layer samples for H_2S, NH_3, and MeOH. This behavior is consistent with a model in which a single layer does not provide sufficient percolation pathways for effective charge transport, while the thicker 15-layer film becomes more compact, causing the gas interaction to occur predominantly at the surface while the electrical current must still percolate through the bulk.

In contrast, all three thicknesses show an approximately 100% response to NO_2, which can be attributed to its strong oxidizing nature and high reactivity.

For H_2, the 1-layer film shows a weaker response compared to the 5-layer sample, similar to the behavior observed for the other gases. However, for the 15-layer film, the response changes sign and resembles that typically associated with oxidizing gases. This has already been reported for In_2O_3 [4].

None of the three film thicknesses shows a significant response to CO, as expected in the absence of catalytic dopants [4].

Acknowledgements

The authors would like to thank the European Union for the founding of the AMUSENS project under grant agreement no. 101130159.

References

[1] P. Najafi et A. Ghaemi, « Chemiresistor gas sensors: Design, Challenges, and Strategies: A comprehensive review », *Chem. Eng. J.*, vol. 498, p. 154999, oct. 2024, doi: 10.1016/j.cej.2024.154999.

[2] A. Turlybekuly, Y. Shynybekov, B. Soltabayev, G. Yergaliuly, et A. Mentbayeva, « The Cross-Sensitivity of Chemiresistive Gas Sensors: Nature, Methods, and Peculiarities: A Systematic Review », *ACS Sens.*, vol. 9, nº 12, p. 6358-6371, déc. 2024, doi: 10.1021/acssensors.4c02097.

[3] G. Bae, M. Kim, W. Song, S. Myung, S. S. Lee, et K.-S. An, « Impact of a Diverse Combination of Metal Oxide Gas Sensors on Machine Learning-Based Gas Recognition in Mixed Gases », *ACS Omega*, vol. 6, nº 36, p. 23155-23162, sept. 2021, doi: 10.1021/acsomega.1c02721.

[4] G. Korotcenkov, M. Ivanov, I. Blinov, et J. R. Stetter, « Kinetics of indium oxide-based thin film gas sensor response: The role of “redox” and adsorption/desorption processes in gas sensing effects », *Thin Solid Films*, vol. 515, nº 7-8, p. 3987-3996, févr. 2007, doi: 10.1016/j.tsf.2006.09.044.

DOI 10.5162/eurosensors2026/Mo−CHS−08

Highly Stable Pt-activated Graphene Gas Sensors with Antimony Oxide Coatings

Ahmet Burak Baloglu, Margus Kodu, Tauno Kahro, Rainer Pärna, Aarne Kasikov, Raivo Jaaniso
University of Tartu, Ülikooli 18, Tartu, Estonia
ahmet.burak.baloglu@ut.ee

Summary:
We report a significant improvement in the thermal stability of graphene-based gas sensors. By depositing a thin antimony oxide layer on graphene via pulsed laser deposition, a protective effect was observed at operating temperatures above 200 °C under humid air and harsh ozone conditions over extended periods, enabling sensors to maintain a stable response. Importantly, this protective layer preserves the CO-sensing capability introduced by Pt functionalization, indicating that the typical sensitivity-stability trade-off can be effectively mitigated without compromising the response to target gases.

Keywords: graphene, antimony oxide, thermal stability, CO detection, chemiresistor

Background, Motivation and Objective

Graphene has emerged as a promising material for next-generation gas sensors, due to its exceptional electronic characteristics and atomically thin structure. However, in its pristine state, graphene is relatively inert, which restricts its effectiveness as a receptor in chemiresistive gas sensors. Previous studies have demonstrated that introducing a functional layer, such as metals [1] or metal oxides [2], onto the graphene can substantially enhance its sensitivity to various toxic and pollutant gases by providing active receptor sites. Despite these improvements, such functionalization often introduces a trade-off between sensitivity and stability, as surface modifications can render sensors susceptible to degradation, particularly during long-term operation at elevated temperatures.

Thermal activation is a widely employed strategy to enhance the performance of both traditional metal-oxide and graphene-based gas sensors [3]. By activating the receptor layer, heating can significantly improve sensitivity and accelerate response and recovery dynamics. Furthermore, temperature modulation strategies have been extensively investigated to enhance selectivity and are already implemented in commercial metal-oxide-based sensing platforms [4]. However, prolonged exposure to elevated temperatures is known to reduce the operational lifetime of the chemiresistive gas sensors. Therefore, ensuring reliable long-term performance and extending the upper temperature limits requires effective protection of the active sensing layer.

In this study, we aimed to improve the long-term stability of graphene-based gas sensors for high-temperature operations in humid air and harsh ozone environments, which we believe is a critical step toward reliable operation as commercial gas sensors.

Description of the New Method or System

Here, we report, for the first time, the protective role of thin antimony oxide layers deposited on graphene-based gas sensors via pulsed laser deposition (PLD) (Figure 1).

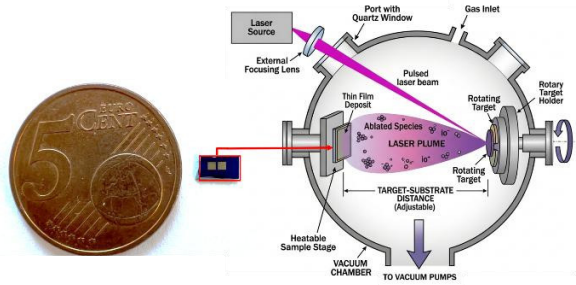

Fig. 1. PLD of graphene sensor. Graphene was previously wet-transferred between the Au electrodes on a Si/SiO_2 substrate (outlined in red). A 5-cent coin for scale.

Our results show that graphene sensors exhibit sensitivity to CO gas only after functionalization with Pt; however, significant degradation occurs at operating temperatures above 200 °C. In contrast, incorporating the antimony oxide interlayer enables the sensor to maintain performance at elevated temperatures without compromising CO sensitivity. This protective effect is highly reproducible, and the improved stability persists for at least two years, indicating that antimony oxide is a promising material for overcoming the long-standing stability limitations in gas sensor research.

Results

Figure 2 demonstrates the change in "relative response," which is the variation of the electrical conductance in time, upon target gas (or heating), and is defined as:

$$\text{Relative response (\%)} = \frac{I_{gas}-I_{air}}{I_{air}} \times 100 \qquad (1)$$

where I_{gas} is the conductance upon a target gas, while the I_{air} is the initial conductance in synthetic air.

Deposition of the Pt layer via PLD enabled the graphene sensor to detect CO gas even at room temperature (RT).

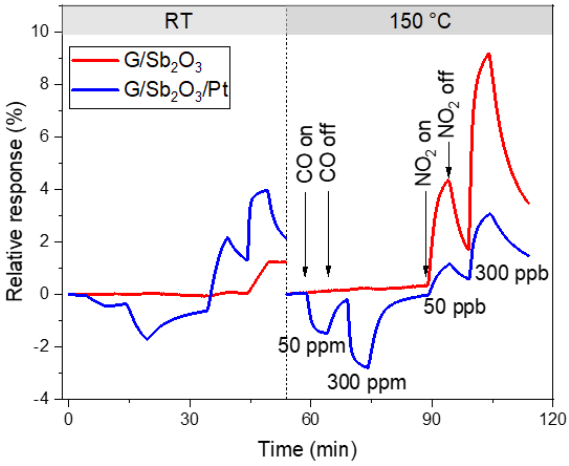

Fig. 2. Relative responses to CO and NO_2 gases in different concentrations at RT and 150 °C.

The long-term stability of the graphene sensors with and without the protective antimony oxide layer is shown in Figure 3. At 200 °C, the unprotected sensor current begins to drop, and at 250 °C, a significant and irreversible decrease occurs, indicating sensor degradation.

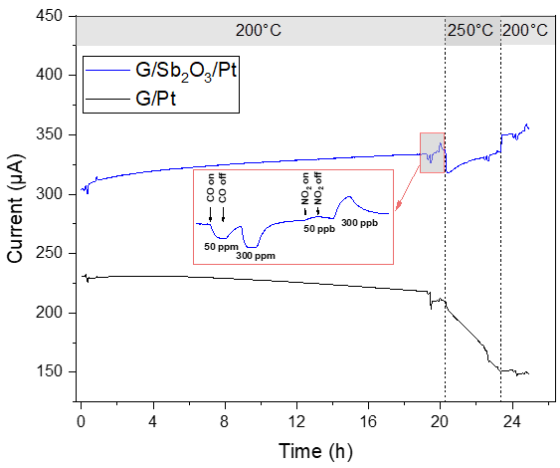

Fig. 3. Long-term stability of the graphene sensors in 40% humid air above 200 °C.

The influence of a harsh environment was investigated by elevating the temperature under an ozone atmosphere. Figure 4 shows that the antimony oxide-coated sensor achieved a stable baseline up to 200 °C, whereas the uncoated sensor exhibited a dramatic degradation trend.

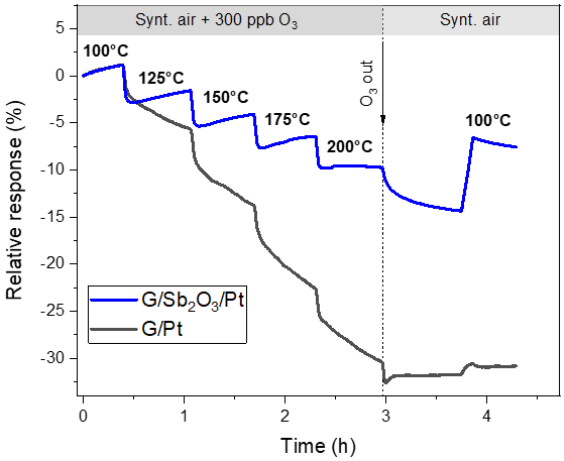

Fig. 4. Stability of the sensors (w/ and wo/ antimony oxide) under an ozone environment.

References

[1] Kodu M, Berholts A, Kahro T, Avarmaa T, Kasikov A, Niilisk A, Alles H, Jaaniso R., Highly sensitive NO2 sensors by pulsed laser deposition on graphene, *Applied Physics Letters* 12;109(11) (2016); doi: 10.1063/1.4962959

[2] Berholts, A., Kodu, M., Rubin, P., Kahro, T., Alles, H. and Jaaniso, R., Layered heterostructure of graphene and TiO2 as a highly sensitive and stable photoassisted NO2 sensor, *ACS Applied Materials & Interfaces*, *16*(33), pp.43827-43837 (2024); doi: 10.1021/acsami.4c08151

[3] Vafaei, P., Lind, M., Kiisk, V., Kahro, T., Baloglu, A.B., Kodu, M., Raabe, R., Kasikov, A., Kikas, A., Kozlova, J. and Jaaniso, R., High-Performance Graphene-Based Gas Sensors with Pulsed Heating and AI Processing. *Advanced Sensor Research*, *4*(12), p.e00083 (2025); doi: 10.1002/adsr.202500083

[4] BME690 gas sensor (BST-BME690-DS001) datasheet, *Bosch Sensortec* (2025); URL: https://www.bosch-sensortec.com/en/products/environmental-sensors/gas-sensors/bme690

Acknowledgements

This research was funded by the Estonian Research Council grant (PRG1580).

DOI 10.5162/eurosensors2026/Mo−CHS−09

Electrosynthesized porous tin oxide film for gas sensors applications

Abhishek Kumar, Sudalaimani Sudalaimuthu, Maxime Minot, Mathilde Rieu
Mines Saint-Etienne, Univ Lyon, CNRS, UMR 5307 LGF, Centre SPIN, 158 Cours Fauriel, F-42023 Saint-Etienne, France
abhishek.kumar@emse.fr

Summary:
Herein, the electrochemical synthesis of porous tin oxide (SnO_2) semiconducting film is demonstrated for application in gas sensors to detect redox gases. The application of a negative electrode potential in a strong acidic precursor solution induces a series of chemical and electrochemical reactions. The interplay of these reactions produces a porous, chemically pure and polycrystalline SnO_2 film over the gas sensor's electrodes. The preliminary tests under different redox gases confirm the enhancement in the sensitivity of the SnO_2 sensors compared to a reference SnO_2 based gas sensors.

Keywords: Metal oxides, Porous materials, Electrosynthesis, gas sensors, Healthcare

Background, Motivation and Objective

There is a growing research interests in developing an electronic nose for breath analysis of a person for the premature diagnostic of disease[1, 2]. Indeed, the human breath contains a complex mixture of oxidizing, reducing and volatile organic compounds (VOCs), which composition and concentrations change depending on the occurrence of a disease. For instance, a kidney infection shoots up ammonia (NH_3) concentration in the breath more than 14 times, while early-stage asthma increases the concentration of nitric oxide (NO) 4 times in the breath compare to a breath of a healthy person [3, 4]. Such disease biomarkers gases have been conventionally detected using gas sensors based on metal oxides, like tin oxides (SnO_2), which are abundant and inexpensive. Current approach of using these materials in gas sensors comprise synthesis of powder by hydrothermal method followed by processing of the corresponding ink on the sensor electrodes into thin film by screen printing or similar solution casting methods. However, the morphologies of such metal oxides films are often compact and that reduces their sensitivity towards the redox gases detection. On the other hand, the detection benchmarks for the disease biomarkers in the breath is often in ppb range, necessitating drastic improvement in the sensitivity of metal oxide-based sensors. In this endeavor, we report an electrosynthesis approach of one step synthesis and deposition of porous film of SnO_2 onto gas sensor electrodes, which is rapid, precise and well-controlled in terms of thickness and porosity.

Description of the New Method

The key novelty of the presented work is the innovative electrochemical methodology, in which *in situ* generated hydrogen bubbles provides a dynamic template for the pores evolution in simultaneously forming SnO_2 deposit. The Dynamic Hydrogen Bubble Template (DHBT) method [5, 6] has been previously explored only for the metal film deposition but never for the metal oxide film. The fine control of the electrochemical conditions could produce a hierarchical porosity in the SnO_2 film deposited over the gas sensors electrodes.

Results

The electrosynthesis is performed by electroreduction at a fixed potential in a precursor solution containing a tin salt, a source of oxygen and a proton source. Notably, the presence of the proton source causes hydrogen evolution reaction at the electrode, producing bubbles at the electrode surface and that behave as a soft dynamic template [2] to induce porosity in the metal oxide deposit. We have modulated the electrosynthesis potential, time and temperature to tune the porosity and microstructures of the SnO_2 porous film. The preliminary results have demonstrated the production of a porous film of SnO_2 (Figure 1a), having multiplicity of pore sizes. Such hierarchical porous morphology is a characteristic feature of DHBT deposition. The microstructure, upon investigation with X-ray diffraction (XRD) exhibits reflection peaks characteristic of rutile or

cassiterite phase of SnO_2. The surface analysis of the film by X-ray photoelectron spectroscopy (XPS) shows characteristic peaks associated to Sn^{4+} oxidation state. The porous coating is of high chemical purity and is devoid of any potential metallic tin contamination, as confirmed by XPS analysis. The electrochemical characterizations of the porous SnO_2 coating further revealed hindered electron transfer reaction of a redox probe $K_3[Fe(CN)_6]$ compared to a conventional gold electrode, which exhibits well-defined redox peaks, highlighting low conductivity of the oxide film. Optimization of the electrosynthesis parameters, evaluation of the associated mechanism and application of porous SnO_2 film in redox gases sensing are the scope of our ongoing activities.

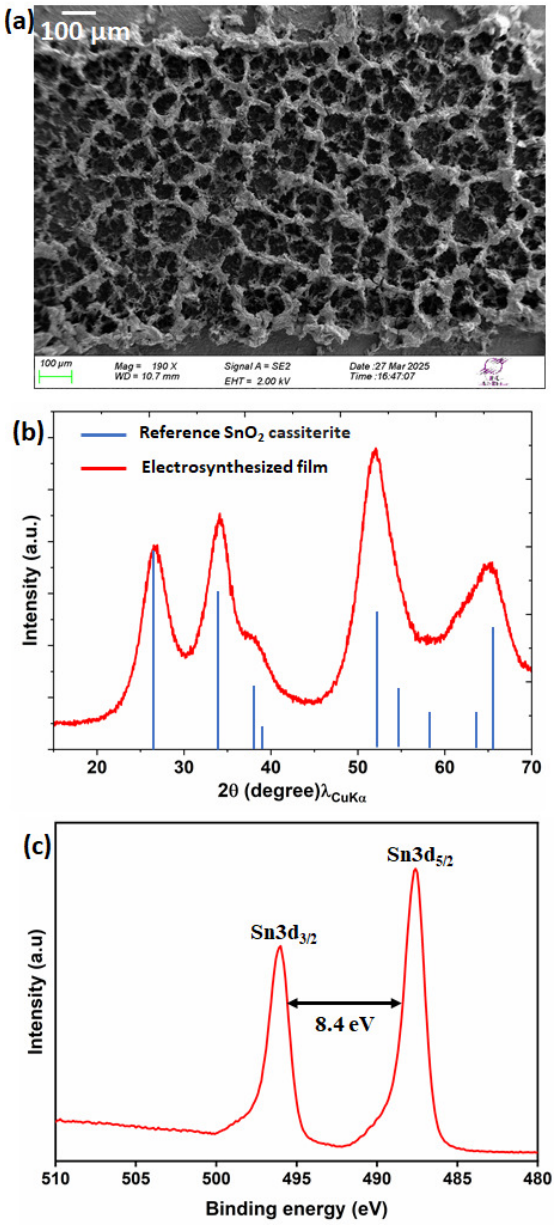

Fig. 1. SEM image (a), XRD profile (b) and XPS high resolution spectrum (c) of SnO_2 film.

References

[1] I. Mondal, A. Zoabi, H. Haick *Adv. Funct. Mater.* 2025, *35*, 2425193.
[2] M. Hijazi, M. Rieu, V. Stambouli, G. Tournier, J.-P. Viricelle, C. Pijolat *Sensors and Actuators B: Chemical*. 2018, *256*, 440-447.
[3] G. Konvalina, H. Haick *Acc. Chem. Res.* 2014, *47*, 66-76.
[4] A. Haccuria, A. Michils, S. Michiels, A. Van Muylem *Journal of Allergy and Clinical Immunology*. 2014, *134*, 554-559.
[5] B. J. Plowman, L. A. Jones, S. K. Bhargava *Chemical Communications*. 2015, *51*, 4331-4346.
[6] A. Kumar, J. Lüder, M. Bertotti, K. Araki, F. Montoro, F. Herbst, R. Meunier-Prest, L. Angnes, M. Bouvet, J. Bettini, J. M. Gonçalves *ACS Applied Nano Materials*. 2024, *7*, 7213-7225.

DOI 10.5162/eurosensors2026/Mo–CHS–10

Sub-ppm Methane Sensing by Spark-Ablation-Synthesized Nano-SnO_2

D. Gounaris[1], A. Baut[2], H. Shin[2] S. E. Pratsinis[2], A. Güntner[2] and G. Biskos[1,3]
[1]Climate and Atmosphere Research Center, The Cyprus Institute, Nicosia, 2121, Cyprus
[2] Department of Mechanical and Process Engineering, ETH Zürich, 8092, Zürich, Switzerland
[3]Faculty of Civil Engineering and Geosciences, Delft University of Technology,2628-CN, Netherlands
d.gounaris@cyi.ac.cy

We present a scalable spark ablation method for producing Sn nanoparticles at atmospheric pressure, followed by air annealing to form SnO_2. Structural characterization confirms nanocrystalline particles, while XPS reveals a high fraction of adsorbed oxygen species. The resulting sensor detects methane down to 0.2 ppm with strong, repeatable responses and high humidity stability. This performance is attributed to the high surface area and enhanced surface reactivity identified by XPS. Overall, our results demonstrate that spark ablation provides a promising route for reliable low-level methane sensors.

Keywords: Spark Ablation, Methane Detection, MOx Gas sensors, SnO_2 NPs

Metal oxide gas sensors are widely employed in various applications due to their low cost, compactness, and robustness. However, their sensitivity and selectivity at low analyte concentrations remain insufficient for environmental monitoring, motivating the development of improved nanostructured sensing materials. [1]

While conventional synthesis approaches such as sol–gel and hydrothermal methods dominate [2], dry techniques like flame spray pyrolysis and spark ablation offer distinct benefits, including reduced contamination, continuous production, and direct formation of porous structures. [3] Spark ablation, in particular, is an environmentally friendly method that produces high-purity nanoparticles through repetitive electrical discharges between conductive electrodes, followed by rapid cooling and particle formation.. The technique, was initially introduced by Schwyn et al.[4] and to date, it has been successfully employed for the synthesis of catalytic, sensing and photovoltaic nanomaterials among others [5].

In this work, [6] Sn nanoparticles are generated using atmospheric-pressure spark ablation with N_2 as a carrier gas and subsequently collected and annealed. The resulting SnO_2 nanoparticles form agglomerates with an average mobility diameter of ~80 nm, while BET analysis indicates a decrease in specific surface area from 105.5 m^2/g (as-prepared Sn) to 45 m^2/g after annealing due to sintering effects. The sensing film, fabricated via doctor blading, exhibits a highly porous and interconnected morphology (see Figure 1), as observed by scanning electron microscopy (SEM), facilitating efficient gas diffusion and surface interaction. [7]

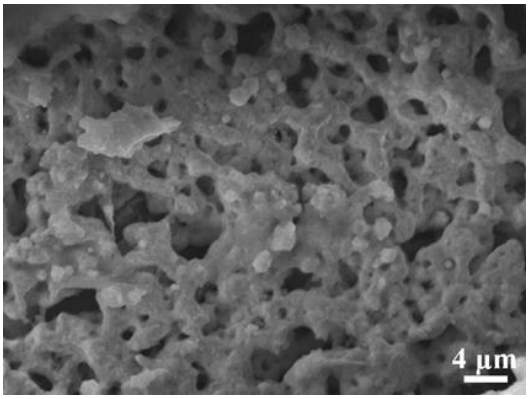

Figure 1. SEM image of the porous sensing film composed of annealed SnO_2 nanoparticles.

The fabricated sensing film, operated at 275 °C for methane detection, reliably measured concentrations between 0.2 and 10 ppm at 20% relative humidity (see Figure 2) with a signal-to-noise ratio of ~58 and a theoretical detection limit of ~7 ppb. Additionally, it exhibited high repeatability over more than ten consecutive cycles at a fixed concentration of 5 ppm (see Figure 3). Furthermore, when exposed to 10 ppm methane, the sensor response remained stable across a broad humidity range (20–80% RH), with variations below 10%. This demonstrates robust performance under varying environmental conditions, highlighting the suitability of the sensor for real-world applications.

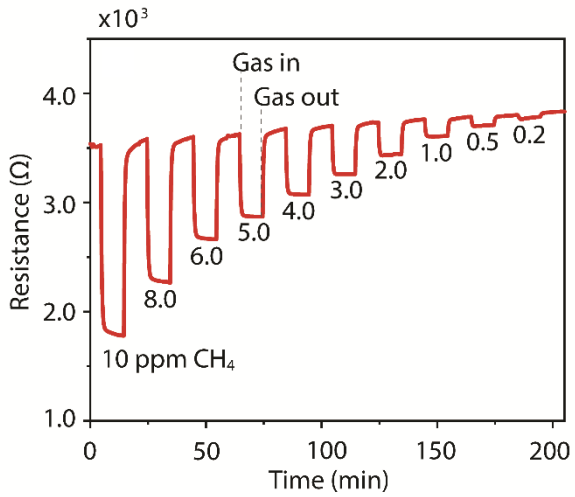

Figure 2. Sensor resistance changes during repeated exposure to different methane concentrations over time at 275 °C and 20% RH.

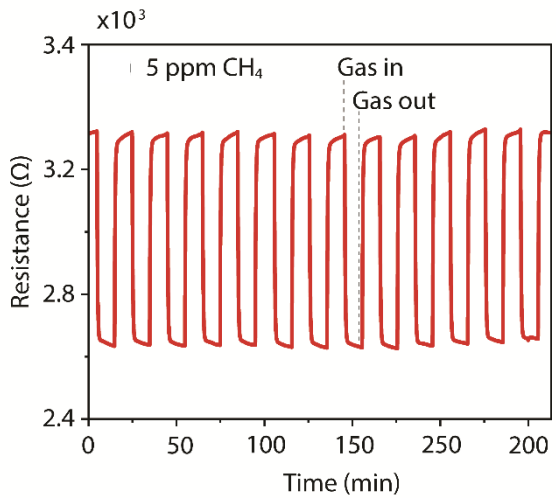

Figure 3. Sensor resistance as a function of time at a constant methane concentration of 5 ppm over 13 cycles at 275 °C and 20% RH.

The performance of the sensor was evaluated in the presence of interfering gases including acetone, ethanol, hydrogen, carbon monoxide and ammonia and was found to follow the behavior of other SnO_2 sensors reported in the literature.

The enhanced sensing performance is linked to the structural and surface characteristics of the nanoparticles, particularly the increased proportion of adsorbed oxygen species revealed by XPS, which facilitates charge transfer during methane oxidation. Overall, this study demonstrates that spark ablation is a powerful and versatile technique for producing high-performance sensing materials, offering a promising route toward reliable sub-ppm methane detection for environmental and industrial applications.

References

[1] N. A. Isaac, I. Pikaar, and G. Biskos, “Metal oxide semiconducting nanomaterials for air quality gas sensors: operating principles, performance, and synthesis techniques,” *Microchim Acta*, vol. 189, no. 5, p. 196, May 2022, doi: 10.1007/s00604-022-05254-0.

[2] A. M. Negrescu, M. S. Killian, S. N. V. Raghu, P. Schmuki, A. Mazare, and A. Cimpean, “Metal Oxide Nanoparticles: Review of Synthesis, Characterization and Biological Effects,” *Journal of Functional Biomaterials*, vol. 13, no. 4, Art. no. 4, Dec. 2022, doi: 10.3390/jfb13040274.

[3] A. T. Güntner, N. J. Pineau, and S. E. Pratsinis, “Flame-made chemoresistive gas sensors and devices,” *Progress in Energy and Combustion Science*, vol. 90, p. 100992, May 2022, doi: 10.1016/j.pecs.2022.100992.

[4] S. Schwyn, E. Garwin, and A. Schmidt-Ott, “Aerosol generation by spark discharge,” *Journal of Aerosol Science*, vol. 19, no. 5, pp. 639–642, Oct. 1988, doi: 10.1016/0021-8502(88)90215-7.

[5] D. P. Debecker *et al.*, “Spark ablation: a dry, physical, and continuous method to prepare powdery metal nanoparticle-based catalysts,” *Chem. Commun.*, vol. 60, no. 79, pp. 11076–11079, Oct. 2024, doi: 10.1039/D4CC03469D.

[6] D. Gounaris *et al.*, “Sub-ppm Methane Sensing by Spark-Ablation-Synthesized Nano-SnO_2,” *ACS Sens.*, vol. 11, no. 3, pp. 1865–1874, Mar. 2026, doi: 10.1021/acssensors.5c02516.

[7] A. T. Güntner, M. Wied, N. J. Pineau, and S. E. Pratsinis, “Rapid and Selective NH3 Sensing by Porous CuBr,” *Advanced Science*, vol. 7, no. 7, p. 1903390, 2020, doi: 10.1002/advs.201903390.

Acknowledgements

This work was supported by the European Union's Horizon Europe research and innovation programme under grant agreement no. NEEDED (GA-101095754)

DOI 10.5162/eurosensors2026/Mo–CHS–11

Harnessing Multi-phase Interactions in Sn/SnO/SnO_2 Tri-phase Material for Gas Sensing

Gunjoo Kim[1], Andreas Güntner[1]
[1]Human-centered Sensing Laboratory, Department of Mechanical and Process Engineering, ETH Zürich, Zürich, Switzerland
andreas.guentner@hsl.ethz.ch

Summary:

Tin oxide is a redox-active material, yet controlled tuning of its surface oxidation states remains elusive due to non-selective reduction pathways. Here, we report a urea-assisted thermal treatment that enables surface-selective transformation of SnO_2, leading to Sn/SnO/SnO_2 multiphase nanocomposites with controlled phase coexistence. This platform allows direct interrogation of multiphase interfaces, revealing distinct roles of metallic Sn and SnO in signal transduction and surface reaction kinetics in gas sensing.

Keywords: Multiphase interface, tin oxide, surface states, signal transduction, gas sensing

Background and objective

Tin oxide is one of the most widely used materials in chemiresistive gas sensing due to its chemical stability, low cost, and compatibility with scalable synthesis methods[1]. Despite its extensive use, however, the role of different oxidation states in governing sensing performance remains insufficiently understood.

Conventional reduction strategies, including hydrogen- and carbon-assisted treatments, inherently lack selectivity and often induce bulk reduction rather than surface-confined transformation[2-3]. This leads to particle coarsening, loss of surface-defined structures, and simultaneous changes in morphology and electronic properties, making it difficult to isolate the intrinsic contribution of surface oxidation states.

Controlled reduction to induce coexistence of metallic, suboxidic, and oxidic phases is therefore highly desirable, as metallic Sn can enhance electronic conduction pathways, while sub-oxide SnO phases affect surface adsorption and reaction kinetics[4-5]. However, achieving such multiphase configurations in a stable and controllable manner remains challenging.

Here, we address this limitation using a urea-assisted thermal treatment that enables surface-selective transformation of SnO_2. Driven by the decomposition chemistry of urea, this single-step and scalable approach allows gradual tuning of phase composition without triggering extensive bulk reduction or sintering. As a result, Sn/SnO/SnO_2 multiphase nanocomposites with preserved morphology and well-defined interfacial structures are obtained.

This platform provides direct access to the coexistence of multiple oxidation states within a single material system, enabling systematic investigation of how multiphase interfaces influence gas sensing behavior.

Results

The urea-assisted thermal treatment enabled controlled transformation of SnO_2 into Sn-containing multiphase nanocomposites. X-ray diffraction (XRD) analysis revealed the gradual emergence of metallic Sn with increasing urea content, while the peak width remained largely unchanged, indicating that the primary effect was the increase in Sn fraction rather than particle growth (Fig. 1a). This suggested that the reduction process proceeded without significant degradation of the oxide framework.

Transmission electron microscopy further confirmed that small, well-dispersed particles were formed on the SnO_2 surface, with comparable particle sizes across samples prepared with different urea ratios. Especially, Sn^0 particles were partially reduced on the surface of SnO_2 (Fig. 1b). These observations indicated that the urea-assisted process enabled compositional tuning while preserving the overall nanostructure.

In addition, controlled post-oxidation led to the formation of SnO, allowing access to Sn/SnO/SnO_2 tri-phase systems.

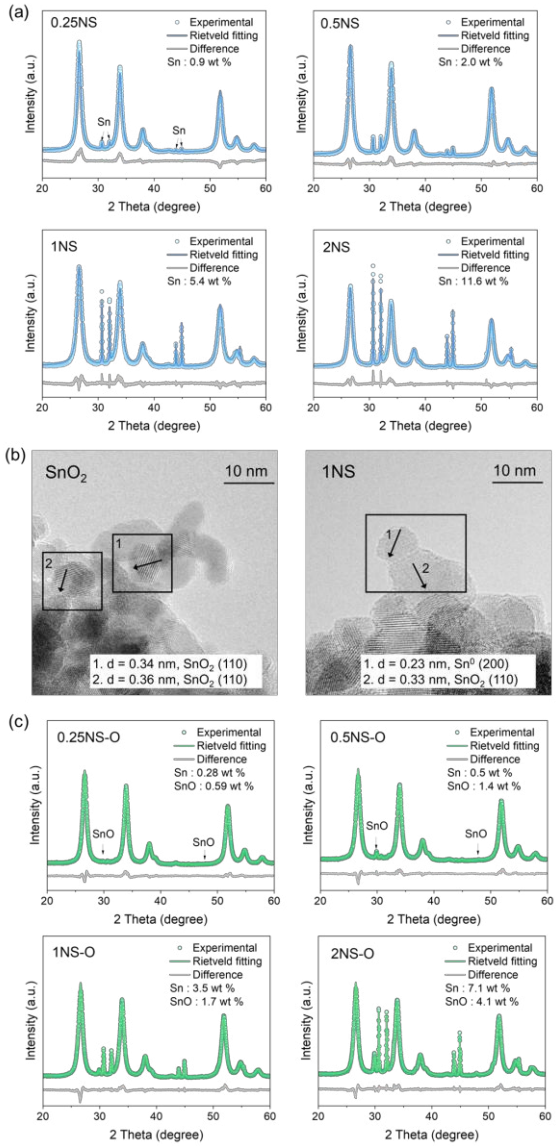

Fig. 1. (a) XRD results of Sn/SnO_2 bi-phase materials, (b) TEM images of SnO_2 and 1NS. (c) XRD results of Sn/SnO/SnO_2 tri-phase materials.

To identify the chemical origin of the reduction process, various species derived from urea decomposition, including H_2, CO, and nitrogen-containing intermediates, were systematically examined. Among them, NH_3 was found to be the key factor enabling partial reduction of SnO_2 while preserving the overall oxide structure, in contrast to other species that led to either insufficient or excessive reduction.

In the resulting multiphase system, metallic Sn acted as an efficient electronic pathway that facilitated charge transport through the sensing layer, thereby lowering the baseline resistance and promoting a stronger transduction response. By contrast, SnO likely played a different role at the surface. Rather than primarily enhancing electronic conduction, it appeared to moderate excessive analyte adsorption and facilitate the oxygen-mediated surface reaction kinetics, which could help suppress irreversible surface accumulation of adsorbates and improve signal recovery. The coexistence of Sn, SnO, and SnO_2 therefore suggested a complementary division of functions within a single material platform, where metallic Sn favored electronic transport, while SnO helped maintain a more balanced and reversible surface state.

References

[1] Y. Masuda, Recent advances in SnO_2 nanostructure based gas sensors, *Sensors and Actuators B: Chemical* 364, 131876 (2022); doi: 10.1016/j.snb.2022.131876

[2] P. Munnik, P. E. de Jongh, and K. P. de Jong, Recent developments in the synthesis of supported catalysts, *Chemical reviews,* 115.14 6687-6718, (2015); doi: 10.1021/cr500486u

[3] H. Rong, S. Ji, J. Zhang, D. Wang, and Y. Li, Synthetic strategies of supported atomic clusters for heterogeneous catalysis. *Nature Communications*, 11(1), 5884 (2020); doi: 10.1038/s41467-020-19571-6

[4] S. Yan, and Q. Wu, Micropored Sn-SnO_2/carbon heterostructure nanofibers and their highly sensitive and selective C_2H_5OH gas sensing performance, *Sensors and Actuators B: Chemical* 205, 329-337 (2014); doi: 10.1016/j.snb.2014.08.062

[5] A. Shanmugasundaram, P. Basak, L. Satyanarayana, and S. V. Manorama, Hierarchical SnO/SnO_2 nanocomposites: Formation of in situ p–n junctions and enhanced H_2 sensing, *Sensors and Actuators B: Chemical*, 185, 265-273, (2013); doi: 10.1016/j.snb.2013.04.097

DOI 10.5162/eurosensors2026/Mo–CHS–12

Room-temperature Drift Reduction in Chemoresistive Gas Sensors by UV Illumination Tuning

Paolo Pellegrino[1,2], Albert Romano Rodriguez[1,2], Guillem Domenech-Gil[1,2,3]
[1] Department of Electronic and Biomedical Engineering, University of Barcelona (UB), 08028 Barcelona, Spain,
[2] Institute of Nanoscience and Nanotechnology (IN2UB), University of Barcelona (UB), 08028 Barcelona, Spain
[3] Department of Thematic Studies - Environmental Change (TEMA M), Linköping University, Sweden
Corresponding Author's e-mail address: guillem.domenech-gil@liu.se

Summary:

Chemoresistive metal-oxide gas sensors are attractive for low-cost sensing but typically require elevated temperatures to operate and suffer from baseline drift that degrades long-term accuracy. We report a room-temperature strategy to mitigate drift by illuminating site-selectively grown tin oxide (SnO_2) nanowire (NW) assemblies with ultraviolet (UV) light. By choosing the illumination wavelength and tuning the light intensity, the nanowire electrical behavior transitions from semiconducting to metallic, and gas-response magnitude and speed can be adjusted, while the baseline slope is reduced 3 orders of magnitude. The approach aims at reducing the need of frequent recalibration against external reference instruments for practical deployments.

Keywords: photoactivation, tin oxide nanowires, baseline drift, room-temperature sensing, sulfur gases

Headlines

- UV activation of semiconducting nanowire assemblies enables control over response speed and magnitude at room temperature.
- Increasing illumination intensity can minimize baseline drift, reducing the need for frequent external calibration.
- In SnO_2 NWs, a light-driven transition in electrical behavior accompanies improved sensing dynamics for sulfur gases.

Background, Motivation and Objective

Crystalline metal-oxide (MOx) chemoresistive gas sensors have been widely investigated and commercialized due to their sensitivity, robustness, miniaturization potential, and comparatively low cost. However, optimal operation often requires heating (typically 100–400 °C) [1], which complicates integration in everyday electronics and increases power consumption. In addition, baseline drift limits precision over time, increasing dependence on reference-grade instruments and frequent recalibration—undermining the low-cost advantage.

Here, our objective is to improve the reliability of MOx chemoresistors by operating at room temperature while reducing baseline drift, paving the way towards denser and more affordable sensing networks to complement limited numbers of reference monitoring stations.

Description of the New Method or System

We use UV light to activate site-selectively synthesized SnO_2 NW sensor devices at room temperature. SnO_2 NWs were site-selectively synthesized by chemical vapor deposition via a vapor-liquid-solid mechanism bridging pre-patterned Cr/Pt electrodes, yielding functional devices within hours. Material quality and crystallinity were confirmed by X-ray diffraction, NW semiconducting nature via I–V electrical measurements, and their indirect bandgap of ~3.5 eV by means of UV–Vis transmission.

Gas measurements were carried out in a custom stainless-steel chamber and using Bronkhorst mass-flow controllers and a Keithley 2400 SourceMeter. Sensors were exposed to 200 $ml \cdot min^{-1}$ flows of dry or humid air with pulses of regulatory-relevant concentrations of H_2S, SO_2, CO_2, CH_4 and CO, under dark conditions and under 360 nm illumination at intensities up to ~90 µW. The novelty resides in the systematic tuning of illumination intensity to simultaneously (i) modulate the nanowire electrical response to

surrounding gases and (ii) reduce baseline drift while maintaining room-temperature operation.

Results

Under increasing UV intensity, n-type SnO_2 NW devices progressively shifted from semiconducting behavior (double-Schottky-like) in the dark to ohmic behavior above approximately 20 µW (see *Fig.1*), whereas p-type NW devices remained ohmic across the studied conditions. Among the tested gases, both device types responded to H_2S and SO_2. Notably, p-type SnO_2 responded to SO_2 only in humid atmospheres, while n-type devices responded under both dry and humid conditions.

Stronger illumination led to faster response dynamics (see *Fig.2*), e.g. reducing response time to 1.25 ppm SO_2 from ~16 minutes in dark conditions to <3 minutes under 50 µW, while the relative response exhibited a maximum of ~40% around ~20 µW (6 minutes). Notably, increasing light intensity, especially above ~20 µW in p-type SnO_2, also reduced baseline drift, i.e., baseline slope changed from $1.8 \cdot 10^{-2}$ Ω/s at 13 µW to $-2.7 \cdot 10^{-5}$ Ω/s at ~90 µW (see *Fig.3*). These trends are consistent with a sequence in which photogenerated carriers reduce the effective barrier, on-setting a tunneling-dominated transport regime, while above certain illumination intensity desorption of pre-adsorbed surface species is promoted. Building on this photon–SnO_2 interaction analysis, we will outline a procedure intended to enable sensor self-recalibration at room temperature, targeting reduced dependence on frequent external calibration.

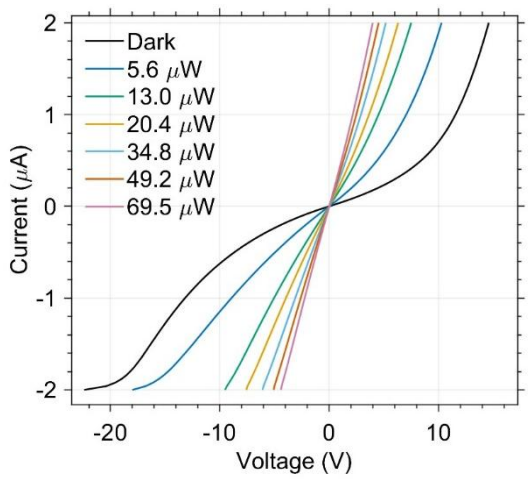

Fig. 1. Current–voltage (I-V) characteristics of Pt/ n-type SnO_2/Pt exhibiting double Schottky behavior under dark conditions and ohmic above ~20 µW.

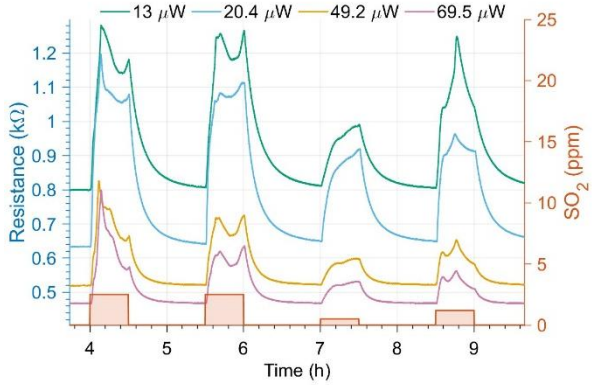

Fig. 2. Resistance as a function of time when n-type SnO_2 is exposed to alternating pulses of sulphur dioxide and to different light intensities where it can be observed the variation magnitude and speed of response.

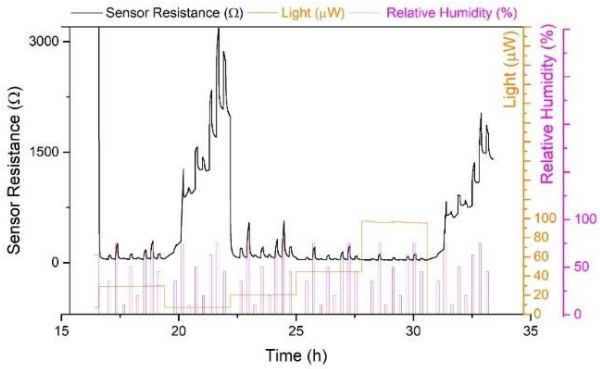

Fig. 3. Resistance over time when p-type SnO_2 is exposed to alternating pulses of relative humidity where the effects of drift reduction and changes in the magnitude and speed of response can be observed when the illumination intensity varies.

References

[1] P. Shankar, J.B.B. Rayappan, Gas sensing mechanism of metal oxides: The role of ambient atmosphere, type of semiconductor and gases - A review, *Science Letters Journal* 4, 126 (2015); doi: NA.

Acknowledgements

This work has been financially supported by the Horizon Europe's Marie Skłodowska-Curie grant agreement No 101109501, MICIU/AEI/10.13039/501100011033 and ERDF, EU under project PID2023-151565OB-C44.

DOI 10.5162/eurosensors2026/Mo–CHS–13

Dataset: Odour sensing in turbulent plumes with high-speed e-nose and PLIF ground truth

Nik Dennler[1], Elle Stark[2], Saimon Collaku[1], Aaron True[2] and Andreas T. Güntner[1]
[1]Human-centered Sensing Laboratory, Department of Mechanical and Process Engineering, ETH Zurich, Zurich, Switzerland
[2]Department of Civil, Environmental and Architectural Engineering, University of Colorado Boulder, Boulder, CO, USA

Summary: Real-world gas sensing requires resolving turbulent odour plumes with rapid concentration fluctuations, yet compact metal-oxide (MOx) sensors strongly low-pass filter these dynamics. Here we present a benchmark dataset combining planar-laser-induced-fluorescence (PLIF) measurements of an acetone plume with synchronised kilohertz-rate recordings from an electronic nose. The measurements enable direct comparison between turbulent plume dynamics and sensor response and thus enable the validation of algorithmic approaches for high-speed olfactory sensing in turbulent environments.

Keywords: turbulence, odour plumes, electronic nose, metal-oxide sensors, PLIF, fast sensing

Introduction

Artificial olfaction in real-world environments requires operation in turbulent flow fields, where odour is transported as intermittent and filamentous plumes with rapid concentration fluctuations rather than smooth gradients [1]. These temporal features carry information relevant to source localisation, plume inference, and—consequentially—odour guided navigation [2]. However, commercially available metal-oxide (MOx) gas sensors strongly low-pass filter the underlying gas signal due to their thermal and surface-kinetic dynamics [3]. Progress in reconstructing fast odour dynamics from the sensors is in principle possible [4], but has been limited by the lack of benchmark datasets that jointly capture realistic plume structure and synchronised sensor response.

To address this, we developed a multimodal dataset that combines non-invasive planar laser-induced fluorescence [5] (PLIF) measurements of an acetone tracer plume with co-located, kilohertz-rate recordings from a custom eight-channel MEMS MOx electronic nose [4] in a laboratory wind tunnel. The contribution is intended as a reusable benchmark for studying sensor dynamics and evaluating reconstruction algorithms under controlled but realistic turbulent conditions.

Dataset design

The dataset was acquired in a low-speed turbulent wind tunnel using acetone as a tracer (see Fig. 1a). Two modalities were measured simultaneously. First, PLIF provided quantitative, two-dimensional concentration fields at high spatial resolution (see Fig. 1b). Second, a custom eight-channel MEMS MOx electronic nose recorded sensor resistances, heater temperatures, and environmental variables on a shared time base at kilohertz rate (see Fig. 1c). The e-nose comprised eight MOx sensors with closed-loop heater control and on-board data logging.

Experiments were performed at three nominal flow velocities (10 cm/s, 15 cm/s, 20 cm/s) and at three sensor positions (see Fig. 1b). Each condition was repeated, yielding a set of experiments that sample distinct plume statistics and sensor exposures. The PLIF measurements were spatially averaged over regions corresponding to the physical sensor housings, and temporally aligned to the e-nose recordings using shared trigger pulses and shape-preserving interpolation.

The released data products consist of: (i) processed PLIF image sequences in HDF5 format, containing concentration fields and calibration information, and (ii) synchronised CSV files containing e-nose measurements together with spatially and temporally aligned PLIF-derived concentration traces for the sensor regions. This structure is designed to support both image-based plume analysis and direct time-series modelling.

Technical validation

A central requirement for the dataset is that both modalities are quantitatively reliable and meaningfully aligned. The PLIF measurements achieved adequate signal quality for this purpose, where time-averaged signal-to-noise ratio exceeded 30, while instantaneous values frequently exceeded 100. The e-nose operated stably throughout the measurements due to closed-loop heater control, maintaining hotplate temperatures near 400 $^{\circ}\mathrm{C}$ with sub-degree variation.

Crucially, the synchronised optical and sensor measurements exhibit clear correspondence despite the expected low-pass behaviour of MOx sensing. Distinct turbulent events, including

DOI 10.5162/eurosensors2026/Mo–CHS–13

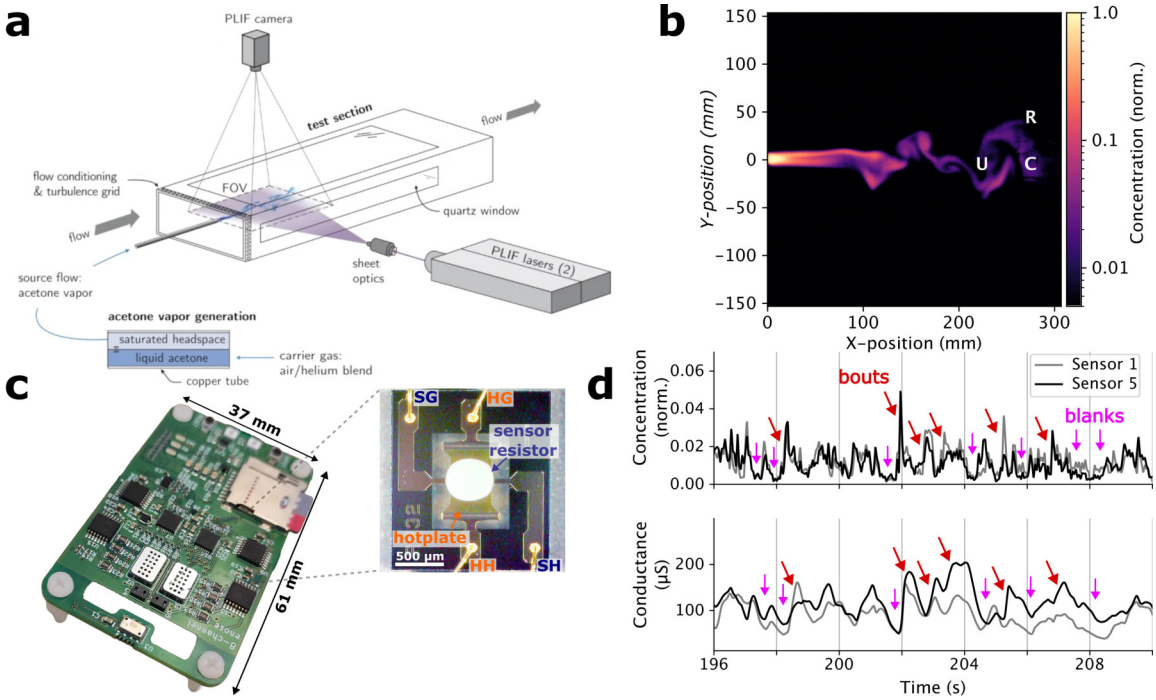

Fig. 1: Benchmark dataset for turbulent odour sensing. ***a*** *PLIF setup in a turbulent wind tunnel (adapted from [6]).* ***b*** *Example PLIF image of the acetone plume with sensor locations.* ***c*** *Custom eight-channel MEMS MOx electronic nose (adapted from [4]).* ***d*** *Representative temporally aligned PLIF concentration and MOx sensor signals, illustrating that salient plume features remain visible in the sensor response.*

bouts and blanks, are clearly visible in both modalities (see Fig. 1d). This confirms that the dataset captures shared plume structure across the optical and sensor domains.

Relevance and outlook

This dataset provides a benchmark for studying how turbulent odour fields are transformed by compact MOx sensors. The resource is directly relevant for deconvolution [7], system identification, transfer-function modelling, and data-driven reconstruction of gas concentration signals from sensor measurements. More broadly, it supports work in olfactory robotics [8], environmental monitoring, and neuromorphic sensing [9], where realistic turbulent statistics are essential but difficult to access experimentally. By combining non-invasive optical ground truth with synchronised high-speed gas sensing, the dataset fills an important methodological gap and offers a practical basis for comparing algorithms under shared experimental conditions.

Acknowledgements

N.D. and A.T.G. acknowledge funding from the Swiss National Science Foundation (Grant SNF #10001714), the ETHZ Postdoctoral Fellowship (Grant #25-1 FEL-031), and the Swiss State Secretary for Education, Research and Innovation (MB22.00041, ERC-STG-21 “HealthSense”). E.S. and A.T. acknowledge funding through the NSF/CIHR/DFG/FRQ/UKRI-MRC Next Generation Networks for Neuroscience Program (#2014217 to JPC and MRC #MR/T046759/1) and the NSF GRFP (#DGE2040434).

References

[1] A. Celani, E. Villermaux, and M. Vergassola, “Odor Landscapes in Turbulent Environments,” *Physical Review X*, vol. 4, no. 4, p. 041015, 2014.

[2] T. Ackels, A. Erskine, D. Dasgupta, A. C. Marin, T. P. Warner, S. Tootoonian, I. Fukunaga, J. J. Harris, and A. T. Schaefer, “Fast odour dynamics are encoded in the olfactory system and guide behaviour,” *Nature*, vol. 593, no. 7860, pp. 558–563, 2021.

[3] E. L. W. Gardner, J. W. Gardner, and F. Udrea, “Micromachined Thermal Gas Sensors—A Review,” *Sensors*, vol. 23, no. 2, p. 681, 2023.

[4] N. Dennler, D. Drix, T. P. A. Warner, S. Rastogi, C. D. Casa, T. Ackels, A. T. Schaefer, A. Van Schaik, and M. Schmuker, “High-speed odor sensing using miniaturized electronic nose,” *Science Advances*, vol. 10, no. 45, p. eadp1764, 2024.

[5] E. G. Connor, M. K. McHugh, and J. P. Crimaldi, “Quantification of airborne odor plumes using planar laser-induced fluorescence,” *Experiments in Fluids*, vol. 59, no. 9, p. 137, 2018.

[6] E. Stark, A. C. True, and J. P. Crimaldi, “Video: Experimental quantification of airborne odor plumes,” in *78th Annual Meeting of the APS Division of Fluid Dynamics - Gallery of Fluid Motion*, DFD 2025, American Physical Society, Nov. 2025.

[7] D. Martinez, J. Burgués, and S. Marco, “Fast measurements with mox sensors: a least-squares approach to blind deconvolution,” *Sensors*, vol. 19, no. 18, p. 4029, 2019.

[8] H. Ishida, Y. Wada, and H. Matsukura, “Chemical Sensing in Robotic Applications: A Review,” *IEEE Sensors Journal*, vol. 12, no. 11, pp. 3163–3173, 2012.

[9] N. Dennler, A. True, A. van Schaik, and M. Schmuker, “Neuromorphic principles for machine olfaction,” *Neuromorphic Computing and Engineering*, vol. 5, no. 2, p. 023001, 2025.

DOI 10.5162/eurosensors2026/Mo−CHS−14

Ethylene Glycol Detection in Pediatric Syrups: Rapid Screening MIP Based Electrochemical Sensor

Eminenur Saritas[1], Begum Sen-Dogan[2], Haluk Kulah[1, 2]
[1] Dept. of Electrical and Electronics Engineering, Middle East Technical University, Ankara, Turkiye,
[2] METU MEMS Center, Ankara, Turkiye
eminenur.saritas@metu.edu.tr

Summary:

A molecularly imprinted polymer (MIP) electrochemical sensor is developed on screen-printed gold electrodes, advancing toward a portable lab-on-a-chip device for screening ethylene glycol (EG) in pediatric syrups. Through optimized 15-cycle electropolymerization and template extraction, validated via Electrochemical Impedance Spectroscopy (EIS), the sensor was able to detect 10 µM EG concentration, below the World Health Organization (WHO) safety threshold. This work presents a highly viable approach for rapid, on-site EG screening.

Keywords: electrochemical sensor, molecularly imprinted polymer, ethylene glycol, rapid screening, field-deployable

Introduction

Glycerin-based pediatric syrups are highly susceptible to toxic contamination by ethylene glycol (EG) [1, 2]. Existing detection methods (e.g., Gas Chromatography-Mass Spectrometry, Spatially Offset Raman Spectroscopy [3]) are cost-prohibitive, lack field applicability, or miss sensitivity targets. Molecularly imprinted polymer (MIP) based sensors offer a robust, cost-effective alternative. They form synthetic matrices with specific template-shaped cavities, exhibiting high affinity and exceptional selectivity [4].

This ongoing research aims to develop a portable lab-on-a-chip MIP sensor. In this study, we optimized the MIP layer on screen-printed gold electrodes (SPE) to establish a highly sensitive recognition matrix, meeting the WHO's 0.1% (~16.1 mM) safety threshold.

Experimental Method

The MIP sensor was fabricated in four steps. Commercial gold working electrodes were cleaned in 0.5 M H_2SO_4 via 20 cyclic voltammetry (CV) cycles using Pt wire as counter and Ag/AgCl as reference electrodes. A self-assembled monolayer (SAM) was formed by dropcasting 100 mM 4-aminothiophenol in ethanol and incubating for 30 min, followed by an ethanol wash.

Recognition cavities were created by co-electropolymerizing 5 mM *o*-phenylenediamine (OPD) and 20 mM EG in acetate buffer via CV. Polymer thickness was optimized by testing 10, 15, and 20 electropolymerization cycles. For template extraction, electrodes were initially immersed in 0.1 M acetic acid-methanol (1:1 v/v) for 20 min. To maximize template removal efficiency from the optimized polymer film, the extraction solution was then upgraded to 0.2 M acetic acid-methanol (1:1 v/v).

Sensor performance was characterized via EIS in the frequency range of 100 kHz - 0.1 Hz and Differential Pulse Voltammetry (DPV) in 10 mM $Fe(CN)_6^{3-/4-}$ with 0.1 M NaCl.

The measurement relies on steric hindrance. Bound targets physically obstruct the redox probe's surface access, decreasing DPV peak current (I_p) and increasing EIS charge transfer resistance (R_{ct}).

Results and Discussion

CV scans during OPD/EG electropolymerization (Fig. 1) exhibited an oxidation peak at ~0.42 V, consistent with OPD oxidation [5]. The progressive current decrease across successive cycles confirmed non-conductive film growth.

To optimize polymer thickness, the current suppression percentage ($\Delta I/I_0$) was evaluated. This yielded suppression values of 9.0%, 16.7%, and 11.3% for polymer films deposited with 10, 15, and 20 cycles, respectively. The 15-cycle polymerization provided the optimal polymer structure, offering more recognition sites than the 10-cycle process without making the polymer film excessively insulating, as observed at 20 cycles.

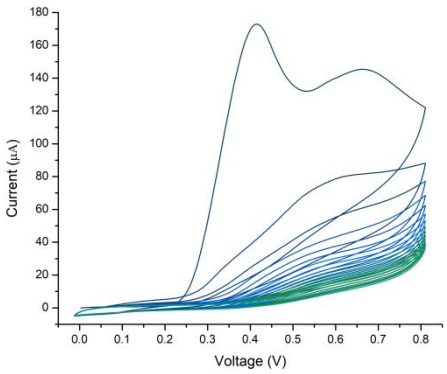

Fig. 1. 15-cycle CV scans during electropolymerization. Current decreases from initial (blue) to final cycles (green), indicating an insulating film growth.

Increasing the extraction solvent to 0.2 M acetic acid demonstrated highly efficient template removal, yielding a 38.9% current suppression ($\Delta I/I_0$) upon rebinding 10 µM EG in acetate buffer (Fig. 2). While the signal recovery trend aligns with typical electropolymerized MIPs on bare gold [6], our modified removal solution drastically improved current suppression.

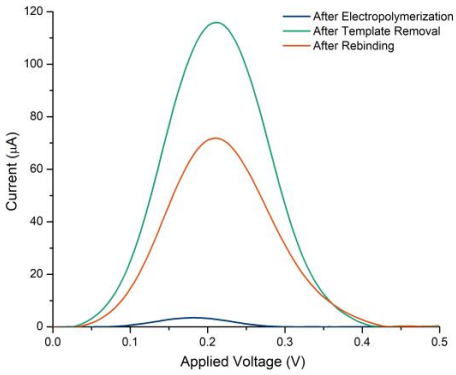

Fig. 2. DPV responses showing a 38.9% current suppression. A voltage window of 0-0.5 V was used.

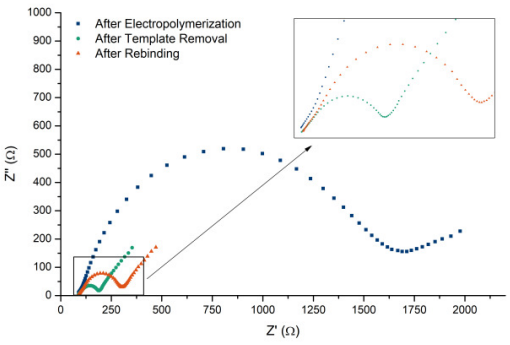

Fig. 3. Nyquist plots of step-wise modification. The semicircle (R_{ct}) expands with the MIP layer, shrinks after extraction, and re-expands upon EG binding.

These findings were quantitatively validated via EIS. Nyquist plots (Fig. 3) were fitted to a modified Randles circuit R_s(CPE[R_{ct}W]), using a Constant Phase Element (CPE) for surface roughness.

Fitted parameters (Tab. 1) revealed a stable solution resistance (R_s ≈ 90 Ω). Post-electropolymerization, R_{ct} increased to 1540 Ω due to the insulating polymer layer. Template removal drastically reduced R_{ct} to 93.0 Ω, confirming successful cavity creation. Upon rebinding 10 µM EG, the sterically hindered cavities raised R_{ct} to 204 Ω.

Tab. 1: Fitted EIS parameters using the modified Randles circuit.

Modification Step	R_s (Ω)	R_{ct} (Ω)
After Electropolymerization	90.6	1540
After Template Removal	89.3	93.0
After Rebinding	92.1	204

Conclusion

A highly sensitive MIP electrochemical sensor for EG detection was successfully established on SPEs. A robust 15-cycle MIP layer and an optimized 0.2 M extraction protocol, verified via DPV and EIS, provide a strong analytical foundation. Future work will integrate custom thin-film electrodes with a microfluidic channel for simultaneous on-chip MIP polymerization and continuous sample measurements.

References

[1] World Health Organization, WHO urges action to protect children from contaminated medicines, (2023); https://www.who.int/news/item/23-01-2023-who-urges-action-to-protect-children-from-contaminated-medicines

[2] J. G. Schier et al., Medication-associated diethylene glycol mass poisoning, N. Engl. J. Med. 388, 1153-1155 (2023); doi: 10.1056/NEJMp2215840

[3] S. Banerjee et al., Handheld spatially offset Raman spectroscopy for rapid non-invasive detection of ethylene glycol and diethylene glycol in medicinal syrups, J. Pharm. Biomed. Anal. 117031 (2025); doi: 10.1016/j.jpba.2025.117031

[4] A. Herrera-Chacón et al., Molecularly imprinted polymers - towards electrochemical sensors and electronic tongues, Anal. Bioanal. Chem. 413, 6117-6140 (2021); doi: 10.1007/s00216-021-03313-8

[5] A. Luo et al., Novel Co MOF with Ionic Liquid Comprised Portable Molecularly Imprinted Polymer-Based Electrochemical Sensor for the Point-of-Care Detection of a Breast Cancer Biomarker, J. Electrochem. Soc. 169, 117504 (2022); doi: 10.1149/1945-7111/ac9ee7

[6] N. Ermiş, N. Tinkiliç, Development of an Electrochemical Sensor for Selective Determination of Dopamine Based on Molecularly Imprinted Poly(p-aminothiophenol) Polymeric Film, Electroanalysis 33, 1491-1501 (2021); doi: 10.1002/elan.202060556

DOI 10.5162/eurosensors2026/Mo–CHS–15

Tuning Selectivity of Electrochemical Sensors through Polymer Modifications

Ines C. Weber,[1] Yann Zosso,[2] Diego Uruchurtu Patino,[2] Laura Rijns,[2] Adrian Düsselberg,[2] Zhenan Bao[2]
[1] Chalmers University of Technology, Kemivägen 10, SE-412 96 Göteborg, SWEDEN
[2] Stanford University, 334 Via Ortega, 94305 Stanford, USA
inesc@chalmers.se

Summary:

Electrochemical sensors are highly promising for emerging applications, including health and environmental monitoring. Yet, a key bottleneck of today's sensors is limited selectivity. While electrode material development can enhance sensor performance, it is often insufficient to achieve the desired selectivity. Here, we introduce a different approach: modifying electrode surfaces with neutral polymeric coatings. Specifically, we demonstrate that poly(4-vinylpyridine) (P4VP) coatings deposited on glassy carbon electrodes systematically shift the oxidation potentials of ascorbic acid (AA) and serotonin (5-HT), thereby separating their oxidation peaks and enabling simultaneous detection in mixture. Importantly, we show that this concept is not limited to this specific example, but can be expanded to varying polymers, additional biomarkers (i.e., estradiol and melatonin), and other carbon electrode materials. Overall, this work demonstrates an alternative strategy to controlling the apparent oxidation potential and selectivity of electrochemical sensors, promising for next-generation sensing applications.

Keywords: electrochemical sensor, selectivity, polymer coating, multi-analyte detection, biomarker

Background, Motivation and Objective

Electrochemical sensors are promising for health applications due to their high sensitivity, repeatability, and compatibility with miniaturized, low-cost platforms [1]. However, their translation into real applications is hindered by limited selectivity: many small-molecule biomarkers, such as 5-HT and AA, exhibit similar oxidation potentials and produce overlapping voltammetric signals that prevent molecular discrimination. Existing approaches to improve selectivity often rely on specific binding receptors [2], but frequently face issues with stability and regeneration due to the strong binding affinity between receptor and target analyte. Receptor-free sensors bear the advantage of repeatability, and material design can improve selectivity; however, this is rarely sufficient to overcome selectivity limitations in complex, real-world fluids.

An alternative strategy is the use of polymeric coatings that modify the electrochemical interface. The most commonly employed polymers are conductive (e.g., PEDOT) or charged (e.g., Nafion [3]), while neutral polymers have received little attention, as they are generally considered to impede diffusion. We show that neutral polymeric coatings are an effective strategy for altering sensor selectivity, providing a novel and so far unexplored route towards selectivity.

Description of the New Method or System

The rationale of our work is to modulate oxidation potentials and currents through polymeric coatings [4]. To this end, we deposit commercial polymers onto glassy carbon electrodes (GCE) via drop-casting. P4VP was selected as the primary coating material because its pyridinic nitrogen can interact with a wide range of molecules, acting as a strong Lewis base and efficient hydrogen-bond acceptor. We hypothesize that polymer–biomarker interactions alter the electron distribution of the biomarker and its adsorption at the electrode interface, resulting in shifts in oxidation potential. We strengthen this hypothesis through chronocoulometry and Fourier-transform infrared spectroscopy (FTIR).

We evaluate the effect of polymeric coatings on the electrochemical detection of ascorbic acid (AA), serotonin (5-HT), melatonin (Mel), and estradiol (E2), chosen for their relevance in clinical applications. We demonstrate that polymeric coatings can selectively modify the oxidation potentials of these biomarkers, thereby enhancing system selectivity, and that this concept extends to other carbon electrode materials and multiple commercial polymers.

Results

The effect of P4VP coatings on GCE is shown in **Fig. 1**. On a bare GCE, the oxidation potentials of AA and 5-HT overlap in the potential range of 0.2 to 0.4 V (**Fig. 1a**). This overlap becomes particularly problematic when measuring the two analytes in a mixture, where physiological AA concentrations exceed 5-HT by orders of magnitude. In fact, in the mixture, the 5-HT signal is obscured by the broad AA shoulder (**Fig. 1b**). In contrast, applying a P4VP coating shifts the 5-HT peak to higher potentials and the AA peak to lower potentials (**Fig. 1c**), yielding a clear peak separation that persists in mixture and enables analyte discrimination (**Fig. 1d**).

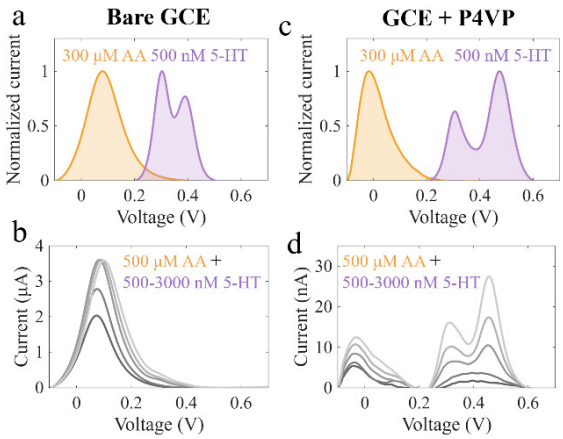

Fig. 1. (a) normalized SWV of ascorbic acid (AA) and serotonin (5-HT) measured as single analytes on a bare GCE. (b) Corresponding mixture measurement (c) normalized SWD detection of AA and 5-HT as single analytes on P4VP-coated GCE. (d) Corresponding mixture measurement [4].

Chronocoulometry and FTIR reveal that the P4VP coating enhances AA adsorption on the GCE surface while reducing 5-HT adsorption, consistent with the observed oxidation potential shifts. FTIR further confirms significant hydrogen bonding between both analytes and P4VP.

Importantly, this concept is not limited to P4VP and these two analytes, but extends to other polymer coatings and biomarkers, each displaying polymer-specific oxidation potentials (**Fig. 2**), as well as to other carbon electrode materials [5]. The ability to control oxidation potentials through a simple polymeric coating represents a significant step towards tunable sensor selectivity: sensor arrays featuring distinct polymeric layers could enable diverse and orthogonal analyte detection, and we have recently shown that polymer-modified electrodes combined with machine learning can differentiate multiple analytes in complex mixtures [6].

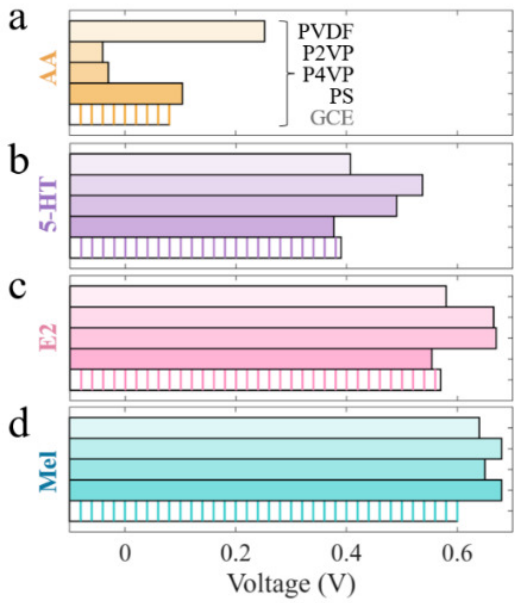

Fig. 2. Oxidation potential of AA, 5-HT, E2, and Mel on the bare GCE and various polymeric coatings (bottom to top: PS, P4VP, P2VP, PVDF) [4].

Conclusion

Polymer coatings offer a simple route to tune the oxidation potentials of electrochemical sensors. We demonstrate that P4VP coatings effectively separate the oxidation potentials of AA and 5-HT, enabling their detection in mixture. This concept extends to various polymers and additional biomarkers, offering a unique handle over the selectivity of label-free electrochemical sensors.

References

[1] S. Chen, Z. Qiao, Y. Niu, J. C. Yeo, Y. Liu, J. Qi, S. Fan, X. Liu, J. Y. Lee, C. T. Lim, *Nat. Rev. Bioeng.* **2023**, *1* (*12*), 950–971. DOI: https://doi.org/10.1038/s44222-023-00094-w.

[2] C. Ye, M. Wang, J. Min, R. Y. Tay, H. Lukas, J. R. Sempionatto, J. Li, C. Xu, W. Gao, *Nat. Nanotechnol.* **2024**, *19* (*3*), 330–337. DOI: https://doi.org/10.1038/s41565-023-01513-0.

[3] J. Han, J. M. Stine, A. A. Chapin, R. Ghodssi, *Anal. Methods*. **2023**, *15* (*9*), 1096–1104. DOI: https://doi.org/10.1039/D2AY01627C.

[4] I. C. Weber, Y. Zosso, D. U. Patino, L. Rijns, A. L. M. Düsselberg, Z. Bao, **2026**, 2026.02.16.706066. DOI: https://doi.org/10.64898/2026.02.16.706066.

[5] I. C. Weber, D. U. Patino, K.-J. Hsu, Y. Zosso, A. L. M. Düsselberg, T. Chen, K. Parkatzidis, S. Wei, A. Mahmud, G. M. G. B. H. Bastide, et al., *Adv. Funct. Mater.* **2026**, *36* (*40*), e28595. DOI: https://doi.org/10.1002/adfm.202528595.

[6] A. L. M. Duesselberg, I. C. Weber, Y. Zosso, P. Salah, Z. Bao, *ACS Electrochem.* **2026**, *2* (6), 1444–1452.DOI: https://doi.org/10.1021/acselectrochem.6c00079.

DOI 10.5162/eurosensors2026/Tu–CHS–01

Manganese Spinels Boost Gas Sensitivity in Humid Environments

Reinaldo dos Santos Theodoro[1,2], Matteo D'Andria[2], Tiago Elias Abi-Ramia Silva[2], Diogo Paschoalini Volanti[1], Andreas T. Güntner[2]
[1] São Paulo State University (UNESP), Rua Cristóvão Colombo 2265, 15054-000 São José do Rio Preto, Brazil,
[2] ETH Zurich, CH-8092 Zurich, Switzerland
andreas.guentner@hsl.ethz.ch

Summary:
In gas sensing, several challenges must be addressed for practical applications, particularly the presence of humidity, which has attracted significant attention. Here, we present manganese-based spinels that can leverage humidity to enhance gas sensitivity.

Keywords: Manganese, Spinel, Flame Spray Pyrolysis, Sensitivity, Humidity

Background

Humidity is a critical challenge for metal oxide (MO_x), based sensing materials, which can detect a wide range of gases and volatile organic compounds (VOCs) [1]. Various strategies have been developed to mitigate this undesired effect, including metal-functionalized MO_x, heterojunctions, and ternary oxides such as perovskite and spinel structures [2]. Here, we demonstrate that *p*-type Manganese spinels exhibit a boost on sensitivity under humid conditions for acetone detection.

Experimental

Manganese spinels-based sensing films were fabricated by flame spray pyrolysis (FSP) [3]. The precursor solutions based on Mn (II) 2-ethylhexanoate and/or Zn (II) 2-ethylhexanoate in xylene were atomized and combusted. Nanoparticles were collected on a filter positioned above the flame. The manganese oxide nanoparticles were directly deposited onto Al_2O_3 substrates with interdigitated Pt electrodes and a resistance temperature detector and annealed at 500 °C for 5 h [4]. Fig. 1 shows the fabrication of nanoparticles and sensing films by FSP. The sensors were mounted on specific holders and connected to a gas mixing system for analysis, using hydrocarbon-free synthetic air and calibrated mass flow controllers to create the desired gas mixture composition [5]. The sensor response (S) was established as follows:

$$S = Rg/Ra - 1 \quad (1)$$

Results

The synthesized materials by the FSP were MnOx (90 mol% Mn_3O_4 and 10 mol% Mn_2O_3) and $ZnMn_2O_4$ spinels, which were characterized by X-ray diffraction (XRD), specific surface area (SSA) via the Brunauer-Emmett-Teller (BET) method, scanning transmission electron microscopy (STEM), X-ray Absorption Spectroscopy (XAS), and Diffuse Reflectance Infrared Fourier Transform (DRIFT) Spectroscopy.

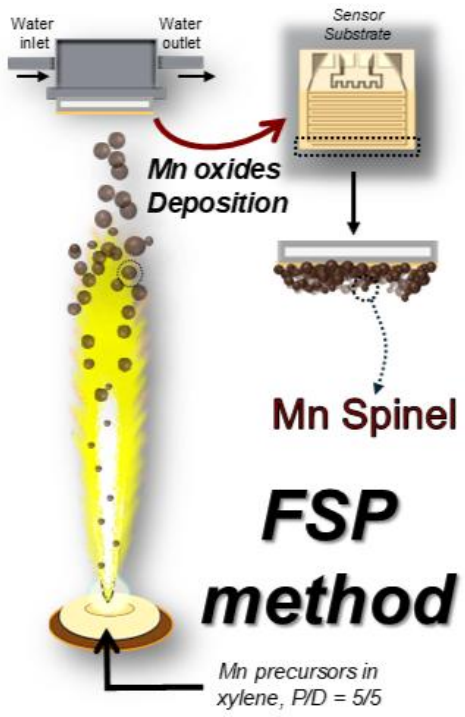

Fig. 1. Schematic illustration of nanoparticles and sensing films of manganese spinel synthesized by the FSP method.

Both sensor materials were tested for the detection of acetone and eleven other interfering gases, including isoprene, ethanol, and methanol, which are relevant interfering analytes in breath analysis. Both materials exhibit high sensitivity for detecting acetone at ppb levels, suggesting an affinity between ketone molecules and manganese-based materials. However, the most notable property of these manganese oxides is their enhanced sensitivity to acetone under humid conditions, as shown in Fig. 2. Both sensors exhibit higher sensitivity to acetone in humid environments than in dry conditions. MnO_x shows the highest normalized response for the detection of 62.5 ppb acetone at 70–80% RH (Fig. 2a), while $ZnMn_2O_4$ exhibits the highest normalized response at 30–60% RH (Fig. 2b). Considering the absolute (non-normalized) sensitivity to acetone, $ZnMn_2O_4$ shows a boost of more than 60% under humid conditions (50% RH) compared to dry conditions, whereas MnO_x exhibits a boost of approximately 17% under humid conditions.

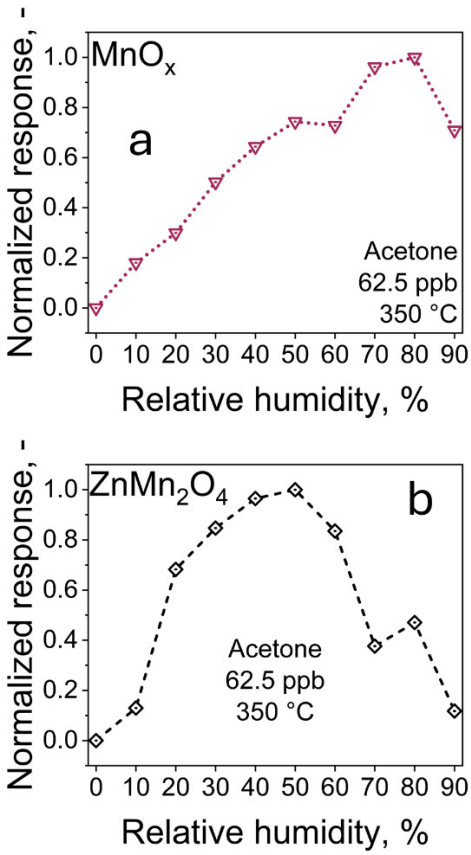

Fig. 2. Normalized sensor response of (a) MnO_x and (b) $ZnMn_2O_4$ spinels at different RH levels (0–90%) toward 62.5 ppb acetone.

DRIFT spectroscopy was used to investigate the adsorption profiles of MnOx and $ZnMn_2O_4$ upon exposure to acetone under dry and humid conditions. Both materials exhibit similar stretching peak profiles; however, the $ZnMn_2O_4$ surface shows greater perturbation, with sharper and more well-defined bands under humid conditions. Notably, two peaks appear in the 1500 – 900 cm^{-1} region, which are indicative of alkoxy (enolate) intermediates formed during acetone adsorption. Reflecting the presence of $Zn(T_d)$ and $Mn(O_h)$ sites, these two bands likely correspond to alkoxide species interacting with different surface sites, such as Zn–OR and Mn–OR. This behavior is not observed in MnO_x, which exhibits only a single, broader, less-defined band.

References

[1] Wang, Y.; Zhou, Y. Recent Progress on Anti-Humidity Strategies of Chemiresistive Gas Sensors. Materials 2022, Vol. 15, 2022, 15 (24). doi:10.3390/MA15248728

[2] Theodoro, R. S.; Santos, G. S. M.; D'Andria, M.; Gropelo, H. S.; Kravecz, S.; Güntner, A. T.; Volanti, D. P. Air Pollution Monitoring with Nanoscaled Materials in Chemoresistive Gas Sensors. ACS Appl. Mater. Interfaces 2026, 18 (10), 14473–14520. doi:10.1021/acsami.5c24099

[3] Mädler, L.; Kammler, H. K.; Mueller, R.; Pratsinis, S. E. Controlled Synthesis of Nanostructured Particles by Flame Spray Pyrolysis. J. Aerosol Sci. 2002, 33 (2), 369–389. doi:10.1016/S0021-8502(01)00159-8.

[4] D'Andria, M., Krumeich, F., Yao, Z., Wang, F. R., Güntner, A. T. (2024). Structure-Function Relationship of Highly Reactive CuO_x Clusters on Co_3O_4 for Selective Formaldehyde Sensing at Low Temperatures. Advanced Science, 11(10), 2308224, (2024); doi:10.1002/ADVS.202308224

[5] Güntner, A. T., Righettoni, M., & Pratsinis, S. E. Selective sensing of NH_3 by Si-doped α-MoO_3 for breath analysis. Sensors and Actuators B: Chemical, 223, 266–273, (2016); doi:10.1016/J.SNB.2015.09.094

Acknowledgements

This work was sponsored by São Paulo Research Foundation (FAPESP); Process numbers: 2020/06421-1, 2022/05381-1, and 2024/12700-1.

DOI 10.5162/eurosensors2026/Tu–CHS–02

Controlling DNA Translocation Velocities through Nanopores by *in-situ* Aperture Size Control

Justin N. Cronk[1], Alessio Angeli Bufalini[1], Morteza Aramesh[1]
[1] Laboratory of Single-Molecule and Single-Cell Biophysics, ETH Zurich
maramesh@ethz.ch

Summary:
Dynamically selecting and modifying aperture size with high resolution allows for size-specific sensing and probing of biopolymers' conformational space. Indeed, in a solution containing single- and double-stranded DNA, we could reduce pore size such that only the single-stranded DNA could translocate, suggesting unparalleled specificity. Dynamic nanopores can also induce conformational changes in biopolymers: we show DNA translocations in its bulk random-walk state, folded states and linearised state through aperture size modification.

Keywords: Nanopore, DNA, Biopolymers, Conformation, Sequencing

Title

Controlling DNA Translocation Velocities through Nanopores by *in-situ* Aperture Size Control

Abstract

The interfacial nanopore is a nascent but proven technique ideally suited to localised detection and fingerprinting of secretions from cells; with dynamic pore sizing, clog-free stability, positionable with nanometre precision and functionalisable, interfacial nanopores provide in-situ aperture size control through the constriction of a solid-state micropore upon contact with and depression of an elastic surface. Nanopore AFMs have already been used to study fibronectin secretion [1], and later an AFM-based interfacial nanopore was used to conduct localised recordings next to single neurons [2].

Using a pipette-elastomer interfacial nanopore (PEIN), in which the aperture of a glass nanopipette is constricted in situ by depression into a soft elastomer, the conformational space of biopolymers can be probed. Indeed, dwell times of double stranded DNA in PEINs show significant increases with smaller apertures. Moreover, additional current levels corresponding to folds in the polymer are only seen at larger aperture sizes, implying greater structural information can be derived and/or that conformational changes are induced in the DNA molecules. This is in accordance with DNA in its bulk random-walk state, folded states and linearised state. Aperture size can also be matched to analyte cross sections in situ, providing selectivity, increasing the range of possible analyte sizes measurable by one pore and allowing biopolymer dwell times to be increased by orders of magnitude over glass nanopipettes [3].

PEINs ultimately enable multidimensional analyte reads, aiding molecular fingerprinting, as well as furthering our understanding of strongly confined biopolymers. We hope to expand the library of biopolymers studied in PEINs and increase the complexity of protein mixtures, aiming to study real-time secretion patterns of live cells.

References

[1] [1] M. Aramesh et al.; Nat. Nanotechnol. 14, 791-798 (2019).

[2] [2] T. Schlotter et al.; ACS Nano 14 (10), 12993-13003 (2020).

[3] [3] N. A. W. Bell et al.; Nat. Commun. 8, 380 (2017).

DOI 10.5162/eurosensors2026/Tu–CHS–03

Sub-ppm Gas Detection with Metal Organic Frameworks Functionalized Quartz Microbalances

Sujitha Murugaiyan[1], Rosamaria Capuano[1,2], Gabriele Magna[2,3], Manuela Stefanelli[2,3], Alexandro Catini[1,2], Kishore Pushparaj[1], Valerio Allegra[1], Yuvaraj Sivalingam[4], Roberto Paolesse[2,3], Corrado Di Natale[1,2]
[1]Dept. of Electronic Engineering, University of Rome Tor Vergata, Rome, Italy
[2]Centre for Volatilomics "A. D'Amico", University of Rome Tor Vergata, Rome, Italy
[3]Dept. of Chemical Science and Technology, University of Rome Tor Vergata, Rome, Italy
[4]Dept. of Electronics and Communication Engineering,
Bannari Amman Inst. of Technology, Sathyamangalam, India
Corresponding author: dinatale@uniroma2.it

Summary:
MOF coated Quartz microbalance show an enhanced sensitivity to gases with sub-ppm limits of detection. The sensitivity pattern of three investigated materials is sufficient for a complete identification, independent from concentration, of gases and vapors of different chemical structure such as methane, CO_2, ammonia, and NO.

Keywords: Gas sensor, MOF, Quartz Microbalance, Sensor Array

Introduction

Quartz microbalances (QMBs) are often associated with limited concentration resolution. This limitation typically arises in sensors functionalized with compact sensitive layers, whereas highly porous materials—with their large effective surface area—are expected to improve detection limits. In this context, metal–organic frameworks (MOFs) represent a promising class of materials for QMB functionalization. Owing to their high porosity and large internal surface area, MOFs provide an abundance of accessible adsorption sites and have therefore attracted significant interest in gas sensing applications.

Despite their inherent sensitivity, the low electrical conductivity of many MOFs can hinder their use in electronic sensing platforms. Thus, mass-sensitive devices offer an opportunity to fully exploit MOF sensitivity. Previous work has demonstrated the detection of carbon dioxide and methane using MOF-functionalized surface acoustic wave sensors and QMBs [1]. In this study, we investigate the response of QMBs functionalized with three different MOFs—Cu-BTC, Ni-doped ZIF-67, and Fe-BDC—to ammonia, nitric oxide, carbon dioxide, and methane.

Methods

The octahedral Cu-BTC MOF was synthesized hydrothermally using copper ions and 1,3,5-benzenetricarboxylic acid (BTC) as the organic linker. The hexagonal micro-spindle-shaped Fe-BDC MOF was prepared hydrothermally using terephthalic acid (BDC). The bimetallic rhombic dodecahedral Ni-doped ZIF-67 was synthesized sonochemically using nickel and cobalt salts with 2-methylimidazole. Structural and morphological characterization was performed using XRD, FTIR, Raman spectroscopy, and SEM (see figure 1). Each MOF was deposited onto 20 MHz QMBs (KVG GmbH, Germany) by drop-casting. Certified gas mixtures were diluted in nitrogen using mass flow controllers (CMA 10B, MKS Instruments, Inc.) and delivered to a Teflon-sealed sensor cell at 100 sccm.

Fig. 1: appearance and SEM figure if MOF films.

Results

Figure 2 shows the response curves of the sensors to the four investigated gases. The adsorption isotherms exhibit an approximately linear trend across the tested concentration ranges. Sensitivities, calculated as the slopes of the linear fits, are compared in Figure 3. All

sensors exhibit the highest sensitivity to nitric oxide and ammonia, whereas the less interactive methane and carbon dioxide produce lower responses.

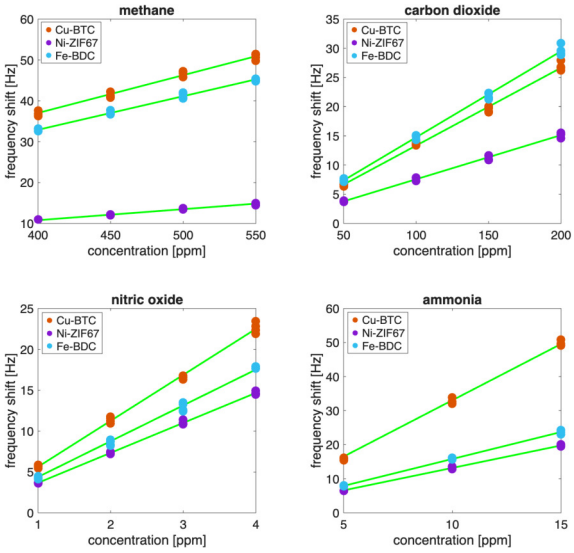

Fig. 2. Response curves of sensors to the four tested gases.

Limits of detection (LOD) were calculated as the ratio between the noise level and the sensitivity [2]. Signal fluctuation varied among sensors, ranging from 0.5 Hz to 3 Hz. These differences likely originate from non-uniform MOF films and interfacial defects between the gold electrode and the MOF layers. The resulting LODs are shown in Figure 3. For nitric oxide, the LOD ranges from 190 to 280 ppb; for ammonia, from 320 to 650 ppb. The LODs for carbon dioxide and methane are substantially higher, between 7–14 ppm for CO_2 and 11–38 ppm for CH_4.

Although the sensitivity patterns (Figure 3) are broadly similar, the remaining differences are sufficient for gas discrimination. This is demonstrated by principal component analysis of the sensor responses. Figure 4 shows the scores of the second and third principal components; the first component, dominated by overall signal magnitude, does not distinguish among gases. In this representation, each gas exhibits a concentration-dependent trajectory, and the divergence between gases increases with concentration. Interestingly, methane does not show a clear concentration trend within these components, although such behaviour appears in the first principal component. This behaviour further supports the presence of distinct sensor–analyte interactions.

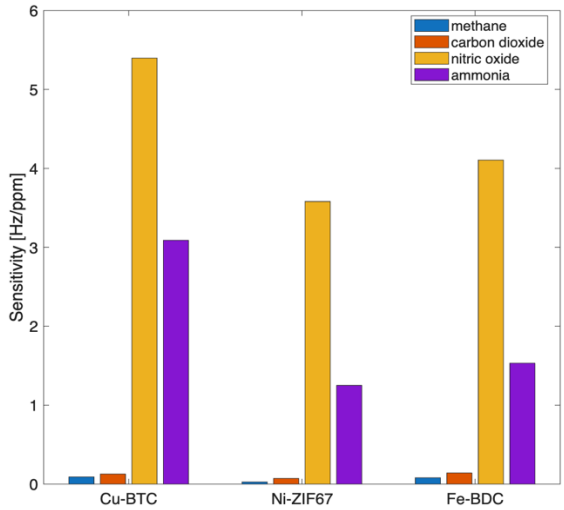

Fig. 3. Sensitivity patterns of the tested sensors

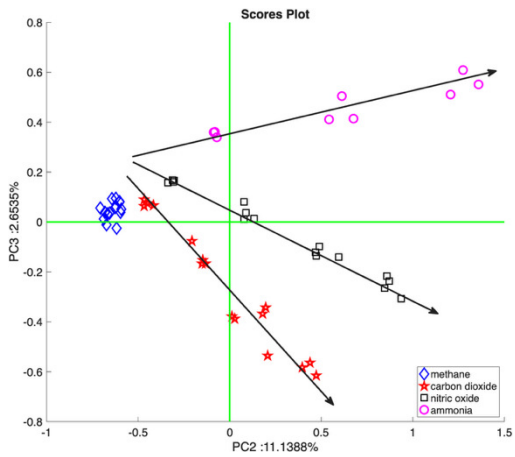

Fig. 4: scores plot of second and third principal components

References

[1] J. Devkota, K.-J. Kim, P.R. Ohodnicki, J.T. Culp, D.W. Greve, J.W. Lekse, Zeolitic imidazolate framework-coated acoustic sensors for room temperature detection of carbon dioxide and methane, Nanoscale 10, 8075–8087 (2013) doi:10.1039/c7nr09536h.

[2] A. D'Amico, C. Di Natale, P.M. Sarro, Ingredients for sensors science, Sens Actuators B 207, 1060-1068 (2015)

DOI 10.5162/eurosensors2026/Tu–CHS–04

W-$Bi_2Sn_2O_7$ Ultrafine Nanocrystals for Chemiresistive Monitoring of Volatile Organic Compound

Yiwen Zhou[1,2,3], Zichen Zheng[1,2,3], Xudong Nie[1,2], Ruiyu Hou[1,2], Carla Bittencourt[3], Chao Zhang[1,2]
[1] College of Mechanical Engineering, Yangzhou University, Yangzhou 225127, PR China,
[2] Jiangsu Key Laboratory of Surface Strengthening and Functional Manufacturing, Yangzhou University, Yangzhou 225127, PR China
[3] Chimie des Interactions Plasma-Surface, University of Mons, 7000 Mons, Belgium
Corresponding Author's e-mail address: zhangc@yzu.edu.cn

Summary:
This work develops a high-sensitivity sensor based on tungsten-doped bismuth stannate (W-$Bi_2Sn_2O_7$) ultrafine nanocrystals for the detection of 4-ethylguaiacol. The sensor demonstrates exceptional response to 4-ethylguaiacol at trace concentrations of 2–10 ppm. The enhanced sensing performance is driven by electronic structure modulation and increased surface oxygen vacancies. This work underscores the potential of defect-engineered nanomaterials for advanced agricultural monitoring and real-time plant health diagnosis.

Keywords: gas sensor, room temperature, 4-ethylguaiacol, metal oxide, doping

Background

Bismuth stannate ($Bi_2Sn_2O_7$), an n-type semiconductor characterized by its stable ilmenite-type lattice, holds immense promise for chemiresistive gas sensing due to its structural flexibility and, notably, its facilitated charge-transfer kinetics [1]. However, achieving high sensitivity at trace-level concentrations remains a formidable challenge for pristine $Bi_2Sn_2O_7$ [2]. Recent studies have demonstrated that the strategic incorporation of tungsten (W) into the metal oxide lattice has significant potential to modulate electronic properties and surface chemistry [3]. By employing a facile hydrothermal route to synthesize W-doped $Bi_2Sn_2O_7$ (W-$Bi_2Sn_2O_7$), this doping strategy synergistically induces the formation of abundant surface oxygen vacancies, creating high-density active sites for gas adsorption. Consequently, the sensor exhibits a superior, stable response to 2-10 ppm 4-ethylguaiacol, enabling reliable trace detection.

4-Ethylguaiacol is a volatile organic compound (VOC) released by plants as a defensive response to biotic or abiotic stressors, such as pathogen invasion or drought [4]. The emission intensity of 4-ethylguaiacol correlates directly with the physiological health status of the crop, providing a real-time diagnostic signature for early plant stress detection. This work demonstrates the successful integration of W-$Bi_2Sn_2O_7$ ultrafine nanocrystals into gas sensing platforms, highlighting their potential as an indispensable tool for precision agriculture and non-invasive plant health monitoring [5].

Sample preparation

A straightforward one-step hydrothermal method was used to synthesize tungsten-doped $Bi_2Sn_2O_7$. During the synthesis, tungsten hexachloride (WCl_6) was used as the dopant precursor, and the molar ratio of W to Bi was adjusted to approximately 0%, 2%, 4%, and 6%. The samples were designated as BSO, 2WBSO, 4WBSO, and 6WBSO, respectively. To evaluate the gas-sensing properties, a four-channel testing system was utilized to capture real-time resistance signals during cyclic exposure to ambient air and the target gases.

Results

Owing to its superior sensing metrics, the 4WBSO sample was selected as the representative sensor for in-depth structural analysis (Fig. 1). The morphological features of the synthesized QDs were examined via high-resolution transmission electron microscopy (HRTEM). As depicted in Fig. 1b, the 4WBSO exhibits an ultra-small grain size of 3-6 nm based on statistical analysis, consistent with the significant broadening observed in the XRD pattern (Fig. 1d), thereby enhancing surface reactivity. The corresponding selected area electron diffraction (SAED) pattern (Fig. 1d) illustrates the well-defined crystalline lattice of the doped stannate structure. Additionally, energy-dispersive X-ray spectroscopy (EDS) mapping (Fig. 3e-3i)

highlights the homogeneous dispersion of Bi, Sn, O, and W atoms, confirming that tungsten has been successfully and uniformly incorporated into the $Bi_2Sn_2O_7$.

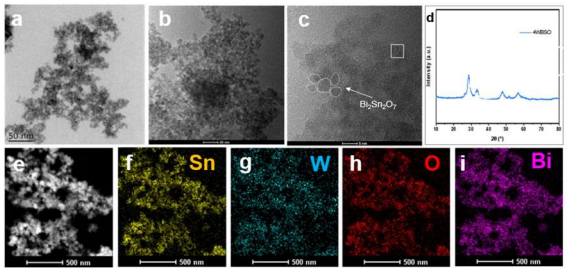

Fig. 1. (a) TEM images and (b-c) HRTEM image of 4WBSO, (d) XRD pattern of 4WBSO, (e) HAADF-STEM image of 4WBSO, (f-i) EDS elemental mapping images of Sn, W, O, and Bi for 4WBSO.

The O 1s spectra were deconvoluted into three Gaussian-Lorentzian components: lattice oxygen (O_L), chemisorbed oxygen (O_C), and oxygen vacancies (O_V). XPS O 1s analysis reveals that W-doping significantly increases the O_V relative concentration ($O_v/(O_c+O_L+O_V)$) from 24.4 % to 50.0 % (Table 1). A corresponding shift in binding energy from 529.7 eV to 530.3 eV confirms the strong electronic modulation by high-valence W^{6+} ions. These abundant O_V sites, combined with size effects, provide a high density of active centers, thereby facilitating enhanced adsorption of 4-ethylguaiacol and superior sensing kinetics.

Tab. 1: Summary of O 1s Binding Energies and Relative concentration of Oxygen Vacancies (O_v) for BSO and 4WBSO Sample.

Sample	Binding Energy (eV)	$O_v/(O_L+O_C+O_v)$ (%)
BSO	529.7	24.4%
4WBSO	530.3	50.0%

Fig. 2 demonstrates that 4WBSO achieves the most significant response toward 4-ethylguaiacol across the 2-10 ppm range at room temperature. The remarkable enhancement is primarily driven by the strategic incorporation of tungsten, which optimizes the amount O_v to a near-ideal level (approx. 50%), significantly modulating the electronic band structure and enhancing charge-carrier mobility. The high valence W^{6+} ions increase the number of chemisorption centers and introduce defect-induced energy levels. These states act as efficient electron traps, facilitating rapid charge transfer during interactions with 4-ethylguaiacol molecules, thereby heightening sensitivity.

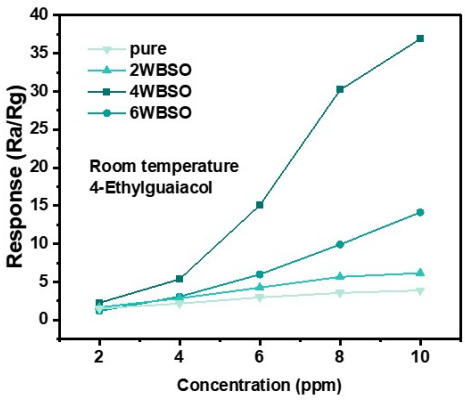

Fig. 2. The response values of WBSO (x = 0, 2, 4, and 5) film to 4-ethylguaiacol (2-10 ppm) at room temperature.

Conclusion

W-doped $Bi_2Sn_2O_7$ ultrafine nanocrystals were successfully synthesized using a facile hydrothermal method. The optimized 4WBSO exhibits abundant oxygen vacancies and size effects. The developed sensor shows a superior response to 2-10 ppm 4-ethylguaiacol at room temperature, providing a valuable tool for real-time plant stress monitoring.

References

[1] T. Wang, W. Tao, X. Kou, L. Zhao, P. Sun, G. Lu, $Bi_2Sn_2O_7$ Overlayer Assists Bilayer Chemiresistor in Humidity-Independent and Highly Selective Detection of Expiratory Acetone, *ACS Sensors* 9, 6717–6727 (2024); doi: 10.1021/acssensors.4c02378

[2] K. Liu, Z. Zheng, Y. Zhou, C. Bittencourt, M. Debliquy, Q. Liu, C. Zhang, Heterovalent-doping-induced ultrasensitive and highly exclusive ethylene sensor: Application to crop quality inspection, *Chemical Engineering Journal* 508, 161075 (2025); doi: 10.1016/j.cej.2025.161075

[3] Z. Li, R. Paul, T. Ba Tis, A. C. Saville, J. C. Hansel, T. Yu, J. B. Ristaino, Q. Wei, Non-invasive plant disease diagnostics enabled by smartphone-based fingerprinting of leaf volatiles, *Nature Plants* 5, 856–866 (2019); doi: 10.1038/s41477-019-0476-y

[4] Z. Li, Y. Liu, O. Hossain, R. Paul, S. Yao, S. Wu, J. B. Ristaino, Y. Zhu, Q. Wei, Real-time monitoring of plant stresses via chemiresistive profiling of leaf volatiles by a wearable sensor, *Matter* 4, 2553–2570 (2021); doi: 10.1016/j.matt.2021.06.009

[5] A. Kumar, V. Krishnan, Vacancy Engineering in Semiconductor Photocatalysts: Implications in Hydrogen Evolution and Nitrogen Fixation Applications, Advanced Functional Materials 31, 2009807 (2021); doi: 10.1002/adfm.202009807M. Mouse, D. Duck, The Beagle Boys for President, *Journal of Applied Nonsense* 13, 123-134 (2011); doi: 10.1234/s10000

DOI 10.5162/eurosensors2026/Tu–CHS–05

Engineering Selective Detection of Hazardous H_2 and NO_2 Using Pd Functionalized MXene/ WS_2 Gas Sensors

Mohamed Elsheshtawy[1], *Shuja Bashir Malik*[1], *Frank Güell*[1,2], *Eduard Llobet*[1], *Fatima Ezahra Annanouch*[1,*]

[1] *Departament d'Enginyeria Electronica, Universitat Rovira i Virgili,Tarragona, Catalunya, Spain.*

[2] *Universitat de Barcelona, Catalan Photonics for Energy (ENFOCAT), Barcelona, Catalunya, Spain.*

*Corresponding Author's e-mail address: fatimaezahra.annanouch@urv.cat

Summary:

Reliable detection of hazardous gases such as hydrogen (H_2) and nitrogen dioxide (NO_2) is essential for industrial safety, environmental monitoring, and emerging hydrogen-based energy technologies. Two-dimensional transition metal dichalcogenides (TMDs), particularly WS_2, have recently garnered attention as promising materials for gas sensing applications, due to their high surface reactivity and tunable electronic properties. In this work, the sensing performance of WS_2 was engineered through hybridization with titanium carbide MXene ($Ti_3C_2T_x$) and palladium nanoparticles. This study presents a highly sensitive Pd functionalized MXene/WS_2 nanocomposite-based sensors operating at low temperature of 100 °C. The WS_2/MXene sensor exhibited a clear sensitivity toward NO_2, with a response of 75%. After Pd functionalization, the sensing behavior shifted from NO_2 toward H_2, giving a dominant H_2 response of approximately 66%, while the response toward NO_2 decreased to nearly half.

Keywords: Gas sensor, TMDs, MXene, nanomaterials, Palladium functionalization.

Background, Motivation and Objective

The development of highly sensitive and selective gas sensors is crucial for environmental monitoring and industrial safety. Nitrogen dioxide (NO_2) is a hazardous air pollutant linked to respiratory diseases, while hydrogen (H_2) is highly flammable and possesses significant explosion risks in hydrogen storage and fuel-cell systems. With the increasing adoption of hydrogen as a clean energy carrier, reliable detection of H_2 leaks has become particularly important for ensuring safe operation [1]. Two-dimensional (2D) materials have recently attracted considerable attention for gas sensing applications due to their high surface-to-volume ratio and tunable electronic properties. Among them, tungsten disulfide (WS_2), a transition metal dichalcogenide (TMD), has shown strong potential for gas detection owing to its edge-rich structure and high surface reactivity [2]. However, pristine WS_2 often exhibits limited selectivity. To address this limitation, hybrid material engineering strategies have been explored. MXenes such as $Ti_3C_2T_x$ offer high electrical conductivity and abundant surface terminations, enabling the formation of conductive heterostructures with semiconducting sensing layers. Additionally, palladium (Pd) nanoparticles exhibit strong catalytic affinity toward hydrogen through dissociation and spillover mechanisms, which can significantly enhance H_2 sensing performance [3]. In this work, two sensing platforms WS_2/MXene and WS_2/MXene/Pd were developed and compared to the pristine WS_2 to investigate how MXene integration and Pd decoration influence the sensing behavior and selectivity of WS_2-based gas sensors.

Materials and Methods

WS_2 was synthesized as reported in our previous study [2]. To fabricate the WS_2/MXene heterostructure sensor, 10 mg of previously synthesized WS_2 powder was dispersed together with 5 mg of $Ti_3C_2T_x$ MXene in 10 mL of absolute ethanol. The mixture was ultrasonicated for 60 minutes to ensure homogeneous dispersion between the two materials. Subsequently, 3 mL of the obtained suspension was airbrushed onto an alumina substrate equipped with platinum interdigitated electrodes on the front side and a platinum resistive heater on the back side. For the preparation of the Pd-functionalized WS_2/MXene sensor (WS_2/MXene/Pd), the previously fabricated WS_2/MXene sensor was decorated with Pd nanoparticles using aerosol-assisted chemical vapor deposition (AACVD) as reported in our previous work [1].

Results

Fig. 1 (a, b) illustrates the FESEM images of the prepared WS_2/MXene and WS_2/MXene/Pd heterostructures respectively. The morphology analysis revealed that the WS_2/MXene heterostructure exhibits relatively smooth and flat flake-like domains, whereas the Pd-functionalized WS_2/MXene/Pd sample shows a noticeably rougher and more corrugated surface decorated with nanoscale protrusions. This morphological evolution is mainly attributed to the nucleation and growth of Pd nanoparticles during AACVD, which preferentially occurs at defects, edges, and active surface sites, thereby increasing the surface roughness and producing a less planar appearance. EDX mapping confirms the presence of MXene in both samples, indicated by the red color across the surface. In the Pd-modified sample, additional blue signals corresponding to Pd appear, confirming the successful decoration of the WS_2/MXene heterostructure with Pd nanoparticles as shown in Fig. 2 (a, b).

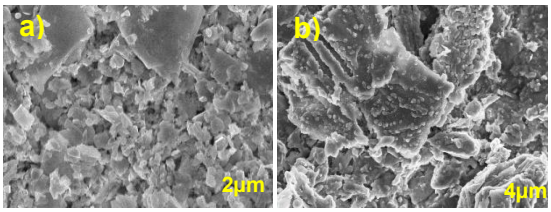

Fig. 1. FSESM images of (a) WS_2/MXene, (b) WS_2/MXene/Pd.

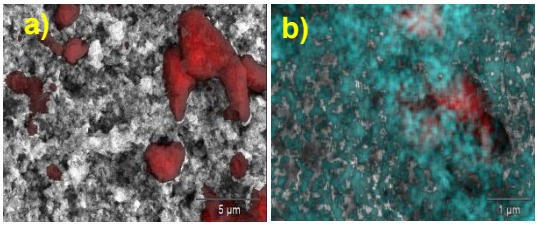

Fig. 2. (a) EDX mapping of WS_2/MXene, (b) EDX mapping of Pd decorated WS_2/MXene sensor.

The sensing performance of the fabricated sensors was compared with the pristine WS_2 sensor at different operating temperatures to identify the optimal working conditions. 100 °C provided the best discrimination between the target gases. Gas sensing measurements were therefore conducted toward 800 ppb NO_2 and 800 ppm H_2 at this temperature. Fig. 3(a, b) shows the dynamic resistance response of the sensors, while the corresponding response values are summarized in Fig. 4. The pristine WS_2 sensor exhibited responses of 48.69% toward NO_2 and 6.1% toward H_2. The WS_2/MXene heterostructure showed an enhanced response toward NO_2 (75.6%), indicating improved interaction due to MXene incorporation. In contrast, the WS_2/MXene/Pd sensor displayed a significantly higher response toward H_2 (66.5%), while the response to NO_2 decreased to 36.8%. The detailed selectivity and humidity sensing responses will be presented at the conference.

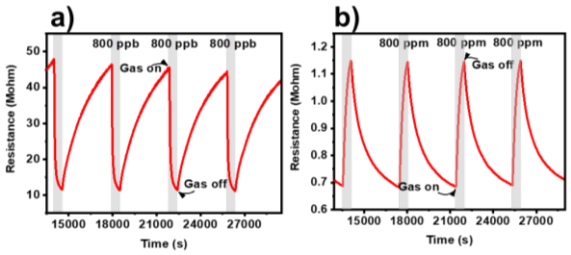

Fig. 3. Resistance dynamics of (a) WS_2/MXene towards 800 ppb NO_2, (b) WS_2/MXene/Pd toward 800 ppm H_2

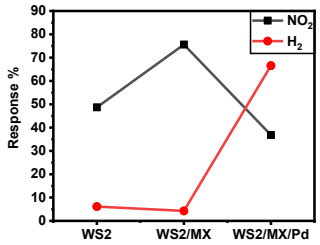

Fig. 4. (a) the sensors response towards NO_2 & H_2 at 100 °C.

Conclusions

This study demonstrates that MXene improves NO_2 sensing performance, whereas Pd functionalization shifts the selectivity toward H_2 gas.

References:

[1] S. B. Malik, F. E. Annanouch, and E. Llobet, "Pd-Nanoparticle-Decorated Multilayered MoS2 Sheets for Highly Sensitive Hydrogen Sensing," *Chemosensors 2023, Vol. 11,* vol. 11, no. 11, Oct. 2023, doi: 10.3390/CHEMOSENSORS11110550.

[2] S. B. Malik, F. E. Annanouch, R. D'Souza, C. Bittencourt, M. Todorović, and E. Llobet, "High-Yield WS2 Synthesis through Sulfurization in Custom-Modified Atmospheric Pressure Chemical Vapor Deposition Reactor, Paving the Way for Selective NH3 Vapor Detection," *ACS Appl. Mater. Interfaces*, vol. 16, no. 36, pp. 48585–48597, Sep. 2024, doi: 10.1021/ACSAMI.4C10077.

[3] M. S. Nam, J. Y. Kim, A. Mirzaei, H. W. Kim, and S. S. Kim, "Pd-functionalized Ti3C2Tx MXenes for realization of flexible, selective, self-heated H2 sensing," *Sens. Actuators B Chem.*, vol. 404, p. 135189, Apr. 2024, doi: 10.1016/J.SNB.2023.135189.

DOI 10.5162/eurosensors2026/Tu–CHS–06

Self-Powered Gas Sensing in Interface Engineered 2D layered Heterostructures

Dipanjana Mondal[1], Vinayak Kamble[1,]*
[1]School of Physics, Indian Institute of Science Education and Research Thiruvananthapuram, Kerala, India 695551.
**email: kbvinayak@iisertvm.ac.in*

Summary:

The development of self-powered gas sensors is critical for enabling low-power, autonomous sensing systems, yet achieving high sensing performance without external bias remains a significant challenge. Self-powered gas sensing, enabled by built-in electric fields at carefully engineered heterointerfaces, offers a compelling pathway beyond this limitation. In this work, we present a comparative investigation of self-powered gas sensors based on both Transition metal dichalcogenide (TMD)-oxide and TMD-TMD interfaces. The three distinct 2D interface devices studied here are, $MoSe_2$-MoO_2, MoS_2-MoO_2 and ReS_2-MoS_2, employed via single-step CVD method. Across all three systems, reproducible zero-bias sensing responses and enhanced performance under photo-activation are observed, pointing to interface-driven charge separation as the governing mechanism. These findings collectively establish a generalized design framework in which interface engineering underpins self-powered sensing behaviour, rather than material choice alone.

Keywords: Self-powered gas Sensor, 2D materials, heterostructure, Transition Metal Dichalcogenides, Interface engineering

Background, Motivation and Objective

The growing demand for continuous environmental and health monitoring has intensified the need for gas sensors that operate reliably without a power supply. Conventional chemiresistive and metal-oxide based sensors typically require elevated operating temperatures (100-400 °C)[1] or continuous external biasing to achieve adequate sensitivity, making them ill-suited for battery-constrained wearables, and remote Internet-of-Things nodes. 2D TMDs have emerged as a promising platform to address this challenge, owing to their atomically thin geometry, large surface-to-volume ration, tunable bandgap, and strong light-matter coupling. Recent studies have demonstrated that heterostructure formation can induce built-in electric fields, enabling spontaneous charge separation and self-powered operation[2].

Despite rapid progress in individual TMD-based sensors, a systematic understanding of interface behaviour governs self-powered sensing performance remains lacking. Most existing studies focus on individual material systems, limiting the ability to derive general design principles. In particular, the interplay between band alignment, defect states, and photo-induced carrier dynamics across diverse heterostructure is not yet fully understood[3].

In this work, we aim to bridge this gap by investigating multiple CVD-grown 2D heterostructures and identifying common physical mechanisms governing self-powered gas sensing[4]. The objective is to move beyond material-specific observations and establish a generalized framework based on interface-driven charge dynamics applicable to next-generation autonomous sensors.

Description of the New Method or System

Here, we have studied three heterostructure systems synthesized by single-step CVD method to ensure clean, scalable, defect free interface formation without intermediate transfer-related contamination. Comprehensive structural and spectroscopic characterization like Raman, PL, XPS, HR-TEM are performed to confirm the integrity of the interface and the compositional gradation within individual flakes.

The first system, $MoSe_2$-MoO_2 heterostructure is a single flake metal-semiconductor heterointerface. Due to heterostructure formation, band-alignment establishes a built-in electric field capable of driving photoinduced carrier separation without external bias. The second system

introduces MoS_2-MoO_2 as a structurally analogous yet chemically distinct TMD-oxide platform[5]. The distinct sulphur-based chemistry relative to the selenide system modifies the charge redistribution at the interface. Thus, this provides a direct opportunity to isolate the role of chalcogen identity on the self-powered sensing response, independent of geometric or structural differences. Finally, the third system, ReS_2-MoS_2, represents a fundamentally different class of interface, i.e., a TMD-TMD van der Waals junction. This heterostructure generates a type-II staggered band alignment, which promotes spatial separation of photoexcited carriers across the junction, enabling self-powered current transduction upon gas exposure.

Results

All investigated heterostructure exhibit measurable gas sensing response towards NO_2 gas under zero external bias as shown in the insets of Figure 1, confirming their self-powered operation. Under illumination, a pronounced enhancement in sensing behaviour is observed across all systems (Figure 1). This photo-induced response indicates that light plays a significant role in facilitating carrier generation and improving charge separation efficiency. Furthermore, the extent of enhancement varies among heterostructures, suggesting that the coupling between optical absorption and interfacial charge transfer is system-dependent. Thus, the cross-system comparative analysis reveals that the built-in electric field at the 2D heterointerface is sufficient to drive measurable zero-bias sensing. Additionally, the enhancement under illumination suggests photoinduced carrier separation as demonstrated in the schematic in Figure 1 (right panel). The relative contribution of each factor depends on the specific heterostructure, but the underlying principle remains consistent across all systems. Therefore, this highlights the importance of interface engineering as a primary design strategy for self-powered sensing devices.

Conclusion

In summary, we demonstrated a comparative study of multiple 2D heterostructure to establish a generalized understanding of self-powered gas sensing. By examining both TMD-oxide and TMD-TMD interfaces, we demonstrate that interface-driven charge dynamics and photo-assisted processes govern sensor performance. The findings move beyond material specific observations and provide a unified framework for designing next-generation self-powered gas sensors.

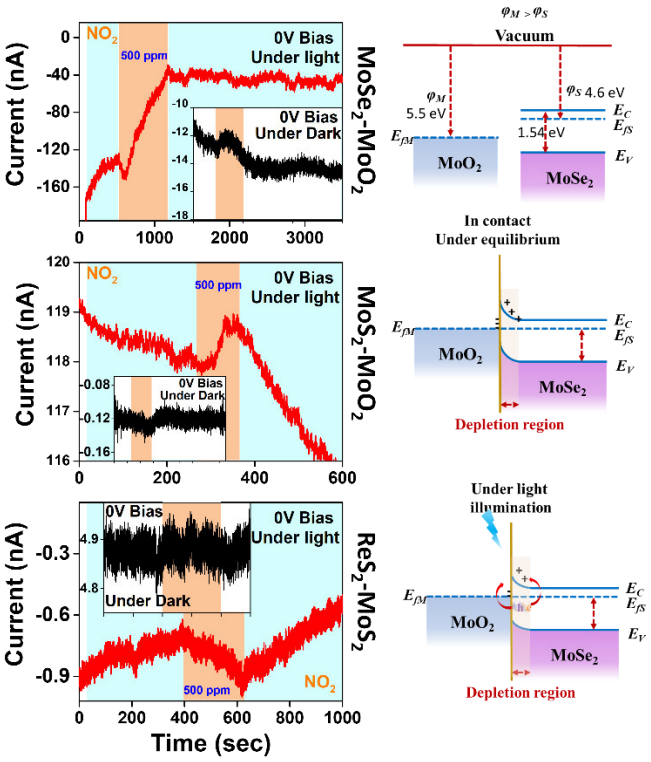

Fig. 1. (left column) The response to NO2 gas (500 ppm) at room temperature under dark and under light illumination for (top to bottom) MoSe2-MoO2, MoS2-MoO2 and ReS2-MoS2 heterostructure flakes. (right column) the band diagram under flat band condition, with heterostructure formation and under light illumination.

References

[1] 1. Barsan, N.; Weimar, U., Conduction model of metal oxide gas sensors. *Journal of Electroceramics* **2001,** *7* (3), 143-167.

[2] 2. Qiao, H.; Huang, Z.; Ren, X.; Liu, S.; Zhang, Y.; Qi, X.; Zhang, H., Self-Powered Photodetectors Based on 2D Materials. *Advanced Optical Materials* **2020,** *8* (1), 1900765.

[3] 3. Lorenz, T.; Ghorbani-Asl, M.; Joswig, J. O.; Heine, T.; Seifert, G., Is MoS_2 a robust material for 2D electronics? *Nanotechnology* **2014,** *25* (44), 445201.

[4] 4. Novoselov, K. S.; Mishchenko, A.; Carvalho, A.; Castro Neto, A. H., 2D materials and van der Waals heterostructures. *Science* **2016,** *353* (6298), aac9439.

[5] 5. Mondal, D.; Sharma, D.; R, K.; N, A. M.; Tiwary, C. S.; Bhat, N.; Kamble, V. B., Native Oxide MoO_2– $MoSe_2$ Heterostructure-Based Self-Powered Gas Sensor for Selective NO_2 and H_2 Detection. *Small* **2025,** *21* (33), 2503284.

DOI 10.5162/eurosensors2026/Tu–CHS–07

Pyrene-Based Probe with Tunable AIE-ICT Emissions for Amyloid Sensing and Imaging

Dharini Arumugam[1], Sarthak Mandal[1]
[1] Spectroscopy and Dynamics Laboratory, Department of Chemistry, National Institute of Technology, Tiruchirappalli, Trichy – 620015, Tamil Nadu, India
e-mail: adharini29@gmail.com

Summary:

Oligomers and amyloid fibrils are central biomarkers in neurodegenerative diseases such as Alzheimer's. Early detection of toxic oligomers remains challenging, as most dyes preferentially recognize fibrils. Dual-responsive probes capable of distinguishing both species are therefore essential for monitoring aggregation dynamics. We preent pyrene-based dye, P1, enabling selective detection of HEWL oligomers and fibrils via distinct aggregation-induced emission (AIE) and intramolecular charge transfer (ICT) channels. P1 exhibit oligomer-specific AIE emissions at 660 nm, while fibril binding induces LE (Locally Excited state) and ICT peaks at 490 nm and 540 nm, respectively, facilitating super-resolution confocal imaging of both aggregation states.

Keywords: Pyrene donor, cyano acceptor, AIE and ICT, sensing of amyloid oligomers and fibrils.

Headlines

Dual-responsive pyrene dye enabling selective visualization of amyloid oligomers and fibrils, advancing early diagnosis and mechanistic insights in neurodegeneration.

Background and Motivation

Misfolded proteins form amyloid aggregates linked to Alzheimer's and Parkinson's. While fibrils mark pathology, short-lived oligomers are more neurotoxic yet difficult to detect due to heterogeneity and instability [1]. These challenges highlight the urgent need for novel, non-invasive, cost-effective diagnostics targeting early oligomeric species during protein aggregation.

Organic π-conjugated materials with aggregation-induced emission (AIE) are widely studied for optoelectronic and biological applications [2]. Pyrene, a planar, electron-rich aromatic molecule with long fluorescence lifetime and high quantum yield, is a versatile scaffold in electronics, self-assembly, and biosensing. Here, we present a pyrene-based ICT dye, P1, synthesized via Knoevenagel condensation, investigated the photophysical properties like solvatochromism, potential AIE behaviour, and biological utility in detecting and imaging amyloid oligomers and fibrils.

Description of the New Approach

We present engineered donor–acceptor fluorophore P1, capable of simultaneously tracking oligomeric and fibrillar protein aggregates via distinct AIE and ICT emissions, enabling spectral discrimination and super-resolution imaging of distinct aggregation states.

Excitation at 430 nm allows P1 [2-(pyren-1-ylmethylene)malononitrile] to distinguish amyloid species: oligomer binding yields a strong 660 nm AIE band, while fibril interaction produces weaker LE and ICT emissions at 490 nm and 540 nm, requiring higher fibril concentrations for detection.

Results

The probe P1 was synthesized *(Fig. 1a)* via Knoevenagel condensation of 1-pyrenecarboxaldehyde (Py-CA) with malononitrile in ethanol/piperidine, yielding P1 (92%) with high purity.

To assess ICT properties, absorption spectra *(Fig. 1b)* of P1 in acetonitrile was compared with that of the precursor Py-CA. Compared to absorption maximum of Py-CA at 393 nm, P1 shifted strongly to 430 nm elucidating that P1 shows better charge transfer than Py-CA. Fluorescence emission spectra *(Fig. 1c)* of Py-CA and P1 illustrated emission maxima at 430 nm and 540 nm respectively, marking that P1 exhbits more charge transfer than Py-CA. These results confirm the presence of efficient excited-state ICT and strong polarity sensitivity suitable for specific amyloid protein aggregate detection.

The photophysical properties of P1 such as solvatochromism and AIE (aggregation induced

emission) in THF:water mixture were also studied to elucidate the pronounced ICT and AIE effects.

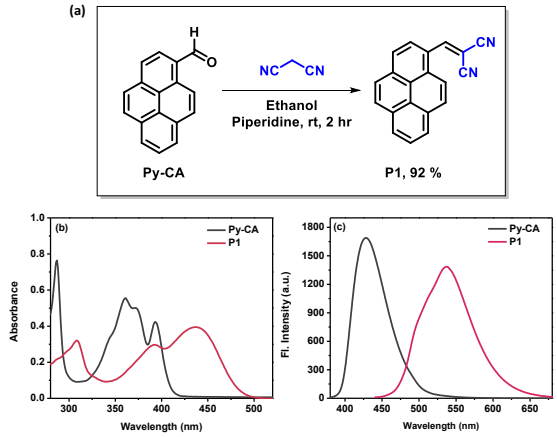

Fig. 1. (a) Synthesis of P1 from precursor Py-CA. Absorption (a) and emission spectra (b) of 20 μM solution of Py-CA, and P1 in acetonitrile (λ_{ex} for Py-CA and P1 are 390 nm and 430 nm).

Then the fluorescence assay *(Fig. 2 a, b)* of aggregated HEWL protein aggregates in presence of P1 was studied in PBS (pH 7.0). Plotting the LE (490 nm) and ICT (540 nm) emissions of P1 against incubation time *(Fig. 2d)* yields sigmoidal kinetics similar to ThT (Thioflavin-T) assay, reflecting fibril growth. In contrast, the AIE intensity at 660 nm *(Fig. 2c)* shows a sharp rise from 0–24 h followed by a decline from 24–120 h. This region appears as a lag phase in ThT assays because ThT cannot detect oligomers, whereas P1's AIE response clearly captures their formation and subsequent depletion during early aggregation.

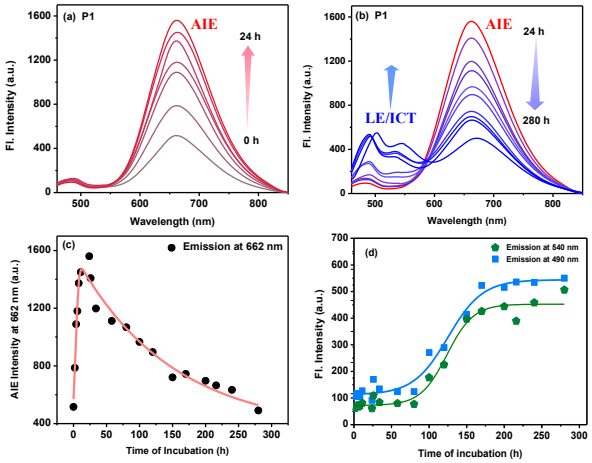

Fig. 2. Fluorescence assay (a, b) and kinetic growth (c, d) of HEWL fibrils and oligomers monitored using 20 μM P1 (λ_{ex} = 430 nm), immediately after mixing with HEWL protein aggregates.

Different protein aggregates of HEWL could be clearly visualized by super-resolution confocal fluorescence microscopy using P1 following photoexcitation at 445 nm *(Fig. 3)*. Significantly, the super-resolution images of amyloid fibrils (t240) obtained using our P1 dye as staining agent could exhibit clear twisted cross-β sheet structural features of mature amyloid fibrils.

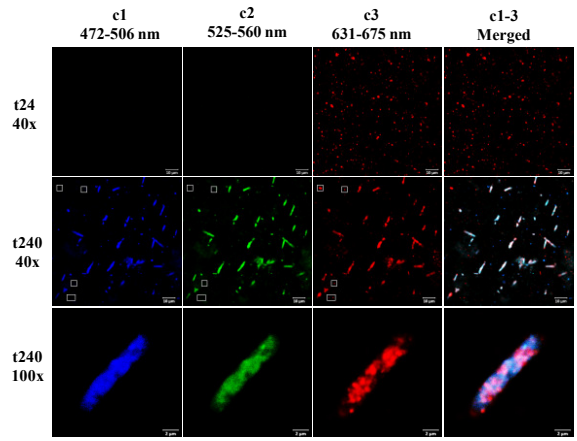

Fig. 3. Super-resolution fluorescence microscopy images of t24 (40x resolution) and t240 (40x and 100x resolution) dry, (λ_{ex} = 445 nm) using 20 μM P1.

Conclusion

Upon binding to oligomers, P1 exhibit AIE peak at 660 nm. In contrast, interaction with mature fibrils induces LE and ICT emissions at 490 and 540 nm respectively. The ability of a single dye to distinguish between oligomeric and fibrillar species based on emission wavelength provides a powerful tool for tracking protein aggregation dynamics and offers promising avenues for early diagnosis and mechanistic studies of amyloidogenic diseases.

Acknowledgements

This work was supported by SPARC (Scheme for Promotion of Academic and Research Collaboration). Dharini Arumugam is thankful to Ministry of Education (MoE) for the research fellowship provided through the National Institute of Technology Tiruchirappalli.

References

[1] R. Limbocker, N. Cremades, R. Cascella, P. M. Tessier, M. Vendruscolo, F. Chiti, Characterization of Pairs of Toxic and Nontoxic Misfolded Protein Oligomers Elucidates the Structural Determinants of Oligomer Toxicity in Protein Misfolding Diseases, *Accounts of Chemical Research,* 56(12), 1395-1405 (2023); doi:https://doi.org/10.1021/acs.accounts.3c00045

[2] P. Jana, S. Kanvah, Aggregation-Induced Emission and Organogels with Chiral and Racemic Pyrene-Substituted Cyanostyrenes, *Langmuir,* 36(10), 2720-2728 (2020); doi: https://doi.org/10.1021/acs.langmuir.9b03946

DOI 10.5162/eurosensors2026/Tu–CHS–08

Morphology-Governed Diffusion Enables CH_4/H_2 Discrimination in Metal Oxide Chemiresistor

Mohit Verma[1], Eduard Llobet[1]
[1] MINOS, Departament d'Enginyeria Electronica, Universitat Rovira i Virgili, Països Catalans 26, 43007 Tarragona, Spain
Corresponding Author's e-mail address: eduard.llobet@urv.cat

Summary:
This work reports a single metal oxide-based chemiresistive sensor with microspherical morphology, capable of diffusion-controlled kinetic discrimination between methane and hydrogen under optimized conditions. Briefly, upon exposure to methane gas, we observe a kink in the response curve at the time of introduction. However, upon hydrogen exposure, no such kinks were observed, confirming that the difference in sensing mechanism is visually distinguishable and can serve as an excellent feature for machine learning algorithms to discriminate methane in a hydrogen mixture. These initial results from our investigation indicate the possibility of extending this work to eventually discriminate and classify flammable gases in mixed, real industrial environments without relying on complex material systems with poor stability, reproducibility, and repeatability.

Keywords: chemiresistive gas sensor, In_2O_3 microspheres, methane sensing, porous metal oxide, kinetic discrimination

Background, Motivation, and Objective

Natural gas typically consists of 70% to 95% methane (CH_4) in pipelines, and leakage and the utilization as fuel from these pipelines account for around 30% of the world's carbon emissions [1]. So, there are two effective way to reduce the carbon emission, first to prevent the leakage from the pipelines while developing a sensor which continuously measure the levels of methane to monitor the status of pipelines around the joints and second by shifting to renewanble source of energy by blending hydrogen gas in the existing natural gas pipeline, often known as Hydrogen Enriched Natural gas (HENG) which also tackle the transport issues of highly reactive and flammable hydrogen gas. However, it also brings major safety concerns and sensor challenges of methane leakage detection in the complex blending environment. So, in the first case, a highly sensitive methane sensor can work, and there is plenty of literature showing that researchers have developed metal-oxide chemiresistive sensors through doping, morphology tuning, and heterostructures [2]. But in the second case of blending, the detection of methane in the presence of hydrogen is quite challenging and, to the best of our knowledge, rarely addressed in literature. Generally, methane gas is large, has slow diffusion, and is inert compared to small, reactive hydrogen gas, making the detection of methane over hydrogen quite challenging. In the methane–hydrogen blending environment, we need a chemiresistive sensor with high methane sensitivity and good selectivity. Thus, to address the above issues, we have fabricated sensors based on In_2O_3 nanomaterials and tested them for CH_4 and H_2 at different temperatures to examine the effect of morphological changes in the sensing material and the kinetic behavior of the gases on the sensing performance.

Description of the New Method or System

The typical synthesis of In_2O_3 involves a two-step process, modified from the literature method to optimize conditions for the desired nanoparticles and microspheres. In the first step, a simple solvothermal method was used to synthesize the In-gly precursor, and in the second step, the sample was heated to high temperature to decompose and form the final In_2O_3 powders. For sensor preparation, 4 mg of sensing material was mixed with 50 µL of 1,3-propanediol solvent and sonicated for 15 minutes to form a uniform dispersion. Then, the sensors were fabricated by drop-casting a 10 µL volume of dispersion onto commercial platinum IDEs on alumina substrates with a 300 µm gap, backside-lining the substrates with a platinum heater. Finally, to decompose and remove 1,3-propanediol from the sensing film, the sensor is heated to 200 °C for 2 hours. A homemade gas-sensing setup with a 35 mL sensing chamber was used for the measurements. Dry air and a gas flow of 100 SCCM were maintained using Bronkhorst mass-flow

controllers, with Methane (0.1%) and Hydrogen (0.1%) from calibrated gas cylinders, which are diluted further with dry air for the desired testing concentration. The electrical resistance of the sensors was measured using Keysight BenchVue. The heater temperature was controlled using an external voltage regulator.

Results

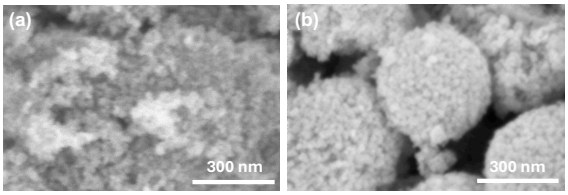

Fig. 1. FESEM images of In_2O_3 nanomaterials (a) nanoparticles (b) microspheres.

Fig. 1 shows the FESEM secondary electron images of synthesized In_2O_3 nanomaterials. FESEM images reveal two distinct morphologies in the synthesized nanomaterials. Fig 1a shows that the In_2O_3 nanoparticles form agglomerated particles. In contrast, Fig. 1b shows that the nanoparticles assemble into a hierarchical pattern to form a well-defined porous spherical shape with a size regime of 300-500 nm.

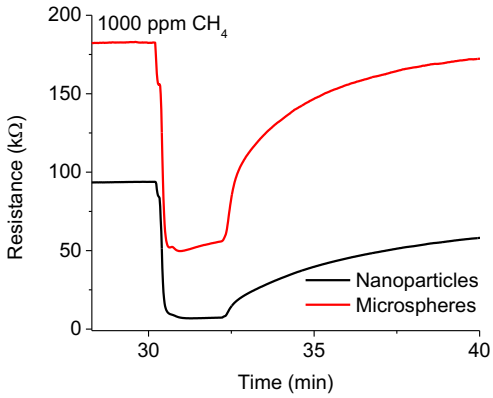

Fig. 2. Methane Sensing performance of In_2O_3 nanoparticles- and microsphere-based chemiresistive sensors at 250 °C and ≤ 5% RH.

Fig. 2 shows the comparative methane sensing performance of two sensors: sensor 1, based on agglomerated nanoparticles, exhibits a larger resistance change than sensor 2, based on microspheres. However, upon closer inspection of the dynamic response kinetics, the nanoparticles exhibit a characteristic steep slope and reach saturation during 4 min of continuous methane exposure. In contrast, in microspheres, on exposure to methane, a kink is observed, and no saturation occurs even after continuous exposure to the gas. This behavior, uniquely observed in the microsphere, indicates the interplay between surface and diffusion reactions; however, the agglomerated particles do not exhibit it. This gave us a good starting point and motivation to explore the material further, including discrimination between methane and hydrogen.

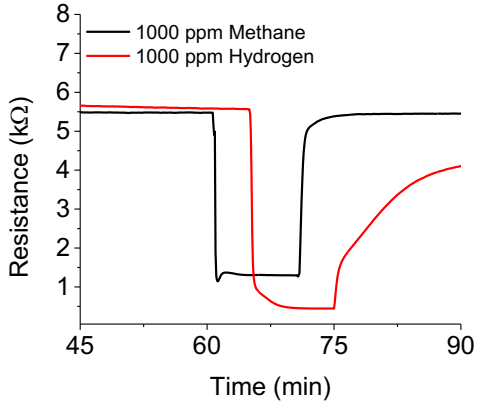

Fig. 3. Sensing performance of In_2O_3 micropspheres based chemiresistive sensors at 400 °C and ≤5%RH towards 1000 ppm methane gas and hydrogen gas.

As shown in Fig. 3, we tested sensor-2 with a microsphere morphology at 400 °C for hydrogen and methane concentrations of 1000 ppm. As expected, the sensor showed a higher response to hydrogen than to methane. Still, interestingly, the microsphere morphology could discriminate between the hydrogen and methane based on their molecular size and thus controlling the kinetics of the reaction, which eventually gives rise to a distinctive kink in the case of methane sensing, which is due to the slow diffusion of methane due to the bigger size of methane molecules in comparison to hydrogen.

Our work reveals an interesting aspect of morphological change in the diffusion-controlled discrimination between low-reactive and high-reactive flammable gases. Further data will be presented at the conference, including the effect of humidity on sensing performance, optimization of temperature-based discrimination between pure-surface and diffusion-controlled reactions, and an understanding of the methane-sensing mechanism using operando NAP-XPS, which is underway to improve material design and machine-learning algorithms, eventually leading to an industry-ready chemiresistive methane sensor.

References

[1] Hureau, G.; Lecarpentier, A.; Serbutoviez, S.; Kaniewicz, J.; Madden, M.; Brooks, C.; Robertson, A.; Harrison, C.; Langston, C.; Ravalec, M. L. Global Methane Emissions from Natural Gas Transmission and Distribution Networks. *Sci. Technol. Energy Transit. 80*, 28 (2025); https://doi.org/10.2516/stet/2025007.

[2] Ke, J.; Xie, X.; Qiu, L.; Liu, F.; Huang, S.; Zhang, Z.; Chen, X. Advances in Chemiresistive Methane Gas Sensors Based on Nanostructured Metal Oxide Semiconductor. *Mater. Sci. Eng. B 323*, 118755 (2026); https://doi.org/10.1016/j.mseb.2025.118755

DOI 10.5162/eurosensors2026/Tu–CHS–09

AuAg Nanocage-based Colorimetric Sensor for Silver Detection

Riann Martin Sarza[1,2], Laura Sutarlie[2], Sam Fong Yau Li[1,3], Xiaodi Su[1,2]
[1] Department of Chemistry, Faculty of Science, National University of Singapore, Blk S8, Lvl 3, 3 Science Drive 3, 117543 Singapore
[2] Institute of Materials Research and Engineering (IMRE), Agency for Science, Technology, and Research (A*STAR), 2 Fusionopolis Way, Innovis #08-03, 138634 Singapore
[3] NUS Environmental Research Institute, National University of Singapore, T-Lab Building, 5A Engineering Drive 1, 117411 Singapore
Corresponding Author: riann.sarza@u.nus.edu

Summary:

Silver ions (Ag^+) are toxic heavy metal pollutants released from industrial wastewater, agricultural runoff, and antimicrobial applications. Existing field-deployable detection tools lack sufficient sensitivity for regulatory thresholds. This work presents a paper-based colorimetric sensor using AuAg nanocages as the sensing material. In the presence of Ag^+, ascorbic acid catalyzes Ag^0 deposition on the inner walls of the nanocages, causing a blue shift in the localized surface plasmon resonance (LSPR) and a visible color change. Currently optimized on Whatman 3 filter paper at 70% nanocage loading, the sensor now achieves a linear response from 5 to 45 ppm (R^2 = 0.990) and a visual detection limit of 1 ppm, without requiring additional reagents, substrates, or instrumentation.

Keywords: AuAg nanocages, colorimetric sensor, silver ion detection, paper-based sensor, LSPR

Background, Motivation and Objective

Silver ions (Ag^+) are toxic heavy metal pollutants released into water systems through industrial wastewater, agricultural runoff, and the widespread use of silver-based antimicrobial agents. Industrial discharge is regulated under frameworks such as the US EPA effluent guidelines and China GB39731-2020 [1,2]. Unlike many contaminants, Ag^+ is particularly concerning because it accumulates in organisms through the food chain [3], making its presence in food and water systems a significant regulatory and public health issue. Drinking water guidelines set a provisional reference value of 100 ppm for Ag^+ [4], while the European Food Safety Authority (EFSA) limits food contact migration to ≤50 ppb [5]. Such threshold values demand sensitive and accessible detection tools. Conventional analytical methods such as ICP-MS and atomic absorption spectroscopy offer excellent sensitivity but require expensive instrumentation and centralized laboratory settings making them unsuitable for routine field monitoring [6]. While commercial test strips offer portability, they typically cannot detect Ag^+ below 10 ppm, falling short of the established safety thresholds. Existing colorimetric approaches in literature have shown promise but often rely on complex reagent systems or multistep procedures that limit practical deployment [7]. There remains an unmet need for a simple, equipment-free, paper-based colorimetric sensor for naked-eye Ag^+ detection at regulatory thresholds. This work aims to develop such a sensor using AuAg nanocages, targeting performance relevant to food and water safety monitoring.

Description of the New Method or System

This work presents a paper-based colorimetric sensor for Ag^+ detection using AuAg nanocages as the sensing material. As earlier reported [8], the hollow, porous structure of AuAg nanocages gives them a highly tunable LSPR response that is sensitive to changes in their inner cavity. In the presence of ascorbic acid as a reductant, Ag^+ is reduced to Ag^0, which nucleates and deposits on the inner cavity walls of the nanocages without altering the outer morphology. We confirmed this mechanism by TEM and EDX characterization. This internal deposition causes progressive wall thickening, resulting in a measurable LSPR blueshift observed as a progressive, distinct, naked-eye color change from blue to purple to orange and then to yellow. To make such sensing platform portable, the nanocages were then deposited onto filter paper strips with an optimal nanocage concentration. Color readout induced by Ag^+ is performed by naked eye or by taking photos and using the CIELAB color system as a

quantitative metric, requiring no instrumentation. Possible interferants, substrate type, and nanocage loading concentration, were systematically screened to optimize reproducibility and selectivity.

Results

Firstly, the selectivity to Ag^+ against seven metal ion interferants were studied with the solution phase reaction. The results revealed that Fe^{3+}, Au^{3+}, and Pt^{4+} caused significant signal distortion in the absence of masking by EDTA, while EDTA chelation effectively suppressed interference from Cu^{2+}, Ni^{2+}, and Zn^{2+}. Au^{3+} and Pt^{4+} remain challenging as they are susceptible to reduction by ascorbic acid, producing interference signals that could not be masked suppressed by EDTA masking alone requiring further investigation. (Fig 1).

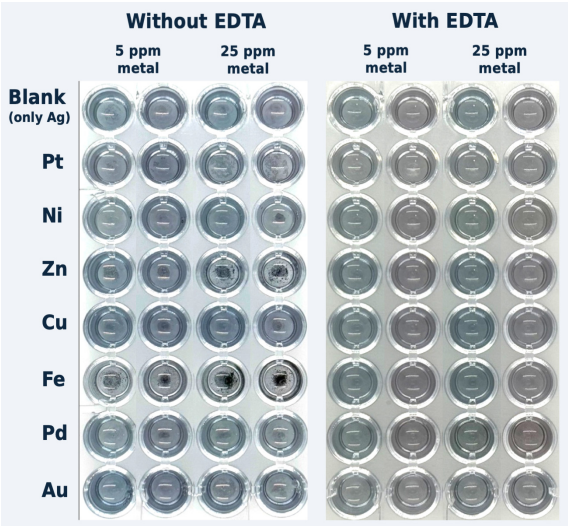

***Fig. 1**. 96 Well plate images showing colorimetric response of AuAg nanocages to Ag^+ in the presence of seven metal ion interferants at 5 and 25 ppm, without (left) and with (right) EDTA masking.*

Systematic optimization of paper substrate and nanocage ink concentration identified Whatman 3 at 70% nanocage loading as the optimal condition, yielding well-defined, uniform sensing spots with a reproducible linear dose-response to Ag^+ from 5 to 45 ppm (R^2 = 0.990) based on CIE b* color analysis (Fig 2). Visual color change was detectable down to 1 ppm, confirmed by statistically significant color difference across replicate measurements. Compared to reported solution-phase colorimetric methods for Ag^+, this paper-based platform achieves competitive detection performance without requiring enzymatic substrates, oxidizing reagents, or benchtop instruments, highlighting its potential for field-deployable food and water safety monitoring.

***Fig 2.** Optimization of paper substrate and nanocage ink for Ag^+ detection. (a) Whatman 1 at 70% shows diffuse spots from lateral wicking. (b) Whatman 3 at 70% shows uniform, well-defined spots. (c) R^2 of Δb^* vs. $[Ag^+]$ for 10–70% nanocage concentrations on both substrates, with Whatman 3 at 70% selected as optimal. (d) Dose–response curve for Whatman 3 at 70% loading with linearity from 5–45 ppm (R^2 = 0.990).*

References

[1] US EPA, Effluent Guidelines for the Electroplating Point Source Category, 40 CFR Part 413. https://www.epa.gov/eg/electroplating-effluent-guidelines

[2] China GB39731-2020, Discharge Standard of Pollutants for Electronics Industry, State Administration for Market Regulation of China (2020).

[3] F. Dang et al., Transfer and toxicity of silver nanoparticles in the food chain, *Environmental Science: Nano* 8, 1519–1535 (2021); doi: 10.1039/d0en01190h

[4] WHO, Guidelines for Drinking-water Quality: Fourth Edition Incorporating the First and Second Addenda, World Health Organization, Geneva (2022); ISBN: 978-92-4-004506-4.

[5] EFSA CEP Panel, Safety assessment of the substance silver nanoparticles for use in food contact materials, *EFSA Journal* 19 (8), 6790 (2021); doi: 10.2903/j.efsa.2021.6790

[6] Y. Gao, Y. Deng, C. Li, Z. Li, S. He, H. Chi, X. Zhou, B. Yan, Simple extraction and ultrasensitive determination of nanoscale silver from environmental waters, *ACS Sustainable Chemistry & Engineering* 10, 1863–1870 (2022); doi: 10.1021/acssuschemeng.1c07368

[7] Y. Ge et al., A multimode detection of silver ions based on peroxidase-like activity and photothermal effect of Prussian blue nanoparticles, *Journal of Food Composition and Analysis* **123**, 105553 (2023); doi:10.1016/j.jfca.2023.105553

[8] Z. Gao, S. Shao, W. Gao, et al., Morphology-invariant metallic nanoparticles with tunable plasmonic properties, *ACS Nano* 2021, 15, 2428-2438, doi: 10.1021/acsnano.0c06123

DOI 10.5162/eurosensors2026/Tu–CHS–10

Pd Decorated Mesoporous TiO_2 Nanospheres for High Performance Hydrogen Gas Sensors at Room Temperature

Thilini Thathsara[1], Dulani Liyanage[1], Caiden J. Parker[2], Christopher J. Harrison[2], Mahnaz Shafiei[1]
[1]School of Engineering, Swinburne University of Technology, Hawthorn, VIC 3122, Australia,
[2]School of Engineering, Royal Melbourne Institute of Technology, Melbourne, VIC 3001, Australia
Corresponding author: mshafiei@swin.edu.au

Summary:

A highly sensitive and selective hydrogen gas sensor operating at room temperature was developed using palladium decorated mesoporous titanium dioxide nanospheres. The sensor was fabricated via a combination of solvothermal and chemical reduction methods to enhance surface area and improve gas surface interactions. The sensor exhibited a high response of 504% with a fast response (35 s) toward 1000 ppm hydrogen at room temperature. In addition, the sensor demonstrated a wide detection range (50-10,000 ppm), with linearity (R^2:0.9912) at low concentrations.

Keywords: Nanospheres, Hydrogen, Titanium dioxide, Room temperature, Pd catalyst.

Background, Motivation and Objective

Hydrogen is widely recognized as a clean energy carrier; however, its high flammability (4-75%) and broad explosive range demand highly reliable sensing technologies for safe handling and practical deployment. Traditional hydrogen sensors often require elevated operating temperatures and commonly show limitations in response time, stability, and power consumption, which restricts their real-world applicability. Metal oxide semiconductors such as TiO_2 have been extensively studied for gas sensing applications due to their chemical stability, low cost, and versatile nano structuring capability. Nevertheless, pure TiO_2 generally exhibits weak sensing performance at room temperature (RT) because of limited surface reaction activity and slow charge transport processes [1].

To overcome these challenges, modification with noble metals has been widely adopted to improve sensing efficiency. Palladium is particularly effective due to its strong catalytic affinity toward hydrogen, enabling efficient dissociation of hydrogen molecules and enhanced electron transfer at the sensing interface [2]. In addition, the mesoporous architecture offers a large specific surface area, which increases the availability of active sites and facilitates rapid diffusion of gas molecules within the sensing layer.

In this study, Pd modified mesoporous TiO_2 nanospheres are designed and developed for hydrogen sensing applications. The main objective is to investigate the combined influence of Pd decoration and mesoporous nanospherical structure on the sensing characteristics, including response magnitude, response time, and RT operation. This work aims to establish an efficient sensing platform enabling high-performance hydrogen detection at RT.

Description of the New Method or System

Pd decorated mesoporous TiO_2 nanospheres were synthesized using analytical grade precursors through a combination of solvothermal processing and chemical reduction methods. Hexadecylamine was employed as a surfactant to direct the formation of a mesoporous shell structure on the TiO_2 nanospheres. The solvothermal treatment was subsequently conducted in an autoclave at 160 °C for 16 hr to facilitate the removal of the surfactant and stabilize the mesoporous architecture.

Results

According to the transmission electron microscope (TEM) images (Fig. 1(a-b)) shows well defined mesoporous TiO_2 nanospheres decorated with randomly distributed Pd nanoparticles. The darker contrast regions correspond to Pd nanoparticles (3.24 ± 0.22 nm) anchored on the surface of the TiO_2 nanospheres. In addition, a highly porous internal structure is clearly observed, confirming the successful formation of nanopores within the nanospheres. The presence of these nanopores provides a large accessible surface area, which is beneficial for hydrogen gas adsorption and diffusion.

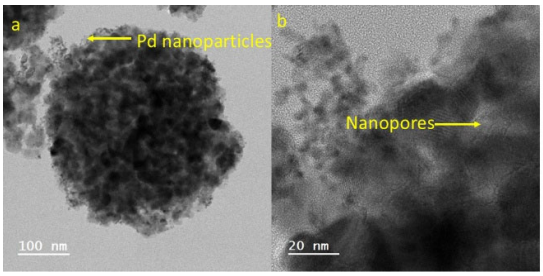

Fig.1. TEM images of (a) Pd-decorated mesoporous TiO_2 nanospheres showing randomly distributed Pd nanoparticles on the nanosphere surface and (b) a well-developed porous network with visible nanopores.

According to Fig. 2, the synergistic effect of Pd nanoparticles and the mesoporous architecture of TiO_2 nanospheres enables the sensor to achieve a high response of 504% (Equation 1), with a rapid response of 35 s toward 1000 ppm hydrogen at RT.

$$R\% = \left(\frac{(I_{gas} - I_{air})}{I_{air}}\right) \quad (1)$$

Where; R: response magnitude, I_{air}: Current of the sensor in the baseline condition and I_{gas}: Current of the sensor in hydrogen environment.

Response time: The time taken to increase the baseline current to 90% of current change after exposure to hydrogen gas.

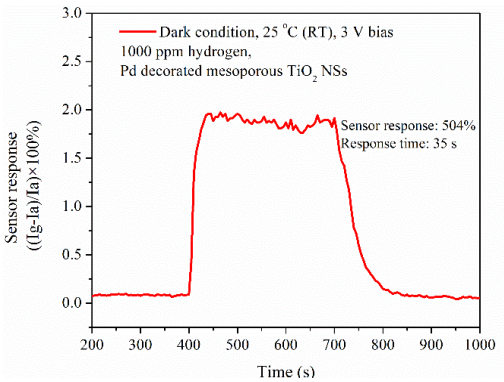

Fig.2.Hydrogen sensing performance of Pd decorated mesoporous TiO_2 nanospheres at RT under 3 V bias.

Fig. 3 shows that the sensor response increases progressively with hydrogen concentration up to 4000 ppm, reaching a current value of 3.17 µA, and then further rises to approximately 4.39 µA at 10,000 ppm, where it begins to plateau, suggesting saturation due to the occupation of most active surface sites on the sensing material. This trend is consistent with Langmuir-type adsorption behavior [3].

Furthermore, Fig. 4 shows that at low hydrogen concentrations (0-4000 ppm), the response exhibits strong linearity ($R^2 = 0.9912$), enabling precise detection in the low concentration range, which is critical for early hydrogen leak detection.

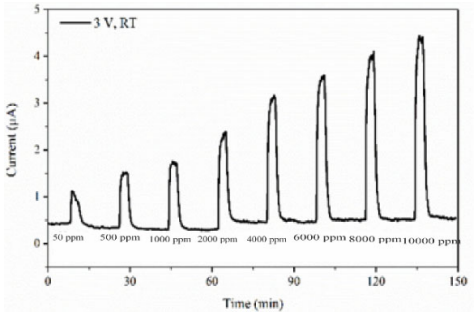

Fig.3. Hydrogen sensing performance towards hydrogen with different concentrations (50–10,000 ppm) at RT under 3 V bias.

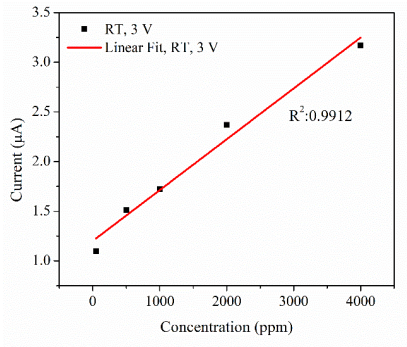

Fig.4. Linear fit of sensor response at RT with corresponding R^2 value.

Conclusion

Pd decorated mesoporous TiO_2 nanospheres enable highly sensitive, fast, room temperature hydrogen sensing for practical applications.

Acknowledgements

The authors greatly appreciate the financial support from the Future Energy Exports Cooperative Research Centre (FEnEx CRC, document no. 2026/24.RP2.0199.PHD-FNX-001) and the Australian Renewable Energy Agency (Contract No. 2018/RND012).

References

[1] D. N. Liyanage, T. Thathsara, C. J. Harrison, P. Kingshott, and M. Shafiei, Recent advances in hydrogen gas sensors based on molybdenum disulfide (MoS_2), *International Journal of Hydrogen Energy,* 161, 150685 (2025); https://doi: 10.1016/j.ijhydene.2025.150685.

[2] Thathsara T, Harrison CJ, Schönauer-Kamin D, Mansfeld U, Moos R, Malherbe FM, et al. Pd Nanoparticles Decorated Hollow TiO_2 Nanospheres for Highly Sensitive and Selective UV-Assisted Hydrogen Gas Sensors. *ACS Applied Energy Materials* 7:5608-20 (2024). https://doi.org/10.1021/acsaem.4c01039.

[3] Thathsara T, Harrison CJ, Hocking RK, Shafiei M. Enhanced Hydrogen Sensing Performance at Room Temperature Employing Photoactive Hybrid Pd Nanoparticle-Decorated SiO_2@TiO_2 Core–Shell Nanospheres. *ACS sensors* 10, 8269-8285 (2025). https://doi.org/10.1021/acssensors.4c03328.

DOI 10.5162/eurosensors2026/Tu–CHS–11

Highly Selective Ethanol Sensor Based on SnO_2/MWCNTs Nanocomposite

Mikayel Aleksanyan, Artak Sayunts, Gevorg Shahkhatuni, Zarine Simonyan, Knarik Hambardzumyan, Gnel Stepanyan, Hayk Kasaparyan and Rima Papovyan
Center of Materials Science and Nanotechnologies, Yerevan State University, 1 Alex Manoogian, 0025, Yerevan, Armenia,
maleksanyan@ysu.am

Summary:
SnO_2/MWCNTs-based ethanol sensor was fabricated using RF magnetron sputtering and e-beam deposition techniques. The linear dependence of the sensor response on ethanol concentration enabled the determination of its concentration in the range of 1-100 ppm, with response and recovery times of 17 and 26 s, respectively. The sensor demonstrated ultra-high selectivity for ethanol vapor relative to acetone, propylene glycol, water, ammonia vapor, methane, and carbon dioxide.

Keywords: gas sensor, ethanol vapors, tin oxide, CNTs, magnetron sputtering

Introduction

Nowadays, the detection of ethanol (ethyl alcohol) is critical for ensuring public safety, verifying regulatory compliance in industries, and health monitoring. It is crucial for detecting environmental leaks, controlling fuel quality in biofuel blending, and analyzing post-mortem samples in forensics. Ethanol detection using metal oxide semiconductor sensors is valued for their low cost, portability, high sensitivity, and real-time monitoring capabilities, which are essential for identifying gas concentrations [1].

Metal oxide (MOX) nanomaterials (e.g., SnO_2, ZnO, TiO_2, Fe_2O_3) are widely used as gas sensing materials, often doped with transition or noble metals (such as Ni, Cu, Os, Pd, and Pt) to enhance their sensing characteristics [2]. Moreover, a combination of MOX with single- or multi-walled carbon nanotubes (SWCNTs or MWCNTs) improves sensitive parameters such as gas response, response and recovery times, and operating temperature. Besides, they increase the effective surface area by creating additional adsorption sites, and at the same time, endow the sensors with flexibility, enhance conductivity, and stability [3].

Motivation and Novelty

Thus, conventional SnO_2-based gas sensors often suffer from limited sensitivity and selectivity to interfering gases. The integration of MWCNTs with SnO_2 offers a promising strategy to overcome these limitations by enhancing charge transport, increasing active surface area, and enabling synergistic interactions at the nanocomposite interface. The fabricated SnO_2/MWCNTs nanocomposite is therefore expected to provide improved selectivity toward ethanol along with enhanced sensitivity, faster response, and better stability compared to conventional materials.

Experimental

The ethanol sensor was fabricated using RF magnetron sputtering from the Cu-doped SnO_2 target prepared earlier by the solid-state reaction method. The SEM image of the SnO_2 powder demonstrated that the grain sizes ranged over a fairly wide range, reaching up to several hundred nanometers. (Fig.1). The sensing film was deposited on the sensor substrate for 25 min using high-purity argon as a working gas, with a generator power of 70 W.

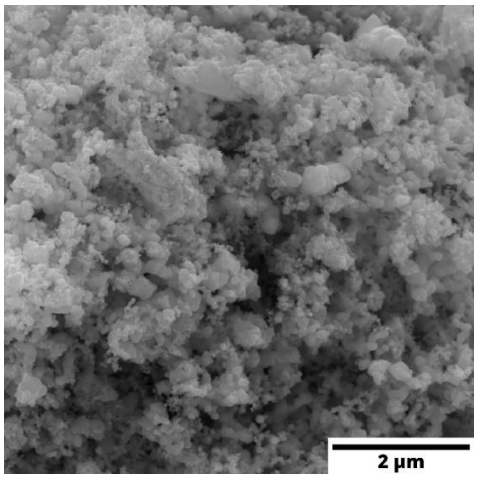

Fig. 1. The SEM image of the SnO_2 powder.

Subsequently, the MWCNTs were deposited onto the film surface by e-beam evaporation for 4 s, which caused the generation of the MWCNT islands on the surface of Cu-doped SnO_2 thin film. SEM image of MWCNTs revealed an intertwined network with diameters of approximately 30-150 nm and lengths of several micrometers, forming a porous architecture that promotes gas adsorption and diffusion (Fig. 2).

A schematic illustration of the fabricated sensing system is presented in Fig. 3.

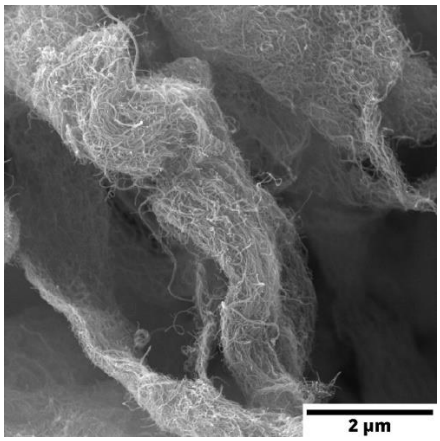

Fig. 2. The SEM image of MWCNTs.

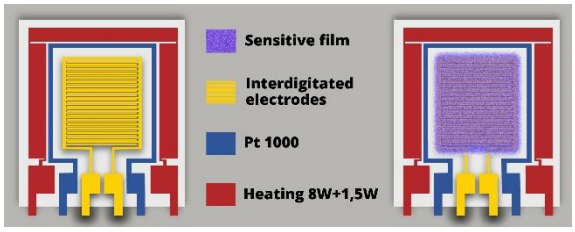

Fig. 3. Schematic illustration of the ethanol sensor.

Results

The response of the sensor was defined as the ratio of its resistance in air and under ethanol exposure, respectively. The ethanol sensor demonstrated its best sensitivity at 150 °C operating temperature under 395 nm UV irradiation. Under those conditions, the sensor showed linear dependence of the response on ethanol concentrations in the range of 1-100 ppm (Fig. 4). The response of the sensor to 1 ppm of ethanol vapor was 1.4, while under exposure to 100 ppm of ethanol vapor, the resistance of the sensor was decreased 7 times.

The inset image of Fig. 4 demonstrated the dynamic resistance curve of the sensor with the injection of 10 ppm ethanol vapor into the chamber, representing a resistance change of 2.4 times. Besides, the response and recovery times of the sensor were 17 and 26 s, respectively.

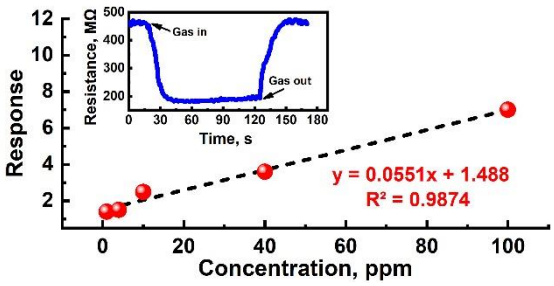

Fig. 4. Linear dependence of the sensor response on ethanol concentration (Inset image: dynamic resistance change of the sensor under 10 ppm ethanol exposure).

The SnO_2/MWCNTs sensor demonstrated ultrahigh selectivity towards ethanol compared to the other interfering gases shown in Fig. 5. The sensor demonstrated no response to 400 ppm of acetone, 3000 ppm of water, 300 ppm of ammonia, and 600 ppm of propylene glycol vapors, and 5000 ppm of methane and carbon dioxide.

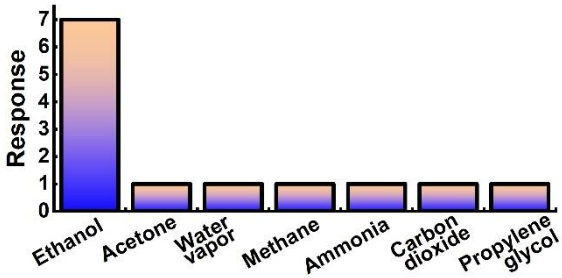

Fig. 3. Selectivity of the SnO_2/MWCNTs sensor.

Thus, the SnO_2/MWCNTs sensor demonstrated a fairly low detection limit for ethanol, high sensitivity, rapidity, and ultrahigh selectivity, making it a potentially applicable system.

Funding

The research was supported by the Higher Education and Science Committee of MESCS RA [Research projects № 24FP-3B001 and Nº 24LCG-2J001]

References

[1] A. M. Laera, M. Penza, Chemiresistive materials for alcohol vapor sensing at room temperature, *Chemosensors* 12(5), 78 (2024); doi: 10.3390/chemosensors12050078

[2] P. Siciliano, Preparation, characterisation and applications of thin films for gas sensors prepared by cheap chemical method, *Sensors and Actuators B: Chemical* 70, 153–164 (2000); doi: 10.1016/S0925-4005(00)00585-2

[3] Y. Kong, Y. Li, X. Cui, L. Su, D. Ma, T. Lai, L. Yao, X. Xiao, Y. Wang, SnO_2 nanostructured materials used as gas sensors for the detection of hazardous and flammable gases: A review, *Nano Materials Science* (2021); doi: 10.1016/j.nanoms.2021.05.006

DOI 10.5162/eurosensors2026/Tu–CHS–12

A Physics-Informed Inverse Problem for Tracking Gas Chromatography Column Degradation

Antoine Riaud[1], Balint Toth[1], Yannick Maret[1], Kai Hencken[1]
[1] ABB Corporate Research Switzerland, Segelhofstrasse 1K, 5405 Baden-Dättwil, Switzerland,
antoine.riaud@ch.abb.com

Summary:
Many sensing systems require inferring a hidden system state from a distorted waveform. In process gas chromatography, column degradation changes the shape of chromatographic peaks, but the underlying physics is nonlinear and difficult to invert. We cast column health estimation as an inverse problem and solve it with a simple physics informed model. The model links peak asymmetry to Langmuir adsorption and converts the inferred loading behavior into a column health metric. On two years of industrial data from six instruments, this metric tracked aging and separated degraded columns early enough to support predictive maintenance.

Keywords: inverse problems, physics informed modeling, condition monitoring, nonlinear transport, gas chromatography

Background, Motivation and Objective

In many sensing systems, the measured signal depends not only on the excitation, but also on the internal state of the system. Recovering that hidden state from the observed signal is a classical inverse problem. In this report, we view gas chromatography as a nonlinear chemical wave propagation problem: a short gas injection travels through a coated separation column and is detected as a chromatographic peak. Usually, the peak area is used to estimate concentration, but we also show that the peak shape contains information about the condition of the column itself.

As the column ages, its molecular coating and active adsorption sites change. This modifies how analytes interact with the stationary phase and leads to broader peaks, stronger or weaker tailing, and in severe cases carryover that interferes with neighboring compounds. Conventional diagnostics such as theoretical plate number capture part of this degradation, but they do not directly explain why the waveform changes or how those changes relate to the chemistry of the column.

The key physical mechanism is nonlinear adsorption. Under low loading, propagation through the column is close to linear and the peak remains nearly symmetric. Under higher loading, Langmuir adsorption makes the transport nonlinear: part of the concentration front moves faster than the rest of the band, producing steep fronts and long tails that resemble shock-like wave propagation [1,2]. From a signal-processing perspective, this means that the observed peak is the output of a nonlinear transport system whose parameters depend on the health of the column.

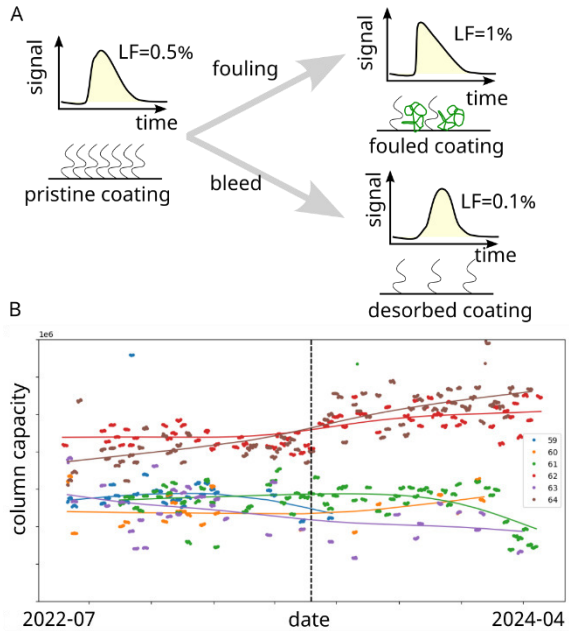

Fig. 1. Physics-informed tracking of gas-chromatography column degradation. Fig. 1.A illustrates a healthy column coating together with two degradation modes, namely stationary phase loss (bleed) and fouling by more active contaminants, and their corresponding peak-shape changes. Fig. 1.B shows the inferred column-capacity trajectories over time, highlighting the early separation of degraded columns from healthy ones. Dashed line indicates maintenance.

The objective of this work is therefore broader than peak fitting used for concentration estimation. We aim to infer column degradation from peak shape by solving a reduced inverse problem: given an observed chromatographic peak, estimate the hidden adsorption state of the column and track how that state evolves over time.

Description of the New Method or System

The exact forward model for this problem is expensive for routine use because it requires simulating nonlinear wave propagation under Langmuir adsorption. That type of model is physically meaningful, but it is not practical to solve repeatedly for every chromatogram in an industrial monitoring workflow. We address this by building a reduced-order surrogate, called HybridMG, that preserves the dominant peak-shape effects of the nonlinear physics while remaining simple to invert.

HybridMG combines two complementary asymmetric peak functions (1): the skewed Gaussian (SG) captures the peak apex well and the exponentially-modified Gaussian (EMG) captures the long tail:

$$\Lambda = \alpha SG + \beta EMG \qquad (1)$$

We constrain the family of admissible peak shapes using Langmuir-based simulations of saturated and unsaturated peaks. This step turns peak fitting into an inverse problem with a meaningful solution. Rather than focusing only on the best-fitting curve, the method uses peak asymmetry to infer the loading factor (LF)of the column $LF = n/CC$, with n the amount of sample and CC the column capacity (total amount of available adsorption sites). In order to determine the latter, validation samples of known composition (n) are used, which yields $CC = nLF$. Each chromatogram then yields not just an analyte estimate, but also a direct estimate of the hidden state of the column. In a nutshell, we find a low-dimensional parameterization of the combined shape, which allows to link the different parameters to easily determinable peak parameters.

In practice, the workflow is simple enough for routine monitoring. After baseline correction and peak segmentation, the dominant methane peak is fitted with HybridMG, the loading factor is recovered, and the derived column-capacity metric is tracked over time.

Results

We evaluated the method on more than 1.1 million chromatograms collected over two years from six industrial gas chromatographs monitoring the same gas mixture. For degradation tracking, the first chromatogram of each day was processed and the dominant methane peak was used to estimate column capacity. The inferred metric separated healthy and degraded columns from the earliest available measurements. Two columns, IP62 and IP64, started with elevated column-capacity values and were later classified as failed within about twelve months, whereas healthy columns remained lower and more stable. This early separation is visible in Fig. 1.B and shows that the hidden degradation state was already encoded in the waveform before conventional maintenance decisions were made.

The significance of the result is broader than gas chromatography. It shows that when a sensor signal is shaped by nonlinear transport, waveform distortion can be treated as information rather than nuisance. A reduced physics-informed model can recover a hidden health variable from the observed signal without repeatedly solving the full nonlinear forward problem. In this work, that hidden variable is linked to column capacity and provides an interpretable health indicator for predictive maintenance.

Overall, the work positions chromatography column monitoring as a signal inversion problem grounded in nonlinear transport physics. The HybridMG model provides a practical bridge between shock-like Langmuir wave propagation and routine industrial diagnostics.

References

[1] S. Golshan-Shirazi, G. Guiochon, Analytical solution for the ideal model of chromatography in the case of a Langmuir isotherm, *Analytical Chemistry* 60(21), 2364-2374 (1988); doi: 10.1021/ac00172a010

[2] G. Guiochon, S. Golshan-Shirazi, A. Jaulmes, Computer simulation of the propagation of a large-concentration band in liquid chromatography, *Analytical Chemistry* 60(18), 1856-1866 (1988); doi: 10.1021/ac00169a005

[3] V.B. Di Marco, G.G. Bombi, Mathematical functions for the representation of chromatographic peaks, *Journal of Chromatography A* 931(1-2), 1-30 (2001); doi: 10.1016/S0021-9673(01)01136-0

[4] E. Grushka, Characterization of exponentially modified Gaussian peaks in chromatography, *Analytical Chemistry* 44(11), 1733-1738 (1972); doi: 10.1021/ac60319a011

DOI 10.5162/eurosensors2026/Tu–CHS–13

Optimising Organic Bilayer Heterojunction Sensors through Device Geometry and Operating Bias

Martin Hruška[1,2], Petr Bečvář[2], Marcel Bouvet[2]
[1] Department of Physics and Measurements, University of Chemistry and Technology, Prague, Technická 5, Praha 6, CZ16628, Czech Republic,
[2] Institut de Chimie Moléculaire de l'Université Bourgogne Europe (ICMUB), UMR CNRS 6302, Université Bourgogne Europe, 21078 Dijon cedex, France
hruskaa@vscht.cz, Marcel.Bouvet@u-bourgogne.fr

Summary:
Organic bilayer heterojunctions (BLHs) are promising chemical sensor devices owing to interfacial charge transport. Here, $CuF_{16}Pc/LuPc_2$ devices are studied for ammonia detection with varied $CuF_{16}Pc$ sublayer thickness, humidity (RH) and applied bias. The response and calibration characteristics show that both geometry and operating conditions strongly affect the device sensitivity. These results provide practical guidelines for tuning organic heterojunction sensor performance.

Keywords: organic semiconductors, bilayer heterojunction (BLH), ammonia sensing, phthalocyanines, sensitivity tuning

Background, Motivation and Objective

Organic bilayer heterojunctions (BLHs) have emerged as promising platforms for chemical sensing because their electrical response is strongly governed by interfacial charge transport between two molecular semiconductors. In such devices, the contact between materials of opposite majority-carrier polarity can lead to charge accumulation at the interface, resulting in enhanced conductivity and improved sensing characteristics [1,2]. Phthalocyanine-based BLHs are particularly attractive for gas sensing because their electronic properties can be modulated by interactions with electron-donating or electron-withdrawing analytes, including ammonia [3].

In $CuF_{16}Pc/LuPc_2$ BLH devices, the highly resistive $CuF_{16}Pc$ sublayer and the more conductive $LuPc_2$ top layer form an interfacial transport pathway, as illustrated in Fig. 1. The nonlinear current–voltage characteristics of these devices indicate the presence of an effective transport barrier, which separates low-bias and high-bias operating regimes. This behaviour suggests that sensor performance may depend not only on the chemical nature of the active layers, but also on the position of the operating point along the I–V curve.

The objective of this work is therefore twofold. First, we investigate whether the effective transport barrier can be tuned by changing the thickness of the $CuF_{16}Pc$ sublayer. Second, we examine how the applied bias voltage can be used as an operating parameter to enhance the relative response and sensitivity of the BLH ammonia sensor.

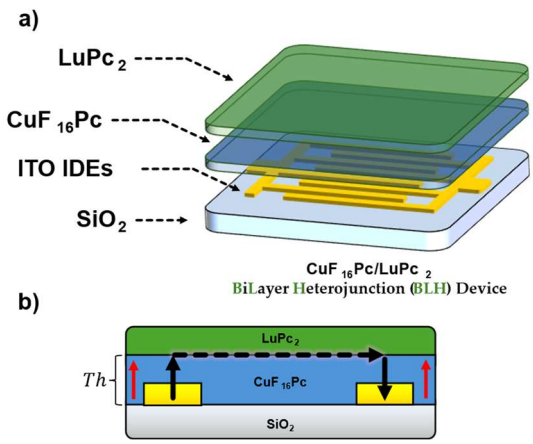

Fig. 1. Bilayer Heterojunction (BLH) sensor device. ***a)*** *Architecture of the heterojunction consisting og highly resistive bottom $CuF_{16}Pc$ sublayer and conductive $LuPc_2$ top layer.* ***b)*** *Sketch BLH cross-section with the indication of current pathway thought the junction.*

Description of the New Method or System

The investigated devices consist of $CuF_{16}Pc/LuPc_2$ bilayer heterojunctions, in which the $CuF_{16}Pc$ sublayer thickness was systematically varied (≈ 50, 75 and 100 nm) while the $LuPc_2$ top layer thickness was kept constant (50 nm). This approach enables the influence of the bottom resistive layer on charge transport and sensing behaviour to be isolated. To the best of our knowledge, this is the first systematic

investigation of the role of $CuF_{16}Pc$ sublayer thickness in tuning the operating regime and sensitivity of this BLH sensor system.

In addition, the ammonia response was investigated under different applied bias voltages within a single automated measurement protocol. The measurements were performed using a Keithley 6517 electrometer controlled by in-house software developed in NI LabVIEW. This setup enabled programmed gas exposure cycles combined with controlled changes in the applied voltage bias, allowing the sensor response, recovery and calibration behaviour to be evaluated as a function of the electrical working point.

This methodology provides a direct way to correlate device geometry, nonlinear electrical transport and gas-sensing performance in organic BLH.

Building on preliminary results presented previously [4], the present work provides a systematic investigation of $CuF_{16}Pc$ sublayer thickness and applied bias voltage as coupled parameters for tuning the sensitivity of $CuF_{16}Pc/LuPc_2$ BLH ammonia sensors.

Results

Original Fig. 2. shows the I–V characteristics of the prepared $CuF_{16}Pc/LuPc_2$ BLH devices with $CuF_{16}Pc$ sublayer thicknesses of 50, 75 and 100 nm, while the $LuPc_2$ top layer thickness was fixed at 50 nm. The curves clearly show that increasing the $CuF_{16}Pc$ sublayer thickness shifts the nonlinear transport regime towards higher voltages. This behaviour indicates that the effective transport barrier of the BLH device can be tuned through the geometry of the heterostructure.

The shift of the transport barrier has a direct influence on the sensing characteristics. When the devices are operated at the same applied voltage, thicker $CuF_{16}Pc$ sublayers exhibit higher baseline resistance. This leads to a larger relative response upon ammonia exposure and, consequently, to a higher calibration sensitivity. The observed trend demonstrates that sublayer thickness is not merely a fabrication parameter, but an active design variable for controlling the operating regime of the sensor.

Following this observation, the applied bias voltage was further investigated as a second tuning parameter. By shifting the working point of the device towards lower voltages, closer to the high-resistance nonlinear regime, the ammonia response was enhanced. This resulted in improved sensitivity of the BLH device. These findings show that the performance of organic heterojunction sensors can be optimised not only by modifying the device architecture, but also by selecting an appropriate electrical operating point.

More generally, this behaviour may be relevant to other chemical sensors exhibiting nonlinear I–V characteristics. The present work therefore provides an in-depth study of how interfacial transport, device geometry and operating bias jointly determine the performance of organic BLH ammonia sensors.

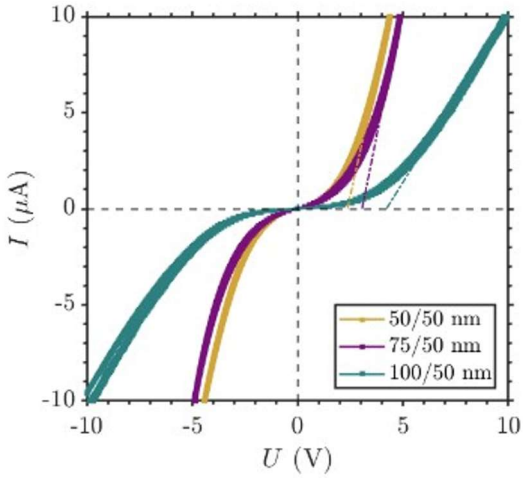

Fig. 2. I-V Characteristics of the prepared BLH devices with the indication of the shifting energy barriers.

References

[1] A. Kumar, R. Meunier-Prest, M. Bouvet, Organic Heterojunction Devices Based on Phthalocyanines: A New Approach to Gas Chemosensing, Sensors 20, 4700 (2020); doi: 10.3390/s20174700

[2] S. Ganesh Moorthy, A. Apoubou, S. Ouedraogo, L. Vachey, M. Bayo-Bangoura, M. Bouvet, In-Depth Study of Ambipolar Charge-Transport Regime through External Triggers and Gas Sensing, ACS Appl. Mater. Interfaces 16, 58991–59003 (2024); doi: 10.1021/acsami.4c14619

[3] A. Kumar, C. H. Devillers, R. Meunier-Prest, D. Sabat, E. Lesniewska, M. Bouvet, Bias-Induced Ambipolar Transport in Organic Heterojunction Sensors, Adv. Electron. Mater. 11, 2400865 (2025); doi: 10.1002/aelm.202400865

[4] M. Hruška, P. Bečvář, M. Vrňata, M. Bouvet, Tuning Sensitivity in Organic Bilayer Heterojunction Sensors via Geometry and Operating Conditions, Barrande-Vltava 2025, 14th French-Czech Chemistry Meeting, Pardubice, Czech Republic (2025)

DOI 10.5162/eurosensors2026/Mo–ESM–01

Porous WS_2 Films for Selective and Humidity-robust NO_2 Sensing at Room Temperature

Simone Hersberger[1], Michael Pereira Martins[1], Selina Fassbind[1], Andreas T. Güntner[1]
[1] Department of Mechanical and Process Engineering ETH Zurich, CH-8092 Zurich, Switzerland
simonehe@ethz.ch

Summary:
Highly porous WS_2 films were developed for selective NO_2 sensing at room temperature. The films were produced by flame aerosol deposition and dry sulfidation, resulting in a nanostructured porous network. This morphology enabled an enhanced sensor response and much faster response kinetics than compact films. NO_2 was detected down to 1 ppb with excellent discrimination from relevant interferents. The sensor performance remained robust over a wide humidity range and stable during long term testing. The presented sensor is promising for low power air quality monitoring and wearable exposure sensing.

Keywords: nanotechnology, semiconductors, thin films, metal sulfides, environmental monitoring

Background, Motivation and Objective

Nitrogen dioxide (NO_2) is a major atmospheric pollutant emitted by fossil fuel combustion, biomass burning, power generation and industrial activities [1], and both short- and long-term exposure have been linked to adverse respiratory and cardiovascular health effects [2]. In response, the World Health Organization lowered the recommended annual mean exposure limit from 40 to 10 µg/m^3, corresponding to about 5 ppb, which increases the need for sensitive monitoring technologies at very low concentrations [4]. Conventional chemiluminescence analyzers are widely used for reference measurements, but they are costly, maintenance intensive and vulnerable to interference from other nitrogen containing compounds [5]. Chemoresistive sensors offer a promising low-cost alternative for distributed and personal monitoring, yet many reported devices still require elevated temperatures or suffer from limited selectivity and humidity dependence [6]. The objective of this work was therefore to develop a room temperature nitrogen dioxide sensor based on porous tungsten disulfide films with improved sensitivity, selectivity and environmental robustness [7].

Description of the New Method or System

A new fabrication route was developed to obtain highly porous tungsten disulfide (WS_2) films for room temperature NO_2 detection. Tungsten trioxide nanoparticles were first deposited directly onto sensor substrates by flame aerosol deposition, forming an open and nanostructured film. These films were then converted by dry sulfidation while preserving the porous architecture. In contrast to compact reference films prepared by spin coating from the same precursor nanoparticles, the resulting porous films provided much more efficient gas transport and a larger accessible surface area. This method enabled a clear improvement in sensing performance, combining very high sensitivity, fast response, strong selectivity and robustness against humidity variations at room temperature.

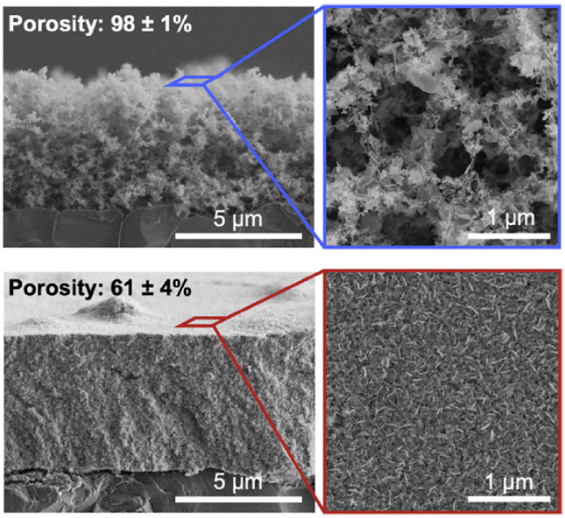

Fig. 1. Cross-sectional and top-view SEM images show the film thickness and film morphology of the flame-aerosol deposited and dry-sulfidized (top) and the spin-coated and dry-sulfidized (bottom) WS_2 films. Reproduced from [7].

Results

Flame aerosol deposition followed by dry sulfidation yielded WS_2 films with a highly open and nanostructured morphology, in clear contrast to the denser spin-coated films (Fig. 1). The porous films consisted of interconnected WS_2

nanosheets arranged in a hierarchical network with pores across multiple length scales, resulting in a porosity of 98 ± 1%. By comparison, the compact films showed a much denser structure with a porosity of 61 ± 4%, with a similar film thickness.

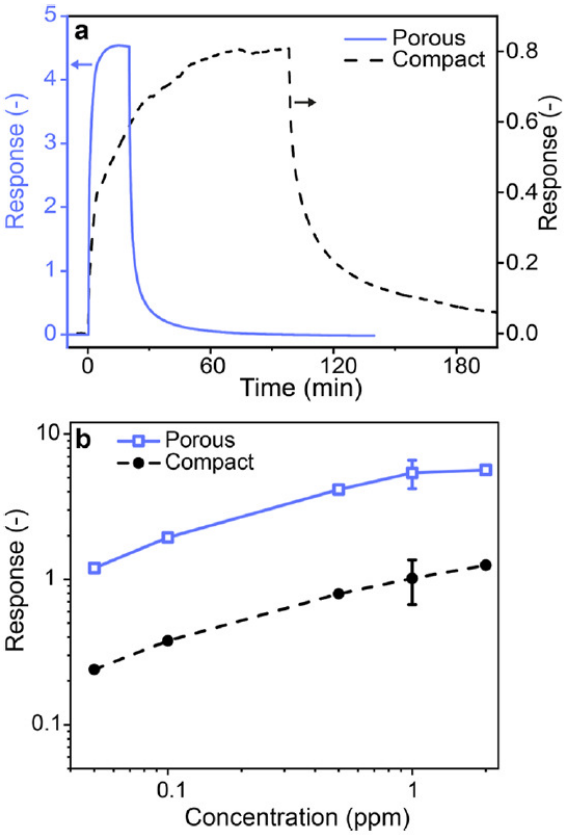

Fig. 2. (a) Response of porous (blue solid line) and compact (black dashed line) WS_2 films to 1 ppm NO_2, shown with different y-axis scales. (b) Sensing response of porous (blue open squares) and compact (black filled circles) WS_2 films exposed to 50-2000 ppb NO_2. At 1000 ppb, the symbols and error bars indicate the mean ± standard deviation for six porous sensors and two compact sensors fabricated under identical conditions. All measurements were carried out at room temperature and 50% RH. Reproduced from [7].

The porous architecture translated directly into superior NO_2 sensing performance. Upon exposure to 1 ppm NO_2 at room temperature and 50% RH, the porous WS_2 films exhibited a response about five times higher than that of the compact films (Fig. 2a). In addition, the porous sensors showed a much faster response time of 60 s, whereas the compact films required about 31 min under the same conditions. The enhanced performance was also maintained over a wider concentration range from 50 to 2000 ppb (Fig. 2b). This improvement is attributed to the open film structure, which facilitates analyte diffusion and provides a larger accessible surface area with more reactive sites.

Beyond sensitivity and speed, the porous WS_2 films also showed excellent selectivity (Fig. 3) and environmental robustness. The response to NO_2 was far stronger than that to a range of interfering gases relevant for air-quality monitoring, demonstrating a high preference for the target analyte. Moreover, the sensor response remained stable across varying humidity conditions and during long-term operation. Together, these results show that tailoring WS_2 into a highly porous film architecture is an effective strategy to enhance sensing performance, yielding faster, stronger, and more selective NO_2 detection under practical operating conditions.

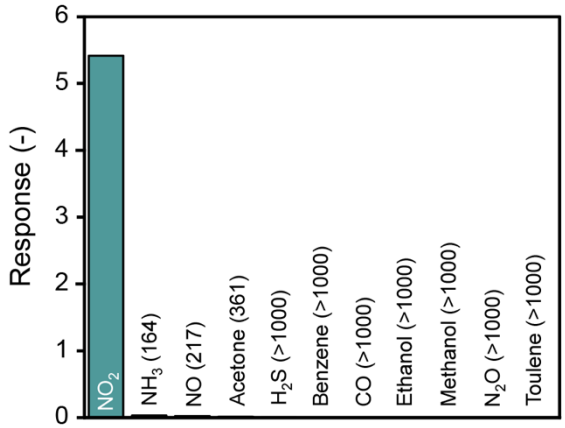

Fig. 3. Sensor response of porous WS_2 film against 1 ppm of air quality-relevant interferents at room temperature and 50% RH. Reproduced from [7].

References

[1] Jion, M. M. M. F. et al., A critical review and prospect of NO2 and SO2 pollution over Asia: Hotspots, trends, and sources. *Sci. Total Environ.* **876**, (2023); doi: 10.1016/j.scitotenv.2023.162851

[2] Meng, X. et al., Short term associations of ambient nitrogen dioxide with daily total, cardiovascular, and respiratory mortality: Multilocation analysis in 398 cities. *BMJ* **372**, (2021); doi: 10.1136/bmj.n534

[3] World Health Organisation. WHO Global Air Quality Guidelines: Particulate Matter (PM2.5 and PM10), Ozone, Nitrogen Dioxide, Sulfur Dioxide and Carbon Monoxide, p1−360 (2021).

[4] Dunlea, E. J. et al., Evaluation of nitrogen dioxide chemiluminescence monitors in a polluted urban environment. *Atmos. Chem. Phys.* **7**, 2691–2704 (2007); doi: 10.5194/acp-7-2691-2007

[5] Abegg, S., Cerrejon, D. K., Güntner, A. T. & Pratsinis, S. E. Thickness optimization of highly porous flame-aerosol deposited WO3 films for NO2 sensing at PPB. Nanomaterials 10, 1–15 (2020); doi: 10.3390/nano10061170

[6] Hersberger, S., Pereira Martins, M., Fassbind, S. & Güntner, A. T. Selective, Stable and Humidity-Robust NO2 Sensing at Room Temperature with Porous WS2 Films. ACS sensors 10, 8596–8605 (2025).

DOI 10.5162/eurosensors2026/Mo–ESM–02

Functionalized MXenes Chemiresistors for Room-Temperature NO Sensing

Eleonora Pargoletti[1,2], Benjamin Davis[3], Yury Gogotsi[3]
[1] Dipartimento di Chimica, Università degli Studi di Milano, golgi 19, Milan, Italy
[2] Consorzio Interuniversitario per la Scienza e Tecnologia dei Materiali, Giusti 9, Florence, Italy
[3] A.J. Drexel Nanomaterials Institute, Materials Science & Engineering, Drexel University, Philadelphia, PA, US
eleonora.pargoletti@unimi.it

Summary:
Pristine and MPTMS-functionalized $Ti_3C_2T_x$ and Nb_2CT_x MXenes were investigated as chemiresistive sensors for nitric oxide under variable humidity at room temperature. Functionalization preserved the layered morphology while modifying the surface chemistry and reducing water interference. $Ti_3C_2T_x$ showed a p-type-like response, whereas Nb_2CT_x displayed n-type behavior. MPTMS increased the response amplitude, especially for the niobium-based MXene, and enabled measurable signals at 5 ppm NO with sub-ppm detection prospects for breath analysis.

Keywords: MXene, nitric oxide, breath analysis, chemiresistor, surface functionalization

Background, Motivation and Objective

Breath analysis is attracting increasing interest as a non-invasive route for monitoring respiratory diseases [1-3]. Among breath biomarkers, nitric oxide is particularly relevant because its concentration correlates with airway inflammation [4,5]. Chemiresistive sensors based on MXenes are promising for this task owing to their high conductivity, large surface area, and room-temperature operation [6,7]. However, strong hydrophilicity and limited selectivity still constrain their practical use under humid conditions. Here, $Ti_3C_2T_x$ and, less studied, Nb_2CT_x MXenes, both pristine and functionalized with 3-mercaptopropyltrimethoxysilane (MPTMS), were investigated, for the first time, to assess whether surface modification can improve NO sensing in breath-relevant humidity.

Synthesis and characterization of pristine and functionalized MXenes

The work compares two MXene chemistries and their MPTMS-functionalized counterparts under the same sensing conditions, enabling a direct evaluation of how surface chemistry affects electronic response and humidity tolerance.
$Ti_3C_2T_x$ and Nb_2CT_x MXenes were synthesized by HF etching and subsequent delamination [6,7]. The obtained materials were freeze-dried and functionalized with 3-(mercaptopropyl)trimethoxysilane (MPTMS) via a silanization process in a 3:1 v/v 2-propanol/water mixture. Hydrolysis of MPTMS was initiated in water and the pH adjusted to 4. The reaction was conducted at 50 °C for 24 h under reflux. The resulting materials were washed with 2-propanol, centrifuged, and dried under vacuum at 60 °C. Different MPTMS concentrations (0–20%) were investigated for optimization.
All the obtained materials were finely investigated on several physicochemical points of view.
Specifically, XRPD and FTIR analyses confirmed successful functionalization through the increase in interlayer distance and the appearance of Si-O-Si and Si-O-M vibrational features, while morphological analyses (HRTEM) showed that the layered morphology was substantially retained. This approach makes it possible to correlate structural modification with gas-response polarity and amplitude at room temperature.

Results and Discussion

Gas sensing tests were carried out at 25 °C using 5 ppm NO under 10-85% relative humidity. $Ti_3C_2T_x$, both pristine and functionalized, exhibited a p-type-like behavior, with resistance increasing upon NO exposure. In contrast, pristine and functionalized Nb_2CT_x showed an n-type response, with conductance increasing in the presence of NO. MPTMS enhanced the response amplitude and mitigated humidity interference, particularly for the niobium-based MXene. All materials provided measurable signals at 5 ppm NO, and preliminary results indicate a detection limit approaching 0.1 ppm, which is relevant for exhaled-breath monitoring, even at high RH%.
Delving deeper into the possible sensing mechanism, the opposite response observed for

$Ti_3C_2T_x$ and Nb_2CT_x indicates that the MXene composition strongly affects charge transport during NO adsorption. MPTMS likely acts by reducing surface hydrophilicity and by promoting specific interactions between thiol groups and NO. These combined effects improve signal readability under realistic humid conditions without requiring elevated temperature.

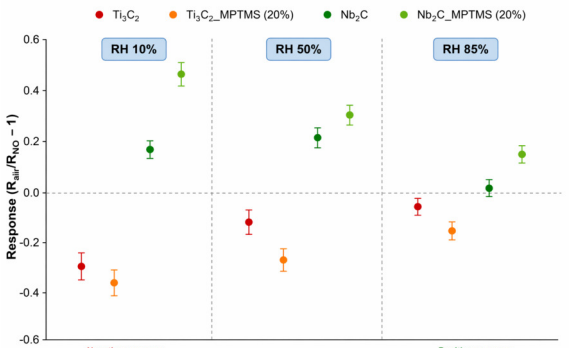

Fig. 1. Comparison of 5 ppm NO sensing response of $Ti_3C_2T_x$ and Nb_2CT_x MXenes and their MPTMS-functionalized counterparts (20%) at different relative humidity levels (10%, 50%, and 85%) at room temperature. Positive and negative responses indicate opposite resistance modulation upon NO exposure. Error bars represent standard deviation from three replicate measurements.

Conclusions

Surface functionalization with MPTMS effectively tunes the NO sensing performance of MXene chemiresistors. $Ti_3C_2T_x$ retained a p-type-like response, whereas Nb_2CT_x showed n-type behavior, and both benefited from stronger signals after modification. Room-temperature operation and reduced humidity interference support the use of functionalized MXenes for portable breath-analysis devices for NO detection.

References

[1] Tricoli, Nasiri, et al., Wearable and Miniaturized Sensor Technologies for Personalized and Preventive Medicine, *Adv. Funct. Mater.*, **2017**, 27, 1605271; doi: 10.1002/adfm.201605271

[2] Pargoletti, Vertova, et al., Boosting Gaseous Acetone Detection by Nanoheterojunctions of p-Type MWCNTs/PANI Integrated into 3D Flame-Synthesized n-Type ZnO, *ACS Sens.*, **2025**, 10, 407−416; doi: 10.1021/acssensors.4c02708

[3] Tessore, Pargoletti, et al., How the Interplay between SnO_2 and Zn(II) Porphyrins Impacts on the Electronic Features of Gaseous Acetone Chemiresistors *ACS Appl. Mater. Interfaces*, **2024**, 16, 41086−41098; doi: 10.1021/acsami.4c05478

[4] Kobayashi, Hanagama, et al., Exhaled nitric oxide: A biomarker for chronic obstructive pulmonary disease, *Respiratory investigation*, **2021**, 59, 364–366; doi: 10.1016/j.resinv.2021.01.003

[5] Maniscalco, M., Mormile, et al., Exhaled Nitric Oxide as Biomarker of Type 2 Diseases *Cells*, **2023**, 12, 2518; doi: 10.3390/cells12212518

[6] Naguib, Kurtoglu, Presser, et al., Two-dimensional nanocrystals produced by exfoliation of Ti_3AlC_2, *Advanced Materials*, **2011**, 23, 4248-4253; doi: 10.1002/adma.201102306

[7] Alhabeb, Maleski, Anasori, et al., Guidelines for Synthesis and Processing of Two-Dimensional Titanium Carbide ($Ti_3C_2T_x$ MXene) *Chemistry of Materials*, **2017**, 29, 7633-7644; doi: 10.1021/acs.chemmater.7b02847

DOI 10.5162/eurosensors2026/Mo–ESM–03

Hybrid Nanomaterial Networks for Dynamic VOC Sensing

Lukas Mielke[1], Yudhajit Bhattacharjee[1], Sophia Caroline Bittinger[2], Gabriele Carelli[1], Hendrik Schlicke[1*]

[1] Leibniz Institute of Polymer Research Dresden, Hohe Straße 6, 01069 Dresden, Germany
[2] University of Hamburg, Institute of Physical Chemistry, Grindelallee 117, 20146 Hamburg, Germany

*schlicke@ipfdd.de

Summary:
We present recent advances in the formation of moleculary cross-linked nanomaterial networks for the selective detection and recognition of volatile organic compounds (VOCs). Using cost-effective ink-based fabrication procedures, we combine inorganic nanomaterials, including gold nanoparticles and $Ti_3C_2T_x$ MXenes, with molecular cross-linkers, such as dithiols or diamines. The resulting hybrid materials exhibit chemiresistivity and composition-tunable selectivity. Our work focuses on tuning analyte/sensor interaction kinetics and exploiting dynamic response patters for VOC recognition.

Keywords: hybrid nanomaterials, VOC sensing, analyte discrimination, nanoparticles, MXenes

Volatile organic compouds (VOCs) comprise multiple hundreds to thousands low-vapor-pressure molecular species, and are found, to name just a few examples, in emissions from industrial processes, in the headspace above food during ripening, in breath, and as environmental pollutants. The chemical diversity of VOCs is associated with distinct properties: While some VOCs pose severe health hazards,[1] others may indicate the degree of ripening or degradation of fruit or vegetables.[2] Specific VOCs or VOC patterns can further act as markers in breath or headspace above body fluids for diagnostic purposes.[3]

Therefore, the mere detection of VOCs is insufficient for several emerging applications. Rather, the identification of individual VOCs or VOC patterns in complex gas mixtures is required for industrial safety monitoring, non-invasive medical diagnostics, food quality control, and environmental monitoring. While methods such as gas chromatography - mass spectrometry (GC-MS) offer excellent selectivity, these techniques are expensive and have limited portability and point-of-care applicability. Hence, there is a strong demand for inexpensive, portable sensing devices that enable analyte classification.

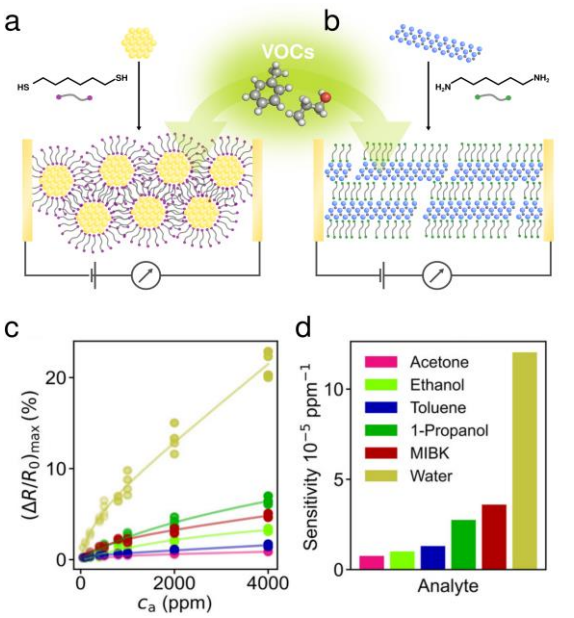

Fig. 1. a,b) Schematics depicting the fabrication of nanomaterial networks from a) dithiol cross-linked gold nanoparticles and b) diamine cross-linked $Ti_3C_2T_x$ MXenes. c) Sorption isotherms and d) vapor sensitivities of 1,6-hexanediamine cross-linked $Ti_3C_2T_x$ chemiresistors. c) Solid lines depict fits of a Langmuir-Henry sorption model.[4]

Hybrid Nanomaterial Networks

Molecularly cross-linked nanomaterial networks are promising and highly configurable candidates for chemiresistive VOC sensors with tunable selectivity. VOC sorption within these materials, particularly at the organic interfaces between the inorganic nanomaterials, sensitively affects charge transport across the composite, resulting in resistance changes that serve as sensing signals. While networks of molecularly stabilized noble metal nanoparticles (Figure 1a) have attracted significant interest in recent years, we here report an entirely ink-based,

efficient process for the deposition of a new class of thin films, namely, diamine cross-linked $Ti_3C_2T_x$ MXenes (Figure 1b), and demonstrate their suitability for chemiresistive sensing (Figure 1c,d).

Dynamic Sensing

Apart from quasi-static response amplitudes, observable after saturation of sorption-based VOC sensors, such devices also exhibit distinct saturation kinetics. While saturation response amplitudes depend on thermodynamic sorption equilibria, dynamic response features are governed by kinetic physicochemical processes. Both contain valuable information, and their combination can significantly enhance analyte recognition.

We tailor nanomaterial networks to deliberately slow down and achieve analyte-selective sorption kinetics (Figure 2a,b). For example, selecting short alkanedithiol molecules as cross-linkers for gold nanoparticle (GNP) networks causes their chemiresistive response kinetics to strongly depend on the size of the analyte molecules.[5] Thus, analyte sorption kinetics complement saturation responses, which are strongly governed by the analyte polarity. By combining suitable nanomaterial networks and evaluation of their dynamic response data using machine-learning algorithms, we achieve robust analyte recognition. Figure 2c exemplarily depicts the result of a linear discriminant analysis of response data aquired using a sensor array of eight sensing elements consisting of different cross-linked gold nanoparticle networks. We demonstrate utilization of these data to classify a set of VOCs at varying concentrations, enabling discrimination even between isomers.[5]

Still, the analysis of real world samples requires the recognition and classification of analytes, as well as the determination of their concentrations in complex mixtures. To understand how analyte mixtures interact with sorption-based nanomaterial network chemiresistors, we present a recent investigation of their response to binary VOC mixtures. As schematically depicted in Figure 2d, we discuss how responses to VOC mixtures can be deconvoluted to assess their composition.

Finally, we discuss recent developments in multilayered chemiresistor stacks, which possess an enhanced capability to kinetically separate analyte mixtures upon entry and provide spatiotemporal sensor responses for further improved analyte recognition.

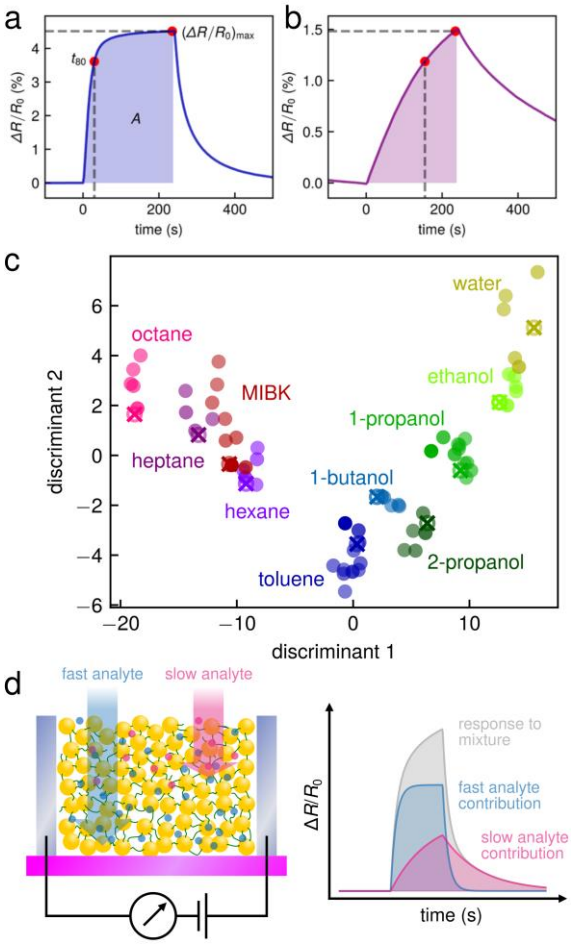

Fig. 2. a,b) Responses of a GNP chemiresistor to a) toluene and b) heptane. c) Linear discriminant analysis of dynamic responses from a VOC sensor array based on GNP sensing elements to different VOCs at varying concentrations. a-c) Adapted with permission from [5]. Copyright 2021 American Chemical Society. d) Schematic depicting the response behavior of a sorption-based chemiresistor to a mixture of analytes having different sorption kinetics. For certain analytes and concentration ranges, the sensor response is a superposition of the individual responses to the pure components.

References

[1] W.-T. Tsai, *Rev. Environ. Health,* **2019**, *34*, 81, doi: 10.1515/reveh-2018-0046.

[2] A. E. Lytou, E. Z Panagou, G.-J. E. Nychas, *Curr. Opin. Food Sci.* **2019**, *28*, 88, doi: 10.1016/j.cofs.2019.10.003.

[3] P. C. Moura, M. Raposo, V. Vassilenko, *Biomed. J.* **2023**, *46*, 100623, doi: 10.1016/j.bj.2023.100623.

[4] Y. Bhattacharjee, L. Mielke, M. Al-Hussein, S. Singh, K. Schaefer, B. Rodriguez-Barea, Q. Li, A. K. Ghosh, A. Erbe, C. Herrmann, Y. Vaynzof, A. Fery, H. Schlicke, *Adv. Funct. Mater.* **2026**, *36*, e18884 doi: 10.1002/adfm.202518884.

[5] H. Schlicke, S. C. Bittinger, H. Noei, T. Vossmeyer, *ACS Appl. Nano Mater.* **2021**, *4*, 10, 10399 doi: 10.1021/acsanm.1c01892.

DOI 10.5162/eurosensors2026/Mo−ESM−04

Plasma-Fabricated Metasurfaces for SERS Detection of Warfare Chemicals

Vasyl Shvalya[1], Oleg Baranov[1,2], Uroš Cvelbar[1,3]
[1] Jozef Stefan Institute, Jamova cesta 39, SI-1000 Ljubljana, Slovenia
[2] O.M. Beketov National University of Urban Economy in Kharkiv, Kharkiv, Ukraine
[3] Jozef Stefan International Postgraduate School, Jamova cesta 39, SI-1000 Ljubljana, Slovenia
Corresponding author: vasyl.shvalya@ijs.si

Summary:
We report plasma grown vertical copper oxide metasurfaces decorated with silver for surface enhanced Raman detection of explosive molecules. The substrates are synthesized directly on copper in a one step oxygen plasma process and converted into broadband plasmonic sensors. The platform delivers nanomolar detection of tetryl and HMX together with good spectral reproducibility. Excitation wavelength dependent shifts in nitro vibrations reveal charge transfer contributions that matter for reliable spectral interpretation. The approach offers a scalable route toward low cost field deployable chemical sensors.

Keywords: chemical sensors, plasmonic metasurfaces, SERS, explosives detection, plasma synthesis

Background, Motivation and Objective

Surface enhanced Raman scattering is one of the most attractive routes for trace chemical sensing because it combines molecular specificity with very high sensitivity. Its practical deployment, however, is still constrained by the need for substrates that are simultaneously strong, reproducible, low cost, and scalable [1-3]. Vertically oriented nanoarchitectures are especially interesting because they expose a large active area and can host dense plasmonic hotspots at ridges, edges, and interparticle gaps. The objective of this work was to develop a simple dry process that directly converts copper into a vertical oxide metasurface and then transforms it into a high performance SERS sensor for explosive molecules.

Description of the New Method or System

Copper samples were cleaned, plasma treated in oxygen at 350 Pa, and processed for 20 min in a glow to arc transition regime at 630 V and 0.25 A while the sample temperature was maintained at about 520 ^{o}C [3]. This one step oxidation route generated densely distributed vertical CuO/Cu2O nanosheets across the substrate. The sheets had typical widths of 5-10 um, heights of 10-12 um, root thickness near 1 um, and sharpened ridges of about 50-100 nm [3]. A 100 nm Ag layer was then sputtered in two 50 nm steps, forming discontinuous nanoparticles and nanoaggregates with typical dimensions around 10-50 nm on ridges and sidewalls. The central novelty is that plasma induced stress, fast oxidation kinetics, and structural disorder are not treated as defects to be removed, but as design variables that promote 2D sheet formation and broadband plasmonic hotspot generation.

Results

Raman spectroscopy, X ray diffraction, electron microscopy, and TEM analysis showed that the walls consist of intergrown CuO and Cu2O domains with wedge like morphology, stacking faults, and local compositional variation [3]. Compared with classical thermal oxidation, model based analysis indicated roughly twenty times faster oxide growth under plasma exposure, consistent with enhanced adsorption and ion assisted transport [3]. After Ag deposition, the metasurface displayed strong electromagnetic confinement in nanoparticle gaps and crevices over a broad excitation range from 488 to 633 nm. Using crystal violet as a marker, the substrate showed relative standard deviation of about 9.7 percent and an analytical enhancement factor of about 6 x 10^6 to 9 x 10^6 [3]. A benchmark detection limit of about 1.5-2.0 nM was obtained for crystal violet [3].

Diffuse reflectance measurements further showed that Ag coating increased the optical response in the visible range, while simulations indicated that the strongest local fields were concentrated in the smallest nanoparticle gaps and in narrow crevices on the vertical ridges [3]. Shorter wavelength excitation preferentially

activated smaller particles and tighter gaps, whereas longer wavelengths coupled more efficiently to larger particles and wider gaps. This broadband behaviour is important because practical sensors must remain informative under different laser configurations and for analytes with different resonance conditions.

The most important application result was the detection of explosive analytes. For tetryl and HMX, clear SERS fingerprints were measured at nanomolar concentrations with estimated limits of detection of about 4-5 nM and 2-3 nM, respectively, under 488 nm excitation [3]. The tetryl spectra also revealed pronounced excitation dependent behaviour: the symmetric NO_2 stretching mode shifted from about 1376 cm^{-1} at 633 nm to about 1334 cm^{-1} at 535 nm and about 1327 cm^{-1} at 488 nm [3]. This trend supports a laser dependent charge transfer contribution from Ag into the analyte LUMO, which is relevant for reference database construction and machine learning workflows that use vibrational fingerprints for hazardous chemical classification [3-5].

Discussion and Outlook

Beyond the specific explosives tested here, the results show how plasma processing can be used to tune both morphology and sensing function in a substrate integrated architecture. The oxide scaffold supplies vertical geometry, mechanical robustness, and a high density of accessible sidewalls, while the discontinuous Ag overlayer creates the local plasmonic environment required for SERS. Because the sensing surface is generated directly on copper, the route avoids lithographic alignment and multistep colloidal assembly. This is attractive for scale up, batch fabrication, and eventual integration into compact sensor heads or disposable cartridges.

The wavelength dependent red shift of tetryl also highlights an important data quality issue. Spectral position is not determined only by the analyte itself, but also by the interplay between hotspot geometry, excitation wavelength, and charge transfer at the metal molecule interface. For practical deployment, this means that reference spectra should be collected under controlled optical conditions and that spectral libraries used for automated classification should contain metadata on the excitation source and substrate type. These requirements are especially relevant for hazardous chemicals, where confident discrimination among chemically similar nitro compounds is essential.

Conclusions

The presented CuO/Cu_2O-Ag platform shows that plasma oxidation can serve as a practical fabrication route for vertical SERS metasurfaces without lithography or wet chemical multistep growth. The combination of anisotropic oxide sheets and discontinuous Ag nanoparticles provides strong hotspot density, good reproducibility, and broadband operation. Because the process is simple and substrate integrated, it is promising for portable chemical sensors aimed at security, environmental, and field analysis applications. Future work should focus on analyte libraries, stability under real sampling conditions, and transfer of the platform into deployable sensing formats.

References

[1] S.-Y. Ding, J. Yi, J.-F. Li, B. Ren, D.-Y. Wu, R. Panneerselvam, Z.-Q. Tian, Nanostructure-based plasmon-enhanced Raman spectroscopy for surface analysis of materials, Nature Reviews Materials 1, 16021 (2016); doi: 10.1038/natrevmats.2016.21

[2] J. Langer, D. Jimenez de Aberasturi, J. Aizpurua, R. A. Alvarez-Puebla, B. Auguie, J. J. Baumberg, et al., Present and Future of Surface-Enhanced Raman Scattering, ACS Nano 14, 28-117 (2020); doi: 10.1021/acsnano.9b04224

[3] V. Shvalya, A. Breus, O. Baranov, D. Vengust, J. Zavasnik, U. Cvelbar, Plasma-Tunable Metasurfaces for SERS Nanosensing of Hazardous Chemicals, Small 21, e202506814 (2025); doi: 10.1002/smll.202506814

DOI 10.5162/eurosensors2026/Mo–ESM–05

Characterization of Aluminum Nitride on vertical side walls

Maria-Theresia Becker[1], Mano Bhavdeep Venkatesan[1], Achim Bittner[1], Alfons Dehé[1,2]
[1] Hahn-Schickard-Gesellschaft für angewandte Forschung e.V., Wilhelm-Schickard-Str. 10, 78052 Villingen-Schwenningen, Germany
[2] Georg H. Endress Chair for Smart Systems Integration, Department of Microsystems Engineering – IMTEK, Albert-Ludwigs-Universität Freiburg, Georges-Köhler-Allee 103, 79110 Freiburg, Germany
Maria-Theresia.Becker@Hahn-Schickard.de

Summary:
AlN is used for actuation of vertical sidewalls e.g. for a MEMS speaker with a high aspect ratio membrane. This actuation of vertical sidewalls by a sputtered AlN layer generates new challenges regarding the characterization of piezoelectric quality along the vertical sidewalls. This work utilizes Fourier transform infrared (FT-IR) microscopy to measure crystallinity and crystal orientation of the layers. FT-IR spectroscopy was found to be a suitable method to characterize vertical AlN sidewalls. Results for crystallinity and crystal orientation of AlN are discussed and compared to surface measurements.

Keywords: piezoelectric AlN, sputter deposition, FT-IR spectroscopy, MEMS, 3D membranes

Background, Motivation and Objective

A novel 3D MEMS speaker concept with high aspect ratio is used to maximize the active surface area [1]. Piezoelectric aluminum nitride (AlN) thin films are used for actuation. In this work, conformal deposited AlN by atomic layer deposition (ALD) is replaced by more crystalline sputtered AlN-layer with higher piezoelectric performance [2] with the drawback of tapered film thickness. As sputtering is a directional process, film properties on vertical side walls will differ from surface properties. This raises the necessity of a reliable characterization method of piezoelectric, structural and mechanical properties at the side wall. The objective of this work is to utilize the high spatial resolution of FT-IR microscopy to characterize the crystallinity, crystal orientation, and residual stress level of AlN layers at vertical side walls.

Description of the new method or system

There are few works on AlN characterization using FT-IR spectroscopy to measure the crystal orientation of AlN films [3]. This work utilizes a Bruker Invenio FT-IR spectroscope coupled with a Hyperion 2000 FT-IR microscope. The high spatial resolution of FT-IR microscopy enables the adjustment on single side-walls of the lamella structure. Side walls were separated by dicing through a trench and aligned horizontally with a mini-vice. The measurement is applied on a side wall sample and results are discussed and compared with surface measurements. Peak positions and widths are extracted using Voigt fitting.

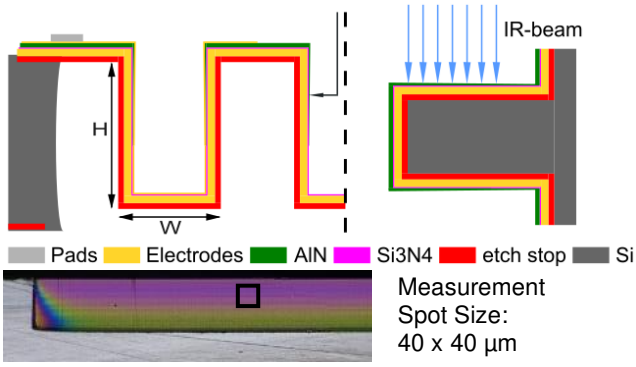

Fig. 1. a) Concept of the MEMS speaker with a high aspect ratio trenches and vertical sidewalls b) alignment for FT-IR measurements; c) LSCOM image of the side wall & measurement spot

Results

AlN thin films were deposited using different sputter conditions on a Si<100> wafer and characterized by FT-IR microscopy. Results are compared with established characterization methods as XRD for crystal orientation and crystallinity, and wafer bow for residual stress measurement. Four different AlN layers were analyzed: two sputtered AlN films with high c-axis orientation and low FWHM (good crystallinity) having different stress states, one sputtered AlN film with crystalline, but not textured crystal structure and one ALD-deposited AlN thin film showing c-axis orientation, but low crystallinity.

FT-IR spectra are shown in Fig. 2a-c. Due to the interaction of the IR beam with AlN, excited phonon modes are dependent on the crystal orientation [3]. If the c-axis is parallel to the incident IR-beam, only the E1 (TO) appears and the A1

(TO) peak vanishes. This can be seen in Fig. 2a. The low FWHM indicates a good crystallinity of AlN. If the crystal structure deviates from an ideal c-axis orientation, the A1 (TO) peak can be detected. This can be due to an additional occurring crystal orientation (Fig. 2b) or due to a lack of crystallinity (Fig. 2c). As excitation of phonon modes is not bound to crystalline materials, also not ordered crystal bonds contribute to the absorption spectrum. The trend in FWHM is similar to the trend detected with XRD. Lowest FWHM was detected in crystalline & c-axis oriented layers (Fig. 2a). A slightly higher FWHM was detected in randomly oriented layers (Fig. 2b) and the highest FWHM was measured in purely crystalline ALD-AlN layers (Fig. 2c). To make an estimation of the residual stress state of AlN-layers, FT-IR peak positions were compared and opposed to wafer bow measurements. A matching trend was not detected. In conclusion, it is possible to conclude on c-axis orientation and crystallinity of AlN by FT-IR measurements.

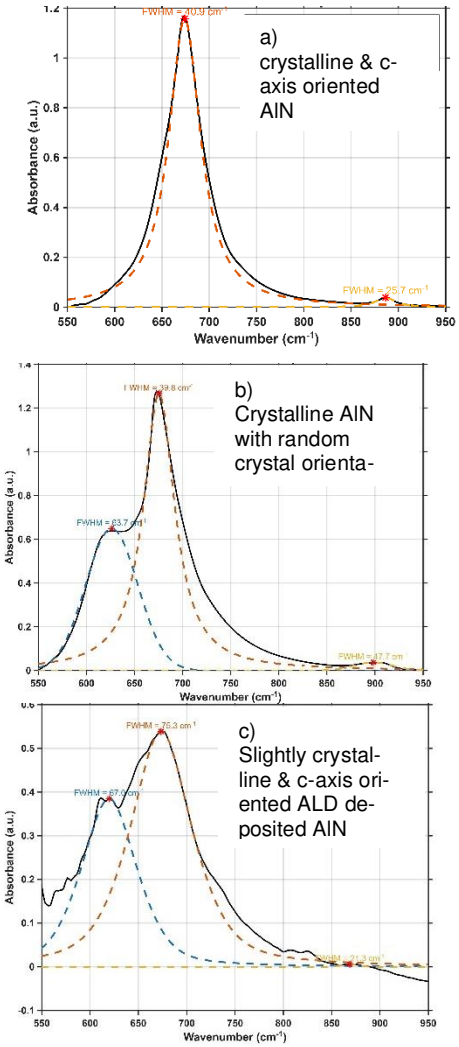

Fig. 2.: FT- IR absorbance spectra of different layers: a) crystalline and c-axis oriented sputtered AlN; b) crystalline, randomly oriented sputtered AlN and c) purely crystalline, c-axis oriented ALD-AlN

The FT-IR measurement of a sidewall coated by AlN is shown in Fig. 3. AlN was grown on a Polysilicon layer, thus measurements were taken in transmission mode. The aperture size was set to 40 x 40 µm (Fig. 1c) to represent a largest possible part of the side wall with a sufficient AlN film thickness.

Both peaks E1(TO) and A1(TO) were detected in the FT-IR spectrum at the side wall. This indicates a deviation from ideal c-axis orientation. As stated in the literature, the c-axis orientation is not perpendicular to the substrate at vertical side walls [4]. Additionally, as also grains are tilted at the side wall, amorphous grain boundaries also contribute to the intensity of the A1 (TO) peak and promote a large FWHM of the E1 (TO) peak.

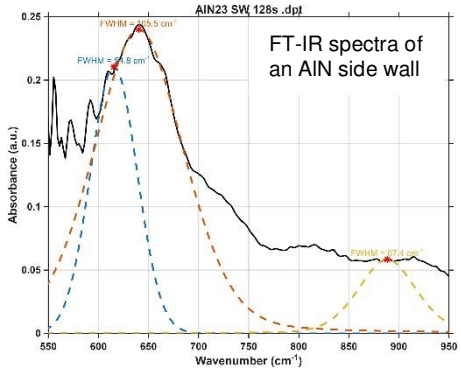

Fig. 3.: FT-IR spectrum of a crystalline AlN layer at the side wall of a trench

In conclusion, FT-IR microscopy can be utilized to measure crystal orientation and crystallinity on trench side walls. Next, it is planned to measure locally resolved at different trench depth to detect the difference occurring with it. Prospectively, FT-IR spectroscopy can be used to optimize AlN for 3D structures.

[1] D. Becker, R. Scharf, T. Leonhard, A. Merz, A. Bittner, A. Dehé, *Meander-shaped piezoelectric MEMS loudspeaker with maximized area efficiency for in-ear applications*, *Sensors and Actuators Reports* 9, 100319 (2025); doi: 10.1016/j.snr.2025.100319

[2] P. Sippola, A. Perros, O.Ylivaara, H. Ronkainen, J. Julin, X. Liu, T. Sajavaara, J. Etula, H. Lipsanen, R.Puurunen, Comparison of mechanical properties and composition of magnetron sputter and plasma enhanced atomic layer deposition aluminum nitride films, *Journal of Vacuum Science & Technology A1 36, 051508 (*2018), doi: 10.1116/1.5038856

[3] M.Kazan, Crystal orientation by unpolarized infrared reflectivity application to aluminum nitride, *Journal of applied Physics* 102, 073532 (2007); doi: 10.1063/1.2795579

[4] M. Ramezani, V. Felmetsger, N. Rudawski, R. Tabrizian, *IEEE Transactions on Ultrasonics, Ferrolelectrics, and Frequency Control* 68 (3), 753 – 759 (2021); doi: 10.1109/TUFFC.2020.30111

DOI 10.5162/eurosensors2026/Mo–ESM–06

Direct Sputter Deposition of Gold Thin-Film Sensors on Wood Substrates toward Chip-on-Wood Integration

Paul Reber[1], Nursultan Daupayev[1], Moritz Lang[1], Sören Hirsch[1]
[1] Brandenburg University of Applied Science, Department of Engineering, Magdeburger Str. 50, 14770 Brandenburg/Havel, Germany
paul.reber@th-brandenburg.de

Summary: This work presents a first step toward realizing Chip-on-Wood systems, a novel integration concept in which microelectronic chips are directly mounted on wood substrates equipped with sputtered thin-film sensors. Gold thin-film structures were deposited on prepared beech wood surfaces via shadow mask sputtering, demonstrating good adhesion and continuous electrical conductivity. The approach eliminates conventional electrode insertion, reduces signal losses, and is fully compatible with future microelectronic integration, offering potential for miniaturized, energy-efficient sensing systems for structural health monitoring in timber construction.

Keywords: Thin-Film Sputtering, Wood Substrate, Structural Health Monitoring, Gold Metallization, Shadow Mask Patterning

Introduction

Wood is widely used as a sustainable building material in the construction industry. However, a key challenge is the high sensitivity of its mechanical properties to climatic fluctuations, which makes continuous structural health monitoring of wooden structures essential. Existing sensing approaches often require inserting electrodes into the wood, which can lead to interfacial failures or loss of signal accuracy [1][2]. Furthermore, due to their size such approaches cannot be integrated with microelectronics components.

To address these limitations, we propose a Chip-on-Wood integration concept, in which thin-film sensor structures are directly sputtered onto the wood surface, enabling future direct mounting of a microelectronic chip on the substrate. This eliminates contact losses at the electrode interface, improves signal integrity, and enables a fully integrated, miniaturized sensing system compatible with scalable deployment in the construction industry.

Fabrication Process

The fabrication process begins with the preparation of the wood substrate. To achieve a surface smooth enough for the sputtering process, the wood-substrates are ground using a metallographic polishing machine under controlled contact pressure and with various grit sizes (Tab. 1). Afterwards the samples were dried at 103 °C for 48 hours to achieve a wood moisture content close to 0 %.

Tab. 1: Grinding Parameters

grit size	contact pressure [N]	Rotation speed [1/min]	time [s]
320	5	130	180
600	5	130	180
1200	10	130	180

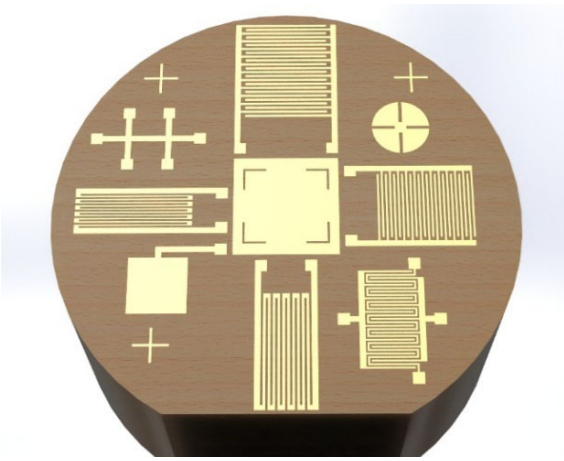

Fig. 1. Schematic representation of the sensor layout: Positioning of various sensor structures on the wood substrate.

The sensor layout is specifically optimized for the sanded wood substrate (Fig. 1). It includes various sensing structures (e.g. interdigital capacitor and strain gauge) in different structural sizes to qualify the aspect ratio of the shadow mask (200 µm). In addition, the layout includes structures for measuring the surface insulation

resistance, contact pads for bond testing, and reference points for orientation and layer thickness measurement.

For the sputtering process, a shadow mask with a thickness of 200 µm was pressed onto the wood substrate (Fig. 2). Through multiple sputtering processes a highly conductive gold layer was deposited.

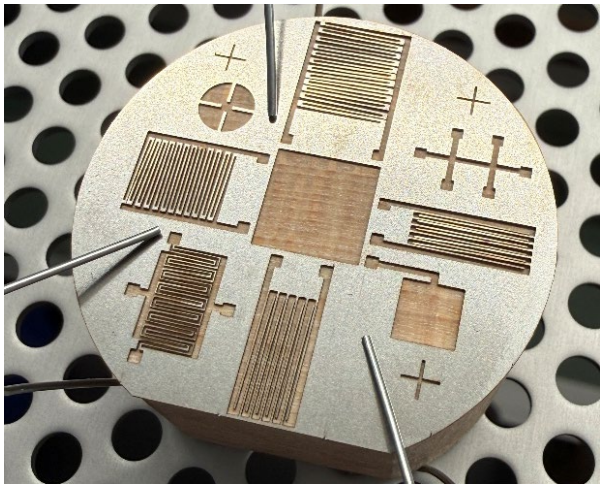

Fig. 2. Implementation of the sensor layout: A shadow mask (200 µm thick) fixed to the prepared wood sample to define the structures during the sputtering process.

Results

The results demonstrate that homogeneous gold layers can be directly deposited onto prepared wood surfaces by sputtering (Fig. 3). To verify the surface adhesion of the metallization to the substrate, a standard tape test was performed using 3M Crystal Tape. The results show a strong interfacial bond between the gold layer and the wood substrate.

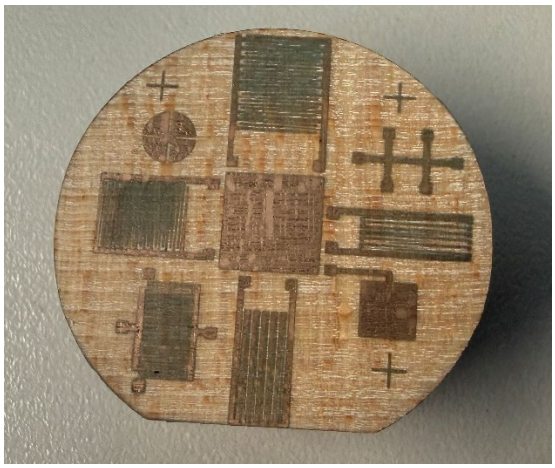

Fig. 3. Result of the sputtering process, a deposited and patterned gold thin film on a prepared beech wood surface.

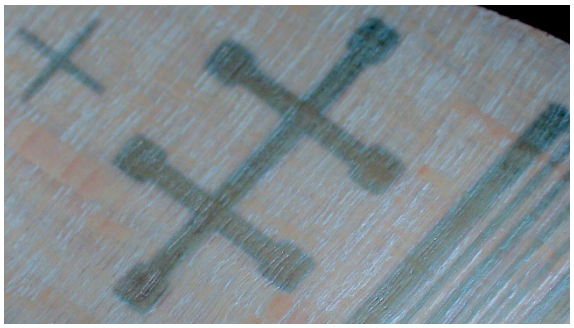

Fig. 4. Close-up of the macroscopic test structure used to determine the surface insulation resistance. Resistance values of 2 kΩ (long arm) and 1 kΩ (short arm) were successfully measured on this cross-shaped geometry.

The limited resolution of the shadow mask process currently prevents functional electrical characterization of microscopic IDC and strain gauge designs. Nevertheless, the overall metallization process has been validated. Using the macroscopic test structures, the surface insulation resistance of the sputtered gold thin film on the beech substrate was successfully quantified. The measured resistances were 2kΩ for the long arm and 1 kΩ for the short arm.

Conclusions

We present a new fabrication process for direct integration of sensor structures on wood substrates. The results confirm continuous electrical conductivity of the film and establish a key parameter for future high resolution sensor integration, opening up prospects for accurate and reliable sensing directly on wood substrates.

Future work will focus on optimizing the aspect ratio of the shadow mask to enable functional IDC and strain gauge structures. In addition, a capacitor-to-digital converter will be integrated directly on the wood substrate to realize a fully self-contained Chip-on-Wood sensing node for structural health monitoring.

References

[1] M. He, M. Li, J. Zhang, Experimental Study on the Bonding Performance of FFRP Reinforced Timber Interface, *Journal of Natural Fibers* 20 (2023); doi: 10.1080/15440478.2023.2175761

[2] R. Hafsa, A. Sbartaï, M. El Ganaoui, Assessment of moisture content profile in Douglas-fir wood using electrical resistivity-based tomography, *Construction and Building Materials* 366, 130230 (2023); doi: 10.1016/j.conbuildmat.2022.130230

DOI 10.5162/eurosensors2026/Mo−ESM−07

Synthesis of Nitrogen and Phosphorus doped carbon dots and study of their photoluminescence in the solid state

Spyridon N. Katsantonis[1,2], Spiros Gardelis[3], Marko Bošković[4], Danijela Randjelović[4], Nikola Vuković[5], Srđan Matijašević[5], Sowmya Dean[6], Maryam A. Saeed[6], Yaaqoub Malallah[6], Konstantinos V. Kordatos[2], Christos Tsamis[1]

[1] Institute of Nanoscience and Nanotechnology, NCSR Demokritos, Patr. Grigoriou E' & 27 Neapoleos Str., Agia Paraskevi, 15341 Athens, Greece

[2] Department of Chemical Sciences, School of Chemical Engineering, National Technical University of Athens, 9 Iroon Polytechniou Str., 15772 Athens, Greece

[3] Condensed Matter Physics Section, Physics Department, National and Kapodistrian University of Athens, Panepistimioupolis Zografos, 15784 Athens, Greece

[4] Institute of Chemistry, Technology and Metallurgy, National Institute of the Republic of Serbia, University of Belgrade, Njegoševa 12, 11000 Belgrade, Serbia

[5] Institute for Technology of Nuclear and Other Mineral Raw Materials, Bulevar Franš d'Eperea 86, 11000 Belgrade, Serbia

[6] Energy and Building Research Center, Kuwait Institute for Scientific Research, 13109 Kuwait city, Kuwait

c.tsamis@inn.demokritos.gr

Summary:

In this work, the solid-state photoluminescence of different carbon dot types was examined. The carbon dots were synthesized solvothermally with variations in dopant species and solvent. Incorporation of heteroatoms such as nitrogen and phosphorus altered the optical properties of carbon dots. For photoluminescence measurements, thin films of carbon dots were prepared on Si/SiO_2 substrates using spin coating.

Keywords: carbon dots, doping, photoluminescence, solid state

Introduction

Carbon dots (CDs) is a class of carbon nanomaterials with sizes less than 10 nm, which has attracted widespread attention due to its excellent optical properties, biocompatibility and low cost of synthesis. Doping of CDs with heteroatoms like nitrogen, phosphorus, sulfur and boron can lead to modification of their properties, including their photoluminescence [1]. Another factor that influences the optical properties of CDs is the solvent used during synthesis or in which they are dispersed [2]. While photoluminescence of CDs has been extensively studied in solution-form, strategies to control solid-state photoluminescence of CDs are still in development, mainly due to challenges that arise from aggregation-caused quenching [3].

In this work, the photoluminescence of various types of CDs in the solid state was investigated. CDs doped with nitrogen (N), phosphorus (P) or co-doped with nitrogen and phosphorus (NP), were prepared by a solvothermal method. Ultrapure water and glycerol were used as solvents. The novelty of this work lies in the combination of the precursor materials used for the synthesis of CDs and the study of their photoluminescence in the solid state.

Materials and Methods

CDs with different types of doping were solvothermally synthesized by varying the precursor materials. Citric acid was used as source of carbon, while urea and phosphoric acid were used as sources of nitrogen and phosphorous, respectively. Specific amounts of each precursor material were dissolved in ultrapure water or glycerol, and the mixture was transferred to a Teflon-lined stainless-steel autoclave, where heating was applied. The solution obtained was purified by centrifugation and filtration. Thin films of the various CDs were prepared by spin coating on Si/SiO_2 substrates. Then, the substrates were heated on a hotplate to evaporate the solvent. The names of the samples indicate their doping type. The samples N-CDs-1, P-CDs-2 and NP-CDs-1 were prepared by using ultrapure water as solvent while P-CDs-1 glycerol was used as solvent.

The optical, structural and morphological properties of the CDs were characterized by scanning electron microscopy (SEM), energy dispersive X-ray spectroscopy (EDS), ultraviolet-visible (UV-Vis) spectrometry and Fourier-transform infrared (FT-IR) spectrometry. The photoluminescence (PL) spectra of the thin films were collected, after laser excitation 355 nm.

Results

Representative SEM images of the thin films prepared from the samples P-CDs-1 and NP-CDs-1 as well as EDS spectrum for NP-CDs-1 are presented in Fig. 1. The thin film of P-CDs-1 is uniformly spread on the surface of the Si/SiO_2 substrate. On the other hand, the thin film of NP-CDs-1 exhibits a patterned surface morphology with 3D texture, which could be attributed to the co-existence of two different dopants.

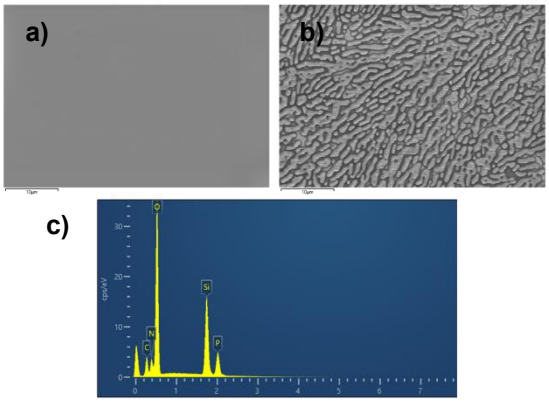

Fig. 1 SEM image of the thin films prepared from the sample (a) P-CDs-1 and (b) NP-CDs-1 captured at 20 kV and x2500 magnification, and (c) EDS spectrum of sample NP-CDs-1.

The UV-Vis spectra of the different types of CDs are presented in Fig. 2. It is observed that all types of CDs strongly absorb light in the UV region. A primary peak at 199-232 nm is present in all the samples and is attributed to π-π* electronic transitions of C=C bonds. Moreover, a secondary peak at 262-336 nm is present in N-CDs-1, P-CDs-1 and NP-CDs-1. This peak is attributed to n-π* electronic transitions of C=O or C=N bonds.

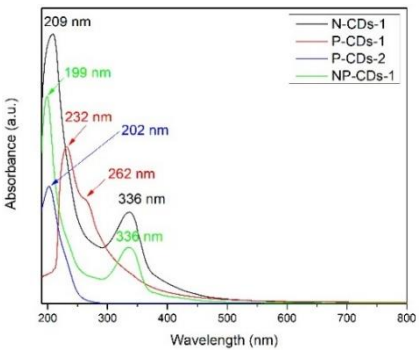

Fig. 2 UV-Vis spectra of the different types of CDs.

The PL spectra of the different types of CDs after excitation with a 355 nm laser are shown in Fig. 3. Photoluminescence is observed in all the samples by exhibiting broad peaks. The samples N-CDs-1, P-CDs-2 and NP-CDs-1 emit mainly light in the region of blue-green color with peaks at 467 nm, 462 nm and 490 nm, respectively.

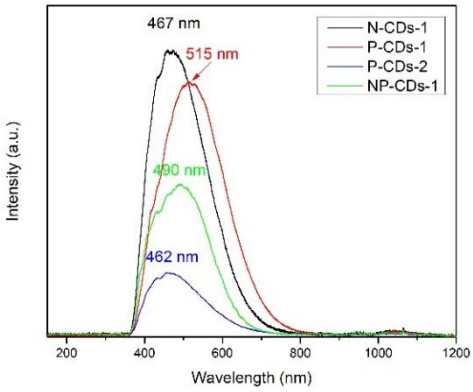

Fig. 3 PL spectra of the different types of CDs at an excitation wavelength of 355 nm.

The sample P-CDs-1 emits mainly light in the region of green-orange color with a peak at 515 nm. Moreover, down-conversion is observed in all samples, since irradiation with a UV-laser at 355 nm leads to emissions with higher wavelength, between 462 nm and 515 nm. This could be explained by the presence of various surface states and defects in the structure of CDs.

References

[1] L. Li and T. Dong, Photoluminescence tuning in carbon dots: surface passivation or/and functionalization, heteroatom doping, *Journal of Materials Chemistry C,* 30, 7944-7970 (2018); doi: 10.1039/C7TC05878K.

[2] Y. Wang and S. Wu, High-performance green fluorescent carbon dots: Synthesis, Properties, and applications in temperature sensing, and information anti-counterfeiting, *Materials Science & Engineering B*, 319, 118355, (2025), doi: 10.1016/j.mseb.2025.118355.

[3] H. Wang, L. Ai, H. Song, Z. Song, X. Yong, S. Qu and S. Lu, Innovations in the Solid-state Fluorescence of Carbon Dots: Strategies, Optical Manipulations, and Applications, *Advanced Functional Materials*, 33, 2303756 (2023), doi: 10.1002/adfm.202303756.

Acknowledgements

This research was sponsored by the NATO Science for Peace and Security Programme under the Multi-Year Project NextGenVLC (grant id. [G7264]) and partially supported by the Ministry of Science, Technological Development and Innovation of the Republic of Serbia (Contract No. 451-03-136/2025-03/200026).

DOI 10.5162/eurosensors2026/Mo–ESM–08

Sputtered permalloy as novel material for THz-thin film technology: fabrication process, physical and electro-magnetic properties

Pranesh Kondamarri[1], Julien Petit[1], András Kovács[1], Ulrich Mescheder[1], Volker Bucher[1], Anil Badisa[2], Michał Herbko[2], Adam Żywica[2], Marcin Ziółkowski[2], Przemysław Łopato[2]
[1] Furtwangen University, Robert-Gerwig Platz 1, 78120, Germany
[2] West Pomeranian University of Technology, Szczecin, al. Piastow 17, Poland
ReddyPranesh.Kondamarri@hs-furtwangen.de

Summary:
Sputtered permalloy thin-film technology has been developed for terahertz (THz) filters. The current work describes its fabrication process and characterisation process. The investigated thickness range of the films is 100-1000 nm. The film surfaces and the growth of the film is analysed using FIB-SEM measurements. The magnetic behaviour is evaluated with vibrating sample magnetometer. The THz behaviour is characterised using sheet-resistance measurements followed by time domain spectroscopy (THz-TDS). It is demonstrated that films with thickness greater than 400 nm show a large out-of-plane magnetisation and a THz-shielding performance of more than -50 dB at 1 THz.

Keywords: THz-filters, magnetic films, Metasurface, MEMS, sputtering, permalloy, THz-TDS, resonant frequency, split-ring resonators.

Introduction

Terahertz (THz) waves ((0.1-30) x 10^{12} Hz) and their interaction with materials gained an increased research-interest in the past two decades. Invention of THz sources (such as photoconductive antennas, backward-wave oscillators, quantum-cascade lasers [1]) paved a way towards THz-TDS technology e.g., for biosensors. Currently, there is a growing need to develop tunable filters for sensing different frequency ranges. One possible way to realize this is through so-called 'metasurfaces (MS) [2].'

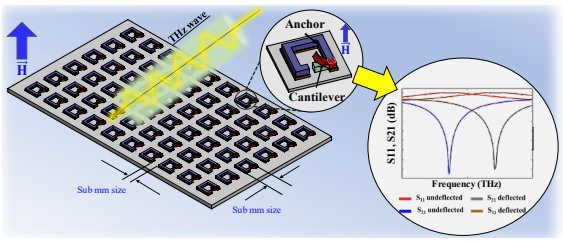

Figure 1 Magnetically tunable THz MS. SRR with a cantilever arm in red (in inset) which is sensitive to external H leading to f_R shift shown using S_{21} transmission parameters [5].

MS are 2D artificial materials which respond unusually to EM waves (compared to natural materials) due to sub-wavelength size structural units. Typical examples of such units are cross structures or split-ring resonators (SRR) which behave as an LC oscillator and are realized by suitable high conductive thin film metal structures with sufficient shielding properties in the THz range. As the SRR dimensions determine the resonance frequency f_R, they can be tailored to operate in THz range [3].

The current work is a part of a project which aims to develop magnetically tunable THz metasurfaces using MEMS processes (Figure 1). The structural unit is an SRR whose one arm is a deflecting cantilever (cl) while the rest is an anchor. In case that the cl is made of ferromagnetic material, the cl can be deflected by an appropriately chosen external magnetic field ($\vec{H}$), and thereby leads to a shift in f_R. Permalloy ($Ni_{80}Fe_{20}$ or Py) has a high permeability (μ_r~100,000), low resistivity (ρ_{bulk} = 16 μΩ-cm) and is therefore in principle very well suited for magnetically tunable filters [4]. However, the THz shielding behavior must be investigated which is the purpose of this study. Therefore, films are characterised based on thickness (*t*), surface and layer growth. The magnetic hysteresis behavior is studied using a vibrating sample magnetometer (VSM). The sheet resistance (R_s) and the shielding behavior are also evaluated. Based on this evaluation, passive MS structures of Py are further fabricated and tested for their THz absorption performance. The processes and results are described in detail in the following sections.

Material and methods

Thin film fabrication

Py films are sputtered at room temperature (RT) in DC mode (Alcatel SCM650). To minimize THz absorption in substrate, low doped Si wafers with ρ > 10 kΩ-cm are used. The base pressure is kept at 7.5 x 10^{-7} mbar. Argon pressure is set to 0.09 mbar. Films are sputtered at 75 W and at a target-substrate distance of 60 mm with a sputter rate of 0.084 nm/s. The range of *t* for the films is in 93-975 nm.

Passive metasurface fabrication using lift-off process.

Based on the characterisation of the complete Py layers, a process flow is developed to fabricate SRR based MS structures described in Figure 2. A positive resist AZ1518 is used as a liftoff layer. This is spin coated using KarlSüss RC8 CT-62 at 4250 RPM, 2500 Accn for 25 s. Diluted HMCTS is applied prior to resist as an adhesion promoter. The coated AZ1518 is soft-baked at 100°C for 50 s and subjected to UV exposure with SRR mask using KarlSüss MA6 SN-50 for 11 sec at RT and 44% humidity. The exposed resist is patterned in diluted AZ351B for 60 s. A layer of Py is then sputtered onto the resist and as a final step, the sample is immersed in acetone placed in ultrasonic shaker for 300 s for lift-off.

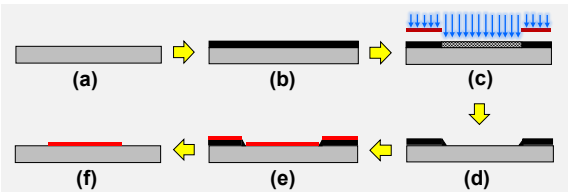

Figure 2 Process flow for passive structure fabrication. (a) Uncoated Si substrate (b) Spin coated AZ1518 photoresist, t = 1.8 µm (c) UV exposure using SRR mask (d) Resist patterning with AZ351B diluted in 5 parts of water (e) Sputter deposition of py layer. (f) Lift-off in Acetone in an ultrasonic bath.

Characterization methods

The metal film thickness is measured using a Dektak profilometer. FIB-SEM device (Zeiss Crossbeam 550 L117442) and laser-confocal microscope (Keyence VK-X3100) are used to evaluate surface topography, layer growth and surface roughness. The hysteresis behaviour of the film is studied in Out-of-plane (OP) direction with a vibrating sample magnetometer (VSM). 4-point measurement is used to measure R_s of the films. The transmission properties are evaluated in 0-6 THz frequency range using THz-TDS spectroscope (Toptica Teraflash Smart). In contrast to vector network analyzers, where the frequency is physically swept during the measurement, THz-TDS performs time-domain measurements, and the frequency response is obtained using Fast Fourier transform (FFT) technique. The blank substrate is taken as reference.

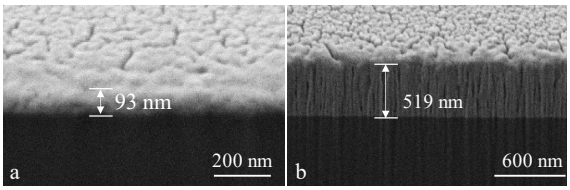

Figure 3 FIBSEM cut of deposited films. The film is crack-free but ridged. The roughness is in nm scale initially at 93 nm (a) but, results in a columnar layer growth at higher thickness (b).

Results and conclusion

Complete layers

The film surface is shown in Figure 3. At 93 nm, the surface is complete, crack-free but, ridged. The roughness of the film is in the nm-scale. As *t* rises, the layer grows in columnar fashion. The magnetisation curve for a film with *t* = 436 nm is presented in Figure 4. The curves exhibit a large magnetisation ($\vec{M}$) in OP direction which is essential for a deflection in applied external $\vec{H}$.

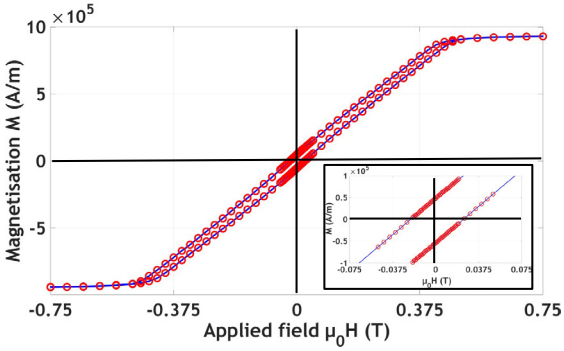

Figure 4 Hysteresis behaviour of a 436 nm-thick Py in the OP direction. The sample has a large $\vec{M}$ and a satruation around 600 mT and have a remanence (M_r) is at 54 kA/m and $\mu_0 H_c$ is at 23 mT.

The THz transmission (|T|) for varying *t* is shown in Figure 5. The inset describes the R_s drops between 93 and 219 nm and saturates at higher thicknesses and the fitted curve follows R_s = a/ (t + b) where a = 4363, b = -33.97. In the region of interest (ROI, 0-3 THz), as *t* rises from 93 to 219 nm, the signal attenuates by more than -20 dB at 1 THz. With further rise in *t*, signal reaches noise level. The according absorption coefficients are analyzed under assumption of constant Py-reflectivity in that range. Absorption coefficients between 10-30 µm^{-1} were found with a maximum at around 1 THz. It results in an attenuation of -50 dB for *t* = 400 nm implying that Py is a potential material for MS-based THz-filters.

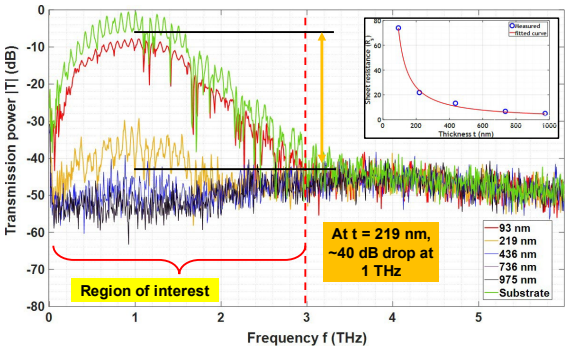

Figure 5 THz transmission in Py films. With increase of t signal attenuates rapidly and reaches noise level for t > 436 nm. The inset describes the variation of R_s with t. The blue circles represent mean in R_s (5 values around the wafer). The error is negligeable.

Structured passive SRR metasurface

The fabricated passive MS is presented Figure 6a. The outer dimensions of SRR are ~ 110 x 110 µm and the capacitive plates are ~25 µm wide and have separation distance of ~16 µm. The Py has a t = 589 ± 46 nm, which is higher than 400 nm, the minimal thickness required for reasonable THz shielding and exert an $\vec{M}$ in OP for a deflection in external-$\vec{H}$. The THz response is presented in Figure 6b. The incident THz wave was polarized with its electric field vector ($\vec{E}$) oriented horizontally, with respect to the SRR ($\vec{E}$ horizontal in Fig. 6a), to maximize the coupling between the $\vec{E}$-field and the LC resonant mode of the structure. This configuration enables efficient excitation of the SRR fundamental resonance and enhances the observed THz response. Its response is compared with the response of an unstructured 436 nm-thick Py layer. Also, for the comparison of THz resonance peaks, an SRR chip fabricated with Al as metal layer, t = 536 ± 40 nm is considered too. Compared to the total attenuated response (in the ROI) of the unstructured Py layer, both Al and Py-SRR samples exert a resonance at 0.57 THz. For an in-depth analysis, the de-embedded response is computed where the influence of the Silicon substrate is eliminated. The obtained-response is further subjected to low-pass filtering and presented in Figure 7. The results show that for the same SRR structures, the THz transmission of a ~ 600 nm-thick Py exerts a resonance of 11 dB which is considerably lower than the 35 dB attenuation for the ~500 nm thin Al-SRRs. To conclude, Py as a complete unstructured layer is a suitable material for THz absorption. In case of SRR structures, a resonance exists but, further design optimisations are necessary to address the specific properties of Py and Si-wafer as it has a high ρ value compared to Al. Also, thermal annealing can be implemented to minimise the intrinsic stress of the Py layer and reduce ρ value. Further, a bi-layer approach with Al for THz shielding and Py for magnetic deflection can also be implemented.

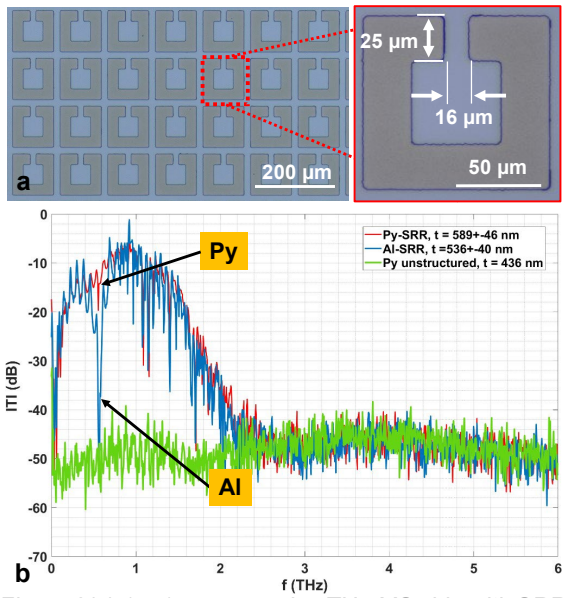

Figure 6(a) 15x15 mm passive THz-MS chip with SRR as a structural unit. For THz-response, the spot-size of the incident wave at 1 THz is expected to be around 2 mm (frequency-defendant). In that case, the unit cells within the array pertaining to the spot-size are ~ 1256 in number. (b) Raw THz response for SRR metasurfaces. In the ROI, both layers exert a resonance at 0.57 THz.

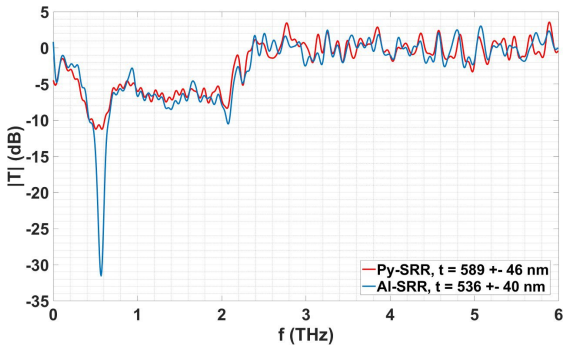

Figure 7 De-embedded-filtered THz response of passive SRR metasurface chip. At 0.57 THz, the transmission drops by ~31 dB for Al layer. In case of Py, there is a drop but, of a weaker magnitude of ~11 dB.

Acknowledgement

This work is funded by German Research Foundation (DFG, Project Nr. 525135725) and the National Science Centre, Poland (NCN, grant no. 2022/47/I/ST7/02055). FIBSEM device is funded by the DFG within the program Major Research Instrumentation (Project number: 505067193) under GG91b and by the state Baden-Württemberg as well as by Furtwangen University. VSM measurements are carried out at the Centre de compétences Magnétisme & Cryogénie, Institut Jean Lamour, Uni-Lorraine, France.

References

[1] H. A. Hafez *et al.,* "Intense terahertz radiation and their applications," *J. Opt.*, vol. 18, no. 9, p. 93004, 2016, doi: 10.1088/2040-8978/18/9/093004.

[2] S. S. Bukhari, J. Vardaxoglou, and W. Whittow, "A Metasurfaces Review: Definitions and Applications," *Applied Sciences*, vol. 9, no. 13, p. 2727, 2019.

[3] X. Zang *et al.,* "Metasurfaces for manipulating terahertz waves," *Light: Advanced Manufacturing*, vol. 2, no. 2, p. 148, 2021, doi: 10.37188/lam.2021.010.

[4] S. Tumański, *Handbook of Magnetic Measurements,* 1st ed. (Series in Sensors Ser). Baton Rouge: Taylor & Francis Group, 2011.

[5] B. Szymanik *et al.,* "MP69 - Simulation and Optimization of Magnetic Field Actuated MEMS-Based Metasurface for Terahertz Applications," in *Poster I*, Wroclaw, 2025, pp. 341–342, doi: 10.5162/EUROSENSORS2025/MP69.

DOI 10.5162/eurosensors2026/Mo−ESM−09

A New Approach for Production of Nanofilament-Based Chemoresistive Sensors

A. Schmidt-Ott[1,2], L. Sacco[1], K.C. Petallidou[2], P. Kováčik[4], G. Biskos[2,3]
[1]VSParticle B.V, Oostsingel 209, 2612HL Delft, The Netherlands,
[2]Climate and Atmosphere Research Centre, The Cyprus Institute, 2121 Nicosia, Cyprus,
[3]Faculty of Civil Eng. and Geosciences, Delft University of Technology, 2628 CN Delft, Netherlands,
[4]National Research Council of Canada, K1A 0R6, Ottawa, Canada,
a.schmidt-ott@vsparticle.com

Summary:

Nanofilament bridges offer a route to low-power chemoresistive sensors. From nanoporous layers (NPLs) consisting of 5 nm particles, which can be produced by a one-step spark-ablation and impaction-printing process, we produce such nanofilaments by current-driven sintering. They are supported by the un-sintered matrix of the original NPL, which has a negligible conductivity with respect to the filaments. Current limitation basically tunes the number of filaments formed. This scalable approach may extend to many metals and alloys as Joule-heated sensing materials for extremely low-power sensor operation.

Keywords: chemoresistive sensor, nanofilaments, nanofibers, nanoporous, nanoparticulate layer, current-driven sintering

Background, Motivation and Objective

Nanofilaments or nanofibers that bridge electrodes offer promising platforms for chemoresistive sensors [1,2]. Joule heating can raise these structures to the required operating temperature, while the temperature-dependent sensor response can improve selectivity. Because heating is localized within the sensing material, power consumption is far lower than in conventional MEMS devices that use separate heaters. However, lithography-based fabrication of chemoresistive sensors typically involves multiple process steps [2]. Recent work has shown that spark-ablation nanoparticle generation in a gas environment combined with impaction printing can produce nanoporous layers (NPLs) in a single step [3]. In particular, the VSParticle VSP-G1 used with the VSP-P1 has demonstrated unique chemoresistive sensing properties [4]. As-deposited NPLs usually require annealing to sinter the typically 5 nm particles to remove highly resistive barriers between them. The spark-ablation-printing approach is inexpensive and scalable. Its unique flexibility regarding composition and structure of nanoparticulate layers, make it a versatile platform for optimizing sensor properties [6].

This study focuses on sintering such NPLs by passing an electric current through them. The objective is to form conductive nanofilaments between the electrodes through current-driven sintering. The remaining un-sintered particle-particle junctions in the NPL then act as a supporting network that holds the conductive filaments in place, while contributing negligibly to the overall conductivity.

Description of the New Method

A Pd NPL track approximately 1 mm long, 60 µm wide, and 1 µm thick was printed on a test chip (Fig. 1), bridging the electrodes. The circuit shown in Fig. 2 was used to measure its electrical characteristics during electrical sintering.

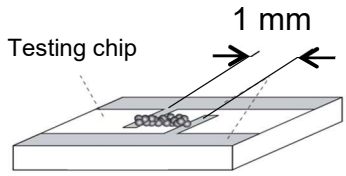

Fig. 1. Testing chip

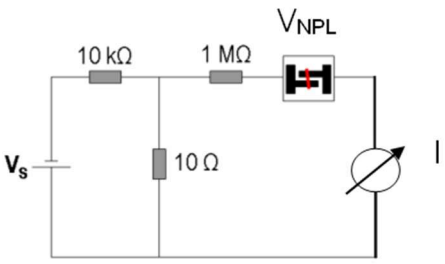

Fig. 2. Testing circuit

Results and Interpretation

The resistance of an un-sintered NPL of metallic nanoparticles is initially governed by contact resistances between particles. A gradual increase in V_{NPL} produces a sharp, three-order-of-magnitude rise in current at the sintering voltage, V_S =

1.2 mV (Fig. 3), indicating the formation of metal-metal connections along particle chains that bridge the electrodes, as illustrated in Fig. 4b) and c). By Ohm's law, an increasing current I at constant voltage shows that conductance rises proportionally with current during sintering.

This behavior is consistent with a model in which the sintering voltage creates a sufficiently large voltage drop across a specific barrier resistance between two nanoparticles to trigger sintering. Once one contact in an electrode-bridging chain sinters, the remaining contacts in that chain experience larger voltage drops, initiating a runaway process that sinters an entire chain, which is then a conducting filament. If the current I between the electrodes is not limited, the same process forms a second nanofilament and then additional ones until current limitation is reached. Assuming similar conductance for all filaments, I is proportional to the number of conducting filaments formed. Estimating the conductance of a chain-like nanofilament composed of 5 nm particles over a length of 1–2 mm therefore allows the approximate number of nanofilaments to be derived from the measured current. Fig. 4 illustrates the sintering states corresponding to the estimated corresponding electrode-to-electrode resistances. The resulting structure c) consists of conducting filaments suspended within a matrix of un-sintered NPL. Allen et al. [5] previously demonstrated the transition shown in Fig. 4a) directly to Fig. 4d), in which particles sinter and coalesce into a highly conducting bridge. Our results show that current limitation can be adjusted to generate a controlled number of nanofilaments embedded within an NPL. Although the model assumes similar resistances for all formed chains and neglects nanofilament branching, it captures the key features of the process.

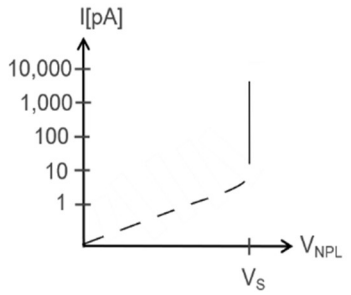

Fig. 3. Plot of the current vs. Voltage during NPL sintering through slow current increase above V_S = 1.2 mV. The dashed line is qualitative and was not measured, while the solid line corresponds to the measured data.

This approach can be applied to a wide range of metals and alloys. Its extension to metal oxide semiconductors remains to be tested. During sensor operation, Joule heating is expected to be adjustable within a wide temperature range, in which the filaments remain stable. Such tests remain to be carried out. Because thermal coupling to the supporting network is minimal, the power consumption is expected to be extremely low compared with any previously reported concept.

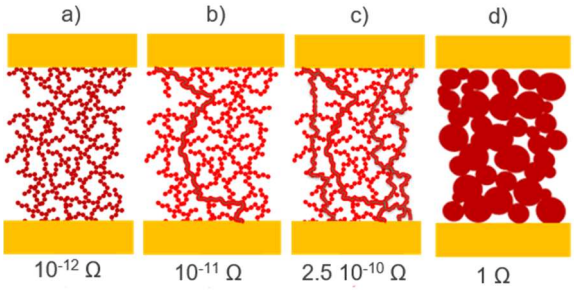

Fig. 4. Illustration of sintering model consistent with measurement: a) NPL before sintering; b)-c) Formation of 1-4 conducting filaments; d) Sintering and coalescence forms strongly conducting connection [5]

References

[1] T.M. Ngoca, N. Van Duya, N. Duc Hoaa, C. M. Hunga, H. Nguyenb, N. Van Hieuc, Effective design and fabrication of low-power-consumption self-heated SnO_2 nanowire sensors for reducing gases, Sensors and Actuators B: Chemical 295, 144-152, DOI: 10.1016/j.snb.2019.05.074

[2] M.-S. Jo, S.-H. Kim, S.-Y Park, K.-W. Choi, S.-H. Kim, J.-Y. Yoo, B.-J. Kim, J.-B. Yoon, Fast-Response and Low-Power Self-Heating Gas Sensor Using Metal/Metal Oxide/Metal (MMOM) Structured Nanowires, ACS Sens. 2024, 9, 1896−1905 DOI: 10.1021/acssensors.3c02613

[3] K.C. Petallidou, P. Kováčik, A. Schmidt-Ott, G. Biskos, Single-step Aerosol-based Synthesis of Nanostructured Thin Films for Hydrogen Sensing, RSC Nanoscale Adv., 2025, 7, 1505. DOI: 10.1039/d4na00884g

[4] M. Zanotti, E. Rolfi, S. Freddi, S. Pagliara, V. Mazzola, F. Ricciardella, L. Sacco, L. Sangaletti, Interfacing a nanostructured nickel oxide layer displaying fractal-like features with graphene: chemiresistive behaviour and GFET implementation, RSC Adv., 2026, 16, 22488. DOI: 10.1039/D5RA06573A

[5] M.L. Allen et al, Electrical sintering of nanoparticle structures *Nanotechnology* 19 175201, 2008. DOI: 10.1088/0957-4484/19/17/175201.

[6] W. Fu, et al. Scalable fabrication of gas sensors via spark-ablation printing of semiconductive metal oxide nanoparticles and heterostructures. Microsyst Nanoeng 12, 141 (2026). DOI: 10.1038/s41378-026-01208-1

DOI 10.5162/eurosensors2026/Mo–EHS–01

Multiplexed Power Management Circuit for Low-Power Thermoelectric Generators

Filippo Leoncini[1], Mohamad Ridwan[2], Ferran Reverter[2]
[1] Department of Information Engineering, Università Degli Studi di Brescia, Brescia, Italy
[2] Department of Electronic Engineering, Universitat Politècnica de Catalunya—BarcelonaTech, 08860 Castelldefels, Spain
ferran.reverter@upc.edu

Summary:
In the field of autonomous sensors powered by energy harvesters, this work proposes and experimentally characterizes a power management circuit (PMC) for low-power thermoelectric generators (TEG). The proposed circuit combines and interconnects, in a multiplexed approach, two off-the-shelf PMCs so as to achieve the benefits of both. Thanks to this interconnection, the resulting circuit is able to start operating from a low input voltage (40 mV) with a satisfactory efficiency (up to 78 %), features that are difficult to achieve exclusively using one of these PMC alternatives.

Keywords: Autonomous sensors, energy harvesting, maximum power point tracker, power management circuit, thermoelectric generator.

Introduction

A large-scale deployment of autonomous sensors (including sensor nodes related to Internet of Things) is no exempt from limitations, and probably the most critical issue is their power supply. The most viable and sustainable alternative seems to be the use of an energy harvester, which converts "free" environment energy to electrical energy. Energy harvesters can rely on different types of input energy [1]: optical, thermal, mechanical, and radio frequency. This work is focused on thermal energy harvesters based on a thermoelectric generator (TEG). The output power of a low-area TEG (say, with a few tens of cm^2) is usually in the range of units or tens of milliwatt [2], but this highly depends on the available thermal gradient.

The DC voltage obtained at the TEG output is generally quite low (i.e., tens or hundreds of millivolts), which is not valid to directly power the electronics of a sensor node. Consequently, an intermediate power management circuit (PMC) performing a DC/DC conversion is required. Among other tasks, this PMC is in charge of ensuring that the TEG operates around its maximum power point (MPP), which corresponds to an operating voltage equal to half of the open-circuit voltage. Therefore, an MPP tracking (MPPT) technique, such as the fractional open-circuit voltage (FOCV) [3], must be automatically applied to adapt the operating point of the TEG to the varying thermal operating conditions.

The semiconductor market offers two alternatives of PMC for TEGs: 1) PMCs able to operate from a very low input voltage but without the ability to apply any MPPT method; and 2) PMCs able to apply an MPPT method but operating from higher values of input voltage. Off-the-shelf PMCs for TEGs offering both abilities (i.e., low-input voltage operation and MPPT) are not available, although these have been suggested with application specific integrated circuits.

This work aims to propose and experimentally characterize a circuit for TEGs that combines the two off-the-shelf PMC alternatives indicated before so as to achieve the benefits of both.

Preliminary characterization of a TEG

For the ensuing characterization of the circuit, the data corresponding to a commercial TEG was used as a reference: GM250-241-10-12 (European Thermodynamics) with an active area of 40×40 mm^2. This TEG was attached to a heatsink (TDEX6015/TH with 60×60×47 mm^3) and then characterized under thermal gradients (ΔT) from 5 to 40 ºC, which are expected indoors [4], generated by a thermal plate (QInstruments ColdPlate 2016-0110). Table 1 summarizes the main experimental results, including the open-circuit voltage (V_{OC}), short-circuit current (I_{SC}), and power at the MPP (P_{MPP}) for different ΔT. The power was in the range of units of mW for $\Delta T \geq 20$ºC, which is appropriate for sensor nodes, but the DC output voltage was in the mV range, which is too low for a direct supply voltage connection.

Tab. 1: Experimental results for the TEG.

ΔT (ºC)	V_{OC} (mV)	I_{SC} (mA)	P_{MPP} (mW)
5	38.0	6.2	0.06
10	91.1	12.5	0.29
20	212.6	27.7	1.51
30	345.7	43.1	3.81
40	482.9	57.8	7.18

Multiplexed PMC for a TEG

A block diagram of the proposed circuit to handle the power coming from a TEG is represented in Fig. 1. The circuit has three main blocks: 1) PMC1 that operates from a very low input voltage, but without the ability to apply any MPPT method; 2) PMC2 that is able to apply an MPPT method but operating from higher values of input voltage; and 3) a switching stage that selects one of the two potential paths depending on the voltage level of the TEG output signal. In the prototype designed, PMC1 and PMC2 were implemented with LTC3108 and ADP5092 (both from Analog Devices), respectively. In addition, PMC2 was set to apply the FOCV with a fraction of 0.5. The switching stage was implemented by ADG839, which is a solid-state switch with an ultra-low on-resistance.

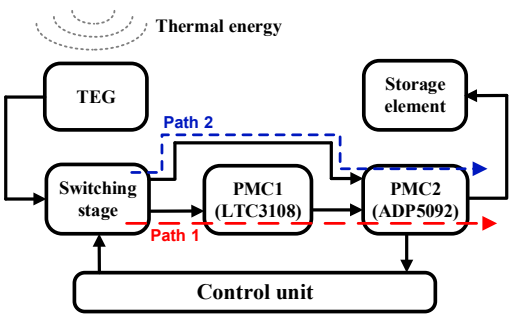

Fig. 1. Block diagram of the proposed circuit combining two PMCs in a multiplexed approach.

When the voltage provided by the TEG is low, path 1 (highlighted in red in Fig. 1) is selected so that the TEG is mainly handled by PMC1 and, then, connected to the storage element using an auxiliary input (BACKUP) of PMC2. On the other hand, when the TEG voltage is high enough, path 2 (shown in blue in Fig. 2) is chosen so that the TEG is directly connected to the main input of PMC2. Note that using always path 1 is not advisable since PMC1 efficiency is low, whereas path 2 cannot be always selected because the minimum operating voltage of PMC2 can be higher than that provided by the TEG. For this reason, this multiplexed solution combing both alternatives is proposed herein.

Experimental Results

The power efficiency of the circuit in Fig. 1 was experimentally evaluated. In order to have a characterization independent of potential drifts affecting the TEG, this was emulated by a source and measurement unit (Keysight B2961A) with a resistor (7 Ω) connected in series to mimic its internal resistance. On the other hand, the output was connected to another source and measurement unit (Agilent B2901A) behaving as a voltage source (3 V) to emulate an energy storage element, such as a supercapacitor or a rechargeable battery.

The efficiency results are represented in Fig. 2. While 40 mV ≤ V_{OC} < 200 mV, path 1 in Fig. 1 was selected and the efficiency was between 25 and 30 % in most of the range. However, when 200 mV ≤ V_{OC} < 500 mV, path 2 was chosen and the efficiency increased up to 78 %. Accordingly, the circuit in Fig. 1 is able to start operating from a low input voltage (i.e., 40 mV, which almost corresponds to ΔT = 5 ºC) with a satisfactory efficiency (78%) at high values of input voltage, features that will not be achievable in a non-multiplexed topology.

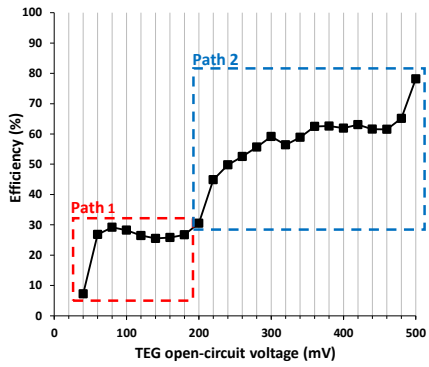

Fig. 2. Experimental results of circuit efficiency.

References

[1] E. Ferré *et al.*, Low-Area PV Cells Under Indoor Artificial Lighting: A Comparative Study, *IEEE Trans. Instrum. Meas.* 74, 1–9 (2025).

[2] M. Ridwan *et al.*, Principle and Applications of Thermoelectric Generators: A Review, *Sensors* 25 (8) (2025).

[3] M. Azlor *et al.*, Study of the Applicability and Limitations of the FOCV Technique for Indoor Low-Area PV Cells, *IEEE Trans. Instrum. Meas.* 74, 1–9 (2025).

[4] M. Ridwan *et al.*, Study of TEG-heatsink pairs for indoor thermal energy harvesting applications, *IEEE Sensors Applications Symposium* 2025.

Acknowledgements

This work was supported in part by MICIU/AEI/10.13039/501100011033 under Grant PID2022-139505OB-I00.

DOI 10.5162/eurosensors2026/Mo–EHS–02

Powering a Sensor Node with an Organic PV Module Under Low-Light Indoor Conditions

Ricardo Alan Retana-González[1], Ferran Reverter[2], Manel Gasulla[3]
Dept. Electronic Eng., Universitat Politècnica de Catalunya-BarcelonaTech, Castelldefels, Spain
ricardo.alan.retana@upc.edu[1], ferran.reverter@upc.edu[2], manel.gasulla@upc.edu[3]

Summary: This work presents an optical harvesting system to power a wireless sensor node operating under low-light indoor conditions. By integrating an organic photovoltaic cell with an optimized power management and storage sizing, self-sustained operation is achieved at low-light indoor conditions. Experimental and in-situ testing demonstrate continuous functionality, offering a robust, battery-less solution for sustainable indoor IoT deployments under indoor illuminance levels as low as 182 lx.

Keywords: autonomous sensors, energy harvesting, low illuminance, photovoltaic cell.

Introduction

The massive deployment of wireless sensor nodes (WSN) is currently transforming fields such as healthcare, Industry 4.0, and residential monitoring. With approximately half of these devices expected to operate in indoor environments, sustainable powering remains a critical challenge [1]. Transitioning away from conventional batteries is essential to reduce maintenance costs and environmental impact. In that sense, Energy Harvesting (EH) systems have emerged as a robust alternative by scavenging ambient energy. Among them, optical EH stands out, in part due to the emergence of novel photovoltaic (PV) technologies such as perovskite and organic (OPV). However, developing PV-based EH systems for indoor applications is challenging, as indoor light sources provide significantly lower irradiance than outdoor sunlight. Furthermore, these systems must balance small form factors with high sensitivity to artificial spectra. Despite previous research has extensively explored the use of PV cells to power WSN [2], this work presents the development of a complete EH system optimized to power a WSN under low-light indoor conditions by using an OPV cell. Its functionality is validated through lab and in-situ testing, proving the system ability to maintain operation of the WSN under real-world, low-illuminance conditions.

Optical Energy Harvester and Sensor Node

Fig. 1 shows a block diagram of the proposed EH system to power an indoor WSN. This comprises three main blocks: an OPV cell, a power management circuit (PMC), and an energy storage unit (ESU). The OPV cell (Dracula Tech.), with an area of 22 cm^2, was selected for its high sensitivity under indoor LED lighting [3]. As for the PMC, the AEM30940 (e-peas) was chosen. This features a Maximum Power Point Tracking (MPPT) stage relying on the Fractional Open Circuit Voltage (FOCV) method [4], an energy storage control circuit, and a regulated voltage output. On the other hand, the ESU was implemented by an array of low-cost electrolytic capacitors.

The SHT43 (Sensirion), with a nominal supply voltage of 3.3 V, was used as an WSN to demonstrate the feasibility of the EH system. This WSN is capable of measuring temperature and humidity while transmitting data via Bluetooth Low Energy (BLE) and displaying results on an integrated LCD.

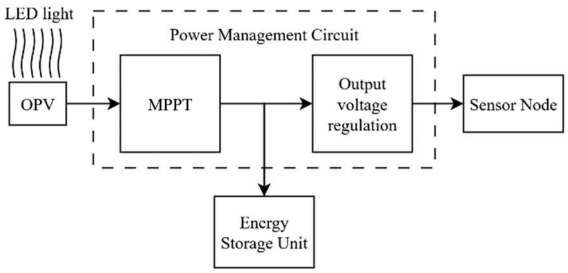

Fig. 1. Block diagram of the EH system powering a WSN.

Experimental Results

Fig. 2 shows the profile of the current consumption of the WSN at 3.3 V. Four distinct operational phases were identified. Phase 0 corresponds to a start-up pulse, whereas phase 3 to steady-state conditions in terms of measurement and communication. The intermediate phases (1 and 2) are similar to phase 3, but the frequency of measurement and communication is higher than that in phase 3. The energy metrics for each stage are summarized in Table 1.

Tab. 1: Charge (Q), energy (E), and mean power (P) consumption of the WSN per phase.

Phase	Interval (s)	*Q* (mC)	*E* (mJ)	*P* (µW)
0	0-1	2.979	9.791	9791
1	1-32	2.840	9.356	309.4
2	32-303	4.749	15.65	58.38
3	303-500	1.998	6.582	33.11

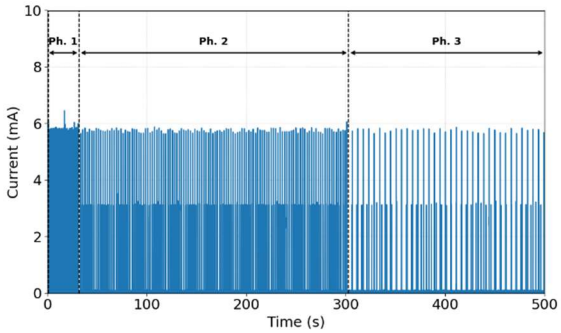

Fig. 2. Profile of the WSN current consumption.

Fig. 3 shows the power-voltage (*P-V*) characteristics of the OPV cell under different illuminance levels (from 100 to 1500 lx) of cold LED (C-LED). The maximum power (highlighted with circular markers) is 40.4 µW at 100 lx and 585 µW at 1.5 klx. Therefore, assuming an ideal scenario without losses, the selected PV cell should be able to power the WSN in phase 3 at an illuminance as low as 100 lux. Regarding the PMC, this was set to provide a FOCV ratio of 0.8.

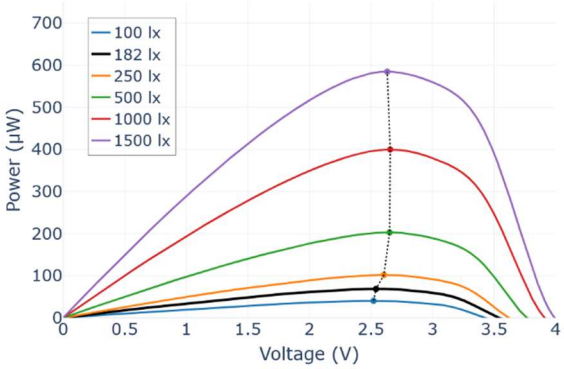

Fig. 3. P-V characteristics for the OPV cell under different C-LED illuminance levels.

The ESU was selected to cope with the more power demanding phases (i.e., phases 0, 1, and 2). In other words, once the WSN is activated (and phase 0 starts), the ESU capacitance should be able to maintain the voltage across it within a given interval. This capacitance was computed as $Q/[V_{CHRDY} - V_{OVDIS}]$, where V_{CHRDY} is the voltage (across ESU) at which the PMC output regulator starts powering the WSN, and V_{OVDIS} is a undervoltage protection limit for the ESU. On the other hand, *Q* is the charge required during phases 0, 1 and 2 minus the charge already provided by the PV cell assuming that it delivers a power equivalent to that required in phase 3 in the first 303 s (i.e., 3.04 mC). Since V_{OVDIS} = 3.6 V and V_{CHRDY} = 4.04 V, the minimum capacitance is 17.1 mF, although a value of 21 mF was selected.

The complete system in Fig. 1 was validated. Fig. 4 shows the voltage waveforms under 250 lx of C-LED. The WSN starts (supply voltage in blue rises to 3.28 V) when the ESU reaches 4.045 V (in green). Afterwards, during the first 32 s (phases 0 and 1), there is a transient voltage drop at the ESU, but not sufficient to be below V_{OVDIS}. Next, the OPV successfully sustains both the node operation and the recharging of the ESU. This behavior was verified down to 182 lx, which is higher than that determined before theoretically. This is due to the power losses, especially the leakage of the selected capacitor. A capacitor with less leakage could make the system autonomous at lower levels of illuminance.

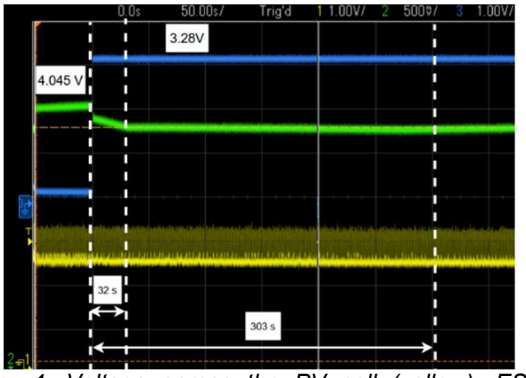

Fig. 4. Voltage across the PV cell (yellow), ESU (green), and WSN supply (blue) at 250 lx. The ground reference of channel 2 is at –1 V.

References

[1] I. Mathews *et al.*, Technology and Market Perspective for Indoor Photovoltaic Cells, *Joule* 3, 6, 1415–1426, (2019).

[2] B. Y. León Ávila *et al.*, Energy harvesting techniques for wireless sensor networks: A systematic literature review, *Energy Strategy Rev.* 57, 101617, (2025).

[3] E. Ferré, *et al.*, Low-Area PV Cells Under Indoor Artificial Lighting: A Comparative Study, *IEEE Trans. Instrum. Meas.* 74, 1–9, (2025).

[4] M. Azlor *et al.*, Study of the Applicability and Limitations of the FOCV Technique for Indoor Low-Area PV Cells, *IEEE Trans. Instrum. Meas*. 74, 1–9 (2025).

Acknowledgements

This work was supported by MICIU/AEI/10.13039/501100011033 under Grant PID2022-139505OB-I00, by the European Union under Grant 101071179, by AGAUR under Grant 2025 FI-SDUR 00274, and by SECIHTI with CVU 1148043 (Mexico).

DOI 10.5162/eurosensors2026/Tu–FSW–01

Fully Printed MWCNT/PEDOT: PSS/Ecoflex Tactile –Thermal Sensor with Dual-Mode Piezoresistive and Thermoresistive Transduction

Nadeem Tariq Beigh[1], Mohammed Al Hadi[1], Nouha Alcheikh[1]
[1] Department of Mechanical and Nuclear Engineering, Khalifa University, Abu Dhabi, United Arab Emirates
Nadeem.beigh@ku.ac.ae; Nouha.alcheikh@ku.ac.ae

Summary:

1. Fully printed, flexible tactile–thermal sensor using a single MWCNT/PEDOT: PSS/Ecoflex (MPE) active film on printed two-terminal, interdigitated electrodes (IDEs) for scalable e-skin integration.
2. Pressure sensing up to ~95 kPa with two linear regimes: ~0.0035 kPa^{-1} (0–20 kPa) and ~0.0085 kPa^{-1} (20–95 kPa).
3. Temperature sensing over ~20–80 °C with near-linear NTC behavior (~0.0045 $°C^{-1}$).
4. Fast pressure dynamics (reported ~0.4 s response/recovery) and distinct thermal kinetics (~2.5 s response, ~18 s recovery) support robust multimodal tactile sensing.

Keywords: Printed e-skin; multimodal sensor; Ecoflex composite; MWCNT/PEDOT:PSS; tactile–thermal sensing

Background, Motivation, and Objective

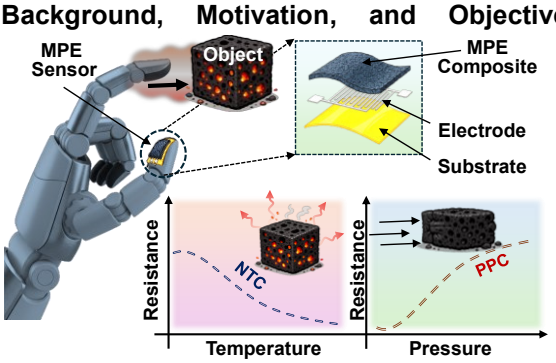

Fig. 1 Printed MPE tactile–thermal sensor concept and principle: NTC response to temperature and PPC response to pressure on a robotic fingertip.

Soft robotic grippers and wearable e-skins increasingly require co-located pressure and temperature perception to safely interpret contact state, object thermal condition, and interaction dynamics. Recent progress in flexible pressure/tactile sensors has been accelerated through micro-structured elastomers and conductive networks that provide large piezoresistive signals with simple readout [1]. However, when pressure and temperature must be sensed from the same contact region, conventional resistive composites face a fundamental limitation: the resistance is simultaneously modulated by mechanically driven junction/tunneling changes and by temperature-dependent carrier transport/percolation, producing coupled outputs that are difficult to interpret under real touch events [2]. Prior multimodal solutions often pursue device-level separation by integrating dedicated pixels/functional units (e.g., active-matrix multimodal arrays), hybrid optoelectronic/structured fibers, or ionic/impedance-derived multimodal receptors. While powerful, these strategies typically require multilayer stacks, specialized readout electronics, or complex integration workflows that limit rapid manufacturing and scaling [3,4].

Here, the objective is to demonstrate a new route to multimodal tactile–thermal sensing that preserves fabrication simplicity: a fully printed, two-terminal sensor in which a single composite film provides both pressure and temperature responses.

Experimental Details

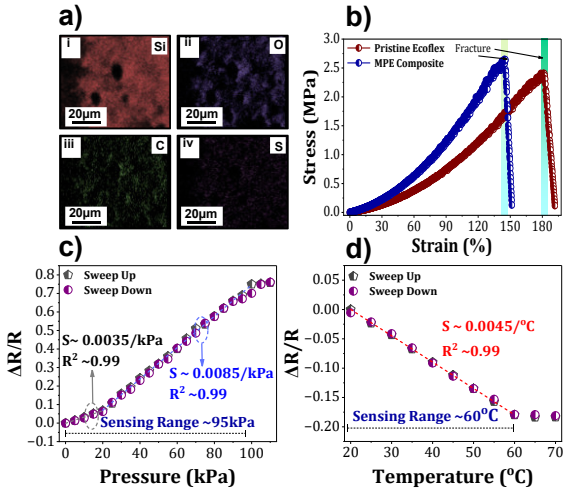

Fig. 2. (a) EDS maps (Si, O, C, S) of the MPE composite. (b) Tensile stress–strain of pristine Ecoflex vs MPE composite. (c) Pressure calibration (0–95 kPa; two linear regimes). (d) Temperature calibration (~60 °C range; NTC response).

The sensing composite uses Ecoflex 00-30 loaded with 5 wt% (multi-walled carbon nanotubes) MWCNTs and 3 wt% (Dimethyl sulfoxide) DMSO-activated PEDOT: PSS nanoparticles. MWCNTs are first dispersed in IPA by bath ultrasonication for 30 minutes, followed by the

addition and further sonication of dried PEDOT: PSS powder. The suspension is then mixed into Ecoflex prepolymer (A: B = 1:1), degassed, and the solvent is allowed to evaporate to produce a homogeneous composite precursor. IDTs are printed on polyimide (Kapton) using a Voltera V-One printer (finger width approximately 200 µm, gap approximately 500 µm, 12 fingers), then cured and lightly surface conditioned for adhesion. The composite is pattern-coated over the IDEs to form a continuous film about 1 mm thick and cured at 60 °C for 8 hours. Electrical measurements are conducted in a two-terminal setup using a Keithley 2450 (3 V bias, 100 ms sampling). Pressure is applied with an instrumented PTI-03 setup, while temperature is controlled via a heater stage managed by a W1209 controller and powered by a GW Instek GP8-4303 DC supply.

Description of the New Method

We present a fully printed, single-film tactile–thermal sensor where one composite layer simultaneously provides (i) a positive pressure coefficient (PPC) of resistance response, which is governed by reversible junction/tunneling modulation within a MWCNT/PEDOT: PSS percolation network, and (ii) a negative temperature coefficient (NTC) of resistance response, dominated by temperature-dependent transport in the same network; all using a minimal, two-terminal resistive architecture (see Fig. 1).

Results

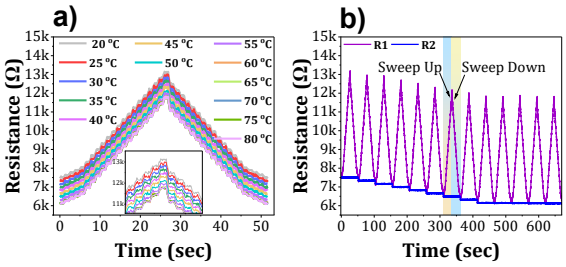

Fig. 3. Mixed pressure–temperature response: (a) pressure sweeps at different temperatures; (b) real-time pressure cycling during a temperature changes.

The MPE composite was thoroughly analyzed to verify its composition and multifunctional performance (Fig. 2). EDS maps reveal strong Si/O signals from the Ecoflex matrix and a spatially distributed S signal from PEDOT: PSS, indicating a well-dispersed conductive phase (Fig. 2a). The composite (160% strain at 2.6MPa) shows enhanced elastomeric mechanics compared to pristine Ecoflex (180% strain at 2.25MPa) , supporting repeatable deformation during sensing. Pressure calibration covers a wide range up to approximately 95 kPa with two linear regimes (S ≈ 0.0035 kPa^{-1} for 0–20 kPa; S ≈ 0.0085 kPa^{-1} for 20–95 kPa), consistent with progressive densification under load. Temperature calibration displays a near-linear NTC response (~0.0045 $°C^{-1}$) over about 60 °C, confirming effective thermoresistive behavior. Collectively, these results confirm the material's structure and baseline pressure/temperature sensing capabilities needed for printed tactile–thermal skins.

Fig. 3 demonstrates the sensor's intrinsic thermo-mechanical coupling under conditions where pressure and temperature co-vary. For identical pressure sweeps at different temperatures (Fig. 3a), the pressure-induced modulation is preserved while the baseline shifts with temperature, confirming mixed sensitivity in the composite resistance. In real-time cycling (Fig. 3b), pressure pulses remain clearly resolved despite baseline drift during a temperature transition (highlighted), showing the device can capture dynamic tactile events under changing thermal conditions—critical for robotic tactile skins handling objects at different temperatures.

Conclusion

We demonstrated a fully printed Ecoflex–MWCNT–PEDOT: PSS tactile–thermal sensor with a simple two-terminal resistive readout. The device senses pressure up to ~95 kPa with two linear regimes and shows a near-linear NTC temperature response over ~60 °C, supported by EDS and mechanical characterization. Mixed tests confirm pressure signals remain resolvable under temperature changes, highlighting suitability for robotic skin integration and scalable printed fabrication.

Acknowledgment

The authors acknowledge the support from Khalifa University of Science and Technology (Award No. KU-INT-FSU-2023-028).

References

[1] J. A. Rogers, T. Someya, Y. Huang, Materials and Mechanics for Stretchable Electronics, Science 327,1603–1607(2010); doi: 10.1126/science.1182383

[2] U. Jeong, Z. Bao, et al., Artificial Multimodal Receptors Based on Ion Relaxation Dynamics, Science 370, 961–965 (2020); doi: 10.1126/science.aba5132

[3] F. Zhang, Y. Zang, D. Zhu, Flexible and Self-Powered Temperature–Pressure Dual-Parameter Sensors Using Microstructure-Frame-Supported Organic Thermoelectric Materials, Nat. Commun. 6, 8356 (2015); doi: 10.1038/ncomms9356

[4] V. Losing, M. Hasenjäger, A multi-modal gait database of natural everyday walking in an urban environment. Scientific data, 9,473 (2022); doi:10.1038/s41597-022-01580-3

DOI 10.5162/eurosensors2026/Tu–FSW–02

Influence of Piezoresistive Material and Thickness on the Electromechanical Response of Flexible Pressure Sensors

Rachel Neveu[1], Gurvan Jodin[1], Sara Bretin[1], Florence Razan[1],
[1] Univ Rennes, ENS Rennes, CNRS, IETR - UMR 6164, F-35000 Rennes, France
Corresponding author: [rachel.neveu; gurvan.jodin; sara.bretin; florence.razan]@ens-rennes.fr

Summary:
Flexible piezoresistive sensors based on carbon-filled polyethylene (PE) and thermoplastic polyurethane (TPU) were compared. TPU sensors were fabricated by fused filament fabrication, enabling thickness control from 0.2 to 5 mm. Electrical resistance was measured under cyclic loading up to 250 kPa. TPU shows improved repeatability and a sixfold reduction in drift (35 Ω vs 330 Ω). Increasing thickness reduces sensitivity but limits saturation, enabling tuning of the sensor response. TPU provides a more stable and configurable alternative to PE.

Keywords: piezoresistive sensors, flexible sensors, thermoplastic polyurethane, polyethylene, pressure sensing

Background, Motivation and Objective

Flexible piezoresistive sensors are widely used for pressure sensing, but performance depends on materials and fabrication, affecting sensitivity, repeatability, and stability [1,2]. For motion analysis and health monitoring, reliable sensors are required. This study compares carbon-filled PE and TPU sensors under cyclic compression, focusing on TPU thickness (0.2-5 mm).

Sensor Architecture and Materials

All sensors share a multilayer architecture composed of polyimide encapsulation layers, copper electrodes, and a piezoresistive layer (Fig. 1). The electrical response is measured under a normal compressive force applied over a 1 cm² area.

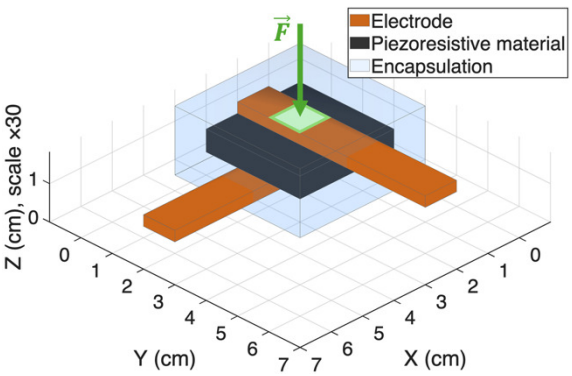

Fig. 1. Multilayer architecture of the piezoresistive sensor under a normal compressive force $\vec{F}$ applied over a 1 cm² area.

Two materials were investigated: carbon-filled polyethylene (PE, Velostat®, 3M, USA, thickness of 0.1 mm) and carbon-filled thermoplastic polyurethane (TPU, Recreus, Spain). PE-based sensors (PC-PE) were fabricated by assembling polyimide (P) layers, adhesive copper (C) electrodes, and a PE film. For TPU-based sensors (PC-TPU), the piezoresistive layer was first fabricated by fused filament fabrication (FFF) with full infill (100%), then assembled with polyimide encapsulation and copper electrodes. The TPU thickness was varied from 0.2 to 5 mm to study its influence on the electrical response, the lower limit being set by the printing resolution of the FFF process and the upper limit by the loss of flexibility at higher thickness. PC-PE sensors were developed in previous work [3].

Electrical Characterization Methods

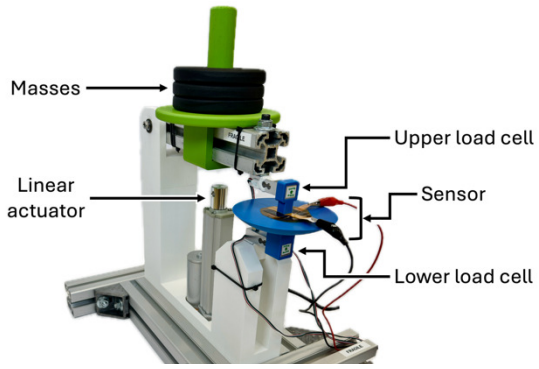

Fig. 2. Experimental setup for electromechanical characterization with force and resistance measurements under calibrated loading.

Electrical characterization was performed using a custom test bench applying controlled normal loads to the sensors (Fig. 2). The load was generated by calibrated masses. Three types of tests were conducted: (i) short-term cyclic tests

(3 cycles, 1 min without load / 1 min under load) to evaluate repeatability; (ii) reproducibility tests on three samples per configuration; and (iii) long-term cyclic tests (1 min period) to assess conditioning effects. Resistance was recorded continuously at a 300 ms sampling interval.

Results and Discussion

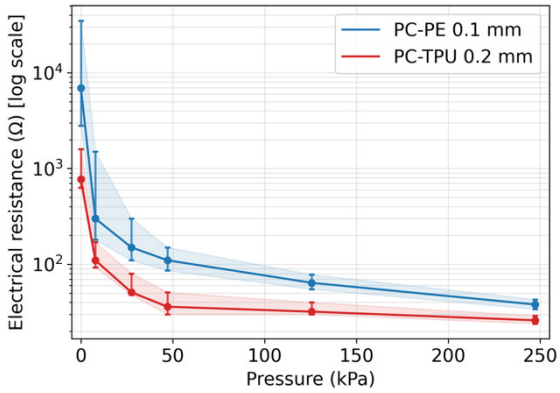

Fig. 3. Electrical resistance as a function of applied pressure for PC-PE and PC-TPU 0.2 mm sensors. Shaded areas represent the min-max range, and markers indicate median values.

Figure 3 compares the electromechanical response of PC-PE (0.1 mm) and PC-TPU (0.2 mm) sensors. The PC-PE sensor exhibits a higher initial resistance and a larger dispersion, as highlighted by the wide min–max range (over repeated cycles and across different samples), particularly at low pressures. In contrast, the PC-TPU sensor shows a more stable and reproducible response, with reduced variability across measurements. As the applied pressure increases, the difference between both materials decreases. At higher pressures (>100 kPa), the electrical resistance tends to converge, indicating a saturation of the piezoresistive effect and reduced sensitivity for both materials.

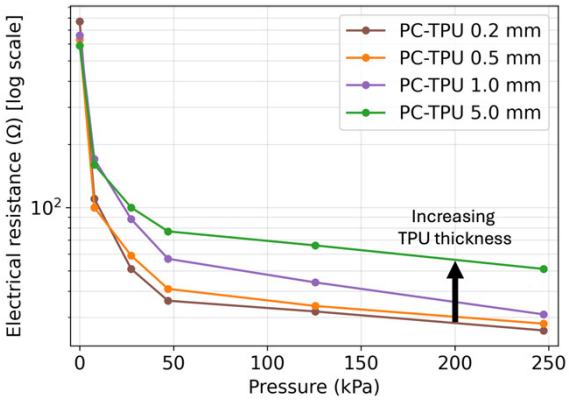

Fig. 4. Electrical resistance as a function of applied pressure for PC-TPU sensors with varying TPU thickness (0.2 to 5 mm). Median values are shown for each configuration.

Figure 4 highlights the influence of TPU thickness on the sensor response. Increasing the thickness from 0.2 mm to 5 mm leads to a systematic increase in resistance between 25 kPa and 250 kPa. At these pressures, the curves exhibit nearly constant spacing on a logarithmic scale, indicating a similar relative sensitivity across all thicknesses. However, in absolute terms, thicker layers show a reduced slope of the resistance-pressure response, corresponding to a lower sensitivity. Thinner layers exhibit a sharper response and earlier saturation, while thicker layers provide a more gradual response and an extended usable pressure range up to 250 kPa. This demonstrates that TPU thickness governs a trade-off between sensitivity and dynamic range.

Tab. 1: Electrical resistance drift (ΔR) measured after stabilization. The stabilization cycle number corresponds to the cycle from which ΔR measured between 0 and 27.5 kPa no longer shows significant evolution.

Sensor	ΔR (Ω)	ΔR (%)	Cycles
PC-PE [3]	330	110%	500+
PC-TPU	35	117%	330

Table 1 shows the electrical resistance drift (ΔR) after stabilization. While both sensors exhibit comparable relative variations (~110-117%), the absolute drift is substantially reduced for PC-TPU, indicating improved stability and more reliable electrical behavior under repeated loading.

Conclusion

TPU improves repeatability, reproducibility and reduces drift compared to PE. Thickness tuning enables a trade-off between sensitivity and dynamic range: increasing thickness raises resistance and reduces absolute sensitivity while extending the usable pressure range. TPU-based sensors thus provide a stable and configurable approach for flexible pressure sensing. A thickness-dependent model may apply at moderate pressures, with deviations at low pressures.

References

[1] F. Xu et al., Recent developments for flexible pressure sensors, *Micromachines* 9, 580 (2018); doi: 10.3390/mi9110580

[2] J. Hu et al., Recent progress in flexible micro-pressure sensors for wearable health monitoring, *Nanoscale Advances* 5, 3131-3145 (2023); doi: 10.1039/D2NA00866A

[3] A.-R. A. Laaraibi et al., Flexible dynamic pressure sensor for insole based on inverse viscoelastic model, *IEEE Sensors Journal* 23, 7634-7643, 2023, doi: 10.1109/JSEN.2023.3245822

Acknowledgment

This work was funded by ANR under the France 2030 programme (ESOS project, ANR-23-CMAS-0007).

DOI 10.5162/eurosensors2026/Tu–FSW–03

Stretchable Carbon Flower Sensors for Sensitive Estradiol Detection

Ines Weber, Manoj Jayarame Gowda, Zhenan Bao
Chalmers University of Technology, Gothenburg, Sweden
ines.weber@chalmers.se, manoj.gowda@chalmers.se

Summary:

Monitoring estradiol is crucial for female reproductive health, fertility, and hormone therapy, however existing sensor technologies often suffer from limited sensitivity and poor selectivity. Here, we present carbon flower sensors fabricated via a scalable spray-coating process on soft, stretchable substrates. The carbon flowers are obtained from polymerization of acrylonitrile followed by carbonization. They exhibit a hierarchical morphology, high surface area and excellent conductivity, enabling sub-nanomolar estradiol detection that exceeds state-of-the-art carbon-based sensors. The sensor operates under physiological conditions and demonstrates good repeatability. These results highlight the potential of carbon flower materials for sensitive estradiol detection and can be extended to other molecules such as ascorbic acid, melatonin, serotonin, and uric acid.

Keywords: estradiol sensing, stretchable sensors, electrochemical sensors, hierarchical carbon, spray coating

Background, Motivation and Objective

Estradiol plays an important role in female reproductive health and endocrine regulation. Real-time monitoring of estradiol levels is crucial for hormone replacement therapy, and disease management of endometriosis [1]. Conventional detection methods such as liquid chromatography-mass spectrometry provide high accuracy but require complex instrumentation and are not suitable for continuous monitoring. Electrochemical sensors offer portability, rapid detection, and compatibility with wearable devices. However, many sensing materials suffer from limited sensitivity, fouling, and selectivity in complex biological environments [2]. This work focuses on developing hierarchical carbon-based material for enhanced estradiol detection.

Description of the New Method or System

Hierarchical carbon flowers are a relatively new material studied in catalysis and supercapacitors [3] but remain largely unexplored for electrochemical sensing. They are synthesized via free radical polymerization of acrylonitrile precursors, followed by oxidative stabilization and carbonization processes [4]. The resulting microstructures exhibit petal-like morphology (see Fig. 1a) with high surface area and conductive graphitic domains [5].

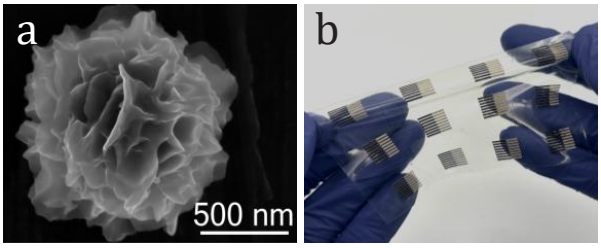

Fig. 1 (a) SEM image of carbon flower. (b) Photograph of stretchable sensor array.

The carbon flower material is dispersed into a printable ink and deposited onto flexible polystyrene-block-poly(ethylene-ran-butylene) block-polystyrene (SEBS) substrates using spray coating through metal masks [6]. This fabrication approach enables scalable patterning of stretchable sensor arrays (Fig.1b), offering advantages such as cost effectiveness and simple fabrication steps, without requiring expensive cleanroom facilities. The electrochemical performance for estradiol

detection is evaluated using square wave voltammetry (SWV), yielding concentration dependent current response.

Results

The electrochemical performance for estradiol detection is evaluated using SWV, which is shown in Fig. 2a. A pronounced oxidation peak appears at approximately 0.51 V and the current response increases for estradiol concentrations between 1 and 100 nM, exhibiting a linear dependence of peak current on estradiol concentration [5].

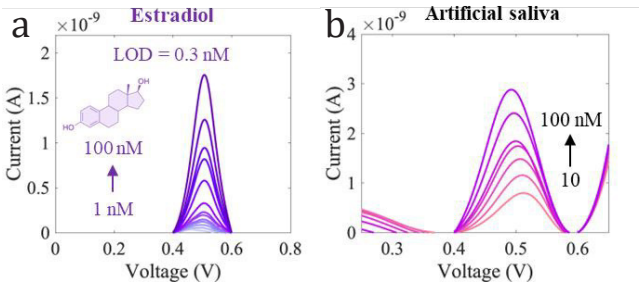

Fig. 2 (a) Detection of 1-100 nM estradiol via SWV. (b) Detection of 10-100 nM estradiol in artificial saliva.

The hierarchical carbon flower sensors achieve a limit of detection of 300 pM, outperforming state-of-the-art carbon-based sensors. We associate the improved sensitivity to the carbon flower morphology and the high surface area [6]. The sensors further demonstrate good stability during repetitive measurements, maintaining substantial responsiveness over 100 cycles. Robust performance is also observed under physiologically relevant conditions: within the saliva-relevant pH range, the peak position remains largely unchanged, while varying KCl concentrations up to 50 mM results in stable peak currents of 6.4 ± 0.5 nA [6]. Additionally, estradiol concentrations between 10 and 100 nM are successfully detected in artificial saliva (see Fig. 2b), confirming reliable sensing performance in complex media.

Conclusions

Carbon flowers are a promising material for electrochemical sensing. Using a simple spray coating process, they can be patterned onto flexible substrates in a scalable and low-cost manner. Their unique hierarchical morphology and defect-rich structure lead to high surface area, enabling sensitive estradiol detection with a sub-nanomolar limit of detection. The sensors show good stability during repeated measurements and maintain reliable performance under physiologically relevant pH and salt conditions, as well as in artificial saliva. These results highlight carbon flowers as a practical and effective platform for stretchable and wearable sensors in sensitive electrochemical detection of estradiol, with potential extension to other molecules [6].

References

[1] Å. Johansson, et al., Investigating the effect of estradiol levels on the risk of breast, endometrial, and ovarian cancer, *Journal of the Endocrine Society* 6, 8 (2022); doi: 10.1210/jendso/bvac100

[2] I.C. Weber, et al., Tuning selectivity of electrochemical sensors with polymer coatings, *Advanced Materials,* e74000 (2026); doi: 10.1002/adma.74000

[3] H. Gong, et al., An emerging class of carbon materials: Synthesis and applications of carbon flowers, *Matter* 6, 2206-2234 (2023); doi: 10.1016/j.matt.2023.04.027

[4] S. Chen, et al., Highly tunable and facile synthesis of uniform carbon flower particles, *Journal of the American Chemical Society* 140, 10297-10304 (2018); doi: 10.1021/jacs.8b05825

[5] I.C. Weber, et al., Sensitive Hormone and Neurotransmitter Detection with Carbon Flower Electrodes, *Advanced Functional Materials,* e28595 (2026); doi: 10.1002/adfm.202528595

[6] AL. Duesselberg, et al., Machine Learning-Driven Multiplexed Biomarker Detection with Polymer-Enhanced Electrochemical Sensors, *ACS Electrochemistry,* 2.6 (2026); doi: 10.1021/acselectrochem.6c00079

DOI 10.5162/eurosensors2026/Tu–FSW–04

Aerosol-jet printed carbon for stretchable sensors

HongZe Zhu,[1,2] Noureddine Adjeroud,[1] Yves Decoster,[3] and Sebastjan Glinsek[1]
[1]Smart Materials Unit, Luxembourg Institute of Science and Technology, 41 rue du Brill, L-4411 Belvaux, Luxembourg
[2]Department of Physics and Materials Science, University of Luxembourg, 41 rue du Brill, L-4422 Belvaux, Luxembourg
[3]Goodyear Innovation Center Luxembourg, Avenue Gordon Smith, L-7750 Colmar-Berg, Luxembourg
sebastjan.glinsek@list.lu

Summary:
This ongoing research investigates aerosol-jet printed carbon dogbones, which can be used in the future as stretchable deformation sensors. A pneumatic atomizer was used to print the ink, and the process conditions were optimized for stable deposition on rubber. Resistance of the printed dogbones remains stable with time, with the change below 0.01 % over 60 h. The dogbones can be stretched to at least 20 %, with gauge factors between 3.5 and 5.2. This validates a robust additive manufacturing route for durable strain sensors that can be integrated into tire systems.

Keywords: Aerosol jet printing, strain sensors, carbon ink, smart tires, additive manufacturing

Background, Motivation and Objective

Following deformation in tires has large benefit for their performance optimization. Conventional accelerometers function well between 40–140 km h^{-1},[1] but they exhibit low signal-to-noise ratios outside this range. Integrated strain sensors are required to monitor tire conditions mechanical strains up to 15% [3]. Additive manufacturing via aerosol jet printing allows for seamless sensor integration directly. While silver-based inks are common, they react with sulfur in the rubber, leading to rapid degradation of the sensor material [4]. This research focuses on utilizing carbon-based inks (EXP 2619-44, CMI) to ensure chemical stability and mechanical robustness. Our objective is to optimize the pneumatic atomization process to fabricate stretchable sensors with high sensitivity.

Experimental and Process Optimization

The strain sensors were fabricated using an aerosol jet printing process on rubber substrates. We used stretchable carbon-based ink (EXP 2619-44, CMI), which was diluted to a 40% concentration with Carbitol Acetate to ensure stable printing. The printing was performed with a pneumatic atomizer using a 300 µm nozzle. For characterization of the samples, a profilometer was used to measure the profile. Resistance of samples were also measured, with a fixing platform for static tests and a stretching for strain/resistance tests. A Keithley 2470 SMU was used for resistance measurement in these tests.

To improve quality of the printing, we optimized the printing parameters by adjusting gas flows. This optimization prevented ink drops from forming at the nozzle tip and resulted in clearer print borders (see Fig. 1). After printing, the samples were annealed at 180 °C for 10 min.

This optimized printing route represents practical advancement, as the carbon-based material remains chemically stable and avoids the sulfur-induced degradation which is common for silver-based materials on rubber.

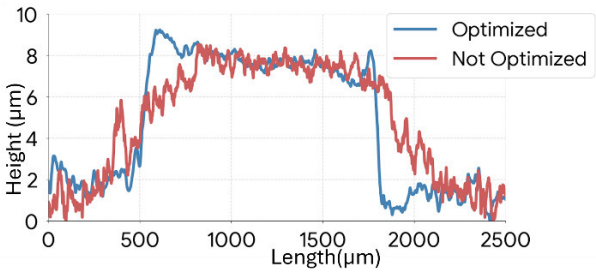

Fig. 1. Profilometry of the prints printed before and after optimization.

Results

Example of a dogbone printed with optimized conditions is shown in Fig.2. Resistivity was 1.86 Ω·cm, which is close to the material specifications from data sheet of the ink.

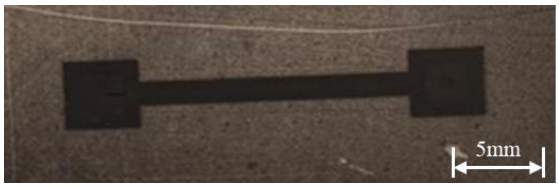

Fig. 2. Optical appearance of a printed dogbone.

The electrical performance of the printed sensors was evaluated through static and dynamic measurements. Static tests confirmed that the resistance of the carbon prints remained stable with time, with the change below 0.01% over 60 h.

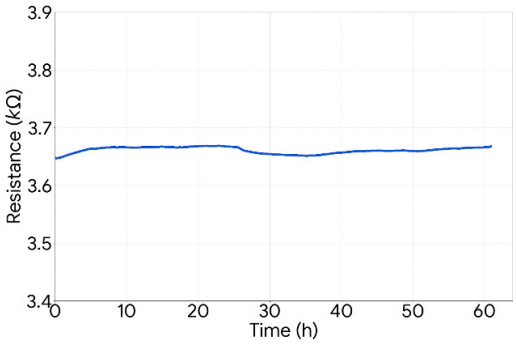

Fig. 3. Resistance of a printed dogbone as a function of time.

Mechanical measurements were also performed. Initial tests at low strain levels revealed a drop in resistance with increasing strain. As reported in literature for similar composite materials [5], this behavior was stabilized by applying a pre-stretch cycle to the samples. After this pre-stretch, the dogbone response became repeatable and stable. The samples were tested up to 20 % strain (see Fig. 4).

The sensitivity of the strain sensors was quantified by calculating Gauge Factor (GF). The measured GF values ranged between 3.5 and 5.2. This is higher than typical GF of commercial gauges, which is usually 2.1. These results demonstrate that this aerosol jet printed carbon sensors provide both the good sensitivity and the wide sensing range necessary for monitoring deformations in tires.

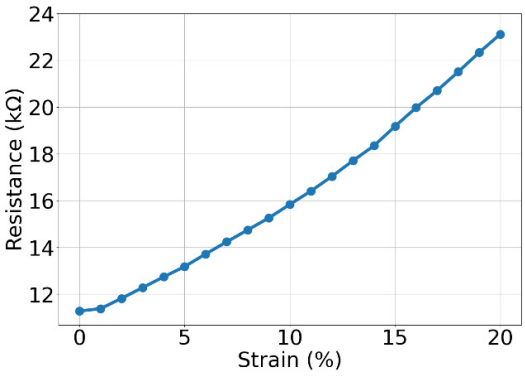

Fig. 4. Resistance as a function of strain.

Conclusion

In this work, we successfully developed a robust carbon-based aerosol-jet printed structure for potential applications in tires. The deposits are stable with time and under large mechanical strain. With gauge factors reaching 5.2 and stable performance at 20% strain, these prints are promising for sensors with high sensitivity and strain-range requirements in tires.

Acknowledgments

This research was funded in whole, or in part, by the Luxembourg National Research Fund (FNR), grant reference IPBG2023/MS/18347824/FURI-OSO. For the purpose of open access, and in fulfilment of the obligations arising from the grant agreement, the author has applied a Creative Commons Attribution 4.0 International (CC BY 4.0) license to any Author Accepted Manuscript version arising from this submission.

References

[1] A. Tota, G. Rigazzi, M. Velardocchia, Integration of active systems for a global chassis control design, *Mechanical Systems and Signal Processing* 119, 437-455 (2019); doi: 10.1016/j.ymssp.2018.10.001

[2] Y. Zhang, Q. Yin, L. Zhao, Design of Direct-Type Tire-Pressure Monitoring System Based on SP37 Sensor, *Journal of Physics: Conference Series* 435, 012022 (2013); doi: 10.1088/1742-6596/435/1/012022

[3] S. K. Clark, *Mechanics of Pneumatic Tires*, NIST Monograph 122, 165-180 (1981); doi: 10.6028/NBS.MONO.122

[4] K. Tsumura, M. Nakano, T. Ohba, Estimation of Emission Characteristics of Sulfur Gas from Rubber, *Journal of the Society of Materials Science, Japan* 54, 638-644 (2005); doi: 10.2472/jsms.54.638

[5] X. Tian, S. G. King, L. S. McCaffrey, J. L. Tanner, Highly stretchable and sensitive strain sensors based on carbon nanotube/thermoplastic polyurethane with a pre-stretching process, *Composites Part A: Applied Science and Manufacturing* 130, 105707 (2020); doi: 10.1016/j.compositesa.2020.105707

DOI 10.5162/eurosensors2026/Tu–FSW–05

Stretchable Piezoelectrics Based on PVDF-Elastomer Blends

Gulshan Khurana[1, 2], Junling Zhao[3], Sebastjan Glinsek[1]
[1] Luxembourg Institute of Science and Technology, Smart Materials Unit
[2] University of Luxembourg, Faculty of Science, Technology and Medicine
[3]The Goodyear Tire & Rubber company, Akron, United States
Corresponding Author: sebastjan.glinsek@list.lu

Summary:

In this work, we present the development of a highly stretchable piezoelectric sensor based on a blended polymer system composed of poly(vinylidene fluoride-co-trifluoroethylene) (PVDF-TrFE) and the elastomer nitrile butadiene rubber (NBR), fabricated via bar-coating & vulcanization. A polymer blending approach is employed, in which PVDF-20TrFE is dispersed within an elastomeric NBR matrix, followed by vulcanization of the NBR phase to enhance mechanical stability and elasticity. Furthermore, the polarization–electric field (P–E) hysteresis is investigated, and the material is electrically poled to improve its piezoelectric performance, indicating their potential for stretchable piezoelectric applications.

Keywords: Piezoelectric sensors, Stretchable electronics, PVDF-TrFE, NBR, Bar-coating technique

Background, Motivation and Objective

Stretchable piezoelectric sensors are key components for next-generation flexible and wearable systems, where reliable electromechanical sensing under large mechanical deformation is required. However, achieving an optimal balance between piezoelectricity, mechanical stretchability, higher strain sensing range and long-term durability remains a major challenge in polymer-based systems [1].

Commercial piezoelectric sensors are typically either rigid or flexible but lack sufficient stretchability to withstand high-strain environments [2]. In applications involving large deformation, these sensors often fail due to mechanical fatigue and poor strain accommodation.

In this work, we aim to develop flexible and stretchable piezoelectric blends by blending piezoelectric polymer PVDF-20TrFE and elastomer NBR, targeting improved stretchability, durability and sensing capabilities.

Description of the New Method or System

In this work, we introduce scalable bar-coating approach to fabricate PVDF-TrFE/NBR blend films for stretchable piezoelectric applications. We systematically investigate the polarization-electric field hysteresis behavior for these blends to understand how the elastomer matrix influences the ferroelectric and piezoelectric response. The results highlight the potential of this approach to optimize mechanical properties and move towards more reliable stretchable piezoelectric sensors.

Results

Mechanical properties were investigated by measuring the stress–strain curves of the blend films. Mechanical characterization reveals a significant reduction in Young's modulus with increasing NBR content, decreasing from 1.6 GPa for pure PVDF-20TrFE to approximately 50 MPa for the 40:60 (PVDF-20TrFE: NBR) blend (Fig. 1). Additionally, the elongation at break increases up to ~16% for the 40:60 blend, indicating enhanced stretchability, compared to only 2% for the pure PVDF-20TrFE film (Fig. 1). These results demonstrate that the incorporation of NBR significantly improves the mechanical compliance and flexibility of the polymer films.

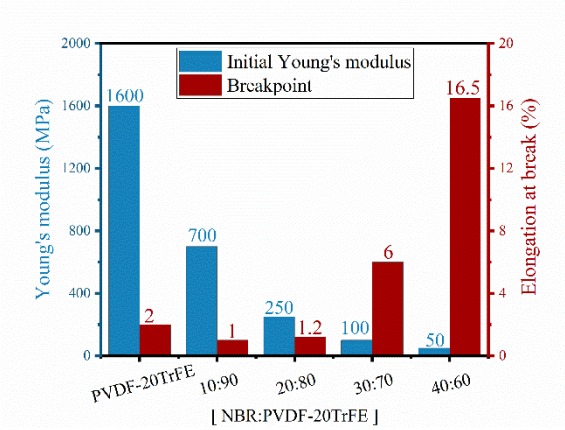

Fig. 1. Graph of Young's modulus and elongation at break for various blend ratios.

Electromechanical measurements confirm clear ferroelectric switching in blends containing ≥50% PVDF-20TrFE, with coercive fields in the range of 30–60 V/µm (Fig. 2), indicating the retention of ferroelectric functionality within the blended system. At higher NBR content, particularly for the 40:60 [N:P] composition, noticeable leakage current are observed, which can be attributed to the increased presence of the elastomeric phase influencing dielectric behaviour.

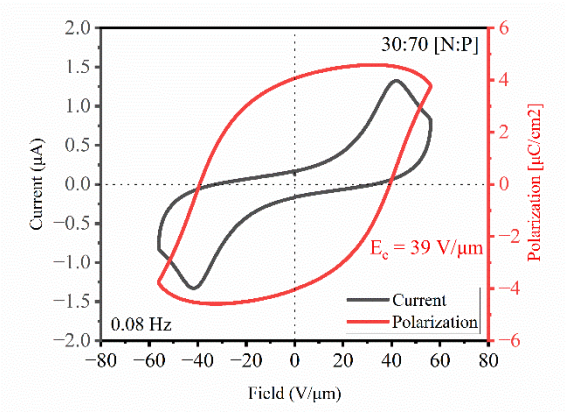

Fig. 2. Polarization-Electric field (PE) hysteresis loop for blend film 30:70

The piezoelectric coefficient (d_{33}) measured using a Berlincourt d_{33} meter for pure PVDF-20TrFE and its blends containing 10 – 40% NBR, provides insight into the effect of polymer composition on electromechanical performance. The d_{33} value gradually decreases from −23 pC/N for pure PVDF-20TrFE to −2.0 pC/N for the 40:60 [N:P] blend ratio, as summarized in Table 1, reflecting the reduced ferroelectric phase contribution with increasing elastomer content.

Tab. 1: piezoelectric coefficient d_{33} of the blends

Samples	d_{33} (pC/N)
PVDF-TrFE	-23
20:80 [N:P]	-9.6
30:70 [N:P]	-2.4
40:60 [N:P]	-2.0

Furthermore, the voltage output was measured using an oscilloscope under repetitive finger-tapping conditions (Fig. 3), which confirms stable and reproducible signal generation across all compositions. The output voltage shows a composition-dependent variation, with values that can be tuned by adjusting the NBR content in the blends, highlighting the compositional control over piezoelectric performance.

Atomic force microscopy (AFM) analysis reveals an elongated distribution of PVDF-TrFE domains within the NBR matrix, which varies with composition. The large contrast in Young's modulus between PVDF-TrFE (3–5 GPa) and NBR (1–2 MPa) enables stiffness mapping, providing insight into the phase distribution and microstructure of the blends (Fig. 4).

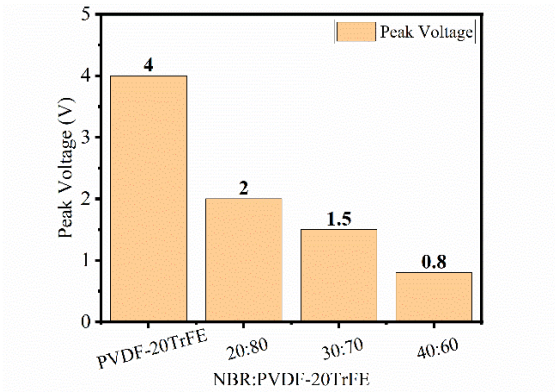

Fig. 3. Graph of peak voltage signal output through tapping mode

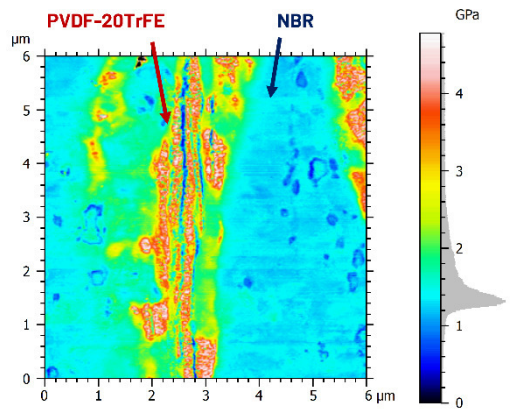

Fig. 4. AFM stiffness mapping: PVDF-20TrFE and NBR phases

Acknowledgment

This research was funded in whole, or in part, by the Luxembourg National Research Fund (FNR), grant reference IPBG2023/MS/18347824/FURI-OSO. For the purpose of open access, and in fulfilment of the obligations arising from the grant agreement, the author has applied a Creative Commons Attribution 4.0 International (CC BY 4.0) license to any Author Accepted Manuscript version arising from this submission.

References

[1] Tu, Ruowen, Sodano, Henry A., Highly Stretchable Printed Poly(vinylidene fluoride) Sensors through the Formation of a Continuous Elastomer Phase, *ACS Applied Materials & Interfaces* 2023 *15(18)*,22320-22331 DOI:10.1021/acsami.3c01168

[2] Rogers JA, Someya T, Huang Y. Materials and mechanics for stretchable electronics. Science. 2010 Mar 26;327(5973):1603-7. doi: 10.1126/science.1182383. PMID: 20339064.

DOI 10.5162/eurosensors2026/Tu–FSW–06

Flexible Wearable MXene – Based Printed Temperature Sensor for Multifunctional Applications

Hamid Nawaz[1], Nadeem Tariq Beigh[1], Nouha Alcheikh[1]
[1] Department of Mechanical and Nuclear Engineering, Khalifa University, Abu Dhabi, United Arab Emirates
100065803@ku.ac.ae; Nouha.alcheikh@ku.ac.ae

Summary:

1. Fully printed flexible wearable temperature sensor was realized on polyimide (PI) substrate using dimethyl sulfoxide (DMSO)-enhanced $Ti_3C_2T_x$ MXene ink through a customized, scalable 3D-printing approach.
2. The sensor demonstarted reliable 20–60 °C sensing, with pronounced negative temperature coeffcient (NTC), a temperature coefficient of resistance (TCR) of −0.84%/°C, and high linearity (Coefficient of Determiantion (R^2) = 0.98).
3. It maintained stable response and recovery with negligible drift over 90 days, demonstrating excellent long-term reliability.

Keywords: Flexible sensor; Temperature; Enhanced MXene; Wearable electronics; Multifunctional

Background, Motivation, and Objective

Flexible wearable sensors are conformable, non-invasive platforms for real-time monitoring in healthcare, environmental systems, human-machine interfaces, and soft robotics [1,2]. Among the physical variables they measure, temperature is particularly important because it reflects both physiological state and local thermal conditions, enabling on-body diagnostics and thermal mapping [1,2]. Despite progress, flexible temperature sensors face trade-offs among sensitivity, mechanical compliance, signal stability under deformation, and scalable manufacturing [2,4,6]. At the material level, polymer systems require molecular engineering to combine softness with strong thermal response [3], inorganic or metal-oxide thin films suffer from poor toughness and limited deformation tolerance [4], and carbon-based conductive networks often need explicit strain–temperature decoupling to avoid cross-signal interference [5]. In parallel, fabrication depends on tight control of ink formulation, printing precision, conformal deposition, and device integration, complicating reproducible, low-cost, and scalable production [6]. Here, we report a fully printed temperature sensor on a flexible substrate using a customized process, enabling high-performance sensing for multifunctional applications under bending-prone conditions.

Experimental Details

The sensing material consisted of DMSO-enhanced $Ti_3C_2T_x$ MXene ink, prepared by repeatedly exchanging the aqueous solvent with DMSO, followed by filtration and drying to obtain a DMSO-rich MXene mud (Fig. 1a). MXene formation was verified by SEM and XRD: SEM (Fig. 1b) showed stacked, accordion-like flakes with clear interlayer galleries, indicating effective etching and delamination, while XRD (Fig. 1c) confirmed conversion of Ti_3AlC_2 MAX to $Ti_3C_2T_x$ MXene through the shift of the (002) peak from 9.5° to ~6.8° and suppression of MAX-phase reflections, evidencing increased interlayer spacing and layered MXene formation. The dried MXene was redispersed in DMSO to produce a homogeneous 45 mg mL^{-1} ink, with its conductivity–viscosity relationship shown in Fig. 2a. Temperature sensor was fabricated on 150 µm-thick PI substrate, which was cleaned with isopropyl alcohol (IPA) and UV-treated for 120 s to enhance adhesion. The ink was printed through a 230 µm disposable nozzle on a Voltera V-One printer using a custom alignment and material-swap method (Fig. 2b). After systematic optimization of feed rate, flow rate, trim length, baking temperature, and baking time, the device was cured at 45 °C for 6 h. The fabricated sensor (Fig. 2c) was electrically characterized in a closed thermal chamber using a Keithley 2450 source meter at 1 V bias and 100

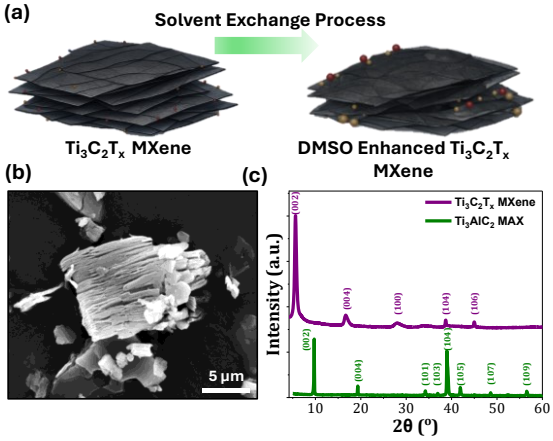

Fig. 1. (a) Solvent-exchange process for MXene ink preparation, (b) SEM image showing accordion-like layered morphology, and (c) XRD patterns confirming conversion of Ti_3AlC_2 MAX to $Ti_3C_2T_x$ MXene with enlarged interlayer spacing.

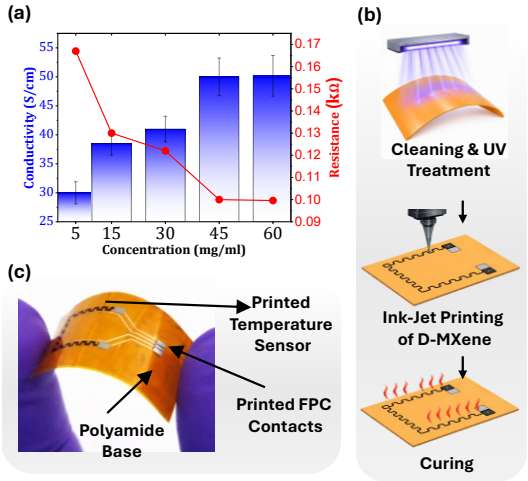

Fig. 2. (a) Conductivity and viscosity relation of the MXene ink, (b) Shematic illustration of the printing process used in sensor fabrication (c) Photograph of the final printed temperature sensor with FPC.

ms sampling interval, while chamber temperature was regulated by a heater with a REX-C100 controller and K-type thermocouple feedback. Silver-based flexible printed circuits (FPCs) were also fabricated to support future IoT integration.

Description of the New Method

We report a fully printed strategy for the fabrication of flexible wearable temperature sensors based on DMSO-enhanced $Ti_3C_2T_x$ MXene ink. The sensing material shows pronounced NTC and a TCR value. Combined optimization of ink formulation, material characterization, and printing parameters enabled the realization of sensors on flexible substrates with high sensitivity, and excellent repeatability.

Results

The temperature-sensing performance of the device was systematically evaluated by increasing the chamber temperature stepwise and recording the stabilized resistance at each setpoint. The resistance decreased continuously with increasing temperature, confirming NTC behavior over the 20–60 °C range (Fig. 3a). The corresponding resistance–temperature relationship (Fig. 3b) exhibited an approximately linear trend, with an R^2 value of 0.98 and a TCR of −0.84%/°C. This behavior is attributed to thermally activated carrier tunneling across interflake barriers, which becomes more favorable at elevated temperatures and thereby reduces junction resistance. The transient response (Fig. 3c) was evaluated by heating the sensor to 40 °C and allowing it to return to ambient conditions, yielding a response time of ~278 s and a recovery time of ~242 s. Long-term repeatability was assessed at 30-day intervals over 90 days, and the results in Fig. 3d show only marginal variation in the response curves and corresponding linear fits, with sensitivity changing by less than 1% after 90 days, confirming reliable long-term operation.

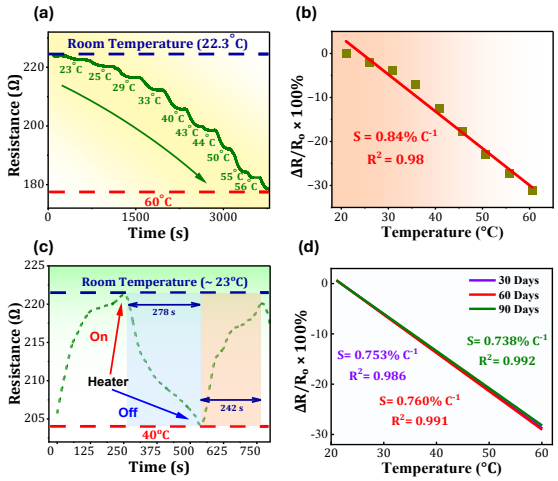

Fig. 3. (a) Stepwise resistance response of the printed flexible temperature sensor (b) Temperature response of the sensor relationship showing sensitivity and linearity (c) Response-recovery dynamics during heating and cooling (d) Long-term repeatability analysis of the sensor.

Conclusion

This work presents a fully printed flexible wearable temperature sensor based on DMSO-enhanced $Ti_3C_2T_x$ MXene ink on PI substrate. The device showed reliable NTC behavior over 20–60 °C, with near-linear response (R^2 = 0.98), a TCR of −0.84%/°C, stable response–recovery performance, and less than 1% sensitivity variation after 90 days. The method provides a scalable route to wearable temperature sensors for diverse monitoring applications.

References

[1] He, X.; Shi, X.-L.; Wu, X.; et al., Three-dimensional flexible thermoelectric fabrics for smart wearables, Nature Communications, 16, 2523 (2025); doi: 10.1038/s41467-025-57889-1

[2] Wagih, M.; Shi, J.; Li, M.; et al., Wide-range soft anisotropic thermistor with a direct wireless radio frequency interface; Nature Communications, 15, 452 (2024); doi: 10.1038/s41467-024-44735-z

[3] Kim, T. H.; Zhou, Z.; Choi, Y. S.; et al., Flexible biomimetic block copolymer composite for temperature and long-wave infrared sensing. Science Advances, 9(6), eade0423 (2023). doi: 10.1126/sciadv.ade0423.

[4] Liu, Z.; Tian, B.; Zhang, B.; et al., A thin-film temperature sensor based on a flexible electrode and substrate. Microsystems & Nanoengineering, 7, 42 (2021); doi: 10.1038/s41378-021-00271-0

[5] Yang, L.; Chen, X.; Dutta, A.; et al., Thermoelectric porous laser-induced graphene-based strain-temperature decoupling and self-powered sensing. Nature Communications, 16, 792 (2025); doi: 10.1038/s41467-024-55790-x

[6] Shao, Y.; Wei, L.; Wu, X.; et al., Room-temperature high-precision printing of flexible wireless electronics based on MXene inks. Nature Communications, 13, 3223 (2022); doi: 10.1038/s41467-022-30648-2

DOI 10.5162/eurosensors2026/Tu–FSW–07

Endometrial Receptivity Monitoring by Impedance Technology on a Soft and Adhesive MEA

Dongyang Tang[1], Liubov Izmaylova[2], Sven Ingebrandt[1], Rudolf E. Leube[2], Ziyu Gao[1,*]
[1] Institute of Materials in Electrical Engineering 1, RWTH Aachen University, 52074 Aachen, Germany
[2] Institute of Molecular and Cellular Anatomy, Uniklinik RWTH Aachen, D-52074 Aachen, Germany
* Corresponding author: Dr. Ziyu Gao, Email: ziyu.gao@iwe1.rwth-aachen.de

Summary:

To investigate hormone-dependent changes in endometrial epithelial receptivity to embryo attachment, an impedance-based microelectrode array was used for monitoring steroid hormone-induced changes in cellular state. Estradiol and progesterone were used to model the proliferative and secretory phase of the menstrual cycle, respectively. Impedance measurements distinguished these two hormonal conditions. This approach offers a route towards miniaturized, non-invasive and real-time platforms for time-resolved *in vitro* assessment of implantation-relevant endometrial responses.

Keywords: embryo implantation, endometrial receptivity, steroid hormones, soft and adhesive microelectrode array (SA-MEA), transepithelial electrical impedance (TEI)

Introduction

The human uterine endometrium undergoes cyclic remodeling during the menstrual cycle to facilitate embryo implantation. Endometrial embryo receptivity is confined to the short window of implantation (WOI) during the mid-secretory phase of the menstrual cycle. The transition towards the receptive state is associated with hormone-regulated alterations in epithelial polarity, cell-cell junction organization, and barrier function, largely driven by estradiol and progesterone signaling [1]. Yet, reliable and minimally invasive approaches capable of monitoring functional endometrial property changes are lacking.

During WOI the progesterone-driven increase in paracellular permeability is accompanied by partial loss of epithelial polarity [1]. These changes are reflected by the electrical properties of the epithelial barrier, making transepithelial electrical measurements a powerful, label-free approach for investigating endometrial receptivity-associated processes. Transepithelial electrical resistance (TEER) studies have shown that steroid hormone-induced resistance changes correlate with altered polarity in cultured endometrial cells [2]. However, single-point, low-frequency TEER only provides a resistive readout, whereas broadband transepithelial electrical impedance (TEI) resolves resistive and capacitive contributions to barrier, membrane and adhesion properties [3]. Moreover, due to the heterogeneity of the endometrial epithelium, single-site TEER working electrodes capture less representative information than a dense, uniformly distributed microelectrode array (MEA). These limitations motivated the development of a soft and adhesive MEA (SA-MEA) to enable non-invasive and real-time monitoring of hormone-dependent endometrial receptivity by TEI. Unlike conventional TEER, SA-MEA requires no auxiliary counter electrode and records signals solely from the apical epithelial surface (Fig. 1a).

Results and discussion

Ishikawa monolayers were exposed either to estradiol (E2) alone or E2 + medroxyprogesterone acetate (MPA) to model progesterone-associated secretory-phase signaling. These monolayers as well as untreated control monolayers were monitored for 4 days using PEDOT:PSS-coated gold SA-MEAs. The conditions were selected to capture hormone-driven epithelial responses while minimizing culture-caused drift and avoiding prolonged hormone exposure (Fig. 1b).

Impedance and phase spectra between 100 Hz and 100 kHz were recorded across the monolayer using 32 electrodes uniformly distributed over a 1,500 × 1,500 µm² area. Valid data were averaged (Fig. 1c). Preliminary (N=1) day 1-normalized impedance spectra revealed distinct hormone-dependent responses in Ishikawa monolayers. E2 increased impedance across the measured frequency range, particularly between 100 Hz and 10 kHz, whereas E2+MPA exposure attenuated this response and reduced the impedance below baseline. Phase spectra further indicated a more capacitive response at 10 – 100 kHz with E2 treatment, but more resistive profile in E2+MPA exposure. By contrast, the no-hormone group showed minor changes, suggesting limited spontaneous remodeling. The

standard deviation in Fig. 1c reflects site-to-site variation arising from epithelial heterogeneity, indicating that the array resolves local epithelial states. The increased impedance, the more pronounced capacitive phase response and preserved morphology in the presence of E2 are consistent with a barrier-like epithelial state, marked by stronger tight junction organization, reduced paracellular permeability and increased polarity. By contrast, the reduced TEI and less capacitive response after E2+MPA exposure may reflect polarity-associated epithelial remodeling towards a receptive-like state, involving junctional redistribution, increased paracellular permeability and reduced membrane-associated capacitive contributions to the impedance [1]. In all groups, the epithelial layer kept confluent confirming that the observed effects are caused by rearrangements of cell-cell junctions and not by monolayer disruption (Fig. 1d).

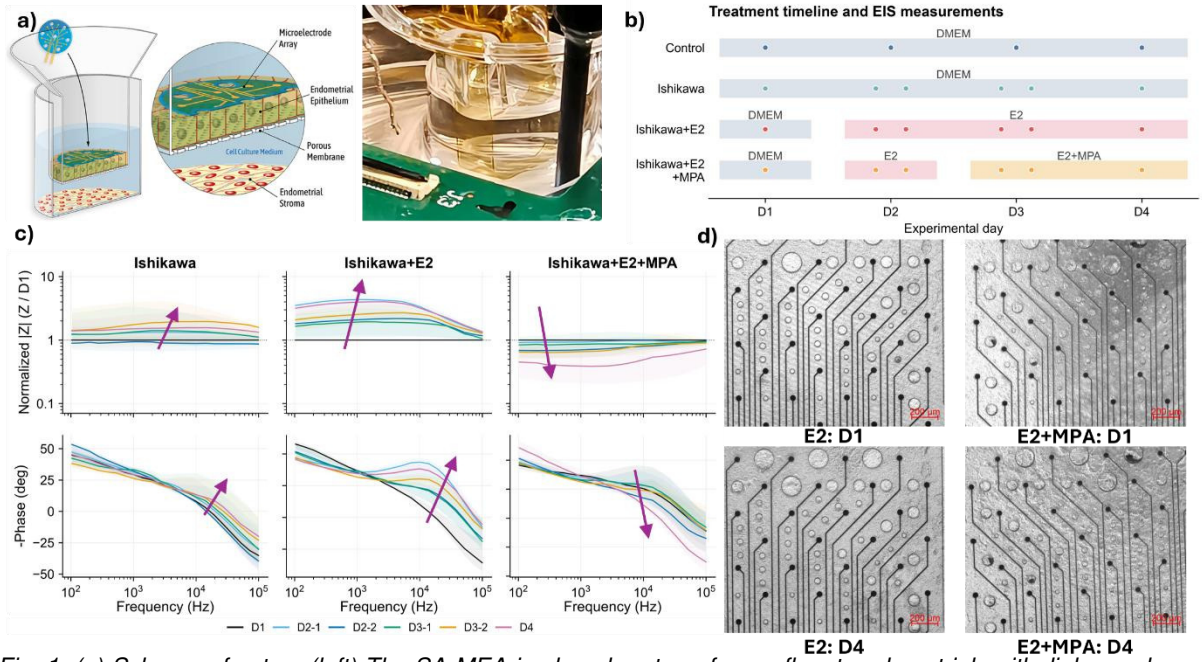

Fig. 1. (a) Scheme of setup. (left) The SA-MEA is placed on top of a confluent endometrial epithelial monolayer. The monolayer was cultured in an insert that is composed of a permeable polymer membrane. Endometrial stromal cells were placed at the bottom of the reservoir below to provide regulatory signals. (right) Photo of measuring setup that contains Pt counter electrode and Ag/AgCl reference electrode. (b) timeline of treatment. The media are changed after each measurement. Confluent layer formed before day 1 (D1). (c) Impedance spectra normalized to D1 and phase spectra of three treatment groups (N=1). Arrows indicate passage of time (D1→D4) (d) Microscopy pictures of E2 and E2+MPA treated Ishikawa monolayers growing below SA-MEAs after D1 and D4.

Conclusion and outlook

These findings identify the SA-MEA as a sensitive platform for real-time monitoring of hormone-dependent epithelial remodeling in Ishikawa monolayers. The impedance and phase spectra report this remodeling through changes in junctional organization, apical barrier continuity and paracellular permeability that reshape frequency-dependent current pathways. Future integration with wireless readout and higher-throughput formats could support quantitative *in vitro* screening of endometrial receptivity-like states and drug responses.

Acknowledgement

Authors thank Ms. Sarah Göbbels for support in biological experiments. This work is funded under the Excellence Strategy of the Federal Government and the Länder (ERS-OPSF906). The authors also thank the funding support from Deutsche Forschungsgemeinschaft (DFG, 363055819/GRK2415), the Deutscher Akademischer Austauschdienst (DAAD, Research ENHANCE.R programme), the Profile Area Materials Science and Engineering of RWTH (MatSE, Conference Funding for Young Talent).

References

[1] Sternberg, A. K., et al. How Mechanical Forces Change the Human Endometrium during the Menstrual Cycle in Preparation for Embryo Implantation. Cells, 10(8) (2021); doi: 10.3390/cells10082008

[2] Heng, S., et al. Podocalyxin promotes an impermeable epithelium and inhibits pro-implantation factors to negatively regulate endometrial receptivity. Sci Rep, 11(1), 24016 (2021); doi: 10.1038/s41598-021-03425-2

[3] Tang, D., et al. Time-resolved monitoring and circuit modeling of trophoblast invasion in a model of human embryo implantation by electric cell-substrate impedance sensing. Biosensors and Bioelectronics: X, 31 (2026). doi: 10.1016/j.biosx.2026.100797

DOI 10.5162/eurosensors2026/Tu–FSW–08

A Flexible Wearable Platform with On-Device TinyML for Context-Aware Bio-Signal Monitoring

Shu-Wei Shen[1], Shin-Lan Lin[1], Chris Buchowiecki[2], Chen-Hao Hong[1], Jui-En Lee[1], Yan-Ling Chen[1], Yung-Chun Yang[1], Si-Yuan You[1], Shi-Yu Hung[1], Hsu-Fan Tseng[1], Hiroyuki Fujita[3, 4], and Cheng-Yao Lo[1, 2, 3, *]

[1] *Department of Power Mechanical Engineering, National Tsing Hua University, Hsinchu 300044, Taiwan*
[2] *College of Semiconductor Research, National Tsing Hua University, Hsinchu 300044, Taiwan*
[3] *Institute of NanoEnginerring and MicroSystems, National Tsing Hua University, Hsinchu 300044, Taiwan*
[4] *Advanced Research Laboratories, Tokyo City University, Tokyo 158-8557, Japan*

Summary: This paper presents a flexible, standalone wearable platform for context-aware bio-disgnal monitoring for emergency scenarios; and introduced heart rate detection as the proof-of-concept. On-device TinyML model running on a resource-constrained microprocessing unit to distinguishing motion states was realized using synchronized photoplethysmography and inertial measurement unit data. This low-power context awareness forms the critical foundation for active noise-filtering to ensure robust, immediate physiological alerts for first responders and elder care without external networks.

Keywords: Flexible sensors, heart rate monitoring, motion artifacts, photoplethysmography, TinyML, wearable sensors.

Background, Motivation and Objective

Continuous monitoring of physiological signals is critical for early-warning health systems and emergency first response [1]. While commercial wearable devices (e.g., smartwatches) are widely available, they are primarily engineered for long-term lifestyle and exercise habit tracking, relying heavily on continuous cloud data accumulation and smartphone pairing [2]. In specific emergency situations such as running exercise in remote area or natural disasters, this dependence on external web infrastructure introduces unacceptable latency and vulnerability. There is a distinct need for a standalone and one-shot alarming system that provides immediate, reliable physiological feedback directly on the edge. To address this gap, we designed and are currently prototyping a flexible, wearable platform addressing that specific niche.

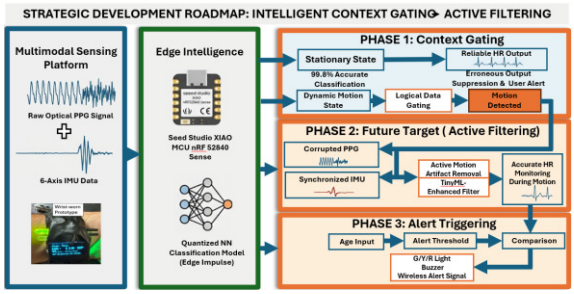

Figure 1: Strategic development roadmap of the context-aware wearable platform. Phase 1 : the on-device TinyML gating mechanism for classifying stationary versus dynamic motion. Phase 2 : active signal filtering for continuous, reliable monitoring during dynamic movement. Phase 3 : alert triggering based on bio-signal.

Research strategy

A primary challenge in ambulatory photoplethysmography (PPG) is signal corruption from motion artifacts [3]. Rather than transmitting raw data to the cloud for processing, the objective is to achieve an intelligent understanding of the user's situation entirely on-device using minimal computational power. As illustrated in Fig. 1, achieving robust heart rate (HR) extraction during dynamic movement and triggering timely alert requires a multi-stage approach. The necessary first step is accurate context awareness via motion state detection. By synchronizing the PPG sensor with an inertial measurement unit (IMU) and deploying a tiny machine learning (TinyML) classification model, the device successfully distinguishes between stationary and in-motion states. The second phase is to use this context awareness to trigger active, on-device filtering algorithms, extracting relevant HR data from highly disturbed signals. The third phase concerns the decision to ensure a fully autonomous, reliable alert transmission for caregivers. Here, we report on the implementation of the first phase.

Experimental

The wearable platform integrates sensing, processing, and feedback mechanisms on a flexible printed circuit board (FPCB) mounted on a polydimethylsiloxane (PDMS) substrate. The sensing elements comprise an optical module (Osram, SFH7072) for capturing the PPG and IMU (LSM6DS3) signals. These components are driven by a microprocessing unit (MCU, Seeed Studio, XIAO nRF52840), which handles data acquisition, manages multimodal feedbacks with

a LED, a piezoelectric buzzer, and an OLED display with the TinyML classification model on the edge (Fig.2).

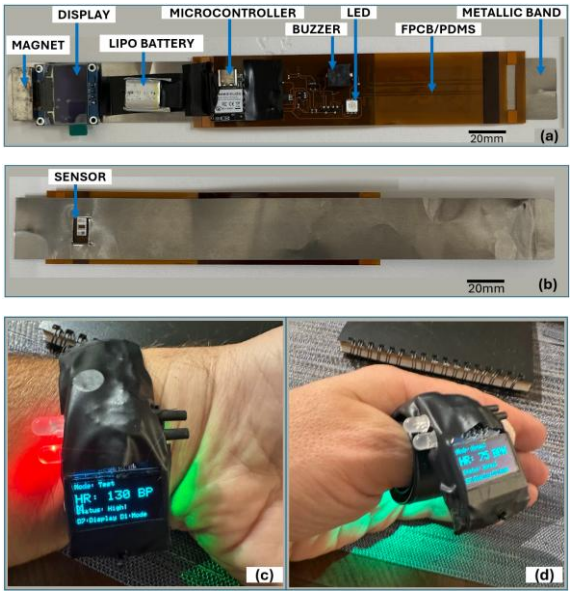

Figure 2: The (a) front and (b) back side of the proposed platform with corresponding components mounted before packaged for prototyping with (c) wrist-worn configuration (d) thumb-worn configuration.

To enable real-time motion classification, a neural network was trained utilizing the edge impulse platform. IMU data streams across dynamic (walking) and static (seating) activity states were collected. A signal processing pipeline employing spectral analysis extracted essential frequency features, training a compact neural network that achieved a validation accuracy of 99.8%. The resulting model was quantized and deployed directly into the device firmware as a self-contained library for continuous, low-power inference.

Results and Conclusion

System validation showed a precise correlation between the classified motion context and PPG signal integrity. Validation against a commercial smartwatch benchmark during these periods yielded a high correlation (linear coefficient of determination of 0.9291, Fig. 3(a)). During static periods, the IMU registered minimal activity, yielding a clean, periodic PPG signal for reliable HR extraction (Fig. 3(b) and 3(d)). On contrary, dynamic states generated large, high-frequency IMU transients that directly corrupted the PPG waveform (Fig. 3(c) and 3(e)). Operating entirely on-device, the TinyML model successfully recognized these dynamic transients in real-time. This validates the claimed context-aware, low-power gating mechanism in Phase 1 of our strategy (Fig. 1). Leveraging this accurate edge-classification framework, we are working on the integration of active filtering algorithms to extract valid HR waveforms during dynamic motion (Phase 2), and a fully autonomous, context-aware emergency alert platform (Phase 3).

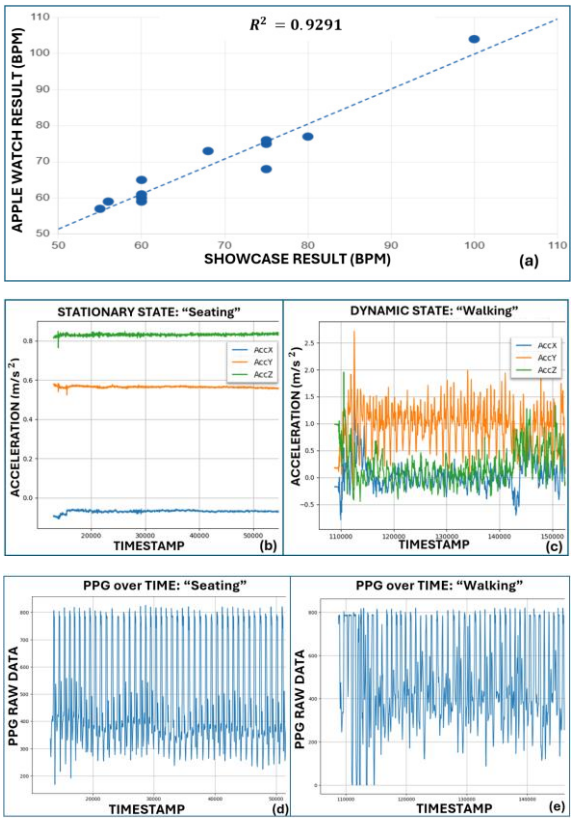

Figure 3: System validation and motion classification. (a) HR correlation between the proposed prototype and an Apple Watch. (b) Baseline IMU data and (d) the resulting stable HR profile during the static "seating" state. (c) High-frequency IMU transients and (e) the corresponding corrupted HR profile during the dynamic "walking" state, demonstrating the necessity of the on-device TinyML gating.

References

[1] K. C. Graham and M. Cvach, "Monitor alarm fatigue: standardizing use of physiological monitors and decreasing nuisance alarms," Am. J. Crit. Care, vol. 19, no. 1, pp. 28-34, Jan. 2010.

[2] A. Ali et al., "An Innovative IoT and Edge Intelligence Framework for Monitoring Elderly People Using Anomaly Detection on Data from Non-Wearable Sensors," Sensors, vol. 25, no. 6, Art. no. 6, Jan. 2025.

[3] R. Ramadhan and I. A. Akbar, "Exploration of Factors Influencing Noise Detection on Health Wearable Devices during Hand Motion Artifacts: Study on Noise Impact," in 2024 International Seminar on Intelligent Technology and Its Applications (ISITIA), Jul. 2024, pp. 349-354.

DOI 10.5162/eurosensors2026/Tu–FSW–09

Natural Flax Fibres for Sustainble Sensor Applications

Yi Chen[1], Anna de Lena[1], Sansan Shen[1,3], Robert Abbel[1], Sofiane Guessama[2], Kate Parker[1], Xuejun Li[3]
[1] Bioeconomy Science Institute, Rotorua, 3010, New Zealand
[2] INRAE, Research Unit BIA UR1268, Rue Geraudiere, Nantes, F-44316, France
[3] Department of Electrical and Electronic Engineering, Auckland University of Technology, Auckland, 1010, New Zealand
yi.chen@scionrsearch.com

Summary: This study demonstrated the potential of functionalised natural flax fibres for sustainable sensor applications. Flax yarn coated with reduced graphene oxide (rGO) exhibited promising electrical properties for e-textiles application. In contrast, flax fibres coated with conductive polymer, polyaniline (PANI) showed high sensitivity to ammonia, highlighting their potential for seafood freshness monitoring.

Keywords: flax fibre, conductive coating, e-textile, ammonia sensing

Introduction

Electronic textiles (e-textiles) and smart packaging are rapidly emerging as key enabling technologies for product and environmental monitoring, healthcare, and the Internet of Things (IoT). However, these systems are predominantly manufactured using petroleum-derived synthetic materials, raising concerns regarding their environmental impact and end-of-life disposal.

The growing demand for sustainable materials has accelerated the development of bio-based alternatives to conventional petroleum-derived materials used in sensors and electronics. Flax (*Linum usitatissimum*) is one of the world's oldest and most widely cultivated natural bast fibres. It possesses an attractive combination of high specific strength, low density, renewability, and low embodied energy, making it an excellent candidate for sustainable advanced materials [1]. Flax fibres exhibit good flexibility, breathability, and moisture management, which have led to their widespread use in textiles and fibre-reinforced composites. More recently, flax has attracted increasing attention for electronics and sensors, particularly in applications requiring lightweight, flexible, and environmentally friendly substrates, such as wearable electronics and smart packaging [2].

This work investigates the development of functional flax materials using conductive coating strategies based on reduced graphene oxide (rGO) and conductive polymer polyaniline (PANI). Two commercial flax substrates were evaluated for their potential applications in e-textiles and smart packaging demonstrating the versatility of natural fibres for next-generation electronic and sensing technologies.

Materials and methods

For e-textile application, flax yarn supplied by Linificio (Italy) was cut into pieces of 15 cm length and sequentially cleaned with deionised water and isopropanol to remove surface contaminants, followed by drying in an oven at 60 °C for 5 minutes. The pre-cleaned yarns were then fully immersed in a graphene oxide (GO) solution (5 mg/mL) for 1 minute then air-dried at room temperature until completely dry. This dip-coating process was repeated to prepare yarns with different GO loading levels. The GO-coated yarns were placed in an ascorbic acid solution (8 mg/mL) and kept in at 90 °C for 24 hours to reduce GO to reduced graphene oxide (rGO).

For ammonia sensing, New Zealand native flax, harakeke (*Phormium tenax*) fibre sheets were investigated as a sustainable substrate for ammonia gas sensing. Ammonia has been identified as a reliable indicator of seafood freshness. The conductive flax paper-based sensor was fabricated via an in-situ chemical oxidative polymerisation process. Briefly, a pristine flax fibre paper substrate was vertically suspended in 1.0 M HCl aqueous solution. Subsequently, 3.84 mmol of aniline monomer and 5.48 mmol of ammonium persulfate (APS) oxidant were sequentially added to the solution. The in-situ polymerisation reaction was conducted in an ice-water bath (0-5 °C) for 7 hours under mild agitation to facilitate the deposition of PANI onto the flax fibre template. Upon completion, the functionalised paper was rinsed with ethanol and deionised water to eliminate unreacted monomers, oligomers, and residual oxidant. Finally, the composite substrate was dried in an oven at 50 °C overnight, yielding the final sensor substrate.

Results

Scanning electron microscopy (SEM) was employed to investigate the morphology of rGO coated flax yarn (10 coating cycles). As shown in Fig. 1, compared with the uncoated yarn, the GO coating and reduction process generated gaps between individual fibres of yarn, while the deposited rGO sheets assembled into an interconnected three-dimensional network throughout the yarn structure. Rather than coating only the surface of individual fibres, the rGO bridged adjacent fibres and formed conductive pathways across multiple fibre layers. This interconnected architecture is expected to facilitate efficient electron transport, making it well suited for potential e-textile integration applications.

The electrothermal performance of the rGO-coated yarn was further evaluated. Compared with the uncoated yarn, the rGO-coated yarn exhibited a measurable surface temperature increase of ~1.56 °C under an applied voltage of 30 V. Infrared thermal imaging also confirmed a uniform heating distribution along the yarn, demonstrating its potential for wearable heating textiles applications.

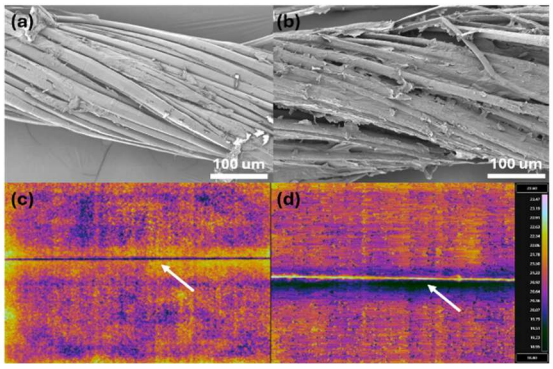

Fig. 1. SEM images of (a) flax yarn, (b) rGO coated yarn (10 times coating cycles), infrared thermal images of flax yarn (c) and rGO coated yarn (d) with applied voltage of 30 V.

PANI coated New Zealand flax fibres were further fabricated for ammonia sensing. The PANI-coated flax fibres exhibited a rougher surface morphology than the uncoated fibres (Fig. 2a and 2b), indicating the successful and uniform deposition of the PANI layer across the fibre surface while preserving the porous fibre structure. Maintaining this porous morphology is advantageous for gas sensing, as it facilitates gas diffusion and interaction with the sensing material. As shown in Fig. 2c, the electrical resistance of the sensor increased upon exposure to ammonia at 80% relative humidity (RH) and 20 °C, owing to the dedoping of the protonated PANI chains by ammonia molecules. The sensor exhibited a response of 15.5% at an ammonia concentration as low as 6 ppm, which increased to 193.0% at 70 ppm. These results demonstrate the high sensitivity of the PANI-coated flax fibres to ammonia and highlight their potential for seafood freshness monitoring.

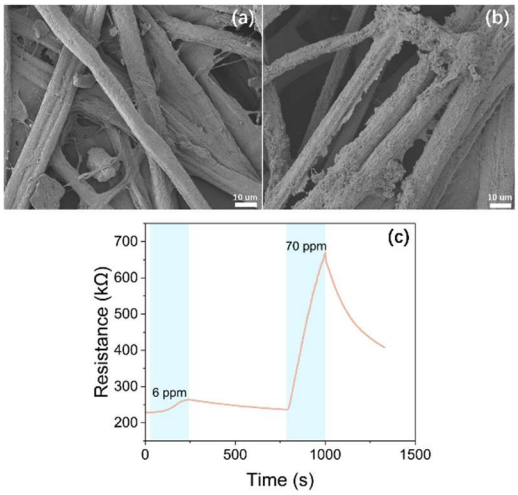

Fig. 2. SEM images of (a) pristine flax sheet, (b) PANI coated flax fibre sheet, (c) ammonia sensing performance of PANI coated flax fibre at 80% relative humidity (RH) and 20 °C.

Conclusions

This study demonstrated potential sensor applications of flax fibres through functionalisation. The rGO-coated flax yarn exhibited good rGO coating and electrothermal heating performance, highlighting its potential for wearable heating textiles and e-textile integration applications. In contrast, the PANI-coated New Zealand flax fibres demonstrated good sensitivity towards ammonia, indicating their suitability for ammonia sensing and smart packaging applications, particularly for seafood freshness monitoring.

References

[1] H. Li, et al, Recent progress in flax fiber-based functional composites, Advanced Fiber Materials 4, 171-84 (2022); doi:10.1007/s42765-021-00115-6

[2] K. Zeng, et al, Design, fabrication and assembly considerations for electronic systems made of fibre devices, Nature Reviews Materials 8, 552-561 (2023); doi:10.1038/s41578-023-00573-x

Acknowledgements

This work has received financial support from the UPWEARS project, which is part of the Horizon Europe programme (grant agreement no. 101130741). Views and opinions expressed are however those of the author(s) only and do not necessarily reflect those of the European Union or HADEA. Neither the European Union nor the granting authority can be held responsible for them. The work was also supported by the Smart Idea Project (No. AUTX2302) from the Ministry of Business, Innovation & Employment (MBIE), New Zealand.

DOI 10.5162/eurosensors2026/Mo–MLO–01

Full-Hydrogel-based Real-Time Sensor and Drug Deliverer in Organ-on-Chip Devices

G. Antonelli[1,2], E. Debbi[1,2], Francesca Corsi[3], Andrea Idili[4], A. Mencattini[1,2], E. Martinelli[1,2]

[1] Department of Electronic Engineering, University of Rome Tor Vergata, Rome, Italy
[2] Interdisciplinary Center for Advanced Studies on Lab-on-Chip and Organ-on-Chip Applications (ICLOC), Rome, Italy
[3] Department of Biology, University of Rome Tor Vergata, Rome, Italy
[4] Department of Chemical Sciences and Technologies, University of Rome Tor Vergata, Rome, Italy

Corresponding Author's e-mail address: g.antonelli@ing.uniroma2.it

Summary:
Integrating sensors into Organ-on-Chip devices is a crucial step toward fully exploiting these powerful platforms for biomedical research, especially in drug development. In this work, we used a custom stereolithography setup to embed hydrogels within a low-cost thermoplastic Organ-on-Chip. These micrometric hydrogels could absorb the drug, permitting a controlled release during the experiment. Moreover, the absorbed drugs acquired intrinsic fluorescence, which was exploited to train a machine learning algorithm, enabling quantitative tracking of absorption and release during the experiment.

Keywords: Hydrogel Sensor, Organ-on-Chip, Continuous Monitoring, Drug Delivery, Machine Learning

Background, Motivation and Objective

In recent years, the introduction of Organ-on-Chip technology into biomedical research has enabled this field to make significant strides [1]. These devices enable the replication of tissue and organ functions at the micrometric scale, allowing a deeper understanding of their biological mechanisms in a more realistic environment than in classical culture dishes. Moreover, in the context of a personalised medicine paradigm, it is crucial to understand the response of a patient's specific pathological tissue to a specific drug treatment.

However, obtaining useful information locally from the biological entity can be challenging, especially when done in real time [2]. In fact, continuous monitoring is crucial for a complete understanding of the dynamics of a certain phenomenon.

However, data coming from these real-time sensors can be difficult to interpret straightforwardly and to manipulate while maintaining the continuous monitoring paradigm. In this context, machine learning algorithms have proven their power by generating data-driven models that can correlate sensor inputs with known outputs. This initial information can subsequently be used during the dynamic monitoring of the biological entity in the Organ-on-Chip [3].

In this work, we present a technique for integrating hydrogel sensors using a custom stereolithographic approach. These hydrogels can absorb a drug or a combination of drugs and subsequently release them during the biological experiment. Using fluorescence imaging and a custom machine learning model based on hydrogel geometric features, we tracked in real time the evolution of this absorption/release process. In the meantime, we monitored the biological entity using brightfield microscopy.

We validated this technique by locally measuring the concentrations of doxorubicin and curcumin during a dynamic microfluidic experiment, revealing distinct absorption/desorption profiles for the drugs. We believe this technique will be extremely useful for local drug delivery and sensing in Organ-on-Chip experiments, especially to study personalised therapies for prostate cancer patients, where this drug combination could be more effective [4].

Methods

The Organ-on-Chip were laser-cut from Poly Methyl Methacrylate and Cyclic Olefin Polymer slabs using a Trotec Speedy 100 and adhered together using a biocompatible adhesive.

The Organ-on-Chip chambers were then filled with a prepolymer formulation consisting of Polyethene glycol diacrylate (PEGDA) and the LAP photoinitiator. A custom stereolithographic setup, obtained by mounting a commercial projector (E4500MKII, EKB Technologies Ltd) on the infinity port of an inverted microscope (Leica Dmi8), permitted the patterning of UV light on the surface of the Chip and locally generated the hydrogel (see Fig.1).

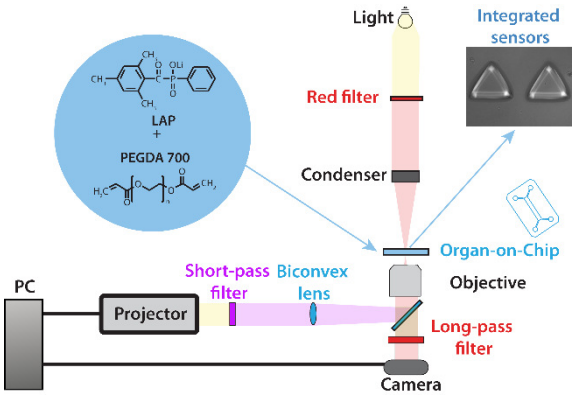

Fig. 1. A scheme of the concept of the experimental setup for integrating the hydrogel sensor and deliverer. The patterned UV light from the projector is focused on the Organ-on-Chip to crosslink the hydrogel. Red-filtered light from an inverted microscope enables monitoring their growth.

Fluorescence images of the sensors were acquired at different drug concentrations in the channels usually associated with FITC and RHOD. A machine learning algorithm was trained to recognise the sensors against the background, extract different geometric regions, and estimate the concentrations of doxorubicin and curcumin.

This model was then used to track drug delivery during a dynamic microfluidic experiment, in which the drugs were allowed to flow through the chambers using syringe pumps at a flow rate of 100 µL/min.

Results

Once the images of doxorubicin and curcumin absorption were obtained, we observed that both fluorescence channels were excited by the drugs. To better separate the information for the two case studies, we used a Partial Least Squares model, obtaining good predictive performance (RMSE = 3.83 ± 1.51 µM in a 10-fold test; see Fig. 2).

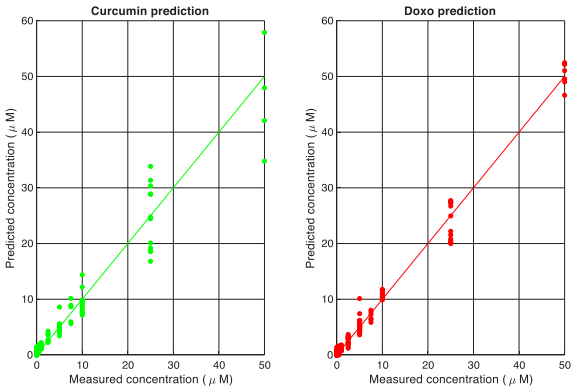

Fig. 2: The performances of prediction for curcumin and doxorubicin prediction using a PLS model. Performances are shown in test.

We could so exploit this model to track the absorption and release of the drugs within a dynamic microfluidic environment (See Fig. 3).

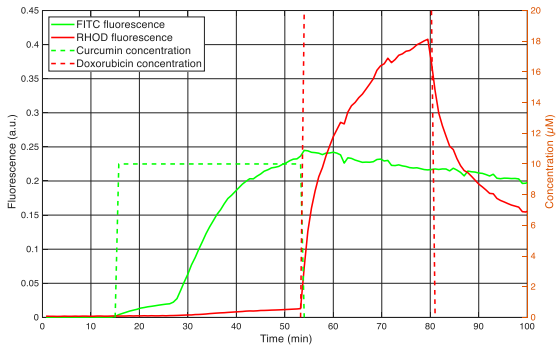

Fig. 3: The evolution of the absorbed/desorbed drugs during a dynamic drug experiment.

The developed model enabled real-time spatio-temporal monitoring of drug distribution within the chip, providing a quantitative description of the absorption and release dynamics during the experiment.

References

[1] D.E. Ingber, Human organs-on-chips for disease modelling, drug development and personalized medicine, *Nature Review Genetics* 23, 467-491 (2022), doi: 10.1038/s41576-022-00466-9

[2] S. Ling et al., Toward continuous monitoring systems: emerging trends of on-chip sensors in organ-on-a-chip, *Microsystems and Nanoengineering* 12 (2026), 61, doi: 10.1038/s41378-025-01142-8

[3] G. Antonelli et al., Continuous pH Monitoring in Organ-on-Chip Devices with Single-Step Fabricated DNA Scaffold Sensors Conjugated Hydrogels and Machine Learning, *Advanced Functional Materials* 35 (2025), 36, 2501659, doi: 10.1002/adfm.202501659

[4] R. Klippstein et al., doxorubicin enhances curcumin's cytotoxicity in human prostate cancer cells in vitro by enhancing its cellular uptake, *International Journal of Pharmaceutics* 514 (2016), 1, 169-175, doi: 10.1016/j.ijpharm.2016.08.003

DOI 10.5162/eurosensors2026/Mo–MLO–02

Microwell for EIS Based Viability Analysis of Cells

Lilia Bató[1,2], János M. Bozorádi[1,2], Zoltán Vizvári[3] Péter Fürjes[2]
[1] Microsystems Lab., Inst. Of Technical Physics and Material Science, HUN-REN Centre for Energy Research, Budapest, Hungary
[2] Óbuda University Doctoral School on Materials Science and Technologies, Budapest, Hungary
[3] Óbuda University, Bioimpedance Technologies Research Center, Budapest, Hungary
Corresponding Author: bato.lilia@ek.hun-ren.hu

Summary:

Microphysiological systems enable advanced in vitro studies for drug development and personalized medicine with integrated sensors that allow real-time monitoring of cell behavior in a microfluidic environment. This work presents a compact microwell platform with integrated platinum microelectrodes for electrochemical impedance spectroscopy analysis of cultured cells. The custom designed electronic board enabled real-time EIS measurements on MES-SA human uterine cervical sarcoma cells. In case of UV-irradiation the cells showed decreased impedance, indicating cytoplasmic release and increased ionic concentration.

Keywords: electrochemical impedance spectroscopy (EIS), microphysiological systems, cell viability, integrated electrodes, microfluidics

EIS analysis of cell cultures

Microphysiological systems designed for the examination of in vitro cell cultures represent a significant advancement in drug discovery, screening, and the development of therapeutic applications [1]. Application-oriented devices integrating microfluidic and sensing systems are capable of maintaining cell cultures and tissues under artificial conditions, exposing them to various chemical agents, and monitoring their behavior in real time. This multifunctional operation is essential in personalized medicine and drug development [2].

Electrochemical Impedance Spectroscopy (EIS) is a powerful technique for characterizing physiological properties of cells and cell cultures through their frequency-dependent electrical parameters, while also enabling non-invasive, real-time monitoring. By incorporating integrated microelectrodes, these microfluidic systems become capable of performing impedance-based cell analysis on single cells or cell cultures [3].

Our work demonstrates the applicability of compact microelectrode system for viability testing of cell cultures.

Fabrication and validation of integrated system for EIS analysis

In this work, we present a compact, microwell-based microphysiological platform with an integrated platinum microelectrode array for real-time EIS measurements (Fig. 1.). Pt electrodes were fabricated on Borofloat™ glass by vacuum sputtering and lift-off lithography. The microwells are made by milling a narrowing cone of 4 to 3 mm into a 6 mm tall polycarbonate cube by CNC machine. The microwell was fixed to the glass chip using a biocompatible Norland UV Curig Adhesive. The electrodes were connected to the PCB by wire bonding. All measurements were performed using the custom-designed PCB.

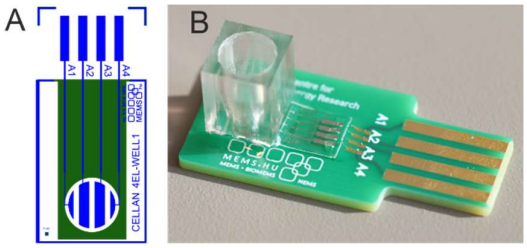

Fig. 1. (A) The layout of the system (green) and the electrodes (blue) and (B) the device itself presenting the PCB and the microwell on top of the chip

The influence of a 30-minute UV irradiation (253.7 nm) on cell viability was tested by following the EIS signal of MES-SA human uterine cervical sarcoma cells cultured in DMEM medium. The microwells were filled with 200 µl of cell solution. Time-resolved EIS measurements were performed before and after

the UV irradiation of an example system and was compared to a control system that received no light exposure. Measurements were made by a PalmSense4 potentiostat. The impedance of the system was measured immediately after the irradiation, after 2 hours and 3 hours and finally overnight incubation of the cells at 37°C temperature and 5% CO_2 environment. To minimize the evaporation, the chips were placed into a Petri dish with wet tissues and then sealed by Parafilm between measurements to keep the humidity constant and to decrease evaporation.

Results

Measurements against a control revealed differences in the EIS measurments of the UV irradiated sample. The control showed no significant diffrence even after 3 hours while the cells exposed to UV showed a decrease in impedance and a shift in phase (Fig. 2-4.). The change is caused by the death of cells due to UV light exposure that leads to cytoplasmic release and thus increased ionic concentrations. Slight changes are present in the control spectra as well, either signifying cell death independent of the irradiation or the slight evaporation of the medium changing the spectra.

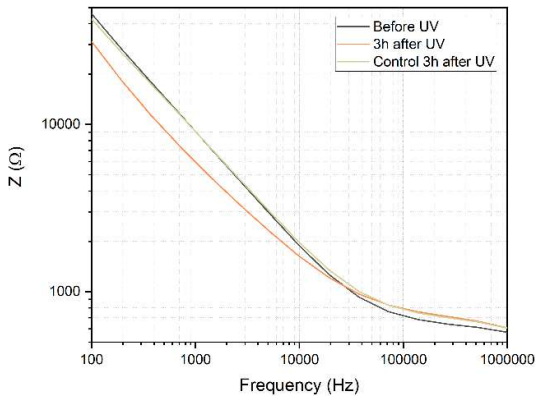

Fig. 2. Difference in impedance of the control and the UV irradiated system before and after 3 hours of light exposure.

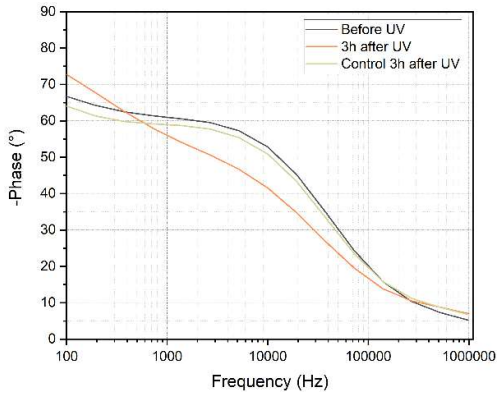

Fig. 3. Difference in phase of the control and the UV irradiated system before and after 3 hours of light exposure.

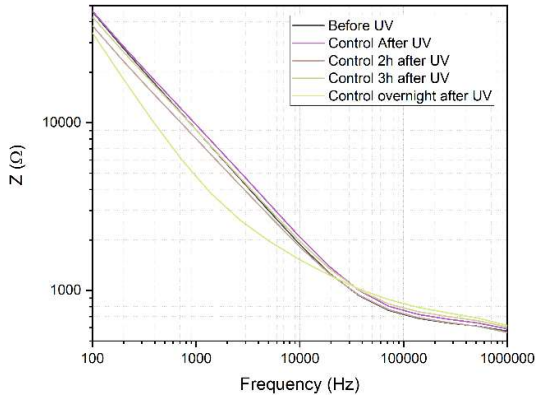

Fig. 4. Difference in impedance of the control system before and after light exposure.

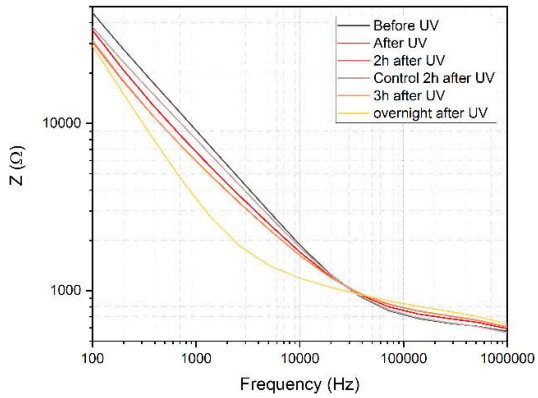

Fig. 5. Difference in impedance of the UV irradiated system before and after light exposure.

Based on the experiments, the system is suitable for longterm mointoring of cells with EIS. In order to follow the changes optically, we are considering modifying the electrodes from Pt to ITO for its transparency. This way the cells could be observed with an inverted microscope that would allow optical characterization with fluorescence methods as well.

References

[1] N. Azizipour, R. Avazpour, D. H. Rosenzweig, M. Sawan, A. Ajji, Evolution of Biochip Technology: A Review from Lab-on-a-Chip to Organ-on-a-Chip, *Micromachines,* 11, 599 (2020); doi: 10.3390/mi11060599

[2] X. Li, H. Zhu B. Gu, C. Yao, Y. Gu, W. Xu, J. Zhang, J. He, X. Liu, D. Li, Advancing Intelligent Organ-on-a-Chip Systems with Comprehensive In Situ Bioanalysis, *Advanced Materials,* 36, 599 (2024); doi: 10.1002/adma.20230526

[3] Z. Zhang, X. Huang, K. Liu, T. Lan, Z. Wang, Z. Zhu, Recent advances in electrical impedance sensing technology for single-cell analysis, *Biosensors,* 11, 470, (2021); doi: 10.3390/bios111104

DOI 10.5162/eurosensors2026/Mo−MLO−03

Acquisition System for Real-Time Monitoring of Glucose and Lactate in Recirculating Multi-Organ-on-Chip

Killian Montiège[1], Valentin Saunier[2], Matthieu Raoux[2], Antoine Pirog[3], Sylvie Renaud[1],
[1] Univ. Bordeaux, Bordeaux INP, CNRS, IMS, UMR 5218, Talence, France
[2] Univ. Bordeaux, Bordeaux INP, CNRS, CBMN, UMR 5248, Pessac, France
[3] ICL, JUNIA, Université Catholique de Lille, LITL, F-59000 Lille, France
killian.montiege@u-bordeaux.fr

Summary:

This study presents a multi-channel electrochemical acquisition system for glucose and lactate biosensing in Multi-Organ-on-Chip (MOoC) platforms. A custom potentiostat-based setup achieving a theoretical current resolution of 3 pA over a ±500 nA range. Comparative tests with a commercial system show fast (<40 s), stable, and linear responses with R^2=0.9992 in both glucose and lactate. The system was designed as the core instrumentation of a diabetes-focused MOoC, with flexibility for further sensor integration.

Keywords: electrochemical sensing, real-time, multi-organ-on-chip, recirculation, online acquisition

Introduction/Background

The emergence of Multi-Organ-on-Chip systems offers a powerful platform for studying complex, systemic diseases such as diabetes by recreating dynamic interactions between multiple tissues in vitro [1]. In this context, continuous and reliable monitoring of key metabolic biomarkers, such as glucose and lactate, is essential to capture organ cross-talk and metabolic regulation in real time. In particular, electrochemical biosensors are well-suited for this purpose due to their high sensitivity and compatibility with microfluidic environments. However, current MOoC platforms still largely rely on off-chip, end-point, and offline measurements, limiting temporal resolution and preventing true in situ analysis. Which is essential when MOoC are configured for fluid recirculation to better mimic closed-loop interactions between organs. This work addresses these shortcomings through the development of a customizable, multi-channel electrochemical acquisition system tailored for sensing in microfluidic MOoC applications under continuous flow and in recirculation.

Materials and Methods

Our MOoC sensing platform relies on a first-generation electrochemical glucose and lactate sensor (*B.LV5*, *Jobst Technologies*), selected for its microfluidic flow compatibility and reliability. Measurements were performed using a custom-developed acquisition system (Fig. 1) based on a digitally tunable potentiostat (−1.5 V to +1.5 V) and six acquisition channels. Each channel consists of a transimpedance amplifier (TIA), a low-pass filter (LPF), and a differential input to an 8-channel, 24-bit sigma-delta ADC. The system is completed and powered with an *ESP32-S3-DevKitM-1* for hardware management and USB communication. Our design is derived from the open hardware, single-channel acquisition board *DStat* [2] (licensed under the CERN OHL v.1.2.), although the original ATmega-based firmware and software were not retained in our implementation. Because of the ADC architecture, channels are sampled sequentially. However, the high effective sampling rate (~1 ms/channel) is sufficient relative to the enzymatic response time for quasi-simultaneous acquisition. The TIA with its 3-fA input bias current precision amplifier LMP7721 coupled with the 3 MΩ current/voltage gain and the low noise 24b ADC (21.8b effective resolution) gives a theoretical current resolution of ~3 pA over a ±500 nA range.

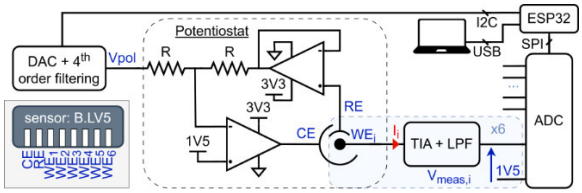

Fig. 1. *Acquisition system architecture and connections to the enzymatic sensor.*

Firmware was developed in C with the Espressif IoT Development Framework as core and a graphical user interface (GUI) was developed in

Python for sampling configuration, electrode selection, real-time visualization, and data logging.

Experimental setup

The system's linearity and response time were evaluated under flow (10 µL/min) at room temperature using a peristaltic pump (*ISMATEC, Reglo ICC*), the *B.LV5* sensor, a custom microfluidic chip (cell-free), and a flow meter (*Sensirion, LG16-0430D).* A solution designed for hepatic gluconeogenesis experiments was used for sensor calibration. It had the following composition, SILAC RPMI 1640 Flex media (*A24942-01, Fisher*) supplemented with Bovine Serum Albumine 0.5% w/v, DMSO 0.5% v/v, Penicilin 100U/mL, Streptomycin 100 µg/mL, Amphotericin 0.25 µg/mL, 10 mM HEPES, 1 mM Pyruvate and 10 µM Forskolin. pH was checked as being at 7.4 before experiments. Several solutions this of medium containing varying concentrations of glucose, lactate, or a mixture of both were prepared to characterize sensor response. Punctual measurements were performed after the sensor reached steady state, with response times not exceeding 40 s across the tested range (Fig. 2A). For comparison, the same protocol was performed using the commercial acquisition system provided by the sensor manufacturer (SIX Biotransmitter).

Results

In both cases the sensor demonstrated linearity (R^2>0.9966) over the range of measurements and near identical models (Fig. 2B and 2C). A linear model was used for this concentration range, although a Michaelis–Menten model may be more appropriate for broader, non-linear ranges in enzyme-catalyzed systems or with different medium [3].

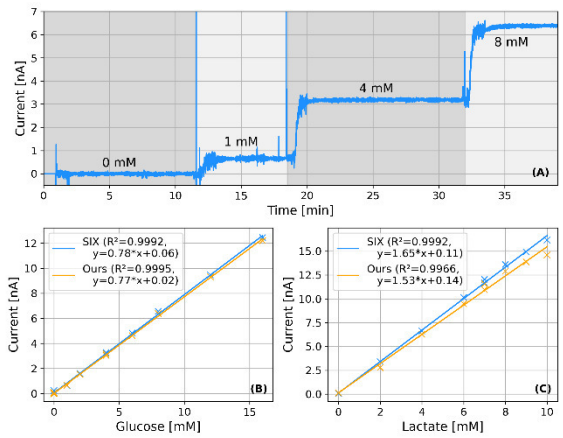

Fig. 2. *(A) Glucose sensor raw response for successive glucose solutions. Linear model of the sensor response for glucose (B) and lactate (C) for two acquisition systems: our system and the commercial reference (SIX Biotransmitter).*

Conclusion and Outlook

This study presented an acquisition system for the real time monitoring of biomarkers in MOoCs. It demonstrated excellent stability and linearity in the physiological range of the tested biomarkers.

Unlike the commercial system, our potentiostat's reference tension is tunable over a −1.5 V to +1.5 V range, enabling the exploration of additional electrochemical and enzymatic sensing modalities. In particular, one of our initial objectives is the development of an integrated oxygen sensor for MOoC applications.

To validate compatibility with recirculating MOoC applications, hepatic gluconeogenesis experiments in recirculation are in progress. In the medium and experimental conditions of these experiments, cell-free controls have already been performed (Fig. 3) and have allowed us to evaluate the lactate sensor drift at 0.11 mM/h. This drift is consistent with that announced by the manufacturer (0.15 mM/h), which further confirm the need to calibrate these sensors for every experimental session.

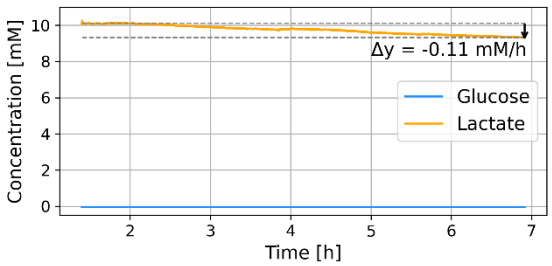

Fig. 3. *Cell-free control gluconeogenesis in a recirculation loop.*

References

[1] Lu, S., Dugan, C. E., Kennedy, R. T. 'Microfluidic Chip with Integrated Electrophoretic Immunoassay for Investigating Cell–Cell Interactions', *Anal. Chem.* 2018, *90* (8), 5171–5178; doi: doi.org/10.1021/acs.analchem.7b05304.

[2] M. D. M. Dryden and A. R. Wheeler, 'DStat: A Versatile, Open-Source Potentiostat for Electroanalysis and Integratio', *PLoS ONE*, vol. 10, no. 10, p. e0140349, 2015; doi: 10.1371/journal.pone.0140349.

[3] Heller, A., Feldman, B. 'Electrochemical Glucose Sensors and Their Applications in Diabetes Management', *Chem. Rev.* 2008, *108* (7), 2482–2505; doi: doi.org/10.1021/cr068069y.

Acknowledgements

This work was funded by ANR DIAMOCHIP (ANR-22-CE19-0032).

DOI 10.5162/eurosensors2026/Mo–MLO–04

Centrifugal Microfluidic Automation of Protein Sample Preparation for Nanopore Sensing

Carolin Kleber[1], Carolin Hensel[1], Ida Suppanz[3], Michelle Hinrichs[2], Sebastian Gutsch[2], Tobias Hutzenlaub[1,2], Felix von Stetten[1,2], Nils Paust[1,2], Gerhard Mittler[3], Andreas Schreiber[1,2], Jan-Niklas Klatt[1,2]
[1] Laboratory for MEMS Applications, IMTEK-Department of Microsystems Engineering, University of Freiburg, Georges-Koehler-Allee 103, 79110 Freiburg, Germany,
[2] Hahn-Schickard, Georges-Koehler-Allee 103, 79110 Freiburg, Germany,
[3] Max Planck Institute of Immunobiology and Epigenetics, Stübeweg 51, 79108 Freiburg, Germany,

Summary:
We present a microfluidic LabDisk automating the solid-phase-enhanced sample preparation (SP3) workflow for nanopore sensing. Using myelin basic protein (MBP), the system produces nanopore-compatible samples preserving membrane stability and enabling reliable detection with the aerolysin AeL-R220S nanopore variant. A distinct MBP peptide marker supports confident identification. Automated and manual workflows show identical nanopore signals ($I/I_0 \approx 0.75$, <0.2 % deviation) and comparable missed cleavage rates, demonstrating robust, standardized, and user-friendly sample preparation.

Keywords: Proteomics, nanopore sensing, microfluidics, sample preparation automation, SP3

Background, Motivation and Objective

Nanopore technology is a biohybride single-molecule sensing platform that enables peptide identification through ionic current modulation across a nanoscale membrane pore [1]. Its universal application as a sensor platform is however limited by the need for detergent-free, highly controlled sample preparation, as detergents used in proteomic workflows can destabilize the sensitive membrane. Moreover, in some measurement setups, nanopores operate in highly diluted electrolyte environments, making analyte enrichment a critical prerequisite for reliable detection. SP3 is a magnetic bead-based method that provides an effective strategy for protein sample preparation with efficient detergent removal [2, 3]. Existing SP3 automation approaches based on liquid handling systems [4, 5] improve throughput and reproducibility but rely on complex instrumentation, large reagent volumes and manual intervention during critical steps. We hypothesize that using a microfluidic system with beads confinement in a column format enables precise handling and efficient processing of miniaturized sample volumes, thereby establishing a scalable route toward automation of sample preparation workflows for nanopore biosensing.

Description of the New Method or System

As illustrated in Fig. 1, the manual SP3 workflow and subsequent nanopore measurements are shown. The LabDisk enables full automation of the SP3 workflow, covering MBP sample processing from denaturation to peptide recovery (n=1/disk). The process begins with manually loading 40 µg MBP sample, bead suspension, digestion mixture and alkylation, reduction mixture into the LabDisk, which is then sealed and inserted into the analyzer. Fluid handling is governed by a combination of thermally induced pneumatic pressure and centrifugal force following a pre-defined protocol. First, denaturation, reduction and alkylation of the protein solution is performed in the incubation chamber, illustrated in Fig. 2. From there, the solution is transferred into the bead column chamber containing 8 µl carboxylated magnetic beads (>37 µm), which are retained by microchannels. Upon release of the binding buffer (acetonitrile) from preloaded stickpacks, it is transferred to the column chamber, where it mixes with the sample and facilitates protein binding to the beads. The bead column is then washed, and the tryptic digestion medium is transferred onto the beads, where digestion is carried out for one hour at 37°C, reducing the total workflow time compared to conventional overnight digestion. Finally the miniaturized peptide eluate (~14 µl) is centrifuged and collected in the outlet chamber from which it can be retrieved.

Results

Nanopore analysis of LabDisk and manually processed samples confirmed full compatibility with nanopore measurements and effective contami-

nant removal by the SP3 workflow. A characteristic peak pattern was observed for both sample types, with peak 4 at $I/I_0 \approx 0.75$ showing <0.2 % deviation across all replicates (n = 10 technical replicates from 3 biological samples) (Fig.3) Spike-in experiments with synthetic peptides identified peak 4 as MBP [H24–R29], establishing it as a unique marker for MBP identification. [3] Data were complemented by LC-MS/MS analysis revealing comparable digestion performance with 40.6 ± 6.4 % (LabDisk) vs. 35.5 ± 1.3 % (manual) missed cleavages, demonstrating equivalent digestion quality. The observed digestion efficiency is consistent with the deliberately shortened 1 h digestion time, chosen to accelerate the workflow. This work demonstrates the proof-of-principle for automated, microfluidic sample preparation enabling reliable peptide identification by nanopore sensing.

Illustrations, Graphs, and Photographs

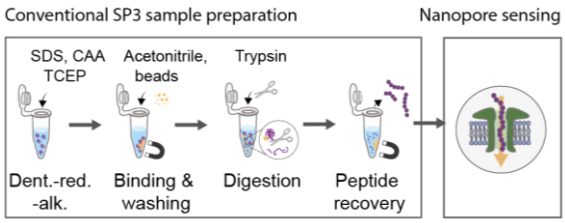

Fig. 1. Schematic of the manual SP3 workflow including denaturation, reduction and alkylation followed by binding, washing, digestion and peptide recovery. The resulting peptides are identified using nanopore sensing. Thereby, a negative voltage is applied across the membrane, causing peptides to translocate electrophoretically through the nanopore. As they pass through, they generate unique current blockades that reflect their physicochemical properties.

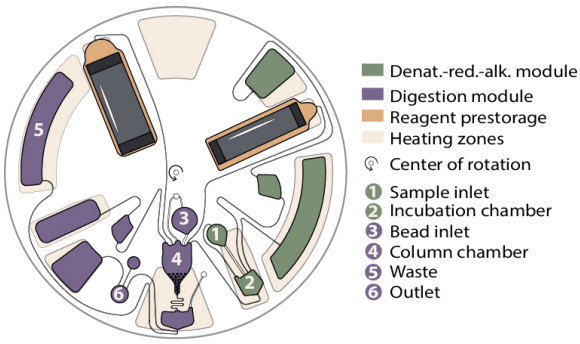

Fig. 2. Illustration of the LabDisk layout comprising modules for denaturation, reduction and alkylation (green), as well as SP3 digestion (purple). Magnetic beads are mechanically retained by filter channels, forming a bead column for solid-phase extraction. Liquid transfer is driven by a combination of thermally induced pneumatic pressure and centrifugal force.

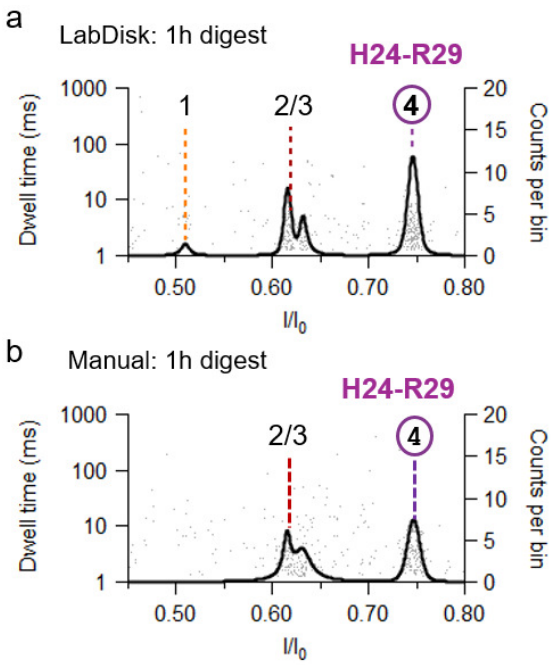

Fig. 3. Nanopore measurements of tryptic MBP digests were performed using the AeL-R220S pore in 4 M KCl, 100 mM Tris (pH 7.5) at −60 mV. Dwell time versus I/I_0 scatter plots with Voigt fits are shown for samples prepared via automated LabDisk and manual workflows. A 5 µL aliquot was analyzed in each case, corresponding to estimated well concentrations of 3.90 µM (LabDisk) and 1.09 µM (manual), reflecting differences in final eluate volumes (14 µL vs. 50 µL).

References

[1] Afshar Bakshloo M, Kasianowicz JJ, Pastoriza-Gallego M, Mathé J, Daniel R, Piguet F, Oukhaled A., Nanopore-Based Protein Identification, *J Am Chem Soc.*, 144, 2716-2725 (2022); doi:10.1021/jacs.1c11758

[2] Hughes, C., Moggridge S., Müller T., Sorensen P., Morin G., Krijgveld J., Single-pot, solid-phase-enhanced sample preparation for proteomics experiments, *Nature Protocols,* 14, 68-85 (2019); doi: 10.1038/s41596-018-0082-x

[3] Hensel, C, Kleber C, Suppanz I, Gutsch S, Hutzenlaub T, Behrends JC, von Stetten F, Mittler G, Klatt JN, Schreiber A, Sample preparation for direct nanopore based identification of a biological protein via tryptic peptide recognition, *in prep.*

[4] Müller T, Kalxdorf M, Longuespée R, Kazdal DN, Stenzinger A, Krijgsveld J., Automated sample preparation with SP3 for low-input clinical proteomics, *Mol Syst Biol.* 16 (2020); doi:10.15252/msb.20199111

[5] Reder A, Hentschker C, Steil L, Gesell Salazar M, Hammer E, Dhople VM, Sura T, Lissner U, Wolfgramm H, Dittmar D, Harms M, Surmann K, Völker U, Michalik S., MassSpecPreppy-An end-to-end solution for automated protein concentration determination and flexible sample digestion for proteomics applications, *Proteomics*, 24 (2024); doi: 10.1002/pmic.202300294.

DOI 10.5162/eurosensors2026/Mo–MLO–05

Integrated Resistive Heating Systems in a Microfluidic Platform for Biological Applications

Michał Żółtowski [1], Adrianna Cieślak [2], Agnieszka Krakos [1], Jerzy Detyna [2], and Rafał Walczak [1]

[1] Department of Microsystems, Faculty of Electronics, Photonics and Microsystems, Wrocław University of Science and Technology, Wrocław, Poland.

[2] Department of Mechanics, Materials and Biomedical Engineering, Faculty of Mechanical Engineering, Wrocław University of Science and Technology, Wrocław, Poland.

adrianna.cieslak@pwr.edu.pl

Summary:

In contrast to traditional heating solutions described in the literature, which often rely on complex and time-consuming lithographic processes or metal thin-film deposition [1], this work utilizes the innovative technology of rapid, direct printing of carbon nanotube (CNT) resistive heaters onto a glass substrate. This method offers the tremendous advantage of unparalleled flexibility in forming heaters of arbitrary shapes. By integrating these heaters into a microfluidic LOC platform, we provide a reliable system that enables precise temperature control for cell studies, allowing for more advanced *in vitro* research.

Keywords: heating system, carbon nanotubes, lab-on-chip, microfluidics, hydrogels

Background, Motivation, and Objective

Rising cancer rates underscore the urgent need for bioengineering innovations that can faithfully replicate the human physiological environment. In this study, we present a lab-on-chip (LOC) platform designed to push the boundaries of cell engineering. Using advanced and biocompatible hydrogel matrices and microfluidic structures, our platform creates a dynamic microenvironment, providing a crucial link between traditional *in vitro* models and the complexities of living systems. A key aspect and innovation of the presented solution is the adaptation of resistive heater technology for precise biological applications. While previous work by the team focused on thermoresponsive phenomena induced by carbon nanotubes (CNTs) for the rapid micropatterning of hydrogel systems [2], the current approach presents a fully functional, modular research workstation. Its fundamental component is a precise heating system (HS), in which the resistive layer consists of CNTs 3D printed directly onto a glass substrate. This bio-platform is complemented by an external peristaltic pump, which continuously and controllably pumps liquid (culture medium) into the system, accurately simulating the circulation of fluids.

Description of the New Method or System

Figure 1 shows the main components of the developed and advanced LOC platform. As mentioned, the HS of a special design incorporated into the bio-platform was fabricated utilizing the additive manufacturing (AM) technique (Fig. 2).

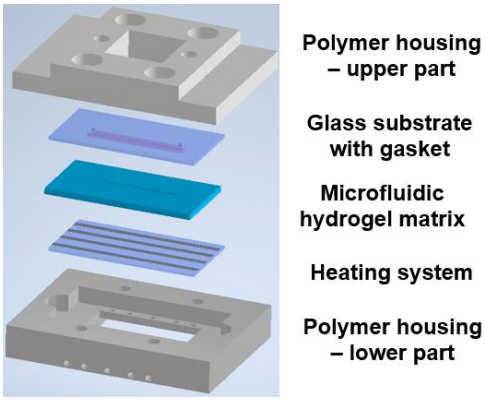

Fig. 1. Microfluidic LOC device scheme.

Conductive layers *(5 layers per HS)* of single-walled carbon nanotubes SWCNTs (OCSiAl's Tuball Batt with 0.4% SWCNT and 0.8% poly(vinylpyrrolidone) (PVP) in H_2O) of various geometries were extruded on the borosilicate glass substrate (Borofloat 3.3 glass), being a part of the sandwiched type platform with hydrogel matrix. The extrusion parameters were as follows: printing speed 5 mm/s, nozzle temperature 28 °C, print bed temperature 30 °C, printing pressure 25 – 30 kPa, and nozzle size 0.25 mm.

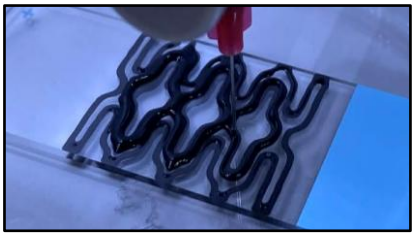

Fig. 2. Extrusion of the SWCNT.

To validate the platform's capabilities, diverse flow tests were conducted using water and a cultivation medium by the standard gravimetric method. The flow speed was set to 50 µL/min.

Results

Using AM technology, three types of such heaters were manufactured and tested, as shown in Fig. 3.

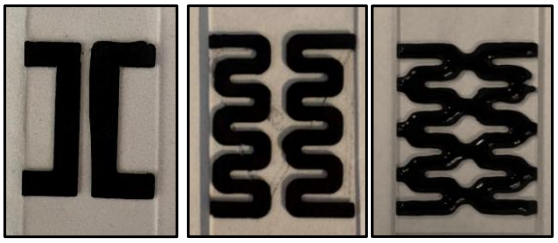

Fig. 3. Conductive layers of the HS with varying geometries: simple, meander, and connected.

Representative dimensions of a simple heater are shown in Fig. 4. Furthermore, the 3D printing fidelity of the heaters was evaluated by comparing the fabricated geometric dimensions with their nominal values specified in the design files. For simple heaters, the dimensional deviation was merely about 3%. However, for arbitrary, more complex patterns, which represent a core advantage of this technique, the deviation reached over 14% due to material spreading on rounded edges during the 3D printing process.

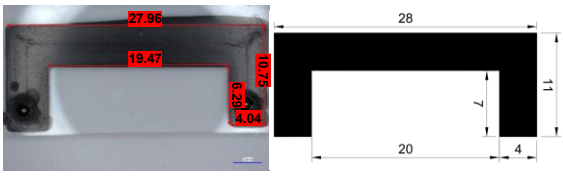

Fig. 4. Representative dimensions of a resistive heater [mm].

Electrical connections were implemented using two distinct methods: a standard mechanical connection utilizing alligator clips and a customized, low-resistance soldered connection. Notably, the measured resistance of the heaters was, on average, ≈ 27% higher with alligator-clip connections than with non-standard soldered joints. The soldered joint (≈ 1 mm in height) significantly facilitates the soldering of a lead wire and ensures a highly reliable ohmic contact, a notable achievement when working with carbon-based materials.

The heaters were driven by a DC voltage of up to 20 V, and the power dissipated within them results from the flow of electric current according to the Joule-Lenz law. The electrical power consumption and all relevant heater parameters are summarized in Tab. 1. By optimizing the power supply parameters, a target surface temperature of ≈ 30 °C was successfully attained on the glass substrate for all heater configurations, confirming the high efficacy of this direct-write approach.

Tab. 1: Resistive heater parameters

Parameter	Simple	Simple	Meander	Meander	Connected
	Soldered joint	Alligator clip	Soldered joint	Alligator clip	Alligator clip
Average absolute dimensional deviation [%]	-2.84	-1.36	10.68	7.94	14.45
Resistance value [Ω]	138.5	207.5	501.5	661.0	255.0
Electric power [mW]	12.44	13.32	25.14	31.45	17.53
Temperature [°C]	30.2	29.8	30.9	30.1	30.3

The flow characteristics of the tested liquids are shown in Fig. 5, exhibiting a positive correlation between the mass increase over time. The highest flow rate was observed for the culture medium. In turn, water flow exhibits the best consistency between the pumped mass and the set flow rate (50 µL/min).

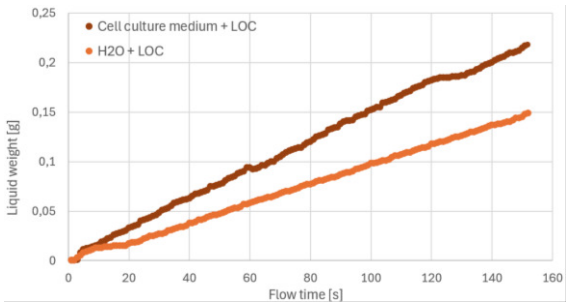

Fig. 5. Positive results of microflows for water and cultivating medium.

References

[1] S. Khan *et al.*, Technologies for Printing Sensors and Electronics Over Large Flexible Substrates: A Review, *IEEE*, 15, 6, 3164-3185 (2015); doi: 10.1109/JSEN.2014.2375203.

[2] M. Żółtowski *et al.*, Rapid hydrogel micropatterning utilizing CNT-induced thermoresponsive effect, *Scientific Reports*, (2026); doi: 10.1038/s41598-026-47758-2.

DOI 10.5162/eurosensors2026/Mo–MLO–06

A miniaturized portable device for continuous sensing of environmental contaminants

Manel López[1], Angel Diéguez[1], J.-Pablo Salvador[2], Giacomo Saviozzi[3]
[1] Departament d'Enginyeria Electrònica I Biomèdica, Universitat de Barcelona, Spain
[2] Nanobiotechnology for diagnostics (Nb4D), IQAC, CSIC, Barcelona, Spain
[3] Marine Robotics, The BioRobotics Institute, Scuola Superiore Sant'Anna (SSSA),Pontedera, Italy

Summary:

This paper presents a compact, low-cost, and low-power device for multiplexed in situ detection of environmental contaminants in seawater. The system integrates microfluidics, electronics, and amperometric biosensors to perform up to eight simultaneous measurements. A novel pulsed-flow method ensures uniform fluid distribution across sensor chambers while reducing energy consumption. The device demonstrates good reproducibility (CV ~7%) and comparable performance to commercial potentiostats. Its portable design enables autonomous operation for real-time environmental monitoring. The platform shows strong potential for scalable and field-deployable biosensing applications.

Keywords: Lab-on-a-chip, time multiplexing, electrochemical sensors, environmental measurements

Introduction

In the last decade, the environmental, economic, and societal importance of marine ecosystems—particularly in Europe—has increased, with sectors such as aquaculture and fisheries strongly impacted by water quality [1]. Chemical contamination of coastal waters poses significant risks to ecosystems and public health, creating a need for early-warning systems capable of providing reliable, real-time data. Conventional analytical techniques, such as chromatography coupled with mass spectro-metry, offer high sensitivity but are limited by cost, complexity, and lack of in situ applicability [2].

To address these limitations, electrochemical biosensors, especially immunosensors, have emerged as promising alternatives due to their miniaturization, low power consumption, and suitability for field deployment [3]. Combined with microfluidic technologies, they enable automated handling, improved accuracy, and continuous monitoring. In this context, this work presents a validated, compact, low-cost, and low-power device for simultaneous detection of multiple contaminants in seawater. The proposed platform integrates microfluidics, electronics, and amperometric biosensors into a multiplexed system. A key contribution is the introduction of a pulsed-flow method that ensures uniform fluid distribution across multiple sensing chambers while significantly reducing energy consumption, paving the way for scalable and autonomous environmental monitoring solutions.

Description of the System

The proposed device is a compact, portable platform designed for in situ and real-time monitoring of environmental contaminants in seawater. It integrates three main subsystems: a microfluidic module, an electronic control system, and an electrochemical sensing unit (Fig. 1). The module is responsible for handling and distributing the liquid samples and reagents through a network of channels, valves, and a peristaltic micropump. It includes two main manifolds: a mixing manifold, where the sample and antibodies are combined, and a sensing manifold, which distributes the processed fluid into eight independent microchambers. Each chamber hosts an electrochemical biosensor, enabling simultaneous multiplexed measurements. The electronic system is divided into two custom-designed systems (PCBs): The Sensor Unit (SU) and the Central Unit (CU). The SU is based on a 32-bit microcontroller and includes the analog front-end, implementing a miniaturized potentiostat for amperometric measurements, along with signal conditioning and data acquisition. The CU, also based on a microcontroller, manages the overall operation of the system, including fluidic control (microvalves and micropump), synchronization, power management, and communication with the user interface.

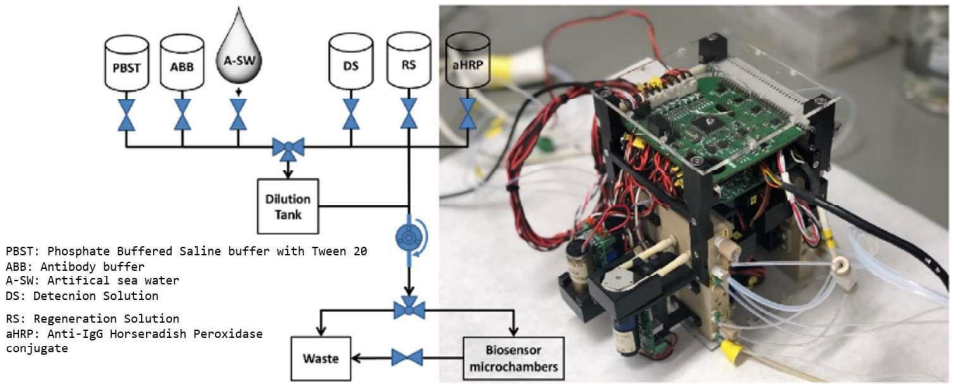

Fig. 1. On the left, the microfluidic schematic of the microfluidic system. On the right, the final device

The measurement method combines amperometric immunosensing with a pulsed-flow technique, where controlled fluid pulses are sequentially delivered to each microchamber instead of continuous flow. This ensures uniform reagent distribution while reducing energy consumption. The analyte interacts with immobilized biomolecules, generating an electrochemical current signal [4-5]. This approach enables reproducible parallel detection across multiple channels with low power consumption and efficient reagent use.

Results

The platform was validated by detecting the marine contaminant Irgarol 1051® as a model analyte. Measurements were performed using an amperometric immunosensing approach [4,5], where the analyte competes with an immobilized antigen (4e-BSA) for binding to a specific antibody (As87). Detection relies on an enzymatic reaction with HRP-labeled secondary antibody, generating an electrochemical current signal in the presence of TMB/H_2O_2 [5], proportional to the analyte concentration. Signal acquisition was performed simultaneously across eight channels using the pulsed-flow multiplexing method, ensuring uniform reagent delivery and consistent conditions. The chronoamperometric response reached a stable regime after an initial transient, with periodic variations due to pulsing. Final signals were extracted from the steady-state region, achieving reproducible results with a coefficient of variation of ~7% across channels. Calibration experiments were conducted by measuring different concentrations of Irgarol 1051®, allowing the construction of dose–response curves for each sensing channel (Fig. 2). The system achieved a mean IC50 of approximately 16 nM and a limit of detection in the sub-nanomolar range.

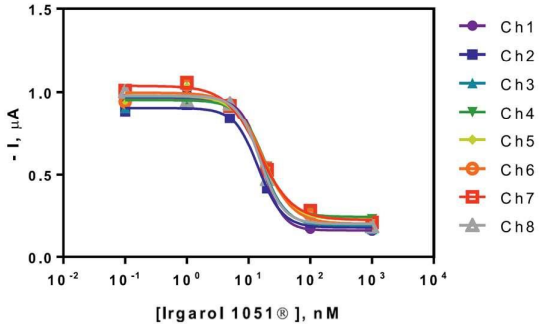

Fig. 2. Calibration curves obtained for the detection of Irgarol 1051® in the eight individual chambers.

The measurements presented in Fig. 2 illustrate the system performance, showing the calibration curves obtained simultaneously across the eight sensors. The consistency between channels demonstrates the robustness of the microfluidic distribution and the reliability of the electronic acquisition system. Overall, the results validate the proposed platform as a suitable solution for low-cost, low-power, and multiplexed in situ environmental monitoring.

Acknowledgments

This paper has been partially funded by the FP7 EU program 614168 and the National Program of Information and Communication Technologies PID2022-136833OB-C21

References

[1] EC. https://eceuropaeu/info/food-farming-fisheries_en, 2020 https://ec.europa.eu/jrc/en/news/eu-aquaculture-report-2020.
[2] M. Farre, L. Kantiani, M. Petrovic, S. Perez, D. Barcelo, J. Chromatogr. A 1259 (2012), 86–99.
[3] M.-P. Marco, S. Gee, B.D. Hammock, Trends Anal. Chem. 14 (1995). 341–350.
[4] P. Fruhmann et al., Anal. Bioanal. Chem. 410 (2018) 5923-5930
[5] J. P. Salvador, M. P. Marco, Electroanalysis 28, (2016) 1833-1838

DOI 10.5162/eurosensors2026/Tu–MLO–01

Electrohydrodynamic oscillatory deformation of viscoelastic droplets as an interfacial microrheometer

Chintak Kamalesh Parashar[1], *Omkar S Deshmukh*[1], *Dipankar Bandyopadhyay*[1*]
[1] *Indian Institute of Technology Guwahati, Guwahati, Assam-781039 India,*
[*]*dipban@iitg.ac.in*

Summary:
A water-based polymer droplet suspended in silicone oil is driven by an AC electric field and used as a non-contact rheological sensor. The work links interfacial Maxwell stress, transient droplet deformation and oscillatory relaxation to viscosity, interfacial tension and elasticity. A perfect-conductor approximation is justified within the experimental range frequency, enabling a compact electromechanical description. The resulting electrohydrodynamic response provides a compact route for classifying liquid-like and solid-like behaviour as well as measure of interfacial tension during relaxation behavior at small volume.

Keywords: electrohydrodynamics, droplet rheometry, viscoelasticity, Maxwell stress, microfluidic sensing

Title

Electrohydrodynamic oscillatory deformation of viscoelastic droplets as an interfacial microrheometer.

Background, Motivation and Objective

Droplet electrohydrodynamics provides a sensitive way to convert electric forcing into a measurable mechanical response through interfacial stress. Classical work by Taylor established that electric-field-induced circulation and deformation depend on the electrical properties of the two phases [1]. More recent studies have expanded this framework to transient AC excitation, finite charge relaxation and high-fidelity small-deformation theory [2,3]. In parallel, microfluidic rheometry has emerged as an attractive route for low-volume characterization of complex fluids [4]. The present work combines these ideas and asks whether the time-dependent deformation of a single droplet can act as a compact sensor for viscosity, interfacial tension and viscoelasticity. The objective is to translate droplet shape dynamics, phase lag and recovery into rheological descriptors that are relevant for publication oriented screening of complex liquids.

Description of the New Method or System

A water-based polymer droplet was suspended in silicone oil and excited at 300 V rms over an external frequency range of approximately 15-500 Hz as shown in Fig. 1. Time-scale analysis using the Maxwell-Wagner relaxation time, bulk charge relaxation and the frequency-dependent Clausius-Mossotti factor indicates negligible polarization lag in this operating window; the droplet can therefore be treated as a nearly perfect conductor. Under electroquasistatic conditions, the electric field generates a normal Maxwell stress jump at the interface, with the strongest tensile stress at the poles and weaker response at the equator [1,2]. The deformation signal is quantified through the standard deformation parameter as a time dependent strain.

Results

Experiments were carried out by varying droplet diameter, viscosity, viscoelasticity, interfacial tension and thereby sample rheology. The transient response shows a DC component in the mean deformation and an AC component in the oscillatory amplitude, consistent with AC EHD theory [2]. Validation against Taylor-type small-deformation behaviour indicates that larger droplets achieve larger peak deformation because the total interfacial electrical loading increases with size, whereas the oscillation magnitude is governed primarily by the surrounding medium viscosity. The creep time increases with both droplet size and oil viscosity, showing that hydrodynamic damping dominates the time required to reach steady oscillation. As the forcing frequency increases, the droplet can no longer follow the field and the oscillation amplitude decreases. For higher elastic droplets the loading and unloading traces nearly collapse, while viscoelastic samples display hysteresis and higher viscous droplets display broader loops, delayed recovery and non-zero area hysteresis. These signatures are consistent with energy storage

and dissipation occurring simultaneously in complex fluids [4]. The relaxation segment after switching off the field is especially informative: fast decay indicates stronger capillary restoration, while slower recovery indicates viscoelastic stress storage and structural reorganization within the droplet

Sensor Implication and Material Classification

The method was examined on DI water, glycerol, honey, sauce, egg white and PVA+borax. Increasing viscosity broadens the temporal response and reduces interface velocity, while increasing elasticity introduces memory between cycles. The most elastic samples exhibit partial recovery after field removal, limit-cycle rotation and oval trajectories with larger eccentricity, all of which are indicative of increasing Deborah number. In this sense, the droplet operates as a soft transducer: the electric field is the calibrated input and the deformation waveform is the sensor output. Compared with a conventional rheometer and DWS measurements, the EHD signal captures the same qualitative progression from fluid-like to solid-like behaviour (as seen in Fig. 1), but with small sample volume and without direct mechanical contact. This makes the platform attractive for rapid screening of biological and food-like fluids where sample amount is limited and interfacial phenomena cannot be ignored.

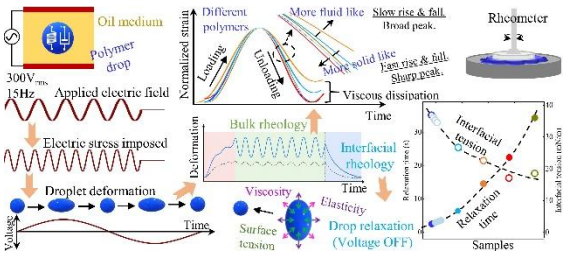

Fig. 1. Schematic of the AC-driven droplet microrheology concept. Interfacial Maxwell stress deforms a conducting polymer droplet in silicone oil, and the resulting waveform is used to infer viscosity and elasticity. Relaxation test is used to infer the surface tension.

Qualitative Material Map

Tab. 1 summarizes the qualitative material progression observed in the study. Low-viscosity samples respond rapidly with narrow loops and negligible recovery, whereas increasingly elastic samples show slower rise and fall, stronger damping and persistent memory during repeated forcing. This trend supports the use of droplet EHD as a compact physical-sensing modality for rheological fingerprinting.

Tables

Tab. 1: Qualitative relation between sample rheology and droplet EHD response

Sample	Dominant property	Observed EHD signature
DI water	High interfacial tension	Fast rise/fall
Honey/ Glycerol	Higher viscosity	Incomplete oscillation
Eggwhite/ PVA+borax	Strong elasticity; Lowest Interfacial tension	Slow rise/fall; Complete oscillation

References

[1] G. I. Taylor, Studies in electrohydrodynamics. I. The circulation produced in a drop by an electric field, Proc. R. Soc. A 291, 159-166 (1966); doi: 10.1098/rspa.1966.0086.

[2] A. Esmaeeli, Transient electrohydrodynamics of a liquid drop in AC electric fields, Eur. Phys. J. E 41, 135 (2018); doi: 10.1140/epje/i2018-11745-1.

[3] D. Das, D. Saintillan, A three-dimensional small-deformation theory for electrohydrodynamics of dielectric drops, J. Fluid Mech. 914, A22 (2021); doi: 10.1017/jfm.2020.924.

[4] F. Del Giudice, P. S. Wilson, A review of microfluidic devices for rheological characterisation, Micromachines 13, 167 (2022); doi: 10.3390/mi13020167.

DOI 10.5162/eurosensors2026/Tu–MLO–02

Finite element modeling, design and characterisation of SAW transducers for acoustofluidic systems

Anita Bányai[1], Eszter Leelőssyné Tóth[1], M. Varga[2], Péter Fürjes[1]

[1] HUN-REN Centre for Energy Research, Microsystems Laboratory, Konkoly Thege Miklós Str. 29-33, H-1121 Budapest, Hungary

[2] 77 Elektronika Ltd., Fehérvári Str. 98, H-1111 Budapest, Hungary

Corresponding author: banyai.anita@ek.hun-ren.hu

Summary:

The aim of our work is to design an interdigital electrode that generates standing waves on a Lithium niobate substrate and enables particle separation in a fluidic channel in the particle range below 4 µm. Before manufacturing the actual fluidic device, the frequency dependence of the designed electrode and the position of the nodes and anti-nodes created by the standing waves excited on the surface were tested FEM simulation using COMSOL code.

Keywords: microfluidic system, particle separation, standing acoustic wave, lithium niobate, FEM simulation

Acoustic waves in microfluidic applications

Among the active separation methods applicable to microfluidic particle separation, acoustophoresis is considered, in which migration can be induced by acoustic pressure waves, without affecting the viability of the applied cells. Surface acoustic waves are more common in microfluidic applications to manipulate flows and the suspended particles, generating droplets [1], enhancing reagent mixing, or managing cell focusing, separation, sorting or target concentration [2], respectively. Moreover, the SAW technology enable sensitive biological or chemical molecule detection.

The generated SAWs (such as Rayleigh waves, Leaky SAW, Love waves, Bleustein–Gulyaev waves) can be used for size dependent separation even in a submicron range [3]. G. Destgeer et al. [4] were able to separate polystyrene beads with a size resolution of only 200 nm (beads with a diameter of 3 µm and 3.2 µm). Shupeng Ning et al. [5] even performed standing surface acoustic waves (SSAWs) in a serpentine microfluidic channels, and separated E. coli bacteria from human RBCs achieving 92.7% purity besides high flow rate.

The advantages of the method are its label-free and contact-free characteristics, and the cells can be focused in physiological solutions without dilution. In terms of reliability and robustness, the method is not extremely sensitive to the composition of the medium, and the vulnerability of living cells is not critical either, since the negligible deflection is performed using acoustic pressure waves.

The method can be widely used for particle capture, but the primary objective is the separation of bacteria from urine from a fairly large sample volume (500 µl). In this case not only the different sizes of the variously shaped elements of urine pose a challenge (60 µm - 1 µm), but also the tight time frame in which the filtration and separation must be performed.

Generation acoustic waves

The acoustic wave theory can describe the formation of bulk (BAW) and surface acoustic waves (SAW) in piezoelectric materials. The SAW waves travel in the surface region, while the BAW waves propagate vertically in the bulk material. The BAW devices are typically used in the higher frequency range over 2 GHz, although for formation surface acoustic waves, the moderated (10 MHz - 1 GHz) frequencies are applicable.

The piezoelectric materials most popularly used in SAW devices include quartz, lithium tantalate (LT, $LiTaO_3$) and lithium niobate (LN, $LiNbO_3$). Also preferred choices are gallium arsenide (GaAs), cadmium sulfide (CdS), zinc oxide (ZnO), lithium tetraborate ($Li_2B_4O_7$), and langasite ($La_3Ga_5SiO_{12}$). SAW devices today not just only utilise the waves propagated along the symmetric crystal, but rather different rotated cuts were discovered and gained popularity in various applications. The SAW related microfluidics application majority use 128° YX LN [6].

For wave generation primarily interdigital transducers (IDT) are used, which are mounted on a piezoelectric substrate. The design of the IDT is quite critical regarding the applications and the adequate propagation of travelling waves (TSAW) or the development the required standing wave pattern in the microfluidic chamber.

In this work the design, fabrication and characterisation of an IDT structure are highlighted, considering its further integration in a microfluidic system. Finite element modelling was applied to define the frequency dependence of the designed electrode system for supporting the microfluidic design and integration.

Design considerations and modelling

An acoustic wavelength was selected considering the 40 µm periodicity of the interdigitated electrode system, having electrode widths and gaps of 10 µm, respectively, and a metal thickness of 200 nm. Considering the SAW phase velocity of $LiNbO_3$ (v_{SAW}=3990 m/s), the expected resonance frequency can be estimated as (1):

$$f = \frac{v_{SAW}}{\lambda} \quad (1)$$

where λ = 40 µm and $f \approx$99.75 MHz.

A single-unit-cell IDT geometry was implemented in COMSOL Multiphysics to evaluate the eigenfrequency spectrum of the device. The piezoelectric response was modelled coupling Solid Mechanics with Electrostatics. A rotated coordinate system was introduced to represent the crystallographic orientation of the 128° YX-cut $LiNbO_3$ substrate. Periodic boundary conditions were applied on the lateral boundaries of the unit cell, while a perfectly matched layer (PML) was introduced at the bottom boundary to suppress artificial wave reflections. The IDT electrodes were driven with an applied potential of 1 V. The material properties of $LiNbO_3$ were assigned according to literature values.

Results

Based on the numerical simulation two surface-localized SAW mode candidates were identified at 97.284 MHz and 98.314 MHz, corresponding to a symmetric and an antisymmetric mode shape, respectively (see Fig. 1).

The IDT systems of the SAW devices is fabricated on $LiNbO_3$ crystal using aluminium electrode materials, and the eigen frequencies are to be characterised by integrated detectors.

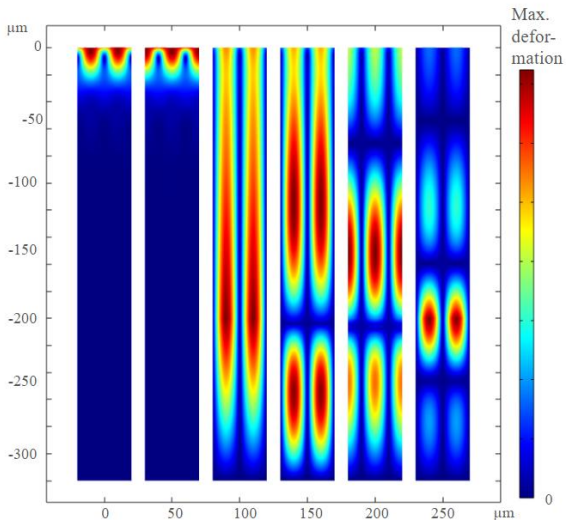

Fig. 1. Calculated eigenmodes visualized at different displacement scales. The first two modes correspond to the identified SAW candidates: the symmetric mode at 97.284 MHz and the antisymmetric mode at 98.314 MHz. The remaining modes are bulk acoustic modes with different nodal distributions, appearing at 101.90 MHz, 102.15 MHz, 102.67 MHz, and 103.38 MHz.

References

[1] K. Chen, C. Sui, Y. Wu, Z. Ao, S. Guo, and F. Guo, ‘A digital acoustofluidic device for on-demand and oil-free droplet generation’, *Nanotechnology*, vol. 30, no. 8, Art. no. 8, Feb. 2019, doi: 10.1088/1361-6528/aaf3fd.

[2] Y. Chen *et al.*, ‘Continuous enrichment of low-abundance cell samples using standing surface acoustic waves (SSAW)’, *Lab. Chip*, vol. 14, no. 5, pp. 924–930, 2014, doi: 10.1039/C3LC51001H.

[3] T. Zhang *et al.*, ‘Focusing of sub-micrometer particles in microfluidic devices’, *Lab. Chip*, vol. 20, no. 1, Art. no. 1, 2020, doi: 10.1039/C9LC00785G.

[4] G. Destgeer, B. Hang Ha, J. Ho Jung, and H. Jin Sung, ‘Submicron separation of microspheres via travelling surface acoustic waves’, *Lab. Chip*, vol. 14, no. 24, Art. no. 24, 2014, doi: 10.1039/C4LC00868E.

[5] S. Ning, S. Liu, Y. Xiao, G. Zhang, W. Cui, and M. Reed, ‘A microfluidic chip with a serpentine channel enabling high-throughput cell separation using surface acoustic waves’, *Lab. Chip*, vol. 21, no. 23, pp. 4608–4617, 2021, doi: 10.1039/D1LC00840D.

[6] W. Connacher *et al.*, ‘Micro/nano acoustofluidics: materials, phenomena, design, devices, and applications’, *Lab. Chip*, vol. 18, no. 14, pp. 1952–1996, 2018, doi: 10.1039/C8LC00112J.

DOI 10.5162/eurosensors2026/Tu–MLO–03

Towards a Bronchus-on-a-Chip Device with Integrated Sensing for Monitoring of the Cell Culture

Elisa Simioni[1,2,4], Suzana Macuvele[2,3], Arsénio M. Fialho[2,3], Catarina R. F. Caneira[1]
[1] Instituto de Engenharia de Sistemas e Computadores – Microsistemas e Nanotecnologias (INESC MN), Rua Alves Redol, 9, 1000-029 Lisbon, Portugal,
[2] Institute for Bioengineering and Biosciences (iBB), Instituto Superior Técnico, Avenida Rovisco Pais 1049-001, Lisbon, Portugal
[3] Department of Bioengineering, Instituto Superior Técnico, University of Lisbon, Lisbon, Portugal
[4] Department of Information Engineering, University of Padova, Padova, Italy
elisa.simioni@tecnico.ulisboa.pt

Summary:
This work presents a proof-of-concept Organ-on-a-Chip platform for culturing epithelial bronchial cells and modelling bacterial adhesion in the human airway epithelium under physiologically conditions. The project focuses on device production and integration of an interdigitated electrode sensor, fabricated through lift-off process. The system aims to overcome the limitations of conventional static in vitro models by incorporating continuous flow. Future developments will assess anti-adhesive therapies.

Keywords: Microfluidics, Cyclic Olefin Copolymer, Impedance sensing, Interdigitated electrodes, 16HBE14o- cell line

Background, Motivation and Objective

Respiratory infections are a major global health concern, particularly in patients with chronic lung diseases such as cystic fibrosis, where impaired mucociliary clearance promotes persistent bacterial adhesion and colonization. Among opportunistic pathogens, certain species pose a severe threat due to multidrug resistance and association with life-threatening complications [1]. However, these processes remain poorly understood, mainly due to limitations of conventional models, which fail to reproduce dynamic airway conditions [2].

In this work, we propose a microfluidic Organ-on-a-Chip (OoC) device integrating impedance-based sensors for real-time, label-free monitoring of epithelial barrier formation and bacterial adhesion under physiological flow and oxygen gradients. To achieve this, two designs were developed: a hybrid system exploiting differential gas permeability of the two materials, and a device relying on controlled perfusion of media with different oxygen levels, a key novelty.

Finally, the platform is intended as a versatile tool to investigate bacterial adhesion under flow in physiologically relevant disease models, enabling the study of host–pathogen interactions and supporting the therapy development for infectious and epithelial barrier-related diseases.

Description of the New Method or System

The coexistence of normoxic and hypoxic conditions within a single device is replicated in novel microfluidic platforms, developed for adherent 16HBE14o- epithelial cells, featuring an 800 µL culture chamber to support monolayer formation and ensure compatibility with standard epithelial culture conditions.

The hybrid device (Fig. 1A) is composed of 2.5 mm PDMS (polydimethylsiloxane) and COC (cyclic olefin copolymer) layers and a PET (polyethylene terephthalate) membrane (0.4 µm pore size) is placed in between, supported by micropillars of the PDMS part.

In the fully COC-based device (Fig. 1B), a flat COC surface (0.1 mm foil or 2.5 mm plate) is associated with a machined plate, which includes microchannels for the inflow and outflow of two different culture media.

COC structures are fabricated by CNC (Computer Numerical Control) milling, while the PDMS components are produced via soft lithography, involving hard mask fabrication followed by SU-8 mold processing. Bonding between the two components uses a 143 µm-thick PSA (pressure-sensitive adhesive) layer.

Device fabrication is followed by design and fabrication of gold interdigitated electrodes (IDE) by photolithography (pre-development time: 40s, exposure energy: 75 mJ·cm^{-2}), development,

metal deposition (10 nm Cr and 100 nm Au), and lift-off. Sensors were designed with 5 µm and 50 µm spacing with linear or circular fingers.
The epithelial bronchial cells used, derived from the 16HBE14o- cell line, are seeded in the devices with a density of 25000 cells/cm^2. Biological validation include coated (LHC basal medium, BSA, collagen, human fibronectin) and uncoated conditions, with optical cell tracking.

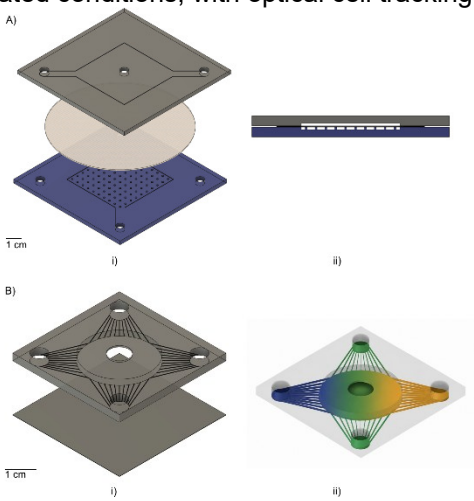

Fig. 1: Microfluidic devices
A) Hybrid PDMS-COC device:
i) Schematic representation of different device layers,
ii) Assembled device cross view
B) Full-COC device:
i) Schematic representation of different device layers,
ii) Illustration of O_2 gradient (normoxia (blue), hypoxia (yellow))

Results

Fabrication results indicate that CNC milling is the most reliable method for rigid thermoplastics devices, providing high-precision rapid prototyping, and that PDMS casting allows reproducibility using a master mold. PSA provides reversible sealing and fast assembly, and its replacement does not affect components, allowing device reuse and improving cost-effectiveness for iterative workflows.
Biological tests confirm adhesion and growth of 16HBE14o- cells, with better performance on COC flat surfaces, validating material compatibility for airway epithelial models (Fig. 2). Surface coating improves adhesion but is not essential for cell viability, as cells exhibit the expected phenotype. Physiologically relevant oxygen gradients mimicking in vivo bronchial conditions are under evaluation.

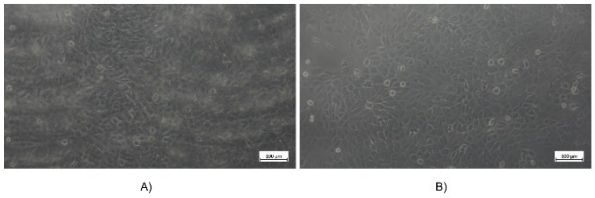

Fig 2. Micrograph (Bright-field, 10x magnification) of cells adhered at day 5 to non-coated (A) PET membrane (PDMS-COC device) and (B) COC foil (COC device)

A key outcome is the integration of IDE sensors, enabling quantitative and non-invasive analysis of cell behaviour and tracking responses to stimuli in future experiments.
The fabricated IDE sensors, with electrode spacings of 50 µm and 5 µm (Fig. 3, Fig. 4), exhibit uniform and well-adhered metallic layers, confirming fabrication protocol suitability. Future results are expected to identify which design performs best in terms of sensitivity and stability for real-time impedance monitoring of epithelial barrier formation.

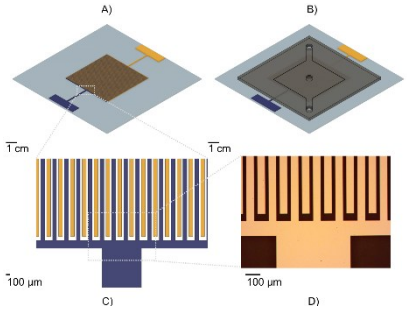

Fig. 3: IDE sensor for PDMS-COC device
A) 3D CAD design, B) Integration with device,
C) Magnified view of 50 µm-spaced patterned lines,
D) Micrograph of final sensor (Bright-field, 5x magnification)

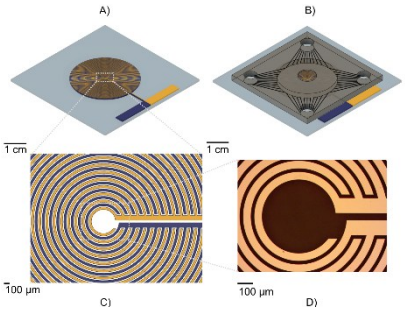

Fig. 4: IDE sensor for COC device
A) 3D CAD design, B) Integration with device,
C) Magnified view of 50 µm-spaced patterned lines,
D) Micrograph of final sensor (Bright-field, 5x magnification)

Overall, this work advances the state of the art by providing a modular, reproducible, physiologically relevant system combining oxygen gradient control and real-time sensing, supporting advanced studies in next-generation OoC systems, particularly for epithelial barrier function and host–pathogen interactions.

References

[1] Scoffone, Chiarelli, Trespidi, Mentasti, Riccardi, Buroni, “*Burkholderia cenocepacia* Infections in Cystic Fibrosis Patients: Drug Resistance and Therapeutic Approaches”. Front Microbiol. 2017 Aug 22;8:1592. doi: 10.3389/fmicb.2017.01592. PMID: 28878751; PMCID: PMC5572248.
[2] Dichtl, Posch, Wilflingseder, “The breathtaking world of human respiratory in vitro models: Investigating lung diseases and infections in 3D models, organoids, and lung-on-chip,” Mar. 01, 2024, John Wiley and Sons Inc. doi: 10.1002/eji.202250356.

DOI 10.5162/eurosensors2026/Tu–MLO–04

Fully Automated Skeletal Muscle-on-chip Platform for Contraction Analysis

Giorgia Curci[1], Daniele Durante[2], Corrado Mazzaglia[1], Arianna Mencattini[1], Monica Ballarino[2], Eugenio Martinelli[1]
[1] Department of Electronic Engineering, University of Rome Tor Vergata, Rome, Italy
[2] Department of Biology and Biotechnologies "Charles Darwin", Sapienza University, Rome, Italy
Corresponding Author's e-mail address: giorgia.curci@uniroma2.it

Summary:

Lab-on-chip technology enables the in vitro analysis of biological processes with simultaneous monitoring of various physiological aspects. In this context, muscle-on-chip systems allow for the study not only of classical parameters but also of contractile function, thanks to the integration of electrodes for electrical stimulation that simulate nerve impulses. In this work, we present an automated platform based on time-lapse microscopy, which enables an in-depth analysis of contraction of hIPSC-derived myotubes, using machine learning algorithms for the extraction of fundamental contraction parameters.

Keywords: Lab-on-chip, Skeletal Muscle Contraction, Time-Lapse Microscopy, Machine Learning

Background, Motivation and Objective

In recent years, biomedical research has shifted toward advanced in vitro models that more accurately reproduce human pathophysiology, overcoming the limitations of animal models. In this context, the transition from conventional cultures to more complex systems has improved the structural representation of tissues, highlighting the need to integrate dynamic functionalities and continuous monitoring systems. Lab-on-chip platforms represent a promising solution, combining microfluidics, sensors, and data-acquisition systems into miniaturized devices that enable precise, real-time analysis with reduced resource consumption. The integration of time-lapse microscopy (TLM) techniques and advanced data analysis algorithms also allows for the extraction of complex quantitative information from dynamic biological systems. Among the various applications, muscle-on-chip systems play a key role, enabling not only structural but also functional analysis of muscle tissue through electrical stimulation and contraction monitoring [1]. These systems enable quantitative study of physiological and pathological responses, offering new perspectives for disease modeling, drug testing, and the development of personalized medicine. Currently, most advanced skeletal muscle models rely on three-dimensional systems, where cells are embedded within a matrix and form contractile tissues anchored to flexible pillars. The deflection of these structures, combined with their known mechanical properties, allows for the estimation of contractile force. While these models provide a physiologically relevant environment, force alone represents a limited descriptor of muscle functionality. In this work, we propose an automated platform based on a two-dimensional muscle-on-chip system integrated with TLM and machine learning algorithms. Particle image velocimetry [2] (PIV) based algorithms are employed to extract key parameters of contractile dynamics, enabling a more comprehensive characterization of muscle function beyond force measurement alone.

Description of the New Method or System

The muscle-on-chip device is based on the platform presented in our work [3]. Briefly, each layer was fabricated using laser cutting techniques on sheets of Polystyrene (PS) from Petri dishes, Polymethyl Methacrylate (PMMA) and Cyclic Olefin Polymer (COP). The electrodes made of laser induced graphene [4] (LIG) were synthesized through the CO2 laser on commercial PI tape, which was directly bonded onto PS substrates. After the laser processing, the non-functionalized residual portions of the tape were carefully peeled off, leaving only the patterned conductive regions adhered to the substrate. Micro-grooves approximately 70 µm wide were created on the substrate to aid myocyte alignment, forming compact myofibrils oriented along the distance between the electrodes (see Fig. 1). Human Induced Pluripotent Stem Cells (hiPSCs)

were seeded onto the device and differentiated into skeletal myotubes over ~15 days. After maturation, the chips were electrically interfaced via a dedicated connector and placed in a microscope-compatible incubator, ensuring controlled temperature, CO_2, and humidity. Electrical stimulation was applied using biphasic pulse trains (6 V peak-to-peak, 0.5 Hz, ~5% duty cycle), while contraction dynamics were recorded using 20× TLM. Videos were processed using a multi-step PIV-based pipeline. A fast PIV-based prescreening was first applied on downsampled data to identify regions of interest (ROIs) exhibiting significant contractile activity. Local velocity fields were computed using FFT-based cross-correlation, and temporal signals were extracted by averaging velocity magnitude within spatial windows. From these signals, amplitude, variance, and slope were extracted, normalized, and combined into an aggregated activity score. ROIs were selected based on a 95th percentile threshold of the extracted features. A high-resolution PIV analysis was then performed on selected ROIs to extract accurate velocity fields and local motion signals. These were used to compute representative contraction profiles and cumulative displacement dynamics. Finally, spatial mapping of contraction signals enabled identification of contraction centers, both in instantaneous and cumulative conditions.

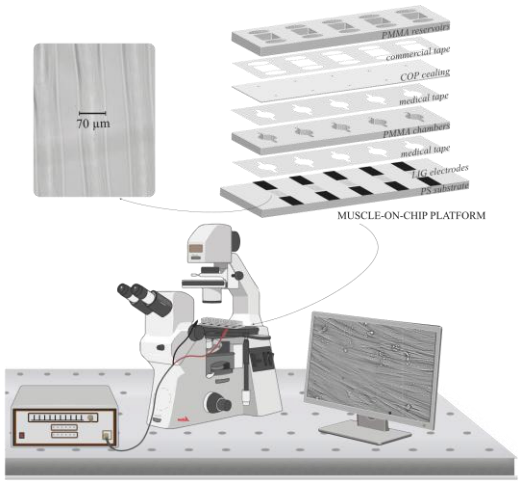

Fig. 1. Schematic view of the platform

Results

The microfluidic device supported the maturation and differentiation of iPSC-derived cells into mature skeletal muscle fibers, characterized by elongated, aligned morphology. Electrical stimulation successfully induced repeatable contractile responses synchronized with each applied pulse. A database of TLM videos was analyzed using the fully automated pipeline based on PIV. The proposed framework enables the identification of contraction centers directly from raw video data and the extraction of their local dynamics (see Fig. 2). For each identified contraction center, the system reconstructs the temporal evolution of motion, including instantaneous velocity signals and cumulative displacement profiles. This allows the spatiotemporal distribution of contractile activity to be quantified, providing a detailed characterization of how mechanical signals propagate across the tissue over time. The combined analysis of local and cumulative descriptors enables a robust functional fingerprint of the tissue, capturing both the intensity and temporal organization of contraction events. This automated approach provides a scalable tool for quantitative assessment of muscle functionality, with potential applications in drug screening, disease modeling, and personalized medicine. In particular, the ability to resolve contraction dynamics at the level of individual functional regions may enable discrimination between different cellular populations and pathological states, as well as systematic evaluation of pharmacological responses.

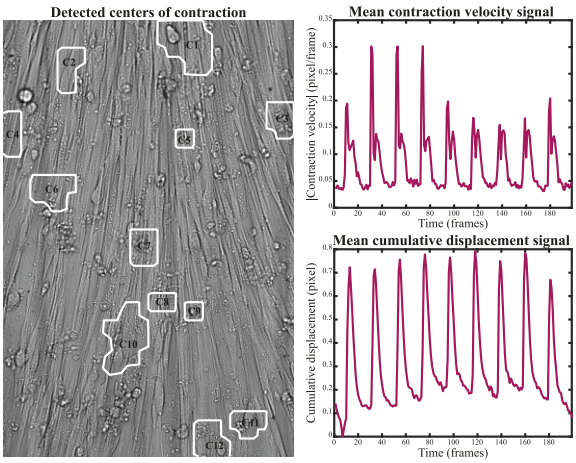

Fig. 2. Example of information extracted from the tool: detected centers of contraction and corresponding mean velocity and cumulative displacement

References

[1] J. M. Fernández-Costa et al., Training-on-a-Chip: A Multi-Organ Device to Study the Effect of Muscle Exercise on Insulin Secretion in Vitro, *Advanced Materials Technologies*, 2022, doi:10.1002/admt.202200873

[2] W. Thielicke, R. Sonntag, Particle Image Velocimetry for MATLAB: Accuracy and Enhanced Algorithms in PIVlab. *Journal of Open Research Software*, 2021, *9* (1), 12, doi: 10.5334/jors.334

[3] G. Curci et al., A Microfluidic Platform Based on Laser-Induced Graphene Electrodes and Machine Learning for Real-Time Skeletal Muscle Analysis, *Advanced Materials Technologies*, 2026, doi: 10.1002/admt.70847

[4] Y. Ruquan, D.K. James, J. Tour, Laser-induced graphene, *Accounts of Chemical Research, 2018, 5(1) 5714,* doi: 10.1021/acs.accounts.8b00084

DOI 10.5162/eurosensors2026/Tu–MLO–05

A Microreactor Workflow for Spatial Proteomics Sample Preparation

Manuel Metzger[1,2], Maximilian Maldacker[3,4], Tobias Hutzenlaub[1,2], Nils Paust[1,2], Oliver Schilling[3], Jan-Niklas Klatt[1,2]
[1] Hahn-Schickard, Georges-Koehler-Allee 103, 79110 Freiburg, Germany,
[2] Laboratory for MEMS Applications, IMTEK-Department of Microsystems Engineering, University of Freiburg, Georges-Koehler-Allee 103, 79110 Freiburg, Germany,
[3] Institute for Surgical Pathology, Faculty of Medicine, Medical Center – University of Freiburg, Breisacher Strasse 115a, 79106 Freiburg, Germany,
[4] Faculty of Biology, University of Freiburg, Schaenzlestrasse 1, 79104 Freiburg, Germany
Corresponding Author's e-mail address: niklas.klatt@hahn-schickard.de

Summary:

We present MR-SP² [1] (microreactor-based sample preparation workflow for spatial proteomics) that addresses key loss mechanisms in laser capture microdissection (LCM) coupled to liquid chromatography–tandem mass spectrometry (LC-MS/MS). MR-SP² integrates specimen capture, one-pot processing, and pipetting-free transfer to LC-MS/MS via Evotip precolumns. Evaluated using formalin-fixed paraffin-embedded (FFPE) murine kidney tissue, MR-SP² reduced the adsorptive surface area by 64% compared to tube-based workflows, yielding more than a 3-fold increase in protein identifications.

Keywords: spatial proteomics, sample preparation, LCM, LC-MS/MS, few-cell proteomics, FFPE

Background, Motivation and Objective

Spatial proteomics enables protein mapping within tissue at cellular resolution, with laser capture microdissection (LCM) coupled to liquid chromatography-tandem mass spectrometry (LC-MS/MS) being the predominant approach [2]. The legacy Zeiss PALM MicroBeam remains the second most widely used LCM platform despite its discontinuation [1], yet no dedicated low-loss sample preparation workflow exists for it. Conventional tube-based workflows suffer from three compounding loss mechanisms: incomplete specimen transfer during pressure-catapulting LCM capture, adsorptive losses of proteins and peptides to reaction vessel surfaces during processing, and a final pipetting step into the LC-MS/MS interface. At the few-cell level, a single pipetting step alone can reduce proteome identifications by 50% [3]. These losses disproportionately affect low-abundance peptides, fundamentally limiting the achievable proteomic depth in spatially defined tissue microregions [4].

Description of the New Method or System

MR-SP² centers on a novel microreactor fabricated from cyclic olefin copolymer (COC) foil via thermoforming, with a 3D-printed COC cap and holder (Fig. 1 A+B). The microreactor geometry for MR-SP² (Fig. 1C) is compatible with the Zeiss PALM RoboMover, occupying the position of a conventional tube cap for direct specimen capture in 20 µL acetonitrile – half the volume of the conventional workflow (Fig 1D). This eliminates the centrifugation step required to transfer specimens from tube cap to tube body, which is a primary source of specimen loss. All processing steps (protein extraction at 95°C, reductive alkylation, tryptic digestion, and acidification) are performed in the sealed microreactor in a total volume of 20 µL, minimizing the inner surface area exposed to the sample from 92.8 mm² in the conventional workflow to 33.4 mm² (64% reduction). Sample transfer to LC-MS/MS is achieved by clipping the microreactor directly onto an Evotip disposable precolumn, entirely eliminating pipetting of the sample. The complete workflow is depicted in Fig. 1. Workflow performance was benchmarked against a conventional tube-based workflow using FFPE murine kidney tissue sections analyzed on a timsTOF flex coupled to an Evosep One system.

Results

MR-SP² improved specimen capture success rate from 75% (12/16) to 94% (15/16) compared to the conventional workflow. At 22-cell input (50,000 µm³), both workflows performed comparably in protein identifications (3381 ± 80 vs. 3174 ± 59 proteins, Fig. 2B), with MR-SP² showing improved peptide depth (16,021 ± 1009 vs. 13,514 ± 740 peptides, $p < 0.05$ Mann-Whitney U (MWU), Fig. 2A). The advantage of MR-SP2

became pronounced at lower inputs where adsorptive losses are more severe. At 5–6 cells (12,500 µm³), MR-SP² identified 1145 ± 188 proteins with match-between-runs (MBR) versus 302 ± 126 proteins for the conventional workflow (>3-fold increase, $p < 0.05$ MWU). At 1–2 cells (3,125 µm³), MR-SP² reached 695 ± 112 proteins (MBR) compared to 206 ± 51 for the conventional workflow (>3-fold increase, $p < 0.05$ MWU). Quantitative reproducibility (Fig. 2C) remained high across all input levels, with mean coefficients of variation (CV) below 0.10 for MR-SP².

References

[1] M. Metzger, M. Maldacker, et al., MR-SP²: A Microreactor-Based Workflow for Few-Cell Spatial Proteomics on the Legacy Zeiss PALM MicroBeam. *J. Proteome Res.* (2026); doi: 10.1021/acs.jproteome.5c01231

[2] P. Horvath, F. Coscia, Spatial Proteomics in Translational and Clinical Research, *Mol. Sys. Biol.* 21, 526-530 (2025); doi: 10.1038/s44320-025-00101-9

[3] A. Momenzadeh, J. G. Meyer, Single-Cel Proteomics Using Mass Spectrometry, *Cell Genomics,* 5 (9) (2025); doi: 10.1016/j.xgen.2025.100973

[4] R. Konno, M. Ishikawa, D. Nakajima, et al., Universal Pretreatment Development for Low-input Proteomics Using Lauryl Maltose Neopentyl Glycol, *Mo. Cell. Proteomics,* 23 (4) (2024); doi: 10.1016/j.mcpro.2024.100745

Illustrations, Graphs, and Photographs

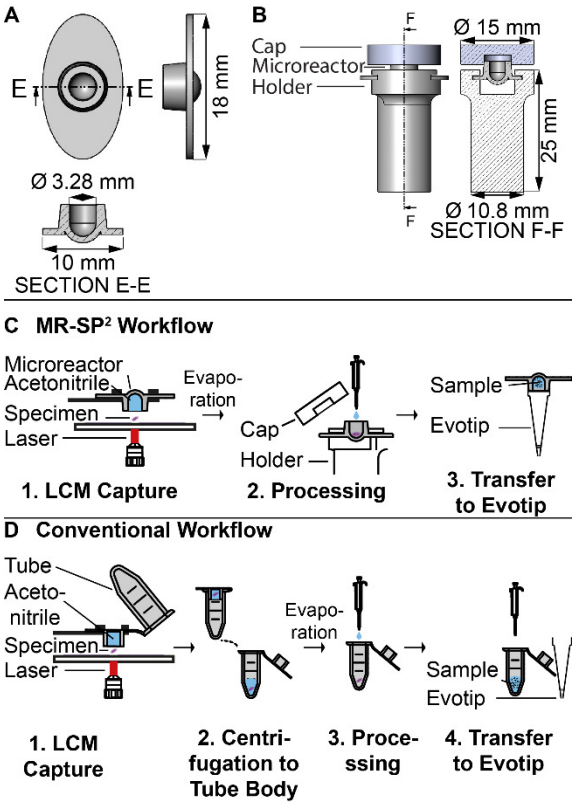

Fig. 1. (A) Microreactor and dimensions. (B) Components used for MR-SP² including microreactor, cap and holder. (C) The MR-SP² workflow including LCM capture, processing, and Evotip transfer. (D) Conventional workflow using a standard tube including LCM capture, centrifugation of specimen to tube body, processing, and Evotip transfer.

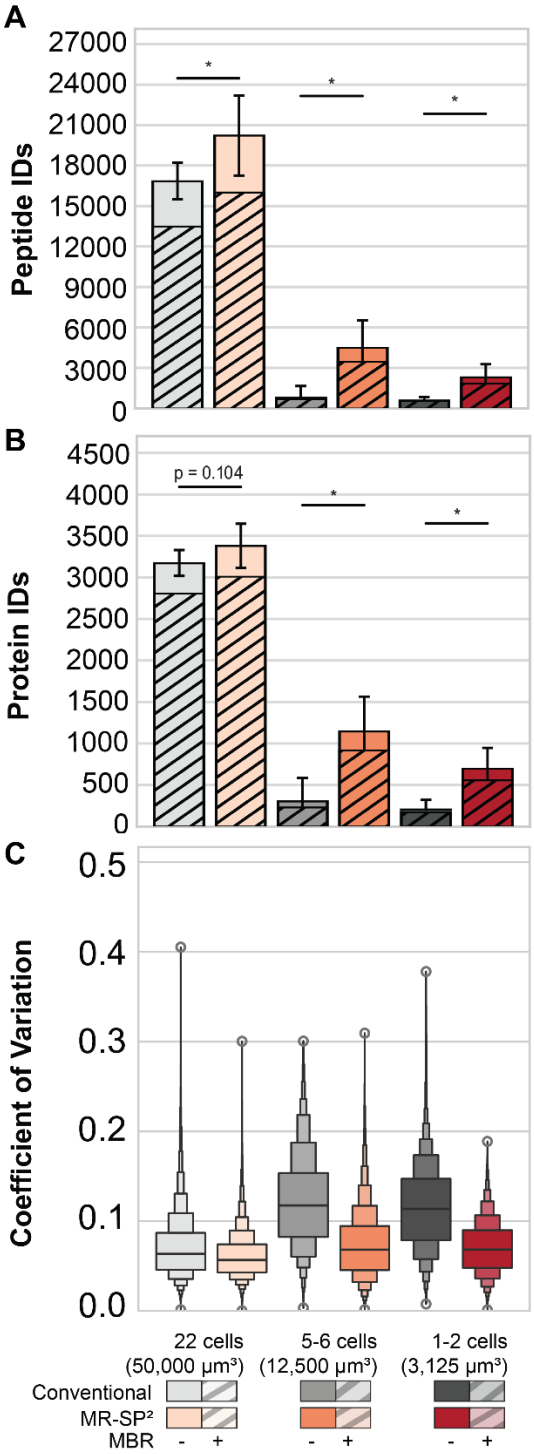

Fig. 2. Results of LC-MS/MS analysis for different input volumes including (A) peptide identifications, (B) protein identifications, and (C) coefficient of variation for $\log_2$ peptide intensities among peptides identified in at least 3 precursors.

DOI 10.5162/eurosensors2026/Tu–MLO–06

A Microfluidic Device Integrating Electrical Impedance Spectroscopy Enables Label-Free Monitoring of *C. elegans* in Egg-Laying

Song Yu[1], Yulu Geng[1], Juncheng Fan[1], Hanye Lu[1], Zhen Zhu[1]*

[1] Southeast University, School of Integrated Circuits, Key Laboratory of MEMS of Ministry of Education, Wuxi Campus, Zhuangyuan Road 5, Wuxi 214125, China
Corresponding Author's e-mail address: zhuzhen@seu.edu.cn

Summary:

Accurate characterization of reproductive phenotypes in *Caenorhabditis elegans* (*C. elegans*) is essential for investigating underlying physiological processes and hereditary mechanisms. However, monitoring of the egg-laying process, one of the central reproductive behaviors in *C. elegans*, has relied on counting expelled embryos, while overlooking organ-level dynamics within the animal, particularly those of the uterus. Here, we present a microfluidic device integrating a microelectrode array to perform electrical impedance spectroscopy measurements of *C. elegans* uterus. Both simulation and experimental results demonstrate that impedance signals at 40 MHz are correlated with the uterine state changes during egg-laying.

Keywords: Lab-on-a-Chip, Electrical impedance spectroscopy, *C. elegans*, Uterus, Egg-laying

Background

The reproductive system is characterized by tightly coordinated processes of organ patterning and morphogenesis across the lifespan, playing a fundamental role in species propagation and organismal health [1]. The nematode *Caenorhabditis elegans* (*C. elegans*) has been widely adopted as a model organism for studying neural regulation, inheritance mechanisms, and reproductive phenotypes [2]. In adult wild-type hermaphrodites, reproduction proceeds through self-fertilization followed by egg-laying [3]. Despite the central role of egg-laying in *C. elegans* reproduction, most existing approaches assess this process indirectly by quantifying expelled embryos, rather than probing the uterus itself [4]. In addition, imaging-based techniques often depend on transgenic strains expressing fluorescent reporters under tissue-specific promoters, which increases experimental complexity and limits accessibility [5]. In this work, we develop a microfluidic device incorporating a microelectrode array (MEA) to enable electrical impedance spectroscopy (EIS)-based monitoring of the *C. elegans* uterus during egg-laying.

System and Methods

The device was fabricated through a three-step microfabrication process. A Cr/Au microelectrode array was first patterned on a glass substrate, followed by deposition of a SiNx passivation layer with defined openings for impedance sensing. A polydimethylsiloxane (PDMS) layer containing a single microchannel and a pneumatic valve was subsequently bonded onto the substrate. The central sensing region of the device is illustrated in Fig. 1. The pneumatic valve, positioned at the outlet of the microchannel, was used to immobilize individual worms for EIS measurement. For EIS acquisition, a pair of microelectrodes was selected as the stimulus electrode (S) and recording electrode (R). A swept-frequency AC excitation was applied at the stimulus electrode, while the response current was collected at the recording electrode to obtain EIS signals.

Results

We first established a finite element model (FEM) of the microfluidic device and *C. elegans* to mimic EIS measurements during egg-laying. Four egg-laying states were defined by varying the number of embryos in the worm uterus (Fig. 2). Fig. 3a shows the raw EIS magnitudes simulated by the S - R electrode pair, ranging from 10 kHz to 100 MHz. Since the impedance variation caused by expelled embryos is small, we calculated the relative EIS signals, which demonstrate that EIS signals at high-frequency (> 40 MHz) can monitor uterine changes in *C. elegans* during egg-laying (Fig. 3b). To verify this conclusion, we performed EIS measurements in the microfluidic device during egg-laying. The results show that the post-laying EIS signals

increase most significantly at 40 MHz compared to those of the pre-laying state (Fig. 4).

References

[1] V. Lorenzi, et al., Spatiotemporal cellular map of the developing human reproductive tract, *Nature* 650.8101, 428-437 (2026); doi: 10.1038/s41586-025-09875-2

[2] C. C. Kern, et al., *C. elegans* ageing is accelerated by a self-destructive reproductive programme, *Nature Communications* 14.1, 4381 (2023); doi: 10.1038/s41467-023-40088-1

[3] J. Noiphung, et al., Based Analytical Device for Real-Time Monitoring of Egg Hatching in the Model Nematode *Caenorhabditis elegans*, *ACS Sensors* 5.6, 1750-1757 (2020); doi: 10.1021/acssensors.0c00412

[4] N. Ringstad, H. R. Horvitz, FMRFamide neuropeptides and acetylcholine synergistically inhibit egg-laying by *C. elegans*, *Nature Neuroscience* 11.10, 1168-1176 (2008); doi: 10.1038/nn.2186

[5] E. R. Galimov, et al., Coupling of rigor mortis and intestinal necrosis during *C. elegans* organismal death." *Cell Reports* 22.10, 2730-2741 (2018); doi: 10.1016/j.celrep.2018.02.050

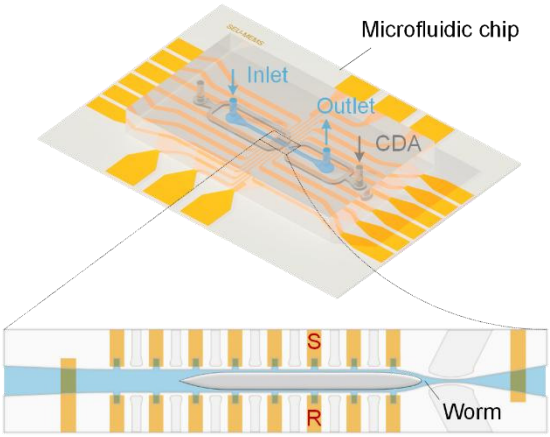

Fig. 1. The microfluidic device and its sensing region for measuring EIS signals of C. elegans.

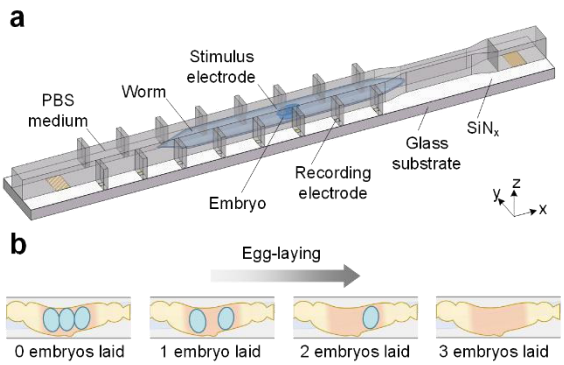

Fig. 2. Modeling and simulation of C. elegans egg-laying. (a) FEMs of the sensing region of microfluidic sensing region. (b) Four worm models at different egg-laying states were established by adjusting the embryos in the uterus.

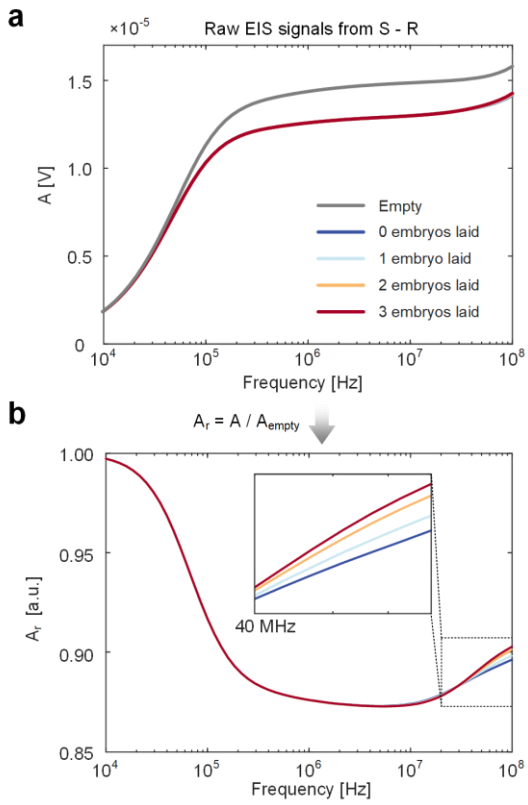

Fig. 3. Simulated EIS signals during egg-laying. (a) Raw EIS signals of the empty microchannel and four states during egg-laying, simulated by the selected electrode pair. (b) Relative EIS signals of the four egg-laying states.

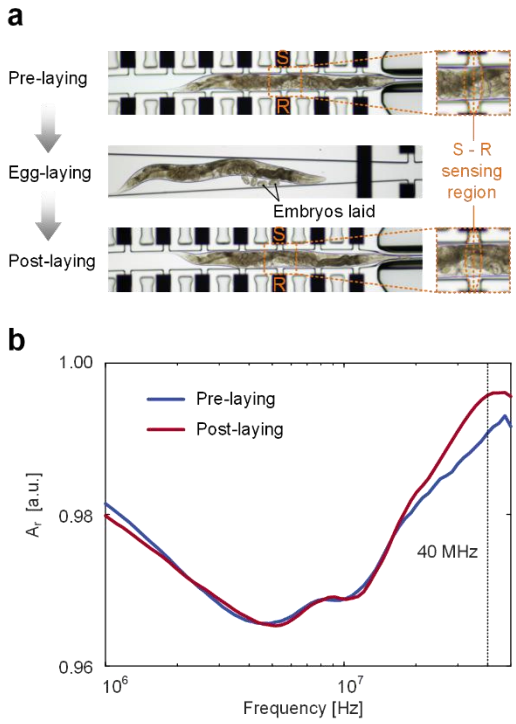

Fig. 4. Monitoring an egg-laying process in the microfluidic device. (a) The EIS measurements were performed in pre-laying and post-laying. (b) The relative EIS signals measured by S - R electrode pair.

DOI 10.5162/eurosensors2026/Mo–POS–01

SPR-grating: spectral vs intensity interrogation for ethanol detection

Miquel Giménez-Conejo[1], Víctor González -Morote[1,2], Sergi González-Martínez[1,2,3], Ignasi Fort-Grandas[1,2,3], Anna Estany-Macià[1,2], Daniel Sainz[2,3], Albert Romano-Rodriguez[1,2], Mauricio Moreno-Sereno[1,2]

[1]Department of Electronics and Biomedical Engineering, Universitat de Barcelona, Barcelona, Spain
[2]Institute of Nanoscience and Nanotechnology, Universitat de Barcelona, Barcelona, Spain
[3]Department of Inorganic and Organic Chemistry, Universitat de Barcelona, Barcelona, Spain

mauricio.moreno@ub.edu

Summary:

In this work we present a comparison of the response of SPR-grating sensors covered with ZIF8 for vapors ethanol detection, using spectral interrogation and intensity interrogation. We show that using the spectral interrogation method we can detect a value of 200 ppm of ethanol.

Keywords: Gas sensor, optical detection surface plasmon resonance, metal-organic frameworks (MOFs), volatile organic compounds, ethanol.

Introduction.

Chemical sensors are attractive because they are sensitive, fast, compact, and consume limited power, although they often lack selectivity. Commercial gas sensors are mainly based on three technologies: electrochemical, chemoresistance or NDIR. NDIR sensors operate by measuring gas absorption in the infrared spectrum. They are highly selective, but detecting low gas concentrations requires a long optical path length and, consequently, they are bulky.

Alternative optical sensing methods include Fabry–Pérot interferometry, fiber-optic gratings, and surface plasmon resonance (SPR). Since gases induce only very small refractive index changes when compared to air, sensitive coatings are often used to enhance detection. Metal-organic frameworks (MOFs) are porous materials with high surface area that are suitable for gas adsorption and sensing applications. Among them, ZIF-8 (zeolitic Imidazolate Framework) is especially promising due to its large pore size and hydrophobic nature, which minimizes humidity interference [1-3].

Sensing method and results.

In this work, a nanostructured gold diffraction grating coated with ZIF-8 is used as the sensing platform. The sensor is fabricated on oxidized silicon wafers with a gold-coated diffraction grating structure. The diffraction grating (period of 500nm) is created using electron beam lithography, followed by reactive ion etching and gold deposition (50nm). A thin ZIF-8 film is then synthesized on selected gratings through immersion in a solution containing zinc nitrate and 2-methylimidazole. The resulting ZIF-8 layer has a thickness of approximately 280 nm.

Two optical interrogation methods were tested. 1) In Spectral interrogation measurements, a white light source is focused on the sample inside a gas chamber. The reflected light was collected and analyzed with a spectrometer to obtain the reflectivity spectrum. 2) In intensity interrogation, the white light source was replaced with a 780 nm laser diode, and the spectrometer was replaced with a silicon photodiode used to measure reflectivity at a fixed wavelength.

In the spectral interrogation experiments, exposure to ethanol vapor caused a redshift in the SPR resonance, indicating an increase in the refractive index of the ZIF-8 film as ethanol molecules were adsorbed. Fig. 1 shows the resonance spectra during exposure to the reference gas, synthetic air, with a resonance at about 755 nm, while under saturated ethanol vapor, using a bubbling system, the resonance shifted to 781 nm ($\Delta\lambda$=26 nm). Using a reference gas cylinder and mass flow controllers, we have been able to detect 200 ppm (Fig. 2).

In the intensity interrogation setup, which is much simpler, the reflected light intensity decreases with increasing ethanol concentration In Fig. 3, the variation of reflectivity between pure synthetic air and different pulses of ethanol dissolved in SA.

The minimum ethanol concentration that produces a measurable variation within a 1-minute

measurement cycle is ≅ 2000 ppm, which is a tenfold increase compared to spectral interrogation previously described.

In Figure 1, the vertical line represents the laser diode wavelength (780 nm). The variation in reflectivity between the two extreme cases, synthetic air and ethanol (EtOH), is shown by the red and magenta lines. These correspond to the green and black dotted lines in Figure 3, which represent the response to a pulsed concentration.

In this work the results of both methodologies will be presented and critically discussed.

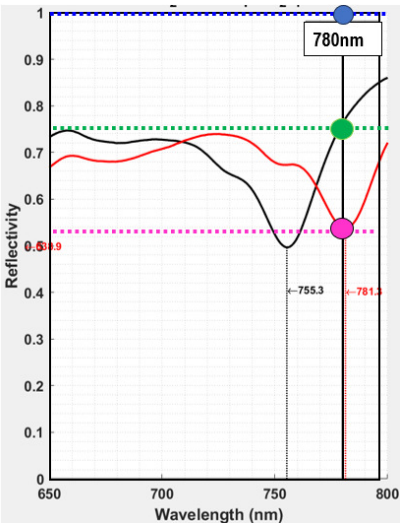

Fig. 1. The black spectrum corresponds to the cleaning state, synthetic air, while the red spectrum shows the redshifted response for fully saturated ethanol vapor. The total redshift observed is Δλ = 26 nm.

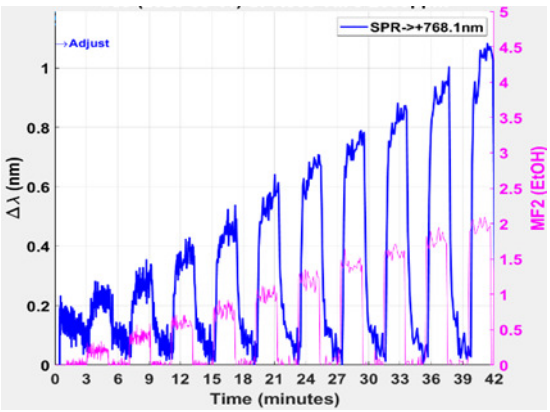

Fig. 2. Redshift of a 500 nm diffraction grating under different ethanol vapor concentrations. The minimum concentration tested is 200ppm

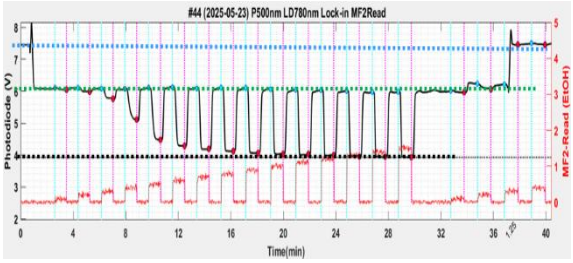

Fig. 3. Decrease of reflectivity using a 780nm laser-diode. Blue line is the 100% of reflectivity in flat-gold. Green line is the maximum reflectivity on difraction grating in cleaning cicles. Black line is the reflectivity under diferent concentrations. Red line is the Mass-flow voltage. Reflectivity decrease from 80% to 53% at maximum concentration of EtOH.

References

[1] G. Lu and J. T. Hupp., “Metal-Organic Frameworks as sensors: A ZIF-8 based Fabry-Perot device as a selective sensor for chemical vapors and gases,” J. Am. Chem. Soc., vol. 132, pp. 7832–7833 (2010); doi: 10.1021/ja101415b.

[2] N.C. Keppler, K. E. J. Hindricks and P. Behrens, “Large refractive index changes in ZIF-8 thin films of optical quality,” RSC Adv., vol. 12, pp. 5807–5815, (2022); doi: /10.1039/D1RA08531J.

[3] A. Estany et al., “ZIF-8-Based Surface Plasmon Resonance and Fabry–Pérot Sensors for Volatile Organic Compounds,” Sensors Sensors 24, 4381, (2024); doi: /10.3390/s24134381

DOI 10.5162/eurosensors2026/Mo–POS–02

Real-time resonance tracking for acoustic resonator enhanced photoacoustic gas sensors

Daniel Sieg[1], Raj Patel[1], Vincent Kuczius[1], Stefan Palzer[1]
[1]Technical University Dortmund, Professorship for Sensors, Otto-Hahn-Straße 8, 44227 Dortmund, Germany
Stefan.palzer@tu-dortmund.de

Summary:

Trace gas detection is crucial for environmental monitoring and numerous industrial applications. Direct photoacoustic is a promising technique for reliable gas sample analysis and their performance may be improved by employing acoustic resonators to enhance sensitivity. However, changes in gas conditions alter both resonance frequency and quality factor, making robust, long-term stable operation challenging. Here a locking scheme for real-time tracking based on a frequency modulation scheme is presented. Inspired by Pound–Drever–Hall locking, the method exploits the resonator's phase response and enables fast, stable PAS measurements in a lean implementation.

Keywords: trace gas sensing, photoacoustics, acoustic resonators, resonance tracking

Introduction

Direct photoacoustic spectroscopy (PAS) is a powerful method for selective trace-gas detection. In order to enhance sensitivity, PAS systems often employ acoustic resonators to amplify the light-induced acoustic wave, where the optical modulation frequency is matched to an acoustic eigenmode. The resulting resonant amplification significantly increases the photoacoustic signal amplitude and consequently improves sensitivity and the limit of detection [1].

Nonetheless, long-term stability hinges on accounting for fluctuations of the exciting light intensity as well as tracking the resonator properties. Since the signal strength scales approximately with the quality factor Q, it is paramount to reliably determine this quantity in order to relate the recorded acoustic signal strength to the target gas concentration. In practical sensing conditions the thermophysical properties of the gas are altered by variations in gas composition, concentration, pressure, or temperature, leading to shifts in the acoustic resonator's resonance frequency f_0 and changes in the Q-factor. To this end, locking schemes to track both the Q-factor and the resonance frequency are necessary for long-term stable operation of PAS sensors. Methods to achieve this include point-by-point frequency scanning [2], chirped modulation [3], light-induced wall signal techniques [4], and transient heterodyne excitation [5].

While these approaches can track the resonance frequency, they increase system complexity or require complex setups. Here an active locking scheme for real-time tracking of the resonance frequency and determination of the Q factor based on mixing three modulation frequencies is presented. It does not require frequency sweeping, which enables fast, real-time tracking of the acoustic eigenmode and gas concentration determination.

Method

The scheme is akin to the Pound-Drever-Hall laser locking scheme [6] and relies on the phase shift acoustic signals experience when interacting with acoustic resonators. To implement the scheme, a carrier frequency, which in this case is the modulation frequency f_c to excite photoacoustic signals is accompanied by two sidebands located at $f_{-1,+1} = f_c \pm f_m$, where f_m is the sideband modulation frequency. Depending on the respective position with respect to the frequency of the resonator eigenmodes, each frequency experiences an individual phase shift. By comparing the amplitude and the phase of the signal originating from the two sidebands, an error signal may be generated to determine and adjust f_c.

Experimental

In order to demonstrate the approach a cylindrical, open resonator with inner diameter of d = 5 mm and a length of 55 mm is employed. An analog MEMS microphone (IvenSense ICS-40619)

is mounted at the back wall and its signal is amplified using a low noise circuit prior to digitization via a differential amplifier circuit with bandpass filter, containing operational amplifiers (Analog Devices LT6235). Control of the sound source, determination of the amplitude and phase of the microphone signal and calculation of f_c and Q-factor, respectively, is embedded in a PSoC 5 microcontroller. The microcontroller generates a composite waveform consisting of the carrier frequency at f_c and the two sidebands and outputs that signal via its internal DAC to an amplifier which drives the capacitor. Simultaneously the lock-in values are calculated by using the microphone signal digitalized by the internal ADC. A new carrier frequency is estimated from the calculated amplitudes and phases measured at the carrier frequency and the sidebands.

Figure 1 depicts the schematic setup. To demonstrate the approach a ceramic capacitor (10 µF, X7R, 1206, Kemet C1206C106K4RAC7800) is used to excite acoustic waves.

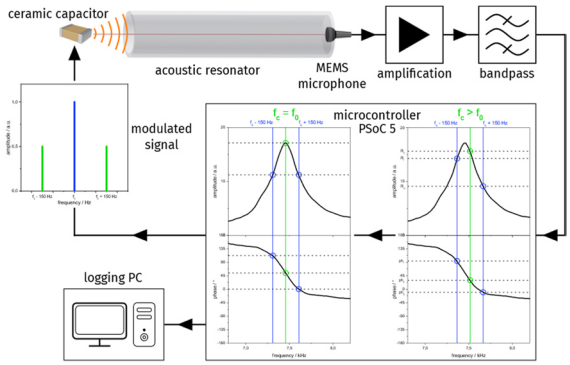

Figure 1: The figure shows the schematic setup. The microcontroller corrects the carrier frequency f_c to fit the resonance mode of the resonator.

Results

A frequency sweep in the range from 1 – 20 kHz confirms the location of the longitudinal eigenmodes and the amplitude as determined by the lock-in algorithm along with the phase between modulation source and microphone signal are depicted in Figure 2. By mixing the signals originating from the sidebands both the error signal and the Q-factor are extracted. Figure 3 shows the results of the determination of resonance frequency for varying temperature, and gas composition. The characterization has been performed in a controlled environment.

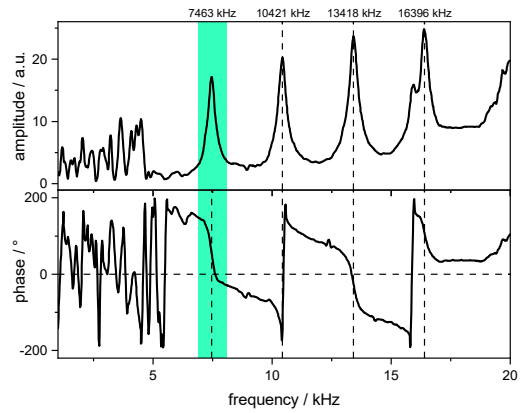

Figure 2: Determined amplitudes and phases by the lock-in algorithm when outputting a frequency sweep from 1 kHz to 20 kHz.

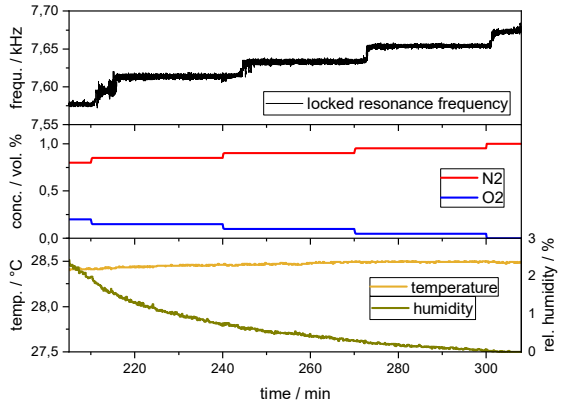

Figure 3: The plot shows the automatically locked resonance frequency for changing gas concentrations.

Conclusion

The use of three frequency modulation of sound sources to excite acoustic resonators enables the real-time determination of both the resonance frequency and the Q-factor, which in turn allows for stable and continuous real-time concentration measurements in direct photoacoustic setups. The speed of resonance tracking is limited only by the sampling rate of the ADC and consequently allows for establishing long-term stable operation without the need for adding complexity to the direct photoacoustic setup. The scheme is scalable in the sense that various eigenmodes of the resonator may be tracked simultaneously.

References

[1] S. Palzer, „Photoacoustic-Based Gas Sensing: A Review," sensors, 2020.

[2] G. Rodriguez Gutierrez et al., „Frequency multiplexing in direct, resonator-enhanced photoacoustic gas sensing setups to establish a reference channel," Sensors and Actuators: B., 2026.

[3] M. Szakáll et al., „Novel resonance profi ling and tracking method for photoacoustic measurements," Applied Physics B, 2009.

[4] C. Weber et al., „Novel approach for efficient resonance tracking in photoacoustic gas sensor systems based on a light-induced wall signal," Photoacoustics, 2023.

[5] T. Wei et al., „Heterodyne photoacoustic gas sensing with real-time resonance tracking in high-Q resonators," Photoacoustics, 2026.

[6] R. W. P. Drever et al., „Laser Phase and Frequency Stabilization Using an optical Resonator," Applied Physics B, 1983.

DOI 10.5162/eurosensors2026/Mo−POS−03

Atomic Structure and Temperature-dependent Photoluminescence of Si-doped Epitaxial Diamond Layer on Nitrogen-rich HPHT Single Crystal Diamond

T. Izsak[1], I. Kozak[1], V. Vretenar[2], M. Matko[2], M. Hulman[1], A. Kozak[1], M. Varga[1]
[1] Institute of Electrical Engineering, Slovak Academy of Sciences,
Dubravska cesta 9, 841 04 Bratislava, Slovak Republic
[2] Centre for Nanodiagnostics of Materials, Faculty of Materials Science and Technology, Slovak University of Technology, 812 43 Vazovova 5, Bratislava, Slovakia
tibor.izsak@savba.sk

Summary:
A single crystal diamond was epitaxially overgrown by MWCVD in the presence of Si wafer pieces. Such a simple approach enables direct growth of Si-doped diamond films (containing SiV color centers) on the nitrogen-rich substrate (containing NV color centers). The sample was studied by means of its atomic structure and its correlation with the temperature- (5–500 K) and excitation wavelength-dependent (405, 488, 532 and 633 nm) photoluminescence properties. Combining and understanding the behavior of different color centers in a single diamond sample opens up new possibilities for various applications.

Keywords: diamond, MWCVD, color centers, Raman spectroscopy, TEM

Background, Motivation and Objective

Diamond, as one of the wide-bandgap materials, is characterized by outstanding properties (such as biocompatibility, chemical and radiation inertness, etc.) that can be further improved by light-emitting color centers in the visible or infrared regions of the light spectrum. Diamonds with sharp, intense, and well-recognizable emission peaks are of significant interest for bio-imaging [1] and integrated quantum photonics [2] applications. Combining different color centers, e.g. NV and SiV, in one diamond sample is an interesting approach that opens up new possibilities in these research fields.

Description of the New Method or System

A high-temperature high-pressure (HPHT) type Ib (100) single crystal diamond (SCD) substrate (E6 Technologies Ltd., UK) with a high nitrogen content ([N]: < 200 ppm), was overgrown in a microwave plasma chemical vapor deposition (MWCVD) system in the presence of clean silicon wafer pieces. The main advantage of this method is that it enables the direct growth of silicon-doped epitaxial diamond films containing silicon-vacancy (SiV) centres [3].

Another advance related to the state of research in this field, is the complex analysis of the color centers (NV and SiV, both present in the prepared sample), including excitation wavelength- and temperature-dependent Raman and photoluminescence spectra measured by different excitation wavelengths (405, 488, 532 and 633 nm) in a wide temperature range of 5-500 K. In addition, the Raman and PL spectra were correlated with HRTEM, SAED, and EDS data.

Results

The epitaxially grown diamond layer (approximately 2 μm thick) is characterized by crystals with a size of 2-4 μm (Fig. 1a). TEM image (Fig. 1b) showed preferential diamond growth normal to the (111) crystallographic planes, resulting in a polycrystalline surface texture characterized by high surface roughness and significant thickness variation (1.8−2.6 μm).

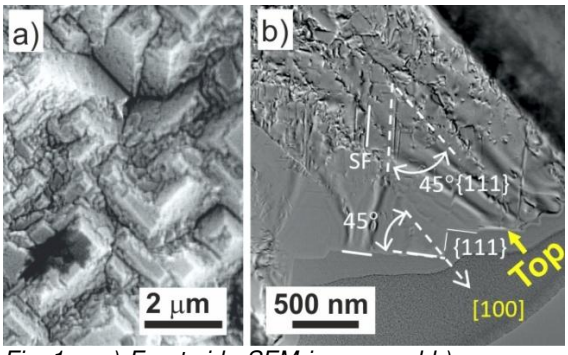

Fig. 1. a) Front-side SEM image and b) cross-section TEM of epitaxially overgrown SCD substrate.

The grown layer exhibits numerous stacking faults and dislocations, which induce local internal strain. Additional strain is also observed at the film–substrate interface. These structural defects are likely associated with Si doping. The

structure and elemental composition were further analyzed using selected-area electron diffraction (SAED) and energy dispersive spectroscopy (EDS) methods.

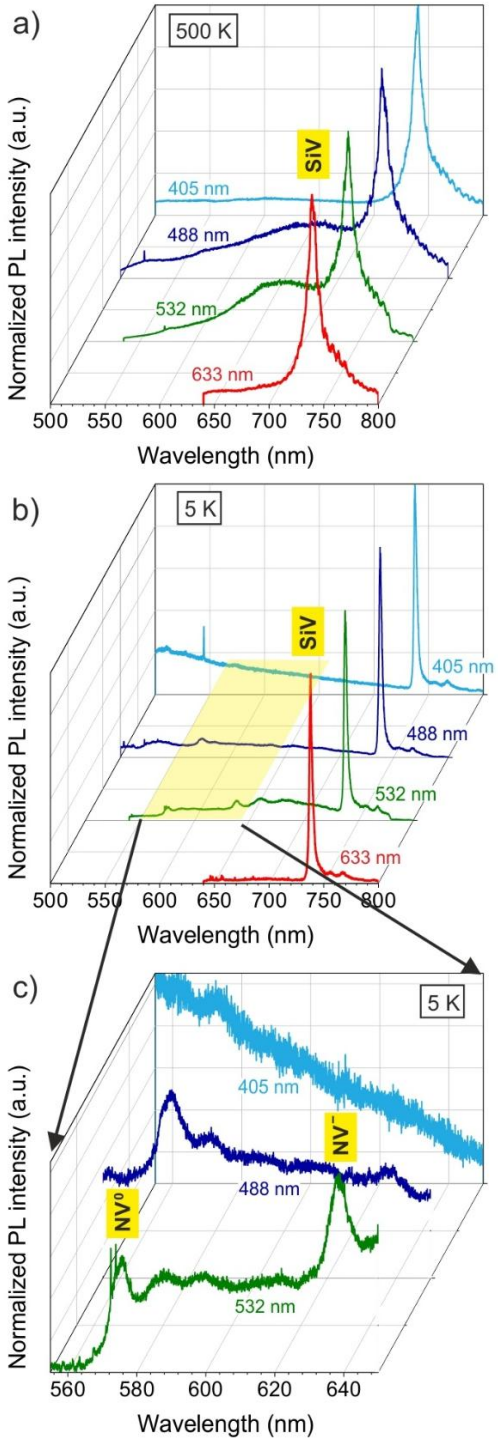

Fig. 2. PL spectra of epitaxially overgrown Ib (100) SCD substrate measured at 500 K (a) and at 5 K (b) with four excitation wavelengths of 405, 488, 532 and 633 nm. c) Detail on the PL spectra of NV centers measured with three excitation wavelengths at 5 K.

Raman spectroscopy showed only a sharp diamond peak at ~1332 cm^{-1} at room temperature. However, within the temperature range 5-500 K, its position shifted from 1333.3 to 1330.5 cm^{-1}. This shift is caused by thermal expansion. Increasing temperature increases the average interatomic distance, causing the crystal lattice slightly to expand.

Photoluminescence spectra revealed three PL peaks corresponding to the NV^0 (575 nm), NV^- (638 nm) and SiV (738 nm) centers, whereas only a strong SiV peak was observed for the whole temperature range (5-500 K). The NV^0 and NV^- are visible only at < 250 K (see Fig. 2).

The NV peaks are more visible when excited by a green laser (Fig. 2c). This is related to several factors including also an increase in the absorption coefficient from approx. 0.15 to 0.3 cm^{-1} as the excitation wavelength decreases from 532 nm to 405 nm [4]. Thus, the epitaxially grown diamond layer absorbs more light from the 405 nm laser than from the 532 nm laser, and suppresses the information from the nitrogen-rich HPHT substrate. The zero-phonon line of the SiV was red-shifted by around 2 nm, while the positions of the NV^0 and NV^- peaks only deviated slightly. A significant decrease in the FWHM of the SiV peak was observed, from 14 cm^{-1} to 2 cm^{-1}, as the temperature decreased from 500 K to 5 K.

Acknowledgements

This work was supported by the Slovak Research and Development Agency (project nr. APVV-23-0361). M.V. acknowledges support from the project IM-2023-87 funded by the Slovak Academy of Sciences via the programme IMPULZ 2023.

References

[1] A. Ermakova, Fluorescent Nanodiamonds for High-Resolution Thermometry in Biology. *Nanomaterials* 14, 1318 (2024,); doi:10.3390/nano14151318

[2] P. K. Shandilya, S. Flågan, N. C. Carvalho, E. Zohari, V. K. Kavatamane, J. E. Losby, P. E. Barclay, Diamond Integrated Quantum Nanophotonics: Spins, Photons and Phonons, *Journal of Lightwave Technology* 40, 7538-7571 (2022), doi:10.1109/JLT.2022.3210466

[3] A. Kromka, M. Varga, K. Aubrechtová Dragounová, O. Babčenko, R. Pfeifer, A. M. Flatae, F. Sledz, F. Akther, M. Agio, Š. Potocký, Š. Stehlík, *ACS Appl. Nano Mater.* 7, 24766–24777 (2024); doi: 10.1021/acsanm.4c04676

[4] A. M. Bennett, B. J. Wickham, H. K. Dhillon, Y. Chen, S. Webster, G. Turri, Mi. Bass, Development of High-purity Optical Grade Single-crystal CVD Diamond for Intracavity Cooling, *Proc. SPIE 8959, Solid State Lasers XXIII: Techn. and Devices*, 89590R (2014); doi: 10.1117/12.2037811

DOI 10.5162/eurosensors2026/Mo–POS–04

Enhanced Optical NO_2 Sensing at Room Temperature through Chemical Reaction-Mediated Plasmonic Interaction

Michael Pereira Martins[1], Andreas T. Güntner[1]
[1] Human-centered Sensing Laboratory, Department of Mechanical and Process Engineering, ETH Zurich, CH-8092 Zurich, Switzerland,
andreas.guentner@hsl.ethz.ch

Summary:
Recently, the interest in plasmonic nanoparticles for sensing applications has been growing due to their ability to colorimetrically quantify gas concentrations, even by naked eye. Specifically, localized surface plasmon resonance (LSPR) results in strong light absorption and enhanced sensing specifically through chemical reaction-mediated LSPR. Here, this is leveraged for the detection of relevant levels of NO_2 at room temperature with high selectivity over significant confounders using TiO_2 nanoparticles decorated with Au. Additionally, the interaction between the Au-TiO_2 nanoparticles and NO_2 has been investigated.

Keywords: plasmonic, nanoparticle, chemical sensor, environmental monitoring, air quality

Background, Motivation and Objective

Most of the urban population is frequently exposed to air pollution, leading to severe health effects and even death [1]. Gas sensing is therefore of interest to monitor the concentration of hazardous compounds and minimize exposure. Chemoresistive nanoparticles have proven to be attractive for on-site monitoring by converting chemical information into electrical signals but lack in selectivity [2], unless enhanced with filters [3], and may require heating resulting in significant power consumption and a bulky device. Therefore, plasmonic nanoparticles are of emerging interest for optical read-out due to their high light absorption, even at room temperature, through LSPR.

The presence of an analyte can change the LSPR peak absorption caused by its refractive index, but volatile organic compounds have rather similar refractive indices [4], limiting selectivity. On top of that, high concentrations are required to obtain a detectable peak shift [5]. On the other hand, through chemical reaction-mediated LSPR, high sensitivity and selectivity can be achieved [6] as shown with Ag/AgO_x-TiO_2 nanohybrids to detect concentrations as low as 5 parts-per-billion (ppb) of formaldehyde with high selectivity (e.g., 600 against ethanol).

Here, TiO_2 nanoparticles are decorated with plasmonic Au clusters through synthesis by flame spray pyrolysis (FSP). These materials are used for relevant ppb-levels detection of NO_2 and have shown high selectivity towards a variety of confounders such as ketones, aldehydes, alcohols and more, all at room temperature and 50% relative humidity (RH). Additionally, the interaction between NO_2 and the sensing material has been investigated

Description of the New Method or System

The synthesis of the Au-decorated TiO_2 nanoparticles was achieved by FSP [7]. A precursor was prepared by first mixing gold(III) acetate (Thermo Scientific, 99.9%) with acetic acid (Fluka, 99.8%) and stirred overnight. Separately, titanium(IV) isopropoxide was dissolved in a 1:1 (v/v) mixture of acetonitrile (Merck, 99.8%) and 2-ethylhexanoic acid (Merck, 99%), and stirred overnight as well. The final precursor solution consisted of 20 vol% acetic acid and had a metal content of 0.5 M.

Particles were then collected from a water-cooled glass fiber filter positioned at 57 cm above the burner. The sensing performance was evaluated using a Cary 5000 spectrophotometer equipped with a Praying Mantis and a high temperature reaction chamber (Harrick Scientific). The following gases were tested: NO_2, NO, ethanol, benzene, NH_3, toluene, methanol, isoprene, acetone, CO_2, H_2, formaldehyde, N_2O, CO, and H_2S. In addition to the sensing performance, X-ray photoelectron spectroscopy (XPS) was used before and after NO_2 exposure to get insights into the sensing mechanisms.

Results

The optimal composition of Au and TiO_2 nanoparticles were exposed to varying concentrations of NO_2 at room temperature to assess the sensing performance (Fig. 1). The performance was characterized by a shift of the LSPR

absorption peak upon exposure to the gas. This shift is explained by a change in the electron density of the plasmonic Au clusters, with a red-shift indicating a reduction of the electron density through chemical interactions. At 500 ppb, a high response of ~15 nm was achieved at room temperature and 50% RH. Even at 25 ppb NO_2, a response of ~3 nm was obtained, considerably higher than previous works.

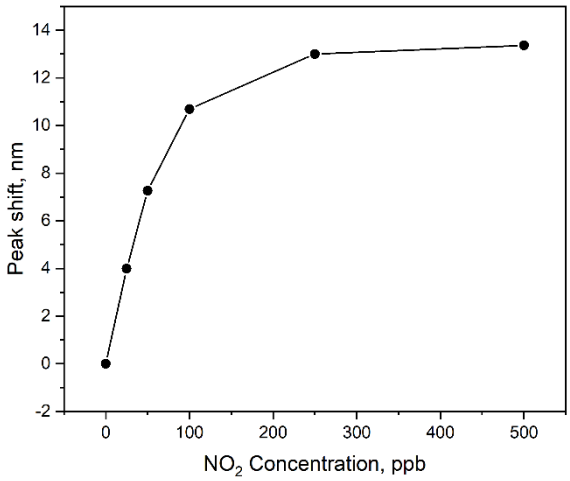

Fig. 1 Plasmonic Au peak shift as a function of NO_2 concentration, error bars represent variation between 3 samples.

The selectivity (Fig. 2) was assessed by exposing the particles to a variety of gases consisting of ketones, aldehydes, alcohols, and more, all at 500 ppb at room temperature and 50% RH. The highest response at 15 nm was obtained for NO_2, followed by NO with a shift of 1 nm, showing promising selectivity. The particles have additionally been exposed to much higher concentrations of CO, CO_2, and ethanol, up to 250 ppm under realistic conditions of 50% RH and at room temperature. There, the highest response was obtained for ethanol with a shift of 0.67 nm at 250 ppm, significantly lower than for NO_2 at 500 ppb.

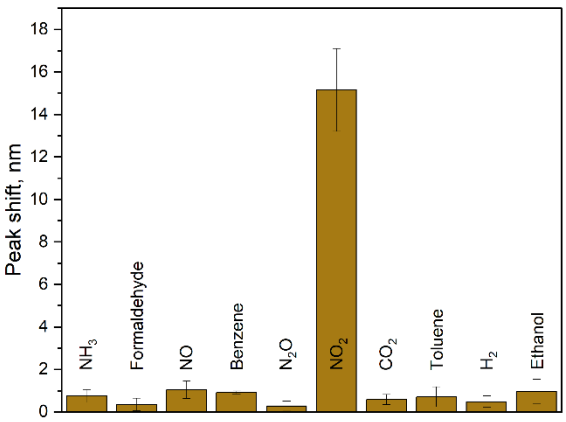

Fig. 2 Selectivity comparison at 500 ppb between NO_2 and a variety of confounders, at room temperature and 50% RH.

The particles have additionally been characterized by XPS before and after exposure to NO_2, showing a significant increase in Au^+ and a decrease in Ti suboxides, indicating reduction in electron density on the Au clusters and the oxidation of the Ti support material. This decrease in electron density of Au is consistent with the observed red-shift upon exposure to NO_2 and corroborates, together with the oxidation of the Ti support, the theorized sensing mechanism for NO_2 sensing.

Fig. 3 Selectivity comparison of 500 ppb NO_2 to 5, 50, and 250 ppm of CO_2, ethanol, and CO.

References

[1] H. Ritchie, M. Roser, Air Pollution, *Our World in Data* (2021) Available online: https://our-worldindata.org/air-pollution#citation (accessed on 14.04.2026)

[2] A. Lewis, P. Edwards, Validation personal air-pollution sensos, *Nature* 535, 29-31 (2016); doi: 10.1038/535029a

[3] S. Abegg, L. Magro, J. van den Broek, S.E. Pratsinis, A.T. Güntner, A pocket-sized device enables detection of methanol adulteration in alcoholic beverages. *Nat. Food* 1, 351-354 (2020); doi: 10.1038/s43016-020-0095-9

[4] W.M. Haynes, *CRC Handbook of Chemistry and Physics*, 97th ed.; CRC Press: Boca Raton, USA, 2016; pp.1-2670

[5] Z. Fusco, M. Rahmani, R. Bo, R. Verre, N. Motta, M. Käll, D. Neshev, A. Tricoli, Nanostructured Dielectric Fractals on Resonant Plasmonic Metasurfaces for Selective and Sensitive Optical Sensing of Volatile Compounds, *Adv Mater.* 30, 1800931 (2018); doi: 10.1002/adma.201800931

[6] A.T. Güntner, F.M. Schenk, Environmental formaldehyde sensing at room temperature by smartphone-assisted and wearable plasmonic nanohybrids, *Nanoscale* 15, 3967-3977 (2023); doi: 10.1039/d2nr06599a

[7] L. Mädler, H.K. Kammler, R. Mueller, S.E. Pratsinis, Controlled synthesis of nanostructured particles by flame spray pyrolysis, *J Aerosol Sci.* 33, 369-389 (2002); doi: 10.1016/S0021-8502(01)00159-8

DOI 10.5162/eurosensors2026/Mo–POS–05

DMOAP-Aligned Bimesogenic Dimers for Wide-Band Spectral Tuning

Rohan Sonar[1], Agus Budi Dharmawan[1], Ismael Benito-Altamirano[1,2,3], J. Daniel Prades[1]
[1] Institute of Semiconductor Technology (IHT) & Laboratory for Emerging Nanometrology (LENA), Technische Universität Braunschweig, Braunschweig, Germany
[2] eHealth Centre, Faculty of Computer Science, Multimedia and Telecommunications, Universitat Oberta de Catalunya, Barcelona, Spain
[3] Department of Electronics and Biomedical Engineering, Universitat de Barcelona, Barcelona, Spain
Email: rohan.sonar@tu-braunschweig.de

Summary:
The objective of this work is to build a wide-range liquid crystal tunable filter (LCTF) designed using a simplified fabrication process, bypassing the need for specialized cleanroom facilities. A central concept involves using a strategic mixture of three commonly available liquid crystals and a chiral dopant to get the right HTP (Helical Twisting Power) and thus an initial pitch exactly where we needed it. For the assembly, since commercial agents like SE-1211 are harder to access, we coated our ITO (Indium Tin Oxide) substrates with DMOAP ((Dimethyloctadecyl[3-(trimethoxysilyl)propyl]ammonium chloride)), which has proved to be a reliable and cheaper alternative for homeotropic alignment. After assembly and filling the cells with our LC (Liquid crystal) mixture, we could precisely drive the device as a voltage-controlled variable optical filter. This approach shows that with a combination of bimesogens and surface anchoring, we can achieve high-end spectral tuning controlled via field-dependent modulation.

Keywords: Non-Mechanical Tunable Optical Filter, Wavelength Tuning, Liquid Crystal Optics, Hyper-spectral Microscopy, Lensless micoscopy.

Background and Motivation

Optical filters are essential for isolating spectral bands in photonic systems, yet conventional static filters are limited by logistical and mechanical constraints. Tunable filters address these challenges by enabling real-time spectral characterization and improved experimental throughput. While many existing tunable systems are prohibitively bulky or expensive, LC technology is re-emerging as a powerful alternative. LCs provide a cost-effective, high-performance solution that is easy to handle and can operate without the need for specialized industrial hardware. This makes them an ideal platform for high-end spectral tuning that remains accessible to the broader research community. [1-4]

This study shows a wide-band tunable optical filter that operates across the visible spectrum. While most studies rely on restricted industrial polyimides like PI-1211 to achieve homeotropic alignment, we utilized a highly diluted DMOAP solution as a benchtop alternative [5]. This approach bypasses the need for specialized industrial hardware and proprietary chemicals, providing a reliable, cost-effective method for achieving alignment in a standard laboratory setting.

Methodology

For our system, the liquid crystal was optimized by substituting CB6OCB with the more commercially accessible CB9CB (4′,4‴-(nonane-1,9-diyl)bis(([1,1′-biphenyl]-4-carbonitrile))), creating a novel ternary bimesogenic mixture with a chiral dopant concentration calculated to set the precise starting pitch. Our fabrication process compared a BY (Bright Yellow) planar alignment against a DMOAP-based homeotropic alignment; as expected, the planar configuration failed to allow for pitch tuning at lower voltages [6], whereas the DMOAP treatment, which was applied via a simple chemical bath, has successfully facilitated the heliconical transition as mentioned in literature [5]. The cells were assembled at a fixed thickness and filled with the LC mixture, and while the work is in its initial stages, we have successfully reproduced the Ch_{OH} (Oblique Helicoidal) state.

Specifically, the observed "blue-shift" (wavelength shortening) under increasing field strengths confirms the relationship described in Eq. 1 [7], where the heliconical pitch P exhibits an inverse proportionality to the electric field E

$$P(E) = \frac{2*\pi*K}{\epsilon_0*\Delta\epsilon*E^2} \qquad (1)$$

where, K = bend elastic constant, ϵ_0 = vaccum permittivity, $\Delta\epsilon$ = Dielectric anisotropy, E = Elec field. Furthermore, the continuous tuning of the reflection peak illustrates the direct proportionality between the pitch and the reflected wavelength (λ) as defined in Eq. 2

$$\lambda = n \cdot P \qquad (2)$$

where, n is average refractive index and P is the helical pitch of LC.

Results

As seen in Fig 1, the device successfully demonstrated the tuning of this filter. Under a stable AC electrical field of 1 kHz (sine) on a temperature controlled stage, as the voltage was incrementally reduced, the system successfully transitioned through a sequence of distinct spectral peaks, shifting from blue to yellow and finally to red. Due to the manual assembly and variations in cell gap uniformity (d ≈ 7 µm), the observed reflection was locally non-homogeneous; however, this is a minor technical variation that can be readily mitigated through the use of calibrated spacers or automated cell-sealing techniques.

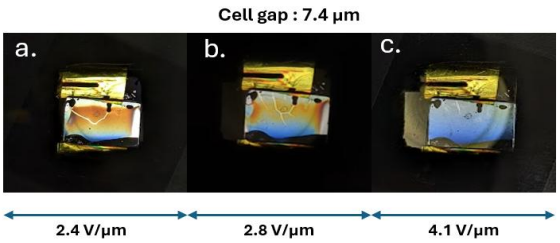

Fig. 3. Field-induced wavelengths in the optical filter. (a) Red, (b) orange, and (c) blue states under crossed polarizers as a function of voltage. Active area: 5mm x 5mm, Filter thickness: 2mm.

Under crossed polarizers, the cell appeared dark in its high-voltage state, indicating that the field had pushed the system beyond the critical threshold (E_C ≈ 5 V/µm). At this saturation point, the heliconical structure collapsed into a homeotropically aligned isotropic state, making the cell totally transparent. This transition was reversible.

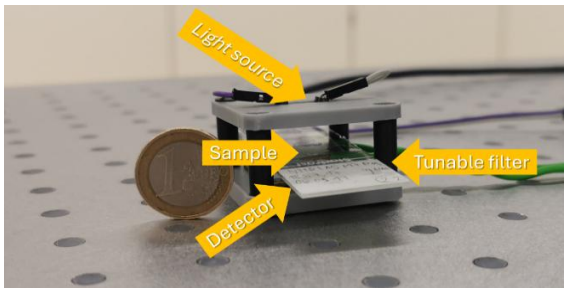

Fig. 4. The integration of the tunable filter and lensless microscope, facilitates a compact, portable imaging platform.

A prominent application for this technology is in lensless microscopy (Fig 4), where LCTFs enable a compact and versatile imaging platform [8]. By integrating tuning directly for either excitation or emission filtering, these systems provide high-resolution spectral data without the need for bulky mechanical hardware. This configuration captures enhanced spatial and spectral information while maintaining a portable, small-scale form factor.

Acknowledgments

This work is supported by the Alexander von Humboldt Professorship of the Humboldt Foundation, and the Federal Ministry for Education and Research, Germany. I.B. greets the support for the Spanish MCIU under the CAS24/00369 José Castillejo grant and the RA 2026 program from UOC.

References

[1] Xiang, Jie, et al. "Electrically tunable selective reflection of light from ultraviolet to visible and infrared by heliconical cholesterics." Advanced Materials (2015): 3014; doi: 10.1002/adma.201500340

[2] Xiang, Jie, et al. "Electrically tunable laser based on oblique heliconical cholesteric liquid crystal." Proceedings of the National Academy of Sciences 113.46 (2016): 12925-12928; doi: 10.1073/pnas.1612212113

[3] Yang, Qing, et al. "Fast tunable biological fluorescence detection device with integrable liquid crystal filter." Crystals 11.3 (2021): 272; doi: 10.3390/cryst11030272

[4] Nava, G., et al. "Heliconical cholesteric liquid crystals as electrically tunable optical filters in notch and bandpass configurations." Liquid Crystals 48.11 (2021): 1534-1543; doi: 10.1080/02678292.2021.1884911

[5] Aouini, Abir, et al. "Chemical-physical characterization of a binary mixture of a twist bend nematic liquid crystal with a smectogen." *Crystals* 10.12 (2020): 1110.; doi: 10.3390/cryst10121110

[6] Iadlovska, Olena S., et al. "Tuning selective reflection of light by surface anchoring in cholesteric cells with oblique helicoidal structures." Optics Letters 43.8 (2018): 1850-1853; doi: 10.1364/OL.43.001850

[7] Mrukiewicz, Mateusz, et al. "Wide temperature range of an electrically tunable selective reflection of light by oblique helicoidal cholesteric." Liquid Crystals 46.10 (2019): 1544-1550; doi: 10.1080/02678292.2019.1587528

[8] Dharmawan, Agus Budi, et al. "Nonmechanical parfocal and autofocus features based on wave propagation distribution in lensfree holographic microscopy." *Scientific Reports* 11.1 (2021): 3213; doi : 10.1038/s41598-021-81098-7

DOI 10.5162/eurosensors2026/Mo–POS–06

Real-time imaging of Microcrystal Growth and Dynamics by Lensless Microscopy in a Cell

Alexey Rybakov[1], Agus Budi Dharmawan[1], J. Daniel Prades[1]
[1] Institute of Semiconductor Technology (IHT) and Laboratory for Emerging Nanometrology (LENA), Technische Universität Braunschweig, Braunschweig, Germany
Email: alexey.rybakov@tu-braunschweig.de

Summary:
We present a lensless microscopy setup for real-time imaging of germanium dioxide microcrystals forming directly inside an incubator. The system enables simultaneous observation over a large detection area, allowing tracking of crystal motion. A variable tilt angle modulates crystal dynamics. Post-processing enables quantification of particle-substrate and particle-solution interactions.

Keywords: microscopy, lensless, microcrystals, crystallization, tracking

Background, Motivation and Objective

Lens-based in situ microscopy of crystals is a classical approach for studying their dynamics in a liquid environment, for example, the growth and dissolution of immobilized crystals, or the diffusion and directed motion of mobile crystals [1]. However, under non-standard conditions (such as variable sample tilt angles, simultaneous detection over a large area, or space-constrained and temperature-controlled settings inside an incubator) this type of microscopy may encounter significant challenges. Lensless, chip-based microscopy circumvents these difficulties and has already demonstrated considerable promise for in situ observation and characterization of both micron-sized particles and bacteria directly within an incubator [2], [3]. Building on these advances in lensless microscopy, we investigated its applicability to the detection of micron-sized crystals.

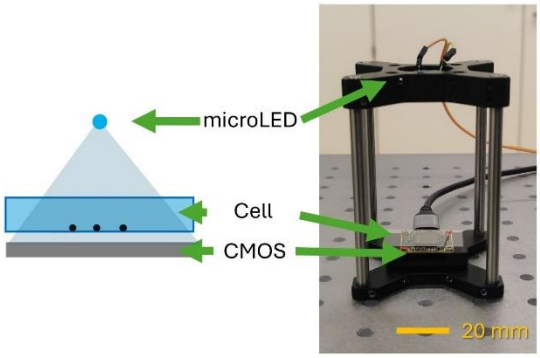

Fig. 1. The lensless microscope's streamlined architecture, comprising only a microLED, a CMOS sensor, and a sample holder, facilitates high-portability observations across diverse environments, including real-time monitoring inside an incubator.

The present work aims to observe the entire process, from the growth of the first detectable crystals in a solution, through their motion, to the accumulation at a preferred location. The study also focuses on the influence of temperature on the crystallization process, as well as on the effects of gravity represented by the tilt angle relative to the horizontal on crystal dynamics.

Description of the New System

Our setup consists of a lensless microscope in which a cell is placed between the microLED (75 µm size and λ = 450 ± 5 nm) and the CMOS sensor, as shown in Fig. 1. The cell consists of two quartz glass windows separated by a PTFE spacer 2 mm in thickness. This portable configuration facilitates experimentation under both ambient conditions and regulated incubator environments, supporting real-time data acquisition through both high-frame-rate video and continuous capture modes.

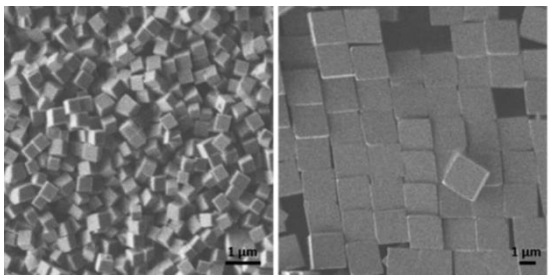

Fig. 2. SEM images of disordered and ordered assemblies of hexagonal GeO_2 cubes.

The cell contains a GeO_2 solution from which cubic-shaped crystals of hexagonal GeO_2 form, with sizes of approximately 0.5–2 µm (Fig. 2). The entire setup is mounted on a stand that allows the tilt angle to be varied from 0° to 90°, and

is placed inside an incubator in which the temperature can be adjusted from 5 °C to 40 °C.

The novelty of our system is threefold. First, we can detect the appearance of new crystals in real time and directly within the incubator, and investigate the dependence of this onset time on the liquid temperature. Second, simultaneous detection over a large area of approx. 35 mm² enables the study of particle dynamics driven by convective flows in the solution. Third, the variable tilt angle allows the crystal dynamics to be actively modulated. Together, these capabilities open new perspectives for in situ microscopy of microcrystal growth, as well as for investigating fundamental aspects of their dynamics governed by interactions with both the solution and the substrate. In addition, raw images are reconstructed via the angular spectrum method to enhance spatial resolution and overall image quality [2].

Results

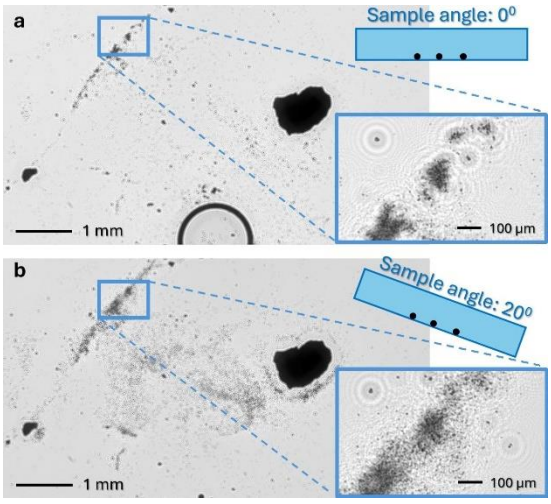

Fig. 3. The large dark spot is the region where particles accumulate due to convective flows in the liquid. Two different crystal densities are shown in the reconstructed images: (a) the cell is parallel to the floor, and in (b) it is slightly tilted to the right.

Over time, the number of newly formed GeO_2 crystals increases. As seen in Fig. 3, they are subject to convective flows and accumulate in a single region located approximately at the center of the cell. By varying the tilt angle of the cell relative to the floor, the crystal density and its spatial distribution can be influenced, as is clearly visible in Fig. 3a and 3b in the regions to the left and right of the cell. In post-processing, the full trajectory of an individual crystal can be reconstructed, and its displacement over a defined time interval calculated. This makes it possible to characterize numerically the interaction of a particle with the solution and the substrate through parameters such as the diffusion coefficient, friction coefficient, and hydrodynamic radius. These parameters depend on the cell tilt angle, as well as on the material and surface properties of the substrate, which opens the possibility for broader systematic investigation.

By varying the distance between the sample and the CMOS sensor, the size of the detected diffraction patterns can also be adjusted. In Fig. 4a, this distance is 2 mm and the diameter of the outer ring is approx. 90 µm, while in Fig. 4b the distance is 17 mm and the diameter is approx. 350 µm. In both cases, the size of the patterns is about two orders of magnitude larger than the size of the microcrystals themselves (Fig. 2), which facilitates their detection.

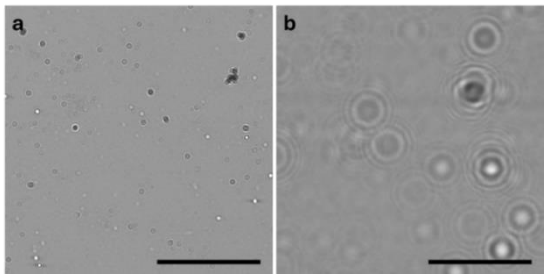

Fig. 4. Increase in diffraction pattern size as a function of distance between the crystals and the CMOS sensor: from 2 mm (a) to 17 mm (b). Scale bar: 500 µm.

Experimental results demonstrate that the lensless microscope maintains high-resolution imaging and an expanded field-of-view (FOV) even under harsh conditions, such as within regulated incubator environments. Furthermore, this approach introduces novel opportunities for in situ measurements, exceeding the technical limitations of conventional instrumentation. Current investigations are extending these findings by systematically modulating thermal parameters and illumination geometries as well as improving the resolution, to further enhance analytical precision and characterization accuracy.

Acknowledgement

This work is supported by the Alexander von Humboldt Professorship of the Humboldt Foundation, and the Federal Ministry for Education and Research, Germany.

References

[1] K. Tsukamoto, “In-situ observation of crystal growth and the mechanism,” Progress in Crystal Growth and Characterization of Materials, vol. 62, no. 2, pp. 111–125, Jun. 2016, doi: 10.1016/j.pcrysgrow.2016.04.005.

[2] A. B. Dharmawan et al., “Nonmechanical parfocal and autofocus features based on wave propagation distribution in lensfree holographic microscopy,” Scientific Reports, vol. 11, no. 1, p. 3213, Feb. 2021, doi: 10.1038/s41598-021-81098-7.

[3] G. Scholz et al., “Continuous Live-Cell culture imaging and Single-Cell tracking by computational lensfree LED microscopy,” Sensors, vol. 19, no. 5, p. 1234, Mar. 2019, doi: 10.3390/s19051234.

DOI 10.5162/eurosensors2026/Mo–POS–07

Label-Free Detection of Exosome Components via a Novel SPR-Raman Platform

Yong Ai Wu[1], Nan-Fu Chiu[1,2], Jou-Chen Lin[1], Tien-Hsiung Ku[3,4,5]
[1] Institute and Undergraduate of Electro-Optical Engineering, National Taiwan Normal University, No. 88, Sec. 4, Ting-Chou Road, Taipei 11677, Taiwan
[2] Research Center for Applied Sciences, Academia Sinica, 128 Academia Road, Section 2, Nankang, Taipei, 11529, Taiwan
[3] Department of Applied Chemistry, Providence University, Taichung 43301, Taiwan
[4] Department of Anesthesiology, Changhua Christian Hospital, Changhua 500209, Taiwan
[5] Artificial Intelligence Development Center, Changhua Christian Hospital, Changhua 500209, Taiwan
nfchiu@ntnu.edu.tw

Summary:
This study introduces a novel biosensing platform that integrates surface plasmon resonance (SPR) and Raman spectroscopy for the quantification of exosomes and the biochemical profiling of their contents, with promising implications for early cancer diagnostics. We successfully determined the concentrations of three exosomal transmembrane proteins—CD63, CD9, and CD81—while simultaneously characterizing the internal molecular cargo using Raman spectroscopy. This dual-modality approach enables real-time, quantitative detection and comprehensive structural analysis of exosomes.

Keywords: surface plasmon resonance (SPR), Raman spectroscopy, exosomes, cancer.

Background, Motivation and Objective

The global epidemiological landscape of lung cancer is undergoing a significant paradigm shift. Although tobacco use remains the dominant risk factor, a growing incidence among never-smokers has been increasingly reported worldwide. Accumulating evidence identifies ambient air pollution, particularly fine particulate matter (PM2.5) and associated carcinogens, as a critical contributor to this trend. Recognizing its impact, the International Agency for Research on Cancer has classified outdoor air pollution as a Group 1 human carcinogen [1,2]. These findings highlight the urgent need for effective early diagnostic strategies. Exosomes have emerged as promising non-invasive biomarkers for precision diagnostics [3]. However, their nanoscale size and structural complexity present analytical challenges. To address these limitations, this study proposes an integrated biosensing platform combining surface plasmon resonance (SPR) with Raman spectroscopy [4,5]. This SPR–Raman system enables real-time quantification of exosomes while providing detailed biochemical profiling of their molecular cargo. By integrating quantitative and qualitative analyses, this multimodal approach enhances sensitivity, specificity, and diagnostic accuracy for early lung cancer detection, particularly in high-risk populations exposed to environmental pollutants.

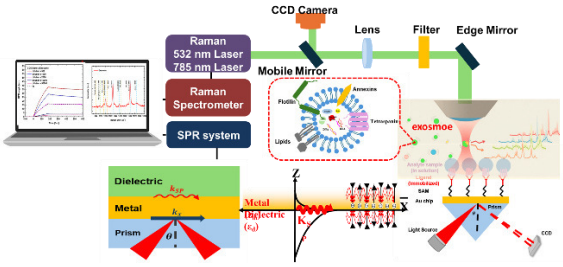

Fig. 1. Schematic representation of the integrated SPR and Raman spectroscopy platform for real-time exosome quantification and molecular profiling.

Description of the New Method or System

In this study, a novel biosensing platform integrating a microscope-based surface plasmon resonance (SPR)–Raman system was developed for real-time, highly sensitive, and label-free detection of exosome biomarkers. The system architecture is illustrated in Figure 1. This enables precise, real-time monitoring of binding kinetics and analyte concentration, while also providing quantitative information on mass accumulation at the sensor surface. However, SPR alone cannot resolve detailed molecular structures or functional groups. To address this limitation, Raman spectroscopy is incorporated to

obtain molecular fingerprint information. Using 532 nm excitation lasers, the microscope-based Raman module detects characteristic vibrational modes, enabling label-free identification of biochemical components without additional labeling. During operation, SPR is first used to monitor biomolecular immobilization and interaction dynamics, followed by Raman analysis to characterize biochemical composition. This integrated platform combines quantitative and qualitative capabilities, offering a comprehensive approach for cancer biomarker detection, early diagnosis, and therapeutic monitoring.

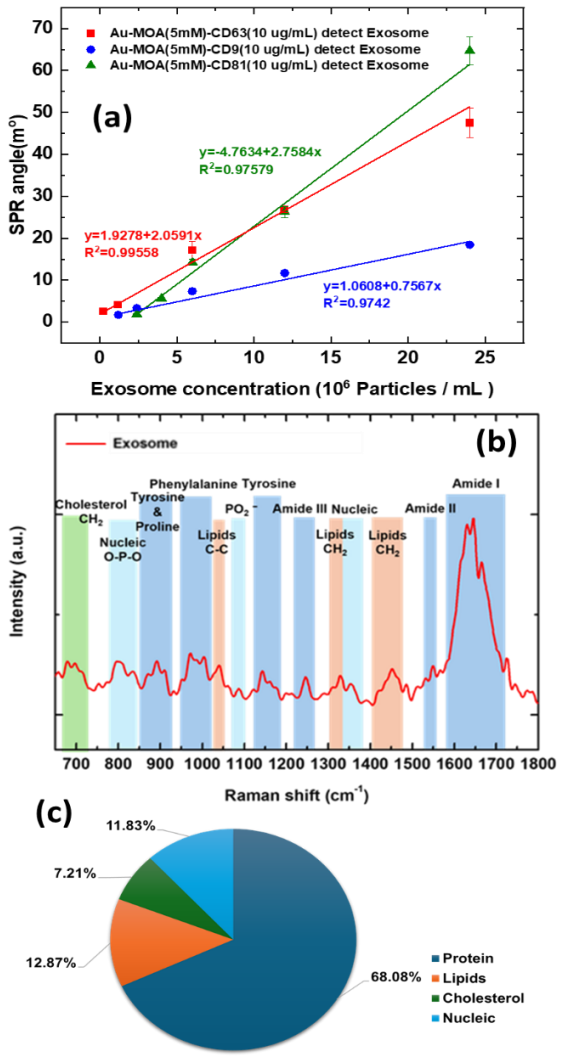

Fig. 2. (a) SPR sensor response demonstrating a linear correlation between biomolecular interactions of exosome surface markers (CD63, CD9, and CD81) and variations in exosome concentration. (b, c) Raman spectra of exosomes acquired using a 532 nm excitation wavelength, together with corresponding spectroscopic characterization and quantitative analysis of molecular composition.

Results

Through SPR analysis, we preliminarily confirmed the presence of key exosomal transmembrane proteins, including CD63, CD9, and CD81, at a measured concentration of 2.4 × 10^6 particles/mL. As shown in Figure 2(a), the SPR sensor demonstrates excellent linearity and a low limit of detection (LOD), indicating high sensitivity and reliable quantitative performance. Figures 2(b) and 2(c) present real-time Raman spectral and compositional analyses of the exosome samples. These results reveal distinct variations in the molecular signatures associated with transmembrane proteins (CD63, CD9, and CD81), reflecting differences in exosome surface composition. The integrated SPR–Raman platform enables simultaneous real-time quantification and biochemical characterization, allowing precise evaluation of protein expression levels and surface binding affinities. Overall, the results provide detailed insights into the molecular characteristics of exosomes. This capability facilitates more accurate discrimination between healthy individuals and those in different physiological or pathological states, highlighting the platform's potential for disease diagnostics and biomarker profiling.

References

[1] International Agency for Research on Cancer (2013). Outdoor air pollution a leading environmental cause of cancer deaths. Lyon: IARC Press.

[2] C.B. Berg et al., Air pollution and lung cancer: mechanistic insights from epidemiology and biology, *Nature* 607, 241-249 (2022); doi:10.1016/j.jtho.2023.05.024

[3] H. Valadi et al., Exosome-mediated transfer of mRNAs and microRNAs is a novel mechanism of genetic exchange between cells, *Nature Cell Biology*, 9, 654-659 (2007); doi:10.1038/ncb1596

[4] C.-L. Chiang, N.-F. Chiu, J.-H. Yang, D.-J. Chang, C.-W. Lin, Layer-by-Layer Characterizations of Protein Complexes by Surface Plasmon Resonance Enhanced Raman System-Detection of Heparin-Platelet Factor IV Complexes as an Example, *Sens. Actuators B Chem.* 452, 139461 (2026). doi:10.1016/j.snb.2026.139461

[5] J.-C. Lin, N.-F. Chiu, Development of an SPR-Raman biosensor for early lung cancer biomarker detection, *Proc. SPIE*, Optical Sensors 2025, 135270S (23 May 2025). doi:10.1117/12.3056355

DOI 10.5162/eurosensors2026/Tu–POS–01

Rapid Vaccine Screening and Component Analysis via a SERS Platform with Plasmonic Concentric Nanostructure Enhancers

I-Ju Chen[1], Yong-Ai Wu[1], Yu-Tien Cheng[1], Hsiao-Yu Ko[1], Nan-Fu Chiu[1,2] ,Ka-Kwan (David) Kuo[3]*
[1] Institute and Undergraduate of Electro-Optical Engineering, National Taiwan Normal University, No. 88, Sec. 4, Ting-Chou Road, Taipei 11677, Taiwan
[2] Research Center for Applied Sciences, Academia Sinica, 128 Academia Road, Section 2, Nankang, Taipei, 11529, Taiwan
[3] Taipei Union Hospital for Women and Children, No.5, Ln. 85, Song-Jiang Rd., Jhong-Shan Dist., Taipei, 10486, Taiwan
nfchiu@ntnu.edu.tw

Summary:
This study presents a highly sensitive SERS platform based on plasmonic concentric nanostructures (PCN) for rapid, label-free analysis of the Spikevax mRNA vaccine. The nanorings generate strong hotspots, enabling clear identification of mRNA, lipid nanoparticles (LNPs), and excipients (e.g., sucrose, PEG) with high reproducibility, offering an efficient tool for vaccine quality control and stability monitoring.

Keywords: plasmonic concentric nanostructures (PCN), surface-enhanced Raman scattering (SERS), mRNA vaccine.

Background, Motivation and Objective

Vaccines are essential in modern healthcare, with mRNA vaccines transforming prevention during the COVID-19 pandemic [1-3]. Their clinical success relies on rigorous quality control (QC) to ensure the integrity and stability of complex mRNA–lipid nanoparticle (LNP) formulations, such as Moderna (Spikevax). However, conventional QC methods are often time-consuming, destructive, and require large sample volumes, limiting efficiency. To address these challenges, this study proposes a surface-enhanced Raman scattering (SERS) platform based on plasmonic concentric nanostructures. This approach enables rapid, label-free, and ultra-sensitive characterization using minimal, non-destructive samples. The generated electromagnetic hotspots amplify weak biomolecular signals, allowing precise identification of mRNA, LNPs, and excipients. This platform offers a powerful solution for real-time stability monitoring and scalable vaccine QC.

Description of the New Method or System

The core of the measurement system is based on PCN biosensors precisely fabricated using electron beam lithography (EBL). The circular grating defines a functional area of 1.2 × 1.2 mm². The PCN biosensors are specifically designed with a linewidth of 400 nm and a pitch of 800 nm. This optimized geometric architecture enables highly efficient excitation of surface plasmon polaritons (SPPs) under illumination [4-6]. As SPPs are generated and propagate along the concentric rings, they constructively interfere, significantly enhancing the localized interfacial electric field, particularly near the center of the structure. This strong electromagnetic confinement creates intense “hotspots,” which greatly amplify the SERS signals of target analytes, as shown in Figure 1. Consequently, this design markedly improves the optical sensing performance of the integrated system, providing ultrasensitive and reliable detection.

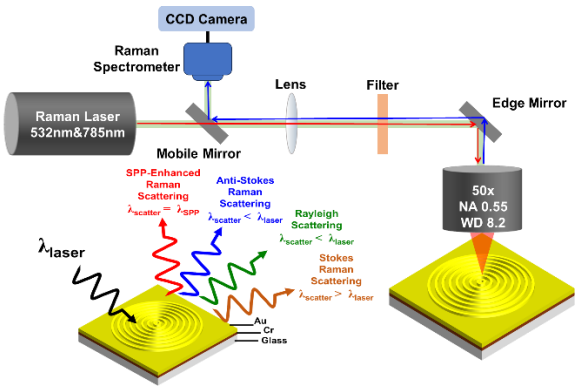

Fig. 1. A novel PCN biosensing platform designed for the highly sensitive detection of vaccines, enabling the accurate acquisition of amplified SERS signals.

Results

SERS spectroscopic analysis of the Moderna Spikevax COVID-19 vaccine was performed using the PCN-based biosensor across concentrations ranging from 2 to 200 µg/mL. Compared with a conventional Au film, the PCN structure exhibited an approximately 50-fold enhancement in Raman signal intensity (Lipids C-C) under optimized water conditions, as shown in Figure 2. Measurements were conducted using a 785 nm excitation laser with a power density of 0.0126 W/µm² (NA = 0.55). Overall, the results demonstrate that excitation wavelength, laser power, and measurement environment strongly influence SERS signal intensity and spectral features, highlighting the capability of the PCN platform for sensitive detection of vaccine biomolecular signatures under both dry and physiological-like conditions.

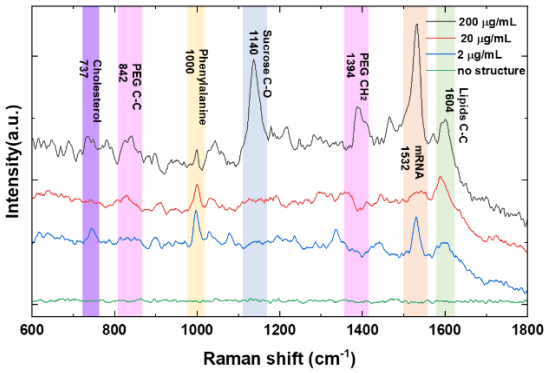

Fig. 2. SERS spectra of the Moderna (Spikevax) mRNA vaccine acquired using a PCN-based biosensor under varying measurement conditions.

References

[1] N. Pardi, M.J. Hogan, F.W. Porter, D. Weissman, mRNA vaccines—a new era in vaccinology, *Nat Rev Drug Discov.* 17, 261-279 (2018). doi:10.1038/nrd.2017.243

[2] U. Sahin, Ö. Türeci, Personalized vaccines for cancer immunotherapy, *Science* 359, 1355-1360 (2018). doi:10.1126/science.aar7112

[3] L. Schoenmaker, D. Witzigmann, J.A. Kulkarni, R. Verbeke, G. Kersten, W. Jiskoot, D.J.A. Crommelin, mRNA-lipid nanoparticle COVID-19 vaccines: Structure and stability. *Int. J. Pharm.* 601, 120586 (2021). doi: 10.1016/j.ijpharm.2021.120586

[4] N.-F. Chiu, C.-H. Hou, C.-J. Cheng, F.-Y. Tsai, Plasmonic circular nanostructure for enhanced light absorption in organic solar cells, *Int. J. Photoenergy,* 502576 (2013). doi:10.1155/2013/502576

[5] D.T. Nurrohman, G.R.A. Cagayan, N.-F. Chiu, Characterization of SPR and cavity modes in one-dimensional (1D) gold nanograting chips: figure of merit analysis and implications for Raman signal enhancement, *Optics Express* 33, 1542-1555 (2025). doi:10.1364/OE.547581

[6] C.-L. Chiang, N.-F. Chiu, J.-H. Yang, D.-J. Chang, C.-W. Lin, Layer-by-Layer Characterizations of Protein Complexes by Surface Plasmon Resonance Enhanced Raman System-Detection of Heparin-Platelet Factor IV Complexes as an Example, *Sens. Actuators B Chem.* 452, 139461 (2026). doi:10.1016/j.snb.2026.139461

DOI 10.5162/eurosensors2026/Tu–POS–02

MEMS-based microplasma devices on glass substrates for optical emission spectroscopy

Enrique Escobedo-Cousin[1,], Karolina Milenko[1], Michael Getz[1], Do Chi Huong Hoang[1], Aina Kristin Herbjørnrød[1] and Elizaveta Vereshchagina[1]*
[1] SINTEF Digital, Smart Sensors and Microsystems, Gaustadalléen 23C, 0373 Oslo, Norway
**enrique.escobedo-cousin@sintef.no*

Summary:

This work presents the design, fabrication, and characterisation of MEMS-based microplasma devices implemented on glass substrates for optical emission spectroscopy (OES). The use of glass substrates is explored to reduce substrate-related leakage currents compared to conventional silicon-based devices. Devices were fabricated using thin-film metallisation and dielectric passivation layers compatible with available processing routes. Plasma ignition was achieved at applied voltages in the kV range and excitation frequencies around 10 kHz. The device behaviour observed indicates that the use of glass substrates does not provide a clear advantage in terms of stability or lifetime under the conditions tested. The results suggest that device performance is primarily governed by dielectric properties and electrode configuration, rather than substrate conduction.

Keywords: MEMS, microplasma, dielectric barrier discharge, optical emission spectroscopy, gas analysis

Introduction

Non-thermal microplasmas have been widely explored for gas analysis using optical emission spectroscopy (OES). Plasma OES enables identification of molecular species through their characteristic emission spectra, providing a compact and versatile approach to gas sensing. Integration of plasma sources into micro-electromechanical systems (MEMS) platforms enables miniaturisation and supports the development of portable, point-of-need systems [1-3].

In this work, we investigate microplasma devices based on the dielectric barrier discharge (DBD) principle, fabricated on glass substrates. The use of glass substrates is explored to reduce substrate-related leakage currents present in silicon-based devices. While silicon substrates are convenient for MEMS processing, their finite conductivity may introduce parasitic losses and influence device operation. Glass substrates provide electrical insulation, potentially reducing substrate coupling and associated losses in the device.

The objective of this study is to assess the impact of substrate choice on device behaviour, focusing on plasma ignition, stability, and qualitative performance under comparable operating conditions.

Design

A minimal configuration for microplasma generation consists of two metal electrodes patterned on an electrically insulating substrate and covered with a dielectric passivation layer. Plasma ignition occurs when the applied voltage generates an electric field in the gas that exceeds the breakdown threshold, while remaining below the limits that would damage the dielectric.

The devices investigated in this work are based on planar electrode configurations with characteristic gap sizes of 10, 25, and 50 µm. Both single devices and linear arrays were implemented. The total chip size is 8 × 8 mm². The dielectric passivation layer consists of an ALD-deposited Al_2O_3 film with thicknesses in the range of 0.25–1 µm.

Compared to silicon-based designs, the use of a glass substrate removes direct electrical coupling to the substrate. Under these conditions, the device capacitance and operating behaviour are primarily governed by the dielectric stack and electrode geometry.

Fabrication

Devices were fabricated using MEMS-compatible processes adapted to glass substrates. Thin-film metal electrodes were deposited and patterned using standard lithographic techniques.

Due to process constraints, gold (Au) was used as the electrode material.

A dielectric passivation layer of Al_2O_3 was deposited over the electrodes to mitigate sputtering-induced erosion and to define the active plasma region. Openings were formed in the passivation layer to provide electrical access for wire bonding. The devices were subsequently diced and mounted on custom printed circuit boards (Fig. 1a).

The fabrication flow differs from the silicon-based process primarily in substrate material, metallisation, and dielectric deposition.

Characterisation

Following fabrication and packaging, the devices were tested for plasma ignition and operation under controlled conditions. A high-voltage excitation setup was used, consisting of a waveform generator and a voltage amplifier providing peak-to-peak voltages in the range of 1.0–2.0 kV at frequencies of 10 kHz. The plasma emission was monitored optically using a microscope and a spectrometer, with integration times in the ms range.

Plasma ignition was observed in ambient air at pressures of 200-500 mbar (Fig. 1c). The plasma emission was monitored optically using a microscope and a spectrometer. Representative emission spectra show characteristic peaks corresponding to species present in air.

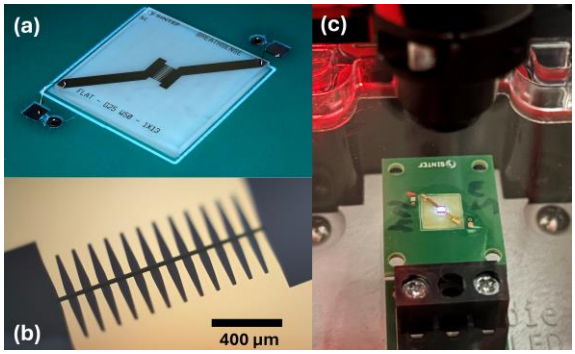

Fig. 1. MEMS DBD microplasma device on glass: (a) chip bonded to PCB, (b) 13-finger electrode array detail, (c) plasma in operation.

In comparison to silicon-based devices with standard dielectric passivation, the glass-based devices exhibited similar qualitative behaviour in terms of ignition and emission. However, no clear improvement in device lifetime or stability was observed. In several cases, localised sparking and degradation of the dielectric passivation were observed during operation.

The increased capacitance associated with the Al_2O_3 dielectric layer is consistent with its higher relative permittivity compared to SiO_2/Si_3N_4 stacks used in previous designs [4, 5]. This increased capacitance may influence the electrical behaviour and energy dissipation in the device.

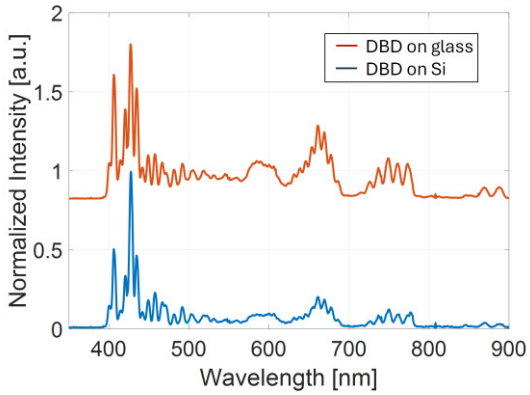

Fig. 2. Comparison of spectra collected in air from DBD microplasmas on glass (red line) and silicon substrates (blue line). The spectrum peaks observed correspond to the emission wavelengths expected for nitrogen.

Conclusion

MEMS-based microplasma devices were fabricated and operated on glass substrates. Under the tested conditions, no clear improvement in performance was observed compared to silicon-based devices. The results indicate that device behaviour is primarily governed by dielectric properties and electrode configuration rather than substrate material. Further optimisation of the dielectric stack and geometry is required to improve stability and lifetime.

References

[1] Kogelschatz, U. (2007), Applications of Microplasmas and Microreactor Technology. Contrib. Plasma Phys., 47: 80-88.

[2] Park S.J. et al. (2005), 40000-pixel arrays of ac-excited silicon microcavity plasma devices, Appl. Phys. Lett. 86, 111501.

[3] R. Brandenburg et al., Barrier Discharges in Science and Technology Since 2003. Plasma Chem. Plasma Process. 43 (2023), 1303–1334.

[4] A. Ellingsen et al., Integration of MEMS-based plasma emission sources in a low-volume flow cell. Proc. of Eurosensors XXXVI 2025, Wroclaw, Poland.

[5] E. Vereshchagina et al., MEMS-based microplasma sources for gas analysis. Proc. of Eurosensors XXXVII 2025, Wroclaw, Poland.

Acknowledgements

The work in this project is financed by Horizon Europe (grant agreement number 101115028).

DOI 10.5162/eurosensors2026/Tu–POS–04

Interface-Controlled Transport and Broadband Photoresponse in ZnO photodetectros modified with Nitrogen and Phosphorus-Doped Carbon Dots

Nikolaos Ganotis[1], Spyridon N. Katsantonis[1,2], Spiros Gardelis[3], Marko Bošković[4], Danijela Randjelović[4], Maryam A. Saeed[5], Sowmya Dean[5], Yaaqoub Malallah[5], Konstantinos V. Kordatos[2], Emmanouel Hourdakis[6], Christos Tsamis[1]
[1]Inst. of Nanoscience and Nanotechnology, National Center for Scientific Research (NCSR) "Demokritos",Patr. Grigoriou E' &27 Neapoleos Str., Aghia Paraskevi, 15341, Athens, Greece
[2]Department of Chemical Sciences, School of Chemical Engineering, National Technical University of Athens (NTUA), 9 Iroon Polytechniou Str., 15772, Athens, Greece
[3]Condensed Matter Physics Section, Physics Department, National and Kapodistrian University of Athens (NKUA), Panepistimioupolis Zografos, 15784, Athens, Greece
[4]Institute of Chemistry, Technology and Metallurgy (ICTM), National Institute of the Republic of Serbia, University of Belgrade, Njegoševa 12, 11000 Belgrade, Serbia
[5]Energy and Building Research Center, Kuwait Institute for Scientific Research, Kuwait City, Kuwait
[6]School of Electrical and Computer Engineering, National Technical University of Athens (NTUA), 9 Iroon Polytechniou Str., 15772, Athens Greece
c.tsamis@inn.demokritos.g

Summary:

In this work we investigate the influence of N- and P-doped carbon dots on ZnO thin films and their applications as photodetectors. Our results indicate that aqueous deposition leads to nonuniform interfaces and asymmetric I–V behavior, while glycerol deposition gives more uniform and symmetric transport. Under illumination, conductivity increases via photogeneration and electron injection from the carbon dots, consistent with a photogating effect. The photocurrent spectrum broadens from the UV (300–500 nm) to the visible–NIR (~1100 nm) due to carbon dot absorption and interfacial states.

Keywords: ZnO; phosphorus-doped carbon dots; photogating effect; interfacial charge transfer; asymmetric transport

Introduction

ZnO is widely employed in sensing and photodetection, predominantly in the ultraviolet range due to its wide bandgap (3.37 eV) and large exciton binding energy (~60 meV) at room temperature. Incorporating nitrogen-doped and phosphorus-doped carbon dots (CDs) with ZnO offers a route to extend sensitivity into the visible and near-infrared regions [1,2]. Understanding how these carbon dots affect charge transport and interfacial properties is crucial for developing broadband photodetectors and advanced optical sensors. In this study, we investigate the impact of Nitrogen and Phosphorus-Doped carbon dots on the optical and electrical properties of thin ZnO films.

Materials and Methods

For the fabrication of the photodetectors, silicon samples with a 100nm silicon dioxide on the surface were used. A 30nm ZnO thin film was deposited on the surface of the samples using spin-coating technique Subsequently, the ZnO layer was patterned, and aluminum electrodes were deposited on top of the ZnO layer using lift-off process. A photograph of the device is shown in figure 1. Various types of carbon dots were deposited on top of the electrodes and the ZnO film using drop-casting. CDs with two different types of doping were solvothermally synthesized by using citric acid, urea and phosphoric acid as sources of carbon, Nitrogen and Phosphorous, respectively. P-doped, N-doped and N,P-co-doped carbon dots were synthesized. Aqueous as well as glycerol solutions were used for the dispersion of the CDs

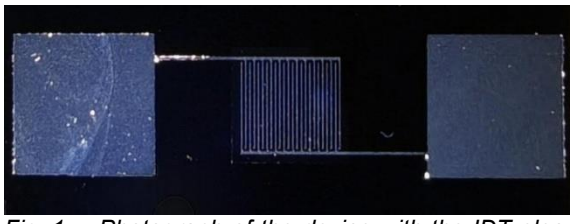

Fig. 1. Photograph of the device with the IDT electrodes.

Photocurrent measurements were carried out using a xenon (Xe) arc lamp coupled to an Oriel 7200 Monochromator for wavelength-selective excitation while photoluminescence measurements were performed using a 355 nm UV laser as the excitation source.

Results and discussion

Pristine ZnO samples show linear and symmetric current–voltage (I–V) characteristics, confirming ohmic transport. Under illumination, the photocurrent increases linearly with applied voltage, indicating classical photoconductive behavior (Fig.2).

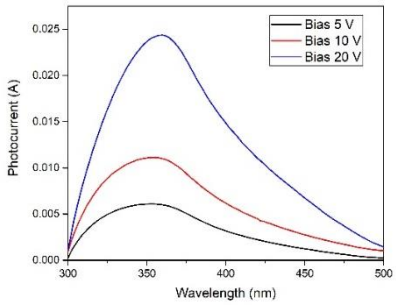

Fig. 2. Spectral dependence of photocurrents of pristine ZnO.

Following deposition of phosphorus-doped carbon dots (P-CDs) from either glycerol or aqueous dispersions, ZnO exhibits a pronounced increase in resistivity and a transition to non-ohmic transport. This behavior is attributed to interfacial charge transfer at the ZnO/P-CD interface. Electron-withdrawing surface states associated with phosphorus doping and functional groups deplete electrons from the near-surface region of ZnO, resulting in upward band bending and formation of a space-charge layer. An asymmetry in the I–V characteristics is observed after P-CD deposition, particularly for aqueous processing. This asymmetry originates from nonuniform interfacial modification of ZnO. Rapid evaporation of water leads to inhomogeneous carbon dot distribution, often with enhanced accumulation near electrode edges. These effects result in unequal band bending and trap densities at the two electrode interfaces, giving rise to asymmetric carrier injection barriers and polarity-dependent transport. In contrast, deposition from glycerol solutions results in more symmetric I–V characteristics and photocurrent in both polarities. The higher viscosity and slower evaporation rate of glycerol promote more uniform carbon dot coverage, leading to homogeneous interfacial modification and more balanced carrier injection at both electrodes.

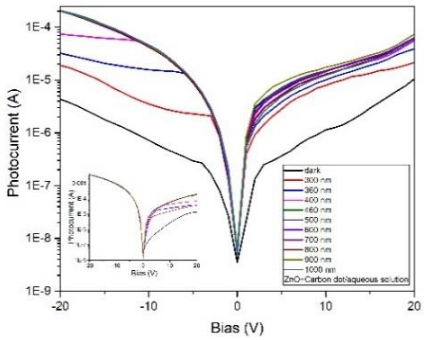

Fig. 3. Current-voltage (I-V) characteristics in dark and under illumination for deposition from glycerol solution. Inset: I-V for deposition from aqueous solution.

Under illumination in the 300–1000 nm spectral range, conductivity increases in all P-CD-modified samples. Illumination reduces the depletion region and lowers the interfacial barrier through a combination of photogenerated carriers in ZnO, photoexcitation of P-CDs, electron injection into the ZnO conduction band, and trap depopulation. This behavior is consistent with a photogating effect, where photoinduced trapped charges modulate the conductivity of the ZnO channel (Fig. 3). Detailed results for the N- as well as N,P-co-doped samples will be presented.

References

[1] J. Wang, C. Chen, M. Jin, Y. Zhu, N. Zhang, The carbon dots modified ZnO films photodetector with broadband and fast photoresponse, Optical Materials 135, 113341 (2023); doi: 10.1016/j.optmat.2022.113341

[2] Y. Zhang, Z. Luo, J. Li, X. Yu, X. Yu, Q. Qiao, H. Zhang, Z. Li, Y. Zhou, Coffee grounds carbon quantum dots modified ZnO nanorods for Near-UV photodetectors Optical Materials 151, 115371 (2024); doi:10.1016/j.optmat.2024.115371

Acknowledgments

This research was sponsored by the NATO Science for Peace and Security Programme under the Multi-Year Project NextGenVLC (grant id. [G7264]) and partially supported by the Ministry of Science, Technological Development and Innovation of the Republic of Serbia (Contract No. 451-03-136/2025-03/200026).

DOI 10.5162/eurosensors2026/Tu–POS–05

A Low-Cost Fully 3D-Printed Automated Magnetic Bead Capture System with Real-Time Optical Monitoring

Pulkit Saluja[1], Sirio Vittorio Feltrin[1], Maria Dimaki[1], Winnie Edith Svendsen[1]
[1] Technical University of Denmark, DTU Bioengineering Søltofts Plads, Kgs. Lyngby-2800, Denmark
wisv@dtu.dk

Summary:
In this work we present a low-cost, 3D-printed magnetic bead-capturing system that uses an automatic magnet-retraction mechanism to control magnetic bead capture, and a (LDR) light-dependent resistors and LED (light-emitting-diode) based optical monitoring system integrated in a custom-made 3D printed microtube rack that was added to monitor real-time bead accumulation for up to eight microtubes simultaneously.

Keywords: 3D printing, paramagnetic beads, magnet-retraction mechanism, photoresistor, optical detection

Background, Motivation and Objective

Magnetic beads are widely used in biosensing, diagnostics, and sample preparation, and are typically separated from solution using magnetic racks or separators [1–4]. The magnetic bead-capturing step usually relies on manual visual inspection to determine whether the beads have fully migrated toward the magnet and whether the remaining liquid can be extracted. This manual reliance on the operator's judgment can make the process tedious when handling multiple samples with different bead concentrations, as the operator must repeatedly verify that all beads have been fully captured [5,6]. Even in automated sample-preparation systems, bead capture is typically controlled by a fixed, time-based protocol rather than real-time sensing [7]. Operators often need to adjust capture time manually because time-based methods do not account for variations in bead concentration, viscosity, or sample composition. To address this, we developed a low-cost, 3D-printed bead-capturing system that combines an automatic magnet-retraction mechanism with an LED–LDR sensing module for real-time monitoring of bead accumulation. This makes the system suitable for automated sample-preparation workflows.

Description of the New Method or System

The automatic bead-capturing system consists of two integrated modules: a magnet-retraction mechanism with eight permanent magnets and a custom 3D-printed rack for eight 2 mL microtubes. The mechanism actuates four linked arms, each carrying two magnets that move toward the tubes for bead capture or retract for releasing the beads, the mechanism is driven by a single micro-servo motor. The microtube rack aligns with the mechanism and incorporates eight pairs of green LEDs and LDRs for optical sensing. The fully integrated system is shown in Fig. 1.

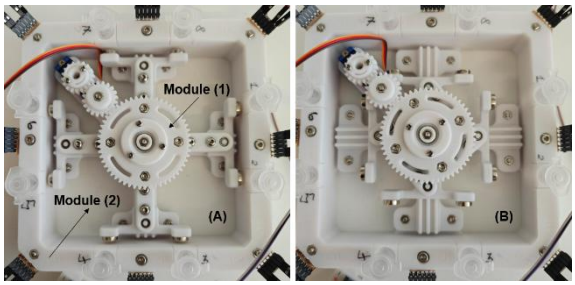

Fig. 1. 3D-printed setup of the integrated system showing Module 1 (permanent-magnet retraction mechanism) and Module 2 (LED–LDR optical detection system). In (A), the mechanism is fully extended, positioning the magnets close to the microtubes to capture the magnetic beads. In (B), the mechanism is retracted, moving the magnets away from the tubes to allow the beads to redisperse.

When a microtube containing suspended magnetic beads is placed in the rack, the beads initially remain dispersed and partially block the light, which increases the LDR's resistance. When the magnet-retraction mechanism is activated, the magnets move toward the microtubes and pull the beads to the microtube wall and clearing the optical path. This allows more LED light to reach the LDR, causing a sharp drop in resistance that indicates bead capture. (Fig.2) shows the alignment of the LEDs, LDRs, and microtubes inside the rack, ensuring the LED light passes through the tube before reaching the

sensor. This setup integrates magnet actuation with real-time optical sensing, forming what we believe is the first low-cost, 3D-printed platform combining an eight-magnet retraction mechanism with LED–LDR detection for automated bead accumulation. This enables feedback-controlled bead capture and improves the reliability of automated sample-preparation workflows.

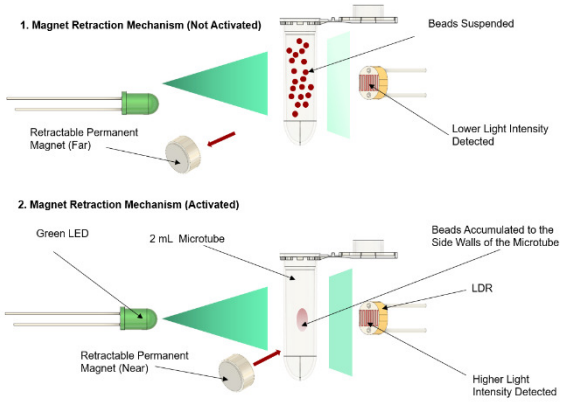

Fig. 2. Physical arrangement of the microtube, LED, and LDR inside the custom 3D-printed microtube rack. The proximity of the permanent magnet determines whether the beads accumulate along the tube wall (magnet near) or remain dispersed in the solution (magnet far).

Results

Magnetic beads were added in DI water to prepare six concentrations (2x, 1x, 0.5x, 0.25x, 0.125x, 0.0625x) using a 1:2 serial dilution, where 1x corresponded to 50 µL of beads in 1 mL DI water. Two additional tubes were included: a DI-water baseline and a 2x reference. For the reference tube, the magnet was physically removed from the mechanism at that specific position so that this tube remained unaffected during the magnetic bead capture.

All eight tubes were placed in the custom microtube rack. The magnet actuation mechanism was initially in the retracted position (Fig. 1B) and then activated after a short delay. Each tube was measured five times. Between runs, bead containing tubes including the 2x reference were manually shaken to redisperse the beads, while the baseline microtube remained undisturbed. Voltage signals from the LDRs were recorded at 10 Hz for 30 s as the beads migrated toward the magnet. For each microtube, the five voltage–time curves were averaged to obtain a representative response. The baseline produced a low, nearly horizontal signal (0–0.3 V), while the 2x reference produced the highest and similarly stable signal (3.5–4.0 V). The six bead concentrations produced averaged curves between these two extremes, with higher concentrations showing greater initial optical blockage and faster signal decay after magnet activation. Although individual runs occasionally showed some irregularities between the 1x and 2x samples at early time points which might need further investigation. However, the averaged curves preserved the expected concentration-dependent trend. The resulting eight averaged curves are shown in Fig. 3.

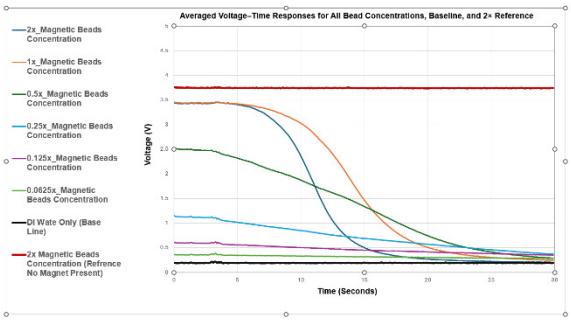

Fig. 3. Averaged voltage–time curves for six bead concentrations, the baseline, and the 2x reference. Each curve represents the average of five measurements, with the 2x reference measured without magnetic capture.

References

[1] Paleček, E.; Fojta, M. Magnetic beads as versatile tools for electrochemical DNA and protein biosensing. Talanta. Elsevier December 15, 2007, pp 276–290. doi:10.1016/j.talanta.2007.08.020.

[2] Aytur, T.; Foley, J.; Anwar, M.; Boser, B.; Harris, E.; Beatty, P. R. A novel magnetic bead bioassay platform using a microchip-based sensor for infectious disease diagnosis. Journal of Immunological Methods **2006**, 314(1–2), 21–29. doi:10.1016/j.jim.2006.05.006.

[3] Guckenberger, D. J.; Pezzi, H. M.; Regier, M. C.; Berry, S. M.; Fawcett, K.; Barrett, K.; et al. Magnetic System for Automated Manipulation of Paramagnetic Particles. Analytical Chemistry **2016**, 88(20), 9902–9907. doi:10.1021/acs.analchem.6b02257.

[4] Gijs, M. A. M. Magnetic bead handling on-chip: New opportunities for analytical applications. Microfluidics and Nanofluidics. November 2004, pp 22–40. doi:10.1007/s10404-004-0010-y.

[5] Safarik, I.; Safarikova, M. Magnetic techniques for the isolation and purification of proteins and peptides. BioMagnetic Research and Technology. November 26, 2004. doi:10.1186/1477-044X-2-7.

[6] Bu, M.; Christensen, T. B.; Smistrup, K.; Wolff, A.; Hansen, M. F. Characterization of a microfluidic magnetic bead separator for high-throughput applications. Sensors and Actuators, A: Physical **2008**, 145–146(1–2), 430–436. doi:10.1016/j.sna.2007.12.014.

[7] Berensmeier, S. Magnetic particles for the separation and purification of nucleic acids. Applied Microbiology and Biotechnology. December 2006, pp 495–504. doi:10.1007/s00253-006-0675-0.

DOI 10.5162/eurosensors2026/Tu–POS–06

Beyond iSCAT Sensitivity: Mechanistic Control of Photodamage in Label-Free Biosensing

Beyza Nur Küçük[1], Andrea Sottini[1], Jaime Ortega Arroyo[1,*], Romain Quidant[1,*]
[1] Nanophotonic Systems Laboratory, Department of Mechanical and Process Engineering, ETH Zurich, Tannenstrasse 3, Zurich 8092, Switzerland
bkuecuek@ethz.ch

Summary:
This work investigates photodamage in optical biosensors by examining antibody–antigen binding kinetics in label-free digital immunoassays. Blue light induces a rapid loss of bound analyte, while orange light provides a more stable response, highlighting strong wavelength dependence. Mechanistic studies identify immobilized antibodies as the most sensitive component, undergoing irreversible, ROS-mediated degradation under blue illumination. These results show that biosensor performance must be evaluated beyond sensitivity, and that shifting to longer wavelengths, such as orange, can mitigate photodamage while maintaining functionality.

Keywords: Digital immunoassays, interferometric scattering microscope (iSCAT), photodamage

Introduction

Ultrasensitive optical imaging based on interference provides a powerful route to probe nanoscale biological systems by converting small phase variations of an electromagnetic field into measurable intensity changes [1]. Interferometric scattering (iSCAT) microscopy has emerged as a particularly robust form of image-plane based inline holography that detects the interference between light scattered by a nanoparticle and a well-defined reference field, typically the back-reflection from a planar interface such as a glass/solution. This configuration enables detection of weak scattering signals, allowing quantitative and sensitive measurements down to single viruses or proteins. [2], [3].

Blue light has become a commonly used illumination source for label-free imaging due to better resolution, higher scattering crossections, smaller depth of fields which lead to optimal signal-to-noise measurement regimes. Nevertheless, beyond sensitivity, photodamage induced by short-wavelength illumination poses a challenge, as it is a well-established concern in biological imaging, particularly in the context of live cells and organisms[4]. Yet its impact on surface-based biosensing platforms has remained largely unexplored. For instance, photo-induced chemical reactions and degradation of biological components, may affect the stability and functionality of sensing interfaces [5]. In response to these limitations, there has been a gradual shift in optical methods toward the use of longer wavelengths, such as red or near-infrared light, in optical detection techniques including fluorescent labeled and interferometric scattering microscopy approaches without describing the underlying mechanisms of photodamage [6], [7].

In this context, one possible mechanism underlying such destructive effects is the generation of reactive oxygen species (ROS) under short-wavelength illumination [4], [5]. In confined environments such as closed microfluidic channels, locally produced ROS can accumulate and interact with both the sensing interface and the analyte. These species are known to induce oxidative damage to biological components, including lipid membranes, proteins, and capture probes such as antibodies, potentially altering their structure and binding capability.

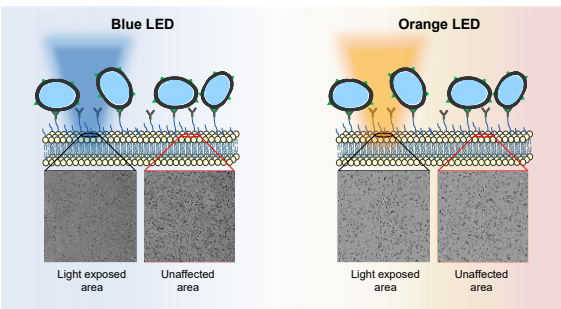

Fig. 1. Schematic representation and corresponding iSCAT images illustrating analyte detection in regions exposed to blue and orange illumination, compared to non-illuminated areas.

Within this study, the influence of blue LED illumination on the integrity of the surface chemistry

and sensing performance was systematically investigated. In parallel, alternative illumination conditions based on longer wavelengths, such as orange LED light, were explored to reduce photodamage while maintaining sufficient detection sensitivity.

Materials and Methods

Binding kinetics of biotin-functionalized liposomes, were investigated on a cell-mimicking supported lipid bilayer (SLB) to model an immunoassay-type sensing interface (*Fig. 1*). Two illumination sources were used to monitor analyte binding within the illuminated region. Specifically, short-wavelength blue LED light (455 nm) and longer-wavelength orange LED light (615 nm) were sequentially applied to the sensing area, while real-time measurements were performed using iSCAT microscopy.

To investigate the mechanism behind the reduced binding observed under blue light (Fig. 1), the stability of the main components of the sensing system was evaluated: (i) the SLB, (ii) the immobilized biorecognition element (anti-biotin antibodies), and (iii) the analyte (biotinylated liposomes). In addition, binding kinetics were measured at different light intensities to determine the operational range and safe monitoring time for both blue and orange LED illumination to identify dose-dependent effects and characteristic time scales of degradation. SLB integrity was assessed by evaluating surface passivation after light exposure. Since intact SLBs suppress non-specific adsorption, any light-induced disruption would be reflected as an increase in background binding. Antibody stability and functionality were probed by comparing analyte capture efficiency on antibody-functionalized regions that were either pre-exposed to light or kept as non-illuminated controls. Analyte stability was examined using biotinylated gold nanoparticles (AuNP) as a structurally robust sample. Additionally, AuNPs were introduced as local ROS scavengers to probe the contribution of ROS to the observed reduction [8].

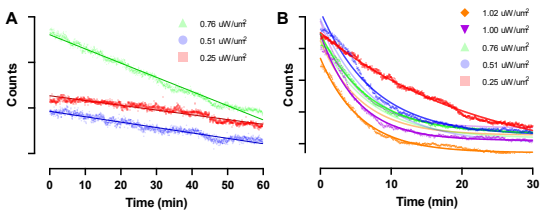

Fig. 2. Real time monitoring of liposome binding kinetics under (A) orange LED for 60 minutes and (B) blue LED for 30 minutes were depicted.

Results

A clear dose-dependent response to illumination intensity was observed for both blue and orange light sources (*Fig. 2*). Under orange illumination, the assay maintained >80% binding efficiency after one hour, indicating stable sensing conditions. In contrast, blue illumination led to a rapid and pronounced decrease in particle counts. Even at low power densities, an initial loss of bound analyte was observed, followed by a plateau phase where a fraction of particles remained on the surface. Importantly, this effect occurred at power densities significantly lower than those typically used and reported in iSCAT and related interferometric techniques, suggesting that blue light can perturb the sensing system under relatively mild conditions. This limits its suitability for long-term kinetic measurements and indicates it may be more appropriate for single measurement endpoint-type assays.

Mechanistic studies indicated that the immobilized antibodies were the most affected component, as reduced binding was observed for both liposome and gold nanoparticle analytes on pre-exposed areas. The damage to antibodies was irreversible; however, the presence of local ROS scavengers reduced the extent of degradation when binding occurred prior to light exposure, supporting the role of ROS in this process.

References

[1] R. W. Taylor and V. Sandoghdar, “Interferometric Scattering Microscopy: Seeing Single Nanoparticles and Molecules via Rayleigh Scattering,” *Nano Lett.*, vol. 19, no. 8, pp. 4827–4835, Aug. 2019, doi: 10.1021/acs.nanolett.9b01822.

[2] P. Kukura, H. Ewers, C. Müller, A. Renn, A. Helenius, and V. Sandoghdar, “High-speed nanoscopic tracking of the position and orientation of a single virus,” *Nat. Methods*, vol. 6, no. 12, pp. 923–927, Dec. 2009, doi: 10.1038/nmeth.1395.

[3] J. Ortega Arroyo *et al.*, “Label-Free, All-Optical Detection, Imaging, and Tracking of a Single Protein,” *Nano Lett.*, vol. 14, no. 4, pp. 2065–2070, Apr. 2014, doi: 10.1021/nl500234t.

[4] Y. Nakashima, S. Ohta, and A. M. Wolf, “Blue light-induced oxidative stress in live skin,” *Free Radic. Biol. Med.*, vol. 108, pp. 300–310, Jul. 2017, doi: 10.1016/j.freeradbiomed.2017.03.010.

[5] E. Kim, S. Kim, M. Kim, and D. Min, “Photooxidative molecular damage under blue light,” *Exp. Mol. Med.*, pp. 1–18, Jan. 2026, doi: 10.1038/s12276-025-01609-8.

[6] A. L. Antaris *et al.*, “A small-molecule dye for NIR-II imaging,” *Nat. Mater.*, vol. 15, no. 2, pp. 235–242, Feb. 2016, doi: 10.1038/nmat4476.

[7] D. Loewenthal *et al.*, “Continuous mass photometry by single molecule trapping,” Feb. 03, 2026, *bioRxiv*. doi: 10.64898/2026.02.02.703204.

[8] J. Kim, H. Park, G. Saravanakumar, and W. J. Kim, “Polymer/Aptamer-Integrated Gold Nanoconstruct Suppresses the Inflammatory Process by Scavenging ROS and Capturing Pro-inflammatory Cytokine TNF-α,” *ACS Appl. Mater. Interfaces*, vol. 13, no. 8, pp. 9390–9401, Mar. 2021, doi: 10.1021/acsami.0c15727.

DOI 10.5162/eurosensors2026/Tu–POS–07

Equivalent Emissivity of Poly-Si, SiO_2, and SiN_x for Accurate Heated-Membrane Optical Radiator Design

Reinoud F. Wolffenbuttel
Laboratory for Electronic Instrumentation, Department of Microelectronics, Delft University of Technology, 2628 CD Delft, The Netherlands
Corresponding Author's e-mail address: R.F.Wolffenbuttel@TUDelft.NL

Summary:
The temperature-dependent spectral emissivity for poly-Si, SiO_2 and SiN_x of different composition have been extracted from wideband data on the index of refraction available in literature and used to obtain the temperature-dependent equivalent emissivity of these materials. The constraints of the Kirchhoff law of optics are not necessarily satisfied for these materials in combination with the thickness typically used in silicon MEMS devices, which is taken into consideration when applying the data obtained in realistic multi-layered structures.

Keywords: heated-membrane, MEMS optical data, emissivity, optical database, Kirchhoff

Background, Motivation and Objective

The Kirchhoff law of optics states that the power radiated by an object in thermal equilibrium must be equal to the power absorbed, which implies that the spectral emissivity of a material can be expressed in terms of its spectral absorbance. Full emissivity, $\epsilon\infty$, (which is actually the value described in literature and described by $\epsilon\infty$= (1-*R*), with *R* the reflectance can develop only if the layer (or stack of layers) of which the membrane is composed is thick enough to ensure that the radiation is fully absorbed (absorbance A=1-exp(-α×t)~1, with α the absorption coefficient of the material and t the membrane/layer thickness).

This condition is not necessarily satisfied for the silicon-compatible materials used in MEMS microheater design. This applies especially to SiO_2 and SiN_x. Data on the temperature dependence of the emissivity of a material, $\epsilon(T)$, is scarce and often a temperature independent value is taken, which limits the accuracy of the simulation. This study aims to obtain accurate values of the spectral emissivity of these materials for realistic layer thicknesses and over the temperature range between 0-800 °C.

Description of the Approach

Literature data on the wavelength dependent complex index of refraction, $n^*= n- jk$, of polysilicon, SiO_2, N-rich SiN_x and Si-rich SiN_x, as available in literature, is used to build a database. For polysilicon, special emphasis is put on free-carrier absorption and the description using a parameterized model was found sufficiently accurate [1-5]. For SiO_2 and SiN_x, modeling based on Brendel oscillator parameters, which is often used for modeling the complex index of refraction of a dielectric material, was found sufficiently accurate [6]. Subsequently, the data was used in matrix calculation of reflectance, transmittance and absorbance using optical admittances [7].

Results

The equivalent emissivity, ϵ_{eq}, is defined as the wideband emissivity applied to a black radiator that would result in the same radiance as the layer and material considered.

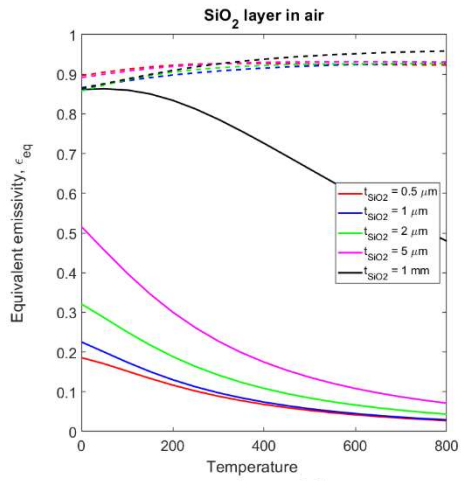

Fig. 1. Equivalent emissivity for an SiO2 layer in air at temperatures in the range 0 – 800 °C.

The equivalent emissivity of SiO_2 layer with a thickness in the range 0.5-5 μm and suspended

in air is shown in Fig. 1. The emissivity for a macroscopic layer is included for comparison. The Kirchhof constraint is disregarded in the dashed lines. Comparison between the dashed and solid lines reveals that full absorption is not reached in a typical MEMS device.

Although the Si-rich SiN_x is often preferred in the design of a suspended MEMS membrane, because of its tensile stress to keep the surface taut, the optical losses are significantly higher as compared to the N-rich SiN_x. Therefore, the equivalent emissivity, ϵ_{eq}, of an N-rich SiN_x layer deposited on a standard silicon substrate is presented in Fig. 2.

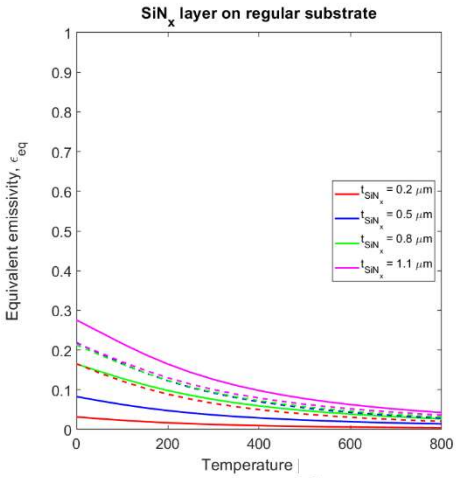

Fig. 2. Equivalent emissivity for a N-rich SiN_x layer on a Si substrate in the temperature range 0–800 °C.

As the membrane is typically suspended from the Si substrate, a realistic simulation of the membrane emissivity should also include such a structure (see Fig. 3).

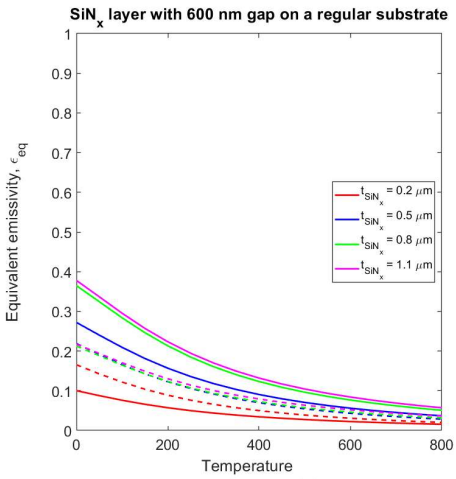

Fig. 3. Equivalent emissivity for a suspended N-rich SiN_x layer in the temperature range 0–800 °C.

Finally, a realistic structure is typically composed of a multi-layer membrane. The results for a poly/SiN_x membrane are shown in Fig. 4 in comparison to the poly-Si layer of the same thickness in air (dashed lines).

The approach is suitable for the calculation of the equivalent emissivity of more complex membranes that are fabricated using the set of conventional silicon-compatible materials. Testing, by applying this approach to the results for measurement results of heaters presented in literature shows good agreement.

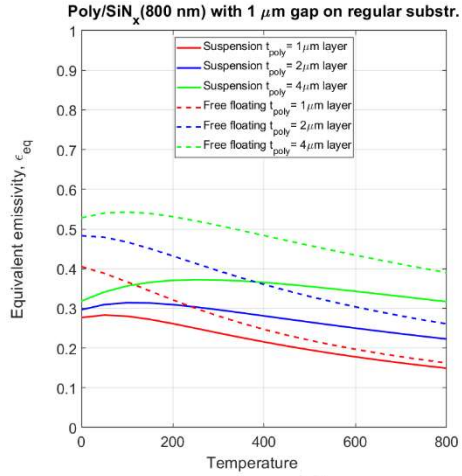

Fig. 4. Equivalent emissivity for a suspended poly-Si/SiN_x multilayer in the range 0–800 °C.

References

[1] A.R. Forouhi, I. Bloomer, Optical Properties of Crystalline Semiconductors and Dielectrics. Phys. Rev. B, 38(3), 1865–1874 (1988).

[2] A. Tarifa, N. Ravindra (2023). Optical Properties of Crystalline Silicon in the Infrared, TMS 2023 Annual Meeting & Exhibition, San Diego, CA, USA (2023)

[3] D. K. Schroder, R. N. Thomas, J. C. Swartz, Free carrier absorption in silicon, IEEE J. Solid State Circuits SC-13(1), 180–187 (1978C)

[4] S.C. Baker-Finch, K.R. McIntosh, D.Yan, K.C. Fong, T.C. Kho, Near-Infrared Free Carrier Absorption in Heavily Doped Silicon, J. of Appl. Phys. 116, 063106 (2014); doi: 10.1063/1.4893176

[5] R. R. Vardanyan, V. K. Dallakyan, U. Kerst, C. Boit, Modeling Free Carrier Absorption in Silicon, J. of Contemporary Physics (Armenian Academy of Sciences), 47 (2), 73–79 (2012)

[6] J. Kischkat, S. Peters, B. Gruska, M. Semtsiv, M. Chashnikova, M. Klinkmüller, O. Fedosenko, S. Machulik, A. Aleksandrova, G. Monastyrskyi, Y. Flores and W.T. Masselink, Mid-Infrared Optical Properties of Thin Films of Aluminum Oxide, Titanium Dioxide, Silicon Dioxide, Aluminum Nitride, and Silicon Nitride, Applied Optics, 51 (28), 6789-6798 (2012)

[7] H.A. Macleod, Thin-Film Optical Filters, 3rd edn. Institute of Physics Publishing,U.K., 2001

DOI 10.5162/eurosensors2026/Tu–POS–08

Irreversible Microstructured Optical RH Threshold Indicator with a Binary Visual Readout

Jakub Orlikowski[1], Joanna Cybińska[1,2]
[1] Łukasiewicz Research Network – PORT Polish Center for Technology Development, Wrocław, Poland,
[2] University of Wrocław, Faculty of Chemistry, Wrocław, Poland
jakub.orlikowski@port.lukasiewicz.gov.pl

Summary:
A passive optical relative humidity threshold indicator is presented for irreversible recording of selected humidity exceedance events. The system is based on a low-cost, humidity-responsive biopolymer film with functional additives selected with future application and biocompatibility requirements in mind. Exposure to the assigned humidity threshold triggers disappearance of a visible structural-optical response, which remains absent after return to the reference humidity. Representative threshold variants showed complete visual loss of diffraction after exposure to RH values of 60, 70 and 80 percent, while the diffractive response remained visible after exposure to the highest sub-threshold RH level tested under the applied exposure protocol. The transition was confirmed by reflected optical intensity measurements. The concept offers a simple, battery-free route toward passive humidity threshold labels.

Keywords: humidity sensor, optical sensor, threshold indicator, irreversible sensor, structural color

Background, Motivation and Objective

Relative humidity (RH) is a critical parameter in packaging, storage, logistics and environmental monitoring, especially when exposure above a defined RH limit can affect material or product stability. In many practical cases, continuous RH monitoring is not required; instead, a low-cost indicator providing direct information that a selected RH threshold has been reached is sufficient. Conventional electronic humidity sensors offer quantitative readout, but they require power supply, electronics and data acquisition. This creates a need for passive, single-use indicators capable of permanently recording RH exceedance events.

Optical humidity sensors based on changes in light transmission, reflection, refractive index, diffraction or structural color have attracted considerable attention due to their simple readout and potential for visual detection [1–4]. Photonic and structural-color humidity sensors typically translate water uptake into reversible spectral or color changes. In contrast, the present work explores a passive RH threshold indicator in which exposure to the assigned RH threshold produces an irreversible binary visual response based on the loss of a visible structural-optical signal.

The objective of this work was to demonstrate a dye-free optical prototype of an irreversible RH threshold indicator operating in a binary readout mode. The proposed system is designed as a reader-free threshold label, where state 0 corresponds to a visible optical response and state 1 corresponds to its permanent disappearance after exposure to an assigned RH threshold.

Description of the New Method or System

The sensor consists of a humidity-responsive biopolymer-based film containing functional additives selected to support threshold activation, low-cost implementation and future application-oriented material requirements. The film carries a microstructured optical surface that produces a visible diffractive response in the initial state. Upon exposure to the assigned RH threshold, water uptake induces swelling and structural relaxation of the microstructured surface, leading to disappearance of the optical response. After return to the reference humidity, the response remains absent, confirming the irreversible character of the transition.

The readout principle is binary. State 0 corresponds to visible diffraction before activation, while state 1 corresponds to no visible diffraction after exposure to the assigned RH threshold. The indicator is therefore designed to record threshold exceedance rather than to reconstruct the full humidity-time profile. The visual response was additionally verified by monitoring the reflected optical intensity before exposure and after return to the reference humidity.

The operating principle of the indicator is schematically shown in Fig. 1. The initial state corresponds to a visible diffractive response, whereas exposure to the assigned RH threshold activates the system and leads to irreversible loss of the structural-optical signal.

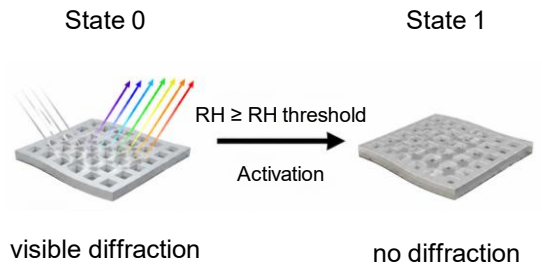

Fig. 1. Conceptual scheme of the irreversible microstructured optical RH threshold indicator. State 0 corresponds to visible diffraction before activation. Exposure to RH at or above the assigned threshold leads to State 1, in which no visible diffraction is observed after return to reference RH.

The platform is expected to be adaptable to selected RH thresholds through material and structural tuning. Response-time control is also considered an important development parameter, but it is not addressed quantitatively in the present disclosure. The present contribution focuses on the sensing principle and functional performance; detailed formulation and fabrication parameters are not disclosed at this stage due to ongoing intellectual property protection.

Results

The response of selected threshold variants was evaluated by combining visual inspection with reflected optical intensity measurements. The initial state was defined by a clearly visible diffractive pattern. After exposure to target RH levels and return to the reference humidity, the final state was classified according to whether the diffractive pattern remained visible or disappeared.

Three representative threshold variants were selected for public presentation: 60, 70 and 80% RH. For each selected variant, the visible diffractive response was retained after exposure to the highest sub-threshold RH level tested under the applied protocol. In contrast, exposure to the assigned RH threshold resulted in complete disappearance of the visible optical response. The absence of the response was retained after return to the reference humidity, confirming irreversible activation under the applied test conditions.

The protocol included controlled RH exposure, RH stabilization and reflected-intensity monitoring, while detailed response-time mapping is considered a subject of ongoing work. The observed optical transition was accompanied by a strong loss of reflected intensity, confirming that the visual change corresponded to degradation of the structural-optical response rather than to a temporary humidity-induced optical fluctuation.

Tab. 1: Binary RH-threshold response under the applied exposure protocol. V = visible diffraction; ND = no diffraction after return to reference RH.

Assigned RH [%]	Below threshold	At threshold
60	50% RH → V	60% RH → ND
70	60% RH → V	70% RH → ND
80	70% RH → V	80% RH → ND

The results confirm that humidity-induced loss of a microstructured optical response can be used as a passive memory of RH threshold exceedance. The system does not aim to continuously track RH changes or reconstruct humidity history, but to provide an irreversible 0–1 indication that a selected RH limit has been reached. Further work will focus on sharpening the transition window, improving below-threshold stability, evaluating response-time tuning and transferring the concept toward a practical low-cost label format. The dye-free prototype presented here may also serve as a platform for future integration with colorimetric components, if required by the target application.

References

[1] X. Rao, L. Zhao, L. Xu, Y. Wang, K. Liu, Y. Wang, G. Y. Chen, T. Liu, Y. Wang, Review of Optical Humidity Sensors, Sensors 21, 8049 (2021); doi: 10.3390/s21238049

[2] H. Wang, K. Q. Zhang, Photonic Crystal Structures with Tunable Structure Color as Colorimetric Sensors, Sensors 13, 4192-4213 (2013); doi: 10.3390/s130404192

[3] E. Tian, J. Wang, Y. Zheng, Y. Song, L. Jiang, D. Zhu, Colorful Humidity Sensitive Photonic Crystal Hydrogel, Journal of Materials Chemistry 18, 1116-1122 (2008); doi: 10.1039/B717368G

[4] S. Cesnik, G. Hernández Rodríguez, A. M. Coclite, A. Bergmann, Structural Colored Based Humidity Sensor Consisting of High Resolution 3D Printed Photonic Crystal Coated with Ultrathin Responsive Hydrogels, Macromolecular Rapid Communications 45, 2400111 (2024); doi: 10.1002/marc.202400111

Acknowledgements

This work was supported by the Ministry of Science and Higher Education in Poland under the Science for Society II grant No. NdS-II/SN/0278/2024/01.

DOI 10.5162/eurosensors2026/Tu–POS–09

Nanowire Geometry Engineering for Enhanced Fluorescence Biosensing Performance

Farhana Akter Mou* and Nicklas Anttu
Physics, Faculty of Science and Engineering, Åbo Akademi University, FI-20500 Turku, Finland.
*email: farhana.mou@abo.fi

Summary:

We introduce a dual-function nanowire architecture consisting of a tapered tip integrated with a cylindrical base, enabling enhanced optical concentration while the cylindrical base preserves the imaging advantages of conventional nanowire biosensor. Our optics modelling shows that the proposed nanowire achieves >1000× fluorescence enhancement over planar substrates and outperforms a full-length cylindrical nanowire. We propose also an alternative nanowire geometry that eliminates the need for selective functionalization while retaining performance comparable to the top-tapered configuration.

Keywords: Nanowires, Biosensor, Fluorescence, Signal Enhancement, Imaging.

Background, Motivation and Objective

Optical biosensors are of great interest over electrochemical, electrical, or piezoelectric sensors because they offer exceptional sensitivity, allow label-free or fluorescence-based detection, and real-time monitoring [1]. Industry-standard planar fluorescence biosensors are popular for their simplicity and cost-effectiveness but are often limited by sensitivity and detection limits [2]. Nanowire (NW) biosensors are currently attracting significant attention because of their high surface-to-volume ratios and engineered geometries that enhance light-matter interaction and photon collection, enabling ultra-low-concentration biomolecule detection that surpasses conventional planar biosensors [3-4].

Recently, our group demonstrated through modelling that vertically oriented GaP NW achieved >100× fluorescence signal enhancement over planar biosensors and enabled imaging-based detection with 25-fold sharper images than conventional diffraction-limited microscopy [4].

The principal objective of this work is to advance fluorescence-based biosensing through the computational design and analysis of nanowire for enhanced signal and imaging performance. Accordingly, we propose a top-tapered nanowire with a cylindrical base to further enhance fluorescence signal and evaluate its imaging performance. The proposed nanowire achieves >1000× fluorescence enhancement compared with planar substrates and outperforms cylindrical nanowires in low numerical aperture (NA_{exc} and NA_{coll}) setups. These results are calculated assuming fluorophore binding only on the cylindrical region, which necessitates selective functionalization and may pose practical challenges. To address this, we also investigate an inverted-taper geometry that removes the need for selective functionalization while preserving performance comparable to the top-tapered design.

Proposed Nanowire design

The nanowire consists of a cylindrical base that preserves the imaging performance of a non-tapered nanowire, combined with a tapered top section designed to enhance the optical signal (Fig. 1). Silicon (Si) is used as the nanowire material, compared to GaP, it is more cost-effective but exhibits some parasitic absorption, particularly at shorter visible wavelengths. We optimize for the operating wavelengths λ_{exc} = 640 nm and λ_{em} = 670 nm. The optical response is modeled using the finite element method in COMSOL Multiphysics. The cylindrical base length is fixed at C_L = 1500 nm, while the tapered length (T_L) is varied from 500 nm to 8500 nm.

To avoid selective functionalization, we also propose an inverted geometry (Fig. 2) where the nanowire tapered part is placed inside a lower refractive index substrate (e.g., n ≈ 1.5). This configuration prohibits fluorophores from binding to the low-enhancement (tapered) region, removing the need for surface selectivity.

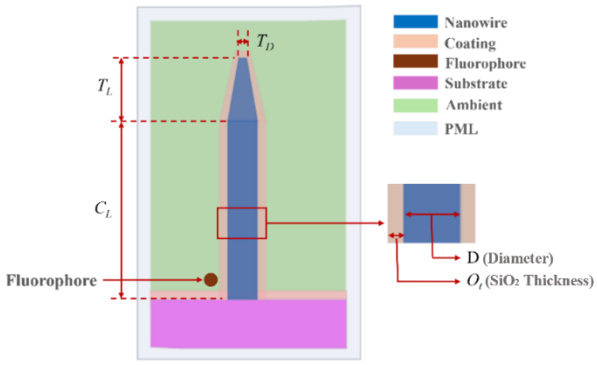

Fig. 1. Cross sectional view of the proposed top-tapered nanowire

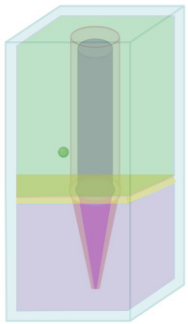

Fig. 2. 3D view of the proposed geometrical setup for avoiding selective functionalization.

Results

The proposed top-tapered NW provides more than three orders of magnitude higher fluorescence enhancement compared with the planar reference and approximately 10-fold improvement over the non-tapered configuration across all investigated fluorophore quantum yields under low NA. The enhancement continues further with taper length (Fig. 3). Fig. 3 also shows that the signal enhancement of the alternative inverted geometry, in which the tapered section is embedded in the substrate, achieves comparable performance while avoiding the need for selective functionalization. We further evaluate the imaging performance by analyzing the spatial localization of the collected signal around the nanowire position. Imaging is assessed from both top and bottom collection sides and presented in Fig. 4. For top-side imaging, $<REL_{img}>$ decreases with increasing taper length due to the more directional emission induced by the taper. In contrast, for bottom-side imaging toward the cylindrical binding region, $<REL_{img}>$ remains stable, with approximately 15% better image sharpness compared with a cylindrical nanowire. The inverted geometry also maintains comparable performance to the top-tapered design in both imaging configurations (Fig. 4).

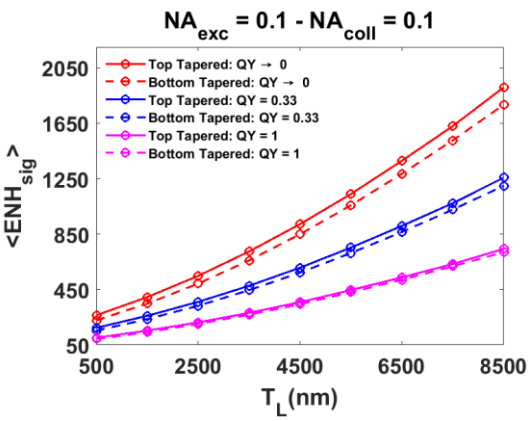

Fig. 3. Signal enhancement relative as a function of tapering length at low numerical aperture for both top and bottom tapered geometry.

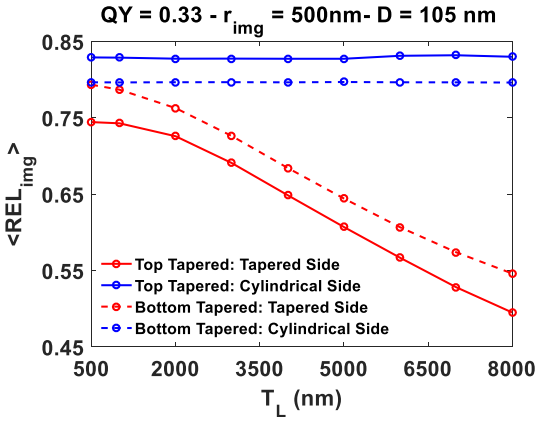

Fig. 4. $< REL_{img} >$, the integrated counts in a disc of 500 nm in radius in the image plane, relative to all counts in the image plane for both top-tapered and bottom tapered situations and imaging from either top or bottom side.

Conclusion

Overall, the proposed nanowire architecture combines cylindrical and tapered geometries to achieve dual functionality. It enables strong fluorescence signal enhancement at low numerical aperture while maintaining stable imaging performance. In addition, the inverted configuration provides a practical route to eliminate the need for selective functionalization. This favorable low-NA performance supports improved signal strength and reliable imaging, making it well suited for cost-effective, compact, and easily integrable biosensing applications.

Acknowledgement

We acknowledge the financial support of the Finnish Ministry of Education and Culture through the PREIN/I-DEEP doctoral pilot (VN/3137/2024-OKM-4).

References

[1]. S. Mostufa, B. Rezaei, S. Ciannella, P. Yari, J. Gómez-Pastora, Advancements and Perspectives in Optical Biosensors, *ACS Omega*, vol. 9, pp. 24181–24202, 2024.

[2]. E. Benito-Peña, M. Granda Valdés, B. Glahn-Martínez, M. C. Moreno-Bondi, Fluorescence-based fiber optic and planar waveguide biosensors: A review, *Analytica Chimica Acta*, vol. 943, pp. 17–40, 2016.

[3]. H. Zhang, N. Kikuchi, N. Ohshima, T. Kajisa, T. Sakata, T. Izumi, H. Sone, Design and fabrication of silicon nanowire-based biosensors with integration of critical factors: Toward ultrasensitive specific detection of biomolecules, *ACS Appl. Mater. Interfaces*, vol. 12, no. 46, pp. 51808–51819, 2020.

[4]. N. Anttu, Fluorophore signal detection and imaging enhancement in high refractive index nanowire biosensors, *Nano Express* 6, 015005, 2025.

DOI 10.5162/eurosensors2026/Tu−POS−10

Tailoring Acoustic Modes for Ultra-Sensitive Photoacoustic Gas Detection

Mh. S. Moussa[1], R. Viard[2], J-F Lampin[1], Sophie Eliet[1], S. Khattou[3], M. Amrani[3], A. Mazzamurro[1], O. Bou Matar[1], B. Djafari-Rouhani [1], P. Pernod[1], E. H. El Boudouti[3], A. Talbi[1]
[1] Univ. Lille, CNRS, Centrale Lille, UPHF, UMR 8520 - IEMN, Lille, France
[2] Groupe Endress+Hauser, Fribourg-en-Brisgau, Allemagne.
[3] *LPMR, Département de Physique, Faculté des Sciences, Univ. Mohammed I, 6000 Oujda,Morocco*

Summary:
Photoacoustic gas sensing is experiencing rapid development due to its high sensitivity and selectivity. In this work, we introduce a novel methodology for the design of photoacoustic cells based on a rigorous analysis of acoustic eigenmodes and excitation mechanisms. We demonstrate that the nature of excitation (acoustic versus photoacoustic) strongly influences modal selection and efficiency. A finite element framework is developed to identify optimal resonant modes under realistic conditions. Based on this approach, a photoacoustic system was fabricated and experimentally validated. High sensitivity detection of volatile organic compounds is demonstrated, achieving detection limits in the ppb range.

Keywords: photoacoustic spectroscopy, acoustic resonators, gas sensing, VOC detection

Background, Motivation and Objective

Trace gas detection is crucial for applications ranging from medical diagnostics to environmental monitoring. Photoacoustic spectroscopy (PAS) offers high sensitivity and background-free detection, further enhanced by resonant cells operating above 1 kHz to reduce noise. Various geometries have been proposed, including cylindrical [1], T-type [2], H-type [4], TT-type [5], differential Helmholtz designs [6], and other advanced configurations mainly based on geometric optimization. However, while these designs exploit acoustic eigenmodes, the choice of mode is rarely physically justified. In this work, we address this gap by identifying, from a modal perspective, the modes most favorable to photoacoustic excitation. We show that the fundamental mode is not always optimal and introduce a physics-based approach, based on eigenmode analysis and optical–acoustic overlap, to select resonant modes maximizing the photoacoustic response, enabling more efficient and sensitive cell designs.

Material and Method

We propose a multi-physics finite element framework combining acoustic and photoacoustic modeling. The acoustic field is described by the linearized wave equation with either boundary-driven excitation (pressure or velocity) or volumetric photoacoustic generation proportional to absorbed optical energy.

Eigenmodes are first computed from the homogeneous Helmholtz problem, and the frequency response is obtained by introducing excitation terms under realistic boundary conditions, including thermoviscous losses.

A key contribution is the direct comparison between excitation mechanisms. Acoustic excitation mainly couples through boundary conditions, while photoacoustic excitation preferentially excites modes with strong spatial overlap with the optical absorption profile.

This leads to the emergence of dominant resonant states, including modes approaching quasi-bound states in the continuum (quasi-BIC), which enhance acoustic confinement and signal amplification.

Results and discussion

The finite element model is first validated under acoustic excitation using a surface boundary condition mimicking a loudspeaker. The system exhibits classical resonator behavior with a dominant fundamental mode under rigid-wall conditions, but the response is strongly affected by boundary conditions and losses, which redistribute energy among higher-order modes (Fig. 1(b)).

The analysis is then extended to the photoacoustic regime, where a volumetric heat source induced by a Gaussian laser beam in stubs $d_2$and $d_3$drives the excitation (Fig. 1(a)). In this case, modal selection is governed by spatial overlap between optical absorption and acoustic eigenmodes. Simulations show that the strongest photoacoustic coupling is obtained for the second eigenmode, rather than the fundamental one (Fig. 1(b)). This mode is particularly interesting, as it corresponds to perfect absorption under excitation from infinity at the entrance of d_3, and becomes a bound state in the continuum (BIC) when $d_1 = d_2$. In this regime, variations of $d_3$have negligible impact on the modal response, making this configuration highly attractive for photoacoustic spectroscopy, since $d_3$can be

used as a gas inlet or reduced without affecting the measurement, ensuring both flexibility and robustness.

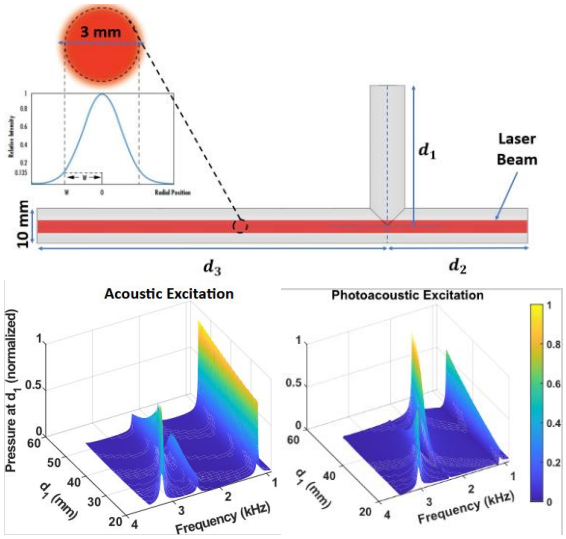

Fig. 1: a) Schematic of the Gaussian laser injected into stubs d_3 and d_2, with its intensity profile. b) 3D map of the simulated pressure versus d_1 and frequency under photoacoustic and acoustic excitation.

For experimental validation, we developed an aluminum photoacoustic cell composed of three stubs (Fig. 3.a). The geometry was selected to excite the BIC state, with $d_1 = d_2 = 40$ mm. Pressure field at the frequency of BIC state is shown on Figure 3.b. Sensitivity measurements were performed by injecting isopropanol vapor with calibrated generator through the d_3 stub, which also serves as the gas outlet. The system employs a MIRCAT QCL laser (Daylight Solutions) emitting at 8.73 µm (maximum absorption of isopropanol), with modulation provided by a mechanical chopper tuned near the acoustic resonance frequency. A TDK membrane microphone is positioned at the end of the $d_3$stub for pressure measurement.

Figure 3 shows the measured photoacoustic signal for different isopropanol concentrations. The signal was acquired using a high-resolution system (200 kHz sampling rate, 24-bit resolution), and the square root of the PSD is plotted in linear scale, revealing a high signal-to-noise ratio. In pure air, the background level is extremely low. Wavelength-dependent tests (not shown here) confirm good agreement with the isopropanol absorption spectrum. The system exhibits good linearity, with an estimated sensitivity of about 6 mV/ppm, enabling a projected detection limit in the few-ppb range.

Acknowledgements

This work was funded by the region Hauts de France and the INSERM through the project SNOOP-I. The authors thank RENATECH, the French national nanofabrication network.

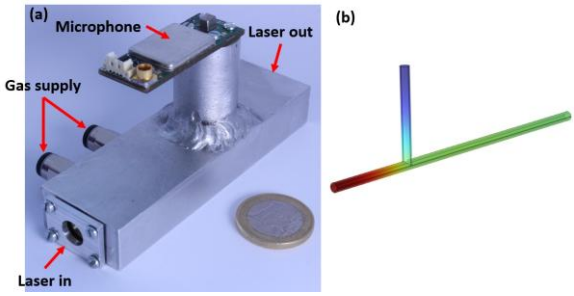

Fig. 3: a) Photograph of the fabricated acoustic cell. b) Presuure field distribution at the ferquency oft he BIC mode.

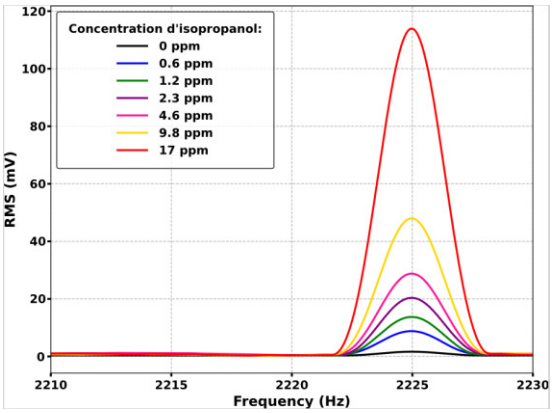

Fig. 4: Measured photoacoustic signal for different isopropanol concentrations.

References

[1] L. Fu, J. Zhang, Y. Pan, P. Lu, Differential photoacoustic spectroscopy for flow gas detection based on single microphone, *Photoacoustics* 38, 100624 (2024); doi: 10.1016/j.pacs.2024.100624

[2] L. Liu, H. Huan, L. Zhang, X. Zhang, J. Tang, X. He, Z. Mou, Y. Liang, H. Xu, Y. Ma, A. Mandelis, T-resonator based adsorbent enhanced photoacoustic sensor for multiple exhaled gas simultaneous monitoring, *Sensors and Actuators B: Chemical* 458, 139810 (2026); doi: 10.1016/j.snb.2026.139810

[3] Y. Ma, Y. Hong, S. Qiao, Z. Lang, X. Liu, H-shaped acoustic micro-resonator-based quartz-enhanced photoacoustic spectroscopy, *Optics Letters* 47(3), 601–604 (2022); doi: 10.1364/OL.448810

[4] F. Wang, J. Zhang, P. Cui, L. Fu, Q. Wang, High-sensitivity photoacoustic spectroscopy gas sensor enhanced by a microphone-array-coupled differential resonator, *IEEE Sensors Journal* (2024); doi: 10.1109/JSEN.2024.

[5] Z. Li, J. Liu, G. Si, Z. Ning, Y. Fang, Design of a high-sensitivity differential Helmholtz photoacoustic cell and its application in methane detection, *Optics Express* 30(16), 28984–28996 (2022); doi: 10.1364/OE.466123

[6] J. Zhou, P. Gong, L. Xie, Z. Er, Y. Chang, X. Jiang, Y. Wang, A new design method for miniature dual-resonance photoacoustic structure based on piezoelectric ceramics slice, *Infrared Physics & Technology* 134, 104849 (2023); doi: 10.1016/j.infrared.2023.104849

DOI 10.5162/eurosensors2026/Mo–PHS–01

Improving Cavity Pressure Stability as Enabler for High-Performance 2-Cavity MEMS Chips

Achim Breitling
Robert Bosch GmbH, Tübinger Str. 123, 72062 Reutlingen, Germany
Achim.Breitling@de.bosch.com

Summary:
The integration of multiple sensors, such as gyroscopes and accelerometers for Inertial Measurement Units (IMUs), onto a single MEMS chip requires separate, stable cavity pressures. This paper presents a systematic analysis to quantify mechanisms which lead to changes in cavity pressure using a dedicated test vehicle. We demonstrate that gas diffusion through buried oxide layers is the dominant cause of pressure drift. Based on this finding, we developed and validated a gas diffusion barrier that reduces pressure drift by 97%, enabling the fabrication of high-performance, long-life 2-cavity MEMS chips.

Keywords: MEMS, IMU, cavity pressure, gas diffusion, desorption

Background, Motivation and Objective

Modern Inertial Measurement Units (IMUs) combine multi-axis gyroscopes and accelerometers to provide comprehensive motion sensing. For optimal performance, these sensors have conflicting environmental requirements: gyroscopes require a high-vacuum cavity to achieve a high quality-factor, while accelerometers are typically operated in a damped environment at a higher pressure. Integrating both sensor types onto a single 2-cavity MEMS chip is desirable for miniaturization and cost reduction, but it presents two significant challenges. The first challenge is to seal different cavity pressures on one and the same chip. This has been enabled by enhanced process techniques such as laser reseal [1]. The second challenge is to prevent gas diffusion between the adjacent, pressure-differentiated cavities over the product's lifetime. Any drift in the gyroscope's vacuum cavity pressure degrades its performance. Therefore, understanding and mitigating the mechanisms of pressure change - such as gas diffusion, adsorption, or desorption - is essential for enabling high-performance, single-chip IMUs. This paper describes a detailed analysis to identify the dominant leakage paths and presents a structural solution to ensure cavity pressure stability.

Description of the New Method or System

To accurately measure smallest changes in cavity pressure, the quality-factor measurement of a yaw rate sensor was employed, which is highly sensitive to smallest changes in damping and thus in gas pressure [2] as shown in *Fig.1*. In order to analyze potential cavity pressure affecting mechanisms such as gas diffusion, adsorption and desorption separately, a MEMS chip layout including dedicated test structures on one and the same wafer was developed and utilized as sketched in *Fig. 2*. Each test structure addressed a different mechanism. The left picture shows the concept of a group of structures in which the eutectic AlGe separator was varied in width and designed with and without an interruption aiming for diffusion effects via the separator. In the second group shown in the center an additional material (Al, Ge or AlGe) was deposited on Si and a direct access to the gyroscope cavity was implemented through the separator addressing de-/adsorption effects. The right group featured an accelerometer core which was enclosed by a rectangle where certain buried layers were removed. This meant that if these layers act as diffusion path, this path was interrupted. By measuring all test structures before and after High Temperature Storage Life (HTSL: 150 °C, 1000 h), the cavity pressure change due to each individual mechanism could be quantified.

Results

The cavity pressure change of all test structures upon HTSL is shown in *Fig.3*. The test structures clustered in the blue and red rectangles, addressing gas diffusion via the eutectic AlGe separator between the cavities (blue) and potential outgassing from the Al / Ge / AlGe material (red), respectively, led to cavity pressure changes below 0.01 mbar of N2 damping equivalent. The test structures clustered in the green rectangle were designed to investigate the gas diffusion via the buried SiO_2 and Poly-Si layers. For these test structures with accelerometer MEMS structure, the change in gyroscope cavity pressure

was much higher than for the other test structures, ranging from 0.08 – 0.16 mbar. To activate this diffusion path, these test structures incorporate an accelerometer MEMS structure with direct contact between the gases of the accelerometer cavity and the buried SiO_2 / Poly-Si layers. In the test structures of the blue and red groups this path was blocked by a closed Si surface. Nevertheless, within the green group, the interruption of the lower and upper oxide layers reduces the pressure increase when compared to the test structure where the poly-Si layers were interrupted. This indicates that gas diffusion between the cavities via the buried SiO_2 layers is the dominant mechanism leading to gyroscope pressure changes upon HTSL [3].

As a layout measure to reduce the observed gyroscope cavity pressure drift, a 2-cavity MEMS layout was introduced featuring a gyroscope core enclosed by a gas diffusion barrier. This barrier consists of a line where the oxide is removed and the gap is filled with the subsequently deposited poly-Si layer [4].

In *Fig.* 4, the gyroscope cavity pressure drift of a reference 2-cavity MEMS chip without the measure is compared to the drift of a chip with the implemented measure of an enclosing gas diffusion barrier. The measure reduces the resulting cavity pressure change by 97%. This enables the positioning of an accelerometer and a gyroscope on the same chip (2-cavity MEMS) while keeping the gyroscope cavity pressure stable over its lifetime.

Illustrations, Graphs, and Photographs

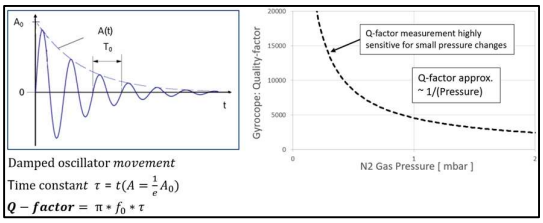

Fig. 1. Left: Damped oscillator movement with decaying amplitude. Quality-factor as a quantity to describe damping. Right: Measured gyroscope quality-factor versus N_2 cavity gas pressure.

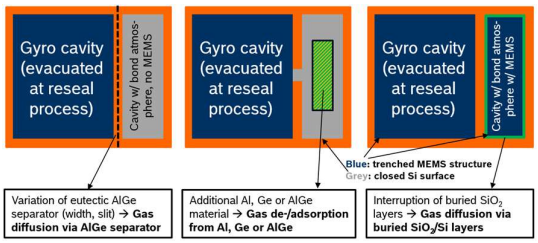

Fig. 2. Sketch of test structures to analyze different mechanisms affecting gyroscope cavity pressure on a 2-cavity MEMS chip with two different cavity pressures and atmospheres. Blue: Trenched MEMS structure, Grey: Closed Si dummy area.

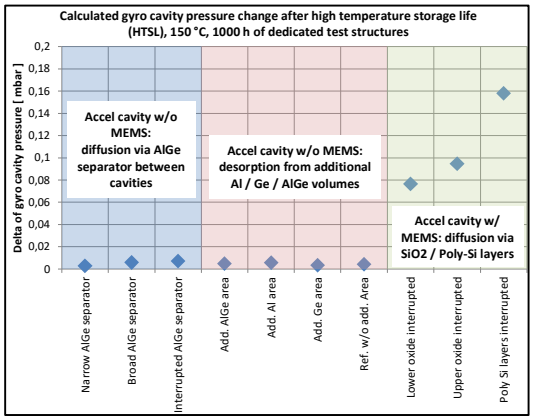

Fig. 3. Change in cavity pressure after HTSL of different test structures addressing various mechanisms contributing to changes in gyroscope cavity pressure.

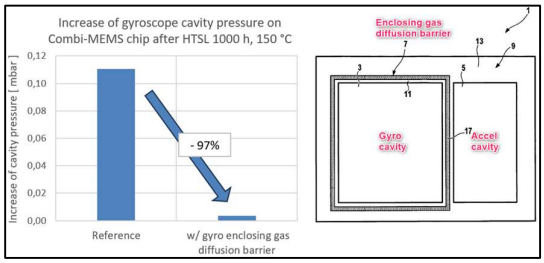

Fig. 4. Change in gyroscope cavity pressure on a 2-cavity MEMS chip after HTSL without (left) and with (right) gyroscope enclosing gas diffusion barrier [4].

References

[1] A. Breitling, E. Graf, J. Frey, J. Reinmuth, M. Ametowobla, “MEMS component having two different internal pressures“ (2020), US patent US10752498B2

[2] Q. Li, J. F. L. Goosen, F. van Keulen and J. T. M. van Beek, "Gas ambient dependence of quality factor in MEMS resonators," *SENSORS, 2009 IEEE*, pp.1040-1043; doi: 10.1109/ICSENS.2009.5398588

[3] M. Kopf, “Langzeitstabilität der Innendrücke von Kavernen benachbarter MEMS-Sensoren auf Siliziumbasis”, *PhD thesis 2022*, *Karlsruhe Institute of Technology (KIT)*; doi: 10.5445/KSP/1000136062

[4] A. Breitling, C. Schwenk, H. Kueppers, N. Schittenhelm, V. Schmitz, „Micro-mechanical component“ (2018), US patent US10059583B2

DOI 10.5162/eurosensors2026/Mo–PHS–02

Surface-Micromachined 3-Omega Gas Sensor

Philipp Raimann[1], Guy Laurent Tchoffo[1], Frank Hedrich[1], Sophie Billat[1], Alfons Dehé[1,2]
[1] Hahn-Schickard, 78052 Villingen-Schwenningen, Germany,
[2] Georg H. Endress Chair for Smart System Integration, Department of Microsystems Engineering–IMTEK, Albert-Ludwigs-University Freiburg, 79110 Freiburg, Germany

Summary:
In this paper a miniaturized thermal gas sensor with a n-doped polysilicon heating element on a thin silicon nitride membrane is presented. The sensor's thermal response is dominated by the gas properties, leading to a signal minimum in the out-of-phase component at a frequency proportional to the gas concentration. Operation at excitation frequencies between 3 and 9 kHz minimizes intrinsic 1/f noise sources and allows frequency-based control strategies with linear sensitivity.

Keywords: Thermal Gas Sensor, SNR improvement, 3-Omega-Method, Surface Micromachining, Lumped-Element-Modelling

Motivation

Micro-machining enables the fabrication of highly miniaturized thermal gas sensors with low power consumption. However, the performance of thermal conductivity sensors is often limited by intrinsic noise and non-linear signal behavior. N-doped polysilicon is widely used for micro-fabricated heaters due to its long-term stability and tunable temperature coefficient of resistance (TCR), but exhibits significant 1/f noise [1]. Therefore, optimizing thermal gas sensors for higher frequency operation is a key strategy to improve sensor performance and enables new possibilities for sensor signal evaluation, particularly through frequency-based analysis approaches.

Description of the New Method

Surface micromachining is employed to reduce the thermal time constant of the sensor, enabling an operation at higher modulation frequencies. Heat transfer between the heater and the surrounding structure occurs primarily through a well-defined gap, which is determined by the thickness d of a sacrificial silicon oxide layer used during fabrication. This controlled geometry ensures reproducible and well-defined thermal coupling to the surrounding gas. To enable accurate signal extraction, a half-bridge configuration is utilized, in which one structure is released by etching and suspended in the gaseous medium, while the other remains fixed on the bulk silicon. This arrangement suppresses the excitation component (1ω) and facilitates precise measurement of the 3ω response.

Sensor Theory

The 3-omega method is a powerful frequency modulation technique for detecting gases [2]. In this paper, the heater is driven with an AC voltage (1ω) at different frequencies and the resulting in- and out-of-phase components of the 3ω signal are detected with a lock-in amplifier.

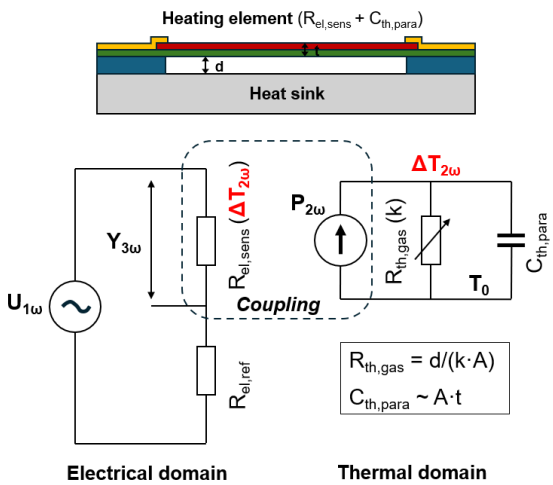

Fig. 1. Lumped element model of the thermal gas sensor with a single thermal time constant.

The low-pass behavior can be effectively captured using a thermal lumped-element model, which accounts for both parasitic contributions and gas-dependent thermal parameters.

$$\tau = R_{th,gas} \cdot C_{th,para} \sim k^{-1} \qquad (1)$$

Due to the high degree of miniaturization, the thermal time constant τ is primarily determined by the thermal conductivity k dependent thermal resistance $R_{th,gas}$ and the parasitic thermal capacitance $C_{th,para}$ of the sensor structure.

Analyzing the temporal thermal behavior offers the advantage of a reduced influence on the applied heating power [3]. Gauthier [2] describes a signal minimum in the out-of-phase-component (Y-signal), which corresponds to dominant thermal frequency of the system.

Fabrication Process

The fabrication begins with the growth of a 1 µm sacrificial thermal oxide layer. A low-pressure chemical vapor deposition (LPCVD) silicon nitride layer is then deposited to form the membrane. The heater is defined in n-doped polysilicon and patterned in a honeycomb geometry for mechanical robustness. Perforations enable etchant access for controlled release and gas access to the cavity for sensing. A PECVD passivation layer protects the membrane during vapor HF (vHF) etching and is removed in the release step. The final device consists of an n-doped polysilicon heater suspended on an 80 nm-thick membrane with reduced thermal mass for enhanced gas sensitivity.

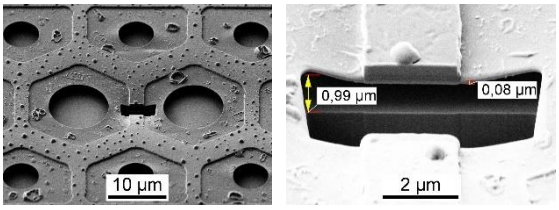

Fig. 2. Honeycomb-shaped heater structure (left) and FIB cross-section for structural analysis (right).

Experimental Results

The half-bridge is excited with a frequency sweep with a 3 V_{pk} input voltage, and the 3 ω is recorded using a lock-in amplifier from Zurich Instruments.

Tab. 1: Overview of different sensor designs

A (mm^2)	$R_{el,sens}$ (Ω)	$f_{1\omega}$ @ $Y_{3\omega,\,min}$ (kHz)
0.011	384±15	3,02±0,10
0.0165	588±28	3,14±0,05
0.022	802±40	2,95±0,09

Despite variations in sensor dimensions, a minimum in the Y-component at similar frequencies is observed, indicating that the thermal response is predominantly governed by the gas properties. This behavior can be explained by the fact that an increase in the area is accompanied by a proportional reduction of the gas thermal resistance (see Fig. 1), resulting in a nearly constant characteristic frequency, corresponding with the calculated frequency of approximately 3.3 kHz for N_2.

In contrast to conventional steady-state thermal conductivity sensors, which exhibit a 1/k-dependence and thus reduced sensitivity at higher thermal conductivities [4], the characteristic frequency of the Y-component minimum shows a linear dependence on the gas concentration. This is attributed to the dynamic measurement principle, where the excitation frequency is inversely proportional to the dominant thermal time constant and therefore directly linked to the effective thermal conductivity of the gas mixture.

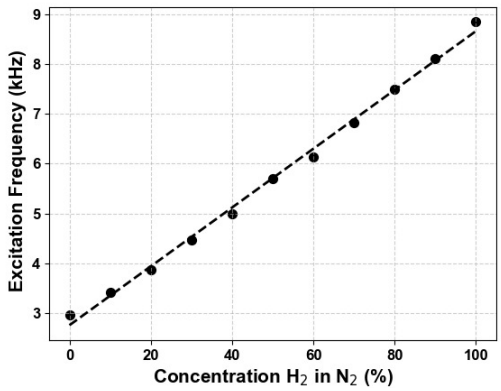

Fig. 3. Excitation frequency $f_{1\omega}$ at the $Y_{3\omega}$ minimum for N_2/H_2 mixtures using a sensor chip with an active area of A = 0.022 mm^2.

Outlook

The potential of surface micromachined sensor for frequency modulated thermal gas detection has been successfully demonstrated. Further optimization of the fabrication process is required, as selectivity issues during vHF etching necessitate the use of a front-side nitride passivation layer. Although this layer is fully removed during etching, it can leave residues on the surface, which need to be addressed in future process refinements.

References

[1] R. Brederlow et al., Low-Frequency Noise of Integrated Poly-Silicon Resistors, IEEE Trans. Electron Devices 48, 1180–1187 (2001); doi: 10.1109/16.925245

[2] S. Gauthier, P. Combette, A. Giani, Gas thermal conductivity measurement based on the three-omega method, IEEE Sensors 2012; doi: 10.1109/ICSENS.2012.6411023

[3] Z. Cai et al.; A Phase-Domain Readout Circuit for a CMOS-Compatible Hot-Wire CO2 Sensor, IEEE J. Solid-State Circuits 53, 3303-3313 (2018); doi: 10.1109/JSSC.2018.2866374

[4] S. Kenari et al., Towards a Gas Independent Thermal Flow Meter, IEEE MEMS 2023; doi: 10.1109/MEMS49605.2023.10052491

DOI 10.5162/eurosensors2026/Mo–PHS–03

Synthesis and sensing properties of SnS_2/rGO composite towards NO_2 gas at room temperature

Julia Coelho Tagliaferro[1], Amanda Akemy Komorizono[1], Valmor RobertoMastelaro[1]
[1] Institute of Physics of São Carlos, São Carlos, Brazil
julia.tagliaferro@usp.br

Summary:
In the present work, a SnS2/rGO composite was prepared via mechanical mixing with different rGO proportions with the objective of sensing NO2 at room temperature. The SnS2/rGO 15% sample showed a high response and good selectivity at room temperature, with a 40% humidity level being determined as ideal for increasing the sensors' response.

Keywords: gas sensing, dichalcogenides, reduced graphene oxide

Background, Motivation and Objective

NO2 gas is linked to increased mortality from respiratory and cardiovascular diseases1; therefore, the development of efficient gas sensors is extremely important to monitor exposure. In this context, composites based on tin disulfide (SnS2) and reduced graphene oxide (rGO) have been reported as excellent choices for NO2 sensing, combining the strong chemical affinity between NO2 and SnS2 and the high electron conductivity of rGO2.
Presently, we propose combining SnS2 and rGO into a mechanically mixed composite for a NO2 sensor that offers selective detection, high sensitivity, and operates effectively at room temperature.

Description of the New Method or System

In this work, a mechanical mixing method was employed in order to form the SnS2/rGO composite. This allows for the freedom to choose the appropriate synthetic route for each component, avoiding the formation of secondary phases while also enabling precise control of the components' characteristics before the composite is formed.

Results

The samples were prepared by mechanically mixing pre-synthesized rGO and SnS2 in fixed proportions (15 wt% and 25 wt% rGO) to achieve a NO2 sensor that is selective and operates at room temperature. In Figure 1, the scanning electron microscopy (SEM) image shows that the small SnS_2 particles are adhered underneath the rGO sheets in agglomerates.

Figure 1: SEM image of the SnS_2/rGO 15% sample.

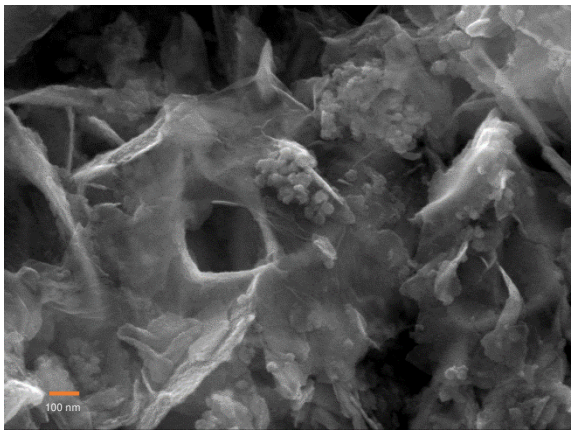

For the gas sensing measurements, the response was calculated as follows:

$$\text{Response (\%)} = ((R_a - R_g)/R_a) \times 100 \quad (1)$$

Figure 2 illustrates the relationship between the sensor response and NO_2 concentration.

As can be observed, the composition containing 15 wt% rGO in SnS_2 exhibited two times higher response compared to the pure rGO sample and 1.7 times the response observed for the 25 wt% formulation at room temperature.

Figure 2: response x concentration data for the pure rGO, SnS2/rGO 15%, and SnS2/rGO 25%.

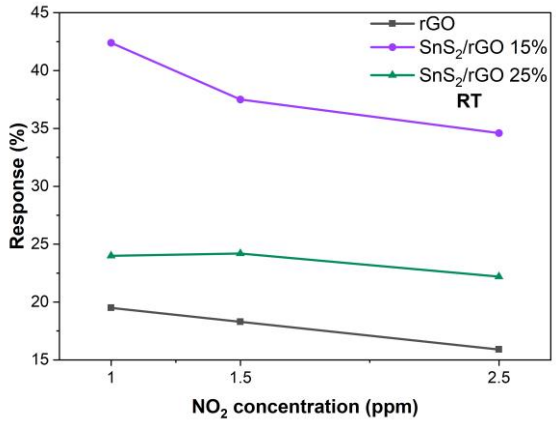

Since the SnS2/rGO 15% presented the best characteristics among the evaluated samples, this sensor was chosen for the selectivity test. The selectivity test was performed using O3, NH3, H2S, H2, and ethanol gases, as displayed in Figure 3. It can be observed that although the SnS2/rGO 15% composite shows some response to NH3 and O3, its response to NO2 is much higher, indicating good selectivity towards NO2. The sample did not show a significant response to H2S, H2, or ethanol.

Figure 3: selectivity test of the SnS_2/rGO 15% sample towards NH_3, O_3, H_2S, H_2, ethanol and NO_2 gases.

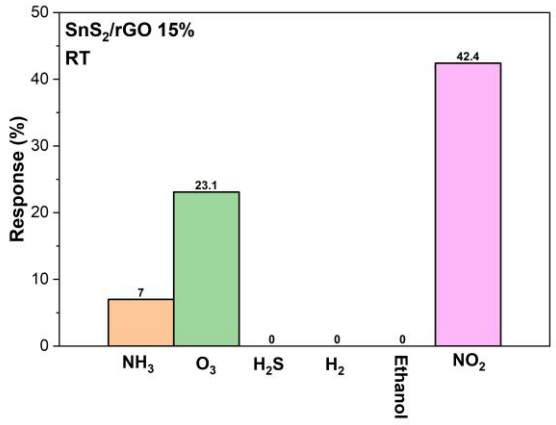

Furthermore, tests concerning the effect of humidity in the performance of the sensor were conducted. The results of the humidity test are displayed in Figure 4, where it can be seen that the sensor presents a higher response for a 40% humidity, and as the humidity increases, the response of the sensor tends to decrease.

Figure 4: variation of the response of the SnS_2/rGO 15% with varying humidity levels.

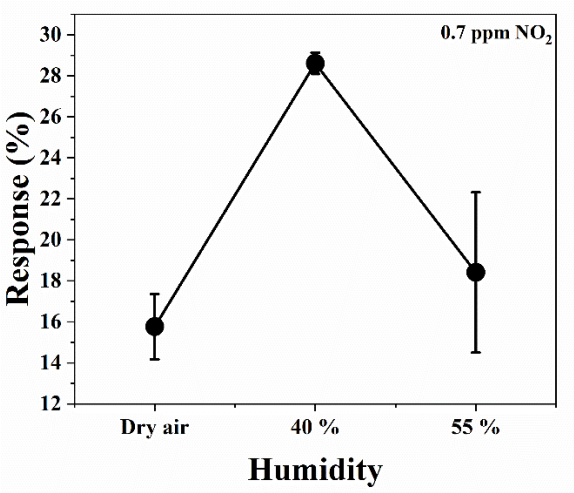

In conclusion, the mechanical mixing dispersion method was effective in forming a composite sensor based on SnS2 and rGO that operates at room temperature and exhibits good selectivity for NO2. The humidity plays a significant part in the detection of NO_2, with a 40% humidity level being determined as ideal for increasing the sensors' response.

References

1. Chen, X., Qi, L., Li, S. & Duan, X. Long-term NO2 exposure and mortality: A comprehensive meta-analysis. *Environmental Pollution* **341**, 122971 (2024).
2. Cheng, M. *et al.* Highly sensitive sensors based on quasi-2D rGO/SnS2 hybrid for rapid detection of NO2 gas. *Sensors and Actuators B: Chemical* **291**, 216–225 (2019).

DOI 10.5162/eurosensors2026/Mo−PHS−03

DOI 10.5162/eurosensors2026/Mo–PHS–04

ZnO nanowires-based micro-sensor for wall pressure measurement in hydrodynamical flow

A. Serrure[1], M. Manrique Reyes[2], M. Abolhassan Araghi[3], L. Simonet[1,4], L. Gimeno[4], V. Consonni[5], B. Salem[2], S. Hoerner[3], G. Ardila[1], C. Ghouila-Houri[1].
[1] Univ. Grenoble Alpes, Univ. Savoie Mont Blanc, CNRS, Grenoble INP, CROMA, F-38000 Grenoble, France
[2] Univ. Grenoble Alpes, CNRS, CEA/LETI Minatec, Grenoble INP, LTM, F-38000 Grenoble, France
[3] Univ. Grenoble Alpes, CNRS, Grenoble INP, LEGI, F-38000 Grenoble, France
[4] Univ. Grenoble Alpes, CNRS, Grenoble INP, G2Elab, F-38000 Grenoble, France
[5] Univ. Grenoble Alpes, CNRS, Grenoble INP, LMGP, F-38000 Grenoble, France

agnes.serrure@grenoble-inp.fr

Summary:
Nanowires-based technology using zinc oxide (ZnO) has been widely investigated in recent years, for its combination of semiconducting and piezoelectric properties. Here, we designed a wall pressure sensor made of vertical ZnO nanowires (NWs) embedded in a polymer matrix, for measurements in hydrodynamical flow. Finite element analysis have been performed, demonstrating the sensor sensitivity to pressure fluctuations. Depending on the nanowires height, the sensitivity can theoretically achieve up to 1.3mV/kPa. The sensor will be wall-mounted in a water tunnel for flow characterization.

Keywords: ZnO nanowires, piezoelectric sensors, wall pressure sensors, active flow control, hydrodynamical flow sensor.

Background

In hydrodynamics, understanding and controlling wall-bounded flows could improve lifespan and performance of hydrokinetic turbines [1]. To achieve this goal, miniaturized and watertight wall pressure sensors are required.

Meanwhile, ZnO thin films, both piezoelectric and semiconducting, have been studied for energy harvesting and sensing applications as an alternative to toxic, non-renewable materials like PZT [2]. In the past twenty years, ZnO NWs, enhancing piezoelectric properties, have also been developed with low-cost fabrication processes and encouraging results for sensing [3].

Our collaborative work focuses on providing a miniaturized sensor device based on ZnO NWs to supply system feedback in a closed loop flow control experiments with an actuated hydrodynamic profile [1].

Sensor fabrication

The sensitive part of the sensor exploits piezoelectric ZnO NWs to measure the wall pressure fluctuations. The fabrication process starts with the deposition of an 80 nm-thick ZnO seed layer, on which nanowires are grown by chemical bath deposition [4]. The NWs are typically 1µm to 10µm high, and 40nm in radius. They are then encapsulated with Parylene-C, a polymer with relevant mechanical and electrical insulation properties [5].

For impedance and piezoelectric response to flow pressure measurements, ZnO NWs must be sandwiched between electrodes. The low-resistivity Si substrate and a 50nm/150nm-thick sputtered gold (Cr/Au) layer play the role of bottom and top electrodes respectively. The sensor design can be appreciated on Fig. 1, and a SEM image of one of the devices, realized with 1µm high nanowires, can be seen on Fig. 2.

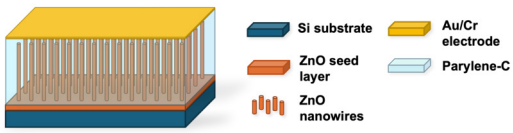

Fig. 1. Wall pressure sensor architecture.

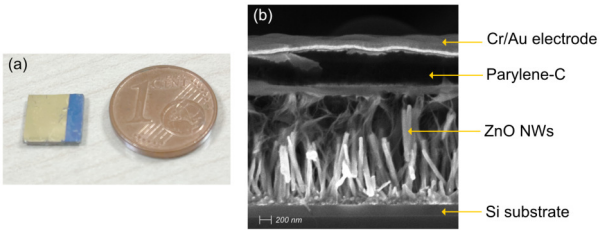

Fig. 2. Cross-sectional SEM image of the wall pressure sensor, with ZnO nanowires 1µm high.

Simulation results

Finite element analysis (FEA) simulations have been performed using COMSOL Multiphysics software. The model includes ZnO coupled piezoelectric and semiconductor properties.

The presented simulation is based on a single-cell 3D model (Fig. 3). In the zoomed window, the square section shows a quarter of a nanowire in each corner, and the inner gap, filled with the Parylene-C encapsulation. The top electrode is metallic and the bottom one semiconductor, so as to remain as close as possible to the real device. Periodic conditions are applied to the sidewalls of the cell, to model a forest of nanowires in x and y directions.

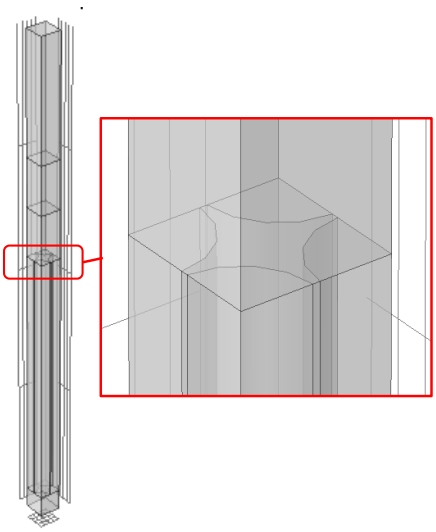

Fig. 3. Single-cell model designed in COMSOL simulation.

Wall pressure is applied on top, with values ranging from -10kPa to 10kPa, corresponding to typical experimental values of wall pressure for flows under 10 m/s in a water tunnel. Zero potential is imposed to the bottom electrode.

Fig. 4 presents the simulation results, showing the electrical voltage variation at the top electrode, for three different nanowires heights: 1 µm, 5 µm and 10µm, corresponding to achievable nanowires heights.

The sensor exhibits a linear behavior with a theoretical sensitivity of 0.133 mV/kPa, 0.642mV/kPa and 1.28mV/kPa for nanowires of respectively 1µm, 5µm and 10µm high. For extreme simulated values of wall pressure, the measured electric potential is in the order a few mV. These values are compatible with commercially available electronics (high precision signal conditioners and instrumentation amplifiers), simplifying future work on sensor interfacing.

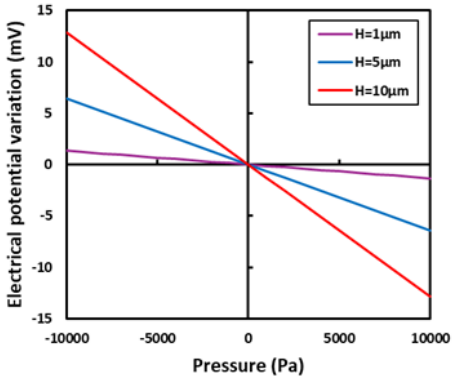

Fig. 4. Electric potential variation measured in top electrode simulation, for P=[-10kPa,10kPa] and for H={1µm, 5µm, 10µm}.

Outlook

In the near future, the sensor will be integrated and made watertight to allow wall-mounting. Finally, the sensor will be characterized electromechanically then tested in a hydrodynamic tunnel, with flow velocities varying from 2m/s to 10m/s. These results, as well as further numerical investigations, will be presented at the conference.

Acknowledgements

This work is funded by Univ. Grenoble Alpes (Physics Engineering and Materials center).

References

[1] S. Abbaszadeh, S. Hoerner, T. Maître, R. Leidhold, Experimental investigation of an optimised pitch control for a vertical-axis turbine, *IET Renewable Power Generation*, 13: 3106-3112 (2019); doi : 10.1049/iet-rpg.2019.0309

[2] J. Zhou, N. Xu, Z. Wang, Dissolving behavior and stability of ZnO wires in biofluids: A study on biodegradability and biocompatibility of ZnO nanostructures, *Advanced Materials*, 18(18), 2432 - 2435 (2006); doi : 10.1002/adma.200600200

[3] R. Tao, M. Parmar, G. Ardila, P. Oliveira, D. Marques, L. Montès, M. Mouis, Performance of ZnO based piezo-generators under controlled compression, Semiconductor Science and Technology, 32 (6) (2017); doi: 10.1088/1361-6641/aa691f

[4] R. Parize, J. Garnier, O. Chaix-Pluchery, C. Verrier, E. Appert, V. Consonni, Effects of Hexamethylenetetramine on the Nucleation and Radial Growth of ZnO Nanowires by Chemical Bath Deposition, *The Journal of Physical Chemistry C*, 120 (9), 5242-5250 (2016); doi : 10.1021/acs.jpcc.6b00479

[5] M. Manrique, V. Consonni, G. Ardila, A. Ghouma, G. Le Rhun, B. Salem, Performance optimization of ZnO nanowire/parylene-C composite-based piezoelectric nanogenerators, *Nano Trends*, 9 (2025); doi : 10.1016/j.nwnano.2024.100066

DOI 10.5162/eurosensors2026/Mo–PHS–05

Harmonic Generation to Improve Ultrasound Image Using Piezoelectrical Micromachined Ultrasound Transducers

Francesc Torres, Arantxa Uranga, Núria Barniol
Universitat Autònoma de Barcelona, Dept. Enginyeria Electrònica, Edifici Q, Campus UAB, Cerdanyola del Vallès, Spain
Francesc.Torres@uab.cat

Summary:
Non-linear excitation of Piezoelectrical Micromachined Ultrasound Transducers (PMUTs) produces harmonics generation in sound waves. These harmonics can be used for enhancing image resolution, acousto-optic modulators or multiplexing. In this work we have demonstrated electrical and mechanical non-linear behavior in a PMUT with high frequency resonance and high order harmonics generation.

Keywords: PMUT, Ultrasound Image, Non-linearity

Background, Motivation and Objective

Ultrasound transducers are used for a huge number of techniques, from imaging to communications, chemical and structural analysis. PMUTs have become good candidates for ultrasound transduction for their low-energy consumption, good sensitivities and well-known fabrication techniques. PMUTs are a special case of flexural microelectromechanical systems (MEMS) resonators subjected to non-linear response depending on the excitation.

Under nonlinear response conditions, the spring constant relating the force acting on the PMUT to its vibration amplitude depends on this amplitude through quadratic, cubic and higher-order terms. This amplitude dependence enables the force to act not only at the excitation frequency but also at its harmonics. This nonlinear behavior enables applications such as second-harmonic imaging [1], acousto-optic modulation [2], multiplexing [3], and other multifrequency applications.

For tissue imaging, second harmonic imaging has become of great importance to increase image resolution because of its capacity to reduce artifacts; the energy is concentrated around the main lobe, and the grating lobes and side lobes will have less energy making this less sensitive to off-axis scatters than the fundamental, giving cleaner images [1]. When a single, small PMUT is used, the acoustic energy is radiated in an almost omnidirectional manner, which significantly degrades lateral resolution. In contrast, excitation at higher harmonics results in a more spatially confined radiation pattern.

In addition, it is demonstrated that the combination of higher harmonics (mainly 3rd, 4th and 5th) in a single superharmonic component is a beneficial way to increase the amount of detected energy, preserving the advantages of higher harmonics [4, 5].

Moreover, high-frequency ultrasounds enable the imaging of small-scale features. By exploiting nonlinear effects and applying external pumping, the amplitudes of high-frequency modes can be enhanced.

PMUTs and measurement set-up

PMUTs have a square shape with an 80 µm side and clamped edges. They are built with a 1.2 µm thick scandium-doped (9.5%) aluminum nitride piezoelectric layer and a 1.5 µm silicon nitride passive layer. The piezoelectric layer is sandwiched between two 0.4 µm aluminum layers, one grounded and the other divided into central and peripheral electrodes to enable differential excitation or detection, with a width ratio of 0.7.

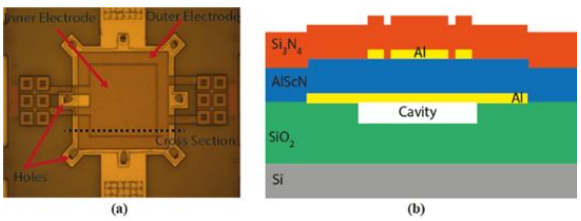

Fig. 1. Optical image (a) and cross section of the PMUT (b)

Fabrication was performed in a commercial CMOS (Silterra) suitable to produce good performance PMUTs for ultrasound purposes [6].

Characterization of the PMUTs non-linearities and measurement of their harmonics were

performed in air, using a home-made interferometer equipped with a He-Ne laser, an avalanche photodiode and a lock-in amplifier.

To characterize the non-linearity, we have driven the PMUT with a relatively high voltage, Vac = 26.7 V peak to peak amplitude, using both electrodes in a differential configuration. PMUT exhibits mechanical (or positive) non-linearity. We can see the characterization in Fig. 2.

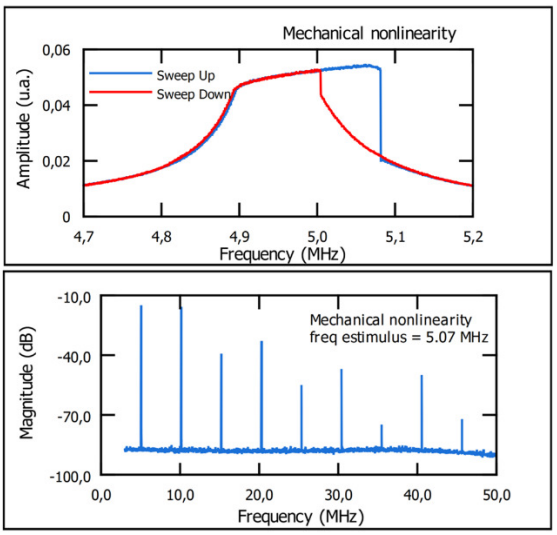

Fig. 2. Optical characterization of PMUT exhibiting mechanical non-linearity (a) and harmonics generation (b)

Results

To generate the harmonics, we have applied a stimulus of a fixed frequency using the lock-in amplifier as a signal source and we have performed the readout using a spectrum analyser obtaining a comb response (see Fig. 2). The frequency used is the one that allows the maximum vibration of PMUT. We have applied a stimulus with frequency of 5.07 MHz to the PMUT with mechanical non-linearity (just near the high frequency jump) and, as can be seen multiple harmonics appear.

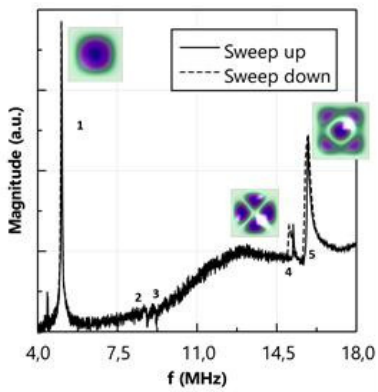

Fig. 3. Excited modes until the fifth. The first, fourth and fifth modes exhibit electrical non-lineariries.

We measured the higher-order modes of another PMUT (see Fig. 3) up to the fifth mode, mode (1,3). The results show that nonlinear effects also appear in high-frequency modes (electrical non-linearities in this case). By applying pumping to the fifth mode, its amplitude can be enhanced, primarily using a phase difference of 30° between excitation and pumping (see Fig. 4), at the expense of the amplitude of the first mode.

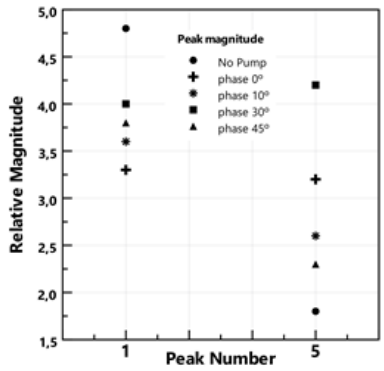

Fig. 4. Pumping of fifth mode of PMUT.

This work was supported by MICIU/AEI/ 10.13039/501100011033 under Project PID2022-136624OB-I00

References

[1] A. Bouakaz *et al*., Native tissue imaging at superharmonic frequencies, transactions on ultrasonics ferroelectrics and frequency control 50, 496-506 (2003); doi: 10.1109/TUFFC.2003.1201462

[2] G. Pillai *et al*., Controllable multichannel acousto-optic modulator and frequency synthesizer enabled by nonlinear MEMS resonator, Scientific Reports 11, 10898-1 10898-13 (2021); doi: 10.1038/s41598-021-90248-w

[3] K. Bhosale *et al*., Nonlinearity driven higher order harmonics in CMOS-MEMS resonators, IEEE IFCS-ISAF Conference 2020; doi: 10.1109/IFCS-ISAF41089.2020.9234852

[4] A. Bouakaz *et al*., Superharmonic imaging: A new imaging technique for improved contrast detection, Ultrasound in Medicine & Biology 28, 59-68 (2002); doi: 10.1016/S0301-5629(01)00460-4

[5] N.D. Londhe *et al*., Superharmonic imaging for medical ultrasound: a review, Journal of Medical Systems 40, 279-1 279-16 (2016); doi: 10.1007/s10916-016-0635-x

[6] I. Zamora *et al*., Monolithic single PMUT-on-CMOS ultrasound system with +17 dB SNR for imaging applications, IEEE Access 8, 142785-142794 (2020): doi: 10.1109/ACCESS.2020.3013763

DOI 10.5162/eurosensors2026/Mo–PHS–06

Robust In-Cavity Thin-Film Temperature Sensor Array for Real-Time Flow-Front Monitoring in Recycled Material Injection Molding

Martin Rekowski[1], Li Zhao[1], Anna Schott[1], Christoph Herrmann[1]
[1] Fraunhofer Institute for Surface Engineering and Thin Films IST, Riedenkamp 2, 38108 Braunschweig, Germany
martin.rekowski@ist.fraunhofer.de

Summary:

We propose a robust thin-film sensing system for in-mold monitoring during injection molding of PP–glass fiber and recycled-content materials. A compact array of resistive temperature sensors is integrated directly on the tool surface with a total layer thickness below 10 µm. The thin-film stack withstands high shear and abrasive glass-fiber flow while showing no drift. Spatiotemporal analysis of the temperature signals across the array provides real-time estimates of local flow-front velocity and direction. Experiments over 500 cycles with varied parameters demonstrate durable operation. The approach supports data-driven process optimization, reduced ramp-up scrap, and future closed-loop process control.

Keywords: injection molding, thin-film sensors, flow-front monitoring, process control

Background, Motivation and Objective

In-cavity sensing is essential for data-driven injection molding. Conventional cavity pressure or temperature sensors are typically bulky, mechanically fragile, and limited in spatial resolution, which restricts their ability to resolve local melt behavior near critical features on the tool surface [1]. Thin-film sensors have previously been successfully integrated into a 2D mold cavity for data-driven quality control in thermoplastic injection molding [2].

We develop a durable multi-sensor thin-film system designed to (i) survive high shear and abrasion for at least 10^5 injection cycles, (ii) fit into highly confined tool geometries, and (iii) provide spatiotemporally resolved temperature data that can be used to infer local flow-front velocity and direction in real time.

Method

A multilayer thin-film system was developed for long-term operation under glass-fiber abrasion. A polished stainless-steel substrate (Rz = 0.1 µm) served as the base material for the thin-film system. A 6 µm amorphous hydrogenated diamond-like carbon (DLC) layer was deposited on the tool by plasma-enhanced chemical vapor deposition (PECVD). Round metallic electrodes for resistive temperature sensing were patterned at selected positions using photolithography from a 0.2 µm chromium layer deposited by physical vapor deposition (PVD). A 1 µm robust insulating amorphous hydrocarbon layer modified with silicon and oxygen (SICON®) was then applied using PECVD. The conductive paths were patterned from an additional 0.2 µm thick chromium layer. A 3 µm thick SICON® layer was used as a wear-protection layer. The contact areas and lead wires were positioned outside the mold cavity to avoid damage. The total layer thickness was kept below 10 µm, which preserves thermal responsiveness and adds only negligible thermal mass compared with the mold insert. Furthermore, an alternative sensor concept based on an Al_2O_3-insulated thin-film stack with thermoresistive chromium PTC temperature sensors was implemented on a second mold insert. Its architecture and performance, together with a detailed comparison to the DLC/SICON® system, will be discussed in the extended version of this work.

To achieve a high information density in confined regions, the sensor layout was miniaturized so that each temperature sensor has a circular temperature-sensing area with a diameter of 1.6 mm. The four outer sensing points form a square with a side length of about 7 mm (diagonal $\approx$ 9.9 mm), and the fifth sensing point is located at the center of this square, as shown in Fig.1.

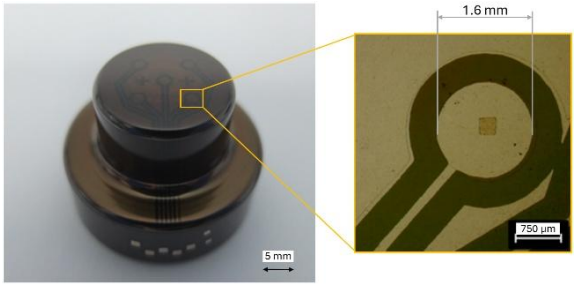

Figure 1. Photograph and close-up of the fabricated sensor system.

To verify the sensor functionality, a thermoresistive characterization was carried out. A Pt100 resistance thermometer was mounted on the surface of the metal insert and served as a reference. The insert with the integrated thin-film sensor system was heated and cooled at a controlled rate in a climate chamber. The measurements revealed an exponentially decreasing dependence of the sensor resistance on temperature over the investigated range.

Sensor signals were acquired using a National Instruments CompactDAQ data acquisition system during injection-molding trials at a sampling rate of 1 kHz. Time-of-arrival and temperature-gradient analyses across the sensor array were implemented to compute local flow-front velocity and direction in real time. As shown in Fig. 2, the thin-film temperature sensor array is arranged on the left half of the mold cavity. The thermocouples are positioned in locations that are mirror-symmetric to thin-film sensors T1, T3, and T4 with respect to the cavity centerline.

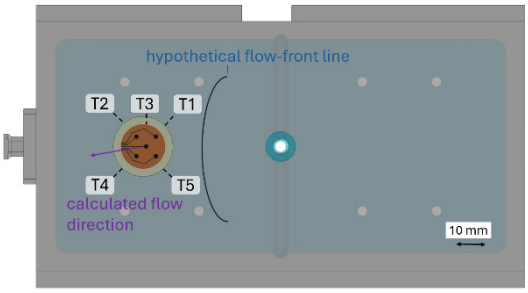

Figure 2. Thin-film sensor system with five temperature sensors installed on the left half of the mold.

Experimental validation was carried out over 500 injection cycles using PP–glass fiber and recycled-content materials with varying levels of recycled content and material quality. Process parameters, including melt temperature, mold temperature, injection speed, holding pressure, and holding time, were systematically varied within industrially relevant ranges.

Results

The thin-film sensors exhibited stable, drift-free signals over 500 shots, with no delamination, cracking, or electrical failure of the sensor paths. As illustrated in Fig. 3, the temperature curves from the thin-film sensors enable clear identification of the turning points that mark the start and end of each stage in the injection-molding cycle: filling, packing, cooling (after the mold clamping force is released), and demolding. This stage-resolved information can significantly support the maintenance of process stability across batch production for different DOE settings.

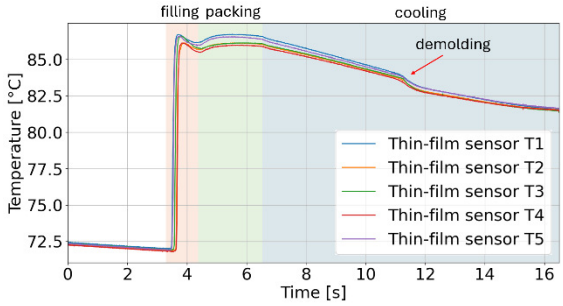

Figure 3. Temperature profiles measured by the thin-film sensor system.

The measured flow-front velocity and direction obtained from the thin-film sensors were compared with those derived from reference sensors, demonstrating excellent agreement. For example, for a high-quality recycled material with 40% recycled content, at a mold temperature of 200 °C, an injection speed of 30 mm/s, a holding pressure of 39 MPa and a holding time of 9 s, the measured average flow-front velocity was 77.4 mm/s at an angle of −85.9°.

In conclusion, this novel thin-film design successfully integrates multiple sensing functions into confined tool spaces without adversely affecting the injection-molding behavior.

Outlook

Future work will further miniaturize the tool insert, increase the sensor count, and integrate the sensing system into closed-loop control strategies with machine-learning-based evaluation in order to enhance process stability and energy efficiency.

References

[1] T. Ageyeva, S. Horváth, J. G. Kovács, In-mold sensors for injection molding: On the way to Industry 4.0, Sensors 19, 3551 (2019); doi: 10.3390/s19163551

[2] M. Rekowski, F. Timmann, H. Hupfeld, A. Schott, A. Hürkamp, K. Dröder, C. Herrmann, Thin-Film Sensors for Data-Driven Quality Control in Thermoplastic Injection Molding, Production at the Leading Edge of Technology (WGP 2024), pp. 377–384 (2024); doi: 10.1007/978-3-031-86893-1_41.

DOI 10.5162/eurosensors2026/Mo−PHS−07

Development of a dipole antenna sensitive to corrosion of steel

Benjamin MUGABO NDUHURA[1], Stéphane Rioual[1], Benoit Lescop[1], Philippe Talbot[1]
[1] Univ Brest – CNRS – LabSTICC, CS 93837 - 6 avenue le Gorgeu – Brest - France,
benjamin.mugabonduhura@univ-brest.fr

Summary:
Monitoring corrosion of reinforcing steel is critical for ensuring the durability and structural safety of civil engineering infrastructures. This paper presents a corrosion-sensitive antenna for detecting corrosion of metallic element in free space, serving as a preliminary step toward UHF RFID-based corrosion monitoring systems for civil engineering structures.

Keywords: Corrosion monitoring, steel, dipole antenna, resonance frequency.

Introduction

The service life of reinforced concrete infrastructures is highly dependent on the corrosion resistance of steel. Indeed, in marine environments, carbonation and chloride penetration from the surrounding environment are known to initiate steel corrosion processes, subsequently leading to the weakening of the structure and, eventually, to its collapse. Traditional corrosion detection methods, such as visual inspections, are time-consuming and costly, and do not allow early detection of corrosion, since the steel is inaccessible. Recently, Radio Frequency Identification (RFID) technology has been proposed as an innovative method for corrosion detection. It is particularly attractive due to the small size of RFID tags, their low cost, and their ability to operate wirelessly. Furthermore, the absence of batteries and cables facilitates their integration into concrete during construction or maintenance/repair operations. Over the past several years, we have therefore proposed several solutions to incorporate corrosion-sensing capabilities into RFID tags. In particular, we recently proposed a UHF-RFID sensor based on an additional sensitive metallic layer exposed to corrosion and located very close, in the mm range, to the RFID antenna [1]. This approach relies on the electromagnetic coupling between the antenna and this metallic layer. The principle is straightforward: as corrosion progresses, the thickness of the thin metal layer decreases, leading to an increase in its electrical resistance and, consequently, to a variation in the properties of the coupled antenna.

This method was applied to produce an UHF-RFID sensor embedded in concrete in close proximity to a steel foil which acts as the sensitive element[2] and more recently to prestressed infrastructures [3]. Despite of the interest of the method, the short-range distance between the antenna and the sensitive material limits the applications. Indeed, due to the aggressive nature of the environment (pH=13), ensuring a long lifetime of an embedded antenna in concrete remains a challenge. Within this context, the use of a remotely located antenna appears to be a relevant alternative. The present work therefore focus on the sensitivity of a dipole antenna positioned in the centimeter range from a steel foil exposed to corrosion. As it will be shown, its performance progressively degrades as corrosion evolves, thereby offering a robust and promising solution for civil engineering applications.

Materials et methods

The development of the dipole antenna sensitive to a distant metallic element was carried out using the ANSYS HFSS software, based on the finite element method with a tetrahedral mesh. The fabricated antenna was produced via a LPKF prototyping machine. Figure 1 illustrates the experimental setup. As observed, an antenna-steel distance d_{as} = 12 mm is used, a value which extend the distance currently used in UFH-RFID corrosion sensors. Experimental results were obtained using a steel sheet (300 x 50 x 0.05 mm). Since corrosion is a low process, it is accelerated through sodium chloride deposition, periodic addition of water approximately every 24 hours, and exposure to ambient air. The refection parameter S_{11} of the antenna was measured using a vector network analyzer (Anritsu MS2037C) connected to the antenna via a coplanar transmission line, then acquired and processed using a computer. On Fig. 1, the

resonance associated with the operating antenna is well observed on the computer.

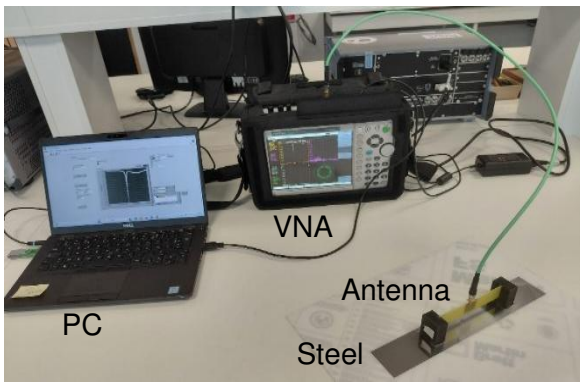

Fig. 1. The experimental setup

Experimental results

Figure 2 displays the S_{11} parameter during corrosion of the steel foil. Before corrosion, in red, a well-defined resonance is observed indicating the good impedance matching of the antenna with the presence of the metallic plate. During corrosion, a degradation of antenna performance is observed, accompanied by a resonance frequency shift associated with the changes in the surrounding environment. This behaviour could be induced by the formation of rust on the steel plate, or due to the presence of hydrated species on the surface. Finally, when the 50 µm of steel are corroded, in yellow color, the antenna does not work properly. The change of operating state of the antenna, is consequently indicative of a mass los of steel. The inset of Fig. 2 displays the state of the steel corresponding to S_{11} parameter displayed in yellow color.

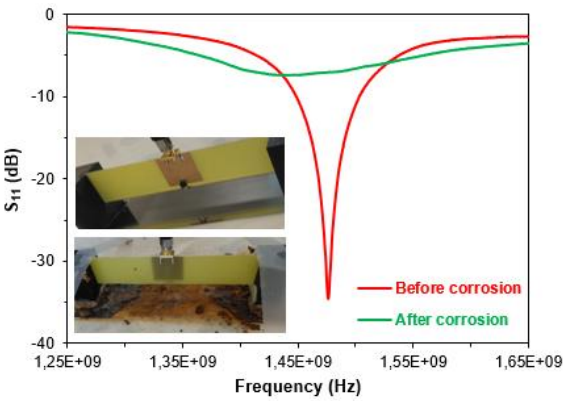

Fig. 2. S_{11} versus frequency during the corrosion of the steel foil. Inset: Steel foil before and after corrosion.

Conclusion

The results demonstrate that monitoring corrosion of a metallic foil is possible when the antenna and the sensitive metallic foil are separated. They provide an improvement of the method with respect to the existing RFID corrosion sensors. An application of this method to corrosion monitoring in civil engineering structures will be investigated in future work. In particular, the aim will be to locate the steel sensitive element near rebars and the antenna at the concrete surface.

Acknowledgment

The authors would like to thank the Britany region for funding a PhD contract (Benjamin MUGABO NDUHURA)

References

[1]El Masri I, Lescop B, Talbot P, Nguyen Vien G, Becker J, Thierry D, Rioual S. Development of a RFID sensitive tag dedicated to the monitoring of the environmental corrosiveness for indoor applications. *Sensors and Actuators B: Chemical*; 322:128602 (2020); doi:10.1016/j.snb.2020.128602

[2]K. Bouzaffour, B. Lescop, F. Gallée, P. Talbot, and S. Rioual. Development of embedded UHF-RFID corrosion sensor for monitoring corrosion of steel in concrete, *IEEE Sensor journal*. Vol. 21(2021); doi: 10.1109/JSEN.2021.3064970

[3]L. Gaillet, C. Sarr, Y. Falaise, S. Chataigner, P. Talbot, B. Lescop, S. Rioual. RFID sensor development for corrosion monitoring in bridges cables, , *Nondestructive Testing and Evaluation*, *41*(2), 981–999 (2026); doi: 10.1080/10589759.2025.2477685

DOI 10.5162/eurosensors2026/Mo–PHS–08

Experimental Investigation of the Thermal Conductivity Behavior of Ne-Ar, Ne-N_2 and Ar-N_2 Binary Gas Mixtures

Svenja Jung[1,2], Mike Benkendorf[1], Hans-Fridtjof Pernau[1], Markus Graf[2,3], Laura Maria Comella[2], Jürgen Wöllenstein[1,4], Katrin Schmitt[1,4]
[1] Fraunhofer Institute for Physical Measurement Techniques IPM, Georges-Köhler-Allee 301, 79110 Freiburg im Breisgau, Germany,
[2]University of Applied Sciences Karlsruhe, Moltkestraße 30, 76133 Karlsruhe, Germany,
[3]University of Hamburg, Luruper Chausee 149, 22761 Hamburg, Germany,
[4]Albert-Ludwig-University Freiburg, Georges-Köhler-Allee 102, 79110 Freiburg im Breisgau, Germany
svenja.jung@ipm.fraunhofer.de

Summary

Binary gas mixtures provide a basis for the investigation of the thermal conductivity behavior and create a starting point for extending the analysis to more complex gas mixtures. Nonlinear behavior already appears in fundamental binary gas mixtures, indicating that even simple systems exhibit complex composition-dependent interactions. Improved prediction of these nonlinearities enables enhanced simulation and calibration of thermal conductivity detectors.

Keywords: Thermal conductivity, binary gas mixtures, nonlinear mixing behavior, thermal conductivity detector, lock-in amplifier

Introduction

Precise theoretical prediction of the properties for gas mixtures is challenging because intermolecular interactions depend on the molecular model, temperature, and pressure, and determine the energy transfer between translational and internal degrees of freedom [1]. Therefore, the thermophysical properties of each pure component in the binary gas mixture are analyzed to assess its influence on transport and thermal behavior. Even in binary mixtures of monatomic gases, nonlinear thermal conductivity behavior is observed. Consequently, the concentration-dependent nonlinearity of the thermal conductivity of binary gas mixtures requires experimental determination, as a precise theoretical prediction remains complex, but is crucial to understand more complex gas mixtures, e.g. air. In this paper, the binary gas mixtures of Ne-Ar, Ne-N_2 and Ar-N_2 are considered, enabling a fundamental investigation of the nonlinearity.

Experimental method

Most advanced, precise gas measurements via thermal conductivity are based on variations of the hot-wire method. This method uses a simple and robust tungsten wire as a thermal conductivity detector (TCD), which simultaneously serves as a heating element and temperature sensor, configured as Wheatstone half bridge. The TCD's reference elements adjust to the ambient gas temperature, thus compensating for temperature influences. Since cross-sensitivity to temperature and humidity affects thermal conductivity, this was additionally measured to assess its potential for use in compensation. The schematic of the TCD measurement for a controlled binary gas mixture is shown in Fig. 1. The increased measurement requirements are met by the lock-in amplifier principle, which are composed of an advanced, compact microcontroller electronic and a benchtop lock-in amplifier.

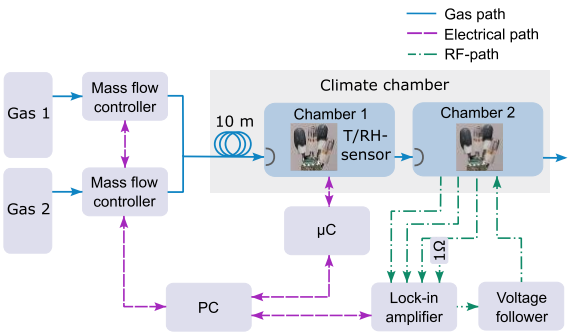

Fig. 1. TCD measurement setup for controlled binary gas mixture measurements. The mixed gas is passed through a 10 m long extended thermalization unit to both measurement chambers with an additional temperature/humidity sensor ScioSense (ENS210), which are located inside the climate chamber. The TCDs operate through a microcontroller electronic and a lock-in amplifier (Zurich Instruments HF2LI) with external voltage follower and a 1 Ω shunt-resistor for current measurement.

Results

Literature values on the nonlinear behavior of the binary gas mixtures Ne-Ar, Ne-N_2 and Ar-N_2 were compiled from various sources [1,2], as no systematic compilation exists that considers the influence of temperature. Therefore, Ne-Ar, Ne-N_2 and Ar-N_2 measurements were performed to investigate the influence of the nonlinear behavior at 25 °C and 38 °C for atmospheric pressure. The bridge voltage measurement using constant gas steps was carried out to determine the nonlinear behavior of the noble gases Ne–Ar (Fig. 2).

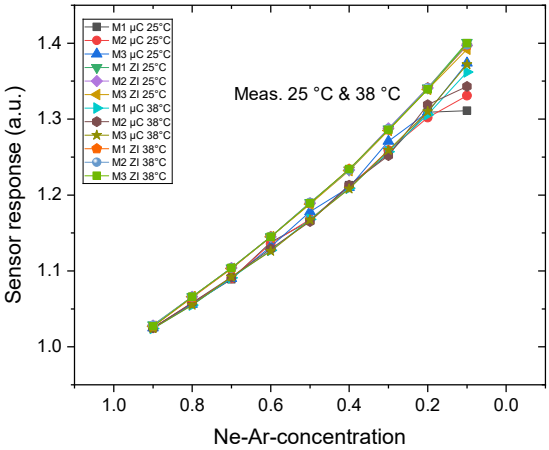

Fig. 2. Nonlinear behavior of Ne-Ar gas steps at 25 °C and 38 °C with 0 % RH. The TCDs were driven via the microcontroller electronic (µC) and the lock-in amplifier (ZI).

The nonlinear behavior is determined by dividing the bridge voltage difference by the corresponding linear gas concentration factor. The relationship at 25 °C and 38 °C shows a nonlinear increase up to a factor of 1.4. The pronounced nonlinearity results from the large difference in the thermal conductivity of Ne-Ar, with a ratio of 49:17.7. The binary gas mixtures of Ne–N_2 (Fig. 3) show a similar nonlinearity as Ne–Ar.

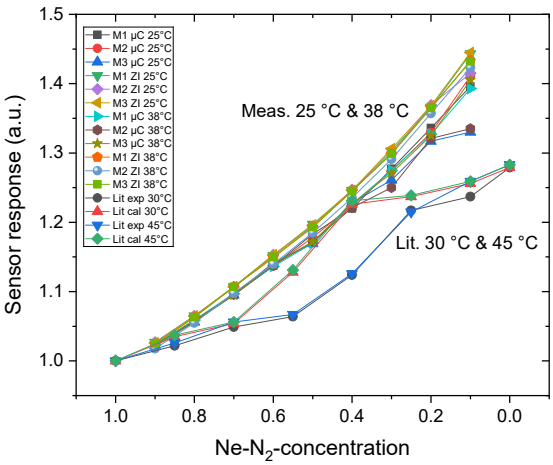

Fig. 3. Nonlinear behavior of Ne-N_2 gas steps at 25 °C and 38 °C, which are compared with the literature of Barua [2] at 30 °C and 45 °C.

The difference in the thermal conductivity of Ne and N_2 (49:25.8) increases up to a factor of 1.45. The literature data of Barua [2] are below the measured values and exhibit irregular behavior. The binary gas mixtures of Ar–N_2 (Fig. 4) show a lower nonlinear behavior as observed for Ne.

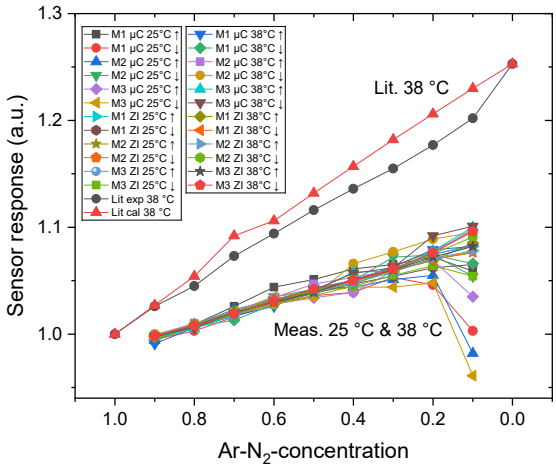

Fig. 4. Nonlinear behavior of Ar-N_2 gas steps at 25 °C and 38 °C, which are compared with the literature of Srivastava and Srivastava [1] at 38 °C.

The difference in the thermal conductivity of Ar and N_2 (17.7:25.8) increases nearly linearly up to a factor of 1.1, whereas the literature data of Srivastava and Srivastava [1] reach up to 1.25, with a significantly steeper increase. The two readout electronics are located close together and the small temperature difference between 25 °C and 38 °C with atmospheric pressure is for the gas combinations not noticeable.

Conclusion

The experimental results of the binary gas mixtures for Ne-Ar, Ne-N_2 and Ar-N_2 at 25 °C and 38 °C with atmospheric pressure show a pronounced concentration-dependent nonlinearity. The nonlinear behavior for Ne-Ar and Ne-N_2 can be attributed to the larger thermal conductivity difference. The marked nonlinearities in binary gas mixtures indicate that simple linear models are inadequate for accurately describing the physical behavior, which is a critical factor for the accurate calibration and reliable operation of TCDs.

References

[1] B. N. Srivastava, R. C. Srivastava; Thermal Conductivity and Eucken Correction for Diatomic Gases and Binary Gas Mixtures. *J. Chem. Phys.* 1 May 1959; 30 (5): 1200–1205. https://doi.org/10.1063/1.1730155

[2] A.K. Barua. „Thermal conductivity and Eucken type correction for binary mixtures of N2 with some rare gases“. In: Physica 25.7–12 (Jan. 1959), S. 1275–1286. issn: 0031-8914. doi: 10.1016/0031-8914(59)90049-7.

DOI 10.5162/eurosensors2026/Mo–PHS–09

Enhancing Cardiac Magnetomechanical Sensing via a Tunable Non-Linear Spring Transduction Layer

Alessandro Ascani Orsini[1], Yijun Lai[1], Haoyu Xu[1,2], Daniel Guo[1], Chang Liu[2], Nitish Thakor[1,2]
[1] Department of Electrical and Computer Engineering, Johns Hopkins University, Baltimore, MD 21218 USA,
[2] Department of Biomedical Engineering, Johns Hopkins University, Baltimore, MD 21218 USA
E-mail: aascani2@jh.edu

Summary:

Conventional wearable cardiac monitoring predominantly uses optical or electrical modalities, which are highly susceptible to skin variability and motion-induced noise. Here, we introduce a magneto-mechanical sensing approach that captures cardiac signals through skin vibrations mechanically coupled into a magnetic spring transduction layer. This tunable, non-linear interface improves mechanical coupling and signal amplification, promising more robust and sensitive heartbeat detection

Keywords: Pulsatility, Magnetics, Magneto Mechanical Transduction, Wearables, Contactless Coupling

Introduction

Cardiovascular diseases remain the leading cause of mortality worldwide, driving demand for continuous, non-invasive wearable monitoring technologies capable of capturing early physiological changes [1]. Mechanical vibration–based modalities such as ballistocardiography and seismocardiography enable unobtrusive sensing of cardiogenic micro-motions within the low-frequency physiological band (~0.5–5 Hz), offering rich information on cardiac mechanical dynamics while avoiding optical attenuation and electrical contact limitations [2]. However, these approaches suffer from low signal-to-noise ratio, motion artifacts, and strong dependence on sensor placement and mechanical coupling, which significantly degrade reliability in real-world use. Existing solutions largely rely on signal processing rather than improving the physical sensing interface [2]. Magneto-mechanical sensing (MMS) provides a low-power alternative by converting vibration-induced displacement into measurable magnetic field variations [3], yet it has been rarely implemented with current designs employing fixed mechanical structures that limit adaptability and sensitivity. Here, a magnetic spring–based architecture is introduced to enable impedance-matched coupling to the skin while passively amplifying signals through non-linear stiffness oscillatory dynamics. This tunable compliance enhances displacement-to-field conversion by increasing mechanical response without active power input. Magnetic springs offer non-linear, adjustable compliance without mechanical wear, improving robustness to placement variability and noise [4]. This approach establishes a framework for mechanically amplified, magnetic biosensing in wearable cardiovascular monitoring.

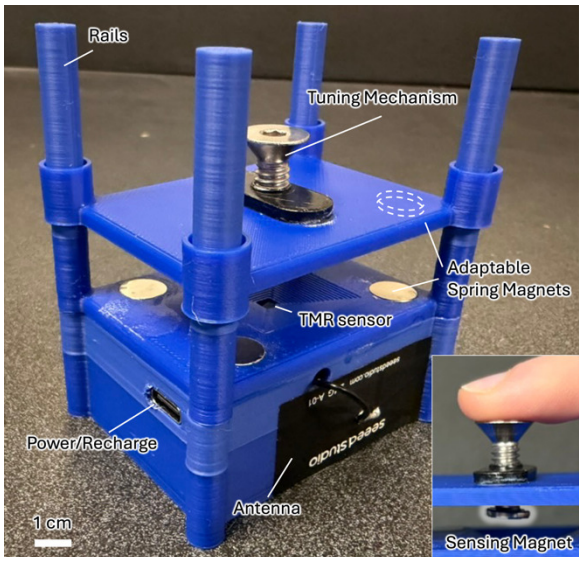

Fig. 1. Design of the tunable transduction mechanomagnetic Cardiac Sensor, showing the spring-mounted magnets and the tunable mechanism for precise transduction in the sensors' regime.

Methods

The sensor (Fig.1) comprises a tunnel magnetoresistive (TMR) element positioned parallel to a disk Neodymium permanent magnet (Total

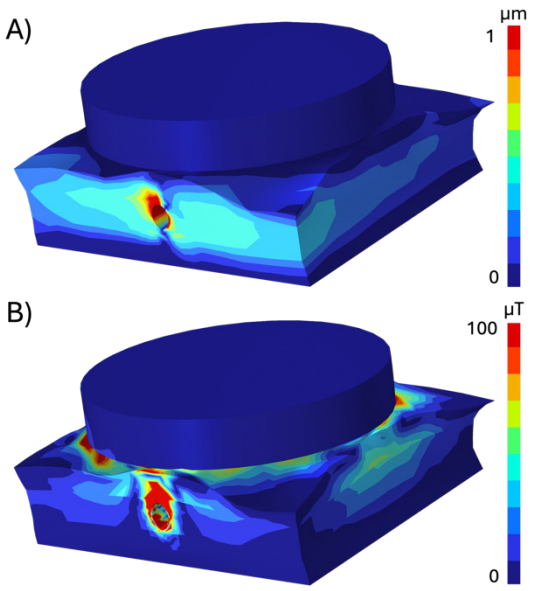

Fig. 2. COMSOL simulation of the expected displacement in rigid setup, when magnet is coupled to skin above a pulsing blood vessel. A) Change in Displacement B) Change in magnetic field

$$\boldsymbol{G} = \begin{array}{c} \text{Displacement} \\ \begin{pmatrix} G_{xx} & G_{xy} & G_{xz} \\ G_{yx} & G_{yy} & G_{yz} \\ G_{zx} & G_{zy} & G_{zz} \end{pmatrix} \end{array} \text{MagField}$$

$$\boldsymbol{G_{Sim}} = \begin{pmatrix} \boxed{1376} & 51 & 614 \\ -265 & -10 & -118 \\ -199 & -7 & -89 \end{pmatrix}$$

Fig. 3. Tensor of Displacement/MagneticField relationship at the skin-magnet interface obtained from COMSOL simulation

Elements) which is mounted on a magnetically levitating platform held via rails. Cardiac-induced skin vibrations drive magnet displacement, modulating the local magnetic field and resistance of the TMR. COMSOL simulations were done to establish the transfer from the skin over a pulsing blood vessel and the sensing magnet upon contact (Fig. 2). Two models of the sensor were done: 1) using traditional fixed platform 2) using magnetic springs. Both devices' responses were characterized via palmar-recording and compared to ElectroCardioGram (ECG) obtained simultaneously through Apple Watch on the same arm (n=3). Signal to Noise Ratio (SNR) was evaluated via spectral analysis.

Results and Discussion

The simulations (Fig. 2-3) show a passive amplification of the mechanical displacement through the magnetic field of almost 3 orders of magnitude. Experimental results using both MMS recording systems show cardiac activity peaks matching Q peaks in ECG lead I (Fig. 4). Rigid transduction exhibits weak cardiac activity, yielding low-amplitude signals with correspondence to ECG peaks (Fig. 4, top). The tunable magnetic spring markedly improves peak amplitude (~10x) and SNR of the system by about 11 dB while maintaining visible alignment with ECG (Fig. 4, bottom), indicating enhanced transfer of cardiac-induced skin vibrations no additional power cost. These results arise from nonlinear stiffness–mediated impedance matching, where distance-dependent restoring forces increase oscillatory amplitude and enhance displacement-to-field transduction. While promising, the approach remains limited to testing via mechanical pulsatility and further characterization is necessary, for validation of real-world robustness.

References

[1] K. Bayoumy, et al., Smart wearable devices in cardiovascular care: where we are and how to move forward, *Nature Reviews Cardiology* **18**, 581–599 (2021); doi: 10.1038/s41569-021-00522-7

[2] F. Santucci, D. Lo Presti, C. Massaroni, E. Schena, R. Setola, Precordial vibrations: A review of wearable systems, signal processing techniques, and main applications, *Sensors* **22**, 5805 (2022); doi: 10.3390/s22155805

[3] C. Romano, C. Massaroni, E. Schena, Wearable magnetic sensing technologies for cardiac and respiratory monitoring: A review, *IEEE Sensors Reviews* (2025); doi: 10.1109/SR.2025.3620252

[4] Q. Zhu, K. Chai, Magnetic negative stiffness devices for vibration isolation systems: A state-of-the-art review from theoretical models to engineering applications, *Applied Sciences* **14**, 4698 (2024); doi: 10.3390/app14114698

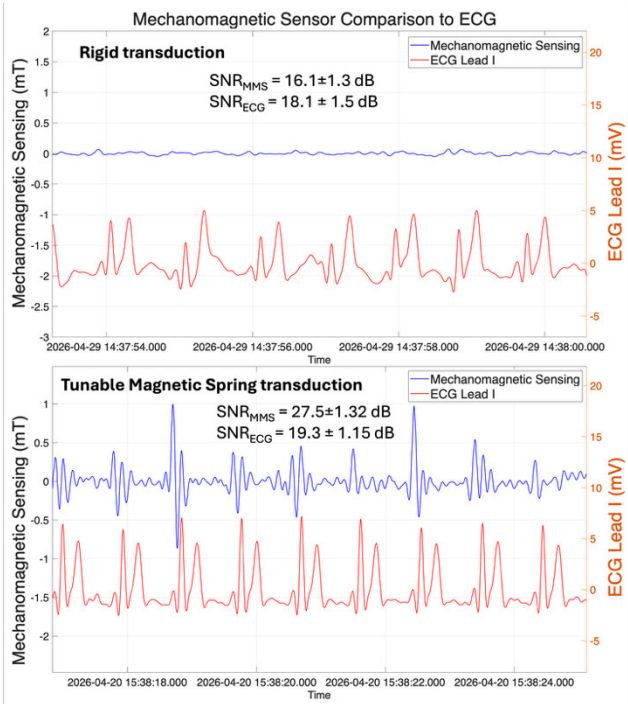

Fig. 4. Measured Comparison of rigid transduction to the tunable magnetic spring transduction. Peaks aligning with Lead I ECG are visible in both, but are more evident in the second by almost a factor of 10.

DOI 10.5162/eurosensors2026/Mo–PHS–10

Piezoelectrically Induced Resonance Frequency Tuning of Buckled-Diaphragm MEMS Ultrasonic Sensors for Multi-Frequency Measurement

Kaoru Yamashita, Junpei Yamamoto
Kyoto Institute of Technology, Matsugasaki, Kyoto 606-8585, Japan

Summary:
The resonance frequency of a piezoelectric MEMS ultrasonic sensor with a buckled diaphragm was controlled by piezoelectrically induced stress for multi-frequency measurement. The sensitivity-enhancing buckled shape in the sensing region was maintained over the tuning-voltage range of 0 V to 10 V, despite changes in the overall buckling profile. Tuning voltages of 2 V and 9 V provided resonance frequencies of 90.6 kHz and 43.3 kHz, respectively, with vibration modes yielding adequate piezoelectric output. These results identified practical operating conditions for resonance control in this scheme.

Keywords: piezoelectric ultrasonic sensor, resonance frequency, vibration mode, resolution, buckling

Background, Motivation and Objective

Phased-array technology enables beam steering in ultrasonic measurement. In conventional phased arrays, angular resolution is improved by increasing the array aperture, while the element spacing must be smaller than half the wavelength to suppress grating lobes [1]. This generally requires a large number of sensor elements in a dense array. In contrast, it has been shown that multi-frequency measurement can improve angular resolution and suppress grating lobes in a sparse array [2], and that, if a single sensor element can operate at all required frequencies, the number of elements can be reduced. Figure 1 illustrates the grating-lobe elimination mechanism based on multi-frequency measurement. In the simplest design, multi-frequency measurement using a base frequency and half of that frequency reduces the required number of elements in a two-dimensional array to one quarter of that in the conventional arrangement. However, realizing such measurement requires sensors capable of stable multi-frequency operation.

Figure 2 shows the structure of the frequency-tunable piezoelectric MEMS ultrasonic sensor used in this study. The sensor has a circular diaphragm composed of a piezoelectric PZT capacitor and a silicon dioxide (SiO_2) film with strong compressive stress. This stress buckles the diaphragm into an upward-convex shape, which enhances the sensitivity [3]. The top electrode is divided into an inner electrode for ultrasonic sensing and an outer electrode for frequency tuning. By applying a voltage to the outer electrode, the resonance frequency can be tuned through piezoelectrically induced in-plane stress.

In a flat diaphragm, such stress mainly shifts the resonance frequency of the same vibration mode. In contrast, in a buckled diaphragm, the applied stress also changes the static buckling profile, which can in turn affect the vibration mode. Therefore, to realize stable multi-frequency operation in the present sensor, resonance control

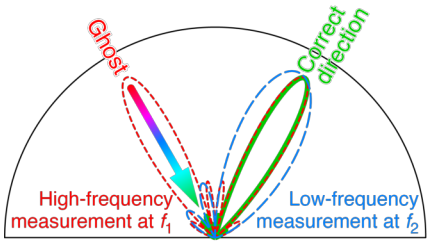

Fig. 1. Grating-lobe suppression in a sparse array by multi-frequency measurement. The grating lobe appearing in the high-frequency measurement at f_1 is suppressed by combining the f_1 and f_2 results so that a null of the f_2 response overlaps the f_1 grating lobe.

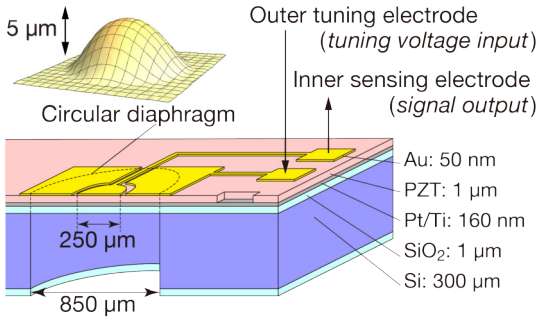

Fig. 2. Schematic illustration of the frequency-tunable MEMS ultrasonic sensor with a circular diaphragm. The diaphragm has an upward-convex buckling shape with buckling deflection up to 1.5% of the diameter.

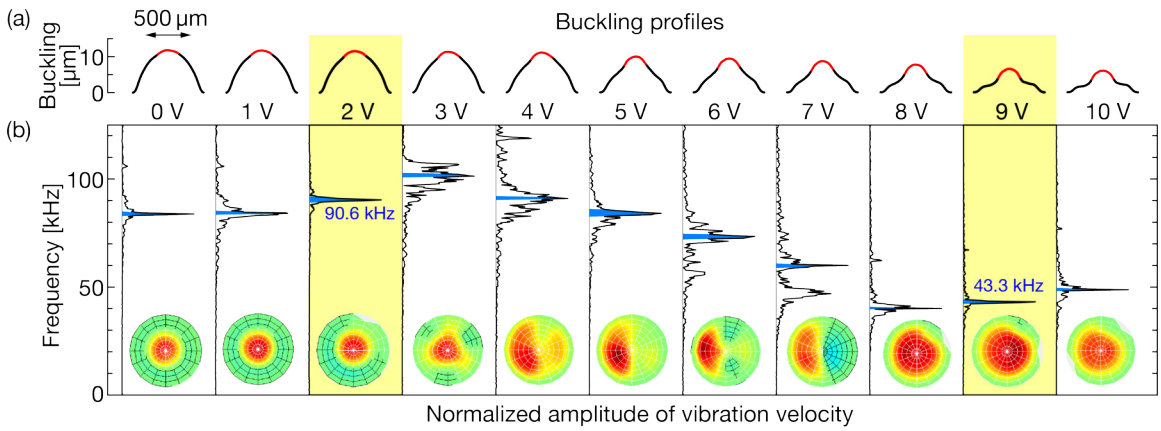

Fig. 3. Results of resonance control over the tuning-voltage range of 0 V to 10 V. (a) Buckling profiles of the diaphragm, showing that the diaphragm maintains the sensitivity-enhancing shape in the sensing electrode region (red part). (b) Vibration spectra and vibration modes corresponding to the dominant peaks indicated in blue in the respective spectra. Resonance frequencies of 90.6 kHz and 43.3 kHz were obtained at 2 V and 9 V, respectively, providing a frequency ratio greater than two, while maintaining single dominant peaks and axisymmetric modes.

must simultaneously provide suitable resonance frequencies, maintain the sensitivity-enhancing buckled shape in the sensing region, and preserve axisymmetric vibration modes within the sensing electrode region to avoid cancellation of piezoelectric output. The objective of this work is to identify tuning-voltage conditions that satisfy these three requirements.

Experiments

A diaphragm sensor with an initial buckling deflection of 12 µm was used in this study. The buckling deflection was controlled through the PZT stress during fabrication [4]. A dc tuning voltage in the range of 0 V to 10 V was applied to the outer electrode to generate piezoelectrically induced stress for resonance control. The static buckling profile of the diaphragm was measured using an optical profiler. Pulse ultrasound generated by electrical discharge was then applied to the sensor. The resulting vibration modes and resonance frequencies were evaluated using a two-channel scanning laser Doppler vibrometer [5].

Results and Discussion

Figure 3 summarizes the experimental results. As shown in Fig. 3(a), the sensing region under the inner electrode (red part) maintained the sensitivity-enhancing buckled shape over the entire voltage range. In contrast, the outer region of the diaphragm gradually deformed toward a flatter shape with increasing tuning voltage due to the piezoelectrically induced stress under the outer electrode. A marked change in the overall buckling profile started at 4 V, corresponding to the ferroelectric coercive field of the PZT film.

Figure 3(b) shows the vibration spectra of the diaphragm in response to an ultrasound pulse. The main resonance peak shifted to higher frequencies with increasing tuning voltage in the ranges of 0 V to 2 V and 8 V to 10 V because of the in-plane tension generated by the piezoelectric stress. In contrast, the peak shifted to lower frequencies in the range of 3 V to 7 V owing to the decrease in the total buckling deflection. In this intermediate range, the dominant mode was non-axisymmetric, with many sub-peaks appearing around it.

Tuning voltages of 2 V and 9 V provided resonance frequencies of 90.6 kHz and 43.3 kHz, respectively, covering the 2:1 frequency ratio required for multi-frequency measurement. At these voltages, the vibration modes were axisymmetric within the sensing electrode region. Together with the maintained buckled shape in the sensing region, these results indicate that the voltages of 2 V and 9 V satisfy the three requirements for resonance control in the present sensor: appropriate frequency selection, preservation of the sensitivity-enhancing buckled shape, and suitable vibration modes for piezoelectric output. Thus, practical operating conditions were identified for multi-frequency measurement using the buckled-diaphragm frequency-tunable sensor.

References

[1] C.-S. Wooh, et al., Review of Progress in Quantitative Nondestructive Evaluation, vol. 17, Plenum Press, New York, pp. 883–890, 1998.

[2] K. Yamashita, et al., Proc. WAC, Kobe, Japan, Sep. 19–23, 2010, IFMIP163.

[3] K. Yamashita, et al., IEEJ Trans. Sensors and Micromachines, vol. 131, pp. 235–239, 2011.

[4] K. Yamashita, et al., Proc. IEEE ISAF, Lausanne, Switzerland, July 14–19, 2019, TuPOii107.

[5] K. Yamashita, et al., Proc. IEEE NEMS, Matsushima, Japan, Apr. 17–20, 2016, B2L-A-2.

DOI 10.5162/eurosensors2026/Mo–PHS–11

Calculation of Far Field Acoustic Radiation from Transmission Line Models of PMUT–Horn Systems

Philipp Möhrle[1], Gabriele Schrag[1]
[1] [1]Technical University of Munich, MSA, Munich, Germany
philipp.moehrle@tum.de

Abstract:
In this paper, we present an extension of an acoustic transmission-line model for PMUT–horn systems that enables the prediction of acoustic pressure using a Rayleigh far-field formulation. The approach is validated against finite element method (FEM) simulations, showing consistent prediction of radiation directivity at 200 kHz. The model provides a computationally efficient alternative to FEM simulations for the design of horn-assisted PMUT systems.

Keywords: Piezoelectric-micromachined-ultrasound-transducer PMUT, acoustic horn, acoustic transmission line, rayleigh-integral, system-level modeling

Introduction and Motivation

Piezoelectric micromachined ultrasonic transducers (PMUTs) are used in airborne ultrasound applications, e.g. for the detection of persons in a room [1]. For such applications, it is necessary to improve the acoustic output and directivity. This can be achieved by coupling PMUTs to acoustic horns, which enhance impedance matching between the vibrating membrane and the surrounding air. Optimizing such systems requires efficient, yet physical models, since simulation by Finite Elements is tedious and computationally very expensive. To tackle this, previous work has demonstrated that the acoustic behavior of PMUT-horn systems can be modeled using a Butterworth-Van Dyke (BVD)- based PMUT model, combined with a transmission-line model of the horn [2]. This approach has been extended with a far-field approximation to estimate the radiated acoustic pressure along the acoustic axis [3]. However, a quantitative evaluation of the angular distribution of the radiated sound pressure and a validation against FEM simulations have not yet been implemented.

In this work, we provide a quantitative assessment of the acoustic radiation from a transmission-line-based acoustic-horn model coupled to a far-field approximation. The radiated sound field is evaluated both on and off the acoustic axis by comparison with a Rayleigh integral formulation and FEM simulations.

Modeling Approach

To compute the acoustic field, a simplified Kirchhoff integral based on the Helmholtz equation, commonly referred to as the Rayleigh integral, is employed.[4, 5]

$$\boldsymbol{p(x,y,z)} = \frac{j\,\rho_0\omega}{2\pi} \cdot \int_S v_{\mathrm{n}} \frac{e^{-\frac{j\omega A}{c}}}{A}\, dS \qquad (1)$$

$$\boldsymbol{A} = \sqrt{(x - x_S)^2 + (y - y_s)^2 + z^2} \qquad (2)$$

Eg. (1) calculates the acoustic pressure at the observation point (x, y, z); (x_s, y_s, z_s) represents a point on the acoustic source. Here v_n, is the normal particle velocity in the z-direction, ρ_0 the air density, c the speed of sound and A the observation distance.

Under far-field conditions (see [4, 5], i.e. for an observation distance A much larger than both, the acoustic wavelength λ and the PMUT diameter d_{PMUT} , the Rayleigh integral can be approximated by the analytical far-field expression [4, 5]:

$$p_{far}(x,y,z) = j\rho_0 c k v_{throat} R_{troa}^2 \left(\frac{J_1(kR\,sin\theta)}{kasin\theta}\right)\frac{e^{(-jkA)}}{A} \qquad (3)$$

J_1 is the first-order Bessel function v_{throat} is the normal velocity at the horn aperture and R_{troa} is the opening radius of the horn. Angle θ is defined as the angle between the acoustic axis (Fig. 1 (a), z-axis) and the direction towards the observation point.
Model validation is performed using finite element simulation of the system in COMSOL® Multiphysics. A uniform pressure of 100 Pa is applied for the simplified horn geometry, shown in Fig.(1) at excitation frequencies of 1 kHz and 200 kHz. The resulting pressure field is evaluated at a distance of 15 cm. At 1 kHz, the wavelength is comparable to the observation distance, which may lead to deviations due to near-field effects, whereas at higher frequencies, the far-field assumptions are better fulfilled. The input for the far-field model is obtained from the transmission-line model, while the full Rayleigh model is excited using pressure data extracted from FEM simulations.

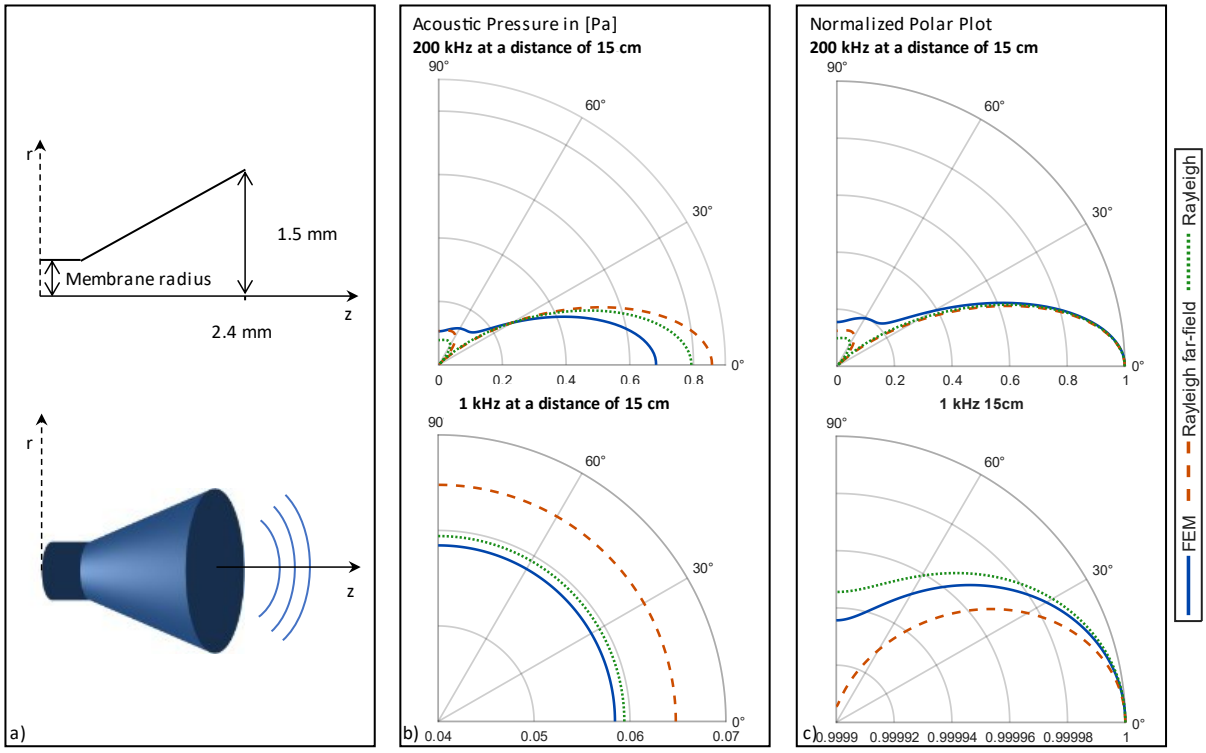

Fig.1 (a) Geometry and profile of the acoustic horn coupled to the PMUT. (b) Polar plots of the acoustic pressure calculated using FEM (blue), the Rayleigh integral (green), and the Rayleigh far-field approximation (orange) at excitation frequencies of 1 kHz and 200 kHz. (c) Corresponding normalized polar plots illustrating the radiation directivity for the different modeling approaches. The deviation at 1 kHz highlights the model's limitations, as described in the text.

Results

The comparison of the different simulation approaches demonstrates that, for acoustic pressure prediction, the transmission line model can be effectively combined with a Rayleigh far-field formulation to calculate the radiation directivity. However, the absolute acoustic pressure is overestimated by the far-field model. For an excitation frequency of 200 kHz, the Rayleigh far-field model predicts the maximum sound pressure with a worst-case deviation of approximately 25% compared to FEM simulations, while showing good agreement in radiation directivity (see Tab.1).

The discrepancies with respect to FEM results are primarily caused by modeling assumptions. In particular, radial velocity components at the horn aperture are neglected, since they are not captured by the transmission-line model. The Rayleigh integral shows improved agreement compared to the far-field approach, as it directly uses the pressure distribution obtained from FEM simulations.

Current work focuses on investigating different horn geometries and carrying out experimental measurements to characterize the samples. Further, we will extend the model to explicitly include PMUT membrane dynamics and investigate the influence of radial air-velocity components.

Tab. 1: Comparison of the different simulation methods at 200 kHz excitation frequency

Simulation-method	Directivity $D = \frac{p_{max}}{p_{avg}}$	Difference to FEM of max. pressure in percent
FEM	2.66	-
Rayleigh	3.15	16.22
Rayleigh Far-Field	3.09	25.72

References

[1] G.-L. Luo, Y. Kusano, and D. A. Horsley, Airborne Piezoelectric Micromachined Ultrasonic Transducers for Long-Range Detection, *J. Microelectromech. Syst.* **30**, S. 81–89 (2021); doi: 10.1109/JMEMS.2020.3037298

[2] G. Bosetti, S. Hofstetter-Spona, and G. Schrag, On the Use of 3D-printed Ultrasonic Horns to Tune the Frequency Response of Airborne MEMS Transducers, *2023 22nd International Conference on Solid-State Sensors, Actuators and Microsystems (Transducers)*, S. 873–876 (2023)

[3] G. Bosetti, S. Hofstetter-Spona, and G. Schrag, Analysis of the Coupling Mechanism between Airborne MEMS Ultra-sonic Transducers and Ultrasonic Horns, *MikroSystemTechnik Kongress 2023; Kongress*, S. 303–306 (2023)

[4] R. S. Lerch, and R. Lerch, Technische Akustik: Grundlagen und Anwendungen, 971 S. (2009); doi: 10.1007/978-3-540-49833-9

[5] M. Möser, Technische Akustik, 544 S. (2012); doi: 0.1007/978-3-642-30933-5

DOI 10.5162/eurosensors2026/Tu–PHS–01

LVIT position sensor with improved linearity

Mehran Mirzaei, Jiri Maier, Pavel Ripka
Faculty of Electrical Engineering, Czech Technical University, Prague 16627, Czech Republic,
mirzameh@fel.cvut.cz

Summary:
This paper presents a design optimization of a linear variable inductive transducer position sensor to extend the linearity range and decrease the nonlinearity error. The linear variable inductive position sensor has only two coils, serially connected, and the voltages across both coils are measured. The voltage difference is a function of the armature position, which is used for the position estimation. The position sensor has a cylindrical structure with toroidal coils. The optimized linear variable inductive sensor features segmented coils to control wire distribution in the axial direction, or along the armature's movement. The measurement of prototype position is conducted to validate the analysis and design. A measured nonlinearity error of approximately 1.0% can be achieved for a ±30 mm movement range.

Keywords: LVIT, nonlinearity error, measurement, modeling, position sensor

Introduction

The linear variable differential transformer (LVDT) position sensor is the most common type of transducer used for measuring linear positions. LVDT position sensors offer primary advantages, including cost-effectiveness, low maintenance, a long lifespan, high sensitivity, high resolution, and excellent mechanical durability [1]-[3]. They have three coils: one excitation coil and two pickup coils. In linear variable inductive transducer (LVIT) position sensors, there are only two coils in series. Achieving the maximum nonlinearity range and minimum nonlinearity error is critical for the efficient and accurate operation of position sensors. They are challenging when a limited axial length constraint is demanded. Design optimization is performed to extend the linearity range with low nonlinearity error. The 2D axisymmetric finite element method is used for analysis and optimization of LVIT position sensors. The shape and number of turns are optimized to minimize nonlinearity errors to extend the linearity range. Two cylindrical LVIT sensors with different armature dimensions are considered for the design, prototyping, and measurement.

Design

Fig. 1 presents the models of LVIT position sensors with two coil structures connected in series, with their generated magnetic fields aligned. It shows a cylindrical ferrite armature moving within the coils. The first structure uses two identical cylindrical coils. The second structure uses conical-shaped coils [2]-[3]. The 2D FEM calculated normalized inductive voltages difference, U_d=U_1-U_2, versus armature position is presented in Fig. 2. The LVIT sensor with conical-shaped coils exhibits a considerably higher linearity range, corresponding to the voltage difference, U_d, versus armature position. It is shown to be within ±30 mm, compared to ±15 mm for the LVIT sensor with cylindrical coils. Segmented coils are used in the optimized LVIT model with 14 slots, as illustrated in Fig. 3, enabling more precise control over the number of turns per coil segment.

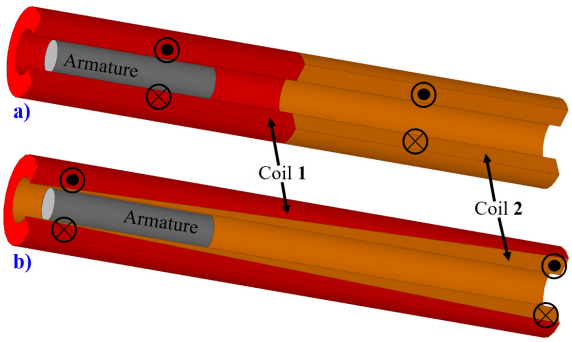

Fig. 1. 3D model of the LVIT position sensor, a) cylindrical shape coils, b) conical shape coils - total axial length of the coils is 100 mm

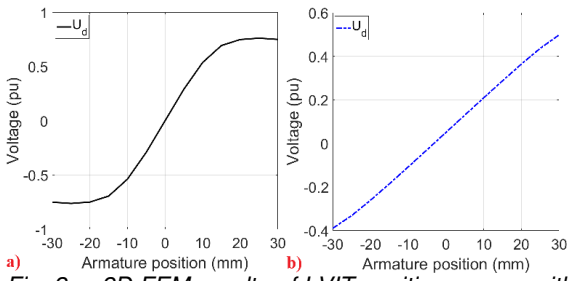

Fig. 2. 2D FEM results of LVIT position sensor with Ferrite armature length of 30 mm- normalized inductive voltage difference versus armature position, a) cylindrical shape coils, b) conical shape coils

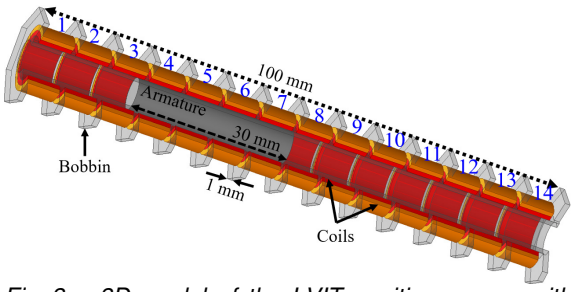

Fig. 3. 3D model of the LVIT position sensor with segmented coils

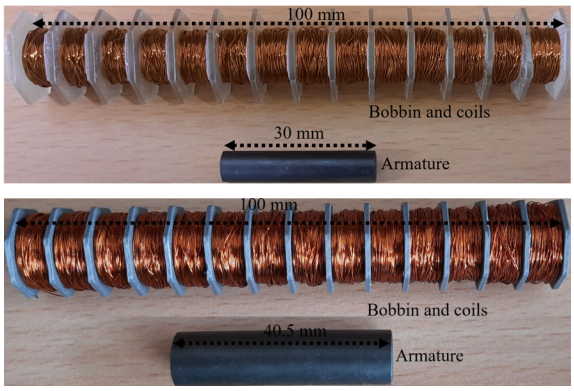

Fig. 4. Experimental LVIT, the coils and the Ferrite armature, a) position sensor 1 with a smaller armature b) position sensor 2 with a larger armature

Experiment

Fig. 4 shows the two prototypes of LVIT position sensors. Sensor 1 has a smaller Ferrite armature measuring 30 mm long and 6 mm in diameter. Sensor 2 has a larger Ferrite armature with a 10 mm diameter and a 40.5 mm length. The voltage ratio, $r = (U1-U_2)/(U_1+U_2)$ versus armature position is shown in Fig. 5 for sensor 1, which shows a lower nonlinearity error of about 0.5% for FEM results and less than 1.0% for experimental results. Fig. 6 presents the voltage-ratio results and the corresponding nonlinearity error for sensor 2. The linearity range with nonlinearity error less than 1.0% is ±30 mm for sensor 1 and ±25 mm for sensor 2. The higher nonlinearity error in sensor 2 compared to sensor 1 for movement ranges above ±25 mm is due to its longer axial length and higher armature diameter, which amplify the effect of the sensor's finite length.

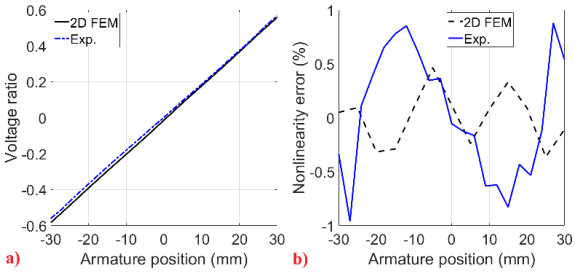

Fig. 5. Experiments vs 2D FEM results of LVIT position sensor 1 with a smaller armature and segmented coils, a) inductive voltage ratio versus armature position, b) nonlinearity error versus armature position

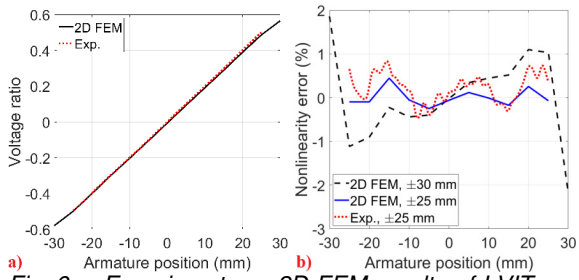

Fig. 6. Experiments vs 2D FEM results of LVIT position sensor 2 with a larger armature and segmented coils, a) inductive voltage ratio versus armature position, b) nonlinearity error versus armature position

The larger armature causes the finite length of the LVIT position sensors to affect the flux uniformity in the inner tube of the coils, reducing it in the larger-armature position. The magnetic flux reduction in the larger armature position decreases sensor voltages at larger positions, thereby increasing the nonlinearity error. The linearity range to total coils axial range ratio is 0.6 (2·30 mm / 100 mm) for sensor 1 and 0.5 (2·25 mm / 100 mm) for sensor 2, corresponding to a nonlinearity error below 1%.

Using the voltage ratio, *r*, also helps compensate for variations in frequency, current, and temperature, and it is well-suited for extending the linearity range. This compensation is essential for the accurate and efficient operation of LVIT position sensors.

Conclusion

The linearity extension of LVIT position sensors was developed and presented. The number and distribution of turns in the coils are optimized using a 2D FEM analysis to extend the linearity range and reduce the nonlinearity error in LVIT position sensors. The nonlinearity error can be reduced to below 1.0% for a ±30 mm armature movement range using the voltage ratio. The segmented coils were used to simplify the winding and improve the accuracy of wire distribution in the two-winding coils. The LVIT position sensor has a simpler structure than the standard LVDT position sensors, which have a separate excitation coil.

References

[1] G.Y. Tian, Z.X. Zhao, R.W. Baines, Computational Algorithms for Linear Variable Differential Transformers (LVDTs), *Proc. Inst. Elect. Eng.* 144, 189–193 (1997), doi: 10.1049/ip-smt:19971262

[2] M. Mirzaei, J. Maier, and P. Ripka, Linearity Range Enhancement of LVDT Position Sensors using Optimized Coils, *IEEE Sensors J.* 25, 24441 - 24450 (2025); doi: 10.1109/JSEN.2025.3568547

[3] A. Ali, G. Y. Tian, D. Wang, A. Asif, X. Lu, C. Peng, and H. Xu, Design and Development of High Linearity of Trapezoidal Winding LVDT, *IEEE Trans. Instrumentation & Measurement* 74, 9539014 (2025); doi: 10.1109/TIM.2025.3617803

DOI 10.5162/eurosensors2026/Tu–PHS–02

Frequency Mixing Magnetic Detection for Viscosity Sensitive Biosensing Using Magnetic Nanoparticle Relaxation

Ali Mohammad Pourshahidi[1], Timur Bikulov[1], Amirreza Gholivand[2], Abdalhalim Abuawad[1], Ulrich M. Engelmann[3] and Hans-Joachim Krause[1,3]
[1] Institute of Biological Information Processing, Bioelectronics (IBI-3), Forschungszentrum Jülich, 52425 Jülich, Germany,
[2] Institute of Epileptology and Cognition Research, Sensory Dynamics and Behavior Lab, University of Bonn, Faculty of Medicine, 53127 Bonn,
[3] Medical Engineering and Applied Mathematics, FH Aachen University of Applied Sciences, 52428 Jülich, Germany
a.pourshahidi@fz-jeulich.de

Summary:

Frequency Mixing Magnetic Detection (FMMD) enables magnetic biosensing by probing the nonlinear dynamic response of magnetic nanoparticles (MNPs) under dual-frequency (f_1, f_2) excitation. Known Brownian-relaxation dominated MNPs BNF-Dextran 80 nm were studied in media with varying viscosities. The complex signal components at the mixing harmonics $f_1 + 2 \cdot f_2$ and $f_1 + 4 \cdot f_2$ were analyzed as a function of the low frequency excitation field, and the harmonic ratio $R = A_{(f_1+2f_2)}/A_{(f_1+4f_2)}$ was evaluated as a sensitive metric. The measured ratios show a pronounced dependency on viscosity and field amplitude. The complex-plane trajectories additionally reveal viscosity-dependent changes in both amplitude and phase. These findings show that harmonic-ratio analysis in FMMD can provide environment-sensitive readout beyond conventional single-harmonic amplitude detection. The approach is therefore promising for viscosity-sensitive biosensing, where target binding or matrix changes modify the local hydrodynamic environment of the MNPs.

Keywords: Magnetic Nanoparticles, Magnetic Biosensor, Viscosity sensing, Frequency mixing magnetic detection

Introduction

Frequency Mixing Magnetic Detection (FMMD) is a sensitive magnetic readout technique based on the nonlinear response of magnetic nanoparticles (MNPs) under dual-frequency excitation [1]. While FMMD is commonly used for MNP characterization [2] and concentration-dependent detection in biosensing applications [3], its mixing harmonics also encode information on nanoparticle relaxation processes [4]. Since these magnetic relaxation processes depend on the local hydrodynamic environment, FMMD can provide viscosity-sensitive biosensing, particularly for particles with larger hydrodynamic size.

This aspect is highly relevant for bioassays in which target recognition does not only change the quantity of magnetic markers, but also affects their mobility, aggregation state, and rotational freedom. Such changes are expressed in Brownian relaxation and can therefore modify the amplitude, phase, and relative spectral content of the FMMD signal. Relaxation-sensitive analysis may thus provide an additional biosensing dimension beyond pure particle quantification. Here, we investigate the viscosity dependence of FMMD relaxation signatures using commercially available MNPs across a physiologically relevant viscosity range. The complex amplitudes of selected mixing harmonics were analyzed under varying driving field conditions.

Method description

In this study, BNF-Dextran 80 nm (1.5 mg/mL) magnetic nanoparticles (from Micromod GmbH Rostock Germany) were investigated in glycerol water mixture media covering a viscosity range from 0.8 to 612 mPa·s. The particles were excited by two sinusoidal magnetic fields of a form

$$B(t) = B_1 \sin(2\pi f_1 t) + B_2 \sin(2\pi f_2 t). \quad \text{(Eq.1)}$$

The excitation settings are presented in Tab.1.

The complex FMMD response was evaluated at the mixing harmonics $f_1 + 2 \cdot f_2$ and $f_1 + 4 \cdot f_2$. Furthermore, the harmonic ratio $R = A_{(f_1+2f_2)}/A_{(f_1+4f_2)}$ defined here as the amplitude of

$(f_1 + 2 \cdot f_2)/(f_1 + 4 \cdot f_2)$, was obtained as a viscosity sensitive metric.

Tab. 1: Measurement excitation settings

Excitation field	Frequency [Hz]	Magnetic field [mT]
Low frequency magnetic field B_2	62.95	Varied from 1.0 to 18.7
High frequency magnetic field B_1	40500	1.2

Results

The complex FMMD trajectories show smooth, non-monotonous and reproducible viscosity-dependent evolution in both magnitude and phase (Fig. 1). The $A_{(f_1+2f_2)}$ component remains dominant, while the $A_{(f_1+4f_2)}$ component shows lower amplitude response as expected.

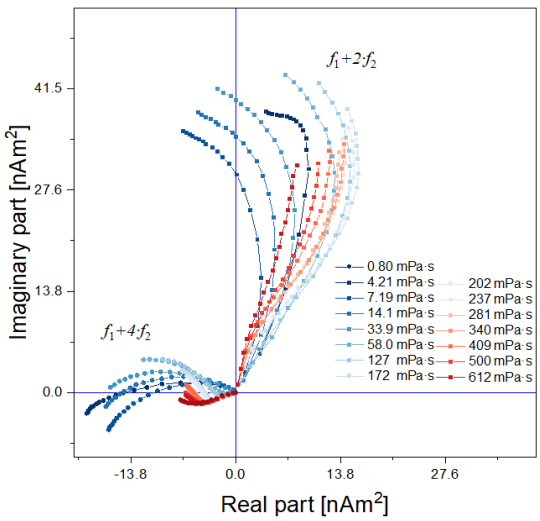

Fig. 1. Complex representation of measurement signals f_1+2·f_2 and f_1+4·f_2 under varying B_2 magnetic field. Colors represent media viscosity.

The ratio R shown in Fig. 2 depends on both viscosity and excitation field. It can be seen that for the lower viscosity regime, it decreases with increasing B_2 and the ratio approaches 2 at the highest fields. At intermediate viscosities, the ratio is larger, while at higher viscosities the ratio slightly increases, compared to the lower viscosity levels after the initial drop. Over the measured field range, the ratio shows the most separation between viscosities in the intermediate to high B_2 region, approximately above 10 mT. At lower fields, the spread is larger and less stable, while at higher fields, the curves move closer together.

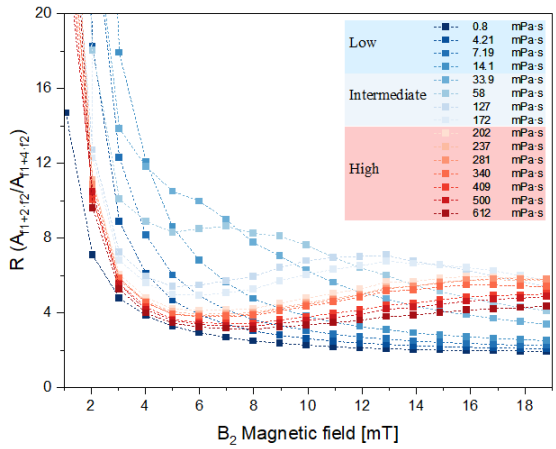

Fig.2. The obtained ratio R for varying viscosities as a function B_2 magnetic field.

Conclusion

The results demonstrate that harmonic-ratio analysis in FMMD can serve as viscosity-sensitive signature beyond single-harmonic amplitude readout. In particular, the ratio R captures changes in the dynamic state of Brownian relaxation-dominated particles, in this case BNF-Dextran 80 nm, over a wide viscosity range, and therefore represents a metric feature for biosensing tasks involving binding, gelation, aggregation, or microenvironmental changes. The presented approach supports the development of FMMD toward relaxation-based and environment-sensitive magnetic biosensing.

References

1. Krause, H.-J.; Engelmann, U.M. Fundamentals and Applications of Dual-Frequency Magnetic Particle Spectroscopy: Review for Biomedicine and Materials Characterization. *Adv. Sci.* **2025**, *12*, 2416838, doi:10.1002/advs.202416838.
2. Pourshahidi, A.M.; Jean, N.; Kaulen, C.; Jakobi, S.; Krause, H.-J. Impact of Particle Size on the Nonlinear Magnetic Response of Iron Oxide Nanoparticles during Frequency Mixing Magnetic Detection. *Sensors* **2024**, *24*, 4223, doi:10.3390/s24134223.
3. Achtsnicht, S.; Neuendorf, C.; Faßbender, T.; Nölke, G.; Offenhäusser, A.; Krause, H.-J.; Schröper, F. Sensitive and Rapid Detection of Cholera Toxin Subunit B Using Magnetic Frequency Mixing Detection. *PLOS ONE* **2019**, *14*, e0219356, doi:10.1371/journal.pone.0219356.
4. Bikulov, T.; Eivazi, F.; Offenhäusser, A.; Krause, H.-J. Multicontrasting MPS by Dual-Tone Nonlinearity Probing. *Int. J. Magn. Part. Imaging IJMPI* **2024**, *10*, doi:10.18416/IJMPI.2024.2403014.

Acknowledgements

Funded by the Deutsche Forschungsgemeinschaft (DFG, German Research Foundation) – Project number 574089568.

The authors thank Oumaima Chig and Ibrahem Nasr Allah for conducting parts of the measurements.

DOI 10.5162/eurosensors2026/Tu–PHS–03

A Drift-Resistant Amine-based Chemiresistive Printed Sensor for Carbon Dioxide Monitoring

Pavlos Tzourmpakis[1], Mohammad Vaseem[2], Igor Getmanov[2], Adarsh Sivan Pillai[3], Atif Shamim[2]
[1]Materials Science and Engineering Program, King Abdullah University of Science and Technology (KAUST), Thuwal, 23955-6900, Saudi Arabia
[2]Electrical and Computer Engineering Program, KAUST, Thuwal, 23955-6900, Saudi Arabia
[3]SMART Lab, School of Computing, Engineering & the Built Environment
Edinburgh Napier University, Edinburgh EH10 5DT, Scotland, UK
pavlos.tzourmpakis@kaust.edu.sa

Summary:

Flexible CO_2 sensors based on carbon nanotubes (CNTs) modified with a Polyethyleneimine (PEI)-1,5-Diaminonaphthalene (DAN) composite are presented. DAN is introduced for the first time in CO_2 sensing, stabilizing the amine environment and reducing baseline drift. The device shows a 6.04% response at 2500 ppm (50% RH) with a sensitivity of 1.68×10^{-3} ppm^{-1}. Screen-printed CNT sensors, functionalized with the same layer, achieve a 27.36% response at 2000 ppm and a sensitivity of 0.92×10^{-2} ppm^{-1}, demonstrating scalable, drift-resistant CO_2 sensing.

Keywords: CO_2 Sensor, Drift, Carbon nanotubes, DAN, Screen printing

Introduction

Accurate CO_2 sensing under varying environmental conditions remains challenging for low-power gas sensors. Signal drift, humidity sensitivity, and limited stability often hinder practical deployment. Although sensitivity is widely reported, drift remains a critical yet insufficiently addressed issue.

Nanomaterials such as CNTs offer advantages over traditional metal oxide sensors due to their large surface area, high conductivity, and and room-temperature operation [1]. Functionalization with PEI enhances CO_2 sensitivity, but PEI–CNT systems often suffer from signal drift. In this work, DAN, an NH_2-rich aromatic molecule, is introduced. π–π interactions between DAN and CNTs enhance interfacial coupling and charge transfer, effectively reducing drift during response–recovery cycles.

Materials, Fabrication and Functionalization

Sensors were fabricated on Kapton flexible substrates with screen-printed silver interdigitated electrodes and drop-casted CNT sensing layers functionalized with a PEI–DAN composite [2]. In addition, CNT deposition was investigated via screen-printing of a single-walled CNT (SWCNT) ink. CNTs (42 mg in 5 mL ethanol) were sonicated with sodium dodecylsulfate (SDS, 5 mg) as dispersant and mixed with ethyl cellulose and an ethanol-terpineol solvent system [3]. After ethanol evaporation, the semi-dried CNT material was diluted 40× in ethyl cellulose/terpineol binder, screen-printed, and cured at 100 °C for 120 min (Fig. 1).

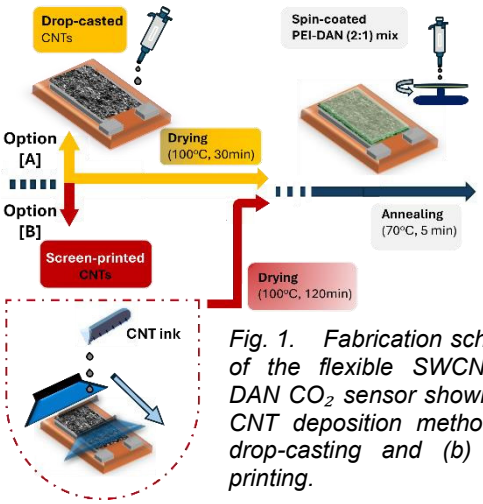

Fig. 1. Fabrication schematic of the flexible SWCNT/PEI–DAN CO_2 sensor showing two CNT deposition methods: (a) drop-casting and (b) scree-printing.

Mechanism, Characterization and Results

The fabricated sensors were evaluated by tesing under varying CO_2 concentrations ranging from 500 to 2500ppm (RT, RH 50%) and the response was calculated using Equation 1:

$$\Delta R(\%) = \frac{R_f - R_0}{R_0} x100\% \quad (1)$$

where R_f denotes sensor resistance in the pre-

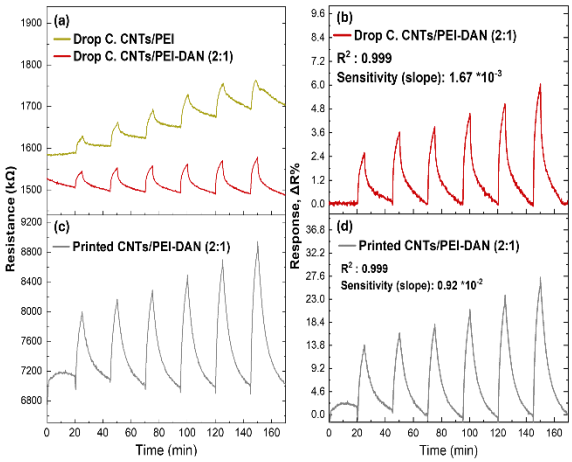

Fig. 2. (a, c) Baseline drift comparison of drop-casted CNT/PEI, CNT/PEI–DAN, and screen-printed CNT/PEI–DAN sensors under six different CO_2 concentrations; (b, d) corresponding response changes of the CNT-based PEI–DAN sensors.

sence and R_0 in the absence of target gas, respectively.

The sensing mechanism of amine-based chemiresistive CO_2 sensors arises from interactions between CO_2 (Lewis acid) and amine groups (Lewis bases) in the PEI–DAN layer [1]. CO_2 diffusion into the polymer leads to amine protonation and formation of bicarbonate species under humid conditions (Eq. 2), decreasing SWCNT conductivity (sensing signal). The reversible reaction enables room-temperature operation and recovery upon CO_2 desorption:

$$RNH_2 + CO_2 + \mathrm{H_2O} \leftrightharpoons RNH_3^+ + \mathrm{HCO_3^-} \qquad (2)$$

As shown in Fig. 2a,c, baseline drift is significantly reduced after DAN addition. In contrast, the CNT/PEI sensor exhibits drift due to partial poisoning and humidity-induced swelling of PEI during adsorption-desorption cycles. The improvement is attributed to π–π interactions between DAN and CNTs, which stabilize the sensing layer, reduce moisture sensitivity [2], and limit bicarbonate trapping, leading to near-complete recovery after CO_2 removal.

Consequently, the sensor shows a 6.04% response at 2500 ppm (50% RH) with a sensitivity of 1.68×10^{-3} ppm^{-1}. Screen-printed CNT sensors yield a higher response of 27.36% at 2000 ppm and a sensitivity of 0.92×10^{-2} ppm^{-1} (Fig. 2b,d). This enhancement is attributed to a more uniform and interconnected CNT network, enabling more homogeneous functionalization, more efficient CO_2 diffusion, and improved charge transport.

SEM images (Fig. 3) reveal clear morphological differences between drop-cast and screen-printed CNT networks, with the latter forming a denser and more interconnected structure. In both cases, PEI deposition leads to inhomogeneous coverage/pore formation. The addition of DAN results in a more uniform and smoother morphology. This improved organization facilitates more efficient CO_2 adsorption–desorption cycles by limiting trapping and PEI chain swelling, leading to enhanced reversibility and minimal drift.

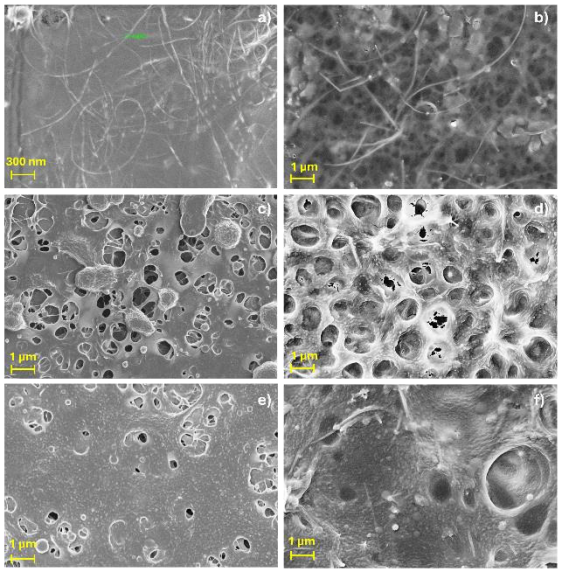

Fig. 3. SEM images of SWCNT-based sensing layers. (a,c,e) Drop-cast CNT networks: (a) pristine CNTs, (c) CNTs functionalized with PEI, and (e) CNTs functionalized with PEI–DAN. (b,d,f) Screen-printed CNT networks: (d) pristine CNTs, (d) CNTs. functionalized with PEI, and (f) CNTs functionalized with PEI–DAN.

Conclusion

CNT-based CO_2 sensing is often limited by drift and humidity effects, which also impact highly sensitive PEI-based sensors. Introducing DAN stabilizes the sensing layer through interactions with CNTs, reducing CO_2 trapping and improving reversibility. In addition, screen-printed sensors form a more uniform and interconnected network, leading to enhanced overall performance.

References

[1] J. Hack, N. Maeda, D. M. Meier, Review on CO_2 Capture Using Amine-Functionalized Materials, ACS Omega 7, 39520–39530 (2022); doi: 10.1021/acsomega.2c03385

[2] P. Tzourmpakis, A. S. Pillai, S. Rauf, M. Vaseem, I. Getmanov, A. Shamim, Drift-Minimized, Highly Sensitive Carbon Nanotube and Amine-Based CO_2 Sensors with Humidity Compensation for Indoor/Outdoor and Breath Monitoring, ACS Sensors (2026); doi: 0.1021/acssensors.5c01565

[3] N. Zavanelli, W.-H. Yeo, Advances in Screen Printing of Conductive Nanomaterials for Stretchable Electronics, ACS Omega 6, 9344–9351 (2021); doi: 10.1021/acsomega.1c00638

DOI 10.5162/eurosensors2026/Tu–PHS–04

Detection of the Oscillation of a Magnetic Artificial Cilium using an Electromagnetic Pickup

Jonas Astl[1], Wolfgang Hilber[1], Sebastian Lang[1], Bernhard Jakoby[1]
[1] Institute for Microelectronics and Microsensors, Johannes Kepler University Linz, 4040 Linz, Austria
jonas.astl@jku.at

Summary:
Inspired by biological cilia used for nutrient transport, locomotion or sensing, researchers fabricated artificial counterparts that are supposed to perform equivalent tasks. Previous studies have primarily focused on the ability of an artificial cilium regarding fluid transport. In contrast, our study focuses on the sensing ability, and in a first step, the oscillation modes and the associated resonance properties were investigated. Magnetizable artificial cilia were devised and fabricated using poly(dimethylsiloxane) enriched with Iron(II,III) oxide nanoparticles. The resulting composite material simultaneously features elasticity and magnetic properties and thus, the movement of the cilium can be evaluated using an electromagnetic pickup. Experiments show a decreasing oscillation frequency with increasing distance between pickup and cilium which converges towards 5 Hz at large distances. By using digital image processing, the natural frequency of the cilium without interaction with a magnetic field was evaluated to be 5.29 Hz and matches the data obtained by simulation and calculation.

Keywords: Magnetic artificial cilia, PDMS mould technology, Composite material, Electromagnetic pickup, bioinspired

Introduction

Thin, hair-like structures (cilia), found in a variety of biological organisms, are used for nutrient transport, locomotion, or sensing [1]. Inspired by these structures, researchers fabricated artificial cilia that mimic the behaviour of the biological counterparts. In previous studies, active motion [2], [3] and sensing ability [4] of these bioinspired structures have been investigated in isolation, with focus on motile artificial cilia. Motile as well as passive cilia rely on the change in motion based on fluidic parameters or changes regarding the actuation [5]. The characterization of the motion of cilia is crucial for further processing regarding the aforementioned applications. Active cilia, which are typically actuated using an external magnetic field as well as electric forces, light or pneumatics [1], optical approaches like digital image processing [3] are used, while passive cilia can consist of an integrated structure resembling a resistive strain gauge [4]. For the fabrication of artificial cilia, lithography processes [2], [3], template-based processes [4] and template-free processes [6] are of greater interest.
This work focuses on the sensing ability of a magnetizable artificial cilium and, in a first step, the characterization of its movement and resonance properties. The artificial cilium is fabricated using a mould-based process and evaluated using an electromagnetic pickup device, similar to the pickup of an electric guitar.

Fabrication Process

In a mould-based process, the cilia are made out of poly(dimethylsiloxane) (PDMS – SYLGARD™ 184 Silicon Elastomer Kit) enriched with Iron(II,III) oxide (Fe_3O_4) nanoparticles (50 nm) from Sigma Aldrich in a mass concentration of 10:1. The combined use simultaneously enables elasticity and introduces magnetic properties. The nanoparticles and PDMS base are mixed for 5 min after which the curing agent is added followed by another 5 min mixing period. After degassing the mixture in vacuum, it is filled into an aluminium mould. An additional degassing step ensures air bubble free fabrication after curing at 100°C for 2 h and cooling down to room temperature.

Fig. 1 Cilium ($d = 1$ mm, $l = 35$ mm) fabricated in a mould-based approach.

Experimental Setup

The sensing setup combines the use of an electromagnetic pickup, consisting of a custom-wound coil with 1500 turns utilizing a neodymium (NdFeB) magnet as a core, and a camera to

track mechanical displacement via digital image processing. The cilium ($d = 1\,\mathrm{mm}$, $l = 35\,\mathrm{mm}$, see Fig. 1) is attached to an XYZ-stage (THORLABS components), which is primarily used to vary the distance between the tip of the cilium and the pickup's pole piece and adjust slight XY-mismatches. The electromagnetic pickup is used to measure the oscillation of the cilium based on electromagnetic induction inside the coil. The induced voltage is amplified by about 94 dB and monitored using an oscilloscope. To actuate the cilium, compressed air directed at its tip used, ensuring mechanical displacement followed by an oscillation until the cilium is back in the initial position. The resulting measurement setup is depicted in Fig. 2.

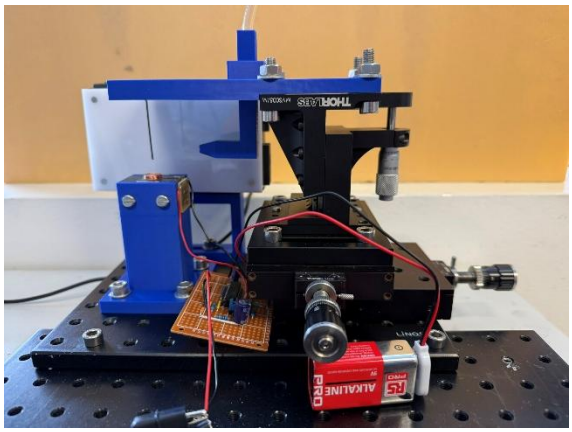

Fig. 2 Setup to measure the movement of the magnetic artificial cilium using a guitar pickup.

Results and Discussion

The oscillation of the artificial cilium for different distances between the tip of the cilium and the surface of the pickup's pole piece was measured where the determined oscillation frequencies are depicted in Fig. 3. With increasing distance between cilium tip and pickup, the resonance frequency decreases approaching 5 Hz. Observations show that the pickup affects the mode shapes of the oscillation. When considering the cilium as a Euler-Bernoulli beam, the cilium approximately operates in a clamped-clamped configuration for distances below $z = 4.5\,\mathrm{mm}$, where the attraction force of the pickup is high, while for larger distances, the cilium's configuration resembles that of a clamped-free beam. Besides the determination of the oscillation frequency from the pickup's signal, the natural frequency of the cilium without interaction with the pickup is obtained using digital image processing and is given by $f_r = 5.29 \pm 0.12\,\mathrm{Hz}$. This value approximately corresponds to the calculated first natural frequency of an Euler-Bernoulli beam in a clamped-free configuration [7].

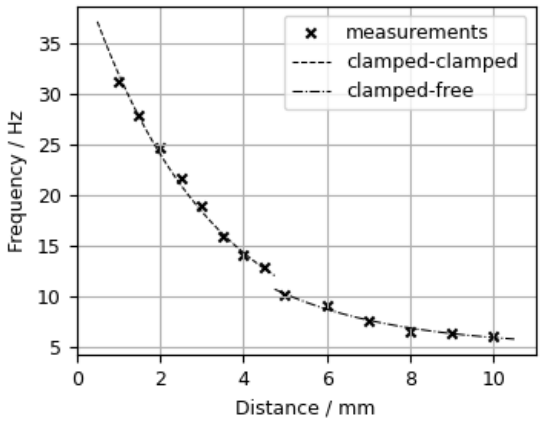

Fig. 3 Oscillation frequency of the cilium versus distance between the tip of the cilium and the pickup's pole piece.

Outlook

The work shows that the detection of the oscillation of a magnetic artificial cilium using an electromagnetic pickup is possible even for large distances of $z = 10\,\mathrm{mm}$, with the oscillation frequency being off resonance. In a next step, the size of the magnetic artificial cilium will be reduced and the concentration of the nanoparticles inside the PDMS material will be varied. Stimulation of the cilium by using a varying external magnetic field to evaluate its active sensing properties is planned.

References

[1] T. ul Islam *et al.*, 'Microscopic artificial cilia – a review', *Lab. Chip*, vol. 22, no. 9, pp. 1650–1679, 2022, doi: 10.1039/D1LC01168E.

[2] J. M. J. D. Toonder and P. R. Onck, 'Microfluidic manipulation with artificial/bioinspired cilia', *Trends Biotechnol.*, vol. 31, no. 2, pp. 85–91, Feb. 2013, doi: 10.1016/j.tibtech.2012.11.005.

[3] S. Hanasoge, M. Ballard, P. J. Hesketh, and A. Alexeev, 'Asymmetric motion of magnetically actuated artificial cilia', *Lab. Chip*, vol. 17, no. 18, pp. 3138–3145, 2017, doi: 10.1039/C7LC00556C.

[4] J. Han *et al.*, 'Actuation-enhanced multifunctional sensing and information recognition by magnetic artificial cilia arrays', *Proc. Natl. Acad. Sci.*, vol. 120, no. 42, p. e2308301120, Oct. 2023, doi: 10.1073/pnas.2308301120.

[5] C. Eloy, 'Kinematics of the Most Efficient Cilium', *Phys. Rev. Lett.*, vol. 109, no. 3, 2012, doi: 10.1103/PhysRevLett.109.038101.

[6] M. Asadnia *et al.*, 'From Biological Cilia to Artificial Flow Sensors: Biomimetic Soft Polymer Nanosensors with High Sensing Performance', *Sci. Rep.*, vol. 6, no. 1, p. 32955, Sep. 2016, doi: 10.1038/srep32955.

[7] W. R. Chen and H. Chang, 'Closed-Form Solutions for Free Vibration Frequencies of Functionally Graded Euler-Bernoulli Beams', *Mech. Compos. Mater.*, vol. 53, no. 1, pp. 79–98, Mar. 2017, doi: 10.1007/s11029-017-9642-3.

DOI 10.5162/eurosensors2026/Tu–PHS–05

Sensing of Microplastics in Water Using Gold Nanoparticle-Coated Multimode Optical Fiber

Vikas Kumar[1], Shrabya Shukla[1], Maria Asunción Illarramendi[2], Joel Villatoro[1,3],
[1]Department of Communication Engineering, UPV/EHU, E-48013 Bilbao, Spain
[2]Department of Applied Physics, UPV/EHU, E-48013 Bilbao, Spain
[3]IKERBASQUE—Basque Foundation for Science, E-48011 Bilbao, Spain
Corresponding Author's e-mail address vikas.kumark@ehu.eus

Summary:

The detection of microplastics in aquatic environments is significant due to their growing impact on ecosystems and human health. Gold nanoparticles were immobilized on the facet of a conventional multimode optical fiber to create a sensor based on localized surface plasmon resonance for detecting microplastics in water. In aqueous media, the interaction of the evanescent field with the nanoparticle layer produces a distinct plasmonic absorption response. Experimental observations show systematic spectral variation with increasing microplastic concentration. The observed trends are further supported by numerical simulations based on Maxwell–Garnett effective medium theory. The proposed platform demonstrates a promising approach for real-time, label-free environmental monitoring of microplastics.

Keywords: Gold nanoparticles deposition, Multimode fiber, Localized surface plasmon resonance, Maxwell-Garnett theory, Optical fiber Sensing, Microplastics sensing

Introduction, Motivation and Objective

Because of their persistence, bioaccumulation, and possible effects on ecosystems and human health, the pervasiveness of microplastics and nanoplastics in aquatic habitats has become a major worldwide concern [1]. These particles, which are now present in rivers, oceans, and even drinking water systems, are the result of the breakdown of larger plastic debris [1]. Reliable detection techniques are desperately needed because of their small size and intricate interactions with biological systems, which make them challenge to monitor and evaluate. As a result, one of the main goals of environmental research is the creation of sensitive and effective methods for detecting microplastics in water [1, 2].

For the examination of microplastics, conventional detection techniques like spectroscopy and microscopy are frequently employed, however they frequently have serious drawbacks [2]. These methods are not appropriate for real-time or in situ monitoring since they usually involve substantial sample preparation, expert operation, and heavy apparatus. Additionally, it is still difficult for them to identify low concentrations or tiny particles. Compact, label-free, and extremely sensitive sensing devices that can continuously monitor microplastics in aquatic environments are therefore in greater demand.

To overcome these obstacles, we have developed a multimode optical fiber sensor that uses gold nanoparticles immobilization and localized surface plasmon resonance (LSPR) to detect microplastics in water. The sensing technique is based on how microplastics alter the local refractive index, which in turn affects the nanoparticle layer's plasmonic response. The composite optical behavior is modeled using numerical simulations based on Maxwell-Garnett effective medium theory to corroborate the experimental data. Demonstrating a dependable, label-free sensing method with the potential for real-time environmental monitoring is the goal.

Methodology

A stable amine-terminated layer is produced by silanization utilizing 3-Aminopropyl)triethoxysilane (APTES) after the silica optical multimode fiber tip surface is initially activated by plasma treatment to produce hydroxyl groups [3]. Gold nanoparticles with a high optical density can be uniformly and robustly immobilized on the fiber surface thanks to this functionalization. Sensitive detection of refractive index fluctuations caused by microplastics is made possible by the resulting nanostructured interface, which improves the interaction between the guided light's field and the surrounding medium.

When exposed to fluids containing microplastics, the gold nanoparticle layer's LSPR response is modulated, which is how the sensing mechanism works. Measurable changes in the plasmonic absorption spectrum result from the presence and quantity of polystyrene (PS) microparticles in water, which alter the local dielectric environment. Through improved modal interaction and efficient light-matter coupling along the

sensing region, the adoption of a multimode fiber further improves the sensing performance. This method is appropriate for real-time and in situ monitoring since it enables label-free detection without requiring intricate surface chemistry targeting particular analytes.

A numerical model based on Maxwell-Garnett effective medium theory [4] is used to characterize the composite optical response of the gold–silica–microplastic system to validate and interpret the experimental data. The model predicts the spectrum behavior of the LSPR signal after considering the gradual addition of polystyrene to the effective medium. An important development that offers both a qualitative and mechanical knowledge of the sensing process is the integration of theoretical modeling and actual data. Using fiber-optic plasmonic devices, this integrated approach shows a scalable and adaptable platform for environmental microplastic sensing.

Results

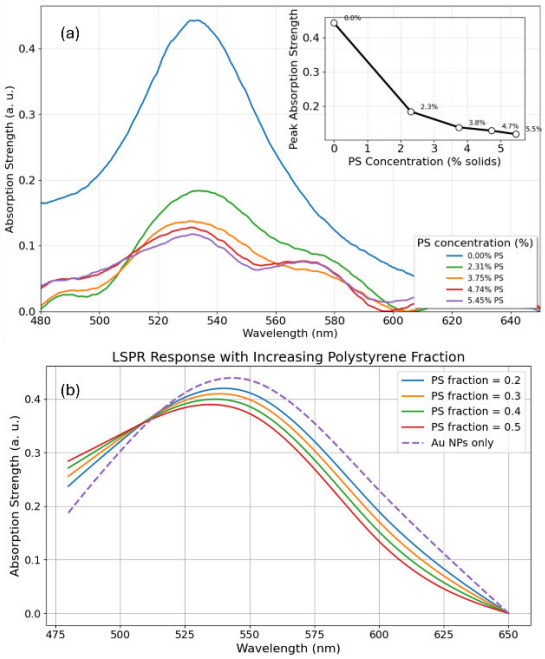

Fig. 1. (a) Experimental measurement of absorption spectrum due to LSPR when the gold deposited multimode fiber is put in water and subsequently immersed in increasing PS solutions. Inset shows peak absorption vs PS concentration. (b) Numerical simulation of the LSPR and its response when added the PS microparticles in the gold-silica composite.

When exposed to aqueous PS microplastic solutions, the gold nanoparticle-coated multimode fiber sensor's experimental response clearly demonstrates a wavelength-dependent absorbance fluctuation. Around the visible area at wavelength of 530nm, a clear localized surface plasmon resonance characteristic is seen, with predictable variations in spectral intensity (absorption strength) as the concentration of polystyrene microplastics rises as shown in Fig. 1(a). The addition of microplastics causes detectable variation in both peak amplitude and spectral form as shown in Fig. 1(a). These fluctuations confirm the sensitivity of the suggested platform to the presence of microplastics by showing a shift in the effective refractive index surrounding the nanoparticle layer.

Numerical simulations based on Maxwell–Garnett effective medium theory were carried out by modeling PS microparticles inclusion inside the gold–silica composite system to further validate the experimental data. The simulated spectra exhibit a steady trend as the microplastic volume fraction increases, indicating a slow shift in the plasmonic response and spectrum modulation in Fig 1(b). Good qualitative agreement between the simulated and experimental data confirms that refractive index changes brought on by microplastic adsorption. The slight difference in strength is because the simulations neglect water medium. These findings demonstrate the sensor's label-free detection capabilities and offer a potential basis for microplastic monitoring in water environments.

ACKNOWLEDGEMENTS: This work was supported by the Spanish Ministry of Science, Innovation and Universities, the State Research Agency (MCIN/AEI/10.13039/501100011033) and the European Regional Development Fund (ERDF)/'European Union', under project PID2023-152763NB-I00 and OPERAS (HORIZON-MSCA-2024-PF-01-01, PID 101204661)

References

[1] M. Kumar, et al., Microplastics, their effects on ecosystems, and general strategies for mitigation of microplastics: A review of recent developments, challenges, and future prospects, *Environmental Pollution and Management* 2, 87-105 (2025); doi: 10.1016/j.epm.2025.03.001

[2] D. Kalaronis, et al., Microscopic techniques as means for the determination of microplastics and nanoplastics in the aquatic environment: A concise review, *Green Analytical Chemistry* 3,100036 (2022); doi: 10.1016/j.greeac.2022.100036

[3] J. Barroso, et al., Selective Ultrasensitive Optical Fiber Nanosensors Based on Plasmon Resonance Energy Transfer, *ACS Sensors* 5(7), 123-134 (2020); doi: 10.1021/acssensors.0c00418

[4] V. Kumar and R. K. Varshney, "Real-time monitoring of toxic CS_2 with high concentrations using a suitable terahertz photonic crystal fiber," J. Opt. Soc. Am. B 40, 239-246 (2023); doi: 10.1364/JOSAB.4706

DOI 10.5162/eurosensors2026/Tu–PHS–06

A Robust Capacitive Sensor Platform for On-Line Dielectric Constant Measurement of Liquid Mixtures

Pascal Schläpfer[1], Julia Schläpfer[1], Marcel Giger[1]
[1] Innovative Sensor Technology iST AG, Stegrütistrasse 14, CH-9642, Ebnat-Kappel
pascal.schlaepfer@ist-ag.com

Summary:
Continuous on-line monitoring of liquid composition is important for process control and analytics. In this work, a ceramic-based capacitive sensor platform for dielectric constant measurement is presented. The sensor consists of an alumina substrate with printed metal and glass layers. Readout was performed using a capacitance to digital converter (CDC) device while the sensing side was immersed in DI water/ethanol mixtures. Literature-based dielectric constants of approximately 80, 57, and 42 were compared with 3D COMSOL simulations and capacitance measurements, demonstrating proof-of-concept liquid differentiation.

Keywords: dielectric constant, capacitive sensing, liquid monitoring, CDC, multifunctional sensor platform

Background and Motivation

Continuous, on-line measurement of liquid properties is important for industrial process monitoring. In particular, the dielectric constant is a useful parameter because it supports differentiation and quantification of liquid compositions. Relevant examples include methanol concentration control in direct methanol fuel cells [1] and ethanol monitoring in fermentation processes, where dielectric measurements have been shown to correlate strongly with ethanol concentration [2]. Dielectric characterization of binary water–alcohol mixtures has been demonstrated over broad frequency ranges and can be used to identify mixture composition [3]. However, existing dielectric measurement approaches still show practical limitations: commercial probe- and RF-based methods are often comparatively expensive and complex and may require non-negligible sample volumes [4]. In this contribution, a robust capacitive sensor platform for on-line dielectric constant measurement is presented. The approach is based on a ceramic material platform that additionally allows the integration of further sensing functions, such as temperature or conductivity measurement, on the same substrate. This makes the concept attractive not only for proof-of-concept dielectric sensing, but also as a basis for compact multifunctional liquid sensor systems. Due to material choice and production methods, the underlying material platform has been shown to be robust against chemically demanding electrolyte-containing and alkaline media, such as concentrated NaCl and NaOH solutions.

Simulation

To support the experimental work, a 3D COMSOL model of the capacitive sensor was established. On the active side of the sensor, a semi-infinite half-space filled with liquid medium was assumed, and the dielectric constant of this region was varied between 1 and 80. The dielectric constant of the glass passivation was modeled as 12, based on a combination of datasheet information and empirical experience. On the back side of the sensor, a semi-infinite air region with dielectric constant 1 was assumed.

Fabrication

The sensor is built on an alumina substrate (96% purity) with silver through-contacting. On the front side, gold interdigital electrodes form the active capacitive structure, which is covered by a glass passivation layer. Metal and glass layers were formed using screen printing. Finger width and separation were chosen to be 150 µm.

Experimental setup

During measurement, the active side of the sensor was immersed into the liquid under test, while the back side remained exposed to air. The liquid volume was chosen much larger than the active sensor area. The readout was performed using a CDC device with an external reference capacitance of 15 pF. The CDC used utilizes discharge-time-based capacitance measurement. Three liquid states based on DI water and ethanol were investigated experimentally. Details are given in Table 1. The experimental

measurements were performed at room temperature (~25 °C).

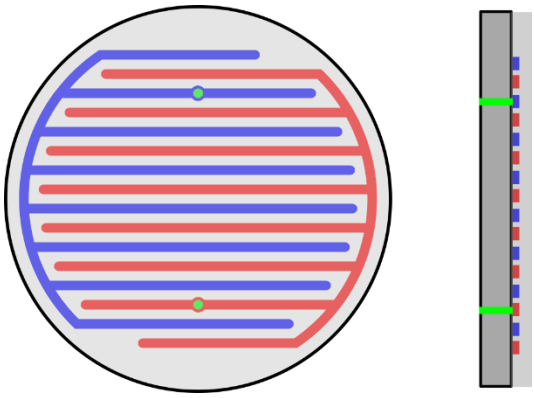

Fig. 1: left: top view of sensor element (active side); right: cross-sectional view of sensor element (not to scale). Finger width and separation was chosen to be 150 µm, outer diameter of the chip is 10 mm.

Proof-of-Concept Results

The COMSOL simulation of sensor capacitance for a medium dielectric constant between 1 and 80 shows an expected monotonic increase in capacitance with increasing dielectric constant of the medium. The gradient of this curve changes with dielectric constant. This is due to the passivation layer over the electrodes. In simulations without this passivation glass (not shown here), the capacitance gradient with dielectric constant appears linear. However, this passivation layer is instrumental for the used readout electronics, since dominant electrical conduction between the electrodes would introduce significant errors in the measurement. Both measurement values and simulation output are given in Figure 2. Numerical values are given in Table 1.

The results demonstrate that the sensor platform can differentiate liquid states with different dielectric constants by means of capacitive readout. The agreement between literature-based medium permittivity estimations, simulation trend, and measured response lies within 8%. At the current stage, the study should be interpreted as platform validation rather than a full quantitative dielectric metrology study. A broader concentration series, temperature-dependent characterization, and evaluation of possible conductivity-related cross-sensitivities will be instrumental for future work. The use of ceramic substrate materials and high-temperature, chemically resistant sensing and protection materials enables the combination with multiple additional sensing parameters, such as temperature, conductivity, or liquid flow.

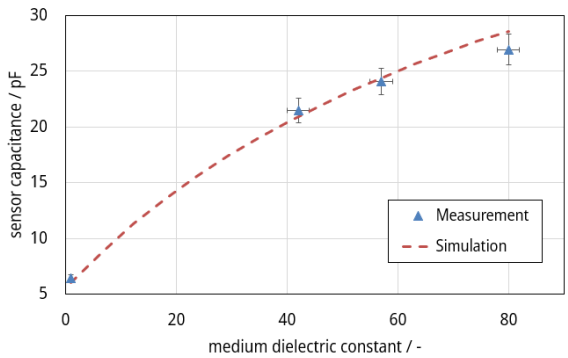

Fig. 2: measured capacitance values in air and in three different liquid media. The red dashed line shows simulated sensor capacitance values.

Tab. 1: comparison between simulated and measured capacitance values for measurements in air and in three liquid media. ε_r values were estimated according to [5].

Medium (ε_r)	$C_{simulation}$ / pF	$C_{measured}$ / pF
Air (1)	5.99	6.45 ± 0.32
70 vol.% ethanol (42)	20.95	21.47 ± 1.07
37 vol.% ethanol (57)	24.40	24.07 ± 1.20
DI water (80)	28.59	26.94 ± 1.35

References

[1] S. Andoh, A. Fujita, T. Miitsu, Y. Kuroda, S. Mitsushima, Practical and Reliable Methanol Concentration Sensor for Direct Methanol Fuel Cells, *Electrochemistry* 89 (3), 250–255 (2021); doi: 10.5796/electrochemistry.21-00012

[2] Z.P. Jákói, B. Lemmer, R. Dobozi, C. Hodúr, S. Beszédes, Using Dielectric Constant Measurement to Monitor Ethanol Fermentation and Anaerobic Co-Digestion of Lignocellulosic Biomass, *Fermentation* 9, 902 (2023); doi: 10.3390/fermentation9100902

[3] J.-Z. Bao, M.L. Swicord, C.C. Davis, Microwave dielectric characterization of binary mixtures of water, methanol, and ethanol, *Journal of Chemical Physics* 104 (12), 4441–4450 (1996); doi: 10.1063/1.471197.

[4] A. Salim, M.U. Memon, H. Jeong, S. Lim, Simplified Approach to Detect Dielectric Constant Using a Low-Cost Microfluidic Quarter Mode Substrate-Integrated Waveguide, *Sensors* 20, 4985 (2020); doi: 10.3390/s20174985

[5] Lechner, M.D. (ed.), Static Dielectric Constants of Pure Liquids and Binary Liquid Mixtures: Supplement to IV/6. Landolt-Börnstein, New Series, Group IV: Physical Chemistry, Vol. 17, *Springer*, Berlin Heidelberg (2008); doi: 10.1007/978-3-540-75506-7

DOI 10.5162/eurosensors2026/Tu–PHS–07

Overcoming Thermal Inertia in Robust Anemometers via Observer-Based Virtual Thermal Isolation

Samuel Huber[1], Mathias Mächler[1], Tobias Lamprecht[1], Lars Kamm[1], Dietmar Bertsch[1], Christoph Würsch[1]
[1] OST Eastern Switzerland University of Applied Sciences, Buchs, Switzerland
samuel.huber@ost.ch

Summary:
This paper presents a novel approach to thermal anemometry that replaces fragile physical thermal isolation structures with algorithmic "virtual" thermal isolation. By applying a discrete-time Linear Quadratic Integral (LQI) controller and a Kalman filter (KF) to a miniaturized bulk-silicon sensor, the high physical thermal inertia is dynamically compensated. The system locks the sensor to a constant temperature difference above ambient and extracts the fluid velocity directly from the optimal control effort enabling fast, noise-filtered flow measurements yet using robust, un-etched silicon substrates.

Keywords: Constant temperature anemometer, digital control, LQI, Kalman filter

Background and Motivation

Miniaturized thermal flow sensors commonly rely on delicate micro-electromechanical systems (MEMS), such as suspended thin-film membranes, to minimize thermal mass and achieve fast response times. Conversely, monolithic bulk-silicon designs offer superior mechanical resilience without fragile post-processing, but inherently suffer from significant thermal inertia that limits their dynamic bandwidth [1, 2].

To overcome these limitations, Constant Temperature Anemometers (CTAs) and closed-loop PID architectures are employed to mitigate environmental variables like ambient temperature drift [3, 4]. However, analog feedback or simple digital bridges struggle to quickly compensate for high thermal mass [2]. Recent advancements demonstrate that integrating optimal state estimators, such as Kalman filters (KFs), into digital control loops enhances dynamic response and provides crucial noise filtering [5].

In this work, we combine a discrete-time Linear Quadratic Integral (LQI) controller with a 1D KF to establish algorithmic "virtual" thermal isolation. Rather than relying on the physical removal of silicon, the digital closed-loop system mathematically compensates for the lumped-capacitance dynamics of the bulk die. The controller forces the heater to a strict temperature difference above ambient, allowing a noise-free fluid velocity signal to be extracted directly from the optimal control effort.

Description of the Sensor-Actuator-System

The sensor system consists of a bulk-silicon die with two thin-film Platinum meander resistors acting as both Joule heater and temperature sensor, upstream and downstream Si pn-junctions, and an off-the-shelf Nordic microcontroller.

The latter hosts LQI control and KF algorithms running presently at a $\Delta t = 5$ ms cycle time thereby reading the voltages of the temperature sensors with a 12-bit ADC at $V_{ref} = 3.3$ V and providing 8-bit PWM duty-cycle to the heater resistor via low-side switch transistor.

The sensactor microchip was fabricated with 225-nm-thick Pt deposition and structuring on a 500-nm-thick SiO2 layer on top of the 300-µm-thick 4” Si substrate containing custom doping forming pn-junctions. The substrate was mounted on a 500-µm-thick BF33 glass wafer. For thermal and electrical isolation, dicing streets between heater, upstream, and downstream temperature sensors were introduced reaching only partly into the glass substrate. A schematic diagram and micrograph of the system are shown in Fig. 1.

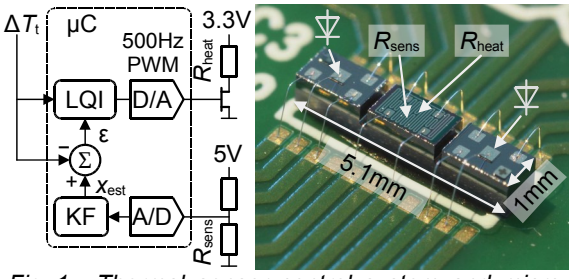

Fig. 1. Thermal sensor control system and micrograph of the sensactor microchip.

The continuous-time thermal dynamics are discretized into a state-space formulation with prediction including thermal behavior $x_{pred,k} = x_{est,k-1}(1-\Delta t/\tau)+u_{k-1}\,\Delta t/C_{th}$. State vector x in our case is the scalar quantity of temperature difference, Δt the time interval, τ the thermal time constant, and C_{th} the thermal capacitance. To handle thermal noise as well as quantization noise from the analog-to-digital converter, a 1D discrete-time KF provides an optimal, noise-free estimate $x_{est,k} = x_{pred,k}+K(\Delta T_{meas}-x_{pred,k})$ of the true temperature state engaging Kalman gain K.

An LQI controller forces the system state derivative to zero, locking the sensor at a strict target temperature difference of presently $\Delta T_t = 15$ K above ambient (fluid) temperature through $u_k = G_{th}\Delta T_t + K_p\varepsilon + K_i\Sigma\varepsilon\Delta t$ with $\varepsilon = \Delta T_t - x_{est,k}$. Therefore u_k, i.e., the heating power, first overcomes thermal conductance G_{th} and corrects the remaining error ε by minimizing a penalty that increases quadratically with dimensions u_k, ε, and integral error. Because the control loop dominates the substrate dynamics, the instantaneous quasi-static flow velocity v_k is extracted mathematically from the control effort u_k via power law [1], bypassing the physical thermal lag.

Results

System Identification. Empirical step-response experiments revealed a step response time $\tau = 0.88$ s, and stationary condition with $\Delta T = 30.4$ K at a power of $P_h = 76.8$ mW. The extraction of the required baseline parameters yielded a static thermal conductance of $G_{th} = 2.5$ mW/K and a total thermal capacitance of $C_{th} = 2.2$ mJ/K. Step response results are shown in Fig. 2.

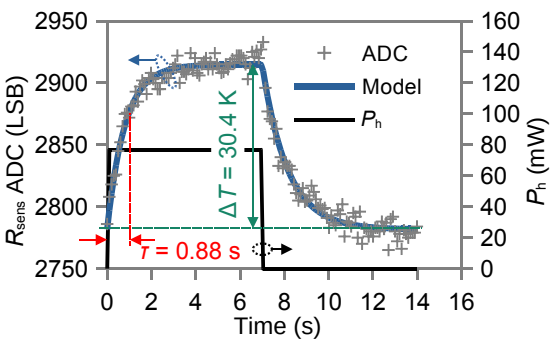

Fig. 2. Thermal step response of the Pt heater on Silicon chip at v = 0 m/s and T_{amb}=22°C.

Closed-Loop Stability. The implementation of the LQI controller with $K_p = 0.018$ W/K and $K_i = 0.05$ W/(K·s) on a microcontroller demonstrated robust temperature locking, with the integral state ensuring zero steady-state error against continuous flow. The desired $\Delta T = 15$ K was reached at a PWM duty-cycle of 15.7% (40 LSB). The KF effectively reduced noise by feeding the system with the best estimate of the actual temperature.

Measurements in the wind tunnel revealed the expected power law (King's law). The Control effort u_k and the corresponding PWM duty-cycle as a function of flow velocity are shown in Fig. 3.

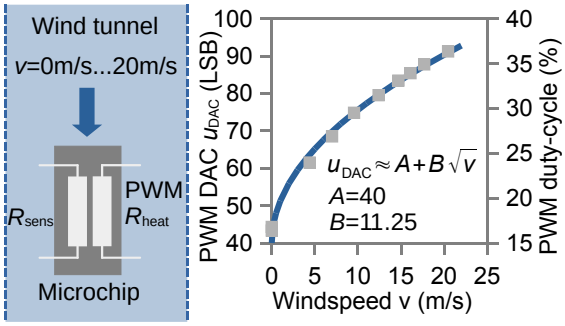

Fig. 3. PWM duty-cycle as a function of flow velocity at T_{amb}=22°C.

Characterisation at low velocity, changing fluid temperatures, and with respect to dynamic properties are subject of future work.

References

[1] T.L. Hacket et al, A Dual-Mode Anemometer Fabricated in 65-nm CMOS BEOL Without Post-processing, *IEEE Sensors Letters* 10, 1-4 (2025); doi:10.1109/LSENS.2025.3636592

[2] D.M. Birch and J.F. Morrison, An Innovative Low-Profile Monolithic Constant-Temperature Anemometer, *Journal of Wind Engineering and Industrial Aerodynamics* 100, 38-45 (2011); doi:10.1016/j.jweia.2011.10.010

[3] M. Domínguez-Pumar et al., Dynamics of constant temperature anemometers for the Martian Atmosphere, *Measurement*, 239 (2025); doi:10.1016/j.measurement.2024.115427

[4] B. Idjeri, M. Laghrouche, E-B. Bourennane, Advanced Calibration of Multisystem Hot-Wire Anemometers Using PID Temperature Control and ANN Techniques, *IEEE Sensors Journal*, 25 (2025); doi:10.1109/JSEN.2025.3599328

[5] V. R. Augesta et al., Kalman Filter-Based Enhancement of PID Control in Water Flow Systems, *5th International Symposium on Materials and Electrical Engineering (ISMEE)*, (2025); doi:10.1109/ISMEE68179.2025.11473032

Acknowledgements

The authors would like to thank P. Zbinden and R. Willi of the Institute for Microelectronics (IMES) and O. Schreiber of the Institute for Computational Engineering (ICE) for their support. Microchips were designed at the Institute for Microtechnology (IMP) and fabricated at the Sensor Innovation Hub (SIH), the open access clean room facilities at Campus Buchs.

DOI 10.5162/eurosensors2026/Tu–PHS–08

LVDT Position Sensor with external armature

Mehran Mirzaei, Jiri Maier, Pavel Ripka
Faculty of Electrical Engineering, Czech Technical University, Prague 16627, Czech Republic, mirzameh@fel.cvut.cz

Summary:
This paper presents a novel position sensor based on a linear variable differential transformer (LVDT). The position sensor consists of one excitation coil and one pickup coil, which are perpendicular to each other. The position sensor is a flat-type, featuring a block-shaped armature that moves in parallel with a rectangular-shaped excitation coil. The initial shape of the pickup coil is a rectangular coil, whose dimensions and position are optimized to extend the linearity range of the position sensor and reduce nonlinearity errors. The shape of the pickup coil is optimized to extend the linearity range further. The measurements are conducted to validate the design optimization of the position sensor.

Keywords: Design and analysis, LVDT, linearity range, measurement, position sensor.

Introduction

Extending the linearity range while reducing nonlinearity error is a challenging task when the maximum axial length of the position sensor and the maximum armature movement range are constrained. Electromagnetic optimization can be applied to extend the linearity range by optimizing the coil shape and armature dimensions [1]-[3]. Implementing an external signal-processing unit is an alternative method for extending the linearity range. However, it complicates the position-measuring system and reduces reliability, especially in harsh environments. Achieving an adequate linearity range in flat-type LVDT sensors with an external armature is more complex because they have an open magnetic-circuit structure. A novel position sensor with an external armature based on a linear variable differential transformer (LVDT) is developed and presented. The design optimization of the LVDT position sensor is performed using the 3D finite element method (FEM) to reduce nonlinearity errors and extend the linearity range. The dimensions, position, and structure of the pickup coil are optimized to achieve the objectives. The proposed position sensor has a simpler structure than a conventional LVDT, with only one pickup coil instead of two.

Structure

Fig. 1 a) shows the 3D model of the LVDT position sensor's basic design. The excitation and pickup coils are perpendicular to each other. The induced voltage in the pickup coil is proportional to the magnetic flux difference through it, which depends on the armature position. The total net flux linkage in the pickup coil is zero for the zero position of the armature, and it is nonzero when the armature moves from the zero position. A new structure of the pickup coil is presented in Fig. 1 b), with its dimensions and position altered. The pickup coil axis is rotated relative to the excitation coil axis with an angle of θ, as shown in Fig. 1 b). Fig. 2 a) presents the induced voltage in the pickup coil for the basic and enhanced designs, covering a ±30 mm movement range, where the curve for the basic structure is not linear; thus, it results in a high nonlinearity error. The corresponding nonlinearity errors (enhanced) for the ±20 mm and ±25 mm ranges are shown in Fig. 2 b) for θ = 3.0 deg. Linearity is considerably improved in the enhanced structure compared to the basic structure.

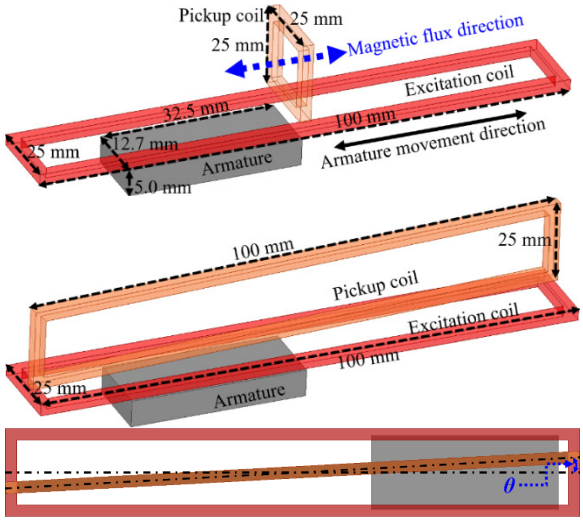

Fig. 1. 3D model of LVDT position sensor, a) basic structure (up), b) the enhanced structure of the LVDT position sensor (bottom), where the pickup coil was rotated with an angle of θ

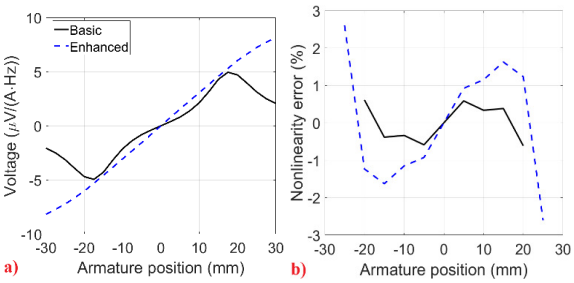

Fig. 2. 3D FEM results of LVDT position sensors with Ferrite armature (θ=3.0 deg. for enhanced structure), a) voltage to current and frequency ratio versus armature position, b) nonlinearity error versus armature position (enhanced structure)

Experiments

Fig. 3 shows the prototyped sensor for the measurement. The experimental results for voltage and nonlinearity error in the ±20 mm range for the enhanced sensor using Ferrite armature (Fig. 1 b)) are presented in Fig. 4 and agree well with the calculations in Fig. 2 a) for the voltage. The measured nonlinearity error is about 1.5%, which is higher than the simulated nonlinearity values, which are below 1.0%. Imperfections in the 3D-printed coil bobbin manufacturing process cause the discrepancy between the 3D FEM and measurements for the nonlinearity error. The measured nonlinearity error can be reduced to the calculated level by improving manufacturing precision. The armature length can be decreased from 32.5 mm to a smaller value. It helps achieve a higher linearity range despite the LVDT position sensor's decreasing sensitivity.

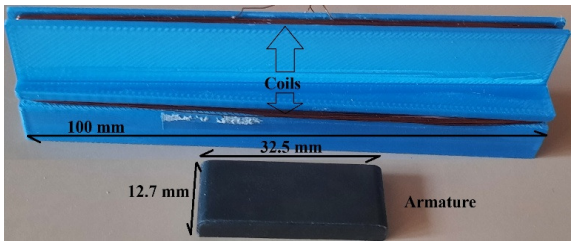

Fig. 3. Prototype of enhanced LVDT sensor- Bobbins, coils, and Ferrite armature (θ=3.0 deg.)

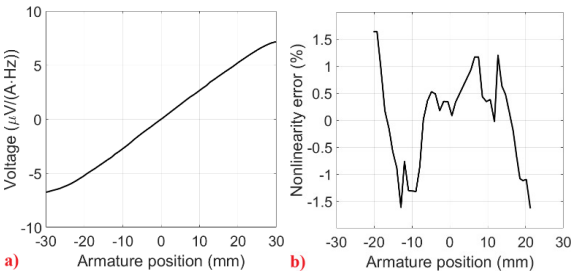

Fig. 4. Experiment results of enhanced LVDT position sensor, a) voltage to current and frequency ratio versus Ferrite armature position, b) nonlinearity error versus Ferrite armature position (The voltage was processed by a phase-sensitive detector (lock-in amplifier)

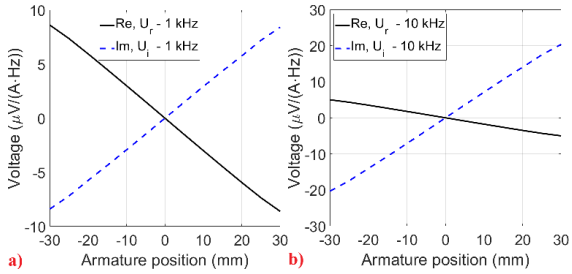

Fig. 5. 3D FEM results of LVDT position sensors (θ=3.0 deg. for enhanced structure) with nonmagnetic conductive armature – real (Re) and imaginary (Im) components of voltage to current and frequency ratio versus armature position, a) 1 kHz, b) 10 kHz

Using Nonmagnetic Conductive Armature

The armature material is changed from Ferrite armature to a nonmagnetic conductive one with an electrical conductivity of 30 MS/m. Fig. 5 shows the real (Re) and imaginary (Im) components of voltage at 1 kHz and 10 kHz. The voltage graph versus armature position shows adequate linearity with a nonmagnetic conductive armature, comparable to that of a magnetic Ferrite armature. Increasing frequency enhances the sensor's sensitivity with a nonmagnetic conductive armature. The real and imaginary components of voltages are obtained relative to the excitation coil current as a reference signal.

The design, analysis, and measurements of a novel LVDT position sensor were presented. The presented sensor features only one pickup coil, which simplifies manufacturability and enables a cost-effective position sensor. The shape and dimensions of the pickup coil have been optimized to extend the linearity range and reduce nonlinearity error below 1.0% using 3D FEM. Optimizing the pickup coil shape and armature length can increase the linearity range to ±25 mm and ±30 mm with low nonlinearity error. The proposed position sensor features a structure with an external armature, isolating the coils from the moving armature. It makes a suitable position sensor for various industrial applications in a harsh environment.

References

[1] M. Mirzaei, P. Ripka, and J. Maier, Design Optimization of a Position Sensor for Linearity Range Extension, *IEEE Trans. Magnetics* 61, 4001705 (2025); doi: 10.1109/TMAG.2025.3534916

[2] M. Mirzaei, J. Maier, and P. Ripka, Linearity Range Enhancement of LVDT Position Sensors using Optimized Coils, *IEEE Sensors J.* 25, 24441 - 24450 (2025); doi: 10.1109/JSEN.2025.3568547

[3] A. Ali, G. Y. Tian, D. Wang, A. Asif, X. Lu, C. Peng, and H. Xu, Design and Development of High Linearity of Trapezoidal Winding LVDT, *IEEE Trans. Instrumentation & Measurement* 74, 9539014 (2025); doi: 10.1109/TIM.2025.3617803

DOI 10.5162/eurosensors2026/Tu–PHS–09

Investigating Slip-Induced Frequency Relationship in Dual-Channel PVDF Sensor Applied to Robotic Grippers

Zerun Wang[1], Vivek Kamat[1], Shekhar Bhansali[1]*
[1]Department of Electrical and Computer Engineering, Vanderbilt University, Nashville, TN 37240, USA
shekhar.bhansali@vanderbilt.edu

Summary:
Robotic handling implements sensors (pressure, tactile, acoustic) for slip sensing and regulating grasping forces. We investigated dual-channel PVDF acoustic sensors embedded in a compliant gripper and characterized them in the frequency domain across 159 grasp trials (72 slip, 87 non-slip). Slip was shown to significantly alter the frequency-selective relationship between the inner and outer sensors, which is absent below 100 Hz and strongly amplified above it (effect size up to 0.97). A threshold model was developed and achieved 81.7% cross-validated accuracy in distinguishing slip from no-slip events.

Keywords: Sensors, slip detection, robotics, signal processing, MEMS

Title

Investigating Slip-Induced Frequency Relationship in Dual-Channel PVDF Sensor Applied to Robotic Grippers

Background, Motivation and Objective

One of the challenges in robotic grasping is sensing slippage for reliable object manipulation and damage avoidance, for which optical, pressure, tactile, and acoustic sensors are common approaches [1]. Piezoelectric polyvinylidene fluoride (PVDF) sensors have been deployed for slip detection [2] but have lacked robustness [3]. Multi-channel configurations are one solution to improve accuracy, reliability, and repeatability attributed to their ability to cancel out noise [4]. We instrumented two independently acquired PVDF channels on the inner and outer surfaces of a fin-ray finger, providing a low-cost and convenient solution for slip sensing, and investigated the frequency-domain relationship between the two channels as well as their correlation with slip events.

Description of the New Method or System

A compliant Fin Ray gripper [5] (Fig. 1) was instrumented with two PVDF sensors (TE Connectivity Measurement Specialties DT4-028K/L), each connected to one channel of the charge amplifier with the exact same configurations (OPA2134, Fig. 2), and output AC-coupled to a UGREEN USB audio interface sampling at 48kHz using a NVIDIA Jetson Orin Nano. For each of 159 grasp trials performed by a myCobot 280 robotics arm, spanning three object types (Fig. 3), a 1 second segment was extracted from the onset of the lifting motion and labeled with visual inspection. Power spectral density was estimated per channel using Welch's method (4096-sample Hann windows, 50% overlap), from which spectral centroid (1), bandwidth (2), and energy (3) in three frequency bands (10-100, 100-2000, 2000-10000 Hz) were calculated per trial.

Results

Inner is systematically higher than outer in both conditions (Fig. 4); slip trials show 10-15 dB higher overall PSD across the broadband spectrum than no-slip.

As shown in Tab. 1, in slip trials, inner exceeds outer across all five features. Under no-slip, this holds for centroid and Band 1/2 energy, but reverses for bandwidth (114.9 vs 223.8 Hz). Slip, therefore, does not merely amplify an existing bias, but restructures which channel dominates.

Accordingly, the inter-channel energy difference is significantly larger during slip than no-slip in Band 2 and Band 3, with no difference in Band 1 (Tab. 2; Fig. 4), which is directionally consistent across all three tested objects, suggesting a structural rather than object-specific origin. Beyond statistical characterization, we tested whether this spectral relationship supports a coarse slip/no-slip distinction.

A single fixed-threshold classifier on Band 2 ΔE achieved 81.7% accuracy and an F1 score of 0.79, indicating the relationship carries directly usable information even without a learned model. Fusing the full feature set (centroid, bandwidth, all bands) across a broader sensing and control pipeline is the subject of ongoing system-level work.

DOI 10.5162/eurosensors2026/Tu–PHS–09

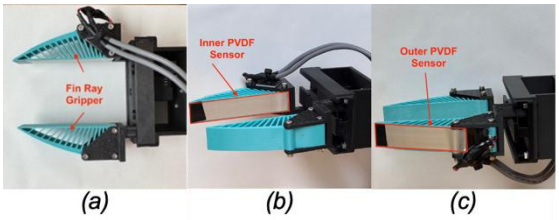

Fig. 1 Hardware setup of the Fin Ray Gripper (a), attached with inner (b) and outer (c) PVDF Sensors

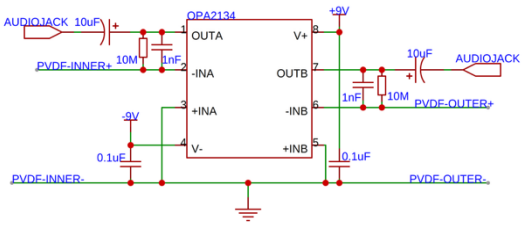

Fig. 2 Schematic for OPA2134 Amplifier Circuit

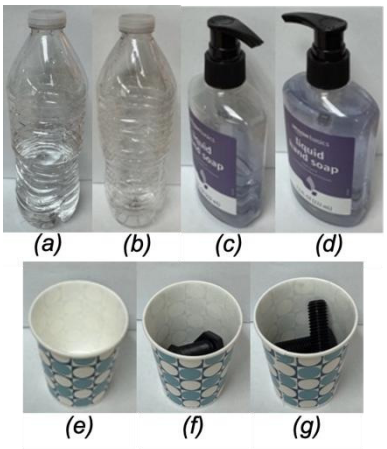

Fig. 3 Object used for slip data collection, including plastic water bottle (a: 243.51g, b: 10.77g), hand soap bottle (c: 215.25g, d: 289.84g), and paper cup (e: 2.29g, f: 61.78g, g: 68.14g)

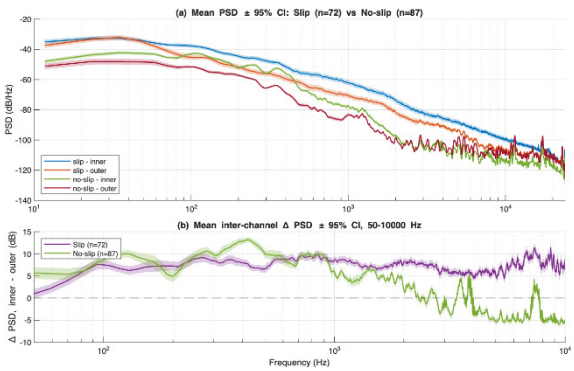

Fig. 4 (a) Mean PSD (±95% CI) of inner and outer channels for slip (n=72) and no-slip (n=87) trials. (b) Mean inter-channel PSD difference (inner − outer, dB) ±95% CI, 50–10000 Hz, for slip vs no-slip trials.

Tab. 1 Inner vs outer statistics, slip (n=72)/no-slip (n=87); note the sign reversal for bandwidth and Band 3 (ES, rank-based). ES = effect size; energy in a.u.

Feature	Slip: In/Out	No-slip: In/Out	ES: Slip/NS
Spectral centroid (Hz)	108.9/72.9	126.6/111.0	0.88/0.38
Spectral band-width (Hz)	182.4/133.4	114.9/223.8	0.83/-0.86
Band 1 energy (10-100 Hz)	0.047/0.040	0.0071/0.0063	0.31/0.44
Band 2 energy (100-2000 Hz)	0.023/0.008	0.0051/0.0007	1.00/1.00
Band 3 energy (2000-10000 Hz)	6.0e-4/1.4e-4	4.35e-7/3.24e-7	1.00/-0.54

Tab. 2 Inter-channel energy difference (ΔE), slip vs no-slip (Mann-Whitney U). ES = effect size.

Band	Slip	No-slip	p (ES)
Band 1 (10-100 Hz)	5.3e-3	7.2e-4	0.107 (n.s.)
Band 2 (100-2000 Hz)	1.56e-2	4.37e-3	<0.001 (0.75)
Band 3 (2000-10000 Hz)	8.45e-5	1.1e-7	<0.001 (0.97)

Equations

$$f_c = \frac{\sum f \cdot P(f)}{\sum P(f)} \quad (1)$$

$$BW = \sqrt{\frac{\sum (f - f_c)^2 \cdot P(f)}{\sum P(f)}} \quad (2)$$

$$E_{band} = \sum_{f_1}^{f_2} P(f) \quad (3)$$

References

[1] X. Zhang, L. Wu, S. He, et al., Recent Advances of Slip Sensors for Smart Robotics, *Advanced Materials Technologies*: e02251 (2026); doi: 10.1002/admt.202502251

[2] M. H. Rosle, A. R. Saffiai, A. Nasir, M. N. F. Saniman, PVDF-based flexible piezoelectric tactile sensor for slip estimation using robotic gripper, *Front. Robot. AI* 12:1691688 (2025); doi: 10.3389/frobt.2025.1691688

[3] K. Van Wyk, J. A. Falco, Slip Detection: Analysis and Calibration of Univariate Tactile Signals, *arXiv*:1806.10451 (2018); doi: 10.48550/arXiv.1806.10451

[4] Q. Yao, L. Xie, X. Guo, F. Yu, X. Zhao, PVDF Membrane-Based Dual-Channel Acoustic Sensor Integrating the Fabry–Pérot and Piezoelectric Effects, *Sensors* 23, 3444 (2023); doi: 10.3390/s23073444

[5] C. Chi, Z. Xu, C. Pan, E. Cousineau, B. Burchfiel, S. Feng, R. Tedrake, S. Song, Universal Manipulation Interface: In-The-Wild Robot Teaching Without In-The-Wild Robots, *Proceedings of Robotics: Science and Systems (RSS)* (2024); doi: 10.48550/arXiv.2402.10329

DOI 10.5162/eurosensors2026/Tu–PHS–10

High Temperature Investigation of Polymer-Free Strain Gauges for Integration in DED-LB Components

Eileen Müller, Julia Eisfelder, Rico Ottermann, Folke Dencker, Daniel Klaas, Marc Christopher Wurz
Institute of Micro Production Technology, Leibniz University Hannover, An der Universitaet 2, 30823 Garbsen, Germany
mueller@impt.uni-hannover.de

Summary:
Strain gauges integrated into additively manufactured metal components allow precise internal strain measurement for lifetime prediction. To withstand process temperatures up to 1,200 °C, thin-film sensors were fabricated on stainless steel substrates. After annealing, insulation maintained sufficient dielectric strength. The k-factor of the sensor doubled to 2.3, while resistance dropped by 50% and TCR remained constant up to 800 °C. The diffusion barriers prevented diffusion up to at least 800 °C. These results confirm the suitability of thin-film strain gauges for sensor integration in DED-LB components.

Keywords: high-temperature, thin-film, strain gauges, insulation layer, diffusion barrier

Introduction

Sensors are essential in industrial applications for real-time monitoring and predictive maintenance. Integrating sensors directly into components using additive manufacturing, particularly Laser Based - Directed Energy Deposition (DED-LB), offers unique advantages as the layer-by-layer process allows the precise placement of sensors in the component that are inaccessible via conventional methods, but requires the development of high-temperature-resistant sensor systems [1]. Previous integration methods often relied on robust and bulky encapsulations and used different methods like Laser Powder Bed Fusion [2]. This work aims to investigate thin-film strain gauges suitable for DED-LB integration, focusing on using high process temperatures for sensor annealing rather than shielding. The study analyzes the sensor system's k-factor, temperature coefficient of resistance (TCR), resistivity, the insulation's dielectric strength and resistivity and diffusion behavior before and after annealing.

Manufacturing and Annealing of the Sensor

All strain gauges were fabricated on 800 µm thick stainless steel (1.4301) substrates, chosen for future integration into machine tool components using DED-LB. The use of stainless steel ensures a strong bond and efficient transfer of strain between the sensor and the component. Substrate surface roughness was measured at R_a = 31 ± 3 nm and R_z = 842 ± 143 nm. A schematic of the manufactured sensor is shown in Fig. 1a. Al_2O_3 was used as insulation material (2 µm) due to its excellent high-temperature insulating properties and its thermal expansion compatibility with both substrate and sensor materials. Tantalum (Ta) was applied as a diffusion barrier (0.2 µm) between the sensor and insulation layers, providing thermal stability and good adhesion. NiCr (50/50 wt.%) was used as sensor layer (0.4 µm) due to its linear k-factor, low TCR, and high-temperature stability. A gold layer was deposited as protective layer on the contact pads (0.5 µm) for reliable electrical contact after annealing. All layers were deposited by sputtering. The fabricated sensors were separated into 1.5 × 1.5 cm chips and annealed at 600 °C, 800 °C, and 1,200 °C (Fig. 1b) in a ceramic oven for 60 s in ambient atmosphere, simulating the short-term thermal loads typical in DED-LB. Three samples per temperature were analyzed and were cooled to room temperature post-annealing. Temperature choices were based on prior heat simulations of DED-LB processes [1].

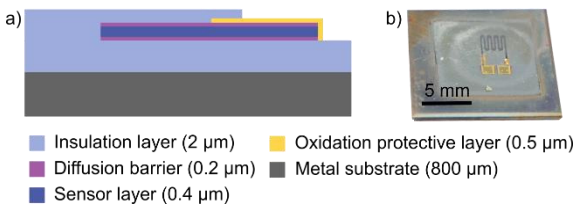

Fig. 1. a) Schematic of the integrable strain gauge system, b) strain gauge annealed at 1,200 °C

Electrical and mechanical characterization

The electrical resistivity ρ and dielectric strength E of the insulation layer were evaluated before and after annealing. A significant increase in ρ and E was observed after annealing at 800 °C.

Tab. 1: Electrical and mechanical characterization of insulation and sensor layer

Properties		As-deposited	600 °C	800 °C	1,200 °C
Al_2O_3	ρ [Ωcm]	$1.35 \cdot 10^{11} \pm 4.08 \cdot 10^{10}$	$2.06 \cdot 10^{11} \pm 8.81 \cdot 10^{10}$	$1.03 \cdot 10^{14} \pm 5.16 \cdot 10^{13}$	$7.71 \cdot 10^{8} \pm 3.13 \cdot 10^{8}$
	E [kV/mm]	40.00 ± 4.7	39.38 ± 2.7	76.25 ± 26.7	46.25 ± 5.9
Sensor	$\Delta R/R$ [%]	-	1.0 ± 0.8	-2.4 ± 1.2	-58.3 ± 1.6
	k [-]	1.1 ± 0.1	1.4 ± 0.2	1.8 ± 0.1	2.3 ± 0.1
	TCR [ppm/°C]	21.9 ± 0.3	51.7 ± 0.8	40.4 ± 4.5	1237.2 ± 53.9

This may be caused by phase transformations of Al_2O_3 to γ-Al_2O_3 at 800 °C and δ-/θ-Al_2O_3 at 1,200 °C [3]. Additionally, at 1,200 °C, cracks and delamination in the thin-film insulation are clearly observable, which explains the significant drop in resistivity. All samples still retained functional insulation, confirming their suitability for integration via DED-LB. The effectiveness of the diffusion barrier was examined through XPS analysis. For temperatures up to 800 °C (Fig. 2), the Ta barrier successfully prevented inter-diffusion. However, at 1,200 °C, XPS could no longer distinguish clear separations between layers, which seems to be due to loss of layer adhesion, rather than interdiffusion. Furthermore, XPS data revealed a NiCr concentration of 40:60 at.% (43:57 wt.%), which deviates from the nominal 50:50 wt.% ratio and could indicate local alloy variations after annealing.

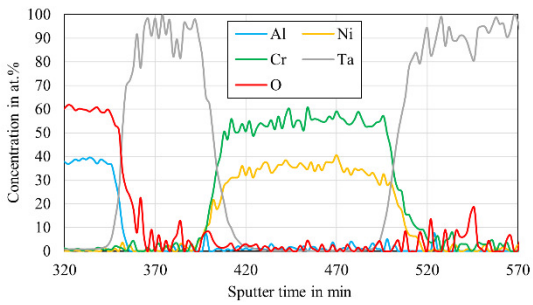

Fig. 2. XPS analysis for a sensor system after 60 s annealing at 800 °C.

Strain gauge resistance R was measured at room temperature before and after annealing. Only minor resistance changes occurred, except after annealing at 1,200 °C, where resistance decreased by about 58%. This reduction is likely caused by annealing-induced reduction of lattice and point defects in the NiCr thin-film, leading to lower resistivity. The k-factor k was characterized through cyclic tensile tests, with strain measured up to 208 µm/m. Annealing at higher temperatures caused significant increases of up to 217%. This is comparable to literature values for NiCr thin films (k = 2.3) and Ta thin films (k = 2.8) and exceeds values for commercial strain gauges typically around 2.0 ± 1% in a temperature range of only -269 °C to +250 °C [4]. The increase is attributed to relaxation of residual stresses and possible phase separation in the NiCr layer (formation of Ni-rich and NiCr regions), as expected from the phase diagram and supported by XPS-measured concentration gradients. TCR measurements revealed a sharp increase by a factor of 30 after annealing at 1,200 °C. This change is likely related to the same phase transformations and microstructural reorganization responsible for the increase in k-factor. A low TCR is preferred for strain gauges to ensure minimal thermal drift and noise; literature typically cites values below 200 ppm/°C for NiCr (50/50 wt.%) and Ta, a criterion met by all except the samples annealed at 1,200 °C. Nevertheless, the higher-TCR samples remain suitable for temperature-stable strain gauge applications. These results confirm the suitability of thin-film strain gauges for sensor-integrated components in additive manufacturing, with further studies recommended to optimize layer adhesion and investigate phase transformations.

Acknowledgment

Funded by the Deutsche Forschungsgemeinschaft (DFG, German Research Foundation) – Project-ID 511263698 – TRR 375

References

[1] M.N. Kishore, et.al. Comprehensive study of the cold-temperature directed energy deposition: Multi-physics modelling and experimental validation, *J. Manuf. Process.* 112, 290-301 (2024); doi: 10.1016/j.jmapro.2024.01.046

[2] M. Binder, et.al. Integration of Strain Gauges in Components Manufactured by Laser Powder Bed Fusion, *Proc. Machining Innov. Conf. (MIC),* 030-041 (2020); doi: 10.2139/ssrn.3724097

[3] M.L. Grilli, et.al. A Comparative Study of the Mechanical and Tribological Properties of Thin Al2O3 Coatings Fabricated by Atomic Layer Deposition and Radio Frequency Sputtering, *Phys. Status Solidi A 219,* 2100398 (2022); doi: 10.1002/pssa

[4] HBM Dehnungsmessstreifen – Erste Wahl für Dehnungsmessungen, *S01264 07 G00 00* (2026); https://www.hbm.com/fileadmin/media-pool/hbmdoc/technical/S01264.pdf

DOI 10.5162/eurosensors2026/Mo–SMD–01

A Miniaturized Electrochemical Biosensor for Real-Time In Vivo Potassium Monitoring in the Inner Ear

Faezeh Arshadi[1], Mahsa Esfandiari[1], Robert Gay[2], Ya Lang Enke[2], Nona Farbehi[3], Christopher Pastras[1*], Mohsen Asadnia[1*]

[1] *School of Engineering, Macquarie University, Sydney, Australia*

[2] *Cochlear Limited, 1 University Avenue, Macquarie University, NSW 2109, Australia*

[3] *Graduate School of Biomedical Engineering, University of New South Wales, Sydney, NSW, 2052, Australia*

Email: Faezeh.arshadi@hdr.mq.edu.au

Abstract:

This work presents a novel miniaturized potassium-selective biosensor with an integrated solid-state reference electrode (RE), designed for real-time, in vivo monitoring of potassium ion (K^+) dynamics in the cochlea. K^+ is essential for auditory transduction and mechano-electrical signal conversion in the inner ear, where sensory hair cells depend on potassium-rich endolymph. Disruptions in K^+ homeostasis are linked to disorders such as Ménière's disease (1). Despite its importance, current diagnostic methods cannot provide real-time, in vivo monitoring of K^+ in the inner ear, limiting our understanding of the ionic mechanisms involved in auditory function and disease progression (2).Unlike prior studies that focused on K^+ monitoring in interstitial fluid, transdermal applications, or the brain (3, 4), this system addresses a critical need for real-time monitoring of K^+ fluctuations, providing valuable insights into both physiological and pathological changes within the inner ear.

A 50 µm copper wire was used as the substrate for both the working electrode (WE) and RE. For the WE, a palladium layer was deposited to enhance surface roughness, followed by electrochemical polymerization of PEDOT/PSS[1], which served as an ion-to-electron transducer. A potassium-selective membrane was then applied to enable ion selectivity toward K^+. To fabricate the RE, the copper wire was coated with a silver layer and further chlorinated using HCl/KCl solution to make Ag/AgCl RE. A reference membrane was then applied to ensure stable performance across varying ionic environments (Fig.1a). The final sensor assembly consisted of two miniaturized electrodes (WE and RE) designed to fit within the confined structure of the cochlea.

After surface characterization, extensive benchtop validation confirmed the performance of the sensor (Fig.1b-f), demonstrating high sensitivity (~52.8 mV/dec), a broad linear range (10^{-5}–10^{-1} mol/L), a limit of detection of $10^{-5.16}$ mol/L, strong selectivity coefficients (−2.62 for Na^+, −4.10 for Mg^{2+}, and −3.85 for Ca^{2+}) (Table1), and excellent stability over two months. Additional experiments using artificial perilymph validated the device's selectivity under physiologically relevant ionic conditions, confirming minimal interference from interfering ions.

To evaluate in vivo functionality, the biosensor was implanted in the guinea pig's cochlea from dorsal and ventral approaches. Following the application of 500 mM KCl at the cochlear base, the sensor detected a rapid increase in potential, indicating elevated K^+ levels. This response plateaued for approximately 15 minutes before gradually returning to baseline within 28 minutes, likely due to cerebrospinal fluid influx via the cochlear aqueduct after cochlear perforation, confirming the sensor's responsiveness and ability to dynamically track ionic changes in vivo.

[1] 3,4-ethylenedioxythiophene / poly (4-styrenesulfonic acid) solution

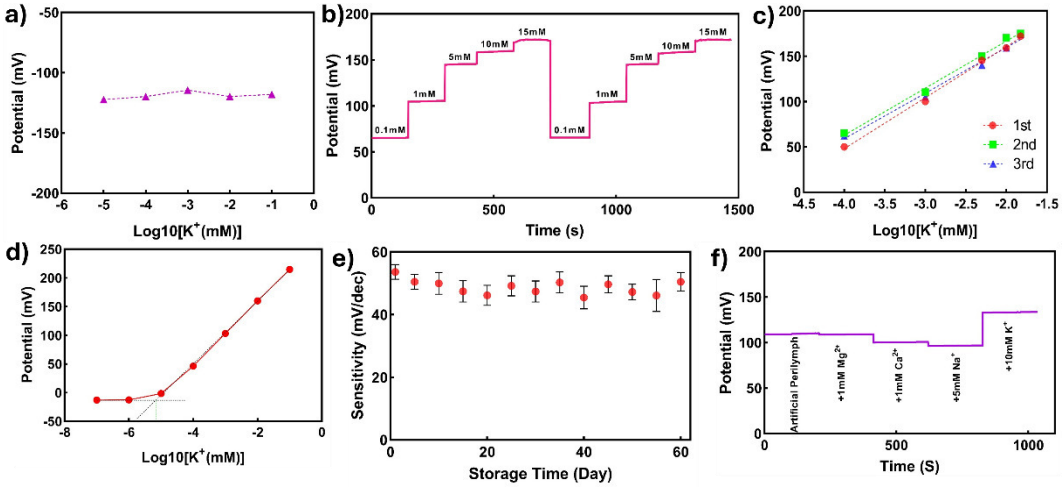

Figure 1: a) Potential stability of the RE. Characterization of the WE: b) Repeatability, c) Sensitivity, d) Linear detection range, e) Long-term stability, and f) Selectivity against interfering ions.

Ion	Log of selectivity coefficient
Na^{+}	-2.62±0.1
Mg^{2+}	-4.10±0.03
Ca^{2+}	-3.85±0.0.6

Table1: Selectivity coefficients of the proposed potassium sensor determined using the fixed interference method.

REFERENCES

[1] D. V. Lindberg and H. K. H. Lee, “Optimization under constraints by applying an asymmetric entropy measure,” *J. Comput. Graph. Statist.*, vol. 24, no. 2, pp. 379–393, Jun. 2015.
[2] M. S. MacNealy, Strategies for Empirical Research in Writing. Boston, MA: Allyn and Bacon, 1999.
[3] J. H. Watt and S. A. van den Berg, Research Methods for Communication Science. Boston, MA: Allyn and Bacon, 1995.
[4] S. Kleinmann, “The reciprocal relationship of workplace culture and review,” in Writing in the Workplace: New Research Perspectives, R. Spilka, Ed. Carbondale, IL: Southern Illinois University Press, 1993, pp. 56–70.

DOI 10.5162/eurosensors2026/Mo–SMD–02

Enhanced Split-Ring Resonator Sensing Platform for Gas Monitoring in Medical Applications

David Bailey[1], Moritz Hitzemann[1], Christian Thoben[1], Tobias Hennig[2], Erik Rohloff[2], Andreas Schneider[2], Andreas Schaate[2], Stefan Zimmermann[1]
[1] Leibniz University Hannover, Institute for Electrical Engineering and Measurement Technology, Hannover, Germany
[2] Leibniz University Hannover, Institute of Inorganic Chemistry, Hannover, Germany
Correspondence E-Mail: david.bailey@geml.uni-hannover.de

Summary:
Split-Ring resonators (SRR) are simple electric structures that can be used for a variety of sensing applications. In this contribution, we focus on their use in medically relevant monitoring systems, and present multiple improvements that make it feasible to use SRRs in patient safety and occupational hazard monitoring during surgeries under anesthesia.

Keywords: Split-Ring Resonator, gas sensing, occupational exposure monitoring, anesthesia safety

Motivation

The detection of very low concentrations of specific compounds is a critical component of many environmental monitoring, safety and security and medical applications. One such application lies in the protection of patients in so-called trigger-free anesthesia, for which exposure limits of below 5 ppm_v of the anesthetic gasses must be observed to avoid malignant hyperthermia [1]. Another application relates to the increasing occupational safety concerns of the long term effects of anesthetic gasses [2]. Monitoring such low concentrations of anesthetic gasses requires an especially sensitive and fast sensor. SRRs can provide such highly sensitive sensor technology, benefitting from simple, low-cost construction and high flexibility, allowing them to be used in a multitude of applications [3–5]. By themselves, however, they are not suitable for selectively sensing volatile compounds in air. Multiple improvements, such as improving selectivity as well as faster data acquisition, need to be made to make SRRs feasible for these types of gas analyses.

Description of the new SRR methodology

Multiple improvements to the SRR sensor system have been made. Firstly, novel 3D split electrodes are used instead of the typical flat split, providing similar benefits to those presented in [6], while making use of cost-optimized and more easily accessible methods of fabrication.

Secondly, Metal-Organic Frameworks (MOFs) are applied to the sensitive region of the resonator. These provide flexible chemical binding sites [7,8], and thusly allow the SRRs to be used as sensitive and selective gas detectors.

Lastly, the use of our newly designed RF electronics provides a stand-alone solution to SRR handling and electronics, providing improved data acquisition speed and precision as well as thermal control.

Results

Through simulation models as well as experiments, an optimal height for the 3D printed electrodes was found that increases the SRR quality factor to approximately 200, a significant increase over bare PCB SRRs with a quality factor of around 40-80 [4], while also improving resonator sensitivity by optimizing the ratio between unwanted parasitic capacitance C_p and the beneficial split-capacitance C_{split}.

The MOF compound used, a UiO-66 MOF, also proved capable of detecting anesthetic gas concentrations in the low ppm_v region with an integrating sensor behavior, making it highly suitable for the long-term monitoring of occupational exposure. Limits of detection as low as 1 ppm_v are feasible.

Finally, the constructed tracking electronics were able to improve over existing solutions. A dedicated RF mixing path with analog frontend and 24-bit ADC provides fast data acquisition of the S_{21} parameter, with a sampling rate of 1 kSps, sub-hertz frequency resolution up to 1.2 GHz, and an amplitude resolution of below 0.01 dB. This highly sensitive data readout is combined with an on-board data processing system and

specialized software algorithms for fast resonance tracking, providing a tracking precision of below 100 Hz while tracking resonance changes at 50 Sps. This makes it possible to observe sudden and small changes in resonator behavior, making it suitable for precision monitoring applications. It also includes thermal control to keep the SRR temperature at a set level, making it a complete stand-alone solution for SRR management and readout. A plot of the step-response of the new sensor platform is shown in Figure 1. Figure 2 shows a picture of the constructed measurement electronics with annotations to the various highlights and capabilities.

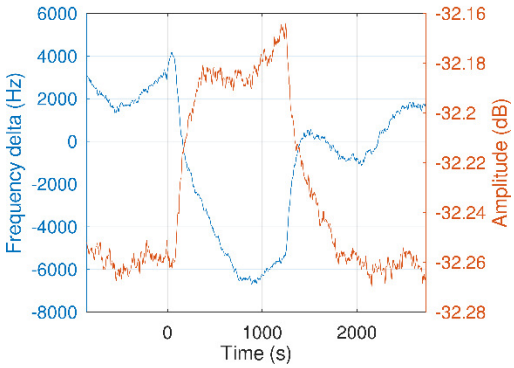

Figure 1: Plot of a measurement using the new electronics with a UiO-66-coated SRR, showing the response to a 500 ppm$_v$ step change in water concentration in dry, synthetic air at 0s. Both amplitude and frequency show a notable shift.

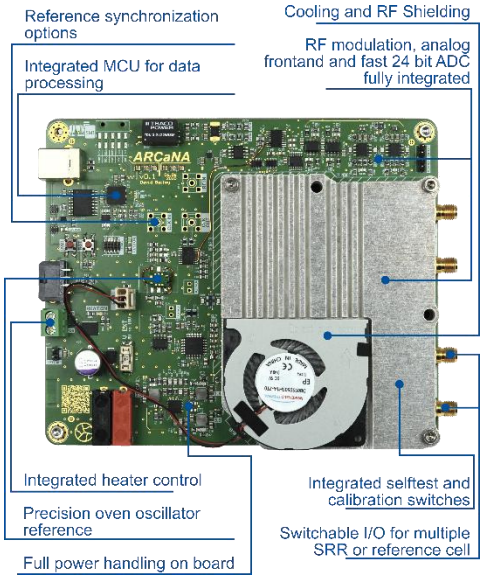

Figure 2: A picture of the completed electronics, with annotations of various highlights.

Acknowledgements

Funded by the Deutsche Forschungsgemeinschaft (DFG, German Research Foundation)—511400779.

References

[1] H. Rüffert, B. Bastian, D. Bendixen, T. Girard, S. Heiderich, et al. (2021): Consensus guidelines on perioperative management of malignant hyperthermia suspected or susceptible patients from the European Malignant Hyperthermia Group, *Br. J. Anaesth.* **126**, 120–130; doi: 10.1016/j.bja.2020.09.029.

[2] K. M. Souza, L. G. Braz, F. R. Nogueira, M. B. Souza, L. F. Bincoleto, et al. (2016): Occupational exposure to anesthetics leads to genomic instability, cytotoxicity and proliferative changes, *Mutat. Res.* **791-792**, 42–48; doi: 10.1016/j.mrfmmm.2016.09.002.

[3] K. J. Dehning, M. Hitzemann, S. Zimmermann (2024): Split-ring resonator with interdigital Split electrodes as detector for liquid and ion chromatography, *Sens. Bio-Sens. Res.* **44**, 100645; doi: 10.1016/j.sbsr.2024.100645.

[4] T. Reinecke, J.-G. Walter, T. Kobelt, A. Ahrens, T. Scheper, et al. (2018): Design and evaluation of split-ring resonators for aptamer-based biosensors, *J. Sens. Sens. Syst.* **7**, 101–111; doi: 10.5194/jsss-7-101-2018.

[5] K. J. Dehning, M. Hitzemann, S. Fisahn, S. Zimmermann (2019): Split-ring resonator: A new detector in liquid chromatography, *Dresdner Sensor-Symposium*, 167–171; doi: 10.5162/14dss2019/P2.02.

[6] A. Salim, S. Ghosh, S. Lim (2018): Low-Cost and Lightweight 3D-Printed Split-Ring Resonator for Chemical Sensing Applications, *Sensors (Basel, Switzerland)* **18**; doi: 10.3390/s18093049.

[7] M. Schulz, A. Gehl, J. Schlenkrich, H. A. Schulze, S. Zimmermann, et al. (2018): A Calixarene-Based Metal-Organic Framework for Highly Selective NO2 Detection, *Angew. Chem. Int. Ed.* **57**, 12961–12965; doi: 10.1002/anie.201805355.

[8] J. F. Olorunyomi, S. T. Geh, R. A. Caruso, C. M. Doherty (2021): Metal-organic frameworks for chemical sensing devices, *Mater. Horiz.* **8**, 2387–2419; doi: 10.1039/D1MH00609F.

DOI 10.5162/eurosensors2026/Mo–SMD–03

Engineering Spatially Patterned Selective Membranes for Scalable Multiplex Electrolyte Sensors

Azadeh Nilghaz[1], *Citsabehsan Devendran*[2], *and Nicolas H. Voelcker*[*1,3]
[1] *Monash Institute of Pharmaceutical Sciences, Monash University, Parkville, Victoria 3052, Australia*
[2] *Proton Intelligence Australia Pty Ltd, Clayton, VIC 3168, Australia*
[3] *Melbourne Centre for Nanofabrication Victorian Node of the Australian National Fabrication Facility, Clayton, Victoria 3168, Australia*
Corresponding Author's e-mail address: nicolas.voelcker@monash.edu

Summary:

This work presents a multiplex wearable sodium-potassium sensor based on spatially patterned ion-selective membranes (ISMs) integrated onto miniaturized microelectrodes. Using masked airbrushing (AB) and doctor blading (DB) techniques, ISMs were precisely deposited onto closely spaced electrode sites, enabling scalable fabrication of compact multiplex devices. The sensors show a near-Nernstian sensitivity of 54.4 ± 0.6 mV per decade, a rapid response, good selectivity against interfering ions, and stable performance over extended operation. Linear detection ranges of 50-200 mM for sodium and 2-8 mM for potassium were achieved, with negligible pH sensitivity from pH 5.5 to 8. This platform offers strong potential for continuous electrolyte monitoring in wearable and point-of-care applications.

Keywords: wearable sensor; multiplex sensing; ion-selective membranes; sodium-potassium detection

Background, Motivation and Objective

Continuous monitoring of electrolytes is essential for maintaining physiological homeostasis and for managing disorders related to hydration, kidney function, and cardiovascular health [1]. Electrolytes such as potassium and sodium play key roles in nerve signalling, muscle contraction, fluid balance, and cardiac activity, and even small deviations from normal levels can lead to serious clinical complications [1]. For example, hyperkalemia affects more than 3.7 million people in the United States and is strongly associated with chronic kidney disease and life-threatening cardiac events [2]. In this context, wearable electrochemical sensors have emerged as promising platforms for real-time and non-invasive electrolyte monitoring in biofluids such as sweat and interstitial fluid [3].

Although wearable electrolyte sensors show considerable potential, their translation into practical devices is still limited by challenges in scalable fabrication and reliable multiplex sensing. Wearable systems must be compact, flexible, and lightweight, which requires sensing electrodes to be miniaturised to very small dimensions. However, as electrode dimensions decrease, the accurate and reproducible deposition of ISMs, which are essential for ion recognition and sensing performance, becomes increasingly difficult [4]. This challenge is further amplified in multiplex sensor configurations, where multiple ISMs with different compositions and formulations (F1 and F2) must be patterned precisely on adjacent electrodes without overlap, cross-contamination, or loss of reproducibility.

The objective of this study is to develop multiplexed electrolyte sensors based on spatially patterned ISMs for scalable manufacturing. Specifically, this study aims to establish a fabrication strategy that enables precise and reproducible deposition of multiple ISMs onto miniaturised electrode arrays, allowing simultaneous detection of different electrolytes within a compact wearable platform. By addressing the fabrication limitations associated with multiplex ISM integration, this work seeks to support the development of scalable and high-performance wearable sensors for continuous electrolyte monitoring.

Description of the New Method or System

In this work, we developed a dual gold electroplated working electrode platform for multiplexed sodium-potassium sensing based on a conductive polymer as a transducer and spatially patterned ISMs. A common reference electrode was also designed to provide a stable potential for simultaneous multiplex measurements. ISM deposition was performed using spatial patterning strategies, including masked airbrushing (AB) and doctor blading

(DB), to achieve controlled and selective deposition of membrane formulations onto predefined electrode regions with well-defined dimensions and thicknesses. The device incorporates microfabricated electrodes with edge-to-edge spacing as low as 300 µm, together with a shared Ag/AgCl reference electrode in a compact architecture suitable for wearable applications. These patterning approaches enable precise membrane placement, minimise cross-contamination between adjacent sensing sites, and provide a promising route toward scalable fabrication of multiplex wearable electrolyte sensors.

Results

The developed sodium- and potassium-selective membranes were successfully deposited onto the microelectrode array to produce a multiplex wearable sensing platform capable of simultaneous detection of these two clinically relevant electrolytes. Spatial patterning enabled selective localisation of the sodium- and potassium-selective membranes onto closely spaced electrode sites while maintaining separation between adjacent sensing regions, demonstrating the suitability of the proposed fabrication approach for multiplex sensor integration at the microscale.

The resulting sensors with both deposition methods and different compositions exhibited near-Nernstian potentiometric performance, with an average sensitivity of 54.4±0.6 mV per decade (Fig.1) [5]. The potassium sensor showed a linear response over the concentration range of 2-8 mM, while the sodium sensor operated linearly from 50-200 mM, covering concentration ranges relevant to physiological monitoring. In addition, the sensors were evaluated over a pH range of 5.5 to 8 and showed no significant pH dependence within this interval, confirming that the potentiometric response was primarily governed by the target ion activity rather than changes in sample pH.

The platform also demonstrated rapid sensor behaviour, with an immediate change in potential observed upon analyte addition, indicating fast response to concentration variations. Over extended operation, the sensors maintained stable performance for 72 h with an average drift of only 0.32 mV h^{-1}. Good selectivity was also observed against common interfering ions, including magnesium, lithium, and ammonium, confirming the ability of the ion-selective membranes to distinguish the target ions in complex electrolyte environments.

Importantly, the multiplex platform retained stable potentiometric performance for up to one week, supporting its potential for continuous electrolyte monitoring in wearable applications. Overall, these results demonstrate that the proposed sensing platform combines miniaturised electrode architecture, precise membrane patterning, and reliable analytical performance, providing a practical pathway toward the scalable fabrication of multiplex wearable electrolyte sensors for continuous health monitoring and point-of-care diagnostics.

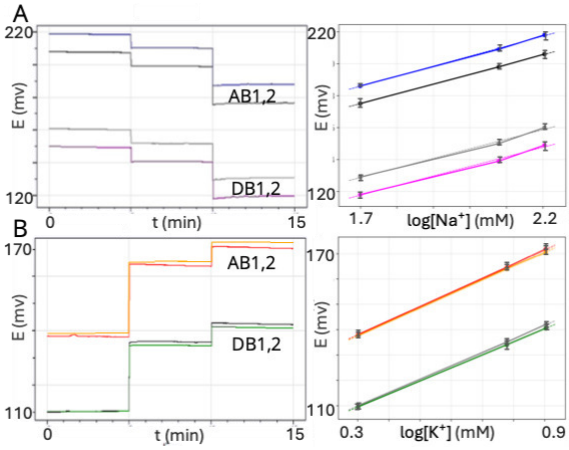

Fig. 1. Potentiometric response of the multiplex Na^+/K^+ sensor, fabricated using different deposition methods and formulations (AB1, AB2, DB1, and DB2), to mixed ion solutions with inversely varied Na^+ and K^+ concentrations. (A) The Na^+ concentration was stepped from 160 to 120 to 50 mM, while (B) the K^+ concentration was increased from 2 to 6 to 8 mM KCl, to evaluate sensor behaviour in the presence of both target ions.

References

[1] A. A. Deabes, A. Essa, Fluid and electrolyte imbalance in renal dysfunction, *Anaesthesia & Intensive Care Medicine,* 25(5), 316-319 (2024).

[2] K. A. Betts, J. M. Woolley, F. Mu, E. McDonald, W. Tang, E. Q. Wu, The prevalence of hyperkalemia in the United States, *Current Medical Research Opinion,* 34(6), 971-978 (2018).

[3] I. L. Salih, A. H. Alshatteri, K. M. Omer, Role of wearable electrochemical biosensors in monitoring renal function biomarkers in sweat: a review, *Analytical Sciences,* 40(11), 1969-1986 (2024).

[4] C. Li, Z. Li, T. Nguyen, S. Ingebrandt, X. T. Vu, Real-time and multiplexed detection of sodium and potassium ions using PEDOT:PSS OECT microarrays integrated with ion-selective membranes, *Electrochimica Acta,* 507, 145111 (2024).

[5] S. Liu, T. Yin, Z. Li, J. Wang, Potentiometric time resolved chronopotentiometric sensing for an all solid state ion selective electrode based on MXene/MWCNTs as solid contact, *Sensors Actuators B: Chemical,* 405, 135269 (2024).

DOI 10.5162/eurosensors2026/Mo–SMD–04

High-Sensitivity Electrochemical Detection of Point Mutations: Optimization of *BRAF* V600E Analysis from Liquid Biopsy

Ludmila Moráňová[1], Karolína Itterheimová[1, 2], Johana Strmisková[1, 2], Martin Bartošík[1]
[1] Research Centre for Applied Molecular Oncology, Masaryk Memorial Cancer Institute, Zluty Kopec 7, 656 53 Brno, Czech Republic
[2] National Centre for Biomolecular Research, Faculty of Science, Masaryk University, Kamenice 5, 625 00 Brno, Czech Republic
karolina.itterheimova@mou.cz

Summary:
This study presents electrochemical approaches for detecting the *BRAF* V600E mutation in circulating tumor DNA (ctDNA) from liquid biopsies. The V600E mutation was successfully identified in clinical samples using SNP-specific primers in Loop-mediated isothermal amplification (LAMP). Additionally, a novel strategy employing CRISPR/Cas12a cleavage to selectively degrade wild-type (WT) sequence was evaluated to enhance mutation-specific detection.

Keywords: *BRAF*, V600E point mutation, ctDNA, liquid biopsy, electrochemistry

Background

The *BRAF* proto-oncogene encodes serine/threonine protein kinase, a key component of the MAPK/ERK signaling pathway. BRAF mutations drive tumorigenesis; specifically, the V600E mutation is present in up to 50% of melanoma and 10% of metastatic colorectal carcinomas and is associated with poorer prognosis and treatment response. Accurate detection is therefore essential for optimizing personalized treatment.

Since ctDNA concentrations are typically low, highly sensitive detection methods are required. This challenge can be addressed by combining isothermal amplification techniques (IATs) with electrochemical (EC) detection. This approach offers a low-cost, simple, and highly selective method for point mutation detection [1].

IATs enable nucleic acid amplification at constant temperatures using specialized polymerases with strand-displacement activity, providing simplicity and rapidity for point-of-care (POC) diagnostics. Furthermore, EC detection enhances the method's potential for integration into fast, simple and cost-effective instrument in clinical diagnostics [2].

Methods

The first approach for point mutation detection utilizes single nucleotide polymorphism (SNP)-specific primers in Loop-mediated isothermal amplification (LAMP). These primers were designed to selectively recognize the V600E variant of the *BRAF* gene while excluding the wild type (WT) sequence (Fig. 1). This ensures that only mutant sequences will be amplified for subsequent endpoint detection.

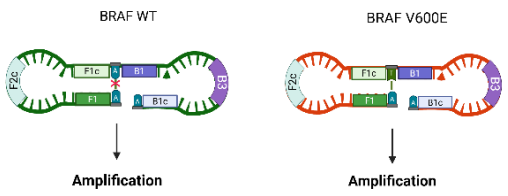

Fig. 1. Principle of SNP-specific recognition of WT and V600E mutation of BRAF gene

Second approach relies on CRISPR/Cas12a cleavage of the WT sequence. The guide RNA (gRNA) was designed to specifically recognize the WT *BRAF* sequence, leading to its degradation while keeping the mutated sequence intact and allowing further recombinase-polymerase (RPA) amplification and detection (Fig. 2).

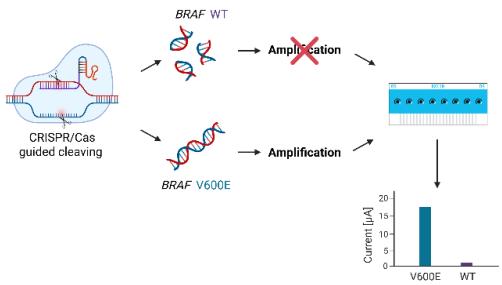

Fig. 2. Principle of CRISPR/Cas12a guided detection of BRAF V600E mutation

In both approaches, biotin-labeled dUTPs alongside classical dTTP are randomly incorporated into newly synthesized strands. Additional specificity is achieved by mutation-specific locked nucleic acid (LNA) capture probes attached to magnetic beads (MBs), enabling sample washing and preconcentration. The incorporated biotin-dUTPs are subsequently conjugated with a streptavidin peroxidase polymer (SPP) for EC detection.

The EC measurement is performed on screen printed carbon electrodes (SPCE), where the prepared magnetic beads are loaded and covered with hydroquinone (HQ) and H_2O_2 substrate. During measurement, H_2O_2 is reduced while HQ is oxidized to benzoquinone; the subsequent reduction of benzoquinone back to HQ generates changes in electric current measured via amperometry (Fig. 3).

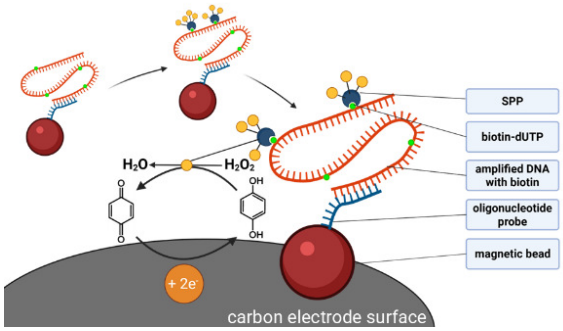

Fig. 3. Electrochemical detection of nucleic acids on screen printed carbon electrode

Results and Discussion

SNP-specific LAMP combined with EC detection was successfully applied to detect the *BRAF* V600E mutation in clinical liquid biopsy samples. Fig. 4 shows the analysis of 27 blood serum samples, which successfully distinguished mutated from WT samples. These results correspond perfectly with prior validation via sequencing.

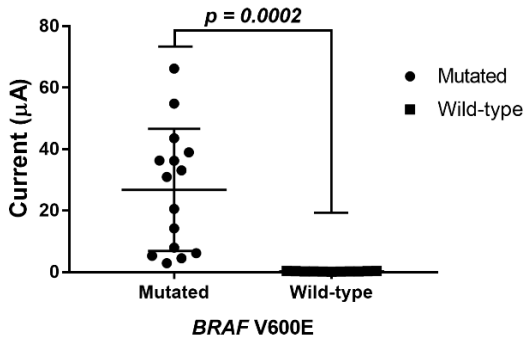

Fig. 4. EC detection of 27 blood samples successfully distinguishing WT and BRAF V600E mutated samples

The CRISPR-based approach was tested on cell lines under several conditions. Fig. 5 demonstrates performance across different Cas12a:gRNA ratios (excess Cas12a, equimolar, and excess gRNA). The results indicate that an excess of gRNA over Cas12a enzyme significantly improves the ability to distinguish between mutated and WT DNA samples.

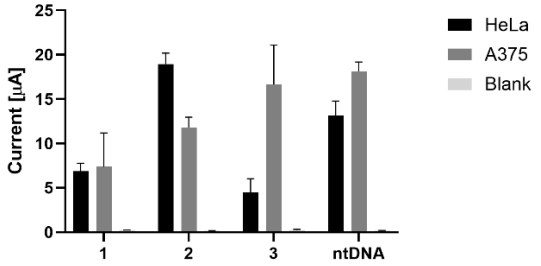

Fig. 5. Electrochemical detection of BRAF V600E mutation in cell lines (HeLa – homozygote WT; A375 – homozygote mutant) using CRISPR approach in various ratios of Cas12a and gRNA – 1: excess of Cas12a; 2: equimolar ratio; 3: excess of gRNA

Conclusion

This study validates two electrochemical platforms for sensitive *BRAF* V600E detection. The LAMP-based approach demonstrates high clinical accuracy, while the CRISPR system offers a promising, selective alternative. Together, these methods provide a rapid, cost-effective framework for point-of-care diagnostics and personalized oncology monitoring.

References

[1] *L.Moranova, J.Strmiskova, K.Ondraskova, M.Bardelcik, M.Cwik, I.Kiss, R.Hrstka, M.Bartosik, Electrochemical Detection of BRAF V600E Mutation in a Liquid Biopsy Format: LAMPing the Way to an Improved Diagnostics and Treatment. Adv. Mater. Technol.2025, 10, 2401404.* https://doi.org/10.1002/admt.202401404

[2] *Ondraskova, K., Sebuyoya, R., Moranova, L. et al. Electrochemical biosensors for analysis of DNA point mutations in cancer research. Anal Bioanal Chem 415, 1065–1085 (2023).* https://doi.org/10.1007/s00216-022-04388-7

Acknowledgements

The financial support of the Czech Health Research Council (No. NU21-08-00078 and NU21-09-00031), project SALVAGE (OP JAC; reg. no. CZ.02.01.01/00/22_008/0004644) – co-funded by the European Union and by the State Budget of the Czech Republic, BBMRI.cz (No. LM2023033) and MH CZ – DRO (MMCI, 00209805) is greatly acknowledged.

DOI 10.5162/eurosensors2026/Mo–SMD–05

Online Bacterial Headspace Sampling Setup for Medical Microbiology Diagnostics with Sensors

Mehmet Berk Bilgin[1], Norma Toccalino[1], Emma Slack[2,3,4], Adrian Egli[5], Andreas Güntner[1]
[1] Human-centered Sensing Laboratory, D-MAVT, ETH Zürich, Zürich, Switzerland
[2] Laboratory for Mucosal Immunology, Department of Health Sciences and Technology, ETH Zurich, Zurich, Switzerland
[3] Botnar Institute of Immune Engineering, Basel, Switzerland
[4] Sir William Dunn School of Pathology, University of Oxford, Oxford, UK
[5] Institute of Medical Microbiology, University of Zurich, Zurich, Switzerland
andreas.guentner@hsl.ethz.ch

Summary:
We introduce a headspace sampling setup for longitudinal monitoring of volatile emissions from microbial species that is compatible with various sensor methodologies. The setup was validated using mass spectrometry and chemoresistive sensors, showing reliable extraction with gas standards and *Escherichia coli* isolates over 24 h. Results show bacterial metabolic activity is mirrored in headspace volatile concentrations, with acetaldehyde serving as a key proliferation indicator. This proof-of-concept system enables continuous monitoring for rapid pathogen detection and antibiotic susceptibility evaluation.

Keywords: Volatilomics, Headspace sampling, Gas sensing, Microbiological sensing, Novel diagnostics.

Background, Motivation and Objective

Bacterial volatilome contains invaluable information on the bacterial metabolism that can be exploited to identify and characterize the organism. With the emergence of high-resolution analytical techniques like gas chromatography–mass spectrometer [1], ion mobility spectrometer [2], and secondary electrospray ionization spectrometer [3], quantitative analysis of headspace biomarkers has become feasible, and promising results were obtained for the identification of the bacteria [4] and the assessment of the antimicrobial resistance (AMR) risk [1]. Using sensitive and selective [5, 6] sensors, compact devices for volatilome analysis can be developed for rapid diagnostics. A crucial aspect of this analysis is the sampling method of the bacterial headspace. However, not only was the importance of sampling underestimated in the literature, but also the differences in sampling tools employed limited the direct comparability between studies. Proposed sorption methods are dependent on the sorptive material selection[7] and they can only perform integrated timepoint measurements. Employed commercial devices are not suitable for longitudinal monitoring[8], and custom-made solutions do not fully address the requirements for a reliable volatilome analysis[9]. The ideal method should be able to provide (i) robust sampling control in terms of extracted volume and humidity for (ii) longitudinal monitoring with (iii) incubation conditions to account for the growth phase differences, (iv) online calibration for accurate volatilome quantification, and (v) controlled dilution of the sampled volume to accommodate dynamic range limitations. None of the proposed approaches provide such a standardized solution. Furthermore, this mismatch of volatilome sampling rendered analysis results incomparable, making the comprehensive understanding of the relationship between the volatilome and microbial metabolism an open challenge. We aim to close this critical gap between volatilome and microbial functions by proposing a standardized tool for controlled headspace volume extraction for both mass spectrometric and chemoresistive sensor measurements. The presentation starts with the essential factors for headspace sampling before introducing the setup with the corresponding design features to satisfy a representative sampling that can be used both for biomarker investigations and diagnostic sensing applications.

Description of the System

We defined the requirements for a reproducible volume extraction in bacterial volatilomics studies and designed a microbiological sample headspace sampling system to meet these

requirements (Figure 1). The setup is divided into two parts, the main line and the sampler line, to maintain a baseline flow for the analytical tool while precisely controlling the sampling, and to enable dilution of the extracted volume for dynamic range adjustments with limited humidity fluctuations. The flow rates and the flow humidity levels are controlled by the mass flow controllers; sample volume is extracted by a solenoid valve. The setup is enclosed and heated to 37 °C to deliver optimal incubation conditions to the microbiological samples. We have validated the approach with mass spectrometry using analyte gas standards. The sampling parameters were optimized for longitudinal analysis with target volatile organic compounds (VOCs). *In vitro* operation was validated with *Escherichia coli* isolates.

Results

Measurements with gas standards confirm reliable volume extraction, as measured down to 50 ppb. The dilution is shown to be an essential component of the volatilome analysis, for analytical tool operational range can be a limiting factor for higher concentrations. The sampling is validated using VOCs from various chemical classes, namely ketones, alcohols, aldehydes, and aromatics. The key aspects of headspace sampling are discussed through preliminary *Escherichia coli* measurements on MHB agar plates (Figure 2). We demonstrate that different classes of VOCs can be measured and bacterial proliferation can be monitored by quantifying the headspace VOC concentrations over the incubation period. The acetaldehyde emerged as the main indicator of bacterial proliferation in our conditions, as early as 4 h after inoculation.

Conclusion:

The versatile system is tailored to accurately sample the headspace of the bacterial culture while providing optimal incubation conditions for longitudinal monitoring. We validated our proof-of-concept device with demonstrative bacteria measurements; it enables standardized biomarker studies, as well as point-of-care testing by ensuring reproducible sampling.

Figures

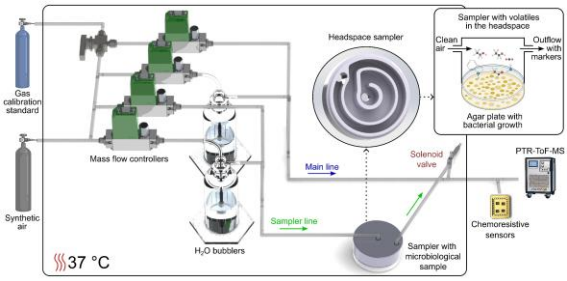

Fig. 1. 3D rendering of the headspace sampling setup

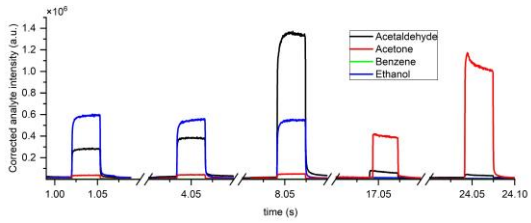

Fig. 2. Headspace concentrations of selected molecules from Escherichia coli inoculated on MHB agar.

References

[1] Q. Ding, W. Zhang, Y. Guo, J. Wang, H. Chen, L. Zhang, β-Lactamase Sensitive Probe for Rapid Detection of Antibiotic-Resistant Bacteria with Gas Chromatography-Tandem Mass Spectrometry, Analytical Chemistry 95, 6098–6106 (2023); doi: 10.1021/acs.analchem.3c00381.

[2] F. Li, S. Gu, C. Zhao, Y. Zheng, J. Zhu, L. Hu, Y. Hang, The Detection and Utilization of Volatile Metabolomics in Klebsiella Pneumoniae by Gas Chromatography-Ion Mobility Spectrometry, Scientific Reports 14, 26122 (2024); doi: 10.1038/s41598-024-77746-3

[3] H. Li, J. Zhu, Differentiating Antibiotic-Resistant Staphylococcus Aureus Using Secondary Electrospray Ionization Tandem Mass Spectrometry, Analytical Chemistry 90, 12108–12115 (2018); doi: 10.1021/acs.analchem.8b03029

[4] R. Vangravs, L. Mežmale, D. Ślefarska-Wolak, E. Dauss, C. Ager, et al. Volatilomic signatures of different strains of Helicobacter pylori, Helicobacter 29, e13064 (2024); doi:10.1111/hel.13064

[5] A.T. Güntner, M. Wied, N.J. Pineau, S.E. Pratsinis, Rapid and Selective NH3 Sensing by Porous CuBr, Advanced Science 7, 1903390 (2020); doi: 10.1002/advs.201903390

[6] I.C. Weber, H.P. Braun, F. Krumeich, A.T. Güntner, S.E. Pratsinis, Superior Acetone Selectivity in Gas Mixtures by Catalyst-Filtered Chemoresistive Sensors, Advanced Science 7, 2001503 (2020); doi: 10.1002/advs.202001503

[7] F.A. Franchina, G. Purcaro, A. Burklund, M. Beccaria, J.E. Hill, Evaluation of different adsorbent materials for the untargeted and targeted bacterial VOC analysis using GC×GC-MS, Analytica Chimica Acta 1066, 146-153 (2019); doi: 10.1016/j.aca.2019.03.027

[8] M. Trincavelli, S. Coradeschi, A. Loutfi, B. Söderquist, P. Thunberg, Direct Identification of Bacteria in Blood Culture Samples Using an Electronic Nose, IEEE Transactions on Biomedical Engineering 57, 2884-2890 (2010); doi: 10.1109/TBME.2010.2049492

[9] J. Lan, G. Greter, B. Streckenbach, B. Wanner, M. Arnoldini, R. Zenobi, E. Slack, Non-invasive monitoring of microbiota and host metabolism using secondary electrospray ionization-mass spectrometry, Cell Reports Methods 3, 100539 (2023); doi: 10.1016/j.crmeth.2023.100539

DOI 10.5162/eurosensors2026/Mo−SMD−06

Electrochemical and Electrochemiluminiscence *in vitro* Detection Methods of a Human Cytomegalovirus in Oncology Patients

Ludmila Moranova[1], Aneta Fried[1,2], Karolina Itterheimova[1,2], Michal Hendrych[3], Martin Bartosik[1]
[1] RECAMO, Masaryk Memorial Cancer Institute, Brno, Czech Republic,
[2] NCBR, Faculty of Science, Masaryk University, Brno, Czech Republic
[3] 1st Dept. of Pathology, St. Anne's Univ. Hospital and Faculty of Medicine, Masaryk University, Brno, Czech Republic
ludmila.moranova@mou.cz

Summary:

The study focuses on the detection of human cytomegalovirus (hCMV) in oncology patients, particularly in glioblastoma, and its potential role in tumor biology. Electrochemical (EC) and electrochemiluminescence (ECL) methods were developed and optimized in combination with different amplification techniques (PCR, RPA, and LAMP). The results showed that EC detection achieved a lower limit of detection than ECL, while LAMP provided the strongest signal in the shortest time. A total of 112 clinical samples were analyzed for viral DNA and RNA to identify suitable biomarkers.

Keywords: human cytomegalovirus, screen-printed carbon electrode, electrochemical bioassay, isothermal amplification technique, cancer biomarker.

Introduction

Human cytomegalovirus (hCMV) is a widespread herpesvirus proposed to exert oncomodulatory effects on several cancers by influencing cell proliferation, inflammation, and immune evasion [1]. hCMV DNA and proteins have been detected in tumors, such as glioblastoma and colorectal cancer, suggesting a possible role in tumor biology. However, detection rates in clinical samples vary dramatically from 0 to 100%, reflecting both biological heterogeneity and methodological differences [2]. Standard detection methods, such as immunohistochemistry, qPCR, and sequencing, provide good sensitivity, but each has limitations, including inconsistent antibody performance, costly instrumentation, and limited suitability for routine screening in point-of-care settings.

Methodology

Here, we address these diagnostic issues by developing new electrochemical (EC) and electrogenerated chemiluminescence (ECL) bioassays that offer attractive alternatives, providing rapid, simple, and low-sample-consumption approaches that are well-suited for point-of-care testing. In this study, we optimized and compared EC and ECL bioassays coupled with various amplification strategies, including PCR, recombinase polymerase amplification (RPA), and loop-mediated isothermal amplification (LAMP), for the detection of hCMV in real samples.

Results

First, we developed and tested three amplification strategies and combined them with EC or ECL readouts. The EC approach achieved a lower LOD and, although its linear range is narrower than that of ECL, EC appears to be a more suitable method (Fig. 1).

Amperometric EC readout combined with PCR or RPA showed high specificity, reliably distinguishing hCMV-infected from uninfected cells and demonstrating its potential for use in tumor tissue analysis. In terms of signal intensity versus amplification time, LAMP showed the best performance but suffered from nonspecific amplification. Surprisingly, the ECL assay failed to detect viral DNA under our conditions [3].

Clinical samples study

After the protocol optimization phase, a set of 112 glioblastoma IDH wild-type samples was tested for the presence of viral DNA and RNA (Fig. 2). In this study, we aim to compare different genes and their RNA products to determine which can serve as the best biomarker. DNA positivity shows the presence of the virus and

RNA can prove their activity and help with a better understanding of viral activity and its oncomodulation role in the tumor microenvironment.

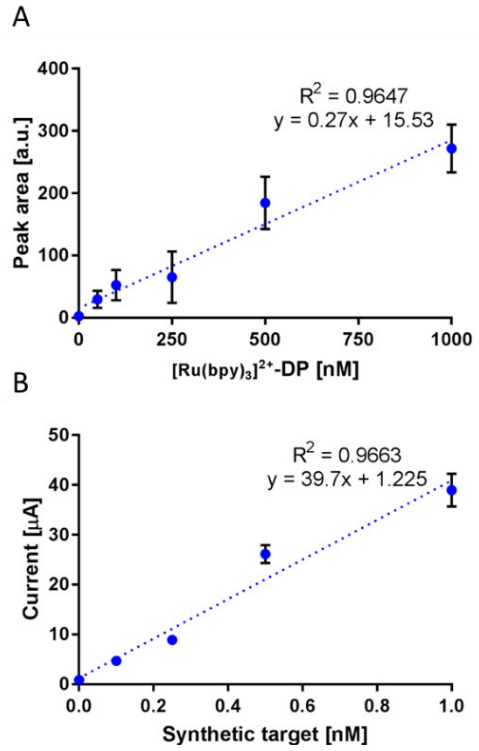

Fig. 1. Linear range of developed the methods. A: ECL of [Ru(bpy)3]2+-DP measured on a photodiode with 100× amplification in the range of 1–1000 nM (LOD = 8.88 nM). B: EC of synthetic target in the linear range of 0 to 1 nM (LOD = 0.01 nM).

Our electrochemical results are compared with those obtained using a commercial kit (IVDF certified) and RT-PCR.

Conclusion

Given the specific aim of detecting viral nucleic acids rather than proteins or antibodies, diagnostic tools for oncology patients remain limited. Our results contribute to clarifying the presence and representation of hCMV in glioblastoma. To our knowledge, no previous study has systematically applied and compared a broad range of both established and newly developed technical approaches for this purpose.

Acknowledgment

This research was funded by Czech Health Research Council (AZV No. NU23J-08-00006), Czech Science Foundation (No. 25-15990S), project SALVAGE (OP JAC; reg. no. CZ.02.01.01/00/22_008/0004644) – cofunded by the European Union and by the State Budget of the Czech Republic, MUNI/A/1843/2025, and MH CZ – DRO (MMCI, 00209805).

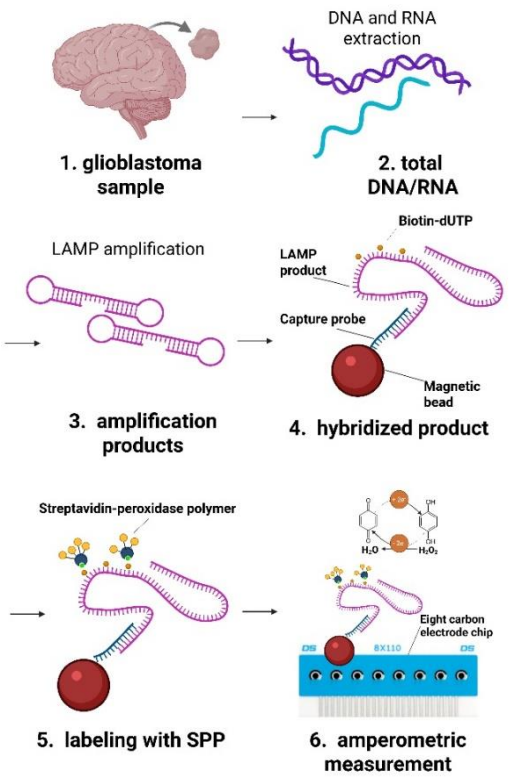

Fig. 2. Methodology scheme of the research method. (1.) Sample of glioblastoma is homogenized and used for either (2.) DNA or RNA extraction. (3.) NA is introduced into the LAMP amplification with biotin-dUTP. (4.) The amplified product with incorporated biotin-dUTP is hybridized on magnetic beads with a specific capture probe and (5.) labeled with streptavidin-peroxidase polymer. (6.) The final complex is measured on 8-electrode carbon chip with hydroquinone/hydrogen peroxide substrate.

References

[1] D. F. El Shazly, A. A. Bahnassey, et al.,Detection of Human Cytomegalovirus in Malignant and Benign Breast Tumors in Egyptian Women, Clin Breast Cancer 18, e629-e642 (2018); doi: 10.1016/j.clbc.2017.10.018

[2] I. Peredo-Harvey, A. Rahbar, et al.,Presence of the Human Cytomegalovirus in Glioblastomas—A Systematic Review, Cancers 13, 5051 (2021); doi: 10.3390/cancers13205051

[3] A. Fried, K. Itterheimova, et al.,Shining a light on viral detection: a comparative study of electrochemical and electrochemiluminescence techniques for human cytomegalovirus, Anal Bioanal Chem 418, 2823-2837 (2026); doi: 10.1007/s00216-026-06410-8

DOI 10.5162/eurosensors2026/Mo–SMD–07

A Data Management Platform for Early Diagnosis and Follow-Up of Human Diseases: Architecture Design, Development and Analysis

Michele Sansone[1], Jolanda Palmisani[1*], Alessia Di Gilio[1], Marirosa Rosaria Nisi[1], Lucia Pastore[1], Miriana Cosma Mazzola[1], Egidio De Benedetto[2], Gianluigi de Gennaro[1]*
[1] Department of Biosciences, Biotechnologies and Environment, University of Bari, via Orabona, 4, 70126, Bari, Italy
[2] Department of Electrical Engineering and Information Technologies, University of Naples Federico II, 80125, Naples, Italy
**co-first authors*
Corresponding Author's e-mail address: m.sansone24@phd.uniba.it

Summary

The growing application of sensor devices in the healthcare field is leading to the production of large datasets, whose effective management represents a critical challenge for current clinical processes. Although affected by high complexity, the heterogeneity of the collected data may enable healthcare professionals and researchers to extract relevant insights for the diagnosis and follow-up of diseases. Accordingly, this work proposes an integrated digital platform for the acquisition, management and analysis of multi-source clinical data, with the aim of improving healthcare and supporting patient treatment and monitoring.

Keywords: On-line breath analysis, Sensor technologies, Integrated data platform, Early Diagnosis, Telemedicine

Background, Motivation and Objective

The digital revolution in the healthcare system is redefining the way clinical data are collected, managed and interpreted [1]. The widespread adoption of electronic health records (EHRs) and sensor devices to detect and measure biomarkers in human biofluids has generated a large volume of clinical data (e.g., demographic and biometric information, diagnostic data, biomarkers and physiological signals) [2]. The use of target-analyte sensors in breath analysis represent a promising frontier for the diagnosis of several human diseases, due to their capability to detect and monitor the disease-related biomarkers pattern in a non-invasive and cost-effective way [3]. These devices enable the quantitative measurement of specific compounds in the exhaled breath, facilitating the identification of biomarkers associated with diseases such as lung cancer, myocardial infarction, and diabetes mellitus [4]. This wealth of information, combined with advances in computational methods, paves the way for new opportunities to support evidence-based decision-making [5].

A robust architecture is needed for the acquisition, management and analysis of data deriving from a variety of sensor devices and analytical platforms, bridging the gap between raw data and the healthcare professionals who need to interpret it [6]. Moreover, early diagnosis and long-term patient follow-up require scalable data management solutions and the integration of analytical pipelines that combine statistical methods and machine learning techniques, with the aim of supporting the clustering of diseases and continuous monitoring of healthcare conditions.

Based on these considerations, this work describes the design of a data management platform focused on early diagnosis and clinical follow-up. The clinical platform aims to integrate data from multiple sensor technologies (e.g., target analyte-sensors, multi-sensor array devices) and analytical platforms such as GC/MS platform for the chemical characterization of human breath. The platform is intended to be the 'space' where all the clinical data can be also matched with other physiological parameters (e.g., heart rate, blood pressure, respiratory rate) and environmental data (e.g., air quality data), in the view of providing a comprehensive overview of the patient's health status. In line with the principles of telemedicine and exposomics, the overall goal of this study is to provide healthcare professionals a flexible solution that optimizes diagnostic accuracy, supports personalized patient care, and establishes the foundation for personalized healthcare applications.

Description of the System

The effective governance of healthcare data requires the development and implementation of a dedicated platform capable of the categorization,

integration and treatment of multiple-sources data, through the application of advanced statistical and AI-driven tools, complying at the same time with regulatory requirements, as the assurance of data security and the confidentiality of patient privacy. *Figure 1* illustrates the general architecture of the proposed platform.

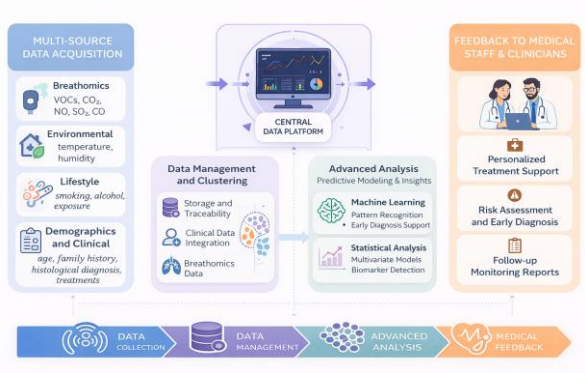

Fig. 1. Architecture of a multimodal clinical data platform for integrated data management, advanced analytics, and clinical decision support.

The central data platform employs a Role-based Access Control (RBAC) model, in which data access privileges are governed by security policies specific to each role. The architecture of central platform is structured in three sequential layers:

- *Presentation Layer*: the user interface was developed as a web app using Flutter, a cross-platform framework that enables deployment across heterogeneous environments from a single codebase. The system supports multi-source data acquisition, integrating breathomics parameters, environmental variables, and patient demographic and clinical data;
- *Application Layer*: the middle layer is involved in communication and clustering processes. The integration with backend services is handled via Firebase, a Backend-as-a-Service (BaaS) platform that provides real-time data synchronization, authentication, and cloud functions. Additionally, this layer manages data parsing prior to storage, clustering the data based on filters such as age, gender and smoking habits;
- *Data Layer*: data persistence is guara teed by a NoSQL database, chosen for its flexibility in managing heterogeneous data. Prior to storage, the data is processed through a normalization pipeline, thereby rendering the dataset available for further analysis workflows. The information provided to healthcare professionals includes a longitudinal history of visits, diagnostic reports, laboratory test results, and multi-sensor physiological measurements.

The proposed platform aims to provide an innovative contribution to the spectrum of tools supporting patient diagnosis and follow-up. The modularity of the architecture, the capability to manage large volumes of heterogeneous data, and flexible communication between the operator and healthcare professionals are distinctive features. Further developments in the near future will be focused on the validation of the developed platform in the clinical practice to manage data from populations of individuals affected by chronic and oncologic diseases as well as of subjects in therapeutic follow-up.

Acknowledgements

The authors thank Dr. Giovanni Liso and all the team of the enterprise MAV Reality srl (Italy) for the precious support in the development of the architecture of the digital platform.

This work is contextualized in the framework of the project INNOVA – Italian Network of Excellence for Advanced Diagnosis (PNC-E3-2022-23683266), funded by the Italian Ministry of University and Research under the National Complementary Plan to the PNRR.

References

[1] Nazir, S., Khan, S., Khan, H. U., Ali, S., Garcia-Magarino, I., Atan, R. B., & Nawaz, M. (2020). A comprehensive analysis of healthcare big data management, analytics and scientific programming. *IEEE Access*, *8*,95714-95733; doi: 10.1109/ACCESS.2020.2995572

[2] Harb, H., Mansour, A., Nasser, A., Cruz, E. M., & de la Torre Diez, I. (2020). A sensor-based data analytics for patient monitoring in connected healthcare applications. *IEEE Sensors Journal*, *21*(2), 974-984; doi: 10.1109/JSEN.2020.2977352

[3] Hooshmand, S., Kassanos, P., Keshavarz, M., Duru, P., Kayalan, C. I., Kale, I., & Bayazit, M. K. (2023). Wearable nano-based gas sensors for environmental monitoring and encountered challenges in optimization. *Sensors*, *23*(20), 8648; doi: doi.org/10.3390/s23208648

[4] Kaloumenou, M., Skotadis, E., Lagopati, N., Efstathopoulos, E., & Tsoukalas, D. (2022). Breath analysis: a promising tool for disease diagnosis—the role of sensors. *Sensors*, *22*(3), 1238; doi: doi.org/10.3390/s22031238

[5] Lu, S., Yang, J., Gu, Y., He, D., Wu, H., Sun, W., ... & Guo, C. (2024). Advances in machine learning processing of big data from disease diagnosis sensors. *ACS sensors*, *9*(3), 1134-1148; doi: 10.1021/acssensors.3c02670

[6] Emeakaroha, V. C., Fatema, K., Healy, P., & Morrison, J. P. (2015). Contemporary analysis and architecture for a generic cloud-based sensor data management platform. *Sensors & Transducers*, *185*(2), 100.

DOI 10.5162/eurosensors2026/Mo−SMD−08

An Adaptable Electrochemical Platform for Detection of Oncogenic Point Mutations Using Rolling Circle Amplification

Sarka Sevcikova[1,2], Karolina Itterheimova[1,2], and Martin Bartosik[1]
[1] RECAMO, Masaryk Memorial Cancer Institute, Zluty kopec 7, 656 53 Brno,
[2] NCBR, MU, Kamenice 5, 625 00 Brno,
sarka.sevcikova@mou.cz

Summary:
We report two electrochemical biosensors for rapid detection of oncogenic mutations based on rolling circle amplification and amperometric detection. The platform enables highly selective identification of mutations in *KRAS* and *PIK3CA*, with sensitivity down to ~61 pM and <1% mutant allele fraction. An ultrafast hyperbranched RCA strategy reduces amplification time to 5 minutes while preserving single-nucleotide specificity. The method shows strong agreement with NGS and offers a rapid, cost-effective solution for point-of-care diagnostics.

Keywords: electrochemical biosensor, rolling circle amplification, point mutation detection, *PIK3CA*, *KRAS*

Background

Oncogenes such as *KRAS*, *BRAF* and *PIK3CA* play key roles in oncogenic signaling pathways, where point mutations often drive pathway dysregulation and contribute to cancer development [1]. These biomarkers are commonly associated with poor prognosis, resistance to treatment, or predict response to targeted therapy (e. g. *PIK3CA* E545K is predictive for the response of alpelisib) [2]. Therefore, their reliable detection is crucial.

Conventional detection methods like NGS, or PCR-based techniques are often time consuming, require expensive instrumentation, involve complex data analysis and can be prone to reaction inhibitors. Isothermal amplification techniques, such as rolling circle amplification (RCA), do not require thermal cyclers and are well suited for mutational analysis. When combined with electrochemical (EC) detection, they represent a promising alternative. [3]. However, many RCA-based EC assays remain limited by relatively long amplification times [4].

Description of the New Method or System

We present two EC RCA-based biosensing platforms for the detection of oncogenic point mutations. The first platform is our previously established biosensor for *KRAS* G12V detection, while the second extends this approach to the clinically relevant *PIK3CA* E545K mutation [5]. The biosensors employ variant-specific padlock probe (PP)-mediated RCA with amperometric readout on screen-printed eight-electrode carbon chips. Additionally, we enriched our *PIK3CA* platform with hyperbranched RCA (HRCA) an exponential amplification variant, to further improve the sensitivity of the biosensor. In both biosensors, target sequences are pre-amplified by recombinase-polymerase amplification and subsequently subjected to (H)RCA, enabling highly selective amplification of either wild-type (wt) or mutant variants. The amplified products are then hybridized to complementary LNA (*KRAS* G12V biosensor) or DNA (*PIK3CA* E545K biosensor) capture probes. Incorporation of biotin-labelled nucleotides during amplification facilitates binding of a streptavidin–horseradish peroxidase conjugate, which catalyzes an electrochemically detectable reaction between hydrogen peroxide and hydroquinone (Fig. 1).

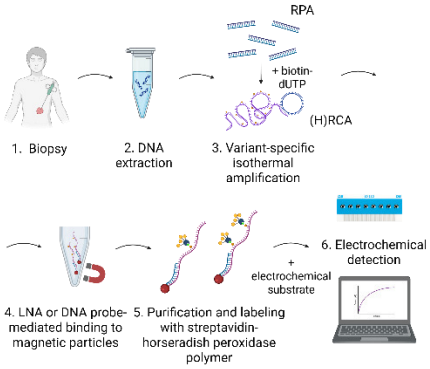

Figure 1: Schematic overview of the experimental workflow for the oncogenic point mutations analysis

In addition, the *KRAS* biosensor incorporates an AI-based logistic regression model that enables automated classification of the G12V mutation presence.

The proposed *PIK3CA* biosensor features an ultrafast HRCA strategy, reducing amplification time from 60 min to 5 min) and total assay time to ~1 h, while maintaining comparable limits of detection (~61 pM) and single-nucleotide specificity. In contrast to our previous designs relying on LNA capture probes, the current approach streamlines the assay architecture by replacing these components with cost-effective DNA probes while maintaining analytical performance.

Results

Both biosensors exhibited a concentration-dependent amperometric response with comparable limits of detection of ~61 pM, whereas the (H)RCA time for the *PIK3CA* biosensor was only 5 minutes, compared to 60-minutes RCA for the *KRAS* biosensor. (Fig. 2).

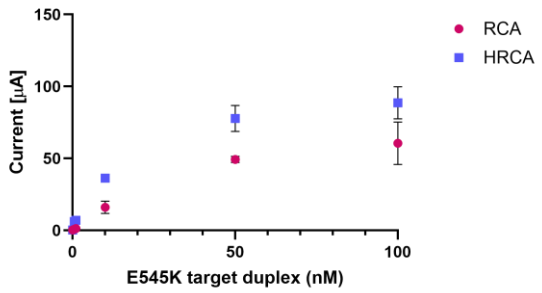

Figure 2: Dependence of electric current values on concentration of PIK3CA E545K target (using E545K PP and E545K capture probes). Red dots represent RCA samples, and blue dots represent HRCA samples.

Clear discrimination between mutant and wt sequences, as well as non-complementary controls, confirmed single-nucleotide specificity of both biosensors. This was validated across multiple targets (*KRAS*, *PIK3CA*, *BRAF*, hCMV, HPV), where each padlock probe produced a signal exclusively with its corresponding target.

Furthermore, the system enabled reliable detection of increasing mutant allele fractions in the presence of excess wt DNA, with sensitivity down to <1% mutant allele fraction, demonstrating its applicability for analysis of heterogeneous samples.

The *KRAS* biosensor was validated on 8 cell lines and 11 clinical samples, achieving 100% agreement with NGS in clinical samples (Fig. 3).

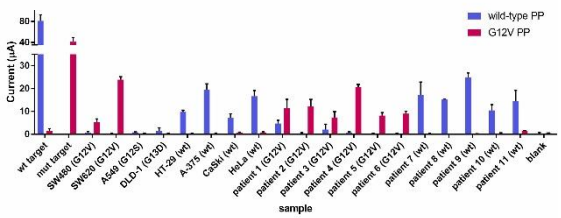

Figure 3: Real sample analysis included 8 cell lines and 11 CRC patient samples with known KRAS status (in parenthesis), alongside two synthetic positive controls (wt and G12V mutant targets) and a non-template control.

Ongoing experiments with the *PIK3CA* biosensor focus on validation using cancer cell lines, while future work will address clinical sample validation to assess applicability in real diagnostic settings.

This approach represents a rapid, sensitive, and cost-effective platform for point mutation detection, with strong potential for point-of-care and decentralized diagnostic applications.

References

[1] Y. Huang, S. Cai, Y. Zhang, X. Wang, Mutation patterns and prognostic analysis of BRAF, KRAS and PIK3CA in colorectal cancer, Journal of Gastrointestinal Oncology 13, 1320–1332 (2022); doi: 10.21037/jgo-22-320

[2] D.-Y. Chang, W.-L. Ma, Y.-S. Lu, Role of Alpelisib in the Treatment of PIK3CA-Mutated Breast Cancer: Patient Selection and Clinical Perspectives, Therapeutics and Clinical Risk Management 17, 193–207 (2021); doi: 10.2147/TCRM.S251668

[3] Y. Zhao, F. Chen, Q. Li, L. Wang, C. Fan, Isothermal Amplification of Nucleic Acids, Chemical Reviews 115, 12491–12545 (2015); doi: 10.1021/acs.chemrev.5b00428

[4] R. M. Bialy, A. Mainguy, Y. Li, J. D. Brennan, Functional nucleic acid biosensors utilizing rolling circle amplification, Chemical Society Reviews 51, 9009–9067 (2022); doi: 10.1039/D2CS00613H

[5] R. Sebuyoya, S. Sevcikova, B. Yusuf, M. Bartosik, Integrating isothermal amplification techniques and LNA-based AI-assisted electrochemical bioassay for analysis of KRAS G12V point mutation, Talanta 288, 127709 (2025); doi: 10.1016/j.talanta.2025.127709

Acknowledgements

The financial support of the Czech Science Foundation (No. 25-15990S), project SALVAGE (OP JAC; reg. no. CZ.02.01.01/00/22_008/0004644) – co-funded by the European Union and by the State Budget of the Czech Republic, BBMRI.cz (No. LM2023033) and MH CZ – DRO (MMCI, 00209805) is greatly acknowledged.

DOI 10.5162/eurosensors2026/Mo–SMD–10

High-Performance Miniaturized Reference Electrodes for Electrochemical Sensors

Davide Migliorelli[1], Guillaume Bouilly[1], Ayian Speck[2], Silvia Demuro[1], Jakoba Heidler[1], Jaemin Kim[1], Loïc Burr[1], Felix Kurth[1], Eric Bakker[2]
[1] CSEM, Bahnhofstrasse 1, 7302 Landquart, Switzerland
[2] Department of Inorganic and Analytical Chemistry, University of Geneva, Quai Ernest-Ansermet 30, 1211 Geneva, Switzerland
davide.migliorelli@csem.ch

Summary:
Screen-printed electrochemical sensors are increasingly adopted for low-cost, disposable sensing platforms in medical diagnostics and patient monitoring. While substantial progress has been achieved in the development of printed working electrodes, the reference electrode remains a critical and often underestimated limitation. Conventional printed Ag/AgCl pseudo-reference electrodes are compact and easy to manufacture; however, their potential is intrinsically dependent on chloride activity and sample matrix composition. This dependence results in signal drift, calibration bias, and compromised reliability when measurements are performed in complex biological fluids, limiting their suitability for clinical and point-of-care applications

Keywords: reference electrode, pulstrode, biofluids, screen-printing, ionic liquid

Background, Motivation and Objective

Screen-printed electrochemical sensors are increasingly adopted for low-cost, disposable analysis in healthcare and life-science applications. Despite major progress in printed working electrodes, the reference electrode remains a critical and often overlooked bottleneck. Conventional printed Ag/AgCl pseudo-reference electrodes are compact and easy to manufacture, but their potential directly depends on chloride activity and matrix composition, leading to drift, calibration errors, and unreliable readout in real biofluids.

The objective of this work is to develop and validate a fully solid-state, chloride-independent reference electrode compatible with scalable screen-printing technologies and capable of reliable operation in complex biofluids [1].

Description of the New Method or System

Here we present a fully solid-state, self-referencing pulstrode integrated on screen-printed electrodes, designed to fundamentally overcome chloride-related instability. The concept relies on an Ag/AgI element operated by a pulsed protocol, where a defined quantity of iodide is locally released by a short cathodic current pulse, the reference potential is measured at zero current, and the interface is subsequently regenerated by iodide recapture.

This self-contained mechanism decouples the reference potential from the bulk chloride concentration and enables a stable, reproducible reference without liquid junctions or internal electrolytes.

Results

The pulstrode was fabricated using printing-compatible and scalable processes and evaluated under conditions relevant for disposable sensing. In non-stirred environments and climate-chamber testing at 20 °C and 80 % relative humidity, the pulstrode reference potential remained stable within 2-3 mV over 48 h (see Fig. 1), whereas conventional printed Ag/AgCl pseudo-reference electrodes typically exhibit potential shifts of several tens of millivolts due to their chloride-dependent (≈ 59 mV dec^{-1}) response [2].

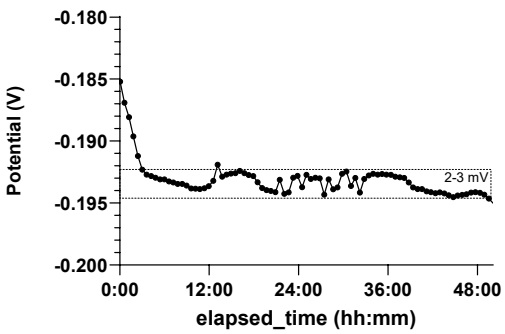

Fig. 1. Continuous pulsing stability test of the pulstrode over 48 h in a climate chamber at 20 °C and 80 % relative humidity.

When applied to a potassium ion-selective electrode in highly viscous artificial saliva, pulstrode-referenced measurements showed excellent agreement with a commercial Horiba reference (see Fig. 2), with a mean percent difference of ~1 % (n = 5) (Tab. 1).

Tab. 1: Quantitative deviation of potassium concentration measured using the Pulstrode reference electrode in artificial saliva compared to a commercial Horiba analyser

Sensor	Estimated concentration in saliva (mM)	Variation with Horiba (%)
Horiba	43.7	0.0
Pulstrode 1	45.1	3.1
Pulstrode 2	44.1	0.9
Pulstrode 3	45.1	3.2
Pulstrode 4	43.2	−1.0
Pulstrode 5	43.1	−1.4

These results demonstrate robust and accurate operation under chloride variations representative of real biofluids.

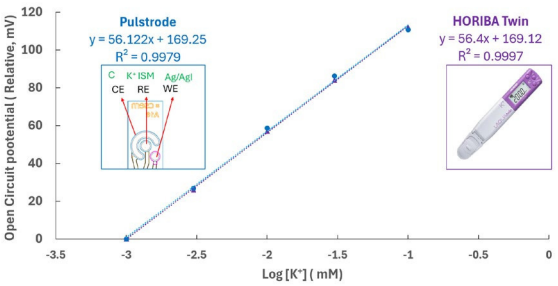

Fig. 2. Potassium ion-selective electrode response in artificial saliva, using the Pulstrode electrode as reference and benchmarked against measurements obtained with a commercial Horiba analyser.

Since chloride sensitivity represents the main limitation of printed reference electrodes, alternative chloride-independent strategies were also explored. Ionic-liquid salt-bridge (ILSB) reference electrodes were investigated as a complementary approach. A moderately hydrophobic ionic liquid embedded in a polymer matrix provides a stable phase-boundary potential over a wide range of buffer solutions and biofluids and can operate with carbon screen-printed transducers, eliminating the need for silver. However, compared to the pulstrode, challenges remain in terms of long-term robustness and full system integration.

Overall, the pulstrode concept introduces a fundamental shift in reference-electrode design, enabling chloride-independent, stable, and manufacturable reference electrodes fully compatible with screen-printed sensor platforms for reliable electrochemical sensing in complex biofluids

References

[1] E. Bakker, E. Pretsch, P. Bühlmann, Selectivity of Potentiometric Ion Sensors, Analytical Chemistry 72, 1127–1133 (2000); doi: 10.1021/ac991146n

[2] E. Zdrachek, E. Bakker, Potentiometric Sensing, Analytical Chemistry 93, 72–102 (2021); doi: 10.1021/acs.analchem.0c04249

DOI 10.5162/eurosensors2026/Tu–SMD–01

Measurement of Stress Relaxation During the Indentaion of Human Gastric Tissues

János M Bozorádi[1,2], Géza Papp[3], Zsófia Sz Bérces[2], Karolina Gáspár[4], Gábor Battistig[5] Péter Fürjes[2]
[1] Microsystems Lab., Inst. of Technical Physics and Materials Science, HUN-REN Centre for Energy Research, Budapest, Hungary
[2] Óbuda University, Doctoral School on Materials Sciences and Technologies, Budapest, Hungary
[3] Uzsoki Hospital, Budapest, Hungary
[4]Budapest University of Technology and Economics, Faculty of Electrical Engineering and Informatics, Budapest, Hungary
[5]University of Debrecen, Inst. of Physics, Department of Electrical Engineering, Debrecen, Hungary

Summary:

Modern gastric and bariatric surgical trends point toward the widespread use of laparoscopy and robotics. The most advanced tools of minimally invasive surgeries (MIS) now include tactile sensory feedback, motorization and other safety improvements to help surgeons achieve better patient outcomes. Neither of these are readily available in everyday cases moreover their optimization depends largely on the basic understanding of soft tissue behavior. In this work we compile a set of measurement parameters which we believe to be of outmost importance to take into consideration while carrying out compression type tissue characterizations.

Keywords: biomechanics, compression, stress relaxation, MEMS force sensor, gastric surgery

Mechanics of soft tissues

Biomechanics in general is the overlapping or interdisciplinary field of biology and physics. It can include any mechanical effect affecting a biological system, be it a single cell, blood flow or an entire body part. The sub-section of soft tissue biomechanics is a niche area with relatively few groups focusing on different tissue types, each using their own methodology [1]. Some of these measurements use derivatives of ISO standard measurements, such as different versions of ISO 527 for example. Some use systems designed for the testing of mediums with viscosity similar to soft tissues. SHORE 00 type durometers can be applicable tools. To ensure modularity and to provide more complex parametric data, we developed an indentation type tabletop measurement system and a set of modified stapler cartridges to test the application of MEMS force sensors for laparoscopic use [2].

Compression Type Tissue Testing

Uniaxial mechanical compression in one or two directions is a popular choice for tissue characterization, due to the measurement setup is robust and can be easily adopted from pre-existing systems with simple modifications for proper clamping of the sample. Similarly to polymers, the resulting stress-strain curves will have their notable points and regions such as yield strength, ultimate tensile strength, necking point, etc. Since soft tissues have viscoelastic behavior, in this case the time dependency is also a key factor. Parameters derived from these measurements such as Young's modulus, or the time dependency of failure rate provide useful insight into individual tissue characteristics, moreover can provide clear clinical relevance [3].

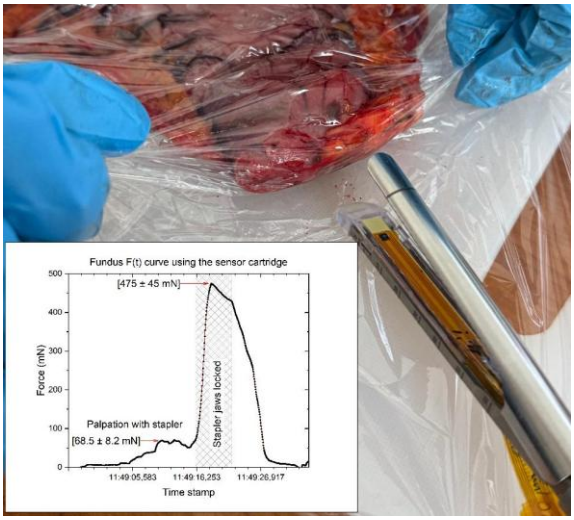

Fig. 1. Time dependent mechanical measurements made on human gastric tissue sample with MEMS force sensor integrated into laparoscopic stapler

The indentation is important, because numerous surgical maneuvers exert a compression type loading on soft tissues of the human body. Indentation type measurement systems yield force-displacement and time dependent force characteristics. While similar metrics can be attributed to these characteristics such as maximum load, relative thickness change,

cumulative force as well as Young's modulus, time dependency is often neglected. Since stress-relaxation has been defined already as an important consideration, time dependency can be important from multiple perspectives. During indentation—similarly to live surgery—tissues are not loaded to failure, but instead are exposed to transient and sustained loading conditions where time-dependent effects must be considered [4].

Results

Different artificial viscoelastic polymers were mechanically characterized by our dedicated measurement system containing self-developed 3D MEMS force sensors. The time-dependent nature of tissue response is illustrated in Fig. 2, where stress relaxation can be observed even between discrete displacement steps of the stepper motor during the compression of human gastric tissue. This highlights that viscoelastic effects are present not only during sustained loading, but also on short timescales.

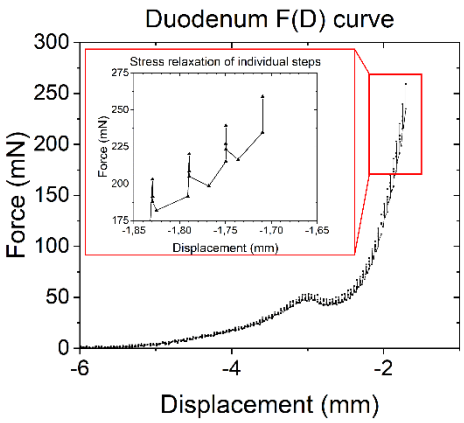

Fig. 2. Stress relaxation effect of real human duodenum sample

The measurement protocol was controlled via a custom LabVIEW interface, allowing precise definition of compression rate and hold time. Measurements were carried out with varying hold times following a force–displacement loading phase at constant compression rate. Experiments were conducted on a PDMS sample (with curing agent : elastomer ratio of 1:30) and a synthetic bowel model (Limbs & Things) used for surgical training, with dwell times of 1, 5, 15, 30, and 60 seconds.

In the artificial bowel model, a clear relaxation behavior was observed. (see Fig 3.) Following initial compression, the material exhibited a continuous decrease in counterforce at constant indenter position, confirming its viscoelastic nature. Measurable relaxation persisted throughout the full 60-second interval, and no steady-state stress value was reached within this timeframe.

As a result, the measured force depended strongly on the selected hold time. Short dwell times (1–5 s) resulted in higher, whereas longer hold times (30–60 s) yielded progressively reduced apparent force values due to the time scale of stress relaxation processes. Similar trends were observed in case the PDSM sample.

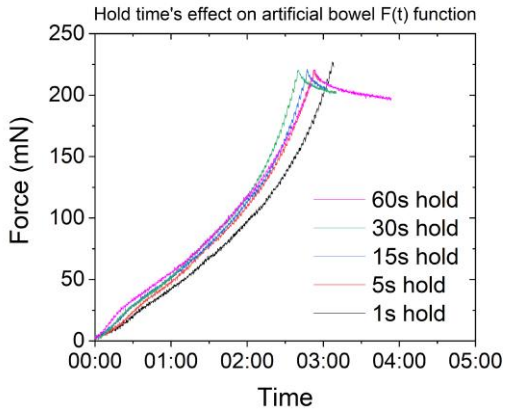

Fig.3. The effect of holding time at the end of the loading cycle of an artificial bowel sample

These findings indicate that final tissue thickness under compression is not a fixed quantity, but depends on the measurement protocol. From a clinical perspective, this introduces a trade-off between allowing sufficient time for relaxation and maintaining a feasible procedural duration, suggesting that standardized hold times may be required for consistent intraoperative assessment. Ongoing work will extend this analysis by systematically investigating the effect of compression rate on tissue response and apparent stiffness.

References

[1] L. Li *et al.*, "Transformative biomechanics and mechanobiology breakthroughs shaping the future of health and medicine," *The Innovation*, vol. 7, no. 4, p. 101307, Apr. 2026, doi: 10.1016/j.xinn.2026.101307.

[2] J. M. Bozorádi, Zs. Sz. Bérces, P. Fürjes, M. B. Maros, and G. Papp, "TP66 - Force measurement in Laparoscopic Stapler for Ex-Vivo Tissue Characterization," in *Poster II*, Wroclaw: AMA Service GmbH, Von-Münchhausen-Str. 49, 31515 Wunstorf, 2025, pp. 486–487. doi: 10.5162/EUROSENSORS2025/TP66.

[3] S. Pouwels *et al.*, "The Role of Artificial Intelligence and Information Technology in Enhancing and Optimizing Stapling Efficiency in Metabolic and Bariatric Surgery: A Comprehensive Narrative Review," *Gastrointestinal Disorders*, vol. 7, no. 4, p. 63, Sep. 2025, doi: 10.3390/gidisord7040063.

[4] M. A. Mahan, S. Yeoh, K. Monson, and A. Light, "Rapid Stretch Injury to Peripheral Nerves: Biomechanical Results," *Neurosurg.*, vol. 85, no. 1, pp. E137–E144, Jul. 2019, doi: 10.1093/neuros/nyy423.

DOI 10.5162/eurosensors2026/Tu–SMD–02

A Non-Invasive Biosensor for Albumin Detection in Tear Fluid Based on Molecularly Imprinted Polymers

Geoffrey Ndege, Sotiria D. Psoma
The Open University, Walton Hall, Milton Keynes, MK7 6AA, United Kingdom
Corresponding Author's e-mail: Sotiria.Psoma@open.ac.uk

Summary:

Tears are biomarker-rich biofluids enabling non-invasive monitoring of disease progression. We present a molecularly imprinted polypyrrole electrochemical sensor for albumin detection, targeting future integration into contact lenses for ocular inflammation monitoring. Sensor performance was evaluated in simulated tear fluid prepared in phosphate-buffered saline. High selectivity was observed against major interferents. The sensor achieved a detection limit of 0.154 mg/L and a 76.77% recovery rate, indicating effective regeneration and suitability for reusable, tear-based healthcare monitoring applications.

Keywords: biosensors, tears, albumin, molecularly imprinted polymers (MIPs), diagnostics.

Background, Motivation and Objective

Albumin concentration in tears ranges from 10 to 200 µg/ml [1], with increased ocular levels potentially indicating vascular leakage across the ocular tear-blood barrier, offering an opportunity as a biomarker of ocular inflammation and an indicator of ocular integrity [2]. Conventionally, albumin concentrations are measured using bulk methods such as liquid chromatography-mass spectrometry (LC-MS) and high-performance liquid chromatography (HPLC), enzyme-linked immunosorbent assays (ELISA), radioimmunoassay, turbidimetry, and nephelometry. These methods require lengthy sample preparation and sometimes large instruments, which limit their applications beyond lab environments [3]. Integration of sensing platforms into contact-lens-based detection offers the advantages of minimal invasiveness, potential for continuous monitoring, and remote applications, and addresses the challenges of bulkiness and sample preparation [4]. Furthermore, molecularly imprinted polymers' (MIPs) ability to act as biomimetics that imitate the antigen-antibody interaction in biosensing applications opens up opportunities for biomarker monitoring [5].

The objective of this study was to develop a proof-of-concept sensor protocol for the detection of human serum albumin in tear fluid using molecularly imprinted polymers (MIPs), with the aim of future integration into contact lens-based biosensing applications.

This was accomplished through the fabrication of a polypyrrole MIP electrochemical sensor on a carbon screen-printed electrode, followed by optimisation of albumin sensitivity and selectivity and testing under simulated tear fluid conditions.

Description of the New Method or System

The electrochemical sensor was prepared by running 7 scans of a solution containing 100 mg/L albumin in 1X PBS buffer and pyrrole on a carbon screen-printed electrode over the potential range -0.2V to +0.8V at a scan rate of 50 mV s using a PalmSens 4 potentiostat. The buffer acted as an electrolyte, with the applied potential oxidising pyrrole to produce radical cations that initiated the chain reaction leading to polypyrrole MIP. To create the MIP, sodium hydroxide (NaOH) was used to disrupt the albumin bonds in the polymer, with sodium chloride (NaCl) to adjust the ionic strength for effective removal. Cyclic voltammetry was then performed to evaluate the performance of the MIP sensor, and simulated tears containing interferents were used for selectivity studies.

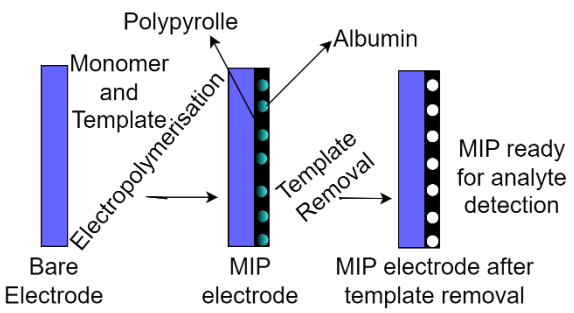

Fig. 1. Schematic representation of the molecularly imprinted polypyrrole electrochemical sensor fabrication for albumin concentration detection.

Results

The measured peak currents during rebinding of the prepared MIP showed an inverse relationship with human serum albumin concentration. An increase in albumin concentration decreased peak currents, with higher concentrations indicating MIP saturation, as shown in Figure 2.

The developed MIP achieved a 450% binding capacity compared to 84.06% for the non-imprinted (NIP), indicating selective binding to the target analyte by the MIP.

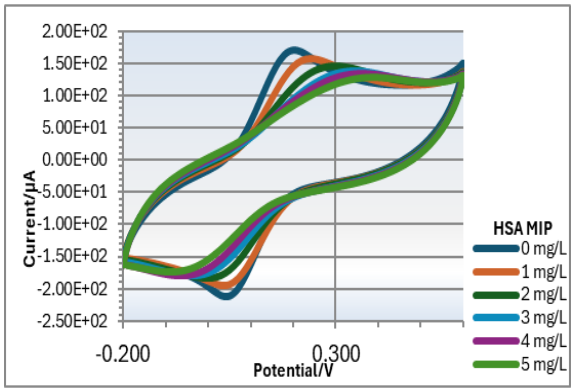

Fig. 2. Cyclic voltammetry rebinding curves recorded at albumin concentrations of 0–5 mg/L, showing a progressive decrease in peak currents with increasing albumin concentration

A recovery attempt of the MIP achieved a 76.77% recovery. This was achieved by washing the rebinded analyte with NaOH, NaCl, and H_2SO_4, then performing a cyclic voltammetry scan and comparing it with the first wash performed during MIP development.

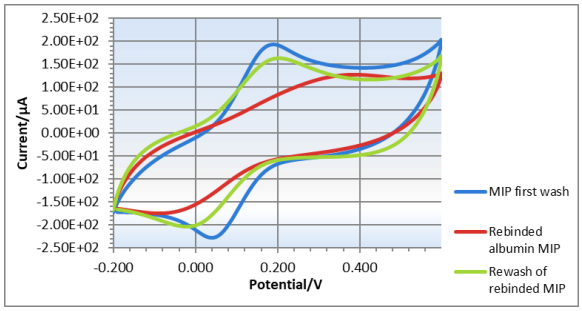

Fig. 3. Recovery experiments of the MIP sensor evaluating reusability, showing a recovery rate of 76.77%.

Further studies were carried out using simulated tears and the principal tear proteins as interferents to assess selectivity. Secretory IgA, lysozyme, lactoferrin, and albumin solutions were prepared in 1X PBS at the tear concentration levels, and dropcast on the MIP on a SPE. The results showed an imprinting factor of 1.74 for albumin, compared to 0.36, 0.4, and 0.29 for lysozyme, IgA, and lactoferrin, respectively.

Potential and Clinical Relevance

The MIP demonstrates significant potential as an electrochemical sensor for integration into wearable platforms for albumin concentration monitoring, particularly in tear fluid. Advances in microelectronics and microelectrode fabrication have enabled increasing miniaturisation, paving the way for lab-on-a-chip and smart sensing applications. This work represents an initial step in the development process; future studies should focus on further reducing non-specific binding and mitigating biofouling to enable reliable performance in in vivo applications.

Conclusion

A polypyrrole electrochemical sensor was developed and tested in buffer and simulated tear fluid, achieving detection and quantification limits of 0.154 mg/L and 0.466 mg/L, respectively. The biocompatibility and high conductivity of polypyrrole make it an attractive material for biosensor development targeting albumin and other diagnostic analytes.

References

[1] M. Aihara, H. Jinnouchi, A. Yoshida, H. Ijima, Y. Sakurai, T. Hayashi, C. Koizumi, T. Kubota, S. Usami, T. Yamauchi, T. Sakata, T. Kadowaki, & N. Kubota, Evaluation of glycated albumin levels in tears and saliva as a marker in patients with diabetes mellitus. *Diabetes Research and Clinical Practice*, *199*, 110637(2023); doi: 10.1016/j.diabres.2023.110637

[2] G. Runstrom, A. Mann, B. Tighe, The fall and rise of tear albumin levels: a multifactorial phenomenon. *Ocul Surf*, *11*(3), 165–180(2013); doi: 10.1016/j.jtos.2013.03.001

[3] R. Molinario, K. Pocino, P. D. Daloiso, A. Giannace, G. Spirito, C. Zuppi, M. Antenucci, Urinary Albumin Detection: Comparison of Two Different Methods. *J Clin Lab Anal*, *30*(6), 888–891(2016); doi: 10.1002/jcla.21952

[4] S. D. Psoma, G. Ndege, Emerging Smart Contact Lens Technology for Wearable Biosensors and Drug Delivery: Biomarkers in Tears. *EMJ Innovations* (2025); doi: 10.33590/emjinnov/FGTG8403

[5] D. A. Gkika, A. K. Tolkou, D. A. Lambropoulou, D. N. Bikiaris, P. Kokkinos, I. K. Kalavrouziotis, G. Z. Kyzas, Application of molecularly imprinted polymers (MIPs) as environmental separation tools. *RSC Applied Polymers*, *2*(2), 127–148 (2024); doi: 10.1039/d3lp00203a

DOI 10.5162/eurosensors2026/Tu–SMD–03

Fatigue Detection During Wall-Sit Exercise Using Statistical Features of Chest ECG-Derived EMG

Chanki Park[1], Chul Huh[1], Hyung Ju Park[1]
[1] Digital Biomedical Research Division, Digital Convergence Research Laboratory, Electronics and Telecommunications Research Institute (ETRI), Republic of Korea
chanki@etri.re.kr

Summary:
Muscle fatigue monitoring during isometric exercise can support safer training and rehabilitation, but conventional limb sEMG setups can be inconvenient in daily use. This work investigates four-class fatigue detection from the myoelectric component extracted from chest ECG during wall-sit exercise. Six healthy adults performed wall-sit until task failure, and the signal was segmented into non-overlapping 1 s windows labeled as rest, low fatigue, moderate fatigue, and high fatigue. Standard deviation, skewness, and kurtosis were used to train a bagging tree classifier. The proposed approach achieved an overall accuracy of 67.5% in 10-fold cross-validation and demonstrates that simple distribution-based features from chest ECG-derived EMG can support low-complexity fatigue sensing.

Keywords: muscle fatigue, wall-sit, chest ECG-derived EMG, statistical features, bagging tree

Background, Motivation and Objective

Muscle fatigue assessment is important in exercise coaching, rehabilitation, and wearable monitoring [1,2]. Surface EMG is widely used to characterize myoelectric manifestations of fatigue, and both amplitude-related and distributional signal properties change during sustained contraction [1-3]. Recent studies have also explored exercise fatigue analysis using ECG and EMG together [4]. In this work, we investigate whether a practical four-class fatigue model can be built from the EMG component extracted from a chest ECG measurement during wall-sit exercise. The objective is to distinguish rest, low fatigue, moderate fatigue, and high fatigue using a small number of features that are suitable for embedded or wearable implementation.

Description of the New Method or System

Six healthy adults performed wall-sit until failure while a chest ECG signal was recorded. To isolate the myoelectric component, the ECG was band-pass filtered between 100 and 500 Hz, and the resulting ECG-derived EMG was divided into non-overlapping 1 s segments. Rest data were labeled as the rest class. For each wall-sit trial, the initial 33% of the time-to-failure interval was labeled as low fatigue, the middle 33% as moderate fatigue, and the final 34% as high fatigue. The dataset comprised 1,958 labeled segments in total: 480 rest, 486 low fatigue, 486 moderate fatigue, and 506 high fatigue. Three statistical descriptors were extracted from each segment: standard deviation (STD), skewness, and kurtosis. A bagging tree classifier [5] was trained to predict the four fatigue classes, and performance was evaluated by 10-fold cross-validation.

Results

Fig. 1 shows the temporal evolution of the statistical features during rest and wall-sit. As wall-sit progressed, STD increased gradually, indicating that the EMG amplitude and the level of muscle activation became larger as fatigue accumulated. In contrast, the magnitude of skewness decreased toward zero, which suggests a more symmetric signal distribution at higher fatigue levels. Kurtosis decreased from approximately 20-30 in the early stage to about 5 near task failure, implying a transition of EMG distribution from a super-Gaussian toward a more Gaussian [3]. These consistent trends confirm that the selected features capture both amplitude changes and distributional reshaping associated with sustained isometric exertion.

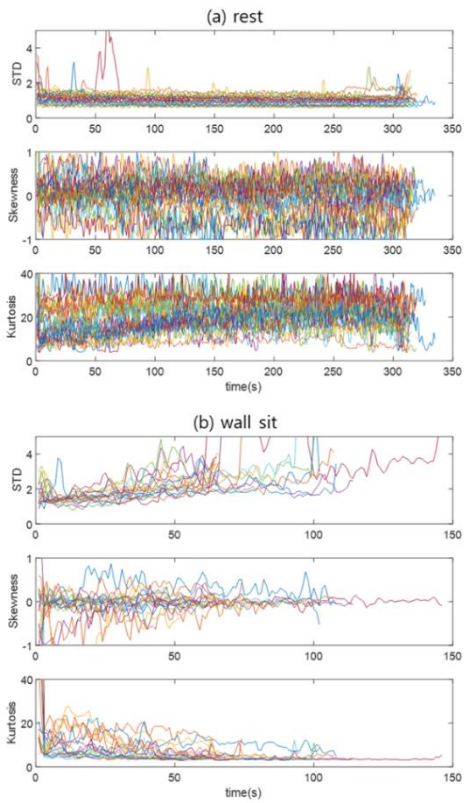

Fig. 1. Temporal variation of STD, skewness, and kurtosis for rest and wall-sit segments. (a): rest and (b): wall sit.

The fatigue classification performance is depicted in Table. 1. The proposed classifier achieved an overall accuracy of 67.5%. The rest class showed the highest recall at 80.6% (387/480), whereas low fatigue and moderate fatigue were more difficult to separate because their physiological characteristics partly overlapped. Most misclassifications occurred between adjacent fatigue stages, especially low versus moderate fatigue and moderate versus high fatigue, rather than between distant states. The high-fatigue class still reached a recall of 69.6% (352/506), which is encouraging for practical monitoring because the late stage is the most relevant for preventing performance collapse.

Overall, chest ECG-derived EMG features enabled meaningful fatigue-state discrimination. In future works, we plan to advance the fatigue analysis based on multi-modal electrophysiological signals.

Tab. 1: Confusion matrix of four-class fatigue classification.

Actual Class \ Predicted Class	rest	low fatigue	moderate fatigue	high fatigue
rest	387	72	10	11
low fatigue	70	288	78	50
moderate fatigue	9	73	294	110
high fatigue	14	21	119	352

References

[1] J. Sun, G. Liu, Y. Sun, K. Lin, Z. Zhou, J. Cai, Application of surface electromyography in exercise fatigue: a review, Frontiers in Systems Neuroscience 16, 893275 (2022); doi: 10.3389/fnsys.2022.893275.

[2] M. Gazzoni, A. Botter, T.M. Vieira, Surface EMG and muscle fatigue: multi-channel approaches to the study of myoelectric manifestations of muscle fatigue, Physiological Measurement 38, R27-R60 (2017); doi: 10.1088/1361-6579/aa60b9.

[3] K. Nazarpour, A.H. Al-Timemy, G. Bugmann, A. Jackson, A note on the probability distribution function of the surface electromyogram signal, Brain Research Bulletin 90, 88-91 (2013); doi: 10.1016/j.brainresbull.2012.09.012.

[4] D. Mu, F. Li, L. Yu, C. Du, L. Ge, T. Sun, Study on exercise muscle fatigue based on sEMG and ECG data fusion and temporal convolutional network, PLoS One 17, e0276921 (2022); doi: 10.1371/journal.pone.0276921.

[5] L. Breiman, Bagging predictors, Machine Learning 24, 123-140 (1996); doi: 10.1007/BF00058655.

ACKNOWLEDGEMENTS

This project was supported the Institute of Information & Communications Technolo-gy Planning & Evaluation (IITP) grant funded by the Korean government (MSIT-2022-0-00025).

DOI 10.5162/eurosensors2026/Tu–SMD–04

Clinical Validation of a New Radar System for Multi-Parameter Vital Sign Detection in Patients

Michael Gottinger[1], Samuel Kranz[1], Nicola Notari[2], Tindaro Pittorino[1], Christoph Würsch[2]
[1] Institute for Electronics, Sensorics and Actorics (ESA), Ostschweizer Fachhochschule, Werdenbergstrasse 4, 9470 Buchs, Switzerland,
[2] Institute for Computational Engineering (ICE), Ostschweizer Fachhochschule, Werdenbergstrasse 4, 9470 Buchs, Switzerland
Corresponding Author: michael.gottinger@ost.ch

Summary:
This work presents a 77 GHz radar system for contactless monitoring of motion, respiration, heart rate, and heart rate variability. The system improves signal-to-noise ratio, spatial flexibility, and temporal resolution compared to previous designs. Clinical measurements over multiple nights demonstrate reliable detection of respiratory patterns, apnea events, and cardiac features. Advanced signal processing enables robust separation of respiration and heartbeat signals. The results highlight the system's potential for real-world clinical monitoring.

Keywords: FMCW radar, patient monitoring, signal analysis, sensor arrays, heart rate variability

Introduction

Contactless monitoring of vital signs has gained significant importance in clinical and home-care environments, as conventional wearable sensors can cause discomfort and limit patient mobility. Radar-based approaches, particularly frequency modulated continuous wave (FMCW) systems, enable non-invasive detection of physiological motion such as respiration and heartbeat [1,3].

Recent research has extended these systems toward more advanced applications, including heart rate variability (HRV) estimation and sleep apnea detection [2,4]. However, accurate extraction of cardiac features remains challenging due to the dominance of respiratory motion in the radar signal.

The integration of multiple-input multiple-output (MIMO) radar architectures significantly improves spatial resolution and interference suppression, enabling reliable measurements even in complex environments [3].

Background, Motivation and Objective

Most existing studies focus on individual vital parameters, whereas clinical practice requires a comprehensive monitoring solution. A previously developed system demonstrated the feasibility of radar-based monitoring but suffered from several limitations [6]. In particular, the transmit power and resulting signal-to-noise ratio were insufficient for reliable heart rate and HRV estimation. The system required placement beside the bed, which is impractical in clinical environments, and its temporal resolution was too low to capture rapid cardiac dynamics.

The objective of this work is to overcome these limitations by introducing an improved radar system and to validate its performance in a clinical setting over extended monitoring periods.

Description of the New System

The proposed system is based on a 77 GHz INRAS RadarLog MIMO radar and a Microsoft Kinect depth camera as reference, see Fig. 1.

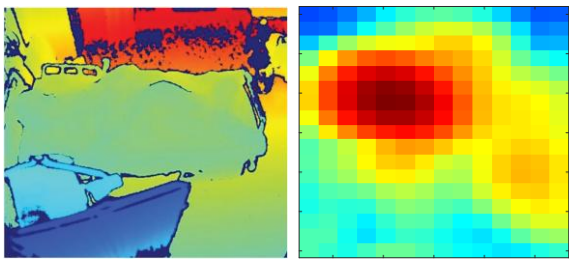

Fig. 1. Illustration of the depth camera image (left) and the radar image (right) for a patient in bed.

The radar signal is segmented into time windows of approx. 30 s. For each window, a range-angle representation is computed using a 2D fast Fourier transform (FFT). Static reflections are suppressed, and the $k \in \{1, \dots, \mathrm{K}\}$ strongest reflection points are selected for further processing.

The phase evolution $\varphi_k[t]$ of these points is analyzed. A low-pass filter is applied to extract the respiratory component $\varphi_k^{\mathrm{LP}}[t]$ and the respiration

rate is estimated via FFT using the fundamental frequency and its first two harmonics. This also enables the detection of apnea events.

To extract cardiac information, the second order derivative of the phase signal

$$\ddot{\varphi}_k[t] = \frac{1}{16}\left(\varphi_k[t+3] + \varphi_k[t-3] + 2\varphi_k[t+2] + 2\varphi_k[t-2] - \varphi_k[t+1] - \varphi_k[t-1] - 4\varphi_k[t]\right) \quad (1)$$

is computed, following the approach in [5]. The computation of $\psi_k[t] = \ddot{\varphi}_k[t] - \ddot{\varphi}_k^{\mathrm{LP}}[t]$ further suppresses low-frequency respiratory components, where $\ddot{\varphi}_k^{\mathrm{LP}}[t]$ is the second derivative of the low-pass filtered phase.

The temporal spacing between detected peaks is used to estimate HRV, while heart rate is additionally determined in the frequency domain. Patient motion is identified by thresholding of the phase acceleration signal.

Results

The system was initially validated in laboratory conditions using reference sensors, including inductive belts for respiration and a pulse oximeter for cardiac measurements. Subsequently, clinical measurements were conducted on five patients with multiple sclerosis in a rehabilitation clinic. In total, more than 20 nights of data (approx. 12 hours each) were recorded. The radar system was mounted on the ceiling 2.8 m away from the patient, ensuring unobtrusive operation.

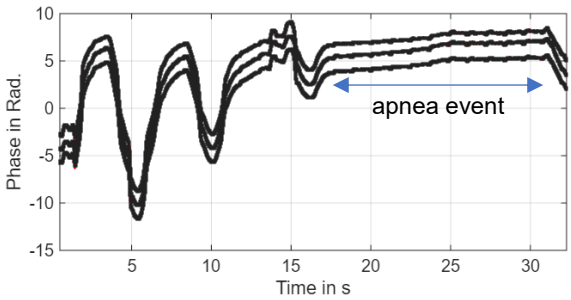

Fig. 2. Measured phase evolution generated by respiration in three reflection points.

The results demonstrate that respiratory patterns and apnea events can be clearly identified (Fig. 2). The phase signal shows distinct variations corresponding to breathing cycles, and apnea events are detectable as interruptions in the periodic pattern, consistent with findings in [4].

Cardiac signals are also successfully extracted, see histogram in Fig. 3. The heartrate varies over the course of the night, reflecting different physiological states.

The second derivative of the phase signal reveals distinct peaks corresponding to heartbeats (Fig. 4), enabling reliable estimation of heart rate and HRV, in agreement with prior work [2,5].

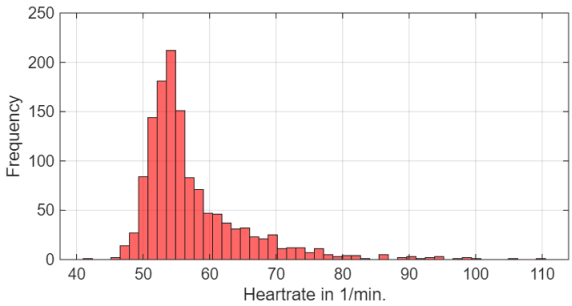

Fig. 3. Measured heartrate over the whole night.

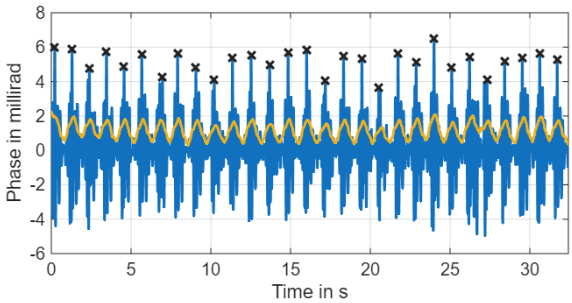

Fig. 4. Acceleration signal during normal respiration. Individual peaks are clearly visible.

In addition, the system reliably detects patient motion and presence, allowing differentiation between resting and active periods.

Discussion

In this study, a manual evaluation was performed by medical staff after one night to assess the health status. The measurement system can be enhanced by immediate data analysis, thus providing real-time information for nursing care.

References

[1] C. Gu, J. Wang, Radar-based Healthcare: A Review of Vital Signs Monitoring, *IEEE Reviews in Biomedical Engineering* 15, 210-225 (2022); doi: 10.1109/RBME.2020.3023256

[2] M. Alizadeh, G. Shaker, S. F. P. Almeida, Remote Monitoring of Heart Rate Variability Using FMCW Radar, *IEEE Access* 7, 54958-54968 (2019); doi: 10.1109/ACCESS.2019.2912893

[3] S. S. Ram, M. M. S. J. Al-Nuaimi, MIMO Radar for Vital Signs Monitoring and People Counting, *IEEE Sensors Journal* 21, 20544-20555 (2021); doi: 10.1109/JSEN.2021.3093256

[4] J. Zhang et al., Contactless Monitoring of Sleep Apnea Using 77 GHz FMCW Radar, *IEEE Journal of Biomedical and Health Informatics* 25, 24-34 (2021); doi: 10.1109/JBHI.2020.2982161

[5] R. Nosrati, S. Tavassolian, Second derivative of the complex radar signal for heart rate monitoring, *IEEE Transactions on Biomedical Circuits and Systems* 12, 1111-1120 (2018); doi: 10.1109/TBCAS.2018.2849503

[6] M. Gottinger, N. Notari, S. Dutler, S. Kranz, R. Vetsch, T. Pittorino, C. Würsch, G. Piai, G, Key Vital Signs Monitor Based on MIMO Radar, *Sensors* 25, 4081 (2025); doi: 10.3390/s25134081

DOI 10.5162/eurosensors2026/Tu–SMD–05

Miniaturized GC-MOS Platform for Exhaled Breath Analysis

Asya Kalinichenko[1], Antonio Rodrigo Murgia[1], Tasnim Kassabi[1], Jan Mitrovics[1], Christian Bur[2], Andreas Schütze[2]
[1]JLM Innovation GmbH, Tübingen, Germany
[2]Lab for Measurement Technology, Saarland University, Saarbrücken, Germany
asya.kalinichenko@jlm-innovation.de

Summary: The research aimed to overcome a key barrier to the clinical translation of breath analysis – the limited selectivity of portable sensor systems for analyzing complex volatile mixtures. To address this challenge, a miniaturized platform integrating analyte preconcentration, rapid chromatographic separation, and metal oxide sensing was developed. Initial modelling and validation demonstrate the feasibility of this approach for future medical diagnostics and monitoring.

Keywords: breath analysis, miniaturized gas chromatography, MOS-detector, in silico GC modelling.

Introduction

Volatile organic compounds (VOCs) in exhaled breath are of endogenous and exogenous origin and are generated by normal physiological and pathophysiological processes. During pulmonary gas exchange, a fraction of these volatile molecules enters the alveolar air, thereby becoming detectable in exhaled breath and providing indirect information about biochemical changes occurring throughout the body [1]. Over the past two decades, research has focused on the potential of exhaled VOCs as biomarkers for a wide range of diseases, from respiratory conditions to systemic disorders such as liver disease and cancer. Exhaled breath analysis is non-invasive and has potential for early screening, triage, and disease monitoring. However, significant challenges in standardization, reproducibility, and clinical translation remain [2].

GC-MS remains the gold standard for VOC identification and quantification, offering high sensitivity and specificity. Recent advances have enabled real-time analysis and multi-analyte detection with SIFT-MS, PTR-MS, and IMS, as well as enhanced separation and identification of complex VOC mixtures at low concentration levels using GCxGC-TOF MS. However, their complexity and cost limit widespread clinical use, driving innovation toward more accessible technologies. Sensor-based technologies meet this need by enabling the detection and quantification of trace-level biomarkers, with metal oxide semiconductor (MOS) sensors being widely explored due to their low cost and ease of integration into portable point-of-care devices.

GC-MOS systems can overcome limitations of standalone MOS sensors, which often suffer from poor selectivity, drift, and interference from environmental factors. Combining MOS sensors with GC enables the pre-separation of complex VOC mixtures in breath before detection, improving sensitivity, reducing cross-sensitivity, mitigating sensor-to-sensor variability, and increasing the informativeness of the VOC profile by reducing the influence of background profiles of healthy controls and other sources of interference. In addition, the integration of ML algorithms further refines VOC classification and compensates for sensor drift, making these systems more robust for clinical diagnostics.

Description of the new GC-MOS platform and results

The GC-MOS platform (Fig. 1) comprises three main functional modules corresponding to: (i) sampling and preconcentration, (ii) chromatographic separation, and (iii) detection. The system operates at atmospheric pressure and uses purified air as the carrier gas, cleaned upstream by a hydrocarbon/moisture trap (Agilent).

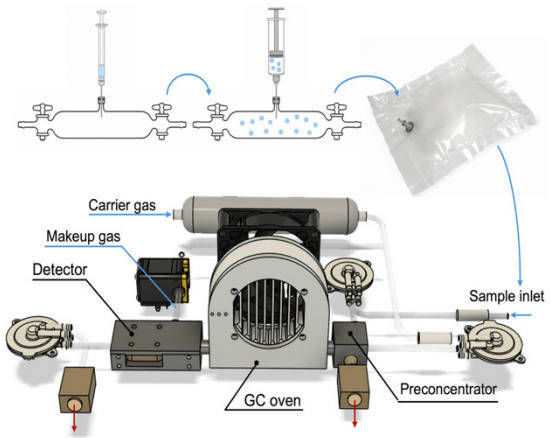

Fig. 1. Miniaturized GC-MOS Platform with synthetic breath mixture preparation for analytical validation

Gas handling is provided by a piezoelectric micropump system, while flow switching between sampling and analysis is controlled by solenoid valves integrated into the injector module. During sampling and preconcentration, the sample passes through a temperature-controlled injector containing an internal MOF preconcentrator coated with UiO-66-BDC [3], which also serves as a focusing trap. Analytes are trapped at 30°C and then desorbed at 220°C, generating a narrow injection plug that is transferred onto the separation column by the carrier-gas stream. In parallel, purified carrier gas continuously flows through the chromatographic line, while the injector-line flow is monitored by a flow sensor.

Chromatographic separation is carried out in a PID temperature-programmable circular oven, which can be operated either isothermally or under temperature ramps from 30 to 100°C with a thermal stability of ±0.1°C. A stepwise flow program is applied to improve the separation of analytes with different volatilities. In addition, a make-up flow is introduced at the detector inlet to increase the total flow through the sensor chamber and minimize peak dispersion, while the outlet flow is monitored by another flow sensor.

After separation, the analytes enter a PID-controlled MOS detector chamber (ca. 100 µL dead volume, PEEK; see Fig. 2) equipped with two ENS160 (ScioSense) and two SGP43 sensors (Sensirion). Temperature modulation is applied independently to each sensor hotplate. In addition, a humidity sensor (SHT4x, Sensirion) continuously monitors the carrier-gas relative humidity (RH). The RH signal is used as an input for a compensation algorithm, improving the stability and comparability of the sensor responses.

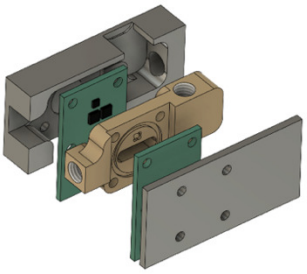

Fig. 2. MOS sensor chamber

As a starting point for developing an analytical method for the miniaturized GC-MOS platform, an ***in silico* chromatographic modelling tool** was developed for the prediction and optimization of rapid GC separations. Stationary phases covering a broad polarity range were compared, including Rtx-1 (non-polar dimethyl polysiloxane), Rxi-624Sil MS (mid-polar 6% cyanopropyl/phenyl, 94% polydimethylsiloxane), and Stabilwax (polar polyethylene glycol phase). The tool was used to predict the retention behavior of target analytes on the selected capillary columns and to identify the best compromise between chromatographic resolution and analysis time under the selected operating conditions, including purified air as carrier gas, a constant column flow of 0.5 mL/min, an oven temperature window of 35 to 100°C, and a column length of 5 m (Fig. 3). Retention times were calculated by numerical integration of the analyte migration equation using a temperature-dependent van't Hoff model for the retention factor and a gas-flow model based on the Hagen-Poiseuille equation with James-Martin compressibility correction [4]. Thermodynamic parameters were taken from the Restek chromatogram modeler. Since not all target analytes were available in the database, the simulations were used primarily for comparative evaluation of stationary-phase selectivity and expected co-elution patterns.

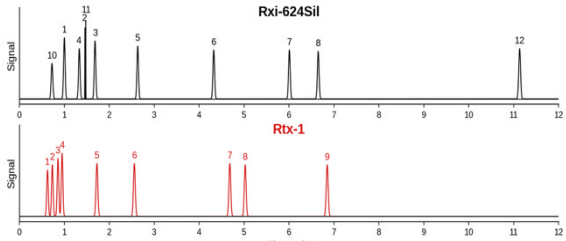

#	Compound	RT (Rxi-624Sil), min	RT (Rtx-1), min
1	Methanol	1.000	0.625
2	Ethanol	1.458	0.733
3	Acetone	1.683	0.858
4	n-Pentane	1.333	0.950
5	n-Hexane	2.633	1.725
6	Benzene	4.325	2.558
7	Toluene	6.008	4.683
8	Hexanal	6.650	5.025
9	Phenol	—	6.850
10	Formaldehyde	0.725	—
11	Isoprene	1.475	—
12	D-Limonene	11.133	—

Fig. 3. Predicted chromatographic separation of target analytes

This enabled the selection of an initial shortened column configuration and an optimized temperature program for rapid breath VOC analysis. The analytical performance of the platform is currently being evaluated on synthetic exhaled breath mixtures using the Rxi-624Sil column. In parallel, based on the complementary selectivity of stationary phases with different polarities observed in the simulations, a dual-column approach with split flow to two detector channels is being investigated for improved compound discrimination.

References

[1] King, J. et al. (2020) *Breathborne Biomarkers and the Human Volatilome.* https://doi.org/10.1016/B978-0-12-819967-1.00003-7

[2] Miekisch, W. et al. (2024) *Trends Anal. Chem.* https://doi.org/10.1016/j.trac.2024.117977

[3] Brieger, O. et al. (2026) Zenodo. https://doi.org/10.5281/zenodo.19481019

[4] Boswell, P.G. et al. (2012) *J. Chromatogr. A.* https://doi.org/10.1016/j.chroma.2012.09.048

DOI 10.5162/eurosensors2026/Tu–SMD–06

Enabling Large-Area Tactile Imaging via Multiplexed CB–PDMS Flexible Pressure Sensor Arrays

Mohammad Ariful Islam Bhuyan, Md Mayen Uddin, Liang Xiuqian, Hyeon Cheol Kim
University of Ulsan, Ulsan, South Korea
hckim08@mail.ulsan.ac.kr

Abstract:
In this work, a large-scale flexible pressure sensor array based on a carbon black–polydimethylsiloxane (CB–PDMS) conductive composite is presented. The array is configured in an approximately 110 × 16 matrix, enabling high-resolution spatial pressure mapping. Crosstalk and leakage are minimized through optimized scanning with precise timing control. A multiplexed row–column addressing scheme is employed for efficient data acquisition with reduced interconnect complexity. The proposed system is scalable, low-cost, and suitable for applications like electronic skin, human–machine interfaces, and tactile imaging.

Keywords: Flexible pressure sensor, Conductive, CB–PDMS, Multiplexed readout, Crosstalk.

Background, Motivation and Objective

Flexible pressure sensor arrays have attracted significant attention for applications such as tactile sensing [1], electronic skin [2], wearable devices, and human–machine interfaces [3]. Among various sensing materials, piezoresistive composites based on carbon fillers dispersed in polydimethylsiloxane (PDMS) are widely utilized due to their low cost, mechanical flexibility, and ease of fabrication [4].

However, the development of large-area, high-density sensor arrays presents several technical challenges, including increased wiring complexity and degraded signal integrity. As the array size scales up, issues such as crosstalk, leakage currents, and switching errors become more pronounced, leading to reduced measurement accuracy and reliability. Furthermore, conventional readout architecture often requires a large number of interconnects and complex circuitry, which limits scalability.

In this work, we present the design, fabrication, and performance evaluation of a high-resolution CB–PDMS-based flexible pressure sensor array, addressing the key challenges associated with large-scale integration.

Description of the Method

The pressure sensor array is fabricated using a CB–PDMS conductive composite as the sensing layer. The composite is prepared by dispersing carbon black particles into the PDMS matrix at a concentration of ~15 wt%, which is near the percolation threshold to achieve high sensitivity for the intended application. The PDMS matrix consists of a silicone elastomer base and a curing agent mixed at a 10:1 weight ratio. The mixture is thoroughly stirred and degassed for 1 hour to ensure uniform dispersion. The conductive polymer mixture is then poured onto the flexible PCB die using a drop-casting method and cured at 100°C for 1 hour to form a flexible conductive film shown in Figure 1.

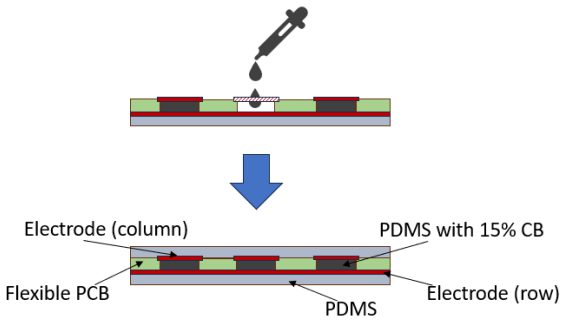

Fig. 1. Fabrication process of the proposed sensor.

The flexible sensor PCB is structured in a “U” shape, as the system is designed to map the localized pressure of the human jaw, as shown in Figure 3(a). The sensor consists of an approximately 110 × 16 matrix formed by arranging row and column electrodes, where each intersection represents an individual sensing unit, as shown in Figure 3(b). When pressure is applied, the resistance at each node changes due to deformation of the conductive network within the CB–PDMS layer.

For electrical readout, a multiplexed row–column addressing scheme is employed, as illustrated in Figure 2. Multiple analog multiplexers are used

to sequentially select rows, while column signals are measured through an ADC readout path. Each selected row is driven by a controlled voltage, and the corresponding column response is recorded. Parasitic effects such as crosstalk and leakage currents are minimized using the Zero Potential Method (ZPM), along with optimized scanning and circuit design.

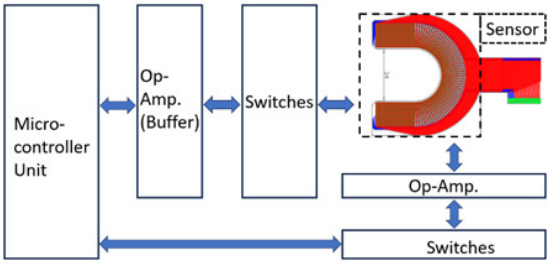

Fig. 2. Block diagram of the data readout system.

Results and Discussion

A buffer circuit is shared across the row lines before the switching stage to reduce leakage currents through unselected rows.

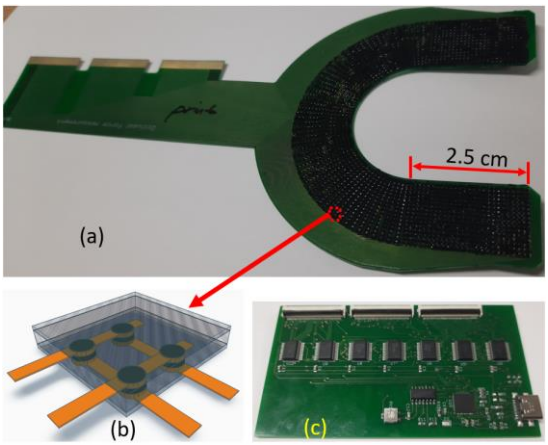

Fig. 3. Fabricated design of (a) sensor array, (b) sensor node within the array, and (c) proposed electronic data readout system.

For the column lines, each channel is connected to an operational amplifier to maintain unselected columns at virtual ground. The implemented electronic hardware system is shown in Figure 3(c). Data acquisition is performed through a sequential scanning process. Data acquisition test platform shown in Figure 4(b).

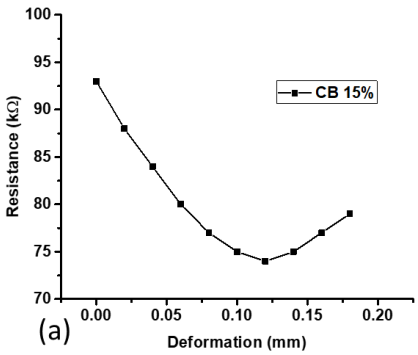

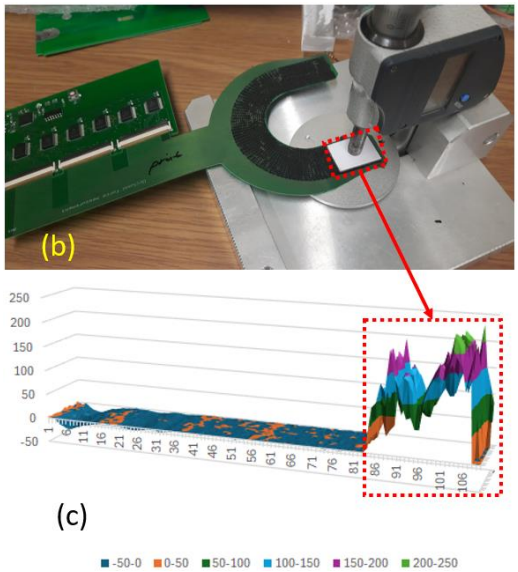

Fig. 4. (a) Response of a single cell of the sensor array, (b) Data acquisition test platform, and (c) Localized pressure mapping using the sensor array.

As pressure increased, resistance decreased due to reduced spacing between CB particles in the PDMS matrix. Beyond a certain threshold, resistance increased again, likely due to particle displacement and structural changes that disrupt conductive paths shown in Figure 4(a). Figure 4(c) shows the localized pressure map, where the x-axis represents the number of rows and the y-axis represents the pressure level. The acquired signals are processed using a microcontroller-based system to reconstruct the spatial pressure distribution across the array.

Conclusion

At high pressures, resistance slightly increased, likely due to particle displacement and matrix over strain. The sensor array showed good sensitivity, repeatability, and stability over a wide pressure range.

References

[1] A. Drimus, G. Kootstra, A. Bilberg, and D. Kragic, “Design of a flexible tactile sensor for classification of rigid and deformable objects,” Robot. Auto. Syst., vol. 62, no. 1, pp. 3–15, Jan. 2014.

[2] N. Fiedler, P. Ruppel, Y. Jonetzko, N. Hendrich, and J. Zhang, “Low cost fabrication of flexible tactile sensor arrays,” HardwareX, vol. 12, Oct. 2022, Art. no. e00372, doi: 10.1016/j.ohx.2022.e00372.

[3] Wang, J. Liu, F. Hou, D. Chen, Z. Xia, and S. Guo, “Organization and understanding of a tactile information dataset TacAct for physical human–robot interaction,” in Proc. IEEE/RSJ Int. Conf. Intell. Robots Syst. (IROS), Sep. 2021, pp. 7328–7333.

[4] D. Ahn, H. J. Choi, H. dong Kim, and S. Y. Yeo, “Properties of conductive polyacrylonitrile fibers prepared by using benzoxazine modified carbon black,” Polymers (Basel), vol. 12, no. 1, 2020, doi: 10.3390/polym12010179.

DOI 10.5162/eurosensors2026/Tu–SMD–07

Sugar-based electrochemical biosensors for quantification of a secreted protein in human fluids

Jia Guo[1], Hervé Le Stunff[2], Yacir Benomar[2], Laurent Salmon[1] and Hafsa Korri-Youssoufi[1]
Email :jia.guo@universite-paris-saclay.fr
[1] Université Paris-Saclay, CNRS, Institut de Chimie Moléculaire et des Matériaux d'Orsay (ICMMO), 17 Avenue des Sciences, bâtiment 670 Henri Moissan, 91400 Orsay, France
[2] Université Paris-Saclay, Institut des Neurosciences, NeuroPSI, CNRS UMR 9197, Allée des Neurosciences, bâtiment 151, 91190 Gif-sur-Yvette, France

Summary:
Obesity is a major risk factor for Type 2 diabetes mellitus (T2DM) and metabolic dysfunction-associated steatotic liver disease (MASLD), two highly prevalent metabolic disorders with substantial clinical burden. Phosphoglucose Isomerase (PGI), classically recognized as a key glycolitic enzyme, has recently emerged as a candidate biomarker for metabolic disease because of its extracellular function as a cytokine. In this study we report the development of electrochemical biosensors for the sensitive detection of PGI in plasma and evaluated their performance in high-fat diet-induced mouse models of obesity. We show that these biosensors reliably detects circulating PGI and enables monitoring of its levels in the context of diet-induced obesity. Together, these findings identify circulating PGI as a potential early biomarker of obesity-associated metabolic disporders and highlight electrochemical biosensing as a promising non-invasive approach for the early diagnosis and monitoring of obesity-driven metabolic diseases progression.

Keywords: Glyco-sensor, graphene-pyrene transducer, PGI, diet-induced obesity, Type 2 diabetes, High fat mouse.

Background, Motivation and Objective

Diabetes mellitus, a metabolic disorder marked by hyperglycemia, is a major global health challenge. It is classified into Type 1 diabetes (T1DM, ~6% of cases), an autoimmune disease destroying pancreatic beta cells; Type 2 diabetes (T2DM, ~92%), driven by insulin resistance in muscle, liver, and fat; and rare forms (~2%), including gestational diabetes, MODY, and monogenic diabetes. The surge in T2DM is closely linked to obesity, sedentary lifestyles, and genetic factors, reflecting the interplay between environment and heredity.

Globally, 436 million adults wotlwide live with T2DM, with 65% also affected by metabolic-associated steatotic liver disease (MASLD). This coexistence highlights the intricate relationship between diabetes and metabolic disorders, such as cardiovascular disease, nephropathy, and fatty liver disease, which collectively increase morbidity and mortality [1,2].

Modern lifestyles—high-calorie diets, physical inactivity, and obesity—exacerbate insulin resistance and T2DM progression, posing a multifaceted public health challenge. Addressing this requires comprehensive strategies for prevention, early diagnosis, and management of obesity and associated metabolic diseases [3].
Phosphoglucose Isomerase (PGI), classically recognized as a key enzyme of glycolysis and gluconeogenesis, is now considered as a multifunctional protein with both intracellular and extracellular activities. Beyond catalyzing glucose-6-phosphate and fructose-6-phosphate interconversion, PGI is also secreted as autocrine motility factor (AMF), influencing cancer cell migration and invasion. This dual role places PGI at the interface between metabolic homeostasis and disease mechanisms, highlighting its relevance as an attractive molecule for biomedical research [4].

PGI is implicated in several pathological conditions, including cancer, rheumatoid arthritis, and metabolic disorders. In tumors, it promotes metastasis; while in inflammatory and metabolic diseases, elevated extracellular PGI levels have been reported [4]. Its presence in plasma and urine suggests its potential as a biomarker for early disease diagnosis. Accordingly, innovative tools, such as electrochemical biosensors, are being developed to measure pathological PGI levels,

offering non-invasive approach for monitoring MASLD and T2DM [5].

This work explores the roles of PGI in health and disease, with particular focus on its diagnostic and therapeutic potential. Here, we report the development of electrochemical biosensors for sensitive PGI detection in plasma, and their application as preclinical model of T2DM in high-fat diet (HFD) mouse models, to evaluate PGI as a candidate biomarker for early diagnosis of HFD-induced metabolic disorders.

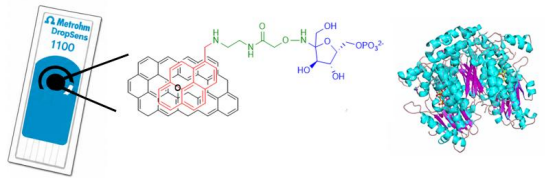

Fig. 1. Schematic representation of the biosensor: The transducer consists of a nanocomposite formed by RGO/pyrene/glucose-6-phosphate as the biomarker. The nanocomposite was synthesized, and the resulting ink was drop-casted onto a screen-printed carbon electrode (SPCE) to form the biolayer.

Description of the Method

The sensor consists of a screen-printed carbon electrode modified with graphene/pyrene biolayers covalently bound to the carbohydrate D-fructose-6-phosphate, the enzyme substrate, which serves as a bioreceptor, as described in our previous work [6].

This study was designed to investigate the temporal evolution of the biosensor response to PGI present in plasma by comparing plasma samples from control and HFD-fed mice. The HFD is known to induce a prediabetic state. Five distinct groups of plasma samples were analyzed: short-term control, long-term control, HFD for 3 days, 8 days, and 8 weeks (long-term). The experimental protocol consisted of four independent experiments per group, under strictly controlled conditions and repetition to highlight the scalability of the measures. This approach allowed for a robust assessment of how the biosensor responds over time to dietary-induced metabolic changes. The plasma are diluted with buffer at various level and then PGI concentration was measured with the electrochemical biosensors using electrochemical impedance spectroscopy. The variation of charge transfer resistance of the E-Biosensors was measured by fitting the data with equivalent circuit.

Results:

Our findings revealed a progressive, time-dependent increase in biosensor signal in plasma from HFD-fed mice, with signal intensity correlating with the duration of high-fat diet exposure. This demonstrates the biosensor's ability to discriminate normal from metabolically stressed conditions, while sensitively capturing the progressive metabolic deterioration induced by HFD.

The evaluation of PGI concentration in high-fat diet mice was conducted using a calibration curve obtained in vitro, where normal mouse plasma was doped with increasing concentrations of PGI. The results demonstrated a good correlation with previous studies [5].

Overall, these findings highlight that the biosensor is highly sensitive to dynamic changes in plasma, making it a promising tool for monitoring metabolic health and disease progression.

All results obtained will be discussed in detail during the presentation.

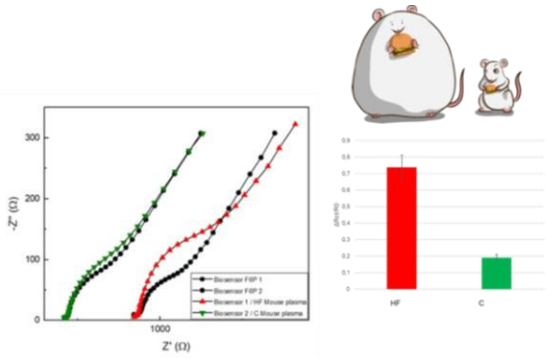

Fig. 2. Impedance characterization of the glycosensor. (Left) Nyquist plots illustrating the impedance variation for plasma samples from high-fat diet mice and control mice. (Right) Histogram showing the variation in charge transfer resistance.

References

[1] Zobair M. Younossi et al., Clin. Gastroenterol. Hepatol. 2024, 22, 1999

[2] A.G. Holleboom, S.M. Francquec, K. Cusi, C. Caussy, Metabolism Open 28 (2025) 100424.

[3] Lancet 2025; 405: 813–38.

[4] H. Lin, L. Zhu, S. S. Baker, R. D. Baker, T. Lee, Biochem. Biophy. Res. Com. 529 (2020) 1101e 1105

[5] Y. Niinaka, S. Paku, A. Haga, H. Watanabe, A. Raz, Cancer Res. 58 (1998) 2667–2674

[6] J. Guo, H. Korri-Youssoufi, L. Salmon, Electrochim. Acta 2025, 543, 147587

DOI 10.5162/eurosensors2026/Tu–SMD–08

Inductive wireless power transfer for miniature rodent brain implants enabling untethered neural recordings

Pegah Haghshomar[1], Baard Nossum[2], Florian Albert Dapsance[3,4], Cantin Ortiz[3,5], Charlotte Boccara[3,5,6], Enrique Escobedo-Cousin,[2] and Kian Mehdi Azadmehr[1]*
[1] Department of Microsystems, University of South-Eastern Norway, Borre, Norway. [2] SINTEF Digital, Oslo, Norway. [3] Norwegian Centre for Molecular Medicine, University of Oslo, Oslo, Norway. [4] Department of Physics, University of Oslo, Oslo, Norway. [5] Institute of Basic Medical Sciences, University of Oslo, Oslo, Norway. [6] Department of Neurology, Oslo University Hospital, Oslo, Norway.
**enrique.escobedo-cousin@sintef.no*

Summary:
This work presents a compact inductive wireless power transfer system for miniature brain implants to be used in neural recordings of freely moving juvenile rat studies. The solution eliminates wired power connections and enables uninterrupted neural recording during natural sleep behavior. A multi-coil architecture combines a cage-embedded transmitter, an auxiliary compensation coil, and a lightweight head-mounted receiver. The system provides sustained spatially uniform power delivery under realistic misalignment conditions. Stable operation across the entire cage volume is experimentally demonstrated, facilitating long-term in vivo neuroscience experiments.

Keywords: wireless power transfer, inductive coupling, neural implants, biomedical sensors, smart cages

Background

Neural recording experiments in freely moving animals mostly rely on wired connections for power delivery and data transmission. In juvenile rat studies, implanted electrodes are fixed to the skull using dental cement and protected by a plastic head cap, while external cables restrict natural behavior and interfere with sleep patterns [1]. These constraints limit experimental validity and animal welfare.

The objective of this work is to deliver continuous wireless power to an existing miniature neural recording module incorporating an analogue front-end based on the Intan RHD2132 digital electrophysiology interface chip, an FPGA, a microcontroller with Bluetooth, power management unit, and supporting circuitry. The system is designed to operate under a strict head-mounted mass constraint of less than 5 g, while ensuring robust power delivery across unrestricted movement inside the cage.

Numerous studies have investigated inductive wireless power transfer for implantable systems using different coil geometries and circuit architectures. Representative approaches include the works of Jow et al. (2014) and Jia et al. (2016), which are summarized in the comparative table in the following [1], [2]. In both cases, flat planar coils are employed, making the power transfer efficiency highly sensitive to angular misalignment between the transmitter and receiver.

Experimental methods and results

The proposed wireless power transfer system consists of three inductively coupled elements:

1. A helical rectangular transmitter coil is integrated into the animal cage and coupled to a driver coil to improve the effective quality factor.
2. An auxiliary coil is positioned beneath the cage floor to compensate for coupling degradation and eliminate identified power blind spots.
3. A compact two-part receiver coil mounted on top of the implant head cap with a total mass below 3 g.

The system operates at 6.78 MHz and is engineered to provide spatially robust power transfer across the animal's free-moving range. Coil geometries and resonant circuits were optimized to reduce impedance mismatch and maintain power transfer efficiency under lateral displacement and angular misalignment.

Experimental measurements were performed at 20 points within the cage in four heights: 0, 36, 56, and 101 mm at 0°, 45° and 90° angles. The results confirm stable power delivery throughout the cage volume. A maximum power transfer

efficiency of 12% and a peak delivered load of 19.6 mW were achieved, sufficient for continuous operation of the implant electronics. The inclusion of the auxiliary coil significantly improved spatial uniformity and reduced sensitivity to misalignment, enabling unrestricted animal movement without power dropout.

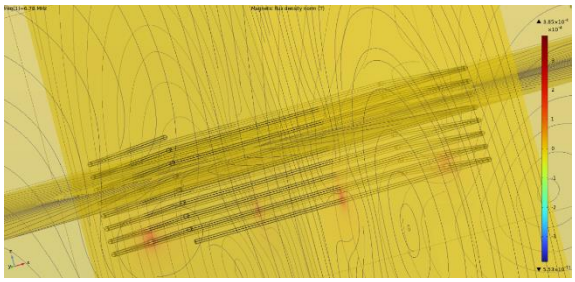

Fig. 1 Electromagnetic field distribution at 6.78 MHz obtained from 3D COMSOL simulations.

Fig. 2 System overview: (a1) cage-integrated helical transmitter coil, (a2) driver coil, (b) auxiliary coil below the cage floor, and (c) two-part receiver coil mounted on the implant cap.

Results

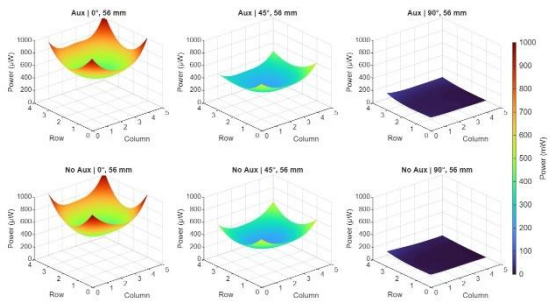

Fig. 3 Measured 3D power distribution inside the cage at a height of 56 mm at three angles with and without the auxiliary coil.

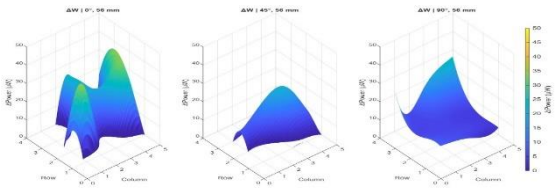

Fig. 4 Improved power distribution inside the cage at a height of 56 mm with the auxiliary coil.

Tab. 1: Comparison of previous work employing inductive links for free moving animals in neuroscience

Work	Year	PTE	PDL	Weigt of headpiece (g)
[1]	2014	5.60%	20 mW	1.7 (wire only)
[2]	2016	14% on average	42 mW	5.1
[3]	2023	19.60%	1.93 W	< 7

Tab. 2: Parameters of the proposed coils

Coil	Inductance (µH)	Number of turns	Wire diameter (mm)
Tx	32	8	4.76
Aux	7	6	4
Rx	9	19	0.4

Conclusion

A compact inductive wireless power transfer system for miniature neural implants has been developed and experimentally validated. The proposed multi-coil architecture ensures robust and spatially uniform power delivery across the full cage volume, mitigating the effects of misalignment and animal movement. The achieved power levels are sufficient for continuous operation of the implant electronics, enabling fully untethered neural recordings. This approach represents a practical step towards long-term, behaviourally unconstrained in vivo studies in juvenile rodents, with potential for further optimisation in efficiency and integration.

References

[1] U. M. Jow et al, “EnerCage: A smart experimental arena with scalable architecture for behavioral experiments,” *IEEE Transactions on Biomedical Engineering*, vol. 61, no. 1, 2014.

[2] Y. Jia et al., “A wirelessly-powered homecage with animal behavior analysis and closed-loop power control,” in *Proceedings of the Annual International Conference of the IEEE Engineering in Medicine and Biology Society, EMBS*, 2016.

[3] J. Kim et al, “Cage-Embedded Crown-Type Dual Coil Wireless Power Transfer Based Microwave Brain Stimulation System for Untethered and Moving Mice,” *IEEE Transactions on Biomedical Circuits and Systems*, vol. 17, no. 2, 2023.

Acknowledgements

The BrainChip project is financed by the Research Council of Norway (project no. 332004).

DOI 10.5162/eurosensors2026/Tu–SMD–09

Development of a transistor-based gas sensor for biomedical applications

Dieu-Linh NGUYEN[1], Thi-Thu VU[2], Benoît PIRO[1]
[1] ITODYS Laboratory, CNRS UMR 7086, Université Paris Cité, 15 rue Jean-Antoine de Baif, 75013, Paris, France
[2] University of Science and Technology of Hanoi (USTH), Vietnam Academy of Science and Technology (VAST), 18 Hoang Quoc Viet, Cau Giay, 100000 Hanoi, Vietnam
Corresponding author: piro@u-paris.fr

Summary:
In this PhD's project, we aim to fabricate a transistor-based gas sensor for screening and analysis of human volatile organic compounds (VOCs) which are exhaled or emitted from human body odor. With the use of porous polyaniline (PANi) as the channel material, decorated with catalytic nanoparticles (PdNPs, PtNPs), the response of the sensor while being exposed to targeted gas molecules is relatively high.

Keywords: Gas sensor, gas sensor array, printed electronics, organic electrochemical transistors, biomedical application, volatile organic compounds.

Title

Development of a transistor-based gas sensor for biomedical applications.

Background, Motivation and Objective

The human body can generate a variety of volatiles organic compounds (VOCs), which could be exhaled gas or emitted gas from body odor [1], [2]. The profiles of human VOCs can reflect underlying pathological and metabolic processes, subtle alterations of their compositions and concentrations might indicate some health conditions, such as lung cancer, diabetes, kidney dysfunction, and inflammatory diseases [2], [3]. Therefore, human VOCs have emerged as non-invasive biomarkers for health monitoring and early diagnosis. The use of gold-standard, traditional analytical methods like gas chromatography-mass spectrometry (GC-MS) might offer good selectivity and sensitivity; however, they are limited by their specialized operations, complications, and high cost. Therefore, with an emerging interest in the development of point-of-care devices, we would like to develop a compact gas sensor array that could operate like an electronic-nose system by combining the arrays of selective sensing transistors, with pattern-recognition or machine learning algorithms to study the complex VOCs mixture. Among several gas sensing platforms such as chemiresistors, optical-based sensors, electrochemical sensors, we would like to investigate a sensor array that is transistor-based. Owing to the advantages of signal amplification, low operating voltage, and room-temperature operation conditions. Within this context, we study a sensor array that is based on organic electrochemical transistors (OECTs) using conducting polymers as the channel material, and with some catalytic NPs (PdNPs, PtNPs) for hydrogen gas and ethanol gas detection, respectively.

Description of the New Method or System

The sensor array composed of 8 side-gate transistors was fabricated by photolithography and gold evaporation. Thereafter, the PANi channel and catalytic NPs were electrodeposited by cyclic voltammetry approach. For the electrical characterizations and gas sensing studies, the sensor array was operated in the form of a solid-state transistor, with an acidic gel electrolyte deposited on top of each transistor, covering all the gate and the channel. The gel electrolyte was printed by direct ink writing method using a Kelenn DMD100 ink-dispensing printer. A 3D-printed gas chamber was installed for gas sensing experiments. Preliminary results indicate that the gas sensor shows a promising response to hydrogen and ethanol, with high sensitivity.

Results

Polyaniline (PANi) nanofibers were electrochemically deposited on the channel by cyclic voltammetry approach with a deposition staircase of -0.2 V to 0.8 V; 50 mV/s, 5 cycles in 0.1 M aniline in 0.5 M H_2SO_4 solution. Also, PdNPs catalytic NPs were electrodeposited by scanning from the same CV staircase in 2 mM $PdCl_2$ in 0.1 M

H_2SO_4 + 0.2 mM HCl solution. To increase the working area of the gate electrode, PANi was also deposited on the Au gate; thus, the gate capacitance will increase, that will further improve of the gating effect of the OECT. For all the electrical characteristic and gas sensing studies, an acidic gel of PVA and H_2SO_4 (1 M) was printed on the side-gate transistors by direct ink-writing method. Electrical studies on PANi-based OECT (with PANi redox active gate) exhibits the ambipolar signature of PANi, which resulted from the redox-state switching of PANi itself with varying gate voltage applied. After the decorations of NPs, although the inhibit the gating effect of the system, they promotes better selectivity towards gas molecules. Preliminary tests on gas sensing study were conducted with a 3D printed gas chamber with H_2 gas collected from a PEM Hydrogen generator machine (provided by Domnick Hunter). The gas sensing was studied by monitoring I_{DS} as a function of time while applying a fixed drain voltage (V_{DS}) bias and gate voltage (V_{GS}) bias at 0.2 V. Initial studies with PdNPs@PANi-based sensor on the array exhibited a high selectivity with high response% value to hydrogen gas. The response% was calculated by:

$$Response = \frac{I_{air} - I_{gas}}{I_{air}} \times 100\%$$

Figure 1 below shows significant responses of H_2 on PdNPs@PANi-based sensor. PdNPs are known to exhibit a selective sensing activity towards hydrogen based on the spill-over effect. As a reducing gas, H_2 will be adsorbed on PdNPs, dissociated into H atoms, forming PdHx and released electrons. The electrons released from PdNPs then will reduce PANi, making PANi become deprotonated, and decrease the conductivity of the material. Thus, the I_{DS} obtained while being exposed to H_2 decreased. The PdNPs@PANi-based sensor exhibited response% of 97%, with an estimated response time of 20s and recovery time of 50s.

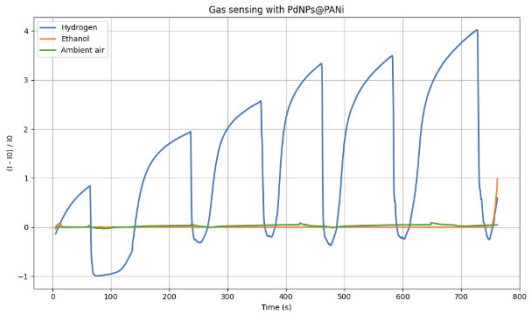

Fig.1. Normalized signal of gas sensing study with PdNPs@PANi transistor with hydrogen, ethanol, and ambient air.

References

[1] P. C. Moura, M. Raposo, and V. Vassilenko, “Breath volatile organic compounds (VOCs) as biomarkers for the diagnosis of pathological conditions: A review,” *Biomed. J.*, vol. 46, no. 4, p. 100623, Aug. 2023, doi: 10.1016/j.bj.2023.100623.

[2] A. Amann *et al.*, “The human volatilome: volatile organic compounds (VOCs) in exhaled breath, skin emanations, urine, feces and saliva,” *J. Breath Res.*, vol. 8, no. 3, p. 034001, Jun. 2014, doi: 10.1088/1752-7155/8/3/034001.

[3] N. Nasiri and C. Clarke, “Nanostructured Chemiresistive Gas Sensors for Medical Applications,” *Sensors*, vol. 19, no. 3, p. 462, Jan. 2019, doi: 10.3390/s19030462.

DOI 10.5162/eurosensors2026/Tu–SMD–10

Discriminating between viable and non-viable bacteria with a field-effect transistor based on Nano-Channels

Gil Shalev[1,2]
[1] School of Electrical Engineering, Ben-Gurion University of the Negev, POB 653, Beer-Sheva 8410501 Israel
[2] The Ilse-Katz Institute for Nanoscale Science and Technology, Ben-Gurion University of the Negev, POB 653, Beer-Sheva 8410501, Israel
glshalev@bgu.ac.il

Summary:
The Meta-Nano-Channel (MNC) bioFET performs specific, label-free, and real-time quantitative sensing of *E. coli* bacteria. The sensing is performed for 0.5 µL unprocessed samples of Lysogeny Broth spiked with *E. coli*. Furthermore, the device capacity to distinguish viable from non-viable bacteria is demonstrated

Keywords: *E. coli*, bioFET, specific sensing, bacteria viability

Background, Motivation and Objective

Bacterial infections remain a leading cause of global morbidity and mortality [1]. Among these, foodborne diseases—arising from contamination across production, distribution, and consumption supply chains—present a major public health burden, causing pathologies ranging from acute gastroenteritis to chronic malignancies. Low-cost, point-of-need biosensors enable rapid on-site bacterial detection; however, most platforms fail to distinguish viable from non-viable cells—a critical limitation in assessing active contamination risks. To address this, we present a Meta-Nano-Channel field-effect transistor (MNC FET) that mitigates molecular localized gating limitations through multiple parallel nano-channels, each coupling surface binding events to channel conductance with distinct efficiencies.

Description of the New Method or System

This study utilizes the MNC bioFET, a platform specifically engineered to overcome traditional interface challenges such as molecular gating and solution gating. The MNC bioFET's unique multi-gate architecture allows for the excitation of various conducting channels that differ in size, shape, and spatial orientation. This diversity ensures that each channel is uniquely coupled to the potential variations at the sensing area, which are often non-uniform due to the irregular distribution of molecular interactions. Furthermore, the device enables the switching of these channels between off and on states while preserving the electrochemical equilibrium of the solution and surface-bound biomolecules—a critical factor for accurate real-time measurements. Functionalized with anti-*E. coli* antibodies, the platform operates directly in unpurified 0.5 µL droplets of Lysogeny Broth (LB, 197 mM ionic strength, 200 mg/L background protein) without sample pre-treatment or wash steps.

Results

The device achieves a limit of detection (LoD) of a single bacterium in LB with excellent sensitivity and linearity [2]. This study presents the first direct bioFET detection of bacteria in complex matrix, achieved without any preprocessing or washing steps. Assay specificity was validated using bacterial controls subjected to antibiotic treatment, metabolic inhibition, and thermal inactivation. Furthermore, the platform's capacity to assess bacterial viability was validated by comparing the MNC FET response of live *E. coli* against populations subjected to thermal denaturation, antibiotic exposure, or metabolic inhibition. The sensor reliably differentiates viable from non-viable cells with a single-cell resolution, offering a robust foundation for real-time viability diagnostics. Leveraging standard CMOS fabrication, the MNC FET platform enables scalable, cost-effective biochip production with high multiplexing density and excellent sensing performance. Manufacturing costs remain low due to relaxed, micron-scale design rules that allow accessible photolithography. Furthermore, the platform's ability to resolve real-time temporal variations in electrical signals introduces a dy-

namic analytical dimension beyond conventional amplitude-based readouts

References

[1] World Health Organization. Foodborne diseases. *World Health Organization Web* https://www.who.int/news/item/04-06-2026-unsafe-food-causes-866-million-illnesses-and-1.5-million-deaths-annually--young-children-at-highest-risk (2026).

[2] Chen, **S**. et al. Discriminating between living and dead bacteria with a field-effect transistor based on Meta-Nano-Channels. *Small* Accepted (2026)

.

DOI 10.5162/eurosensors2026/Mo−EFS−01

Remote Sensing for Monitoring Hydric Stress in Farm Animals

Elise Saoutieff[1], Sébastien Brulais[1], Ilaria Sorrentino[1], Marie Escudé[1], Mahfod Benessalah[1], Laurabelle Gauthier[1], Claire Verplanck[1], Romain Anciant[1], Isabelle Texier[1], Caroline Xavier[2], Lucile Hervé[2], Anne Boudon[2], Florence Gondret[2]
[1] Univ. Grenoble Alpes, CEA, Leti, Grenoble, France,
[2] INRAE, Institut Agro PEGASE, Saint Gilles, France
elise.saoutieff@cea.fr

Summary:

The rapid acceleration of global climate warming is presenting unprecedented challenges for agricultural systems worldwide. Particularly, enhancing livestock resilience to environmental stressors, notably represented by more frequent acute heat waves and feeds of poorer and inadequacy qualities, is one of the challenges.
In the Wait4 project, we aimed to quantify and characterize animal adaptation to heat and hydric stress. From this perspective, the development of new wearable sensors, based on microneedle patches to perform measurements of physiological parameters that are minimally invasive for animals were developed to monitor interstitial hydraulic conductivity which represents intrinsic permeability of the cells and saturation of the fluid, as a proxy of dehydration to inform about hydric stress.

Keywords: adaptation to heat stress, interstitial fluid, micro-needles, remote sensing, wearable

Background, Motivation and Objective

The consequences of global warming of 1.5 °C above pre-industrial levels and the resulting greenhouse gas emission trajectories require us to assess the impact of associated environmental changes on both humans and animals [1]. In France, a plan based on a Reference Warming Trajectory for Climate Change Adaptation (TRACC) [2] of +3°C by the end of the century was even launched in 2026 by the government to develop a climate change adaptation strategy This includes planning water management and implementing vulnerability assessment of farm animals and resilience of farming systems as top priorities.

Farm animals are negatively affected by the climate change [3]. One of the biggest impacts is the temperature increase, especially more frequent and acute heat waves, that affects the hydration quality of feeds (especially forages), changes the feeding and drinking behaviors of the animals, and challenges thermoregulation mechanisms including sweating, respiratory hyperventilation, hyperthermia, and cellular responses in blood and tissues. Thus, moisture and heat were the most commonly perceived adverse factors in hot environment.

The WAIT4 project (Welfare: Artificial Intelligence and new Technologies for Tracking Key Indicator Traits in Animals Facing Challenges of the Agro-ecological Transition) aims to monitor animal physiology in response to climate change in controlled and ha in controlled and harsh environments [4]. Indeed, IoT technologies offer new opportunities in precision livestock farming [5] to understand and improve animal's responses. However, sensor techniques are still barriers [6] for monitoring physiology of large farm animals.

Conductivity Sensor

A wearable sensor for dermal interstitial fluid (ISF) analysis, focusing on conductivity as an indicator of electrolyte balance, hydration, and metabolic changes was developed [7]. Based on poly(lactic-co-glycolic acid) (PLGA) microneedle arrays, sensors were fabricated via hot molding and coated with metallic layers to function as electrodes.

ISF, a biofluid similar to blood but more accessible, presents a promising non-invasive solution for health monitoring. During stress period, water quantity will decrease in the ISF and its conductivity increase.

System Architecture

The overall system architecture of the wearable device is shown schematically in Figure 1.

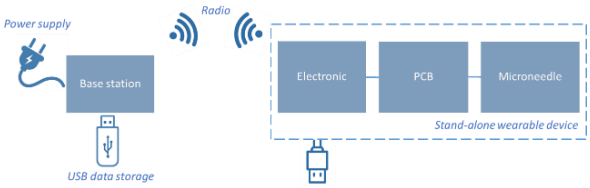

Fig. 1. Architecture of the autonomous wearable device

Each sensor (microneedle patch) is connected to a small circular printed circuit board (PCB) containing a temperature sensor and making contact with the patch via spring-loaded test pins. The sensor/PCB assembly is then connected via a ribbon cable to the data acquisition board (the mother board), which collects, processes and transmits the data to a base station with a radio signal (fig.2).

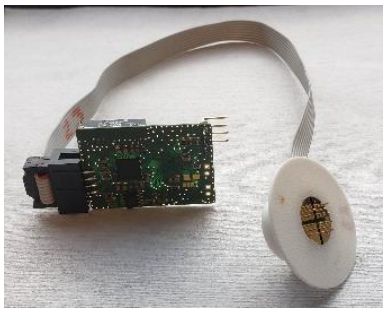

Fig. 2. Assembled patch connected to the mother board

The electronic mother board, embedded a AD5941 potentiostat to perform the impedance and so conductivity measurement.

Results

This study presents wearable sensors based on microneedle arrays, focusing on conductivity as an indicator of electrolyte balance, hydration, and metabolic changes. Their performance was first tested on skin models in labs. Then, sensors were inserted on living pigs and dairy cows under different conditions (from 24 hours until 1 week of implementation, followed by a period of thermal or hydric stress).

This minimally invasive solution supports sustainable, welfare-oriented livestock farming to address agro-ecological transition challenges.

Acknowledgements

This research was funded by Agence Nationale de la Recherche under the France 2030 program with the reference ANR-22-PEAE-0008.

References

[1] GIEC report, 2023 Available: https://www.ipcc.ch/report/ar6/syr/ (accessed: Ap. 27, 2026)

[2] TRACC report, Available: https://www.ecologie.gouv.fr/sites/default/files/documents/27012026_DP_TRACC.pdf (accessed: Ap. 30, 2026)

[3] A. Anuta, X. Wang, P. Kinay, The impacts of climate change on livestock: An interdisciplinary, scoping review of health, production, and adaptation strategies, Climate Smart Agriculture, Vol. 2, Issue 4, 2025, 100082, ISSN 2950-4090, doi: 10.1016/j.csag.2025.100082

[4] I. Sorrentino, C. Verplanck and Y. R. J. Thomas, Electrochemical Sensors for Animal Welfare, Proceedings 2024, 97, 45. doi: 10.3390/proceedings2024097045

[5] V. Choudhary, P. Guha, G. Pau, S. Mishra, An overview of smart agriculture using internet of things (IoT) and web services, Environmental and Sustainability Indicators, Volume 26, 2025, 100607, doi: 10.1016/j.indic.2025.100607

[6] C.H. Knight, Review: Sensor techniques in ruminants: more than fitness trackers, Animal, Volume 14, Supplement 1, 2020, Pages s187-s195, doi: 10.1017/S1751731119003276

[7] L. Gautier, S. Wiart-Letort, A. Massé, C. Xavier, L. Novais-Gameiro, A. Hoang, M. Escudé, I. Sorrentino, M. Bonnet, F. Gondret, C. Verplanck, I. Texier, Micromachines 16 (9), (2025), 1015, doi : 10.3390/mi16091015

DOI 10.5162/eurosensors2026/Mo–EFS–02

Development of a Radiofrequency Sensor for Detecting Bacteria in the Food Industry

Youness Hsana[1,2], Anne-Gabrielle Mathot[1], Olivier Couvert[1], Philippe Talbot[2], Stéphane Rioual[2], Benoit Lescop[2]
[1] Univ Brest, INRAE, LUBEM, 29000 Quimper, France
[2] Lab-STICC, University Brest, CNRS, UMR 6285, 29200 Brest, France
Corresponding Author's e-mail address: lescop@univ-brest.fr

Summary:
Microbiological safety is a critical concern in the food industry, as it requires continuous monitoring for potential bacterial contamination along production lines. In this context, developing low-cost sensors capable of providing real-time data is of paramount importance. To this end, an open-ended coaxial probe controlled by a miniVNA Tiny (Vector Network Analyzer) was selected to detect bacterial growth. First, the effect of temperature on the sensor response was characterized. Subsequently, variations in the S11 reflection coefficient of the probe were correlated with the concentration of *Bacillus licheniformis*

Keywords: RF sensor, biofilm, bacteria, monitoring, low-cost sensor

1. Introduction

Controlling bacterial contamination is a key challenge for the food processing industry. Indeed, the contamination of food products by pathogenic and/or spoilage bacteria (*Bacillus cereus*, *Salmonella* spp., …) can have serious sanitary and economic consequences [1]. As bacteriological analyses are often carried out by external laboratories, the detection of contamination is not immediate. The delayed recall of the products concerned therefore has a major impact on manufacturers, both financially and in terms of brand reputation.

Our team recently demonstrated the feasibility of real-time monitoring of bacterial growth and biofilm formation using Radio Frequency measurements [2]. A truncated coaxial line was immersed in the bacterial solution under study, and S11 parameter measurements were performed over a frequency range of 0.1 to 3 GHz. Application in the food processing industry requires not only *in situ*, real-time monitoring, but also the deployment of a large number of sensors. These constraints require the use of a low-cost system. We therefore opted to use of a mini-VNA tiny to carry out the measurements.

2. Materials and methods

The probe used consists of an open-ended coaxial line. Reflection measurements (S11 parameters) are performed using a mini-VNA Tiny. As illustrated in Figure 1, all measurements were carried out in an incubator using saline solutions or bacterial cultures. Acquisition of the RF parameter values was made by a computer.

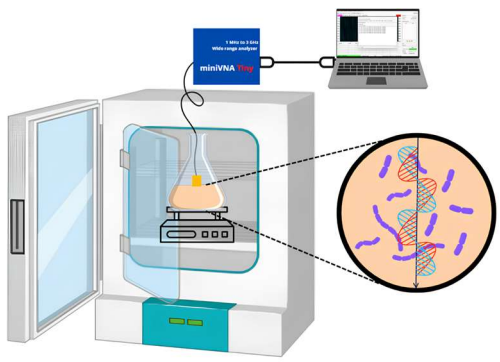

Fig. 1. Drawing of the experimental set-up

Prior to initiating measurements, the mini-VNA is allowed to warm up overnight, after which calibration is carried out using the SOL (Short – Open – Load) method. Temporal monitoring of the S11 parameter was conducted at a fixed frequency of 100 MHz.

The temperature monitoring of the solution was continuously performed by a thermometric data logger (Dutscher). This device is programmable and enables both temperature tracking and data storage.

Measurements were performed on the industrial spoilage bacterium *Bacillus licheniformis* 16 (BL16), a biofilm-forming bacterium isolated from skimmed milk powder by the LUBEM

laboratory. The bacterial growth was made in NB (Nutrient Broth) medium.

3. Results and discussion

Temporal stability

Monitoring bacterial growth requires measurement durations from 24 to 48 hours. We initially assessed the temporal stability of the sensor response by performing measurements on saline solutions. Measurements were conducted in the incubator at 40°C, which corresponds to the optimal growth temperature of the BL16 strain.

During the first four hours of measurement, the system was found to require a stabilization period. Subsequently, a drift of between 0.05 and 0.1 dB/day was observed. The system exhibits relatively stable behavior, although it may be sensitive to temperature fluctuations.

Temperature

As previously demonstrated [2], the RF sensor response is dependent on the solution's electrical conductivity, which is itself temperature-dependent. The sensitivity of the sensor to temperature variations was therefore investigated using a physiological liquid. A temperature gradient ranging from 33°C to 42°C was applied by incrementally increasing the temperature over a total experimental duration of eight hours.

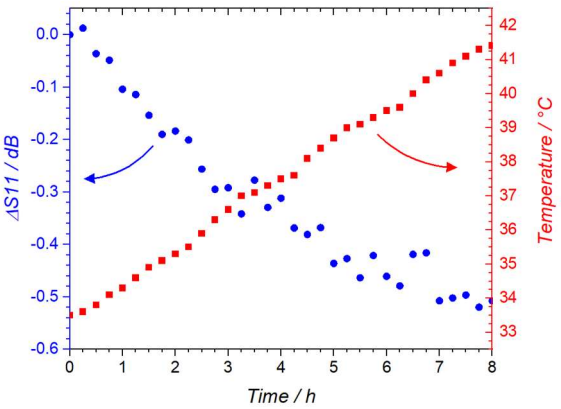

Fig. 2. ΔS11 and temperature in function of time.

Figure 2 presents the ΔS11 evolution and temperature in function of time. A negative correlation between temperature and the S11 parameter is reported: the S11 response decreases as temperature increases. Note that a linear behavior can be observed. These results therefore confirm the sensitivity of the sensor to temperature variations during experiments. Furthermore, this finding suggests that temperature-induced variations could be corrected for in subsequent bacterial analyses.

Bacteria concentration

Figure 3 illustrates the relative ΔS11 response as a function of BL16 concentration in the liquid medium. ΔS11 is normalized to the initial liquid medium value *i.e.*, in the absence of bacteria. The increase of bacteria concentration leads clearly to the variation of the S11 values, even if the ΔS11 variation is weak for values below 2 x 10^7 CFU/ml. However, the highest concentration values show high ΔS11 variation.

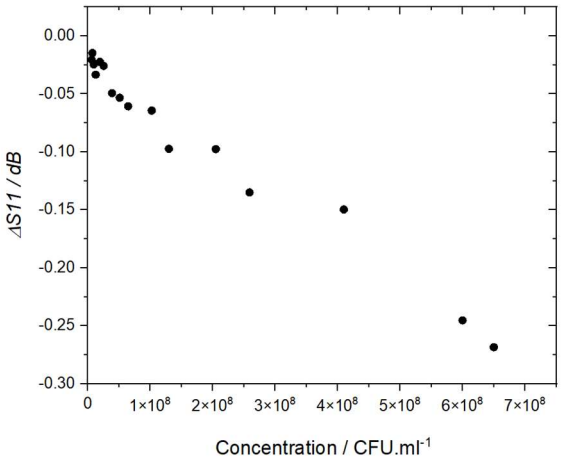

Fig. 3. Relative S11 data in function of BL16 concentration

Additional data on another *Bacillus licheniformis* strains present similar results. The comparison between our data and those reported by Longo *et al* [2] shows that the S11 variation seems to depend to the nature of the bacteria.

4. Conclusion

This work focuses on the application of an open-ended coaxial line for the detection of bacteria in the food processing industry. Our preliminary results demonstrate the capacity of the sensor to monitor changes in the test medium attributable to the presence of bacteria. This can be possible with a low-cost system. In upcoming experiments, bacteria growth will be monitored over time. In addition, the goal will be to test our sensor under conditions similar to those found in industrial settings.

References

[1] O. Fysun, H. Kern, B. Wilke, and H.-C. Langowski, Evaluation of factors influencing dairy biofilm formation in filling hoses of food-processing equipment, *Food Bioprod. Process.*, 113, 39-48 (2019).

[2] M. Longo, S. Rioual, P. Talbot, F. Faÿ, C. Hellio, and B. Lescop, A high sensitive microwave sensor to monitor bacterial and biofilm growth, *Sens. Bio-Sens. Res.*, 36, 100493 (2022).

DOI 10.5162/eurosensors2026/Mo–EFS–03

Synthesis of Gold Nanostructures for Optical Fiber Biosensors Towards the Detection of *Salmonella* Typhimurium

Khent Ivan Duerme[1], Maciej Ptak[1], Roberto Scotti[2]
[1] Institute of Low Temperature and Structure Research, Polish Academy of Sciences, Wrocław, Poland
[2] University of Milano-Bicocca, Milan, Italy
k.duerme@intibs.pl

Summary:
This work presents a proof-of-concept for the rapid detection of *Salmonella* Typhimurium for food safety applications. The sensing approach is based on localized surface plasmon resonance in tapered single-mode-multimode-single mode fibers functionalized with synthesized gold nanostructures. Gold nanoparticles and gold nanostars were successfully synthesized and optically characterized; with distinct plasmonic responses suitable for sensing applications. The preparation of optical fiber probe and functionalization with nanostructures and antibodies are currently in progress.

Keywords: gold nanoparticles, gold nanostars, LSPR, optical fiber, *Salmonella*

Background, Motivation and Objective

Salmonella Typhimurium is a major foodborne pathogen faced by the world. In fact, *S.* Typhimurium infections account for approximately 420,000 deaths annually, highlighting the urgent need for rapid and highly sensitive detection methods [1], [2]. The plate culture method remains the gold standard for identifying bacterial contamination. However, confirmation of contamination usually takes several hours to days, making it insufficient for meeting the rapid response demands of modern food industries. Several rapid methods have emerged, but they usually suffer from high cost or lower sensitivity. Optical fiber (OF)-based biosensors, particularly those utilizing localized surface plasmon resonance (LSPR), have shown promise as powerful platforms for real-time detection due to their high sensitivity, lower cost, and potential for portability [3], [4], [5]. In our study, we will be evaluating the performance of a tapered single-mode-multimode-single-mode (SMF-MMF-SMF) fibers functionalized with various synthesized nanostructures exhibiting LSPR: gold nanoparticles (Au NPs), gold nanostars (Au NSs), Au NP@ZrO_2, and Au NS@ZrO_2 core-shell particles. To enhance the biosensor's selectivity and specificity towards *S.* Typhimurium, monoclonal antibodies will be immobilized on the sensor surface. The study aims to fabricate an optical biosensor that is cost-effective, robust, and allows for real-time detection to meet the current demands of the food industry.

Description of the New Method or System

In this work, a tapered SMF-MMF-SMF platform functionalized with gold nanostructures is proposed for bacterial detection in food. The novelty of the proof-of-concept lies in the integration and comparative evaluation of different gold-based nanostructure—Au NPs, Au NSs, Au NP@ZrO_2 core-shell particles, and Au NS@ ZrO_2 core-shell particles— on the optical fiber platform. This approach would allow a systematic investigation of how nanostructure morphology influences both enhanced sensor performance and sensor stability in the presence of the target bacteria. This integrated design combines robustness, cost-effectiveness, and enhanced sensing performance, offering a promising approach for rapid, selective, and reliable pathogen detection in food safety applications.

Preliminary Results

Au NPs were synthesized using the Turkevich method. To strike the balance between the desired nanoparticle size ranging from 15-30 nm and keeping the precursor consumption at a minimum, optimization studies were done. The identified conditions were therefore 1.0 mM $HAuCl_4$ starting concentration, 1:5.1 $HAuCl_4$:citrate ratio, 15 min reaction time at 500 rpm stirring speed at a boiling temperature. This allowed the formation of spherical Au NPs with LSPR peak at 423 nm

(Fig. 1) and an average particle diameter of 18 ± 3 nm with a normal size distribution (Fig. 2). The same Au NPs were used as seeds for the synthesis of Au NPs through a surfactant-free approach. $AgNO_3$ was used to block high-energy facets of the Au NP seeds, allowing the specific migration of Au atoms from the growth solution onto the low-energy surface of the nanoparticle, which then form the branches [6] . Fig 3 shows the TEM micrograph of the synthesized Au NSs, with a characteristic LSPR peak at 822 nm. These results confirm the successful synthesis of gold nanostructures with desired optical properties, which will then be used for the functionalization of the optical fiber structure.

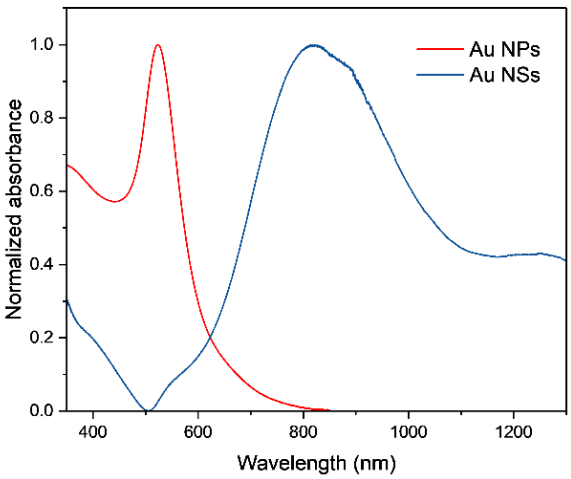

Fig. 1. UV-Vis-NIR absorbance spectra of Au NPs and Au NSs with corresponding LSPR peak at 423 nm and 822 nm, respectively.

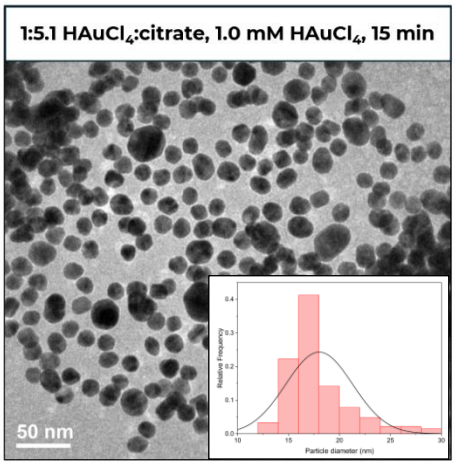

Fig. 2. TEM micrograph of Au NPs synthesized at the optimized precursor:reducing agent ratio, initial precursor concentration, and reaction time. Captured with 24k magnification and at 160 kV. (Inset: particle size distribution.)

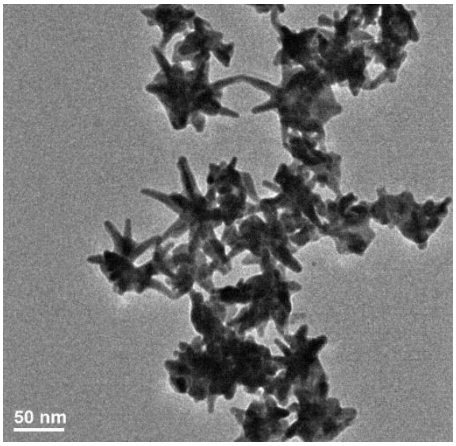

Fig. 3. TEM micrograph of Au NSs with well-defined branches. Captured with 24k magnification and at 160 kV

References

[1] S. Kaushik, A. Pandey, U. K. Tiwari, and R. K. Sinha, “A label-free fiber optic biosensor for Salmonella Typhimurium detection,” *Opt. Fiber Technol.*, vol. 46, pp. 95–103, Dec. 2018, doi: 10.1016/j.yofte.2018.09.012.

[2] S. Wang *et al.*, “Nanostructure-Modified Optical Fiber Sensors for Detection of *Salmonella typhimurium* in Food,” *ACS Appl. Nano Mater.*, p. acsanm.6c00082, Feb. 2026, doi: 10.1021/acsanm.6c00082.

[3] Q. Zhang *et al.*, “Dual nanoparticle-enhanced biophotonic fiber sensor for highly sensitive and selective detection of pseudomonas aeruginosa in food safety applications,” *Sens. Actuators Rep.*, vol. 10, p. 100409, Dec. 2025, doi: 10.1016/j.snr.2025.100409.

[4] X. Lang, “Chitosan-coated iron(III) oxide nanoparticles and tungsten disulfide quantum dots-immobilized Fiber-based WaveFlex Biosensor for Staphylococcus Aureus bacterial detection in real food samples,” 2024.

[5] A. Moslemi *et al.*, “Highly sensitive gold nanostar based optical fiber sensor with tunable plasmonic resonance,” *Sens. Actuators Rep.*, vol. 9, p. 100326, Jun. 2025, doi: 10.1016/j.snr.2025.100326.

[6] A. L. Siegel and G. A. Baker, “Bespoke nanostars: synthetic strategies, tactics, and uses of tailored branched gold nanoparticles,” *Nanoscale Adv.*, vol. 3, no. 14, pp. 3980–4004, 2021, doi: 10.1039/D0NA01057J.

Acknowledgment

The study has received funding from the European Union’s Horizon Europe research and innovation program under the Marie Skłodowska-Curie Grant Agreement No 101169415 (FunctiGlass project).

Funded by
the European Union

DOI 10.5162/eurosensors2026/Mo–EFS–04

Smell-Based Molecular Communication for Mobile Robots Using Gas Sensing

Ali Abdali[1], Dadi Bi[2], Hayeong Lee[1], Ruifan Zhu[3], and Yansha Deng[1]

[1] Department of Engineering, King's College London, London, UK.
[2] James Watt School of Engineering, University of Glasgow, Glasgow, UK.
[3] Department of Electrical and Electronic Engineering, Imperial College London, London, UK.
Corresponding Author's e-mail address: yansha.deng@kcl.ac.uk

Summary:

We present an experimental demonstration of smell-based molecular communication for mobile robots using gas sensing. Inspired by biological systems, information is encoded in chemical signals that propagate through the environment as volatile plumes and are detected by a gas-sensor-equipped receiver as transient responses. A robotic-compatible platform enables autonomous emission, detection, and interpretation of these signals. Representative sensor measurements exhibit distinct transient dynamics, enabling reliable detection of individual chemical pulses. The received signal shows clear attenuation with increasing transmitter–receiver distance and sensitivity to transmission pulse duration. The system demonstrates stable and reproducible communication behavior under varying spatial configurations. These results establish chemical sensing as a viable communication modality and provide a foundation for smell sensing-driven information exchange and coordination among autonomous robotic systems.

Keywords: molecular communication, gas sensors, robotic communication, chemical sensing, volatile organic compounds

Background, Motivation and Objective

Communication between autonomous robots is predominantly based on radio frequency or optical technologies, which can degrade in cluttered, confined, or electromagnetically noisy environments. In contrast, biological systems widely employ chemical signaling to enable robust and decentralized information exchange. Inspired by these natural mechanisms, molecular communication has emerged as an alternative paradigm [1]. However, its practical realization in mobile robotic systems remains largely unexplored despite recent advances in robotic olfaction and gas-sensing platforms [2, 3]. In particular, the integration of chemical sensing and actuation into autonomous platforms, and understanding signal propagation under realistic conditions, remain open challenges. In this work, we develop a gas sensor-based molecular communication framework for mobile robots and investigate its behavior under varying spatial and environmental conditions.

Description of the New Method or System

We present a molecular communication system designed for integration with robotic platforms and evaluated under controlled experimental conditions. The transmitter emits controlled pulses of aerosolized vinegar vapor, while the receiver captures the resulting signals using a metal-oxide gas sensor. The system is designed to operate under realistic conditions, where signal propagation is influenced by spatial configuration and environmental factors.

Unlike most existing studies based on highly simplified setups, the proposed framework enables experimental investigation of chemical signal propagation under controlled yet spatially varying conditions. The design allows systematic evaluation of how distance, pulse duration, and environmental factors affect signal detectability. This approach establishes chemical sensing as a practical mechanism for communication in robotic systems.

Results

Experimental observations demonstrate distinct sensor responses to controlled chemical pulse transmissions. The experimental setup, shown in Fig. 1, consists of a transmitter that emits periodic bursts of volatile molecules and a receiver equipped with a gas sensor positioned at a

defined spatial offset. This configuration enables systematic investigation of signal propagation under controlled geometric conditions. The measured signals exhibit a characteristic transient response to chemical pulse transmission, consisting of a rapid rise upon arrival followed by a gradual decay. As shown in Fig. 2, the sensor response varies systematically with the transmitter–receiver distance. Increasing distance results in a clear reduction in peak amplitude. This behavior reflects the attenuation and temporal spreading of the chemical plume during propagation. Despite these effects, the signal remains clearly distinguishable across all configurations.

As shown in Fig. 3, increasing the pulse duration leads to a stronger received response and a more prolonged decay profile. Despite these variations in amplitude and temporal extent, all cases retain a similar overall transient shape. This result indicates that the measured signal is sensitive to transmission duration and reflects the temporal characteristics of the emitted chemical pulse.

Extended periodic transmissions demonstrate repeatable sensor behavior over long durations. As shown in Fig. 4, successive chemical pulses produce distinguishable transient responses with similar overall temporal profiles across cycles. The responses maintain similar amplitude and temporal profiles across cycles, indicating stable system performance over time. These results highlight the capability of the sensing mechanism to support continuous signal transmission with clear event separation, suggesting its suitability for low-rate information exchange.

These findings demonstrate that smell sensing can support reliable information exchange, providing a foundation for autonomous robotic systems operating in environments where conventional communication methods are limited. Additional results, including mobile robotic implementation aspects, will be presented at the conference.

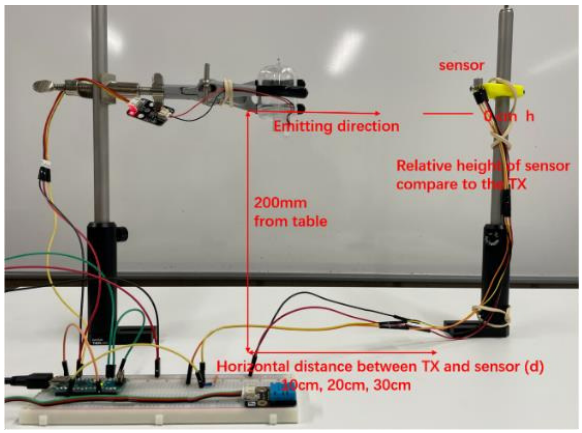

Figure 1: Experimental setup for smell-based molecular communication.

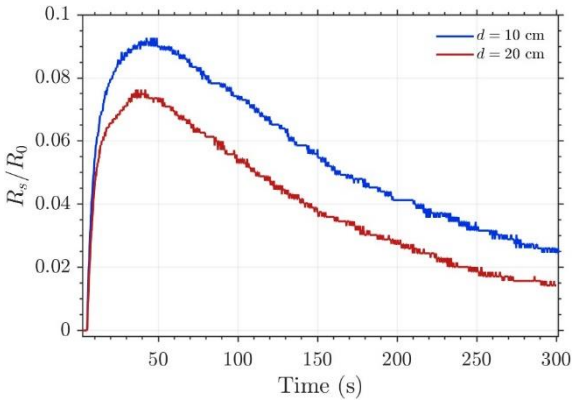

Figure 2: Representative gas sensor responses to a chemical pulse at two transmitter–receiver distances.

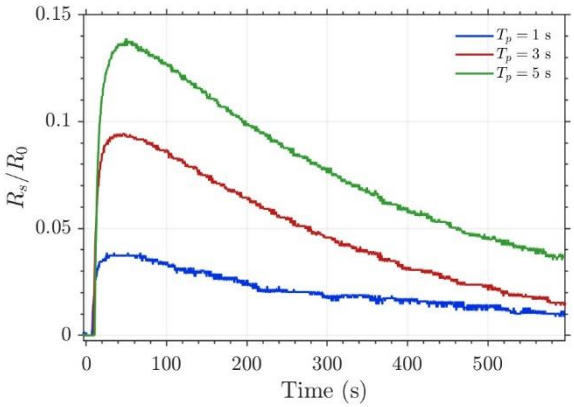

Figure 3: Representative gas sensor responses to chemical pulses of different pulse durations.

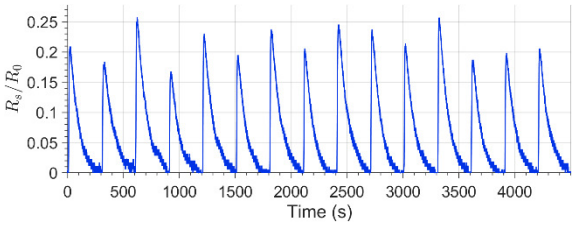

Figure 4: Representative sensor responses under periodic chemical pulse transmission.

References

[1] N. Farsad et al., “A Comprehensive Survey of Molecular Communication,” IEEE Commun. Surveys Tuts., 2016.

[2] W. Zhang, W. Tang, Z. Wan, and Z. Fan, “Advanced electronic noses for future robotic olfaction,” npj Flexible Electronics, vol. 9, no. 1, 2025.

[3] Xiang S.Y., Wang T.Y., Zhang Z.K., Jin H., “Harnessing interfacial and gas-phase reaction engineering to enhance sensing performance for autonomous gas leak detection in smell-based robot,” Rare Metals, 2025.

Acknowledgments

This work was supported in part by the European Research Council (ERC) under the European Union Horizon Europe research and innovation program through the ERC Starting Grant Nr. 101221728 REACTION.

DOI 10.5162/eurosensors2026/Mo–EFS–05

MOS Sensors Characterization for Fermentation Monitoring Using GC-SOMSA

Lucia Corrà[1], Gina Zeh[2], Tilman Sauerwald[2], Laura Capelli[1], Michael Czerny[2]
[1]Department of Chemistry, Materials and Chemical Engineering "Giulio Natta", Politecnico di Milano, Piazza Leonardo da Vinci 32, Milan, Italy,
[2]Fraunhofer Institute for Process Engineering and Packaging, Giggenhauser Strasse 35, D-85354 Freising, Germanyy
lucia.corra@polimi.it

Summary:
Headspace monitoring is a promising strategy for fermentation control, with ammonia representing a key fermentation marker. In this work, MOS sensor characterization for headspace measurement of aqueous ammonia solutions (pH > 10) was carried out using gas chromatography mass spectrometry (GC-MS) coupled with a sensor array. All four sensors exhibited a power law response to ammonia concentration, with one (SGP40, Sensirion) achieving a limit of detection below 1 ppm. These results establish a foundation for the characterisation of MOS sensor for fermentation processes.

Keywords: GS-SOMSA, MOS, fermentation, ammonia.

Background, Motivation and Objective

Monitoring of fermentation processes in the headspace has become increasingly attractive to standardize products characteristics, detect faults and optimize the process [1]. Fermentation refers to the enzymatic conversion of organic substrates by the action of microorganisms into a variety of metabolites [2]. Among the various metabolites, ammonia is widely reported, particularly as a product of the fermentation of protein-rich foods such as cheese, natto, and miso [2]. Metal oxide semiconductor (MOS) sensors can be an inexpensive and compact technology to monitor a large range of metabolites generated throughout the fermentation processes including ammonia [3]. However, due to their low selectivity and lack of specificity, a sensor characterization towards the target analytes needs to be carried out to identify suitable sensors and their operating modes as well as other potential system components for sampling and separation [4]. To this end, the gas chromatography selective odorant measurement sensor array (GS-SOMSA) has been developed [4,5] focusing on volatile organic compounds (VOCs). In this work the methodology is enhanced to the characterization of ammonia to enable a more comprehensive sensors characterization.

Materials and Methods

The GC-SOMSA system described by [5] consisted of a gas chromatograph (Trace 1610 gas chromatograph; Thermo Scientific, USA) coupled in parallel with a mass spectrometer (ISQ 7610 Single Quadrupole Mass Spectrometer; Thermo Scientific, USA) and a sensor chamber was used. For direct ammonia quantification without derivatization, the SPME-GC-MS method proposed by Zidouhia et al., 2025 was adapted to our work [6]. Aqueous ammonia was prepared in triplicate at different concentrations from ammonium hydroxide solution (Sigma-Aldrich, USA). The pH of the ammonia solutions (2 mL) were adjusted with 200 µL NaOH solution (1 M) to pH ≥10 [6]. The concentrations tested ranged from 0.5 ppm to 1000 ppm. Ammonia was extracted for 32 min at 40°C by a acrylate SPME fiber (, Sigma-Aldrich, USA) and analyzed by GC-MS using a DB-5 (Agilent Technologies, USA) capillary GC column. The sensor chamber housed an SGP40 gas sensor featuring four sensing elements. The sensor signals were evaluated by an in-house software. The heights of the ammonia signals were used for calibration plots evaluation and limit of detection estimation. The estimated limit of detection was obtained by comparing the peak height of water blank (adjusted at pH >10 with NaOH) with the four sensing elements when compared to the lowest concentrations of ammonia tested.

Results

The characteristic m/z-ion 16 was used for monitoring ammonia in GC-MS analyses. It was tentatively identified using the NIST database (match >90%). The retention time determined by GC-MS was used to identify ammonia in the SOMSA-chromatograms of the four sensors.

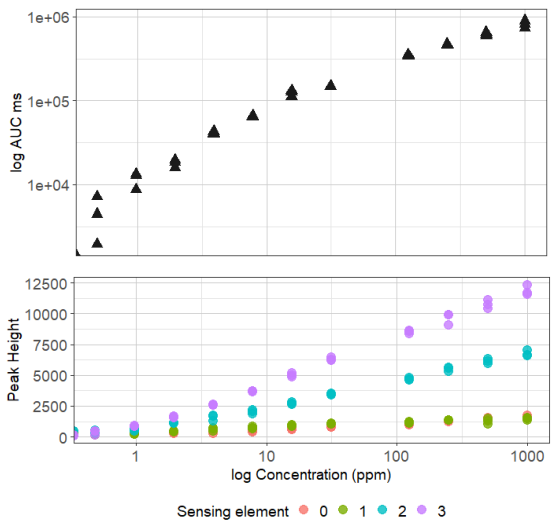

Fig. 1. Calibration plot of MS signal (logarithm of AUC for ms vs logarithm) of ammonia concentration and calibration plot for sensor response (peak height vs logarithm of ammonia concentration)

Fig. 1 shows first the calibration plot of MS results obtained using the AUC of m/z of 16. These preliminary results were used as reference to compare with the calibration curves for sensors responses. From the sensors responses, which are proportional to the logarithm of the sensor conductance [5] the peak height was derived. Subsequently, a calibration plot was constructed by plotting the peak height against the logarithm of ammonia concentration. As displayed in Fig. 1 the sensor response can be all estimated by a power law with R^2 as follow per sensing element 0 (0.9563), 1 (0.9354), 2 (0.9873) and 3 (0.9922). Following peak height extraction, the mean peak height amongst replicates of the water blank was compared to the mean ammonia peak at low concentrations (0.5, 1 and 2 ppm) as displayed in Fig. 2.

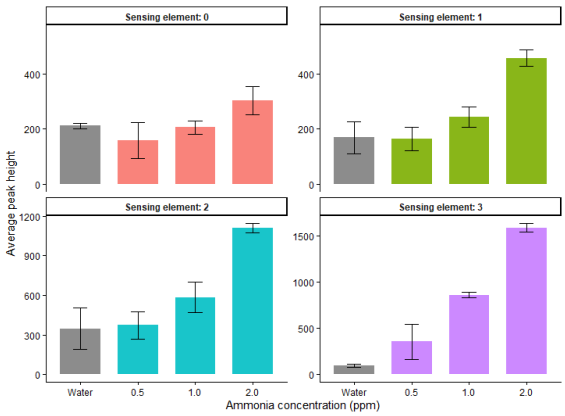

Fig. 2. Average peak height vs concentration of ammonia (0.5, 1 and 2) and water blank (grey) for the 4 sensing elements: 0: red, 1: green, 2: light blue and 3: purple

As shown in the histogram, at 1 ppm only sensing element 3 (purple) exhibited a peak height exceeding that of the water blank. At 2 ppm, sensing elements 1 and 2 (green and light blue respectively) displayed higher peak height than the water blank, while sensing element 0 (red) didn't show a significant response below 2 ppm. The differing estimated limits of detection across the four sensing elements suggest that their selection should be tailored to the expected concentration range, as some sensing elements may be more suitable for specific applications. A method for GC-SOMSA measurements of ammonia was established. By the choice of the sampling technique and GC column it is expected that VOC key markers from fermentation can be measured with the same apparatus. This would enable a highly functional approach to characterize additional fermentation markers.

References

[1] S. A. Siddiqui, Z. Erol, J. Rugji, F. Taşçı, H. A. Kahraman, V. Toppi, R. Castro-Muñoz, An overview of fermentation in the food industry-looking back from a new perspective, Bioresources and bioprocessing, 10(1), 85 (2023); https://doi.org/10.1186/s40643-023-00702-y

[2] C. S. Yee, N. A. Zahia-Azizan, M. H. Abd Rahim, N. A. Mohd Zaini, R. B. Raja-Razali, M. A. Ushidee-Radzi, W. A. A. Q. I. Wan-Mohtar, Smart fermentation technologies: Microbial process control in traditional fermented foods, Fermentation, 11(6), 323 (2025); https://doi.org/10.3390/fermentation11060323

[3] T. Seesaard, C. Wongchoosuk, Recent progress in electronic noses for fermented foods and beverages applications, Fermentation, 8(7), 302 (2022); https://doi.org/10.3390/fermentation8070302

[4] M. Koehne, O. T. Penagos Carrascal, M. Czerny, G. Zeh, T. Sauerwald, A versatile development platform for odor monitoring systems, Journal of Sensors and Sensor Systems, 14(1), 75-88 (2025); https://doi.org/10.5194/jsss-14-75-2025

[5] T. Hofmann, P. Schieberle, C. Krummel, A. Freiling, J. Bock, L. Heinert, D. Kohl, High resolution gas chromatography/selective odorant measurement by multisensor array (HRGC/SOMSA): a useful approach to standardise multisensor arrays for use in the detection of key food odorants, Sensors and Actuators B: Chemical, 41(1-3), 81-87 (1997); https://doi.org/10.1016/S0925-4005(97)80280-8

[6] D. Zidouhia, E. Grau, D. M. Bassani, Direct Quantification of Ammonia and Alkylamines in Aqueous Environments Using Solid-Phase Microextraction-Gas chromatography-Mass spectrometry, Chemistry-Methods, 5(8), e202400095 (2025); https://doi.org/10.1002/cmtd.202400095

DOI 10.5162/eurosensors2026/Mo–EFS–06

Portable and Smart Ion Analyser for Automated Monitoring of Alkali Metals in Battery Recycling Industries towards Circular Economy

Renato Gil[1], Samuel Silva[1], Olesia Dudik[1], Álvaro Geraldes[1], João Piteira[1], Ana Carolina Costa[2,3], Maria João Regufe[2], Rui Jorge Sousa[2], Raquel Queirós[1]
[1]INL-International Iberian Nanotechnology Laboratory, Avenida Mestre José Veiga, 4715-330 Braga, Portugal
[2] B.again SA, Rua de Pitancinhos, ap. 208, 4700-727 Braga, Portugal
[3]LSRE-LCM, ALiCE, Faculty of Engineering, University of Porto, Rua Dr. Roberto Frias, 4200-465 Porto, Portugal
raquel.queiros@inl.int

Summary:
A portable, accessible, and smart ion analyser is presented herein for automated monitoring of Li^+ and Na^+ in battery recycling processes, integrating potentiometric sensing, automated fluid handling, embedded data processing, and remote dashboard access in a compact modular platform. The system enables quasi-parallel multi-electrode measurements, autonomous recalibration, and near-real-time operation with minimal human intervention. The prototype shows wide linear ranges, low detection limits, and strong agreement with ICP-MS/MS reference measurements. Deployed in a battery recycling facility, it demonstrated reliable on-site monitoring of process streams over a 4-week trial. Overall, the system supports sustainable recycling, operational decision-making, and scalable industrial metal recovery.

Keywords: Alkali-metals, Potentiometry, Smart Ion Analyser, Battery recycling, Circular economy.

Background, Motivation and Objective

With the increasing demand for lithium-ion batteries and the growing need for efficient recycling strategies, accurate, fast, and accessible monitoring solutions for strategic metals are crucial to support sustainable recycling, raw material recovery, and quality control processes [1]. While conventional instrumental procedures are effective for benchtop analysis, the high cost, results delay, and laborious sample pre-treatment are still challenges to address. In context, we present a portable and smart ion analyser for automated and real-time monitoring of alkali metals (i.e. Li^+ and Na^+) in battery recycling processes.

Description of the New Method or System

The ion analyser (Fig. 1) combines potentiometric sensing, embedded signal processing, fluidic monitoring, and networked data communication into a compact digital-physical platform (50 cm × 35 cm × 30 cm). The system integrates eighteen ion-selective electrodes (nine Na-ISEs and nine Li-ISEs) and six solid-contact Ag/AgCl reference electrodes in a screen-printed configuration, assembled in a modular 3D-printed multi-flow cell, to enable multi-point statistical acquisition and multiple analyses over time. A syringe pump, two rotary selection valves, three pillow bags with standard solutions (recalibration Li/Na solutions and ionic strength adjuster), and a custom-made 3D-printed module for sample dilution are integrated for sample and carrier delivery, enabling automated sensor recalibration and sample processing. A single EmStat-4M potentiostat was extended by a custom-made multiplexer hardware adaptor to quasi-parallel multi-electrode operation (1s interval). Beyond sensing, the system is embedded with a flowmeter for real-time flow characterisation and a derivative flat-region detection algorithm for data analysis. In addition, the ion analyser incorporates software with a dashboard interface, accessible via an integrated display or browser connection, supporting standalone, scheduled, or fully automated operation modes.

Results

Under optimal conditions, the analytical figures of merit of the proposed system include a sub-Nernstian sensitivity (≈55 mV dec^{-1}) and a wide linear response range from 0.1 to 100 mM for both metals. The limit of detection was 0.05 and 0.04 mM for Li^+ and Na^+, respectively. Impressive slope reproducibility for the same electrode or between electrode units was demonstrated by relative standard deviation (RSD) values lower than 7.7%, while small discrepancies were

observed for the intercept values (RSD<20%), which are circumvented by sensor recalibration before sample analysis. The system supports up to 45 consecutive measurements without consumable replacement or maintenance, with a sample throughput every 1 hour and 30 minutes. Before deployment, pregnant leaching solutions of black mass (PLS) from Lithium Nickel Manganese Cobalt Oxide batteries and battery discharge waters (BDW) samples were analysed using the ion analyser and compared to analysis performed by ICP/MS-MS at an external laboratory as the reference method. A strong agreement was observed between the two approaches, specifically for Na measurement at the BDW samples (diff ≤16%) and Li measurement at the PLS samples (diff ≤27%).

Tab. 1: Analytical performance of the Ion Analyser.

	Li^+	Na^+
Slope / mV dec^{-1}	56.0	56.1
R^2	0.999	0.999
LRR / mg L^{-1}	0.7 – 700	2.3 – 2300
LOD / mg L^{-1}	0.4	0.8
pH range	2 – 10	2 – 10

As a case study, the ion analyser was deployed at a local battery recycling facility (B.again, Braga, Portugal) to monitor the levels of Li^+ and Na^+ in PLS and BDW samples. During the trial period (4 weeks), the system performed intermittent analysis with a total of 35 measurements, and the samples were sent to an external laboratory to be analysed by ICP/MS-MS (results still pending).

This innovative portable ion analyser represents a step forward to resilient smart sensing solutions and circular economy [2], offering a cost-effective and modular smart system, on-site or near-line operation, automated analysis, and industrial connectivity. Ultimately, this system contributes to more efficient decision-making and sustainable metal recoveries in battery recycling industries [3].

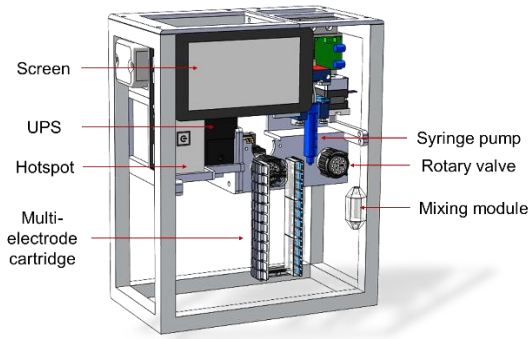

Fig. 1. Ion Analyser visualisation and description.

References

[1] Xing, Z., M. Srinivasan, Lithium Recovery from Spent Lithium-ion batteries Leachate by Chelating, *Chemical Engineering Journal* 474, 145306 (2023); doi: 10.1016/j.cej.2023.145306

[2] C. Beaucillon, Strategic Autonomy: A New Identity for the EU as a Global Actor, *European Papers* 8, 417-428 (2023); doi: 10.15166/2499-8249/664

[3] Kilavuz, E. Sustainable Lithium-Ion Battery Recycling: Challenges, Innovations, and Pathways to a Circular Economy, *ACS Sustainable Resource Management* 2, 1838-1858 (2025); doi: 10.1021/acssusresmgt.5c00408

DOI 10.5162/eurosensors2026/Tu–EFS–01

Direct Comparison between an Analog MOS Sensor Array and a Single Temperature-Modulated Digital MOS Sensor for Food Spoilage Status Classification

Lucia Corrà[1], Christian Ratti[1], Sara Bettinaglio[1], Emanuele Zanni[2], Francesca Pianca[3], Raffaele Dellacà[2], Laura Capelli[1]
[1] Department of Chemistry, Materials and Chemical Engineering "Giulio Natta", Politecnico di Milano, Piazza Leonardo da Vinci 32, Milan, Italy
[2] Department of Electronics, Information, and Bioengineering, Politecnico di Milano, Via Giuseppe Colombo 40, 20133 Milan, Italy
[3] Electrolux Italia s.p.a., 31025, Treviso, Italy
lucia.corra@polimi.it

Summary:
The integration of electronic nose (e-noses) in home appliances is limited by the cost of the hardware. In this study, food spoilage status has been assessed by comparing the performances of a single digital MOS sensor with an array of analog MOS sensors. To carry out this study, an experimental setup has been designed to measure the food sample headspace simultaneously with the two configuration settings. The single digital MOS sensor has shown comparable classification performance across three different machine learning models, demonstrating the potential of substituting sensor arrays.

Keywords: Digital sensor, MOS, Food spoilage, Home appliance, Temperature-Cycle Operation

Background, Motivation and Objective

E-noses based on metal oxide semiconductor (MOS) sensors have been successful in predicting food spoilage status [1]. However, the integration of such systems into home appliances remains limited in real-world applications [2]. One of the key constraints is the cost of the sensing hardware, along with its power consumption and compactness, which must be minimized to ensure their commercial viability [3]. Temperature-cycled operation (TCO) of digital MOS sensors has been proposed as an effective approach to emulate a virtual multi-sensor array using a single sensing element [4]. The TCO determines higher selectivity as the interaction of the sensitive layer with the Volatile Organic Compounds (VOCs) is temperature dependent, as they have different oxidation temperatures [5]. Furthermore, the instantaneous temperature changes from high to low temperatures determine a non-equilibrium condition in which trace amounts of reducing gases can react with the sensitive layer [6]. These features make TCO-operated digital sensors a promising low-cost alternative to analog sensor arrays. Therefore, this study aims to compare the classification performance in predicting food spoilage status using a single digital TCO MOS sensor, and an array of six analog MOS sensors operated at constant temperature.

Description of the New Method or System

The experimental setup (Fig. 1) was designed with four custom-made airtight containers connected to a single e-nose measurement core, consisting of a PCB designed to read six analog MOS sensors and one digital MOS sensor operated under TCO. With a frequency of 12 hours, headspace was drawn sequentially from each container by a diaphragm pump (NMP820KPDC-B, KNF) and routed to the measurement core via a custom PEEK flow distributor controlled by on-off valves (LVM09, SMC, JP). Due to the low headspace volume of the container (~1.5 L), a recirculation mechanism was implemented by adding a return path at the pump outlet via a second flow distributor. Finally, to allow for reference baseline measurement, a clean air inlet was installed at the e-nose measurement core.

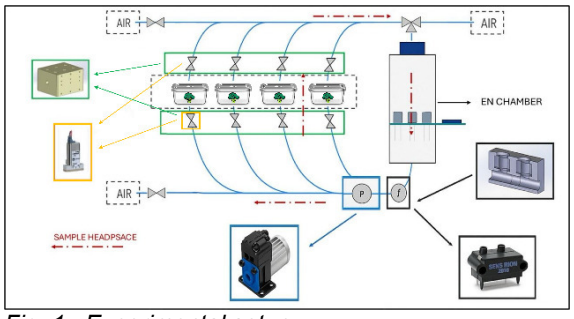

Fig. 1. Experimental setup.

To label the spoilage status of food samples, an internal microbiological method was carried out every 24 hours on a dedicated extra container kept under the same conditions as the headspace samples. Based on the microbiological results, three spoilage labels were defined: “fresh”, “eat it soon”, and “spoiled”. A total of three test sessions were carried out, each including four food samples for the e-nose and one sample for spoilage assessment, all taken from the same production lot.

Raw sensor resistances were pre-processed to remove undesired signal spikes and normalized using reference air. Subsequently, features extraction has been conducted on the sensors' resistance curve, resulting in a total of 102 features from the analog sensors (17 per sensor) and 99 features from the single digital sensor, including transient-dependent resistance changes. Feature selection was then carried out by removing zero-variance and highly correlated features, followed by application of Boruta algorithm to select the most informative features for classification.

Results

The subset of selected features, 7 for the analog sensor and 9 for the digital sensor, was used as input for Principal Component Analysis (PCA).

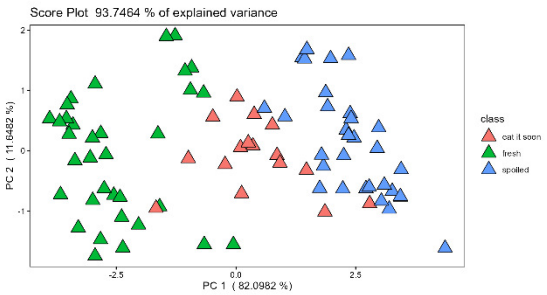

Fig. 2. PCA score-plot for analog sensors array.

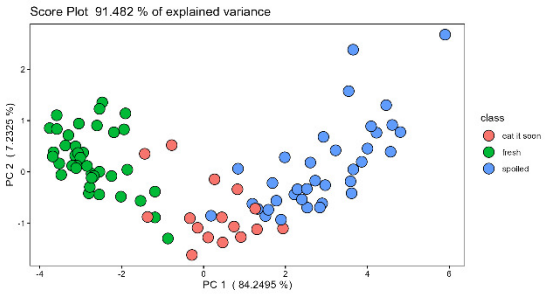

Fig. 3. PCA score-plot for digital sensor.

Both score plots (Fig. 2 and 3) reveal a visually similar distribution of samples, with the three spoilage labels showing comparable clusters along PC1. To quantitatively assess the classification performance, three machine learning models, Random Forest, Linear Discriminant Analysis (LDA), and XGBoost, were developed. Across the three independent test sessions, three containers were used as training and the remaining one as test. Accuracy has been used as figure of merit for model classification performance (Fig. 4). The digital sensor showed similar performance compared to the analog sensor array across all three models yielding the highest accuracy with Random Forest.

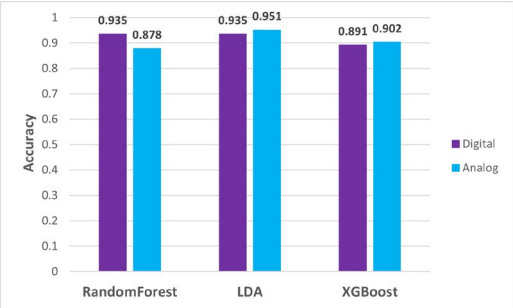

Fig.4. Classification model accuracy.

These preliminary results indicate that the single TCO-operated digital sensor achieves classification accuracy comparable to the analog array, supporting its potential as a low-cost alternative for food spoilage classification. Further experiments will be conducted applying more advanced data processing techniques.

References

[1] M. Falasconi, I. Concina, E. Gobbi, V. Sberveglieri, A. Pulvirenti, G. Sberveglieri, Electronic nose for microbiological quality control of food products, *International Journal of Electrochemistry*, (2012); doi: 10.1155/2012/715763

[2] F. Röck, N. Barsan, U. Weimar, Electronic nose: current status and future trends, *Chemical reviews* 108, 705-725 (2008); doi:10.1021/cr068121q

[3] GC. Green, AD. Chan, RA Goubran, Monitoring of food spoilage with electronic nose: potential applications for smart homes, *3rd International Conference on Pervasive Computing Technologies for Healthcare*, 1-7 (2009); doi: 10.1109/PCTHEALTH.2009.5291419

[4] C. Schultealbert, T. Baur, A. Schütze, T. Sauerwald, Facile quantification and identification techniques for reducing gases over a wide concentration range using a MOS sensor in temperature-cycled operation, *Sensors 18*, 744 (2018); doi: 10.3390/s18030744

[5] JM. Smulko, M. Trawka, CG. Granqvist, R. Ionescu, F. Annanouch, E. Llobet, LB. Kish, New approaches for improving selectivity and sensitivity of resistive gas sensors: a review, *International Journal on Smart Sensing and Intelligent Systems 7*, 1-6 (2020); doi: 10.21307/ijssis-2019-027

[6] T. Baur, C. Schultealbert, A. Schütze, T. Sauerwald, Novel method for the detection of short trace gas pulses with metal oxide semiconductor gas sensors, *Journal of Sensors and Sensor Systems 7*, 411-419 (2018); doi: 10.5194/jsss-7-411-2018

DOI 10.5162/eurosensors2026/Tu–EFS–02

A Lensless Microscope-Based Sensor for 3D Displacement Measurement in Infrastructure Monitoring

Luqi Yan[1], Agus Budi Dharmawan[1], Jan Gülink[2], Izabela Zrazinska[3], Francisco Hernandez[3], J. Daniel Prades[1]
[1] Institute of Semiconductor Technology (IHT) and Laboratory for Emerging Nanometrology (LENA), Technische Universität Braunschweig, Germany
[2] QubeDot GmbH, Braunschweig, Germany
[3] Worldsensing S.L., Barcelona, Spain
luqi.yan@tu-braunschweig.de

Summary:
We developed a cost-effective, compact lensless imaging system designed for 3D displacement tracking in the context of structural health monitoring. Lateral displacement is measured using phase-correlation-based image registration, while axial displacement is estimated from illumination-dependent image shifts using a geometric model. Experiments show lateral resolution down to 5 micrometers (x-y axes) and axial resolution of about 0.1 millimeters (z axis) over a dynamic range up to 18 millimeters. This instrument enables compact non-contact monitoring of microscopic 3D movements in cracks and joints.

Keywords: 3D displacement measurement, optical sensing, lensless imaging, phase correlation, structural health monitoring

Background and Motivation

Structural health monitoring of infrastructure requires reliable displacement sensing to enable long-term assessment of deformation and displacement. Conventional contact-based sensors include electrical crackmeters, vibrating-wire crackmeters, and fiber Bragg grating-based sensors. Despite their high sensitivity, these methods are typically deployed as point-wise measurements and most often provide one-dimensional information at each sensing location.

Vision-based non-contact methods have therefore attracted strong interest for displacement monitoring [1]. However, many existing optical approaches rely on bulky imaging optics and complex calibration, which restrict their use in compact field-deployable systems.

Lensless imaging offers a promising route toward miniaturized optical sensing [2,3]. In this field, phase correlation has been established as a robust method for sub-pixel displacement estimation [4]. Here, we combine these concepts and propose a compact lensless optical sensor based on a monochrome CMOS camera and a microLED array. The objective is to achieve 3D displacement sensing, where lateral motion (x-y axes) is measured by phase correlation and axial motion (z axis) is inferred from illumination-dependent image shifts under different LED positions.

Methodology and Instrument Design

The proposed instrument implements a compact lensless optical architecture for 3D displacement measurement using a QubeDot microLED array (λ = 450 nm), a patterned marker, and a Basler CMOS camera (daA3840-45um) in an in-line configuration. The marker is positioned between the illumination source and the sensor, so that each LED generates a distinct diffraction-based intensity pattern on the CMOS plane. Controlled displacement is introduced using a three-axis translation stage actuated by Thorlabs K-Cube DC servo controllers.

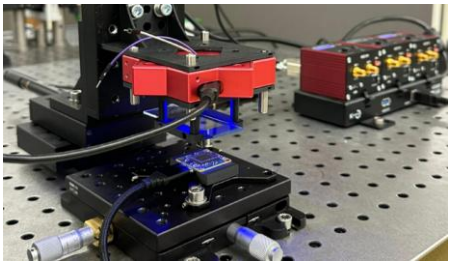

Fig. 1. Experimental setup of the proposed lensless displacement sensing instrument.

For two frames $I_a(x,y)$ and $I_b(x,y)$, the subpixel shift is obtained by phase correlation [4]:

$$(\Delta x, \Delta y), \rho = PhaseCorrelation(I_a, I_b) \quad (1)$$

where $\Delta x, \Delta y$ are pixel displacements and ρ is the correlation response. A key design feature is

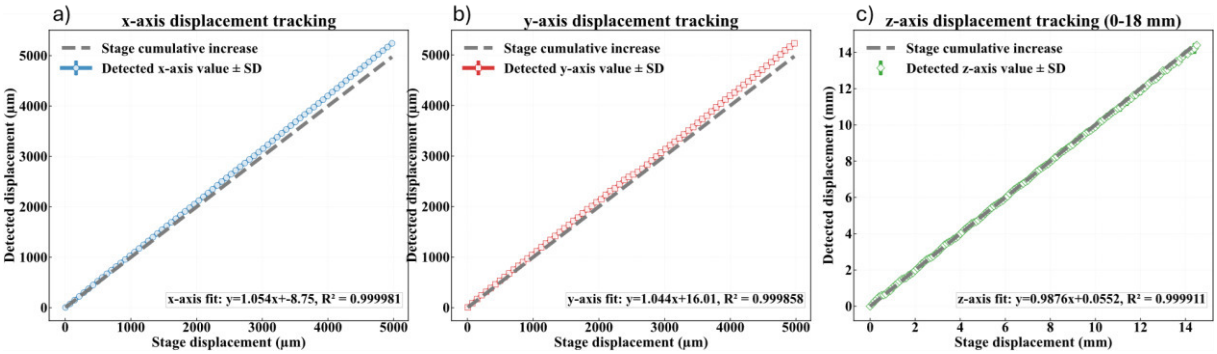

Fig. 2. Measured versus stage-referenced cumulative displacement for lateral (x, y) and axial (z) directions. a) x-axis displacement tracking; b) y-axis displacement tracking; c) axial displacement estimation over 0–18mm.

the decoupled estimation of lateral and axial motion. Lateral (x-y) displacement is estimated from inter-cycle, same-pattern phase correlations, while axial (z) displacement is estimated from intra-cycle, illumination-dependent disparities. This separation reduces cross-axis coupling between lateral drift and depth variation.

Results

In the experiment, a motorized stage driven by three Thorlabs K-Cube DC servo controllers along the x, y, and z axes. The stage moved in fixed step sizes (5 µm in the x-y axes and 100 µm in the z axis). The measured displacements were recorded in real time and compared with a reference displacement of the stage to evaluate the measurement performance.

The displacement estimates follow the commanded stage motion consistently across all three axes. Under representative experimental conditions (CMOS pixel size of 2 µm, exposure time of 1000 µs, and microLED pixel size of 75 µm), the instrument achieves lateral (x-y) resolution down to 5 µm and axial (z) resolution of about 0.1 mm over a dynamic range up to 18 mm.

For detection speed, we tuned the camera readout by reducing the CMOS region of interest (ROI). In our setup with a Basler daA3840-45um, the full-frame mode (3840 × 2160 pixels) provided about 44 fps, whereas cropping to a small ROI (320 × 240 pixels) increased the acquisition rate to about 200 fps. Unlike reconstruction-based lensless or holographic axial methods [3], which rely on numerical propagation across multiple depth planes using wave-propagation models such as the angular spectrum method [5], our instrument estimates displacement directly from illumination-dependent pattern shifts. This avoids full image reconstruction and reduces computational complexity. Processing a 1 MP image via holographic reconstruction typically takes 0.2 s [5], while our instrument processes an image of the same size in only 0.008 s. This speed gain directly improves temporal resolution for real-time displacement monitoring. This combined hardware–algorithm co-design enables compact, real-time, and repeatable 3D displacement sensing in a single optical head.

Acknowledgments

This technology has been developed under TotalScope project (number 7232) funded under the Eurostars programme with co-financing from *Centro para el Desarrollo Tecnológico y la Innovación, E.P.E.* (CDTI) and *Deutsches Zentrum für Luft- und Raumfahrt* (DLR) under European Union's Horizon Europe Framework Programme for research and innovation. And supported by the Alexander von Humboldt Professorship of the Humboldt Foundation, the Federal Ministry of Education and Research (Germany), and the zukunft.niedersachsen program of the Lower Saxony Ministry for Science and Culture and the Volkswagen Foundation.

References

[1] S. Kim, Y. Choi, J. Kim, and H. Na, Review of Image-Processing-Based Technology for Structural Health Monitoring, *Journal of Imaging* 10, 93 (2024); doi: 10.3390/jimaging10040093

[2] W. Bishara, T. Su, and A. Ozcan, Lensfree On-Chip Microscopy over a Wide Field-of-View Using Pixel Super-Resolution, *Optics Express* 18, 11181–11191 (2010); doi: 10.1364/OE.18.011181

[3] A. B. Dharmawan, S. Mariana, G. Scholz, P. Hörmann, T. Schulze, K. Triyana, M. Garcés-Schröder, I. Rustenbeck, K. Hiller, H. S. Wasisto, and A. Waag, Nonmechanical Parfocal and Autofocus Features Based on Wave Propagation Distribution in Lensfree Holographic Microscopy, *Scientific Reports* 11, 3213 (2021); doi: 10.1038/s41598-021-81098-7

[4] H. Foroosh, J. B. Zerubia, and M. Berthod, Extension of Phase Correlation to Subpixel Registration, *IEEE Transactions on Image Processing* 11, 188–200 (2002); doi: 10.1109/83.988953

[5] T. Latychevskaia, H. W. Fink, Practical algorithms for simulation and reconstruction of digital in-line holograms, *Applied Optics* 54, 2424–2434 (2015); doi: 10.1364/AO.54.002424

DOI 10.5162/eurosensors2026/Tu–EFS–03

From Measurements to Perceptions: Sensors and Structural Equation Modelling to Evaluate Indoor Comfort in University Buildings

Chiara Visentin[1,†], Matteo Pellegatti[1], Arianna Rossi[2], Marco Magoni[2,3], Danila Azzolina[4], Domenico Iervolino[5], Elena Marrocchino[4], Maria Grazia Paletta[4], Francesco Aldegheri[6], Giulio Magherini[2], Barbara Fabbri[2,,†]*

[1] Department of Engineering, University of Ferrara - via Saragat 1/A, 44122, Ferrara, Italy,
[2] Department of Physics and Earth Sciences, University of Ferrara - via Saragat 1/C, 44122, Ferrara, Italy,
[3] Center for Sensing Solution, Eurac Research - viale Druso 1, 39100 Bolzano, Italy,
[4] Department of Environmental and Prevention Sciences, University of Ferrara - C.so Ercole I D'Este, 32, 44121, Ferrara, Italy,
[5] Unit of Biostatistics, Epidemiology and Public Health, Department of Cardiac, Thoracic, Vascular Sciences and Public Health, University of Padova - Via Loredan 18, Padova 35131, Italy,
[6] Studio Tecnico Aldegheri - via Padova 27, 44122, Ferrara, Italy
barbara.fabbri@unife.it; [†]These authors are co-first authors of this work

Summary:

How is the Indoor Environmental Quality (IEQ) affecting the university students' satisfaction, comfort, and perceived learning performance? Technical conditions were monitored, while students' perceptions were collected through questionnaires spanning over the four seasons. Structural Equation Modelling (SEM), implemented through a Generalized Structured Component Analysis (GSCA), was used for the first time in university buildings to explore direct and indirect relationships among comfort domains, overall IEQ satisfaction, and perceived performance.

Keywords: Indoor Environmental Quality, multi-domain evaluation, structural equation modelling, comfort in university classrooms, human perception

Introduction

Extensive studies highlight how adequate school climate, particularly its environmental dimension, promotes student development. In this context, the interplay between physical environmental parameters and building layout represents a primary driver of IEQ [1]. Most existing studies addressed the question highlighted in the summary by considering IEQ domains individually, overlooking their combined effects. Conversely, this study adopts a practical multi-domain and multi-level approach to investigate indoor comfort by integrating such challenging long-term in-field measurements over all the four domains of IEQ and students' subjective evaluations, additionally applying for the first time SEM in university classrooms.

Materials and methods

In-field measurements and surveys were carried out in two lecture classrooms, labelled A and B, of Ferrara University (Italy), selected for the study as they share the same volume but differ in all aspects that might impact indoor environmental quality and comfort. Measurements included thermal (temperature and (relative humidity), air quality (CO_2, VOCs, PM10) [2], acoustic (sound pressure level) [3], and lighting (screen and horizontal illuminance) domains of the IEQ.

A questionnaire survey was employed to collect data on students' perceptions and psychological responses to the physical characteristics of the classroom environment, focusing on the key dimensions of IEQ. It included 25 closed-ended questions based on the EN ISO 10551 standard. The questionnaire was completed during 23 lessons in 14 different days. Overall, a total of 614 students participated in the survey.

The relationship among person-related factors, students' subjective response to the individual domains of IEQ, and perceived outcomes (i.e., global satisfaction with the IEQ and perceived performance), was simultaneously investigated through SEM-based approach (see Fig. 1). A GSCA-SEM was implemented with the software GSCA PRO. Before estimating the SEM,

diagnostic checks were performed to confirm that data met modelling assumptions.
Given the qualitative nature of the questionnaire items, Multiple Correspondence Analysis (MCA) was employed.

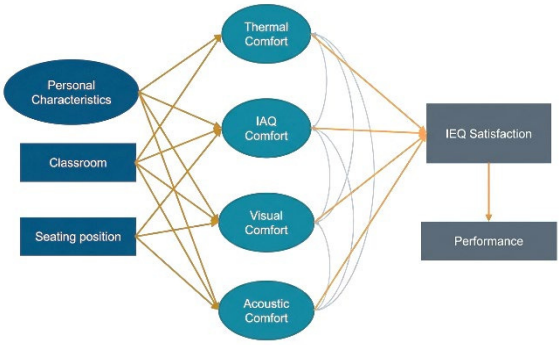

Fig. 1. Conceptual diagram with hypothesized pathways between variables. Rectangles and ellipsoids represent measured and latent variables, respectively.

Results

In order to allow comparison with the survey responses, the technical parameters measured over each two-hour session were aggregated into representative single values (see Fig. 2).

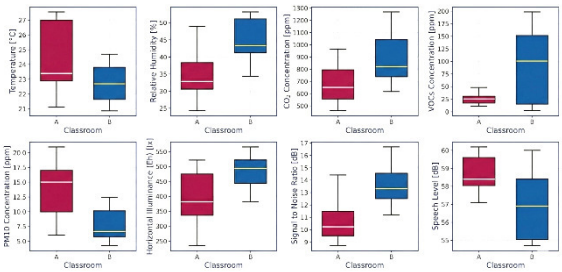

Fig. 2. Boxplots comparing environmental parameters measured during different lessons between Classroom A and B. The plots illustrate median values and interquartile ranges.

Then, the relationship between measured parameters and subjective data was estimated using linear mixed-effects models, with the measured parameter as a fixed effect and lesson as a random intercept to account for the hierarchical structure of the data. Correlations were generally low or non-significant. In the thermal domain, air temperature and relative humidity showed significant positive correlations. However, the effect size is very small and likely attributable to artefacts or to the sample size. In the indoor air quality (IAQ) domain, CO_2 and PM10 were negatively correlated with IAQ. VOCs, lighting parameters (Eh) and acoustic measures (speech levels and SNR) showed non-significant correlations with subjective evaluations. This is consistent with prior IEQ research.
The MCA results suggested that the chosen personal characteristics do not constitute a unified construct but rather reflect multiple distinct factors, then the latent variable representing personal characteristics was not considered in the final version of the SEM. This included 18 out of 28 items from the questionnaire. The model explained 39% of the variance in IEQ global satisfaction, indicating a moderate level of explanatory power. The GSCA-SEM explained 46% of the variance of thermal comfort, 54% in IAQ comfort, 31% in lighting comfort, and 30% in acoustic comfort. The high value for IAQ comfort supports the reliability of these perceptual assessments, in line with previous studies showing that air pollutants produce perceptible sensations of stuffiness, reduced freshness, or fatigue. Overall, IEQ satisfaction was positively associated with thermal, visual, and acoustic comfort. No significant relationship was observed with IAQ comfort, likely because the IAQ conditions during surveys showed limited variation and mostly fell within favourable or acceptable ranges.

Conclusions

Despite generally adequate classroom technical conditions, small or non-significant relationships were found between long-term monitoring and students' perception, suggesting the need to go beyond the separate analysis of the single domains. Indeed, SEM highlighted significant correlations among comfort domains, proving that indoor environment is perceived holistically rather than as a sum of independent factors. The results provided a practical outcome in terms of domains ranking, showing that thermal, visual, and acoustic comfort are the main predictors of overall IEQ satisfaction, while IAQ showed no direct effect. These findings underscore the value of integrated, multi-domain and human-centred assessment frameworks, providing insights to understand hierarchical human–environment interactions supporting the design and management of university classrooms.

References

[1] Y. Zhao, D. Li, Multi-domain indoor environmental quality in buildings: A review of their interaction and combined effects on occupant satisfaction, *Building and Environment* 228, (2023) 109844; doi: 10.1016/j.buildenv.2022.109844

[2] M. Magoni, A. Rossi, F. Tralli, P. Bernardoni, B. Fabbri, A. Gaiardo, S. Gherardi, V. Guidi, Novel Chemoresistive Sensors for Indoor CO_2 Monitoring: Validation in an Operational Environment, *ACS Sens.* 9, (2024) 2999–3008; doi: 10.1021/acssensors.4c00171

[3] M. Pellegatti, C. Visentin, S. Torresin, F. Babich, P. Wargocki, N. Prodi, Combined and cross-modal effects of acoustic and indoor air quality conditions on sensory and cognitive responses of university students, *Building and Environment* 288, (2026) 114005; doi: 10.1016/j.buildenv.2025.114005

DOI 10.5162/eurosensors2026/Tu–EFS–04

Theoretical-Experimental Investigation of a Surface Acoustic Wave Sensor Based on Dual Substrates

Hiba Taleb[1], Meddy Vanotti[1], Virginie Blondeau-Patissier[1]
[1] *Université Marie et Louis Pasteur, SUPMICROTECH, CNRS,* Time and Frequency department, FEMTO-ST Institute Besançon 25000, France,
hiba.taleb@femto-st.fr.

Summary:
To monitor air pollution, an innovative cascade impactor integrating Surface Acoustic Wave (SAW) sensors has been developed within our team. Conventional impaction plates are replaced by SAW sensors to measure PM10 and PM2.5, i.e., particles with aerodynamic diameters below 10 µm and 2.5 µm [1]. These sensors are typically based on bulk piezoelectric materials such as AT-cut quartz, which offers excellent thermal stability but low electromechanical coupling, limiting performance. The study investigates alternative substrates, comparing bulk lithium tantalate with a piezoelectric-on-insulator (POI) configuration in terms of performance. Numerical simulations and experiments demonstrate that the POI substrate provides enhanced sensitivity and improved thermal stability. These results highlight its potential for more efficient particulate matter detection.

Keywords: SAW sensors, Bulk substrate, POI substrate, sensitivity analysis, air monitoring.

Background, Motivation and Objective

Air pollution monitoring requires accurate, real-time detection of particulate matter (PM), which poses serious health risks due to deep respiratory penetration. SAW devices exhibit high gravimetric sensitivity and have been investigated by our team as microbalances for particle detection [1]. These sensors must combine high sensitivity at low concentrations with robustness under varying environmental conditions. Two key parameters are therefore considered: the electromechanical coupling coefficient (k^2), governing wave-surface interaction, and the temperature coefficient of frequency (TCF), affecting stability. Initial sensors based on quartz substrates supporting Love waves exhibited k^2 = 0.14% and TCF = −0.035 ppm/°C at 125 MHz [1]. To improve performance, quartz is replaced by a composite Piezoelectric-on-Insulator (POI) substrate, investigated and compared with its bulk counterpart.

Description of the Substrates Used

The substrates investigated in this study are, in accordance with IEEE standard, Lithium Tantalate (YXl)/42° in bulk form, referred to as LT42, and in piezoelectric-on-insulator form, referred to as LTOI42, as shown in Fig. 1. The bulk substrate consists of a single $LiTaO_3$ layer, whereas the POI structure is composed of a thin $LiTaO_3$ layer bonded onto a SiO_2 layer and supported by a silicon substrate.

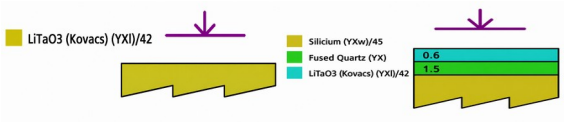

Fig. 1. Bulk and POI lithium tantalate substrates (thickness in µm) used for simulations

Simulation

A numerical tool based on Green's function formalism was used to evaluate the acoustic properties of the substrates. It allows the calculation of key parameters such as the electromechanical coupling coefficient (k^2) and phase velocity [2]. Simulations at 500 MHz show that LTOI42 exhibits higher k^2 (10.984%) and near-zero TCF = 4.103 ppm/°C compared to LT42 (k^2 = 5.282%, TCF = −26.538 ppm/°C), indicating improved sensitivity and thermal stability. To further assess the impact on mass sensitivity, particle deposition is simulated by introducing a gold layer on top of the substrates. Sauerbrey's equation is then used and adapted accordingly:

$$Sg = \frac{\Delta v}{v_0} \cdot \frac{A}{\Delta m} \quad (1)$$

where Sg is the gravimetric sensitivity (cm²/g), Δv/v0 is the normalized phase velocity variation, A is the active sensing area, and Δm is the deposited mass related to the density and thickness of the gold layer. The simulations evaluate the phase velocity and as a function of gold layer thickness from which the gravimetric

sensitivity is estimated. As shown in Fig. 2, and using $\Delta m = d_e \cdot \rho \cdot A$, where d_e is the thickness of gold layer, the thickness range (0.01–0.2 µm) corresponds to 1.5–29.9 µg for LTOI42 and 2.15–43.0 µg for LT42. In this low-mass region, LTOI42 shows higher sensitivity than LT42. This indicates better performance of LTOI42 for thin deposited layers.

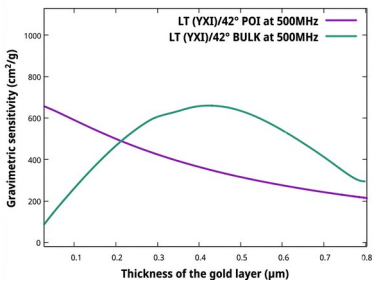

Fig. 2. Gravimetric sensitivity for LTOI42 and LT42

Experiments

Experiments were conducted in a leak-proof chamber where the cascade impactor is placed. Tests were done under a PM2.5* concentration of 250 ± 5 µg/m³. A Gilian® pump of type Gilair™ Plus is then used to collect the generated particles through the impactor at 3 Lpm flowrate. The sampling conducted until the surface of both devices are saturated as shown in Fig. 3.

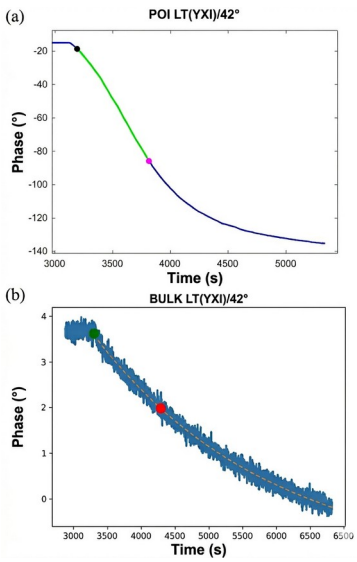

Fig. 3. Phase monitoring upon long term particle collection for (a) LTOI42 and (b) LT42

To relate the simulated gravimetric sensitivity Sg to the experimental sensor sensitivity Ss, a model previously developed within our team is used, based on Sauerbrey's approach [3]. The sensor sensitivity is defined as:

$$S_g = \frac{df}{f_0} \cdot \frac{A}{dm} \quad (2)$$

with *dm* representing the mass of particles deposited on the sensing area *A*. By linking the phase variation to the deposited mass and the operating conditions of the impactor, the following relationship is obtained:

$$S_{s,estimated} = S_g \frac{\alpha f_0 Q}{2A} \quad (3)$$

where $\alpha = d\varphi/df$, f_0 is the operating frequency, Q the flow rate, and A the sensing area. This formulation enables a direct comparison between experimental and theoretical sensitivities, allowing validation of substrate influence on sensor performance.

Substrate	$S_{s,experimental}$ ($°.s^{-1}.g^{-1}.m^3$)	$S_{s,estimated}$ ($°.s^{-1}.g^{-1}.m^3$)
LN42	22.02	189.905
LNOI42	266.85	26814.70

Analysis

The comparison between experimental and estimated sensitivities shows a significant difference in absolute values, while preserving the same trend between substrates. This discrepancy has previously been observed for other substrates and is attributed to the absence of a correction factor β in the theoretical model [3]. Indeed, the estimation of sensitivity based on gravimetric simulations does not account for several real phenomena such as particle surface interactions, particle rebound, and non-uniform deposition within the impactor. These effects are incorporated through a correction factor β (< 1), which must be introduced into the model to match experimental observations.

Conclusion

In both experimental and estimated results, the POI-based substrate shows higher sensitivity than the bulk, consistent with the higher electromechanical coupling coefficient (k^2) and confirming the strong influence of substrate properties. Experiments under controlled particle concentrations will be conducted to characterize sensitivity and its evolution with fooling, enabling improved model validation including the β correction factor and determination of the detection limit.

References

[1] L. Djoumi et al., "SAW-based cascade impactor for PM10 and PM2.5 measurement," Sensors, 18(1), 2018.

[2] A. Clairet et al., "Composite $LiTaO_3$/Si substrates for SAW devices," Forum Acusticum, 2020. 2527–2533

[3] G. Fawaz et al., "SAW devices for real-time monitoring and self-cleaning cascade impactor," Proc. EnvIMEKO, 2022

DOI 10.5162/eurosensors2026/Tu–EFS–05

Magnetic Microfluidics Biosensor for Environmental Applications: A Simulation Approach

F. Shanehsazzadeh [1], R. Askari Moghadam[2], A. Rabehi[1], S. Neveu[3], G. Klisnick, H. Kokabi[2]*
[1]*Group of Electrical Engineering of Paris (GeePs), Sorbonne Université, CNRS UMR 8507, France*
[2] *Laboratoire d'Imagerie Biomédicale, Sorbonne University, CNRS, INSERM, France*
[3]*Laboratoire Physicochimie des Electrolytes et Nanosystèmes, Sorbonne University, CNRS, France*
Corresponding Author's e-mail address: reza.askari_moghadam@sorbonne-universite.fr

Summary:
At the nano scale, certain magnetic materials eliminate hysteresis in their magnetization curves which provide new tools of sensing. In this study, a magnetic sensor including the microfluidics structure between two magnetic coils for sensing the biomaterials or pathogens is simulated by COMSOL Multiphysics. The special characteristics of magnetic nanoparticles, help us to employ the frequency mixing technique for biosensing applications. The magnetic biosensor system is simulated based on previous experimental works that detects pathogens in plants and toxic substances in agricultural products.

Keywords: Biosensor, Magnetic Nano Particles, Frequency Mixing Technique , Microfluidics

Introduction

Magnetic Nano Particles (MNP) with diameters in the order of tens of nanometers exhibits superparamagnetic behavior. The magnetization of MNPs is characterized by a hysteresis-free magnetization curve, featuring both linear and nonlinear regions, and reaching saturation at high field strengths in both directions. This special characteristic of the magnetization curve of MNP motivates scientists to develop a detection mechanism which is named Frequency Mixing Magnetic Detection (FMMD) [1,2]. In FMMD, two excitation signals at low and high frequencies are applied to two coils in order to generate two magnetic fields at two distinct frequencies f_1 and f_2. In the central zone of magnetic fields, the MNPs are placed. Based on its magnetization curve, it will induce a small magnetic field in the third coil (pick-up coil) at different frequency components, including two exciting frequencies and their intermodulation combinations. The mass of MNP in the central zone defines the amplitude of the induced signal in the pick-up coil. To leverage the MNPs' nonlinearity, the response is measured at the frequency f_1+2f_2, enabling the detection and quantification of them. This is a simple and fast technique to measure the mass or concentration of MNP in the central zone of the magnetic field. FMMD has been proposed for biosensing applications as well as bioimaging and material characterization [1,3].

Designing and optimizing such structures traditionally relies on multiple fabrication and experimental cycles, resulting in increased cost and time. Our study aims to provide an accurate modeling approach that directly incorporates measured MNP properties to streamline microchannel development.

Experimental setup

In this section, the main parts of the experimental setup are briefly explained, with detailed descriptions available in [2,4]. The first part includes magnetic excitation and response signal measurement circuits. It is needed to generate low-frequency (LF) and high-frequency (HF) excitation signals. The power of the response signal, measured by the third coil, is very small, and it is amplified by lock-in amplifiers. By applying Fast Fourier Transform (FFT) to the measured signal, the amplitude of the response signal at frequency f_1+2f_2 would be measured. The concentration of MNP in the sample solution is directly proportional to the signal amplitude at this frequency.

The second part of the experimental setup is a microfluidics chip containing the MNP sandwich with target pathogen or biomaterial. The target pathogens or molecules are connected to MNP on one side, and on the other side, they are fixed on the surface of the microfluidic chip. The volume of the microfluidic chip is almost 15 microliters, fabricated by PDMS bonded to the glass, as shown in Fig. 1.

Simulation

The system was modeled using COMSOL Multiphysics through a series of multi domain simulations. These simulations help us to optimize

the microstructure by considering some factors such as the magnetization of nanoparticles, in order to estimate the sensitivity and magnetic field intensity.

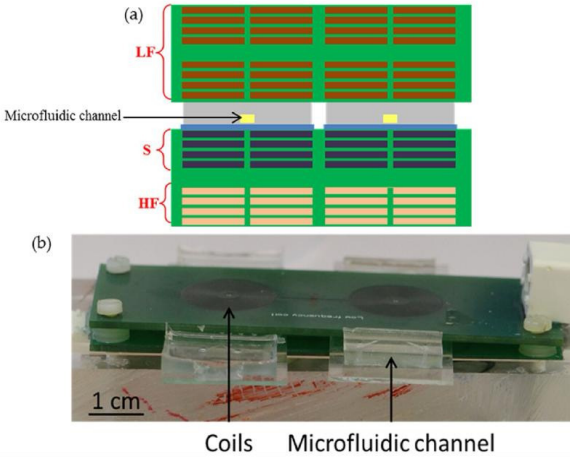

Fig1. (a) Schematic of layers: two green blocks for PCB coils (LF, S, HF); PDMS layer (gray) with microfluidic channel (yellow) bonded to glass (blue). (b) PCB/microfluidic prototype detection structure [4].

The impedance of the coils and the magnetic field intensity at the surface of the detection and sensor coils were measured using an impedance analyzer and a Gaussmeter, respectively. The same conditions are simulated in COMSOL, and the comparison of results, is presented in Table 1.

Table1. Comparison of simulated (S) and measured (M) coil resistance, inductance, and surface magnetic field under input DC voltages of 3V, 4V, and 6V.

				Magnetic Field (mT)		
		R (Ω)	L(mH)	@ 3V	@4V	@6V
HF	M	35	176	697	890	1.3
	S	24	192	727	969	1.45
Sensor	M	44	265	708	1.00	1.45
	S	29.7	245	984	1.31	1.97
LF	M	90	950	581	715	1.11
				600	807	1.39
	S	58	891	604	806	1.2
				706	941	1.4

In addition, two simulations are carried out for cylindrical and serpentine microfluidics channels, as shown in Fig2. In addition, the MNP material was defined in COMSOL, based on the measured magnetic properties by experiments. The experimental results exhibit superparamagnetic behavior of MNP as shown in Fig. 3. To evaluate and compare the entire sensor measured signals with the simulation results, we applied consistent electrical settings to both the simulation and the measurement. The LF coils operated at 65 Hz, powered by a 48 Vpp signal, while the HF coils functioned at 40 kHz, powered by a 40 Vpp signal. The results showed that considering the same mass of nanoparticles, the simulation predicted 12.72 mV which is near to the measured value 14mV.

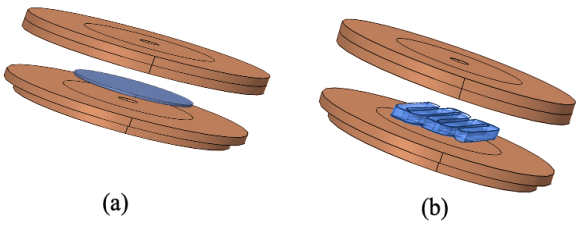

Fig 2. Simulation of different microfluidic structures

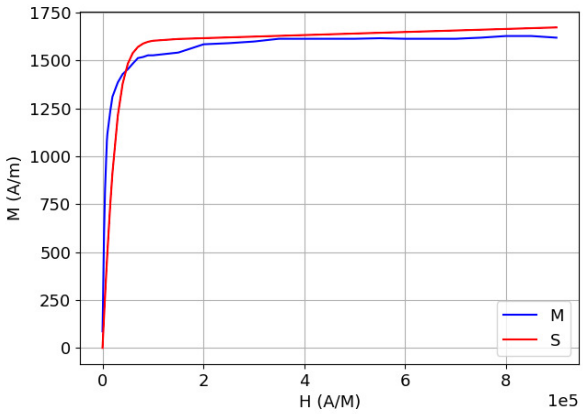

Fig 3. Comparison of nanoparticle material properties in simulation (S) and measurement (M).

References

[1] H.J. Kraus, U.M. Engelmann, Fundamentals and Applications of Dual-Frequency Magnetic Particle Spectroscopy: Review for Biomedicine and Materials Characterization, *Advanced Sciences*, 2025.

[2] A. Rabehi, B. Garlan, S. Achtsnicht, H.J. Krause,A. Offenhäusser, K. Ngo, S. Neveu, S. Graff-Dubois, H. Kokabi, Magnetic Detection Structure for Lab-on-Chip Applications Based on the Frequency Mixing Technique, *Sensors*, Vol. 18, 2018. https://doi.org/10.3390/s18061747

[3] S.M. Choi, J.C. Jeong, J. Kim, E.G. Lim, C.B. Kim, S.J. Park, D.Y. Song, H.J. Krause, H. Hong, I. S. Kweon, A Novel Three Dimensional Magnetic Particle Imaging System Based on the Frequency Mixing for the Point-of-Care Diagnostics, *Scientific Reports*, 2020.

[4] B. Garlan, A. Rabehi, K. Ngo, S. Neveu, R. Askari Moghadam, H. Kokabi, Miniaturized Pathogen Detection System Using Magnetic Nano Particles and Microfluidics Technology, *Micromachines*, 15, 1272, 2024

DOI 10.5162/eurosensors2026/Mo–SAN–01

Polymer-Coated Quartz Microbalance Array for Discriminating VOCs and Ammonia

F. Cortese[1], R. Capuano[1], A. Catini[1], E. Stoleru[3], M. Brebu[3], C. Di Natale[1]
[1] Department of Electronic Engineering, Tor Vergata University of Rome, Rome, Italy
[2] "P. Poni" Institute of Macromolecular Chemistry, Iaşi, Romania
Corresponding author capuano@ing.uniroma2.it

Summary:

A quartz microbalance array coated with polymeric sensing layers was investigated for the detection of volatile compounds and ammonia at room temperature. The array included chitosan and polylactic acid based coatings. Measurements performed with isopropanol, xylene, pentanol, octane and ammonia showed analyte dependent response patterns over concentration ranges relevant to environmental monitoring. Chitosan electrospinning coatings provided the largest absolute responses, while signal normalization highlighted complementary sensitivities across the array. t-distributed Stochastic Neighbor Embedding (t-SNE) confirmed that the collective response of the sensors enables discrimination among the tested compounds.

Keywords: quartz microbalance, polymer coatings, volatile organic compounds, sensor array

Background, Motivation and Objective

Quartz microbalances are attractive platforms for room temperature gas sensing because they provide real time mass sensitive transduction with simple readout electronics. Their analytical performance strongly depends on the physicochemical properties of the coating, which control sorption, swelling and specific interactions with the analytes [1-3]. In this context, arrays combining different functional layers are particularly promising, since partial selectivity can be exploited to recognize complex vapors through multivariate analysis. The aim of this work is to evaluate whether a heterogeneous set of polymeric coatings can provide discriminative fingerprints for selected volatile organic compounds and ammonia.

Description of the New Method or System

The sensing platform consists of a set of seven quartz microbalance array coated with different active layers, including chitosan based, polylactic acid (PLA) based materials. The array include four sensors based on a chitosan and gelatine blend coatings, which differ in percentages of the components in the mixture, in microstructure (crosslinked or not) and type of deposition (electronspray or electospinning), and three sensors coated with PLA by electrospray, using different set-up conditions (Tab. 1). Figure 1 shows the surface arrangement of Chitosan 2.5% /Gelatin 10% 7/3 in high Acetic acid, deposited by electrospinning (Fig. 1A) and PLA layer deposited by electrospray (Fig. 1B). The array was tested with isopropanol, xylene, pentanol, octane and ammonia in concentration ranges of about 3500 to 14200 ppm, 544 to 2170 ppm, 88 to 350 ppm, 840 to 3300 ppm and 5 to 20 ppm, respectively. Sensor responses were evaluated as resonance frequency shifts, and the resulting datasets were analyzed both in terms of single sensor sensitivity and collective response using t-distributed Stochastic Neighbor Embedding (t-SNE).

Results and Discussion

All analytes produced concentration dependent responses, with significant differences among coatings. Chitosan 2.5% /Gelatin 10% 7/3 in high Acetic acid (electrospun-Chito 1) and Chitosan 1% /Gelatin 5% 6/4 diluted, crosslinked and deposited by electrospray (Chito4) layers showed the largest absolute signals, especially toward xylene, octane and ammonia, whereas the other coatings contributed more moderate but complementary patterns (Fig. 2). Ammonia emerged as the most sensitive target across the full array, while isopropanol generated the weakest signals (Fig. 3). Pentanol and xylene showed intermediate sensitivities and a stronger dependence on the coating composition, indicating that the array can exploit both adsorption strength and pattern diversity. t-SNE of the linear-normalized responses, calculated using Euclidean distance, provided a good separation of the five vapors, especially for alcohols, supporting the use of the platform for analyte discrimination rather than simple threshold sensing (Fig. 4).

Tab. 1: Sensing material characteristics

Name	Material	Deposition technique
Chito 1	Chitosan 2.5% /Gelatin 10% 7/3 in high Acetic acid	Electrospin (V=19kV, Flow=2µL/min, Dep. Time= 5s,T=40°C)
Chito 2	Chitosan 2.5% /Gelatin 10% 7/3 in high Acetic acid	Electrospray (V=21kV,Flow=3µL/min, Dep. Time= 90s,T=25°C)
Chito 3	Chitosan 2.5% /Gelatin 10% 7/3 in high Acetic acid	Electrospray (V=21kV,Flow=3µL/min, Dep. Time= 90s,T=25°C)
Chito 4	Chitosan 1% /Gelatin 5% 6/4 diluted & crosslinked	Electrospray (V=20kV,Flow=20µL/min, Dep. Time= 540s,T=25°C)
PLA 1	PLA 5%	Electrospray (V=20kV,Flow=5µL/min, Dep. Time= 30s,T=25°C)
PLA 2-PLA 3	PLA 5%	Electrospray (V=20kV,Flow=5µL/min, Dep. Time= 180s,T=25°C)

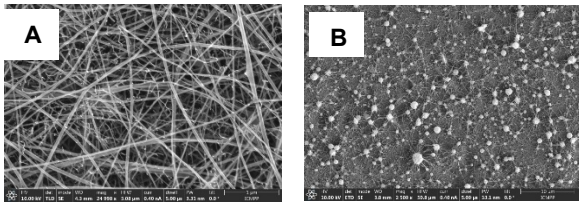

Fig. 1. Surface arrangement of (A) electrospun chitosan-based and (B) electrosprayed PLA-based sensing layer

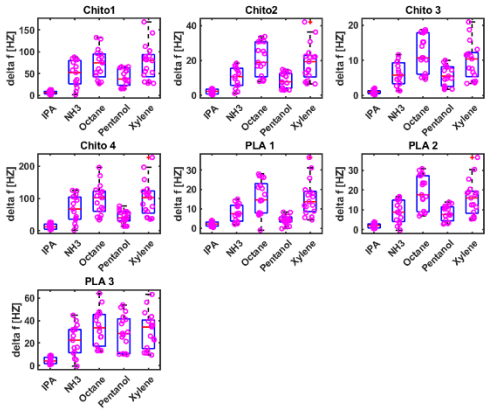

Fig. 2. Box plots of sensor responses to the different considered analytes

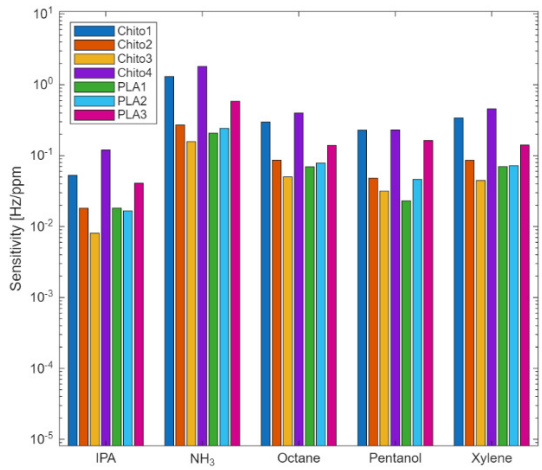

Fig. 3. Bar plot reporting the sensitivity of each sensor to the different analytes

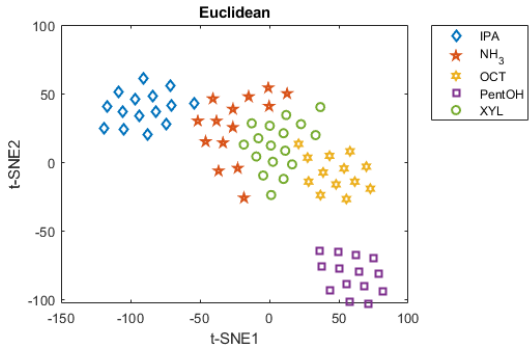

Fig. 4. t-SNE of the linear-normalized sensor responses, calculated using Euclidean distance

Conclusions

These preliminary results indicate that polymer coated quartz microbalance arrays are suitable for room temperature recognition of volatile compounds and ammonia. The combination of high response chitosan based layers with complementary lower amplitude coatings improves the multidimensional fingerprint of the system and enables robust separation in t-SNE space. The study therefore supports further optimization of the coating set and measurement protocol toward an electronic nose strategy for environmental or process monitoring applications.

References

[1] G. Magna, R. Belugina, F. Mandoj, *et al.*, Experimental determination of the mass sensitivity of quartz microbalances coated by an optical dye, *Sensors and Actuators B: Chemical* 320, 128373 (2020); doi: 10.1016/j.snb.2020.128373

[2] A. Catini, R. Kumar, R. Capuano, *et al.*, An Exploration of the Metal Dependent Selectivity of a Metalloporphyrins Coated Quartz Microbalances Array, *Sensors* 16, 1640 (2016); doi: 10.3390/s16101640

[3] K. Triyana, A. Sembiring, A. Rianjanu, *et al.*, Chitosan-Based Quartz Crystal Microbalance for Alcohol Sensing, *Electronics* 7, 181 (2018); doi: 10.3390/electronics7090181

DOI 10.5162/eurosensors2026/Mo–SAN–02

An Adaptive Embedded Readout System for Resistive Sensor Arrays

Deepika Balraj[1], Mohd Tarique[2], Leon Abelmann[2], Peter Woias[1], Suman Kundu[1]*
[1] Department of Microsystems Engineering – IMTEK, Albert-Ludwigs-Universität Freiburg, Georges-Köhler-Allee 102, 79110 Freiburg, Germany
[2] Department of Microelectronics, TU Delft, Mekelweg 4, 2628CD Delft, Netherlands
**Corresponding Author: suman.kundu@imtek.uni-freiburg.de*

Summary: Resistive sensor arrays are extensively used for spatially distributed sensing and acquiring multiparametric data. However, a major challenge is the need of bulky measurement instruments for precise array readout. Here, we report an embedded and adaptive resistance readout system for sensor arrays. The readout yields low errors ±0.5% in 1 kΩ – 33 MΩ resistance range with a high SNR of 70-92 dB. End-to-end operation of the developed readout is demonstrated by utilizing a packaged 4×4 ZnO photodetector-array and accurate monitoring the photocurrents in real-time.

Keywords: resistive sensor arrays, embedded readouts, multiplexed arrays, PCB sensor instrumentation, UV photodetectors

Background and Motivation

Resistive photodetectors based on wide-bandgap semiconductors attractive for solar-blind UV sensing, environmental ozone and flame detection. When constructed as microdimensional sensing elements, these devices generate photocurrents ranging from picoamperes to microamperes, spanning several orders of magnitude in sensor resistance depending on optical intensity, device geometry, and applied bias. Capturing this dynamic range in a single multiplexed measurement without forfeiting accuracy or portability is challenging. Source measure units can deliver the required precision but at a cost and footprint incompatible with embedded deployment [1]. PCB-level alternatives each trade off a different dimension: voltage-divider readouts with adaptive reference tuning [2] cover only ~three decades and scale poorly with array size; diode-steered op-amp interfaces [3] multiplex many pixels but over a narrow resistance range; precision transimpedance amplifiers [4] achieve pA-level sensitivity but only as single-channel instruments. The 2D networked-array literature addresses inter-channel crosstalk at the algorithmic level [5, 6], leaving the analogue front-end untouched. Thus, developing an embedded readout system adaptive to the use-case base requirements would be highly beneficial.

System Description

We report development of an embedded readout that is multiplexed, wide-range, and pA-capable, with end-to-end demonstration of current reading from a 4×4 ZnO-based photodetector array. Fig. 1a shows the Block diagram of the multiplexed readout signal chain. The active sensor pixel is selected by a 32:1 analogue multiplexer and routed to a single OPA380 precision transimpedance amplifier (TIA), configured as a bias-offset non-inverting stage. A bias voltage V_{bias} = 0.56 V is applied across the sensor through a passive divider; the TIA output follows the closed-form transfer function in (1), where R_f is a selectable feedback resistor giving overlapping decade coverage from 1 kΩ to 33 MΩ.

$$V_{out} = V_{bias}\left(1 + \frac{R_f}{R_{pixel}}\right) \quad (1)$$

The output is buffered, anti-alias filtered, and digitised by a 24-bit ΔΣ ADC (ADS124S08) whose internal reference is 2.5 V, setting the full-scale output limit of the chain. An STM32 microcontroller (Nucleo platform) handles channel switching, ADC configuration, and serial transfer. The 16-pixel prototype uses a DIP-packaged ZnO photodetector array (Fig. 1b,c).

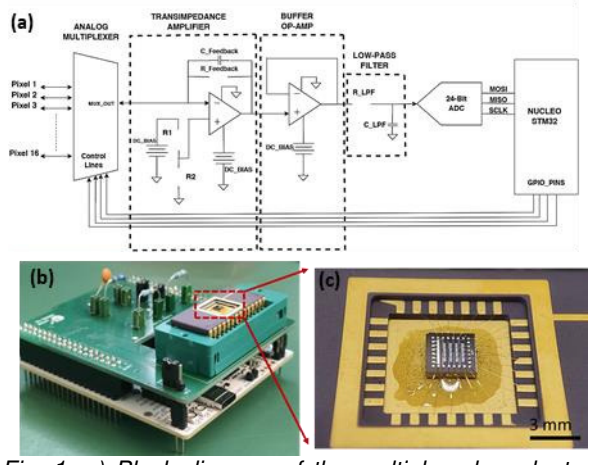

Fig. 1. a) Block diagram of the multiplexed readout signal chain: 4×4 sensor array → 32:1 analogue multiplexer → OPA380 TIA (bias-offset non-inverting) → unity buffer → passive anti-alias filter → 24-bit ΔΣ ADC → STM32 Nucleo microcontroller. b) Image of the developed embedded readout system. c) Image of the 4×4 sensor array.

Characterisation Methodology

The readout is characterised primarily by sweeping the pixel resistance: R_{pixel} from 1 kΩ to 33 MΩ at three representative feedback values (R_f = 33 kΩ, 1 MΩ, 10 MΩ), each chosen to span one decade of the operating range. For every (R_{pixel}, R_f) point, the mean of 100 ADC samples at 4 kSPS is compared against closed-form theory (1) and against an independent PSpice simulation of the full analogue chain. The measurement error is computed via (2), and the signal-to-noise ratio via (3). A representative linearity check is performed by fixing R_{pixel} at 1 MΩ and sweeping R_f to confirm gain linearity and locate the saturation boundary.

$$Error\ (\%) = \frac{V_{measured} - V_{theory}}{V_{theory}} \times 100 \qquad (2)$$

$$SNR\ (dB) = 20\ log_{10}\ \frac{V_{out}}{\sigma} \qquad (3)$$

Results

Fig. 2 shows the V_{out} measured at three R_f values. Hardware, PSpice simulation, and closed-form theory overlap across the full 1 kΩ – 33 MΩ range, with each curve saturating at 2.5 V once V_{out} approaches the ADC's internal reference. The asymptotic approach to V_{bias} = 0.56 V at high R_{pixel} confirms correct operation of the bias-offset topology.

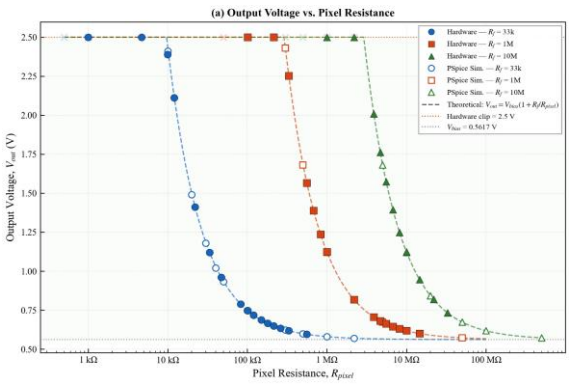

Fig. 2. V_{out} vs R_{pixel} at R_f = 33 kΩ, 1 MΩ, 10 MΩ. Hardware (filled), PSpice simulation (open), and closed-form theory (dashed) overlap across the full 1 kΩ – 33 MΩ range; saturation at 2.5 V is set by the ADC internal reference.

Measurement error is shown in Fig. 3a. Across most of the operating range, error stays within ±0.5%, and within the middle decade of each gain setting it remains within ±0.1%. The worst-case −2.1% excursion appears at R_{pixel} = 10 kΩ with R_f = 33 kΩ, where the closed-loop gain (~4.3) drives V_{out} into the 2.5 V saturation ceiling; this is an input-range limit imposed by the ADC reference, not an amplifier non-linearity.

Fig. 3b shows the signal-to-noise ratio across the pixel-resistance range. SNR exceeds 80 dB over the central operating region of each gain setting, reaching 92 dB at the peak, and remains above 70 dB at the extremes of the sweep.

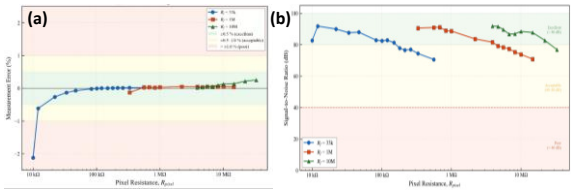

Fig. 3. a) Measurement error (%) vs. R_{pixel} at R_f = 33 kΩ, 1 MΩ, 10 MΩ. b) Signal-to-noise ratio (SNR) vs. R_{pixel}.

Demonstration on ZnO Photodetector Array

To verify end-to-end operation, the 16-pixel microsensor array chip was wire-bonded into a DIP package (Fig. 1c), thereafter ZnO nanoparticles (diameter~100 nm) were dropcoated on top of the microelectrodes. The packaged chip was connected directly to the readout PCB (Fig. 1b). Fig. 4 shows the acquired output current from one of the pixels; first kept at dark and then illuminated with a 365 nm UV LED for 100 s and thereafter kept in dark. The current transitions from a dark baseline of 0.8 nA to 7.385 μA upon UV illumination, and returns to baseline when the source is removed, resolved in real time at R_f = 33 kΩ.

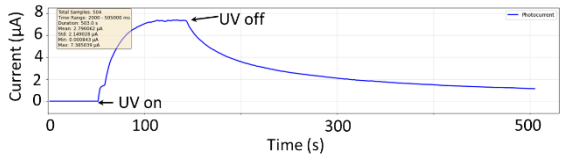

Fig. 4. Current vs. time plot for a ZnO-coated microsensor pixel under dark-UV (365 nm) illumination-dark condition. The data was acquired at R_f = 33 kΩ.

References

[1] G. Ferrari *et al.*, Transimpedance Amplifier for High Sensitivity Current Measurements on Nanodevices, *IEEE J. Solid-State Circuits* 44(5), 1609–1616 (2009); doi:10.1109/JSSC.2009.2016998

[2] S. Lakshminarayana *et al.*, A readout system for high speed interface of wide range chemiresistive sensor array, *IEEE Access* 10, 45726–45735 (2022); doi: 10.1109/ACCESS.2022.3170486

[3] S. Kuankid, J. Jittakort, A. Aurasopon, A Multiplexable Op-Amp Interface for Accurate Readout of Remote Resistive Sensors, *Sensors* 26(2), 461 (2026); doi: 10.3390/s26020461

[4] N. D. Gupta *et al.*, Design and development of low noise transimpedance amplifier for low intensity light level detection applications for UV range, *Integr. Circuits Signal Process.* 126, 43 (2026); doi: 10.1007/s10470-026-02573-7

[5] J. A. Hidalgo-López *et al.*, Improving accuracy in the readout of resistive sensor arrays, *J. Sensors* 2018, 9735741 (2018); doi: 10.1155/2018/9735741

[6] J. A. Hidalgo-López, J. Romero-Sánchez, R. Fernández-Ramos, New approaches for accuracy in resistive sensor array readout, *IEEE Sensors J.* 17(7), 2154–2164 (2017); doi: 10.1109/JSEN.2017.2662803

DOI 10.5162/eurosensors2026/Mo–SAN–03

Engineering Opposing Response Evolution in $ZnWO_4$–WO_3 Sensor Pair for Deterministic Decoding of NO_2 in Reducing Gas

Shivam K Singh[1], Cyrin Neeraj[1], Anuj Kumar Dwivedi[1], Vinayak B Kamble[1]
[1]School of Physics, Indian Institute of Science Education and Research, Thiruvananthapuram, India
Email: shivam21@iisertvm.ac.in

Summary:

The selective detection of NO_2 in a multicomponent gas environment is still limited by the cross-sensitivity of metal oxide sensors. In this study, a $ZnWO_4$-WO_3 sensor pair is created by deliberately using opposing response trends under identical gas circumstances. In the presence of reducing gases such as CH_4 and CO, the reaction rate of $ZnWO_4$ decreases steadily. WO_3 has a significantly higher reaction rate than pure NO_2, sometimes up to 3 times higher, depending on the interferent concentration. This contrast provides a structured response space in which the same NO_2 concentration generates different responses depending on the background gas combination. The distinction makes the dataset ideal for deterministic discrimination and for machine learning algorithms for classification and concentration estimation.

Keywords: Metal oxide sensors, NO_2 sensing, gas mixtures, cross-sensitivity engineering, sensor arrays, machine learning-assisted sensing

Background, Motivation and Objective

Metal oxide semiconductor sensors are widely used for detecting harmful gases due to their high sensitivity and scalability [1]. However, in a multi-component context, their selectivity decreases. In the presence of both oxidizing and reducing gases, they compete for surface reactions, leading to nonlinear responses that are difficult to interpret [2]. Most existing techniques aim to improve selectivity by adding more materials or increasing the number of sensor arrays, but this quickly increases costs and complexity. Here, we adopt a different method. We do not aim to conceal cross-sensitivity; rather, we use it on purpose [3]. By choosing materials with opposing response qualities, we can achieve complementary behavior. The goal is to show that this divergence can be employed as a reliable sensing parameter rather than as a constraint.

Description of the New Method or System

The WO_3 and $ZnWO_4$ thin films were prepared by DC and RF sputtering and then thermally annealed to improve their crystallinity and surface activity. Both sensors were operated simultaneously under the same conditions and exposed to NO_2 concentrations of 5 to 100 ppm in the presence of CH_4 (10-30 ppm) and CO (25-75 ppm). The two materials react with gases in very different ways. WO_3 is sensitized by vacancy-mediated sensitization in reducing environments, thereby facilitating NO_2 adsorption and improving its response. In contrast, $ZnWO_4$ is dominated by electron compensation and competitive adsorption, resulting in a quenched signal. The difference creates a non-collinear two-dimensional sensing space without additional hardware, effectively encoding information about the gas mixture [4].

Results

The $ZnWO_4$–WO_3 pair exhibits quite different response behavior under the same gas conditions. $ZnWO_4$ showed strong suppression of both CH_4 and CO (Fig. 1a and 1b), especially at low NO_2 levels. The response could drop by orders of magnitude, but it could recover at higher concentrations. In WO_3, the opposite trend is seen. Its response increases across all mixed-gas conditions, surpassing the pure NO_2 signal and reaching much higher values, especially in CO-rich environments (Fig. 1c and 1d). The strength of this effect depends on the type and amount of the interfering gas. For example, CO has a stronger, non-monotonic effect than CH_4. Consequently, the response ratio $R(ZnWO_4)/R(WO_3)$ is inverted and exceeds one in pure NO_2, while it is significantly less than one in mixed conditions.

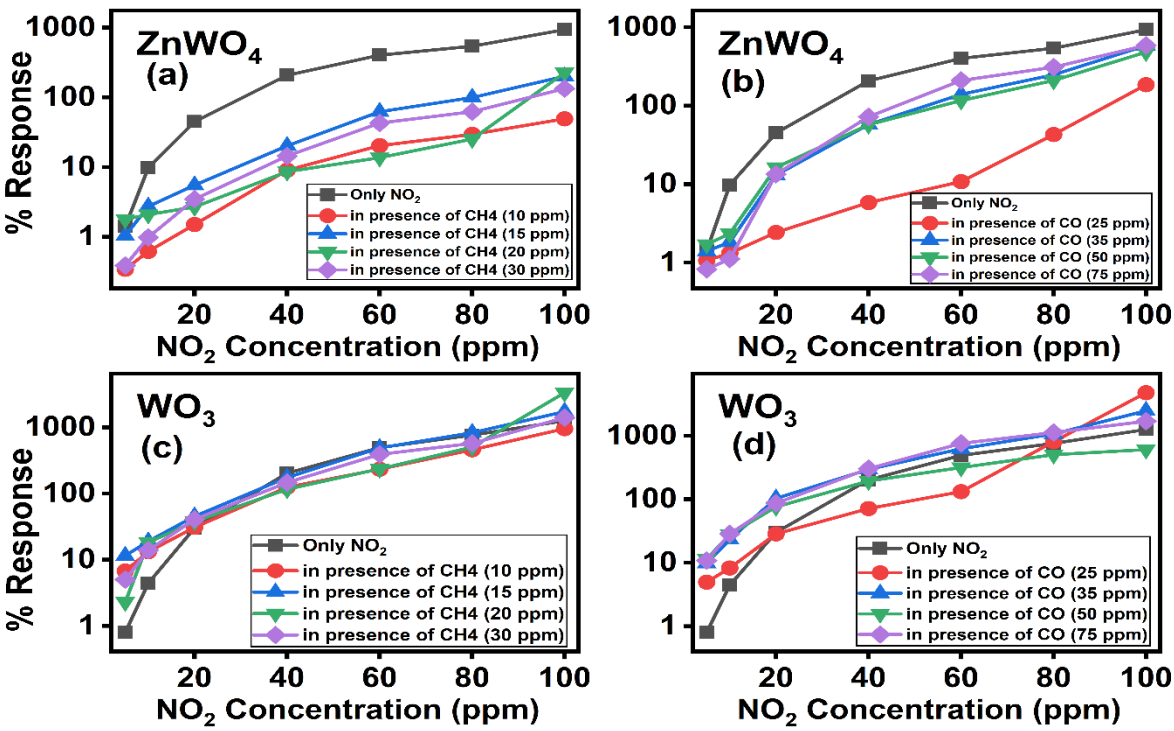

Figure 1: Percentage response as a function of NO_2 concen-tration for $ZnWO_4$ (a, b) and WO_3 (c, d) thin-film sen-sors under pure NO_2 and binary gas mixtures with CH_4 (a, c; 10–30 ppm fixed) and CO (b, d; 25–75 ppm fixed).

This makes a response space that is both organized and separate. It is possible to distinguish between gas identity and background concentration using the paired outputs. $ZnWO_4$ always shows a lower response than the pure-NO_2 baseline, while WO_3 always shows a higher response than the pure-NO_2 baseline at all levels of the interferent tested. This change occurs across the entire 5–100 ppm NO_2 range. The two-dimensional response space comprises the two opposing trends. It contains information about both the target gas and the interfering components, enabling reliable measurement of NO_2 in complex mixtures.

Conclusion

The results show that cross-sensitivity can be used positively rather than seen as a problem. The $ZnWO_4$–WO_3 sensor pair lets you decode NO_2 in multicomponent environments without complicating the system by using materials that react differently. This provides a feasible path-way for developing scalable, data-driven gas sensing systems.

References

[1] Singh, S.; S, S.; Varma, P.; Sreelekha, G.; Adak, C.; Shukla, R. P.; Kamble, V. B., Metal oxide-based gas sensor array for VOCs determina-tion in complex mixtures using machine learning. Microchimica Acta 2024, 191 (4), 196; doi: 10.1007/s00604-024-06258-8

[2] Chu, J.; Li, W.; Yang, X.; Wu, Y.; Wang, D.; Yang, A.; Yuan, H.; Wang, X.; Li, Y.; Rong, M., Identification of gas mixtures via sensor array combining with neural networks. Sensors and Ac-tuators B: Chemical 2021, 329, 129090; doi: 10.1016/j.snb.2020.129090

[3] Sweta Giri, P.N. Anantharamaiah, B. Sahoo, sensing of oxidizing and reducing gases by sen-sors prepared using nanoscale Co3O4 powders: A study through Cu substitution, Advanced Pow-der Technology, Volume 33, Issue 4, 2022, 103529, ISSN 0921-8831, doi: 10.1016/j.apt.2022.103529

[4] K. T. Savio, Amisha Mishra, Aniket K. Pandey, Shivam Kumar Singh, Sajana S., Chandranath Adak, Rajendra P. Shukla, and Vinayak B. Kamble. Data-Driven Approach toward the Quantification of Gases in a Complex Mixture Using a Non-Selective Single Metal Oxide Gas Sensor. *ACS Sensors* Article ASAP; doi: 10.1021/acssensors.5c03553

DOI 10.5162/eurosensors2026/Tu–SAN–01

Sensor Placement in Energy Systems Based on Residual Uncertainty

Philipp Kersten[1], Sören Hirsch[1]
[1] University of Applied Sciences Brandenburg,
Magdeburger Straße 50, 14770, Brandenburg an der Havel, Germany
philipp.kersten@th-brandenburg.de

Summary:

This work investigates the measurement requirements in energy systems from an information-centric viewpoint. The framework models an energy system as a hierarchy of aggregated nodes, represented as the sum of known and unknown load components. The mismatch between measured node power and the estimated system state defines a residual that represents the remaining information uncertainty and serves as the basis of a greedy sensor selection process. The sensor placement task is formulated as an optimization problem, where sensors are selected to minimize the residual-based uncertainty.

Keywords: sensor placement, observability, energy systems, residual uncertainty, greedy optimization

Introduction

Modern energy systems are increasingly characterized by distributed generation, heterogeneous loads, and multi-level system structures. From individual households and buildings to district energy systems and large-scale grids, the number of interacting components continues to grow. Reliable monitoring of these systems is essential for energy management, forecasting, and control [1], [2], [3]. In practice, however, energy systems are only partially instrumented. Installing sensors at every possible point is typically infeasible due to cost, communication constraints, and system complexity. Energy management systems must therefore operate with incomplete information about the underlying system state and rely on state estimation techniques to reconstruct the system state from available measurements [4]. This leads to a central design question: which sensors provide the greatest information value for observing the system? In this work, we focus on optimizing an existing energy system that is modeled as a hierarchy of aggregated nodes. Based on this representation, sensor placement is formulated as an optimization problem, where the goal is to select measurement points that reduce the remaining information uncertainty as efficiently as possible. To evaluate our study, the simulation-based sensor placement method is evaluated using stochastic realizations.

Description of the New Method

The energy system is modeled as a set of aggregated nodes, each representing a local power balance. The balance can be categorized into measured loads (A), modeled loads (B) and unknown loads (C), representing a realistic scenario. The difference between measured node power and estimated power defines a residual $R(t)$, which represents the remaining information uncertainty. The effects of the variability and the maximum deviation of the residual are combined into a single score, referred to as the observability score shown in (1). Adding a sensor reduces the score by transferring loads from modeled to measured, thereby decreasing the residual uncertainty.

$$Score(\mathcal{S}) = Var\big(R(t)\big) + w_{peak} \cdot max|R(t)|^2 \qquad (1)$$

The variance of the residual $Var(R(t))$ of the residual captures overall fluctuations, while the maximum deviation reflects critical peak events. The sensor placement problem is defined over a set of candidate sensors, from which a subset is selected to minimize the observability score. To archive this, a greedy algorithm is applied, iteratively selecting the sensor that provides the largest reduction in uncertainty. This allows an efficient approximation of the optimal sensor configuration without evaluating all possible combinations.

Results

The method is evaluated using stochastic simulations with 50 different random seeds of a representative node with multiple heterogeneous electrical loads. As shown in Fig. 1, the observability score decreases rapidly with the first few sensors, indicating that a small number of measurements already captures most of the relevant information. The shaded areas indicate the variability across the realizations.

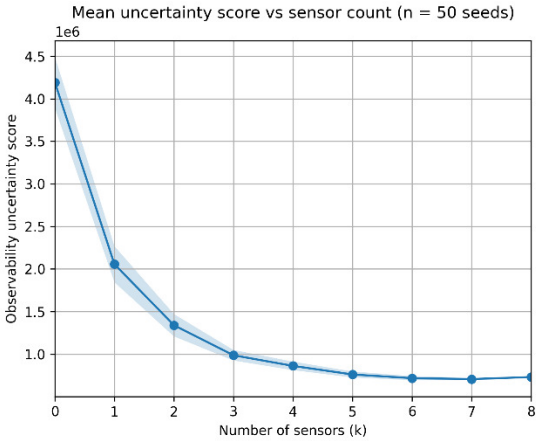

Fig. 1. Mean Observability score as a function of the number of sensors

Consistent with this, Fig. 2 shows that the marginal information gain decreases with each additional sensor, confirming the presence of diminishing returns. The first sensor provides the largest improvement, while later sensors contribute only minor reductions.

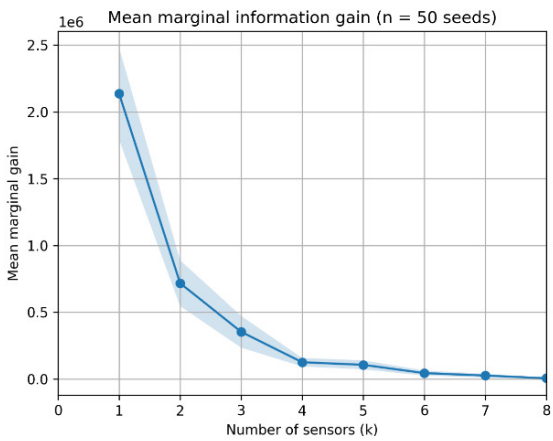

Fig. 2. Mean marginal information gain

The stability analysis in Fig. 3 demonstrates that the selection order of sensors is largely consistent across different stochastic realizations. This indicates that the proposed metric captures meaningful structural properties of the system. It also suggests that the dominant sources of uncertainty are identified consistently across different realizations.

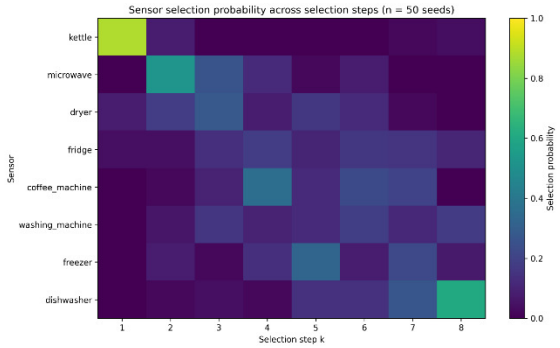

Fig. 3. Sensor selection probability heatmap

Conclusion

The proposed observability metric and greedy sensor placement method provide an effective approach for identifying informative sensors in partially observed energy systems. The framework links sensor placement directly to the reduction of residual information uncertainty at the node level. The simulation experiments show that a small number of strategically placed sensors already reduces the majority of the information uncertainty. Additional sensors lead to progressively smaller improvements, indicating diminishing returns in sensor placement. The stability analysis shows consistent sensor prioritization across realizations, indicating meaningful structural properties. While the present study focuses on the active power balance of a single node, the proposed framework is designed to scale to hierarchical energy systems consisting of multiple interconnected subsystems. Future work may therefore extend the model to incorporate additional system variables such as voltage, reactive power, and environmental inputs, as well as investigate sensor placement strategies in larger multi-node systems. Furthermore, the proposed approach could be applied to other sensor placement problems.

References

[1] W. Lise et al., Study on promoting energy system integration through the increased role of renewable electricity, decentralised assets and hydrogen – Final Report. Luxembourg: Publications Office of the European Union, European Commission, Mar. 2024, doi: 10.2833/560304

[2] G. Li, M. Niu, and J. Huang, “Evolution of energy systems: Patterns and mechanisms,” Energy Strategy Reviews, vol. 50, 2023, Art. no. 101200, doi: 10.1016/j.esr.2023.101200

[3] K. G. Koukouvinos, “Evaluating the Performance of Smart Meters: Insights into Advanced Metering Systems,” Applied Sciences, vol. 15, no. 2, Art. no. 960, 2025, doi: 10.3390/app15020960

[4] O. Darmis, M. Zribi, and A. Al-Hinai, “A Survey on Hybrid SCADA/WAMS State Estimation for Power Systems,” Energies, vol. 16, no. 2, 2023

DOI 10.5162/eurosensors2026/Tu–SAN–02

A multisensor-array device for breath analysis: development of a data quality assessment framework and application in the clinical practice

Valentina Pizzillo[1,2], Jolanda Palmisani[1,2*], Alessia Di Gilio[1,2], Annamaria Catino[3], Alba Quarato[3], Gianluigi de Gennaro[1,2], Sergio Ivan Lopes[4]*

[1] Department of Biosciences, Biotechnology and Environment, University of Bari Aldo Moro, 70125 Bari, Italy
[2] Apulian Regional Centre for the Breath Analysis, Istituto Tumori 'Giovanni Paolo II', 70124 Bari, Italy;
[3] Istituto Tumori 'Giovanni Paolo II', 70124 Bari, Italy;
[4] ADiT-Lab, Instituto Politécnico de Viana do Castelo, 4900-348 Viana do Castelo, Portugal
**co-first authors*

Corresponding Author's e-mail address: v.pizzillo@phd.uniba.it

Summary:

In the present work, a multi-sensor array device for real-time monitoring of target compounds (CO_2, CO, TVOCs, NO_2, H_2S, SO_2) was developed and validated under controlled environmental conditions. To face the critical issue of data quality, a multidimensional Data Quality Assessment (DQA) framework was proposed. Outcomes showed that environmental/external conditions significantly affect sensors behavior and data reliability. The developed approach therefore enabled the identification of reliable acquisition conditions. The validation of the system for diagnostic purposes on a population of malignant pleural mesothelioma patients is ongoing.

Keywords: Breath analysis, Multi-sensor array system, Data Quality Assessment, early diagnosis, malignant pleural mesothelioma

Background, Motivation and Objective

Breath analysis has emerged as a promising non-invasive approach for the early diagnosis and monitoring of chronic and oncological diseases. The chemical characterization of exhaled breath, combined with the real-time detection of selected compounds, enables the identification of metabolic alterations associated with pathological conditions [1,2]. Multisensor array systems have been widely investigated as effective tools for this purpose. However, their performance is strongly influenced by environmental conditions and acquisition-related factors, which may affect baseline stability, sensor response, and measurement reliability. In addition, temporal misalignment and inter-sensor variability complicate the interpretation of multisensor data. Although several studies address data quality in sensor systems [3,4], it is often treated as a preprocessing step rather than as part of system characterization. The system considered in this study is designed for breath acquisition from both healthy subjects and patients affected by oncological diseases (such as lung cancer and malignant pleural mesothelioma).

In this context, this work presents a multi-sensor array device for the real-time monitoring of target compounds (CO_2, CO, TVOCs, NO_2, H_2S, SO_2) in human breath. To face the well-known critical issue of data quality provided by these kinds of systems, a quality-aware workflow for multisensor breath analysis integrating preprocessing for multi-rate synchronization, CO_2-based breath/background segmentation and a multidimensional Data Quality Assessment (DQA) framework was developed and applied to background data. Besides exploring the data quality across multiple complementary dimensions, the present work aims to explore the potentialities of the multi-sensor array device in the clinical practice for diagnosis and prediction purposes. Preliminary results coming from the use of the system on a population of patients affected by malignant pleural mesothelioma (MPM) are also discussed.

Description of the New Method or System

In this work, a multisensor-array system for breath analysis was developed, integrating commercial sensor technologies for the real-time monitoring of selected organic and inorganic compounds within the ppb–ppm concentration range. The system consists of a multi-sensor array for the high temporal resolution monitoring of: 1. TVOCs concentration - photoionization detectors (PIDs); 2. CO_2 concentration and temperature monitoring - infrared (IR) sensor; 3. H_2S, SO_2, CO, and NO concentration monitoring along with relative humidity determination - electrochemical sensors. The system, visualized in Figure 1, operates in continuous acquisition mode, enabling simultaneous multisensor measurements.

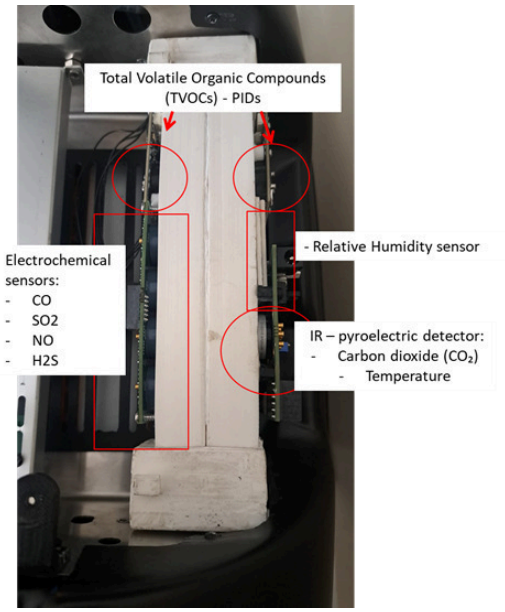

Fig. 1. Overview of the multisensor array chamber.

Sensor data acquired at different sampling rates were temporally aligned within a common time reference. An automatic segmentation procedure was developed to separate breath-related responses from environmental background using CO_2 dynamics as a physiological reference (capnogram). Breath and background data were processed separately, and the background component was used to evaluate system behaviour independently of respiratory signals. Breath data acquired from subjects are also presented in this work, providing preliminary observations, while the main focus remains on background characterization and data quality assessment. System performance was quantified through indicators including baseline stability, signal variability, drift, and inter-sensor correlation. Temporal consistency was evaluated through autocorrelation and timestamp analysis. Experimental measurements were performed under different environmental conditions (e.g., occupancy and ventilation variations), enabling a systematic characterization of sensor behaviour and sensitivity to environmental perturbations. Once exploring the data quality across multiple complementary dimensions and identifying the reliable acquisition conditions, the breath analysis system is currently undergoing validation in collaboration with the medical team of Istituto Tumori 'Giovanni Paolo II' on individuals affected by MPM for diagnosis and prediction purposes.

Results

The obtained outcomes demonstrated that environmental/external conditions may significantly influence sensor responses and baseline stability. More specifically, variations in occupancy and ventilation conditions (rate and mode) may lead to increased baseline variability and higher inter-sensor correlation. Drift analysis highlighted the time-dependent changes in sensor behaviour, more pronounced under perturbed environmental conditions. These findings therefore emphasize the importance of background characterization for reliable multisensor measurements and confirm the effectiveness of the proposed approach in identifying stable acquisition conditions. The use of the system on a population of MPM patients provided promising results, although preliminary.

References

[1] IA. G. Buma et al. Lung cancer detection by electronic nose analysis of exhaled breath: a multicentre prospective external validation study, *Annals of Oncology* 36, 786–795 (2025)

[2] E. A. Chapman, et al. A breath test for malignant mesothelioma using an electronic nose, European Respiratory Journal 40, 448–454 (2012)

[3] E. Hosseinzadeh et al. Data quality assessment in healthcare, dimensions, methods and tools: a systematic review, BMC Medical Informatics and Decision Making 25, 296 (2025)

[4] I. Hayward et al. Low-Cost Air Quality Sensors: Biases, Corrections and Challenges in Their Comparability, *Atmosphere* 15, 1523 (2024)

DOI 10.5162/eurosensors2026/Tu–SAN–03

Integrated Nitrate Sensor for Real-time Soil Monitoring

Elise Saoutieff[1], Arthur Ohl[1], Vincent Elhorga[1], Célia Boko[1], Iris Vogeler[2], Nivedha Surendran[3], Axel Wille[3], Han Shao[4], Alan O'Riordan[4], Patryk Kalkowski[5], Lukasz Kulas[5], Henrique Trindade[6], Safi Ullah[7], Lukas Kohl[7]
[1] Univ. Grenoble Alpes, CEA, Leti, Grenoble, France,
[2] Christian-Albrechts-Universität, Kiel, Germany
[3] Fraunhofer Institute for Electronic Microsystems and Solid State Technologies, Munich, Germany
[4] Nanotechnology Group, Tyndall National Institute, Cork, Ireland
[5] Gdansk University of Technology, Gdansk, Poland
[6] University of Trás os Montes e Alto Douro, Quinta de Prados, Portugal
[7] University of Eastern Finland, Kuopio, Finland
elise.saoutieff@cea.fr

Summary:
Integrated systems for soil monitoring are of growing of interest, especially to detect in real-time the presence of pollutants like nitrate and thus decrease the exploitation cost in field.
This paper presents a wireless multi-sensor system developed during the European FAMOSOS project along with laboratory test results. The system measures the concentration of nitrate in the soil water, the pH, temperature, and soil moisture status using automated data acquisition and wireless LoRa data transmission through the soil.

Keywords: Analog Front-End, Integrated systems, soil monitoring, nitrate, low-power, real-time, wireless sensor network

Background, Motivation and Objective

Guided by the European zero-pollution vision for 2050 and its key 2030 targets "improving soil quality by reducing nutrient losses and chemical pesticides' use by 50%" [1], our work focuses on the detection of nitrate in soil.

Clean water is vital to human health and to natural ecosystems. Nitrogen pollution remains one of the most challenging and costly environmental problems [2]. Nitrate, soluble in water, can easily leach through the soil into the receiving waterways, contaminating groundwater, rivers and lakes.

Monitoring soil environments is thus essential. The FAMOSOS project (Farm Monitoring via Real-time Soil Sensing) [3] from European EJP-SOIL initiative, addresses this challenge by developing a low-cost, real-time electronic system designed to help farmers optimize fertilizer use, reduce greenhouse gas emissions, and minimize water pollution. This paper focus on the Analog Front-End (AFE) specifically developed for an electrochemical nitrate sensor.

System Architecture

A schematic view of the FAMOSOS system architecture and more specifically the electronic architecture interface with others components is represented in Fig.1. The red rectangle highlights the electronic board with IoT power management circuit, along with all other components that can be connected to the board.

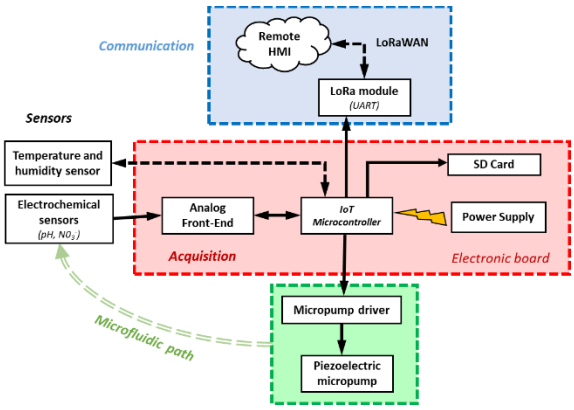

Fig. 1. FAMOSOS simplified design

The multi-sensors system is dedicated to pH and nitrate (NO_3^-) concentration measurements along with soil temperature and moisture in view of our specific application for soil monitoring in the field. It combines a sensor network together with a microfluidic path (composed of porous ceramic cup associated with a micropump and an electrochemical sensor), an analog front-end board for the data acquisition and an antenna for wireless LoRa data transmission through soil.

Analog Front-End for Nitrate Sensor

The previous architecture [4] embedded an Analog Front-End that integrates an STM32 microcontroller unit (MCU) and a portable potentiostat AD5941 from Analog Devices. It was designed to support both analog and digital sensors while also controlling the micropump.
Raw data from the sensors are collected by the AFE and converted into physical values by the microcontroller unit.
Optimizations were performed in this work to operate the bipotentiostat Square Wave voltammetry technique (specific for nitrate sensor) and to improve the robustness and the reproducibility of the electronics. The board also embeds the micropump driver and the LoRa module.

A representation of the FAMOSOS system electronic architecture is shown in Fig.2.

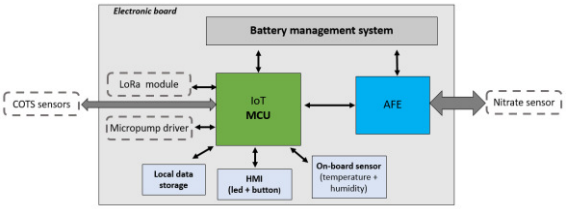

Fig. 2. FAMOSOS Motherboard architecture

The wireless interface for data transmission through the soil, consists of a setup of base stations and wireless end devices, which will be buried underground.
To minimize power consumption, sensors and peripherals remain in standby mode and wake up only when data transmission is required.

Laboratory results

NO_3^- solutions with concentrations of 10, 50 and 100 ppm, were filled into the sensor casing manually with syringe (fig.3).

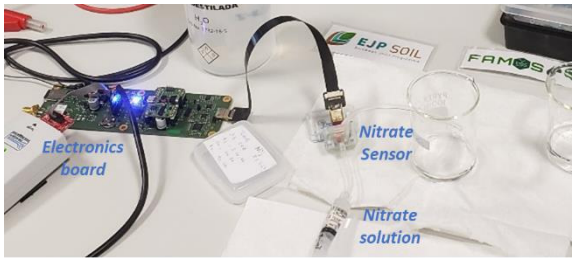

Fig. 3. Laboratory set-up for testing nitrate sensor

The sensor detected changes in nitrate levels over time as shown in Fig 4, providing real-time monitoring of nitrate movement and availability in the soil.

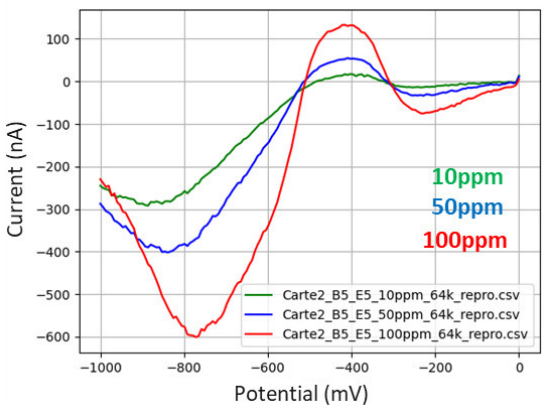

Fig. 4. Nitrate concentration in ppm

The reproducibility and robustness of the electronics were demonstrated through successful laboratory tests.

The next actions will be the deployment in field and Subsequent trials with the overall system and different nitrate concentration.

FAMOSOS will make a significantly contribution to enhancing soil understanding to improve management practices such as optimizing N fertilization strategies.

References

[1] EU Zero Pollution Action Plan [Online] Available : https://environment.ec.europa.eu/strategy/zero-pollution-action-plan_en accessed: Ap. 09 2026.

[2] European Commission Nitrate Directive [Online] Available Ap. 10 2026: https://environment.ec.europa.eu/topics/water/nitrates_en#:~:text=Excess%20nitrogen%20from%20agricultural%20sources,through%20run-off%20from%20agricultural%20fields

[3] E. Saoutieff, C. Boko, P. Fourcade, V. Elhorga, S. Boisseau & al., Real-time soil sensing system for farm monitoring all along FAMOSOS project, Smart System Integration 2025 conference, doi: 10.1109/SSI65953.2025.11107187

[4] C. Boko, E. Saoutieff & al., A low-power wireless sensor platform for real-time monitoring of pH and nitrate in the soil EUROSENSORS XXXVII; 2025 doi: 10.5162/EUROSENSORS2025/T4.3.2.

Acknowledgements

The project is funded as an EJP-SOIL external project by the French National Research Agency (ANR) under grant ANR-23-SOIL-0002-04, the Irish Department of Agriculture, Food and the Marine under grant agreement No. 2022EJPSOIL202, the Finnish Ministry of Agriculture (4400T-0569) and the German Federal Ministry of Education and Research BMBF under grant number 031B1377B.

DOI 10.5162/eurosensors2026/Tu–SAN–04

Scalable flux using chamber embedded integrated selective multigas sensing

Fabian Sievers[1], Moritz Zimmer[1], Álvaro Ortiz Pérez[1], Natalie Schütz[1], Stefan Palzer[1]
[1] TU Dortmund, Professorship for Sensors, Otto-Hahn-Straße 8, 44227 Dortmund, Germany
stefan.palzer@tu-dortmund.de

Summary:
An integrated selective miniaturized multi-gas sensor embedded in a flux chamber enables real-time selective gas flux determination without sample extraction. Using frequency multiplexing multiple gas flux can be measured simultaneously with a single detector. Proving the independent gas flux measurement with a large cost reduction compared to conventional designs, a scalable platform for surface gas emission measurements was designed.

Keywords: photoacoustics, flux sensing, selective gas sensing, scalable flux chamber, sensor network

Introduction

Gas exchange between the Earth's surface and the atmosphere is a key component of global biogeochemical cycles regulating climate and ecosystem functioning. Soils and vegetation emit and consume gases such as carbon dioxide (CO_2), methane (CH_4), and nitrous oxide (N_2O) through respiration and microbial decomposition [1]. In agricultural systems, these fluxes are strongly influenced by management practices such as fertilization, irrigation, and livestock production. Because these processes vary significantly in space and time due to changes in soil moisture, temperature, biological activity, and management events, monitoring approaches with high temporal resolution and dense spatial coverage are required [1].

Currently, fluxes are mainly measured using eddy covariance systems or chamber-based approaches combined with gas chromatography or laser spectroscopy [2]. These methods often require gas sample extraction and complex instrumentation, limiting large-scale deployment. Recently the development of low-cost automated flux chambers with commercially available gas sensors directly inside the head volume have emerged [3]. Those increase complexity by using multiple sensors to achieve the simultaneous measurement of multiple gases and trade-off some selectivity and sensitivity by using lower quality sensors.

Here an approach using an integrated selective miniaturized multi-gas sensor [4] embedded in a chamber is shown to enable real-time gas flux determination without sample extraction. In this approach, gas fluxes are determined from real-time concentration gradients inside the chamber, allowing continuous measurements with minimal system complexity. Such integrated sensing units provide a scalable foundation for dense chamber networks to monitor soil–atmosphere gas exchange across agricultural and natural landscapes.

Method

Fig. 1 depicts the used sensing setup. It uses two temperature-controlled light sources: L15895-0430CN and L15893-0330CN (Hamamatsu Photonics K. K., Japan) with wavelength of 4.3 and 3.3 µm. Amplitude modulation of the LED current with a sine wave of frequency 469 Hz and 541 Hz leads to sound wave generation at those frequencies according to the gas species.

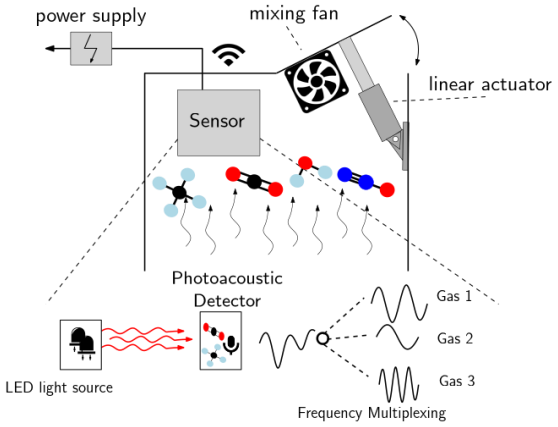

Fig. 1. Schematic Diagram of flux chamber. Multifrequency modulated LEDs excite photoacoustic signals according to each gas species.

The sensor has an absorption path length of 3 cm, where interaction between the gas mixture and light lead to an attenuation according to Beer-Lambert's law. Frequency multiplexing

allows selective multi-gas sensing without cross-sensitivity to humidity or other gases. The setup's compact size, allows sensor integration directly into the flux chamber. The vent, motorized by a linear actuator, can open and close the chamber automatically for intermediate ventilation. The gas sensor itself reports a measurement sample every 10 seconds for CO_2 and CH_4.

The sensor assembly includes a Wi-Fi capable ESP32 (Espressif Systems (Shanghai) Co., Ltd., China), reading and transmitting sensor data to an offsite database. It also controls the motor for the ventilation opening and reads data from an environmental sensor MS8607 (TE Connectivity plc, Ireland), recording air temperature, relative humidity and pressure.

Experimental

For evaluation the flux chamber was placed on top of cattle manure stored in a cut open IBC container. With a ventilation window of 5 minutes and a closed gas accumulation window of 20 minutes the continuous gas concentration inside the flux chamber was recorded for 11 days.

The flux is calculated using a closed chamber approach, meaning CO_2 and CH_4 concentration accumulate inside the closed chamber while being simultaneously measured by the sensor. The ventilation resets the gas concentration inside the chamber to the baseline, starting a new automated measurement cycle. The wireless interface allows for remote management and straight forward setup of multiple flux chambers in a wireless sensing network.

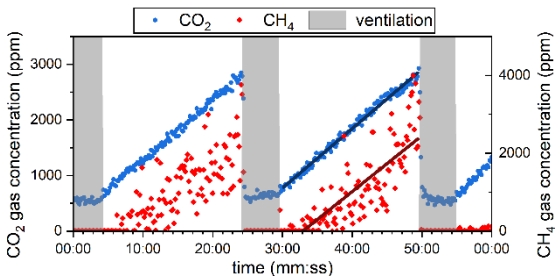

Fig. 2. Flow chamber gas concentration data for CO_2 and CH_4 with exemplary linear fits. The measurements were taken with a 5-minute ventilation window and 20 minutes of gas accumulation.

By applying a linear fit to the independent gas concentration data, while no ventilation occurs, the simultaneous gas flow for multiple gases can be determined independently (see Fig. 2).

Results

Applying the linear fitting method to the whole measurement period, the temporal trend of gas flux emitted from the substrate is created (see Fig. 3). By comparing flux data to the environmental sensor data recorded inside the chamber, investigation of the influence of environment temperature, pressure and relative humidity is possible.

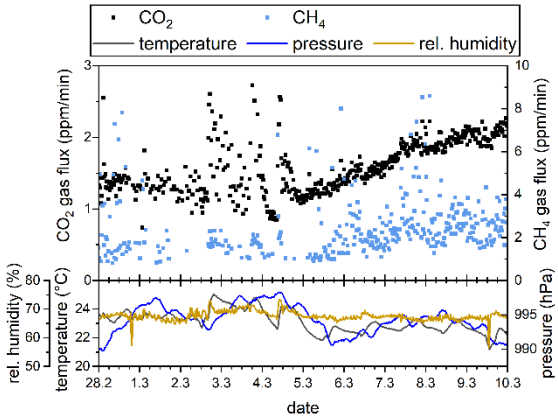

Fig. 3. Top: Flow data derived from flux chamber concentration measurements for CO_2 and CH_4. Bottom: Environmental sensor data during the measurement period.

Conclusion

By integrating a compact novel photoacoustic multi-gas sensor into a flux chamber, a revolutionary cost reducing sensing system for surface gas flux measurements was established, without compromising on selectivity. Cost reduction and integrating the sensor into the chamber, also adding wireless connectivity opens up opportunities for a scalable gas flux measurement network especially useful for dense large-scale soil emission examination. The multi-gas sensor would allow additional simultaneous gas detection of more gases without increasing complexity or cost of the sensor platform for measuring N_2O in soil emission, too.

References

[1] M. Lackner, B. Sajjadi, W.-Y. Chen, eds., *Handbook of Climate Change Mitigation and Adaptation*. Springer International Publishing; Imprint Springer, Cham; 2022.

[2] C. Oertel, J. Matschullat, K. Zurba, F. Zimmermann, S. Erasmi, Greenhouse gas emissions from soils—A review, *Geochemistry* 76, 327–352 (2016); doi: 10.1016/j.chemer.2016.04.002.

[3] B. J. Archer, P. Casper, M. O. Gessner, AutoChamber : A broadly accessible 3D - printed floating chamber to automate measurements of greenhouse gas emissions from surface waters, *Methods in Ecology and Evolution* 17, 979–991 (2026); doi: 10.1111/2041-210x.70222.

[4] G. Rodriguez Gutierrez, A. Ortiz Perez, S. Palzer, Integrated, Selective, Simultaneous Multigas Sensing Based on Nondispersive Infrared Spectroscopy-Type Photoacoustic Spectroscopy, *ACS sensors* 9, 23–28 (2024); doi: 10.1021/acssensors.3c01285.

DOI 10.5162/eurosensors2026/Tu–SAN–05

Biosensing Network for Real-time Water Monitoring

Elise Saoutieff[1], Célia Boko[1], Arthur Ohl[1], Clément Garaffa[1], Guillaume Nonglaton[1], Luana Cuvillier[1], Richard Murray[2], Alan O'Riordan[2], Sana Muzaffar[2], Arjan GJ Tibbe[3], Jinane Elias[3], Gabriela Dudnik[4], Abdessamad Falhi[4], André Fivaz[4], Cecilia Jimenez-Jorquera[5], Josep Maria Margarit-Taulé[5], Enrique Asin Garcia[6], Cécile van der Vlugt[7], Petra Hogervorst[7]
[1] Univ. Grenoble Alpes, CEA, Leti, Grenoble, France
[2] Nanotechnology Group, Tyndall National Institute, Cork, Ireland
[3] OnePlanet Research Center, IMEC, Eindhoven, Netherlands
[4] CSEM, Neuchâtel, Switzerland
[5] IMB-CNM, CSIC, Barcelona, Spain
[6] Wageningen University, Wageningen, Netherlands
[7] RIVM, Bilthoven, Netherlands
elise.saoutieff@cea.fr

Summary:

A biosensor-based monitoring system for water monitoring is growing of interest especially to detect in real-time typical pollutants such as nutrients (nitrates and phosphates), Estrogenic endocrine-disrupters, PFAS (Perfluoroalkyl, and polyfluoroalkyl substances) and Microcystines.

The paper presents a biosensing network developed in the BIOSENSEI project along with the first laboratory results focus on the electronic system architecture. This will enable the first continuous, reliable and robust real-time monitoring and detection of these pollutants in watercourses using cellular-based biosensors.

Keywords: Water monitoring, biosensor, real-time, Nb-IoT, Integrated systems

Background, Motivation and Objective

Water pollution, the leading environmental cause of physical and mental illness, accounted for 1.4 million premature deaths worldwide in 2022 (16% of total deaths) and 12.5% of deaths each year in the EU. Together with the EU Drinking Water Directive from January 2023 [1], there is an urgent need to provide high-quality water, prevent pollution and develop methods to improve the protection of human health.

Better monitor, report and prevent water pollution by providing real-time digital tools directly to users is thus a priority.

In the Horizon Europe project BioSensei (Biosensor-based diagnostic platform enabling real-time monitoring of existing and emerging pollutants), we are addressing these challenges by tackling pollutants of concern, such as PFAS, endocrine disruptors (EDs) and microcystins [2,3].

Based on previous work [4] [5] [6], novel mixed-signal front-ends is developed for the combinatorial sensing approach (electrochemical and fluorescence transducers) and sampling conditions. These systems will transfer sensor data to the project cloud to facilitate long-term autonomous sensing with Nb-IoT communication.

System Architecture

The BioSensei Node (Fig.1) is a subsystem composed by (a) the BioSensei Sensor Head, (b) the BioSensei electronic front-end and (c) the BioSensei IoT.

(a) Cellular biosensors are encapsulated and immobilized at bimodal transducers (nanoelectrochemical and optical) for detection of the target pollutants: Nitrate, Nitrite, Phosphate, Estrogens E1, E2, E3, E12 and PFAS.

(b) the electronic front-end is separated into electrochemical and optical front-end subunits.

(c) the IoT controls the electronic front-end, to which it will request to start a measurement and from which it will collect the values measured by the sensor. The IoT will then store, process and transmit these values to the BioSensei Cloud platform. Up to 10 bio-sensors will be integrated on the BioSensei platform associated to up to 10 sensor front-ends.

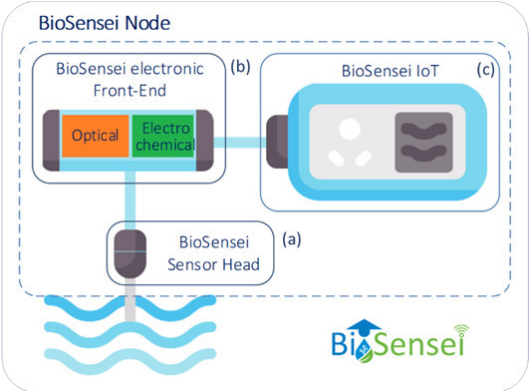

Fig. 1. BioSensei simplified design

IoT node

The IoT node embeds a wireless communication module to link to the BioSensei Cloud platform via the Internet by means of either a Gateway and a mid-range communication infrastructure like on Fig.2.

Nb-IoT communication was chosen as the most appropriate for the BioSensei use cases, using LTE “Long Term Evolution” coverage network.

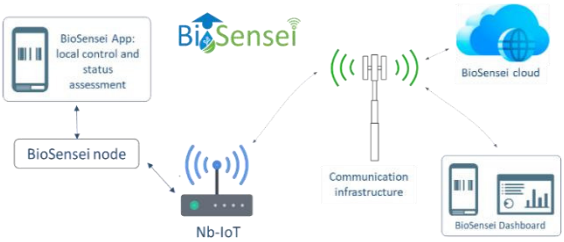

Fig. 2. BioSensei IoT

Laboratory results

The IoT board was connected with the 6 terminals optical sensors AFE (Analog Front-End), the 2 terminals electrochemical AFE and the edge-computing board like shown in Fig. 3.

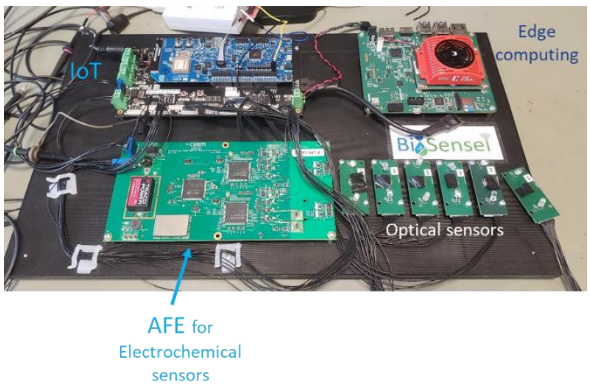

Fig. 3. Set-up for the communication IoT test

Good communication between the different boards were highlighted. The robustness of the electronics and Nb-IoT communication were demonstrated through successful laboratory tests.

The next actions will be the integration of the overall system with 10 cells in laboratory and subsequent trials with different pollutants and finally the deployment in Ireland and Netherlands tests site.

BioSensei will make a significantly contribution to enhancing water understanding to improve management practices.

References

[1] Drinking water directive. [Online]. Available: https://eur-lex.europa.eu/eli/dir/2020/2184/oj (accessed: Ap. 21, 2026)

[2] E. Saoutieff & al., Bio-sensing system for water real-time monitoring in BioSensei project, Smart System Integration 2025 conference

[3] E. Saoutieff, P. Fourcade, C. Boko et al., Real-time water monitoring with advanced biosensor systems, EUROSENSORS XXXVI; 2024, Debrecen, Hungary; doi: 10.5162/EUROSENSORSXXXVI/PT6.304; ISBN 978-3-910600-03-4

[4] A. O'Riordan, H. Shao, T. Narayan, "A working electrode, a reference electrode, a sensor, and a method of manufacture thereof"," UK2309536.7, 2023

[5] E. Saoutieff, T. Polichetti, L. Jouanet, A. Faucon, A. Vidal, et al., “Wearable Smart Sensing platform for environmental and health monitoring: the Convergence project,” Sensors, 21, 1802, 2021

[6] SARMENTI (H2020-ICT-2018-2) Smart multisensor embedded and secure system for soil nutrient and gaseous emission monitoring (https://sarmenti-project.eu/)

Acknowledgements

The project is funded by the European Union’s Horizon Europe Framework Programme (Horizon) under grant agreement 101135241 – BioSensei.

DOI 10.5162/eurosensors2026/Tu–SAN–06

Low-Cost Electronic Nose for Environmental Applications

Guillem Domenech Gil[1], David Bastviken
[1] Department of Thematic Studies - Environmental Change (TEMA M), Linköping University, Sweden

Corresponding Author's e-mail address: guillem.domenech-gil@liu.se

Summary:
Atmospheric methane (CH_4) concentrations are increasing rapidly for reasons that are not entirely clear. To understand the dynamics of this gas, we need a high number of CH_4 sensors widely distributed over the Earth's surface, what would only be possible if such sensors were inexpensive. Low-cost sensors (LCS) could fill this technological need. However, LCS suffer from cross-interference and thus show complications to measure CH_4. We have developed a platform that combines low-cost metal oxide CH_4 sensors with ambient temperature, humidity, and pressure sensors, and an algorithm that trains models enabling to compensate for interferences at low cost. Using mechanistically informed multivariate statistical models trained on reference equipment data, we manage to measure CH_4 changes at sufficient precision to track atmospheric changes. We compare laboratory and field calibrations and describe limitations and practical ways to improve this versatile approach for data from natural and anthropogenic sources.

Keywords: methane, electronic nose, metal-oxide sensors, calibration, machine learning.

Headlines

- Our electronic-nose combines several low-cost metal-oxide CH_4 sensors with temperature, humidity, and pressure sensors.
- Mechanistically informed multivariate statistics models trained against reference equipment are used to compensate cross-interferences and retrieve CH_4 concentrations.
- Laboratory and field calibrations show differences; we discuss limitations and routes to improve reliability for natural and anthropogenic source contexts.

Background, Motivation and Objective

CH_4 is a potent greenhouse gas with a 100-year global-warming potential of 28–34 relative to CO_2 by mass, and atmospheric concentrations are rising rapidly for reasons that are not totally clear [1]. Current ground-based monitoring systems used for national inventories and international reporting are costly and thus far too scarce to help resolve source-sink dynamics details at local scales, exactly where they could help reduce further emissions [2]. This strengthens the need for affordable and accessible CH_4 quantification techniques. In this sense, distributed LCS networks represent an appealing solution that could fairly complement reference approaches. LCS could potentially enable more spatially resolved measurements and support flux analyses to better understand concentration variability, support source attribution, and assess mitigation efforts. However, reliable use of LCSs remains limited due to their need for extensive periodical calibrations and the necessity to compensate for cross-interferences and environmental influences to ensure data quality [3].

Description of the New Method or System

Our system is a multi-sensor platform that integrates various low-cost metal-oxide CH_4 sensors with co-located environmental sensors (temperature, humidity, pressure). Thus, the platform generates multi-channel signals intended to capture both CH_4 response and confounding effects. We calibrated several platforms both in laboratory conditions and outdoors, close to the laboratory and in the final measurement site. Then, we deployed them outdoors close to known anthropogenic emission sources. During field measurements, we observe that these three environmental variables influence the sensor signal, both baseline and response, and are therefore important variables to compensate for during real-world operation if one targets absolute CH_4 accurate concentration. We then applied mechanistically informed multivariate statistics models trained against reference equipment and retrieved CH_4 concentration predictions. An important novelty is the algorithm of the multivariate statistic model, which is adaptative and can return models adapted to the sensor units and platforms. Because each sensor and system

present particularities, the model returning gas concentration can be considerably different. With our data treatment architecture, we can improve the interpretability and reliability of LCS outputs under variable environmental conditions.

Results

By implementing our algorithm to data from electronic noses calibrated with reference instruments, we compensate enough for cross-interferences to resolve CH_4 environmental variability even if the metal-oxide sensors are meant for CH_4 leakage detection at much higher concentration values. In *Fig. 1* one can see the results of the model for one of the LCS systems trained with our algorithm. The graph shows only test data, i.e., data that was not used to train the model (unseen). This is an approximation to how the system will perform after being calibrated and operating in the deployed field as the measurement shown is when operating outdoors and exposed to uncontrolled atmospheric variable changes. The predicted signal is compared to data collected with the reference instrument that was located next to the LCS system to validate the results. In this way, one can understand the level of accuracy we can reach with a ~500€ system compared to what one obtains with a reference system of with a cost of ~60 times higher. Besides, we observed that one metal-oxide sensor is not enough to track atmospheric concentration changes but that three achieve convenient accuracy. Moreover, we also observed that more than three sensors do not relevantly improve the resolution and thus we keep three sensors as cost-accuracy compromise. We present results that highlight differences between laboratory calibrations and field calibrations, and we discuss what these differences imply for deployment strategies and calibration transferability. Finally, we outline limitations of the current calibration strategies, machine learning approaches for data treatment, and practical pathways for improvement based on tests using data associated with both natural and anthropogenic sources. This work aims to support the use of CH_4 LCS networks to complement reference-grade instruments and help assess mitigation strategies efficiency.

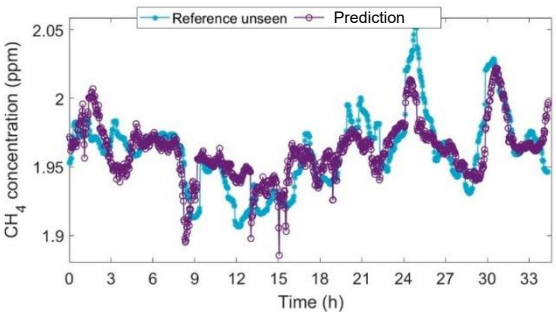

Fig. 1. Comparison between the signal of unseen reference methane data over time (test set, not used during model training) and predictions extracted from a low-cost electronic nose dataset operated during the same time period.

References

[1] G. Myhre et al. *Anthropogenic and Natural Radiative Forcing*. In: Climate Change 2013: The Physical Science Basis. Contribution of Working Group I to the Fifth Assessment Report of the Intergovernmental Panel on Climate Change; Stocker, T., Qin, D., Plattner, G.-K., Tignor, M., Allen, S., Boschung, J., Nauels, A., Xia, Y., Bex, V., Midgley, P., Eds.; Cambridge University Press, United Kingdom and USA, 659-740 (2013); doi: 10.1017/CBO9781107415324.018.

[2] D. Bastviken, J. Wilk, N.T. Duc, M. Gålfalk, M. Karlson, T.-S. Neset *et al.* Critical method needs in measuring greenhouse gas fluxes. *Environmental Research Letters* 17, 104009 (2022); doi: 10.1088/1748-9326/ac8fa9.

[3] G. Domènech-Gil, N.T. Duc, J.J. Wikner, J. Eriksson, S.N. Påledal, D. Puglisi, D. Bastviken, Electronic Nose for Improved Environmental Methane Monitoring. *Environmental Science & Technology* 58, 352-361 (2024). doi: 10.1021/acs.est.3c06945

Acknowledgements

This work has been financially supported by the Horizon Europe's grant agreement no.101120651, Next-2Digits, Formas grant 2018-01794, and Swedish Research Council grants 2016-04829 and 2022-03841.

DOI 10.5162/eurosensors2026/Tu–SAN–07

Is the initial response of gas sensors enough for gas recognition?

Luiz MIRANDA[1,2], Ítalo SANTOS[1], Bernadette DORIZZI[1], Dijana PETROVSKA DELACRETAZ[1], Mossaab HARIZ[1], Jerome BOUDY[1], Nathalie REDON[2], Alberto GREGORI[2], Jugurta MONTALVÃO[3]

Corresponding Author's e-mail address: luiz.miranda@imt-nord-europe.fr

Summary:

This work examines whether early-response features of metal-oxide (MOX) gas sensors enable reliable gas identification without waiting for signal stabilization. Four features are evaluated, the derivative (Dt), relative response (Rs), and area under the curve (AUC), including a truncated version (AUC-20s) using only the first 20 seconds. Using a multilayer perceptron and intrinsic dimensionality analysis on an open dataset of 11 gases across three sensor positions, results show that early features can match or outperform Rs, with AUC-20s performing best for real-time applications.

Keywords: metal-oxide sensors, gas identification, real-time monitoring, feature extraction, intrinsic dimensionality

Introduction

Gas sensing using metal-oxide semiconducting (MOX) sensors has gained traction due to their cost-effectiveness. Although they are a non-selective type of sensor, an array of different MOX sensors can match the performance of more costly selective sensors, when paired with a machine learning post-processing. However, calibration models typically rely on the stable sensor response relative to a baseline resistance, which is impractical for real-time monitoring. In this work, we investigate whether early-response features of MOX sensors, computable within the first few seconds of gas exposure, can support reliable gas identification. We compare the sensor derivative (Dt) against the relative response (Rs), the area under the curve (AUC), and a truncated variant (AUC-20s).

Methodology

As observed in previous studies, Dt can provide significant information for gas identification [1], [2]. To check if this feature is sufficient to recognize a target gas with similar performance to reference methods (Rs), the gold standard for gas sensing, and AUC, we perform the following procedure: (i) From the raw sensor response curves, extract 4 datasets, corresponding to their respective features: Dt, Rs, AUC, and AUC-20s; (ii) Perform a k-fold cross validation to evaluate the average accuracy of each dataset on a fixed model architecture. Here, k = 10; (iii) Perform an information content analysis of each dataset.

To compute Dt, the raw sensor response is truncated between the moment of gas injection and Δ samples after injection. The discrete derivative is then computed as:

$$dt[n] = s[n] - s[n-1]$$

where $s[n-1]$ and $s[n]$ are consecutive measurements at time indices n-1 and n, respectively, across the D sensors in the array. The resulting feature is the average value of *dt* per sensor. For the tests performed in this work, Δ = 20 samples.

Rs is computed from each raw sensor response by extracting R_0, the sensor resistance at the moment of gas injection, and R_g, the resistance at the end of the exposure period. The relative response is then computed as:

$$R_s = \begin{cases} (R_g - R_0)/R_0\,, R_g \geq R_0 \\ (R_0 - R_g)/R_g, R_g < R_0 \end{cases}$$

Finally, AUC is computed by the sum of measurements during an injection. For each *d* sensor:

$$AUC_d = \sum_{n=0}^{N} s_d[n]$$

where n=0 corresponds to the injection time and n=N to the end of the exposure period. A truncated variant, AUC-20s, is also explored, where N is limited to the first 20 seconds of injection.

Experiments

Tests were performed using open dataset collected in [3]. For this work, the details that matter are that, in total 11 target gases are tested, with

a sampling period of 1 s, and measured by 8 individual commercially available sensors. The experimental protocol used to extract the data is as follows: (a) 20 s of clean air; (b) 3 minutes of target gas exposure; (c) 3 minutes of purging with clean air. Sensors are tested in several positions in relation to the gas source[1]: P1, P3 and P4 (according to Figure 2 from the reference), under the assumption that performance degrades with increasing distance from the source. The selected sensing array is consistently the one located at the center of the chamber.

Gas classification was performed using a simple multilayer perceptron (MLP), with 7 neurons in the input layer (one for each sensor[2]), followed by a hidden layer of 15 neurons with a sigmoidal activation function. The output layer consists of 11 neurons (corresponding to the 11 target gases) and uses a softmax activation function to estimate valid class probability distributions. Input data were normalized prior to training and testing. The model was trained using the Adam optimizer with a fixed learning rate of 0.01, over 100 epochs with a batch size of 50. Total number of samples in each dataset was 3075.

An information content analysis was also performed by estimating the intrinsic dimensionality (ID) of the resulting datasets using the multiscale approach developed in [4].

Results and discussion

A summary of the classification results per feature and per position is shown in Table 1. While the AUC is computed during the whole injection period, AUC-20s considers only the first 20 seconds of injection, in the same way as Dt. Even with this limitation, AUC-20s still manages to outperform both Rs and Dt, making it the optimal choice within the tested features for gas classification task. This is especially true for real-time monitoring, since only the initial 11% of the exposure time results more effective than Rs, measured on the whole exposure time.

A summary of the information content analysis is provided in Table 2. It becomes clear that ID for AUC is in general higher, representing a higher complexity of the data, which may be advantageous for the classifier, as reflected in the higher accuracy results[3].

Another interesting result from this analysis comes from the comparable ID of Dt and Rs. This indicates that the complexity of the resulting datasets is almost identical and likely to show even closer results by selecting another classifier. Further study is still required on this point.

Table 1. Summary of gas classification accuracy per feature and per position.

Feature	Position		
	P1	P3	P4
Dt	94.01 ± 1.37 %	92.74 ± 1.59 %	89.75 ± 2.17 %
Rs	94.34 ± 1.61 %	94.08 ± 1.75 %	90.40 ± 1.70 %
AUC	98.66 ± 0.86 %	98.60 ± 0.98 %	97.39 ± 1.14 %
AUC-20s	95.93 ± 1.33 %	95.93 ± 1.54 %	93.46 ± 1.13 %

Table 2. Summary of intrinsic dimensionality (ID) estimation of the resulting datasets.

Feature	Position		
	P1	P3	P4
Dt	1.74	1.52	1.55
Rs	1.73	1.57	1.56
AUC	1.93	2.04	2.13
AUC-20s	2.20	2.11	2.22

Conclusions

In this work, we investigated whether early-response features of MOX gas sensors are sufficient for reliable gas identification. Results show that the sensor derivative (Dt), computed from only the first 20 seconds of exposure, achieves classification accuracy comparable to the standard relative response (Rs), suggesting that the initial transient response carries enough discriminative information for gas recognition. Furthermore, AUC-20s outperforms both Dt and Rs across all tested positions, making it a strong candidate for real-time gas monitoring applications. The information content analysis corroborates these findings, showing that AUC-based features present higher intrinsic dimensionality, indicating a higher level of complexity provided by the feature, which appears to be exploited by the classifier to achieve better performance.

References

[1] P. Le Maout *et al.*, *IEEE Engineering in Medicine and Biology Society (EMBC)*, Jul. 2018. doi: 10.1109/EMBC.2018.8512847.

[2] J. G. Monroy, J. González-Jiménez, J. L. Blanco, *Sensors*, Oct. 2012, doi: 10.3390/s121013664.

[3] A.Vergara *et al*, *Sensors and Actuators B: Chemical*, Aug. 2013, doi: 10.1016/j.snb.2013.05.027.

[4] J. Montalvão, J. Canuto, and L. Miranda, *Journal of Communication and Information Systems*, Dec. 2020, doi: 10.14209/jcis.2020.30.

Acknowledgments

This work is currently supported by the European Union through the HORIZON-CL4-2023-RESILIENCE-01-33 project “Smart sensors for the Electronic Appliances market (RIA),” grant number 101130159 – AMUSENS.

[1]P2 was removed from the testing due to lack of data.
[2]TGS 2611 was removed from analysis due to scaling issues.
[3]High ID alone does not imply high classification accuracy, but it contributes to estimating mutual information between observations and the gas class. Results in this study suggest that higher ID increases the information available about the class, warranting further research.

DOI 10.5162/eurosensors2026/Mo–SFM–01

Physics-Based Power-Law Discrimination of CO_2 and Isoprene Using a Single $NdFeO_3$ Perovskite Sensor

Abhijit Narayan Eshore[1], Subhobrata Banerjee[2], Priyanka Dutta[3], Prasanta Kumar Guha[3]*
[1] Advanced Technology Development Centre (ATDC), IIT Kharagpur, India
[2] School of Nano Science and Technology, IIT Kharagpur, India
[3] Department of Electronics and Electrical Communication Engineering, IIT Kharagpur, India
Corresponding Author: pkguha@ece.iitkgp.ac.in

Summary:

A physics-based framework is presented for $NdFeO_3$ gas sensors, where gas-specific power-law scaling arises from coupled defect transport and surface reactions. At 250° C, CO_2 response follows the expected scaling with exponent agreement $\Delta\alpha<0.05$ (measured $\alpha = 0.297\pm0.007$ vs predicted 0.25; $R^2 =0.987$), identifying the validity regime of the model. Mixed-gas response is analyzed using the shifted power-law formulation without normalizing or masking. The isoprene contribution exhibits enhanced current-response scaling, indicating competitive site-blocking that modulates carrier density at this temperature. These results demonstrate that the scaling exponents can serve as physically interpretable descriptors for dual-analyte discrimination.

Keywords: $NdFeO_3$, gas sensing, power-law scaling, mixed gas, isoprene, competitive adsorption

Background, Motivation and Objective

Metal oxide gas sensors exhibit excellent robustness and sensitivity, yet simultaneous surface interactions often limit selectivity in mixed gas conditions [1]. In perovskite oxides such as $NdFeO_3$, sensing behavior is governed by oxygen vacancy defects and surface adsorption that modulate charge transport across grain-boundary barriers [2, 3]. While CO_2 adsorption typically forms carbonates at basic sites, altering carrier density [4], hydrocarbon (e.g., isoprene) interactions are strongly temperature-dependent and favor site competition over complete oxidation at moderate temperatures [5, 6]. This study examines whether these distinct reaction pathways yield characteristic steady-state power-law exponents suitable as single-sensor discrimination descriptors, and identifies the temperature window for model validity.

Description of the New Method or System

The heart of the resistive sensor was nanomaterial-based sensing layer ($NdFeO_3$). It was synthesized using sol-gel technique and drop-casted on interdigitated electrodes to fabricate the device. The sensing layer was characterized using XRD (orthorhombic perovskite phase found) and SEM (agglomerated grains with porous morphology observed) (shown in Fig 1). The dynamic response was measured using a custom-made gas test set up. The sensing response is described using a coupled transport-reacting framework, where oxygen vacancy transport within the bulk is governed by a Nernst-Planck relation and coupled to surface reactions through boundary kinetics [2]. The electrical response is determined by grain-boundary modulation expressed as

$$I=I_0 \exp(-q\Phi_s/K_BT)\ldots\ldots(i)$$

where I is the measured current, I_0 is the pre-exponential baseline current, q is the elementary charge, k_B is the Boltzmann constant, and T is the absolute temperature, and Φ_s, is the surface potential governed by the charge state of adsorbed species [3]. Under steady state conditions, gas-specific scaling exponent (α) relations emerge between response R and concentration (C) as

$$R = AC^{\alpha}\ldots\ldots(ii)$$

The carbonate formation in CO_2 sensing depletes electrons producing a positive scaling exponent, validating theoretical value of $\alpha \approx 0.25$ [4]. For isoprene, shifted power law in equation (iii) gives the net empirical response. This positive response change implies adsorption on surface oxygen sites rather than oxidative dehydrogenation at 250° C, and the mechanistic assignment is under ongoing investigation. The mixed-gas response is expressed as:

$$R_{mix} = R_{base}+ A_{iso}C_{iso}^{\alpha}\ldots\ldots(iii)$$

Where, R_{base} corresponds to the CO_2 baseline contribution, without normalisation; log-log curvature reflects the superposition of two surface processes. Throughout this work, sensor re-

sponse R is defined as the ratio of steady-state current under gas exposure to current in air (at a constant applied voltage), $R = I_{gas}/I_{air}$; a response value greater than unity therefore indicates a decrease in resistance consistent with enhanced carrier density.

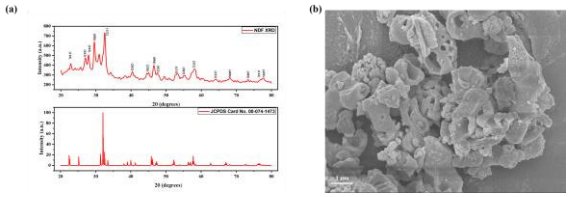

Fig. 1. Structural and morphological characterization of $NdFeO_3$. (a) X-ray diffraction (XRD) pattern with indexed diffraction peaks. (b) Field-emission scanning electron microscopy (FESEM) image at the micrometer scale.

Results

At 250° C, CO_2 response follows a power-law with α_{CO2} = 0.297±0.007 (predicted theoretically 0.250; R^2 = 0.987), confirming the model across 10-160 ppm. The deviation satisfies Δα<0.05. For mixed gas conditions (160 ppm CO_2, and isoprene varying between 0.1 ppm and 5 ppm, as shown in Fig 2b), the response was analyzed using a shifted power-law formulation without baseline subtraction or normalization. The extracted isoprene contribution gives α_{iso} = 0.852±0.021. The extracted exponent of 0.852 is treated as an experimentally characterised discriminator.

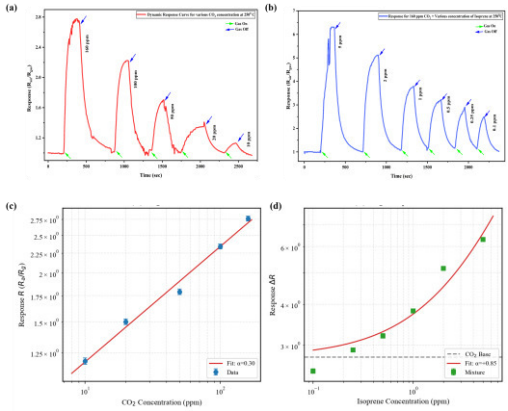

Fig. 2. Gas sensing characteristics of $NdFeO_3$ at 250°C. (a) Dynamic response of the sensor to varying CO_2 concentrations. (b) Dynamic response under mixed gas exposure (CO_2 + isoprene). (c) Log–log plot of steady-state response versus CO_2 concentration showing power-law scaling with fitted exponent. (d) Mixed-gas response as a function of isoprene concentration, fitted using a shifted power-law model. The presence of a baseline contribution from CO_2 results in curvature in the log–log representation.

Response values increase across 0.1–5 ppm; ΔI is predominantly positive, with a small negative deviation at 0.1 ppm near the detection limit (ΔI), which may arise from noise or competing surface processes near the detection limit. At 250° C, isoprene adsorbs on vacancy sites, modifying surface oxygen kinetics and enhancing carrier density. The difference between scaling exponents provides a measure of discrimination capability $|\alpha_{iso} - \alpha_{CO2}|$=0.555. This separation indicates that the contributions of CO_2 and isoprene can be distinguished within a single sensor response. At 200° C, deviations from ideal scaling (α_{CO2} =0.189<0.25) confirm the model boundary and are excluded from validation in this manuscript.

Conclusion

A physics-based framework for gas sensing in $NdFeO_3$ has been established using steady-state power-law scaling. At 250 °C, the CO_2 response demonstrates strong agreement with theoretical predictions (0.297 ± 0.007 vs. 0.250; Δα < 0.05; R^2 = 0.987), validating the coupled transport-reaction model. Mixed-gas response is accurately described using a shifted power-law formulation, enabling extraction of the isoprene contribution without normalization artifacts. The positive current response and elevated exponent (0.852 ± 0.021) indicate competitive site-blocking at surface oxygen sites. The exponent separation of 0.555 provides a direct, physically interpretable metric for dual-analyte discrimination, offering a streamlined approach for compact mixed-gas monitoring platforms.

References

[1] S. Kanaparthi, S.G. Singh, Discrimination of gases with a single chemiresistive multi-gas sensor using temperature sweeping and machine learning, *Sensors and Actuators B: Chemical* 348, 130725 (2021); doi: 10.1016/j.snb.2021.130725

[2] F.A. Kröger, H.J. Vink, Relations between the concentrations of imperfections in crystalline solids, *Solid State Physics* 3, 307-435 (1956); doi: 10.1016/S0081-1947(08)60135-6

[3] N. Bârsan, U. Weimar, Conduction model of metal oxide gas sensors, *Journal of Electroceramics* 7, 143–167 (2001); doi: 10.1023/A:1014405811371

[4] Y. Chen et.al., CO_2 sensing properties and mechanism of $PrFeO_3$ and $NdFeO_3$ thick film sensor, *Journal of Rare Earths* 37, 80–87 (2019); doi: 10.1016/j.jre.2018.06.007

[5] J. Casanova-Chafer et.al., Enhanced CO_2 sensing by oxygen plasma-treated perovskite–graphene nanocomposites, *ACS Sensors* 9, 830–839 (2024); doi: 10.1021/acssensors.3c02166

[6] A.T. Güntner, et.al., Selective sensing of isoprene by Ti-doped ZnO for breath diagnostics, *Journal of Materials Chemistry B* 4, 5466–5474 (2016); doi: 10.1039/C6TB01335J

DOI 10.5162/eurosensors2026/Mo–SFM–02

Artificial Wind-Assisted Control of Hydrogen Gas Leaks for Improved Sensor Detection: A CFD Study

Subhashish Dasgupta[1], Pedro Castro-Fernandez[2], Axel Kramer[2]
[1] ABB Corporate Research, Bangalore, India,
[2] ABB Corporate Research, Baden-Dättwil, Switzerland
pedro.castro@ch.abb.com

Summary:

This CFD study evaluates an artificial wind-assisted approach to actively control, detect, and localize hydrogen gas leak plumes. Detecting hydrogen leaks is challenging due to strong buoyancy and rapid multidirectional dispersion, which may cause leaked gas to bypass stationary sensors. The results show that moderate blower-generated air jets can steer hydrogen plumes over distances exceeding 15 m while maintaining gas concentrations within detectable ranges. Interaction between the airflow and surrounding surfaces promotes near-ground plume transport, mitigating buoyant rise and increasing sensor exposure time. The proposed approach enables more cost-effective sensor deployment and improves detection robustness and localization capability, particularly in scenarios involving multiple simultaneous leaks.

Keywords: CFD, gas leak detection, artificial wind, sensors, hydrogen

Background, Motivation and Objective

Hydrogen leak detection is challenging due to the intrinsic high buoyancy and rapid diffusion of hydrogen, which lead to complex plume trajectories that may compromise safety at industrial facilities if undetected [1]. As a result, leaked gas can bypass conventional point sensors even when these are placed near expected leak locations. Current hydrogen safety systems rely mainly on passive detection, often requiring dense sensor deployment to compensate for uncertain plume paths. This increases system complexity and cost while still leaving detection gaps, particularly in open or semi-open environments [2]. Computational fluid dynamics (CFD) has been widely validated for predicting hydrogen dispersion and supporting safety-oriented design in industrial settings [3].

The objective of this work is to assess, using CFD simulations, an alternative strategy in which blower-generated artificial airflow is used to actively control hydrogen plume trajectories and guide leaked gas toward strategically positioned sensor arrays.

Description of the New Method or System

The proposed system combines strategically positioned air blowers with downstream hydrogen gas sensors to actively manage dispersion following a leak. As illustrated in Fig. 1A, the artificial airflow intercepts the hydrogen plume shortly after release and steers it toward a predefined detection zone, rather than relying solely on passive transport.

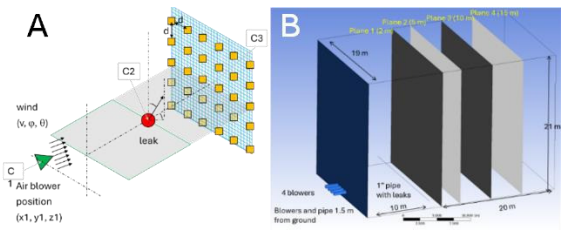

Figure 1. A: artificial wind-assisted gas leak detection system. B: schematic of CFD model. Vertical planes are non-physical, only for viewing gas concentration contours.

Moderate airflow velocities are intentionally targeted, as wind speeds on the order of 5–7 m/s are known to dominate hydrogen plume transport without excessive dilution [4]. The artificial wind-assisted concept is evaluated using CFD, exploiting the established capability of numerical models to capture combined momentum- and buoyancy-driven hydrogen dispersion. The analysis focuses on plume controllability, downstream concentration levels, and sensitivity to blower configuration and leak positioning, with particular attention to maintaining hydrogen concentrations within the detection range of commercially available sensors. By shifting leak detection from a passive to an actively managed process, the proposed approach enables wider

coverage, improved leak localization capability, and greater flexibility in sensor placement for complex industrial environments.

Results

The CFD model geometry and the relative positions of the blowers and multiple hydrogen leak sources are shown in Fig. 1B. Downstream of the simulated leaking pipe, the airflow progressively attaches to nearby ground surfaces, promoting downward deflection of the hydrogen plume and sustained near-ground transport. This behavior, visualized in Fig. 2 (left column), is attributed to the Coanda effect, which has been widely reported for wall-jet and near-surface flows and is reliably captured in CFD simulations [5]. The resulting plume trajectory counteracts rapid vertical rise and increases exposure time for ground-mounted sensors.

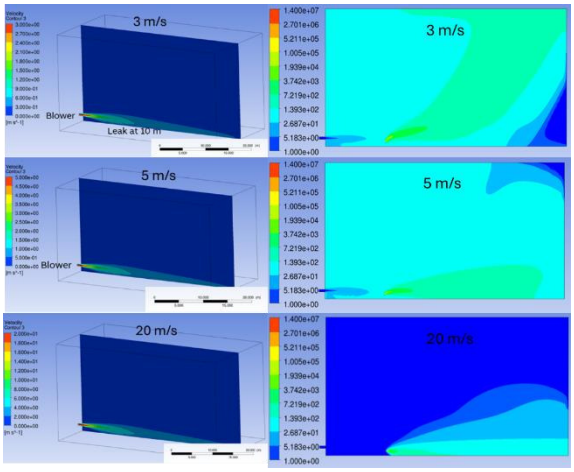

Figure 2. Left column: air stream grazes the ground surface downstream from the blower. Right column: H_2 concentration distribution under air stream at different speeds. Gas leakage rate 0.4 kg/hr.

As shown in Fig. 2 (right column, top), at low air-jet velocities (~3 m/s) the induced airflow is insufficient to counteract buoyancy-driven plume rise, resulting in limited plume steering. Partial control emerges at approximately 5 m/s (Fig. 2, right column, middle), consistent with hydrogen dispersion behavior under moderate cross-flow conditions [4]. Gas concentration profiles extracted at downstream planes reveal a trade-off between plume confinement and dilution. While higher air-jet velocities (~20 m/s; Fig. 2, right column, bottom) further enhance plume control, they reduce hydrogen concentrations below 50 ppm, surpassing the lower detection limits of many commercial hydrogen sensors. Consequently, an air-jet velocity of ~7 m/s provides the most favorable balance between controllability and detectability.

Subsequently, multi-leak scenarios distributed along the pipeline were simulated. Spatially distributed blowers enable simultaneous steering of multiple plumes toward a common downstream detection region (Fig. 3), while preserving detectable hydrogen concentrations (>50 ppm) at distances exceeding 15 m from the leak sources. These results demonstrate the robustness of the proposed approach for diverse industrial layouts.

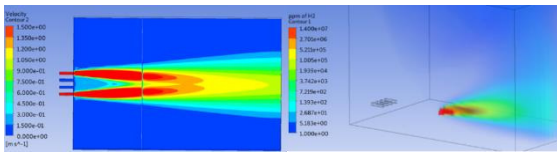

Figure 3. Left: top view of air velocity contours; right: distribution of concentration of H_2 emanating from all leaks.

Conclusion

The CFD results demonstrate that moderate artificial airflow can effectively control buoyant hydrogen gas leak plumes across a broad plane, mitigate rapid vertical rise through surface-attachment effects, and preserve gas concentrations within sensor detection limits across longer distances from the leak source. By shifting hydrogen leak detection from a passive to an actively managed process, the proposed artificial-wind-assisted approach enhances sensing coverage, localization robustness, and flexibility in sensor placement for complex industrial environments. Using CFD modelling, it was possible to optimize the air velocity and blower positioning required to adequately control gas plumes over a broad leakage area, as well as to determine how far downstream the target gas could still be detected. The promising results from these studies are planned to be demonstrated throughout future field testing.

References

[1] K. Prasad, *et al*, A numerical study of the release and dispersion of a buoyant gas in partially confined spaces, *Int. J. Hydrogen Energy* 33, 6208–6219 (2008);doi:10.1016/j.ijhydene.2008.07.037

[2] S. K. Menon, *et al*, Advancements in hydrogen gas leakage detection sensor technologies and safety measures, *Clean Energy* 9, 263–277 (2025); doi: 10.1093/ce/zkae122

[3] V. Agranat, *et al*, CFD modeling of hydrogen releases and dispersion in industrial environments, *Int. J. Hydrogen Energy 29*, 961–971 (2004); doi: 10.1016/S0360-3199(03)00168-5

[4] S. Choi, B. Jeong, CFD simulation of gas dispersion at hydrogen bunkering stations under different wind conditions, J. *Int. Marit. Saf. Environ. Aff. Ship.* 7, 2261350 (2023); doi: 10.1080/25725084.2023.2261350

[5] Lemos, *et al*. Numerical effects of a turbulent flow with Coanda effect in hydrodynamics profiles. *FME transactions*, 45, 412-420 (2017); doi: 10.5937/fmet1703412L

DOI 10.5162/eurosensors2026/Mo–SFM–03

Impact of Water on the Temperature Homogeneity in a High-Temperature Gas Sensor

Julia Herrmann[1], Gunter Hagen[1], Ralf Moos[1]
[1]Department of Functional Materials, University of Bayreuth, Bayreuth, 95440, Germany

Summary:
The study investigates the impact of water in the exhaust gas on the temperature homogeneity of high-temperature gas sensors. The sensors are equipped with a rear-side platinum heater and five front-side thermocouple junctions to monitor the temperature distribution. Experimental results show that increasing water content has a cooling effect, requiring higher heating power to maintain the target temperature. It also leads to local temperature variations across the sensor substrate. These temperature inhomogeneities may lead to significant measurement errors in temperature-sensitive gas sensors.

Keywords: high-temperature, gas sensor, impact, water, temperature homogeneity

Introduction

In many exhaust gas applications, such as in the automotive sector or biomass combustion, gas sensors are exposed to harsh environmental conditions. This includes, on the one hand, very high flow velocities, particle-loaden exhaust gases, and high exhaust temperatures. To withstand these conditions, high-temperature gas sensors are employed [1-4]. An example of such a high-temperature gas sensor is a thermoelectric hydrocarbon sensor. This sensor utilizes the thermoelectric voltage as the measurement signal. Here however, a temperature variation of 2 °C can correspond to a propene concentration of 1000 ppm [1, 5]. Therefore, a precise temperature control is of great importance for these sensors, as temperature fluctuations can lead to erroneous measurement signals [1-3]. For this reason, the cooling effect of water (H_2O) in the gas atmosphere plays a significant role.

Methods and Setup

Typical high-temperature gas sensors are fabricated on ceramic substrates. The dimensions of these sensors are 50.8 mm in length, 6.35 mm in width, and 0.63 mm in height. To maintain the sensors at their operating temperature, a screen-printed platinum heater structure is located on the rear side of the sensor. It enables heating to the desired operating temperature of 600 °C and allows temperature control via a four-wire resistance measurement and subsequent heater control. On the front side, thermocouples made of gold (Au) and platinum (Pt) conductors are printed, providing five thermocouple junctions (see Fig. 1). These measurement points are positioned in a way that they represent the temperature distribution in a region relevant to gas sensing. The temperature at the measurement points can be calculated from the measured thermoelectric voltage using the Seebeck coefficient for Pt/Au [2].

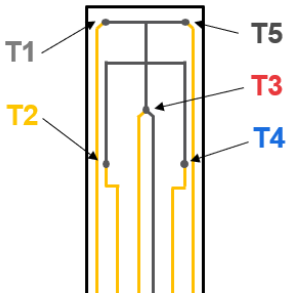

Fig. 1: Schematic representation of a sensor with five thermocouple junctions

Results and Discussion

To investigate the influence of water on the temperature homogeneity of the sensor substrate, the sensor was mounted horizontally (with the thermocouple junctions facing upwards) in an exhaust gas pipe. At a constant total flow rate, the H_2O-content was increased from 0 to 10 vol.% in steps of 2.5 % and subsequently decreased again. The base gas consists of 10 % oxygen (O_2) in nitrogen (N_2). Fig. 2 a) shows the measured temperatures (T1–T5, corresponding to the thermocouple junctions shown in Fig. 1) on the front side of the sensor, the dosing of the water content (see Fig. 2 b).

The heater was operated at a constant voltage, resulting in a temperature of 600 °C at the central temperature measurement point T3 under exposure to the base gas (see red curve in Fig. 2 within the first 300 s).

When examining the temperature measurements, it is immediately apparent that the temperature at all measurement points decreases significantly with increasing water content. The temperature at the central measurement point (T3) decreases by 5 °C when the water content is increased from 0 to 10 %. While the temperatures at the sensor tip (T1 and T5) show a stronger cooling of 7 °C, the temperature decrease at the more inward measurement points T2 and T4 is lowest, amounting to 4 °C.

In addition, the cooling behavior reveals that the lateral temperature decrease at the left edge of the sensor (T1 and T2) is comparable to that at the right edge (T4 and T5). This behavior is expected, as the water content changes uniformly within the surrounding gas. Furthermore, the diagram shows a uniform cooling behavior both during an increase and a decrease in water content, indicating a linear relationship between cooling and water concentration.

It can also be observed that the absolute temperature on the left side of the sensor (T1 and T2) is higher than the corresponding values on the right side (T5 and T4). Possible reasons for this include a slightly tilted installation of the sensor relative to the horizontal orientation. Another potential cause could be a slightly off-centered, asymmetric printed heater structure on the rear side of the sensor.

Despite these inaccuracies, the cooling effect of water on the sensor temperature is clearly evident.

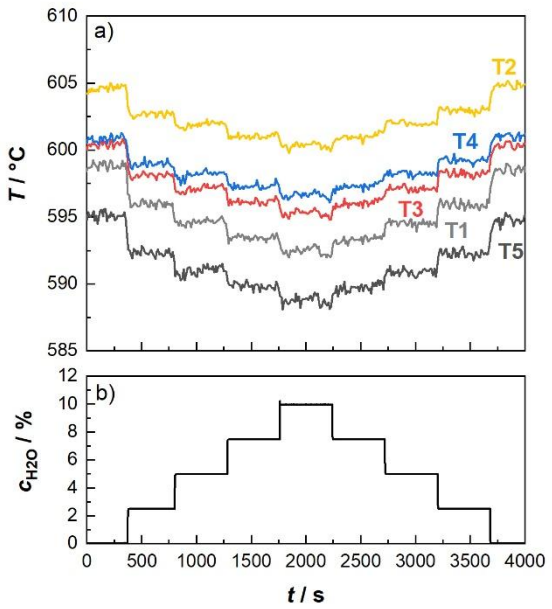

Fig. 2: a) Measurement of the temperature at five thermocouple junctions, b) concentration of H_2O

Conclusion and Outlook

The results show that increasing water content in the exhaust gas causes a clear and nearly linear cooling of the sensor, affecting all measurement points. Temperature reductions of several degrees Celsius, especially at the sensor tip, are critical for thermoelectric hydrocarbon sensors due to their high temperature sensitivity. Consequently, water-induced cooling effects must be considered in sensor operation and calibration to ensure reliable measurements under realistic exhaust gas conditions.

In further steps, the cooling influence of the water content will be investigated for a heater operated under constant temperature control. Here, the heating power of the platinum heater applied to the tip of the rear side, can serve as an additional signal to correct the sensor signal with respect to the cooling effect of water. It has to be considered that an increasing heater power might lead to additional individual temperature inhomogeneities due to installation or production anomalies.

References

[1] G. Hagen, J. Herrmann, X. Zhang, H. Kohler, I. Hartmann, R. Moos, Application of a Robust Thermoelectric Gas Sensor in Firewood Combustion Exhausts, *Sensors* 23 (6), (2023), DOI: 10.3390/s23062930

[2] T. Wöhrl, J. Herrmann, J. Kita, R. Moos, G. Hagen, Methods to investigate the temperature distribution of heated ceramic gas sensors for high-temperature applications, *Journal of Sensors and Sensor Systems* 12 (2), 205–214 (2023), DOI: 10.5194/jsss-12-205-2023

[3] G. Hagen, A. Harsch, R. Moos, A pathway to eliminate the gas flow dependency of a hydrocarbon sensor for automotive exhaust applications, *Journal of Sensors and Sensor Systems* 7 (1), 79–84 (2018), DOI: 10.5194/jsss-7-79-2018

[4] T.V. Johnson, Review of diesel emissions and control, *International Journal of Engine Research* 10 (5), 275–285 (2009), DOI: 10.1243/14680874JER04009

[5] S. Wiegärtner, G. Hagen, J. Kita, W. Reitmeier, M. Hien, P. Grasse, R. Moos, Thermoelectric hydrocarbon sensor in thick-film technology for on-board-diagnostics of a diesel oxidation catalyst, *Sensors and Actuators B: Chemical* 214, 234-240 (2015), DOI:10.1016/j.snb.2015.02.083

DOI 10.5162/eurosensors2026/Mo–SFM–04

Revealing and Modeling Frequency-Dependent Field Redistribution for Calibration-Free Wideband Four-Electrode Impedance Spectroscopy

Lihong Pan[12], Ding Han[1], Yongyao Niu[1], Jiahe Zheng[1], Junbo Wang[12], Jian Chen[12]*, Xiaoye Huo[1]**

[1] State Key Laboratory of Transducer Technology, Aerospace Information Research Institute, Chinese Academy of Sciences, Beijing 100190, People's Republic of China.

[2] School of Advanced Interdisciplinary Sciences, University of Chinese Academy of Sciences, Beijing 100049, People's Republic of China.

Xiaoye Huo[1]: huoxy@aircas.ac.cn*

Summary:

Wideband impedance spectroscopy of conductive liquids is fundamentally limited by frequency-dependent distortion that cannot be removed by conventional calibration. This work shows, for the first time, that such distortion originates from redistribution of internal electric fields and current paths induced by loading of the measurement system, rather than a simple additive error. A system-aware field–circuit coupled framework is proposed that enables calibration-free extraction of intrinsic electrical properties and accurate fitting of impedance spectra from 10 kHz to 10 MHz, outperforming conventional models.

Keywords: Wideband impedance spectroscopy, Four-electrode configuration, Field–circuit coupling, Field redistribution, Calibration-free measurement

Background

Wideband impedance spectroscopy is widely used for electrical characterization of conductive liquids [1]. Although four-electrode configurations suppress electrode polarization at low frequencies, significant distortion appears at higher frequencies and cannot be removed by conventional calibration methods [2]. This indicates that the error is not purely additive. In fact, frequency-dependent loading of the measurement system, alters boundary conditions and redistributes internal electric fields and current paths within the liquid. As a result, the effective impedance becomes strongly frequency-dependent, making accurate extraction of intrinsic properties challenging.

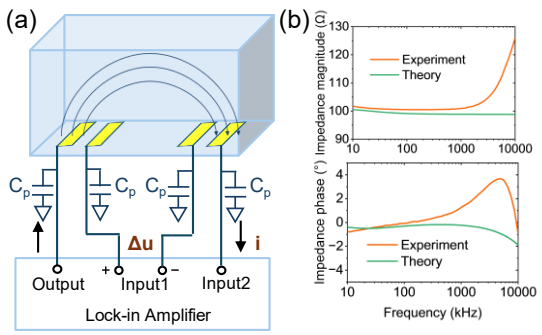

Fig. 1. (a) Schematic of Four-electrode impedance measurement setup. A lock-in amplifier (HF2LI, Zurich, CH) excites and measures the voltage and current through coaxial cables with parasitic capacitance. (b) Representative experimental impedance spectra showing frequency-dependent distortion under wideband conditions.

Description of the System

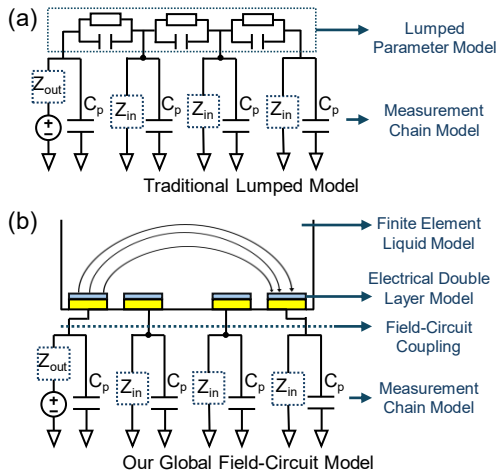

Fig. 2. (a) Conventional lumped-parameter model, neglecting the interaction between the measurement system and the internal field distribution. (b) Proposed system-aware field–circuit coupled model integrating the liquid domain with the measurement chain.

Conventional lumped or liquid-only models fail to capture the interaction between the measurement system and the internal field distribution. A system-aware field–circuit coupled framework is developed, where the liquid is modeled by finite

elements and the measurement chain is described by its equivalent circuit including instrument impedance and parasitic. These components are coupled through electrical ports to jointly solve the frequency-dependent response. By fitting measured spectra with forward simulations, intrinsic electrical properties can be extracted without reference-based calibration.

Results

The proposed method achieves accurate fit-ting of impedance spectra from 10 kHz to 10 MHz and significantly outperforms conventional models (Fig. 3). The results show that internal electric field distribution and current paths vary with frequency, even under fixed electrode and fixture conditions, confirming that high-frequency distortion arises from frequency-dependent field redistribution rather than a fixed additive error. The liquid-only finite-element model cannot explain the distortion, whereas the field–circuit coupled method can capture this process and explains several seemingly unintuitive results in wideband four-electrode liquid impedance measurement (Fig. 4). Consistent fitting across solutions with different conductivities further demonstrates the capability of calibration-free wideband characterization (Fig. 5).

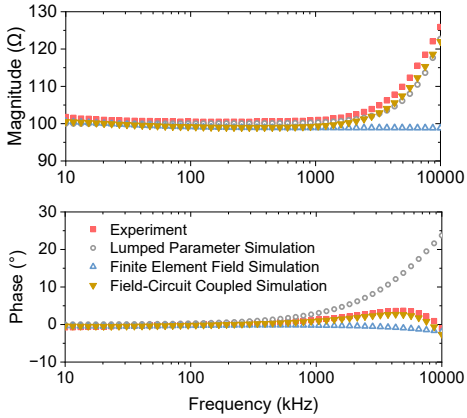

Fig. 3. Comparison of measured and fitted impedance magnitude and phase for PBS solution using different models.

This work reveals the physical origin of high-frequency distortion in wideband four-electrode impedance measurement and establishes a unified modeling framework that explicitly ac-counts for the measurement system. By trans-forming the problem from empirical calibration to physics-based forward modeling, the proposed approach enables accurate and calibration-free extraction of intrinsic electrical properties over a wide frequency range, providing a new foundation for high-frequency impedance sensing in biological and microfluidic applications.

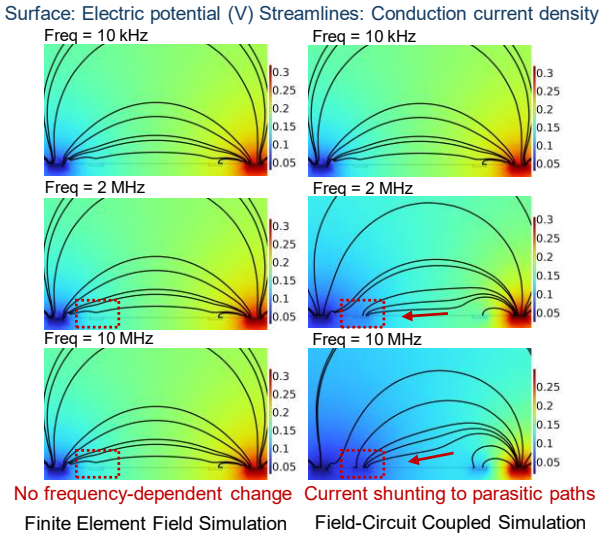

Fig. 4. Simulated evolution of the internal field distribution in the liquid under wideband conditions, illustrating frequency-dependent redistribution of current paths under realistic measurement conditions.

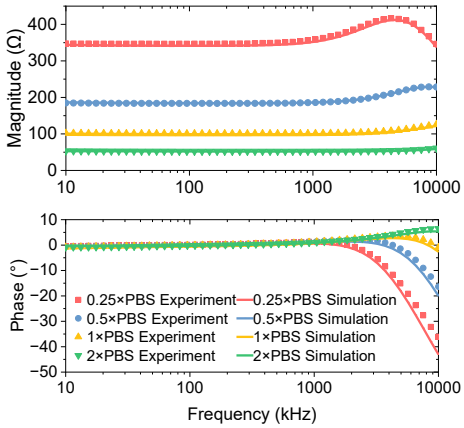

Fig. 5. Comparison between measured and field–circuit coupled simulated impedance magnitude and phase for solutions with different conductivities, showing consistent wideband fitting without calibration.

References

[1] H. Li, Y. Fu, Impedance Cell Sensing Technology From Single-Frequency to Multifrequency: A Review, IEEE Sensors Journal 24, 4150-4160 (2024); doi: 10.1109/JSEN.2023.3347539.

[2] B. A. Mazzeo, A. J. Flewitt, Two- and Four-Electrode, Wide-Bandwidth, Dielectric Spectrometer for Conductive Liquids: Theory, Limitations, and Experiment, Journal of Applied Physics 102, 104106 (2007); doi: 10.1063/1.2815666

Acknowledgements

Natural Science Foundation of Beijing: 4254075
National Natural Science Foundation of China：62501573

DOI 10.5162/eurosensors2026/Tu–SFM–01

Precision in Gas Sensing: A Quantitative and Qualitative Analysis of Comparative Bias in Reported Metrics

Pedro P. Ortega[1], Sandro Gherardi[2,3], Michele Astolfi[2,3], Miguel A. Ponce[4], Cesare Malagù[2,3], Elson Longo[1]
[1] Federal University of São Carlos (UFSCar), 13565-905, São Carlos, Brazil,
[2] SCENT S.r.l. - Via Quadrifoglio 11, - 44124 Ferrara, Italy
[3] University of Ferrara (UNIFE), Via Saragat 1, 44122, Ferrara, Italy
[4] Physics and Engineering Research Center CIFICEN (UNCPBA-CICPBA-CONICET), B7000GHG, Tandil, Argentina.
pedro.ortega@ufscar.br

Summary:
Gas-sensing performance is commonly assessed through metrics such as sensitivity and response time, often compared across studies without considering experimental variability. Here, we demonstrate that experimental variables significantly influence these metrics. By systematically isolating these parameters, we show that apparent performance differences may arise from measurement artifacts rather than intrinsic material properties. These findings highlight a critical limitation in cross-study comparisons and emphasize the need for standardized reporting and experimental transparency in gas-sensing research.

Keywords: gas sensors, reproducibility, chamber dynamics, flow rate, pre-conditioning

Background, Motivation and Objective

Gas-sensing research relies strongly on performance indicators such as sensitivity, response time, and recovery time to evaluate and compare sensing materials [1]. However, these comparisons typically assume equivalent experimental conditions across different studies. In practice, variations in chamber design, gas delivery systems, and sensor conditioning protocols introduce uncontrolled variables that may significantly bias reported results [2]. Although the influence of these parameters is acknowledged within the community, they are often not explicitly accounted for in comparative analyses, leading to quantitative comparisons that may overlook the qualitative differences among experimental setups. In this sense, this study aims to quantify how chamber volume, flow rate, and pre-conditioning influence the measured sensing performance, highlighting the risk of comparing data from non-equivalent systems.

Description of the New Method or System

A modular gas-sensing chamber with adjustable volume was developed to allow a controlled variation of the parameters under investigation to minimize the influence of other variables. The stackable ring architecture of the chamber allowed changing the chamber volume (550 and 860 cm^3) while maintaining identical sensor positioning and electronic interfaces. Different flow rates (100–1000 sccm) were also used, and their influence in response and time parameters were investigated. Sensor temperature and gas-flow were varied pre-measurement to assess their impact on subsequent transient responses. A first-order mass transport model was employed to describe gas concentration dynamics and correlate them with experimentally observed sensing responses.

Results

The experiments were conducted on two different sensors, based on ZnO (S1) and STN (S2), operating at their optimal operating temperature. The sensors' response profile showed a significant change when the chamber volume increased from 550 cm^3 (V_1) to 860 cm^3 (V_2) (see Fig. 1). For a 20 ppm CO exposure at 500 sccm, the response magnitude varied up to ~50% in the larger volume. The volume increase was more critical to the time parameters. The response and recovery times increased by about 75% and 85%, respectively. These variations were attributed to the increased dilution time of the target gas, which delayed the attainment of the steady-state concentration.

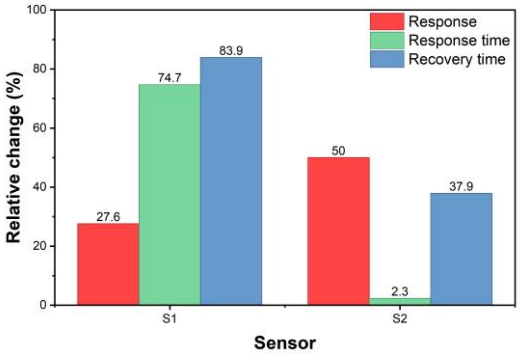

Fig. 1. Relative change of response, response time, and recovery time to 20 ppm of CO when increasing the volume of the chamber from 550 cm³ to 860 cm³.

By varying the flow rate from 100 to 1000 sccm, we observed that the kinetics of the sensing process are dominated by the gas delivery system rather than the adsorption/desorption rates associated with the sensing material. At 100 sccm, the response takes a long time to achieve the steady-state (22 min and 19.8 min for S1 and S2, respectively), while at 1000 sccm, the same sensors present response times of 1 min (S1) and 3.6 min (S2, see Fig. 2). Interestingly, the response magnitude was not significantly influenced by the flow-rate, indicating that the steady-state response is intrinsic to the sensing material.

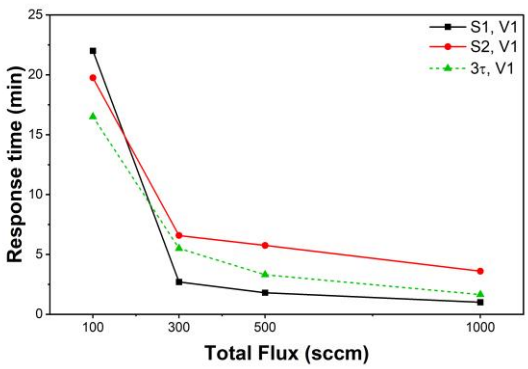

Fig. 2. Variation of response times to 20 ppm of carbon monoxide for different applied flow rates and comparison with the theoretical 3τ curve (95% chamber filling of V1; green dashed line).

Finally, another influencing factor in performance indicators is the sensing history of the sensors. After being exposed to a flow-rate higher than that used during the sensing experiments (1000 and 500 sccm, respectively), S2 exhibited an increased response to CO, whereas no changes were observed for S1. These results indicate that applying a high flow-rate promotes the regeneration of active surface sites and baseline recovery. The fact that S2 remained unchanged may instead be attributed to its higher operating temperature, which already induces a continuous desorption of surface adsorbates and surface regeneration. Thermal pre-conditioning at 500°C was found to induce increased transient responses that lasted for several measuring cycles (see Fig. 3). Initial exposures following high-temperature cleaning showed response magnitudes up to 30% higher than the stabilized baseline. These effects may be less apparent in single-cycle measurements and can therefore be easily overlooked, as the full transition to steady-state operation is not always captured.

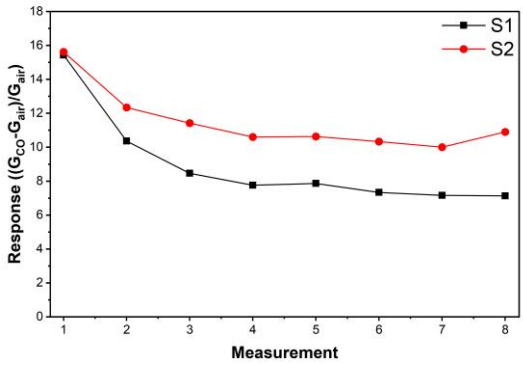

Fig. 3. Stability of the sensors over consecutive sensing measurements after being heated at 500°C for 10 min.

Conclusions

Experiments using two chemoresistive sensors exposed to carbon monoxide (20 ppm) reveal that chamber volume alone can alter response magnitude by up to 50%, and response/recovery times by ~75% and ~85%, respectively. Flow rate strongly influenced time metrics, with response times varying from ~1 min to ~20 min, in agreement with theoretical predictions. Additionally, both flow-induced and thermal pre-conditioning significantly altered sensor responses. These results demonstrate that commonly reported sensing metrics are highly sensitive to experimental conditions, which should be disclosed in detail in sensing studies.

Acknowledgements

This work was founded by the São Paulo Research Foundation (FAPESP), Grant Number #2024/08759-0, #2023/07486-8, and #2013/07296-2.

References

[1] L. Parellada-Monreal, G.G. Mandayo, A. Martín-Mayor, I Souto-Canteli, M.M. Bou-Ali, Influence of the test-chamber shape on the performance of conductometric gas sensors, *Sensors and Actuators B: Chemical* 361, 131694 (2022); doi: 10.1016/J.SNB.2022.131694

[2] W. Zhang, Y. Xian, B. Cheng, R. Han, Y. Zhang, J. Xiang, Fe_2TiO_5 nanoparticle-based novel gas sensor with high response to ethanol and acetone, *Ceramics International* 50, 34027–34036 (2024). doi: 10.1016/J.CERAMINT.2024.06.222.

DOI 10.5162/eurosensors2026/Tu–SFM–02

PMUT and CMUT array – design, technology and experimental validation

Rahul Nagaraja[2], Alexey Shaporin[1], Akshay Rameshbhai Dudhat[1], Shubham Mulay[1], Chris Stöckel, Andrew Tweedie[2], Alexandre Halbach[2]
[1] Fraunhofer ENAS, Technologie Campus, 3, 09126, Chemnitz, Germany
[2] Quanscient Oy, Peltokatu 34 B, 33100 Tampere, Finland
rahul.nagaraja@quanscient.com

Summary:

This work focuses on the design and analysis of piezoelectric micromachined ultrasonic transducers (PMUTs) and capacitive micromachined ultrasonic transducers (CMUTs). Both device types are designed and simulated using finite element methods (FEM). In addition, fabricated microsystems are experimentally characterized to compare design target specifications with measured results.

Keywords: PMUTs, CMUTs, FEM simulations, experimental validation

Motivation

In this work, we simulate and systematically validate the technical performance of PMUTs and CMUTs. Owing to a complete in-house MEMS development chain at Fraunhofer ENAS, including design, fabrication, and characterization - experimental data from fabricated arrays are available for design validation. Accordingly, this study has two main objectives. First, to investigate the sensitivity of key design parameters (e.g., film thickness and membrane geometry) on device performance. Second, to compare different modeling approaches with experimental data, identifying discrepancies and their underlying causes.

PMUT

MEMS PMUTs [1–3] are used for portable medical imaging, haptic feedback, non-destructive testing, and microfluidic sensing. PMUT chip cross-section as well as fabricated at FhI ENAS PMUT array is shown in Fig. 1.

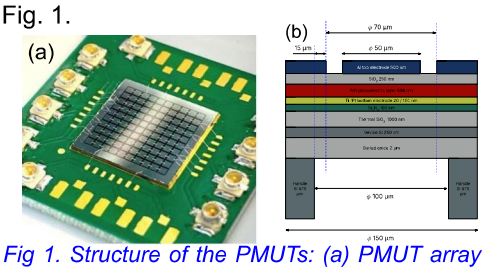

Fig 1. Structure of the PMUTs: (a) PMUT array on a PCB - fabricated at FhI ENAS; (b) Cross-section of a representative PMUT cell.

Finite element (FE) simulations are performed using Quanscient's Allsolve multiphysics platform [8-9], leveraging the domain decomposition method to facilitate the parallelization of large-scale array simulations. Figure 2a-2b shows a PMUT quarter cell modelled in Allsolve and the resonance response in air is plotted in Figure. 3.

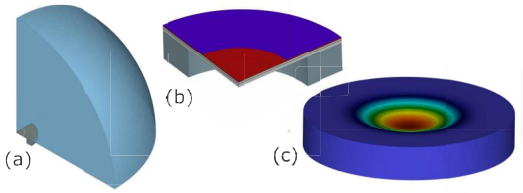

Fig 2. a) A quarter PMUT unit cell with acoustic domain. b) Voltage drive applied on the outer ring of the piezo. c) Membrane deflection (first mode)

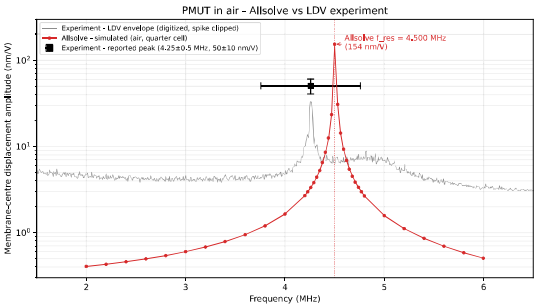

Fig 3. Frequency response of the PMUT cell in air.

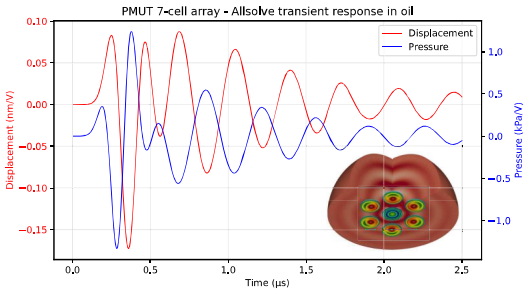

Fig 4. Transient response of 7-cell hex PMUT array.

CMUT

Capacitive micromachined ultrasonic transducers (CMUTs) are widely recognized as key enabling devices for next-generation ultrasonic systems, particularly in medical imaging, non-destructive evaluation, and immersion-based sensing applications [3-6]. Due to their flexural membrane operation, CMUTs exhibit low mechanical impedance and efficient acoustic coupling to liquids, making them well suited for broadband ultrasonic transmission and reception.

The CMUT structure [3-7] consists of a composite membrane suspended over a vacuum gap, forming a variable capacitor between the top membrane electrode and the bottom fixed electrode. The electrostatic gap is defined by sacrificial-layer processing and sealed to form a cavity (see Fig. 4).

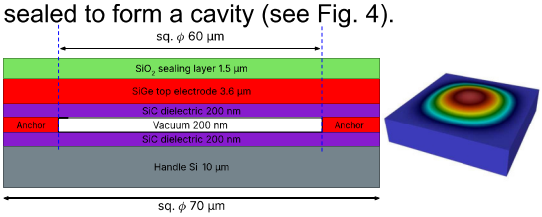

Fig. 5. a) Cross section layer stacks of CMUT [7]. b) Membrane deflection (first mode)

The same model is implemented in Quanscient Allsolve, with its response shown in Fig. 6-7; experimental mechanical and acoustic characterization enables comparison of resonance frequency, quality factor, and transient response.

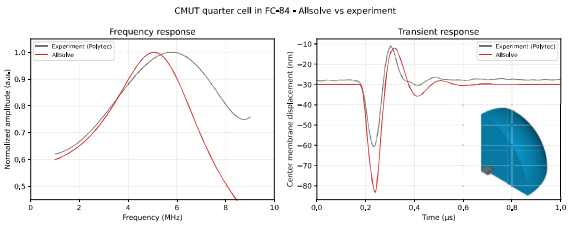

Figure 6. Frequency and transient response of the quarter cell CMUT [7]. Drive voltage: V_{DC} = -160V, V_{pulse} = -60V.

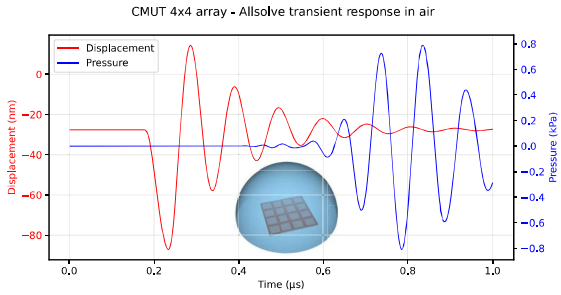

Figure 7. Transient response of a CMUT 4x4 array. Drive voltage: V_{DC} = -160V, V_{pulse} = -60V.

Conclusion

The presented work demonstrates an experimentally validated methodology for the design and simulation of PMUT and CMUT devices. The study compares results from different simulation software and with experimental data.

References

[1] C. Stoeckel et al., "Design and technology for uniform aluminum nitride piezoelectric micromachined ultrasonic transducers with radial array," 2021 Smart Systems Integration (SSI), Grenoble, France, 2021, pp. 1-4, doi: 10.1109/SSI52265.2021.9467017.

[2] E. Moisello, L. Novaresi, E. Sarkar, P. Malcovati, T. L. Costa and E. Bonizzoni, "PMUT and CMUT Devices for Biomedical Applications: A Review," in IEEE Access, vol. 12, pp. 18640-18657, 2024, DOI: 10.1109/ACCESS.2024.3359906.

[3] Subbiah, Nilavazhagan et al. “Modeling and Simulation of Cmut and Pmut Ultrasound Transducers and Package Using a Multiphysics Approach.” 2025 26th International Conference on Thermal, Mechanical and Multi-Physics Simulation and Experiments in Microelectronics and Microsystems (EuroSimE) (2025): 1-7., DOI: 10.1109/EuroSimE65125.2025.11006581

[4] Vishwanatha M., Kraljevski I., Alkhasli I., Saeidi N., Selvam K., Wiemer M., Kuhn H.; Investigating Performance Enhancements of CMUT Based Flow Measurement Using Regression Techniques; (2025) Proceedings of IEEE Sensors, DOI: 10.1109/SENSORS59705.2025.11331011

[5] Saeidi N., Selvam K.F.R.G.M., De Souza Tortato F., Satwara M., Wiemer M.; Characterization of Capacitive Micromachined Ultrasound Transducer (CMUT) for Targeted Applications in Harsh Environments; (2021) Proceedings of the IEEE International Conference on Micro Electro Mechanical Systems (MEMS), 2021-January, pp. 903 – 906; DOI: 10.1109/MEMS51782.2021.9375331

[6] S. P. Mao, X. Rottenberg, V. Rochus, B. Nauwelaers and H. A. C. Tilmans, "FEM simulation and measurement validation of a cMUT cell," 2014 15th International Conference on Thermal, Mechanical and Multiphysics Simulation and Experiments in Microelectronics and Microsystems (EuroSimE), Ghent, Belgium, 2014, pp. 1-7, DOI: 10.1109/EuroSimE.2014.6813847.

[7] https://quanscient.com/allsolve, retrieved on 29.08.2026

DOI 10.5162/eurosensors2026/Tu–SFM–03

A Metasurface Acoustic Fabry-Perot Interferometer for Ultrasonic Passive Strain Sensing

Sira Bielefeldt[1], Roman Furrer[2], Christofer Hierold[1], Mathieu Luisier[1], Cosmin Roman[1]
[1] ETH Zurich, Rämistrasse 101, 8092 Zürich, Schweiz
[2] EMPA, Überlandstrasse 129, 8600 Dübendorf, Schweiz
croman@ethz.ch

Summary:
We propose a passive strain sensor concept based on a Fabry-Perot interferometer. Its two partially transmitting acoustic mirrors consist of air-channel metasurfaces embedded in PDMS. Finite element simulations are used to design the sensor and its acoustic spectral response for 5 MHz ultrasound interrogation. This sensor exhibits an average reflectance 2.9× (9.3 dB) higher compared to a PDMS monolayer, and a gauge factor of 0.48. Further simulations of lateral channel misalignment and non-circular channel cross-sections confirm the robustness of the design to fabrication variations.

Keywords: acoustic metasurfaces, passive implantable sensors, Fabry-Perot interferometer

Background, Motivation and Objective

Acoustic metamaterials have recently been explored as passive implantable sensors. Resonances or bandgap effects encode changes in pressure [1], temperature [2], or deformation [3] into a measurable acoustic spectral response. In this work, we propose an acoustic metamaterial sensor based on a Fabry-Perot interferometer, referred to as m-AFP. The device is made of two metasurfaces implemented as patterned air-channels in Polydimethylsiloxane (PDMS; Fig. 1). These act as the partially transmitting acoustic mirrors of the FP interferometer.

Here, we investigate numerically the acoustic strain sensitivity of m-AFPs as well as their robustness to fabrication variations.

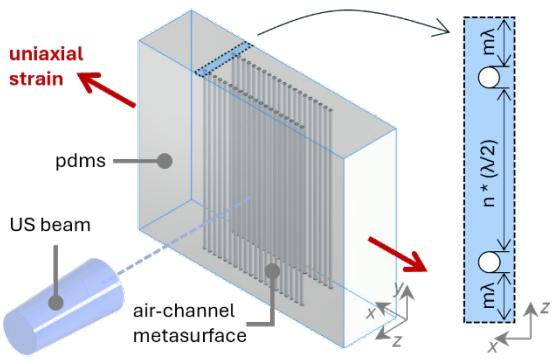

Fig. 1: ***Device concept.*** *An m-AFP interferometer with air-channel metasurface mirrors. The device is strained along the x-direction and interrogated by an ultrasound probe (US beam) in the z-direction.*

Description of the New Method or System

The channels are oriented along the y-direction and have a length of 3 mm, a diameter of 50 µm, and a lateral lattice constant a of 100 µm. The two metasurfaces are separated by $n\lambda/2$, while the PDMS cover layers extend over $m\lambda$ on both sides, λ being the sound wavelength inside PDMS at the design frequency of 5 MHz.

The acoustic spectral response of the undeformed structure was simulated in a 2D unit-cell using the pressure acoustics module of COMSOL Multiphysics. The model consists of two air inclusions in PDMS with water domains, and a perfectly matched layer above and below (Fig. 2, left). PDMS material parameters were $E = 4.5\,\mathrm{MPa}$, $\nu = 0.495$, $\rho = 1030\,\mathrm{kg/m^3}$, $c = 1030\,\mathrm{m/s}$. Water parameters were taken from the material library, and air was treated as a non-computational domain.

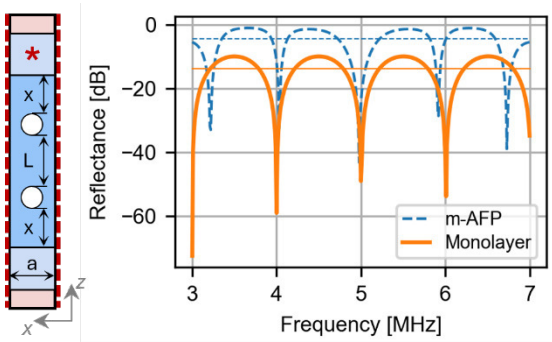

Fig. 2: ***Acoustic spectral response.*** *Schematic of the m-AFP 2D unit-cell (left) and simulated reflectance spectra and average reflectance of the m-AFP compared to a PDMS monolayer of thickness L in the undeformed state (right), with x = 206 µm, L = 515 µm.*

Periodic boundary conditions were applied in the x-direction. The reflectance spectrum was calculated at the point marked with ★ in Fig. 2, by subtracting dB values of the background pressure from the backscattered pressure.

Compared to a PDMS monolayer with a thickness equal to the metasurface spacing *L*, the m-AFP shows the same main resonances at 4, 5, and 6 MHz. However, the m-AFP exhibits a substantially higher average reflectance: -4.3 dB (m-AFP) vs. -13.6 dB (monolayer) (Fig. 2, horizontal lines). This increased average reflectance (2.9×) is a major advantage of the m-AFP, making the sensor easier to localize and increasing the signal-to-noise ratio in real world conditions.

Results

To evaluate strain sensitivity, a 3D solid-mechanics unit-cell model of the device was first simulated. Strain was applied in the x-direction, and the resulting deformation was mapped from the mid-plane of the 3D model onto a 2D geometry for acoustic simulation.

As shown in Fig. 3, tensile strain shifts the reflectance spectrum toward higher frequencies. From f_0 = 4.98 MHz in the undeformed state to 5.1 and 5.22 MHz for 5% and 10% strain, respectively. This corresponds to an absolute sensitivity of approximately 24 kHz/% strain, or a gauge factor $GF = (\Delta f / f_0)/\varepsilon$ of around 0.48 (similar to the monolayer), with an approximately linear scaling with strain in this range.

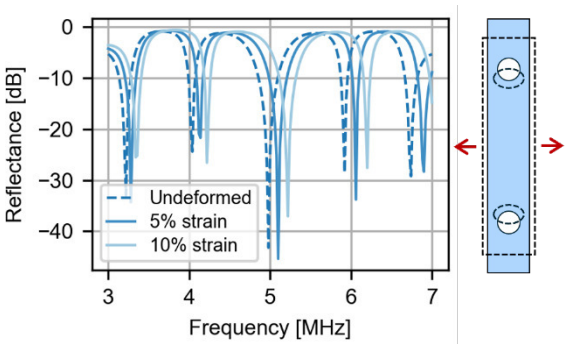

Fig. 3: ***Strain sensitivity of m-AFP.*** *Simulated reflectance spectra of the undeformed structure as well as in the presence of 5% and 10% strain.*

The robustness of the acoustic response to fabrication variations was investigated by varying the relative alignment and the cross-sectional shape of the air channels (Fig. 4). Lateral misalignment between the two metasurfaces had no visible influence on the simulated spectrum for offsets of 25 and 50 µm. Furthermore, changing the channel cross-section from circular to octagonal resulted in a nearly identical response. Square channels showed only minor deviations above 6.5 MHz, while the main resonances at 4, 5, and 6 MHz were preserved.

These results indicate that the proposed m-AFP is robust to relevant geometric variations. This is beneficial for future fabrication, as it allows different manufacturing approaches, e.g., molding from microSLA- or two-photon-polymerized masters, or soft lithography using SU-8 molds and subsequent PDMS bonding.

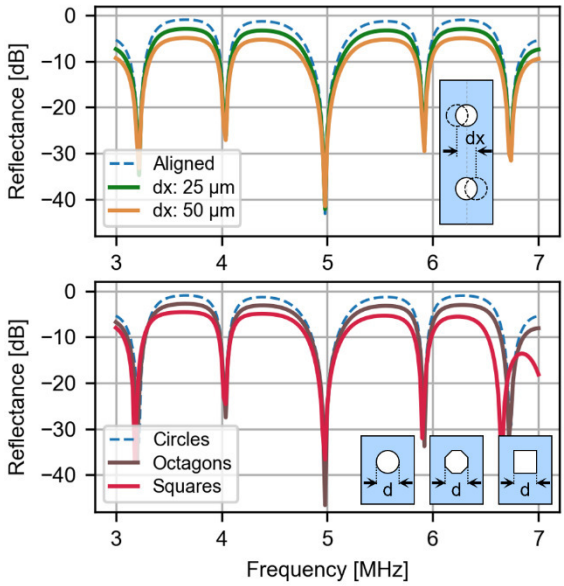

Fig. 4: ***Robustness to fabrication variations.*** *Influence of lateral channel misalignment (top) and channel shape (bottom) on the reflectance spectrum. Curves shifted by -3 and -6 dB for better visualization.*

Conclusion

We proposed a metasurface Fabry-Perot interferometer strain sensor concept. Device simulations show a high reflectance and a strain-dependent frequency shift, with an estimated gauge factor of 0.48 around the 5 MHz resonance. The response remains robust against lateral channel misalignment and moderate changes in channel shape. The proposed design combines a relatively simple two-layer geometry with passive ultrasonic readout for soft implantable strain sensors. Future work will focus on fabrication and experimental validation of the simulated response.

References

[1] H. Tang et al., Injectable ultrasonic sensor for wireless monitoring of intracranial signals, *Nature* 630, 84-90 (2024); doi: 10.1038/s41586-024-07334-y

[2] L. Maini et al., An in vitro demonstration of a passive, acoustic metamaterial as a temperature sensor with mK resolution for implantable applications, *Micro- & Nanosystems* 10, 8 (2024); doi: 10.1038/s41378-023-00632-x

[3] Y. Tian et al., An implantable hydrogel-based phononic crystal for continuous and wireless monitoring of internal tissue strains, *Nat. Biomed. Eng* 9, 1335-1348 (2025); doi: 10.1038/s41551-025-01374-z

DOI 10.5162/eurosensors2026/Tu–SFM–04

Fast Tactile Sensor Array Normalization of an Artificial Silicone Fingertip Using a Pressure Chamber

Katja Meier[1], Florin Püntener[1], Sira Bielefeldt[1], Christofer Hierold[1], Cosmin Roman[1]
[1]Micro and Nanosystems, Dept. of Mechanical and Process Engineering, ETH Zürich, Switzerland
croman@ethz.ch

Summary: We present an approach for normalizing the output of tactile sensor arrays to reduce taxel-to-taxel variations due to manufacturing. The method is applied to a soft, artificial fingertip containing 144 integrated capacitive taxels. A pressure chamber applies uniform forces, to all taxels, simultaneously. Two normalization methods are proposed and compared: one based on the maximum taxel capacitance change and another based on a fitted sigmoid function. Both methods reduce taxel spread (coeff. of variation from 0.41 down to 0.23 and 0.085 respectively), improving tactile image uniformity.

Keywords: Normalization/calibration, tactile sensor array, pressure chamber, sensor linearization.

Background

Soft artificial fingertips with high spatial resolution are expected to significantly advance dexterous robotic manipulation [3]. Fluctuations during fabrication of these complex devices result in taxel-to-taxel variations. This makes rapid and consistent taxel normalization a critical requirement for practical use in robotic grasping and manipulation. To overcome the limitations of sequential single-taxel characterization, which is slow for high-density arrays, a pressure chamber is introduced to enable simultaneous, spatially uniform loading of all taxels. While pressure chamber-based approaches have been explored in prior work, they often rely on deformable membranes [1] or bladder interfaces [2].

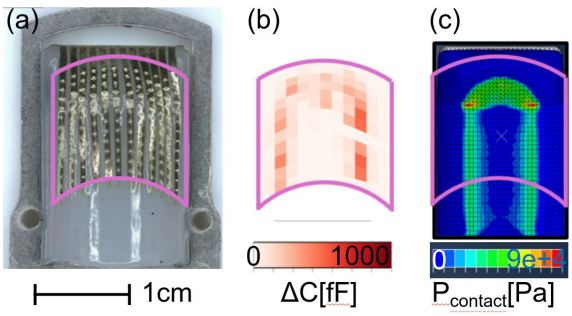

Fig. 1. ***Technology overview****: (a) artificial fingertip with embedded tactile sensing array containing 12x12 tactile sensing units. Sensing area is indicated by pink shape. (b) Tactile image under loading of flat indenter showing ΔC for each taxel. (c) FEM simulation of same load case as in (b) showing contact pressure.*

Description of new Method

Since each capacitive taxel features an air gap fully encapsulated in silicone [3], the fingertip can be characterized using a simple pressure chamber. This avoids using a bladder or membrane that may introduce load inhomogeneities.

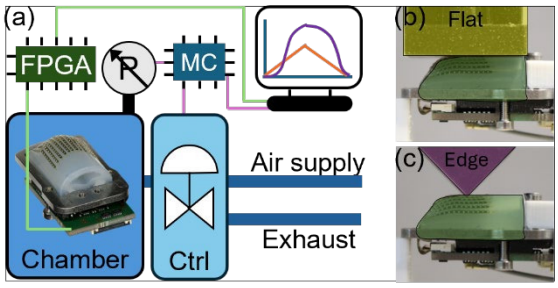

Fig. 2. ***Experimental setup****: (a) schematic representation of setup including pressure chamber, pressure controller (Ctrl), pressure sensor (P), Arduino (MC) and Field Programmable Gate Array (FPGA) to read out artificial fingertip taxel response. (b) Real world load cases where the artificial fingertip is indented with a flat or (c) edged indenter.*

Two taxel array normalization approaches were developed. In the *Maximum Capacitance* normalization (**Max**), the recorded change in capacitance (ΔC) of each taxel is divided by its maximum response at peak pressure (ΔC_{Pmax}), as defined in Eq. (1). The expected taxel outputs are in the range of 0 to 1 and unitless.

$$\Delta C_{norm} = \frac{\Delta C}{\Delta C_{Pmax}} = \frac{\Delta C}{\Delta C(P=3000mbar)} \qquad (1)$$

In the *Inverse Sigmoid Normalization* (**Sig**), the parameters L, k, P_0, α describing a sigmoid function with linear extension, as defined in Eq. (2), were found for each taxel using least squares fitting. Thereafter, Brent's root finding method was applied to predict the input pressure in mbar (P~) from a measured ΔC.

$$\Delta C(P) = \frac{L}{1+\exp(-k(P-P_0))} + \alpha \cdot P \qquad (2)$$

Results and Discussion

Raw sensor responses measured in the pressure chamber exhibit a characteristic "S"-shaped behavior in the ΔC–P curves (Fig. 3a). Taxel variations (average coefficient of variation CV: 0.41) arise from variations in cover layer thickness, taxel orientation, initial membrane gap, and parasitic capacitances. Normalization using **Max** partially compensates for these effects (Fig. 3b, average CV: 0.23), yielding outputs scaled between 0 and 1. However, the response remains strongly nonlinear, with significant variability particularly in the mid-pressure range. While this approach is simple and robust, it does not fully correct taxel-to-taxel variations. In contrast, applying the **Sig** normalization and estimating the pressure at the taxel level results in a substantially more linear response and improved performance across the full pressure range (average CV: 0.085), as shown in Fig. 3c.

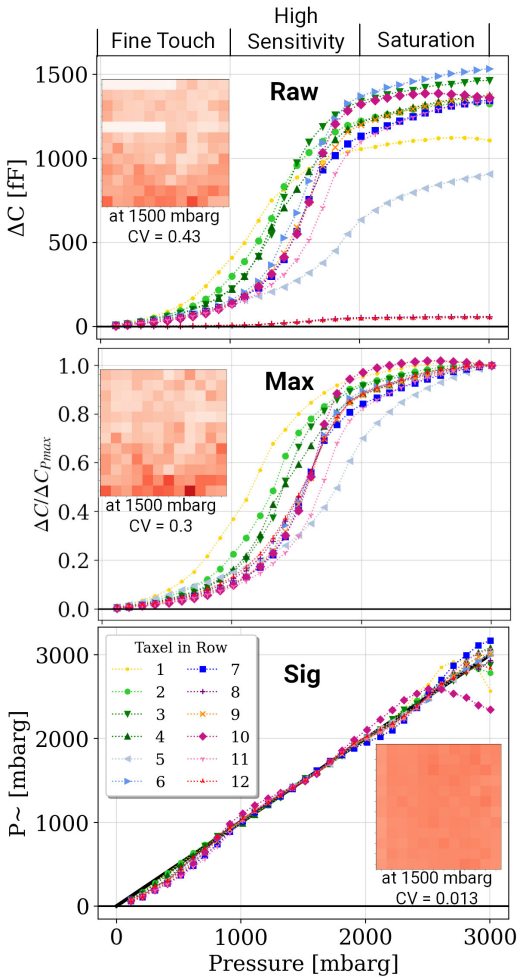

Fig. 3. ***Uniform pressure loading****: (a) Response of 12 taxels showing output variations. (b) Using the* ***Max*** *normalization, the taxel outputs are normalized between 0 and 1. (c) Using the* ***Sig*** *normalization for each taxel response leads to linearization of the output. (Insets) full 12x12 tactile images with CV values.*

The effect of normalization on real finger indentation scenarios is shown in Fig 4 for a flat and an edge rigid indenter. The **Max** normalization resolved the large variation in output intensity and compensated low sensitivity regions, bringing the images closer to simulated contact pressure fields. For the sigmoid fit, this effect was even more pronounced, but also some smearing out was observed due to high sensitivity to non-ideal fitting parameters at very low ΔC and P values. Future work will evaluate the effect of the different normalization procedures on the performance of robotic in-hand object manipulation.

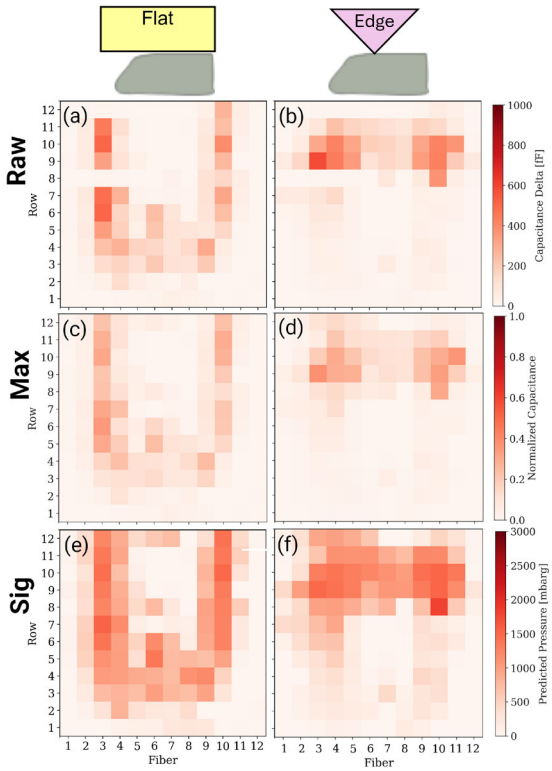

Fig. 4. ***Rigid indenter load cases:*** *Raw capacitance data when pressing on a flat surface (a) and swiping over edge (b). Using* ***Max*** *normalization increased the response of weak taxels, resulting in a more uniform tactile image (c, d). Using* ***Sig*** *normalization, the predicted taxel pressure is further homogenized but also smeared (e, f).*

References

[1] S. Wistreich, et al, DexSkin: High-Coverage Conformable Robotic Skin for Learning Contact-Rich Manipulation, *arXiv preprint* (2025); doi: 10.48550/arXiv.2509.18830

[2] J. Kangro, et al, A Plenum-Based Calibration Device for Tactile Sensor Arrays, *IEEE Robotics and Automation Letters*, (2018); doi: 10.1109/LRA.2018.2857858

[3] Weichart et al, Tactile Sensing with Scalable Capacitive Sensor Arrays on Flexible Substrates, *IEEE Xplore* (2021); doi: 10.1109/JMEMS.2021.3104352

DOI 10.5162/eurosensors2026/Tu–SFM–05

Efficient Prediction of Damping in Acceleration Sensors by Physical Compact Modelling

F. Michael[1], K. Hiller[2], S. Weidlich[2], R. Forke[3], S. Pregl[4], G. Schrag[1]
[1]Technical University of Munich, Munich, Germany
[2]TU Chemnitz, Chemnitz, Germany
[3] Fraunhofer Institute for Electronic Nano Systems ENAS, Chemnitz, Germany
[4] Infineon Technologies AG, Dresden, Germany
friederike.michael@tum.de

Summary:
In this work, we use generalized Kirchhoffian networks (GKNs) composed of physically based compact models to efficiently and accurately predict viscous damping in highly perforated moving micromechanical structures. We introduce compact models for slit-shaped perforations, validated by dedicated test structures, and successfully applied them to an acceleration sensor. Comparison with measurements shows good agreement and prove the feasibility of the approach.

Keywords: compact models, transitional flow, damping ratio, MEMS, simulation

Motivation

Damping phenomena in MEMS are difficult to predict, due to complex fluid–structure interaction and gas rarefaction effects present for small dimensions and low-pressure regimes. Accurate simulations based on finite element methods (FEM) are mostly very costly regarding computational efficiency, especially when it comes to coupling of different energy domains. On the other hand, simplified analytical approaches fail to accurately capture those phenomena. Compact model-based methods have proven to bridge this gap by embedding physically based equations into reduced-order formulations that are compatible with system-level simulators. These are designed to solve standard differential equations in a short period of time, which enables fast and reliable simulation of damping behavior in MEMS.

Compact Modelling of Damping by GKNs

We derived a compact modeling approach based on flux-conserving generalized Kirchhoffian networks (GKNs) [1]. GKNs enhance simulation accuracy by resolving details of the structure in a finite network discretization, thus enabling the spatial resolution of e.g. the pressure distribution underneath a movable membrane or contributions of specific parts to the overall noise of the device [2]. The GKN is assembled modularly from a set of compact models. Those are stored in a dedicated library that contains damping models for basic MEMS perforation structures, usually circular or square holes.

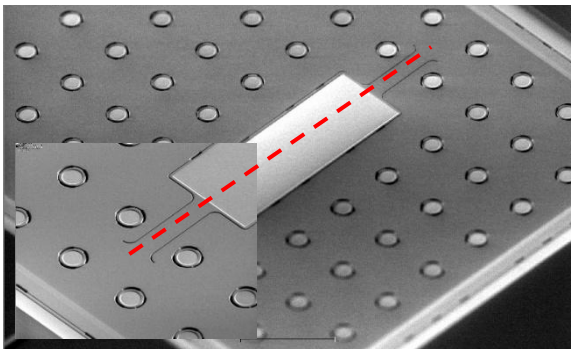

Fig. 1. SEM image of a z-axis accelerometer including a close-up of the perforations. The slits formed in each perforation due to the integrated pillars are clearly visible. The torsion bar is indicated by a red dashed line.

The existing damping models were validated by FEM and measurements for a variety of test structures (cf. sketch in Fig. 2) with different perforation patterns [3]. The models contain correction factors for gas rarefaction and deliver very good results in the range of 1 bar to 1 mbar with an absolute max. error of 10% to 20%.

Compact Model for Slit-shaped Perforations

To cover the impact of regions with high aspect ratio perforations or small slits between the outer edge of the structure and the surrounding material, we derived a new compact model for slit-shaped perforations.

The damping results of the dedicated test structure, whose suspended membrane moves in z-direction like a trampoline generating a piston-like mode shape, displayed in Fig. 2 are in excellent agreement with the simulation from

atmospheric pressure down to the point where the mechanical damping of the device dominates the overall damping behavior at around 2 mbar.

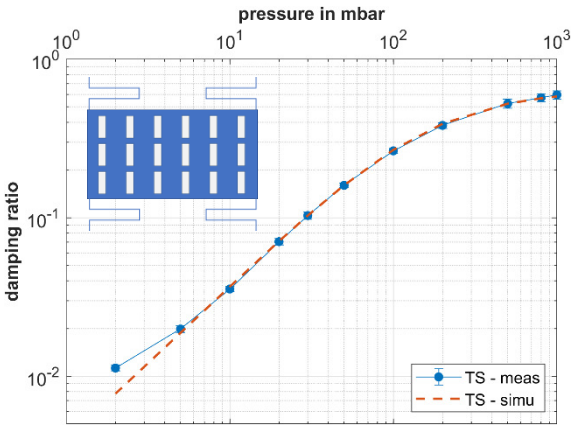

Fig. 2. Damping ratio of test structure with slit-like perforations measured with a laser Doppler vibrometer (LDV) compared with simulation result of respective compact model. A simplified sketch of the test structure is included for explanatory purposes.

Application to Real Sensor

A suitable device to apply the “slit" compact model to is depicted in Fig. 1. The sensor oscillates in z-direction around a torsional spring and has a periodical perforation pattern. Due to the fabrication process each perforation contains a silicon pillar, cf. close-up in Fig. 1. Instead of fully etched holes this creates narrow circular slits for the surrounding gas to flow between the cavity beneath the moving component and the region above it which exerts viscous damping forces. The validated compact model for slit-like perforations is applied to simulate these forces. To preserve the characteristics of the original perforation, the smaller slit dimension and total slit area are kept constant while converting the circular slits into rectangles.

Evaluation of Sensor Results

Fig. 3 shows the measured damping results of the open sensor structure for ambient pressures between 100 mbar and 2 mbar compared with the respective simulation data. Between 20 mbar and 100 mbar the slit model simulation curve is in good agreement with the measured data with an error around 1% - 15% (at the maximum pressure level). At approx. 10 mbar the simulated curve decreases, vastly underestimating the measured damping. One way to explain this behavior is to have a closer look at the Knudsen number (Kn) of the sensor system. Unlike the test structure, which operates at the transitional flow regime for the entire pressure interval, i.e. Kn<10, the sensor enters the molecular flow regime at 10 mbar. At this point the fit parameters used for including gas rarefaction in the compact models are outside their range of validity. Also, the compact model is based on a rectangular slit geometry not a circular one, which could also impact the simulation especially regarding the incoming fluid flow.

The results clearly display the operational limits of the compact models while simultaneously proving their performance within their respective boundaries. Nevertheless, it remains vital make adjustments for higher Knudsen numbers to expand the compact model simulation into the molecular flow regime.

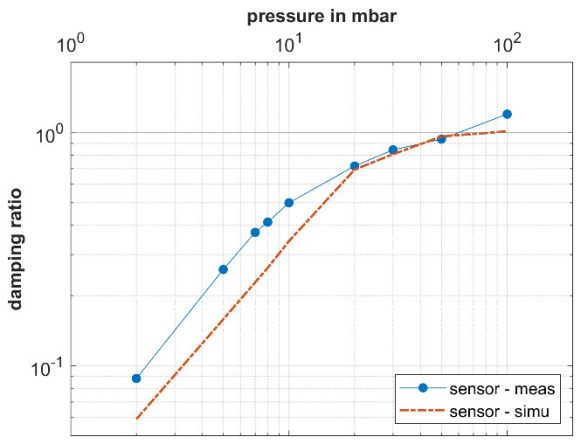

Fig. 3. Damping ratio derived from measurement and simulation of depicted sensor structure for varying surrounding pressures.

Conclusion

We have shown that our approach of implementing compact models in a GKN is highly suitable to give a valid approximation of fluidic damping in the transitional flow regime for standard MEMS devices such as accelerometers. Future investigations will expand into more complex sensor designs. Additionally further research will be done to increase the area of validity of our models into higher Knudsen number areas.

Overall, it becomes clear that by preserving full multi-domain energy coupling, our approach captures the interaction between mechanical motion, fluidic damping, and electrical transduction without sacrificing simulation speed.

References

[1] G. Schrag, G. Wachutka, „System-Level Modeling of MEMS Using Generalized Kirchhoffian Networks – Basic Principles,“ doi:10.1002/9783527647132.ch2.

[2] M. Niessner, G. Schrag, „Mixed-Level Approach for the Modeling of Distributed Effects in Microsystems,“doi:10.1002/9783527647132.ch7.

[3] F. Michael, B. Leikam, G. Schrag, „Reliable Damping Simulation of Highly Perforated Micro-Electro-Mechanical Systems through Physical Compact Modeling,“ doi:10.3390/proceedings2024097176

DOI 10.5162/eurosensors2026/Tu–SFM–06

Engineering Nanopipettes for Probing Neuronal Communication at the Nanoscale

Amelie Viol[1], Morteza Aramesh[1], János Vörös[2]
[1] Laboratory of Single-Molecule and Single-Cell Biophysics, Institute for Biomedical Engineering, ETH Zürich
[2] Laboratory of Biosensors and Bioelectronics, Institute for Biomedical Engineering, ETH Zürich
violam@ethz.ch

Summary:

Nanopipettes offer a geometrically matched interface to the nanoscale structures where neuronal communication occurs, but their use as probes is limited by fundamental physical and chemical constraints. We investigate how the nanopipette–neuron interface, including probe geometry, electrolyte composition, and electrical coupling, determines both access and signal fidelity. Through controlled impalement experiments and systematic variation of recording conditions, we identify key trade-offs that govern successful measurements at this scale.

Keywords: Nanopore, Cell-Cell Communication, Neuroscience

Neuronal communication is governed by ionic and molecular events occurring at spatial scales of tens to hundreds of nanometres, yet most experimental techniques interface with neurons at substantially larger dimensions. This mismatch limits direct access to the subcellular processes that shape signal propagation and synaptic transmission. Nanopipettes offer a geometrically compatible probe for these domains, but their practical use is constrained by the interplay between probe geometry, electrical impedance, and ionic composition at the nanoscale interface.

Axons provide a particularly clear example of this limitation. Rather than acting as passive transmission cables, they are now understood to be active, spatially heterogeneous structures in which local ion channel distributions shape spike generation, propagation dynamics, and synaptic output [1]. However, the sub micrometre diameters of most central axons place them beyond the reach of conventional patch-clamp techniques, leaving the ionic mechanisms underlying their computational role largely inaccessible.

Here, we evaluate the use of glass nanopipettes with submicron tip diameters as probes for neuronal communication. Using controlled membrane impalement experiments, we investigate how nanoscale probe geometry, electrolyte composition, and seal formation influence access and signal fidelity. In this regime, recordings are fundamentally shaped by the electrical properties of the probe, such as high access resistance, stray capacitance, and the small dimensions of the recorded structure impose bandwidth limitations and distort fast voltage signals. Attempts to reduce electrode impedance, for example through high-concentration electrolytes, introduce additional trade-offs by altering ionic gradients and generating junction potentials that can perturb the system under study. As a result, the recorded signal reflects not only the underlying membrane dynamics but also the constraints imposed by the measurement interface and the geometry of the neuronal compartment. In addition, nanopipettes are prone to clogging by membrane fragments or adsorbed biomolecules, leading to progressive changes in resistance and signal quality. We therefore explore surface functionalization and coating strategies to stabilize the pipette interface and improve recording reproducibility.

To systematically explore these constraints, we combine experiments with electrical modelling of the nanopipette–neuron interface. The model (Fig. 1) is used to map how variations in pipette resistance, capacitance, seal quality, and axonal geometry [2] influence the amplitude, shape, and interpretability of recorded signals, thereby defining the parameter space in which meaningful measurements are possible.

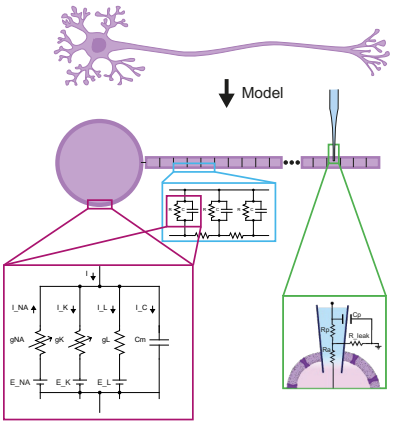

Fig. 1. Electrical model of the pipette-neuron interface.

In parallel, we develop Polydimethylsiloxane (PDMS) microstructures [3] to constrain axonal growth and define accessible geometries for targeted probing. By guiding neuronal connectivity and restricting the spatial location of axons and synapses, these platforms provide a controlled framework for reproducible nanopipette access at subcellular sites. Together, this approach establishes practical design constraints for nanopipette-based sensing and advances the ability to probe neuronal communication at the nanoscale.

References

[1] J. C. Mateus, M. M. Sousa, J. Burrone, and P. Aguiar, “Beyond a Transmission Cable—New Technologies to Reveal the Richness in Axonal Electrophysiology,” The Journal of Neuroscience, vol. 44, no. 11, p. e1446232023, 3 2024. [Online]. Available: http://www.jneurosci.org/content/44/11/e1446232023.abstract

[2] V. J. Oláh, G. Tarcsay, and J. Brunner, “Small size of recorded neuronal structures confines the accuracy in direct axonal voltage measurements,” eNeuro, vol. 8, no. 4, 7 2021.

[3] Duru J, Küchler J, Ihle SJ, Forró C, Bernardi A, Girardin S, Hengsteler J, Wheeler S, Vörös J, Ruff T. Engineered biological neural networks on high density CMOS microelectrode arrays. Frontiers in Neuroscience. Frontiers; 2022. DOI: 10.3389/fnins.2022.829884.

DOI 10.5162/eurosensors2026/Tu–SFM–07

A two-layer Micro-Electrical Impedance Tomography Platform for Three-Dimensional Image Reconstruction using Machine Learning

Chang Liu[1,2], Thomas E. Winkler[1,3], Iordania Constantinou[1,2]**
[1] Institute of Microtechnology (IMT), Technische Universität Braunschweig, Alte Salzdahlumer Straße 203, 38124 Braunschweig, Germany,
[2] Center of Pharmaceutical Engineering (PVZ), Technische Universität Braunschweig, Franz-Liszt-Str. 35a, 38106 Braunschweig, Germany
[3] Department of Micro and Nanosystems (MST), Digital Futures & SciLifeLab, KTH Royal Institute of Technology, Malvinas väg 10, 100 44 Stockholm, Sweden
**Corresponding author e-mail: winklert@kth.se, i.constantinou@tu-braunschweig.de*

Summary:
We present a two-layer micro-electrode system enabling three-dimensional (3D) electrical impedance tomography (EIT) for label-free observation of micro-scale biological samples. The system employs two facing 16-electrode rings with 1 mm diameter and 0.5 mm spacing for high depth sensitivity. A 3D forward model and machine learning-based reconstruction are implemented using simulated datasets. Preliminary simulation results show improved depth discrimination compared to conventional two-dimensional (2D) EIT.

Keywords: Electrical impedance tomography, image reconstruction, 3D imaging, microelectrodes, machine learning

Background, Motivation and Objective

EIT stands out as a cost-effective, non-invasive, and radiation-free imaging technique [1,2,3]. Recently, there have been efforts to push its resolution to the micro-scale for cell biology applications. [4,5,6] We have contributed to this push by developing a glass-based micro-EIT platform to achieve faithful reconstructions of zebrafish eggs and their larval development.[7] This was enabled by a custom convolutional neural network (CNN) reconstruction approach, which we benchmarked against standard methods (one-step Gauss-Newton and total variation).

Despite such advances, key limitations remain. Notably, most existing micro-EIT systems (including our own prior work) rely on planar electrode configurations and 2D reconstruction, which limits depth resolution and introduces ambiguity in volumetric interpretation. Extension to 3D remains a major challenge due to hardware limitations and inverse problem complexity.

This work aims to overcome these challenges by introducing a two-layer electrode architecture and a corresponding 3D reconstruction framework, enabling volumetric imaging and depth-resolved slice visualization.

Description of the New Method and System

Our two-layer micro-EIT platform includes both a novel hardware architecture and a corresponding 3D reconstruction framework. The measurement system consists of two 16-electrode circular arrays 1 mm in diameter (0.125 mm electrode diameter), facing each other across a 0.5 mm deep microfluidic chamber. 3D-printed holders are used to keep the system together, consisting of the two microelectrode ring layers, as well as the polydimethylsiloxane (PDMS)-based microchannel intended to support future in situ biological sample culture (as shown in Fig. 1).

3D forward models are implemented using EIDORS with refined mesh resolution (element size ~0.05), and datasets of simulated measurements (1024 voltage values per data) are generated. Based on these datasets, multiple 1D-CNN models implemented in PyTorch are trained under different parameter settings to learn to map measurement data to volumetric conductivity distributions.

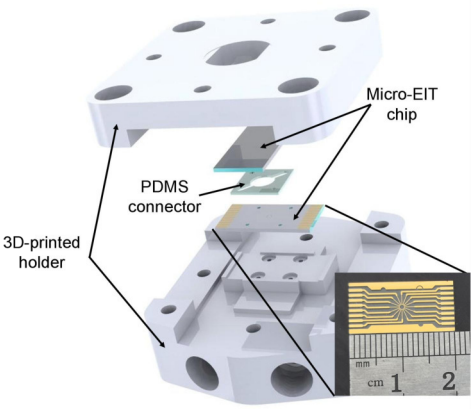

Fig. 1. Exploded view of the two-layer micro-EIT system, including a 3D-printed holder with fluidic connections, PDMS microfluidics for cell culture, and micro-EIT electrode chips (top and bottom). Ruler for chip scale.

Results

Simulation datasets have been generated and used to train multiple CNN models, yielding 3D reconstruction results along with corresponding 2D slices (Fig. 2. a and b). The results indicate that our two-layer structure and reconstruction framework are feasible and enable initial volumetric imaging and slice-based visualization.

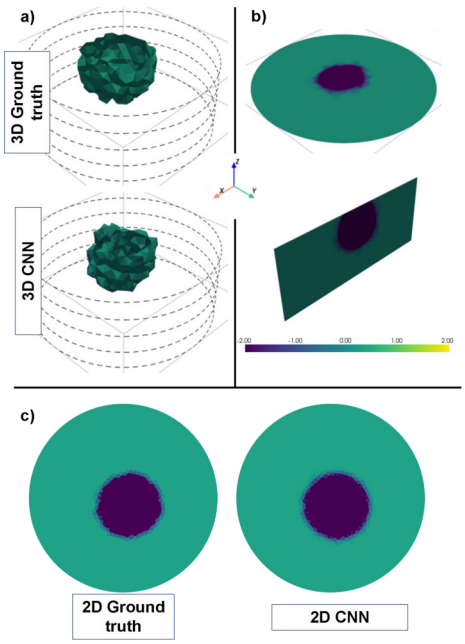

Fig. 2. micro-EIT reconstruction results: a) 3D simulated ground truth and CNN-based reconstructed image, b) corresponding 2D slice extracted at the central plane along the x and z-axis and c) 2D simulated ground truth and CNN-based reconstructed image. The results demonstrate the feasibility of volumetric reconstruction and slice-based visualization of our two-layer micro-electrode system.

Compared to conventional single-layer configurations, which provide limited depth information (as shown in Fig. 2. c), the two-layer design shows improved volumetric sensitivity, suggesting enhanced sensing capability.

Although quantitative evaluation and experimental validation are ongoing, these results demonstrate the potential of our approach for 3D micro-EIT imaging. Future work will focus on optimizing excitation patterns, improving reconstruction accuracy, and experimental validation.

Conclusion

This work represents a step towards 3D micro-EIT imaging through the integration of two-layer system design and machine learning-based reconstruction.

References

[1] A. Adler, A. Boyle, Electrical Impedance Tomography, *Wiley Encyclopedia of Electrical and Electronics Engineering*; John Wiley & Sons, Ltd, 2019; pp 1–16. https://doi.org/10.1002/047134608X.W1431.pub2.

[2] D. S. Holder, Electrical Impedance Tomography, Institute of Physics Publishing: Bristol and Philadelphia, 2005; ISBN 10.1201/9780429399886.

[3] B. Liu, B. Yang, C. Xu, J. Xia, M. Dai, Z. Ji, F. You, X. Dong, X. Shi, F. Fu, pyEIT: A Python Based Framework for Electrical Impedance Tomography, *SoftwareX* 2018, 7, 304–308. https://doi.org/10.1016/j.softx.2018.09.005.

[4] Y. Yang, J. Jia, S. Smith, N. Jamil, W. Gamal and P. -O. Bagnaninchi, A Miniature Electrical Impedance Tomography Sensor and 3-D Image Reconstruction for Cell Imaging, *IEEE Sensors*, vol. 17, no. 2, pp. 514-523, 15 Jan.15, 2017, doi: 10.1109/JSEN.2016.2631263.

[5] L. Yang, H. Wu, K. Liu, B. Chen, S. Huang and J. Yao, A Multicircle Planar Electrical Impedance Tomography Sensor for 3-D Miniature Imaging, *IEEE Sensors*, vol. 23, no. 9, pp. 9697-9706, 1 May1, 2023, doi: 10.1109/JSEN.2023.3262266.

[6] C. Canali, K. Aristovich, L.Ceccarelli, L.B Larsen, G. Martinsen, A. Wolff, M. Dufva, J. Emnéus, A. Heiskanen, Electrical impedance tomography methods for miniaturised 3D systems, *Journal of Electrical Bioimpedance,* vol. 7, no. 1, University of Oslo, 2016, pp. 59-67. https://doi.org/10.5617/jeb.4084.

[7] C. Liu, X. Chen, T. E. Winkler, I. Constantinou, A Comparative Evaluation of Microimpedance Tomography Reconstruction Algorithms for in Vitro Imaging, *ACS Sensors,* 2025 10 (11), 9093-9102, DOI: 10.1021/acssensors.5c03758.

DOI 10.5162/eurosensors2026/Mo–SML–01

Reliable TVOC Sensing: A Lab-to-Field Calibration Approach

Johannes Amann[1], Stefan Schumacher[2], Andreas Schütze[1], Christian Bur[1]
[1] Lab for Measurement Technology, Saarland University, Campus A5 1, 66123 Saarbrücken, Germany
[2] Institute of Energy and Environmental Technology e.V. (IUTA), 47229 Duisburg, Germany
c.bur@lmt.uni-saarland.de

Summary:
A methodology for reliable TVOC measurements of metal oxide semiconductor gas sensors in the example of indoor air quality is presented. It is based on representative lab calibration, dynamic operation, and field validation with release tests and air purifiers together. Volatile organic compounds are represented using substance groups derived from analytical studies. Calibration is performed using randomized gas mixtures and machine learning methods. The root means squared error of validation after the lab calibration was less than 10 %. In field tests, the system showed a high correlation to the PTR-MS used as a reference with deviations in the low parts-per-billion range. Thus, the approach enables robust and application-oriented TVOC measurement using cost-effective sensors.

Keywords: total volatile organic compounds (TVOC), calibration, metal oxide semiconductor (MOS) gas sensor, indoor air quality (IAQ), machine learning, validation

Motivation

Indoor air quality (IAQ) is becoming increasingly important, yet the focus remains on carbon dioxide (CO_2) and particulate matter, even though it has been known since Pettenkofer's time that CO_2 is merely a proxy and that volatile organic compounds (VOC) are the primary cause of poor air quality [1]. Unlike CO_2, the reliable and cost-effective measurement of VOC is a challenge, as VOC represent a complex multi-component problem due to the existence of hundreds of different VOC in indoor environments [2]. Therefore, the sum parameter total VOC (TVOC) is frequently used, although its definition depends heavily on the measurement method [3].

Metal oxide semiconductor (MOS) gas sensors are promising due to their low cost, high sensitivity, and real-time on-site capability, but they exhibit low selectivity and require application-specific calibration [4]. Furthermore, the transferability of laboratory conditions to real indoor environments has not yet been adequately addressed and remains one of the major challenges for chemical sensor systems.

The aim of this work is to develop a comprehensive methodology for reliable calibration of MOS sensors for field applications like indoor air quality (IAQ). This involves the definition of the measurement task, i.e., target and interfering gases, representative lab calibration of TVOC, and field validation - a guideline from the laboratory to the application.

Method

The presented methodology is a unified approach consisting of four main steps: Defining the measurement task, selecting and adapting the sensor system, lab calibration of the system including model building, and field validation, see Fig. 1.

The first step is to understand the measurement task involving major target and interfering gases. Since any (lab) calibration is just a simplification of the real-world application, this step is outmost important. Here, literature research is suggested to identify dominating target and interfering gases including concentration ranges.

To simplify the complex task of, e.g., IAQ with hundreds of VOC, VOC are classified into chemical substance groups first. Each group is described by representative compounds with typical concentration ranges based on extensive studies [2, 5]. The goal of simplification is to reduce the complexity to a feasible number of compounds needed for lab calibration, yet representing the application well. Calibration of seven volatiles representing six substance groups plus hydrogen and carbon monoxide is performed using randomized gas mixtures to simulate realistic indoor air conditions [6].

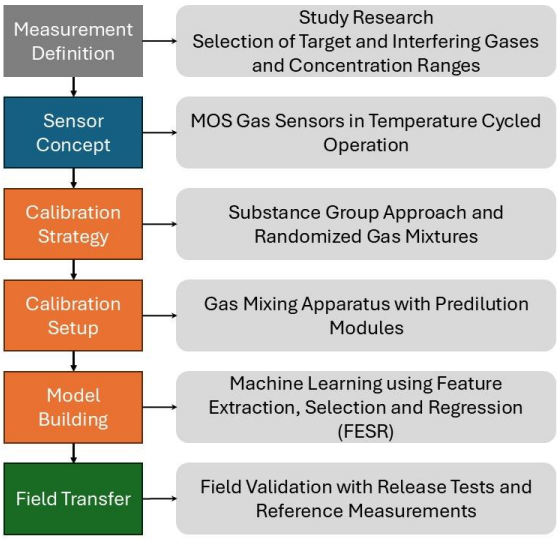

Fig 1. Flow Chart of the methodology showing the four main steps from defining the task to the field transfer.

To improve selectivity and sensitivity, the sensors run in temperature cycled operation (TCO), and the signals are evaluated using machine learning methods, i.e., applying the FESR (feature extraction and selection regression) method [5, 7]. Field phases are specifically integrated to account for drift and ensure transferability (merging lab calibration data and field data).

The novelty of the method lies in the overall approach, which consists of a combination of literature research, a substance-group-based calibration strategy, randomized gas mixtures, and continuous validation from the laboratory to real-world applications. The suggested method is universal and applicable to other use cases.

Results

The calibration provides an accurate prediction of TVOC across a wide concentration range (250 – 3400 ppb) with standardized errors of less than ten percent in the laboratory.

Field validation is demonstrated through release tests and measurements with air purifiers. Dynamic concentration profiles are reliably recorded and correlate well with reference measurements, i.e., a Proton Transfer Reaction – Mass Spectrometer (PTR-MS), see Fig. 2. Here, decay curves of a toluene release with and without an air purifier are compared. With the air purifier turned on, the toluene concentration decreases much faster than with the natural decay curve without an air purifier. The sensor results are identical to those of PTR-MS in relative terms and differ by only a few ppb in absolute terms.

Additionally, successful testing in accordance with VDI/VDE 3518 Part 4 is demonstrated, which allows VOC detectors to be tested for IAQ, confirming their suitability for indoor air quality assessment.

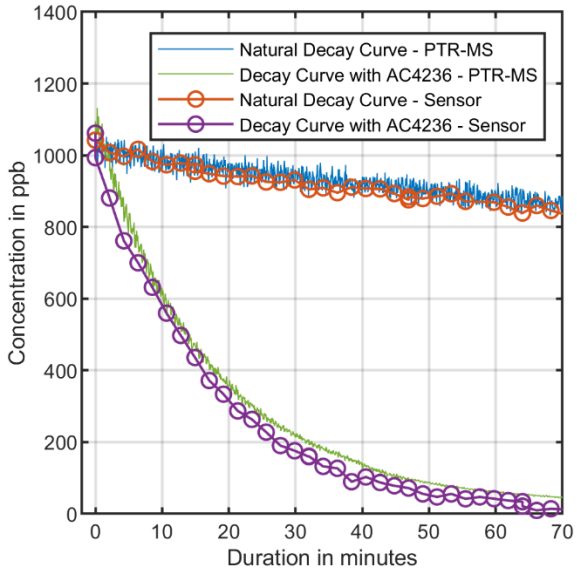

Fig 2. Natural decay curve vs decay curve during operation of an air purifier (Philips AC4236/10) recorded by a calibrated sensor (connected circles) and a PTR-MS during toluene releases (solid line).

References

[1] M. Pettenkofer, Über den Luftwechsel in Wohngebäuden, *Literarisch-Artistische Anstalt der J.G. Cotta'schen Buchhandlung* (1858)

[2] H. Hofmann, P. Plieninger, Bereitstellung einer Datenbank zum Vorkommen von flüchtigen organischen Verbindungen in der Raumluft, in *WaBoLu-Hefte, Umweltbundesamt* (2008); https://www.umweltbundesamt.de/sites/default/files/medien/publikation/long/3637.pdf

[3] T. Salthammer, TVOC-revisited, *Environment international* 167, 107440 (2022); doi: 10.1016/j.envint.2022.107440

[4] L. Spinelle, M. Gerboles, M. Aleixandre, Protocol of evaluation and calibration of low-cost gas sensors for the monitoring of air pollution, *Publications Office of the European Union*, Luxembourg (2013)

[5] T. Baur, J. Amann, C. Schultealbert & A. Schütze, Field study of metal oxide semiconductor gas sensors in temperature cycled operation for selective VOC monitoring in indoor air, *Atmosphere* 12(5), 647 (2021); doi:

[6] T. Baur, M. Bastuck, C. Schultealbert, T. Sauerwald & A. Schütze, Random gas mixtures for efficient gas sensor calibration. *Journal of Sensors and Sensor Systems* 9(2), 411-424 (2020); doi: 10.5194/jsss-9-411-2020

[7] A. Schütze & T. Sauerwald, Dynamic operation of semiconductor sensors. In *Semiconductor gas sensors*, Woodhead Publishing, 385-412 (2020); doi: 10.1016/B978-0-08-102559-8.00012-4

DOI 10.5162/eurosensors2026/Mo–SML–02

Progressive Domain Adaptation under Sensor Drift for Gas Classification with Limited Calibration Labels

Han Fan[1,2], *Achim J. Lilienthal*[1,2]

[1] Chair of Perception for Intelligent Systems (PercInS), Munich Institute of Robotics and Machine Intelligence (MIRMI), Technical University of Munich (TUM), Germany
[2] Robot Navigation and Perception Lab (RNP), Örebro University, Sweden
han.fan@tum.de, achim.j.lilienthal@tum.de

Summary: Metal-oxide electronic noses suffer from sensor drift, in which sensor response characteristics change over time. This creates a data distribution shift (domain gap) that severely degrades gas classification accuracy. To address this drift effect, domain adaptation techniques reduce the distribution discrepancy between the initial source domain and drift-affected target measurements. We study batch-wise adaptation across temporally ordered drift batches, where calibration labels are extremely scarce. To ensure robust adaptation under unpredictable drift patterns, we train a diverse pool of conditional domain-adversarial experts. We then fuse their predictions using a confidence-aware Expectation-Maximization procedure. This fusion mechanism acts as a smart consensus, estimating each expert's reliability using the limited calibration labels without requiring additional annotations. On the UCI drift benchmark, this budget-respecting approach consistently improves target accuracy over a tuned Drift Correction Autoencoder (DCAE) baseline, particularly on later, more severely drifted batches.

Keywords: electronic nose; sensor drift; transfer learning; domain adaptation.

Introduction

Metal-oxide (MOX) electronic noses (e-noses) enable low-cost gas identification, but their long-term reliability is limited by sensor drift and instrumental variation. Such effects induce distribution shifts between an initial training condition and later operating conditions, leading to substantial accuracy degradation in gas classification models. Existing drift-compensation strategies rely on different assumptions about the availability of the target domain. Correction-centric transfer learning can exploit paired transfer measurements to learn drift-corrected yet discriminative representations (e.g., drift correction autoencoder (DCAE)) [1]. At the other extreme, target-domain-free methods (e.g., TDACNN) avoid using any target-domain samples during training and prediction, which improves deployability but prevents adaptation to batch-specific drift patterns as conditions evolve.

In practice, continuously deployed e-noses yield abundant unlabeled measurements, but physical recalibration is costly, restricting us to a strict budget of calibration pairs. Conditional Adversarial Domain Adaptation (CDAN) leverages unlabeled data to align source and target distributions, conditioned on class predictions [2]. However, when drift is severe and heterogeneous, aggressively enforcing domain alignment may degrade target-domain classification performance and lead to negative transfer [3].

To achieve robust gas classification under a strict calibration budget, we propose a two-stage framework. First, we train a diverse pool of CDAN experts. By intentionally varying their adaptation components, we induce a variety of drift-compensation behaviors. Second, we fuse their predictions using a confidence-aware Dawid–Skene EM procedure. This semi-supervised procedure estimates confidence-specific expert confusion matrices from the limited calibration labels and uses them to infer a reliability-aware fused class posterior.

Method

We treat the gas sensor drift as a statistical domain shift between the initial calibration data (source domain, $\mathcal{S}$) and the incoming batch (target domain, $\mathcal{U}_b$). Therefore, by applying domain adaptation to align these two distributions, we can effectively reduce the drift effect. We propose an approach that combines conditional domain-adversarial learning with ensemble learning. To handle heterogeneous drift, we leverage a multi-expert pool to capture diverse adaptation trajectories, then employ a probabilistic consensus mechanism to resolve expert disagreements using the limited calibration data. Our approach consists of two stages:

A. Mechanistically Diverse Domain-Adversarial Experts

Because drift patterns are unpredictable, a single adaptation strategy may over-correct or under-correct the distribution shift. To mitigate this, we train a pool of experts $m \in \{1, \ldots, M\}$

using the following loss function:

$$\mathcal{L}^{(m)} = \mathcal{L}_{\text{cls}} + \lambda_{\text{adv}}^{(m)} \mathcal{L}_{\text{CDAN}} + \lambda_{\text{pair}}^{(m)} \mathcal{L}_{\text{pair}} + \lambda_{\text{pst}}^{(m)} \mathcal{L}_{\text{pst}} \quad (1)$$

Here, $\mathcal{L}_{\text{cls}}$ ensures basic classification on source data; $\mathcal{L}_{\text{CDAN}}$ encourages conditional alignment between source and target representations [2]; $\mathcal{L}_{\text{pair}}$ aligns the few paired source–target transfer samples; and $\mathcal{L}_{\text{pst}}$ performs self-training with predicted high-confidence pseudo-labels. To cover a wide spectrum of drift-compensation behaviours, we systematically vary the hyperparameters (λ) and conditioning strategies across the experts.

B. Confidence-aware Fusion

Since different experts may excel under different drift conditions, we use a semi-supervised Dawid–Skene Expectation-Maximization (EM) procedure to dynamically find the best consensus. For every unlabeled testing measurement, the experts provide class-probability distributions. ConfDS estimates confidence-specific confusion matrices and iteratively infers a fused posterior over gas classes using Dawid–Skene expectation–maximization. To allow an expert's reliability to differ between confident and uncertain predictions, we separate each expert's predictions into high-confidence and low-confidence bins (using a threshold τ), evaluating their reliability separately. By anchoring this estimation on the tiny budget of true calibration labels, the EM algorithm updates the reliability weights and outputs a robust, fused final classification.

Results and Conclusion

We use the open-source UCI Gas Sensor Array Drift Dataset [4] for evaluation. We use the first batch as the source domain and perform batch-wise adaptation and evaluation on the temporally ordered target batches b02–b10. Only 0.62% target measurements are labelled for the confidence-aware fusion (the per-batch fraction varies with batch size). We report target classification accuracy and its average over target batches. The result is obtained by repeating the full pipeline over 6 runs (3 training seeds $\times$ 2 pair-shuffle seeds).

Fig. 1 summarizes the per-batch classification accuracy. Overall, the proposed CDAN diverse-expert pool with ConfDS fusion achieves a higher mean target accuracy than the DCAE baseline trained under the same budget, with the advantage becoming most pronounced on later/harder batches, namely b06–b09. Both our work and the DCAE outperform the target-domain-free baseline implemented by TDACNN [5], which illustrates the typical accuracy degradation under sensor drift when no target-domain adaptation is performed.

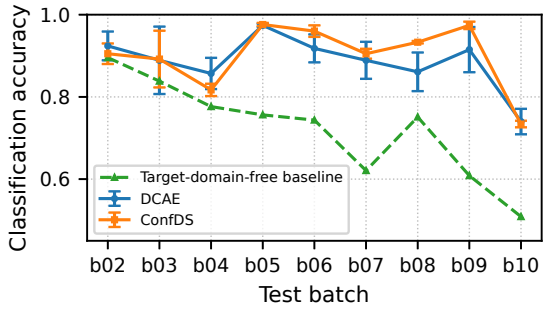

Figure 1: Per-batch classification accuracy on the UCI drift dataset. Our ConfDS fusion (0.899 ± 0.009 overall) consistently outperforms the DCAE baseline (0.885 ± 0.008) under the same strict calibration budget and the target-domain-free baseline, with the largest gains observed on b06–b09.

In conclusion, our results show that combining diverse conditional domain-adaptation experts with confidence-aware fusion can improve gas classification robustness under temporally varying sensor drift and limited target supervision. For reproducibility, the implementation of the proposed framework is publicly available at `https://github.com/TUM-PercInS/confds-enose-domain-adaptation.git`. As a next step, we will validate the approach on long-term robotic olfaction deployments with operationally realistic calibration procedures.

References

[1] Ke Yan and David Zhang. Correcting instrumental variation and time-varying drift: A transfer learning approach with autoencoders. *IEEE Transactions on Instrumentation and Measurement*, 65(9):2012–2022, 2016.

[2] Mingsheng Long, Zhangjie Cao, Jianmin Wang, and Michael I Jordan. Conditional adversarial domain adaptation. *Advances in neural information processing systems*, 31, 2018.

[3] Han Zhao, Remi Tachet Des Combes, Kun Zhang, and Geoffrey Gordon. On learning invariant representations for domain adaptation. In *International conference on machine learning*, pages 7523–7532. PMLR, 2019.

[4] Alexander Vergara, Shankar Vembu, Tuba Ayhan, Margaret A Ryan, Margie L Homer, and Ramón Huerta. Chemical gas sensor drift compensation using classifier ensembles. *Sensors and Actuators B: Chemical*, 166:320–329, 2012.

[5] Yuelin Zhang, Sihao Xiang, Zehuan Wang, Xiaoyan Peng, Yutong Tian, Shukai Duan, and Jia Yan. Tdacnn: Target-domain-free domain adaptation convolutional neural network for drift compensation in gas sensors. *Sensors and Actuators B: Chemical*, 361:131739, 2022.

DOI 10.5162/eurosensors2026/Mo–SML–03

Characterizing Resonance Scaling in Cattle Eructation Sounds for Methane Emission Estimation

Yujia Hu, Jarred Fastier-Wooller, Shun Muramatsu, Michitaka Yamamoto, Toshihiro Itoh
Department of Precision Engineering, School of Engineering, The University of Tokyo
7-3-1 Hongo, Bunkyo, Tokyo 113-8656, Japan
3906910474@g.ecc.u-tokyo.ac.jp

Summary:
We propose an acoustic method for estimating methane emissions from cattle eructation sounds, based on resonance scaling caused by changes in gas molecular weight. To evaluate this method, we reproduced eructation sounds experimentally and extracted resonance-related components using cepstral analysis. The liftered spectra for N_2 and CO_2 showed similar shapes after frequency scaling, suggesting that the gas molecular weight can be estimated with a 2.9% error.

Keywords: Acoustic sensing, Resonance scaling, Cattle, Eructation sounds, Wearable device

Introduction

Methane emissions from cattle and other livestock are a significant source of global warming. Although methane-reducing feeds have been developed, their effects vary among individual cattle and over time [1]. Therefore, long-term monitoring of methane emissions is required. However, existing methods, such as chamber method and sniffing systems, are not suitable for long-term, continuous monitoring of total methane emissions from cattle [2]. We focused on an acoustic approach. Body-transmitted sounds in animals can be measured, and collar-mounted devices have been shown to monitor heart sounds, scratching sounds, and eructation sounds in cattle [3].

We investigate an acoustic method for long-term monitoring of total methane emissions from cattle using eructation sounds. However, it is unclear whether gas molecular weight can be reliably estimated from eructation sounds. In this study, we therefore aim to evaluate the measurement performance of the proposed method by experimentally reproducing resonant sounds in the esophagus of cattle.

Materials and Methods

Figure 1 shows the concept of the proposed method. A collar-mounted device equipped with body-conduction microphones is attached to cattle to measure eructation sounds generated in the esophagus.

Eructation sounds are considered to follow the source-filter theory: sound source generated at the esophageal groove is filtered through the resonance characteristics determined by the

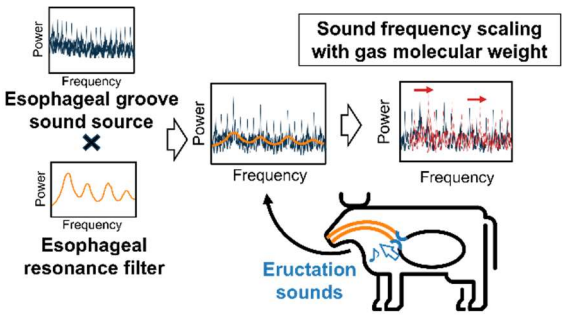

Fig. 1. Concept of methane emission measurement from eructation sound.

concentration alter the molecular weight of the eructated gas, thereby changing the speed of sound and scaling the resonance frequencies. Since the sound velocity c is given by eq. (1) using the specific heat ratio k, gas constant R, absolute temperature T, and molecular weight M, the average molecular weight of the gas can be estimated from the frequency scaling.

$$c = \sqrt{\frac{kRT}{M}} \tag{1}$$

Figure 2 shows the experimental setup used to reproduce eructation sounds under different gas. Since eructation sounds generated in the cattle esophagus occur through a mechanism similar to human phonation, a vocal-tract model was used in this experiment. CO_2 and N_2 were used as test gases. A slit silicone structure was used as an artificial vocal fold [4], and the vocal tract was modeled as an open-ended resonator. The sound was measured using an omnidirectional microphone (Onosokki, MI-1271). The recorded

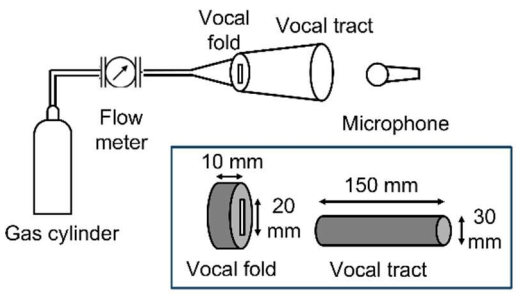

Fig. 2. Experimental system.

sound data were analyzed to obtain the power spectrum and liftered spectrum.

Results and Discussion

Figure 3 shows the power spectrum and liftered spectrum for CO_2 and N_2. The power spectra show both peaks corresponding to the sound source and a spectral pattern associated with resonance characteristics. The liftered spectrum represents the spectral envelope of the power spectrum and can be regarded as extracts the resonance-related component. The peak points of each liftered spectrum are also indicated.

Figure 4 shows a comparison of the corresponding peak frequencies in the liftered spectra of N_2 and CO_2. Averaging the first five peaks of the liftered spectra showed that the CO_2 peak frequencies were 0.78 times those of N_2. The theoretical frequency ratio is expressed by eq. (2), indicating that gas molecular weight could be estimated with an error of 2.9% (absolute error: 1.27)

$$\frac{f_{CO_2}}{f_{N_2}} = \sqrt{\frac{k_{CO_2} \cdot M_{N_2}}{k_{N_2} \cdot M_{CO_2}}} = \sqrt{\frac{1.30 \cdot 28}{1.40 \cdot 44}} \approx 0.77 \qquad (2)$$

The observed error may be attributed to the mixing of air ($M = 29$) in the resonant tube.

Conclusion

In this study, we experimentally reproduced eructation sounds and evaluated an acoustic method for gas molecular-weight estimation based on resonance scaling. The liftered spectra of N2 and CO2 showed similar patterns after frequency scaling, suggesting that the gas molecular weight can be estimated with a 2.9% error. Future work will focus on experiments using geometries closer to the cattle esophagus, evaluating measurement accuracy for various molecular weights, and investigating acoustic changes during propagation through body tissues.

References

[1] J. Rey, R. Atxaerandio, R. Ruiz, E. Ugarte, O. González-Recio, A. Garcia-Rodriguez, I. Goiri Comparison between noninvasive methane measurement techniques in cattle, Animals Vol 9, No 8, p. 563 (2019).

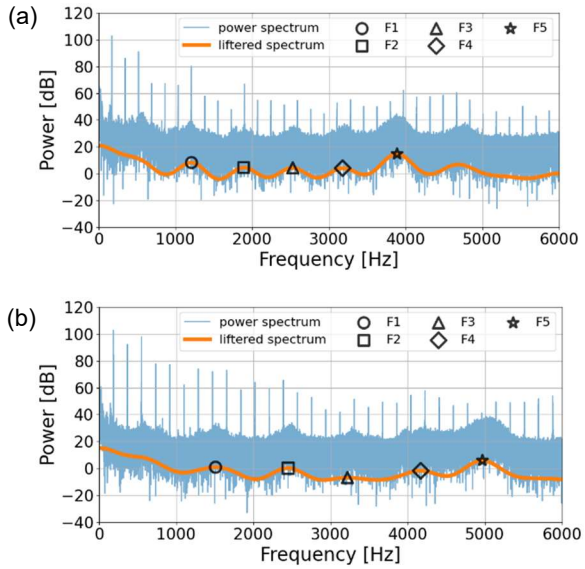

Fig. 3. Power spectrum and liftered spectrum for (a) CO_2 and (b) N_2

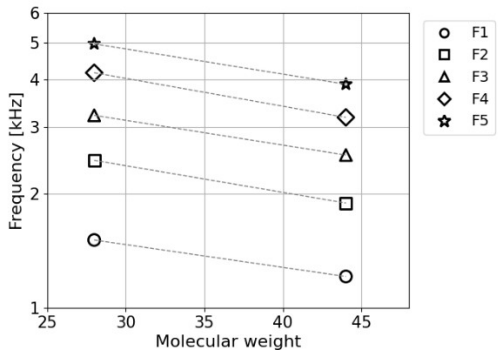

Fig. 4. Comparison of the corresponding peak frequencies in the liftered spectra of N_2 and CO_2.

[2] M. O. Okpara, Methane Emissions in Ruminants: Perspectives on Measurement and Estimation Methods, Russian Agricultural Science, Vol 44, No 3, pp. 290-294 (2018).

[3] S. Muramatsu, N. Mascia, J. Fastier-Wooller, M. Yamamoto, S. Koike, T. Itoh, A Collar Device for Monitoring Cattle Mastication and Eructation Sounds, in Proc. 2025 IEEE Sensors, pp. 1-3 (2025).

[4] P. Luizard, L. Bailly, H. Yousefi-Mashouf, R. Girault, L. Orgéas and N. Henrich Bernardoni, Flow-induced oscillations of vocal-fold replicas with tuned extensibility and material properties, Scientific Reports, Vol 13, p. 22658 (2023).

Acknowledgement

This work was supported by Cabinet Office, Government of Japan, Crossministerial Moonshot Agriculture, Forestry and Fisheries Research and Development Program, “Technologies for Smart Bio-industry and Agriculture” (funding agency: Bio-oriented Technology Research Advancement Institution) (grant number: JPJ009237).

DOI 10.5162/eurosensors2026/Mo–SML–04

Jacobian-Initialized Parametric Physics-Informed Neural Network for Anomaly Position and Size Estimation from Simulated Electrical Impedance Tomography Data

Shilpa Sharma[1], Kerstin Eckert[1,2], Zhe Lei[1,2]
[1] Helmholtz-Zentrum Dresden-Rossendorf, Bautzner Landstrasse 400, 01328 Dresden, Germany
[2] Technical University of Dresden, 01069, Dresden, Germany
s.sharma@hzdr.de, z.lei@hzdr.de

Summary:

Real-time monitoring of the trajectory and size of the particle, droplet or bubble is relevant in many multiphase processes, but imaging techniques often fail in optically inaccessible media. In that case, electrical impedance tomography (EIT) provides a non-invasive alternative. This work presents a simulation-based study of an eight-electrode EIT sensor for monitoring a circular conductivity anomaly. We introduce a preliminary study deploying a parametric physics-informed neural network (PINN) approach that uses the center estimate from conventional Jacobian-based reconstruction to refine the trajectory and estimate the radius of an anomaly from simulated boundary-voltage measurements.

Keywords: Electrical impedance tomography, physics-informed neural network, partial differential equation, particle monitoring, inverse problems.

Introduction

In many multiphase systems, real-time monitoring of the position and size of the dispersed particle/droplet is crucial for process monitoring [1]. Experimentally, we investigated an electrical impedance tomography (EIT) cell constituted of eight electrodes (as shown in Fig. 1). Following a programmed sequence, these eight boundary electrodes excite the current in selected pairs and measure the excited responsive boundary voltages at the remaining electrode pairs to evaluate the internal conductivity distribution.

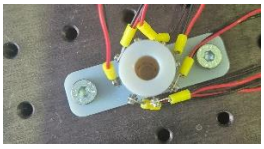

Fig. 1. Experimental eight electrode EIT cell.

However, to reconstruct the conductivity distribution information, a nonlinear and ill-posed inverse problem have to be solved. Conventional linearized methods, such as Jacobian-based reconstruction, are used to solve the EIT-governed partial differential equation (PDE). It is proven to be sufficient to reconstruct the internal conductivity field in simplified systems. However, the reconstructed anomalies are often spatially blurred due to the limited measured degrees of freedom.

This study investigates a simulation-based physics-informed neural network (PINN) approach to estimate the trajectory and radius of the moving circular conductivity anomaly. pyEIT [2] is used to generate the circular conductivity anomalies with the known position, shape and conductivity together with the corresponding boundary-voltage measurements. The initial localization of an anomaly is estimated by the Jacobian-based reconstruction, which is then refined by the subsequent parametric PINN to estimate the radius by combining the voltage consistency, governing PDE, and size-sensitive voltage-amplitude constraint.

Proposed Algorithm

A two-dimensional circular EIT phantom with eight electrodes is simulated using the pyEIT library [2]. The dataset comprises circular anomalies with different positions and radii together with their corresponding boundary-voltage measurements. For each frame, the frame voltage vector $\mathrm{v}_{\mathrm{frame}}$ and the homogeneous reference vector $\mathrm{v}_{\mathrm{ref}}$ are first used to obtain an initial anomaly center using a regularized Jacobian reconstruction.

In the second stage, a parametric PINN is introduced in which the conductivity distribution is represented by a circular model. This model comprises a small number of trainable geometric

parameters: the center coordinates x_c and y_c, the radius r and the anomaly conductivity σ_{in}

$$\sigma(x,y) = \sigma_{bg} + (\sigma_{in} - \sigma_{bg})S(r - d(x,y)), \quad (1)$$

where

$$d(x,y) = \sqrt{(x - x_c)^2 + (y - y_c)^2}, \quad (2)$$

and S denotes a smooth circular boundary. The Jacobian estimate initializes the center coordinates, such that $x_c = x_{jac}$ and $y_c = y_{jac}$, while the same initial radius is used for all frames.

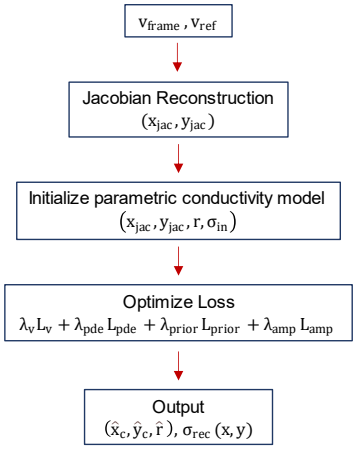

Fig. 2. Workflow of the proposed Jacobian-initialized parametric PINN.

As shown in Fig. 2, the potential-network weights and anomaly parameters are then optimized jointly. The loss terms L_v and L_{pde} ensure agreement with the simulated data and physical consistency, whereas L_{prior} preserves the Jacobian-based initialization. The amplitude loss L_{amp} provides sensitivity to the anomaly size. The output layer returns the refined center coordinates, estimated radius, and corresponding conductivity distribution.

Results

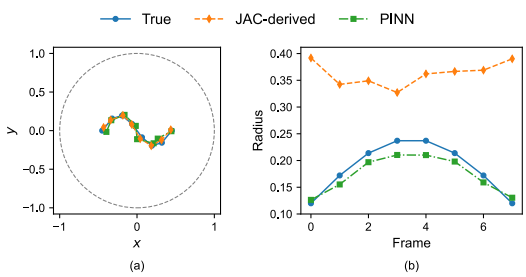

Fig. 3. Comparison over eight simulated frames. True, Jacobian-derived and PINN-estimated (a) center trajectories, and (b) size of anomalies.

The comparison of recovered anomaly trajectory and anomaly size is illustrated in Fig. 3. All three trajectory curves indicate that the center estimation is almost close to the true center location (Fig. 3(a)). Fig. 3(b) shows that the effective radius estimation of the proposed parametric PINN remains closer to the ground truth in comparison to the conventional Jacobian-based reconstruction. Fig. 4 demonstrates that the PINN recovers the approximate extent of an anomaly. The absolute error maps suggest that the largest deviations appear near the circular interface.

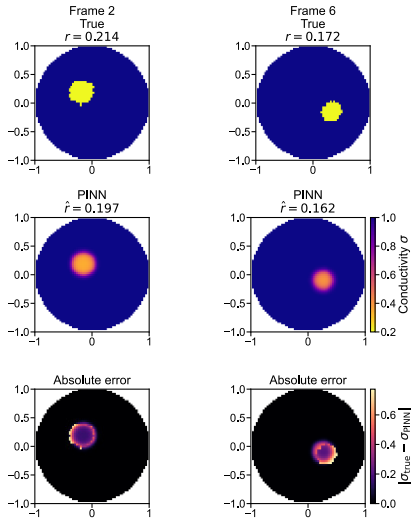

Fig. 4. Representative parametric PINN reconstructions for frame 2 and frame 6. Each row shows the ground truth, PINN estimation, and an absolute reconstruction error.

Conclusion

The Jacobian-based reconstruction localized the anomaly efficiently, but it blurred the anomaly interface and overestimated the effective radius. In comparison, the parametric PINN preserved the estimated trajectory and recovered the radius more closely to the ground truth. The results demonstrate the robustness of combined Jacobian initialization and physics-informed parameter estimation for position and size monitoring.

Acknowledgements

We acknowledge the German Federal Ministry of Research, Technology and space (BMFTR) with funds provided in the context of DATIPilot - Sprint under Grant 03DPS1187 (Project KepRE)

References

[1] Y. He, K. Ortmann, K. Eckert, and Z. Lei, “Rectilinear magnetophoresis of a single oil droplet in a paramagnetic rare-earth solution”, *Physical Review Fluids* 10(3), 033603 (2025); doi: 10.1103/PhysRevFluids.10.033603

[2] B. Liu, B. Yang, C. Xu, J. Xia, M. Dai, Z. Ji, F. You, X. Dong, X. Shi, and F. Fu, “pyEIT: A Python based framework for electrical impedance tomography”, *SoftwareX* 7, 304–308 (2018); doi: 10.1016/j.softx.2018.09.005

DOI 10.5162/eurosensors2026/Tu–SML–01

Recovery of Characteristic Thiabendazole Raman Peaks from Ethanol-Dominated Spectra Toward Microfluidic SERS-Based Pesticide Sensing

Karolina Mileńko[1], Kari Anne Hestnes Bakke[1], Elizaveta Verschegina[1], Angela Baracu[2], Adrian Dinescu[2], Oana Rasoga[3], Konrad Giżyński[4]
[1]Smart Sensors and Microsystems Department, SINTEF Digital, Gaustadalléen 23C, 0373, Oslo, Norway,
[2]National Institute for R&D in Microtechnologies - IMT Bucharest, Romania,
[3]National Institute of Materials Physics, 405 A, Atomistilor Street, P.O. Box M.G. 7, 077125 Magurele, Romania
[4]Institute of Physical Chemistry, Polish Academy of Sciences, Kasprzaka 44/52, 01-224 Warsaw, Poland
kgizynski@ichf.edu.pl

Summary:

We present a reference-guided Raman analysis workflow developed as a signal processing module for a microfluidic SERS sensor targeting pesticide detection. A two-component linear model based on ethanol and dry thiabendazole (TBZ) reference spectra was used to recover analyte contributions from ethanol-dominated spectral data. The recovered TBZ component preserved key diagnostic peaks and enabled automated peak identification. The current results are based on measurements of a dried sample of 2 µL and serve as a proof-of-concept for future flow-through sensing systems.

Keywords: thiabendazole, Raman spectroscopy, SERS, microfluidics, spectral unmixing

Background, Motivation and Objective

Thiabendazole (TBZ) is a benzimidazole fungicide relevant for residue monitoring in environmental and food-related samples. Raman and surface-enhanced Raman spectroscopy (SERS) provide molecular specificity; however, in liquid-phase measurements the analyte signal is often obscured by strong solvent contributions. This limitation persists even when using advanced plasmonic substrates engineered for efficient excitation at near-infrared wavelengths [1].

In this work, we develop a compact spectral unmixing workflow intended as a signal processing component of a microfluidic SERS sensor, where analyte-containing solutions will flow over an active sensing substrate. As an intermediate step, we evaluate the recovery of TBZ Raman features from spectra dominated by ethanol using a controlled static measurement configuration.

Description of the New Method or System

Corrected spectra measured on SERS substrates - Au-based nanostructures fabricated via electron-beam lithography and designed to achieve plasmonic resonance in the 800–900 nm range, matching 785 nm excitation—were analyzed in the 300–1800 cm⁻¹ spectral range. Each measured spectrum was modeled as a linear combination of reference spectra [2]:

$$I_{mix} = \alpha \cdot I_{ethanol} + \beta \cdot I_{TBZ}$$

where $I_{ethanol}$ and I_{TBZ} correspond to ethanol and dry TBZ references, respectively. To improve robustness, the dominant ethanol band region (850–910 cm⁻¹) was excluded from fitting.

The recovered analyte contribution ($\beta \cdot I_{TBZ}$) was further processed using prominence-based peak detection to identify characteristic Raman bands. The approach is computationally lightweight and compatible with real-time data processing in flow-through sensing configurations. SERS measurements were performed using a fiber-optic probe coupled to a 785 nm excitation source, consistent with the substrate design.

The overall sensing concept is illustrated in Fig. 1a, where a microfluidic SERS platform is envisioned. In this system, analyte-containing solution flows over a nanostructured Au substrate, and the Raman signal is collected via a fiber-optic probe. The proposed spectral unmixing approach is intended as a signal processing module within this architecture.

Results

The proposed decomposition successfully isolated a TBZ-like spectral component even when the raw spectra were strongly dominated by ethanol. As shown in Fig. 1b, the measured spectra exhibit a dominant ethanol contribution, particularly in the 850–910 cm^{-1} region, which obscures direct identification of analyte features. Following spectral unmixing, the recovered TBZ component (Fig. 1c) preserves characteristic Raman bands near 782, 1009, 1275, 1377, 1450, and 1592 cm^{-1}, enabling reliable peak identification. The averaging of the reconstructed TBZ spectra across concentrations further enhances the visibility of diagnostic features.

The concentration dependence of the unmixing coefficient β is presented in Fig. 1d. Despite inter-series variability, a monotonic trend is observed for most measurement series, supporting the use of β as a semi-quantitative indicator of TBZ concentration.

References

[1] J. Langer et al., Present and Future of Surface-Enhanced Raman Scattering, ACS Nano **14**, 28 (2020).

[2] P. Yin, Y. Xiao, C. Feng, X. Wu, X. Wang, D. Klyuyev, Z. Wu, Y. Zhao, and B. Hu, Decoding Complex Spectra with Machine Learning: Advances in Spectral Unmixing for Chemical Analysis, Anal. Chem. **98**, 4432 (2026).

Acknowledgements

The authors would like to thank the European Commission and the Research Council of Norway for funding in the frame of the collaborative international consortium STARDUST financed under the 2022 Joint call of the European Partnership 101060874 - Water4All. This work was supported by a grant of the Ministry of Research, Innovation and Digitization, CNCS/CCCDI - UEFISCDI, project number COFUND-WATER4ALL-STARDUST-2, within PNCDI IV. Project no. WATER4ALL/I/20/STARDUST/2024 is co-financed/financed by the National Centre for Research and Development under the Water4All Partnership Programme

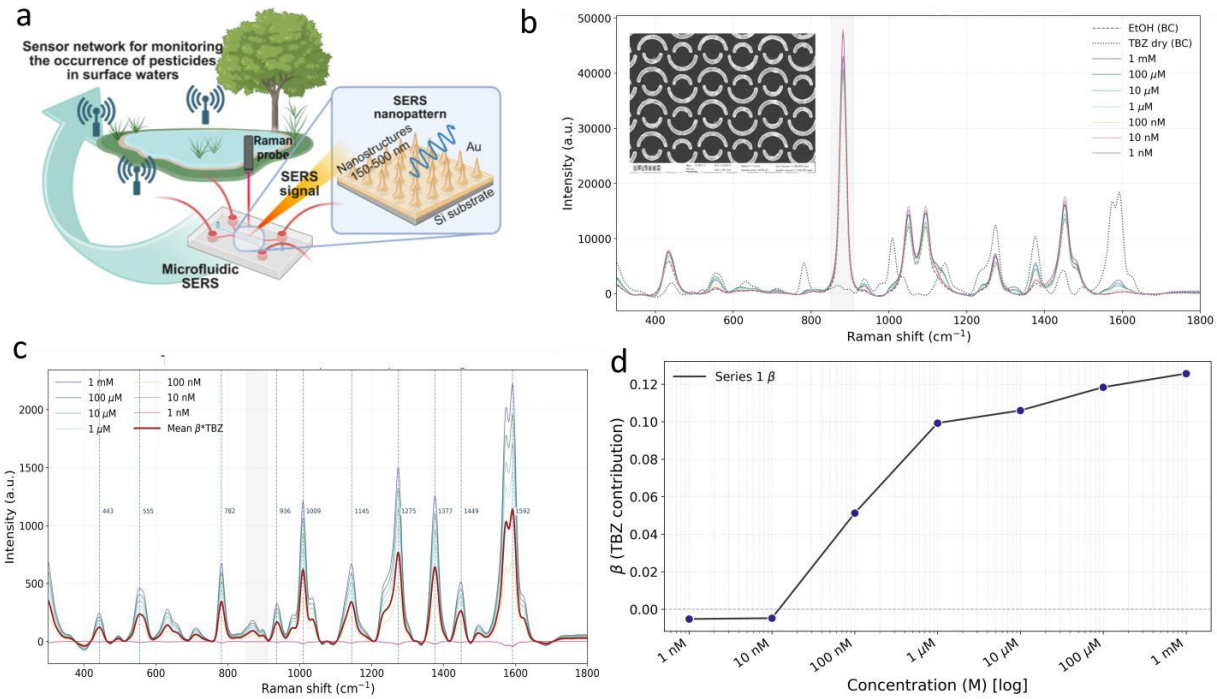

Fig. 1. (a) Concept of a microfluidic SERS sensing platform for pesticide detection, where analyte-containing solution flows over a nanostructured Au substrate and Raman signal is collected using a fiber-optic probe. (b) Raw Raman spectra of TBZ in ethanol at different concentrations, dominated by solvent contribution; inset: SEM image of the SERS substrates showing Au nanostructures. (c) Recovered TBZ spectral component obtained by two-component unmixing, showing enhanced visibility of characteristic Raman bands. (d) Dependence of the unmixing coefficient β (TBZ contribution) on concentration.

DOI 10.5162/eurosensors2026/Tu–SML–02

Dual-Descriptor VAE Characterisation of AE-Band Structural Signals in Reinforced Concrete

Xiang Zhang[1]
[1] HafenCity University Hamburg, Henning-Voscherau-Platz 1, 20457 Hamburg, Germany
xiang.zhang@hcu-hamburg.de

Summary:
We report an offline baseline-relative VAE study for fixed-window characterisation of continuous high-frequency structural acoustic signals from AE-band piezoelectric sensors in reinforced concrete. RMS-normalised spectra represent spectral shape, while pre-normalisation log-RMS preserves amplitude-related energy. In a bending test, principal load cycles were dominated by energy increases, with weaker spectral-shape shifts, latent-space drift, and broader latent dispersion during final load-to-failure. Results support unsupervised descriptor-based continuous signal characterisation under varying load.

Keywords: Continuous high-frequency structural signals, reinforced-concrete bending test, variational autoencoder, baseline-relative descriptors, AE-band sensing

Background, Motivation and Objective

We use AE-bandwidth piezoelectric sensors (30–120 kHz) but treat the recorded signals as continuous high-frequency structural acoustic time series, without hit detection or onset picking. AE-band sensing is widely used in concrete monitoring [1,2], where conventional hit-based workflows depend on threshold and onset choices - a well-known limitation across general AE signal processing [2,3]. Dense fixed-window processing avoids committing to a single hit definition and yields continuous time-series descriptors that can be aligned with the loading history. Normal-state Variational Autoencoder (VAE) [4] reconstruction has been used in related work to detect deviations from a reference state [5]. Building on this baseline-relative idea, this proof-of-concept study investigates an offline dual-descriptor VAE workflow during one reinforced-concrete bending test, with RMS-normalised spectrograms representing spectral shape and pre-normalisation log-RMS retained as the energy descriptor.

Description of the New Method

Two AE-band piezoelectric sensors mounted diagonally on a full-scale reinforced-concrete (RC) beam recorded continuous signals at 10 MHz, decimated to 1 MHz and segmented into 10 ms windows with 2 ms hop (80% overlap). The two synchronised channels were stacked as a joint two-channel spectrogram tensor. The joint pre-normalisation RMS was stored as the energy descriptor; waveforms were normalised by this RMS before STFT. STFT used a 1024-sample Hann window, 256-sample hop, 2048-point FFT, cropped to 30–120 kHz and standardised against baseline statistics. Load was synchronously recorded by the testing-machine load cell; load values are used here to define load-cycle boundaries but are not used as input to the descriptor pipeline.

The VAE used a 128-dimensional latent space and was trained on 50,000 baseline spectrograms from 20–130 s. Training used Adam with an initial learning rate of 0.001 and cosine learning-rate decay, up to 100 epochs with early stopping, and a loss combining reconstruction MSE, a spectral-consistency term penalising frequency-band and time-envelope energy mismatch, and KL regularisation with β warmed up linearly to 0.003 over 15 epochs. The spectral-shape score is a one-sided RMS combination of the robust-standardised reconstruction MSE and spectral-consistency residual; negative deviations from the baseline median are clipped to zero. The energy score is the robust-standardised pre-normalisation log-RMS, using baseline median and robust scale. Encoder mean vectors are used to compute a robust-standardised latent-drift score relative to the baseline latent centre.

The loading programme comprised an initial zero-load reference period, a first load cycle peaking at ~24 kN (140–210 s), two intermediate ~10 kN holds (505–620 s and 900–940 s), a second load cycle peaking at ~51 kN (1100–1290 s), and a final load-to-failure cycle reaching ~70 kN (1380–1630 s). The present analysis focuses on baseline-relative drift across the three principal load cycles.

Results

The threshold-free descriptor view showed an energy-dominated response during the principal

load cycles, while the spectral-shape descriptor changed more gradually. This supports interpreting the two descriptors as parallel summaries of amplitude-driven and spectral-shape evolution in this single loading sequence, rather than as validated damage-class labels.

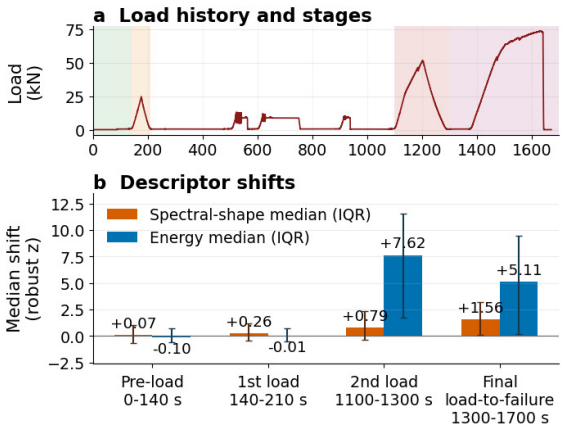

Fig. 1. Load history and baseline-relative descriptor shifts across the selected load stages. Bars show stage-wise medians and IQRs of robust-z-standardised descriptors without percentile-based event selection.

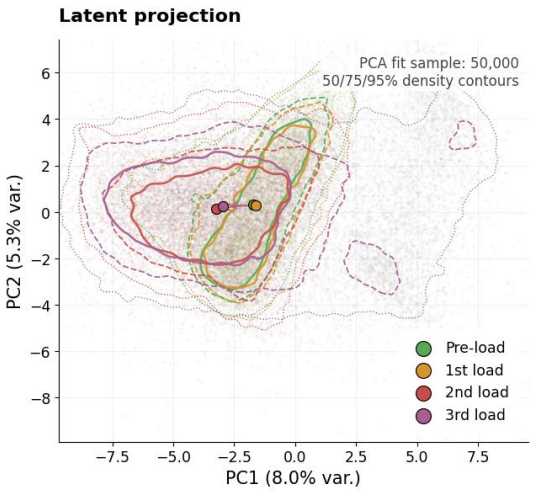

Fig. 2. Latent projection by load stage. PCA contours and centroids summarise stage-wise drift and dispersion in the VAE latent space.

The latent projection showed continuous stage-to-stage drift rather than isolated clusters. The later loading stages broadened in the displayed PCA space, consistent with a more variable latent representation during the high-load and failure sequence.

The framework provides parallel baseline-relative descriptors for offline characterisation of high-frequency structural acoustic signals under varying load in this case study. Operating-point calibration for engineering deployment is left to follow-up work, where multi-specimen baselines will enable systematic sensitivity analysis.

Acknowledgements

This work was carried out within the SBMuW project, Smart Building Systems through Recombination of Materials and Wireless Technologies, at HafenCity University Hamburg (HCU).

References

[1] C. U. Grosse, M. Ohtsu (Eds.), Acoustic Emission Testing: Basics for Research-Applications in Civil Engineering, Springer, Berlin Heidelberg (2008); doi: 10.1007/978-3-540-69972-9.

[2] RILEM Technical Committee, Recommendation of RILEM TC 212-ACD: Acoustic emission and related NDE techniques for crack detection and damage evaluation in concrete: Test method for damage qualification of reinforced concrete beams by acoustic emission, Materials and Structures 43, 1183-1186 (2010); doi: 10.1617/s11527-010-9639-z.

[3] J. F. Piñal-Moctezuma, M. Delgado-Prieto, L. Romeral, An acoustic emission activity detection method based on short-term waveform features: Application to metallic components under uniaxial tensile test, Mechanical Systems and Signal Processing 142, 106753 (2020); doi: 10.1016/j.ymssp.2020.106753.

[4] D. P. Kingma, M. Welling, Auto-Encoding Variational Bayes, Proc. ICLR (2014); arXiv:1312.6114; doi: 10.48550/arXiv.1312.6114.

[5] I. Komorska, A. Puchalski, Condition monitoring using a latent space of variational autoencoder trained only on a healthy machine, Sensors 24, 6825 (2024); doi: 10.3390/s24216825.

DOI 10.5162/eurosensors2026/Tu–SML–03

Field Measurement-Based Analysis of Impulsive Bridge Vibrations for Energy Harvesting

Shucen Du[1], Marcus Illguth[1], Gesa Kapteina[1]
[1] HafenCity University Hamburg, Hamburg, Germany
shucen.du@hcu-hamburg.de

Summary:
This work presents a harvester-oriented analysis of field-measured bridge vibrations. Impulsive events were detected using a dual-threshold envelope method and classified by burst organization. Velocity-weighted spectral analysis was used to identify harvester-relevant low-frequency content. The results show that useful mechanical input is governed more by burst morphology and low-frequency structural response than by the highest acceleration peaks. These findings support the selection of harvester bandwidth, tuning frequency, and impact-response design concepts. This work was conducted within the SBMuW project at HafenCity University Hamburg

Keywords: Field vibration measurement, impulsive events classification, velocity-weighted STFT, energy harvesting, burst morphology

Background, Motivation and Objective

Vibration energy harvesting offers a promising route to power low-power sensing nodes for structural health monitoring, particularly in bridge and transport infrastructure where battery replacement is difficult. Piezoelectric harvesters are attractive for this purpose because they can convert local mechanical vibration into electrical energy and support self-powered monitoring systems [1,2]. However, their performance depends strongly on the actual vibration source, including amplitude, frequency, duration, direction, and event morphology. Therefore, vibration intensity alone is insufficient for harvester design. This work analyzes impulsive vibration events measured at a bridge expansion joint, classifies their time-domain morphology, and extracts harvester-relevant spectral features to support the selection of suitable energy harvesting concepts.

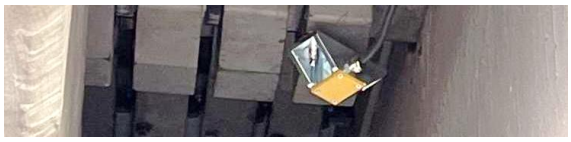

Fig. 1. Kionix KX134-1211 accelerometer module with a ±8 g range and a bandwidth of approximately 8 kHz, mounted on the expansion joint of Köhlbrand Bridge in Hamburg, Germany

Description of the New Method or System

This work proposes a harvester-oriented method for analysing bridge expansion-joint vibrations (Fig.1.), based on one week of daytime measurements with 60 s continuous recordings collected every 30 min. Impulsive events are detected by a dual-threshold envelope method and classified by burst organization using a data-driven characteristic burst time. By combining time-domain morphology with velocity-weighted spectral analysis, the method links real impulsive vibration features to harvester bandwidth, tuning frequency, and response design requirements.

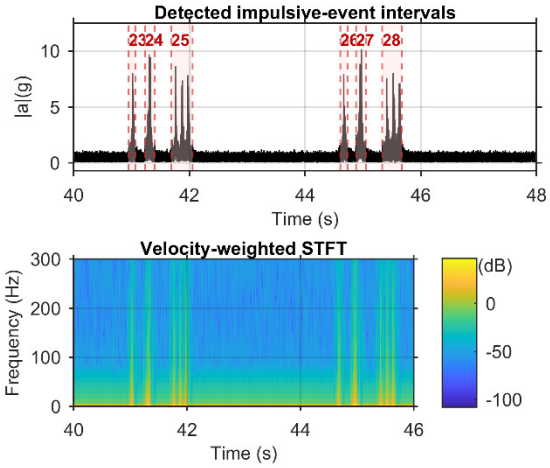

Fig. 2. Fig. 2. Impulsive-event intervals and velocity-weighted STFT. Detected intervals in |a| are compared with the corresponding velocity-weighted time–frequency response.

Results and Discussion

The measured expansion-joint response is dominated by intermittent impulsive events rather than continuous stationary vibration. As shown in Fig. 2, these events appear as short high-amplitude intervals in the resultant acceleration |*a*|, while the velocity-weighted STFT shows that the harvester-relevant response is concentrated in a

lower-frequency band rather than at the highest acceleration peaks. This is consistent with Fig. 5, where Type2 and Type3 events show similar dominant velocity-weighted spectral content despite different burst organizations.

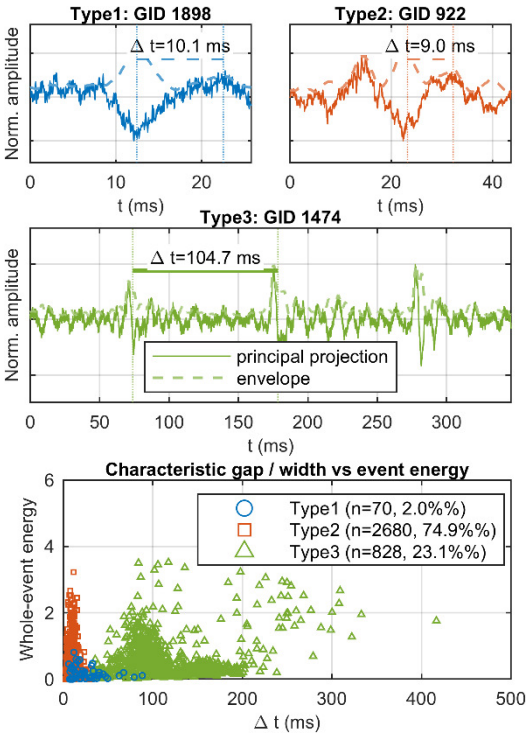

Fig. 3. Time-domain classification of impulsive events. Representative waveforms and the Δt–energy distribution distinguish single-burst, continuous multi-burst, and discrete burst-cluster events.

The time-domain classification in Fig. 3 shows that the events are not uniform single-burst responses. Continuous multi-burst events dominate, while discrete burst clusters form another important group. Together with the envelope similarity shown in Fig. 4, this suggests that laboratory reproduction should use representative event templates, including single bursts, continuous multi-burst events, and discrete burst clusters, rather than only single impacts or steady sinusoidal excitation.

These results provide direct implications for harvester design. The low-frequency velocity-weighted energy concentration supports resonant cantilever harvesters with adjustable proof mass as a basic option. The observed spectral spread and different burst organizations suggest multi-degree-of-freedom systems or cantilever arrays for broader bandwidth. The intermittent impulsive excitation further motivates impact-excited, stopper-assisted, or nonlinear bistable/multi-stable designs, while weak background vibration and event tails may benefit from strain-amplifying structures such as cymbal-type transducers or auxetic substrates. [3,4]

Overall, the expansion-joint vibration should be considered as low-frequency structural response triggered by impulsive events. Suitable harvester concepts should therefore account for event morphology, burst organization, velocity-weighted spectra, and bandwidth.

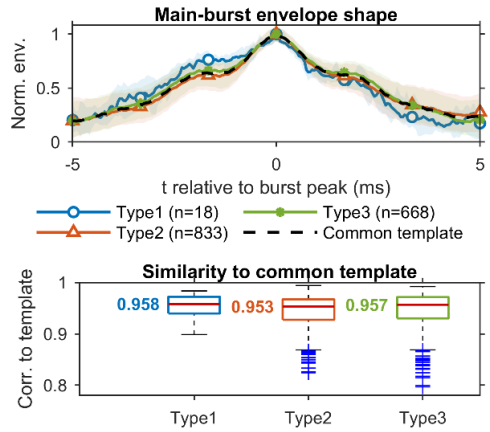

Fig. 4. Burst envelope similarity based on 3000 randomly sampled bursts from all measurement files.

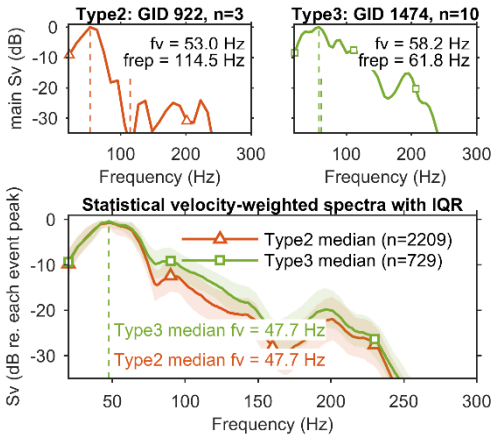

Fig. 5. Peak-centred burst spectra of Type2 and Type3 events. Example spectra show f_v and f_{rep}, while the lower panel summarizes all burst windows identified around main envelope peaks. Both types show a dominant velocity-weighted band around 50 Hz.

References

[1] S. Hassani, U. Dackermann, A systematic review of advanced sensor technologies for non-destructive testing and structural health monitoring, Sensors 23, 2204 (2023); doi: 10.3390/s23042204

[2] L. Castellini, et al., Self-powered wireless structural sensors for long-term monitoring of bridges, Procedia Structural Integrity 62, 824-831 (2024); doi: 10.1016/j.prostr.2024.09.111

[3] L. Shehu, J. H. Yeon, Y. Song, Piezoelectric Energy Harvesting for Civil Engineering Applications, Energies 17, 19 (2024); doi: 10.3390/en17194935

[4] T. Li, P. S. Lee, Piezoelectric Energy harvesting technology: from materials, structures, to applications, Small Structures 3, 2100128 (2022); doi: 10.1002/sstr.202100128

DOI 10.5162/eurosensors2026/Tu–SML–04

Impact of Sensor Selection on Signal Quality of Physiological Monitoring in Demanding Conditions

Aline F.Renz[1], Ekaterina Maevskaia[1], Frederik Bauer[1], Denis Bron[2], Andreas Stier[3], René M. Rossi[1,4], Simon Annaheim[1]
[1] Empa, Laboratory for Biomimetic Membranes and Textiles, 9014 St. Gallen, Switzerland
[2] Swiss Air Forces, Aeromedical Center, Dubendorf, Switzerland
[3] Armasuisse, Bern, Switzerland
[4] Department of Health Sciences and Technology, ETH, Zurich, Switzerland

aline.renz@empa.ch

Summary:
Monitoring vital signs becomes increasingly important beyond stationary medical settings for real world applications. With the rise of wearable sensor systems, monitoring over various time windows and in dynamic environments requires new evaluation of signal quality and suitable sensor selection. In this work we highlight the importance of evaluating the signal quality of wearable electrocardiography (ECG) derived data prior to further interpretation in the highly dynamic and demanding operational environment of fighter jet pilots.

Keywords: physiology, health monitoring, sensor, wearable, signal quality

Background, Motivation and Objective

Measuring physiologically important parameters such as heart rate and heart rate variability are widely adopted across the medical and physical performance field with different sensor interfaces widely available. However, in dynamic and demanding conditions, current sensors often lack the capability for highly accurate measurements beyond the heart rate itself. However, besides heart rate, the heart rate variability provides important insight to assess stress levels and potential fatigue. Here the sensor-skin interface as well as signal robustness in high-motion environments such as fighter jets with various noise sources become important.[1] Short-term recordings often pose an additional limitation in dynamic, real-world monitoring environments. Therefore, high signal quality is required to gain relevant insight for health and performance investigations in high-pressure and demanding tasks pilots face. Evaluating signal quality before interpreting sensor data is therefore a key step for non-stationary measurement conditions where sudden changes have to be identified fast and reliable to ensure pilot safety. In this study we assessed the signal quality of a commercial and a newly developed in-house wearable sensor system [2] monitoring heart activity through textile-based electrodes under extreme conditions such as G-force exposure.

Tab. 1: The signal quality requirements based on Pearson correlation coefficient r for the collected ECG signals. [3]

	r of QRS complex	r of PQRST complex
Class 1	≥ 0.98	≥ 0.98
Class 2	≥ 0.98	< 0.98
Class 3	< 0.98	< 0.98
Class 4	any	any

Methodology

The signal quality was assessed using a previously established signal quality algorithm [3] for ECG measurements. The signal classification in table 1 show the specific requirements for the ECG derived QRS and PQRST complex. The signals were collected from a 2 lead (commercial) and a 1 lead (in-house) wearable sensor system, both equipped with textile-based electrodes placed across the chest area. 30-second time windows pre- and post G-force exposure

were selected for the signal quality analysis. The vital sign monitoring of fighter pilots was conducted using a standardized G-Force exposure protocol (15-second exposures to 4G, 5.5G, and 7G) in a dedicated centrifuge setup (Fig. 1.1).

Results

The signal quality for both systems was assessed by using the collected data and applying the signal quality assessment algorithm and evaluating the performance for each window of interest highlighted in Figure 1.1 in yellow.

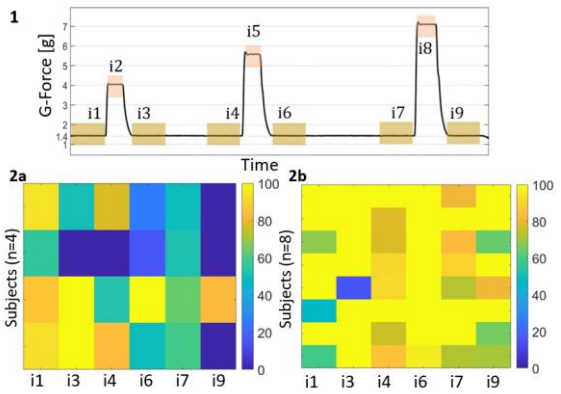

Fig. 1. Overview of G-Force profile (1) with the allocated 30-second time windows pre- and post-exposure (yellow). The corresponding ECG signal quality analysis Heatmap for the commercial (2a) and in house build (2b) wearable sensor system highlighting the percentage of data in class 1 and 2 for each subject and window.

Table 2. highlights a clear difference between the two systems across all classes, with almost equal distribution for the commercial system between class 1 and 2 to class 3 and 4. To further depict the signal quality a heatmap highlighting class 1 and 2 distribution across subjects and windows is mapped in Figure 1.2a. It shows that especially window i9 should be discarded for further heart rate variability interpretation as it would falsify the outcome. The overall low class 1 allocation for the commercial system should be considered when the aim is to investigate heart rate variability measures.

Tab. 2: Overview of Class allocation across subjects and time windows of interest for the commercial (C) and in-house (H) sensor system.

	M_C	SD_C	M_H	SD_H
Class 1	1.2%	5.8%	16.1%	29.8%
Class 2	52.7%	35.6%	72.8%	33.7%
Class 3	26.8%	31.9%	5.7%	14.9%
Class 4	19.3%	25.9%	5.5%	11.5%

Conclusion

As shown in Figure 1. (2a and 2b), the difference varies across subjects; hence, we can conclude that the superior performance of the in-house sensor system is not representative of population differences alone. In addition, the difference in signal quality couldn't be attributed to any specific subjects. This is important to note, as the two systems cannot be worn simultaneously and therefore limit the direct comparison.

Despite the better performance of the in-house solution, 20% of subjects for both sensor systems had to be excluded from the analysis due to contact issues of the sensors. This is mainly attributed to the additional gear worn on top of the sensor as well as body movements prone to errors in loose sensor-to-skin-contact. Although preliminary results, these findings highlight the importance of evaluating signal quality of sensors and potential noise sources prior to measurement interpretation, especially in human health context for dynamic conditions. Overall, the combination of our in-house developed textile-based sensor system with the consecutive signal quality analysis is a suitable tool for dynamic vital sign measures in extreme conditions. In future work a more in-depth investigation assessing the impact of dynamic parameters and environmental noise should be considered including an initial quality control prior to monitoring dedicated protocols to further reduce low signal quality recordings and subject exclusion.

References

[1] BS. Bradke, TA. Miller, B. Everman, Photoplethysmography behind the Ear Outperforms Electrocardiogram for Cardiovascular Monitoring in Dynamic Environments, *Sensors* 21(13), 4543 (2021); doi: 10.3390/s21134543

[2] F. Baty, D. Cvetkovic, M. Boesch, F. Bauer, NRA. Martins, RM. Rossi, O. Schoch, S. Annaheim, MH. Brutsche, Validation of a Textile-Based Wearable Measuring Electrocardiogram and Breathing Frequency for Sleep Apnea Monitoring, *Sensors* 24(19), 6229 (2024); doi: 10.3390/s24196229

[3] NRA. Martins, F. Bauer, F. Baty, M. Boesch, MH. Brutsche, RM. Rossi, S. Annaheim, Introduction to electrocardiogram signal quality assessment and estimated accuracy for textile electrodes Acknowledgements, *Scientific Reports,* 15:41365 (2025); doi: /10.1038/s41598-025-25365-x

DOI 10.5162/eurosensors2026/Tu–SML–05

Multi-Season Field Evaluation of a Temperature-Modulated SMOX Sensor Array for NO_2 and O_3 Monitoring

Felix Schmidt[1], Arne Kobald[1], Pietro Tosato[2], Andrea Gaiardo[2], Udo Weimar[1], Nicolae Barsan[1]
[1] Institute of Physical and Theoretical Chemistry, University of Tuebingen, Tuebingen, Germany,
[2] Sensors and Devices Center, Bruno Kessler Foundation, Via Sommarive 18, Trento, 38123, Italy
nb@ipc.uni-tuebingen.de

Summary:
Semiconducting metal oxide gas sensor arrays, when combined with temperature modulation, have demonstrated promising performance in laboratory tests for outdoor air-quality applications. However, their suitability for long-term field deployment across multiple seasons remains insufficiently validated. In this study, the system was deployed alongside an air-quality reference station over 17 months. The model for predicting NO_2 and O_3 achieved a normalized root-mean-square error of less than 8%, demonstrating robust multi-season outdoor performance.

Keywords: Outdoor Air Quality, SMOX, Temperature Modulation, Gas Sensor, Convolutional Neural Networks

Introduction

Driven by the need for spatially resolved air pollution monitoring in urban areas, low-cost gas-sensing solutions have attracted increasing attention [1], [2]. Temperature-modulated semiconducting metal oxide (SMOX) gas sensor arrays are promising due to their low-cost, small size and high sensitivity. Laboratory studies have demonstrated the ability to quantify mixtures of four major air pollutants (CO, NO_2, O_3, SO_2) within concentration ranges relevant to outdoor air-quality applications [3]. So far, demonstrations in real outdoor air have been limited to ozone prediction during a three-month summer period [3]. Due to cross-sensitivity to environmental factors, long-term and multi-season validation is essential. This study, therefore, presents a 17-month field evaluation of the sensor array for predicting NO_2 and O_3.

Materials and Methods

The custom-built E-Nose module mainly consists of a micropump (mp6, Bartels Mikrotechnik, Germany), responsible for creating a continuous flow of air through the sensor chamber, and a commercially available gas sensor array SGP40 (Sensirion, Switzerland). The gas sensor consists of four subsensors, each made of a different material, that can be temperature-controlled. A temperature-modulation profile ranging from 25 °C to 375 °C was applied in a descending-then-ascending staircase pattern, with a sudden decrease in temperature at the center. Each modulation cycle lasted 190 seconds and was applied simultaneously to all pixels, except for subsensor four, which was limited to a maximum temperature of 300 °C due to material constraints. The E-Nose was deployed in close proximity to the reference station Parco Santa Chiara in Trento, Northern Italy. The station is situated in an urban background environment and provides hourly mean concentrations of ozone (O_3), nitrogen dioxide (NO_2), and sulfur dioxide (SO_2), measured in accordance with European standards. The reference data were obtained via the European Environment Agency's (EEA) publicly accessible download service.

To align the reference data with the sensor modulation frequency, the air-quality measurements were interpolated using cubic splines. A logarithmic transformation was applied to the sensor resistance, while a $log(x+1)$ transformation was applied to the pollutant concentrations to approximate a linear relation between the inputs and targets. The complete dataset was split into blocks of three days and randomly assigned to the train (70%), validation (10%), or test (20%) set. The convolutional neural network (CNN) architecture consists of three convolutional layers followed by two fully connected layers, as previously proposed by Kobald et al.[3]. As input, the model receives the two-dimensional sensor response (190×4) corresponding to a single modulation cycle. The output layer predicts the concentrations of both target pollutants.

Results and Discussion

The outdoor air-quality dataset spans from October 2024 to February 2026 and comprises approximately 12,000 hourly mean values. Since

the maximum concentration of SO_2 is below 5 ppb and therefore well under the threshold of 38 ppb for “Very good” air-quality, this pollutant was excluded from further analysis. The concentration distributions of O_3 and NO_2 are depicted in Figure 1 and exhibit pronounced seasonal variability. Nitrogen dioxide concentrations are higher during the colder months (October-March) and mostly remain within the “very good” levels in summer. A maximum of 53 ppb is reached, with a single outlier of 112 ppb likely attributable to a local emission event. Even more dependent on seasonal changes is the ozone concentration: The median concentration rise by approximately one order of magnitude from winter (3.6 ppb) to summer (33.6 ppb). During the warmer months (April-September), approximately 19% of hourly values fall into the “medium” air-quality category or worse, with peak ozone concentration reaching up to 101 ppb.

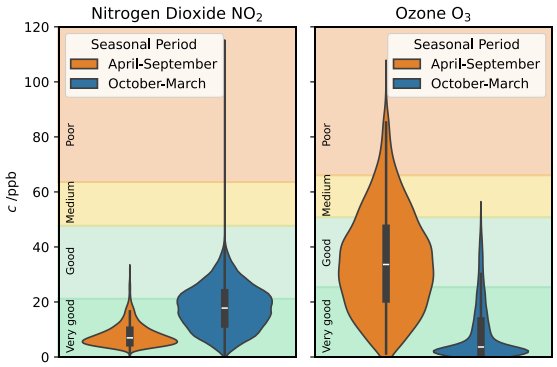

Figure 1: Distribution of NO_2 and O_3 concentration for the summer and winter seasons. In the background is the air quality index as defined by the EEA.

The sensor dataset acquired over the same time frame comprises approximately 200,000 modulation cycles, corresponding to 88% of the expected data. The predicted and reference concentrations for the test dataset are shown in Figure 2. At higher concentration levels, the majority of predictions fall within the 25% relative error margin indicated by the dashed black lines. In contrast, predictions at low concentrations (NO_2: < 20 ppb, O_3: < 40 ppb) exhibit substantial deviation. This is further reflected in the increased mean relative prediction errors of 17.5% for NO_2 and 28.8% for O_3, as reported in Table 1. However, as this concentration regime corresponds predominantly to the “good” or “very good” air-quality index, the deviations may still be acceptable for applications focusing on elevated pollution levels. Further, prediction outliers often appear as drifting patterns and occur in temporally adjacent clusters. The root mean squared error (RMSE) was normalized by the concentration range, enabling comparison of predictive performance between the two pollutants. Overall, the model performs similarly well, but slightly better for ozone prediction, with a normalized RMSE of 6% compared to 7.5% for NO_2. The obtained prediction errors are comparable to those reported by Kobald et al. [3] for experiments conducted using a gas mixing system, with normalized RMSEs of 7.3% for O_3 and 6.3 % for NO_2.

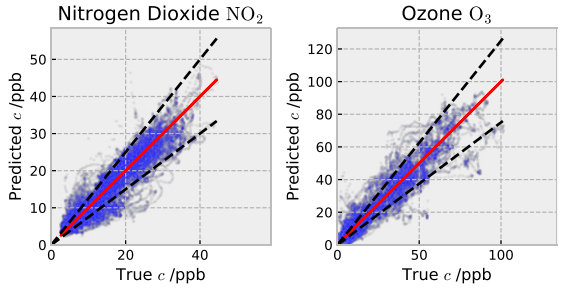

Figure 2: Prediction results based on the test dataset consisting of over 39,000 predictions from 93 days. The red line indicates the perfect prediction and the dashed black lines the 25% relative error margin.

Tab. 1: Prediction error for the test dataset.

Error Metric	NO_2	O_3
Mean Relative Error / %	17.5	28.8
RMSE / ppb	3.2	6.0
Normalized RMSE / %	7.5	6.0
Mean Absolute Error / ppb	2.3	3.3

Future work in this ongoing field evaluation should include external validation using a test set derived from the final portion of the dataset. Additional improvements in predictive performance should be evaluated by incorporating environmental variables (e.g., humidity and temperature) as inputs to the model. Overall, this study demonstrated the feasibility of temperature-modulated SMOX sensor arrays for real-world outdoor air-quality monitoring of NO_2 and O_3.

References

[1] F. Concas *et al.*, “Low-Cost Outdoor Air Quality Monitoring and Sensor Calibration: A Survey and Critical Analysis,” *ACM Trans Sen Netw*, vol. 17, no. 2, p. 20:1-20:44, May 2021, doi: 10.1145/3446005.

[2] I. Gryech, C. Asaad, M. Ghogho, and A. Kobbane, “Applications of machine learning & Internet of Things for outdoor air pollution monitoring and prediction: A systematic literature review,” *Eng. Appl. Artif. Intell.*, vol. 137, p. 109182, Nov. 2024, doi: 10.1016/j.engappai.2024.109182.

[3] A. Kobald, U. Weimar, and N. Bârsan, “Towards understanding temperature modulated SMOX gas sensor arrays for outdoor air quality applications,” *Sens. Actuators B Chem.*, vol. 440, p. 137879, Oct. 2025, doi: 10.1016/j.snb.2025.137879.

DOI 10.5162/eurosensors2026/Tu–SML–06

Generation and Real-Time Detection of High-Fidelity Odour Plumes

Amirreza Gholivand[1], Anantha Padmanabhan[1], Florian Paul Schmidt[2], Tobias Ackels[1]
[1] University of Bonn, Faculty of Medicine, Sensory Dynamics and Behaviour Laboratory, Institute of Experimental Epileptology and Cognition Research, Venusberg-Campus 1, 53127 Bonn, Germany,
[2] Bielefeld University, Faculty of Biology, Biological Cybernetics, Universitätsstr. 25, 33615 Bielefeld, Germany
tobias.ackels@ukbonn.de

Summary:
Understanding how animals navigate their environment requires experimental tools capable of generating plumes and detecting odour fluctuations. We present a unified framework comprising the temporal Odour Delivery Device (tODD) and the detection method with compact passive chemical sensors coupled with WaveNet-based signal recovery architecture. The delivery system achieves rapid onset latencies and decay times to precisely reproduce naturalistic plumes. In combination with the sensor system, this creates a high-dynamics framework suitable for use in behaving animals.

Keywords: Signal reconstruction, Odour delivery, Deep learning model, MOX, Sensor dynamic

Background, Motivation and Objective

Olfactory navigation is crucial for survival-related behaviours in animals. In natural environments, odours are transported in turbulent plumes, generating highly intermittent and rapidly fluctuating signals rather than smooth gradients. These fluctuations contain rich temporal information about the structure and origin of odour sources. Reproducing these naturalistic stimuli in a controlled lab environment remains a significant challenge. Capturing their real-time dynamics in freely behaving animals adds further complexity.

Unlike visual or auditory systems, chemical stimuli are constrained by fluid dynamics, requiring vaporization, transport, and clearance that introduce temporal delays and concentration variability [1-3]. Standard olfactometers often lack the millisecond precision required to reproduce the rapid "whiff" and "blank" sequences of turbulent plumes, typically relying on slow onset/offset dynamics or steady state concentrations [2]. Furthermore, recording these dynamics in combination with behaving animals presents a parallel bottleneck. While Photoionisation Detectors (PID) offer high sensitivity, their size and active suction mechanisms distort local flow streams, making them unsuitable for head-mounted applications [4]. Conversely, miniature Metal Oxide Chemical Sensors (MOX) are compact but suffer from slow response times that filter out the high-frequency fluctuations that might aid navigation. To bridge this gap between stimulus generation and sensory recording, a unified system capable of both delivering and resolving fast temporal odour dynamics is required.

To overcome these dual limitations, we present a comprehensive framework comprising the temporal Odour Delivery Device (tODD) and a compact detection strategy combined with a robust signal processing pipeline based on the WaveNet architecture.

Description of the New Method or System

Odour Delivery Device

To overcome these limitations, we developed tODD, designed specifically to replicate the fast temporal dynamics of natural odour plumes. Figure 1 shows the assembled setup and a schematic of the device. This allows the precise and reproducible generation of fast odour dynamics, thereby providing a tool to capture the complex structure of natural odour plumes (Fig. 1d).

Sensing and Reconstruction

To overcome the constraints of conventional detection techniques, we utilize a miniature Micro Chemical Sensor (MiCS). Its compact size and low weight make it ideal for head-mounted implantation on freely behaving mice. Crucially, as a passive sensor, MiCS does not distort local plume structures or flow streamlines. However, MiCS inherently suffers from slower response dynamics compared to reference detectors. To address this latency, we established a WaveNet-based deep learning

architecture. This model learns the non-linear mapping between raw, low-bandwidth MiCS responses and high-fidelity PID references. By effectively deconvolving sensor inertia, our method restores the temporal resolution lost to hardware constraints, creating a virtual "high-dynamics" sensor. Together, tODD and the WaveNet decoder form a closed-loop experimental platform that synchronizes high-precision stimulus delivery with real-time, high-fidelity plume reconstruction.

Results

Characterization of tODD using 100 ms square pulses revealed an average onset latency of 5.6±0.1 ms, a rise time of 8.5±0.6 ms, and a decay time of 43±3.7 ms for Ethyl Butyrate at a concentration of 10% (Fig. 1c). These metrics demonstrate the system's capability of fast odour pulse generation, satisfying the requirement for naturalistic plume reproduction. To verify the high-fidelity generation of complex stimuli, we compared device output against empirical plume recordings for two distinct odorants: Ethyl Butyrate and Limonene. As shown in Fig. 1d, tODD reliably reproduced rapid concentration fluctuations. The coefficient of variation across five repeated trials remained below 6%, confirming robust stimulus stability essential for behavioural studies.

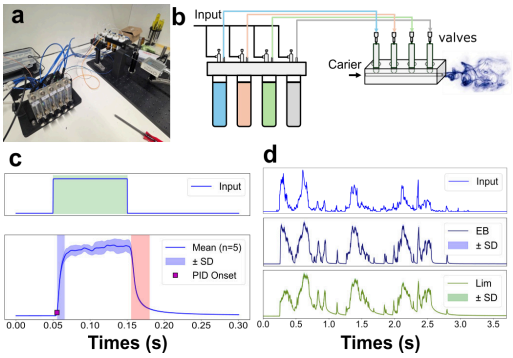

Fig. 1. Temporal Odour Delivery Device. (a) Photo of the assembled setup, (b) schematic design of the tODD, where pressurized air is guided through odour bottles towards high speed valves to generate odour plumes. (c) 100 ms pulse command (top panel) with corresponding tODD odour output (bottom panel). The blue area represents the 90% rise time and the red area represents the 10% decay of the signal. (d) Exemplary plumes. Input signal (top) and reproduced odour signals using Ethyl Butyrate (EB; middle) and Limonene (Lim; bottom). Solid line: average of 5 different repeats, shaded area: SD. All plots are normalized.

Finally, we evaluated the deep learning model's ability to recover high-frequency dynamics from MiCS recorded signals. The model successfully reconstructed transient features with a correlation coefficient of R^2 = 0.92±0.05 against PID ground truth, effectively resolving "whiff" events that were otherwise smoothed out by the raw sensor data (Fig. 2c). The detection system was systematically evaluated across varying odorant concentrations and distances within the test arena. Results demonstrate that the sensor array reliably captures low odorant concentrations at distal recording positions (Fig. 2b), highlighting the system's sensitivity and spatial range. This integrated detection platform enables real-time odorant concentration monitoring, with potential applications in olfactory navigation paradigms and behavioural studies. Furthermore, the incorporation of a deep learning model in principle could facilitate source discrimination, allowing the decomposition and identification of individual odour sources within complex, mixed-signal environments.

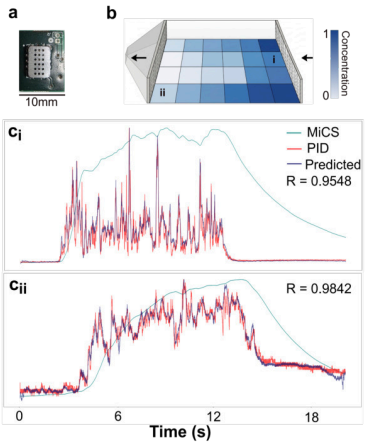

Fig. 2. MiCS (a) Photo of the MiCS mounted on a PCB. (b) Schematic representation of the experimental arena partitioned into 24 spatial grids, illustrating the distribution of odorant concentration across grid positions. (c) Comparative traces of PID (red) and MiCS (teal) signals recorded at two arena positions ((i) and (ii); see Fig. 2b), alongside the model-predicted signal (blue).

References

[1] C. Doyle, J. Wang, E. Galliano, C. Guillaume, A low-cost and open-source olfactometer to precisely deliver single odours and odour mixtures, (2026) 2025.09.11.675563. https://doi.org/10.1101/2025.09.11.675563.

[2] T. Ackels, A. Erskine, D. Dasgupta, A.C. Marin, T.P.A. Warner, S. Tootoonian, I. Fukunaga, J.J. Harris, A.T. Schaefer, Fast odour dynamics are encoded in the olfactory system and guide behaviour, Nature 593 (2021) 558–563. https://doi.org/10.1038/s41586-021-03514-2.

[3] S. Gorur-Shandilya, C. Martelli, M. Demir, T. Emonet, Controlling and measuring dynamic odorant stimuli in the laboratory, J Exp Biol 222 (2019) jeb207787. https://doi.org/10.1242/jeb.207787.

[4] A.C. True, J.P. Crimaldi, Distortion of passive scalar structure during suction-based plume sampling, Sensors and Actuators B: Chemical 367 (2022) 132018. https://doi.org/10.1016/j.snb.2022.132018.

DOI 10.5162/eurosensors2026/Tu–SML–07

Empowering Self-Powered Sensors via Agentic RAG: A Domain-Specific LLM Framework for Building Physics Retrieval

(Sobhan Saadatnasab)[1],
[1] *(Sobhan Saadatnasab), Email: (ssaadatnasab@connect.ust.hk)*

ABSTRACT

Wireless sensor networks deployed in built environments face a critical bottleneck: reliable in-situ powering. Energy harvesting, whether from thermal gradients, ambient airflow, or mechanical vibrations—demands precise, context-aware calculations of building physics parameters such as heat flux, air velocity, temperature differentials, and fluid properties. However, general-purpose Large Language Models lack the domain-specific reasoning required to retrieve and compute these engineering metrics from technical literature, codes, and equipment schedules, as they consistently fail to accurately interpret structured tables, complex mathematical formulas, and chart-based empirical data.

To bridge this gap, we present a domain-specific LLM framework powered by an advanced multimodal Agentic Retrieval-Augmented Generation (RAG) pipeline. Our framework implements an end-to-end pipeline that converts heterogeneous technical literature into a high-quality Markdown corpus and leverages vision-language extraction to index information from figures, schematics, and images.

A core innovation lies in its agentic architecture, which features autonomous planning and a dedicated pathway that executes Python code within a secure sandbox. This ensures strict mathematical precision for engineering calculations—a necessity for tasks such as power density estimation, conversion efficiency analysis, and storage sizing in energy-constrained sensors.

We rigorously validate our approach using a comprehensive benchmark of 1,487 technical questions spanning 12 core building science domains (heat transfer, HVAC, thermodynamics, fluid mechanics, and automation) across five question types and three difficulty levels. Our evaluation of 15 state-of-the-art LLMs reveals a base accuracy of only 58.7%, confirming the inadequacy of off-the-shelf models. To address this, we implement a hybrid retrieval stack combining BM25 sparse retrieval, dense MiniLM embeddings (fused at 0.4/0.6), MMR diversification, and a bge-reranker-v2-m3 cross-encoder. Extending this with an Agentic RAG workflow yields a +4% overall accuracy boost and a remarkable +8.2% improvement on hard questions, with specific models like Claude Opus 4.6 gaining up to +22.5 points over their base versions.

By integrating these capabilities, our approach delivers a robust, high-fidelity reasoning and retrieval tool specifically designed for specialized engineering domains. This framework empowers engineers to rapidly query, calculate, and verify energy-harvesting potential from building data, significantly accelerating the design and optimization of self-powered, maintenance-free wireless sensing systems.